

Academic Press  
Library in Mobile  
and Wireless  
Communications

# Academic Press Library in Mobile and Wireless Communications

## Transmission Techniques for Digital Communications

Edited by

**Sarah Kate Wilson**

Santa Clara University, Santa Clara, CA, USA

**Stephen Wilson**

University of Virginia, Charlottesville, VA, USA

**Ezio Biglieri**

Universitat Pompeu Fabra, Barcelona, Spain,  
and University of California, Los Angeles  
Los Angeles CA, USA



AMSTERDAM • BOSTON • HEIDELBERG • LONDON  
NEW YORK • OXFORD • PARIS • SAN DIEGO  
SAN FRANCISCO • SINGAPORE • SYDNEY • TOKYO

Academic Press is an imprint of Elsevier



Academic Press is an imprint of Elsevier  
125 London Wall, London EC2Y 5AS, United Kingdom  
525 B Street, Suite 1800, San Diego, CA 92101-4495, United States  
50 Hampshire Street, 5th Floor, Cambridge, MA 02139, United States  
The Boulevard, Langford Lane, Kidlington, Oxford OX5 1GB, United Kingdom

© 2016 Elsevier Ltd. All rights reserved.

No part of this publication may be reproduced or transmitted in any form or by any means, electronic or mechanical, including photocopying, recording, or any information storage and retrieval system, without permission in writing from the publisher. Details on how to seek permission, further information about the Publisher's permissions policies and our arrangements with organizations such as the Copyright Clearance Center and the Copyright Licensing Agency, can be found at our website: [www.elsevier.com/permissions](http://www.elsevier.com/permissions).

This book and the individual contributions contained in it are protected under copyright by the Publisher (other than as may be noted herein).

### Notices

Knowledge and best practice in this field are constantly changing. As new research and experience broaden our understanding, changes in research methods, professional practices, or medical treatment may become necessary.

Practitioners and researchers must always rely on their own experience and knowledge in evaluating and using any information, methods, compounds, or experiments described herein. In using such information or methods they should be mindful of their own safety and the safety of others, including parties for whom they have a professional responsibility.

To the fullest extent of the law, neither the Publisher nor the authors, contributors, or editors, assume any liability for any injury and/or damage to persons or property as a matter of products liability, negligence or otherwise, or from any use or operation of any methods, products, instructions, or ideas contained in the material herein.

### Library of Congress Cataloging-in-Publication Data

A catalog record for this book is available from the Library of Congress

### British Library Cataloguing-in-Publication Data

A catalogue record for this book is available from the British Library

ISBN: 978-0-12-398281-0

For information on all Academic Press publications  
visit our website at <https://www.elsevier.com/>



*Publisher:* Joe Hayton

*Acquisition Editor:* Tim Pitts

*Editorial Project Manager:* Charlotte Kent

*Production Project Manager:* Melissa Read

*Cover Designer:* Greg Harris

Typeset by SPi Global, India

*To Paul*

SKW

*To the memory of CES*

EB

# Contributors

**S. Ahmadi**

Xilinx Inc., San Jose, CA, United States

**J. Barry**

Georgia Institute of Technology, Atlanta, GA, United States

**L.T. Berger**

University of British Columbia, Vancouver, BC, Canada;  
BreezeSolve, Paterna (Valencia), Spain

**H.L. Bertoni**

NYU Tandon School of Engineering, Brooklyn, NY, United States

**M. Brandt-Pearce**

University of Virginia, Charlottesville, VA, United States

**O. A. Dobre**

Memorial University, St. John's, NL, Canada

**M. Erez**

University of Texas at Austin, Austin, TX, United States

**A. Eryilmaz**

Ohio State University, Columbus, OH, United States

**M. Fanaei**

Minnesota State University at Mankato, Mankato, MN, United States

**A. Gatherer**

Huawei United States, Plano, TX, United States

**S. Gorshe**

PMC-Sierra, Portland, OR, United States

**E. Hossain**

University of Manitoba, Winnipeg, MB, Canada

**L. Lampe**

University of British Columbia, Vancouver, BC, Canada

**K.G. Madushan Thilina**

University of Manitoba, Winnipeg, MB, Canada

**S.L. Miller**

Texas A&M University, College Station, TX, United States

**M. Moeneclaey**

Ghent University, Ghent, Belgium

**N. Noels**

Ghent University, Ghent, Belgium

**M. Noshad**

University of Virginia, Charlottesville, VA, United States

**C.B. Papadias**

Athens Information Technology, Athens, Greece

**M. Rice**

Brigham Young University, Provo, UT, United States

**E.G. Ström**

Chalmers University of Technology, Gothenburg, Sweden

**S.A. Torrico**

Comsearch, Ashburn, VA, United States

**M.C. Valenti**

West Virginia University, Morgantown, WV, United States

**S. Weinstein**

Communication Theory and Technology Consulting, NY, United States

**S.K. Wilson**

Santa Clara University, Santa Clara, CA, United States

**S.G. Wilson**

University of Virginia, Charlottesville, VA, United States

**H. Wymeersch**

Chalmers University of Technology, Gothenburg, Sweden

**T. Xie**

SanDisk Corporation, Milpitas, CA, United States

**H. Zhu**

University of Texas at Austin, Austin, TX, United States

# Introduction

Digital transmission is constantly evolving. Yet many fundamentals within the field of digital transmission remain constant. This book serves as an introduction both to digital transmission theory and to current applications.

Since early times people have used digital transmission as a way to send important messages: from signaling with beacons of light to today's cellular systems and the Internet. Digital transmission is a way to send messages over various media with the minimal amount of confusion at the receiver. The earliest electronic communications system, the telegraph, was digital using Morse code. Using digital communications with the early telegraph was necessary to avoid the problem of electronic noise and its effect on a low-power signal. It is much easier to distinguish between a dot and a dash and then to reconstruct alphanumeric messages, than it is an analog voice message. Moreover, digital transmission easily admits encryption for security and message routing in networks. Twentieth-century analog communications is in some ways an anomaly in the history of communications and has mostly, although not entirely, been replaced by digital transmission.

This book provides both a foundation in modern digital communications as well as an exploration of current digital transmission issues. [Chapters 1–5](#) present the basics of digital communications theory and would represent material covered in a graduate course in digital communications. [Chapters 6–10](#) delve deeper into the field of communications by exploring particular types of digital communications, (spread-spectrum, single-carrier, multicarrier) as well as required receiver methods such as synchronization and equalization. [Chapters 11–16](#) focus on more specific applications of communications, for example, power line and optical communications. This book should serve both as an introduction and reference to the field of digital transmission.

[Chapter 1](#) by Stephen Weinstein introduces the history and general issues associated with digital information. It provides context for the rest of the book and the field in general. [Chapter 2](#) by Stephen Wilson and Tingjun Xie outlines the principle of baseband (low-frequency) representation of passband (assigned carrier frequency) modulation in digital communications. Michael Rice introduces single-carrier modulation in [Chapter 3](#); this is a basis for all other types of communications and provides a fundamental lesson in how to send digital signals. [Chapter 4](#) by Erik Strom explains how to optimally demodulate/decode these signals in an additive white Gaussian noise environment. [Chapter 5](#) by Matthew Valenti and Mohammed Fanaei explains how coding and modulation relate. Note that a more complete book on error control coding can be found in our sister book, *Error Control Coding*.

[Chapter 6](#) by Henry Berton and Saul Torrico describes the propagation issues and challenges associated with the radio channel. This leads to two chapters on how to resolve issues due to channel conditions: [Chapter 7](#) by Marc Moeneclaey and Nele Noels, and [Chapter 8](#) by John Barry. [Chapter 7](#) focuses on how to synchronize a digital transmission signal while [Chapter 8](#) focuses on how to compensate for

frequency-selective channels with equalization. [Chapter 9](#) by Sarah Kate Wilson and Octavia Dobre focuses on multicarrier modulation, a technique that simplifies the equalization that is required for single-carrier signals found in [Chapter 8](#). [Chapter 10](#) by Scott Miller introduces spread-spectrum modulation, a technique developed in military communication, but now used in the third-generation cellular system.

[Chapter 11](#) on MIMO by Constantinos Papadias expands on how to increase the efficiency of digital communications through the use of multiple antennas at the transmitter and/or the receiver. [Chapter 12](#) by Henk Wymeersch and Attila Eryilmaz discusses how to accommodate several users in communications system.

[Chapter 13](#), Cognitive Radio and Spectrum Sensing, by Ekram Hossain shows how we can further increase the number of users in a communications system through smart sensing and use of the radio spectrum. [Chapters 14](#) and [15](#), by Steven Gorshe and Ahmad Sassani respectively, are devoted to communications standards. [Chapter 14](#) focuses on wireline standards while [Chapter 15](#) focuses on wireless standards. [Chapters 16](#) and [17](#) focus on power line transmission and optical transmission. In [Chapter 16](#) Maite Brandt-Pearce and Mohammad Noshad focus on the issues associated with digital transmission in an optical channel. In [Chapter 17](#), Lutz Lampe and Lars Berger discuss the issues associated with another challenging channel, the power line. Finally, Alan Gatherer addresses issues associated with building transceivers in a cellular system in [Chapter 18](#).

# Introduction to digital transmission

# 1

**S. Weinstein**

*Communication Theory and Technology Consulting, NY, United States*

## CHAPTER OUTLINE

<b>1.1 Why Digital?</b> .....	2
<b>1.2 Historical Perspective on Digital Transmission</b> .....	3
1.2.1 The Sampling Theorem: Transitioning Media from Analog to Digital ....	4
1.2.2 Pulse Code Modulation .....	6
1.2.3 Digital Transmission Hierarchy and SONET .....	7
<b>1.3 Microwave, Optical, and Satellite Transmission Systems</b> .....	11
1.3.1 Optical Transmission in the Backbone Network .....	12
1.3.2 Communication Satellites for Backbone Transmission and Broadcasting	14
<b>1.4 Evolutionary Steps in Digital Access Networkings</b> .....	16
1.4.1 Voice Channel Modems .....	17
1.4.2 ISDN and DSL .....	21
1.4.3 Cable Data Networks .....	24
1.4.4 Passive Optical Network .....	26
<b>1.5 Origins of Data Communication Networks and Voice-Data Integration</b> .....	28
1.5.1 Packet Transmission .....	28
1.5.2 ATM and B-ISDN .....	31
1.5.3 Contention Systems: AlohaNet and Ethernet .....	33
<b>1.6 Wireless Transmission Systems</b> .....	35
1.6.1 Cellular Mobile: 1G to 4G.....	36
1.6.2 5G Cellular Mobile .....	40
1.6.3 Wireless Transmission in the Cloud .....	42
1.6.4 IEEE 802.11 Wireless LANs and Some Alternatives .....	43
<b>1.7 All the Rest</b> .....	45
<b>References</b> .....	46

This first chapter is a broad introduction to digital transmission that introduces basic concepts and techniques and their application in major wired and wireless networks. It leaves detailed development to the later chapters. Topics in this chapter cover backbone and access technologies and networks, the rise of data communications

and Internet technologies, and the wireless networks that are the current focus of development. The following concise guide may help to tie the sections together.

---

## 1.1 WHY DIGITAL?

There are still a few exceptions, notably analog amplitude modulation (AM) and frequency modulation (FM) radio broadcasting that have surprised us all with their longevity, but digital transmission is dominant for all media in wired and wireless communications, terrestrial and satellite television, and everything that comes through the Internet. Consumers today do not expect anything else and the phrase “analog communication” is rarely heard. Before embarking on the weightier technical content of this book, which specifically addresses digital transmission, it helps our understanding and appreciation of these digital technologies to look back at the motivations, the technical basics, and the social and economic pressures to work with digital representations and transmission of information, particularly voice and video information. We recognize that digital transmission has a very long history and in fact, for long-distance transmission, was used millennia before long-distance analog transmission. The demand for high-quality long-distance transmission was, in fact, one of the main motivators for digitizing analog voice in modern times.

But let us begin thousands of years ago, when people began using drumbeats and smoke signals to convey simple messages. It is likely, although we cannot know for sure, that information was not sent as continuous variations in smoke or drumbeat volume but rather as the presence or absence of signal or as a coarse quantization of volume such as “lots of smoke” versus “not much smoke” or “no smoke.” This reflected, in part, the reality that humans had not yet created signal analogs of information waveforms such as speech, although they could have conceived of a signal analog of a nearly continuously varied parameter such as, for example, the amount of food on hand. But more relevant to contemporary digital communications, this coarse quantization was de facto recognition of the noise immunity advantage of digital signaling. Continuous variations of smoke or sound (or any other detectable-from-a-distance representation) would be difficult to do, degraded by both human error and environmental influences such as wind. Quantized, easily differentiated digital signals could, in contrast, be correctly received and interpreted almost all the time despite (usually) small perturbations caused by these impairing factors. This was especially important for information relayed over several hops, where the effects of noise might add and cause even more perturbation of continuous analog signals but would, with an appropriate digital quantization, have only a small probability of causing a detection error for the digital signal. Similarly for information storage, digital representation of information avoids distortions due to the degradation of the medium used for information storage, most obvious in phonograph records. The information will very likely be as accurate the 1000th time it is read as the first. These properties are as true for electrical communication as they were for smoke signals, and with current achievements in very large-scale integration (VLSI) of semiconductor memories, we have an additional advantage of very large digital memories in very small volumes.

More sophisticated digital transmission systems also evolved quite early. In Greece in 350 BC, Aeneas documented a sight-based relay network in which the information data were represented by different water levels in a visible container [1]. Without telescopes, the water levels would have to be quantized into just a few values readable from a distance. This system had a control mechanism in which the raising of torches signaled the beginning and end of transmission of data, a separate channel demonstrating that today's software defined network (SDN) is not the first example of a system separating control and data planes.

Jumping forward to modern times and coding of analog information waveforms such as speech and video into digital data streams for transmission and/or storage, we recognize that the absence of analog noise perturbation enjoyed by digital transmission does not mean the absence of any noise perturbation. Quantization noise, the difference between a sample value of an analog waveform and its quantized representation, is an aspect of the digital coding process explained below, and the design of a transmission or storage system requires selection of parameters that result in an acceptable quantization noise level. Not surprisingly, lower quantization noise requires higher transmission rate with its attendant cost in bandwidth and other transmission and storage resources.

Another motivation for going digital is the relative ease of implementing coding for secrecy, authentication, and error detection and correction. Secrecy, meaning protection from interception and reading by a third party, always vital in espionage and war, is more important than ever in a global business environment in which hacking into corporate databases has become a common crime. Authentication, proof that a message comes from the claimed source and not a "spoofers," also has great importance to the value and safety of communications. Coding for error detection and correction covers a broad range of techniques that, at the cost of adding a little redundancy to a digital data stream, make it possible to learn that an error has occurred in transmission and, with a little more redundancy, to correct at least occasional errors.

Finally, digital transmission is appropriate and convenient for very low rate channels, initially long wires in the early 19th century and more recently radio channels linking spacecraft with Earth, characterized by a low ratio of signal to noise (SNR) and interference. An information object, such as a speech segment, photograph, or video clip, can be digitally "compressed," meaning removal of redundancy that can consume transmission resources without adding much if any information, and then transmitted at any feasible speed to be reconstructed later and, for voice and video, displayed at a "real time" rate. Of course, there are delay penalties for this processing, and compromises must be made among the available tradeoffs.

---

## 1.2 HISTORICAL PERSPECTIVE ON DIGITAL TRANSMISSION

Electrical telegraphy was one of the greatest technical innovations of the 19th century. Although the poorly understood and generally uncompensated transmission characteristics of a long pair of wires forced very low transmission rates, these rates were sufficient for transmission of the most urgent news and personal

A ··	B ....	C --- ·	D ---	0 -----	1 -----
E ·	F ....	G --- ·	H ....	2 -----	3 -----
I ··	J -----	K --- ·	L --- ·	4 -----	5 -----
M --	N --	O ---	P --- ·	6 -----	7 -----
Q ---	R --- ·	S --- ·	T -	8 -----	9 -----
U ---	V --- ·	W --- ·	X --- ·		
Y --- ·	Z --- ·				

FIG. 1.1

Morse code for basic letters and numbers (there are additional codes for other characters and punctuation).

communications. Samuel Morse devised, in 1838, a variable-length coding from one digital representation (letters and numbers) to another digital representation (brief presses of the telegraph key called “dots” and twice as long presses called “dashes”) that achieved a remarkable data compression of the information stream. In Morse’s coding scheme, frequently used letters received the shortest representations such as one dot for “e,” two dots for “i,” and one dash for “t,” while the less frequently used (in those days) numbers are represented by various combinations of five dots and dashes (Fig. 1.1).

Morse code has the drawback of not being prefix free; that is, the representations for some letters could be misinterpreted as the beginnings of other letters, such as “e” (one dot) being a prefix of “a” (two dots), or “s” (three dots). Telegraphers had to leave a considerable space between letters to avoid ambiguous reception. Huffman coding [2], the best variable-length coding that systematically assigns the number of bits as the log of the inverse of the probability of occurrence, is prefix free, as are all fixed-length codes including the popular ASCII. Fixed-length codes do not generate any compression of alphabetic letters.

Alexander Graham Bell, remembered today principally for the analog telephone, was in fact funded to develop a multitone digital transmission system. The objective was to multiply the capacity of telegraph (ie, digital) transmission lines by simultaneously communicating using tones of different frequencies. Although Bell retreated to his family’s farm in Canada to escape from this work and focus on the telephone, he developed and patented a workable two-tone apparatus, shown in Fig. 1.2. This accomplishment, in heated competition with other inventors just as with the telephone, received US Patent 174465 and was an early example of digital frequency-division multiplexing (FDM). Bell’s telephone company later was desperate to develop analog FDM for analog voice traffic, which was not really effective until application of vacuum tubes to provide amplification at relay points [3].

### 1.2.1 THE SAMPLING THEOREM: TRANSITIONING MEDIA FROM ANALOG TO DIGITAL

Digital transmission of voice traffic had to wait many more decades, requiring first the discovery of the “sampling theorem.” This was a mathematical demonstration, often credited to Harry Nyquist, that an analog (continuous) waveform can be exactly

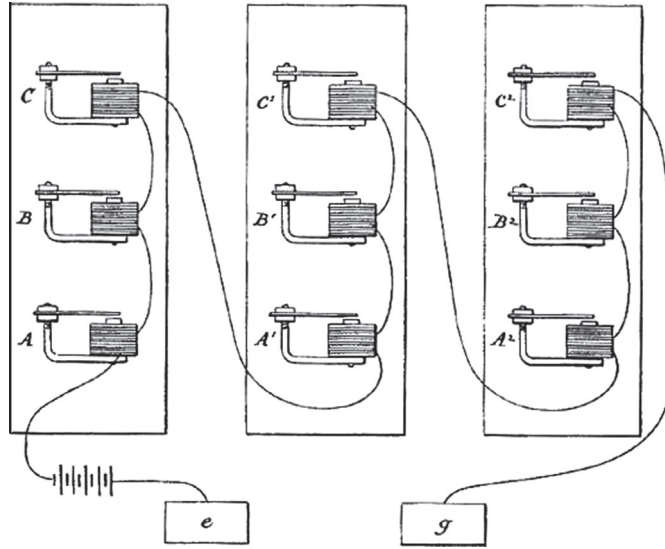


FIG. 1.2

Diagram in US Patent 174465 for Alexander Graham Bell's "harmonic telegraph" in which armatures vibrating at different frequencies may be modulated to produce noninterfering telegraph signals. Similar tuned devices respond as receivers.

reconstructed from just a set of *samples* taken at a rate equal to (at least) twice the highest frequency component of the analog waveform. Credit is also due to Vladimir Kotelnikov, E.T. Whittaker, and others working in this area in the late 1920s and early 1930s. This powerful *sampling theorem* [4] is expressed and proved as follows:

**Theorem 1.1.** *If a continuous time function  $x(t)$  is bandlimited to frequencies in the range  $-W < f < W$  Hz, then*

$$x(t) = (1/2W) \sum_n x(n/2W) [\sin 2\pi W(t - n/2W)/2\pi W(t - n/2W)], \quad (1.1)$$

where the samples of  $x(t)$  are taken at time intervals of  $1/2W$ .

*Proof.* Since the Fourier transform  $X(f)$  of  $x(t)$  is limited to  $|f| < W$ , we can represent it (in the frequency domain) by a Fourier series for a periodic function, with period  $2W$ , that equals  $X(f)$  in the interval  $-W < f < W$ :

$$X(f) = \left\{ \begin{array}{ll} \sum_n c_n \exp[-j2\pi nf/2W], & |f| \leq W \\ 0 & \text{elsewhere} \end{array} \right\} = \sum_n c_n \exp[-j2\pi nf/2W] U_W(f), \quad (1.2)$$

where  $U_W(f)$  equals 1 for  $|f| < W$  and is 0 otherwise, and the  $\{c_n\}$  are Fourier coefficients to be determined below. Recalling that multiplication in the frequency domain corresponds to convolution (indicated by a star " $*$ ") in the time domain, and denoting the inverse Fourier transform by  $F^{-1}$ ,

$$\begin{aligned}
x(t) &= F^{-1} \left[ \sum_n c_n \exp[-j2\pi nf/2W] \right] * F^{-1} U_W(f) = \sum_n c_n \delta[t - n/2W] \\
&\quad * 2W [\sin(j2\pi Wt)/2\pi Wt] \\
&= 2W \sum_n c_n [\sin 2\pi W(t - n/2W)/2\pi W(t - n/2W)], \tag{1.3}
\end{aligned}$$

where we have used the facts that the Fourier transform of the delta time function  $\delta[t - n/2W]$  is the exponential  $\exp[-j2\pi nf/2W]$ , the Fourier transform of the time function  $2W [\sin(j2\pi Wt)/2\pi Wt]$  is  $U_W(f)$ , and the convolution of a delta function with a time function simply picks out a specific sample of that time function. We determine the values of the Fourier coefficients  $\{c_n\}$  in Eq. (1.3) as follows to complete the proof:

$$x(m/2W) = \int_{-\infty}^{\infty} X(f) e^{j2\pi f(m/2W)} df = \sum_n c_n \int_{-W}^W e^{j2\pi f(m-n)/2W} df = 2W c_m, \tag{1.4}$$

where Eq. (1.2) has been substituted for  $X(f)$  and it has been noted that all integrals are 0 except when  $n = m$ . Thus

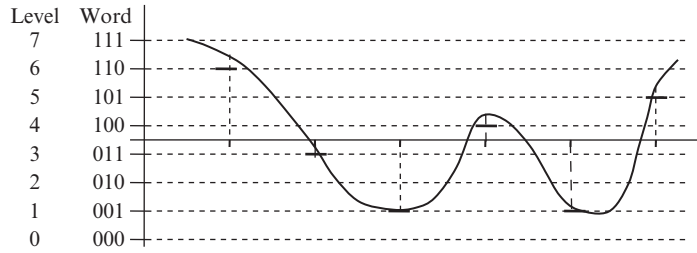
$$c_m = x(m/2W)/2W, \tag{1.5}$$

and substitution into Eq. (1.3) completes the proof.  $\square$

### 1.2.2 PULSE CODE MODULATION

Digital transmission was not seriously implemented in the telephone network until the 1960s although the foundation for it was the invention of pulse code modulation (PCM) by Alec Reeves in the UK in 1938 [5]. PCM saw limited use during World War II, notably for encrypted communication between President Roosevelt and Prime Minister Churchill. PCM started with the sampling theorem, presuming samples taken at (typically) 8000 samples/s to represent a telephone voice signal bandlimited to 4 kHz. Reeves' big additional step was to define a fixed set of discrete quantization levels over the dynamic range of the signal and to represent each level by a fixed-length digital word, normally 8 bits long. He demonstrated that good quality speech could be reproduced from a sequence of these approximate sample values rather than the actual ones. Each sample is rounded off to 1 of 256 quantization levels, each of which is represented by an 8-bit digital word, that with 8000 samples/s results in a 64 kbps data stream. Fig. 1.3 shows a simplified PCM coding into eight quantization levels, each represented by a 3-bit digital word. For the waveform shown, the six quantized samples result in the digital data stream 110 011 001 100 001 101.

The difference between an actual sample value and the nearest quantization level is the quantization noise. SNR is a common criterion for transmission quality. When the only noise is quantization noise, the quantization levels are uniformly spaced, as

**FIG. 1.3**

Pulse-code modulation (PCM) rounds off a sample to the nearest quantization level and represents that quantization level with a fixed-length digital word.

shown in Fig. 1.3, and both the signal and the noise can be statistically described, the SNR is the ratio of signal power to noise power expressed as [6]:

$$\text{SNR} = \text{Signal variance} / \text{Quantization noise variance} = 3(\sigma_x^2 / x_{\max}^2)2^{2b}, \quad (1.6)$$

where  $\sigma_x^2$  is the signal variance,  $x_{\max}^2$  is the square of the maximum signal amplitude, and  $b$  is the number of bits per digital word, eight in the usual case for voice. This expression makes the important point that although digital transmission is not without noise, it has the great advantage that this noise level is set in advance, as small as possible consistent with the capacity of the transmission channel, and is not increased during transmission or storage. Of course, digital errors can occur during transmission due to channel noise and distortion that the design of digital transmission systems must take into account. Later chapters of this book will describe in detail many of the mechanisms used in modern telecommunications to realize high transmission efficiencies (bits per second per hertz of bandwidth) while keeping the digital error rate below an acceptable level.

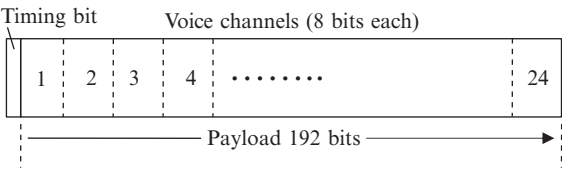
Although digital transmission is commonly associated with efficient use of bandwidth, uncompressed PCM is not necessarily bandwidth efficient. For example, baseband bipolar encoding (that transmits 2 bits/s per Hz) of a PCM data stream will require 32 kHz bandwidth for a 64 kbps PCM stream, far more than the 4 kHz bandwidth of the original analog speech waveform. It is only through highly effective compressive coding that we realize rates as low as 8 kbps for speech signals of reasonably good quality. Together with efficient modulation techniques, this can result in spectrum occupancy significantly lower than 4 kHz.

### 1.2.3 DIGITAL TRANSMISSION HIERARCHY AND SONET

A major motivation for applying PCM in the public switched telephone network (PSTN) was to realize efficient time-division multiplexed (TDM) transmission for multiple voice channels between telephone offices. For the relatively short distances within a local exchange network, existing copper circuits could carry not just 1 but

24 simultaneous conversations. TDM operates with a frame containing one word from each of a number of digitized voice streams, as illustrated by the 128  $\mu$ s DS-1 frame representing digitized samples of 24 voice channels (8 bits each) and 1 synchronization bit shown in Fig. 1.4, which transmits data at 1.544 Mb/s. Frames are transmitted synchronously—strictly clocked and regular—8000 times/s, suitable for regularly sampled signals such as voice and (some) video. This rate was widely implemented on T1 carrier facilities. As time went on and transmission rates increased on microwave and optical facilities, a TDM hierarchy developed with much higher rates (Table 1.1) to accommodate far more voice channels on high-speed media, up to the Synchronous Optical Network (SONET) standards extending to the OC-768 rate of almost 40 Gbps.

Software-controlled electronic switching systems were deployed even before the voice signals themselves were digitized, with “stored program control” of switching functions. And when PCM transmission was introduced, so was fully digital circuit switching. Internally, the telephone network became a fully digitized line-switched system, with analog telephone signals from subscriber access lines converted in the central office channel banks into digitized signals. Only 4 kHz of the bandwidth

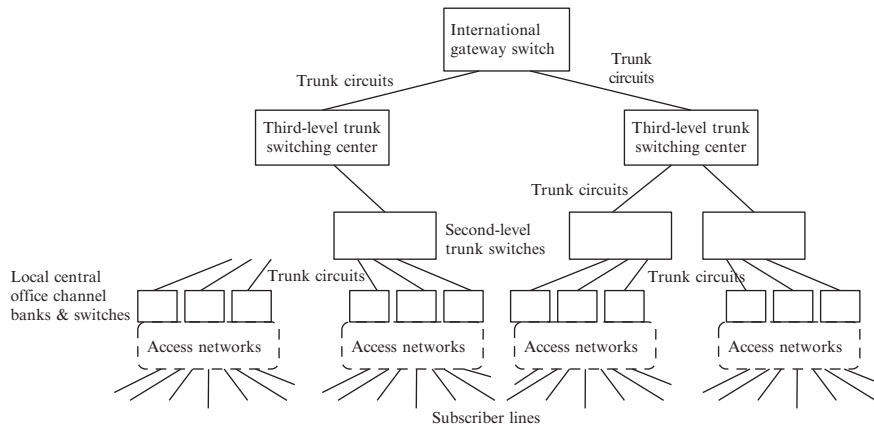


**FIG. 1.4**

The 128  $\mu$ s DS-1 frame. Each slot contains the bits representing one PCM sample of a particular source.

**Table 1.1** Digital Transmission Hierarchies [7]

DS-0:	64.000 kbps (one voice channel)
DS-1:	1.544 Mbps in North American and 2.048 Mbps in Europe
DS-2:	6.312 Mbps
DS-3:	44.736 Mbps
DS-4:	273.000 Mbps
<i>SONET commonly used rates</i>	
OC-1:	51.84 Mbps
OC-3:	155.52 Mbps
OC-12:	622.08 Mbps
OC-48:	2.48832 Mbps
OC-192:	9.95328 Gbps
OC-768:	39.81312 Gbps

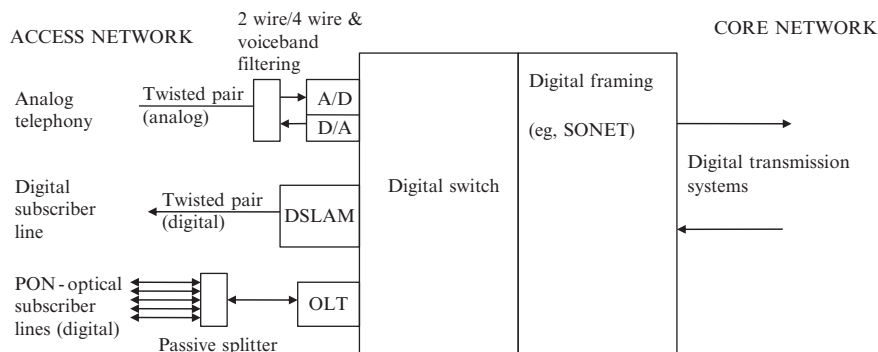
**FIG. 1.5**

The digitized public network.

Source: Drawn in part from R.J. Chapuis, *100 Years of Telephone Switching (1878–1978)*, North Holland Publishing Company, 1982.

available on the subscriber access line was used, assured by cutoff filters. Fig. 1.5 provides an overview of the organization of the digitized public telephone network, including assembly of traffic from diverse access systems, subscriber and trunk lines, and digital switches in a hierarchy of functions and capacities.

Fig. 1.6 illustrates three typical access systems: a two-wire analog telephone line converted into four-wire (separate in each direction) circuits, in which the

**FIG. 1.6**

Assembling traffic in a central office for digital transmission systems. *DSLAM*, digital subscriber line access multiplexer; *OLT*, optical line termination; *PON*, passive optical network.

upstream analog voice signal from the subscriber line is converted to digital and the downstream digital voice signal from the transmission system is converted to analog; digital subscriber line (DSL); and passive optical network (PON). Note that a low-pass filter in the analog to digital (A/D) converter limits use of the copper subscriber line to 4 kHz, appropriate for voice but a severe limitation for data transmission. The digitized information streams from these access systems may be combined (multiplexed) in the frames used for digital transmission systems, from the modest DS-1 frame at 1.544 Mbps to SONET frames at the high rates described in Table 1.1.

SONET, an international standard since 1988, enabled high speed transmission in the international public backbone network of both synchronous (regularly clocked) traffic, such as PCM speech, and asynchronous traffic such as asynchronous transfer mode (ATM) and IP. SONET originated and is most widely used in North America, while a similar international standard, synchronous digital hierarchy (SDH), is more widely used in Europe.

Fig. 1.7 shows the earliest and lowest rate SONET frame. The frame consists of 9 rows of 90 bytes, that is, 9 rows of 720 bits each. Frames are transmitted

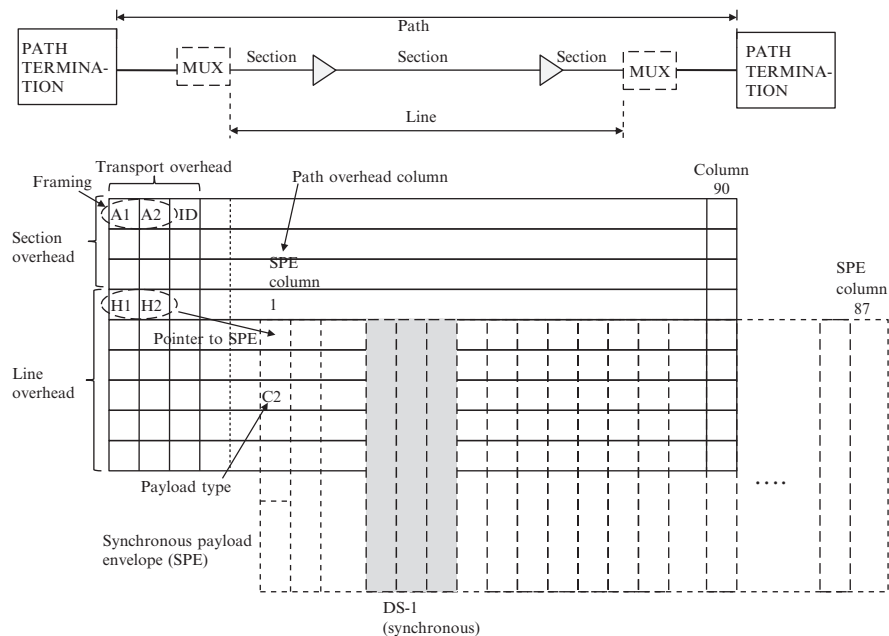


FIG. 1.7

A SONET frame for transmission at the OC-1 rate. Each square represents 1 byte (8 bits). The rows of 90 bytes are transmitted sequentially.

Source: Drawn in part from R. Gitlin, J. Hayes, S. Weinstein, *Data Communications Principles*, Plenum, 1992.

8000 times/s, so that a single byte per frame can carry a 64 kbps PCM data stream. The total transmission rate is  $8000 \times 9 \times 720 = 51.84$  Mbps, the OC-1 rate shown in Table 1.1. With three columns of frame overhead and one of path overhead, the user data payload is 49.536 Mbps. It is carried in a subframe called the synchronous payload envelope (SPE), with 9 rows and 87 columns including the path overhead column, leaving 86 columns for user data. The SPE may be contained in a single frame or overlap two frames as illustrated in Fig. 1.7. When it overlaps, bytes shown to the right of the frame wrap around into the slots to the left of the SPE. Bytes shown underneath the frame map into columns 4–90 of the next transmitted frame. A multiple of OC-1 frames are byte interleaved to realize a higher SONET rate, but path overhead may be constrained to one column instead of the multiple number of columns. Fig. 1.7 illustrates transport of a single DS-1 stream at 1.544 Mbps, corresponding to 24.125 bytes in each SONET frame, in three columns, a bit wasteful since three columns imply 27 bytes/frame.

Although for trunk circuits, digital TDM largely replaced the analog FDM systems for carrying multiple telephone calls, FDM has returned in optical transmission systems where use of multiple carrier wavelengths can vastly increase the capacity. Each wavelength in such a wavelength division multiplexed (WDM) system is likely to carry one of the SONET TDM rates shown in Table 1.1.

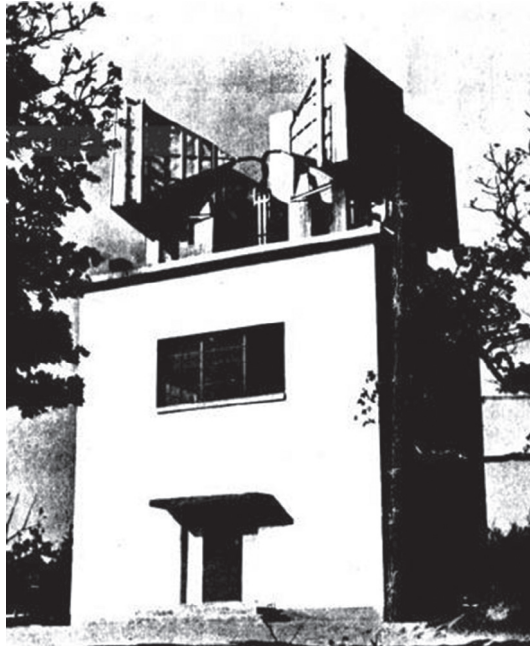
Many different kinds of traffic can be multiplexed into a SONET frame, not only PCM voice streams. Although SONET is designed for synchronous traffic only, of which DS-1 is an example, other traffic types such as ATM and IP, both described later in this chapter, can be encapsulated into synchronous streams. Ordinarily a single SPE will carry only one type of traffic since traffic requirements may differ, such as a delay for IP packets that may be unacceptable for synchronous voice traffic; but mixes are possible. The path overhead column allows identification of the traffic type.

---

## 1.3 MICROWAVE, OPTICAL, AND SATELLITE TRANSMISSION SYSTEMS

Before optical transmission systems became the workhorses of the backbone network, analog voice and the early digitized voice traffic were transmitted over long distances using either coaxial cables or (on land) through fixed microwave transmission systems. A voice channel often used both coaxial and microwave transmission segments. In 1932 Marconi designed what was probably the first regular microwave relay link for telephony, connecting Vatican City with the Pope's summer residence at Castel Gandolfo ([www.seas.columbia.edu/marconi/history.html](http://www.seas.columbia.edu/marconi/history.html)). However, it was the invention of a good microwave amplifier, the klystron, in the late 1930s, that made microwave carrier systems practical.

The earliest implementation in the public network was probably the 1947 microwave transmission carrier system linking New York and Boston through a sequence of seven microwave relay towers [8]. It used four radio channels in the

**FIG. 1.8**

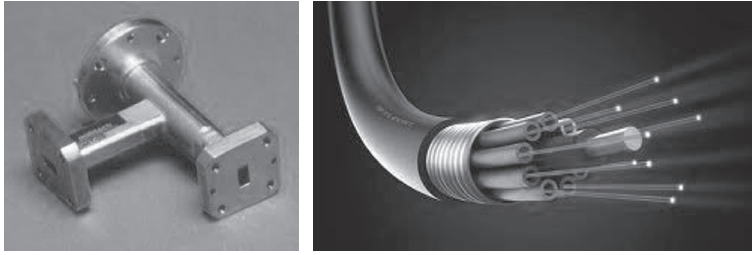
The Bear Hill microwave relay tower near Waltham, Massachusetts in 1947.

Source: [www.long-lines.net/documents/latest-word/PO6.html](http://www.long-lines.net/documents/latest-word/PO6.html).

4 GHz band, each carrying 480 analog telephone circuits or 1 analog television signal. Fig. 1.8 shows one of the relay towers. Microwave relay was a relatively low cost option for long-haul transmission and its use expanded rapidly until optical transmission systems, with their vast capacity and high reliability, took over in the 1980s.

### 1.3.1 OPTICAL TRANSMISSION IN THE BACKBONE NETWORK

The huge and rapidly increasing demands for high-rate digital communication, created in large part by streaming of video content, drove introduction of optical transmission systems beginning in the 1970s. Experimentation with fiber optic transmission had begun much earlier. In 1960, glass fibers showed a loss of around 1 dB/m, not yet usable for communication over a reasonable distance [9]. The laser (Light Amplification by Stimulated Emission of Radiation) needed to generate a strong light carrier signal was invented about the same time, prototyped by Theodore Maiman with reference to the theoretical work of Charles Townes and Arthur Schawlow, who had invented the microwave “maser.” The great advance in low-loss optical fiber came from the pioneering experimental work of Charles Kao at the

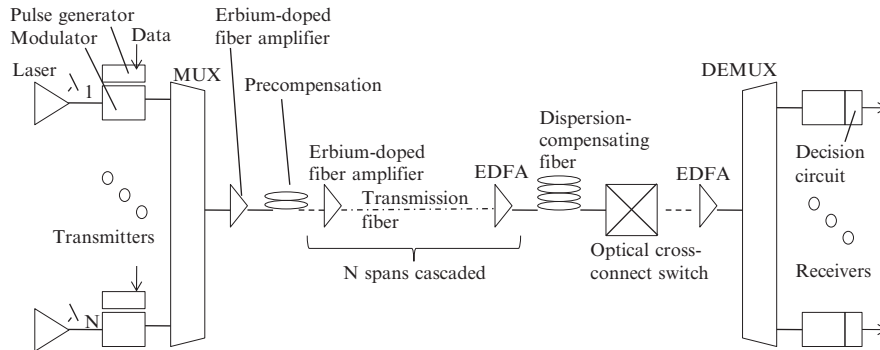
**FIG. 1.9**

Transmission media for millimeter microwave and optical transmission systems.

Standard Telecommunications Laboratories in the UK. He realized that impurities in glass led to high loss but predicted in 1966 that loss could be driven below 20 dB/km even though it was still, at that time, of the order of 100 dB/km. He demonstrated a physically robust structure with a glass core of 3–4  $\mu\text{m}$  diameter clad in glass of slightly smaller refractive index, with a total waveguide diameter of 300–400  $\mu\text{m}$ . Optical waves were propagated along the interface between the core and the cladding. By 1970 the Corning Glass Works, using fused silica, had realized single-mode fibers with loss below 20 dB/km at 633 nm wavelength [9]. Semiconductor diode lasers were developed at about the same time. By the 1980s, fiber loss was well below 1 dB/km and long distance fiber transmission was a reality.

While this history was evolving, it was, for some time, not sure that optical transmission would be adopted rather than millimeter microwave systems of small waveguides, both illustrated in Fig. 1.9. The rapid reduction in the transmission loss of single-mode (one coherent optical wave) transmission, together with development of low-loss splicing and other favorable attributes, carried the day in favor of optical transmission.

There followed a rapid development of long-haul optical transmission (Fig. 1.10), achieving a span of more than 1000 km with repeaters at 80–100 km intervals and offering an effective bandwidth of several THz when wavelength division multiplexing (WDM) is employed [10]. Tunable lasers also helped. Each wavelength in a set of carriers feeding a WDM long-haul optical transmission system is individually modulated by, for example, a Mach-Zehnder modulator, typically at a rate a little over 40 Gbps to accommodate an OC-768 data stream; 100 Gbps transmission was also being deployed as this book was sent to press. The modulation initially used on-off keying, but current preference, to achieve very high rates, appears to be for coherent (phase-sensitive) modulation such as quadrature phase-shift keying (QPSK) together with use of quadrature polarizations. Orthogonal frequency division multiplexing (OFDM) is also a serious candidate for optical transmission systems with its potential to “eliminate virtually all intersymbol interference (ISI) caused by chromatic dispersion and polarization mode dispersion (PMD),” together with its spectrum utilization flexibility that “makes it an ideal candidate for networks with many reconfigurable optical add and drop multiplexers (ROADMs).” [11]

**FIG. 1.10**

A long-haul WDM optical transmission system.

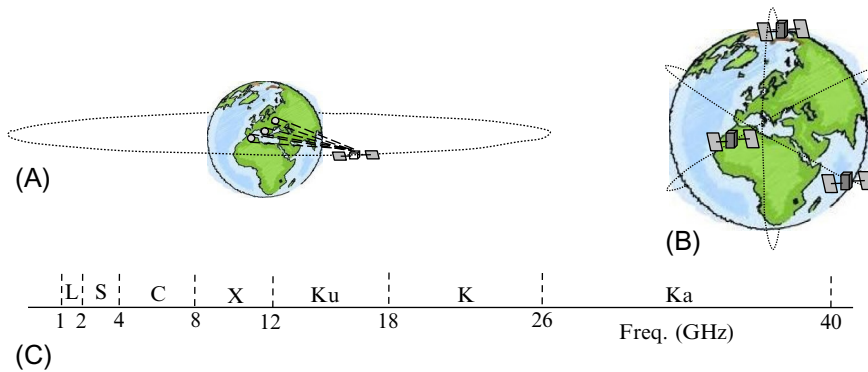
Source: Adapted from S. Pachnicke, *Fiber-Optic Transmission Networks*, Springer-Verlag, Berlin, 2012.

Optical fiber transmission, with its freedom from interference and attenuation beyond that of the fiber, dominates optical transmission but free space optical transmission, used since ancient times, still has a role. It is found in infrared transmission within a room and in campus-scale building-to-building transmission systems. Outdoor use is constrained by vulnerability to high transmission loss in bad weather.

### 1.3.2 COMMUNICATION SATELLITES FOR BACKBONE TRANSMISSION AND BROADCASTING

Satellite applications may be roughly organized in to three categories: Backbone transmission similar to that of the microwave and optical systems just described; broadcasting of programming to local distributors (cable operators and telcos) and to end users (direct broadcast satellite or DBS); and point-to-point communications. The British scientist and writer, Arthur C. Clarke, in 1945 envisioned DBS via a system of three space stations in geosynchronous orbit 36,000 km above the surface of the Earth, with a large population of users receiving with 30 cm antennas [12]. Although acceptable for broadcasting purposes, the propagation delay up to a geosynchronous satellite and back down again is a bit more than 1/4 s, which combined with other network delays can be unpleasant for real-time voice communication. Echo cancelers mitigate but do not entirely eliminate this disadvantage. For this reason low earth orbiting (LEO) satellite systems were also introduced into the global communications infrastructure although they have been largely overtaken by terrestrial and undersea optical fiber transmission systems.

The first communications satellite, Echo 1, a passive reflective balloon, launched in 1960, was not in geostationary orbit, nor were the active Telstar satellites of the early 1960s [13]. In 1964, when the international consortium Intelsat was formed, the first geostationary satellite, Syncom 3, was put into orbit, followed in 1965

**FIG. 1.11**

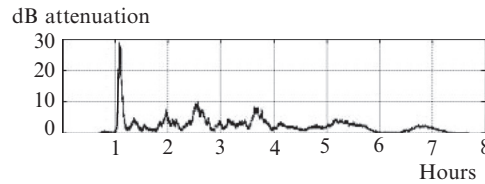
(A) Geosynchronous satellite with spot beams. (B) Low earth orbiting satellite system with moving satellites. (C) Frequency bands in which satellites operate. K band is sometimes included in Ka band.

Source: [www.esa.int/Our\\_Activities/Telecommunications\\_Integrated\\_Applications/Satellite\\_frequency\\_bands](http://www.esa.int/Our_Activities/Telecommunications_Integrated_Applications/Satellite_frequency_bands).

by Intelsat 1 (“Early Bird”) that supported two-hundred forty 4 kHz voice circuits between the United States and Europe. These satellites and others that followed still relayed analog, not digital, signals.

Intelsat satellites began the full operational use of digital time-division multiple access (TDMA) in the mid-1980s, with Intelsat-V transponders operating in the C-band, with frequency bands defined in Fig. 1.11C. Each transponder was capable of 120.8 Mbps transmission in a 72 MHz bandwidth and the satellite also performed dynamic beam switching [14]. Spot beams covering relatively small areas on the Earth’s surface permit reuse of frequencies for customized content and even individual communications channels to a much larger population of users than if everyone received the same broadcast content. Digital transmission advanced to a much higher frequency band in 1993 with NASA’s ACTS experimental geosynchronous satellite [15]. It operated in a portion of the lightly used Ka band (26–40 GHz) and featured onboard switching and the use of “hopping” (rapidly switched) very thin spot beams (Fig. 1.11A).

Fig. 1.11B illustrates a LEO system, with satellites that are not stationary but instead move in several different orbits at low altitudes, typically 800 km above the surface of the Earth. The much shorter transmission path results in short propagation delays that make this system suitable for real-time applications. Signals from the satellite are also much stronger, when received by communications devices on the Earth’s surface, than those from the distant geosynchronous satellites. Traffic is relayed among satellites in addition to the links to earth stations. The famous Iridium system, with 66 satellites, was launched in 1998 using C-band uplinks and downlinks for compressed digital voice at 2.4 kbps. It was a commercial failure in terms of return on the huge investment it required but continues in operation with large upgrades in data rates underway.

**FIG. 1.12**

Attenuation of a received 20 GHz signal at different times during a rainstorm [17].

Even before digital transmission, distribution of video programming to cable headends had become a major business for satellite operators. Unlike real-time voice communication, this broadcast application was tolerant of the long propagation time through geosynchronous satellites. By the mid-1980s several C-band geosynchronous satellites were devoted largely to supplying cable programming to cable headends [16]. A single video channel initially required the full 36 MHz bandwidth of an early transponder, but digitally compressed video now has more modest capacity requirements.

Consumers first had direct access to satellites through C-band receiving stations, with relatively large (2-m) and expensive dish antennas that tapped into programming intended for cable operators. DBS with small (46 cm) antennas began with geosynchronous satellite orbital assignments made by World and Regional Administrative Radio Conferences in the late 1970s and early 1980s, with eight satellites allocated to the United States. Currently, DBS services are available in the C-band (3.7–4.2 GHz), Ku-band (11.7–12.7 GHz), and Ka-band (18.3–18.8 and 19.7–20.2 GHz) (<https://sbca.com/receiver-network/satellite-overview.htm>). A high-powered Ku-band satellite radiates 120–240 W per transponder, 10 times as much as a typical C-band transponder, making possible the small dish antennas and reception in moving vehicles. In addition to downstream video and satellite radio programming, DBS satellites also support two-way broadband Internet access that is sometimes the only option for people living in rural areas.

Satellite propagation is usually in line of sight (LOS) channels with consistently reliable performance, but at the higher frequencies rain may significantly attenuate signal strength. Fig. 1.12 illustrates attenuation, over time, of a downstream signal at the lower end of the Ka-band during an initially heavy rainstorm.

## 1.4 EVOLUTIONARY STEPS IN DIGITAL ACCESS NETWORKINGS

Digital transmission was deployed in the backbone network well before it appeared in access networks available to consumers. But the need for digital access came early in banking, commercial transactions, and information access applications.

The first step was to use the existing analog voice telephone network for this new digital traffic, doing the best one could with facilities designed to optimize analog voice transmission. The device required to do this was the MODulator-DEModulator (modem).

### 1.4.1 VOICE CHANNEL MODEMS

End users, both residential and small business, had access only to twisted pair copper access lines running to telephone switches in central offices. A great deal of effort from the 1960s through the 1990s went into developing faster and more adaptive modems for dial-up access despite the severe limitations imposed by telephone network architecture. Cable modems followed, as cable access systems deployed data capabilities (Section 1.4.2).

The largest bottleneck was the constraint on bandwidth imposed on twisted pair telephone subscriber lines. Most twisted pairs, up to about 5 km, can provide about 1 MHz bandwidth, permitting data transmission at speeds of several megabits per second. However, the telephone networks included 4 kHz filters in the central offices to support multiplexing of voice channels in both TDM (Section 1.3) and analog FDM carrier systems, as suggested in Fig. 1.13. As a consequence, modem signals had to be limited to less than 4 kHz. The earliest modems used frequency-division duplexing (FDD), with completely separate transmission bands in the two directions. Data were initially sent at 300 bps in each direction using frequency-shift keying (FSK). By the 1970s modems incorporated the data-driven echo canceler, shown in Fig. 1.14, to cancel self-interference from local transmitted signal and distant reflections of transmitted signal [18]. This permitted use of the same full channel bandwidth in both transmission directions at the same time, opening the door to significantly faster full-duplex performance, reaching 9600 bps in each direction by the late 1970s.

Of course, in a low-noise environment but with distorted voice channels causing ISI, relatively high rates, that exceeded 50 kbps full duplex by the 1990s, were nevertheless attained by use of various techniques. These included partial response pulses, multilevel pulse amplitude modulation (PAM), a range of carrier modulation

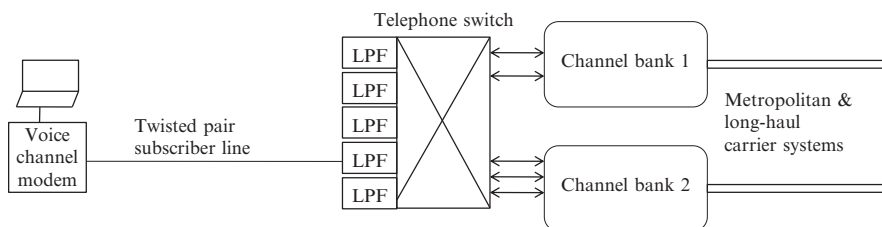
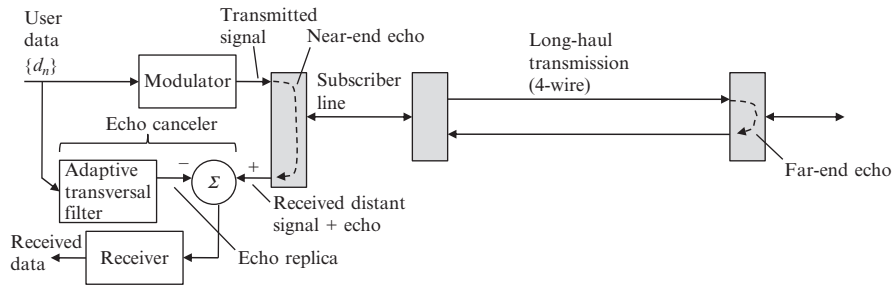


FIG. 1.13

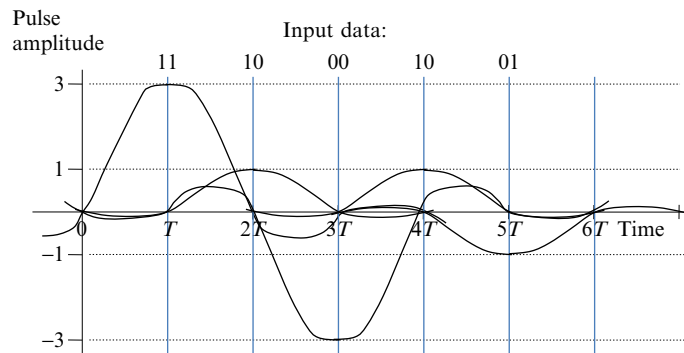
The dial-up access speed bottleneck: voiceband low-pass filters in the central office.

**FIG. 1.14**

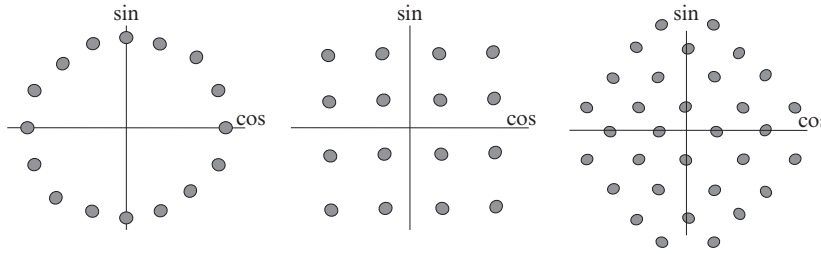
Data-driven echo cancellation supported full-duplex data transmission in the same telephone channel bandwidth. The adaptive transversal filter is similar to that of an adaptive equalizer, Fig. 1.19. Shaded boxes: directional couplers.

formats including phase-shift keying (PSK) and quadrature amplitude modulation (QAM), and sophisticated channel equalization and detection algorithms. In this brief introductory overview, we offer only a few capsule descriptions.

PAM is simply the coding of bits from a string of data into pulse levels. The available bandwidth determines the maximum number of noninterfering pulses transmitted per second, which can be shown to be twice the bandwidth [19]. Given a desired data rate in bits per second (bps), a sufficient number of bits must be coded into each pulse in order not to exceed the limitation on pulse rate. For example, if we are transmitting 8000 pulses/s, also called 8000 baud, requiring 4 kHz bandwidth, and wish to carry data at a rate of 16 kbps, 2 bits must be encoded into each pulse. This corresponds to a choice among four pulse amplitudes as illustrated in Fig. 1.15.

**FIG. 1.15**

Four-level pulse-amplitude modulation (PAM) coding 2 bits into a pulse level.  $T$  is the symbol interval, for example,  $1/8000$  s.

**FIG. 1.16**

16-PSK, 16-QAM, and 32-point CCITT V.32 signal constellations.

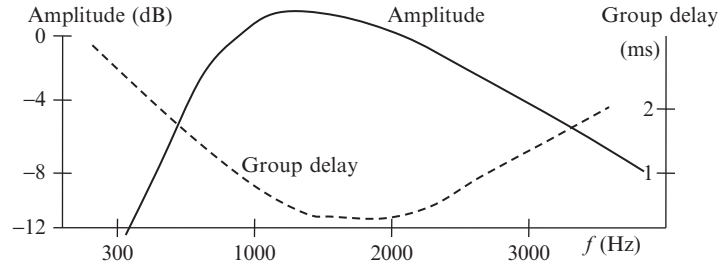
The pulses (Nyquist or Equivalent Nyquist) are designed to not mutually interfere, with their tails taking the value 0 at the centers of neighboring pulses. The actual signal waveform is the sum of the pulses shown. The spectral efficiency is 4 bits/s per Hz. As this example illustrates, bandwidth, baud, and data rate, often confused, are three different things.

For phase modulation and QAM, cosine and sine waveforms at a convenient carrier frequency (such as 1800 Hz) within the voiceband are each modulated by a sequence of pulse levels. 16-PSK, 16-QAM, and 32-CCITT (International Consultative Committee on Telephone and Telegraph) V.32 are represented by the “signal constellations” of Fig. 1.16. For each signal point, the horizontal coordinate is the amplitude of the cosine carrier and the vertical coordinate is the amplitude of the sine carrier. Note that the more signal points to choose from with a fixed power constraint, the closer together the points are and more vulnerable to detection errors due to noise and distortion. It was common for voiceband modems to dynamically select the largest constellation, and thus highest bit rate possible, without exceeding an acceptable bit error rate.

These are “passband” signal constellations because they represent modulation on carrier waveforms. Each again codes four data bits into each symbol. However, a special coding is used for the V.32 constellation with its constellation of doubled size as required for performance-enhancing channel trellis (convolutional) coding [20]. The increased size of the signal constellation implies, as the previous paragraph notes, some cost in immunity to noise and distortion. Nevertheless, the minimum Euclidean distance between coded line signal sequences is significantly increased, realizing a net gain. As a result, data can be reliably sent at the same rate as 16-QAM in channels with lower SNR than 16-QAM would require.

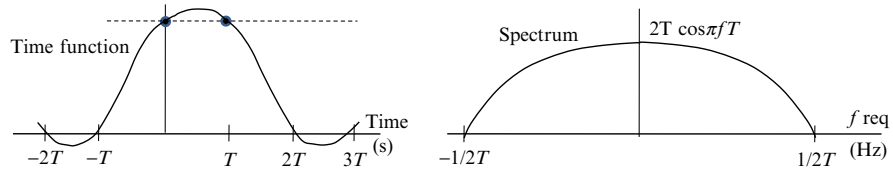
Voice channels in the telephone network are characterized by additive noise and by both linear and nonlinear distortions. Fig. 1.17 illustrates the amplitude and group delay (first derivative of phase) characteristics of linear distortion typical in telephone channels of the 1960s to 1990s period.

The technical response to linear distortion was both clever pulse design and powerful channel equalizers. The pulse design advances of the 1960s included

**FIG. 1.17**

Typical linear distortion of a telephone voice channel.

Source: Adapted from R. Gitlin, J. Hayes, S. Weinstein, *Data Communications Principles*, Plenum, 1992

**FIG. 1.18**

The duobinary partial response pulse, in the time and frequency domains [22].

“partial response” pulses, which caused intentional ISI between adjacent pulses in order to shape the spectrum so as to minimize the negative effects of channel distortion. This interference was predictable and could be removed during detection. The “duobinary” pulse, illustrated in Fig. 1.18, was one of the most successful in this regard.

Adaptive channel equalizers [21], self-tuning linear filters in the receiver of a modem, in large part compensated for linear channel distortion. Pioneered by Robert Lucky and others in the 1960s, they made possible large gains in voice channel transmission rate, from 300 bps to over 50 kbps, between the late 1960s and the mid-1990s. These instruments usually minimized the residual mean-squared error in the sample value presented to the detector. Fig. 1.19 illustrates the basic concept of an adaptive equalizer realized as a tapped delay line, with the delay elements possibly shorter (“fractionally spaced equalization”) than in a “synchronous” equalizer which has tap delays equal to the symbol interval  $T$ . The simple least mean square adaptation algorithm is:

$$\mathbf{c}_{n+1} = \mathbf{c}_n - \beta[y(nT + t_0) - \mathbf{r}_n \hat{\mathbf{a}}_n],$$

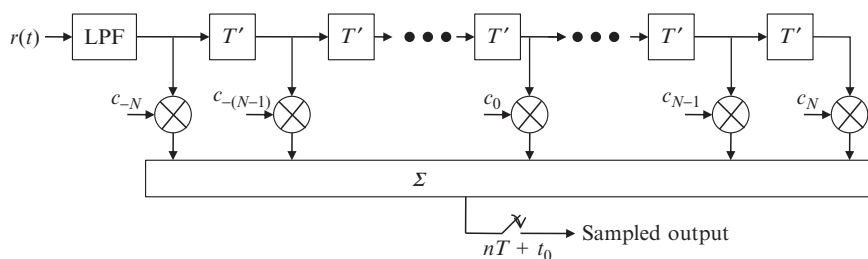


FIG. 1.19

An adaptive equalizer. The delay elements of  $T'$  seconds may be a fraction (typically half) of the symbol interval  $T$  to permit independent shaping of the filter's spectrum on both sides of the rolloff region [19].

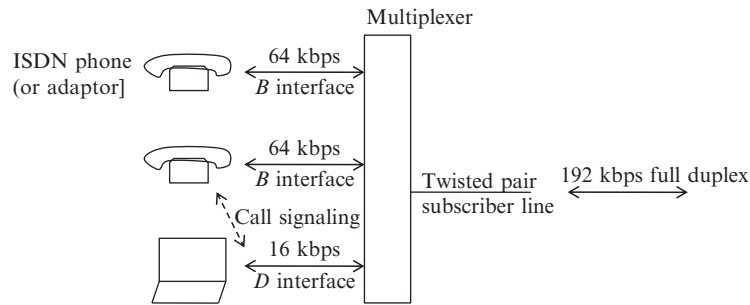
where  $\mathbf{c}_n$  is the vector of tap weights at the  $n$ th iteration of the algorithm,  $y(nT + t_0)$  is the signal sample correspondence to the  $n$ th transmitted symbol,  $\beta$  is a small weighting factor,  $\hat{a}_n$  is the decision made for the  $n$ th transmitted symbol, and  $\mathbf{r}_n$  is the vector of voltages at the outputs of the individual delay elements [19].

Dial-up modems made data services and, in the 1990s, the Internet available to ordinary people. They were the beginning of the transition to relying on communications processing “intelligence” at the edges of the network, rather than only inside the network as was the long tradition of the public telephone network. Wireless devices similarly use modems for transmission over wireless access links, described in Section 1.6. Signal modulation, timing and synchronization, detection, and channel equalization have been important elements in many phases of the history of digital transmission.

### 1.4.2 ISDN AND DSL

The development of high-speed digital switching and digital transmission within the public network left the subscriber access line as the bottleneck, still analog and, from a bandwidth perspective, grossly underutilized. Engineers were acutely aware that, aside from modest-rate modem traffic, digital transmission did not extend all the way to the subscriber. The Integrated Services Digital Network (ISDN) [23] was an attempt to overcome this limitation. The basic ISDN interface shown in Fig. 1.20 offered two 64 kbps channels for PCM voice and one 16 kbps channel for control and data, thought to be sufficient in the 1970s. At the telephone office, the voiceband filters were removed to allow the transmission of the approximately 200 kHz bandwidth required for the upstream and downstream ISDN channels. A “primary” ISDN interface, intended for business users, provided twenty-three 64 kbps channels for voice and one 16 kbps data channel.

The telephone industry expended considerable effort to deploy ISDN but it never really caught on, being perceived as too little, too late. It was followed, in the 1980s

**FIG. 1.20**

The basic ISDN interface.

and 1990s by DSL, introduced in the next paragraph, and by Broadband ISDN (B-ISDN) described in the following section in the context of ATM.

DSL took the same perspective of avoiding voiceband filters in the telephone office and using more of the bandwidth of the twisted pair subscriber line. It went a large step further, offering downstream rates, in Asymmetric Digital Subscriber Line (ADSL), of 1.5–8 Mbps, depending on distance from the central office. ADSL, a concept largely credited to Joseph Lechleider at Bellcore, offers downstream transmission at a rate typically 4–10 times the upstream transmission rate. This reflects the far greater likelihood, at least in most communication sessions, that a residential customer will receive a high-rate video stream than send one. It makes this service possible on a wide variety of telephone “local loops” (twisted-pair subscriber lines) in spite of severe crosstalk interference, introduced later in this section.

The much faster ADSL service doomed ISDN for anything beyond telephony. But it gave the telephone companies a way to become video services providers well before the expected triumph of fiber to the home (FTTH). Experiments at Bellcore proved the feasibility of linking servers on a high-performance multiservice backbone network, such as an ATM network ([Section 1.5.2](#)), to provide content for ADSL subscribers. These experiments proved the feasibility of an effective video delivery service even if a truly broadband network could not yet be extended to residential subscribers [24]. Fiber in the home did eventually become practical with the introduction of the PON ([Section 1.4.4](#)), but DSL has itself advanced with much faster speeds and remains a viable technology for residential access to the Internet. [Fig. 1.21](#) shows an xDSL access system, where the “x” represents any of several versions including ADSL and very high speed DSL (VDSL). A DSL Access Multiplexer (DSLAM) in the central office terminates a multiplicity of subscriber lines and provides an interface to ATM transport or directly to high-speed routers and the Internet. [Table 1.2](#) defines many of the xDSL formats.

xDSL historically began with two alternative modulation formats: carrierless amplitude-phase, very similar to QAM ([Section 1.4.1](#)), and discrete multitone

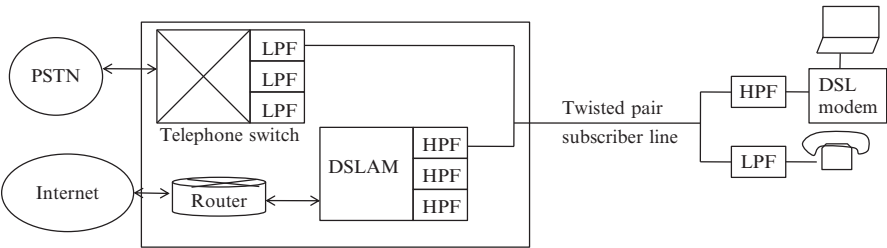


FIG. 1.21

xDSL access system.

Table 1.2 xDSL Formats

xDSL	Standard	Downstream	Upstream	Symmetry
ADSL	ITU-T Rec. G.992.1	Up to 8 Mbps	Up to 1 Mbps	Asymmetric
HDSL	ITU-T Rec. G.991.1	784 kbps, 1.544 Mbps, 2.0 Mbps	784 kbps, 1.544 Mbps, 2.0 Mbps	Symmetric
SDSL	–	Up to 2 Mbps	Up to 2 Mbps	Symmetric
VDSL	ITU-T Rec. G.993.1	Up to 100 Mbps	Up to 100 Mbps	Both
VDSL-2	ITU-T Rec. G.993.2	Up to 100 Mbps	Up to 100 Mbps	Both

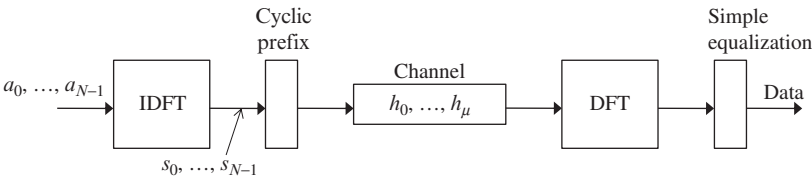
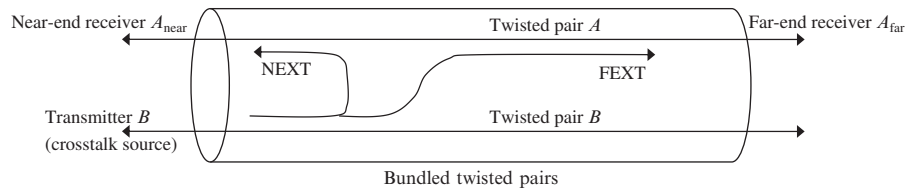


FIG. 1.22

An OFDM transmission system [25].

(DMT), a version of OFDM. DMT now dominates xDSL because of its superior ability to compensate seriously distorted channels, essentially avoiding the placement of energy in segments of the transmission band with very bad characteristics. OFDM/DMT transmits a data stream as a set of slower rate data streams modulating narrowly spaced subcarriers in parallel, contiguous frequency channels, a form of frequency division multiplexing in which all the streams are generated in one efficient computational algorithm, the fast Fourier transform implementation of the discrete Fourier transform (DFT), operating on the input data [25]. Fig. 1.22 is a simplified illustration of a point-to-point OFDM transmission system. Channel equalization is

**FIG. 1.23**

Introduction of crosstalk into xDSL systems.

much simpler in such a system as compared with single-carrier data transmission. OFDM is also used in fourth-generation cellular mobile, WiFi, and wireless over-the-air audio and video broadcasting.

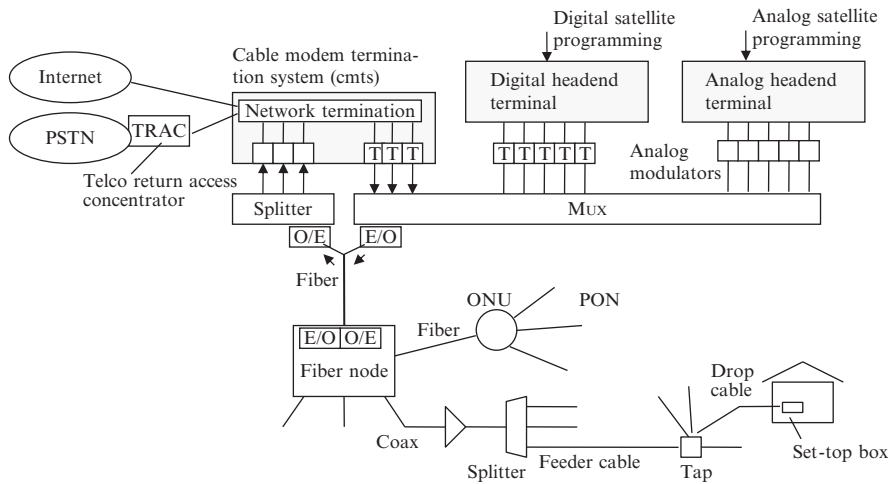
xDSL transmission is hampered by crosstalk interference between different twisted pair subscriber lines that are bundled together. Fig. 1.23 illustrates how this crosstalk appears, in both near-end (NEXT) and far-end (FEXT) components.

VDSL can provide very high rates in large part because of vectoring techniques addressing the significant FEXT interference [26]. Vectoring coordinates the detection of the separate VDSL signals on bundled groups of twisted pair subscriber lines, using a process of successive cancellation that is reminiscent of echo cancellation techniques used in modems. This strategy of coordinating multiple communications channels appears in wireless communications as well, in particular current initiatives in cellular mobile systems introduced in Section 1.6.

### 1.4.3 CABLE DATA NETWORKS

From a business perspective, the telephone companies' pursuit of xDSL was primarily an effort to compete with the already successful cable television (CATV) industry that not only delivered video programming, but was becoming the main provider of high-speed Internet access. From its origins as a "community antenna" system, CATV quickly acquired satellite-delivered programming including lucrative "pay" channels, and even toyed, quite early, with interactive programming [16].

As a local access system, a typical CATV system operates a tree-like network with a metropolitan area scope. A cable headend may use trunk cables to serve several hubs, which spread out into feeder cables and drop cables. Originally all of this was in coaxial cable, but reliable transmission was hampered by the need for up to 20 consecutive amplifiers in a large system. It was obvious, as soon as fiber optic cable became available, to replace the trunk cables and (later) even some of the feeder cables with fiber optic lines, leaving the expensive task of replacing all the drop cables to some future time. Thus the common model for a CATV network became the hybrid fiber-coaxial (HFC) architecture shown in Fig. 1.24. Further improvement, such as addressable taps, made it unnecessary to send service personnel to change

**FIG. 1.24**

A hybrid fiber-coaxial (HFC) CATV system.

the filters assigned to individual drop cables when a subscriber's choice of program packages changed.

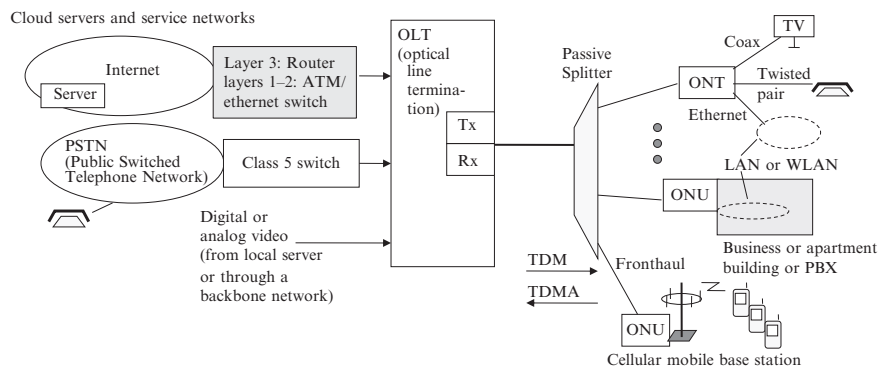
The higher quality of the transmission system further made it possible to use high spectral efficiency modulation schemes, such as 64-QAM, supporting digital video programming including HDTV with much greater efficiency than had previously been possible for distribution of analog video programs. In particular, each 6 MHz channel previously used for 1 analog television signal could carry up to 30 Mbps digital data, enough for at least 6 digital television signals or 1 HDTV signal plus 2 regular digital television signals. As FTTH becomes more practical with the advances in PON (see next section), the lower, coaxial cable part of the HFC system may be gradually replaced by the all-optical distribution tree shown above the coax portion.

The first technical standard for OFC systems was the Data Over Cable Service Interface Specification DOCSIS-1, promulgated by Cable Television Laboratories in 2000; DOCSIS 3.1 is a later (2013) version, available from Cable Labs ([www.cablelabs.com](http://www.cablelabs.com)). Its objective was bi-directional transparent transfer of IP traffic between a cable headend and customer locations. Within the headend, transmission resources were under the control of the Cable Modem Termination System. In the downstream direction, QAM modulators, using signal constellations of either 64 or 256 points, generated data signals at 27 Mbps or more in each 6 MHz channel. For upstream traffic, the rate was much less and a medium access control protocol assigned time slots and resolves contention. The upstream data rate was 0.2–3.2 Mbps. Some parameters have changed as the standard has evolved, particularly faster transmission in both directions, but the architecture is still very much the same.

### 1.4.4 PASSIVE OPTICAL NETWORK

Still seeking to bring fiber all the way to residences to beat the performance promises (which may not always be the performance delivered) of cable operators, telephone companies are exploiting the relatively low-cost PON architecture. PON is a high-performance “last mile” technology, with low-cost passive (not electrically powered) equipment in the field and the possibility of offering rates of up to 1 Gbps to each subscriber in the upstream as well as the downstream direction [27]. Its reach is actually much more than a mile; it can be 40 km in some cases. In addition to serving residential and business subscribers, PON has an important application to “fronthaul” transmission between cellular mobile base stations and cloud-based processing nodes, and “backhaul” from local area WiFi networks and from local communication systems such as private branch exchanges (PBXs). It is likely that as small base stations proliferate, the fast, economical backhaul capabilities of PON will become even more in demand. Fig. 1.25 shows the generic PON architecture delivering voice, video programming, and Internet access services and providing backhaul services as well, although it is unlikely that these would all be provided through a single PON.

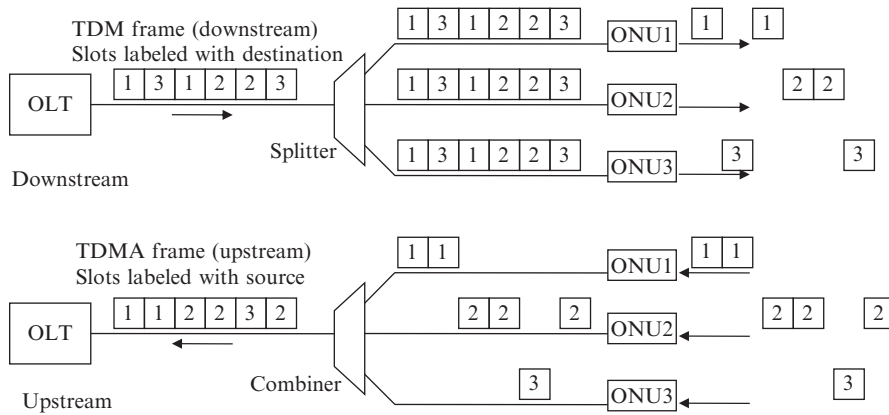
The principal elements of a PON are the optical line termination (OLT) in a central office, the passive splitter which typically shares the power of the downstream signal among 32 outgoing subscriber links (all optical fiber), and the optical network termination (ONT) at a subscriber location. There are three principal standards: the original broadband PON (BPON), ITU-T G.983.1; Ethernet PON (EPON), IEEE 802.3ah; and gigabit-capable PON (GPON), ITU-T G.984.1, and G.987. GPON and EPON, that share 10 Gbps among the attached users in current implementations, are competitors, with EPON sometimes seen as having a cost edge while GPON,



**FIG. 1.25**

Generic passive optical network (PON) architecture.

Source: Adapted from S. Weinstein, T. Wang, Y. Luo, *The ComSoc Guide to Passive Optical Networks: Enhancing the Last Mile Access*, Wiley-IEEE Press, 2011.

**FIG. 1.26**

Data transmission by TDM downstream and TDMA upstream.

to telephone companies, uses more of the traditional technologies such as SONET. Both use synchronous time division multiple access (TDM and TDMA) technologies, shown in Fig. 1.26, for the downstream and upstream directions, respectively. EPON additionally can use, for the appropriate kinds of bursty traffic, the original Ethernet carrier sense multiple access-collision detection (CSMA-CD) scheme for contention access, or one of its variants.

WDM PON will become the next generation standard. It can be configured such that each of up to 40 attached user lines gets one wavelength all to itself, at up to 10 Gbps in each direction. In this architecture the field unit is a (passive) wavelength multiplexer/demultiplexer, not a splitter. Of course, splitters can also be used so that each wavelength can be shared by multiple users.

In single wavelength (in each direction) PONs, the downstream wavelength is typically 1490 nm and the upstream wavelength 1310 nm. A second downstream wavelength of 1550 nm can be used for special video broadcasting purposes. At these wavelengths in the available single-mode fiber, the physical span of the network depends on the loss budget allowed in view of the input power. The power classes range from the low power class of PONs with transmission loss not exceeding 20 dB, a split of as many as 1:16, and a reach of at least 10 km, to the extended power budget class of PONs with transmission loss not exceeding 34 dB, a split of as many as 1:64, and a reach of at least 20 km ([www.ieee802.org/3/ad\\_hoc/ngepon/public/14nov/ngepon\\_1114\\_hajduczenia\\_01.pdf](http://www.ieee802.org/3/ad_hoc/ngepon/public/14nov/ngepon_1114_hajduczenia_01.pdf)). Tradeoffs are available, going beyond the bound of one parameter in return for lowering the bound of another.

With the rise of PON solutions, optical transmission now covers the entire span from access network to long haul, including trans-oceanic, network. It is an essential partner of wireless communications which, far from being a separate networking operation, depends heavily upon a very high speed, low-latency backbone network.

---

## 1.5 ORIGINS OF DATA COMMUNICATION NETWORKS AND VOICE-DATA INTEGRATION

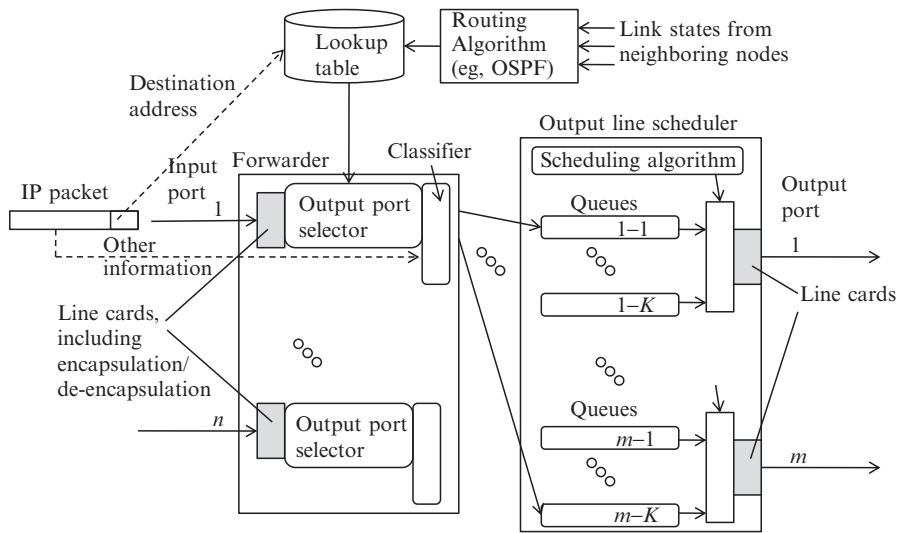
The dawn of the computer age began very early to make special demands on digital communication. One of the first communications-dependent applications, when computers were rare and expensive, was time-shared computing, the “computer utility,” for a widely distributed community of users. M.I.T. housed Project MAC beginning with a Defense Advanced Research Projects Agency grant in 1963, and the concept is once again widely used, albeit in an even more distributed way and with a new set of cost-saving justifications, under the banner of “cloud computing.” Dedicated private line data communication networks provided access to time-shared computing for large participating institutions, and dial-up modems allowed limited-speed access for individuals, but there was early interest in new communications techniques and networks that were better suited to computer traffic. Packet communications was perhaps the biggest and most revolutionary idea.

### 1.5.1 PACKET TRANSMISSION

Computer communications applications are bursty and demand additional flexibility from data communication networks. The time and effort to set up and tear down a switched circuit was impractical for a short keyboard burst, and the uniform-capacity switched circuits of the telephone network were inappropriate for the varying rate, duration, and quality requirements of data transmissions.

It was, however, unclear for some time just what mechanisms would be best suited not only for computer-oriented data communications but also for the digitized voice and video streams heavily loading today’s Internet. The community of researchers and developers interested more in computer-generated traffic than in voice calls favored message or packet transmission, the first defined as store and forward transport of a digital string representing an entire message, and the second defined as segmentation of a digital information object or stream into one or more bundles called packets that are individually routed through the transmission network. A fixed route and transmission resources do not necessarily have to be allocated in advance, so that call setup signaling may not be needed. Researchers in the 1960s, notably Paul Baran in the United States and Donald Davies in the United Kingdom, defined the packet concept and noted its value for “survivable” networks that could route traffic in alternate paths if a portion of a data network were damaged. The best known prototype of a packet network was the ARPAnet, a government-funded research network beginning in the late 1960s and initially linking a few locations, mainly university research centers, over 56 kbps leased lines.

The story is widely available elsewhere (see in particular the Internet Society’s history page, <https://internetsociety.org/internet/what-internet/history-internet/brief-history-internet>) and we only note here the conception, by Vinton Cerf and Robert Kahn, of the Transport Control Protocol/Internet Protocol (TCP/IP) mechanism facilitating the movement of packets in the ARPAnet and adopted today in the

**FIG. 1.27**

Routing and forwarding at a node of an Internet Protocol network.

immense commercial Internet. Packets are transferred from one transmission link to the next, in the general direction of the final destination and possibly in entirely different physical networks, by a router/forwarder. This IP router, unlike a switch in a switched circuit network, does not have to maintain the state of a connection, which is a well-defined path and information flow between endpoints, since there is no connection, just individual packets being forwarded in the right direction. Fig. 1.27 shows the generic structure of a typical router/forwarder, in which a routing algorithm, informed about the condition of links to neighboring nodes, decides which output line best conveys the packet closer to its destination. There may be several different possible routes to the destination device and it is possible for the routing to change between individual packets of a particular flow, although they usually traverse the same route.

There is an important detail in Fig. 1.27: Each input and output port includes a line card that exercises the underlying protocols used by the network to which it is connected. Thus, one output port might connect to an ATM/optical network, while another might connect to a switched Ethernet, and similarly for input ports. IP packets are encapsulated into lower-level frames or protocol data units (PDUs) of a particular network at an output port of the router, and de-encapsulated at the end of the link to enter the router at the next node. The internal functions of the router are independent of whatever networks (with line cards) are attached, showing why IP is an internet-working protocol that works with all physical networks for which encapsulation protocols exist.

Although the IP service is “best effort,” with no guarantee that the packet will not be delayed or dropped because of congestion, it saves a lot of effort in control signaling and offers a great deal of flexibility in routing. Different packets of the same “call” might take different routes. Reliability measures can and frequently are offered at a higher protocol level, notably TCP, which establishes a “connection” and retransmits lost packets. Moreover, although communication quality is not guaranteed as in circuit switching, there is the opportunity, through classification of a packet into different quality classes and specification of priorities in the scheduling algorithm, to grant preferential treatment, such as minimized delay, to quality-sensitive traffic types. Packet transmission with this kind of selective treatment allows convenient mixing of traffic at radically different rates while realizing, or at least approaching, the quality demands of all users.

It may be difficult for today’s Internet users to believe that IP was hardly visible in early commercial computer communication networks. Table 1.3 lists a number of these early networks [28]. The mechanisms they employed included X.25 [29], a packet forwarding protocol, that, unlike IP, operates over preestablished paths. It implements virtual calls and, as in ATM, virtual circuits as in ATM (defined in the next section). It follows a complex set of rules for realizing quality of service (QoS). Leased digital lines interconnected the store and forward nodes. Other networks forwarded whole messages or even used something close to traditional circuit switching. By the late 1970s, these commercial data networks were widely used and important to the global economy long before the commercial Internet appeared in the 1990s.

Today packet transmission and switching, dominated by IP, increasingly rules in wireless as well as wired networks. The mixture of different traffic types continues

**Table 1.3** Early Commercial Computer Communication Networks

DATAPAC	Canadian packet switching network using the X.25 host interface packet protocol that offers “reliable,” dedicated resources
TELENET	Packet-switched network that also was a forerunner of the Internet and used X.25
TYMNET	Computer time sharing. Store-and-forward message switching along a virtual circuit (defined in the next section)
DATRAN	Circuit (line) switched
SITA	Early message-switched network for the air travel industry
SNA	IBM’s System Network Architecture. Packet forwarding along fixed routes and the Synchronous Data Link Control (SDLC) protocol
SWIFT	The international banking network that employed a proprietary protocol, changing to X.25 in 1990 and an IP network in the early 2000s
Credit authorization networks	Leased-line and dial-in facilities, operated by credit card issuers such as banks participating in Visa and Mastercard and other issuers such as American Express, for authorizing credit card purchases. Generally used X.25

to drive deployment of packet transmission. Interestingly, packet transmission is adapting, under new names, some of the resource reservation and circuit switching aspects that were so successful in maintaining transmission quality in the PSTN. One of the most prominent innovations in this category is multiprotocol label switching (MPLS) [30], which switches, rather than routes, packets based on identifying labels and preallocated transmission resources. It goes part way toward the transmission capacity reservation properties of ATM. The gulf between the “telephone” and “computer communication” perspectives is not as large as it once was.

The actual transmission facilities used as links in data networks, including the Internet, are the same optical, microwave, satellite, cellular mobile, and copper facilities used by what is left of the legacy telephone network. Packet traffic may, as noted earlier, be included in the SONET and other synchronous frames used over such facilities even though the packet traffic is not synchronous, that is, packets arrive at input nodes on an irregular schedule. The obvious translation mechanism is buffering in which packets enter buffers at irregular times but are discharged from buffers at regular time intervals. This was the intent for ATM, a special packet mode that was, in the 1980s, the telephone companies’ answer to the question “how can we efficiently transport all kinds of traffic on the same network?”

### 1.5.2 ATM AND B-ISDN

Packet switching was only reluctantly embraced by the telephone industry. Telco managers feared a degradation of the quality inherent in switched circuits with their preauthorized transmission resources. A kind of compromise was realized in ATM [31] that, in contrast to IP with its variable-length packets, utilized a fixed size packet, called a cell, of 53 bytes including a 5-byte header, as shown in Fig. 1.28. ATM is very effective at providing whatever capacity is needed by different kinds of traffic; a higher-rate source simply issues cells at a higher rate than a lower-rate source and the ATM switch figures out how to mix this traffic in a fair way.

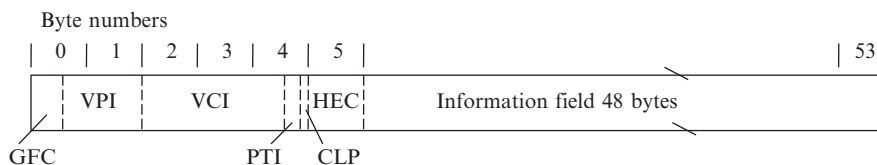


**FIG. 1.28**

The ATM cell. *GFC*, generic flow control (to manage flows from different sources); *VPI*, virtual path indicator (for aggregations of virtual circuits between the same end points); *VCI*, virtual circuit indicator (connection-oriented node-to-node channel); *PTI*, payload type indicator (3 bits) identifies data, maintenance, end of message, etc.; *CLP*, cell loss priority (1 bit); *HEC*, header error correction, computed as a polynomial operator on the header.

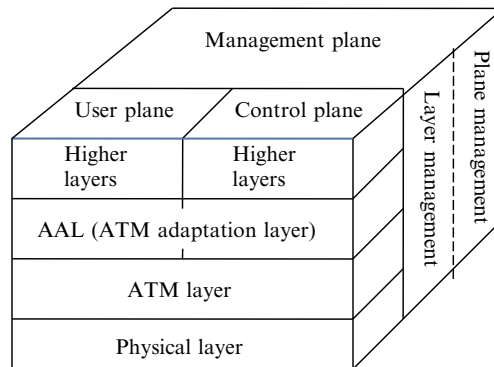
Transmission resources are preallocated to calls or sessions via *virtual circuits*. A virtual circuit may be defined as a point-to-point connection in a transmission system with a fixed path and assigned capacity, as in an ordinary circuit, but without dedicating a particular set of physical resources such as particular slots in transmission frames. The necessary capacity is realized as either a fixed rate or a statistical commitment. Furthermore, cell switches in the 1980s were much cheaper, for a given total throughput, than routers handling variable-sized packets. The 48-byte payload was a further compromise. The computer communication community had wanted a larger cell size to accommodate big data transfers, while the telephone industry, especially in Europe, wanted a smaller cell size to avoid cell-loading delays in real-time speech communication that could exacerbate echo problems.

In the 1980s and 1990s, telephone companies had great hopes that the 155 Mbps Broadband ISDN (B-ISDN) basic interface for residential subscribers, relying on ATM, would support both ordinary voice telephony and digital video services, especially video on demand to compete with cable operators. Devices performing digital video coding and decoding (codecs) with a high digital compression ratio, taking advantage of in-frame and frame-to-frame redundancies, were not yet available at an acceptable cost. The general presumption at the time was that an uncompressed digital video stream required about 140 Mbps in transmission capacity. Like circuit-switched networks, the virtual circuit ATM networks required an elaborate signaling protocol that appeared as the international standard Q.2931 [32].

B-ISDN was a broadband network consisting largely of optical transmission facilities including optical fiber to subscriber residences; ATM switches; the Q.2931 signaling protocol for setting up and managing virtual circuits and paths; and a set of protocols, above the ATM layer, for encapsulating different types of traffic into ATM cells. The principal rates specified for the user-network interface (UNI) were 155.52 and 622.08 Mb/s, including the possibility of asymmetric interfaces with different upstream and downstream rates [33].

The B-ISDN protocol reference model [34], shown in Fig. 1.29, consists of three planes: a user plane, a control plane, and a management plane. The physical transmission layer is shared by the user and control planes and consists, for example, of physical transmission media such as optical transmission systems and a framing mechanism using the medium, such as SONET, which is able to encapsulate ATM cells. The next layer up is the ATM layer, providing data transfer for all types of traffic. The ATM adaptation layer (AAL) above that provides service-dependent functions to higher layers, for example, mapping QoS dependent voice or video traffic into ATM cells, or alternatively encapsulating IP packets into ATM cells. Encapsulation, an important concept in digital transmission, means placing an unchanged PDU, such as a complete IP packet, into the information fields of a lower-level PDU such as one or more ATM cells.

Above the AAL in the control plane are call control and connection control, while in the user plane there may be mechanisms for creating application-specific PDUs from original sampled audio and video streams. The management plane oversees

**FIG. 1.29**

The B-ISDN reference model.

faults, alarms, and corrective measures; performance issues; network configuration; accounting; and security.

When B-ISDN was planned in the 1980s, telephone engineers were optimistic that a large portion of the telephone subscribing public would be using it by the year 2000 and that this would enable telephone companies to successfully compete with well-established coaxial cable operators. This failed to happen for a number of reasons, first and foremost that it simply cost too much. Also, by the 1990s cable operators were already introducing optical fiber in hybrid fiber-coaxial (HFC) systems, described in [Section 1.4.3](#), that used fiber transmission to hubs in the field but retained the copper coaxial cables in the part of the system closest to subscribers, thus avoiding the large expense of running fiber to every subscriber location. Another factor in the failure of B-ISDN was that video compression became cheap and available, significantly reducing the required data rate for a video channel to the point (about 1.5 Mbps) where more economical services, such as DSL, provided a better entry point into broadband services.

Over a longer period of time, optical access from subscriber locations has become relatively widespread and the (former) telephone companies that operate them have become successful video programming providers, relying heavily on PON access systems described in [Section 1.4.4](#).

### 1.5.3 CONTENTION SYSTEMS: ALOHANET AND ETHERNET

Most transmission systems provide either guaranteed transport, over circuits or virtual circuits, or “best effort” transport as with the Internet protocol, where packets are queued at routers and a packet is sometimes dropped if there is not enough capacity on the desired outgoing link. There is a third option that has been implemented in several important communication systems, that of contention access

on a shared medium, in which a packet or frame of data offered to the shared medium might collide with someone else's, and the collision is resolved by a "backoff" mechanism in which each of the contenders wait a specified time before trying again. This is the basis of the very widely used Ethernet, invented in the early 1970s by Robert Metcalfe at the Xerox Palo Alto Research Center (PARC), although it should be noted that many enterprises now use switched Ethernet in which there is no longer any real contention or collision.

AlohaNet, a radio contention system invented by Norman Abramson and others at the University of Hawaii, was a network linking computers scattered over the Hawaiian Islands. Remarkable for its simplicity as a multiple access system, it began with the "pure" Aloha protocol in which a transmitter would simply begin sending, but if no acknowledgment of successful transmission returned from the designated receiver it would back off for a randomly selected interval and then try again [35]. For light traffic it worked well, but when utilization approached 20% there began to be many collisions and performance quickly degraded. The system was enhanced with "slotted Aloha" which offered synchronized transmission time slots that significantly improved the collisions threshold, but still could not be considered a high-utilization network.

Ethernet was invented to aid communication sessions among the advanced Alto personal computers that were one of the pioneering advances at the Xerox PARC [36]. It was quickly generalized to serve any communicating host machine. Its great advance over Aloha was to listen first ("carrier sense") and transmit only if no other station was heard, a protocol labeled CSMA-CD. For two active stations, a collision may nevertheless occur because of the propagation and receiver processing delays. When this collision is detected, each transmitter waits either 0 or 1 (random choice) frame times before transmitting again. If either transmitter should detect another collision, it waits 0, 1, 2, or 3 frame times before transmitting again, and so on, by a power of 2, quitting after 16 attempts. Fig. 1.30 illustrates a possible collision and retransmission sequence, with the  $T1$  (transmitter 1) frames shown in actual time and the  $T2$  (transmitter 2) frames when they are heard by  $T1$ , which will be some time after they are sent. Upon hearing the first collision,  $T1$  chooses randomly

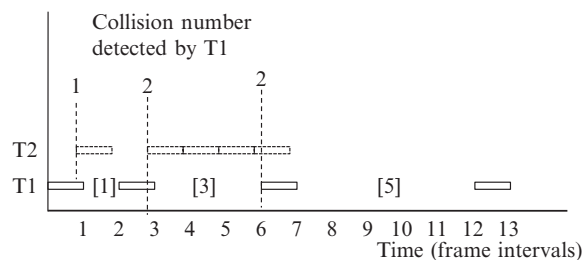


FIG. 1.30

Illustration of operation of the Ethernet retransmission protocol.

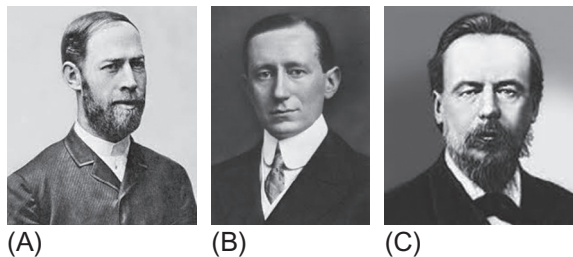
between waiting zero frames or one frame and the random choice turns out to be one frame, represented as Holzman and Pehrson [1]. Not hearing anyone else,  $T1$  sends its frame again. Transmitter 2, who also may have heard the collision, also waits one frame and, not hearing  $T1$  because of the propagation delay, transmits again, detected by  $T1$  as collision no. 2. This time  $T1$  randomly selects a delay of three frames from the choices (0, 1, 2, 3) before its third attempt. A third collision is detected and this time  $T1$  waits five frames randomly selected from the set (0, 1, 2, 3, 4, 5, 6, 7).

Multiple access backoff protocols advanced further, but there are now commercial Ethernet switches that avoid contention altogether, using the Ethernet frame specification for communication through an Ethernet switching hub with individual dedicated channels to the participating computers. Switched resources are requested and granted or denied, with no collisions occurring. Ethernet is almost universally used in residential and enterprise local-area wired networks using cable media.

---

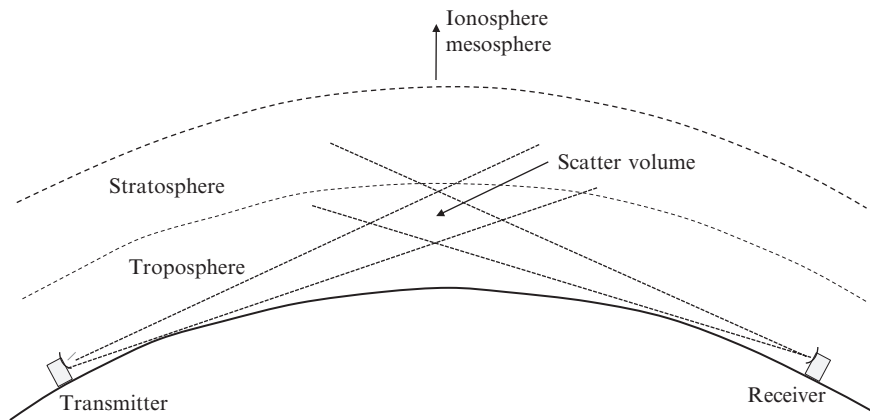
## 1.6 WIRELESS TRANSMISSION SYSTEMS

Wireless transmission has a long history in many forms, including the terrestrial microwave relay transport of multiple voice circuits introduced in Section 1.3. The earliest commercial use of digital wireless transmission, beginning around 1900, was for radiotelegraphic ship-to-shore communications, driven by the safety and convenience needs of navies and passenger liners. Marconi was a leading figure in this early application, making many early demonstrations of radio transmission over both land and water in England and Italy, and later in the United States [37]. He was not the first or only implementer of radio transmission; Hertz offered demonstrations in the late 1880s but he did not use it for conveying information. Popov in Russia was another practical innovator like Marconi, demonstrating ship-to-shore communications to the Russian Navy in the late 1890s; but the Navy's insistence on secrecy may have kept Popov from receiving much recognition in Europe and the United States [38] (Fig. 1.31).



**FIG. 1.31**

(A) Hertz, (B) Marconi, and (C) Popov.

**FIG. 1.32**

Tropospheric scatter data transmission.

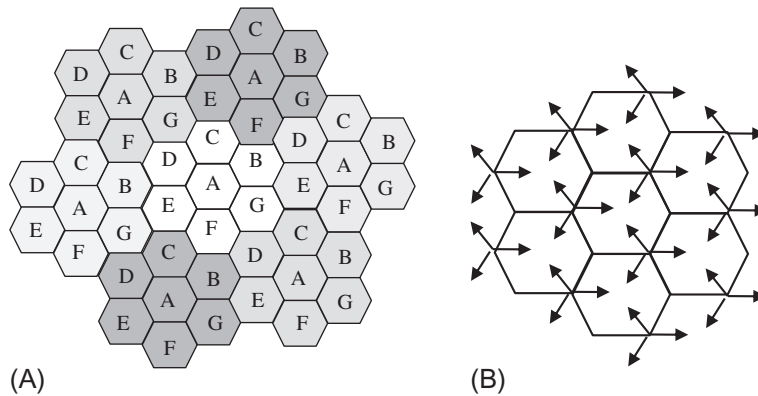
The spark gap transmitters used in these early systems generated electromagnetic waves over a very wide range of frequencies, so that the dimensions and resonant frequencies of the antennas structures effectively determined the transmitted frequency. Hertz's early demonstrations were at relatively high (60–500 MHz) frequencies. Marconi's long-distance transmissions, made much later, used huge antennas that effectively radiated at frequencies ranging from 45 to 850 kHz [39]. These low frequencies are appropriate for low-loss “ground wave” transmission over long distances and helped make Marconi's experiments great successes.

By 1920 analog voice largely replaced digital telegraphy traffic in wireless systems. It was not until the advent of military high-frequency radio systems in the 1960s that data, including digitized voice, reappeared as the main traffic type. These systems, some of which implemented over-the-horizon transmission of data by low-altitude tropospheric scatter as illustrated in Fig. 1.32, suffered from frequency-selective fading that attenuated parts of the signal spectrum.

Full-bandwidth channel equalization for channels suffering deep selective fades is very difficult, which is why military VHF data transmission systems, in the 1960s, were among the earliest users of OFDM, introduced in Section 1.4.2. The KATHRYN high-frequency radio, described in a 1967 paper [40], was a notable example. Its transmitter generated 34 subchannels within a total 3 kHz bandwidth using an analog DFT. Deep fades within the passband could be addressed by simply not putting energy into the lossy subbands, the same basic principle that later was so successful in DSL.

### 1.6.1 CELLULAR MOBILE: 1G TO 4G

The first generation (1G) of cellular mobile communication systems, called Advanced Mobile Phone System (AMPS) in North America, used analog FM in

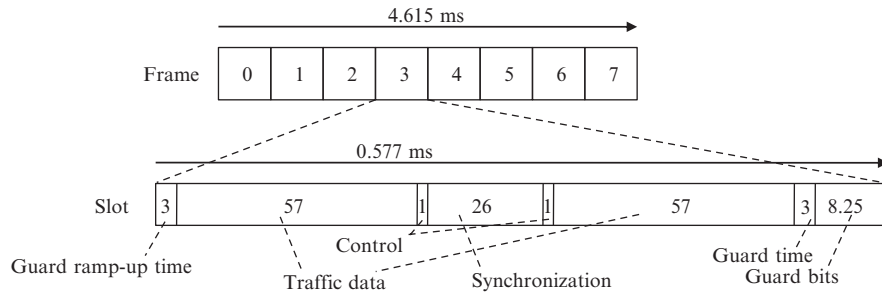
**FIG. 1.33**

(A) Cellular structure based on a reused seven-cell pattern. Each letter represents a different set of carrier frequencies. (B) Sectorization, increasing frequency reuse with directional antennas.

Source: Adapted from G. Stuber, *Principles of Mobile Communication*, second ed., Kluwer Academic Publishers, 2001.

30 kHz channels and accommodated multiple users through frequency division multiple access in the 800–900 MHz band allocated by the 1976 World Allocation Radio Conference (WARC) [41]. The critical cellular structure (Fig. 1.33A) came into commercial practice with the 1979 NTT deployment in Japan, followed by the 1981 Nordic mobile telephone service and the 1983 AT&T AMPS (Advanced Mobile Phone Service) in the United States. The cellular structure made possible multiple reuse of frequencies in different (separated) cells in contrast with earlier mobile systems that often had one antenna for an entire city and a very limited number of simultaneous channels. The separation between cells with the same carrier set is sufficient to attenuate signals to a noninterfering level. Additional frequency reuse within a single cell is possible with directive antennas at the vertices, a system that is called *sectorization*, with directional antennas represented by arrows in Fig. 1.33B.

Wireless *digital* transmission came with 2G, the second-generation cellular mobile systems deployed in the early 1990s exemplified by the North American IS-54 and IS-136 standards using TDMA, the European Group Speciale Mobile (GSM) standard that also used TDMA, and the North American IS-95 code-division multiple access (CDMA) standard. By use of digital voice compression, the TDMA standards supported three times as many voice channels in the same bandwidth as the old analog systems. In GSM, the first deployed of the TDMA standards, carriers separated by 200 kHz each carried “frames” of eight time slots each, with a time slot illustrated in Fig. 1.34. This provided just under 198 kbps for traffic data, mainly multiple compressed digital voice streams but also including data from the 9.6 kbps voiceband data modems of that time and from ISDN. The upstream and downstream

**FIG. 1.34**

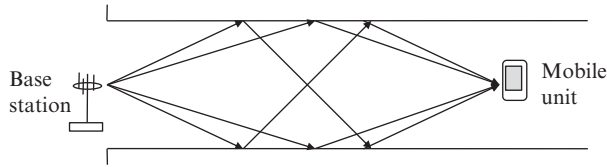
GSM time slot is carried in an eight-slot frame on one of the carrier frequencies spaced at 200 kHz.

Source: Adapted from G. Stuber, *Principles of Mobile Communication*, second ed., Kluwer Academic Publishers, 2001.

signals were conveyed full duplex on entirely separate carrier frequencies. IS-54, in contrast, kept the 30 kHz spacing of carrier frequencies and implemented a 40 ms frame containing three slots. Both systems implemented several compressive voice coders with data rates ranging from about 7 to 13 kb/s.

In the alternative IS-95 CDMA system [42] the user information stream (primarily compressed voice), at 9.6 kb/s, was spread over a much wider transmission bandwidth by multiplying it with a pseudo-noise (PN) bit sequence with a clock, or chip, rate 128 times faster, or 2.2288 Mchips/s. The PN sequences of different users were mutually orthogonal, making detection possible by multiplication with the correct, synchronized PN sequence. With a very large number of available orthogonal PN sequences, increasing numbers of simultaneous users were possible, with conversations already in progress experiencing a little more background noise each time a new user was added. This accommodation of more users led to forecasts of huge gains in spectral efficiency. In practice, for comparable quality, IS-95 showed gains of 6–10 times over 1G AMPS compared to IS-54's factor of 3. There are additional levels of coding beyond the scope of this brief overview and additional measures were required to regulate signal levels to overcome the near-far effect in which mobile units close to a base station overpower the signals from mobile units farther away and to meet other special needs of CDMA. As an historical note, CDMA appears to have been described in the 1930s by a Russian researcher, Dmitri Ageev [43].

The channel between a transmitter and a receiver is typically not the ideal unobstructed LOS, but rather a complex set of paths due to scattering, resulting in frequency-dependent fading. Fig. 1.35 illustrates nonisotropic scattering in a city street between tall buildings. The phase differences between multipath components arriving at the receiver may, due to small variations in the path delays, result in a constructive or destructive combination. Addressing the fading wireless channel is a major topic for the rest of this book.

**FIG. 1.35**

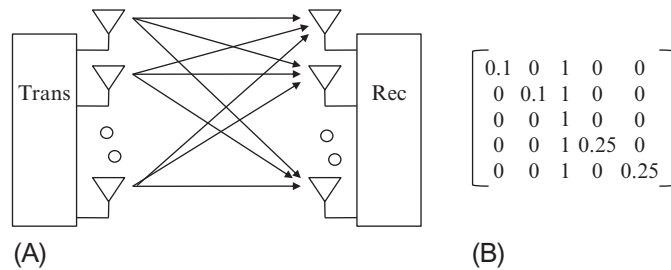
Multipath propagation between rows of buildings [41].

The motivation for 3G cellular mobile was to move beyond the heavily voice-oriented architecture of 2G to provide at least equal emphasis on delivering data and media (audio and video) content. The IMT-2000 concept, with spectral allocations assigned by the 1992 WARC, had specific goals for transmission rates, including 144 kb/s in vehicles, 384 kb/s for pedestrians, and (asymmetric) 2 Mb/s downstream indoors. A second phase defined data rates as high as 20 Mb/s, although in practice this was left to 4G systems.

There are two major 3G standards: Universal Mobile Telecommunications System (UMTS), a successor to the 2G GSM promulgated by the 3GPP industry consortium, and CDMA2000 system, promoted by the 3GPP2 industry consortium, which is largely a successor to the IS-95 CDMA standard. Both of these standards operate in frequency bands from 1850 to 2200 MHz and utilize CDMA, but in different configurations. UMTS employs wideband CDMA (W-CDMA), with carrier spacing starting at 5 MHz and asynchronous operation of base stations, while CDMA2000 has carrier spacing starting at 1.25 MHz, the same as IS-95, and operates base stations synchronously. W-CDMA has implemented several upgrades with increasing speeds, notably High Speed Packet Access (HSPA) with 14.4 Mb/s downstream rate. CDMA2000 has evolved to similar rates.

Fourth-generation (4G) cellular mobile employs a range of techniques to realize a large increase in capacity, with the goal of full accommodation of Internet applications migrating from computers to personal handsets. Peak data rate can reach 3 Gbps in the downlink and 1.5 Gbps in the uplink. Carriers have acquired or reassigned additional bandwidth for 4G services in segments between 700 and 2700 MHz. This is still within the familiar frequency range so that propagation conditions are similar to those for the previous generations of cellular mobile systems.

The characteristics of 4G cellular mobile, defined in 3GPP's Long Term Evolution-Advanced (LTE-A) specifications, include use of OFDM with its resilience against multipath delay and pulse dispersion; carrier aggregation through use of multiple frequency channels for one communication session; multiple antennas in multiple antennas out (MIMO) spatial multiplexing, a way to profit from relatively uncorrelated multipath propagation [44]; and coordinated multipoint, the collaboration of multiple base stations in communicating with a mobile unit that is near a cell boundary [45]. Relay nodes, essentially microcells embedded in ordinary cells near their boundaries to improve performance, are also supported. Either FDD or time-division duplex operation can be used.

**FIG. 1.36**

(A) MIMO with multiple antennas at transmitter and at the receiver. (B) A possible channel variance matrix for a  $5 \times 5$  MIMO system [46].

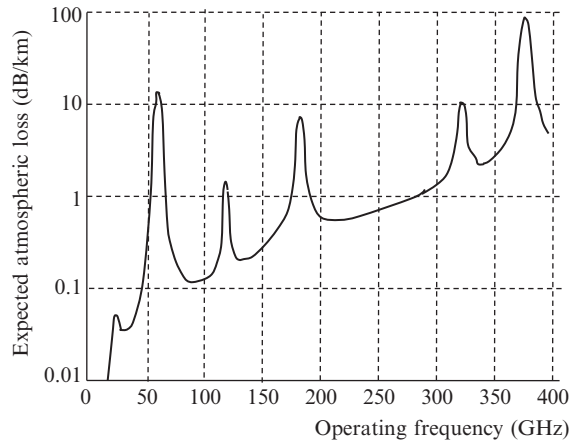
Carrier aggregation groups up to five component carriers, each with a bandwidth up to 20 MHz for a maximum of 100 MHz. The component carriers may come from different overlapping service cells offering different frequency channel sets, not the same as the spatially disjoint cells in the basic cellular mobile concept.

MIMO, a major enhancer of high speed digital wireless communication, provides the physical environment for spatial coding. For each transmitter-receiver pair, a transmitter uses multiple transmitting antennas to send appropriately designed signals to multiple receiving antennas, as illustrated in Fig. 1.36. This figure also shows a possible channel variance matrix when the matrix channel contains two very small scatterers, two larger ones, and one large scattering cluster. LTE-A supports up to  $8 \times 8$  MIMO in the downlink and  $4 \times 4$  MIMO in the uplink. A range of available transmission modes supports a variety of different user equipments.

Although 4G is still early in its deployed lifecycle, the relentless demand for greater bandwidth and flexibility drives efforts to devise technologies and techniques for reliable wireless access in much higher frequency bands, as described in the next section.

### 1.6.2 5G CELLULAR MOBILE

There are many views of what 5G is, since, at the time of writing, it is still not defined in a standard, which 3GPP anticipates will be issued in 2020. There is agreement that the scope of 5G includes the smooth integration of different network types of wireless access and local area networks and the use of new frequency allocations in much higher bands than those used for currently deployed cellular systems. As defined in METIS, a major European project, “the goal is a system that supports 1000 times higher mobile data volume per area (10–100 times higher number of connected devices and 10–100 times higher use data rate), 10 times longer battery life for low power massive machine communication, and 5 times reduced end-to-end latency, all of them at a similar cost and energy dissipation as today” [47]. In addition to going to frequency bands up to 86 GHz, the 5G system will exploit “new network

**FIG. 1.37**

Atmospheric path loss as a function of frequency [48].

topologies and technologies such as moving networks, multi-hop communications, self-configuration networks, and direct device-to-device communications.”

Transmission studies for the development of 5G focus on understanding of the transmission characteristics of the higher frequency bands and the extremely high speed digital logic required to use them. As noted in Rappaport et al. [48], “spectrum at 28 GHz, 38 GHz, and 70–80 GHz looks especially promising for next-generation cellular systems.” Although oxygen in the air attenuates electromagnetic waves at 60 GHz, adjacent frequency bands experience relatively low attenuation, as illustrated in Fig. 1.37. Rain also degrades propagation at higher frequencies, as much as 20 dB/km above 50 GHz for a heavy rain, compared with negligible attenuation in the 2G-4G frequency bands. However, high-speed wireless communication is becoming shorter range through deployment of microcells and picocells to reduce load on the macrocellular base stations, making the attenuation associated with higher frequencies a less significant limitation. The 60 MHz region is a serious candidate for LAN and small-cell communication because the high attenuation is actually a benefit in avoiding inter cellular interference.

In urban environments where 5G is expected to be heavily used, the millimeter-wave frequencies are characterized by long delay spreads from the multiple reflection paths. These long spreads can be partly avoided using directional beamforming, but designers must keep in mind the complexity tradeoff between beamforming (which reduces the need for equalization of long delay spreads) and channel equalization (which reduces the need for directional transmission).

Channel modeling for simulation studies and system design is an important part of current work on millimeter-wave communication. Several models are described in Raschkowski et al. [47] and Rappaport et al. [48]. Ray tracing “uses computer

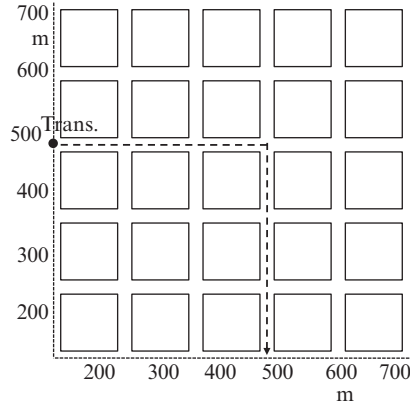


FIG. 1.38

Example of METIS simplified ray tracing model [47].

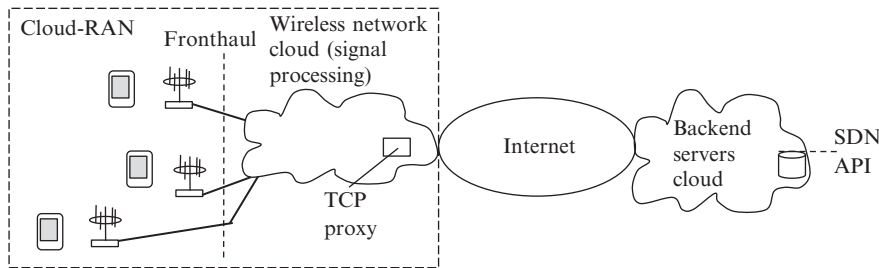
simulation to model and discretize the energy radiated in space as it interacts with a computer model of the physical environment [48].” A model can include reflections, scattering, and atmospheric attenuation. The METIS map-based model, based on simplified ray tracing, begins with a simple geometric description of the propagation environment using geographic maps or 3D models of indoor environments. Fig. 1.38 illustrates such a simplified geometric description for a rectangular city grid. Modeling also can be done through empirical measurements, such as channel soundings in selected environments such as city streets and university campuses. Analytical models form a third category, beginning with the simple log-distance path loss model:

$$P_r(d) = P_t K_{fs} (d_0/d)^\alpha \quad (1.7)$$

for a propagation distance  $d$ , a close-in (but in the far field) free space path loss reference distance  $d_0$ , and a constant  $K_{fs}$  and path loss exponent  $\alpha$  that are selected in accordance with empirical measurements [48].

### 1.6.3 WIRELESS TRANSMISSION IN THE CLOUD

Aside from transmission through literal clouds, the precipitation mentioned above, wireless communication is increasingly taking advantage of the economies and performance gains of shared distributed resources. The Radio Access Network (RAN) is an unseen but vital part of the wireless digital transmission system. Traditionally, baseband radio signal processing, mapping information streams from the wired service network into radio signals destined for user devices and the reverse for radio signals coming from the user devices, occurs at the base station. These signal processing actions are computing tasks that might be handled more efficiently by shared computing resources located somewhere within the computing

**FIG. 1.39**

The Cloud-RAN with signal processing in the wireless network cloud rather than at each base station, and software-defined network functions in a backend server, cloud.

Source: Adapted from Y. Cai, F. Yu, S. Bu, *Cloud Radio Access Networks (C-RAN) in Mobile Cloud Computing Systems*, in: *Proc. 2014 IEEE INFOCOM Workshop on Mobile Cloud Computing*.

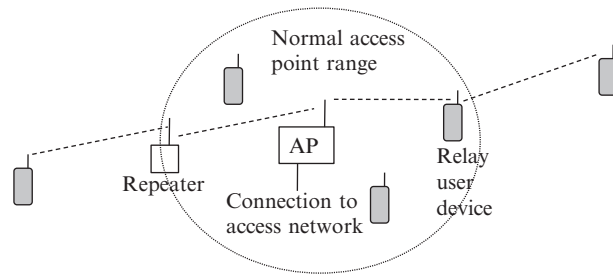
resources cloud. As noted in Cai et al. [49], “This transition from distributed to centralized infrastructure for baseband processing can have significant benefits: saving the operating expenses due to centralized maintenance; improving network performance due to advanced coordinated signal processing techniques; reducing energy expenditure by exploiting the load variations.” This is the essence of the Cloud-RAN, a concept particularly applicable to the many very small base stations that are promising to become ubiquitous in 5G access networks.

Fig. 1.39 illustrates the Cloud-RAN concept and further introduces the possibility of SDN control of network and service configuration and management. There are two clouds, one handling the immediate signal processing needs of a RAN serving a several-base station, and the other the SDN functions that may serve multiple RANs and include, for example, association of base stations with RANs, managing handoff between RANs, performance monitoring, usage measurement for billing, distributing signal processing load among multiple servers within the wireless network cloud, and facilitating redundant functionality for robustness.

The fronthaul from base stations, which may only contain power amplifiers and antennas, is likely to be radio over fiber (RoF), carrying either analog or digitized radio frequency (RF) or intermediate frequency data streams. RoF transmission requires considerably larger capacity than in conventional base station networks where only user data are carried and all RF processing occurs in the base stations. Nevertheless, the cost savings from sharing signal processing functions in the wireless network cloud are likely to offset the increased cost of transmission.

### 1.6.4 IEEE 802.11 WIRELESS LANS AND SOME ALTERNATIVES

IEEE 802.11 (“WiFi”) networks very likely carry the bulk of the world’s digital transmission traffic. They are primarily one-hop local area systems in which all mobile units communicate directly with a single access point connected to an access

**FIG. 1.40**

An IEEE 802.11 network with relay and repeater extensions.

Source: Adapted from D. Zhao, T. Todd, *Real-time traffic support in relayed wireless access networks using IEEE 802.11*, *IEEE Wireless Communications*, April, 2004.

network. But extensions through relay nodes are also possible, as Fig. 1.40 illustrates, and such self-organizing networks can significantly extend the range and utilization rate of the access point. The relay nodes may be dedicated network extension nodes or user devices with added relay capabilities. A repeater is a simpler range extension device, lying between an access point and client terminals, which simply retransmits everything it hears. This increases the usable distance between access points and client terminals but reduces the overall traffic capacity of the access node because the repeater retransmits data frames, duplicating traffic and possibly halving the total capacity [50]. A repeater also requires powering that a battery-powered relay node does not.

IEEE 802.11 is, like Ethernet, a contention system with users competing for transmission time on each of the available carrier frequencies, primarily within the unlicensed (ISM and RF devices) portions of the 2.4 and 5 GHz frequency bands [51]. The link-level protocol used to resolve the contention is carrier sense multiple access/collision avoidance (CSMA-CA) with an explicit acknowledgment and exponential backoff, differing from Ethernet's CSMA-CD by avoiding collisions rather than detecting them and trying again. A sender listens, backs off (delays) transmission according to the exponential protocol similar to that of Ethernet, transmits a frame, waits for an acknowledgment (ACK) and, if there is a timeout waiting for the ACK, goes again to the backoff procedure. Several generations of IEEE 802.11 standards, listed in Table 1.4, have steadily increased data rate.

Propagation conditions determine range as in wireless access networks. Table 1.5 illustrates typical in-building losses over distance and through walls for IEEE 802.11g and 802.11n signals. Note that increasing distance and walls increases signal loss, but at a decreasing rate.

IEEE 802.11 is generally not used for very short distances, for example, for personal computer and smartphone peripherals such as earpieces, speakers, mice, and keyboards. These and a range of rising body-area applications are more likely to

**Table 1.4** IEEE 802.11 Major Standards

Standard	Modulation	Band (GHz)	Max. Data Rate (Mbps)
802.11b	Direct-sequence spread spectrum	2.4	11
802.11a	OFDM/64QAM	5	54
802.11g	OFDM/64QAM	2.4	54
802.11n	MIMO/OFDM/64QAM	2.4 and 5	200
802.11ac	MultiuserMIMO/OFDM/256QAM	5	1300

**Table 1.5** Distance and Absorption Indoor Losses for IEEE 802.11 Signals

Distance (m)	10	15	20	25	30
Number of walls	1	2	4	5	6
Absorption (dBm)					
802.11g	−10	−16	−20.8	−22.5	−24
802.11n	−9	−14	−25	−26.8	−28

Source: Adapted from S. Japertas, et al., *Research of IEEE 802.11 standard signal propagation features in multi partition indoors*, in: *IEEE Second Int. Conf. on Digital Information Processing & Communications*, 2012.

use the very low powered Bluetooth [52] transmission system. Bluetooth employs a frequency-hopping system in which short time slots are sent on different subchannels in a random hopping pattern.

Free-space infrared optical communication is another alternative for room-area communications, for applications as simple as television remote controls but going beyond to higher rates. Recent research suggests that OFDM, with signals modified to accommodate the nonnegative nature of optical signals, might be a successful technique to combat the serious multipath interference seen in room-area environments [53].

## 1.7 ALL THE REST

The brief introduction in this chapter to digital transmission history and the major digital transmission areas sets the stage for the in-depth discussions of the rest of the book. To keep this broad overview to a reasonable size, several topics such as undersea digital transmission systems, were regrettably not included. We hope the reader will understand and find this book a helpful guide to what digital transmission is, how it works, and how it is likely to advance in the years to come.

## REFERENCES

- [1] G.J. Holzmänn, B. Pehrson, *The Early History of Data Networks*, Wiley-IEEE Computer Society Press, 1994.
- [2] D.A. Huffman, A method for the construction of minimum-redundancy codes, in: *Proc. of the I.R.E.*, 1952.
- [3] G. Squier, Multiplex Telephony and Telegraphy by Means of Electric Waves Guided by Wires, *Trans. AIEE* 30 (2) (1911) 1675–1680.
- [4] H.D. Luke, The origins of the sampling theorem, *IEEE Commun. Mag.* 37 (4) (1999) 106–108.
- [5] A.H. Reeves, The past, present, and future of PCM, *IEEE Spectr.* (1965).
- [6] M. Konate, P. Kabal, Quantization noise estimation for long-PCM, in: *Proc. IEEE CCECE 2011, 24th Annual Canadian Conference on Electrical & Computer Engineering*, Niagara Falls, Ontario, Canada, May 8–11, 2011.
- [7] D.R. Smith, *Transmission Systems*, third ed., Springer, 2004.
- [8] AT&T Bell Labs Staff, *A History of Engineering and Science in the Bell System: Transmission Technology*, AT&T Bell Labs, 1985.
- [9] J. Hecht, *City of Light: The Story of Fiber Optics*, Oxford University Press, New York, 1999.
- [10] S. Pachnicke, *Fiber-Optic Transmission Networks*, Springer-Verlag, Berlin, 2012.
- [11] S. Jansen, I. Morita, T. Schenk, D. van den Borne, Optical OFDM—a candidate for future long-haul optical transmission systems, in: *Proc. IEEE OFC/NFOEC*, 2008.
- [12] A.C. Clarke, *Extra-Terrestrial Relays*, *Wireless World (U.K.)*, 1945.
- [13] IEEE Communications Society, *A Brief History of Communications*, 2nd edition, 2012.
- [14] D. Martin, *Communication Satellites*, fourth ed., Aerospace Corporation, 2000.
- [15] R. Gedney, Advanced communications technology satellite (ACTS), *Acta Astronaut.* 26 (11) (1992).
- [16] S.B. Weinstein, *Getting the Picture: A Guide to CATV and the New Electronic Media*, IEEE Press, 1984.
- [17] J. Riera, Ka-band propagation characterization: Madrid experiment, in: *Proc. IEEE Int. Symp. on Broadband Multimedia Systems and Broadcasting*, Bilbao, Spain, 2009.
- [18] S. Weinstein, V. Koll, Simultaneous two-way data transmission over a two-wire circuit, *IEEE Trans. Comm.* 21 (1) (1973) 143–147.
- [19] R. Gitlin, J. Hayes, S. Weinstein, *Data Communications Principles*, Plenum, 1992.
- [20] G. Ungerboeck, Trellis-coded modulation with redundant signal sets, part 1, introduction, and part 2, state of the art, *IEEE Commun. Mag.* 25 (2) (1987) 5–21.
- [21] R. Lucky, Automatic equalization for digital communications, *Bell Syst. Tech. J.* 44 (1965) 547–588.
- [22] A. Lender, Correlative level coding for binary data transmission, *IEEE Spectr.* 3 (1966) 104–115.
- [23] O. Inoue, Implementation in Japan (ISDN), *IEEE Commun. Mag.* 30 (8) (1992) 54–57.
- [24] A. Gelman, et al., A store and forward architecture for video on demand service, in: *Proc. IEEE ICC 91*, Denver, June, 1991.
- [25] S. Weinstein, The history of OFDM, *IEEE Commun. Mag.* (2009) 26–35.
- [26] G. Ginis, J. Cioffi, Vectored transmission for digital subscriber line systems, *IEEE J. Select. Areas Commun.* 20 (5) (2002) 1085–1104.
- [27] S. Weinstein, T. Wang, Y. Luo, *The ComSoc Guide to Passive Optical Networks: Enhancing the Last Mile Access*, Wiley-IEEE Press, 2011.

- [28] M. Schwartz, *Computer-Communication Network Design and Analysis*, Prentice-Hall, 1977.
- [29] S.K. Schlar, *Inside X.25: A Manager's Guide*, McGraw-Hill Information, 1990.
- [30] Ietf, RFC 3031, Multiprotocol Label Switching Architecture, 2001, Available from: <https://tools.ietf.org/html/rfc3031>.
- [31] M. de Prycker, *Asynchronous Transfer Mode: Solution for Broadband ISDN*, Prentice-Hall, 1995.
- [32] B.G. Lee, W. Kim, *Integrated Broadband Networks: TCP/IP, ATM, SDH/SONET and WDM/Optics*, Artech House, 2002.
- [33] CCITT Recommendation I.432, B-ISDN User-Network Interface—Physical Layer Specification, 1991.
- [34] CCITT Recommendation I.321, B-ISDN Protocol Reference Model and Its Application, 1991.
- [35] N. Abramson, The ALOHA system—another alternative for computer communications, in: *Proc. ACM 1970 Fall Joint Computer Conference*, November 1970.
- [36] C.E. Spurgeon, J. Zimmerman, *Ethernet: The Definitive Guide*, second ed., O'Reilly Books, 2014.
- [37] J.A. Fleming, *The Principles of Electric Wave Telegraphy and Telephony*, Longmans, Green & Co., London, 1910.
- [38] O. Vendik, Significant contribution to the development of wireless communication by Professor Alexander Popov, *IEEE Commun. Mag.* 48 (10) (2010) 20–26.
- [39] J.S. Belrose, Fessenden and Marconi: their differing technologies and transatlantic experiments during the first decade of this century, in: *IEEE International Conf. on 100 Years of Radio*, London, September 5–7, 1995, Available from: [www.ieee.ca/millennium/radio/radio\\_differences.html](http://www.ieee.ca/millennium/radio/radio_differences.html).
- [40] M. Zimmerman, A.L. Kirsch, The AN/GS-10 (KATHRYN) variable rate data modem for HF radio, *IEEE Trans. Commun. Technol.* 15 (2) (1967) 197–204.
- [41] G. Stuber, *Principles of Mobile Communication*, second ed., Kluwer Academic Publishers, 2001.
- [42] A.J. Viterbi, *CDMA: Principles of Spread Spectrum Communication*, first ed., Prentice-Hall, 1995.
- [43] N. Tokareva, *Bent Functions: Results and Applications to Cryptography*, Academic Press, 2015.
- [44] A. Paulraj, R. Naar, D. Gore, *Introduction to Space-Time Wireless Communications*, Cambridge Univ. Press, 2003.
- [45] J. Wannstrom, LTE-Advanced, 3GPP, June 2013, Available from: [www.3gpp.org/technologies/keywords/acronyms/97-lte-advanced](http://www.3gpp.org/technologies/keywords/acronyms/97-lte-advanced).
- [46] V. Veeravalli, Y. Liang, A. Sayeed, Correlated MIMO wireless channels: capacity, optical signaling, and asymptotics, *IEEE Trans. Inf. Theory* 51 (6) (2005) 2058–2072.
- [47] L. Raschkowski, et al., M.E.T.I.S. and deliverable D.1.4, European Seventh Framework Programme, METIS (Mobile and wireless communications Enablers for the Twenty-twenty Information Society) project, April 2015, Available from: [https://www.metis2020.com/wp-content/uploads/deliverables/METIS\\_D1.4\\_v2.pdf](https://www.metis2020.com/wp-content/uploads/deliverables/METIS_D1.4_v2.pdf).
- [48] T. Rappaport, R. Heath, R. Daniels, J. Murdock, *Millimeter Wave Wireless Communication*, Prentice-Hall, 2015.
- [49] Y. Cai, F. Yu, S. Bu, Cloud Radio Access Networks (C-RAN) in mobile cloud computing systems, in: *Proc. 2014 IEEE INFOCOM Workshop on Mobile Cloud Computing*, 2014.
- [50] J. Geier, *Designing and Deploying 802.11n Wireless Networks*, Cisco Press, 2010.

- [51] FCC Online Table of Frequency Allocations, August 13, 2015, Available from: <https://transition.fcc.gov/oet/spectrum/table/fcctable.pdf>.
- [52] J.-S. Lee, Y.-W. Su, C.-C. Shen, A comparative study of wireless protocols: Bluetooth, UWB, ZigBee and Wi-Fi, in: IEEE Industrial Electronics Society 33rd Annual Conf., Taipei, November 2007.
- [53] D.J.F. Barros, S.K. Wilson, J.M. Kahn, Comparison of orthogonal frequency-division multiplexing and pulse-amplitude modulation in indoor optical wireless links, *IEEE Trans. Commun.* 60 (1) (2012) 153–163.

# Modulated signals and $I/Q$ representations of bandpass signals

# 2

S.G. Wilson\*, T. Xie†

University of Virginia, Charlottesville, VA, United States\* SanDisk Corporation, Milpitas, CA, United States†

## CHAPTER OUTLINE

<b>2.1 Introduction .....</b>	<b>49</b>
<b>2.2 Bandpass Signal Representation .....</b>	<b>51</b>
2.2.1 Energy/Power Calculations.....	54
2.2.2 Analytic Signal .....	57
<b>2.3 Bandpass Linear Systems .....</b>	<b>59</b>
<b>2.4 Bandpass Random Processes .....</b>	<b>62</b>
2.4.1 Preliminaries.....	62
2.4.2 Bandpass Gaussian Processes .....	63
<b>2.5 Application to Bandpass Nonlinearity .....</b>	<b>64</b>
<b>2.6 Sampling of Bandpass Signals.....</b>	<b>66</b>
2.6.1 More on Demodulation .....	69
<b>References.....</b>	<b>71</b>

## 2.1 INTRODUCTION

Most of the signals that communication engineers encounter are *bandpass* (or passband) signals, loosely meaning that the frequency content of these signals is confined to a relatively small band of frequencies around some identifiable high frequency, often called the carrier frequency. For example, a digital satellite transmission carrying 60 Mbps using quadrature phase-shift keying QPSK modulation of a 12 GHz carrier has a bandwidth of perhaps 36 MHz, less than 1% of the center frequency. A fiber optic link may be conveying binary on/off modulation at a rate of 1 Gbps, but since the center frequency may be nearly 200 THz (1.55  $\mu\text{m}$  wavelength), the percentage bandwidth is even smaller. The same may be said for most analog transmission techniques, including amplitude modulation (AM) and frequency modulation (FM) broadcasting.

This situation exists for two distinct reasons, even though the intrinsic message bandwidth does not require it:

- Sharing the electromagnetic spectrum with other users has meant adoption of steadily higher frequency for spectrum availability.
- Physical propagation-related reasons require, or augur for high frequency transmission. Fiber optic cables propagate only optical-frequency signals for example, and small radio-frequency antennas are more efficient when the wavelength becomes shorter as operating frequency increases.

Furthermore, the signal processing systems used in communication tend to have bandpass nature, either because it is difficult to realize wide bandwidth technology or because it is natural in handling bandpass signals. Notable examples are antennas, amplifiers, and bandpass filters used for frequency selection.

Such signals and systems are described by real (physical) functions and we can study or process, such signals in the same way as we do any lower-frequency signal, applying standard signal analysis tools of transforms and convolution, and can perform power/energy calculations in exactly the same manner. However, it is often convenient, and notationally more compact, to utilize what is called the *complex envelope representation* for such signals, which in essence represents a bandpass signal by an equivalent (complex) low-frequency waveform. (Such equivalences are prevalent in circuit analysis when dealing with sinusoidal excitation, and in representing sinusoidal electromagnetic waves, where the complex equivalent signal, or phasor equivalent, is a constant.) Of course, in the implementation of transmitters and receivers, real signals are utilized throughout, so this mathematical construct eventually ties back to real bandpass signals and systems.

The principal benefits of this representation are the following:

- Analysis is easier—all we really need to be concerned with is the behavior of the modulation signal associated with the bandpass signal.
- Computer simulation is greatly simplified, since we may work with a low-frequency signal that allows a much lower sampling rate.
- The bandpass/lowpass transformations are at the heart of most practical signal processing in receivers and transmitters.

Illustration of these benefits will emerge in examples below.

Our discussion here will be in the context of continuous-time (CT) signals, though many of the same ideas carry over to analysis of discrete-time (DT) signals, and these are important in many modern applications, especially “software-defined radio” [1]. We will begin by regarding the signal of interest to be deterministic, that is, nonrandom. Then we tie bandpass systems together with bandpass signals. Following this development the extension to *bandpass random processes* is relatively straightforward. The chapter concludes with an application of use of the complex envelope in bandpass nonlinear amplifiers and with material on sampling and demodulation of bandpass signals, using an application in digital satcom reception that incorporates many of the ideas presented.

## 2.2 BANDPASS SIGNAL REPRESENTATION

We start by describing a real bandpass signal  $x(t)$  in the frequency domain, sketching its Fourier transform  $X(f) = A(f) \exp(j\alpha(f))$  as shown in Fig. 2.1. We write  $x(t) \leftrightarrow X(f)$  to represent the Fourier transform relationship between these functions.  $X(f)$  will be complex in general, but because it is the transform of a real signal, it will possess conjugate symmetry about zero, that is,  $X(f) = X^*(-f)$ , implying the magnitude function  $A(f)$  is even and the phase function  $\alpha(f)$  is odd in  $f$ . Notice we do not place any restriction on the detailed shape of the spectrum, for example, its fractional bandwidth or symmetry about a center frequency. We only assume that the signal is bandlimited, meaning that the Fourier spectrum is nonzero only over a region around some high-frequency carrier; the percentage bandwidth is not important.

We wish to relate the bandpass signal,  $x(t)$ , or  $X(f)$ , to a corresponding low-pass signal,  $\tilde{x}(t)$ , or  $\tilde{X}(f)$ . We make the following claim, then establish its validity:

$$x(t) = \text{Re} \left\{ \sqrt{2} \tilde{x}(t) e^{j2\pi f_0 t} \right\}, \quad (2.1)$$

where  $\tilde{x}(t)$  is a complex low-pass signal whose Fourier transform is given by

$$\tilde{X}(f) = \tilde{A}(f) e^{j\tilde{\alpha}(f)} = \sqrt{2} [X(f + f_0)]_{\text{LP}}, \quad (2.2)$$

and where “LP” stands for “take the low frequency component of the term in brackets.” In other words, to find  $\tilde{X}(f)$ , simply scale the bandpass signal’s spectrum by  $\sqrt{2}$ , then shift it to the left by  $f_0$  along the frequency axis and retain the zone around zero frequency.

The claim establishes a relation between the real bandpass signal of interest and a unique low-pass signal  $\tilde{x}(t)$ , this uniqueness relying upon the 1–1 property of the Fourier transform operator.

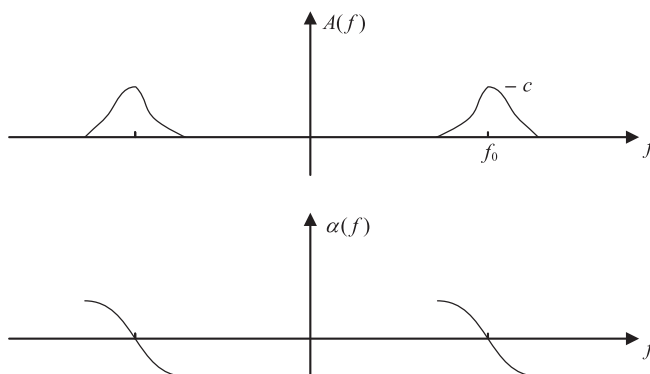
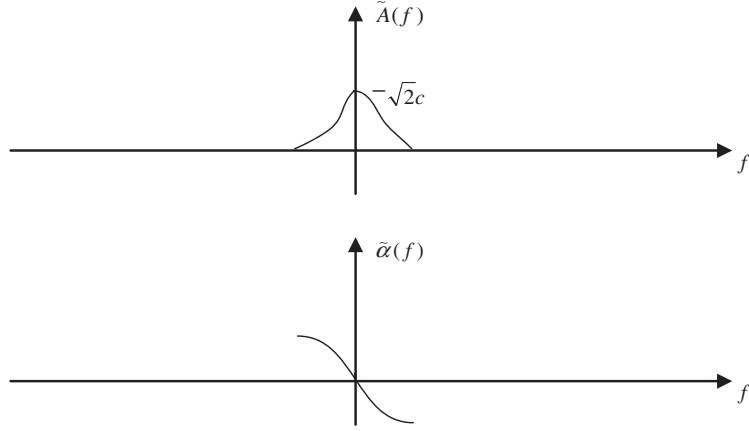


FIG. 2.1

Bandpass signal in frequency domain.

**FIG. 2.2**

Frequency spectrum of complex equivalent signal.

Before proving the correctness of this relation we illustrate the method with the response of Fig. 2.1. We can pick *any positive* frequency  $f_0$  in the region of support of  $X(f)$  and associate  $x(t)$  with a low-pass signal  $\tilde{x}(t)$ . For example, picking  $f_0$  as shown in the figure, and applying the definition (2.2) we find that the Fourier transform of the complex equivalent signal is shown in Fig. 2.2. Note the amplitude scale change. In general  $\tilde{X}(f)$  will not have conjugate symmetry about zero frequency (whenever the bandpass signal spectrum is asymmetric about the adopted reference frequency  $f_0$ ), and thus  $\tilde{x}(t)$  is usually a complex function of time as the name suggests. Examples of this complex envelope are provided below.

To establish the validity of Eqs. (2.1), (2.2) we show the Fourier transform of Eq. (2.1) is correct. By definition, this is

$$X(f) = \int_{-\infty}^{\infty} \text{Re} \left\{ \sqrt{2} \tilde{x}(t) e^{j2\pi f_0 t} \right\} e^{-j2\pi f t} dt. \quad (2.3)$$

Now we use the relation that for any complex quantity  $c$ ,  $\text{Re}\{c\} = (c + c^*)/2$ , leading to

$$\begin{aligned} X(f) &= \int \frac{1}{2} \left[ \sqrt{2} \tilde{x}(t) e^{j2\pi f_0 t} \right] e^{-j2\pi f t} dt + \int \frac{1}{2} \left[ \sqrt{2} \tilde{x}^*(t) e^{-j2\pi f_0 t} \right] e^{-j2\pi f t} dt \\ &= \frac{1}{\sqrt{2}} \tilde{X}(f - f_0) + \frac{1}{\sqrt{2}} \tilde{X}^*(-f - f_0), \end{aligned} \quad (2.4)$$

which follows from operational properties of the Fourier transform. Notice that the right-hand side is a conjugate symmetric function, as it must be to be the transform of a real signal. Now, substituting the relation (2.2),  $\tilde{X}(f) = \sqrt{2}X(f + f_0)_{\text{LP}}$ , into this final expression shows that the first term gives the proper Fourier structure for the

positive frequency portion  $X(f)$ , and the second term properly describes the negative frequency portion.

The signal  $\tilde{x}(t)$  (or  $\tilde{X}(f)$ ) is called the *complex equivalent low-pass signal*, or often the *complex envelope* of  $x(t)$ , since Eq. (2.1) regard  $\tilde{x}(t)$  as the complex envelope signal multiplying  $e^{j2\pi f_0 t}$ , whose real part then provides the actual bandpass signal. It is important to emphasize that  $\tilde{x}(t)$  conveys everything about the original bandpass signal we might wish to determine. However, we obtain a different complex envelope signal if we adopt a different reference frequency  $f_0$ . Thus, we should be precise by saying  $\tilde{x}(t)$  is the complex envelope relative to some frequency  $f_0$ .

When starting with a bandpass signal's Fourier spectrum, Eq. (2.2) provides an easy way to find the complex envelope. It is frequently the case, however, that determination of the complex envelope in the time-domain follows from inspection. Often, we encounter a bandpass signal written in either quadrature modulation form<sup>1</sup>

$$x(t) = \sqrt{2}[i(t) \cos(2\pi f_0 t) + q(t) \sin(2\pi f_0 t)] \quad (2.5)$$

or in magnitude/phase (polar) form

$$x(t) = \sqrt{2}a(t) \cos(2\pi f_0 t + \theta(t)). \quad (2.6)$$

The relationships between these quantities are

$$a(t) = (i^2(t) + q^2(t))^{1/2}, \quad \theta(t) = -\tan^{-1}(q(t)/i(t)) \quad (2.7)$$

and

$$i(t) = a(t) \cos \theta(t), \quad q(t) = a(t) \sin \theta(t). \quad (2.8)$$

Simple calculation shows that the complex envelope, relative to  $f_0$ , is given by

$$\tilde{x}(t) = a(t)e^{j\theta(t)} = i(t) - jq(t), \quad (2.9)$$

which can be verified by substitution into Eq. (2.1). Correspondingly we have  $\tilde{X}(f) = I(f) - jQ(f)$ .

**Example 2.1** (Frequency modulation). In FM, the real bandpass signal can be expressed as

$$x(t) = A \cos \left( 2\pi f_0 t + 2\pi k_f \int_{-\infty}^t m(\tau) d\tau \right), \quad (2.10)$$

where  $A$  is the carrier amplitude,  $f_0$  is the carrier frequency,  $k_f$  is a modulator scale factor, and  $m(\cdot)$  is the modulating signal, carrying either an analog or digital message. By converting Eq. (2.10) to quadrature form using trigonometric identities we can obtain  $i(t)$  and  $q(t)$  signals, then  $\tilde{x}(t)$ . Alternatively it is readily seen using Euler's relation that

---

<sup>1</sup> $i(t)$  and  $q(t)$  are known as the “in-phase” and “quadrature” components, or so-called  $I/Q$  components, of the signal.

$$\tilde{x}(t) = \frac{A}{\sqrt{2}} \exp \left( j2\pi k_f \int_{-\infty}^t m(\tau) d\tau \right), \quad (2.11)$$

which is a low-frequency complex signal whose locus is a circle with radius  $A/\sqrt{2}$ . Back-substitution of this into Eq. (2.1) recovers Eq. (2.10). Such signals are known as *constant envelope* because the standard envelope of the bandpass signal is  $|x(t)| = A$ .

Determination of  $\tilde{X}(f)$  can be made by using a Taylor series expansion of  $e^u$  on Eq. (2.11), then Fourier transforming term-by-term to obtain

$$\tilde{X}(f) = \frac{A}{\sqrt{2}} \left[ \delta(f) + \frac{k_f M(f)}{f} + \frac{k_f^2}{2} \left[ \frac{M(f)}{f} \right] \star \left[ \frac{M(f)}{f} \right] + \dots \right], \quad (2.12)$$

where  $M(f)$  is the Fourier spectrum of  $m(t)$  and  $\star$  denotes convolution. This expresses the well-known broadening of the spectrum in FM, depending on modulation index.

### 2.2.1 ENERGY/POWER CALCULATIONS

The energy of a real signal, bandpass or not, when normalized to a 1 ohm resistance, is

$$E_x = \int_{-\infty}^{\infty} x^2(t) dt. \quad (2.13)$$

By Parseval's relation this is equivalently

$$E_x = \int_{-\infty}^{\infty} |X(f)|^2 df. \quad (2.14)$$

(Here it is assumed that the signal is an energy signal, having finite energy; power signals have similar conclusions dealing with average power.)

Using the bandpass signal representation in Eq. (2.4), Eq. (2.14) becomes

$$E_x = \int \left[ \frac{1}{\sqrt{2}} \tilde{X}(f - f_0) + \frac{1}{\sqrt{2}} \tilde{X}^*(-f - f_0) \right] \left[ \frac{1}{\sqrt{2}} \tilde{X}(f - f_0) + \frac{1}{\sqrt{2}} \tilde{X}^*(-f - f_0) \right]^* df. \quad (2.15)$$

By expanding the integrand, then realizing that under the assumptions about the bandpass signal, terms of the form  $\tilde{X}(f - f_0)\tilde{X}(-f - f_0)$  are 0 for all  $f$ , we find that

$$\begin{aligned} E_x &= \frac{1}{2} \int |\tilde{X}(f - f_0)|^2 df + \frac{1}{2} \int |\tilde{X}(-f - f_0)|^2 df \\ &= \int_{-\infty}^{\infty} |\tilde{X}(f)|^2 df = E_{\tilde{x}}. \end{aligned} \quad (2.16)$$

So, the energy attached to the complex envelope signal equals that of the real bandpass signal.

*Caution: Perhaps half the presentations of this material choose to omit the scale factor  $\sqrt{2}$  in Eq. (2.1), which leads to corresponding scale changes for  $\tilde{x}(t)$  and  $\tilde{X}(f)$ ,*

and also results in the energy of the complex envelope signal being twice that of the bandpass signal. This can cause confusion and one must be careful about which definition is in effect.

Many discussions of this representation of bandpass signals indicate the relations above are only true for *narrowband* signals, which is never precisely defined. Our derivation shows that the relations hold provided only that there is a region around zero frequency devoid of spectral content, and the reference frequency is chosen so that  $\tilde{X}(f - f_0)$  and  $\tilde{X}(-f - f_0)$  do not overlap in frequency. Thus, the relationships hold for such applications as former voice-band modem data transmission, wherein a carrier at 1800 Hz is modulated with a pulse-shaped signal having baseband bandwidth of 1400 Hz. The resulting bandpass signal extends from 400 to 3200 Hz and is not a narrowband bandpass signal by any means. It is nonetheless possible to define the complex envelope relative to, say, an 1800 Hz frequency.

It is perhaps good to remember, however, that no time-limited signal can strictly satisfy the bandlimited property we have assumed here, so one should be cautious in applying this theory to pulsed signals, unless the reference frequency is large relative to the reciprocal of the pulse time, in which case, we may regard the bandpass signal as essentially bandlimited. A case that raises possible abuse of this notation is the following example.

**Example 2.2** (Pulsed bandpass signal). Consider a radio frequency (RF) pulse having 1  $\mu$ s duration, symmetric about  $t = 0$ , and suppose the carrier frequency is 2 MHz. The nonzero portion of the real signal  $x(t)$  is shown in Fig. 2.3.

Letting  $\tau = 10^{-6}$  denote the pulse length, calculation shows that the Fourier transform of the pulse waveform is<sup>2</sup>

$$X(f) = \frac{A\tau}{2} \text{sinc}(\pi(f - 2 \times 10^6)\tau) + \frac{A\tau}{2} \text{sinc}(\pi(f + 2 \times 10^6)\tau), \quad (2.17)$$

plotted in Fig. 2.4. ( $X(f)$  is real since  $x(t)$  is even by construction.) Notice there is no region around zero frequency void of spectral components.

It is possible by inspection to see the complex envelope is

$$\tilde{x}(t) = \frac{A}{\sqrt{2}} \text{rect}\left(\frac{t}{\tau}\right) \quad (2.18)$$

since

$$x(t) = \text{Re} \left\{ \sqrt{2} \tilde{x}(t) e^{j2\pi 2 \times 10^6 t} \right\} \quad (2.19)$$

is the original  $x(t)$ . Then  $\tilde{X}(f) = (A\tau)/\sqrt{2} \text{sinc}(\pi f \tau)/\pi f \tau$ . We cannot find this, however, by appeal to

$$\tilde{X}(f) = \sqrt{2} X(f + 2 \times 10^6)_{\text{LP}} \quad (2.20)$$

---

<sup>2</sup>We use the definition  $\text{sinc}(x) = \sin(x)/x$ .

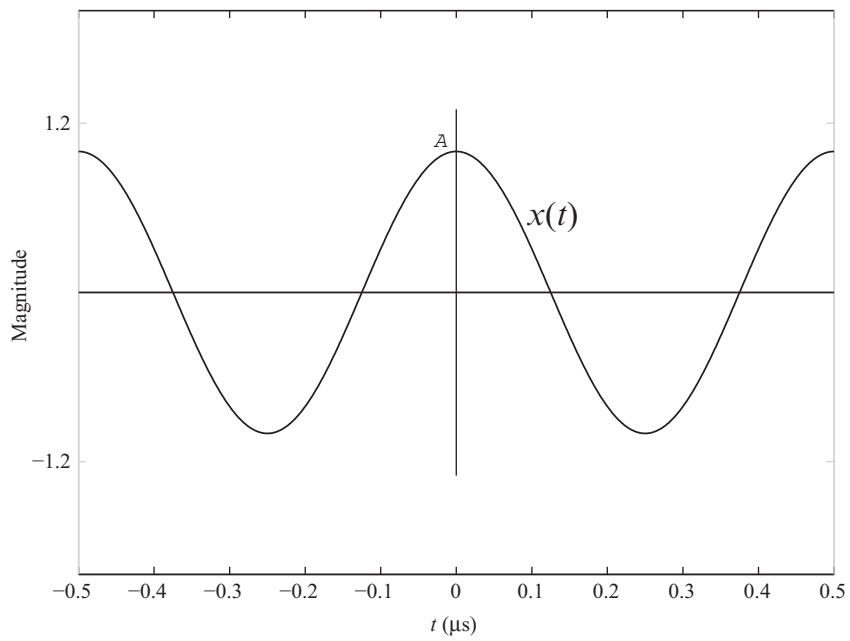


**FIG. 2.3**

Pulsed 2 MHz sinusoid.

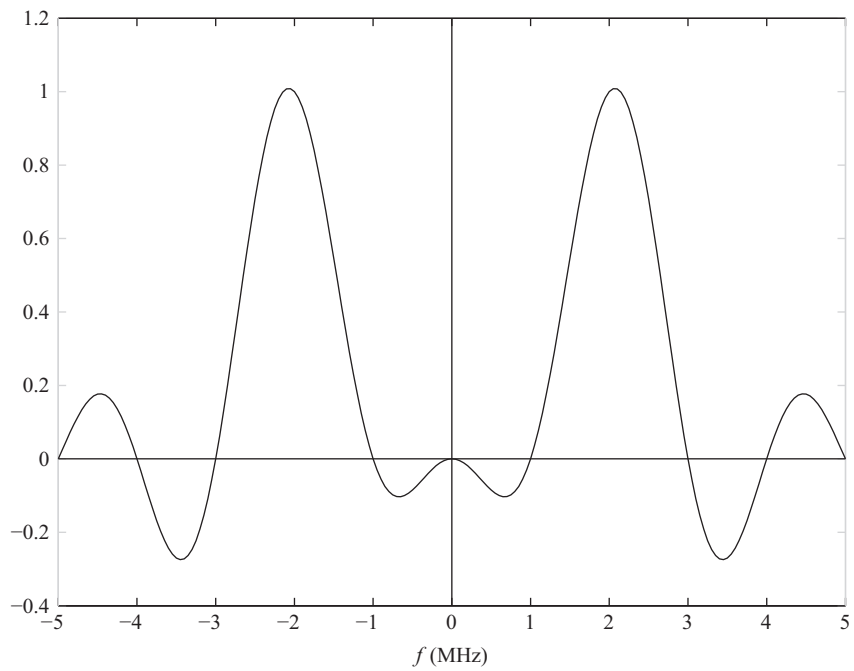


**FIG. 2.4**

Fourier spectrum  $X(f)$  of pulsed 2 MHz sinusoid.

to find the complex equivalent signal. First, there is the question of what bandwidth pertains to the low-pass operator. However, any choice here gives slightly incorrect representation of the original pulsed signal and its energy. Use of Eq. (2.19) is valid, however.

**Example 2.3** (Offset-QPSK). In offset (or staggered) QPSK, the in-phase and quadrature binary symbols  $a_n$  and  $b_n$  are staggered by one original bit duration, then applied to pulse shaping filters whose impulse response is  $p(t)$ , whose outputs then modulate  $\cos(2\pi f_0 t)$  and  $\sin(2\pi f_0 t)$ , respectively. Since the bandpass signal is already in quadrature form, we can immediately write

$$\tilde{x}(t) = i(t) - jq(t), \quad (2.21)$$

where

$$\begin{aligned} i(t) &= \sum_n a_n p(t - nT) \\ q(t) &= \sum_n b_n p(t - nT - T/2) \end{aligned} \quad (2.22)$$

and where  $T$  is called the symbol interval, related to the underlying bit interval by  $T = 2T_b$ , since each symbol conveys 2 information bits.

Fig. 2.5 shows the complex trajectory of  $\tilde{x}(t)$  for a case with  $p(t)$  defined by a square-root raised cosine filter [2], with rolloff factor 0.25. This smoothly evolving trajectory is what allows the bandpass signal to be strictly bandlimited. Staggering the quadrature components of the signal prevents the complex envelope from passing near the origin and helps to reduce the peak-to-rms ratio of the modulated signal, making amplifier design easier.

### 2.2.2 ANALYTIC SIGNAL

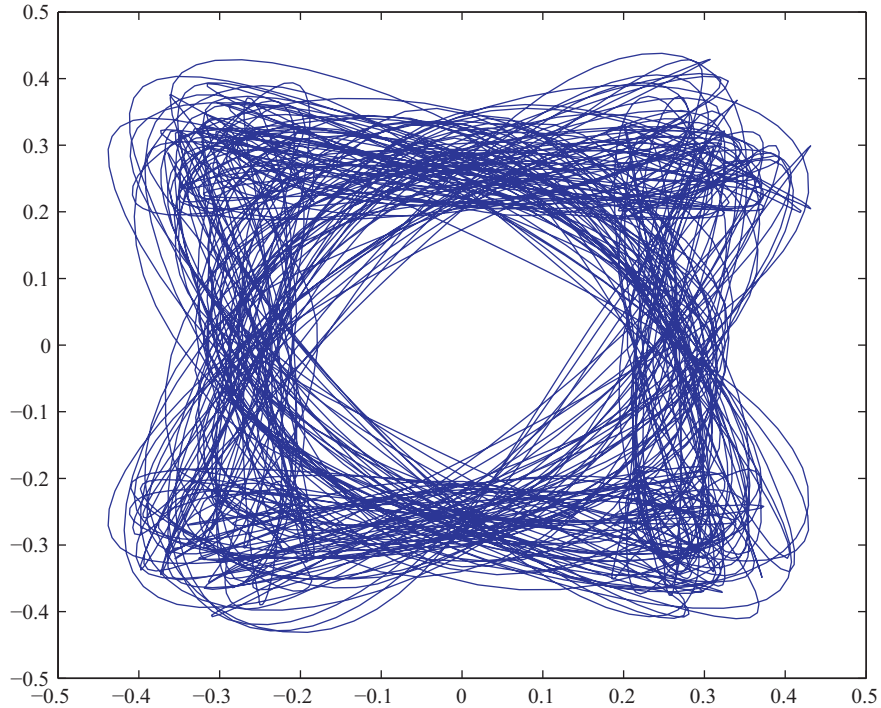
Closely related to the complex envelope of a bandpass signal is the *analytic signal*, an auxiliary complex signal defined to have a Fourier transform that matches the positive frequency portion of the transform of the original real signal, except for a scale factor of 2. We will denote this signal by  $x^+(t) \leftrightarrow X^+(f)$ , as in Haykin [2], where

$$X^+(f) = \begin{cases} 2X(f) & f > 0 \\ 0 & f < 0 \end{cases}. \quad (2.23)$$

At this point it is evident that the analytic signal and the earlier complex envelope are related by

$$\tilde{X}(f) = \frac{1}{\sqrt{2}} X^+(f + f_0). \quad (2.24)$$

In the time domain the relation is  $\tilde{x}(t) = \frac{1}{\sqrt{2}} x^+(t) e^{-j2\pi f_0 t}$ .

**FIG. 2.5**

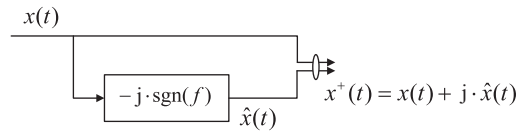
Complex envelope trajectory for offset QPSK with pulse shaping.

We can form this analytic signal with use of a linear filter that forms the *Hilbert transform* of a real signal. The frequency response of the Hilbert transformer is

$$H_{\text{hilb}}(f) = -j \operatorname{sgn}(f), \quad (2.25)$$

which is a linear system that has constant gain = 1 and phase shift of  $-\pi/2$  radians for  $f > 0$ . Implementation of a true Hilbert transformer is impossible, since the phase function is discontinuous at  $f = 0$ , but for bandpass signals we only require Eq. (2.25) to hold over a restricted bandwidth, allowing synthesis with so-called quadrature hybrid RF devices.

If we pass a real bandpass signal through a system shown in Fig. 2.6, and bundle the two real outputs into a single complex signal, its Fourier spectrum is  $X(f) + j(-j \operatorname{sgn}(f))X(f) = 2X(f)$ ,  $f > 0$  as in Eq. (2.23). The corresponding time function is then  $x(t) + j\hat{x}(t)$ , an alternate definition of the analytic signal.

**FIG. 2.6**

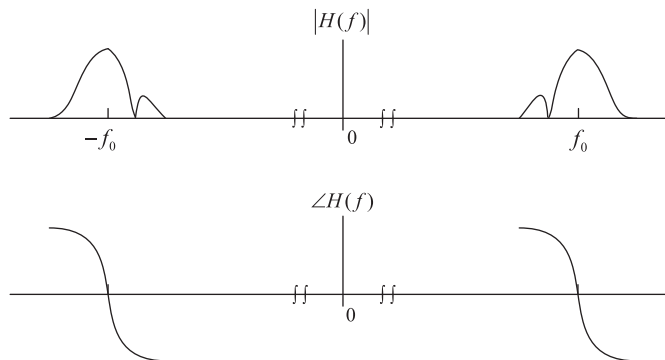
System producing analytic signal  $x^+(t)$ .

By complex heterodyning (multiplying by  $e^{-j2\pi f_0 t}$ ), we obtain the complex envelope signal  $\sqrt{2}\tilde{x}(t)$ .

In modern digital signal processing (DSP) implementation of receivers, this operation is accomplished by beginning with a sampled version of the bandpass signal and implementing the Hilbert transform either with a finite impulse response (FIR) filter or with discrete Fourier transform processing. Heterodyning is performed by multiplying with a DT complex exponential sequence. See Johnson et al. [1] for more details here.

## 2.3 BANDPASS LINEAR SYSTEMS

Any linear, time-invariant system is described by its frequency response  $H(f)$  or by its impulse response  $h(t)$ . A *bandpass* system, or filter, has nonzero  $H(f)$  confined to a region surrounding some high-frequency location, called the center frequency of the filter. Because the filter's impulse response is real, the frequency response will exhibit the same conjugate symmetry that the spectrum of a real signal does. Fig. 2.7 shows a typical bandpass frequency response, intentionally drawn to be asymmetric about  $f_0$ .

**FIG. 2.7**

Frequency response of bandpass system.

The real impulse response of such a bandpass filter will be an oscillatory response that has “period” roughly  $1/f_0$ , for example, of the form

$$h(t) = \operatorname{Re}\{e^{-\alpha t} e^{j2\pi f_0 t}\} = e^{-\alpha t} \cos(2\pi f_0 t), \quad t \geq 0. \quad (2.26)$$

Using methods just described for bandpass signals, we write the bandpass impulse response as

$$h(t) = \operatorname{Re} \left\{ \sqrt{2} \tilde{h}(t) e^{j2\pi f_0 t} \right\}, \quad (2.27)$$

where  $\tilde{h}(t)$  is the *complex equivalent impulse response* of the system. As above, we may define  $\tilde{h}(t)$  through its Fourier transform:

$$\tilde{H}(f) = \sqrt{2} H(f + f_0)_{\text{LP}}. \quad (2.28)$$

As with bandpass signals, we have the low-pass to bandpass relation:

$$H(f) = \frac{1}{\sqrt{2}} \tilde{H}(f - f_0) + \frac{1}{\sqrt{2}} \tilde{H}^*(-f - f_0). \quad (2.29)$$

If we excite the bandpass system with a bandpass signal, the output will be a bandpass signal (as seen by multiplying the Fourier transforms). We can calculate directly, either multiplying transforms or convolving real bandpass responses. However, there is another way, working with the complex equivalent signals themselves. To see how, write the output signal Fourier transform of the input signal transform and the frequency response, each expressed in terms of the complex equivalent frequency function:

$$\begin{aligned} Y(f) &= X(f)H(f) \\ &= \left[ \frac{1}{\sqrt{2}} \tilde{X}(f - f_0) + \frac{1}{\sqrt{2}} \tilde{X}^*(-f - f_0) \right] \times \left[ \frac{1}{\sqrt{2}} \tilde{H}(f - f_0) + \frac{1}{\sqrt{2}} \tilde{H}^*(-f - f_0) \right]. \end{aligned} \quad (2.30)$$

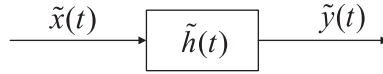
Now assuming that  $\tilde{X}(f - f_0)$  and  $\tilde{H}(f + f_0)$  do not overlap in frequency, two of the four products in Eq. (2.30) vanish, leaving

$$Y(f) = \frac{1}{2} \tilde{X}(f - f_0) \tilde{H}(f - f_0) + \frac{1}{2} \tilde{X}^*(-f - f_0) \tilde{H}^*(-f - f_0). \quad (2.31)$$

We can thus express the system output using complex envelope notation as

$$Y(f) = \frac{1}{2} \tilde{Y}(f - f_0) + \frac{1}{2} \tilde{Y}^*(-f - f_0) \quad (2.32)$$

if  $\tilde{Y}(f) = \tilde{X}(f) \tilde{H}(f)$ . The point is that we can perform operations on the equivalent low-pass signal and system responses, thereby obtaining the complex equivalent signal of the output response, then using this to obtain the actual bandpass signal by

**FIG. 2.8**

Implementation of bandpass filtering using complex equivalent responses.

$$y(t) = \text{Re} \left\{ \sqrt{2} \tilde{y}(t) e^{j2\pi f_0 t} \right\}. \quad (2.33)$$

Because the equivalent low-pass signals are related by  $\tilde{Y}(f) = \tilde{X}(f)\tilde{H}(f)$ , we have also that

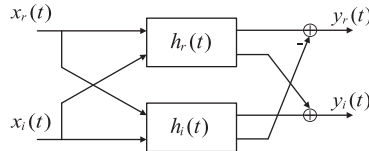
$$\tilde{y}(t) = \tilde{x}(t) * \tilde{h}(t). \quad (2.34)$$

is a time-domain route to calculating the same output response. This relationship is summarized in Fig. 2.8.

For actual signal processing operations or for simulating systems on a computer, we must implement the complex signal operations on real processors.<sup>3</sup> By writing each of the complex responses in Eq. (2.34) as, say,  $\tilde{x}(t) = x_r(t) + jx_i(t)$ , then expanding Eq. (2.34), we find that the output real and imaginary signals that make up  $\tilde{y}(t)$  are

$$\begin{aligned} y_r(t) &= x_r(t) * h_r(t) - x_i(t) * h_i(t) \\ y_i(t) &= x_r(t) * h_i(t) + x_i(t) * h_r(t), \end{aligned} \quad (2.35)$$

where  $h_r(t)$  and  $h_i(t)$  are the real and imaginary components of  $\tilde{h}(t)$ . Thus, to perform the filtering operation at baseband using complex equivalent signals, we implement the process shown in Fig. 2.9, requiring four convolutions. Notice, however, that we may have a system response which is conjugate-symmetric about  $f_0$ , so the corresponding complex equivalent frequency response will be real, in which case half of the required processing indicated in Fig. 2.9 disappears.

**FIG. 2.9**

Implementation of bandpass filtering using real functions.

<sup>3</sup>Packages such as Matlab can handle complex signals directly, but it should be realized that when two such complex signals are multiplied, for example, there are four real multiplications in the background involving the real/imaginary components of the complex signals.

While it may appear that the processing overhead has considerably increased over a direct implementation of filtering at bandpass frequencies, realization of the desired response is often more correctly achieved via baseband processing, then conversion back to bandpass form if desired. Whenever DT processing is involved, the sampling rates involved will generally be much greater in the direct bandpass implementation, even after allowing for the fact that sampling of bandpass signals need not be done at twice the highest frequency for alias-free representation, as discussed below.

## 2.4 BANDPASS RANDOM PROCESSES

We now turn to representation of nondeterministic signals, or *random processes*, that are bandpass in nature. A principal application is in the description of bandpass noise produced as a result of thermal noise and shot-noise processes in receiver circuits, or perhaps from external noise sources. The extension to random processes from the description of deterministic signals in the earlier section is remarkably similar, except that we use the calculus of stationary random processes, for example, correlation functions and power spectra.

### 2.4.1 PRELIMINARIES

In this section, some basic concepts of random processes are summarized prior to the application to bandpass processes. The emphasis shifts here to infinite-duration random signals assumed to be power signals. Readers are invited to consult basic texts in random processes as necessary [3].

A random process  $X(t)$  is *wide-sense-stationary* (WSS) if its mean function is invariant to absolute time and its autocorrelation function depends only on time separation, that is

$$\begin{aligned}\mu(t) &= E[X(t)] = \mu_0, \text{ mean function} \\ R_X(t, t + \tau) &= E[X(t)X^*(t + \tau)] = R_X(\tau), \text{ autocorrelation function.}\end{aligned}\quad (2.36)$$

For a real process, the autocorrelation function is even in  $\tau$ , while for a complex process the autocorrelation function has conjugate symmetry, that is,  $R_X(-\tau) = R_X^*(\tau)$ .

The *power spectral density* of a WSS process is defined as the Fourier transform of the autocorrelation function, and is always a real, nonnegative function of  $f$ , specifying the distribution of average power versus  $f$ . In the case of real random processes, the power spectral density (PSD) is also an even function of  $f$ .

A process is said to be *Gaussian* if any finite collection of random variables associated with the process are jointly Gaussian. Let the random variables be captured by the column vector

$$\mathbf{x} = (x_1, x_2, \dots, x_N)^T. \quad (2.37)$$

In the jointly Gaussian case, the p.d.f. for samples is

$$f(\mathbf{x}) = \frac{1}{(2\pi)^n [\det(\mathbf{K})]^{1/2}} \exp\left(-\frac{1}{2}[\mathbf{x} - \boldsymbol{\mu}]^H \mathbf{K}^{-1}[\mathbf{x} - \boldsymbol{\mu}]\right), \quad (2.38)$$

where  $\boldsymbol{\mu}$  is the mean vector,  $\mathbf{K}$  is the covariance matrix for the set of samples, and  $H$  denotes the conjugate-transpose operation on a vector. Of major analytic importance is that the joint density function, and by extension the process description itself, requires only knowledge of the mean and covariance descriptions, a so-called second-order characterization.

### 2.4.2 BANDPASS GAUSSIAN PROCESSES

Bandpass Gaussian noise typically presents itself in communications applications as the result of bandpass filtering of a wideband Gaussian noise process. This wideband process is physically produced by thermal (or Johnson) noise in lossy circuit elements, by shot-noise associated with electronic and photonic devices, or even by atmospheric and cosmic electromagnetic radiation.

A bandpass process, not necessarily Gaussian, is one that has a power spectrum confined to some region around  $f_0$ . (Notice we use power spectrum here rather than the Fourier spectrum used earlier, since the latter would also be a random process in  $f$ .) Fig. 2.10 illustrates a power spectrum for a real bandpass process. The physical unit for power spectral density is watts/hertz for the vertical scale, or equivalent. Sample functions from this process can be viewed as undergoing amplitude/phase modulation of a sinusoid having frequency  $f_0$ , where the modulation components now are themselves random-processes, but with low-frequency content. We have three representations for such a signal, as before<sup>4</sup>:

$$N(t) = \sqrt{2}[N_c(t) \cos(2\pi f_0 t) + N_s(t) \sin(2\pi f_0 t)] \quad (\text{quadrature form})$$

$$N(t) = \sqrt{2}A(t) \cos(2\pi f_0 t + \theta(t)) \quad (\text{polar form}) \quad (2.39)$$

$$N(t) = \text{Re} \left\{ \sqrt{2} \tilde{N}(t) e^{j2\pi f_0 t} \right\} \quad (\text{complex envelope form}) \quad (2.40)$$

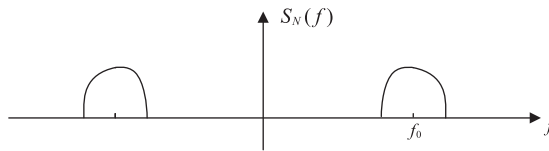
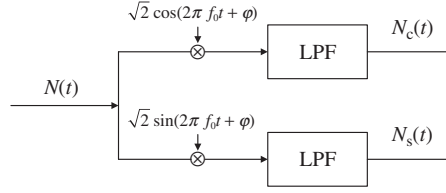


FIG. 2.10

Power spectral density  $S_N(f)$  for bandpass random process.

<sup>4</sup>The factor  $\sqrt{2}$  is embedded as before in the definition.

**FIG. 2.11**

Recovery of in-phase and quadrature components of bandpass random process.

In these above forms,  $N_c(t)$  and  $N_s(t)$  are known as the *in-phase* and *quadrature* components of the bandpass process,  $A(t)$  is the random amplitude function,  $\theta(t)$  is the random phase process, and  $\tilde{N}(t)$  is the (random) complex low-pass signal associated with the bandpass process. We have

$$\tilde{N}(t) = N_c(t) - jN_s(t) = A(t)e^{j\theta(t)}. \quad (2.41)$$

If the bandpass noise process is WSS and Gaussian, it may be shown [2] that the in-phase and quadrature processes are zero-mean Gaussian, and with power spectral densities

$$S_{N_c}(f) = S_{N_s}(f) = \frac{1}{2}[S_N(f - f_0) + S_N(f + f_0)]_{LP}. \quad (2.42)$$

For example, if the bandpass noise has a rectangular PSD with height  $N_0/2$  and bandwidth  $B$ , each of the quadrature components also has PSD with height  $N_0/2$  and positive-frequency extent  $B/2$ .

In addition  $N_c(t)$  and  $N_s(t)$  are uncorrelated at the same time, regardless of symmetry or lack thereof of the bandpass spectrum. So, as with deterministic signals, the power of the bandpass signal matches the power of the complex baseband signal. Finally, the envelope of bandpass Gaussian noise has a Rayleigh probability density function, while the phase angle is uniformly distributed on  $(0, 2\pi)$ .

As with deterministic signals, we may “demodulate” the bandpass process as shown in Fig. 2.11 to recover the in-phase and quadrature components of the bandpass process, except here the recovered processes are random. When a bandpass deterministic signal is also present this demodulator recovers  $I(t) + N_c(t)$  and  $Q(t) + N_s(t)$  in the two arms.

## 2.5 APPLICATION TO BANDPASS NONLINEARITY

The complex envelope notation has benefits even in *nonlinear* bandpass systems, as now illustrated with a power-law nonlinearity that might model a power amplifier, a prevalent source of nonlinearity. Suppose a (deterministic) bandpass signal with carrier frequency  $f_0$  is acted upon by a nonlinearity whose input/output expression is

$$y(t) = a_1 x(t) + a_3 x^3(t - \tau), \quad (2.43)$$

where  $a_i$  are real coefficients and  $\tau$  is a real-valued delay.<sup>5</sup> A third-order model serves to illustrate the method, and we do not include the second-order term since, as seen below, it will not produce “in-band” signal components.

The output bandpass signal is subjected to a *zonal filter* which is a bandpass filter that passes only frequency components near  $f_0$ , rejecting the signal components around  $2f_0$ ,  $3f_0$ , etc. Let the output of this filter be  $z(t)$ . This new bandpass signal has a complex envelope  $\tilde{z}(t)$ , and we can find this directly in terms of  $\tilde{x}(t)$ .

We again write  $x(t) = \text{Re} \left\{ \sqrt{2} \tilde{x}(t) e^{j\omega_0 t} \right\}$  and again use  $\text{Re}\{c\} = (c + c^*)/2$ , where  $c$  is any complex quantity. Defining  $\omega_0 = 2\pi f_0$  and substituting this into the nonlinearity above we obtain

$$\begin{aligned} y(t) = & a_1 \left[ \sqrt{2} \tilde{x}(t) e^{j\omega_0 t} + \sqrt{2} \tilde{x}^*(t) e^{-j\omega_0 t} \right] / 2 \\ & + a_3 \left[ \sqrt{2} \tilde{x}(t - \tau) e^{j\omega_0(t - \tau)} + \sqrt{2} \tilde{x}^*(t - \tau) e^{-j\omega_0(t - \tau)} \right] / 2 \\ & \times \left[ \sqrt{2} \tilde{x}(t - \tau) e^{j\omega_0(t - \tau)} + \sqrt{2} \tilde{x}^*(t - \tau) e^{-j\omega_0(t - \tau)} \right] / 2 \\ & \times \left[ \sqrt{2} \tilde{x}(t - \tau) e^{j\omega_0(t - \tau)} + \sqrt{2} \tilde{x}^*(t - \tau) e^{-j\omega_0(t - \tau)} \right] / 2. \end{aligned} \quad (2.44)$$

Upon expanding the triple product, eliminating terms having frequency  $\pm 3\omega_0$  and regrouping, then applying the identity above for complex variables in reverse, we find the bandpass signal is

$$\begin{aligned} z(t) = & a_1 \text{Re} \left\{ \sqrt{2} \tilde{x}(t) e^{j\omega_0 t} \right\} \\ & + \frac{a_3 (\sqrt{2})^3}{4} [\text{Re}\{\tilde{x}(t - \tau) \tilde{x}^*(t - \tau) \tilde{x}(t - \tau) e^{j\omega_0(t - \tau)}\} \\ & + \text{Re}\{\tilde{x}(t - \tau) \tilde{x}(t - \tau) \tilde{x}^*(t - \tau) e^{j\omega_0(t - \tau)}\} \\ & + \text{Re}\{\tilde{x}^*(t - \tau) \tilde{x}(t - \tau) \tilde{x}(t - \tau) e^{j\omega_0(t - \tau)}\}]. \end{aligned} \quad (2.45)$$

Next, use the fact that the sum of real parts of complex quantities equals the real part of their sum, along with  $z(t) = \text{Re} \left\{ \sqrt{2} \tilde{z}(t) e^{j\omega_0 t} \right\}$  to determine the complex envelope for  $z(t)$  is

$$\tilde{z}(t) = a_1 \tilde{x}(t) + \frac{6a_3}{4} [|\tilde{x}(t - \tau)|^2 \tilde{x}(t - \tau) e^{-j\omega_0 \tau}]. \quad (2.46)$$

This expresses nonlinear distortion of the input signal, with the second term producing spectral broadening of the input signal. System analysis or simulation can be based upon  $\tilde{z}(t)$ . This is an example of a Volterra baseband model for a bandpass nonlinearity.

---

<sup>5</sup>Such models can be applied only over an appropriate range for input signal strength.

As a special case of this result, suppose the input signal is an unmodulated sinusoid with amplitude  $A$  and phase 0. Then  $\tilde{x}(t) = A/\sqrt{2}$ , and

$$\tilde{z}(t) = a_1 \frac{A}{\sqrt{2}} + \frac{3a_3}{4\sqrt{2}} A^3 e^{-j\omega_0 t}. \quad (2.47)$$

As the amplitude of the input signal changes, the output amplitude  $|\tilde{z}(t)|$  changes nonlinearly, and the phase of the output signal changes as well. This is referred to as AM-AM and AM-PM conversion, respectively, in the nonlinear amplifier literature.

## 2.6 SAMPLING OF BANDPASS SIGNALS

Sampling of a CT signal is commonly done to permit storage, digital signal processing, or to enable digital communication of an analog signal. The prevailing question is whether the CT signal can be properly reconstructed from its samples, or alternatively whether the modulation of the bandpass signal can be recovered correctly, which places requirements on the sampling rate relative to the spectral properties of the signal. Sampling is a linear, time-varying operation that produces new frequency components in the sampled signal, known as *aliases*, and a typical goal is to produce sampling capable of reconstruction free from aliasing distortion. The familiar sampling theorem for real signals with nonzero spectrum on  $[-B, B]$  is that sampling frequency must satisfy  $f_s > 2B$ , called the Nyquist rate. The sampling theory can be extended to bandpass signals, with more subtlety. Basically, sampling at rate less, and often much less, than twice the highest frequency is permissible when aliases can be placed in the null regions of the bandpass spectrum.

To frame the problem, suppose we are given a bandpass signal having nonzero spectrum only on the interval  $[f_L, f_U]$  (and its mirror image), with bandwidth  $B = f_U - f_L$ . What sampling rates allow alias-free recovery of the original signal? And what is the smallest of such acceptable sampling rates?

It follows from the standard sampling theorem that sampling at a rate  $f_s > 2f_U$  suffices, but this is often wasteful and produces far more data per unit time than necessary. To see that we can usually sample much slower, consider the right-shifted aliases of the spectral zone originally located at negative frequency, that is, the interval  $[-f_U, -f_L]$ . The bands occupied by these aliases extend from  $-f_U + nf_s$  to  $-f_L + nf_s$ , spaced by  $f_s$  with each alias zone having bandwidth  $B$ . Some of these zones will fall in the null regions of the original spectrum, but for  $f_s$  to allow alias-free reconstruction, we must have, for some integer  $n$ , the  $n$ th right alias lie to the left of  $f_L$  on the positive frequency axis, and at the same time, the  $n + 1$ -st alias must clear the frequency  $f_U$  to the right. The first requires  $nf_s < f_L$  and the second requires  $(n + 1)f_s > 2f_U$ . (Strict inequality holds to allow for possible spectral lines at the band edges.)

The easiest way to interpret these requirements is to consider integer values  $n = 0, 1, 2, 3, \dots$ , and, for each, find sampling rates that satisfy both

**Table 2.1** Listing of Acceptable Sampling Frequency Bands,  $f_L = 2.6$ ,  $f_U = 3.1$

$n$	$f_{\text{slower}} = \frac{2f_U}{n+1}$	$f_{\text{supper}} = \frac{2f_L}{n}$
0	6.20	$\infty$
1	3.10	5.20
2	2.07	2.60
3	1.55	1.73
4	1.24	1.30
5	1.033	1.04

$$f_s < \frac{2f_L}{n} = \frac{2(f_U - B)}{n}$$

$$f_s > \frac{2f_U}{n+1}. \quad (2.48)$$

There will always be the naive solution  $f_s > 2f_U$  for  $n = 0$ , but for increasing  $n$  we find decreasing intervals of acceptable sampling rates, until no such rates exist.

To illustrate, alias-free sampling rate intervals are listed in Table 2.1 for a case with normalized frequencies  $(f_L, f_U) = (2.6, 3.1)$ , that is, where the signal bandwidth is 0.5 Hz. For  $n = 0$  we find the naive solution,  $f_s > 6.2$  Hz. Letting  $n = 1$  reveals a range of sampling rates  $[3.1, 5.2]$  is feasible, and so on, with the smallest acceptable sampling rate corresponding to  $n = 5$ , namely 1.033 Hz, slightly greater than  $2B$ .

A closed-form result for the *minimum* acceptable sampling rate is obtained as follows. Let  $n^*$  be the largest integer  $n$  for which Eq. (2.48) can hold, namely  $n^* = \text{int}(f_L/B) = \text{int}((f_U - B)/B)$ . Substituting this into Eq. (2.48) then yields

$$f_{s\min} = \frac{2f_U}{n^* + 1} = \frac{2f_U}{\text{int}(f_U/B)}. \quad (2.49)$$

This relation is plotted in Fig. 2.12, showing the *minimum* sampling rate normalized to the bandwidth  $B$  as a function of  $f_U/B$ . Notice that as  $f_U/B$  becomes large, the minimum acceptable sampling rate tends to double the bandwidth. Two cautions are in order, however. First,  $f_{s\min}$  is generally not equal to  $2B$  (except when  $f_U/B$  is an integer). Second, having found an acceptable sampling rate, one cannot conclude that a larger sampling rate is acceptable, as shown in the above example. Finally, we should realize that this analysis allows aliases to butt against the desired frequency zone, implying ideal filters are needed to recover the bandpass signal. If we want some guard zone in frequency (perhaps some fraction of the original signal bandwidth), we could reformulate the constraints above, and we would find that the suitable sampling rates change and that the minimum sampling rate will increase.

We have discussed bandpass sampling as if recovery of the original bandpass signal is the objective; but more often we are interested in recovering an alias in a lower frequency region, ideally near zero, that allows easy demodulation, namely recovery of  $\tilde{x}(t)$ . Sampling of a bandpass signal is a kind of heterodyning operation,

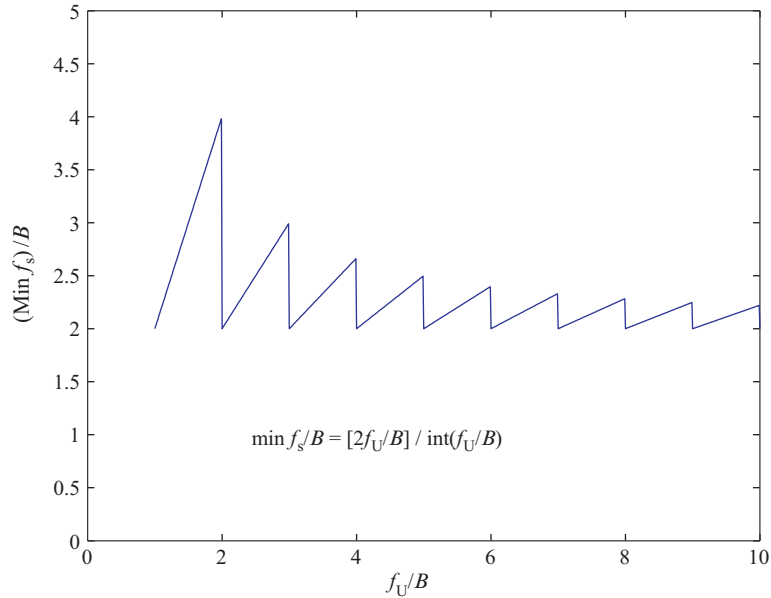


FIG. 2.12

Minimum sampling rate, normalized to  $B$ , versus  $f_U/B$ .

that is, spectral copies are produced at lower frequency. It can also be shown that the conditions discussed above for clearing the original bandpass region of aliasing are exactly those needed to produce nonoverlapping aliases in low-frequency zones, leading to recovery of the complex envelope.

Note that the new center frequency is not identically zero, however, and further “despinning” is necessary to bring the signal to zero frequency. Some sampling rate choices will produce an alias-free zone near zero frequency, but with spectral reversal. When such spectral reversal occurs, it may be undone by changing the heterodyning frequency to rotate the periodic DT spectrum into proper alignment at zero frequency.

**Example 2.4.** Suppose a receiver uses standard analog heterodyne conversion to provide a band of channels centered at 70 MHz, with total bandwidth 2 MHz. Then we have  $f_U = 71$  MHz,  $f_L = 69$  MHz, and  $B = 2$  MHz. Assuming the presampling circuitry in the receiver does a satisfactory job of making the signal bandlimited, the minimum sampling rate is  $2(71)/\text{int}(71/2) = 4.057$  MHz, only slightly greater than  $2B$ . The 17th alias of the original bandpass signal is located near zero frequency with band-center at  $70 - 17(4.057) = 1.029$  MHz, (barely) without aliasing distortion. Further processing can extract a subchannel of interest with digital filtering, then heterodyne it to zero frequency with a digital local oscillator. Alternatively, we could sample at a somewhat higher rate satisfying the rules above to

provide some frequency guard interval. Even though the sampling rate can be much lower than 2(71) MHz, we must have adequate input analog bandwidth in the A/D converter to handle the bandpass signal; specifically a sample-and-hold circuit prior to the sampler must have adequate frequency response to capture the high-frequency signal.

### 2.6.1 MORE ON DEMODULATION

An alternate method of representing a bandpass signal to a digital processor is a more classical method, involving a quadrature demodulator of the bandpass signal to baseband, producing the in-phase and quadrature components of the signal. Each of these has bandwidth  $B/2$  in the above notation, and sampling of each at  $B$  sps can represent each signal. The net sampling rate then for the two streams is exactly  $2B$  sps, and this holds true no matter what the ratio  $f_U/B$  is. The cost is the need for a quadrature demodulator (two mixers and a local oscillator), plus two A/D converters instead of one bandpass sampler. An equivalent process is to first form the analytic signal for the bandpass signal, then heterodyne this complex signal to zero frequency and sample the real and imaginary components separately, each at rate  $B$  sps.

*Direct* recovery of the sampled in-phase and quadrature components of a bandpass signal can be done instead by cleverly sampling the bandpass signal. Specifically if we represent the signal as

$$x(t) = \sqrt{2}[i(t) \cos(2\pi f_c t) + q(t) \sin(2\pi f_c t)] \quad (2.50)$$

and sample at  $f_s = 4f_c$ , with  $t = 0$  as the first sample, we recover the sequence

$$\sqrt{2} \times \{i(0), q(1T), -i(2T), -q(3T), i(4T), q(5T), \dots\}, \quad (2.51)$$

as substitution of sampling times will show. By demultiplexing this sequence into two sequences, then switching the signs of alternate samples in each sequence, we recover two streams (in-phase and quadrature signals), each represented at a sampling rate of  $f_s/2 = 2f_c$ . Provided this is greater than twice the bandwidth of the in-phase/quadrature signals to be recovered, we have thus demodulated using a single sampler acting on the bandpass signal, while avoiding heterodyne processing.

This idea can be extended to allow undersampling of the bandpass signal, as discussed above, yet still provide recovery of the in-phase/quadrature sequences, if the sampling rate is an odd-submultiple of  $4f_c$ , that is,  $f_s = 4f_c/n$ , where  $n$  is odd.<sup>6</sup> The divisor  $n$  cannot be larger than some critical number that leaves  $(f_s)' = f_s/2 > 2W$ , where  $W$  is the baseband message bandwidth of the  $I/Q$  signals. This requires  $2f_c/n > 2W$ , or  $n < \text{int}(f_c/W)$ , with  $n$  odd. This means that the minimum sampling rate associated with this direct demodulation method is

<sup>6</sup>The sign patterns on the  $I/Q$  streams changes to  $I, -Q, -I, Q, \dots$  when  $n \bmod 4 = 3$ . This corresponds to recovery of  $\tilde{X}^*(-f)$  rather than  $\tilde{X}(f)$ .

$$f_{s,\text{min,direct}} = \frac{4f_c}{\max \text{ odd int}(f_c/W)}. \quad (2.52)$$

Some subtleties are tied to this rather convenient idea. First, the sampling will be asynchronous with the carrier, so we cannot claim samples line up with zero crossings of the  $\cos/\sin$  terms. This implies we actually will recover a rotated combination of  $I/Q$  streams, and a phase derotation must be performed to correctly recover the  $I/Q$  streams. Moreover, the sampling clock will not be an exact submultiple of the actual  $4f_c$  due to Doppler shift or oscillator offsets in the transmitter and receiver. So the recovered baseband signal is slowly spinning in  $I/Q$  space versus time. If coherent detection of the signal is desired, both this slow frequency spin and any phase offsets must be removed by digital signal processing of the baseband samples, using some type of carrier phase synchronization scheme.

Finally, note that  $I/Q$  are recovered in time-staggered manner. If we need the  $I/Q$  streams to be represented at the same DT points, then a digital interpolation of one will be needed to time shift one stream by the necessary amount. This is easy, however, and is typically incorporated within symbol timing methods.

**Example 2.5** (Digital satcom receiver). In receivers for direct broadcast satellites, analog receiver processing often converts the received multichannel frequency band, say 12.2–12.7 GHz carrying multiple programs, to an intermediate frequency range 900–1400 MHz, using block down-conversion. Channel selection from this channel multiplex is done by mixing with a local oscillator signal to convert the channel of interest to a center frequency of 140 MHz. We assume the bandwidth of the signal to be processed is  $B = 36$  MHz, carrying one or more digital video streams. A bandpass filter with this bandwidth would typically appear at the output of the frequency converter.

At this point we have a bandpass signal (plus noise), centered at 140 MHz with bandwidth 36 MHz. The complex envelope of this signal has 18 MHz bandwidth, and recovery of the  $I/Q$  components of this complex signal allows demodulation and subsequent recovery of the digital data.

Appealing to the direct recovery sampling procedure just discussed, we have  $f_c = 140$  MHz,  $W = 18$  MHz, and the minimum sampling rate producing direct demodulation without aliasing is

$$f_{s,\text{min,direct}} = \frac{4(140)}{\max \text{ odd int}(140/18)} = \frac{560}{7} = 80 \text{ Msps} \quad (2.53)$$

This is 2.22 times the bandwidth of the IF signal, a considerable reduction over the naive sampling rate of 2(136) Msps and only slightly larger than the 79 Msps minimum alias-free rate from Eq. (2.49).

The adopted sampling rate of 80 Msps places an alias-free copy of the IF signal centered at 20 MHz (though spectrally reversed), which is  $f_c/7$ , meaning that simple demultiplexing and sign-alternation as above recovers the  $I/Q$  samples without further frequency translation. In practice there will be some small frequency offset, in addition to an overall phase rotation that must be removed using a

phase-synchronization algorithm, beyond the discussion here. The  $I/Q$  samples will need to be resampled to a rate appropriate to the underlying symbol rate for purposes of symbol timing and matched filtering [4].

---

## REFERENCES

- [1] C.R. Johnson Jr., W.A. Sethares, A.G. Klein, *Software Receiver Design*, Cambridge, 2011.
- [2] S. Haykin, *Communication Systems*, fourth ed., Wiley, 2006.
- [3] R. Gallager, *Probability and Stochastic Processes*, Cambridge, 2014.
- [4] F. Harris, *Multirate Signal Processing for Communication Systems*, Prentice-Hall, 2004.

## Single-carrier modulation

## 3

**M. Rice***Brigham Young University, Provo, UT, United States***CHAPTER OUTLINE**

<b>3.1 Preliminaries</b> .....	74
<b>3.2 Linear, Memoryless Modulation</b> .....	75
3.2.1 Background.....	75
3.2.2 Mathematical Description .....	81
3.2.3 Modulation .....	83
3.2.4 Power Spectral Density .....	84
3.2.5 Pulse Shape Examples.....	85
3.2.6 Examples .....	89
3.2.7 Concluding Remarks for Linear Modulation .....	94
<b>3.3 Nonlinear Modulation: CPM</b> .....	95
3.3.1 Background.....	95
3.3.2 Mathematical Description .....	98
3.3.3 Modulation .....	102
3.3.4 Power Spectral Density .....	104
3.3.5 CPFSK, MSK, and GMSK .....	108
3.3.6 Concluding Remarks for Nonlinear Modulation .....	112
<b>3.4 Comparisons</b> .....	113
<b>References</b> .....	117

The first radio frequency (RF) systems were based on single-carrier modulations. Limitations imposed by the immature technology rendered anything more sophisticated impossible. Analog modulations, in the form of amplitude modulation (AM) and frequency modulation (FM), were single-carrier modulations and served the needs of radio systems from the early 20th century up to the advent of digital communications. The use of a single carrier for digital modulation was a natural extension of the single-carrier analog modulations, although the mathematics used to

describe a digitally modulated carrier are quite different from those used to describe an AM or FM carrier. Consequently, the first digital communication systems were based on single-carrier techniques, and this remained the case until the 1990s, when multicarrier modulations became popular.

As of this writing, the popular mobile telephony networks (4G/LTE) and wireless networking systems (IEEE 802.11 or WiFi) are based on multicarrier modulation. But multicarrier modulation requires a very linear RF power amplifier. Where this is difficult, single-carrier modulations still dominate, such as with satellite communications, aeronautical and aerospace communication systems, systems with low probabilities of interception or detection, low-cost radio networks (IEEE 802.15.4 and Bluetooth), and 4G/LTE backhaul links operating in the 60/70/80/90 GHz bands. In addition, the terminology used to describe much of the multicarrier modulations derives from the terminology used for single-carrier modulations. Consequently, single-carrier modulation remains an important area of study.

### 3.1 PRELIMINARIES

Modulation is a one-to-one mapping of  $B$  input bits to one of the  $M = 2^B$  waveforms in the following set:

$$\mathcal{S} = \{s_1(t), s_2(t), \dots, s_M(t)\}. \quad (3.1)$$

The situation is illustrated by the example shown in Fig. 3.1. Here,  $B = 2$  bits are mapped to one of the  $M = 4$  waveforms. The input bit sequence is partitioned into nonoverlapping segments of  $B = 2$  bits. Each 2-bit segment maps to one of the four waveforms, as shown. A new waveform is produced every  $T_s$  seconds and corresponds to a  $B$ -bit symbol. Consequently,  $T_s$  can be thought of as the symbol period (with units s/symbol) and the corresponding symbol rate is as follows:

$$R_s = \frac{1}{T_s} \text{ symbols/s}. \quad (3.2)$$

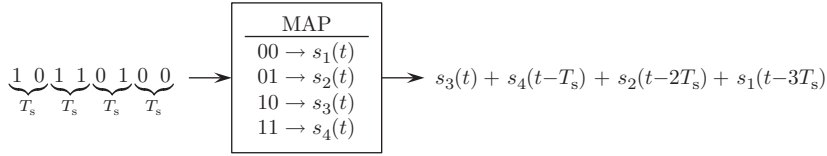
Because  $B$  bits comprise each symbol, the bit period is  $T_b = T_s/B$  s/bit and the corresponding bit rate is as follows:

$$R_b = \frac{1}{T_b} \text{ bits/s}. \quad (3.3)$$

The bit rate and symbol rate are related by

$$R_b = BR_s \text{ bits/s}. \quad (3.4)$$

The symbol-to-waveform mapping may be defined as either memoryless or with memory. The mapping shown in Fig. 3.1 is an example of a memoryless mapping: each  $B$ -bit symbol maps to one of the  $M$  waveforms without regard to the previous  $B$ -bit symbol and its corresponding waveform. The alternative is a mapping with memory: the output waveform is determined from the current and previous  $(L - 1)$

**FIG. 3.1**

An example of modulation as a mapping between  $B = 2$ -bit symbols and  $M = 2^B = 4$  waveforms.

$B$ -bit symbols. The mapper can be conceived as a finite state machine with  $2^{B(L-1)}$  states.

The set of waveforms may be described as linear or nonlinear. For linear mappings, the superposition principle holds in the sense that a linear combination of any two waveforms in  $\mathcal{S}$  is another waveform of the same functional form, but not necessary in the waveform set  $\mathcal{S}$ . When this is not true, the mapping is nonlinear.

This chapter is devoted to linear, memoryless modulations (quadrature amplitude modulation, QAM) and nonlinear modulations with memory (continuous phase modulation, CPM).

## 3.2 LINEAR, MEMORYLESS MODULATION

### 3.2.1 BACKGROUND

The most common linear, memoryless modulation is the class of modulations known as QAM. The conventional description of QAM relies on signal spaces defined by basis functions. Formal definitions are outlined in “[Signal space concepts](#).” Here, a few examples are given to illustrate the concepts.

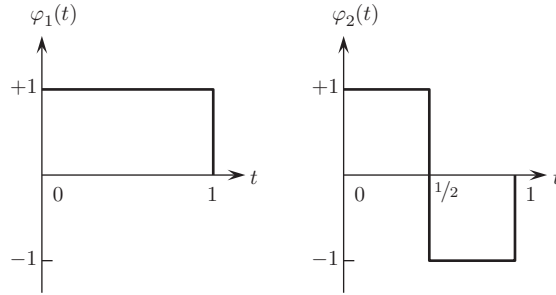
**Example 3.1.** As a first example, consider the basis waveforms shown in [Fig. 3.2](#). The energy in each of the waveforms is

$$E_1 = \int_{T_1}^{T_2} |\varphi_1(t)|^2 dt = \int_0^1 dt = 1$$

$$E_2 = \int_{T_1}^{T_2} |\varphi_2(t)|^2 dt = \int_0^{1/2} dt + \int_{1/2}^1 dt = 1.$$

This shows that each waveform is *normalized* to unit energy. The relationship between the two is defined by their inner product:

$$\begin{aligned} \langle \varphi_1(t), \varphi_2(t) \rangle &= \int_{T_1}^{T_2} \varphi_1(t) \varphi_2^*(t) dt \\ &= \int_0^{1/2} dt - \int_{1/2}^1 dt \\ &= 0. \end{aligned}$$

**FIG. 3.2**

An example of two orthonormal basis waveforms.

This shows that the basis waveforms are *orthogonal*. Because the basis waveforms are orthogonal and normalized to unit energy,  $\varphi_1(t)$  and  $\varphi_2(t)$  form an *orthonormal basis*. A waveform in the span of  $\varphi_1(t)$  and  $\varphi_2(t)$  is of the form

$$s(t) = a_1\varphi_1(t) + a_2\varphi_2(t),$$

for constants  $a_1$  and  $a_2$ . The set of all waveforms in the span of  $\varphi_1(t)$  and  $\varphi_2(t)$  is called a *signal space*. An example of four waveforms in the signal space formed by  $\varphi_1(t)$  and  $\varphi_2(t)$  is shown in Table 3.1. The table shows that each waveform may be represented by the  $(a_1, a_2)$  pair. This observation leads to the concept of a *constellation*. The constellation is a point in a two-dimensional space where the two axes correspond to  $\varphi_1(t)$  and  $\varphi_2(t)$ . The constellation corresponding to the four waveforms of Table 3.1 is shown in Fig. 3.3. The coordinates for each point are the  $(a_1, a_2)$  pairs that define the waveform.

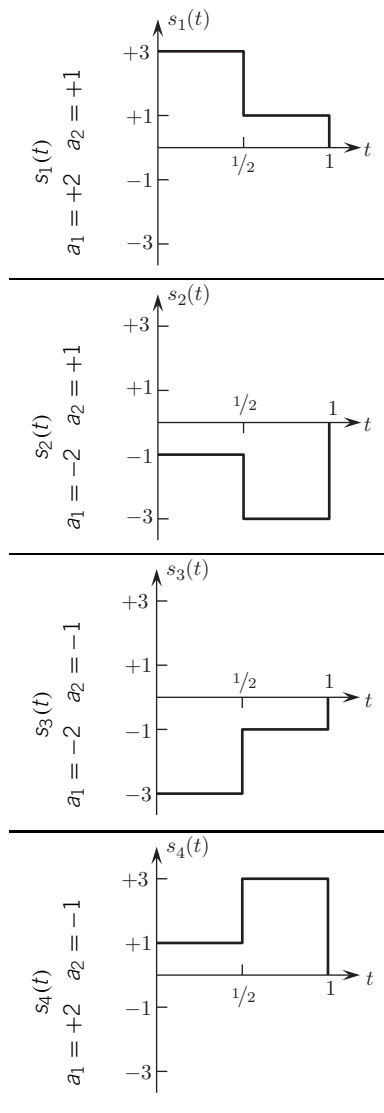
**Example 3.2.** This example is based on the same orthonormal basis waveforms shown in Fig. 3.2 but with a different set of constants to create four waveforms. These waveforms are shown in Table 3.2 and may be expressed as

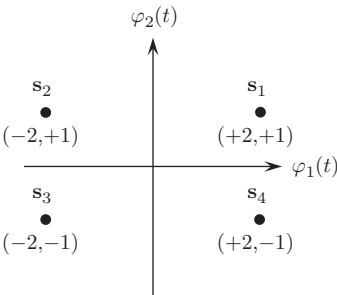
$$\begin{aligned} s_1(t) &= +1 \times \varphi_1(t) + 1 \times \varphi_2(t) \\ s_2(t) &= -1 \times \varphi_1(t) + 1 \times \varphi_2(t) \\ s_3(t) &= -1 \times \varphi_1(t) - 1 \times \varphi_2(t) \\ s_4(t) &= +1 \times \varphi_1(t) - 1 \times \varphi_2(t). \end{aligned}$$

The four waveforms have a very distinctive shape, and one could easily envision using the waveforms  $\varphi'_1(t)$  and  $\varphi'_2(t)$  shown in Fig. 3.4 as an orthonormal basis for these waveforms. In this case, the waveforms may be represented as follows:

$$\begin{aligned} s_1(t) &= \sqrt{2} \times \varphi'_1(t) + 0 \times \varphi'_2(t) \\ s_2(t) &= 0 \times \varphi'_1(t) - \sqrt{2} \times \varphi'_2(t) \\ s_3(t) &= -\sqrt{2} \times \varphi'_1(t) + 0 \times \varphi'_2(t) \\ s_4(t) &= 0 \times \varphi'_1(t) + \sqrt{2} \times \varphi'_2(t). \end{aligned}$$

**Table 3.1** Four Waveforms  
Generated by the Basis  
Waveforms in [Fig. 3.2](#)

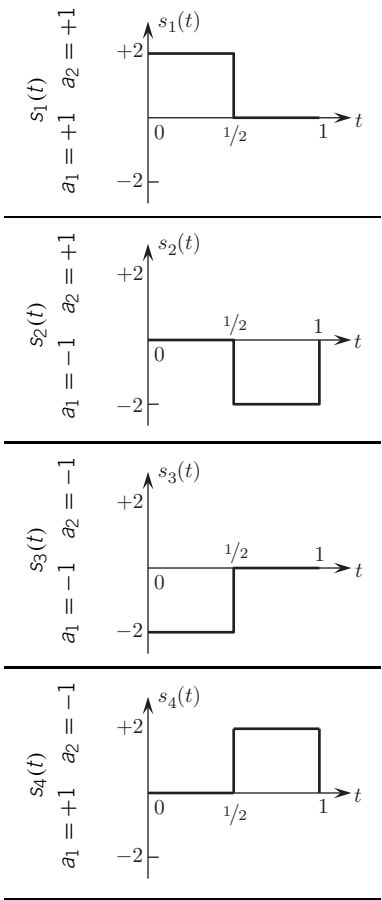


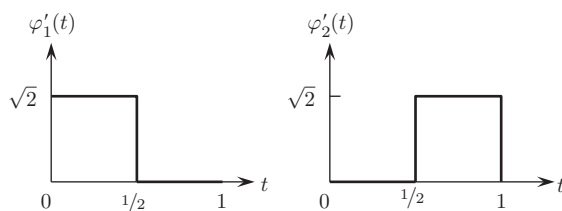


**FIG. 3.3**

The constellation corresponding to the four waveforms in [Table 3.1](#).

**Table 3.2** Four Waveforms  
Generated by the Basis  
Waveforms in [Fig. 3.2](#)



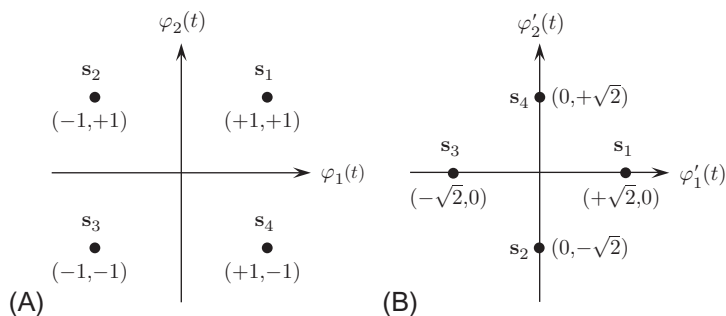
**FIG. 3.4**

An alternate basis for the four waveforms in this example (cf. Fig. 3.2).

This illustrates the fact that a basis set is not unique. Because the coefficients corresponding to each  $s_i(t)$  ( $i = 1, 2, 3, 4$ ) depend on the choice of basis functions, it is not surprising that the constellation also depends on the basis functions. This concept is shown in Fig. 3.5.

These examples demonstrate the signal space concepts outlined in “Signal space concepts.” They show that waveforms may be represented as points in a  $K$ -dimensional space whose basis is a set of orthonormal waveforms. The basis waveforms are not unique. In general, a change of basis also changes the locations of the points in the  $K$ -dimensional space. The notions of energy, unit energy, orthogonality, and orthonormality were also shown.

A linear digital modulation comprises a set of  $M$  points in the  $K$ -dimensional signal space. Associated with each point is a  $\log_2(M)$ -bit pattern. This bit-pattern-to-signal-space-point association is the basis for the mapping between bits and waveforms described in Section 3.1. In the two examples,  $M = 4$  signals were identified. Consequently,  $\log_2(M) = 2$  bits are required to form the bits-to-waveform mapping. Note that there are  $4! = 24$  possible bit-to-waveform mappings, and the

**FIG. 3.5**

Constellations for the four waveforms listed in Table 3.2: (A) the constellation corresponding to the basis waveforms of Fig. 3.2 and (B) the constellation corresponding to the basis waveforms of Fig. 3.4.

modulator and demodulator must agree on which of the mappings to use before reliable communication can be achieved.

A real-valued bandpass QAM signal is based on the  $K = 2$  orthonormal bandpass basis functions:

$$\begin{aligned}\varphi_{1,\text{bp}}(t) &= \sqrt{2}p(t) \cos(2\pi f_0 t) \\ \varphi_{2,\text{bp}}(t) &= -\sqrt{2}p(t) \sin(2\pi f_0 t),\end{aligned}\tag{3.5}$$

where  $p(t)$  is a unit-energy, real-valued pulse shape described below. The waveform associated with the point  $(a_1, a_2)$  in the signal space is of the form

$$\begin{aligned}s_{\text{bp}}(t) &= a_1 \varphi_{1,\text{bp}}(t) + a_2 \varphi_{2,\text{bp}}(t) \\ &= \underbrace{a_1 \sqrt{2}p(t) \cos(2\pi f_0 t)}_{\text{inphase component}} - \underbrace{a_2 \sqrt{2}p(t) \sin(2\pi f_0 t)}_{\text{quadrature component}},\end{aligned}\tag{3.6}$$

where  $a_1$  and  $a_2$  are drawn from the field of real numbers  $\mathbb{R}$ . For one-dimensional signal sets,  $a_2 = 0$ . In QAM, the term “quadrature” derives from the fact that the basis waveforms (Eq 3.5) differ from each other by<sup>1</sup> 90 degrees. By convention,  $\varphi_{1,\text{bp}}(t) = \sqrt{2}p(t) \cos(2\pi f_0 t)$  is taken to be the phase reference (ie, this term corresponds to a phase of 0 degrees). For this reason, the term involving  $\varphi_{1,\text{bp}}(t)$  is called the “inphase component,” as indicated in Eq. (3.6). Because the phase  $\varphi_{2,\text{bp}}(t)$  is 90 degrees behind that of  $\varphi_{1,\text{bp}}(t)$ , the term involving  $\varphi_{2,\text{bp}}(t)$  is called the “quadrature component.” The term “amplitude” derives from the fact that the form of Eq. (3.6) involves an amplitude scaling of the quadrature basis waveforms. The sinusoids give QAM signals their bandpass characteristic. The center frequency of the bandpass signal is  $2\pi f_0$  rads/s.

It is often of use to work the complex-valued baseband equivalents. The complex-valued baseband equivalent of a QAM signal is a point in the  $K = 1$ -dimensional signal space whose basis function is

$$\varphi_{1,\text{bb}}(t) = p(t).\tag{3.7}$$

Here, the complex-valued baseband equivalent of the signal Eq. (3.6) is

$$s_{\text{bb}}(t) = a\varphi_{1,\text{bb}}(t) = ap(t),\tag{3.8}$$

where  $a$  is, in general, drawn from the field of complex numbers  $\mathbb{C}$  and, with reference to Eq. (3.6), is of the form  $a = a_1 + ja_2$ .

---

<sup>1</sup>The word “quadrature” derives from the classical Latin *quadrātūra*, meaning the division of land into squares. In postclassical Latin, the term came to mean a square or the quality of being square. Scientific use of the term dates from the 16th century, when astronomers used “in quadrature” to describe the arrangement of two objects 90 degrees apart on the celestial sphere. Its first use in the sense it is used here was in 1889, when T.H. Blakesly described the relationship between the induced current in a coil and the corresponding magnetic field as “in quadrature” [1].

### 3.2.2 MATHEMATICAL DESCRIPTION

QAM is usually described in terms of its signal set  $\mathcal{S}$ . The signal set  $\mathcal{S}$  comprises  $M$  waveforms. The complex-valued baseband equivalent representation of the signals in  $\mathcal{S}$  are denoted as follows:

$$\mathcal{S} = \{s_{1,\text{bb}}(t), s_{2,\text{bb}}(t), \dots, s_{M,\text{bb}}(t)\}. \quad (3.9)$$

The signal space is the one-dimensional signal space defined by the basis function

$$\varphi_{1,\text{bb}}(t) = p(t), \quad (3.10)$$

where  $p(t)$  is the real-valued, unit-energy pulse shape defined on  $T_1 \leq t \leq T_2$ . Examples are given in [Section 3.2.5](#). Note that for some ideal pulse shapes,  $T_1 \rightarrow -\infty$  and  $T_2 \rightarrow +\infty$ . The  $m$ th member of  $\mathcal{S}$  is thus

$$s_{m,\text{bb}}(t) = a_m p(t) \quad (3.11)$$

for  $m = 1, 2, \dots, M$ , where  $a_m$  is a member of a complex-valued  $M$ -ary alphabet:

$$\mathcal{A} = \{a_1, a_2, \dots, a_M\}. \quad (3.12)$$

The structure of the signal space imparts a one-to-one mapping between the signal set  $\mathcal{S}$  and the alphabet  $\mathcal{A}$ :

$$\begin{aligned} a_1 &\leftrightarrow a_1 \varphi_{1,\text{bb}}(t) = a_1 p(t) = s_{1,\text{bb}}(t) \\ a_2 &\leftrightarrow a_2 \varphi_{2,\text{bb}}(t) = a_2 p(t) = s_{2,\text{bb}}(t) \\ &\vdots \\ \underbrace{a_M}_{\mathcal{A}} &\leftrightarrow a_M \varphi_{M,\text{bb}}(t) = a_M p(t) = \underbrace{s_{M,\text{bb}}(t)}_{\mathcal{S}}. \end{aligned} \quad (3.13)$$

A QAM signal set is often described by listing (or graphing) the members of  $\mathcal{A}$ . A plot of the members of  $\mathcal{A}$  as points in the complex plane is called a constellation. Examples are given in [Section 3.2.6](#).

Using the notation  $a_m = a_{m,i} + ja_{m,q}$ , the complex-valued baseband equivalent form of Eq. (3.11) may be rewritten:

$$s_{m,\text{bb}}(t) = a_m p(t) = |a_m| e^{j\angle a_m} p(t), \quad (3.14)$$

where

$$|a_m| = \sqrt{a_{m,i}^2 + a_{m,q}^2} \quad (3.15)$$

$$\angle a_m = \tan^{-1} \left( \frac{a_{m,q}}{a_{m,i}} \right). \quad (3.16)$$

This shows that the symbol  $a_m$  modulates the magnitude and phase of the carrier. The carrier magnitude is shifted by  $|a_m|$  and the carrier phase is shifted by  $\angle a_m$ .

The real-valued bandpass versions of the QAM signal set are defined as follows:

$$s_{m,\text{bp}}(t) = \sqrt{2} \operatorname{Re} \left\{ s_{m,\text{bb}}(t) e^{j2\pi f_0 t} \right\} \quad (3.17)$$

$$= a_{m,i} \underbrace{p(t) \sqrt{2} \cos(2\pi f_0 t)}_{\varphi_{1,\text{bp}}(t)} - a_{m,q} \underbrace{p(t) \sqrt{2} \sin(2\pi f_0 t)}_{-\varphi_{2,\text{bp}}(t)} \quad (3.18)$$

$$= |a_m| \sqrt{2} p(t) \cos(2\pi f_0 t + \angle a_m). \quad (3.19)$$

Eq. (3.18) reveals the real-valued, bandpass basis functions for QAM (cf., Eq. 3.10) and shows that the real-valued, bandpass signal may be expressed as

$$s_{m,\text{bp}}(t) = a_{m,i} \varphi_{1,\text{bp}}(t) + a_{m,q} \varphi_{2,\text{bp}}(t). \quad (3.20)$$

The energy of  $s_{m,\text{bb}}(t)$  is

$$E_m = \int_{T_1}^{T_2} |s_{m,\text{bb}}(t)|^2 dt = |a_m|^2 \quad (3.21)$$

for  $1 \leq m \leq M$ . Because the complex-valued baseband basis function is orthonormal and the corresponding bandpass basis functions are orthonormal,  $E_m$  is also the energy of the corresponding real-valued bandpass version of the signal. The average energy of the signal set is

$$E_{\text{avg}} = \sum_{m=1}^M E_m P(a_m), \quad (3.22)$$

where  $P(a_m)$  is the probability the source produces  $a_m$ . When the data symbols are equally likely,  $P(a_m) = 1/M$ .

The performance of the maximum likelihood detector in the additive white Gaussian noise (AWGN) environment is determined by the signal-to-noise ratio and the minimum Euclidean distance. The squared Euclidean distance between  $s_{k,\text{bb}}(t)$  and  $s_{m,\text{bb}}(t)$  for  $1 \leq k \leq M$  and  $1 \leq m \leq M$  is

$$d_{k,m}^2 = \int_{T_1}^{T_2} |s_{k,\text{bb}}(t) - s_{m,\text{bb}}(t)|^2 dt. \quad (3.23)$$

Using the relationship Eq. (3.11),  $d_{k,m}^2$  may also be expressed as

$$d_{k,m}^2 = |a_k - a_m|^2 = (a_{k,i} - a_{m,i})^2 + (a_{k,q} - a_{m,q})^2. \quad (3.24)$$

The minimum squared Euclidean distance is

$$d_{\min}^2 = \min_{k \neq m} \{ d_{k,m}^2 \}. \quad (3.25)$$

### 3.2.3 MODULATION

Generally, QAM is generated in two steps. First, the complex-valued pulse train representing the complex-valued baseband equivalent is formed:

$$x_{\text{bb}}(t) = \sum_k a(k)p(t - kT_s). \quad (3.26)$$

Note that the temporal index  $k$  has been added to the notation. For each  $k$ ,  $a(k)$  is one of the  $M$  members of the alphabet  $\mathcal{A}$ . The pulse shape  $p(t)$  is described in Section 3.2.5. The basic approach is illustrated by the block diagram in Fig. 3.6A. The pulse train is formed using a serial-to-parallel converter (S/P), a look-up table (LUT), and a pulse shaping filter whose impulse response is the pulse shape. As explained in the introduction, the input bits are partitioned into nonoverlapping segments of  $\log_2(M)$  bits by the serial-to-parallel converter. Each bit segment forms a  $\log_2(M)$ -bit address to an LUT that stores each constellation point as a complex-valued entry.

To perform pulse shaping, the process is conceptualized by treating the input to the pulse shaping filter as a weighed impulse train:

$$x(t) = \sum_k a(k)\delta(t - kT_s), \quad (3.27)$$

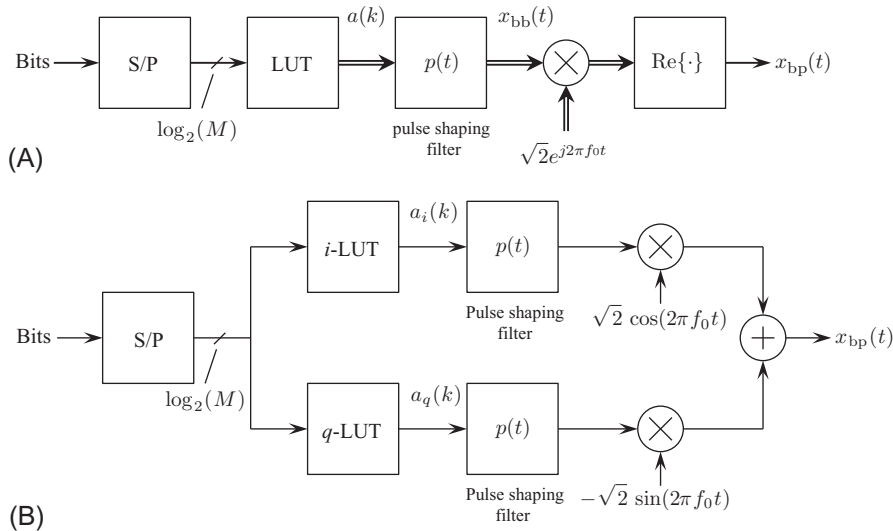


FIG. 3.6

A block diagram illustrating the generation of QAM: (A) generating the real-valued bandpass signal from the complex-valued baseband equivalent and (B) generating the real-valued bandpass signal directly.

where  $\delta(t)$  is the Dirac impulse function. The output of the filter with impulse response  $p(t)$  is the complex-valued pulse train (Eq. 3.26). Practical approaches, using discrete-time signal processing, are described by Dodley and Erving [2], Harris et al. [3], and in Chapter 10 of Rice [4].

Using the notation  $a(k) = a_i(k) + ja_q(k)$ , the real-valued bandpass signal is

$$x_{\text{bp}}(t) = \sqrt{2} \operatorname{Re} \left\{ s_{\text{bb}}(t) e^{j2\pi f_0 t} \right\} \quad (3.28)$$

$$= \sum_k a_i(k) p(t - kT_s) \sqrt{2} \cos(2\pi f_0 t) - \sum_k a_q(k) p(t - kT_s) \sqrt{2} \sin(2\pi f_0 t). \quad (3.29)$$

This shows that the real-valued bandpass signal can be generated directly from the real and imaginary elements in the LUT, as shown in Fig. 3.6B.

### 3.2.4 POWER SPECTRAL DENSITY

The power spectral density of the modulated carrier is an important characterization because the bandwidth of the modulated carrier is defined by the properties of the power spectral density. The power spectral density is computed from

$$x_{\text{bb}}(t) = \sum_{n=-\infty}^{\infty} a(n) p(t - nT_s), \quad (3.30)$$

where  $a(n) \in \mathcal{A}$ . The analysis assumes an infinite number of symbols forming a wide-sense stationary discrete-time process with

$$E\{a(n)\} = 0 \quad (3.31)$$

$$E\{a(n+k)a^*(n)\} = R_a(k). \quad (3.32)$$

Consequently,  $x_{\text{bb}}(t)$  is a cyclo-stationary random process. The power spectral density is given by

$$S_{x,\text{bb}}(f) = \frac{1}{T_s} S_a(f) |P(f)|^2, \quad (3.33)$$

where

$$S_a(f) = \sum_{k=-\infty}^{\infty} R_a(k) e^{-j2\pi k f T_s} \quad (3.34)$$

and  $P(f)$  is the Fourier transform of the pulse shape  $p(t)$ . The two terms in Eq. (3.33) show that the power spectral density is a function of both the symbol sequence correlation function and the pulse shape. Consequently, it is possible to shape the power spectral density of the modulated signal by controlling the correlation properties of the symbols. For a given pulse shape,  $S_a(f)$  tends to be wider for an uncorrelated symbol sequence than for a correlated symbol sequence. The impact of the pulse shape is through its Fourier transform. Pulse shapes with abrupt transitions

tend to have a wider Fourier transform than smoother pulse shapes. Some commonly encountered pulse shapes are described in [Section 3.2.5](#).

For a sequence of equally likely and uncorrelated symbols, the power spectral densities for QAM are scaled versions of the plots in [Fig. 3.8](#) for the nonreturn-to-zero (NRZ), Manchester (MAN), and half-sine (HS) pulse shapes described in [Section 3.2.5](#). For these three pulse shapes, the power spectral density is characterized by a main lobe and a number of sidelobes with decreasing height. For the square-root raised cosine (SRRC) pulse shape, also described in [Section 3.2.5](#), the power spectral density corresponding to a sequence of equally likely and uncorrelated symbols is a scaled version of the plot shown in [Fig. 3.9](#). Unlike the case for the NRZ, MAN, and HS pulse shapes, there are no sidelobes for the infinitely long pulse shape (the lobing occurs in the time domain), as explained in [Section 3.2.5](#).

### 3.2.5 PULSE SHAPE EXAMPLES

Some pulse shapes over the interval  $0 \leq t \leq T_s$  include the NRZ pulse shape,<sup>2</sup>

$$p(t) = \begin{cases} \sqrt{\frac{1}{T_s}} & 0 \leq t < T_s \\ 0 & \text{otherwise} \end{cases} \quad |P(f)|^2 = T_s \operatorname{sinc}^2(fT_s), \quad (3.35)$$

the MAN or biphase pulse shape,

$$p(t) = \begin{cases} +\sqrt{\frac{1}{T_s}} & 0 \leq t < \frac{T_s}{2} \\ -\sqrt{\frac{1}{T_s}} & \frac{T_s}{2} \leq t < T_s \\ 0 & \text{otherwise} \end{cases} \quad |P(f)|^2 = T_s \left( \frac{\pi f T_s}{2} \right)^2 \operatorname{sinc}^4\left(\frac{f T_s}{2}\right) \quad (3.36)$$

and the HS pulse shape

$$p(t) = \begin{cases} \sqrt{\frac{2}{T_s}} \sin\left(\frac{\pi t}{T_s}\right) & 0 \leq t < T_s \\ 0 & \text{otherwise} \end{cases} \quad |P(f)|^2 = \frac{8T_s}{\pi^2} \left[ \frac{\cos(\pi f T_s)}{(2fT_s)^2 - 1} \right]^2. \quad (3.37)$$

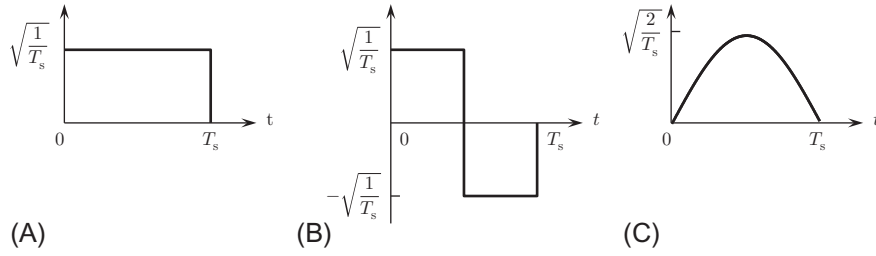
Plots of  $p(t)$  and  $|P(f)|^2$  for these pulse shapes are given in [Figs. 3.7](#) and [3.8](#), respectively.

The power spectral density relationship (3.33) shows that the power spectral density of the modulated carrier is proportional to  $|P(f)|^2$ . Because the NRZ, MAN, and HS pulse shapes have finite support in  $t$ ,  $|P(f)|^2$  has infinite support in  $f$ . Consequently, the power spectral density of the modulated carrier has (at least theoretically) infinite support.

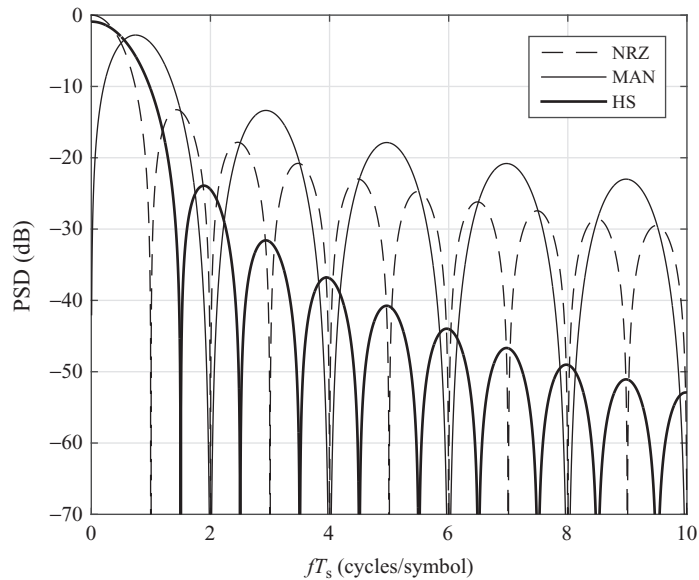
To generate a modulated carrier whose power spectral density is strictly band limited, a pulse shape for which  $|P(f)|^2$  has finite support is required. But this

---

<sup>2</sup> $\operatorname{sinc}(z) = \sin(\pi z)/(\pi z)$ .

**FIG. 3.7**

Three commonly encountered pulse shapes over  $0 \leq t \leq T_s$ : (A) the nonreturn-to-zero (NRZ) pulse shape, (B) the Manchester (MAN) pulse shape, and (C) the half-sine (HS) pulse shape.

**FIG. 3.8**

$|P(f)|^2$  for the three pulse shapes shown in Fig. 3.7.

requirement dictates the use of a pulse shape with infinite support in  $t$ . The use of a pulse shape that spans more than one symbol interval introduces the possibility of a phenomenon called intersymbol interference (ISI). In Chapter 4, it will be shown that the optimum detector in the AWGN environment is one that filters the received signal with a filter matched to the pulse shape (ie, the impulse response of the filter

is  $p(-t)$ ) and samples the matched filter output at  $t = kT_s$ . Neglecting noise, the matched filter output is

$$x(t) = \left[ \sum_n a(n)p(t - nT_s) \right] * p(-t) = \sum_n a(n)R_p(t - nT_s), \quad (3.38)$$

where  $R_p(\tau)$  is the pulse shape autocorrelation function

$$R_p(\tau) = \int_{-\infty}^{\infty} p(t)p(t + \tau)dt. \quad (3.39)$$

Sampling the matched filter output at  $t = kT_s$  gives

$$x(kT_s) = a(k)R_p(0) + \sum_{n \neq k} a(n)R_p((k - n)T_s). \quad (3.40)$$

The second term on the right-hand side of Eq. (3.40) models the ISI. Note that for the NRZ, MAN, and HS pulse shapes, this term is zero because these three pulse shapes span only one symbol interval. But for pulse shapes that span more than one symbol interval, this term can be nonzero. Nyquist proved the necessary and sufficient conditions for the second term in Eq. (3.40) to be zero:

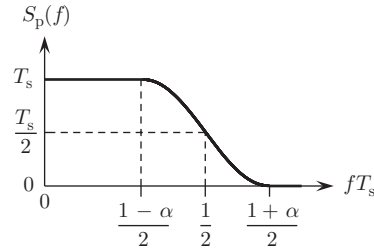
$$R_p(kT_s) = \begin{cases} 1 & k = 0 \\ 0 & k \neq 0 \end{cases} \quad \text{if and only if} \quad \sum_{m=-\infty}^{\infty} S_p\left(f - \frac{m}{T_s}\right) = T_s, \quad (3.41)$$

where  $S_p(f)$  is the Fourier transform of  $R_p(\tau)$ . (The formulation here does not follow Nyquist's original development [5]; it instead follows the more modern approach of Tufts [6].) This condition shows that pulse shapes for which  $S_p(f)$  possesses an odd-symmetric taper produce no ISI at the properly sampled instants of their matched filter outputs. The raised cosine spectrum is the most popular choice:

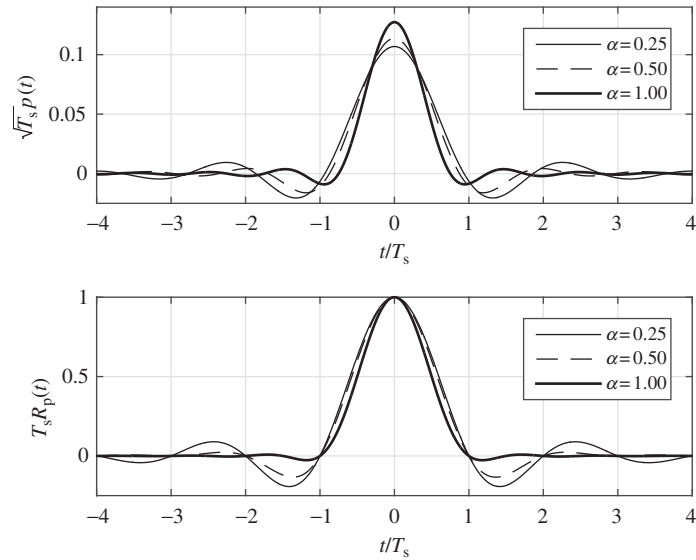
$$S_p(f) = \begin{cases} T_s & 0 \leq |f| \leq \frac{1-\alpha}{2T_s} \\ \frac{T_s}{2} \left[ 1 + \cos\left(\frac{\pi|f|T_s}{\alpha} - \frac{\pi(1-\alpha)}{2\alpha}\right) \right] & \frac{1-\alpha}{2T_s} \leq |f| \leq \frac{1+\alpha}{2T_s} \\ 0 & |f| > \frac{1+\alpha}{2T_s} \end{cases}. \quad (3.42)$$

The raised cosine spectrum is parameterized by  $0 \leq \alpha \leq 1$ , variously called the roll-off factor or excess bandwidth. The raised cosine spectrum is plotted in Fig. 3.9. Using the relationship  $S_p(f) = |P(f)|^2$ , the SRRC pulse shape is the inverse Fourier transform of  $\sqrt{S_p(f)}$ :

$$p(t) = \frac{1}{\sqrt{T_s}} \frac{\sin\left(\pi(1-\alpha)\frac{t}{T_s}\right) + \frac{4\alpha t}{T_s} \cos\left(\pi(1+\alpha)\frac{t}{T_s}\right)}{\frac{\pi t}{T_s} \left[ 1 - \left(\frac{4\alpha t}{T_s}\right)^2 \right]}. \quad (3.43)$$

**FIG. 3.9**

A plot of  $S_p(f)$  for the raised-cosine pulse shape with excess bandwidth  $\alpha$ .

**FIG. 3.10**

Plots of  $p(t)$  and  $R_p(t)$  for the square-root raised cosine pulse shape for  $\alpha = 0.25, 0.50$ , and  $1.00$ .

The SRRC pulse shape  $p(t)$  is plotted in top portion of Fig. 3.10. Note that the zero-crossings of  $p(t)$  vary with  $\alpha$  and that none of them coincide with integer multiples of  $T_s$ . In contrast, the matched filter outputs,  $R_p(t)$ , plotted in the lower portion of Fig. 3.10, have zero-crossings that coincide with the integer multiples of  $T_s$ . Note that as  $\alpha$  decreases, the magnitude of  $R_p(t)$  for  $|t| > T_s$  increases.

Other square-root Nyquist pulses are possible. See Franks [7], Sousa and Pasupathy [8], Scanlan [9], Beaulieu et al. [10], and Assilini and Tonello [11].

The square-root Nyquist pulse shapes described here possess ISI prior to matched filtering. ISI-free pulse shapes both with and without matched filtering are called generalized Nyquist pulses have been described by Xia [12], Demeechai [13], Alagha and Kabal [14], Kisel [15,16], and Tan and Beaulieu [17,18].

### 3.2.6 EXAMPLES

In these examples, constellations and pulse shapes for a number of applications are given. It will be shown in Chapter 4 that in the AWGN environment, the probability of error is a function of the Euclidean distance between the constellation points. For moderate to high signal-to-noise ratios, the probability of error is dominated by the minimum Euclidean distance between constellation points. Because the probability of error is a decreasing function of  $d_{\min}^2/E_{\text{avg}}$ , both values are listed for each example. Here,  $E_{\text{avg}}$  is given by Eq. (3.22) and  $d_{\min}^2$  is given by Eq. (3.25).

#### Pulse amplitude modulation

In pulse amplitude modulation (PAM), the  $a_m$  are purely real, that is  $\text{Im}\{a_m\} = 0$  for  $m = 1, 2, \dots, M$ . Consequently, the constellation points lie on the horizontal line. It is customary to arrange the points so that they are equally spaced and centered at zero. This is shown in Fig. 3.11 for  $M = 2, 4$ , and  $8$ . The waveforms corresponding to the  $M$  constellation points differ only in amplitude. The minimum Euclidean distance and average energy are

$$d_{\min} = 2A \quad (3.44)$$

$$E_{\text{avg}} = \frac{M^2 - 1}{3} A^2. \quad (3.45)$$

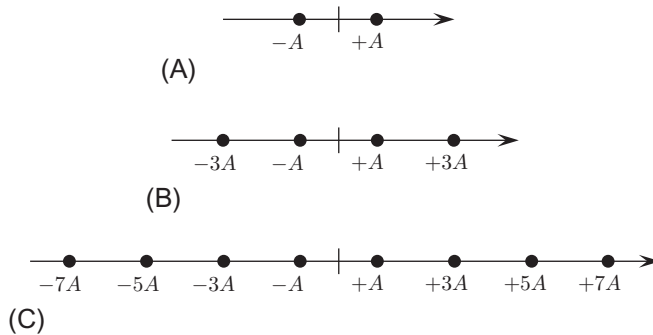


FIG. 3.11

PAM constellations for (A)  $M = 2$ , (B)  $M = 4$ , and (C)  $M = 8$ .

### $M$ -ary phase shift keying

In  $M$ -ary phase shift keying (MPSK), the  $a_m$  are constrained to lie on a circle of radius  $A$ . With reference to Eqs. (3.15), (3.16)

$$\begin{aligned} A_m &= A \\ \theta_m &= (m-1) \frac{2\pi}{M} \end{aligned} \quad (3.46)$$

for  $m = 1, 2, \dots, M$ . This mapping places the constellation points at equally spaced locations on the circle, as shown in Fig. 3.12 for  $M = 2, 4$ , and  $8$ . The waveforms corresponding to the  $M$  constellation points differ only in phase. The minimum Euclidean distance and average energy are

$$d_{\min} = 2A \sin\left(\frac{\pi}{M}\right) \quad (3.47)$$

$$E_{\text{avg}} = A^2. \quad (3.48)$$

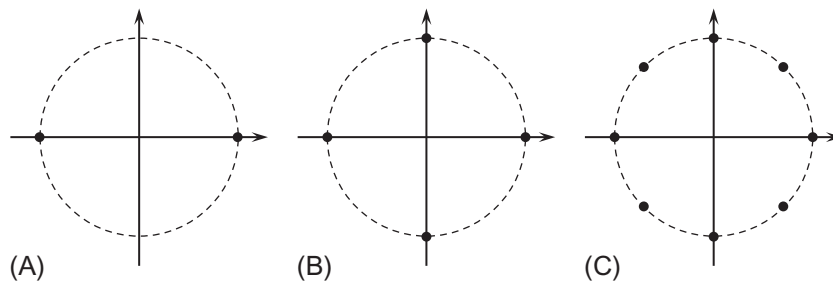
### Rectangular QAM

In this version of QAM, the points are constrained to lie on a grid. If  $B$  (the number of bits per symbol) is even, the points can be arranged on a square grid, as shown in Fig. 3.13 for  $M = 4, 16$ , and  $64$ . If adjacent points are separated by  $2A$ , the minimum Euclidean distance and average energy are

$$d_{\min} = 2A \quad (3.49)$$

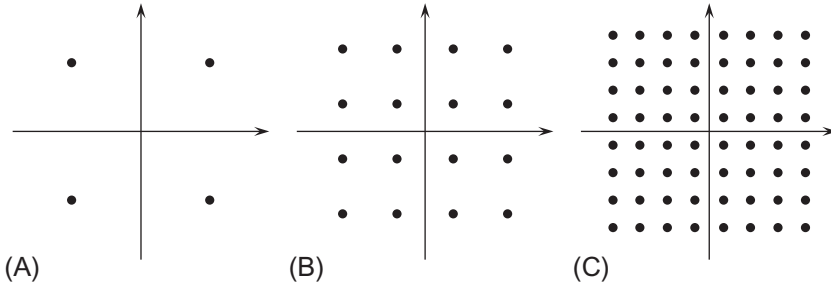
$$E_{\text{avg}} = \frac{2}{3}(M-1)A^2. \quad (3.50)$$

If  $B$  is odd, the points are arranged in what is commonly called a “cross constellation,” such as those shown in Fig. 3.14 for  $M = 8$  and  $32$ . Again, if adjacent points are separated by  $2A$ , the minimum Euclidean distance is  $d_{\min} = 2A$  and the average energy is

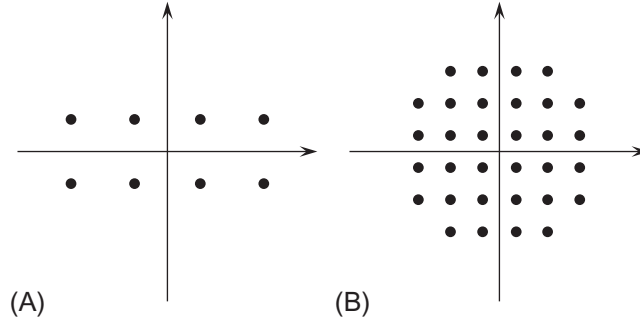


**FIG. 3.12**

MPSK constellations for (A)  $M = 2$ , (B)  $M = 4$ , and (C)  $M = 8$ .

**FIG. 3.13**

Square QAM constellations for (A)  $M = 4$ , (B)  $M = 16$ , and (C)  $M = 64$ .

**FIG. 3.14**

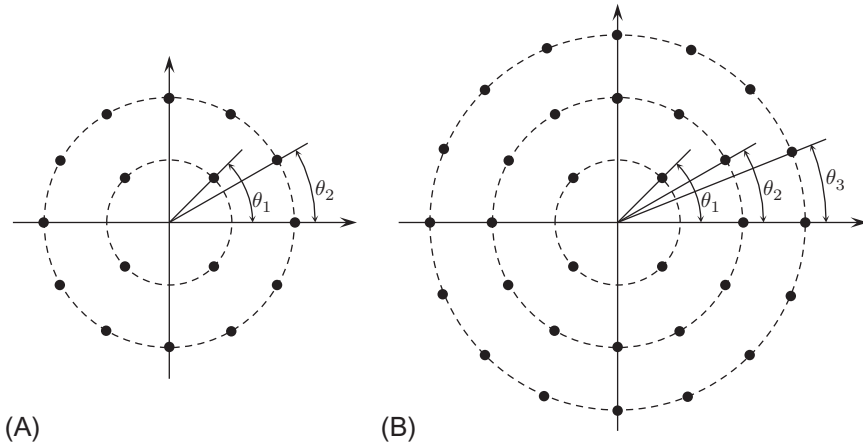
Cross-QAM constellations for (A)  $M = 8$  and (B)  $M = 32$ .

$$E_{\text{avg}} = \begin{cases} 6A^2 & M = 8 \\ 20A^2 & M = 32 \\ 82A^2 & M = 128. \end{cases} \quad (3.51)$$

The DOCSIS 3.1 standard [19], defining wideband Internet access over cable TV systems, specifies the use of the square QPSK, 16-QAM, and 64-QAM constellations shown in Fig. 3.13, together with the SRRC pulse shape with  $\alpha = 0.25$ .

### Amplitude-phase shift keying

In amplitude-phase shift keying (APSK), the constellation points are arranged in equally spaced positions on concentric circles with increasing radii. Two arrangements, known as 4 + 12-APSK and 4+12+16-APSK, are shown in Fig. 3.15. There are four parameters that define the 4+12-APSK constellation in Fig. 3.15A: the radius of the inner circle  $r_1$ , the radius of the outer circle  $r_2$ , and the two angles,

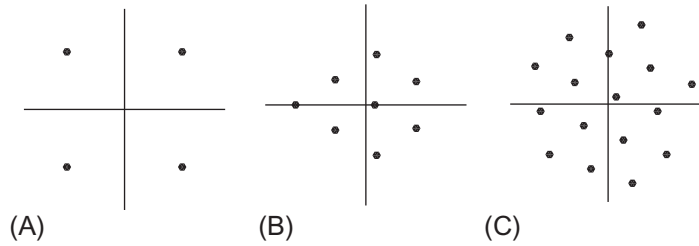
**FIG. 3.15**

APSK constellations: (A) 4 + 12-APSK ( $M = 16$ ) and (B) 4 + 12 + 16-APSK ( $M = 32$ ).

$\theta_1$  and  $\theta_2$ , shown in the figure. Due to the circular symmetry of the constellation, it is often defined by only two parameters: the ratio  $r_2/r_1$  and the phase offset  $\theta_2 - \theta_1$ . These parameters may be chosen to maximize the minimum Euclidean distance or to minimize the peak-to-average power ratio. Similarly, the 4+12+16-APSK constellation, shown in Fig. 3.15B, is defined by six parameters: the radius of the inner circle  $r_1$ , the radius of the middle circle  $r_2$ , the radius of the outer circle  $r_3$ , and the three angles,  $\theta_1$ ,  $\theta_2$ , and  $\theta_3$ , shown in the figure. Because of circular symmetry, the parameters  $r_2/r_1$ ,  $r_3/r_1$ ,  $\theta_2 - \theta_1$ , and  $\theta_3 - \theta_1$  are often used to describe the 4+12+16-APSK constellation. APSK constellations have been thoroughly examined by Lucky and Hancock [20], Weber [21], Salz et al. [22], and Thomas et al. [23]. The two APSK constellations shown in Fig. 3.15, together with the SRRC pulse shape with  $\alpha = 0.35$  (with options for  $\alpha = 0.25$  and  $0.20$ ), form part of the digital video broadcast standard (DVB-S2) published by the European Telecommunications Standards Institute [24].

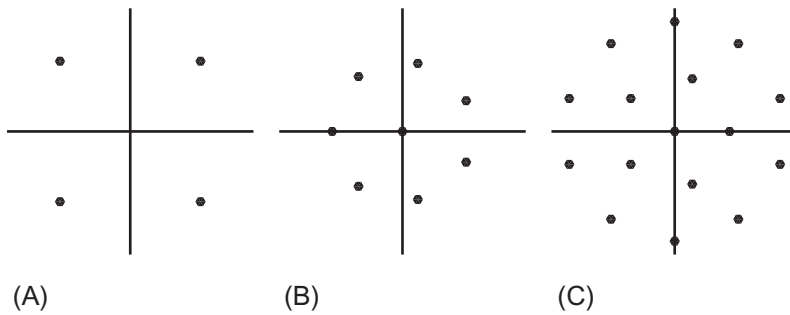
### Minimum probability of error constellations

In Chapter 4, it is shown that the probability of error in the AWGN environment is, asymptotically in  $E_b/N_0$ , a function of the ratio  $d_{\min}^2/E_{\text{avg}}$ . The minimum probability of error constellations maximize the ratio  $d_{\min}^2/E_{\text{avg}}$ . The unconstrained optimizations for  $M = 4, 8$ , and  $16$  were performed by Foschini et al. [25] and are shown in Fig. 3.16. When the constellation points are restricted to lie on a rectangular grid or a set of concentric circles, the optimization produces the constellations shown in Fig. 3.17 for  $M = 4, 8$ , and  $16$ ; in Fig. 3.18 for  $M = 32$  and  $64$ ; and in Fig. 3.19 for  $M = 128$ . These constellations were identified by Thomas et al. [23]. Other possible constellation design criteria are possible. For example, constellations that maximize mutual information were examined by Blachman [26].

**FIG. 3.16**

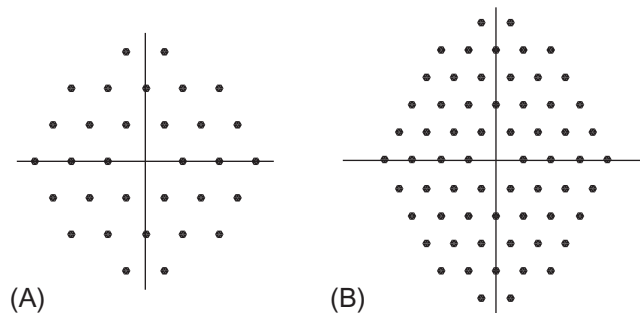
Minimum probability of error constellations: (A)  $M = 4$ , (B)  $M = 8$ , and (C)  $M = 16$ .

Source: Reproduced from Foschini et al. [25].

**FIG. 3.17**

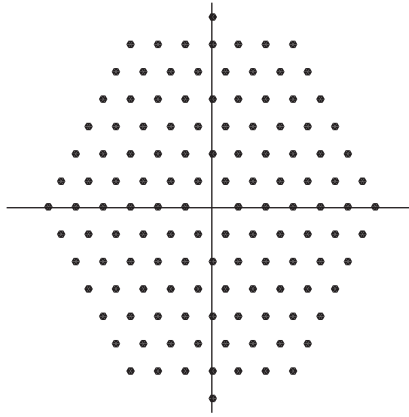
Minimum probability of error constellations constrained to a rectangular grid or a set of concentric circles: (A)  $M = 4$ , (B)  $M = 8$ , and (C)  $M = 16$ .

Source: Reproduced from Thomas et al. [23].

**FIG. 3.18**

Minimum probability of error constellations constrained to a rectangular grid or a set of concentric circles: (A)  $M = 32$  and (B)  $M = 64$ .

Source: Reproduced from Thomas et al. [23].

**FIG. 3.19**

Minimum probability of error constellations constrained to a rectangular grid or a set of concentric circles for  $M = 128$ .

Source: Reproduced from Thomas et al. [23].

### 3.2.7 CONCLUDING REMARKS FOR LINEAR MODULATION

The focus of this section is linear modulations with memoryless mappings. Mappings with memory are also possible. The most commonly encountered form of linear modulations with memory involve a class of mappings called “correlative” encodings, first described by Lender [27] and generalized by Kretzmer [28] and Lender [29]. In the context of the Nyquist No-ISI condition (3.41), this approach produces matched filter outputs with nonzero values for more than one sample. Consequently, ISI is present, but it is controlled-ISI in the sense that the ISI is known and can be accounted for, in the detection process. The advantage of controlled ISI is that the achievable spectral efficiency (with units bits/s per Hz) is greater than that suggested by the Nyquist No-ISI condition and SRRC spectral plots such as those shown in Fig. 3.9.

Offset QPSK (OQPSK) is a commonly encountered variation of QPSK wherein the quadrature component of the modulated carrier is delayed one-half symbol time relative to the inphase component. With reference to Eq. (3.26), the complex-valued baseband equivalent is

$$s_\ell(t) = \sum_k a_i(k)p(t - kT_s) + ja_q(k)p\left(t - \frac{1}{2}T_s - kT_s\right). \quad (3.52)$$

The delay (or offset) of the quadrature component precludes simultaneous transitions on the inphase and quadrature components. This is an advantage when the modulated carrier is subjected to a nonlinearity (such as an RF power amplifier operating at or near full saturation) in the sense that the spectral “regrowth” accompanying the

application of the nonlinearity is less for OQPSK than for QPSK. See Chapter 5 of Rice [4] for more details.

The examples presented in this section were drawn from one-dimensional signal sets (or two real-dimensional signal sets).  $K$ -dimensional signal sets, for  $K > 2$ , are also possible.  $K$ -dimensional constellations are usually conceptualized as a  $K$ -dimensional lattice enclosed within a finite region. The simplest  $K$ -dimensional constellation comprises all the points on a cubic lattice enclosed in a  $K$ -dimensional cube. More densely packed arrangements produce a sort of coding gain whereas using a more sophisticated bounding region produces a shaping gain. For more information, see Forney and Wei [30], Forney [31,32], Livingston [33], and Laroia et al. [34].

### 3.3 NONLINEAR MODULATION: CPM

The most commonly encountered nonlinear modulation is the class of modulations known as CPM. The principle distinguishing feature of CPM is that the information-bearing content is the instantaneous phase. Consequently, a CPM signal has constant amplitude (or envelope), making CPM well-suited for use with nonlinear RF power amplifiers. Because the instantaneous phase of the CPM carrier is defined as the time-integral of the instantaneous frequency, even if the instantaneous frequency is not continuous, the instantaneous phase is continuous, hence the name “continuous phase.” This phase continuity produces a relatively compact power spectral density with advantageous spectral occupancy properties. CPM includes as a special case the continuous phase version of frequency shift keying (CPFSK). The classic references for CPM are the papers by Aulin et al. [35,36]. Because CPM is closely related to FM, this section begins with a short review of FM.

#### 3.3.1 BACKGROUND

The connection between CPM and FM plays a central role in the definition of CPM. The real-valued bandpass equivalent of a generic modulated carrier may be expressed as

$$x_{bp}(t) = A(t) \cos(2\pi f_0 t + \phi(t)), \quad (3.53)$$

where  $A(t)$  is the time-varying amplitude of the carrier and  $f_0$  is the carrier frequency. The formal definitions of phase and frequency are key to understanding FM. The instantaneous phase is the argument of the cosine. The instantaneous frequency is the time-derivative of the instantaneous phase:

$$\begin{aligned} \text{Instantaneous phase} &= 2\pi f_0 t + \phi(t) \\ \text{Instantaneous frequency} &= f_0 + \frac{1}{2\pi} \frac{d}{dt} \phi(t). \end{aligned} \quad (3.54)$$

This shows that the instantaneous phase comprises variations about a ramp whose slope is proportional to the carrier frequency. The instantaneous frequency comprises variations about the horizontal line at  $f_0$ . The instantaneous excess phase and frequency are defined as the variations in the phase and frequency, respectively, relative to the carrier:

$$\begin{aligned}\text{Instantaneous excess phase} &= \phi(t) \\ \text{Instantaneous excess frequency} &= \frac{1}{2\pi} \frac{d}{dt} \phi(t).\end{aligned}\tag{3.55}$$

The instantaneous excess phase and frequency are the instantaneous phase and frequency, respectively, of the complex-valued baseband equivalent waveform:

$$x_{\text{bb}}(t) = A(t)e^{j\phi(t)}.\tag{3.56}$$

In the case of FM, the instantaneous excess frequency is proportional to a real-valued, baseband modulating signal  $m(t)$ :

$$\frac{1}{2\pi} \frac{d}{dt} \phi(t) = k_f m(t),\tag{3.57}$$

where the constant of proportionality  $k_f$  is called the frequency deviation and the amplitude in Eqs. (3.53), (3.56) is a constant:  $A(t) = A$ . Consequently, the instantaneous excess phase is given by

$$\phi(t) = 2\pi k_f \int_0^t m(x) dx\tag{3.58}$$

so that the real-valued bandpass and complex-valued baseband equivalents are

$$x_{\text{bp}}(t) = A \cos(2\pi f_0 t + \phi(t))\tag{3.59}$$

$$x_{\text{bb}}(t) = A e^{j\phi(t)}.\tag{3.60}$$

Often, the FM signal is parameterized by the peak frequency deviation  $f_d$  given by

$$f_d = k_f \max_{\text{all } t} \{|m(t)|\}.\tag{3.61}$$

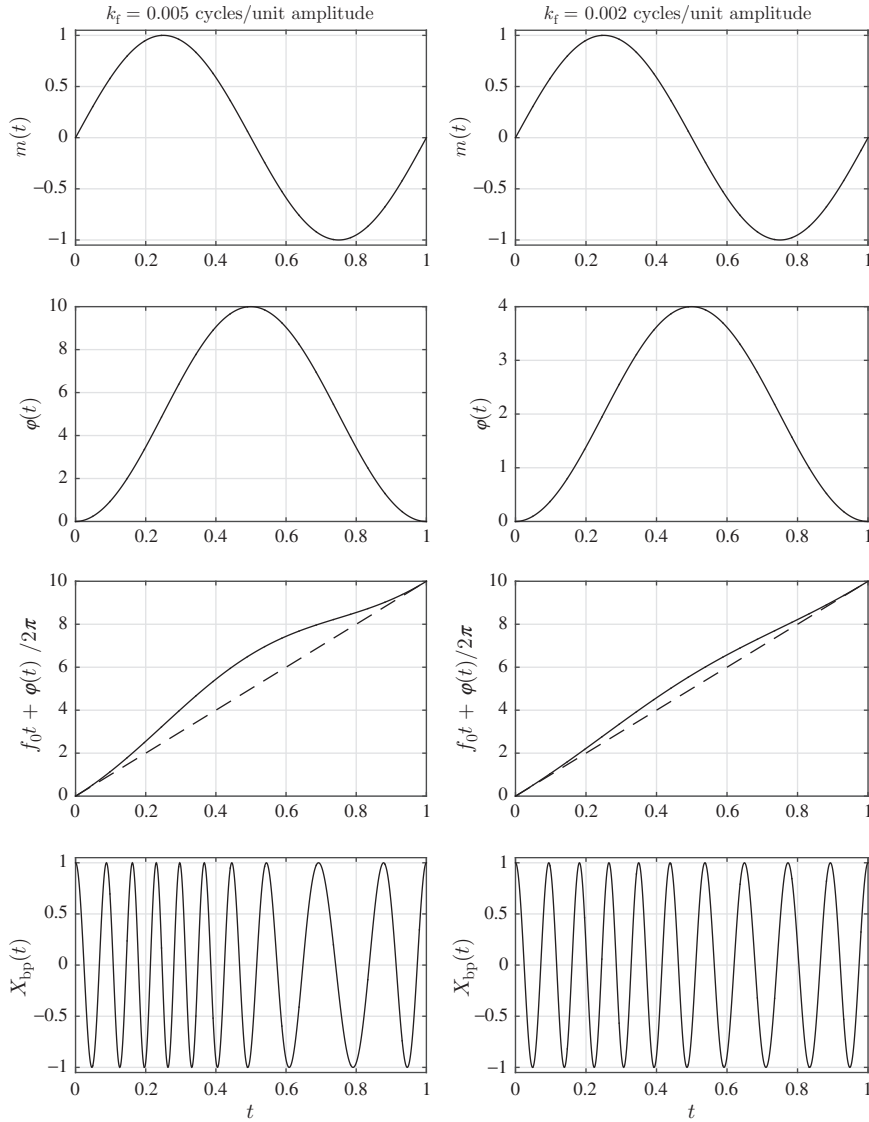
In this way, the instantaneous excess phase may be parameterized by  $f_d$ :

$$\phi(t) = 2\pi \frac{f_d}{\max \{|m(t)|\}} \int_0^t m(x) dx.\tag{3.62}$$

**Example 3.3.** This example illustrates the relationship between the instantaneous frequency and instantaneous phase for the case where

$$m(t) = \sin(2\pi t), \quad 0 \leq t \leq 1.$$

The signals corresponding to  $m(t)$  for  $0 \leq t \leq 1$  are plotted in Fig. 3.20. The left column of this figure corresponds to  $k_f = 0.005$  cycles/unit amplitude whereas the

**FIG. 3.20**

An example illustrating the relationship between instantaneous frequency and instantaneous phase for the simple signal  $m(t)$  for  $k_f = 0.005$  cycles/unit amplitude (*left column*) and for  $k_f = 0.002$  cycles/unit amplitude (*right column*): the *first row* shows the modulating signal  $m(t)$ ; the *second row* shows the instantaneous excess phase  $\phi(t)$ ; the *third row* shows the instantaneous phase  $f_0 t + \phi(t)/2\pi$ ; and the *fourth row* shows the real-valued bandpass signal.

right column corresponds to  $k_f = 0.002$  cycles/unit amplitude. The second row is the time-integral of the first row:

$$\phi(t) = 2\pi k_f \int_0^1 m(x) dx = -k_f [\cos(2\pi t) - 1].$$

The third row is the scaled instantaneous phase:

$$f_0 t + \frac{1}{2\pi} \phi(t).$$

The dashed line on this row is  $f_0 t$ . Note how the instantaneous excess phase comprises variations about the line  $f_0 t$ . The difference between the solid line and the dashed line is a scaled version of the instantaneous excess phase. The fourth row is the corresponding bandpass signal

$$x_{bp}(t) = \cos(2\pi f_0 t + \phi(t)).$$

Note the relationship between  $m(t)$  and the frequency of  $x_{bp}(t)$ . The more positive the amplitude of  $m(t)$ , the higher the frequency of  $x_{bp}(t)$ ; likewise, the more negative the amplitude of  $m(t)$ , the lower the frequency  $x_{bp}(t)$ .

This example also illustrates the impact of  $k_f$  on the waveforms. The larger the  $k_f$ , the larger the change in the instantaneous excess phase per unit change in  $m(t)$ . The corresponding instantaneous frequency also has a larger deviation.

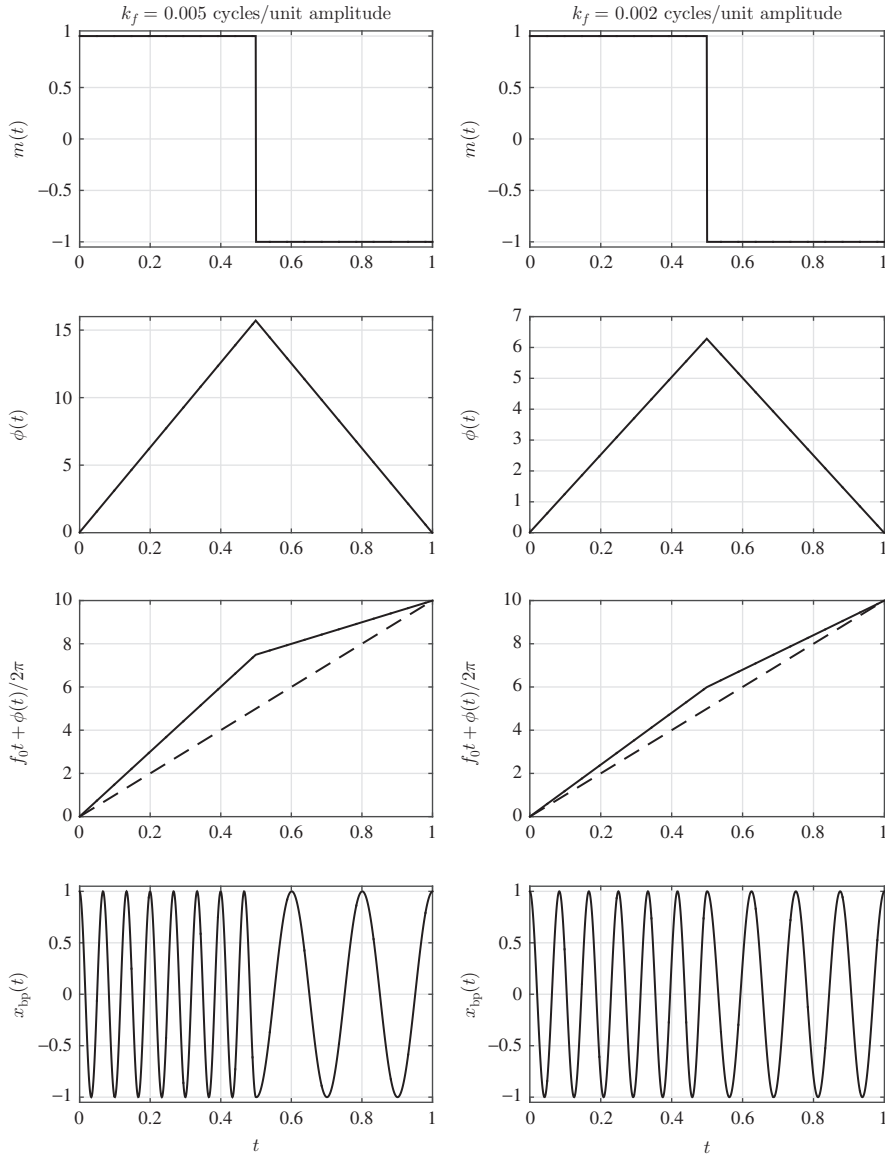
**Example 3.4.** This example is identical to [Example 3.3](#), except that a different  $m(t)$  is used. The modulating signal used here is the square wave plotted in the first row of [Fig. 3.21](#). The corresponding instantaneous excess phases, instantaneous phases, and bandpass signals are plotted in the second, third, and fourth rows, respectively, for  $k_f = 0.005$  and  $k_f = 0.002$  cycles/unit amplitude in the first and second columns, respectively.

Note that a square wave input causes a frequency shift in  $x_{bp}(t)$  between a high and low frequency. The high frequency corresponds to  $m(t) = +1$  whereas the low frequency corresponds to  $m(t) = -1$ . The frequency shift (difference between the high and low frequencies) is controlled by the frequency deviation  $k_f$ . This observation is the basis for *frequency shift keying* (FSK), the most simple form of CPM. FSK will be discussed in [Section 3.3.5](#).

### 3.3.2 MATHEMATICAL DESCRIPTION

The complex-valued baseband equivalent representation of CPM is

$$x_{bb}(t) = e^{j\phi(t;\mathbf{a})}, \quad (3.63)$$

**FIG. 3.21**

An example illustrating the relationship between instantaneous frequency and instantaneous phase for the simple signal  $m(t)$  for  $k_f = 0.005$  cycles/unit amplitude (*left column*) and for  $k_f = 0.002$  cycles/unit amplitude (*right column*): the *first row* shows the modulating signal  $m(t)$ ; the *second row* shows the instantaneous excess phase  $\phi(t)$ ; the *third row* shows the instantaneous phase  $f_0 t + \phi(t)/2\pi$ ; and the *fourth row* shows the real-valued bandpass signal.

where  $\mathbf{a} = \dots, a(0), a(1), \dots$  is the symbol sequence, and the instantaneous phase, for  $nT_s \leq t \leq (n+1)T_s$ , is given by

$$\phi(t; \mathbf{a}_n) = 2\pi h \sum_{k=0}^n a(k)q(t - kT_s). \quad (3.64)$$

The parameters that define the phase are

- $h$  is the digital modulation index.
- $a(k)$  is the  $k$ th symbol, drawn from the alphabet  $\{\pm 1, \pm 3, \dots, \pm(M-1)\}$ . In this notation,  $\mathbf{a}_n = [\dots, a(0), a(1), \dots, a(n)]$ .
- $q(t)$  is the phase pulse. The phase pulse is defined as the time integral of a frequency pulse  $g(t)$  whose support is  $0 \leq t \leq LT_s$  (for some integer  $L$ ) and whose area is  $\frac{1}{2}$ . The reason for defining  $q(t)$  as a time integral is the frequency-phase relationship outlined in [Section 3.3.1](#).

The frequency pulse spans  $L$  symbol intervals, where  $L$  is usually a positive integer. When  $L = 1$ , the modulation is called a full response CPM; otherwise, the modulation is called partial response CPM. Because the phase pulse is defined as the time integral of a frequency pulse with finite support, it is customary to use a piecewise definition for  $q(t)$ :

$$q(t) = \begin{cases} 0 & t < 0 \\ \int_0^t g(u)du & 0 \leq t < LT_s \\ \frac{1}{2} & LT_s \leq t. \end{cases} \quad (3.65)$$

Consequently, Eq. (3.64) may also be expressed in a piecewise fashion:

$$\phi(t; \mathbf{a}_n) = \underbrace{\pi h \sum_{k=0}^{n-L} a(k)}_{\theta_n} + \underbrace{2\pi h \sum_{k=n-L+1}^n a(k)q(t - kT_s)}_{\theta(t; a(n-L+1), \dots, a(n))}. \quad (3.66)$$

Here, the first term is called the phase state of the modulation. Because the phase state may be reduced to modulo- $2\pi$  and because the symbol alphabet is finite, there is a finite number of possible phase states. For  $h = \frac{2m}{p}$  for relatively prime  $m$  and  $p$ , there are  $p$  phase states:

$$\theta_n \in \left\{ 0, \frac{2\pi}{p}, \frac{4\pi}{p}, \dots, \frac{2\pi(p-1)}{p} \right\}. \quad (3.67)$$

Note that the phase states are defined by the modulation index and by the sum of all the symbols prior to  $a(n-L+1)$ . The second term in Eq. (3.66) defines modulation states due to the phase pulse. For a given modulation index and phase pulse, the states defined by this term are only a function of the previous  $(L-1)$  symbols  $\{a(n-L+1), \dots, a(n-1)\}$  and the current symbol  $a(n)$ . The vector comprising the previous  $(L-1)$  symbols is called the correlative state vector. Consequently, during

the interval  $nT_s \leq t \leq (n+1)T_s$ , the CPM signal is completely described by the state vector

$$\mathcal{S}_n = \{\theta_n, a(n-1), \dots, a(n-L+1)\}. \quad (3.68)$$

Two of the most commonly encountered frequency pulses in CPM are the length- $L$  rectangular pulse (LREC), defined by

$$g(t) = \begin{cases} \frac{1}{2LT_s} & 0 \leq t \leq LT_s \\ 0 & \text{otherwise} \end{cases}, \quad (3.69)$$

and the length- $L$  temporal raised-cosine (LRC) defined by

$$g(t) = \begin{cases} \frac{1}{2LT_s} \left[ 1 - \cos\left(\frac{2\pi t}{LT_s}\right) \right] & 0 \leq t \leq LT_s \\ 0 & \text{otherwise} \end{cases}. \quad (3.70)$$

These two pulses, together with their time integrals  $q(t)$ , are shown in Fig. 3.22.

At high  $E_b/N_0$ , the performance of the maximum-likelihood detector in AWGN is determined by  $E_b/N_0$  and the minimum Euclidean distance. The squared Euclidean distance between the signals corresponding to the symbol sequences are as follows:

$$\mathbf{a}_n = a(0), a(1), \dots, a(n) \quad (3.71)$$

$$\mathbf{b}_n = b(0), b(1), \dots, b(n) \quad (3.72)$$

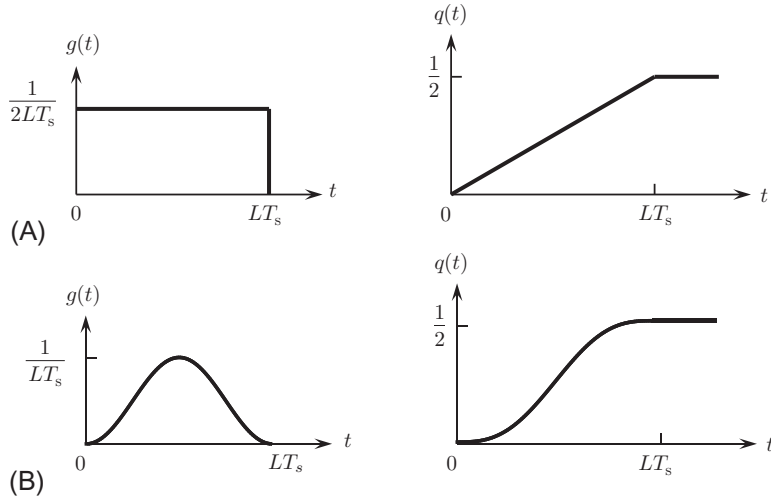


**FIG. 3.22**

Two of the most commonly encountered CPM frequency pulses and their time integrals: (A) the LREC pulse  $g(t)$  and the corresponding time integral  $q(t)$  and (B) the LRC pulse  $g(t)$  and the corresponding time integral  $q(t)$ .

is

$$d_n^2(\mathbf{a}_n, \mathbf{b}_n) = \int_0^{nT_s} \left| e^{j\phi(t; \mathbf{a}_n)} - e^{j\phi(t; \mathbf{b}_n)} \right|^2 dt \quad (3.73)$$

$$= 2 \int_0^{nT_s} \left[ 1 - \cos \left( 2\pi h \sum_{i=0}^n \Delta(i) q(t - iT_s) \right) \right] dt, \quad (3.74)$$

where  $\Delta(i) = a(i) - b(i)$ . Thus, the Euclidean distance is a function of the difference  $\Delta_n = \mathbf{a}_n - \mathbf{b}_n$  and may be expressed as  $d_n^2(\Delta_n)$ . The minimum Euclidean distance is

$$d_{n,\min}^2 = \min_{\Delta_n \neq \mathbf{0}} \left\{ d_n^2(\Delta_n) \right\}. \quad (3.75)$$

Aulin et al. [36] develop an upper bound for  $d_{n,\min}^2$  and describe a sequential algorithm for computing  $d_{n,\min}^2$ .

### 3.3.3 MODULATION

A CPM signal is generated by applying the pulse train,

$$m(t) = \sum_k a(k)g(t - kT_s), \quad (3.76)$$

to a frequency modulator. This technique is shown in Fig. 3.23A. The pulse train, based on the symbol alphabet and the frequency pulse  $g(t)$ , is created using a serial-to-parallel converter, LUT, and pulse shaping filter in the same way these elements were used for QAM in Fig. 3.6. The pulse train frequency modulates a carrier using a peak deviation  $f_d = h/(2T_s)$  as shown.

For the simplest case,  $M = 2$  and  $g(t)$  is the 1REC pulse, and the maximum is

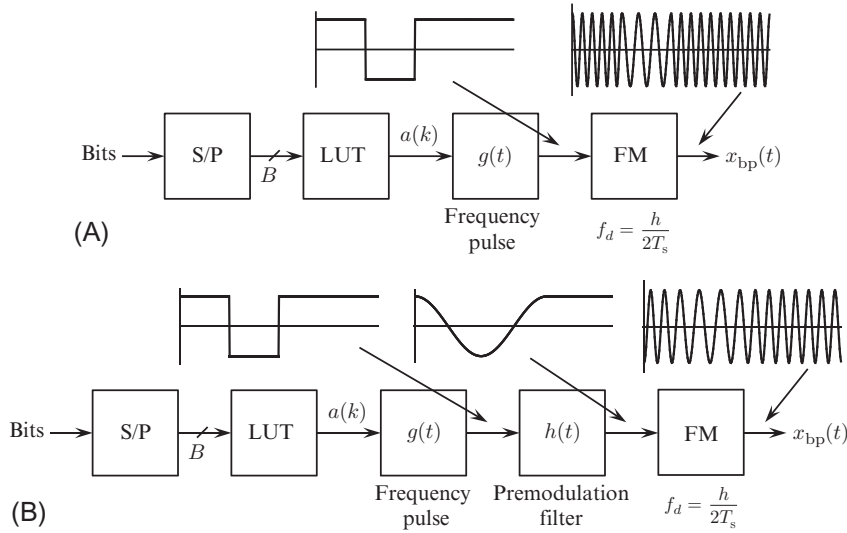
$$\max_{\text{all } t} \{|m(t)|\} = \frac{1}{2T_s} \quad (3.77)$$

so that the instantaneous excess phase for  $nT_s \leq t \leq (n+1)T_s$  may be expressed as

$$\phi(t) = 2\pi \frac{f_d}{2T_s} \int_0^t \sum_{k=0}^n a(k)g(x - kT_s)dx \quad (3.78)$$

$$= 2\pi(2f_d T_s) \sum_{k=0}^n a(k) \int_0^t g(x - kT_s)dx \quad (3.79)$$

$$= 2\pi(2f_d T_s) \sum_{k=0}^n a(k)q(t - kT_s). \quad (3.80)$$

**FIG. 3.23**

A block diagram illustrating the generation of CPM using a frequency modulator: (A) the standard approach and (B) using a premodulation filter.

Comparing Eq. (3.80) with Eq. (3.64) establishes the relationship  $h = 2f_d T_s$ . The comparison also shows that the time-integral relationship between the instantaneous frequency and phase is why the phase pulse  $q(t)$  is defined as the time integral of the frequency pulse  $g(t)$ . The time-integral relationship between the frequency pulse  $g(t)$  and the phase pulse  $q(t)$  means that even if  $g(t)$  contains discontinuities, the phase pulse will not. Because the phase pulse transitions from one symbol to another in a continuous fashion, the name CPM is used.

The impact of the frequency pulse on the power spectral density is described in Section 3.3.4. In general, longer (and sometimes smoother) frequency pulses produce more narrow power spectral densities. Historically, longer, smoother frequency pulses were conceptualized as a lowpass-filtered version of the 1REC frequency pulse as shown in Fig. 3.23B. The lowpass filter with impulse response  $h(t)$  is called a premodulation filter due to its position at the input to the frequency modulator. Conceptualizing the frequency pulse as a lowpass filtered version of the 1REC pulse was motivated by technological limitations: mature analog filter design techniques were applied to the easy-to-generate 1REC pulse. The true frequency pulse is simply the convolution of the 1REC frequency pulse with  $h(t)$ . As advances in digital circuits have made more sophisticated discrete-time signal processing viable, the true frequency pulse is implemented directly. Consequently, using a lowpass filtered 1REC frequency pulse has become less common. Because of this history, some frequency pulses are defined in terms of the 1REC pulse and  $h(t)$ . This is the case with Gaussian minimum shift keying (GMSK), described in Section 3.3.5.

### 3.3.4 POWER SPECTRAL DENSITY

The power spectral density of CPM is computed from Eq. (3.63) using

$$\phi(t; \mathbf{a}) = 2\pi h \sum_{k=-\infty}^{\infty} a(k)q(t - kT_s). \quad (3.81)$$

The analysis assumes an infinite number of uncorrelated and equally likely symbols:

$$P(a(k) = a_m) = \frac{1}{M}, \quad m = 1, 2, \dots, M \quad (3.82)$$

$$E\{a(k)\} = 0 \quad (3.83)$$

$$E\{a^2(k)\} = \frac{M^2 - 1}{3}. \quad (3.84)$$

The power spectral density of the complex-valued baseband equivalent signal is [37]

$$S_{bb}(f) = 2 \operatorname{Re} \left\{ \int_0^{LT_s} R(\tau) e^{-j2\pi f \tau} d\tau + \frac{1}{1 - C e^{-j2\pi f T_s}} \int_{LT_s}^{(L+1)T_s} R(\tau) e^{-j2\pi f \tau} d\tau \right\}, \quad (3.85)$$

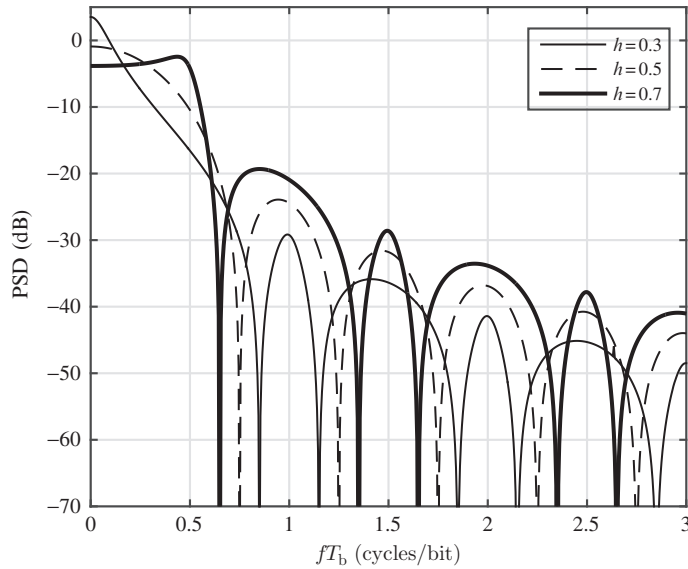
where

$$R(\tau) = \frac{1}{2T_s} \int_0^{T_s} \prod_{k=1-L}^{\lceil \tau/T_s \rceil} \frac{\sin(2\pi h M [q(t + \tau - kT_s) - q(t - kT_s)])}{M \sin(2\pi h [q(t + \tau - kT_s) - q(t - kT_s)])} dt, \quad (3.86)$$

$$C = \frac{\sin(M\pi h)}{M \sin(\pi h)}. \quad (3.87)$$

Because CPM is a nonlinear modulation, the relationship between the modulation parameters (frequency pulse, modulation index, alphabet size) and the power spectral density is not as straight-forward as it is for linear modulation. The main characteristics of the power spectral density are the width of the main lobe and the fall-off rate (ie, the rate at which the power spectral density level decreases with increasing  $fT_s$ ). A few simple examples will illustrate some of the general trends and point out some of the difficulties.

- **Fig. 3.24** plots the power spectral densities of binary CPM using the 1REC pulse shape for three values of the modulation index  $h$ . Each value of  $h$  produces a different main lobe shape and width and different sidelobe structure. For the parameters used here, as  $h$  increases, the main lobe width decreases whereas the height of the sidelobes increases. In general, the fall-off rate improves with decreasing  $h$ . **Table 3.3** shows that the minimum Euclidean distance also decreases with decreasing  $h$ . This suggests a trade-off involving bandwidth and bit error rate performance. The modulation index  $h$  can be used to select the operating point in this trade-off space.

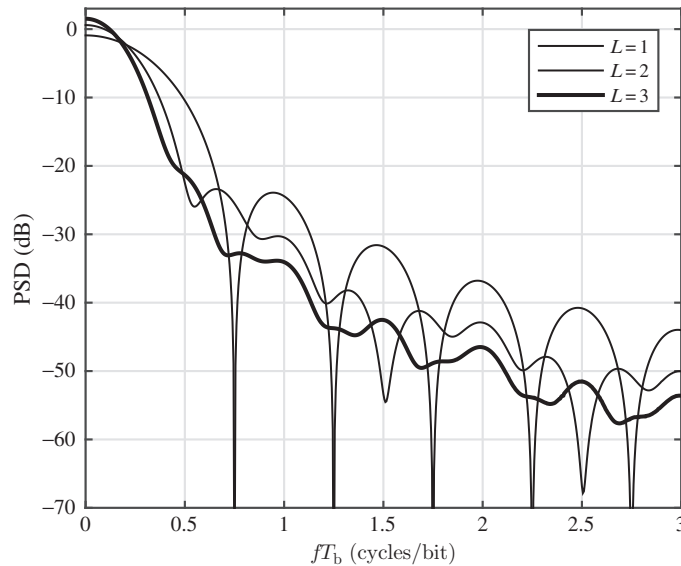

**FIG. 3.24**

Power spectral density plots for CPM using the 1REC frequency pulse with  $M = 2$  for  $h = 0.3, 0.5, 0.7$ .

**Table 3.3** Minimum Euclidean Distances and Normalized 99% Power Bandwidths for the CPM Cases Explored in Figs. 3.24–3.26 and 3.30

Frequency Pulse	$h$ (Modulation Index)	$d_{\min}$	$B_{99}T_b$
1REC	0.3	0.990898	0.360
1REC	0.5	2.000000	0.540
1REC	0.7	2.432473	0.800
2REC	0.5	1.726760	0.380
3REC	0.5	1.346013	0.315
1RC	0.5	2.000000	0.715
2RC	0.5	1.966553	0.490
3RC	0.5	1.764665	0.395
Gaussian, $BT_b = 1.0$	0.5	2.000000	0.515
Gaussian, $BT_b = 0.5$	0.5	1.940487	0.475
Gaussian, $BT_b = 0.4$	0.5	1.892986	0.450
Gaussian, $BT_b = 0.3$	0.5	1.786840	0.415
Gaussian, $BT_b = 0.2$	0.5	1.531934	0.350

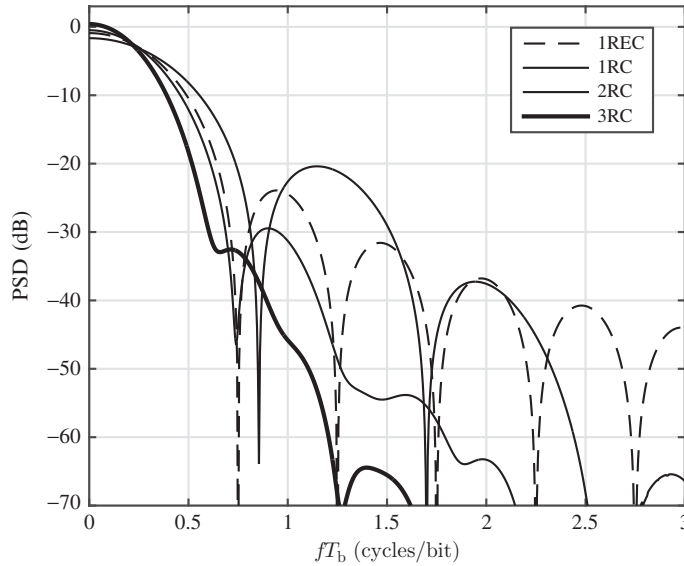
Note: The values for  $d_{\min}$  were computed using the online resource by Perrins [39].

**FIG. 3.25**

Power spectral density plots for CPM using the LREC frequency pulse with  $M = 2$  and  $h = 0.5$  for  $L = 1, 2, 3$ .

- Fig. 3.25 plots the power spectral densities of binary CPM using  $h = 0.5$  and the LREC frequency pulse for  $L = 1, 2, 3$ . Here, the general trend that the fall off rate improves as  $L$  increases is observed. Table 3.3 shows that the minimum Euclidean distance decreases as  $L$  increases. This is a slightly different manifestation of the trade-off involving bandwidth and bit error rate performance. Here the parameter  $L$  selects the operating point in the trade-off space.
- Fig. 3.26 plots the power spectral densities of binary CPM using  $h = 0.5$  and the 1RC, 2RC, and 3RC frequency pulses. The power spectral density corresponding to the 1REC frequency pulse is included for reference. As was the case for the LREC frequency pulse, the fall-off rate improves with an increasing  $L$ , and Table 3.3 shows that the minimum Euclidean distance decreases with increasing  $L$ .

Comparing the power spectral densities corresponding to the 1REC and 1RC pulses is interesting: The main lobe of the power spectral density corresponding to the 1REC pulse is narrower than that corresponding to the 1RC pulse. The first two sidelobes of the power spectral density corresponding to the 1REC pulse are lower than the first sidelobe of the power spectral density corresponding to the 1RC pulse. This is explained by the fact that the peak frequency deviation for the 1RC pulse is twice that for the 1REC pulse. In contrast, the third and higher

**FIG. 3.26**

Power spectral density plots for CPM with  $M = 2$  and  $h = 0.5$  for the 1REC, 1RC, 2RC, and 3RC frequency pulses.

sidelobes of the power spectral density corresponding to the 1REC pulse are higher than the second and higher sidelobes of the power spectral density corresponding to the 1RC pulse. This illustrates the general trend that the fall-off rate at large,  $fT_s$ , is better for smoother frequency pulses. For large  $fT_s$ , the fall-off rate is determined by the number of continuous derivatives of  $g(t)$  [36,38]. Note that the CPM using the 1REC and 1RC frequency pulses achieves the same minimum Euclidean distance (see Table 3.3).

Due to space limitations, the behavior of the power spectral density as a function of the alphabet size  $M$  was not explored. Plots of Eq. (3.85) as a function of  $M$  are given in Aulin et al. [35,36]. The expected outcome is observed: the main lobe width and fall-off rate, both as a function of the equivalent  $fT_b$ , improve with increasing  $M$ .

The power spectral density is the basis for bandwidth definitions for CPM. One common measure of bandwidth is the 99% power bandwidth,  $B_{99}$ . The 99% power bandwidth is the interval on the frequency axis that captures 99% of the area under the power spectral density. The formal definition is

$$\int_0^{B_{99}} S_{bb}(f) df = 0.99 \times \int_0^{\infty} S_{bb}(f) df. \quad (3.88)$$

Note that  $B_{99}$  is the bandwidth of the complex-valued baseband equivalent signal whereas  $2B_{99}$  is the bandwidth for the real-valued bandpass equivalent signal. The

normalized 99% power bandwidths  $B_{99}T_b$  corresponding to the power spectral densities plotted in Figs. 3.24–3.26 and 3.30 are tabulated in Table 3.3.

Finally, because the relationship (3.87) holds for noninteger values of  $h$ , the power spectral density expression (3.85) holds only when  $h$  is not an integer. When  $h$  is an integer, the power spectral density exhibits spectral lines [37,40,41]. For the applications where bandwidth efficiency is important, the spectral lines tend to violate spectral containment requirements. Consequently,  $h < 1$  is used. In contrast, systems operating in severe radio environments rely on noncoherent detection. The probability of error performance for noncoherent detection is maximized when the signals are orthogonal. As explained in Section 3.3.5, an integer value of  $h$  is required to produce an orthogonal signal set under the constraint of noncoherent detection.

### 3.3.5 CPFSK, MSK, AND GMSK

The continuous phase version of binary FSK corresponds to CPM when using the 1REC frequency pulse. The phase for  $nT_b \leq t \leq (n+1)T_b$  is

$$\phi(t; \mathbf{a}_n) = \pi h \sum_{k=0}^{n-1} a(k) + a(n) \frac{\pi h}{T_b} (t - nT_b), \quad (3.89)$$

and the corresponding bandpass signal is

$$x_{bp}(t) = \sqrt{2} \operatorname{Re} \left\{ e^{j\phi(t; \mathbf{a}_n)} e^{j2\pi f_0 t} \right\} = \sqrt{2} \cos \left( 2\pi \left( f_0 + a(n) \frac{h}{2T_b} \right) t + \theta_n - na(n)\pi h \right), \quad (3.90)$$

where  $\theta_n$  is the first term on the right-hand side of Eq. (3.89). For binary CPFSK, the data shifts the carrier frequency by  $\pm h/(2T_b)$ , hence the name FSK. An example corresponding to the symbol sequence  $\mathbf{a} = +1, -1, +1, +1$  is shown in Fig. 3.27. Note the higher frequency during the intervals  $0 \leq t \leq T_b$  and  $2T_b \leq t \leq 4T_b$  and the lower frequency during the interval  $T_b \leq t \leq 2T_b$ . Also note the phase continuity between the frequency shifts.

The real-valued bandpass signal corresponding to binary CPFSK suggests the existence of two waveforms in the signal set: The first is a sinusoid with frequency  $f_0 - h/(2T_b)$  and the second is a sinusoid at frequency  $f_0 + h/(2T_b)$ . For the interval  $0 \leq t \leq T_b$ , the complex-valued baseband equivalent of the two signals may be expressed as follows:

$$\begin{aligned} s_{0,bb}(t) &= \exp \left\{ j \left[ -2\pi \frac{ht}{2T_b} + \theta_0 \right] \right\} \\ s_{1,bb}(t) &= \exp \left\{ j \left[ 2\pi \frac{ht}{2T_b} + \theta_0 \right] \right\}, \end{aligned} \quad (3.91)$$

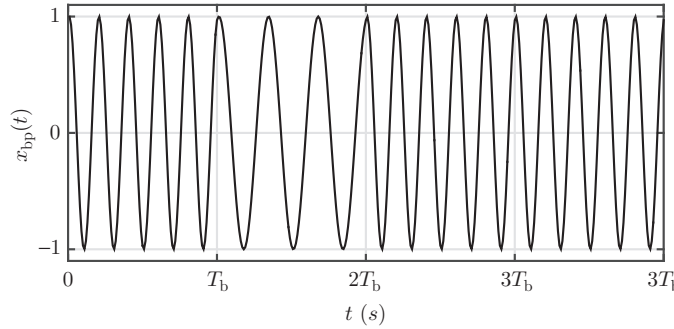


**FIG. 3.27**

A plot of binary CPFSK corresponding to the bit sequence  $\mathbf{a} = +1, -1, +1, +1$  for  $h = 2$ . Note that  $h = 2$  is an unusably large value for the modulation index. It is used here to make the frequency shift in the plot more obvious.

where as before,  $\theta_0$  is the first term on the right-hand side of Eq. (3.89). The inner product is

$$\langle s_{1,bb}(t), s_{0,bb}(t) \rangle = \int_0^{T_b} e^{j2\pi ht/T_b} dt = T_b \frac{\sin(\pi h)}{\pi h} e^{j\pi h}. \quad (3.92)$$

For coherent detection, the probability of error decreases with increasing  $\rho_c$ , where

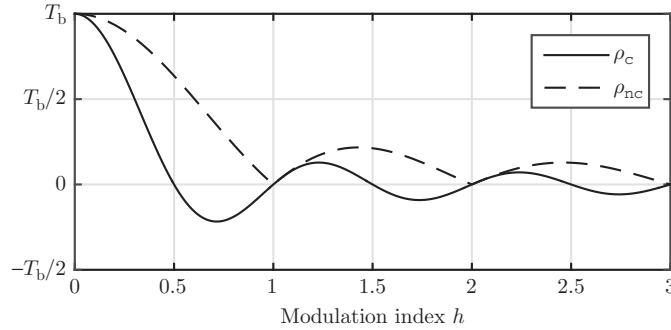
$$\rho_c = \text{Re} \{ \langle s_{1,bb}(t), s_{0,bb}(t) \rangle \} = T_b \frac{\sin(2\pi h)}{2\pi h}. \quad (3.93)$$

For noncoherent detection, the probability of error decreases with increasing  $\rho_{nc}$ , where

$$\rho_{nc} = | \langle s_{1,bb}(t), s_{0,bb}(t) \rangle | = T_b \left| \frac{\sin(\pi h)}{\pi h} \right|. \quad (3.94)$$

In either case, the correlation is a function of the modulation index  $h$ . A plot of  $\rho_c$  and  $\rho_{nc}$  versus  $h$  is shown in Fig. 3.28. Note that for coherent detection, the minimum probability of error corresponds to  $h = 0.715$ . Also for coherent detection,  $\rho_c$  exhibits zero-crossings when  $h$  is a positive integer multiple of  $\frac{1}{2}$ . When  $\rho_c = 0$ , the two signals are orthogonal and unit-energy versions of  $s_{0,bb}(t)$  and  $s_{1,bb}(t)$  may be used as basis waveforms to represent the two waveforms in a signal space. The minimum value of  $h$  that renders  $s_{0,bb}(t)$  and  $s_{1,bb}(t)$  orthogonal is  $h = \frac{1}{2}$ , and the resulting modulation is called minimum shift keying (MSK). For noncoherent detection,  $\rho_{nc}$  exhibits zero-crossings when  $h$  is a positive integer. Here, the minimum frequency shift required for orthogonality is twice that required for coherent detection.

In Section 3.3.4, it was shown that longer (and sometimes smoother) frequency pulses produce a power spectral density with better spectral containment relative to the power spectral density corresponding to the 1REC frequency pulse. Generating

**FIG. 3.28**

A plot of the  $\rho_c$  (Eq. 3.93) and  $\rho_{nc}$  (Eq. 3.94) as a function of the modulation index  $h$ .

more interesting frequency pulses using a lowpass premodulation filter was described in Section 3.3.3. One popular application of this approach to MSK was described by Murota and Hirade [42], who investigated the use of a lowpass filter with a Gaussian impulse response:

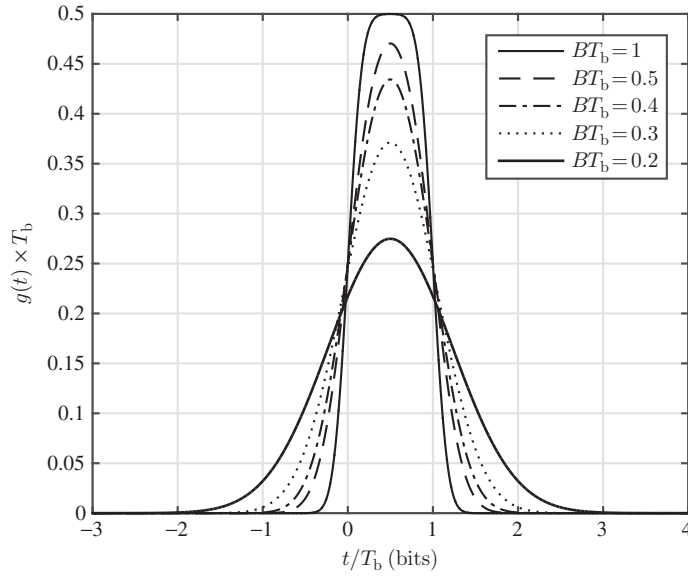
$$h(t) = B \sqrt{\frac{2\pi}{\ln(2)}} \exp \left\{ -\frac{(2\pi Bt)^2}{2 \ln(2)} \right\}, \quad (3.95)$$

where  $B$  is the 3-dB bandwidth of the filter. The resulting frequency pulse is

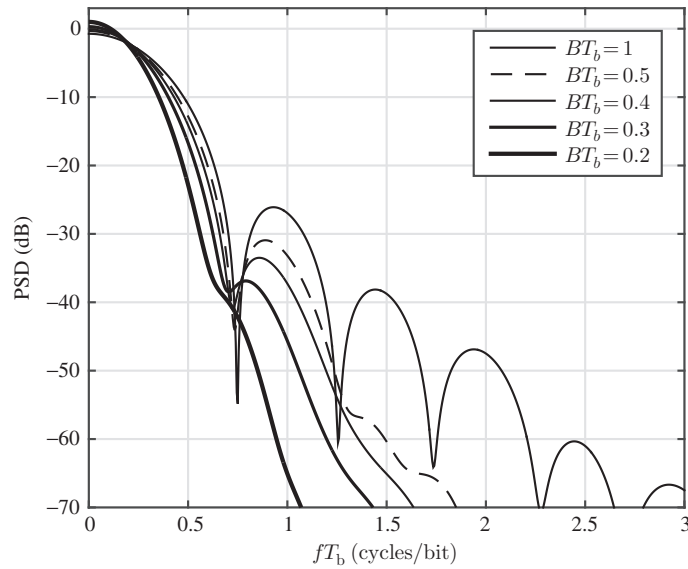
$$g(t) = \frac{1}{2T_b} \left[ Q \left( \frac{2\pi B T_b}{\sqrt{\ln(2)}} \left( \frac{t}{T_b} - 1 \right) \right) - Q \left( \frac{2\pi B T_b}{\sqrt{\ln(2)}} \frac{t}{T_b} \right) \right]. \quad (3.96)$$

Because the pulse was generated from MSK by using a premodulation filter with a “Gaussian” impulse response, Murota and Hirade coined the term “Gaussian minimum shift keying” (or GMSK) for this modulation. The frequency pulse is parameterized by the product of the 3-dB bandwidth and bit time:  $BT_b$ . A plot of  $g(t)$  for  $BT_b = 1, 0.5, 0.4, 0.3$ , and  $0.2$  is shown in Fig. 3.29. The plot shows that even though Eq. (3.96) is defined for  $-\infty < t < \infty$ , the pulse may be truncated without introducing significant errors. The result is a pulse that spans  $L < \infty$  symbols. Observe that as  $BT_b$  decreases, the required pulse width increases. The power spectral densities corresponding to these frequency pulses are plotted in Fig. 3.30. In general, the bandwidth decreases with decreasing  $BT_b$  and Table 3.3 shows that the minimum Euclidean distance decreases with decreasing  $BT_b$ . Fig. 3.30 and Table 3.3 demonstrate the trade-off between bandwidth and bit error rate performance for GMSK. The frequency pulse parameter  $BT_b$  may be used to adjust the operating point in this trade-off space.

GMSK with  $BT_b = 0.3$  is the modulation used for the GSM (for the French Groupe Spécial Mobile) mobile telephony standard [43]. GMSK is also used for the telemetry links for near-Earth and deep-space spacecraft: the CCSDS

**FIG. 3.29**

GMSK frequency pulses for various values of  $BT_b$ . As  $BT_b$  decreases, the pulses become wider.

**FIG. 3.30**

The power spectral density of GMSK for  $M = 2$  and various values of  $BT_b$ .

413.0-G-1 Green Book (for Consultative Committee for Space Data Systems) specifies the use of GMSK with  $BT_b = 0.5$  for interplanetary links with bit rates in excess of 2 Mbites/s [44]. For near-Earth missions, GMSK with  $BT_b = 0.25$  is an option [44]. GMSK is also a commonly used modulation in satellite communications [45,46].

The popular Bluetooth standard uses a version of binary CPM similar to GMSK called Gaussian frequency shift keying (GFSK). The modulator is based on the approach outlined in Fig. 3.23B where the impulse response of the premodulation filter is the Gaussian response given by Eq. (3.95)—the resulting frequency pulse is given by Eq. (3.96) with  $BT_b = 0.5$ . GMSK uses a modulation index  $h = 0.5$  (hence, the “M” in GMSK), and volume 2 of the Bluetooth standard specifies a modulation index  $0.28 < h < 0.35$  for basic rate communications [47]. Volume 6 of the Bluetooth standard specifies a modulation index of  $0.45 < h < 0.55$  for the low energy physical layer [48]. Because  $h$  is not fixed at 0.5, the modulation is not a variant of MSK, and this is why the modulation is called GFSK, not GMSK.

### 3.3.6 CONCLUDING REMARKS FOR NONLINEAR MODULATION

The treatment here focused on CPM where the phase is of the form of Eq. (3.64). A generalization, called multi- $h$  CPM, uses a time-varying modulation index and was introduced by Miyahawa et al. [49] and Anderson and Taylor [50]. In this case the phase is of the form

$$\phi(t; \mathbf{a}_n) = 2\pi \sum_{k=0}^n h_k a(k) q(t - kT_s), \quad (3.97)$$

where the sequence of modulation indexes is a periodic sequence with period  $N_h$ . For a given bandwidth, multi- $h$  CPM tends to have a larger minimum Euclidean distance than the single- $h$  counterpart.

A number of alternate representations for CPM have also been published. Among these, Rimoldi’s “tilted phase” representation [51] decomposes CPM into the cascade of a continuous phase encoder and memoryless modulator. This decomposition has been used to isolate the contribution of the phase encoding from that of modulation in an attempt to identify more powerful phase encodings. Another popular decomposition for binary CPM is as a superposition of amplitude modulated pulses due to Laurent [52]. This decomposition is the basis for power spectral density calculations and reduced-complexity detectors. The generalization of Laurent’s decomposition to nonbinary CPM was performed by Mengali and Morelli [53], to  $M$ -ary CPM with an integer modulation index by Huang and Li [54], and to nonbinary multi- $h$  CPM by Perrins and Rice [55]. Further generalizations were published by Cariolaro [56].

### 3.4 COMPARISONS

One of the broad conclusions from this chapter is that a digital modulation may be characterized by its probability of bit error (through the minimum distance  $d_{\min}$ ) or by its bandwidth (through the power spectral density). The properties of the CPMs described in the previous section are summarized in Table 3.3. These entries demonstrate the general trend that a decrease in  $B_{99}$  (a good thing) is usually accompanied by a decrease in  $d_{\min}$  (a bad thing). In other words, an improvement in spectral efficiency is accompanied by a decrease in power efficiency. The same general trend holds with the linear modulations described in Section 3.2. QAM is described by constellation points. The average energy is the average squared Euclidean distance between the points and the origin, and the minimum Euclidean distance is the smallest Euclidean distance between adjacent points. The power spectral density is determined by the pulse shape and the symbol rate; see Eq. (3.33). For a *fixed bit rate*, increasing the number of bits per symbol increases spectral efficiency. This necessitates an increase in the number of constellation points. Unfortunately, for *fixed average energy*, increasing the number of constellation points decreases the minimum Euclidean distance.

The conclusion is that there is a fundamental tradeoff between spectral efficiency and power efficiency. It is now time to be more precise. Because the occupied bandwidth is proportional to the bit rate, the spectral efficiency is defined as the ratio of the bit rate to bandwidth and has the somewhat unusual units of bits/s per Hz. (For historical reasons, this is never simplified to bits/cycle.) Expressions for the spectral efficiency for QAM and CPM are developed as follows:

- The bandwidth of a linearly modulated signal using a bandlimited pulse shape, such as the SRRC pulse (the most common choice), is governed by the magnitude-squared of the Fourier transform of the pulse shape; see Eq. (3.33). The bandwidth of the SRRC pulse shape is

$$B_p = \frac{1 + \alpha}{2T_s} = \frac{1 + \alpha}{2 \log_2(M) T_b}. \quad (3.98)$$

Hence, the spectral efficiency of the real-valued bandpass  $M$ -ary QAM is

$$R = \frac{1/T_b}{2B_p} = \frac{\log_2(M)}{1 + \alpha} \text{ bits/s per Hz}. \quad (3.99)$$

- For CPM, the bandwidth that is derived from the power spectral density depends on the definition of bandwidth used. The spectral efficiency of real-valued bandpass CPM using the 99% power bandwidth is

$$R = \frac{1/T_b}{2B_{99}} = \frac{1}{2B_{99}T_b}. \quad (3.100)$$

The power efficiency is defined as the value of  $E_b/N_0$  required to achieve a target probability of bit error. Applying the principles described in Chapters 4 and 9

(the AWGN environment is the special case  $H(f) = 1$ ), the probability of bit error as a function  $E_b/N_0$  in the AWGN environment can be derived. This functional relationship can be used to compute the  $E_b/N_0$  required to achieve a target probability of bit error.

For a given modulation and desired bit error probability, the required  $E_b/N_0$  and spectral efficiency define a point in the  $E_b/N_0$ ,  $R$  tradeoff space. The fundamental bound relating the spectral efficiency and power efficiency is given by Shannon's channel capacity for a bandlimited AWGN channel:

$$R < \log_2 \left( 1 + R \frac{E_b}{N_0} \right). \quad (3.101)$$

A graphical representation of the spectral efficiency and power efficiency in the AWGN environment for some of the examples presented in this chapter is shown in Fig. 3.31. Notes:

1. For all points,  $E_b/N_0$  is the value required to achieve a probability of bit error equal to  $10^{-6}$ . The values for the linear modulations were derived using the principles derived in Chapter 4. The union bound was used for all points except square QAM ( $M = 4, 16, 64$ , and  $256$ ) and MPSK. The values of  $E_b/N_0$  for CPM were derived from the mathematical expressions accompanying the  $d_{\min}$  values obtained using the web-based tool developed by Perrins [39].
2. The spectral efficiencies for the linear modulations used Eq. (3.99) with  $\alpha = 0.5$ .
3. The spectral efficiencies for the CPMs used Eq. (3.100) with the values of  $B_{99}T_b$  listed in Table 3.3.
4. The points labeled "QAM" correspond to square QAM constellations for  $M = 4, 16, 64$ , and  $256$  and to the cross-QAM constellations for  $M = 32$  and  $128$ .
5. The parameters of the 4+12-APSK constellation are  $R_2/R_1 = 2.7$ ,  $\theta_1 = \pi/4$ , and  $\theta_2 = \pi/6$ .
6. The parameters of the 4+12+16-APSK constellation are  $R_2/R_1 = 2.64$ ,  $R_3/R_1 = 4.64$ ,  $\theta_1 = \pi/4$ , and  $\theta_2 = \pi/12$  (there is no point on the radius- $R_2$  circle aligned with the inphase axis), and  $\theta_3 = \pi/8$ .
7. All of the CPMs used a binary alphabet,  $M = 2$ .

The best location in a plot like Fig. 3.31 is in the upper left corner: the modulation achieves a very high spectral efficiency and requires very little power. The inequality (3.101)—shown by the dashed line labeled "capacity"—forms a boundary that keeps points out of the most desirable position. This boundary is one form of the channel capacity idea due to Shannon [57]. The proper interpretation is that the channel capacity is a bound in the  $E_b/N_0$ ,  $R$  plane beyond which it is impossible to simultaneously achieve the power and spectral efficiencies on the wrong side of the bound.

In addition to showing the tradeoffs in power and spectral efficiencies for the example modulations presented in this chapter, Fig. 3.31 also reveals some interesting relationships. One way for a point to move closer to capacity is to move vertically.

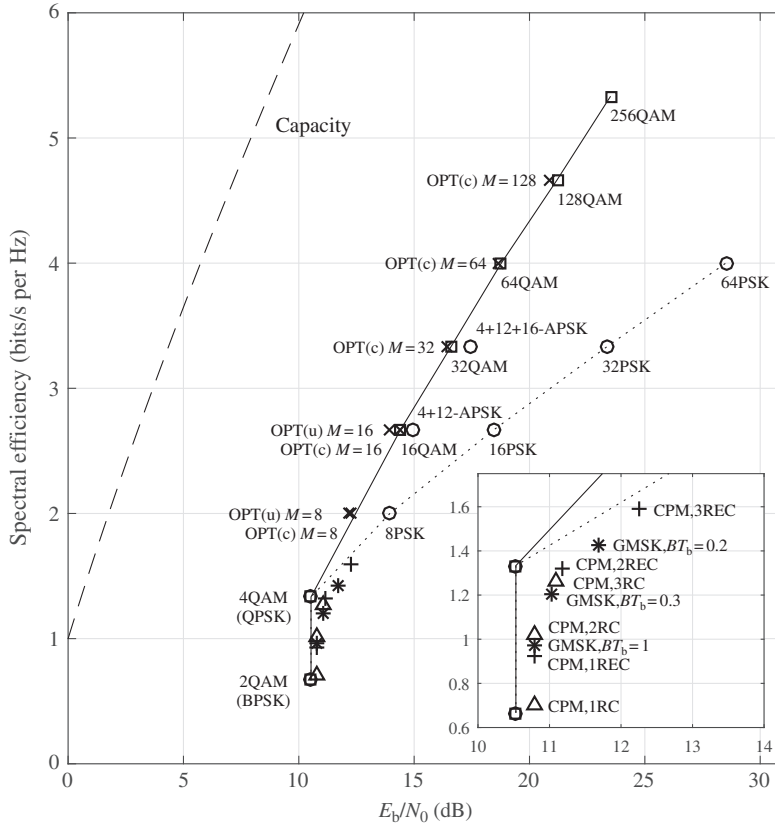


FIG. 3.31

Spectral efficiency vs  $E_b/N_0$  required to achieve  $10^{-6}$  probability of the bit error in the AWGN environment.

This means that there is an increase in spectral efficiency with no change in the required  $E_b/N_0$ . A vertical move only occurs in two places within a family. The reasons in each instance are very different. The move from BPSK to QPSK (or, from the QAM point of view, from binary QAM to quaternary QAM) does not require a corresponding increase in the required  $E_b/N_0$  because the binary versions of the modulations do not exploit the quadrature component of the modulated carrier. The relative positions of the BPSK and QPSK points shows that the transition to using the quadrature component comes for free, but there is a corresponding increase in the complexity of the modulator and detector.

The other place where a vertical move occurs within a modulation family is the set of points involving 1RC, 2RC, 1REC, and GMSK with  $BT_b = 1$  in CPM. (Note that all four cases use  $h = 0.5$ .) These points are all vertically aligned. The

1RC version has the lowest spectral efficiency of the group and the 2RC version has the highest spectral efficiency of the group. The trend does not generalize. For example, 1REC and 2REC are not vertically aligned in the plot. The reasons for this move are harder to visualize than in the BPSK/QPSK case. This is because the modulation is nonlinear. For these four modulations, the frequency pulses are such that the resulting CPM signals have approximately the same  $d_{\min}$  (see Table 3.3) but different power spectral densities. It is difficult to predict when this occurs with CPM and the existence of such a predictor for CPM remains an open question.

Another way for a point to move closer to capacity is a horizontal move to the left. Here, the spectral efficiency remains unchanged but the power efficiency improves. There are a number of examples of this in Fig. 3.31. As an example, consider the linear modulations for  $M = 16$ . All five have the same spectral efficiency ( $4/1.5 = 2\frac{2}{3}$ ). The least power efficient is 16PSK, whereas the most power efficient is the unconstrained minimum probability of the error constellation of Fig. 3.16. A close examination of constellations along this horizontal line shows that the more efficient the packing of the 16 constellation points, the more power efficient the modulation is. This observation is the motivation for the line of research that treats constellation design as a “packing problem.” Before leaving this case, note that the minimum probability of error constellations (either the unconstrained or constrained versions) are not much more power efficient than square 16QAM. This explains why square 16QAM is so commonly used. The power efficiency 4+12-APSK is slightly worse than 16QAM, but it possesses a lower peak-to-average power ratio than 16QAM.

In general, the more spectrally efficient a modulation is, the less power efficient it is. Note that none of the modulations seem to approach the channel capacity limit. For the linear modulations, increasing  $M$  improves the spectral efficiency but decreases power efficiency. With reference to the channel capacity limit, the decrease in power efficiency is more pronounced than the increase in spectral efficiency. The result is that for a fixed constellation family, the operating point moves further away from the channel capacity limit as  $M$  increases.

There are two reasons why the examples in Fig. 3.31 are not closer to channel capacity. First, the derivation of Eq. (3.101) assumes an infinite-dimensional alphabet with a Gaussian probability density function. (This is clearly not the case for the modulations described in this chapter.) Second, the derivation of Eq. (3.101) is based on error correcting codes. The signaling techniques described in this chapter are uncoded. Error correcting codes are beyond the scope of this chapter, but they are described in another book in this series.

On a final note, the points in Fig. 3.31 correspond to a  $10^{-6}$  probability of bit error, the square-root raised-cosine pulse shape with  $\alpha = 0.5$  for the linear modulations, and the use of  $B_{99}$  as the measure of bandwidth for CPM. Changing any one of these parameters moves the points, but not the channel capacity limit. For example, reducing  $\alpha$  from 0.5 to 0.25 moves all the linear modulation points up by a factor  $1.5/1.25 = 6/5$ . Reducing the target bit error probability from  $10^{-6}$  to  $10^{-5}$  moves all points to the left by about 1 dB.

## REFERENCES

- [1] “quadrature, n.”, OED Online, Oxford University Press, 2015 (accessed August 26, 2015).
- [2] C. Dodley, R. Erving, In-building software radio architecture, design and analysis, in: *Proceedings of the IEEE International Symposium on Personal, Indoor and Mobile Radio Communication*, London, UK, 2000, pp. 479–483.
- [3] F. Harris, C. Dick, M. Rice, Digital receivers and transmitters using polyphase filter banks for wireless communications, *IEEE Trans. Microwave Theory Tech.* 51 (4) (2003) 1395–1412.
- [4] M. Rice, *Digital Communications: A Discrete-Time Approach*, Pearson Prentice-Hall, Upper Saddle River, NJ, 2009.
- [5] H. Nyquist, Certain topics in telegraph transmission theory, *AIEE Trans. Commun. Electron.* 47 (1928) 617–644.
- [6] D. Tufts, Nyquist’s problem—the joint optimization of transmitter and receiver in pulse amplitude modulation, *Proc. IEEE* 53 (3) (1965) 248–259.
- [7] L. Franks, Further results on Nyquist’s problem in pulse transmission, *IEEE Trans. Commun. Technol.* 16 (2) (1968) 337–340.
- [8] E. Sousa, S. Pasupathy, Pulse shape design for teletext data transmission, *IEEE Trans. Commun.* 31 (7) (1983) 871–878.
- [9] J. Scanlan, Pulses satisfying the Nyquist criterion, *Electron. Lett.* 28 (1) (1992) 50–52.
- [10] N. Beaulieu, C. Tan, M. Damen, A “better than” Nyquist pulse, *IEEE Commun. Lett.* 5 (9) (2001) 367–368.
- [11] A. Assalini, A. Tonello, Improved Nyquist pulses, *IEEE Commun. Lett.* 8 (2) (2004) 87–89.
- [12] X. Xia, A family of pulse-shaping filters with ISI-free matched and unmatched filter properties, *IEEE Trans. Commun.* 45 (10) (1997) 1157–1158.
- [13] T. Demeechai, Pulse-shaping filters with ISI-free matched and unmatched filter properties, *IEEE Trans. Commun.* 46 (8) (1998) 992.
- [14] N. Alagha, P. Kabal, Generalized raised-cosine filters, *IEEE Trans. Commun.* 47 (7) (1999) 989–997.
- [15] A. Kisel, An extension of pulse shaping filter theory, *IEEE Trans. Commun.* 47 (5) (1999) 645–647.
- [16] A. Kisel, Nyquist 1 universal filters, *IEEE Trans. Commun.* 48 (7) (2000) 1095–1099.
- [17] C. Tan, N. Beaulieu, An investigation of transmission properties of Xia pulses, in: *Proceedings of the IEEE International Conference on Communications*, Vancouver, BC, 1999, pp. 1197–1201.
- [18] C. Tan, N. Beaulieu, Transmission properties of conjugate-root pulses, *IEEE Trans. Commun.* 52 (4) (2004) 553–558.
- [19] Cable Television Laboratories, Inc., Data over cable service interface specifications DOCSIS<sup>®</sup> 3.0, CM-SP-PHYv3.0-I11-130808, 2013.
- [20] R. Lucky, J. Hancock, The optimum performance of N-ary systems having two degrees of freedom, *IRE Trans. Commun. Syst.* 10 (1962) 185–192.
- [21] C. Weber, New solutions to the signal design problem for coherent channels, *IEEE Trans. Inf. Theory* 12 (1966) 161–167.
- [22] J. Salz, et al., Data transmission by combined AM and PM, *Bell Syst. Tech. J.* 50 (1971) 2399–2419.

- [23] C. M. Thomas, M. Weidner, S. Durrani, Digital amplitude-phase keying with M-ary alphabets, *IEEE Trans. Commun.* 22 (2) (1974) 168–180.
- [24] European Telecommunications Standards Institute, Digital video broadcasting (DVB); second generation framing structure, channel coding and modulation systems for broadcasting, interactive services, news gathering and other broadband satellite applications, EN 302 307 V1.1.1, Sophia Antipolis Cedex—FRANCE, 2004.
- [25] G. Foschini, R. Gitlin, S. Weinstein, Optimization of two-dimensional signal constellations in the presence of Gaussian noise, *IEEE Trans. Commun.* 22 (1) (1974) 28–38.
- [26] N. Blachman, A comparison of the informational capacities of amplitude- and phase—modulation communication systems, *Proc. IRE* 41 (1953) 748–759.
- [27] A. Lender, The duobinary technique for high-speed data transmission, *Trans. AIEE I Commun. Electron.* 82 (5) (1963) 214–218.
- [28] E. Kretzmer, Generalization of a technique for binary data communication, *IEEE Trans. Commun. Technol.* 14 (1) (1966) 67–68.
- [29] A. Lender, Correlative data transmission with coherent recovery using absolute reference, *IEEE Trans. Commun. Technol.* 16 (1) (1968) 108–115.
- [30] G.D. Forney, L.-F. Wei, Multidimensional constellations—part I: introduction, figures of merit, and generalized cross constellations, *IEEE J. Sel. Areas Commun.* 7 (6) (1989) 877–892.
- [31] G.D. Forney, Multidimensional constellations—part II: Voronoi constellations, *IEEE J. Sel. Areas Commun.* 7 (6) (1989) 941–958.
- [32] G.D. Forney, Trellis shaping, *IEEE Trans. Inf. Theory* 38 (2) (1992) 281–300.
- [33] J. Livingston, Shaping using variable-size regions, *IEEE Trans. Inf. Theory* 38 (4) (1992) 1347–1535.
- [34] R. Laroia, N. Farvardin, S. Tretter, On optimal shaping of multidimensional constellations, *IEEE Trans. Inf. Theory* 40 (4) (1994) 1044–1056.
- [35] T. Aulin, N. Rydbeck, C.-E. Sundberg, Continuous phase modulation—part I: full response signaling, *IEEE Trans. Commun.* 29 (3) (1981) 196–209.
- [36] T. Aulin, N. Rydbeck, C.-E. Sundberg, Continuous phase modulation—part II: partial response signaling, *IEEE Trans. Commun.* 29 (3) (1981) 210–225.
- [37] T. Aulin, C.-E. Sundberg, An easy way to calculate power spectra for digital FM, *IEE Proc. F Commun. Radar Signal Process.* 130 (6) (1983) 519–526.
- [38] T. Baker, Asymptotic behavior of digital FM spectra, *IEEE Trans. Commun.* 22 (10) (1974) 1585–1594.
- [39] E. Perrins, Minimum distance calculator for continuous phase modulation (CPM), <http://people.eecs.ku.edu/~esp/doku/doku.php?id=cpmdistance>.
- [40] T. Aulin, C.-E. Sundberg, Calculating digital FM spectra by means of autocorrelation, *IEEE Trans. Commun.* 30 (5) (1982) 1199–1208.
- [41] R. Anderson, J. Salz, Spectra of digital FM, *Bell Syst. Tech. J.* 44 (1965) 1165–1189.
- [42] K. Murota, K. Hirade, GMSK modulation for digital mobile radio telephony, *IEEE Trans. Commun.* 29 (7) (1981) 1044–1050.
- [43] M. Mouly, M.-B. Pautet, *The GSM System for Mobile Communications*, Telecom Publishing, 1992.
- [44] G. Sessler, R. Abelló, N. James, R. Baddeè, E. Vassallo, GMSK demodulator implementation for ESA deep-space missions, *Proc. IEEE* 95 (11) (2007) 2132–2141.

- [45] M. Rice, T. Oliphant, O. Haddadin, W. McIntire, Estimation techniques for GMSK using linear detectors in satellite communications, *IEEE Trans. Aerosp. Electron. Syst.* 43 (4) (2007) 1484–1495.
- [46] C. Sacchi, T. Rossi, M. Ruggieri, R. Granelli, Efficient waveform design for high-bit-rate W-band satellite transmissions, *IEEE Trans. Aerosp. Electron. Syst.* 47 (2) (2011) 974–995.
- [47] Specification of the Bluetooth<sup>®</sup> system, 2014, Specification Volume 2: Core System Package [BR/EDR Controller volume].
- [48] Specification of the Bluetooth<sup>®</sup> System, 2014, Specification Volume 6: Core System Package [Low Energy Controller volume].
- [49] H. Miyakawa, H. Harashima, Y. Tanaka, A new digital modulation scheme—multi-mode binary CPFSK, in: *Proceedings of the Third International Conference on Digital Satellite Communications*, Kyoto, Japan, 1975, pp. 105–112.
- [50] J. Anderson, D. Taylor, A bandwidth-efficient class of signal-space codes, *IEEE Trans. Inf. Theory* 24 (11) (1978) 703–712.
- [51] B. Rimoldi, A decomposition approach to CPM, *IEEE Trans. Inf. Theory* 34 (2) (1988) 260–270.
- [52] P. Laurent, Exact and approximate construction of digital phase modulations by superposition of amplitude modulated pulses (AMP), *IEEE Trans. Commun.* 34 (2) (1986) 150–160.
- [53] U. Mengali, M. Morelli, Decomposition of  $M$ -ary CPM signals into PAM waveforms, *IEEE Trans. Inf. Theory* 41 (5) (1995) 1265–1275.
- [54] X. Huang, Y. Li, The PAM decomposition of CPM signals with integer modulation index, *IEEE Trans. Commun.* 51 (4) (2003) 543–546.
- [55] E. Perrins, M. Rice, PAM decomposition of  $M$ -ary multi- $h$  CPM, *IEEE Trans. Commun.* 53 (12) (2005) 2065–2075.
- [56] G. Cariolaro, A system-theory approach to compose CPM signals into PAM waveforms, *IEEE Trans. Commun.* 58 (1) (2010) 200–210.
- [57] T. Cover, J. Thomas, *Elements of Information Theory*, second ed., Wiley-Interscience, 2006.

# Optimal detection of digital modulations in AWGN

# 4

**E.G. Ström**

*Chalmers University of Technology, Gothenburg, Sweden*

## CHAPTER OUTLINE

<b>4.1 Digital Transmission Over Noisy Channels .....</b>	<b>122</b>
<b>4.2 Minimum-Distance Receiver .....</b>	<b>125</b>
<b>4.3 Vector Channel .....</b>	<b>127</b>
<b>4.4 White Gaussian Noise Vector .....</b>	<b>134</b>
<b>4.5 Optimum Message Receivers .....</b>	<b>136</b>
4.5.1 MAP Receiver .....	136
4.5.2 ML Receiver .....	140
<b>4.6 The Irrelevance Theorem .....</b>	<b>141</b>
<b>4.7 Decision Regions and Error Probability .....</b>	<b>144</b>
4.7.1 Decisions Regions for a General Detector .....	144
4.7.2 Decision Regions for the Minimum-Distance Detector .....	146
4.7.3 Decision Regions for the MAP Detector .....	148
<b>4.8 Union Bound .....</b>	<b>149</b>
<b>4.9 Bit Error Probability and Constellation Labelings .....</b>	<b>156</b>
<b>4.10 Optimum Bitwise Receivers .....</b>	<b>160</b>
<b>4.11 Matched Filter .....</b>	<b>163</b>
<b>4.12 Summary .....</b>	<b>166</b>
<b>4.13 Practical Detectors .....</b>	<b>167</b>
<b>4.14 Probability of Received Vector Belonging to a Decision Boundary .....</b>	<b>168</b>
<b>References .....</b>	<b>169</b>

The material developed in this chapter can be found in many other books, but perhaps presented in a different manner. The approach here is inspired by several classical books and countless other sources, including discussions with teachers, students, and colleagues. It would be impossible to list all of them. However, the choice to start the exposition with the minimum-distance detector is inspired by Lee and Messerschmidt [1]. Another important source of inspiration is the classical book from

1965 by Wozencraft and Jacobs [2], which is very readable even today. An accessible introduction to estimation and detection theory is found in Kay's two books [3,4], and a more advanced text is by Poor [5].

Authors are always faced with a dilemma when selecting notation and the level of mathematical rigor to employ. Too little rigor leaves the reader unsure about what exactly is claimed, while too much rigor will obscure the big picture. For readers who would enjoy a more precise and rigorous approach than the one taken here, we recommend the excellent books by Lapidot [6] and by Gallager [7]. In particular, the shortcuts taken here (including the use of white noise and Dirac delta functions, the fearless faith in that all integrals and sums converge, and that it is always allowed to change the order of expectation, integration, and summation) are criticized, explained, and (sometimes) justified in these books. Readers can, however, rely on the fact that the developed detectors and analysis methods in this chapter are indeed the same as would have been obtained with a more rigorous approach.

With some important exceptions, random variables and random processes are denoted with uppercase letters and their realizations with lowercase letters. The main exceptions to this rule are the information bits  $b_k$ ,  $\mathbf{b} = [b_1 \ b_2 \ \cdots \ b_K]$ , and the transmitted message index  $m$ , which are random quantities. General sets are denoted with calligraphic symbols, for example,  $\mathcal{M}$ , while fields are denoted with blackboard bold symbols, for example, the set of all real numbers  $\mathbb{R}$ . An exception to the last convention is  $\mathbb{E}$ , which denotes the expectation operator.

---

## 4.1 DIGITAL TRANSMISSION OVER NOISY CHANNELS

Digital communication implies that the message to be sent can be represented as a sequence of binary digits,  $b_k \in \{0, 1\}$  for  $k = 1, 2, \dots, K$ . For all practical purposes, we can assume that there are a finite number of bits to transmit, that is, that  $K < \infty$ . For sure, all practical messages have finite, but possibly very large, lengths.

When discussing protocol stacks, for example, the TCP/IP stack or the OSI stack, the term message usually refers to an application layer protocol data unit. However, we will use the term message in a broader context—a message refers to a sequence of bits that we need to treat as a unit when specifying optimal receivers.

We collect all transmitted bits into the  $K$ -vector<sup>1</sup>

$$\mathbf{b} \triangleq [b_1 \ b_2 \ \cdots \ b_K] \in \{0, 1\}^K. \quad (4.1)$$

We will model  $b_k$  as random variables with certain distributions later. For now, we will just assume that all  $K$ -bit patterns can occur, that is, that  $\Pr\{\mathbf{b} = \mathbf{u}\} > 0$  for all  $\mathbf{u} \in \{0, 1\}^K$ .

---

<sup>1</sup>We will use the long-standing convention of thinking of vectors over, the binary field as row vectors. However, all other vectors will be column vectors.

The simplest communication system consists of a single link, that is, the cascade of a transmitter, a channel, and a receiver. We will consider the channel to be an additive noise waveform channel, that is, the input  $x(t)$  and output  $y(t)$  of the channel are continuous-time signals and the output is

$$y(t) = x(t) + v(t), \quad (4.2)$$

where  $v(t)$  is the noise waveform. For generality, we will consider the input, noise, and output signals to be complex-valued (and treat real-valued signals as a special case of complex-valued signals). The noise waveform  $v(t)$  will be modeled later in this chapter in [Section 4.4](#). For the time being, we will just assume that  $v(t)$  is completely unknown to the transmitter and receiver. In case  $v(t)$  is known to either the transmitter or the receiver, the communication problem would become trivial since the noise can be canceled by either the transmitter (by transmitting  $x'(t) = x(t) - v(t)$ , which yields  $y(t) = x(t)$ ) or the receiver (by forming  $y'(t) = y(t) - v(t) = x(t)$ ).

The transmitter is a conceptually very simple device. It is a one-to-one mapping of  $\mathbf{b}$  to  $x(t)$ , where  $x(t)$  is a member of the set of signal alternatives  $\mathcal{X} \triangleq \{x_1(t), x_2(t), \dots, x_M(t)\}$ . Since  $\mathbf{b}$  can take on  $2^K$  values, the number of required signal alternatives is  $M = 2^K$ . The signal alternatives are assumed to have finite energies, that is, the energy of  $x_\ell(t)$  is  $E_\ell \triangleq \int_{-\infty}^{\infty} |x_\ell(t)|^2 dt < \infty$  for all  $x_\ell(t) \in \mathcal{X}$ .

**Example 4.1.** Consider the signal alternatives.

$$\begin{aligned} x_1(t) = -x_3(t) &= \begin{cases} \sqrt{6}, & 0 \leq t < 2 \\ 0, & \text{otherwise} \end{cases} \\ x_2(t) = -x_4(t) &= \begin{cases} \sqrt{2}, & 0 \leq t < 1 \\ -\sqrt{2}, & 1 \leq t < 2 \\ 0, & \text{otherwise} \end{cases} \end{aligned}$$

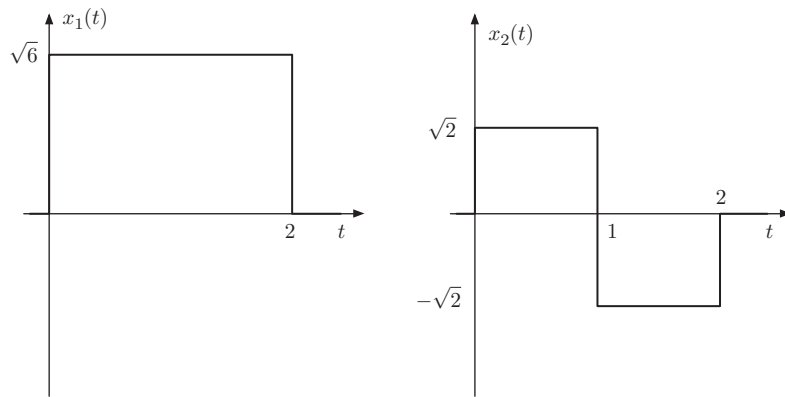
where  $x_1(t)$  and  $x_3(t)$  are depicted in [Fig. 4.1](#).

The signal energies are

$$\begin{aligned} E_1 = E_3 &= \int_{-\infty}^{\infty} |x_1(t)|^2 dt = \int_0^2 6 dt = 12 \\ E_2 = E_4 &= \int_{-\infty}^{\infty} |x_2(t)|^2 dt = \int_0^2 2 dt = 4. \end{aligned}$$

Since there are  $M = 4 = 2^2$  signal alternatives,  $K = 2$ . One of the  $M! = 4! = 24$  possible mapping between bits and signal alternatives is given by [Table 4.1](#).

This transmitter model is actually quite general and also covers the use of channel coding, loss-less source coding, synchronization sequences, etc. However, by restricting the mapping to be one-to-one, there will be a minor loss of generality, as, for example, lossy source coding will not be covered by the transmitter model. This is a minor issue since we can simply prepend the transmitter with a separate lossy source coding block.

**FIG. 4.1**

Signal alternatives.

**Table 4.1** One Possible Bit-to-Signal Alternative Mapping

<b>b</b>	<b><math>\mathbf{x}(t)</math></b>
[00]	$x_1(t)$
[01]	$x_2(t)$
[10]	$x_3(t)$
[11]	$x_4(t)$

Restricting the signal alternatives to have finite energies is quite mild. Practical signal alternatives are always time-limited and have finite amplitudes.

We can think of the transmitter as a special type of digital-to-analog converter and the receiver as a special type of analog-to-digital converter. That is, the task of the receiver is to map the observed received signal  $y(t)$  to a sequence of bits. The output bits are denoted  $\hat{b}_1, \hat{b}_2, \dots, \hat{b}_K$ , where  $\hat{b}_k$  is the decision (ie, the receiver's guess) on the value of  $b_k$ . Likewise, the vector

$$\hat{\mathbf{b}} \triangleq [\hat{b}_1 \ \hat{b}_2 \ \dots \ \hat{b}_K] \in \{0, 1\}^K \quad (4.3)$$

is the receiver's guess on the value of  $\mathbf{b}$ . If  $\hat{\mathbf{b}} \neq \mathbf{b}$ , a message error has occurred. A bit error occurs when  $\hat{b}_k \neq b_k$ . We note that a bit error (in any position  $k$ ) results in a message error, and a message error implies that at least one bit among the  $K$  bits is in error. We will explore how the probability of message and bit errors are related later in [Section 4.9](#). For the time being, we will concentrate our efforts on finding receiver structures that try to avoid message errors.

A final note is that the additive noise channel model implies that the receiver is perfectly synchronized to the transmitter. This is a rather big assumption. In practice, the received signal is delayed by the channel (surely, the propagation speed cannot exceed the speed of light in vacuum) and is attenuated due to losses in the propagation medium (wires, cables, optical fibers, or wireless media). Moreover, clocks and oscillators in the transmitter and receiver are not perfectly matched to each other. Hence, the receiver is often required to synchronize itself in time, phase, frequency, and amplitude. The situation is even more complicated when the channel is fading (time-varying) and time-dispersive; see [Chapters 6 and 8](#). Nevertheless, we will ignore the synchronization issues in this chapter, with the tacit understanding that the synchronization task will also require transmission resources (power and bandwidth) and receiver complexity. For more information about this important issue, see Chapter 7 or refer to the book by Meyr et al. [8].

---

## 4.2 MINIMUM-DISTANCE RECEIVER

In this section, we will introduce the intuitively pleasing minimum-distance receiver, which will turn out to possess some optimality properties, as explained later in [Sections 4.5.1 and 4.5.2](#).

In general, the receiver task is as follows: given the observation of  $y(t)$ , guess which signal alternative was sent. We assume that the receiver has knowledge of the signal alternatives  $\mathcal{X} = \{x_1(t), x_2(t), \dots, x_M(t)\}$  and can invert the bits-to-signal mapping performed in the transmitter. That is, the transmitter knows how to demap  $x_\ell(t)$  to the corresponding bit pattern  $\mathbf{b}_\ell$ .

To understand the minimum-distance receiver, we need to define a notion of distance between signals. As explained in the Appendix, the distance between two finite-energy signals,  $g(t)$  and  $h(t)$ , can be defined as follows:

$$d(g(t), h(t)) \triangleq \|g(t) - h(t)\| = \sqrt{\int_{-\infty}^{\infty} |g(t) - h(t)|^2 dt}. \quad (4.4)$$

In passing, we note that the  $d^2(g(t), 0) = \|g(t)\|^2 = E_g$ , that is, the squared distance from the origin is equal to the signal energy.

Now, the minimum-distance receiver simply selects the signal alternative that is closest to  $y(t)$ . In other words, the minimum-distance guess is  $x_{\hat{m}_{\text{MD}}}(t) \in \mathcal{X}$ , where  $d(y(t), x_{\hat{m}_{\text{MD}}}(t)) \leq d(y(t), x_\ell(t))$  for all  $x_\ell(t) \in \mathcal{X}$ . An equivalent way to state this relation is as follows:

$$\hat{m}_{\text{MD}} = \arg \min_{\ell \in \mathcal{M}} d(y(t), x_\ell(t)) = \arg \min_{\ell \in \mathcal{M}} d^2(y(t), x_\ell(t)), \quad (4.5)$$

where  $\mathcal{M} \triangleq \{1, 2, \dots, M\}$  and the last equality holds since distances are nonnegative.

**Example 4.2.** Suppose the signal alternatives are as in [Example 4.1](#) and the received signal is as depicted in [Fig. 4.2](#). To find the minimum distance decision, we compute the squared distances between  $y(t)$  and the signal alternatives:

$$\begin{aligned} d^2(y(t), x_1(t)) &= \int_0^2 |y(t) - x_1(t)|^2 dt \\ &= (1 - \sqrt{6})^2 + \frac{1}{2} (-1 - \sqrt{6})^2 + \frac{1}{2} (1 - \sqrt{6})^2 \\ &= 14 - 2\sqrt{6} \approx 9.10 \\ d^2(y(t), x_2(t)) &= \int_0^2 |y(t) - x_2(t)|^2 dt = 6 - 2\sqrt{2} \approx 3.17 \\ d^2(y(t), x_3(t)) &= \int_0^2 |y(t) - x_3(t)|^2 dt = 14 + 2\sqrt{6} \approx 18.90 \\ d^2(y(t), x_4(t)) &= \int_0^2 |y(t) - x_4(t)|^2 dt = 6 + 2\sqrt{2} \approx 8.83. \end{aligned}$$

Hence, signal alternative  $x_2(t)$  is the closest to the received signal and the minimum-distance decision is  $\hat{m}_{\text{MD}} = 2$ .

In case there is a two-way tie, that is, if

$$\min_{\ell \in \mathcal{M}} d(y(t), x_\ell(t)) = d(y(t), x_{\hat{m}_1}(t)) = d(y(t), x_{\hat{m}_2}(t)), \quad (4.6)$$

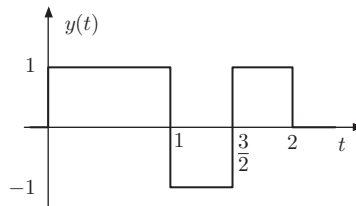


**FIG. 4.2**

Received signal.

we then choose  $\hat{m}_{\text{MD}}$  to be  $\hat{m}_1$  or  $\hat{m}_2$  in an arbitrary manner, for example, at random or as  $\hat{m}_{\text{MD}} = \min\{\hat{m}_1, \hat{m}_2\}$ . This approach generalizes to multiple ties, that is, we can arbitrarily choose any of the tied signal alternatives. As we will see later, when the noise is modeled as a white Gaussian random process, ties can be resolved in the same way (ie, that any of the tied signal alternatives could be chosen) without affecting the error probability.

There are  $M$  possible guesses for  $x(t)$ , namely,  $x_1(t), x_2(t), \dots, x_M(t)$ , and each guess on  $x(t)$  corresponds to a guess on the noise waveform. That is, the guess that  $x(t) = x_k(t)$  implies the guess that  $v(t) = y(t) - x_k(t) = v_k(t)$ . Now, the energy of  $v_k(t)$  is  $\|v_k(t)\|^2 = \|y(t) - x_k(t)\|^2 = d^2(y(t), x_k(t))$ . Hence, we can interpret the minimum-distance receiver as the minimum-noise-energy receiver: we pick the signal alternative that results in the smallest noise energy. The rationale is that it is more likely that the noise has small energy than large energy. This notion will be more formalized later in the chapter, when we model the noise as a Gaussian random process.

### 4.3 VECTOR CHANNEL

In the following, we will show how we can convert the continuous-time waveform channel  $y(t) = x(t) + v(t)$  to a vector channel of the form  $\mathbf{y} = \mathbf{x} + \mathbf{v}$ . The vector channel is very useful for analysis of detector performance, as we see later in this chapter in [Section 4.7](#). Moreover, the vector channel suggests how we can implement the front-end of an optimal receiver.

From the “??,” we recall that  $x_1(t), x_2(t), \dots, x_M(t)$  spans an  $N$ -dimensional vector space  $\mathcal{S} = \text{span}\{\mathcal{X}\}$ , where  $N \leq M$ . Let  $\boldsymbol{\varphi} \triangleq \{\varphi_1(t), \varphi_2(t), \dots, \varphi_N(t)\}$  be an orthonormal<sup>2</sup> basis for  $\mathcal{S}$ . We can now represent all signals in  $\mathcal{S}$  as vectors in  $\mathbb{F}^N$  (where  $\mathbb{F} = \mathbb{R}$  or  $\mathbb{F} = \mathbb{C}$ , depending on whether the signal alternatives are real-valued or complex-valued signals). In particular, we define the signal vectors as

$$\mathbf{x}_\ell \triangleq [x_{\ell,1} \quad x_{\ell,2} \quad \cdots \quad x_{\ell,N}]^T \in \mathbb{F}^N, \quad \ell = 1, 2, \dots, M, \quad (4.7)$$

where

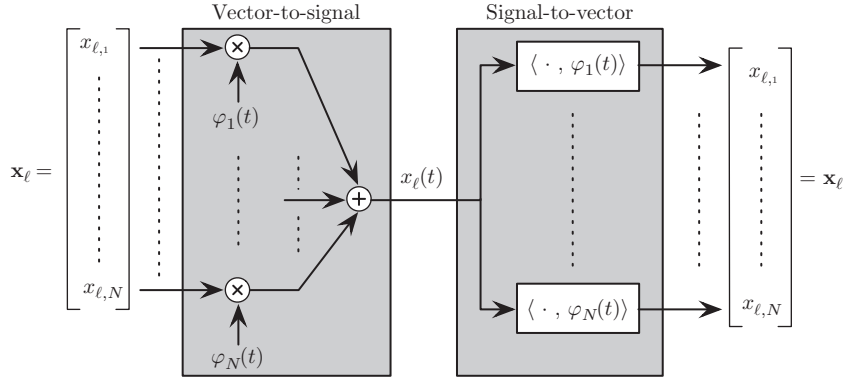
$$x_{\ell,n} \triangleq \langle x_\ell(t), \varphi_n(t) \rangle, \quad n = 1, 2, \dots, N. \quad (4.8)$$

The signal can be constructed from the elements of  $\mathbf{x}_\ell$  as

$$x_\ell(t) = \sum_{n=1}^N x_{\ell,n} \varphi_n(t). \quad (4.9)$$

The conversion from vector to signal and from signal to vector are depicted in block diagram form in [Fig. 4.3](#).

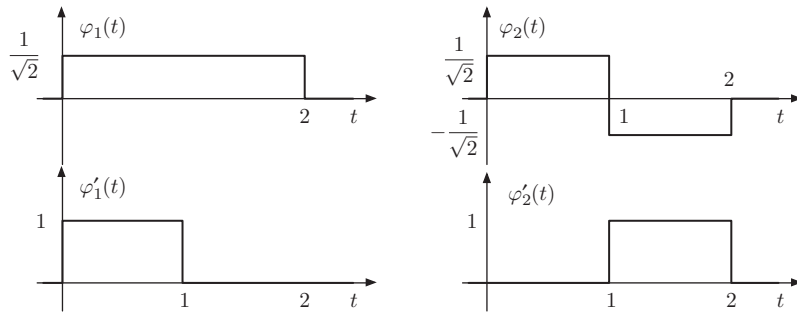
<sup>2</sup>The set  $\{\varphi_1(t), \varphi_2(t), \dots, \varphi_N(t)\}$  is orthonormal if  $\langle \varphi_i(t), \varphi_j(t) \rangle = 0$  for  $i \neq j$  (orthogonal) and  $\langle \varphi_n(t), \varphi_n(t) \rangle = 1$  for  $n = 1, 2, \dots, N$  (normalized).


**FIG. 4.3**

Block diagram illustration of conversion between signals and signal vectors.

It is usually not difficult to find a basis for the signal space. Indeed, in practice, we often construct the signal alternatives from a predefined basis. If this is not the case, then we can always apply the Gram-Schmidt procedure to find a basis. In any event, the basis choice is not important for the communication system performance, and we can select any basis that is convenient for our purposes (eg, for mathematical convenience).

**Example 4.3.** It is easily seen that  $\{\varphi_1(t), \varphi_2(t)\}$  and  $\{\varphi'_1(t), \varphi'_2(t)\}$ , defined in Fig. 4.4, are two orthonormal bases for the signal space spanned by the signal alternatives in Example 4.1. The signal vector for  $x_1(t)$ , with respect to the  $\{\varphi_1(t), \varphi_2(t)\}$  basis, can be found from the defining Eqs. (4.7), (4.8) as the following:


**FIG. 4.4**

Two orthonormal bases for the signal alternatives  $\{x_1(t), x_2(t), x_3(t), x_4(t)\}$  defined in Fig. 4.1.

$$x_{1,1} = \langle x_1(t), \varphi_1(t) \rangle = \int_{-\infty}^{\infty} x_1(t) \varphi_1^*(t) dt = \sqrt{6} \frac{1}{2} 2 = \sqrt{12}$$

$$x_{1,2} = \langle x_1(t), \varphi_2(t) \rangle = \int_{-\infty}^{\infty} x_1(t) \varphi_2^*(t) dt = \sqrt{6} \frac{1}{2} - \sqrt{6} \frac{1}{2} = 0,$$

which implies that  $\mathbf{x}_1 = [x_{1,1} \ x_{1,2}]^T = [\sqrt{12} \ 0]^T$ . We can also find the signal vector by inspection. From Figs. 4.1 and 4.4, we see that  $x_1(t) = \sqrt{12}\varphi_1(t) \Rightarrow \mathbf{x}_1 = \sqrt{12}\boldsymbol{\varphi}_1 = \sqrt{12}[1 \ 0]^T$ . From either the definition or by inspection, we can easily find the remaining signal vectors as

$$\mathbf{x}_2 = -\mathbf{x}_4 = [0 \ 2]^T$$

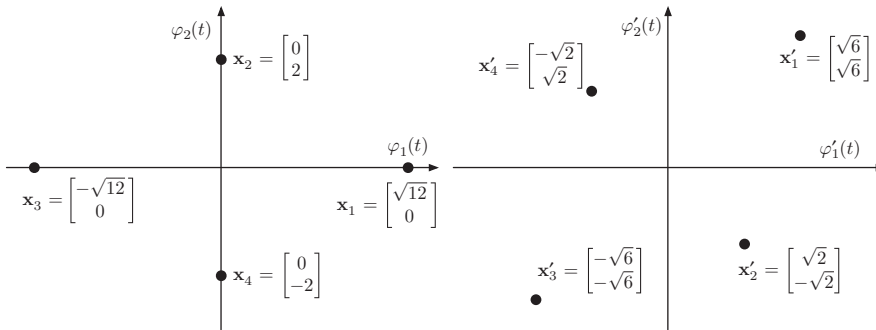
$$\mathbf{x}_3 = -\mathbf{x}_1 = -[\sqrt{12} \ 0]^T.$$

Moreover, the signal vectors with respect to the basis  $\{\varphi'_1(t), \varphi'_2(t)\}$  are

$$\mathbf{x}'_1 = -\mathbf{x}'_3 = [\sqrt{6} \ \sqrt{6}]^T$$

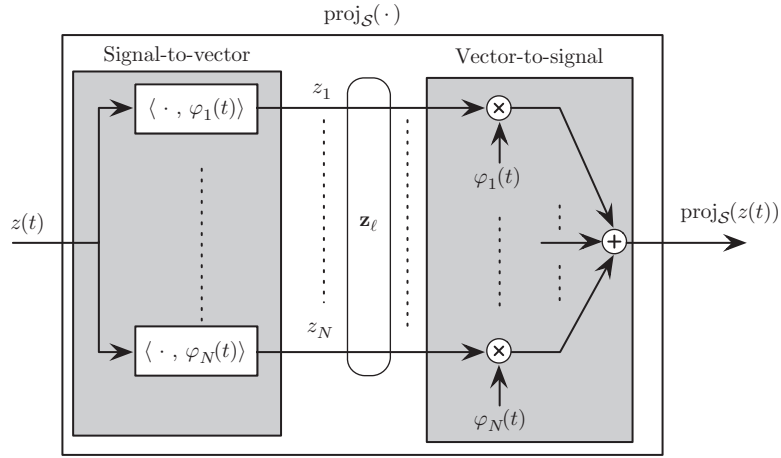
$$\mathbf{x}'_2 = -\mathbf{x}'_4 = [\sqrt{2} \ -\sqrt{2}]^T.$$

The signal vectors are plotted in Fig. 4.5. As seen, the distances between the signal vectors remain the same in both bases. In fact, we see that we can find  $\mathbf{x}'_\ell$  by first reflecting  $\mathbf{x}_\ell$  in the  $\varphi_1$ -axis and then rotating the resulting vector around the origin by  $\pi/4$  radians. This is a general property: a change of basis does not change the norm of the vectors or the distances between them. Hence, a change of basis can always be interpreted in terms of reflections and rotations of the signal vectors.



**FIG. 4.5**

Signal vectors for  $\{x_1(t), x_2(t), x_3(t), x_4(t)\}$  with respect to the basis  $\{\varphi_1(t), \varphi_2(t)\}$  (left) and  $\{\varphi'_1(t), \varphi'_2(t)\}$  (right).

**FIG. 4.6**

Block diagram illustration of the projection onto the signal space.

The projections of a generic signal  $z(t)$  onto the signal space  $\mathcal{S}$  and its orthogonal complement can be computed as follows:

$$z_{\mathcal{S}}(t) = \text{proj}_{\mathcal{S}}(z(t)) = \sum_{n=1}^N \langle z(t), \varphi_n(t) \rangle \varphi_n(t) \quad (4.10)$$

$$z_{\mathcal{S}^\perp}(t) = \text{proj}_{\mathcal{S}^\perp}(z(t)) = z(t) - z_{\mathcal{S}}(t). \quad (4.11)$$

As shown in Fig. 4.6, we can think of the projection onto the signal space in block diagram form as a cascade of a signal-to-vector and a vector-to-signal conversion block. We recall that  $z(t) \in \mathcal{S}$  if and only if  $z(t) = z_{\mathcal{S}}(t) = \text{proj}_{\mathcal{S}}(z(t))$ , or equivalently, when  $z_{\mathcal{S}^\perp}(t) = z(t) - z_{\mathcal{S}}(t) = 0$ .

By definition, the transmitted signal  $x(t)$  is contained in the signal space  $\mathcal{S}$ . However, the noise waveform  $v(t)$  is, in general, not completely contained in the signal space. That is, if we write  $v(t) = v_{\mathcal{S}}(t) + v_{\mathcal{S}^\perp}(t)$ , where  $v_{\mathcal{S}}(t)$  and  $v_{\mathcal{S}^\perp}(t)$  are the projection of the noise signal onto the signal space and the orthogonal complement to the signal space, respectively, then in general  $v_{\mathcal{S}^\perp}(t) \neq 0$ . Likewise, the received signal can be decomposed as  $y(t) = x(t) + v(t) = y_{\mathcal{S}}(t) + y_{\mathcal{S}^\perp}(t)$ . The relationship between the signals and their various projections is depicted in Fig. 4.7. It is clear from the picture that  $y_{\mathcal{S}^\perp}(t) = v_{\mathcal{S}^\perp}(t)$  and  $y_{\mathcal{S}}(t) = x(t) + v_{\mathcal{S}}(t)$ .

We will now show that  $v_{\mathcal{S}^\perp}(t)$  is irrelevant for the minimum-distance receiver. The squared distances needed for the minimum-distance receiver are of the form

$$d^2(y(t), x_\ell(t)) = \|y(t) - x_\ell(t)\|^2 \quad (4.12)$$

$$= \|x(t) + v_{\mathcal{S}}(t) + v_{\mathcal{S}^\perp}(t) - x_\ell(t)\|^2 \quad (4.13)$$

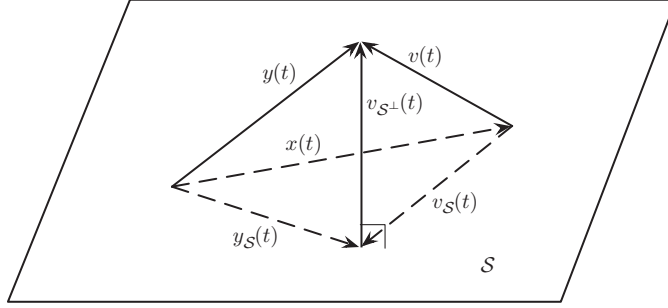


FIG. 4.7

Relation between transmitted, noise, and received signals and their projections. Signals illustrated as *dashed* vectors are completely contained in the signal space  $\mathcal{S}$ .

$$= \|y_{\mathcal{S}}(t) - x_{\ell}(t) + v_{\mathcal{S}^\perp}(t)\|^2 \quad (4.14)$$

$$= \|y_{\mathcal{S}}(t) - x_{\ell}(t)\|^2 + \|v_{\mathcal{S}^\perp}(t)\|^2, \quad (4.15)$$

where the last equality follows from the Pythagorean theorem, since  $y_{\mathcal{S}}(t) - x_{\ell}(t)$  is in the signal space and is therefore orthogonal to  $v_{\mathcal{S}^\perp}(t)$ . Now, since  $\|v_{\mathcal{S}^\perp}(t)\|^2$  does not depend on  $\ell$ , the minimum-distance guess is

$$\hat{m}_{\text{MD}} = \arg \min_{\ell \in \mathcal{M}} \|y_{\mathcal{S}}(t) - x_{\ell}(t)\|^2 + \|v_{\mathcal{S}^\perp}(t)\|^2 \quad (4.16)$$

$$= \arg \min_{\ell \in \mathcal{M}} \|y_{\mathcal{S}}(t) - x_{\ell}(t)\|^2. \quad (4.17)$$

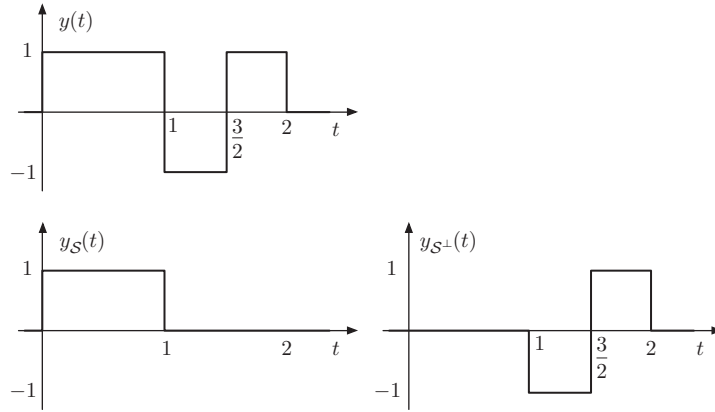
That is, we can compute the minimum-distance guess from  $y_{\mathcal{S}}(t)$  and the signal  $y_{\mathcal{S}^\perp}(t) = v_{\mathcal{S}^\perp}(t)$  is therefore irrelevant.

**Example 4.4.** Consider again the signal alternatives from [Example 4.1](#) and the received signal from [Example 4.2](#). Let us compute the projection of  $y(t)$  onto the signal space. We start by forming the inner products:

$$\begin{aligned} y_1 &= \langle y(t), \varphi_1(t) \rangle \\ &= \int_{-\infty}^{\infty} y(t) \varphi_1^*(t) dt \\ &= \left( \frac{1}{\sqrt{2}} \right) + \frac{1}{2} \left( \frac{1}{\sqrt{2}} (-1) \right) + \frac{1}{2} \left( \frac{1}{\sqrt{2}} \right) = \frac{1}{\sqrt{2}} \\ y_2 &= \langle y(t), \varphi_2(t) \rangle = \frac{1}{\sqrt{2}}. \end{aligned}$$

Hence, the projection of  $y(t)$  onto the signal space is

$$y_{\mathcal{S}}(t) = y_1 \varphi_1(t) + y_2 \varphi_2(t),$$

**FIG. 4.8**

Received signal and its projections onto the signal space and the orthogonal complement of the signal space.

and the projection onto the orthogonal complement of the signal space is  $y_{S^\perp}(t) = y(t) - y_S(t)$ . The projections are depicted in Fig. 4.8. We clearly see that  $y(t) = y_S(t) + y_{S^\perp}(t)$ . It is also clear that  $y_{S^\perp}(t)$  is orthogonal to all signal alternatives and that  $\|y_{S^\perp}(t)\|^2 = 1$ . The squared distances needed for the minimum-distance receiver formulation in Eq. (4.17) are as follows:

$$\begin{aligned} d^2(y_S(t), x_1(t)) &= \int_0^2 |y_S(t) - x_1(t)|^2 dt = 13 - 2\sqrt{6} \\ d^2(y_S(t), x_2(t)) &= \int_0^2 |y_S(t) - x_2(t)|^2 dt = 5 - 2\sqrt{2} \\ d^2(y_S(t), x_3(t)) &= \int_0^2 |y_S(t) - x_3(t)|^2 dt = 13 + 2\sqrt{6} \\ d^2(y_S(t), x_4(t)) &= \int_0^2 |y_S(t) - x_4(t)|^2 dt = 5 + 2\sqrt{2}. \end{aligned}$$

We can verify from Example 4.2 that  $d^2(y(t), x_\ell(t)) = d^2(y_S(t), x_\ell(t)) + \|y_{S^\perp}(t)\|^2 = d^2(y_S(t), x_\ell(t)) + 1$  for all  $\ell$ , exactly as predicted by Eq. (4.15).

Now, since  $\|y_S(t) - x_\ell(t)\|^2 = \|\mathbf{y} - \mathbf{x}_\ell\|^2$ , where  $\mathbf{y}$  is the vector representation of the signal  $y_S(t)$ :

$$\mathbf{y} \triangleq [y_1 \quad y_2 \quad \cdots \quad y_N]^T \in \mathbb{R}^N \quad (4.18)$$

$$y_n \triangleq \langle y_S(t), \varphi_n(t) \rangle, \quad n = 1, 2, \dots, N. \quad (4.19)$$

We can formulate the minimum-distance receiver as follows:

$$\hat{m}_{\text{MD}} = \arg \min_{\ell \in \mathcal{M}} \|\mathbf{y} - \mathbf{x}_\ell\|^2. \quad (4.20)$$

**Example 4.5.** The signal vectors in our running example are depicted in Fig. 4.5. In particular,  $\mathbf{x}_1 = [\sqrt{12} \ 0]^T$ . From Example 4.4, we know that the received signal vector  $\mathbf{y} = [1/\sqrt{2} \ 1/\sqrt{2}]^T$ . Therefore, the squared distance between  $\mathbf{y}$  and  $\mathbf{x}_1$  is as follows:

$$\|\mathbf{y} - \mathbf{x}_1\|^2 = \left(1/\sqrt{2} - \sqrt{12}\right)^2 + \left(1/\sqrt{2}\right)^2 = 13 - 2\sqrt{6},$$

which is equal to  $d^2(y_{\mathcal{S}}(t), x_1(t))$  in Example 4.4. It is easily verified that  $\|y_{\mathcal{S}}(t) - x_\ell(t)\|^2 = \|\mathbf{y} - \mathbf{x}_\ell\|^2$  for all  $\ell$ .

Interestingly, we can compute  $y_n$  directly from  $y(t)$  since

$$y_n = \langle y_{\mathcal{S}}(t), \varphi_n(t) \rangle \quad (4.21)$$

$$= \langle y_{\mathcal{S}}(t), \varphi_n(t) \rangle + \underbrace{\langle y_{\mathcal{S}^\perp}(t), \varphi_n(t) \rangle}_{=0} \quad (4.22)$$

$$= \langle y_{\mathcal{S}}(t) + y_{\mathcal{S}^\perp}(t), \varphi_n(t) \rangle \quad (4.23)$$

$$= \langle y(t), \varphi_n(t) \rangle. \quad (4.24)$$

Moreover,

$$y_n = \langle y(t), \varphi_n(t) \rangle \quad (4.25)$$

$$= \langle x(t) + v(t), \varphi_n(t) \rangle \quad (4.26)$$

$$= \langle x(t), \varphi_n(t) \rangle + \langle v(t), \varphi_n(t) \rangle \quad (4.27)$$

$$= x_n + v_n, \quad (4.28)$$

where  $v_n$  is the  $n$ th element of the noise vector  $\mathbf{v}$

$$\mathbf{v} \triangleq [v_1 \ v_2 \ \cdots \ v_N]^T \in \mathbb{F}^N \quad (4.29)$$

$$v_n \triangleq \langle v(t), \varphi_n(t) \rangle, \quad n = 1, 2, \dots, N. \quad (4.30)$$

Hence, we can write

$$\mathbf{y} = \mathbf{x} + \mathbf{v}, \quad (4.31)$$

which is the input-output relation of the vector channel. The relation between the waveform and vector channels is shown in Fig. 4.9. The vector channel is extremely convenient for analysis of communication systems.

It is, however, important to remember that we cannot recover  $y(t)$  from  $\mathbf{y}$ . In fact, by projecting the received signal onto the signal space, we remove the noise component  $v_{\mathcal{S}^\perp}(t)$ . However, as we showed above,  $v_{\mathcal{S}^\perp}(t)$  is irrelevant for the minimum-distance receiver, and we will later show that  $v_{\mathcal{S}^\perp}(t)$  is also irrelevant

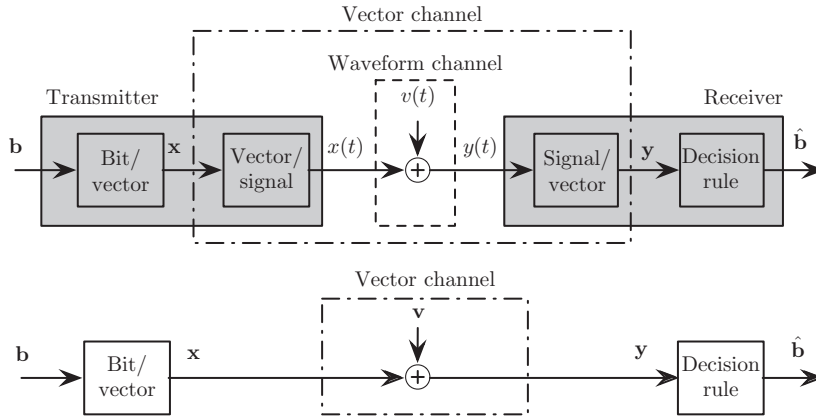


FIG. 4.9

Waveform and vector channels.

for the optimum receivers developed in Sections 4.5.1 and 4.5.2. Hence, for these receivers, there is no loss in performance by considering the vector channel instead of the waveform channel.

## 4.4 WHITE GAUSSIAN NOISE VECTOR

To derive the error probability of different receivers, we need statistical models for both the transmitted bits and the channel noise. In the following, we will derive the pdf of the noise vector, when the continuous-time noise is modeled as a white Gaussian random process.

Suppose we model the noise as real-valued white Gaussian noise with power spectral density  $N_0/2$ . This implies that  $V(t)$  is a stationary Gaussian random process with zero mean and autocorrelation function  $R_V(\tau) = \mathbb{E}[V(t)V(t+\tau)] = (N_0/2)\delta(\tau)$ , where  $\delta(t)$  is the Dirac delta function.<sup>3</sup> Note that we use  $V(t)$  to denote the random noise process and  $v(t)$  to denote a realization of  $V(t)$ . Likewise, we think of  $\mathbf{v}$  as a realization of the random vector  $\mathbf{V} = [V_1 \ V_2 \ \cdots \ V_N]^T$ , where  $V_n \triangleq \langle V(t), \varphi_n(t) \rangle$  for  $n = 1, 2, \dots, N$ .

<sup>3</sup>This model is quite unphysical, as the variance for  $V(t)$  is not finite due to the delta function in the autocorrelation. A more proper (and physical) view is to say that a random process is white if the autocorrelation function can be written as  $R_V(\tau) = (N_0/2)\delta_\epsilon(\tau)$ , where  $\delta_\epsilon(\tau)$  is a very thin pulse that integrates to one, for example,  $\delta_\epsilon(\tau) = (\pi\epsilon)^{-1/2} \exp(-\tau^2/\epsilon)$  for sufficiently small  $\epsilon > 0$ . Nevertheless, we will, for mathematical convenience, continue to use Dirac delta functions. See Gallager [7] for a more careful discussion about noise modeling.

Now, since  $V(t)$  is a Gaussian process, the elements of  $\mathbf{V}$  are jointly Gaussian random variables [7] with the following mean:

$$\mathbb{E}[V_n] = \mathbb{E}\langle V(t), \varphi_n(t) \rangle = \mathbb{E} \int_{-\infty}^{\infty} V(t) \varphi_n(t) dt = \int_{-\infty}^{\infty} \mathbb{E}[V(t)] \varphi_n(t) dt = 0. \quad (4.32)$$

Additionally, it has the following covariance:

$$\mathbb{E}[V_i V_j] = \mathbb{E} \int_{-\infty}^{\infty} V(t) \varphi_i(t) dt \int_{-\infty}^{\infty} V(u) \varphi_j(u) du \quad (4.33)$$

$$= \int_{-\infty}^{\infty} \int_{-\infty}^{\infty} \mathbb{E}[V(t) V(u)] \varphi_i(t) \varphi_j(u) dt du \quad (4.34)$$

$$= \int_{-\infty}^{\infty} \int_{-\infty}^{\infty} \frac{N_0}{2} \delta(t - u) \varphi_i(t) \varphi_j(u) dt du \quad (4.35)$$

$$= \frac{N_0}{2} \int_{-\infty}^{\infty} \varphi_i(t) \varphi_j(t) dt \quad (4.36)$$

$$= \begin{cases} \frac{N_0}{2}, & i = j \\ 0, & i \neq j \end{cases}, \quad (4.37)$$

where the last equality follows since the basis functions  $\{\varphi_1(t), \varphi_2(t), \dots, \varphi_N(t)\}$  are orthonormal. Hence, the noise vector elements are independent, identically distributed (iid) Gaussian random variables, and the pdf for  $\mathbf{V}$  is therefore

$$p_{\mathbf{V}}(\mathbf{u}) = \frac{1}{(\pi N_0)^{N/2}} \exp\left(-\frac{1}{N_0} \|\mathbf{u}\|^2\right). \quad (4.38)$$

It is sometimes convenient to model the noise as circular-symmetric complex white Gaussian noise. That is,  $V(t) = V_I(t) + jV_Q(t)$ , where  $V_I(t)$  and  $V_Q(t)$  are independent white real-valued Gaussian random processes and  $j = \sqrt{-1}$ . We can form the noise vector as  $\mathbf{V} = \mathbf{V}_I + j\mathbf{V}_Q$ , where  $\mathbf{V}_I$  and  $\mathbf{V}_Q$  are iid vectors with pdfs given by Eq. (4.38). The pdf of the complex noise vector is

$$p_{\mathbf{V}}(\mathbf{u}) = \frac{1}{(\pi N_0)^N} \exp\left(-\frac{1}{N_0} \|\mathbf{u}\|^2\right). \quad (4.39)$$

We will not make a notational difference between the pdf for the real-valued noise vector and the complex-valued noise vector. It should be clear from context if the noise vector pdf  $p_{\mathbf{V}}(\mathbf{u})$  should be defined by Eq. (4.38) or (4.39).

The noise vector does not characterize the whole noise process, since the noise process realizations are not contained in the signals space. Indeed, the noise vector is a representation of

$$V_S(t) = \sum_{n=1}^N V_n \varphi_n(t). \quad (4.40)$$

However, we will later show that the suppressed noise component,

$$V_{S^\perp}(t) = V(t) - V_S(t), \quad (4.41)$$

is irrelevant for optimal receivers. Hence, there is no information loss when projecting the received signal onto the signal space.

## 4.5 OPTIMUM MESSAGE RECEIVERS

We are now ready to find optimum receivers, that is, receivers that minimize the error probability. We consider the message error probability in this section and treat bit error probability in [Section 4.9](#).

### 4.5.1 MAP RECEIVER

We model the transmitted bits as binary random variables. The distribution of the transmitted bits and the mapping from bits to signal alternatives determine the distribution of the transmitted signal or, equivalently, the transmitted vector. Suppose  $m$  is the index of the transmitted signal alternative. That is, the transmitted signal is  $X(t) = x_m(t)$ , which implies that  $\mathbf{X} = \mathbf{x}_m$ , an exception to our notation convention that lower case symbols are deterministic. Note that we think of  $m$  as a random variable, since  $m$  is determined by the transmitted bits. Hence,  $x_m(t)$  is a random process and  $\mathbf{x}_m$  is a random vector. The pdf (or more accurately, the pmf) of  $m$  is called the a priori distribution:

$$p_m[\ell] \triangleq \Pr\{m = \ell\} = \Pr\{\mathbf{X} = \mathbf{x}_\ell\} = \Pr\{X(t) = x_\ell(t)\}. \quad (4.42)$$

Without great loss of generality, we will from now on assume that  $p_m[k] > 0$  for all  $k \in \mathcal{M}$ , that is, all signal alternatives are transmitted with nonzero probability.

Suppose the receiver knows the a priori distribution. To derive the optimum receiver for this case, we start with a seemingly strange example: suppose the receiver is forced to make a guess  $\hat{m}$  on  $m$  before observing the received vector. The probability that this guess is correct, which we denote  $P_c[\hat{m}]$ , is given by the following a priori distribution:

$$P_c[\hat{m}] = \Pr\{m = \hat{m}\} = p_m[\hat{m}]. \quad (4.43)$$

The best guess is therefore to choose  $\hat{m}$  as a number in  $\mathcal{M}$  that maximizes  $P_c[\hat{m}]$ , that is, we should form the guess  $\hat{m}$  on  $m$  as

$$\hat{m} = \arg \max_{\ell \in \mathcal{M}} P_c[\ell] = \arg \max_{\ell \in \mathcal{M}} p_m[\ell]. \quad (4.44)$$

We call this detection rule the maximum a priori rule.

**Example 4.6.** Suppose that the a priori distribution is

$$p_m[1] = 2/8, \quad p_m[2] = 1/8, \quad p_m[3] = 2/8, \quad p_m[4] = 3/8.$$

Since signal alternative four is the most probable one, the maximum a priori decision is  $\hat{m} = 4$ .

This somewhat contrived example can be extended to cover the more interesting case when the receiver is allowed to observe the received vector. Suppose that the receiver observes that  $\mathbf{Y}$  takes on the value  $\mathbf{y}$ . Then, from the receiver's perspective, the pdf of  $m$  changes from the a priori distribution to the a posteriori distribution,

$$p_{m|\mathbf{Y}}[\ell | \mathbf{y}] \triangleq \Pr\{m = \ell | \mathbf{Y} = \mathbf{y}\}. \quad (4.45)$$

The probability that the guess  $\hat{m}$  is correct, conditioned on us observing that  $\mathbf{Y} = \mathbf{y}$ , is therefore  $P_c[\hat{m}] = p_{m|\mathbf{Y}}[\hat{m} | \mathbf{y}]$ , and the optimum decision rule is the maximum a posteriori (MAP) rule:

$$\hat{m}_{\text{MAP}} = \arg \max_{\ell \in \mathcal{M}} p_{m|\mathbf{Y}}[\ell | \mathbf{y}]. \quad (4.46)$$

From Eq. (4.46), it is clear that the MAP receiver can be implemented by evaluating the a posteriori pdf of  $m$  conditioned on the event that  $\mathbf{Y} = \mathbf{y}$ . For the additive white Gaussian noise (AWGN) channel this is perhaps most easily done by applying Bayes' rule, which states that the joint pdf of  $\mathbf{Y}$  and  $m$  can be expressed as follows:

$$p_{\mathbf{Y},m}(\mathbf{y}, \ell) = p_{m|\mathbf{Y}}[\ell | \mathbf{y}]p_{\mathbf{Y}}(\mathbf{y}) = p_{\mathbf{Y}|m}(\mathbf{y} | \ell)p_m[\ell]. \quad (4.47)$$

Since  $p_{\mathbf{Y}}(\mathbf{y}) \neq 0$ , we can write

$$p_{m|\mathbf{Y}}[\ell | \mathbf{y}] = \frac{p_{\mathbf{Y}|m}(\mathbf{y} | \ell)p_m[\ell]}{p_{\mathbf{Y}}(\mathbf{y})}. \quad (4.48)$$

To compute  $p_{\mathbf{Y}|m}(\mathbf{y} | \ell)$ , we recall that  $\mathbf{Y} = \mathbf{x}_m + \mathbf{V}$ , where  $\mathbf{V}$  is a Gaussian random variable. Hence, conditioned on  $m = \ell$ , we have that  $\mathbf{Y} = \mathbf{x}_\ell + \mathbf{V}$  is a Gaussian random variable with mean  $\mathbf{x}_\ell$  (a deterministic vector). It follows from Eqs. (4.38), (4.39) that

$$p_{\mathbf{Y}|m}(\mathbf{y} | \ell) = p_{\mathbf{V}}(\mathbf{y} - \mathbf{x}_\ell) = \frac{1}{K} \exp\left(-\frac{1}{N_0} \|\mathbf{y} - \mathbf{x}_\ell\|^2\right), \quad (4.49)$$

where  $K = (\pi N_0)^{N/2}$  for real-valued noise and  $K = (\pi N_0)^N$  for complex-valued noise. Now,

$$p_{\mathbf{Y}}(\mathbf{y}) = \sum_{j \in \mathcal{M}} p_{\mathbf{Y},m}(\mathbf{y}, j) \quad (4.50)$$

$$= \sum_{j \in \mathcal{M}} p_{\mathbf{Y}|m}(\mathbf{y} | j)p_m[j] \quad (4.51)$$

$$= \sum_{j \in \mathcal{M}} \frac{1}{K} \exp\left(-\frac{1}{N_0} \|\mathbf{y} - \mathbf{x}_j\|^2\right) p_m[j]. \quad (4.52)$$

Combining Eqs. (4.48), (4.49), (4.52) allows us to write the a posteriori distribution as follows:

$$p_{m|\mathbf{Y}}[\ell | \mathbf{y}] = \frac{p_{\mathbf{Y}|m}(\mathbf{y} | \ell)p_m[\ell]}{\sum_{j \in M} p_{\mathbf{Y}|m}(\mathbf{y} | j)p_m[j]} \quad (4.53)$$

$$= \frac{\exp(-\|\mathbf{y} - \mathbf{x}_\ell\|^2/N_0)p_m[\ell]}{\sum_{j \in M} \exp(-\|\mathbf{y} - \mathbf{x}_j\|^2/N_0)p_m[j]}, \quad (4.54)$$

where we note that Eq. (4.54) is valid for both real-valued and complex-valued noise, since the factor  $K$  in front of the exponential in Eq. (4.49) cancels.

**Example 4.7.** The pdfs in Eqs. (4.49), (4.54) are plotted in Fig. 4.10, considering the signal vectors in Example 4.3, a priori distribution in Example 4.6, and  $N_0 = 2$ . To compute the a posteriori distribution, we evaluate the pdfs at  $\mathbf{y} = [1/\sqrt{2} \ 1/\sqrt{2}]^T$  and use Eq. (4.54). As seen in Fig. 4.11, the MAP decision is  $\hat{m}_{\text{MAP}} = 2$  for  $N_0 = 2$  and  $\hat{m}_{\text{MAP}} = 4$  for  $N_0 = 6$ . In general, the MAP decision is dependent on both the a priori distribution and the noise variance. Indeed, as the noise variance increases, the observation is that  $\mathbf{Y} = \mathbf{y}$  will be less and less informative. Hence, it then makes sense to trust the a priori distribution more, and at some point, the maximum a posteriori decision becomes equivalent to the maximum a priori decision. This notion is made more precise below.

We can obtain the MAP decision by inserting Eq. (4.54) in Eq. (4.46):

$$\hat{m}_{\text{MAP}} = \arg \max_{\ell \in \mathcal{M}} p_{m|\mathbf{Y}}[\ell | \mathbf{y}] \quad (4.55)$$

$$= \arg \max_{\ell \in \mathcal{M}} \frac{\exp(-\|\mathbf{y} - \mathbf{x}_\ell\|^2/N_0)p_m[\ell]}{\sum_{j \in M} \exp(-\|\mathbf{y} - \mathbf{x}_j\|^2/N_0)p_m[j]} \quad (4.56)$$

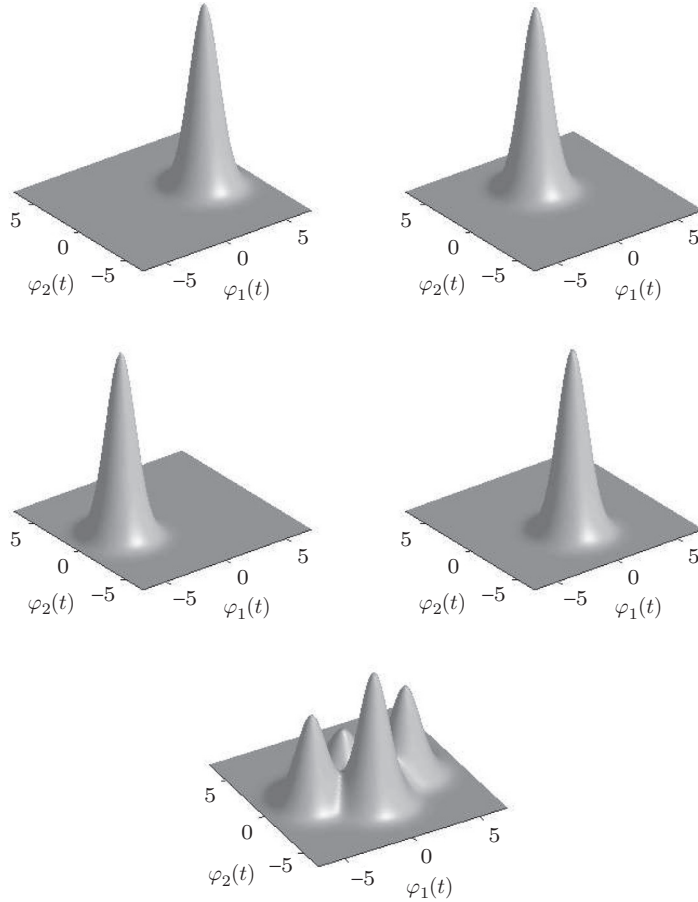
$$= \arg \max_{\ell \in \mathcal{M}} \exp(-\|\mathbf{y} - \mathbf{x}_\ell\|^2/N_0)p_m[\ell] \quad (4.57)$$

$$= \arg \max_{\ell \in \mathcal{M}} -\frac{\|\mathbf{y} - \mathbf{x}_\ell\|^2}{N_0} + \ln p_m[\ell] \quad (4.58)$$

$$= \arg \min_{\ell \in \mathcal{M}} \|\mathbf{y} - \mathbf{x}_\ell\|^2 - N_0 \ln p_m[\ell], \quad (4.59)$$

where Eq. (4.57) is valid since the denominator in Eq. (4.56) does not depend on  $\ell$ , Eq. (4.58) follows since  $\ln(x)$  is an increasing function of  $x$ , and Eq. (4.59) follows since  $N_0 > 0$ . We note that Eq. (4.59) is valid for both the real-valued and complex-valued cases.

We note that the MAP rule is essentially a minimum-distance rule, which penalizes signal alternatives with relative small a priori probabilities. That is, the smaller  $p_m[\ell]$  is, the larger the penalty term  $-N_0 \ln p_m[\ell]$  is. We also note the penalty term is more pronounced the noisier the channel is, that is, when  $N_0$  grows large. In fact, it follows from Eq. (4.58) that the MAP decision becomes the maximum a priori decision as  $N_0 \rightarrow \infty$ .

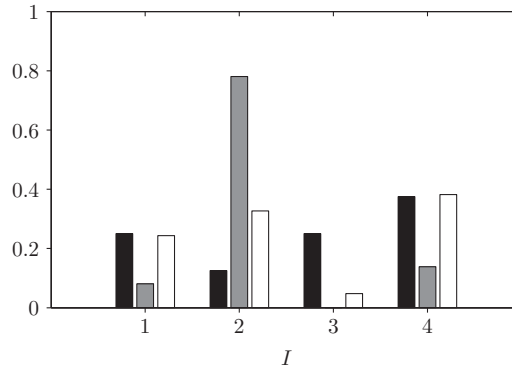
**FIG. 4.10**

Plot of pdf of  $\mathbf{Y}$  conditioned on  $m$ , that is,  $p_{\mathbf{Y}|m}(\mathbf{y} | \ell)$ , for  $\ell = 1, 2, 3, 4$  and unconditional pdf of  $\mathbf{Y}$ , that is,  $p_{\mathbf{Y}}(\mathbf{y})$  (bottom).

Now, consider a generic detector  $\text{dec}: \mathbb{F}^N \rightarrow \mathcal{M}$ , that is, a mapping from the observed received vector to the index set of the possible transmitted vectors. Here,  $\mathbb{F}$  is the set of the real or complex numbers, as appropriate. Given an observed vector  $\mathbf{y}$ , the decision is  $\hat{m} = \text{dec}(\mathbf{y})$  and the probability of the correct decision conditioned on the event  $\mathbf{Y} = \mathbf{y}$  is then  $p_{m|\mathbf{Y}}[\text{dec}(\mathbf{y}) | \mathbf{y}]$ . Hence, the (average) message error probability is

$$P_e = \Pr\{m \neq \text{dec}(\mathbf{Y})\} \quad (4.60)$$

$$= 1 - \Pr\{m = \text{dec}(\mathbf{Y})\} \quad (4.61)$$

**FIG. 4.11**

Plot of the a priori distribution of  $m$ , that is,  $p_m[\ell]$  (left bar) and a posteriori distribution of  $m$  conditioned on  $\mathbf{Y} = \mathbf{y}$ , that is,  $p_{m|\mathbf{Y}}[\ell | \mathbf{y}]$ , for  $N_0 = 2$  (middle bar) and  $N_0 = 6$  (right bar).

$$= 1 - \int_{\mathbf{y} \in \mathbb{R}^N} \Pr\{m = \text{dec}(\mathbf{y}) | \mathbf{Y} = \mathbf{y}\} p_{\mathbf{Y}}(\mathbf{y}) d\mathbf{y}. \quad (4.62)$$

$$= 1 - \int_{\mathbf{y} \in \mathbb{R}^N} p_{m|\mathbf{Y}}[\text{dec}(\mathbf{y}) | \mathbf{y}] p_{\mathbf{Y}}(\mathbf{y}) d\mathbf{y}. \quad (4.63)$$

From this expression, we can prove that the MAP detector is the optimum receiver in the sense that we cannot find a detector that has a smaller average error probability than the MAP detector. The proof is simple: the integral in Eq. (4.63) is maximized by maximizing the integrand for every value of  $\mathbf{y}$ . This is achieved by the MAP detector since, by definition,  $p_{m|\mathbf{Y}}[\hat{m}_{\text{MAP}} | \mathbf{y}] \geq p_{m|\mathbf{Y}}[\text{dec}(\mathbf{y}) | \mathbf{y}]$  for any choice of  $\text{dec}(\mathbf{y})$ .

We will later show how Eq. (4.63) can be manipulated into a form which is easier to either compute exactly or bound.

### 4.5.2 ML RECEIVER

In case we do not know the a priori distribution or  $N_0$ , we cannot compute the MAP decision. While we can think of estimating  $N_0$  from the received signal as a synchronization problem (similar to estimating the propagation delay), the lack of knowledge of the a priori probabilities is more problematic. We can approach the problem of missing knowledge about the a priori distribution in two ways. One approach is simply to change the modeling of the transmitted data from a Bayesian approach to a non-Bayesian approach. That is, we model the data as a deterministic unknown parameter. Another approach, which we will adopt here, is to assume that all signal alternatives are equally likely, that is, that  $p_m[\ell] = 1/M$  for all  $\ell \in \mathcal{M}$ . As will be shown below, the MAP detector reduces to a form that is equivalent to the maximum-likelihood (ML) detector, which is a standard detector

with some optimality properties in a non-Bayesian setting [3]. The reduction of MAP to ML justifies, to some degree, our choice to remain in a Bayesian setting. Further justification for the assumption of equally probable signal alternatives is offered by the fact that this assumption can be viewed as a maximum entropy assumption, that is, an assumption that is the least restrictive in the sense that this will make the receiver maximally unsure about the value of  $m$ . Indeed, the probability of error for the maximum a priori decision rule (which is the minimum error probability receiver in the absence of an observation of  $\mathbf{Y}$ ), that is,  $\hat{m} = \arg \max_{\ell \in \mathcal{M}} p_m[\ell]$ , is  $P_e = 1 - 1/M$ , which is the largest possible among all possible a priori distributions.

Now, under the assumption that  $p_m[\ell] = 1/M$  for all  $\ell \in \mathcal{M}$ , it follows from Eq. (4.59) that the MAP decision is as follows:

$$\hat{m}_{\text{MAP}} = \arg \min_{\ell \in \mathcal{M}} \|\mathbf{y} - \mathbf{x}_\ell\|^2 - N_0 \ln p_m[\ell] \quad (4.64)$$

$$= \arg \min_{\ell \in \mathcal{M}} \|\mathbf{y} - \mathbf{x}_\ell\|^2 - N_0 \ln \frac{1}{M} \quad (4.65)$$

$$= \arg \min_{\ell \in \mathcal{M}} \|\mathbf{y} - \mathbf{x}_\ell\|^2 \quad (4.66)$$

$$= \hat{m}_{\text{MD}}, \quad (4.67)$$

where Eq. (4.66) follows since  $N_0 \ln(1/M)$  is independent of  $\ell$ . The decision rule in Eq. (4.68) is equivalent to the ML decision rule, which is defined, in general, as

$$\hat{m}_{\text{ML}} = \arg \max_{\ell \in \mathcal{M}} p_{\mathbf{Y}|m}(\mathbf{y} | \ell). \quad (4.68)$$

We arrive at the following important conclusion: the MAP and ML detectors are equivalent (and optimum from a minimum average message error probability perspective) when the signal alternatives are equally likely. Moreover, for the AWGN channel, the ML detector is equivalent to the minimum-distance detector.

The name for the ML detector comes from the fact that in Eq. (4.68),  $\mathbf{y}$  is a constant and we view  $p_{\mathbf{Y}|m}(\mathbf{y} | \ell)$  as a function of  $\ell$ . Such functions are commonly called likelihood functions.

Finally, we note that since the ML detector expression in Eq. (4.66) is derived from the MAP expression (4.59), which is valid for both real and complex AWGN channels, the ML detector expression in Eq. (4.66) is also valid for both real and complex AWGN channels.

## 4.6 THE IRRELEVANCE THEOREM

Our objective with this section is to show that the noise component  $V_{\mathcal{G}^\perp}(t)$ , which was ignored in the process of converting  $Y(t)$  to  $\mathbf{Y}$ , is irrelevant to the problem of guessing the value of  $m$  with minimum probability of error. The main idea is to show

that if (in addition to  $\mathbf{Y}$ ) we were able to also observe  $V_{\mathcal{S}^\perp}(t)$ , then this would not change the MAP decision on  $m$ .

We will actually prove this in a slightly restricted form. Instead of observing  $V_{\mathcal{S}^\perp}(t)$  directly, we will observe the random vector  $\mathbf{W}$  defined as

$$\mathbf{W} \triangleq [W_1 \quad W_2 \quad \cdots \quad W_P]^T \quad (4.69)$$

$$W_p \triangleq \langle V_{\mathcal{S}^\perp}(t), w_p(t) \rangle, \quad (4.70)$$

where  $w_p(t)$  for  $p = 1, 2, \dots, P$  are assumed to have finite energy but are otherwise arbitrary. Our main reason for not observing  $V_{\mathcal{S}^\perp}(t)$  directly is that the variance for any time sample of  $V_{\mathcal{S}^\perp}(t)$  is not bounded, which leads to mathematical difficulties. Nevertheless, the observation model in Eq. (4.69) is physically appealing: most, if not all, physical sensors will be bandlimited, which can be accurately modeled by a linear operation of the form in Eq. (4.69). In the following we will show that  $\mathbf{W}$ , and any processing (linear or nonlinear) of  $\mathbf{W}$ , is irrelevant for the decision on  $m$ . A more rigorous approach to the irrelevance theorem can be found in Lapidoth [6] and Gallager [7].

We recall from Eq. (4.41) that we can decompose the noise into two components:

$$V(t) = V_{\mathcal{S}}(t) + V_{\mathcal{S}^\perp}(t), \quad (4.71)$$

where

$$V_{\mathcal{S}}(t) \triangleq \sum_{n=1}^N V_n \varphi_n(t) \quad (4.72)$$

$$V_{\mathcal{S}^\perp}(t) \triangleq V(t) - V_{\mathcal{S}}(t). \quad (4.73)$$

We see that  $V_{\mathcal{S}}(t)$  is completely determined by the vector  $\mathbf{V}$ :

$$\mathbf{V} \triangleq [V_1 \quad V_2 \quad \cdots \quad V_N]^T. \quad (4.74)$$

In the following, we will show that the MAP detector for  $m$  based on the observation  $\mathbf{Y} = \mathbf{y}$ ,  $\mathbf{W} = \mathbf{w}$  reduces to the MAP detector for  $m$  based only on  $\mathbf{Y} = \mathbf{y}$ . That is, the vector  $\mathbf{W}$ , and therefore  $V_{\mathcal{S}^\perp}(t)$ , is irrelevant for the problem of guessing  $m$  with minimum probability of error.

The MAP detector for  $m$  based on the observation  $\mathbf{W} = \mathbf{w}$ ,  $\mathbf{Y} = \mathbf{y}$  is as follows:

$$\hat{m}_{\text{MAP}} = \arg \max_{\ell \in \mathcal{M}} p_{m|\mathbf{W}, \mathbf{Y}}[\ell \mid \mathbf{w}, \mathbf{y}] \quad (4.75)$$

$$= \arg \max_{\ell \in \mathcal{M}} \frac{p_{\mathbf{W}, \mathbf{Y}|m}(\mathbf{w}, \mathbf{y} \mid \ell) p_m[\ell]}{p_{\mathbf{W}, \mathbf{Y}}(\mathbf{w}, \mathbf{y})} \quad (4.76)$$

$$= \arg \max_{\ell \in \mathcal{M}} p_{\mathbf{W}, \mathbf{Y}|m}(\mathbf{w}, \mathbf{y} \mid \ell) p_m[\ell] \quad (4.77)$$

$$= \arg \max_{\ell \in \mathcal{M}} p_{\mathbf{W}, \mathbf{V} | m}(\mathbf{w}, \mathbf{y} - \mathbf{x}_\ell | \ell) p_m[\ell] \quad (4.78)$$

$$= \arg \max_{\ell \in \mathcal{M}} p_{\mathbf{W} | \mathbf{V}, m}(\mathbf{w} | \mathbf{y} - \mathbf{x}_\ell, \ell) p_{\mathbf{V} | m}(\mathbf{y} - \mathbf{x}_\ell | \ell) p_m[\ell] \quad (4.79)$$

$$= \arg \max_{\ell \in \mathcal{M}} p_{\mathbf{W} | \mathbf{V}}(\mathbf{w} | \mathbf{y} - \mathbf{x}_\ell) p_{\mathbf{V}}(\mathbf{y} - \mathbf{x}_\ell) p_m[\ell], \quad (4.80)$$

where we have used Bayes' rule repeatedly, and the fact that  $p_{\mathbf{W}, \mathbf{V}}(\mathbf{w}, \mathbf{y})$  does not depend on  $\ell$  and  $\mathbf{W}$  and  $\mathbf{V}$  are independent of  $m$ .

We see that if the first factor in Eq. (4.80), that is,  $p_{\mathbf{W} | \mathbf{V}}(\mathbf{w} | \mathbf{y} - \mathbf{x}_\ell)$ , does not depend on  $\ell$ , the MAP detector based on the observation  $\mathbf{W} = \mathbf{w}$ ,  $\mathbf{Y} = \mathbf{y}$  reduces to

$$\hat{m}_{\text{MAP}} = \arg \max_{\ell \in \mathcal{M}} p_{\mathbf{V}}(\mathbf{y} - \mathbf{x}_\ell) p_m[\ell], \quad (4.81)$$

which is the MAP detector based on the observation  $\mathbf{Y} = \mathbf{y}$ . Hence, it is sufficient to show that  $\mathbf{W}$  and  $\mathbf{V}$  are independent, as this implies that  $p_{\mathbf{W} | \mathbf{V}}(\mathbf{w} | \mathbf{y} - \mathbf{x}_\ell) = p_{\mathbf{W}}(\mathbf{w})$ , which does not depend on  $\ell$ .

To this end, let us formulate a basis for the space

$$\text{span}\{\varphi_1(t), \dots, \varphi_N(t), w_1(t), \dots, w_P(t)\} \quad (4.82)$$

as

$$\{\varphi_1(t), \dots, \varphi_N(t), \varphi_{N+1}(t), \dots, \varphi_L(t)\}, \quad (4.83)$$

where  $L$  is the dimension of the space in Eq. (4.82). We can write  $w_p(t)$  for  $p = 1, 2, \dots, P$  as

$$w_p(t) = \sum_{n=1}^L w_{p,n} \varphi_n(t) \quad (4.84)$$

$$w_{p,n} = \langle w_p(t), \varphi_n(t) \rangle. \quad (4.85)$$

Hence,

$$W_p = \langle V_{\mathcal{S}^\perp}(t), w_p(t) \rangle \quad (4.86)$$

$$= \langle V(t) - V_{\mathcal{S}}(t), w_p(t) \rangle \quad (4.87)$$

$$= \langle V(t), w_p(t) \rangle - \langle V_{\mathcal{S}}(t), w_p(t) \rangle \quad (4.88)$$

$$= \sum_{n=1}^L \langle V(t), \varphi_n(t) \rangle w_{p,n}^* - \sum_{n=1}^N V_n \langle \varphi_n(t), w_p(t) \rangle \quad (4.89)$$

$$= \sum_{n=1}^L V_n w_{p,n}^* - \sum_{n=1}^N V_n w_{p,n}^* \quad (4.90)$$

$$= \sum_{n=N+1}^L V_n w_{p,n}^*, \quad (4.91)$$

where we have used the standard properties of the inner product<sup>4</sup> and extended the definition of  $V_n = \langle V(t), \varphi_n(t) \rangle$  to hold also for  $n = N + 1, N + 2, \dots, L$ . Following the exact same procedure as before, it is easy to show that  $\{V_1, \dots, V_L\}$  are iid Gaussian random variables. Hence, the elements of  $\mathbf{V}$ , that is,  $\{V_1, \dots, V_N\}$ , are statistically independent of any linear combination of  $\{V_{N+1}, \dots, V_L\}$ , including  $W_p = \sum_{n=N+1}^L V_n w_{p,n}^*$ , for  $p = 1, 2, \dots, P$  and it follows that  $\mathbf{V}$  and  $\mathbf{W}$  are statistically independent. Moreover, any function of  $\mathbf{W}$ , say  $f(\mathbf{W})$ , will also be statistically independent of  $\mathbf{V}$ . Hence,  $f(\mathbf{W})$  is also irrelevant for the MAP decision on  $m$ .

We have now shown that the receiver front-end, that is, the signal-to-vector conversion block in Fig. 4.9, is loss less. That is, no information about  $m$  is lost in the front-end.

## 4.7 DECISION REGIONS AND ERROR PROBABILITY

### 4.7.1 DECISIONS REGIONS FOR A GENERAL DETECTOR

We recall that a detector maps the received vector onto the index set of the transmitted vectors, that is,  $\text{dec}: \mathbb{F}^N \rightarrow \mathcal{M} = \{1, 2, \dots, M\}$ . For the AWGN channel, we can restrict our attention to deterministic detectors, that is, we can think of  $\text{dec}$  as a deterministic function, without loss of optimality [6]. The decision regions  $\Lambda_1, \Lambda_2, \dots, \Lambda_M$  for the detector  $\text{dec}$  are defined such that

$$\Lambda_\ell \triangleq \{\mathbf{y} \in \mathbb{F}^N: \text{dec}(\mathbf{y}) = \ell\}. \quad (4.92)$$

From the definition, it follows that the decision regions is a partitioning of the space  $\mathbb{F}^N$ , that is,  $\bigcup_{\ell=1}^M \Lambda_\ell = \mathbb{F}^N$  and  $\Lambda_\ell \cap \Lambda_i = \emptyset$  for  $\ell \neq i$ .

**Example 4.8.** The decision regions for a certain (non-MAP, non-ML) detector are shown in Fig. 4.12. As seen, the decision regions are nonoverlapping and partition the entire 2-dimensional plane.

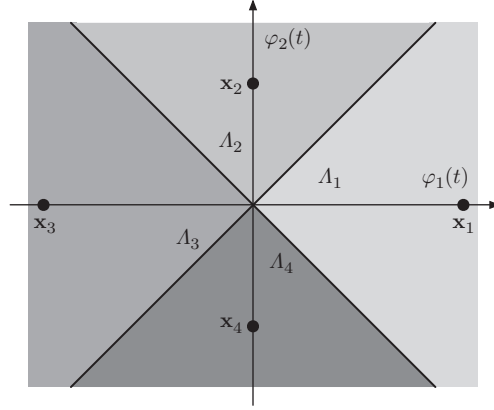
The decision regions are very useful to compute the error probability. To see this, we first find the error probability conditioned on  $m = j$  or, equivalently,  $\mathbf{X} = \mathbf{x}_j$ , as follows:

$$P_{e|j} \triangleq \Pr\{\hat{m} \neq j \mid m = j\} = 1 - \underbrace{\Pr\{\hat{m} = j \mid m = j\}}_{P_{c|j}}, \quad (4.93)$$

where  $P_{c|j}$  is the probability of a correct decision conditioned on  $m = j$ , that is, when  $\mathbf{Y} = \mathbf{x}_j + \mathbf{V}$ . Hence,  $p_{\mathbf{Y}|m}(\mathbf{u} \mid j) = p_{\mathbf{V}}(\mathbf{u} - \mathbf{x}_j)$ , and

$$P_{c|j} = \Pr\{\mathbf{y} \in \Lambda_j \mid \mathbf{x} = \mathbf{x}_j\} \quad (4.94)$$

<sup>4</sup>For the scalar  $a$  and signals  $f(t)$ ,  $g(t)$ , and  $h(t)$ , we have that  $\langle f(t), g(t) \rangle = (\langle g(t), f(t) \rangle)^*$ ,  $\langle f(t), ag(t) \rangle = \langle f(t), g(t) \rangle a^*$ ,  $\langle af(t), g(t) \rangle = a \langle f(t), g(t) \rangle$ ,  $\langle f(t) + g(t), h(t) \rangle = \langle f(t), h(t) \rangle + \langle g(t), h(t) \rangle$ , and  $\langle f(t), g(t) + h(t) \rangle = \langle f(t), g(t) \rangle + \langle f(t), h(t) \rangle$ .


**FIG. 4.12**

Decision regions for an example detector.

$$= \int_{\Lambda_j} p_{\mathbf{Y}|m}(\mathbf{u} | j) d\mathbf{u} \quad (4.95)$$

$$= \int_{\Lambda_j} p_{\mathbf{V}}(\mathbf{u} - \mathbf{x}_j) d\mathbf{u}. \quad (4.96)$$

For the AWGN channel, we know that  $\mathbf{V}$  is a Gaussian random vector with zero mean and covariance  $(N_0/2)\mathbf{I}_N$  in the real case and  $N_0\mathbf{I}_N$  in the complex case. Nevertheless,  $P_{c|j}$  is simply the integral of a Gaussian density centered at  $\mathbf{x}_j$  over the corresponding decision region  $\Lambda_j$ .

**Example 4.9.** For our example detector with decision regions as in Fig. 4.12, the conditional probability of correct detection for the second signal vector is

$$P_{c|2} = \int_{\Lambda_2} p_{\mathbf{V}}(\mathbf{u} - \mathbf{x}_2) d\mathbf{u}.$$

The integral is equal to the volume under a truncated Gaussian pdf, as depicted in Fig. 4.13 when  $N_0 = 6$ .

In some cases, most notably when  $\Lambda_j$  is a cuboid, we can efficiently compute the integral. In the more general case, we can find upper bounds on  $P_{e|j}$  that are tight for an asymptotically small  $N_0$ . We will explore different bounding techniques in more detail in Section 4.8.

Given the conditional probability of correct decision, we can easily compute the unconditional (average) error probability as

$$P_e = \sum_{j \in \mathcal{M}} P_{e|j} p_m[j] = \sum_{j \in \mathcal{M}} (1 - P_{c|j}) p_m[j]. \quad (4.97)$$

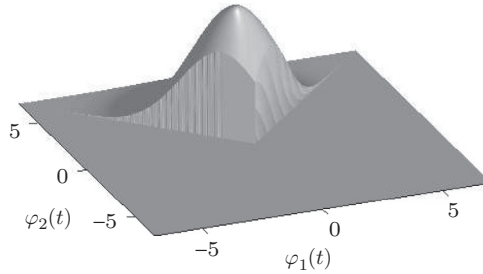


FIG. 4.13

The probability of correct detection conditioned on  $m = 2$ , that is,  $P_{c|2}$ , is the volume under the noise pdf, centered around  $\mathbf{x}_2$  and truncated to  $\Lambda_2$ .

### 4.7.2 DECISION REGIONS FOR THE MINIMUM-DISTANCE DETECTOR

The decision regions for the minimum-distance receiver are closely related to the Voronoi regions,  $\Omega_\ell$ , defined as

$$\Omega_\ell \triangleq \{\mathbf{y} \in \mathbb{F}^N : d(\mathbf{y}, \mathbf{x}_\ell) \leq d(\mathbf{y}, \mathbf{x}_i), i \in \mathcal{M}_\ell\}, \quad \ell \in \mathcal{M}, \quad (4.98)$$

where

$$\mathcal{M}_\ell \triangleq \{i \in \mathcal{M} : i \neq \ell\}, \quad \ell \in \mathcal{M}. \quad (4.99)$$

We can find  $\Omega_\ell$  as the intersection of  $M - 1$  half-spaces. To see this, let us consider the half-space  $\Omega_\ell^{(i)}$ , defined as

$$\Omega_\ell^{(i)} \triangleq \{\mathbf{y} \in \mathbb{F}^N : d(\mathbf{y}, \mathbf{x}_\ell) \leq d(\mathbf{y}, \mathbf{x}_i)\}, \quad i \in \mathcal{M}_\ell. \quad (4.100)$$

Hence, by definition,  $\Omega_\ell^{(i)}$  is the set of vectors in  $\mathbb{F}^N$  that are closer (or at the same distance) to  $\mathbf{x}_\ell$  than  $\mathbf{x}_i$ . Hence, the set of vectors in  $\mathbb{F}^N$  that are closer (or at the same distance) to  $\mathbf{x}_\ell$  than any other signal vector must be a member of all  $\Omega_\ell^{(i)}$ , that is,

$$\Omega_\ell = \bigcap_{i \in \mathcal{M}_\ell} \Omega_\ell^{(i)}. \quad (4.101)$$

Hence,  $\Omega_\ell$  is a convex (possibly unbounded) polytope, as it is formed as the intersection of a number of convex regions (half-planes).

**Example 4.10.** The half-spaces (or more precisely half-planes, since the considered signal space is 2-dimensional),  $\Omega_1^{(i)}$  for  $i = 2, 3, 4$  and the Voronoi region  $\Omega_1$  are shown in Fig. 4.14. In this case, we note that

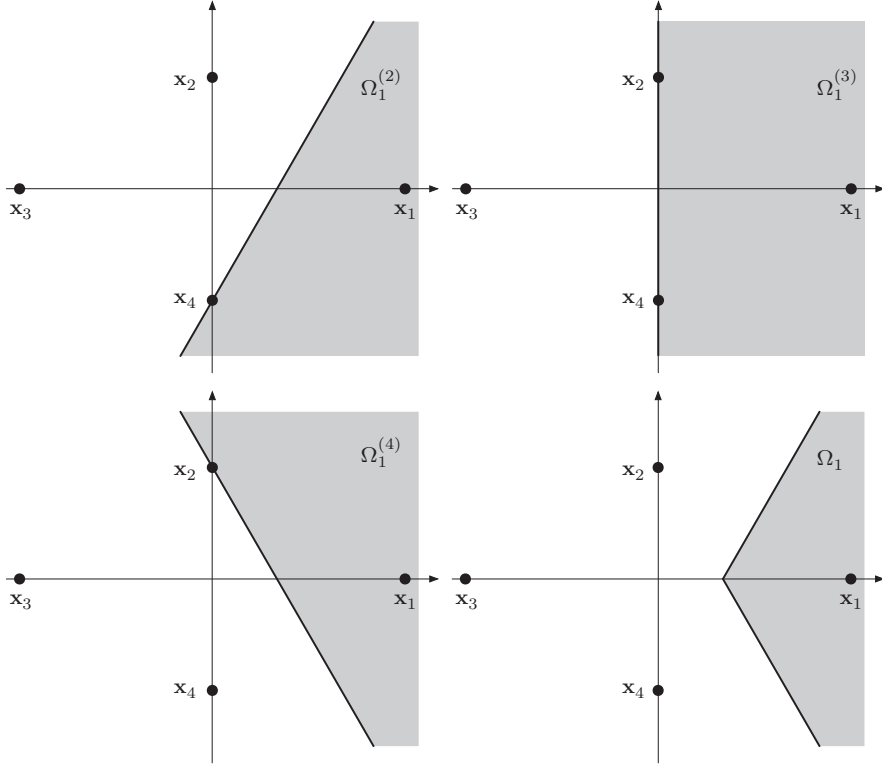


FIG. 4.14

Construction of Voronoi region  $\Omega_1$ .

$$\Omega_1 = \Omega_1^{(2)} \cap \Omega_1^{(3)} \cap \Omega_1^{(4)} = \Omega_1^{(2)} \cap \Omega_1^{(4)},$$

which follows since  $\Omega_1^{(2)} \cap \Omega_1^{(4)}$  is a subset of  $\Omega_1^{(3)}$ . The complete Voronoi diagram is depicted in Fig. 4.15.

As seen in Fig. 4.15, not all half-spaces  $\Omega_\ell^{(i)}$  for  $i \in \mathcal{M}_\ell$  necessarily contribute to the Voronoi region  $\Omega_\ell^{(i)}$ . In fact, we have that

$$\Omega_\ell = \bigcap_{i \in \mathcal{N}_\ell} \Omega_\ell^{(i)}, \quad (4.102)$$

where  $\mathcal{N}_\ell$  is the smallest-cardinality subset of  $\mathcal{M}_\ell$  that satisfies Eq. (4.102). We call  $\mathcal{N}_\ell$  the closest neighbor set to the signal vector  $\mathbf{x}_\ell$ .

**Example 4.11.** For our example constellation (see Fig. 4.15), we have

$$\mathcal{N}_1 = \{2, 4\} = \mathcal{N}_3; \quad \mathcal{N}_2 = \{1, 3, 4\}; \quad \mathcal{N}_4 = \{1, 2, 3\}.$$

Hence,  $\mathcal{N}_\ell = \mathcal{M}_\ell$  for  $\ell = 2, 4$ , while  $\mathcal{N}_\ell$  is a proper subset of  $\mathcal{M}_\ell$  for  $\ell = 1, 3$ .

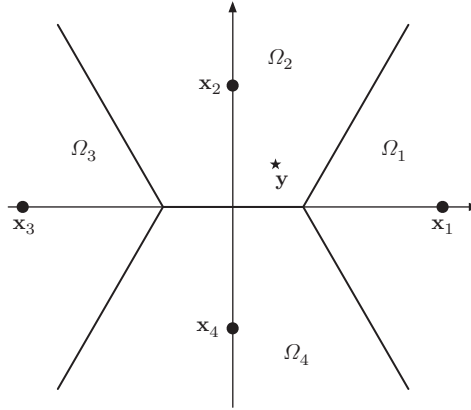


FIG. 4.15

Voronoi regions for the signal constellation  $\{\mathbf{x}_1, \mathbf{x}_2, \mathbf{x}_3, \mathbf{x}_4\}$ . The signal vector  $\mathbf{y}$  from Example 4.4 is indicated with a star.

Moreover, we see that  $\mathbf{y} \in \Omega_2$ , and the ML decision on  $m$  is therefore  $\hat{m}_{\text{ML}} = 2$ .

As the astute reader has discovered, the Voronoi regions cannot be decision regions of any detector, let alone the minimum-distance detector. The problem is that any point  $\mathbf{y}$  such that  $d(\mathbf{y}, \mathbf{x}_\ell) = d(\mathbf{y}, \mathbf{x}_i)$  belongs to both  $\Omega_\ell$  and  $\Omega_i$  (and possibly more Voronoi regions). Nevertheless, we can still use the Voronoi regions to compute the error probability of the minimum-distance receiver for most additive noise channels of practical interest, including the AWGN channel.

To prove this, the key observation is that the boundary of  $\Omega_\ell^{(i)}$  is a hyperplane, which has zero volume. Hence, the event that  $\mathbf{Y}$  ends up on the bounding hyperplane is a zero-probability event for the AWGN channel (see Section 4.14 for a formal proof). Hence, for all practical purposes, we can consider the Voronoi regions to be the decision regions for the minimum-distance receiver. If the received vector ends up on the boundary, we can break the tie in an arbitrary manner, for example, in favor of the smallest signal vector index.

### 4.7.3 DECISION REGIONS FOR THE MAP DETECTOR

Finding the decision regions for the MAP detector for an AWGN channel is similar to the minimum-distance receiver. In fact, it follows from Eq. (4.59) that the  $\ell$ th decision region for the MAP detector is a convex polytope found as the intersection of the  $M - 1$  half-spaces  $\Psi_\ell^{(i)}$ , defined for  $i \in \mathcal{M}_\ell$  as follows:

$$\Psi_\ell^{(i)} \triangleq \{\mathbf{y} \in \mathbb{R}^N: d^2(\mathbf{y}, \mathbf{x}_\ell) - N_0 \ln p_m[\ell] \leq d^2(\mathbf{y}, \mathbf{x}_i) - N_0 \ln p_m[i]\} \quad (4.103)$$

$$= \left\{ \mathbf{y} \in \mathbb{R}^N: d^2(\mathbf{y}, \mathbf{x}_\ell) \leq d^2(\mathbf{y}, \mathbf{x}_i) + N_0 \ln \frac{p_m[\ell]}{p_m[i]} \right\}, \quad (4.104)$$

where the second equality is valid since we assume that  $p_m[\ell] > 0$  for all  $\ell \in \mathcal{M}$ . The  $\ell$ th MAP decision region is

$$\Lambda_\ell = \bigcap_{i \in \mathcal{M}_\ell} \Psi_\ell^{(i)}, \quad (4.105)$$

where we (again) have been a bit sloppy, since boundaries between the decision regions are overlapping. However, just as in the minimum-distance detector case, the error probability can be computed from our sloppy definition (4.105); see Section 4.14 for a formal proof. If the received vector ends up on the boundary, we can break the tie in an arbitrary manner.

It is not hard to show that  $\Psi_\ell^{(i)}$  can be found by pushing the boundary of  $\Omega_\ell^{(i)}$  in the direction from  $\mathbf{x}_\ell$  toward  $\mathbf{x}_i$  with a distance equal to  $N_0/(2d(\mathbf{x}_i, \mathbf{x}_\ell)) \ln(p_m[i]/p_m[\ell])$ . Hence, the distance from  $\mathbf{x}_\ell$  to the boundary of  $\Psi_\ell^{(i)}$  is  $|r_{\ell,i}|$ , where

$$r_{\ell,i} \triangleq \frac{1}{2}d(\mathbf{x}_i, \mathbf{x}_\ell) + \frac{1}{2} \frac{N_0}{d(\mathbf{x}_i, \mathbf{x}_\ell)} \ln \frac{p_m[\ell]}{p_m[i]}. \quad (4.106)$$

We note that  $r_{\ell,i}$  can be negative, in which case  $\Lambda_\ell$  does contain  $\mathbf{x}_\ell$ . In any event, the smallest norm vector from  $\mathbf{x}_\ell$  to the boundary is

$$r_{\ell,i} \frac{\mathbf{x}_i - \mathbf{x}_\ell}{\|\mathbf{x}_i - \mathbf{x}_\ell\|}. \quad (4.107)$$

**Example 4.12.** For our example constellation, a priori distribution,

$$p_m[1] = 2/8; \quad p_m[2] = 1/8; \quad p_m[3] = 2/8; \quad p_m[4] = 3/8,$$

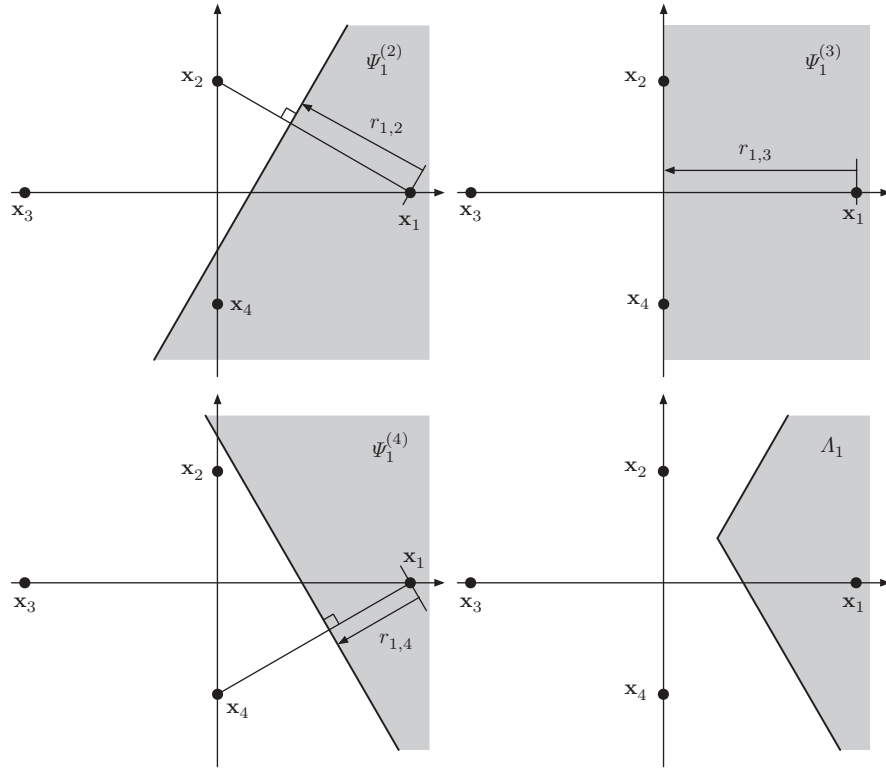
and  $N_0 = 6$ . The MAP decision region for the first signal alternative can be constructed as shown in Fig. 4.16.

Compared with the ML detector (ie, the minimum-distance detector), the MAP decision boundaries are moved toward the signal alternative with the smallest a priori probability. For example, since  $p_m[1] < p_m[4]$ , the boundary between  $\mathbf{x}_1$  and  $\mathbf{x}_4$  is moved toward  $\mathbf{x}_1$ , while the boundary between  $\mathbf{x}_1$  and  $\mathbf{x}_3$  does not move, since  $p_m[1] = p_m[3]$ .

The resulting MAP decision regions are depicted in Fig. 4.17. We see that  $\mathbf{y} \in \Lambda_4$ . Hence, the MAP decision on  $m$  is therefore  $\hat{m}_{\text{MAP}} = 4$ , while we recall from Example 4.11 that the ML decision is  $\hat{m}_{\text{ML}} = 2$ .

## 4.8 UNION BOUND

Computing the error probability is, in general, not a tractable problem. In the following, we will develop a number of upper bounds on the error probability for the ML and MAP detectors that are easily computable, amenable for analytical analysis, and are asymptotically tight as the noise variance becomes small.


**FIG. 4.16**

Construction of the MAP decision region  $\Lambda_1$  from half-planes  $\Psi_1^{(i)}$ .

Recall that we can compute the error probability as

$$P_e = \sum_{j \in \mathcal{M}} P_{e|j} p_m[j], \quad (4.108)$$

where  $P_{e|j}$  is the conditional error probability

$$P_{e|j} = \Pr\{\hat{m} \neq j \mid m = j\} = \sum_{\ell \in \mathcal{M}_j} \Pr\{\hat{m} = \ell \mid m = j\}, \quad (4.109)$$

and where

$$\Pr\{\hat{m} = \ell \mid m = j\} = \Pr\{\mathbf{Y} \in \Lambda_\ell \mid m = j\} \quad (4.110)$$

$$= \Pr\{\mathbf{V} + \mathbf{x}_j \in \Lambda_\ell\} \quad (4.111)$$

$$= \int_{\Lambda_\ell} p_{\mathbf{V}}(\mathbf{u} - \mathbf{x}_j) d\mathbf{u}. \quad (4.112)$$

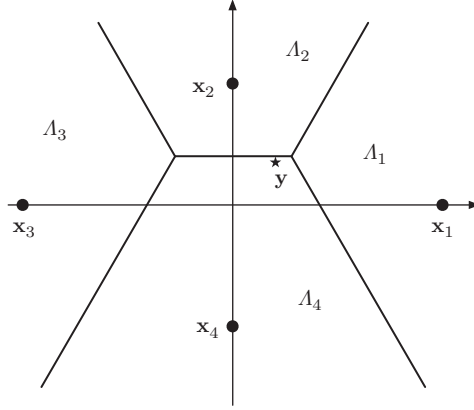


FIG. 4.17

MAP decision regions. The signal vector  $\mathbf{y}$  from Example 4.4 is indicated with a *star*.

It is, in general, difficult or cumbersome to compute this integral. However, we can find an easily computable upper bound to it for the ML (minimum-distance) and MAP detectors. The main idea is to enlarge the integration region, that is, by replacing  $\Lambda_\ell$  with a superset of  $\Lambda_\ell$ , which will result in an upper bound of the integral (since the integrand is positive). Obviously, we want to find a superset to  $\Lambda_\ell$  that makes the new integral tractable.

We will develop the bound for the ML detector first. We remember that for the ML detector,  $\Lambda_\ell$  is the intersection of  $M - 1$  half-planes  $\Omega_\ell^{(i)}$ , that is,  $\Lambda_\ell = \bigcap_{i \in \mathcal{M}_\ell} \Omega_\ell^{(i)}$ , where  $\Omega_\ell^{(i)}$  are all points in the signal space that are closer to  $\mathbf{x}_\ell$  than  $\mathbf{x}_j$ ; see Eq. (4.100). Hence, for all  $j \in \mathcal{M}_\ell$ , we have that  $\Lambda_\ell \subset \Omega_\ell^{(j)}$  and

$$\Pr\{\hat{m} = \ell \mid m = j\} \leq \int_{\Omega_\ell^{(j)}} p_{\mathbf{V}}(\mathbf{u} - \mathbf{x}_j) d\mathbf{u}. \quad (4.113)$$

The right-hand side of Eq. (4.113) can be interpreted as the conditional error probability for the minimum-distance receiver for a signal constellation consisting of only two vectors,  $\mathbf{x}_j$  and  $\mathbf{x}_\ell$ . For this reason, the right-hand side of Eq. (4.113) is called the pairwise error probability<sup>5</sup>

$$P_{j \rightarrow \ell} \triangleq \Pr\{d^2(\mathbf{Y}, \mathbf{x}_\ell) < d^2(\mathbf{Y}, \mathbf{x}_j) \mid m = j\} \quad (4.114)$$

$$= \int_{\Omega_\ell^{(j)}} p_{\mathbf{V}}(\mathbf{u} - \mathbf{x}_j) d\mathbf{u}. \quad (4.115)$$

<sup>5</sup>Since there are only two signal vectors, the conditional error probability for the minimum-distance receiver is also the (unconditional) error probability. Hence, we drop the word “conditional” in the name for  $P_{j \rightarrow \ell}$ .

Now, conditioned on  $m = j$ , we have that  $\mathbf{Y} = \mathbf{x}_j + \mathbf{V}$  and

$$d^2(\mathbf{Y}, \mathbf{x}_\ell) = \|\mathbf{V} + \mathbf{x}_j - \mathbf{x}_\ell\|^2 \quad (4.116)$$

$$= \|\mathbf{V}\|^2 - 2\operatorname{Re}\langle \mathbf{V}, \mathbf{x}_\ell - \mathbf{x}_j \rangle + \|\mathbf{x}_\ell - \mathbf{x}_j\|^2 \quad (4.117)$$

$$d^2(\mathbf{Y}, \mathbf{x}_j) = \|\mathbf{V} + \mathbf{x}_j - \mathbf{x}_j\|^2 = \|\mathbf{V}\|^2, \quad (4.118)$$

and

$$d^2(\mathbf{Y}, \mathbf{x}_\ell) < d^2(\mathbf{Y}, \mathbf{x}_j) \Leftrightarrow -2\operatorname{Re}\langle \mathbf{V}, \mathbf{x}_\ell - \mathbf{x}_j \rangle + \|\mathbf{x}_\ell - \mathbf{x}_j\|^2 < 0. \quad (4.119)$$

Now, since  $\operatorname{Re}\langle \mathbf{V}, \mathbf{x}_\ell - \mathbf{x}_j \rangle \sim \mathcal{N}(0, \|\mathbf{x}_\ell - \mathbf{x}_j\|^2 N_0/2)$ , we can write

$$P_{j \rightarrow \ell} = \Pr\{\operatorname{Re}\langle \mathbf{V}, \mathbf{x}_\ell - \mathbf{x}_j \rangle > \|\mathbf{x}_\ell - \mathbf{x}_j\|^2/2\} \quad (4.120)$$

$$= \Pr\left\{ \frac{\operatorname{Re}\langle \mathbf{V}, \mathbf{x}_\ell - \mathbf{x}_j \rangle}{\sqrt{\|\mathbf{x}_\ell - \mathbf{x}_j\|^2 N_0/2}} > \frac{\|\mathbf{x}_\ell - \mathbf{x}_j\|^2/2}{\sqrt{\|\mathbf{x}_\ell - \mathbf{x}_j\|^2 N_0/2}} \right\} \quad (4.121)$$

$$= Q\left( \frac{\|\mathbf{x}_\ell - \mathbf{x}_j\|^2/2}{\sqrt{\|\mathbf{x}_\ell - \mathbf{x}_j\|^2 N_0/2}} \right) \quad (4.122)$$

$$= Q\left( \sqrt{d_{j,\ell}^2/2N_0} \right), \quad (4.123)$$

where  $d_{j,\ell} = \|\mathbf{x}_\ell - \mathbf{x}_j\|$ .

**Example 4.13.** The bound on  $\Pr\{\hat{m} = 1 \mid m = 2\}$  is shown in Fig. 4.18. The difference between the upper bound and the exact value is the integral over the added

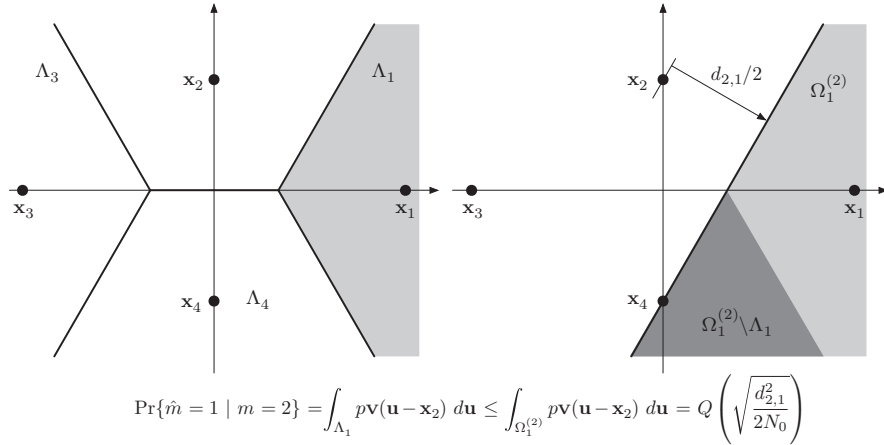


**FIG. 4.18**

An upper bound on  $\Pr\{\hat{m} = 1 \mid m = 2\}$  is found by enlarging the integration region from  $\Lambda_1$  (left) to  $\Omega_1^{(2)}$  (right). The added area is marked with a darker gray.

area,  $\Omega_1^{(2)} \setminus \Lambda_1$ . Hence, for the bound to be tight, this area should be small and far from  $\mathbf{x}_2$ , as the integrand  $P_{\mathbf{V}}(\mathbf{u} - \mathbf{x}_2)$  decreases with  $\|\mathbf{u} - \mathbf{x}_2\|$ .

Now, the conditional error probability can be bounded as

$$P_{e|j} = \sum_{\ell \in \mathcal{M}_j} \Pr\{\hat{m} = \ell \mid m = j\} \leq \sum_{\ell \in \mathcal{M}_j} \int_{\Omega_\ell^{(j)}} p_{\mathbf{V}}(\mathbf{u} - \mathbf{x}_j) d\mathbf{u}. \quad (4.124)$$

The bound in Eq. (4.124) is a so-called union bound on  $P_{e|j}$ . The name stems from the fact that the probability of a union of a finite number of events is less than or equal to the sum of the probabilities for the individual events. In our notation,

$$P_{e|j} = \Pr \left\{ \mathbf{V} + \mathbf{x}_j \in \bigcup_{\ell \in \mathcal{M}_j} \Omega_\ell^{(j)} \right\} \leq \sum_{\ell \in \mathcal{M}_j} \Pr \left\{ \mathbf{V} + \mathbf{x}_j \in \Omega_\ell^{(j)} \right\}. \quad (4.125)$$

Hence, we could have used Eq. (4.125) directly to derive Eq. (4.124), but at the price of less insight into the geometry of the bound.

**Example 4.14.** The bound on  $\Pr\{\hat{m} \neq 2 \mid m = 2\}$  is found by adding the integrals over the three half-planes  $\Omega_1^{(2)}$ ,  $\Omega_3^{(2)}$ , and  $\Omega_4^{(2)}$ ; see Fig. 4.19. Areas that are intersections of exactly two half-spaces are counted twice, areas that are the intersections of exactly three half-spaces are counted thrice, etc. We note, however, that only parts of  $\Omega_3^{(2)} \cap \Omega_4^{(2)}$  and  $\Omega_1^{(2)} \cap \Omega_4^{(2)}$  are counted twice. In this example, the area counted twice is

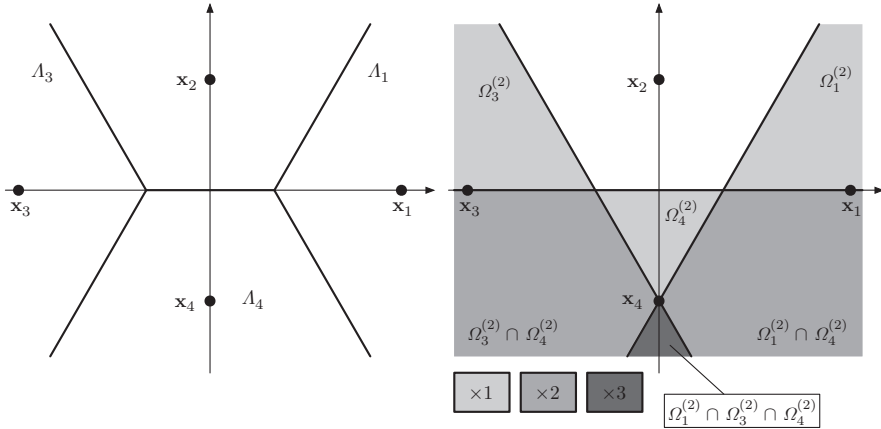


FIG. 4.19

An upper bound on  $\Pr\{\hat{m} \neq 2 \mid m = 2\}$  is found by adding integrals of the three half-spaces  $\Omega_1^{(2)}$ ,  $\Omega_3^{(2)}$ , and  $\Omega_4^{(2)}$ . Areas that are counted more than once are marked with a *darker gray*.

$$[(\Omega_3^{(2)} \cap \Omega_4^{(2)}) \cup (\Omega_1^{(2)} \cap \Omega_4^{(2)})] \setminus (\Omega_1^{(2)} \cap \Omega_3^{(2)} \cap \Omega_4^{(2)});$$

see Fig. 4.19. Clearly, the bound is tight if the areas that are counted multiple times are small and far from  $\mathbf{x}_2$ .

We can use Eq. (4.125) together with the fact that

$$\bigcup_{\ell \in \mathcal{M}_j} \Omega_\ell^{(j)} = \bigcup_{\ell \in \mathcal{N}_j} \Omega_\ell^{(j)} \quad (4.126)$$

to easily show that we can sharpen the bound in Eq. (4.124) by considering only the half-planes that belong to the nearest neighbors,

$$P_{e|j} \leq \sum_{\ell \in \mathcal{N}_j} \int_{\Omega_\ell^{(j)}} p_{\mathbf{V}}(\mathbf{u} - \mathbf{x}_j) d\mathbf{u}. \quad (4.127)$$

$$\leq \sum_{\ell \in \mathcal{M}_j} \int_{\Omega_\ell^{(j)}} p_{\mathbf{V}}(\mathbf{u} - \mathbf{x}_j) d\mathbf{u}. \quad (4.128)$$

We are now ready to form upper bounds on the error probability for the ML detector,

$$P_e = \sum_{j=1}^M p_m[j] \sum_{\ell \in \mathcal{M}_j} \Pr\{\hat{m} = \ell \mid m = j\} \quad (4.129)$$

$$\leq P_{\text{UB},1}^{\text{ML}} \triangleq \sum_{j=1}^M p_m[j] \sum_{\ell \in \mathcal{N}_j} \mathcal{Q}\left(\sqrt{d_{j,\ell}^2/2N_0}\right). \quad (4.130)$$

It is clear that we need to know the distances between all signal alternatives and the nearest neighbor set for all signal alternatives to compute the bound. For very large constellations, these quantities might be unknown or the mere number of calculations needed to compute Eq. (4.130) might be prohibitive. Luckily, we can often use symmetries in the constellation to reduce the number of calculations. For instance, it is clear that all signal alternatives with decision regions of the same shape and size (or more precisely, congruent decision regions) will have the same conditional error probability. For example, we see in Fig. 4.19 that  $\Lambda_1$  and  $\Lambda_3$ , as well as  $\Lambda_2$  and  $\Lambda_4$ , are congruent, and we only need to compute the inner sum in Eq. (4.130) for  $j = 1$  and  $j = 2$ . The computational gain is marginal in this example, but it is more significant for larger symmetrical constellations. For instance, for phase-shift keying (PSK) or orthogonal constellations, all decision regions are congruent, and it is enough to calculate the inner sum in Eq. (4.130) only once.<sup>6</sup>

<sup>6</sup>In fact, for any constellation which results from concatenating a linear binary error-correcting code and binary modulation, the same result applies: the inner sum in Eq. (4.130) is the same for all  $j \in \mathcal{M}$ .

We can also simplify the bound and reduce the number of calculations by bounding the  $Q$ -function terms. To this end, let us define the quantities

$$d_{\min,j} \triangleq \min\{d(\mathbf{x}_j, \mathbf{x}_\ell) : \ell \in \mathcal{M}_j\} \quad (4.131)$$

$$d_{\min} \triangleq \min\{d(\mathbf{x}_j, \mathbf{x}_\ell) : j, \ell \in \mathcal{M}, j \neq \ell\}. \quad (4.132)$$

That is,  $d_{\min,j}$  is the smallest distance from  $\mathbf{x}_j$  to some other signal vector, while  $d_{\min}$  is the smallest distance between any two distinct signal vectors. Since the  $Q(x)$  is a decreasing function for  $x \geq 0$ , we have that

$$Q\left(\sqrt{d_{j,\ell}^2/2N_0}\right) \leq Q\left(\sqrt{d_{\min,j}^2/2N_0}\right), \quad \ell \in \mathcal{M}_j \quad (4.133)$$

$$\leq Q\left(\sqrt{d_{\min}^2/2N_0}\right). \quad (4.134)$$

Hence, we can bound  $P_{\text{UB},1}^{\text{ML}}$  as

$$P_{\text{UB},1}^{\text{ML}} = \sum_{j=1}^M p_m[j] \sum_{\ell \in \mathcal{N}_j} Q\left(\sqrt{d_{j,\ell}^2/2N_0}\right) \quad (4.135)$$

$$\leq P_{\text{UB},2}^{\text{ML}} \triangleq \sum_{j=1}^M p_m[j] |\mathcal{N}_j| Q\left(\sqrt{d_{\min,j}^2/2N_0}\right) \quad (4.136)$$

$$\leq P_{\text{UB},3}^{\text{ML}} \triangleq Q\left(\sqrt{d_{\min}^2/2N_0}\right) \sum_{j=1}^M p_m[j] |\mathcal{N}_j| \quad (4.137)$$

$$\leq P_{\text{UB},4}^{\text{ML}} \triangleq (M-1)Q\left(\sqrt{d_{\min}^2/2N_0}\right), \quad (4.138)$$

where  $|\mathcal{N}_j|$  is the number of elements in the set  $\mathcal{N}_j$  and Eq. (4.138) follows since  $|\mathcal{N}_j| \leq |\mathcal{M}_j| = M-1$ .

Clearly, the bounds  $P_{\text{UB},1}^{\text{ML}}$ ,  $P_{\text{UB},2}^{\text{ML}}$ ,  $P_{\text{UB},3}^{\text{ML}}$ , and  $P_{\text{UB},4}^{\text{ML}}$  are increasingly looser but also increasingly simpler to compute. Interestingly enough, all bounds are tight for asymptotically high signal-to-noise ratio (SNR) (ie, for asymptotically small  $N_0$ ). The asymptotic convergence of the bounds follows since  $Q(x) \leq e^{-x^2/2}$  for  $x > 0$ , which implies that the dominating term in Eq. (4.135) is  $CQ\left(\sqrt{d_{\min}^2/2N_0}\right)$  for some constant  $C > 0$  as  $N_0 \rightarrow 0$ . Hence, all bounds converge to Eq. (4.138).

We will now turn our attention to the MAP detector. Since the error probability for the MAP detector is less or equal to the ML detector error probability, the ML union bounds are valid also for the ML detector. It is, however, not hard to formulate bounds that might be sharper.

For the MAP detector,  $\Lambda_\ell = \bigcap_{i \in \mathcal{M}_\ell} \Psi_\ell^{(i)} \subset \Psi_\ell^{(j)}$  if  $j \in \mathcal{M}_\ell$  and where the half-spaces  $\Psi_\ell^{(j)}$  are defined in Eq. (4.103). Hence, we can write

$$\Pr\{\hat{m} = \ell \mid m = j\} \leq \int_{\Psi_\ell^{(j)}} p_{\mathbf{V}}(\mathbf{u} - \mathbf{x}_j) d\mathbf{u} \quad (4.139)$$

$$= Q\left(r_{j,\ell}\sqrt{2/N_0}\right), \quad \ell \in \mathcal{M}_j, \quad (4.140)$$

where  $r_{j,\ell}$  is defined in Eq. (4.106). Hence,  $|r_{j,\ell}|$  is the distance from  $\mathbf{x}_j$  to the boundary of the half-space  $\Psi_\ell^{(j)}$ ; see Fig. 4.16 (where we recall that  $\Psi_\ell^{(j)}$  and  $\Psi_j^{(\ell)}$  have the same boundary). By following the same procedure as for the ML detector, it is easy to prove the following sequence of bounds:

$$P_e = \sum_{j=1}^M p_m[j] \sum_{\ell \in \mathcal{M}_j} \Pr\{\hat{m} = \ell \mid m = j\} \quad (4.141)$$

$$\leq P_{\text{UB},1}^{\text{MAP}} \triangleq \sum_{j=1}^M p_m[j] \sum_{\ell \in \mathcal{N}_j} Q\left(r_{j,\ell}\sqrt{2/N_0}\right) \quad (4.142)$$

$$\leq P_{\text{UB},2}^{\text{MAP}} \triangleq \sum_{j=1}^M p_m[j] |\mathcal{N}_j| Q\left(r_{\min,j}\sqrt{2/N_0}\right) \quad (4.143)$$

$$\leq P_{\text{UB},3}^{\text{MAP}} \triangleq Q\left(r_{\min}\sqrt{2/N_0}\right) \sum_{j=1}^M p_m[j] |\mathcal{N}_j| \quad (4.144)$$

$$\leq P_{\text{UB},4}^{\text{MAP}} \triangleq (M-1)Q\left(r_{\min}\sqrt{2/N_0}\right), \quad (4.145)$$

where

$$r_{\min,j} \triangleq \min\{r_{j,\ell} : \ell \in \mathcal{M}_j\} \quad (4.146)$$

$$r_{\min} \triangleq \min\{r_{j,\ell} : j, \ell \in \mathcal{M}, j \neq \ell\}. \quad (4.147)$$

Now, in general,  $r_{\min} \leq d_{\min}/2$ , and we have that  $P_{\text{UB},4}^{\text{ML}} \leq P_{\text{UB},4}^{\text{MAP}}$ . Hence, the bound  $P_{\text{UB},4}^{\text{MAP}}$  is of very little interest, since it is never tighter than  $P_{\text{UB},4}^{\text{ML}}$ , which is also a bound on the MAP error probability. Moreover, we recall that  $r_{j,\ell}$  is a function of  $N_0$ , which makes the MAP-specific bounds slightly more complicated to compute and less convenient for analysis.

## 4.9 BIT ERROR PROBABILITY AND CONSTELLATION LABELINGS

To this point, we have been concerned with the message error probability. However, in some applications, we are more interested in the bit error probability.

To characterize the bit error probability and its connection to the message error probability, we introduce the concept of constellation labelings.

A binary labeling  $\lambda$  of order  $K$  is defined as a sequence of  $M = 2^K$  distinct vectors (called labels or codewords),  $\lambda = (\mathbf{b}_1, \mathbf{b}_2, \dots, \mathbf{b}_M)$ , where each  $\mathbf{b}_i \in \{0, 1\}^K$ . The bit-to-signal-point mapping is defined by the labeling in the natural way: the bits in the  $\ell$ th label  $\mathbf{b}_\ell$  is mapped onto the  $\ell$ th signal point  $\mathbf{x}_\ell$ . The transmitted label is therefore  $\mathbf{b}_m = [b_1 \ b_2 \ \dots \ b_K]$ , where we think of  $m$  and  $b_1, b_2, \dots, b_K$  as random variables.

The labeling indirectly determines  $p_m[\ell]$ . Indeed, given the a priori distribution for the bit patterns,

$$p_{\mathbf{b}}[\mathbf{c}] \triangleq \Pr\{b_1 = c_1, b_2 = c_2, \dots, b_K = c_K\}, \text{ and} \quad (4.148)$$

where  $\mathbf{c} = [c_1 \ c_2 \ \dots \ c_K] \in \{0, 1\}^K$ , we have that

$$p_m[\ell] = p_{\mathbf{b}}[\mathbf{b}_\ell], \quad (4.149)$$

where  $\mathbf{b}_\ell$  is the  $\ell$ th label in  $\lambda$ . In essence, the a priori probabilities for bit patterns are permuted to form  $p_m[\ell]$ , where the permutation is determined by  $\lambda$ .

**Example 4.15.** The labeling  $\lambda = (\mathbf{b}_1, \mathbf{b}_2, \mathbf{b}_3, \mathbf{b}_4) = ([00], [01], [10], [11])$  is depicted in Fig. 4.20. If the bit pattern a priori distribution is

$$p_{\mathbf{b}}[[00]] = 2/8, \quad p_{\mathbf{b}}[[01]] = 1/8, \quad p_{\mathbf{b}}[[10]] = 2/8, \quad p_{\mathbf{b}}[[11]] = 3/8,$$

the labeling implies that the message a priori distribution is

$$p_m[1] = 2/8, \quad p_m[2] = 1/8, \quad p_m[3] = 2/8, \quad p_m[4] = 3/8,$$

since  $\mathbf{b} = [00] = \mathbf{b}_1 \Leftrightarrow m = 1$ ,  $\mathbf{b} = [01] = \mathbf{b}_2 \Leftrightarrow m = 2$ , etc.

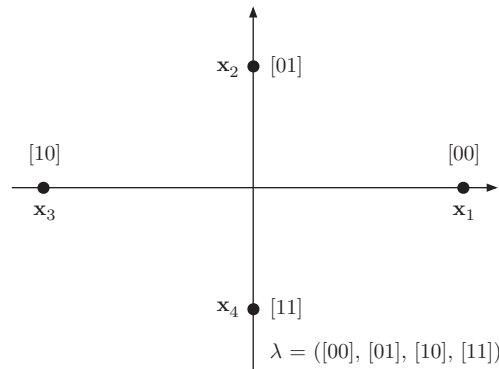


**FIG. 4.20**

Example constellation mapping.

Now suppose the decision on the  $k$ th bit is denoted  $\hat{b}_k$ , then the bit error probability for the  $k$ th bit position in the label is

$$P_{b,k} \triangleq \Pr\{\hat{b}_k \neq b_k\}. \quad (4.150)$$

In general,  $P_{b,k}$  take on different values for different  $k$ .

The (average) bit error probability is defined as the average over the bits in the label:

$$P_b = \frac{1}{K} \sum_{k=1}^K \Pr\{\hat{b}_k \neq b_k\}. \quad (4.151)$$

There are two main ways to find  $\hat{b}_k$  for  $k = 1, 2, \dots, K$  from  $\mathbf{y}$ . The first method is to first compute a decision on the transmitted vector index,  $\hat{m}$ , and then find  $\hat{b}_k$  for  $k = 1, 2, \dots, K$  as the bits in the label  $\mathbf{b}_{\hat{m}}$ . The second method is to directly compute  $\hat{b}_k$  from  $\mathbf{y}$ . We will defer the discussion on bitwise decoding to [Section 4.10](#), and focus on the first method here. Conditioned on  $m = j$ , the transmitted label is  $\mathbf{b}_j$ , and the number of bit errors associated with the decision  $\mathbf{b}_\ell$  is  $d_H(\mathbf{b}_\ell, \mathbf{b}_j)$ , where  $d_H(\mathbf{x}, \mathbf{y})$  is the Hamming distance between  $\mathbf{x}$  and  $\mathbf{y}$ , that is, the number of positions in which the vectors  $\mathbf{x}$  and  $\mathbf{y}$  differ. Hence, the average number of erroneous bits that occur, conditioned on  $m = j$ , is

$$\sum_{\ell \in \mathcal{M}_j} d_H(\mathbf{b}_\ell, \mathbf{b}_j) \Pr\{\hat{m} = \ell \mid m = j\}. \quad (4.152)$$

Since a transmission carries  $K$  bits, the average error probability conditioned on  $m = j$  is

$$P_{b|j} = \frac{1}{K} \sum_{\ell \in \mathcal{M}_j} d_H(\mathbf{b}_\ell, \mathbf{b}_j) \Pr\{\hat{m} = \ell \mid m = j\}, \quad (4.153)$$

and we find the bit error probability by averaging over the a priori distribution,

$$P_b = \sum_{j \in \mathcal{M}} \left( \frac{1}{K} \sum_{\ell \in \mathcal{M}_j} d_H(\mathbf{b}_\ell, \mathbf{b}_j) \Pr\{\hat{m} = \ell \mid m = j\} \right) p_m[j] \quad (4.154)$$

$$= \frac{1}{K} \sum_{j \in \mathcal{M}} p_m[j] \sum_{\ell \in \mathcal{M}_j} d_H(\mathbf{b}_\ell, \mathbf{b}_j) \Pr\{\hat{m} = \ell \mid m = j\}. \quad (4.155)$$

From this equation, we see that the constellation labeling is important for the bit error probability as it determines  $d_H(\mathbf{b}_\ell, \mathbf{b}_j)$  and  $p_m[\ell]$ . In general, there is no labeling that is universally optimum in the bit error probability sense. However, for higher SNRs, the dominant error event is to the closest neighbors and it makes sense to assign similar labels to neighbors, as this will tend to make  $d_H(\mathbf{b}_\ell, \mathbf{b}_j)$  small for  $\ell \in \mathcal{N}_j$ . Indeed, for the special case of PAM, or rectangular quadrature amplitude modulation

constellations, equally likely and independent bits, and ML message decoding, it can be shown that the labeling that has the smallest bit error probability for high SNR is the binary reflected Gray code [9]. Using a Gray labeling for these constellations ensures that labels for closest neighbors differ in only one bit position.

We recall from Section 4.8, that for the ML message decoder,  $\Pr\{\hat{m} = \ell \mid m = j\}$  for  $\ell \in \mathcal{M}_j$  is upper bounded by the pairwise error probability  $P_{j \rightarrow \ell}$ . Hence, we can form an upper bound on the bit error probability as

$$P_b = \frac{1}{K} \sum_{j \in \mathcal{M}} p_m[j] \sum_{\ell \in \mathcal{M}_j} d_H(\mathbf{b}_\ell, \mathbf{b}_j) \Pr\{\hat{m} = \ell \mid m = j\} \quad (4.156)$$

$$\leq \frac{1}{K} \sum_{j \in \mathcal{M}} p_m[j] \sum_{\ell \in \mathcal{M}_j} d_H(\mathbf{b}_\ell, \mathbf{b}_j) P_{j \rightarrow \ell} \quad (4.157)$$

$$= \frac{1}{K} \sum_{j \in \mathcal{M}} p_m[j] \sum_{\ell \in \mathcal{M}_j} d_H(\mathbf{b}_\ell, \mathbf{b}_j) Q\left(\sqrt{d_{j,\ell}^2/2N_0}\right), \quad (4.158)$$

where  $d_{j,\ell} = \|\mathbf{x}_\ell - \mathbf{x}_j\|$ . The expression for the MAP message decoder is similar:

$$P_b \leq \frac{1}{K} \sum_{j \in \mathcal{M}} p_m[j] \sum_{\ell \in \mathcal{M}_j} d_H(\mathbf{b}_\ell, \mathbf{b}_j) Q\left(r_{j,\ell} \sqrt{2/N_0}\right), \quad (4.159)$$

where  $r_{j,\ell}$  is defined in Eq. (4.106).

In general, we can relate the message and bit error probabilities by bounding  $d_H(\mathbf{b}_\ell, \mathbf{b}_j)$ . For instance, inserting the bound  $d_H(\mathbf{b}_\ell, \mathbf{b}_j) \geq 1$  for  $\ell \neq j$  in Eq. (4.155) yields the bound

$$P_b \geq \frac{1}{K} \sum_{j \in \mathcal{M}} p_m[j] \sum_{\ell \in \mathcal{M}_j} \Pr\{\hat{m} = \ell \mid m = j\} \quad (4.160)$$

$$\geq \frac{1}{K} \sum_{j \in \mathcal{M}} p_m[j] P_{e|j} = \frac{1}{K} P_e, \quad (4.161)$$

where  $P_{e|j}$  is the message error probability conditioned on  $m = j$  and  $P_e$  is the message error probability. Similarly, using the bound  $d_H(\mathbf{b}_\ell, \mathbf{b}_j) \leq K$  in Eq. (4.155) yields

$$P_b \leq \frac{1}{K} \sum_{j \in \mathcal{M}} p_m[j] \sum_{\ell \in \mathcal{M}_j} K \Pr\{\hat{m} = \ell \mid m = j\} = P_e. \quad (4.162)$$

Hence, we have that  $P_e/K \leq P_b \leq P_e$ , which holds in general for any channel, constellation labeling, and message detector.

## 4.10 OPTIMUM BITWISE RECEIVERS

In general, the message decoding-demapping method does not minimize the bit error probability, even if the message decoding is done using a MAP decoder (which minimizes the message error probability). Indeed, the optimum decoder for the  $k$ th bit is the bitwise MAP decoder, defined as

$$\hat{b}_{k,\text{MAP}} = \arg \max_{c \in \{0,1\}} p_{b_k|\mathbf{Y}}[c | \mathbf{y}], \quad (4.163)$$

where  $p_{b_k|\mathbf{Y}}[c | \mathbf{y}]$  is the a posteriori distribution of  $b_k$ , that is, the distribution of the  $k$ th bit  $b_k$  given the observation  $\mathbf{Y} = \mathbf{y}$ ,

$$p_{b_k|\mathbf{Y}}[c | \mathbf{y}] \triangleq \Pr\{b_k = c | \mathbf{Y} = \mathbf{y}\}. \quad (4.164)$$

Proving optimality for the MAP detector for  $b_k$  follows the same pattern as for the MAP detector for  $m$ . In short, given the observation  $\mathbf{Y} = \mathbf{y}$ , our task is to choose  $\hat{b}_k = 0$  or  $\hat{b}_k = 1$ . If we choose  $\hat{b}_k = 0$ , the probability of a correct decision is  $\Pr\{b_k = 0 | \mathbf{Y} = \mathbf{y}\}$ , and if we choose  $\hat{b}_k = 1$ , the probability of a correct decision is  $\Pr\{b_k = 1 | \mathbf{Y} = \mathbf{y}\}$ . Obviously, we should select  $\hat{b}_k$  to maximize the probability of a correct decision, and this is precisely what the MAP rule in Eq. (4.163) specifies.

We can express  $p_{b_k|\mathbf{Y}}[c | \mathbf{y}]$  in terms of the a posteriori distribution for  $m$ . To this end, we define the sets

$$\mathcal{M}(c, k) \triangleq \{\ell \in \mathcal{M} : [\mathbf{b}_\ell]_k = c\}, \quad c \in \{0, 1\}, k \in \{1, 2, \dots, K\}, \quad (4.165)$$

where  $[\mathbf{b}_\ell]_k$  denotes the  $k$ th bit in the label  $\mathbf{b}_\ell$ . Hence, the labels  $\mathbf{b}_\ell$  for which  $\ell \in \mathcal{M}(c, k)$  are the labels that have bit  $c$  in the  $k$ th position.

**Example 4.16.** For the labeling  $\lambda = (\mathbf{b}_1, \mathbf{b}_2, \mathbf{b}_3, \mathbf{b}_4) = ([00], [01], [10], [11])$ , we have

$$\mathcal{M}(0, 1) = \{1, 2\}; \quad \mathcal{M}(1, 1) = \{3, 4\}; \quad \mathcal{M}(0, 2) = \{1, 3\}; \quad \mathcal{M}(1, 2) = \{2, 4\}.$$

Now, since the probability that  $b_k = c$  is equal to the probability that  $m \in \mathcal{M}(c, k)$ ,

$$p_{b_k|\mathbf{Y}}[c | \mathbf{y}] = \sum_{\ell \in \mathcal{M}(c, k)} p_{m|\mathbf{Y}}[\ell | \mathbf{y}] \quad (4.166)$$

$$= \sum_{\ell \in \mathcal{M}(c, k)} \frac{p_{\mathbf{Y}|m}(\mathbf{y} | \ell) p_m[\ell]}{p_{\mathbf{Y}}(\mathbf{y})}, \quad (4.167)$$

and we can write the bitwise MAP detector as

$$\hat{b}_{k,\text{MAP}} = \arg \max_{c \in \{0,1\}} \sum_{\ell \in \mathcal{M}(c, k)} \frac{p_{\mathbf{Y}|m}(\mathbf{y} | \ell) p_m[\ell]}{p_{\mathbf{Y}}(\mathbf{y})} \quad (4.168)$$

$$= \arg \max_{c \in \{0,1\}} \sum_{\ell \in \mathcal{M}(c, k)} p_{\mathbf{Y}|m}(\mathbf{y} | \ell) p_m[\ell] \quad (4.169)$$

$$= \arg \max_{c \in \{0,1\}} \sum_{\ell \in \mathcal{M}(c,k)} p_{\mathbf{V}}(\mathbf{y} - \mathbf{x}_{\ell}) p_m[\ell] \quad (4.170)$$

$$= \arg \max_{c \in \{0,1\}} \sum_{\ell \in \mathcal{M}(c,k)} \exp\left(-\frac{1}{N_0} \|\mathbf{y} - \mathbf{x}_{\ell}\|^2\right) p_m[\ell]. \quad (4.171)$$

We note that the bitwise MAP detector is more complicated to compute than the messagewise MAP detector, since the objective function is a sum of exponentials. Moreover, we see that the decision regions for the bitwise MAP detector are, in general, not convex polytopes.

**Example 4.17.** The bitwise MAP decoder decision regions for the bits  $b_1$  and  $b_2$  for our example constellation,  $\lambda = (\mathbf{b}_1, \mathbf{b}_2, \mathbf{b}_3, \mathbf{b}_4) = [00], [01], [10], [11]$ , and  $N_0 = 6$ , are plotted in Fig. 4.21. We note that the decision region boundaries are not straight lines. Hence, the decision regions are not found as the intersection of a number of half-planes, in contrast to the message MAP and ML decoders; see Figs. 4.15 and 4.17.

The bitwise MAP decisions  $\hat{b}_{1,\text{MAP}}$  and  $\hat{b}_{2,\text{MAP}}$  imply a decision on the message  $\hat{m}$ , where  $\mathbf{b}_{\hat{m}} = [\hat{b}_{1,\text{MAP}} \ \hat{b}_{2,\text{MAP}}]$ . This message decoder is, in general, different from the message MAP decoder, as we see in Fig. 4.22. This illustrates the fact that optimum (in the minimum error probability sense) decoders are, in general, different depending on whether we want to minimize bit error probability or message error probability.

Just as the messagewise MAP detector specializes to the messagewise ML detector for equally likely transmitted messages, that is,  $p_m[\ell] = 1/M$ , the bitwise MAP detector specializes to the bitwise ML detector for equally likely and independent transmitted bits. That is, when

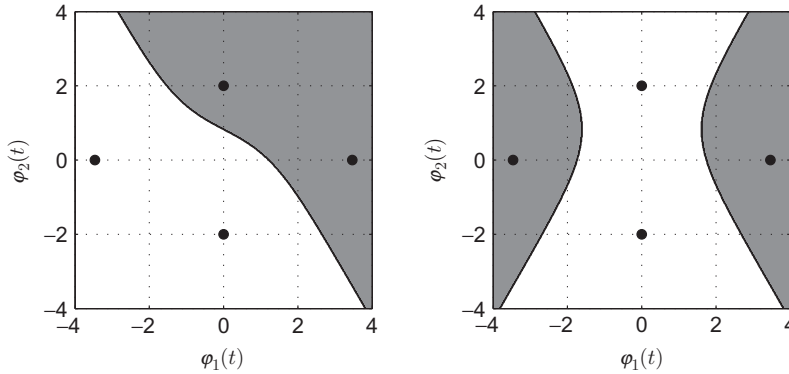


FIG. 4.21

Bitwise MAP decision regions for  $b_1$  (left) and  $b_2$  (right), where the region for  $b_k = 0$  is in gray.

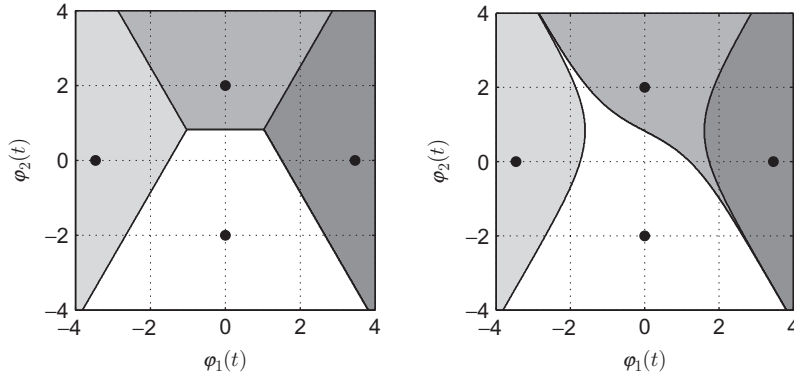


FIG. 4.22

Decision regions for the message MAP decoder (*left*) and the message decoder implied by the bitwise MAP decoder (*right*).

$$\Pr\{\mathbf{b} = \mathbf{u}\} = \prod_{k=1}^K \Pr\{b_k = u_k\} = \left(\frac{1}{2}\right)^K = \frac{1}{M}, \quad (4.172)$$

then

$$p_m[\ell] = \Pr\{m = \ell\} = \Pr\{\mathbf{b} = \mathbf{b}_\ell\} = \frac{1}{M} \quad (4.173)$$

and

$$\hat{b}_{k,\text{MAP}} = \arg \max_{c \in \{0,1\}} \sum_{\ell \in \mathcal{M}(c,k)} \exp\left(-\frac{1}{N_0} \|\mathbf{y} - \mathbf{x}_\ell\|\right) p_m[\ell] \quad (4.174)$$

$$= \arg \max_{c \in \{0,1\}} \sum_{\ell \in \mathcal{M}(c,k)} \exp\left(-\frac{1}{N_0} \|\mathbf{y} - \mathbf{x}_\ell\|^2\right) \quad (4.175)$$

$$= \hat{b}_{k,\text{ML}}. \quad (4.176)$$

We note that, in contrast to the ML detector for  $m$ , the bitwise ML detector, in general, requires knowledge of  $N_0$  and the decision regions are not convex polytopes.

**Example 4.18.** The bitwise ML decision regions for the same conditions as in Example 4.17 are shown in Fig. 4.23. We see that the ML decision regions are symmetric with respect to the  $\varphi_1(t)$  and  $\varphi_2(t)$  axis, as opposed to the MAP regions in Fig. 4.21. Although not shown here, the symmetry with respect to the signal space axes also holds for the message decoder that is implied by the bitwise ML decoder.

It can be shown that for high SNRs, or more precisely, as  $N_0 \rightarrow 0$ , the bitwise MAP and ML detectors converge to the same bitwise detector and the implied

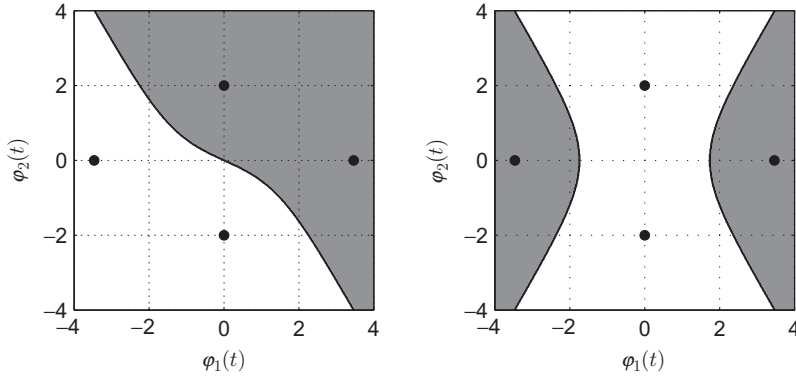


FIG. 4.23

Bitwise ML decision regions for  $b_1$  (left) and  $b_2$  (right), where the region for  $b_k = 0$  is in gray.

message detector converges to the ML message detector. Hence, the choice of detector (MAP or ML, bitwise and messagewise) is not important for high SNRs.

## 4.11 MATCHED FILTER

We will conclude this chapter with a discussion about matched filters.

As discussed in Section 4.3, the receiver front-end projects the received signal onto the basis functions  $\varphi_n(t)$  for  $n = 1, 2, \dots, N$  to form the elements of the received vector. The  $n$ th element of  $\mathbf{y}$  can be computed as

$$y_n = \langle y(t), \varphi_n(t) \rangle = \int_{-\infty}^{\infty} y(u) \varphi_n^*(u) du. \quad (4.177)$$

The above integral is sometimes called the correlation integral, as the result is the correlation between the signals  $y(t)$  and  $\varphi_n(t)$ . We can also compute  $y_n$  by feeding  $y(t)$  to a filter and sample the output at time  $t = T_0$ . In fact, we will prove that we can compute inner products of the form

$$\langle y(t), g(t) \rangle = \int_{-\infty}^{\infty} y(u) g^*(u) du \quad (4.178)$$

for a general  $g(t)$  with finite, but not necessarily unit, energy, as

$$\langle y(t), g(t) \rangle = y(t) * h(t)|_{t=T_0}, \quad (4.179)$$

for a suitable choice of the impulse response  $h(t)$ .

To show this, we simply manipulate the convolution integral into a form that allows us to specify the impulse response:

$$y(t) * h(t)|_{t=T_0} = \int_{-\infty}^{\infty} y(u)h(t-u) du \Big|_{t=T_0} \quad (4.180)$$

$$= \int_{-\infty}^{\infty} y(u)h(T_0-u) du. \quad (4.181)$$

Hence, the right-hand side is equal to  $\langle y(t), g(t) \rangle$  if  $h(T_0-u) = g^*(u)$ , that is, when  $h(t) = g^*(T_0-t)$ .

In general, we define the matched filter to a finite-energy pulse  $g(t)$  with respect to the sampling time  $t = T_0$  as a filter with impulse response  $h(t) = g^*(T_0-t)$ . We see that  $h(t)$  is a conjugated, time-reversed version of  $g(t)$  delayed with  $T_0$ . In practice, we can select  $T_0$  such that  $h(t)$  is causal, which is required for a real-time implementation. However, for theoretical studies, the value of  $T_0$  is not very important and is often set to zero.

If the input to filter matched to  $g(t)$  is  $g(t)$  itself, then the output is

$$g(t) * h(t) = \int_{-\infty}^{\infty} h(u)g(t-u) du \quad (4.182)$$

$$= \int_{-\infty}^{\infty} g^*(T_0-u)g(t-u) du \quad (4.183)$$

$$= \int_{-\infty}^{\infty} g^*(v)g(v+t-T_0) dv \quad (4.184)$$

$$= R_{gg}(t-T_0), \quad (4.185)$$

where  $R_{gg}(\tau)$  is the autocorrelation function for  $g(t)$ , defined as<sup>7</sup>

$$R_{gg}(\tau) = \int_{-\infty}^{\infty} g^*(v)g(v+\tau) dv. \quad (4.186)$$

If  $g(t)$  is real-valued, then  $R_{gg}(\tau)$  is an even function that is maximized for  $\tau = 0$ . (If  $g(t)$  is complex-valued, then  $|R_{gg}(\tau)|$  is even and maximized at  $\tau = 0$ .) This property can be used for synchronization purposes. For example, suppose  $g(t)$  is a real-valued, time-limited pulse such that  $g(t) = 0$  for  $t < 0$  and  $t \geq T$ . Furthermore, if  $g(t)$  is transmitted over a noiseless channel with delay  $\tau$ , the received signal is  $g(t-\tau)$ . To the receiver, the value of  $\tau$  is unknown, but it can be recovered by monitoring the output of a matched filter. Suppose the matched filter impulse response is  $h(t) = g^*(t-T)$ , then the matched filter output is  $R_{gg}(t-\tau-T)$  and will peak at time  $t = \tau + T$ . Since  $T$  is known by the receiver, the receiver can easily recover  $\tau$ . In practice, channel noise will perturb the peak location, which results in a synchronization error. It can, however, be shown that we can make

<sup>7</sup>This should not be confused with the autocorrelation function of a wide-sense stationary process  $X(t)$ , which is defined as  $\mathbb{E}[X^*(t)X(t+\tau)]$ .

the synchronization error small by increasing the transmit power (which improves SNR) or by increasing the bandwidth of  $g(t)$ . Increasing the bandwidth will make the correlation peak more narrow, which intuitively improves noise robustness.

Another property of the matched filter is that it maximizes the SNR in the following setup. Suppose the received signal is  $Y(t) = g(t) + V(t)$  where  $g(t)$  is a deterministic real-valued signal with finite energy and  $V(t)$  is white real-valued Gaussian noise. Furthermore, suppose we form  $Y'$  as the sample at time  $t = 0$  of the output of a filter with impulse response  $h(t)$  and input  $Y(t)$ , that is,

$$Y' = \int_{-\infty}^{\infty} Y(u)h(t-u) du \Big|_{t=0} \quad (4.187)$$

$$= \int_{-\infty}^{\infty} [g(u) + V(u)]h(-u) du \quad (4.188)$$

$$= \langle g(t), h(-t) \rangle + \langle Y(t), h(-t) \rangle, \quad (4.189)$$

where the first term is the signal term and the second term is the noise term. We define the SNR in  $Y'$  as

$$\text{SNR} = \frac{\mathbb{E}[\langle g(t), h(-t) \rangle^2]}{\mathbb{E}[\langle Y(t), h(-t) \rangle^2]}. \quad (4.190)$$

Now, since  $Y(t)$  is a white Gaussian process with autocorrelation  $R_V(\tau) = \mathbb{E}[V(t)V(t+\tau)] = (N_0/2)\delta(\tau)$ , we have that the denominator in Eq. (4.190) is a zero-mean Gaussian random variable with the following variance:

$$\mathbb{E}[\langle Y(t), h(-t) \rangle^2] = \mathbb{E} \left[ \int_{-\infty}^{\infty} Y(u)h(-u) du \int_{-\infty}^{\infty} Y(v)h(-v) dv \right] \quad (4.191)$$

$$= \int_{-\infty}^{\infty} \int_{-\infty}^{\infty} \mathbb{E}[Y(u)Y(v)]h(-u)h(-v) dudv \quad (4.192)$$

$$= \frac{N_0}{2} \int_{-\infty}^{\infty} h(-u)h(-u) du \quad (4.193)$$

$$= \frac{N_0}{2} \|h(-t)\|^2. \quad (4.194)$$

Hence,

$$\text{SNR} = \frac{2}{N_0} \frac{\langle g(t), h(-t) \rangle^2}{\|h(-t)\|^2} \quad (4.195)$$

$$\leq \frac{2}{N_0} \frac{\|g(t)\|^2 \|h(-t)\|^2}{\|h(-t)\|^2} \quad (4.196)$$

$$= \frac{2\|g(t)\|^2}{N_0}, \quad (4.197)$$

where Eq. (4.196) follows from the Cauchy-Schwarz inequality [10], which holds with equality if and only if  $h(-t) = \alpha g(t)$  for some nonzero scalar  $\alpha$ , say  $\alpha = 1$ .

Hence, we see that the SNR is maximized by choosing  $h(t) = g(-t)$ , that is, as the filter which is matched to  $g(t)$  with respect to the sampling time  $t = 0$ . We also note that the SNR is not dependent on  $\alpha$ , which makes intuitive sense as it seems unreasonable that we can affect the SNR by amplifying the noise and desired signal with the same factor.

## 4.12 SUMMARY

In this chapter, we have developed message and bit detectors for the AWGN channel, that is, when the received signal  $Y(t)$  is the sum of the transmitted signal  $x_m(t)$  and white Gaussian noise  $V(t)$ . It was shown in [Section 4.6](#) that the received vector  $\mathbf{Y}$  retains all information contained in the received signal  $Y(t)$  needed for detecting the transmitted information with minimum error probability. Hence, the developed detectors are all based on the observation  $\mathbf{Y} = \mathbf{y}$ .

The main vehicle for minimum error probability detection is the MAP rule, which for detection of the message  $m$  is

$$\hat{m}_{\text{MAP}} = \arg \max_{\ell \in \mathcal{M}} p_{m|\mathbf{Y}}[\ell | \mathbf{y}], \quad (4.198)$$

and for detection of the  $k$ th bit  $b_k$  is

$$\hat{b}_{k,\text{MAP}} = \arg \max_{c \in \{0,1\}} p_{b_k|\mathbf{Y}}[c | \mathbf{y}]. \quad (4.199)$$

These equations are quite general: given an observation  $\mathbf{Y} = \mathbf{y}$ , the MAP rules minimize the error probability. This is true even if transmission is over non-AWGN channels. However, for some channels,  $\mathbf{Y}$  might not capture all relevant information contained in  $Y(t)$ . Hence, even if the above MAP rules are optimal given the observation  $\mathbf{Y} = \mathbf{y}$ , they might not be optimal given the observation  $Y(t) = y(t)$ .

For the AWGN channel with noise parameter  $N_0$ , the MAP rules reduce to

$$\hat{m}_{\text{MAP}} = \arg \min_{\ell \in \mathcal{M}} \|\mathbf{y} - \mathbf{x}_\ell\|^2 - N_0 \ln p_m[\ell] \quad (4.200)$$

and

$$\hat{b}_{k,\text{MAP}} = \arg \max_{c \in \{0,1\}} \sum_{\ell \in \mathcal{M}(c,k)} \exp\left(-\frac{1}{N_0} \|\mathbf{y} - \mathbf{x}_\ell\|^2\right) p_m[\ell]. \quad (4.201)$$

Hence, computing the MAP decision requires knowledge of  $N_0$  and the a priori distribution  $p_m[\ell]$ . Moreover, the bitwise MAP detector depends on  $\mathcal{M}(c, k)$ , which in turn depends on the constellation labeling.

In case of equally probable messages, that is, when  $p_m[\ell] = 1/M$ , both MAP detectors reduce to the corresponding ML detectors

$$\hat{m}_{\text{ML}} = \arg \min_{\ell \in \mathcal{M}} \|\mathbf{y} - \mathbf{x}_\ell\|^2 \quad (4.202)$$

and

$$\hat{b}_{k,\text{MAP}} = \arg \max_{c \in \{0,1\}} \sum_{\ell \in \mathcal{M}(c,k)} \exp \left( -\frac{1}{N_0} \|\mathbf{y} - \mathbf{x}_\ell\| \right). \quad (4.203)$$

We note that the message ML detector does not need knowledge of  $N_0$  and is equivalent to the minimum distance detector. In contrast, the bitwise ML detector, is dependent on  $N_0$  and is not a minimum distance detector.

An alternative to the bitwise detectors is to first detect the message and then detect the bits by inverting the bit-to-message mapping. This procedure is, in general, suboptimal even if the message detector is the MAP detector (which minimizes the message error probability). However, as SNR increases, that is, when  $N_0 \rightarrow 0$ , the difference between all bit detectors becomes negligible.

Finally, we note that the minimum distance detector finds the signal alternative that is closest to the observed received signal. This is the same as finding the noise signal with the smallest energy that can explain the observation  $Y(t) = y(t) = x(t) + v(t)$ . Hence, the minimum distance receiver is reasonable for a wide range of noise signals, Gaussian as well as non-Gaussian, as long as the noise is more probable to have low energy than high energy.

## 4.13 PRACTICAL DETECTORS

In practice, the number of bits in a message is often large. For instance, a common size of an IP packet is  $K = 12,000$  bit (1500 byte). Hence, to find the ML decision by brute force search over all possible transmitted signals, as suggested by Eq. (4.202), would evaluate all  $M = 2^{12,000} \approx 10^{3612}$  signal alternatives! This can safely be assumed to be infeasible for practical implementation.

Luckily, we can design mappings between bits and signal alternatives in ways that allow for ML detection with much lower complexity. There are numerous approaches, but we will only mention two of them here.

The first and simplest example is uncoded transmission of  $K$  independent bits using binary modulation, for example, when

$$x_k = A(2b - 1) = \begin{cases} -A, & b_k = 0 \\ A, & b_k = 1 \end{cases}, \quad k = 1, 2, \dots, K \quad (4.204)$$

for some constant  $A$ . The vector channel in Fig. 4.9 then decomposes into  $K$  mutually independent scalar channels of the form  $y_k = x_k + v_k$ , and the  $k$ th bit can be decoded from only  $y_k$  without loss of performance. For instance, the ML decision on the  $k$ th bit is

$$\hat{b}_{k,\text{ML}} = \arg \min_{c \in \{0,1\}} \|y_k - A(2c - 1)\|^2 = \begin{cases} 0, & y_k \leq 0 \\ 1, & y_k > 0 \end{cases}. \quad (4.205)$$

The ML or MAP message decisions are simply composed by the ML or MAP bit decisions, respectively. The overall receiver complexity for decoding  $K$ -bit messages is therefore linear in  $K$ .

The second example is slightly more complicated, but also more practical. Suppose we use a rate  $1/n$ ,  $L$ -state, binary convolutional encoder and BPSK modulation to transmit  $K$  independent bits over an AWGN channel. A receiver consisting of a soft-output BPSK demodulator (essentially a matched filter) followed by a soft-input Viterbi decoder is able to perform exact ML decoding with a computational complexity  $\mathcal{O}(KL)$ , that is, complexity scales linearly with  $K$ , a dramatic reduction from the exponential dependency  $2^K$  suggested by the general ML-decoder expression.

The Viterbi algorithm can be used to reduce complexity in many different settings [11], such as during ML decoding of block codes, CPM and other modulation schemes with memory, and dealing with intersymbol interference.

Hence, the decoder expressions in this chapter should be viewed as starting points for developing practical algorithms, rather than as final implementation recipes.

---

#### 4.14 PROBABILITY OF RECEIVED VECTOR BELONGING TO A DECISION BOUNDARY

We recall from Sections 4.7.2 and 4.7.3 that the decision regions for the MD, ML, and MAP detectors are intersections of  $M - 1$  half-spaces. A half-space in an  $N$ -dimensional space is bounded by a  $(N - 1)$ -dimensional hyperplane. Let us denote such a bounding hyperplane with  $\Gamma$  and consider transmission over an AWGN channel with  $N_0 > 0$ . For  $N_0 > 0$ , the noise pdf is upper bounded by some finite constant  $C$ , that is,  $p_{\mathbf{V}}(\mathbf{u}) \leq C < \infty$ . The probability that  $\mathbf{Y}$  ends up on  $\Gamma$  conditioned on that  $\mathbf{x}_j$  was transmitted is therefore

$$\Pr\{\mathbf{Y} \in \Gamma \mid m = j\} = \int_{\Gamma} p_{\mathbf{V}}(\mathbf{u} - \mathbf{x}_j) d\mathbf{u} \quad (4.206)$$

$$\leq C \int_{\Gamma} d\mathbf{u} = 0, \quad (4.207)$$

where the last equality follows since the volume of  $\Gamma$  is zero,

$$\int_{\Gamma} d\mathbf{u} = 0. \quad (4.208)$$

Hence,  $\Pr\{\mathbf{Y} \in \Gamma \mid m = j\} = 0$ .

Now, the  $\ell$ th decision region,  $\Lambda_{\ell}$ , is bounded by at most  $M - 1$  truncated hyperplanes, and it follows that the probability for  $\mathbf{Y}$  to be on the boundary of  $\Lambda_{\ell}$  is zero. We can therefore add or subtract the boundary to integration regions when integrating  $p_{\mathbf{V}}(\mathbf{u})$  without changing the value of the integral. In particular, we can write

$$\Pr\{\hat{m} = \ell \mid m = j\} = \Pr\{\mathbf{Y} \in \Lambda_\ell \mid m = j\} \quad (4.209)$$

$$= \int_{\Lambda_\ell} p_{\mathbf{V}}(\mathbf{u} - \mathbf{x}_j) d\mathbf{u} \quad (4.210)$$

$$= \begin{cases} \int_{\Omega_\ell} p_{\mathbf{V}}(\mathbf{u} - \mathbf{x}_j) d\mathbf{u}, & \text{for ML} \\ \int_{\Psi_\ell} p_{\mathbf{V}}(\mathbf{u} - \mathbf{x}_j) d\mathbf{u}, & \text{for MAP} \end{cases}, \quad (4.211)$$

where  $\Omega_\ell$  is the Voronoi region defined in Eq. (4.98) and  $\Psi_\ell$  is defined in Eq. (4.103). Hence, for the purpose of probability calculations, we can regard  $\Omega_\ell$  and  $\Psi_\ell$  as the  $\ell$ th decision region for the ML and MAP detectors, respectively.

---

## REFERENCES

- [1] E.A. Lee, D.G. Messerschmitt, *Digital Communication*, third ed., Springer, 2003.
- [2] J.M. Wozencraft, I.M. Jacobs, *Principles of Communication Engineering*, Wiley, 1965.
- [3] S.M. Kay, *Fundamentals of Statistical Processing, Volume I: Estimation Theory*, Prentice Hall, Upper Saddle River, NJ, 1993.
- [4] S.M. Kay, *Fundamentals of Statistical Signal Processing: Volume II: Detection Theory*, Prentice Hall, Upper Saddle River, NJ, 1998.
- [5] H.V. Poor, *An Introduction to Signal Detection and Estimation*, second ed., Springer, 1998.
- [6] A. Lapidoth, *A Foundation in Digital Communication*, Cambridge University Press, 2009.
- [7] R.G. Gallager, *Principles of Digital Communication*, Cambridge University Press, 2008.
- [8] H. Meyr, M. Moeneclaey, S.A. Fechtel, *Digital Communication Receivers, Synchronization, Channel Estimation, and Signal Processing*, John Wiley & Sons, 1998.
- [9] E. Agrell, J. Lassing, E.G. Ström, T. Ottosson, On the optimality of the binary reflected Gray code, *IEEE Trans. Inf. Theory* 50 (12) (2004) 3170–3182.
- [10] E.W. Weisstein, Schwarz's inequality, from MathWorld—A Wolfram Web Resource, <http://mathworld.wolfram.com/SchwarzsInequality.html>.
- [11] G.D. Forney, Jr., The Viterbi algorithm, *Proc. IEEE* 61 (3) (1973) 268–278.

# The interplay between modulation and channel coding

# 5

M.C. Valenti\*, M. Fanaei†

*West Virginia University, Morgantown, WV, United States\**

*Minnesota State University at Mankato, Mankato, MN, United States†*

## CHAPTER OUTLINE

<b>5.1 Introduction .....</b>	<b>171</b>
<b>5.2 Coded Modulation .....</b>	<b>175</b>
<b>5.3 Reception of Coded Binary Modulation .....</b>	<b>177</b>
5.3.1 Soft Demapping .....	178
5.3.2 Channel Decoding .....	179
5.3.3 Example: Decoding of a Hamming Code .....	180
<b>5.4 Reception of Coded Nonbinary Modulation .....</b>	<b>182</b>
5.4.1 BICM Reception .....	182
5.4.2 BICM-ID Reception .....	184
5.4.3 Example: BICM Versus BICM-ID .....	187
5.4.4 Example: LTE Turbo Codes .....	189
<b>References .....</b>	<b>190</b>

## 5.1 INTRODUCTION

The error rates provided by the digital modulation schemes described in the previous chapters are usually too high to provide the quality of experience demanded by today's applications. Almost all modern communication systems use *error-control coding* to bring the error rate down to an acceptable level. Error-control coding adds controlled redundancy to the transmission, and this redundancy can be used to either correct or detect errors induced by the communication channel. While the correction of errors is preferred, even the detection of uncorrectable errors is useful inasmuch

that it can be used to automatically trigger a retransmission. Error detection is a critical ingredient in any system that uses *automatic request for retransmission* (ARQ). Often, error correction and detection are combined in *hybrid-ARQ* systems, which first attempt to correct errors, but request a retransmission when uncorrectable errors are detected [1].

Particular care must be taken when a system uses both error-control coding and digital modulation. Systems that combine the two are referred to as *coded-modulation* systems, though often the term is reserved for systems that combine a code with a higher-order (nonbinary) modulation format such as quadrature amplitude modulation (QAM). In an uncoded system, modulation symbols are independently selected one at a time (or using a limited memory of past symbols, as in continuous phase modulation (CPM)); if the modulation constellation has  $M$  symbols, then each symbol is selected using only  $m \triangleq \log_2(M)$  information bits. In contrast, a coded-modulation system groups symbols together into modulated codewords that can be fairly long, with a typical codeword containing hundreds or thousands of symbols, and a fairly long *message* is used to pick codewords from a quite large *codebook*.

Let  $N_s$  denote the number of symbols in a modulated codeword and  $N_d$  denote the dimensionality of each symbol. The encoded and modulated message can be represented by a length- $N_s$  vector  $\mathbf{x}$  of symbols called a *codeword*.<sup>1</sup> If a vector modulation is used, then the  $i$ th entry of  $\mathbf{x}$  is in itself a length- $N_d$  vector of real numbers, and it is convenient to arrange the codeword as an  $N_d$ -by- $N_s$  matrix; ie,

$$\mathbf{x} \triangleq [\mathbf{x}_1 \quad \mathbf{x}_2 \quad \dots \quad \mathbf{x}_{N_s}] = \begin{bmatrix} x_{1,1} & x_{1,2} & \dots & x_{1,N_d} \\ x_{2,1} & x_{2,2} & \dots & x_{2,N_d} \\ \vdots & \vdots & \ddots & \vdots \\ x_{N_d,1} & x_{N_d,2} & \dots & x_{N_d,N_s} \end{bmatrix}. \quad (5.1)$$

Alternatively,  $x_i$ ,  $i = 1, 2, \dots, N_s$ , may be a real scalar if the modulation is one dimensional (eg, binary phase-shift keying), or a complex scalar if it is two dimensional (eg, QAM or phase-shift keying). Each symbol in  $\mathbf{x}$  is drawn from the  $N_d$ -dimensional symbol constellation  $\mathcal{X}$ . Since each element of the codeword,  $\mathbf{x}$ , must contain a symbol from  $\mathcal{X}$ , it follows that the codeword,  $\mathbf{x}$ , must be drawn from the *Cartesian product* of  $N_s$  constellations  $\mathcal{X}$ , and this set is denoted by  $\mathcal{X}^{N_s}$ . If the system were uncoded, then all  $M^{N_s}$  elements of  $\mathcal{X}^{N_s}$  could be used to convey  $mN_s$  bits per codeword. However, this is an uninteresting case of usage, as it is the same thing as simply sending a sequence of  $N_s$  uncoded symbols, which will not provide any *coding gain*.

In a coded-modulation system, each codeword must be drawn from a subset of  $\mathcal{X}^{N_s}$  called a *codebook* or simply a *code*. Here, we use  $\mathcal{X}_c$  to denote the codebook, where  $\mathcal{X}_c \subset \mathcal{X}^{N_s}$ . An *encoder* uses a vector of information bits,  $\mathbf{u}$ , to select a codeword,  $\mathbf{x} \in \mathcal{X}_c$ . Let  $K_b$  denote the number of bits in  $\mathbf{u}$ . As there is a one-

<sup>1</sup>Note that in this chapter, a codeword is a vector of modulated symbols rather than a vector of bits. In the case of binary modulation, the two perspectives are equivalent.

to-one mapping between  $\mathbf{u}$  and  $\mathbf{x}$ , it follows that  $K_b = \log_2 |\mathcal{X}_c|$ , which is less than the number of bits that could be mapped when the system is uncoded; ie,  $\log_2 M^{N_s} = mN_s$ . The *rate*  $R_c = K_b/(mN_s)$  of the code is the ratio of the number of information bits actually conveyed by a codeword to the number of bits that could have been sent had a code not been used (ie, had the codeword been drawn from the full set,  $\mathcal{X}^{N_s}$ ). Note that  $R_c \leq 1$  since  $\mathcal{X}_c \subset \mathcal{X}^{N_s}$ , and hence  $K_b \leq mN_s$ . The rate quantifies the loss in spectral efficiency due to the use of a code. A lower rate typically translates to a higher *energy efficiency* due to its ability to correct more errors, though this comes at the cost of requiring more bandwidth for a given data rate, or a reduction in the data rate for a given bandwidth. The *spectral efficiency*,  $\eta_c$ , of the coded modulation is the amount of information conveyed per transmitted symbol; ie,  $\eta_c \triangleq mR_c$ . Spectral efficiency is expressed in units of *bits per channel use* (bpcu). Often, the loss in bandwidth efficiency due to using a lower-rate code, can be compensated by simply using a higher-order modulation. For instance, a system that uses 16-QAM modulation and half-rate encoding ( $R_c = 1/2$ ) might offer better energy efficiency than an uncoded QPSK system, even though the two systems have exactly the same bandwidth efficiency (ie,  $\eta_c = 2$  bpcu).

The encoding operation is therefore characterized as a mapping of information bit sequences of length  $K_b$  to modulation symbol sequences of length  $N_s$ . Conceptually, coded modulation can be considered simply as a type of digital modulation with a very large signal set. Instead of using  $m$  bits to select from among the  $M$  symbols in  $\mathcal{X}$ ,  $K_b$  bits are used to select modulated codewords from  $\mathcal{X}_c$ . Whereas the dimensionality of  $\mathcal{X}$  is  $N_d$ , the set  $\mathcal{X}_c$  has a dimensionality of  $N_d N_s$ . The goal of the decoder is to determine the codeword in  $\mathcal{X}_c$  that lies *closest* to the received signal. In an additive white Gaussian noise (AWGN) channel, the measure of closeness can be the Euclidean distance, just as it is for uncoded modulation. The error performance for a coded-modulation system in the AWGN channel can be found by using the principles in Chapter 4 by using the modulated codewords from  $\mathcal{X}_c$  in place of the symbols from  $\mathcal{X}$ .

While considering a coded-modulation system as a vastly expanded constellation is simple conceptually, there are several practical considerations that must be taken into account when implementing coded modulation. One key issue is how to match the error-correction code with the modulation. Some coded-modulation systems tightly integrate the two operations; for instance, in a *trellis-coded modulation* (TCM) system [2,3], a convolutional encoder is used and the branches of the encoder's trellis are labeled with modulation symbols from  $\mathcal{X}$ . TCM was widely used for telephone-line modems in the late 1980s and early 1990s. However, as many powerful codes are binary, the trend with modern systems is to combine a binary error-correction code with a higher-order modulation. A pragmatic approach to coded modulation is to simply combine an off-the-shelf binary code, such as a convolutional, turbo, or low-density parity check (LDPC) code, with a conventional nonbinary modulation, such as QAM or PSK [4]. The output of the binary encoder is fed into the input of the modulator. Often, for reasons that will be explained later in the chapter, the bits output by the encoder are *interleaved*, ie, their order is permuted, before being fed into the modulator.

Coded-modulation formats that are generated by placing an interleaver between the output of a binary encoder and the input of a nonbinary modulator are called *bit-interleaved coded modulation* (BICM) [5,6]. BICM is known to perform especially well in fading environments [5], but is also often applied in AWGN environments due to its convenience.

A key consideration for engineering coded-modulated systems is how to design the corresponding receiver. If coded modulation is interpreted as an expansion of the signal set, then a naïve brute-force decoder could operate by comparing the received signal against every candidate codeword in  $\mathcal{X}_c$ . While such a brute-force approach is reasonable for an uncoded system with  $M$  candidates, the number of candidates in a coded-modulation system grows exponentially with the length of the codeword. Clearly, such a decoder is not a viable choice, except when the codewords are extremely short. A more pragmatic approach is to perform *demodulation* and *decoding* as two separate operations in the receiver. This is the approach taken in most coded-modulation systems, especially BICM. For such receivers, the interface between the demodulator and decoder is crucial. Here, we use the term *channel decoder* to describe the unit used to decode just the binary channel code. On the one hand, the demodulator could provide hard decisions from the individual coded bits to the channel decoder, and these hard decisions could be processed by a *hard-decision* decoder. However, it is well known that *soft-decision* decoders can significantly outperform hard-decision ones, and it is advantageous for the demodulator to pass appropriately defined soft values to the channel decoder. A key aspect of this chapter is to describe how to compute metrics suitable for soft-decision decoding. Moreover, performance in a BICM system can often be improved by feeding back soft information from the channel decoder to the demodulator, and operating in an iterative mode called *BICM with iterative decoding* (BICM-ID) [7].

This chapter is not meant to be a tutorial on error-control coding. There is by now a vast literature on coding theory and practice; see, for instance, [8–12] and the references therein. Rather than delving into the principles of code design, we consider a code to merely be an arbitrary set of codewords without elaborating on how to design a good code. Similarly, rather than describing the inner workings of the channel decoder, we consider it to be a kind of black box that takes in appropriately defined soft-decision metrics and produces estimates of the message. The main focus of the chapter is on the interfaces between modulation and coding, and in particular, the processing that must be done to the received signal to put it into a format that can be used by an off-the-shelf channel decoder. To this end, the main emphasis of the chapter is on the concepts of BICM and BICM-ID.

The remainder of this chapter is structured as follows. Section 5.2 presents a model of coded modulation. Next, Section 5.3 derives the receiver for the case that the coded-modulation system uses a binary modulation, such as BPSK. The receiver for the case that the modulation uses nonbinary constellations is considered in Section 5.4, and this includes receivers for both BICM and BICM-ID architectures.

## 5.2 CODED MODULATION

A message vector is composed of  $K_b$  consecutive input information bits and denoted by  $\mathbf{u} \triangleq [u_1, u_2, \dots, u_{K_b}]$ , where each  $u_i \in \{0, 1\}$ . As shown by the dashed box at the top of Fig. 5.1, the message vector is passed through a bit-to-symbol encoder that generates a length- $N_s$  vector of  $M$ -ary symbols denoted by  $\mathbf{x} \triangleq [\mathbf{x}_1, \mathbf{x}_2, \dots, \mathbf{x}_{N_s}]$ . Each component of  $\mathbf{x}$  is a length- $N_d$  column vector of real numbers representing a single symbol drawn from the  $N_d$ -dimensional modulation constellation  $\mathcal{X}$ .

In general, the coded modulation can use any arbitrary one-to-one mapping from  $\mathbf{u}$  to  $\mathbf{x}$ . However, for the remainder of this chapter, we will focus specifically on BICM, for which the bit-to-symbol encoder comprises the three components shown inside the top dashed box of Fig. 5.1. In particular, the message vector,  $\mathbf{u}$ , is passed through a binary channel encoder, which adds controlled redundancy to it and produces a length- $K_c$  *binary codeword*  $\mathbf{c} \triangleq [c_1, c_2, \dots, c_{K_c}]$ , where  $K_c \geq K_b$  and each  $c_i \in \{0, 1\}$ . The binary channel codebook is denoted by  $\mathcal{C}$ , which is the set of all valid binary codewords, and the rate of the binary channel code is  $R_c = K_b/K_c$  information bits per coded bit.

The binary codeword,  $\mathbf{c}$ , can be directly fed into a bit-to-symbol mapper to generate the vector of modulated symbols,  $\mathbf{x}$ . However, in a BICM system, each binary codeword is passed through a pseudo-random, bit-wise interleaver  $\Pi$  that randomly permutes its input bits. The interleaver essentially transforms the single channel with  $M$ -ary inputs into a set of  $m$  parallel binary channels. Moreover, it is

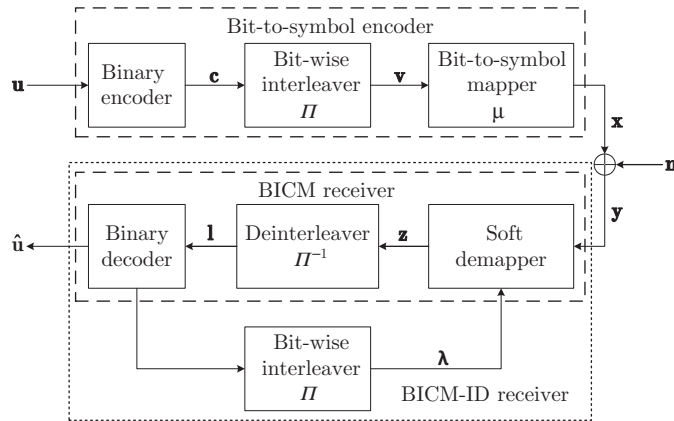


FIG. 5.1

Block diagram of a typical communication system with AWGN channel. The difference between BICM and BISM-ID systems is that in a BICM system, there is no feedback information from the binary channel decoder to the demapper.

also assumed that the interleaver arranges its output in the form of an  $m$ -by- $N_s$  matrix,  $\mathbf{v}$ , as follows:

$$\mathbf{v} \triangleq \begin{bmatrix} \mathbf{v}_1 & \mathbf{v}_2 & \dots & \mathbf{v}_{N_s} \end{bmatrix} = \begin{bmatrix} v_{1,1} & v_{1,2} & \dots & v_{1,N_s} \\ v_{2,1} & v_{2,2} & \dots & v_{2,N_s} \\ \vdots & \vdots & \ddots & \vdots \\ v_{m,1} & v_{m,2} & \dots & v_{m,N_s} \end{bmatrix}, \quad (5.2)$$

where  $N_s \triangleq K_c / \log_2 M$  and  $\mathbf{v}_\ell$  is a (column) vector representing the  $\ell$ th column of the matrix. Placing the interleaved bits into a matrix makes it clear that there is a one-to-one correspondence between the columns of this matrix and the modulated symbols, and it also underscores the perspective that the rows of the matrix correspond to the parallel binary channels created by the BICM.

The bit-to-symbol mapper function  $\mu(\cdot)$ , defined as  $\mu : \{0, 1\}^m \rightarrow \mathcal{X}$ , converts each length- $m$  column of the matrix of interleaved coded bits,  $\mathbf{v}$ , into an  $M$ -ary symbol drawn from a constellation,  $\mathcal{X}$ , where  $\mathbf{x}_\ell \triangleq \mu(\mathbf{v}_\ell)$ ,  $\ell = 1, 2, \dots, N_s$ , is an  $N_d$ -dimensional column vector of real numbers representing the  $M$ -ary modulated symbol associated with the  $\ell$ th column of matrix,  $\mathbf{v}$ . Therefore, the final output of the mapper is an  $N_d$ -by- $N_s$  matrix of modulated symbols,  $\mathbf{x}$ , as defined in Eq. (5.1). The spectral efficiency of the system is  $\eta_c \triangleq K_b \log_2 M / K_c = mR_c$  bits per channel use.

The vector of the modulated symbols,  $\mathbf{x}$ , is assumed to be transmitted over an AWGN channel and is received as

$$\mathbf{y} = \mathbf{x} + \mathbf{n}, \quad (5.3)$$

where  $\mathbf{y} \triangleq [\mathbf{y}_1, \mathbf{y}_2, \dots, \mathbf{y}_{N_s}]$  is the channel output and  $\mathbf{n} \triangleq [\mathbf{n}_1, \mathbf{n}_2, \dots, \mathbf{n}_{N_s}]$  is the uncorrelated, identically distributed, zero-mean Gaussian channel noise, where the variance of each component is  $\sigma_n^2 \triangleq N_0/2$ . The dimensionality of  $\mathbf{y}_\ell$  and  $\mathbf{n}_\ell$ , where  $\ell = 1, 2, \dots, N_s$ , is equal to that of the modulation scheme; ie,  $\mathbf{y}_\ell$  and  $\mathbf{n}_\ell$  are  $N_d$ -dimensional column vectors.

Upon receiving the channel output,  $\mathbf{y}$ , the demapper calculates a metric for each interleaved coded bit,  $v_{i,\ell}$ , where  $i = 1, 2, \dots, m$  and  $\ell = 1, 2, \dots, N_s$ , which denotes the element in the  $i$ th row and  $\ell$ th column of matrix  $\mathbf{v}$ . In a BICM system, the metrics are deinterleaved and then fed to the binary channel decoder. The channel decoder estimates the binary codeword from the set of  $2^{K_b}$  codewords based on the received metrics for the coded bits from the demapper. Since there is a one-to-one mapping between the vectors of information bits and binary codewords, deciding on the most likely codeword is equivalent to the most likely vector of information bits, denoted by  $\hat{\mathbf{u}}$ .

If the binary channel decoder is a *soft-output* decoder, it can produce a metric related to the likelihood of each code bit. In a system with iterative decoding (ID), the soft output of the channel decoder can be fed back to the demapper to improve its performance. In a BICM-ID system, the soft information fed back from the channel decoder is interleaved before being fed back to the demapper.

In the rest of this chapter, we analyze a generic BICM-ID system as shown in Fig. 5.1. To that end, we will first consider a coded-modulation system with a binary signal constellation. Following this, a BICM system is analyzed in a generic case of nonbinary modulations. Lastly, the receiver formulation is modified to consider the iterative decoding procedure.

### 5.3 RECEPTION OF CODED BINARY MODULATION

As a first step in analyzing the formulation of the receiver, consider a system with binary channel coding and BPSK modulation over an AWGN channel. In this section, we study the formulation of the demodulator and channel decoder for such a system. These formulations will be generalized into an arbitrary, nonbinary modulation scheme in the next section. The coded-modulation system under study is shown in Fig. 5.2. Notice that the output of the binary encoder is fed directly into a BPSK mapper. Since the BPSK is binary, there is no need to use an interleaver to partition the encoder output into parallel binary channels; thus, there is no interleaver in this model.

BPSK is a one-dimensional modulation (ie,  $N_d = 1$ ) whose constellation contains  $M = 2$  signal points with equal energy and an opposite phase; ie,  $\mathcal{X} = \{-\sqrt{\mathcal{E}_s}, \sqrt{\mathcal{E}_s}\}$ , where  $\mathcal{E}_s = |x_i|^2$  is the energy per modulated symbol. Each symbol modulates only  $m = 1$  bit; hence,  $N_s = K_c$ . The elements of the vector of modulated symbols,  $\mathbf{x}$ , are scalar and related to the corresponding elements of binary codeword,  $\mathbf{c}$ , by

$$x_i = \sqrt{\mathcal{E}_s}(2c_i - 1), \quad i = 1, 2, \dots, N_s. \quad (5.4)$$

The mapping given by Eq. (5.4) represents a code bit with value  $c_i = 1$  as a positive signal level  $x_i = +\sqrt{\mathcal{E}_s}$ , and a code bit with value  $c_i = 0$ , as a negative signal level  $x_i = -\sqrt{\mathcal{E}_s}$ .

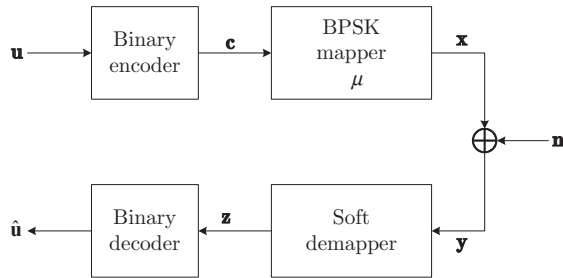


FIG. 5.2

Block diagram of a coded-modulation system with AWGN communication channel.

### 5.3.1 SOFT DEMAPPING

Since BPSK modulation is memoryless, the demodulation of the received vector,  $\mathbf{y}$ , can be decomposed into the *independent* demodulation of its components. Upon reception of  $y_i$ , where  $i = 1, 2, \dots, N_s$ , the soft demapper calculates a metric for the coded bit associated with it. This metric is defined in the form of a *log-likelihood ratio* (LLR), which is defined for the  $i$ th coded bit as

$$z_i \triangleq \log \frac{P(c_i = 1|y_i)}{P(c_i = 0|y_i)}, \quad i = 1, 2, \dots, N_s, \quad (5.5)$$

where  $P(c_i = b|y_i)$ ,  $b = 0, 1$ , is the a priori conditional probability that  $c_i = b$ , given that the received symbol is  $y_i$  and the logarithm is usually assumed to be the natural logarithm (ie,  $\log \equiv \ln$ ). Note that the value of the LLR is a function of the received symbol at the channel output. Based on the relationship between coded bits and modulated symbols in Eq. (5.4), the above LLR can be rewritten as

$$z_i = \log \frac{P(x_i = \sqrt{\mathcal{E}_s}|y_i)}{P(x_i = -\sqrt{\mathcal{E}_s}|y_i)}. \quad (5.6)$$

Using Bayes' rule,  $P(x_i|y_i)$  can be written as

$$P(x_i|y_i) = \frac{f_{Y_i}(y_i|x_i)P(x_i)}{f_{Y_i}(y_i)}, \quad (5.7)$$

where  $f_{Y_i}(y_i|x_i)$  denotes the conditional probability density function (PDF) of the received symbol,  $y_i$ , given that the transmitted modulated symbol is  $x_i$ . Substituting Eq. (5.7) into Eq. (5.6), and canceling the common terms, results in

$$z_i = \log \frac{f_{Y_i}(y_i|x_i = \sqrt{\mathcal{E}_s})P(x_i = \sqrt{\mathcal{E}_s})}{f_{Y_i}(y_i|x_i = -\sqrt{\mathcal{E}_s})P(x_i = -\sqrt{\mathcal{E}_s})}. \quad (5.8)$$

Since the channel is assumed to be AWGN, based on Eq. (5.3),  $y_i$  conditioned on  $x_i$  is a Gaussian random variable with mean  $x_i$  and variance  $N_0/2$ ; ie,  $y_i|x_i \sim \mathcal{N}(x_i, N_0/2)$ . Therefore,

$$f_{Y_i}(y_i|x_i) = \frac{1}{\sqrt{\pi N_0}} \exp\left(-\frac{(y_i - x_i)^2}{N_0}\right). \quad (5.9)$$

Substituting Eq. (5.9) into Eq. (5.8), and assuming equally likely coded bits, ie,  $P(x_i = -\sqrt{\mathcal{E}_s}) = P(x_i = \sqrt{\mathcal{E}_s})$ , will result in the value of the LLR for BPSK modulation over an AWGN channel:

$$\begin{aligned} z_i &= \ln \left( \frac{\frac{1}{\sqrt{\pi N_0}} \exp\left[-\frac{1}{N_0}(y_i - \sqrt{\mathcal{E}_s})^2\right]}{\frac{1}{\sqrt{\pi N_0}} \exp\left[-\frac{1}{N_0}(y_i + \sqrt{\mathcal{E}_s})^2\right]} \right) \\ &= -\frac{1}{N_0} \left[ (y_i - \sqrt{\mathcal{E}_s})^2 - (y_i + \sqrt{\mathcal{E}_s})^2 \right] \\ &= \frac{4\sqrt{\mathcal{E}_s}}{N_0} y_i. \end{aligned} \quad (5.10)$$

The LLR values calculated by the demodulator will be used by the channel decoder to find the most likely transmitted binary codeword,  $\mathbf{c}$ .

### 5.3.2 CHANNEL DECODING

Now let us consider how the channel decoder can use the bit LLRs from the demapper to estimate the binary codeword from  $\mathcal{C}$ . Given  $\mathbf{y}$ , the maximum a posteriori probability (MAP) decoding rule is

$$\hat{\mathbf{c}} = \arg \max_{\mathbf{c} \in \mathcal{C}} P(\mathbf{c}|\mathbf{y}). \quad (5.11)$$

Because the binary codeword,  $\mathbf{c}$ , is mapped to the vector of modulated symbols,  $\mathbf{x}$ , through the one-to-one mapping of  $\mathbf{x} = \mu(\mathbf{c})$ , it can be replaced by the corresponding vector of modulated symbols,  $\mathbf{x}$ , in the previous equation:

$$\hat{\mathbf{c}} = \arg \max_{\mathbf{x} \in \mathcal{X}_c} P(\mathbf{x}|\mathbf{y}) \quad (5.12)$$

where  $\mathcal{X}_c$  is the set of modulated codewords; ie,  $\mathcal{X}_c \triangleq \{\mathbf{x} : \mathbf{c} = \mu^{-1}(\mathbf{x}) \in \mathcal{C}\}$ .

Since the components,  $n_i$ , of the channel noise vector are independent, it follows that the set of conditional probabilities,  $P(x_i|y_i)$ , are independent, and the previous equation can be expressed as

$$\hat{\mathbf{c}} = \arg \max_{\mathbf{x} \in \mathcal{X}_c} \prod_{i=1}^{N_s} P(x_i|y_i). \quad (5.13)$$

By dividing each term in the previous multiplication by  $P(x_i = -\sqrt{\mathcal{E}_s}|y_i)$ , the above equation can be written as

$$\hat{\mathbf{c}} = \arg \max_{\mathbf{x} \in \mathcal{X}_c} \prod_{i=1}^{N_s} \frac{P(x_i|y_i)}{P(x_i = -\sqrt{\mathcal{E}_s}|y_i)}. \quad (5.14)$$

Taking the logarithm, it can be rewritten as

$$\begin{aligned} \hat{\mathbf{c}} &= \arg \max_{\mathbf{x} \in \mathcal{X}_c} \log \left( \prod_{i=1}^{N_s} \frac{P(x_i|y_i)}{P(x_i = -\sqrt{\mathcal{E}_s}|y_i)} \right) \\ &= \arg \max_{\mathbf{x} \in \mathcal{X}_c} \sum_{i=1}^{N_s} \log \left( \frac{P(x_i|y_i)}{P(x_i = -\sqrt{\mathcal{E}_s}|y_i)} \right). \end{aligned} \quad (5.15)$$

If the  $i$ th bit of the candidate codeword,  $\mathbf{c}$ , is  $c_i = 1$ , then  $x_i = \sqrt{\mathcal{E}_s}$ , and the corresponding term in Eq. (5.15) is

$$\log \frac{P(x_i = \sqrt{\mathcal{E}_s}|y_i)}{P(x_i = -\sqrt{\mathcal{E}_s}|y_i)} = z_i. \quad (5.16)$$

Notice that this is the LLR of  $x_i$  for the given  $y_i$ , as defined in Eq. (5.6). Similarly, if the  $i$ th bit of the candidate codeword,  $\mathbf{c}$ , is  $c_i = 0$ , then  $x_i = -\sqrt{\mathcal{E}_s}$ , and the corresponding term in Eq. (5.15) is

$$\log \frac{P(x_i = -\sqrt{\mathcal{E}_s}|y_i)}{P(x_i = \sqrt{\mathcal{E}_s}|y_i)} = 0. \quad (5.17)$$

Generalizing Eqs. (5.16) and (5.17), the  $i$ th term of the sum in Eq. (5.15) is

$$\log \left( \frac{P(x_i|y_i)}{P(x_i = -\sqrt{\mathcal{E}_s}|y_i)} \right) = c_i z_i, \quad (5.18)$$

and thus Eq. (5.15) may be written as

$$\hat{\mathbf{c}} = \arg \max_{\mathbf{c} \in \mathcal{C}} \sum_{i=1}^{N_s} c_i z_i. \quad (5.19)$$

To summarize, decoding proceeds by first finding the LLR of each coded bit,  $c_i$ , which for BPSK modulation over an AWGN channel is found using Eq. (5.10). For each one of the  $2^{K_b}$  candidate codewords,  $\mathbf{c} \in \mathcal{C}$ , the metric

$$\Lambda(\mathbf{c}|\mathbf{y}) \triangleq \sum_{i=1}^{N_s} c_i z_i \quad (5.20)$$

is found. The most likely binary codeword is then the one with the largest metric given by Eq. (5.20).

### 5.3.3 EXAMPLE: DECODING OF A HAMMING CODE

Let us consider the decoding of a simple Hamming code with BPSK modulation over an AWGN channel. Hamming codes are a class of single error-correction codes, characterized by having a codeword length of  $K_c = 2^q - 1$  and a message length of  $K_b = 2^q - 1 - q$  for any integer  $q = K_c - K_b$  [13]. A Hamming code where  $q = 3$  is listed in Table 5.1. For each codeword, a corresponding message is shown. We note that the code is *systematic* since each message is disposed in the first  $K_b$  bits of its corresponding binary codeword. The last two columns in the table will be used in reference to the example decoding operation discussed in this section.

Suppose that the message vector of information bits is

$$\mathbf{u} = [1 \ 0 \ 0 \ 1]$$

so that the corresponding binary codeword is

$$\mathbf{c} = [1 \ 0 \ 0 \ 1 \ 0 \ 1 \ 1]. \quad (5.21)$$

**Table 5.1** Hamming Code with  $K_b = 4$  Information Bits and Binary Codewords of Length  $K_c = 7$ 

Message $\mathbf{u}$	Binary Codeword $\mathbf{c}$	$d_H(\mathbf{c}, \mathbf{r})$	$\Lambda(\mathbf{c} \mathbf{y})$
0 0 0 0	0 0 0 0 0 0 0	3	0.0
0 0 0 1	0 0 0 1 1 0 1	4	2.4
0 0 1 0	0 0 1 0 1 1 1	5	1.4
0 0 1 1	0 0 1 1 0 1 0	6	-3.0
0 1 0 0	0 1 0 0 0 1 1	2	7.6
0 1 0 1	0 1 0 1 1 1 0	5	-3.6
0 1 1 0	0 1 1 0 1 0 0	4	-4.2
0 1 1 1	0 1 1 1 0 0 1	3	5.0
1 0 0 0	1 0 0 0 1 1 0	4	0.6
1 0 0 1	1 0 0 1 0 1 1	3	<b>9.8</b>
1 0 1 0	1 0 1 0 0 0 1	2	9.2
1 0 1 1	1 0 1 1 1 0 0	5	-2.0
1 1 0 0	1 1 0 0 1 0 1	<b>1</b>	8.6
1 1 0 1	1 1 0 1 0 0 0	2	4.2
1 1 1 0	1 1 1 0 0 1 0	3	3.2
1 1 1 1	1 1 1 1 1 1 1	4	5.6

Assume that the binary codeword is BPSK modulated based on Eq. (5.4) and sent over an AWGN channel, where the variance of the additive channel noise is  $\sigma_n^2 = N_0/2 = 1 \equiv 0$  dB. Let the average energy per modulated symbol be  $\mathcal{E}_s = 1$ . Suppose that the received signal at the receiver is

$$\mathbf{y} = [2.1 \quad 0.5 \quad -0.9 \quad -0.5 \quad -1.7 \quad -0.1 \quad 3.4]. \quad (5.22)$$

Using Eq. (5.10), the vector of the LLRs  $\mathbf{z} \triangleq [z_1, z_2, \dots, z_{N_s}]$ , can be found in this example to be

$$\mathbf{z} = \frac{4\sqrt{\mathcal{E}_s}}{N_0} \mathbf{y} = [4.2 \quad 1.0 \quad -1.8 \quad -1.0 \quad -3.4 \quad -0.2 \quad 6.8]. \quad (5.23)$$

Since a positive LLR implies that “1” is more likely than “0”, and a negative LLR implies that “0” is more likely than “1”, a hard decision on the LLR vector of Eq. (5.23) gives the received vector as

$$\mathbf{r} = [1 \quad 1 \quad 0 \quad 0 \quad 0 \quad 0 \quad 1]. \quad (5.24)$$

Comparing Eq. (5.24) with Eq. (5.21), it can be seen that the two vectors differ in the second, forth, and sixth bit positions. Thus, after a hard decision is made, the binary codeword is received with three bit errors. Since the message was encoded with a Hamming code, which can only correct a single error, a hard-decision decoder is unable to correct this received vector. The number of bit positions that the vector

of hard decisions, in Eq. (5.24), is different from each binary codeword is known as the *Hamming distance* between the two vectors, denoted by  $d_H(\mathbf{c}, \mathbf{r})$ , and shown in one of the columns of Table 5.1. Based on the maximum-likelihood (ML) decoding rule for hard-decision decoding, the most likely binary codeword, given the received vector,  $\mathbf{r}$ , is the one with the least number of bit differences with  $\mathbf{r}$ , which is

$$\hat{\mathbf{c}}_{\text{HD}} = [1 \ 1 \ 0 \ 0 \ 1 \ 0 \ 1], \quad (5.25)$$

which is not the transmitted binary codeword.

Now consider the soft-decision decoder. For each binary codeword in  $\mathcal{C}$ , the metric  $\Lambda(\mathbf{c}|\mathbf{y})$  is computed using Eq. (5.20), and the binary codeword with the highest metric is selected. For the Hamming code shown in Table 5.1 and the LLR vector given by Eq. (5.23), the corresponding metric for each one of the  $2^{K_b} = 16$  binary codewords is given in the last column of Table 5.1. The maximum metric is  $\Lambda(\mathbf{c}|\mathbf{y}) = 9.8$ , which corresponds to the binary codeword:  $\hat{\mathbf{c}}_{\text{SD}} = [1 \ 0 \ 0 \ 1 \ 0 \ 1 \ 1]$ . This is the transmitted binary codeword, as specified by Eq. (5.21). Thus, the soft-decision decoder has successfully decoded the received vector, despite the fact that it contained three errors when subjected to a hard decision.

## 5.4 RECEPTION OF CODED NONBINARY MODULATION

In this section, we extend the formulation of the receiver in Section 5.3 to memoryless, nonbinary modulations to include a bit-wise interleaver  $\Pi$  between the channel encoder and bit-to-symbol mapper, as well as an iterative decoder at the receiver.

### 5.4.1 BICM RECEPTION

Since the modulation scheme is assumed to be memoryless, the demodulation of the received vector,  $\mathbf{y}$ , can be decomposed into the *independent* demodulation of its symbols,  $\mathbf{y}_\ell$ ,  $\ell = 1, 2, \dots, N_s$ . Upon reception of  $\mathbf{y}_\ell$ , the soft demapper calculates a metric for each one of the  $m$  bits associated with the  $\ell$ th column of the transmitted matrix  $\mathbf{v}$ . This metric is defined to be in the form of an LLR, which is defined for the  $i$ th bit in the  $\ell$ th column of the matrix  $\mathbf{v}$  as

$$z_{i,\ell} \triangleq \log \frac{P(v_{i,\ell} = 1|\mathbf{y}_\ell)}{P(v_{i,\ell} = 0|\mathbf{y}_\ell)}, \quad i = 1, 2, \dots, m \text{ and } \ell = 1, 2, \dots, N_s. \quad (5.26)$$

Note that the LLR value for each one of the  $m$  bits associated with the  $\ell$ th column of the transmitted matrix of bits only depends on the  $\ell$ th column of the received matrix,  $\mathbf{y}$ . The previous LLR can be rewritten as

$$z_{i,\ell} = \log \frac{\sum_{\mathbf{s} \in \mathcal{X}_i^1} P(\mathbf{s}|\mathbf{y}_\ell)}{\sum_{\mathbf{s} \in \mathcal{X}_i^0} P(\mathbf{s}|\mathbf{y}_\ell)}, \quad i = 1, 2, \dots, m \text{ and } \ell = 1, 2, \dots, N_s, \quad (5.27)$$

where  $\mathcal{X}_i^b$  is the set of the modulated symbols for which the  $i$ th bit in the mapped column  $\mathbf{v}_\ell$  to the symbol  $\mathbf{s} \in \mathcal{X}$  is equal to  $b$ , where  $b = 0, 1$ . In other words,

$$\mathcal{X}_i^b \triangleq \left\{ \mathbf{s} | \mathbf{v} \triangleq \mu^{-1}(\mathbf{s}) \text{ and } \mathbf{v}_i = b \right\}, \quad b = 0, 1 \text{ and } i = 1, 2, \dots, m.$$

Using Bayes' rule,  $P(\mathbf{s} | \mathbf{y}_\ell)$  can be written as

$$P(\mathbf{s} | \mathbf{y}_\ell) = \frac{f_{\mathbf{Y}_\ell}(\mathbf{y}_\ell | \mathbf{s}) P(\mathbf{s})}{f_{\mathbf{Y}_\ell}(\mathbf{y}_\ell)}, \quad (5.28)$$

where  $f_{\mathbf{Y}_\ell}(\mathbf{y}_\ell | \mathbf{s})$  denotes the conditional PDF of the received signal,  $\mathbf{y}_\ell$ , given that the transmitted modulated symbol is  $\mathbf{x}_\ell = \mathbf{s}$ . Substituting Eq. (5.28) into Eq. (5.27), and canceling the common terms, results in

$$z_{i,\ell} = \log \frac{\sum_{\mathbf{s} \in \mathcal{X}_i^1} f_{\mathbf{Y}_\ell}(\mathbf{y}_\ell | \mathbf{s}) P(\mathbf{s})}{\sum_{\mathbf{s} \in \mathcal{X}_i^0} f_{\mathbf{Y}_\ell}(\mathbf{y}_\ell | \mathbf{s}) P(\mathbf{s})}. \quad (5.29)$$

Since the channel is assumed to be AWGN, based on Eq. (5.3),  $\mathbf{Y}_\ell | \mathbf{s}$  is a Gaussian random vector with mean  $\mathbf{s}$  and a covariance matrix  $\frac{N_0}{2} \mathbf{I}_{N_d}$ , where  $\mathbf{I}_{N_d}$  is the  $N_d$ -by- $N_d$  identity matrix; ie,  $\mathbf{Y}_\ell | \mathbf{s} \sim \mathcal{N}\left(\mathbf{s}, \frac{N_0}{2} \mathbf{I}_{N_d}\right)$ . Therefore,

$$\begin{aligned} f_{\mathbf{Y}_\ell}(\mathbf{y}_\ell | \mathbf{s}) &= \frac{1}{(\pi N_0)^{N_d/2}} \exp\left(-\frac{(\mathbf{y}_\ell - \mathbf{s})(\mathbf{y}_\ell - \mathbf{s})^T}{N_0}\right) \\ &\stackrel{(a)}{\propto} \exp\left(-\frac{1}{N_0} \|\mathbf{y}_\ell - \mathbf{s}\|^2\right), \end{aligned} \quad (5.30)$$

where “ $\propto$ ” is read as “is proportional to,”  $\|\cdot\|$  denotes the  $L^2$ -norm of a vector,  $\|\mathbf{y}_\ell - \mathbf{s}\|$  denotes the Euclidean distance between vectors  $\mathbf{y}_\ell$  and  $\mathbf{s}$ , and (a) is because the common terms in the numerator and denominator of Eq. (5.29) can be canceled out. Substituting Eq. (5.30) into Eq. (5.29) results in

$$z_{i,\ell} = \log \frac{\sum_{\mathbf{s} \in \mathcal{X}_i^1} \exp\left(-\frac{1}{N_0} \|\mathbf{y}_\ell - \mathbf{s}\|^2\right) P(\mathbf{s})}{\sum_{\mathbf{s} \in \mathcal{X}_i^0} \exp\left(-\frac{1}{N_0} \|\mathbf{y}_\ell - \mathbf{s}\|^2\right) P(\mathbf{s})}. \quad (5.31)$$

Note that the bit LLR found in Eq. (5.31) is a function of the Euclidean distance between the received signal,  $\mathbf{y}_\ell$ , and each one of the  $M = 2^m$  modulated symbols in the constellation,  $\mathbf{s} \in \mathcal{X}$ .

In a BICM system, all of the modulated symbols are assumed to be equally likely so that the term  $P(\mathbf{s})$  cancels in the numerator and denominator of Eq. (5.31), and the MAP bit metric defined in Eq. (5.26) is reduced to the ML bit metric. Therefore, the bit LLR defined in Eq. (5.26) can be found in a BICM system as

$$z_{i,\ell} = \log \frac{\sum_{\mathbf{s} \in \mathcal{X}_i^1} \exp \left( -\frac{1}{N_0} \|\mathbf{y}_\ell - \mathbf{s}\|^2 \right)}{\sum_{\mathbf{s} \in \mathcal{X}_i^0} \exp \left( -\frac{1}{N_0} \|\mathbf{y}_\ell - \mathbf{s}\|^2 \right)}. \quad (5.32)$$

The bit LLR can be computed using the Jacobian logarithm [14–16]

$$\begin{aligned} \ln(e^\alpha + e^\beta) &= \max(\alpha, \beta) + \ln(1 + e^{-|\alpha - \beta|}) \\ &= \max(\alpha, \beta) + \gamma_C(|\alpha - \beta|), \end{aligned} \quad (5.33)$$

where  $\gamma_C(\cdot)$  is a one-dimensional *correction function*, which is only a function of the difference between the two variables  $\alpha$  and  $\beta$ . Based on this identity, an operator is defined as [16]

$$\max^*(\alpha, \beta) \triangleq \ln(e^\alpha + e^\beta). \quad (5.34)$$

Similar to the property of the “max” operator for which

$$\max(\alpha_1, \alpha_2, \alpha_3) = \max(\max(\alpha_1, \alpha_2), \alpha_3),$$

the “max\*” operator can be extended to more than two variables as

$$\max^*(\alpha_1, \alpha_2, \alpha_3) = \max^*(\max^*(\alpha_1, \alpha_2), \alpha_3).$$

Therefore, the “max\*” operator can, in general, be defined as

$$\max_{\alpha \in \{\alpha_1, \alpha_2, \dots, \alpha_t\}}^* g(\alpha) \triangleq \max^*(g(\alpha_1), g(\alpha_2), \dots, g(\alpha_t)) = \ln \sum_{q=1}^t \exp(g(\alpha_q)), \quad (5.35)$$

where  $g(\cdot)$  is an arbitrary function.

Based on the definition of the “max\*” operator, Eq. (5.32) can be rewritten as

$$z_{i,\ell} = \max_{\mathbf{s} \in \mathcal{X}_i^1}^* \left( -\frac{1}{N_0} \|\mathbf{y}_\ell - \mathbf{s}\|^2 \right) - \max_{\mathbf{s} \in \mathcal{X}_i^0}^* \left( -\frac{1}{N_0} \|\mathbf{y}_\ell - \mathbf{s}\|^2 \right). \quad (5.36)$$

Thus, the BICM receiver computes the LLR of each interleaved code bit by using Eq. (5.36), deinterleaves the resulting LLRs by putting them into a row vector that has the same ordering as  $\mathbf{c}$ , and then passes the result to the binary channel decoder.

### 5.4.2 BICM-ID RECEPTION

In contrast to BICM systems, which assume all of the modulated symbols to be equally likely during the demapping operation (ie,  $P(\mathbf{s}) = 1/M$  for  $\mathbf{s} \in \mathcal{X}$ ), BICM-ID systems attempt to estimate the a priori likelihood of the modulated symbols, iteratively using information fed back from the soft-output binary decoder to the

soft demapper. The soft information fed back from the binary decoder is called the *extrinsic* information. Prior to being fed into the soft demapper, it is interleaved and placed into a matrix  $\lambda$  of the form

$$\triangleq \begin{bmatrix} \lambda_1 & \lambda_2 & \dots & \lambda_{N_s} \end{bmatrix} = \begin{bmatrix} \lambda_{1,1} & \lambda_{1,2} & \dots & \lambda_{1,N_s} \\ \lambda_{2,1} & \lambda_{2,2} & \dots & \lambda_{2,N_s} \\ \vdots & \vdots & \ddots & \vdots \\ \lambda_{m,1} & \lambda_{m,2} & \dots & \lambda_{m,N_s} \end{bmatrix}. \quad (5.37)$$

Rather than assuming equally likely symbols with equal  $P(\mathbf{s})$ , the BICM-ID receiver uses  $\lambda$  to produce an a priori estimate that is used in place of the  $P(\mathbf{s})$  in Eq. (5.31). During the  $\ell$ th symbol interval, the estimate of  $P(\mathbf{s})$  is denoted by  $P(\mathbf{s}|\lambda_\ell)$  to emphasize that the estimate of the symbol probability is found by using the  $\ell$ th column of the matrix  $\lambda$  denoted by  $\lambda_\ell$ . It follows that for the BICM-ID receiver, Eq. (5.31) becomes

$$z_{i,\ell} = \log \frac{\sum_{\mathbf{s} \in \mathcal{X}_i^1} \exp\left(-\frac{1}{N_0} \|\mathbf{y}_\ell - \mathbf{s}\|^2\right) P(\mathbf{s}|\lambda_\ell)}{\sum_{\mathbf{s} \in \mathcal{X}_i^0} \exp\left(-\frac{1}{N_0} \|\mathbf{y}_\ell - \mathbf{s}\|^2\right) P(\mathbf{s}|\lambda_\ell)}. \quad (5.38)$$

Let  $\mathbf{w}$  denote the length- $m$  vector of bits associated with  $\mathbf{s}$ ; ie,  $\mathbf{s} = \mu(\mathbf{w})$  and  $\mathbf{w} = \mu^{-1}(\mathbf{s})$ . Since there is a one-to-one mapping between  $\mathbf{s}$  and  $\mathbf{w}$ , it follows that  $P(\mathbf{s}|\lambda_\ell) = P(\mathbf{w}|\lambda_\ell)$ . Note that if  $\mathbf{s} \in \mathcal{X}_i^b$ , then the  $i$ th bit in the corresponding  $\mathbf{w}$  is fixed to  $w_i = b$ , where  $b \in \{0, 1\}$ . Therefore, for any  $\mathbf{s} \in \mathcal{X}_i^b$ ,

$$P(\mathbf{s}|\lambda_\ell) = P(\mathbf{w}|\lambda_\ell) \Big|_{w_i=b} = P(\mathbf{w} \setminus w_i | \lambda_\ell), \quad (5.39)$$

where  $\mathbf{w} \setminus w_i$  is the vector  $\mathbf{w}$  excluding the element  $w_i$ , and  $P(\mathbf{w} \setminus w_i | \lambda_\ell)$  represents the estimate of the a priori probability of  $\mathbf{w}$ , excluding its  $i$ th bit  $w_i$ , which is found by using  $\lambda_\ell$ .

Since it is a LLR,  $\lambda_{i,\ell} \triangleq \ln \frac{P[w_i=1]}{P[w_i=0]}$  for the  $\ell$ th symbol. It follows that

$$P[w_i = 0] = \frac{1}{1 + e^{\lambda_{i,\ell}}} \quad (5.40a)$$

$$P[w_i = 1] = \frac{e^{\lambda_{i,\ell}}}{1 + e^{\lambda_{i,\ell}}}. \quad (5.40b)$$

Generalizing Eqs. (5.40a) and (5.40b), the a priori probability of each transmitted bit can be written as

$$P[w_i] = \frac{\left(e^{\lambda_{i,\ell}}\right)^{w_i}}{1 + e^{\lambda_{i,\ell}}}. \quad (5.41)$$

If  $w_i = 0$ , Eq. (5.41) reduces to Eq. (5.40a), whereas if  $w_i = 1$ , Eq. (5.41) reduces to Eq. (5.40b). The a priori probability,  $P(\mathbf{w} \setminus w_i | \lambda_\ell)$ , can be written as

$$\begin{aligned}
P(\mathbf{w} \setminus w_i | \lambda_\ell) &= \prod_{\substack{j=1 \\ j \neq i}}^m P[w_j] \stackrel{(a)}{=} \exp \left( \sum_{\substack{j=1 \\ j \neq i}}^m \ln P[w_j] \right) \\
&\stackrel{(b)}{=} \exp \left( \sum_{\substack{j=1 \\ j \neq i}}^m \left[ w_j \ln e^{\lambda_{j,\ell}} - \ln(1 + e^{\lambda_{j,\ell}}) \right] \right) \\
&= \exp \left( \sum_{\substack{j=1 \\ j \neq i}}^m w_j \lambda_{j,\ell} \right) \times \exp \left( - \sum_{\substack{j=1 \\ j \neq i}}^m \ln(1 + e^{\lambda_{j,\ell}}) \right),
\end{aligned} \tag{5.42}$$

where (a) is based on the identity,  $a = \exp(\ln a)$ , and (b) replaces  $P[w_j]$  with Eq. (5.41) and uses the identities  $\log(a/b) = \log(a) - \log(b)$  and  $\log(a^b) = b \log(a)$ . During each iteration, Eq. (5.42) can be used to estimate the a priori probability of the modulated symbol,  $P(\mathbf{s} | \lambda_\ell)$ , by using  $\lambda_\ell$ . The substitution of this a priori information into Eq. (5.38), and the cancelation of the common terms between the numerator and denominator, results in

$$z_{i,\ell} = \log \frac{\sum_{\mathbf{s} \in \mathcal{X}_i^1} \exp \left( -\frac{1}{N_0} \|\mathbf{y}_\ell - \mathbf{s}\|^2 + \sum_{\substack{j=1 \\ j \neq i}}^m w_j \lambda_{j,\ell} \right)}{\sum_{\mathbf{s} \in \mathcal{X}_i^0} \exp \left( -\frac{1}{N_0} \|\mathbf{y}_\ell - \mathbf{s}\|^2 + \sum_{\substack{j=1 \\ j \neq i}}^m w_j \lambda_{j,\ell} \right)}. \tag{5.43}$$

Based on the definition of the “max\*” operator, Eq. (5.43) can be rewritten as

$$\begin{aligned}
z_{i,\ell} &= \max_{\substack{\mathbf{s} \in \mathcal{X}_i^1}}^* \left( -\frac{1}{N_0} \|\mathbf{y}_\ell - \mathbf{s}\|^2 + \sum_{\substack{j=1 \\ j \neq i}}^m w_j \lambda_{j,\ell} \right) \\
&\quad - \max_{\substack{\mathbf{s} \in \mathcal{X}_i^0}}^* \left( -\frac{1}{N_0} \|\mathbf{y}_\ell - \mathbf{s}\|^2 + \sum_{\substack{j=1 \\ j \neq i}}^m w_j \lambda_{j,\ell} \right).
\end{aligned} \tag{5.44}$$

where the reader is reminded that  $\mathbf{w} \triangleq \mu^{-1}(\mathbf{s})$ . As explained before, the above bit LLRs are deinterleaved and fed to the soft-input channel decoder so that it can estimate the vector of the transmitted information bits,  $\hat{\mathbf{u}}$ . The operation of the channel decoder is beyond the scope of this chapter and depends on the structure of the binary channel code.

### 5.4.3 EXAMPLE: BICM VERSUS BICM-ID

As an example, we compare the performance of a BICM system with a BICM-ID system. Throughout this example, we use the same binary code, which is a rate  $R_c = 1/2$  *convolutional* code. The code is generated using the structure shown in Fig. 5.3. Data is fed sequentially through the encoder, which contains a linear shift register. During each bit period, the next message bit is fed into the shift register, and two output bits are determined from the depicted logic. The output bits form the binary codeword. The encoder shown in Fig. 5.3 is said to have a *constraint length* of seven, because each output bit can depend on up to seven bits (the current bit, plus the six bits stored in the shift register). The convolutional code is decoded with the max-log-MAP algorithm [17]. For more information about convolutional codes, the reader is referred to [8,18].

The performance of BICM and BICM-ID depends on the function  $\mu(\cdot)$  used to map the bits to symbols. In this example, we consider 16-QAM modulation with the two mappings shown in Fig. 5.4: a Gray mapping and an anti-Gray mapping. In the Gray mapping, the bits labeling neighboring bit positions differ in just one bit position, whereas in the anti-Gray mapping, the bits labeling neighboring bit positions are common in just one bit position. For reasons discussed in [19], the Gray labeling is optimal when BICM is used, while the anti-Gray labeling is optimal when BICM-ID is used.

The results of a set of simulations using the binary code of Fig. 5.3 and mappings of Fig. 5.4 are shown in Fig. 5.5. For each of the two mappings, both BICM and BICM-ID receivers are considered. The results of BICM are shown as solid lines, while the results of BICM-ID are shown as dashed lines. The curves show the bit-error rate (BER) as a function of the ratio of  $\mathcal{E}_s/N_0$ , where  $N_0$  is the one-sided noise spectral density. An AWGN channel is assumed.

If only BICM is used, then Gray mapping gives a much better performance than anti-Gray mapping. However, the opposite is true for BICM-ID. As shown in Fig. 5.5, the system with Gray mapping shows only a negligible gain from BICM-ID—the figure shows results after 2 and 10 iterations, but there is no gain after the second iteration and hence, the two curves coincide. However, the anti-Gray mapping shows a dramatic gain when BICM-ID is used. For bit-error rates below  $10^{-4}$ , anti-Gray mapping with 10 iterations of decoding outperforms Gray mapping (either with or without BICM-ID).

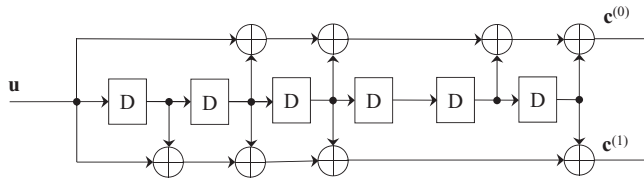
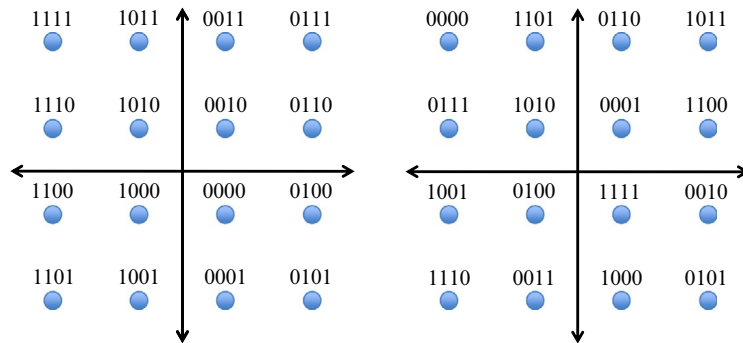
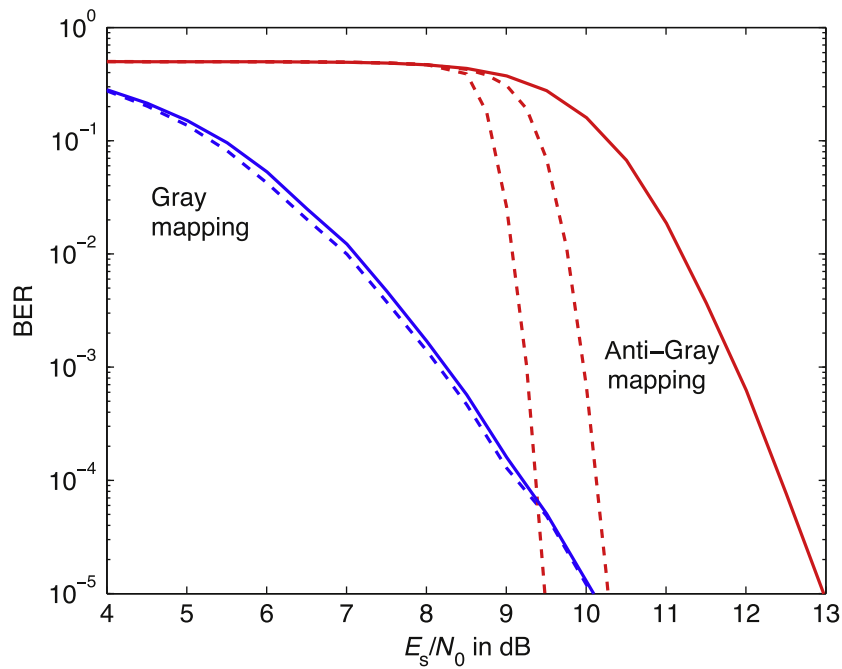


FIG. 5.3

A rate-1/2 convolutional encoder with a constraint length of seven.

**FIG. 5.4**

A Gray mapping (left) and an anti-Gray mapping (right).

**FIG. 5.5**

Simulated bit-error rate (BER) of the rate-1/2 convolutional encoder with 16-QAM using two mappings. Both BICM and BICM-ID are considered. The results for BICM are shown as solid lines, while the results after 2 and 10 iterations of BICM-ID are shown as dashed lines.

### 5.4.4 EXAMPLE: LTE TURBO CODES

As another example of the bit-error performance of a coded-modulation system, we consider the coded modulation used in the long-term evolution (LTE) 4G cellular system [20]. LTE uses a combination of a *turbo* code [21,22] and a higher-order modulation, which may be QPSK, 16-QAM, or 64-QAM. LTE is an adaptive system, where the modulation and coding scheme (MCS) switches on timescales on the order of a millisecond. LTE supports 27 MCS schemes, with each MCS scheme embodied by a particular combination of code rates and modulation types. The MCS index is proportional to the spectral efficiency,  $\eta_c$ . The 11 lowest MCSs (MCS0 through MCS10) use QPSK, the 10 intermediate MCSs (MCS11 through MCS20) use 16-QAM, and the 6 highest MCSs (MCS21 through MCS26) use 64-QAM. All of the MCSs use Gray mapping for the bit-to-symbol mapping function. Because turbo codes are already approaching capacity, and because these modulations all permit Gray mapping, there is no benefit to using BICM-ID or anti-Gray mapping.

Fig. 5.6 shows the simulated BER performance of BICM reception for a subset of the MCS schemes, each with a different spectral efficiency: MCS0 ( $\eta_c = 0.194$ ), MCS4 ( $\eta_c = 0.5$ ), MCS10 ( $\eta_c = 1.233$ ), MCS11 ( $\eta_c = 1.411$ ), MCS14 ( $\eta_c = 2$ ), MCS20 ( $\eta_c = 3.181$ ), MCS21 ( $\eta_c = 3.5370$ ), and MCS26 ( $\eta_c = 5.07$ ). Although

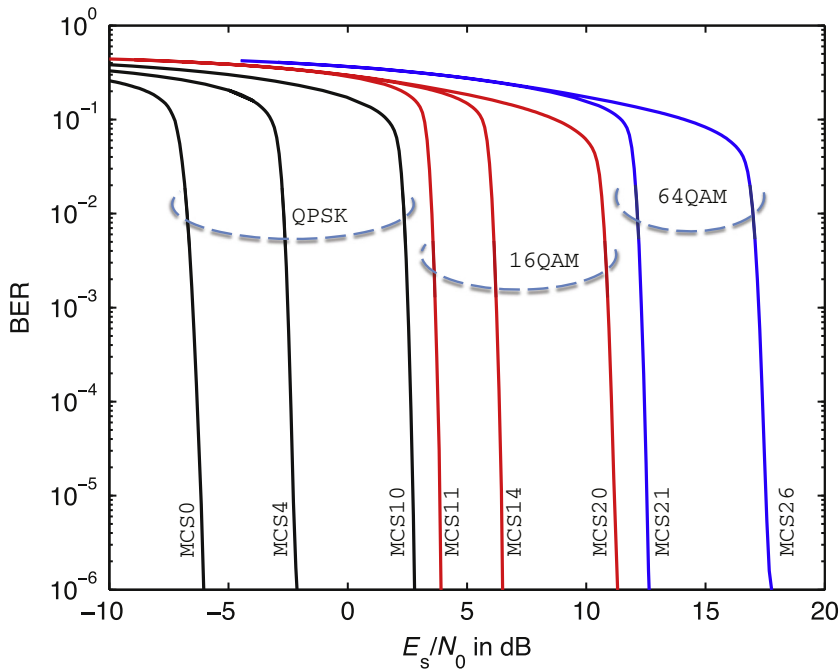


**FIG. 5.6**

Simulated bit-error rate (BER) of the code-modulation used by LTE.

the BICM-ID is not used, the binary decoder for a turbo code is itself iterative, and the curves were produced by using 16 iterations of the turbo decoding algorithm described in [22]. Shown in Fig. 5.6 is the BER versus  $\mathcal{E}_s/N_0$ , which is a signal-to-noise ratio (SNR). Note that the curves are fairly steep, which is indicative of the behavior of strong codes, like turbo codes; they offer poor performance up to some threshold SNR, but then the performance rapidly improves with an increasing SNR. As can be seen, codes of lower spectral efficiency can operate at lower SNR values.

---

## REFERENCES

- [1] G. Caire, D. Tuninetti, The throughput of hybrid-ARQ protocols for the Gaussian collision channel, *IEEE Trans. Inform. Theory* 47 (5) (2001) 1971–1988.
- [2] G. Ungerboeck, Trellis-coded modulation with redundant signal sets—part I: introduction, *IEEE Commun. Mag.* 25 (2) (1987) 5–11.
- [3] G. Ungerboeck, Trellis-coded modulation with redundant signal sets—part II: state of the art, *IEEE Commun. Mag.* 25 (2) (1987) 12–21.
- [4] A.J. Viterbi, J.K. Wolf, E. Zehavi, R. Padovani, A pragmatic approach to trellis-coded modulation, *IEEE Commun. Mag.* 27 (7) (1989) 11–19.
- [5] G. Caire, G. Taricco, E. Biglieri, Bit-interleaved coded modulation, *IEEE Trans. Inform. Theory* 44 (3) (1998) 927–946.
- [6] L. Szczecinski, A. Alvarado, *Bit-Interleaved Coded Modulation: Fundamentals, Analysis and Design*, John Wiley & Sons, New York, NY, 2015.
- [7] X. Li, J.A. Ritcey, Trellis-coded modulation with bit interleaving and iterative decoding, *IEEE J. Sel. Areas Commun.* 17 (4) (1999) 715–724.
- [8] S. Lin, D.J. Costello, *Error Control Coding: Fundamentals and Applications*, second ed., Prentice Hall, Upper Saddle River, NJ, 2004.
- [9] T.K. Moon, *Error Correction Coding: Mathematical Methods and Algorithms*, John Wiley & Sons, New York, 2005.
- [10] D. Declercq, M. Fossorier, E. Biglieri, *Channel Coding: Theory, Algorithms, and Applications*, first ed., Academic Press, New York, NY, 2014.
- [11] W.E. Ryan, S. Lin, *Channel Codes: Classical and Modern*, Cambridge University Press, Cambridge, UK, 2009.
- [12] S.B. Wicker, *Error Control Systems for Digital Communication and Storage*, Prentice Hall, Upper Saddle River, NJ, 1995.
- [13] R.W. Hamming, Error detecting and error correcting codes, *Bell Syst. Tech. J.* 29 (2) (1950) 147–160.
- [14] J. Erfanian, S. Pasupathy, P.G. Gulak, Reduced complexity symbol detectors with parallel structure for ISI channels, *IEEE Trans. Commun.* 42 (2/3/4) (1994) 1661–1671.
- [15] S.S. Pietrobon, Implementation and performance of a serial MAP decoder for use in an iterative turbo decoder, in: *Proceedings of the IEEE International Symposium on Information Theory (ISIT'95)*, Whistler, BC, Canada, 1995, p. 471.
- [16] A.J. Viterbi, An intuitive justification and a simplified implementation of the MAP decoder for convolutional codes, *IEEE J. Sel. Areas Commun.* 16 (2) (1998) 260–264.
- [17] P. Robertson, P. Hoeher, E. Villebrun, Optimal and sub-optimal maximum a posteriori algorithms suitable for turbo decoding, *Eur. Trans. Telecommun.* 8 (2) (1997) 119–125.

- [18] J.G. Proakis, M. Salehi, *Digital Communications*, fifth ed., McGraw-Hill, Inc., New York, NY, 2008.
- [19] D. Torrieri, M.C. Valenti, Constellation labeling maps for low error floors, *IEEE Trans. Wireless Commun.* 7 (12) (2008) 5401–5407.
- [20] E. Dahlman, S. Parkvall, J. Skold, *4G LTE/LTE–Advanced for Mobile Broadband*, Academic Press, New York, NY, 2011.
- [21] C. Berrou, A. Glavieux, Near optimum error correcting coding and decoding: turbo codes, *IEEE Trans. Commun.* 44 (10) (1996) 1261–1271.
- [22] M.C. Valenti, J. Sun, The UMTS turbo code and an efficient decoder implementation suitable for software defined radios, *Int. J. Wireless Inform. Netw.* 8 (4) (2001) 203–216.

# Properties and measures of the radio channel

# 6

**H.L. Bertoni\***, **S.A. Torrico†**

*NYU Tandon School of Engineering, Brooklyn, NY, United States\** *Comsearch, Ashburn, VA, United States†*

## CHAPTER OUTLINE

<b>6.1</b>	<b>Introduction</b> .....	193
<b>6.2</b>	<b>Antenna and Propagation Fundamentals</b> .....	194
6.2.1	Antenna Gain .....	194
6.2.2	Path Gain/Loss .....	196
6.2.3	Fresnel Zones and the Local Properties of Radiation .....	196
<b>6.3</b>	<b>Models of Multipath Propagation</b> .....	197
6.3.1	Channel Response for Isotropic Antennas .....	199
6.3.2	Channel Response With Directive Antennas .....	202
<b>6.4</b>	<b>Measures of Narrowband Multipath Characteristics</b> .....	204
6.4.1	Spatial Fading of Multipath Narrowband Signals .....	204
6.4.2	Frequency Fading of Multipath Narrowband Signals .....	206
6.4.3	Correlation of Narrowband Spatial Fading .....	208
6.4.4	Time Dependence and Doppler Spread of Narrow Band Signals .....	211
<b>6.5</b>	<b>Measures of Multipath for Wideband Signals and Directive Antennas</b> .....	213
6.5.1	Spatial Variation of Pulse Response .....	214
6.5.2	Delay Spread for Wideband Channel Response .....	215
6.5.3	Coherence Bandwidth .....	217
6.5.4	Angle Spread for Highly Directive Antennas .....	217
<b>6.6</b>	<b>Shadow Fading, Range Dependence, and Cross-Polarization</b> .....	219
6.6.1	Separating Shadow Fading From Range Dependence .....	220
6.6.2	Cross-Polarization Coupling .....	222
	<b>References</b> .....	223

## 6.1 INTRODUCTION

Radio transmission has made its impact on communications based on three inherent properties: (1) it can cover large distances; (2) it allows for broadcast (point to multipoint); and (3) it allows for mobility. While some systems still make use of

the first two properties, modern wireless systems primarily depend on radio links to provide for mobility. The new applications demand high data rates, requiring wide bandwidth systems that by necessity have center frequency  $f$  in the UHF band (300 MHz to 3 GHz), or above. As a result it is especially important to understand spatial and frequency variations of the received signal for wavelengths  $\lambda = c/f$  of about 1 m or smaller (speed of light  $c \approx 3 \times 10^8$  m/s). Because the most common radio links are to handheld devices, the propagation conditions of greatest commercial interest are those found where people are, in man-made environments. While many initial studies of the radio channel characteristics in cities were carried out for frequencies in the UHF band, as summarized in [1], frequencies up to about 60 GHz are now being considered for millimeter wave systems [2].

This chapter is intended to provide simple models describing how the physical properties of radiowaves in man-made environments leads to a multipath description of propagation and how this description when filtered through system parameters, such as bandwidth and antenna gain, leads to the observed channel characteristics. We start by discussing some antenna and propagation fundamentals as they impact received power, as well as the local properties of the propagation, under the simplest conditions. Subsequently we identify simple models of propagation that illustrate the sources of multipath and investigate the effects produced by multipath together with various commonly used measures. Finally we briefly examine other sources of channel variability that have weak frequency dependence and affect all systems.

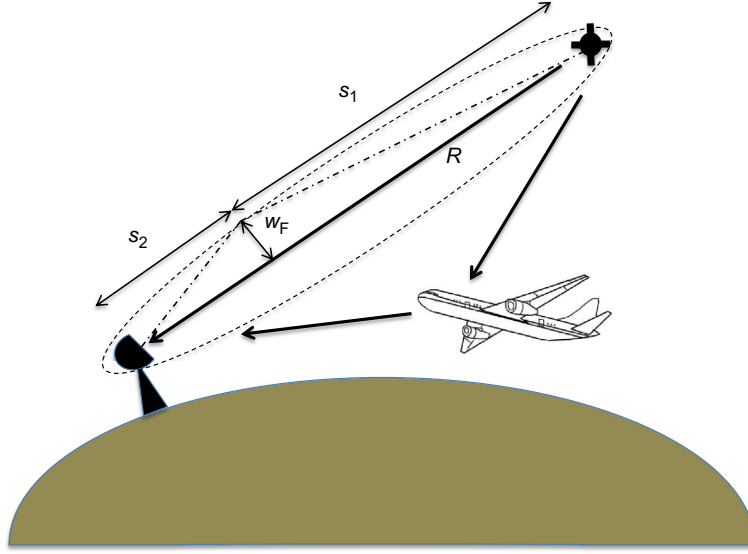
---

## 6.2 ANTENNA AND PROPAGATION FUNDAMENTALS

The radio channel is usually considered to include all cables and hardware between the transmitter box and receiver box, as well as the physical environment around and between the antennas. The cables and hardware are under the control of the designer and can be accounted for independently. In order to focus on the physical environment, we assume that all cables and hardware are matched and loss free. Under these conditions the propagation between antennas is reciprocal. That is to say, if antenna 1 receives power  $P_R$  when antenna 2 transmits power  $P_T$ , then the same power  $P_R$  will be received by antenna 2 when 1 transmits power  $P_T$  [3]. Reciprocity allows us to consider either antenna as the transmitter at our convenience.

### 6.2.1 ANTENNA GAIN

The simplest physical environment occurs when the antennas are located in free space, such as for communication between satellites or from an overhead satellite to ground, as suggested in Fig. 6.1. The satellite antenna radiates electric and magnetic fields that have the radial dependence  $e^{-jkr}/R$  of a spherical wave, where  $R$  is the radial distance and  $k = 2\pi/\lambda = \omega/c$  is the wavenumber. Consistent with conservation of energy, these fields carry power in the radial direction such that the total radiated power  $P_T$  at a distance  $R$  is spread over the area  $4\pi R^2$  of the sphere.

**FIG. 6.1**

Free space propagation from a satellite to a ground station showing the Fresnel zone about the direct ray.

Thus, the power density  $p(R, \theta_1, \phi_1)$  in watts per meter square in the polar direction  $(\theta_1, \phi_1)$  from the source, can be expressed as [1–3]

$$p(R, \theta_1, \phi_1) = P_T \frac{g_1(\theta_1, \phi_1)}{4\pi R^2}. \quad (6.1)$$

Here  $g_1(\theta_1, \phi_1)$  is the directive gain or directivity of the antenna and describes the relative strength of the radiation in different directions. The directivity of any antenna must satisfy the condition

$$\int_0^{2\pi} \int_0^\pi g(\theta, \phi) \sin \theta \sin \phi d\theta d\phi = 4\pi. \quad (6.2)$$

The maximum value of  $g(\theta, \phi)$  is referred to as the antenna gain relative to isotropic or simply the antenna gain, and given the symbol  $G$ .

If it could exist, an isotropic antenna would have directivity  $g = 1$  for all directions. Linear antennas, such as a half-wave dipole, are called omnidirectional because the directivity is the same for all directions  $\phi$  in the horizontal plane. A very short (Hertz) dipole has directive gain  $g(\theta, \phi) = (3/2) \sin^2 \theta$  [3]. Other antennas, such as a parabolic dish or an array of circular shape, can produce spot beams, similar to a flashlight beam. Suppose that the radiation is uniform within a cone of half-angle  $\Omega$  in radians and zero outside. Within the spot  $g(\theta, \phi) = G$  so that the antenna gain

is the ratio of the total area of a sphere to the area of the spot. Thus, for narrow beams  $G = 4\pi/(\pi\Omega^2) = 4/\Omega^2$ . For example, if the half-angle is 5 degrees, then  $\Omega = 0.0873$  radians, and  $G = 525$  or 27.2 dB.

The receiving antenna, shown as the ground station in Fig. 6.1, has an effective receiving area  $A_{e2}$  in the direction of the satellite. Assuming the polarization of the antenna to be the same as that of the incoming field, the received power is  $P_R = pA_{e2}$ . For any antenna, the effective receiving area is related to the directivity through the relation [1,3]

$$A_e = \frac{\lambda^2}{4\pi} g(\theta, \phi). \quad (6.3)$$

If the antenna is large, the effective receiving area can be nearly equal to the physical size of the antenna. Using this approximation, a parabolic dish having spot beam with 5 degrees half-angle would need an area  $A_e = \lambda^2/(\pi\Omega^2)$  or a diameter  $dia = 2\lambda/(\pi\Omega)$  of  $7.3\lambda$ .

## 6.2.2 PATH GAIN/LOSS

When discussing channel characteristics it is usual to take the ratio of received to transmitted power. This ratio is called the path gain and is written  $PG = P_R/P_T$ . For antennas in free space, it is seen from Eqs. (6.1) and (6.3) that the free space path gain is

$$PG = g_1(\theta_1, \phi_1)g_2(\theta_2, \phi_2) \left( \frac{\lambda}{4\pi R} \right)^2, \quad (6.4)$$

where  $(\theta_2, \phi_2)$  is the polar direction of the transmitter as seen from the receiver. The technical literature more commonly refers to the path loss  $L$ , which is the inverse of the path gain. Whereas  $PG$  is always smaller than unity and usually orders of magnitude smaller,  $L$  is greater than unity and commonly expressed in decibel.

Eq. (6.4) embodies the dilemma of using higher frequency to achieve high data rates. Because of the term  $\lambda^2$  in the numerator, for fixed transmitter power  $P_T$  the received power decreases strongly with frequency. Using antenna gain to compensate for the  $\lambda^2$  dependence involves antennas that are larger compared to wavelength, and correspondingly more directive, thus demanding more careful orientation.

## 6.2.3 FRESNEL ZONES AND THE LOCAL PROPERTIES OF RADIATION

Fig. 6.1 illustrates another feature of wave propagation that is important in understanding multipath effects. We have drawn in the Fresnel zone, which is an ellipsoid of revolution about the direct path from the satellite to the ground station. The Fresnel zone is defined such that length of the line from one antenna to the surface and thence to the other antenna is  $\lambda/2$  longer than the direct path. (Strictly speaking this is the first Fresnel zone, but for simplicity we will refer to it as the Fresnel zone.) It is

principally through this region that the direct signal propagates [1]. An object, such as the airplane, outside the Fresnel zone can scatter the signal radiated by the antenna, thereby giving rise to additional contributions to the received signal, but does not alter the direct signal. However, if the object penetrates the Fresnel zone, then the direct signal is no longer that for free space. As a result, the Fresnel zone is a measure of the localization of the region along a particular path by which a radiated signal arrives at the receiver.

For distances  $R$  that are large compared to  $\lambda$ , the radius  $w_F$  of the Fresnel zone can be approximated as [1]

$$w_F = \sqrt{\frac{\lambda s_1 s_2}{R}}, \quad (6.5)$$

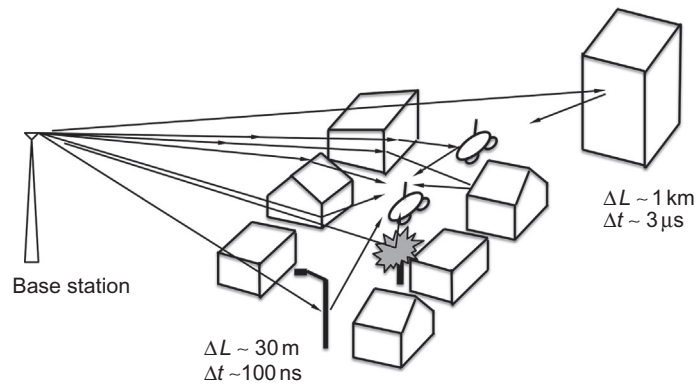
where the distances  $s_1$  and  $s_2$  are shown in Fig. 6.1. The maximum width of the Fresnel zone occurs at the midpoint and is given by  $2w_F = \sqrt{\lambda R}$ . As an example, consider 3 GHz ( $\lambda = 0.1$  m) transmission for a low orbit satellite with  $R = 400$  km. The maximum diameter of the Fresnel zone is then 200 m. Close to the earth station  $s_1 \ll s_2 \approx R$  and the diameter of the Fresnel zone is  $2w_F = 2\sqrt{\lambda s_2}$ . For  $s_2 = 8$  km, the altitude at which commercial airplanes fly, the Fresnel zone diameter is 56 m, which is on the order of the size of a commercial airplane so that significant link degradation can occur as the airplane passes through the Fresnel zone.

On terrestrial radio links in cities, the link distances are typically on the order of 1 km. At 1 GHz ( $\lambda = 0.3$  m), for example, the maximum diameter of the Fresnel zone for  $R = 1$  km is  $2w_F = 17$  m, which is on the order of building dimensions. The significance of this observation is that the electromagnetic waves propagating from transmitter to receiver will undergo interaction with individual buildings and other structures in sequence along the paths linking transmitter and receiver. In other words, we can think of the fields as propagating along rays that are reflected and scattered or diffracted by structures in sequence along the paths. This ray representation in physical space is approximated in communication theory by the multipath representation of the received signal as a series of delayed and scaled versions of the transmitted pulse, as discussed in the next sections.

---

## 6.3 MODELS OF MULTIPATH PROPAGATION

When one or both of the antennas is located among scattering obstacles, such as buildings, there are typically multiple paths by which the transmitted signal can arrive at the receiver. The number and distribution of the multipath arrivals depends on the physical environment and on the placement of the antennas within it. One such case is indicated in Fig. 6.2 for communication between a base station antenna elevated above the surrounding buildings and a mobile at street level. For such links the base station is often not visible from the mobile, so that there is no direct ray path linking the two. As suggested in Fig. 6.2, a cluster of signals from the base

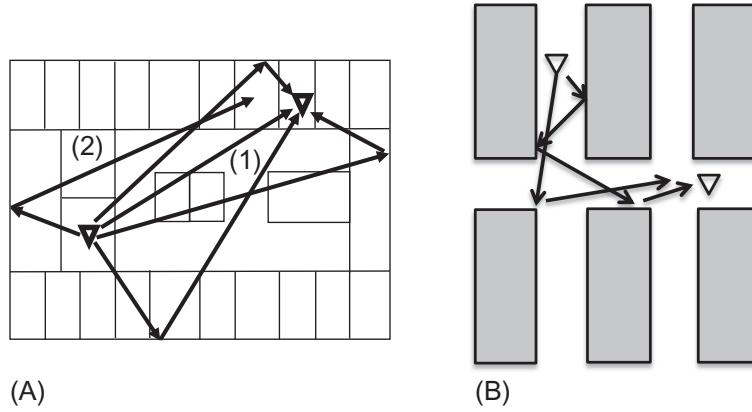
**FIG. 6.2**

For communication between a base station antenna elevated above the surrounding buildings and a mobile located in the building clutter, multiple ray paths arise from scattering by buildings and other objects in the environment.

station reach the mobile after reflection or scattering at building surfaces, lamp posts, vehicles, trees, etc., and as a result of diffraction over or around the building edges, tree canopies, etc., in the vicinity of the mobile [4–6]. In addition, signals reflected or scattered by large distant buildings can reach the mobile as a separate cluster after being rescattered by nearby objects.

Outdoors, the distances from the mobile to nearby objects are on the order of 30 m, so that the various ray contributions in the direct cluster have differences in the time of arrival at the mobile that are on the order of 100 ns. Other clusters may arrive as a result of first being scattered by large distant buildings. Since such scattering involves additional path length on the order of 1 km, arrival of such scattered clusters will exhibit additional delays on the order of 3  $\mu\text{s}$ .

As suggested in Fig. 6.2, and found in outdoor measurements, for example, [4–9], the various ray paths at the mobile take all directions in the horizontal plane and vertically in a wedge of angle up to the rooftops. At the elevated base station antenna the rays are in narrow wedge of angles in both the horizontal and vertical planes. For other link geometries and antenna placements, the foregoing description of the ray paths will be somewhat different. Two examples shown in Fig. 6.3 depict symmetric radio links wherein propagation is between antennas located in similar environments. For links on one floor of an office building, as in Fig. 6.3A, reflections from walls and objects will result in rays taking all directions around the antennas in the horizontal plane with a similar distribution occurring for both transmitter and receiver. In the case of mobile-to-mobile links in a high-rise urban environment, as suggested in Fig. 6.3B, ray paths may be concentrated along the street canyons but are expected to have similar distribution at both antennas.

**FIG. 6.3**

Radio links with symmetric ray distributions for both antennas: (A) on one floor of an office building; and (B) mobile to mobile communications on city streets.

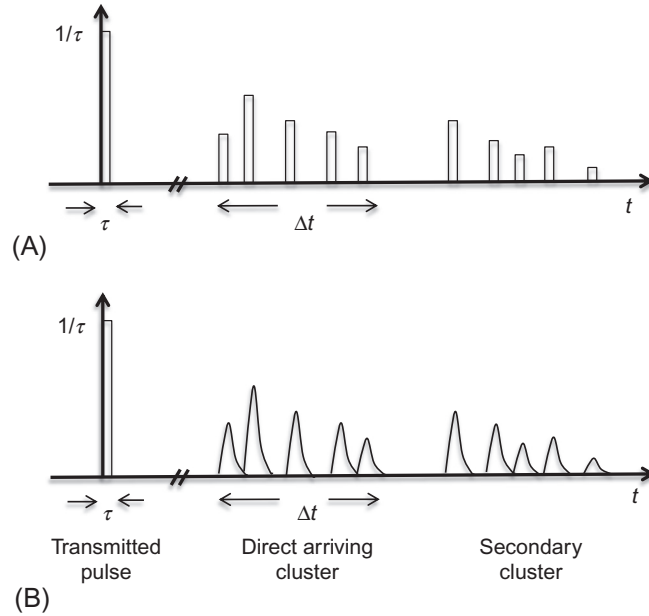
### 6.3.1 CHANNEL RESPONSE FOR ISOTROPIC ANTENNAS

Communication systems will experience the multipath environment in different ways depending on the system bandwidth and antenna beamwidth. In order to explore the influence of bandwidth, we first consider the case of isotropic antennas operating under the conditions suggested in Fig. 6.2. The idealized response for a system having very wide bandwidth is depicted in Fig. 6.4A. For this idealization, a narrow unit amplitude pulse transmitted at the base station is received as a series of impulses, so that the received voltage takes the form

$$V_R(t) = \sum_n a_n \delta(t - L_n/c), \quad (6.6)$$

where  $a_n$  is the amplitude associated with each ray path and  $L_n$  is the length of the ray. As discussed above, the differences in path length for the various rays is on the order of 30 m, so that the individual arrivals in the direct cluster will be spread over a time interval  $\Delta t$  that is several hundred nanoseconds. Other clusters with time delays on the order of microseconds will also be present.

Eq. (6.6) is commonly used for the channel impulse response. This expression is at best an approximation since the individual physical processes of reflection, scattering, and diffraction that give rise to the ray paths are themselves frequency dependent [10]. For example, radiowaves incident on a brick wall will undergo multiple internal reflections that stretch the reflected waves over several nanoseconds. As a result of frequency dependence, each multipath arrival will display a pulse

**FIG. 6.4**

Multipath response for a pulsed source: (A) as idealized; and (B) voltage envelope accounting for the frequency dependence of the physical processes.

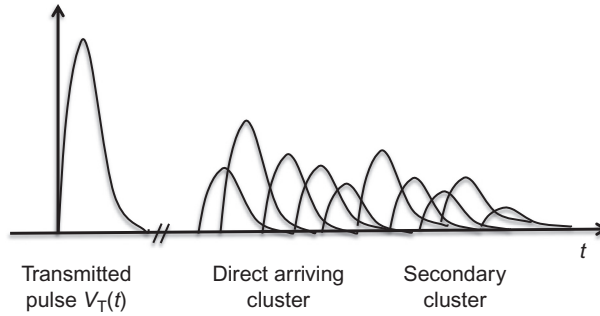
distortion that is dependent of the physical process involved. This distortion is suggested by the voltage envelopes of received multipath pulses in Fig. 6.4B, assuming no overlap between individual arrivals.

Since actual communication systems have a limited bandwidth, transmitted pulses will necessarily be of finite time duration. In order to observe the nanosecond distortion of individual multipath components due to the frequency dependence of the scattering, the system bandwidth would have to be on the order of 1 GHz or greater, as in ultra-wideband (UWB) systems [11]. To resolve individual multipath arrivals separated by 100 ns as expected on outdoor links the bandwidth must be on the order of 10 MHz, while resolving clusters separated by microseconds can be done using a bandwidth on the order of 1 MHz.

Fig. 6.5 suggests the voltage envelopes of the individual multipath components that would be detected for transmitted pulse  $V_T(t) \exp(j\omega_0 t)$  having bandwidth sufficient to separate individual multipath components. Here  $\omega_0$  is the center of the frequency band. In this case, the received phasor voltage takes the form

$$V_R(t) = \sum_n a_n e^{j\phi_n} e^{-j\omega_0 L_n/c} V_T(t - L_n/c), \quad (6.7)$$

where  $\phi_n$  is the additional phase change due to scattering. Because of the phase dependence on  $L_n$  in Eq. (6.7), various terms can add constructively or destructively

**FIG. 6.5**

Voltage envelopes of the multipath contributions for a pulsed source having finite bandwidth.

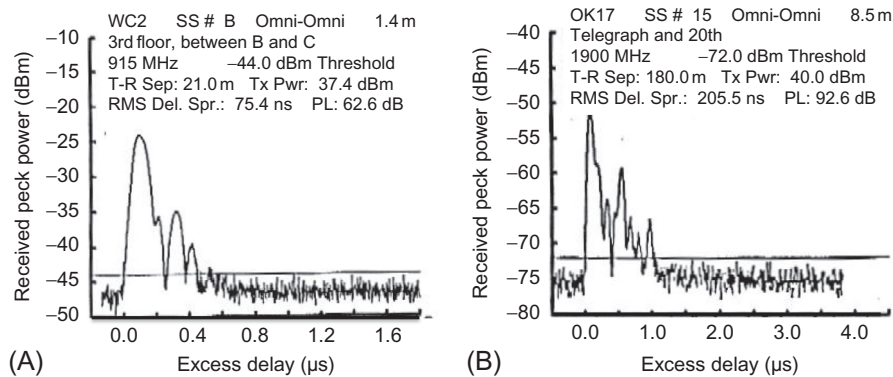
so that the received voltage is sensitive to the exact location of the scatterers and the mobile.

Typical measurement systems determine the received power as a function of time  $P_R(t)$ , which is proportional to  $|V_R(t)|^2$  and is referred to as the power delay profile. Two examples of measured power delay profiles are shown in Fig. 6.6 for omnidirectional antennas: Fig. 6.6A inside a large office building; and Fig. 6.6B in an urban area of mixed buildings [12]. Because it is difficult to determine the absolute starting time of a received pulse, the starting time in the plots is arbitrarily taken to be the first detectable signal. To account for the large dynamic range of the received signal, a decibel scale is used for the power axis. These two examples show many multipath arrivals occurring in clusters over time with dynamic range of more than 20 dB. In general, the amplitude within a cluster decreases with time and later clusters are weaker. On indoor links the path distances are shorter than outdoors, so that the overall time spread of the received signal is smaller [13].

When the carrier modulation  $V_T(t)$  is over time intervals substantially greater than  $10 \mu\text{s}$ , the transmission bandwidth is less than 100 kHz and the time dependence is essentially the same for all terms in Eq. (6.7). For such narrow band signals the modulation can be taken outside the sum so the received phasor voltage is given by

$$V_R(t) = V_T(t - R/c) \sum_n a_n e^{j\phi_n} e^{-j\omega_0 L_n/c}, \quad (6.8)$$

where  $R$  is the separation between antennas. Addition of the various terms in the summation term of Eq. (6.8) sets up a standing wave pattern in space, so that the received voltage is sensitive to the exact position of the mobile. The statistical properties of this standing wave pattern are discussed later.

**FIG. 6.6**

Examples of power delay profiles measured: (A) inside a large office building; and (B) in an urban environment of mixed buildings.

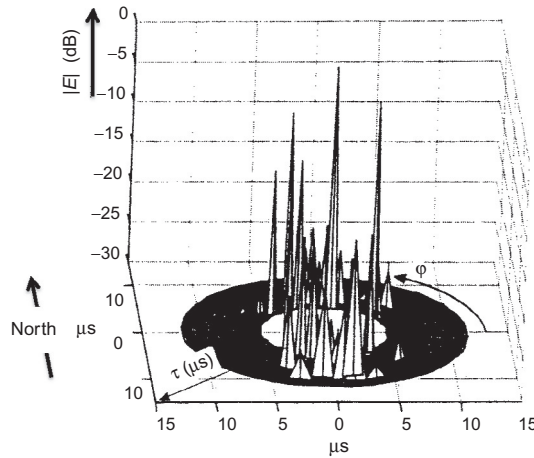
Source: Reprinted from *Experimental License Progress Report to FCC from Telesis Technology Laboratory*, Aug. 1991.

### 6.3.2 CHANNEL RESPONSE WITH DIRECTIVE ANTENNAS

Directive antennas have long been used for microwave links under conditions that are close to free space propagation. Cellular systems use vertical arrays of antennas having 120 degrees beam width in azimuth to give narrower beam width in elevation. To date highly directive array antennas have primarily been used to better document the complexity of the multipath arrivals in channel measurements [4–9]. Often the array is synthetic in that a single receiving antenna is moved systematically over the array locations under static conditions of the channel, such as that occurs at night when there is little or no traffic. Recording the amplitude and phase of the received signal, the measurements are later processed to simulate the response of a complete array. Results of one such set of measurements are shown in Fig. 6.7 for a mobile station at street level on a north-south street in Paris that is surrounded by 25–30 m high buildings [9]. In this 3D polar plot, the angle  $\varphi$  represents the angle of arrival of the multipath component as measured from south, the radial dimension gives the relative time delay  $\tau$  in microseconds, and the vertical dimension is power of the multipath component in decibel. The base station is located towards the northwest, and the system did not distinguish the vertical angle of arrival of the multipath components. Because of wave guiding by the high buildings, arrivals are mostly within  $\pm 45$  degrees from the street direction with strong components observed out to several microseconds from the first strong arrival from the north.

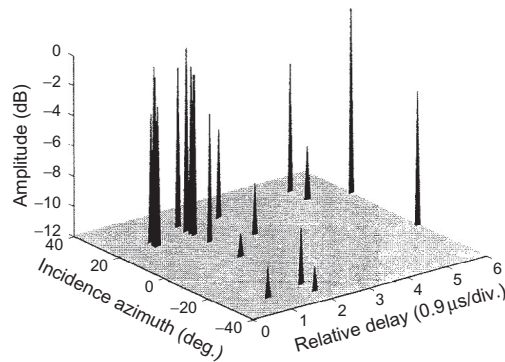
Multipath components have been measured at elevated base stations using pulsed systems with the mobile as source and a receiving array at the base station.

An example of such a measurement at 1800 MHz is shown in Fig. 6.8 [14]. Here the time delay and azimuth angle are plotted as rectangular coordinates, with

**FIG. 6.7**

Space-time pulses observe at street level on a north-south street in Paris from a base station located to the northwest. Resolution of the 890 MHz system is 100 ns in time and 5 degrees in azimuth angle. All elevation angles are included.

Source: © 1997 IEEE. Reprinted, with permission, from J. Fuhl, J.-P. Rossi, E. Bonek, *High-resolution 3-D direction-of-arrival determination for urban mobile radio*, *IEEE Trans. Antennas Propag.* 45 (1997) 672-682.

**FIG. 6.8**

Multipath components measured at an elevated base station in Aalborg, Denmark at 1800 MHz system.

Source: Reprinted with editor's permission from K.I. Pedersen, P.E. Mogensen, B.H. Fleury, F. Frederiksen, K. Olesen, S.L. Larsen, *Analysis of time, azimuth and Doppler dispersion in outdoor radio channels*, in: *Proceedings of ACTS*, 1997.

amplitude in decibel as the vertical coordinate. The main components arrive from the 20 degrees direction with an angle spread of about  $\pm 8$  degrees and relative delays out to several microseconds.

The concept of clusters of related ray paths, as discussed above was first proposed by Saleh and Valenzuela [15] to explain time delay characteristics they observed on indoor links. Since then, two groups, one at Helsinki University of Technology [4] and the other at Eindhoven University of Technology [6,7], have used measurements systems with very high time and space resolution to relate the clusters to groups of ray paths in space for outdoor links. The Helsinki group identified three types of clusters: (1) street-guided propagation; (2) direct propagation over the rooftops; and (3) scattering from high-rise objects [4]. These cluster types incorporate the various ray paths suggested in Fig. 6.2. The cluster type giving the dominant contribution in outdoor links will depend on the separation  $R$  between antennas, antenna height relative to the buildings, and the distribution of building heights. Similar techniques have been used to identify ray clusters on indoor links, as for example in [16].

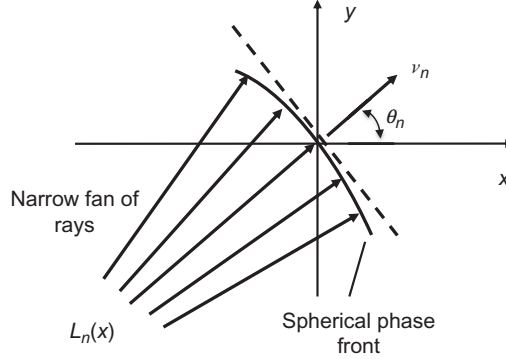
---

## 6.4 MEASURES OF NARROWBAND MULTIPATH CHARACTERISTICS

Various measures of the channel characteristics have been developed in connection with different system applications. Measures of multipath fading were developed early on in connection with narrow band cellular mobile radio channels. Later, measures of delay spread and angle spread became important for more advanced digital systems. Treating the topics in this order is also useful for understanding.

### 6.4.1 SPATIAL FADING OF MULTIPATH NARROWBAND SIGNALS

As suggested in Fig. 6.2 for a street level mobile, the rays at the mobile arrive from all directions in the horizontal plane and over a limited range of angles in the vertical direction. For simplicity we assume the rays to be horizontal and consider the spatial variation in the received signal for small displacements in the horizontal ( $x, y$ ) plane. Consider a narrow family of rays illuminating points in the plane in the vicinity of a mobile, which is assumed to be at the origin  $(0, 0)$ , as shown in Fig. 6.9. The rays are associated with the  $n$ th term in Eq. (6.8) and appear to originate from a common point such as a local scatterer, or the image of the transmitter in a reflecting building surface, etc. In general, the distance from the apparent source to the origin, which is taken here to be the ray length  $L_{n0}$ , is large compared to wavelength. The unit vector  $\nu_n$  in the direction of propagation of this central ray makes an angle  $\theta_n$  to the positive  $x$ -axis, as shown in Fig. 6.9. The phase of the fields along the various rays will be constant over spherical phase fronts centered about the common point. For small displacements from the origin  $(0, 0)$  in Fig. 6.9 the spheres can be approximated by plane phase fronts. With this approximation the length of a ray reaching a point along the  $x$ -axis near to the origin is given by

**FIG. 6.9**

A narrow fan of rays illuminating points near the origin in the  $(x, y)$  plane.

$$L_n(x) = L_{n0} + x \cos \theta_n. \quad (6.9)$$

Assuming for simplicity that  $V_T(t) = 1$ , the received voltage will be independent of time, but will depend on position  $x$ . Using Eq. (6.9) in Eq. (6.8), and defining the wave number  $k = \omega_0/c = 2\pi/\lambda$ , the received voltage  $V_R(x)$  is given by

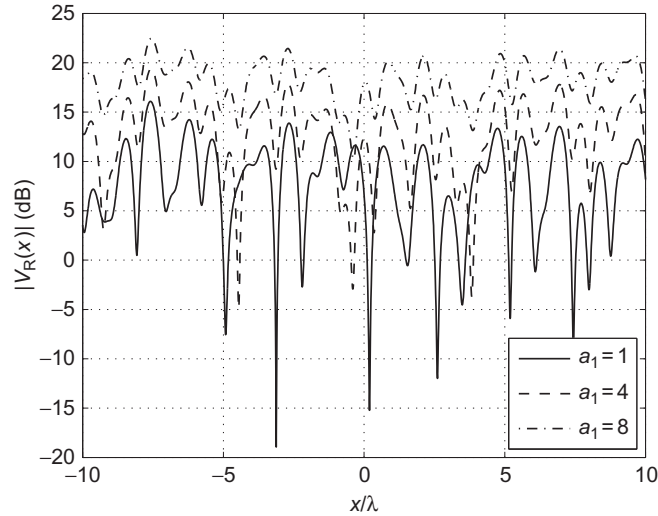
$$V_R(x) = \sum_n a_n e^{j(\varphi_n - kL_{n0})} \exp(-jkx \cos \theta_n). \quad (6.10)$$

In order to illustrate properties resulting from the summation of multiple waves in Eq. (6.10), we have plotted the magnitude of the received voltage computed assuming eight rays arriving at angles randomly selected in the interval  $0 < \theta_n < 2\pi$ , and with randomly selected phase  $\varphi_n - kL_{n0}$ . Results are shown in Fig. 6.10 for displacements up to  $\pm 10\lambda$  on either side of the origin.

The plots in Fig. 6.10 are for three choices of the amplitudes  $a_n$ : Fig. 6.10A all amplitudes equal  $a_n = 1$ ; Fig. 6.10B with  $a_1 = 4$ , and all other  $a_n = 1$ ; and Fig. 6.10C with  $a_1 = 8$ , and all other  $a_n = 1$ . It is seen that when the amplitudes are equal, as might be expected when the base station is not visible from the mobile, there are deep fades of 20 dB. The distance between fades is somewhat greater than  $\lambda/2$ , but less than  $\lambda$ . When the amplitude of one wave is somewhat stronger than the other waves, the fades generally are smaller, but there can still be an occasional deep fade. However, when the amplitude of one wave is as large as the sum of the other waves, as might happen when the base station is within line-of-sight (LOS) of the mobile, the fades are smaller.

Statistical models of the fading can be constructed from the spatial dependence by normalizing  $|V_R(x)|$  to its spatial average  $\langle V_R \rangle$  defined by

$$\langle V_R(x) \rangle = \frac{1}{2W} \int_{-W}^W |V_R(x)| dx, \quad (6.11)$$

**FIG. 6.10**

Variation of received voltage magnitude for eight incident waves with: (A) all amplitudes equal  $a_n = 1$ ; (B) with  $a_1 = 4$ , and all other  $a_n = 1$ ; and (C) with  $a_1 = 8$ , and all other  $a_n = 1$ .

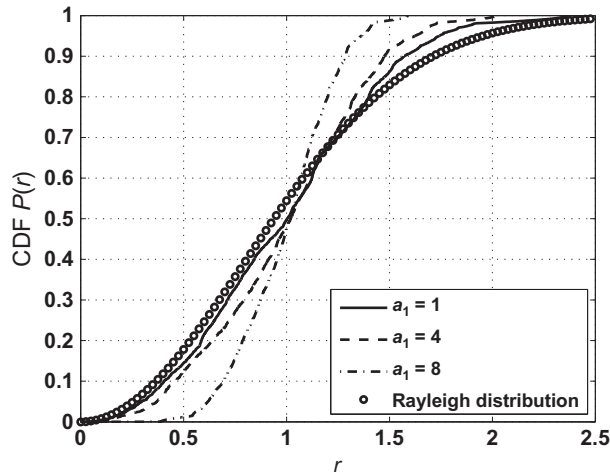
where  $2W$  is a sector length spanning 20 or so wavelengths. The cumulative distribution functions (CDFs) obtained from the three plots in Fig. 6.10 are shown in Fig. 6.11. Also shown is a plot of the Rayleigh distribution having CDF( $r$ ) given by [17]:

$$\text{CDF}(r) = 1 - \exp(-\pi r^2/4), \quad (6.12)$$

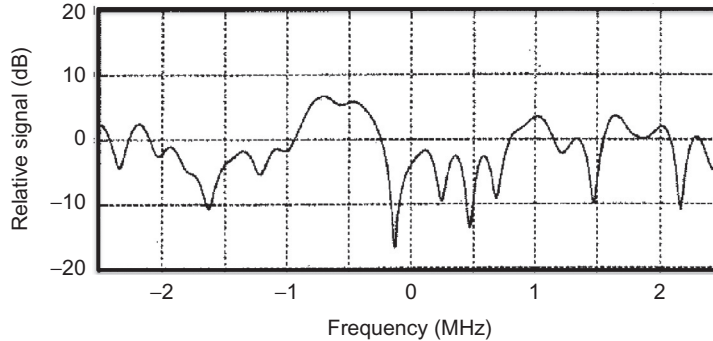
where  $r$  is the random variable. When the amplitudes of the eight waves are equal, the distribution function is close to a Rayleigh distribution, while it departs when amplitude of one ray is significantly larger than the others. In the latter case the distribution function is Rician [17].

### 6.4.2 FREQUENCY FADING OF MULTIPATH NARROWBAND SIGNALS

The phase of each term in the summation of expression Eq. (6.8) for the received voltage due to a narrow band source has an explicit dependence on the center frequency  $\omega_0$ . As the frequency changes, the phases of the terms will change so that the summation can be expected to show fading. This frequency dependence is shown in Fig. 6.12 for measurements made in Toronto, where the frequency was varied about a center frequency of 910 MHz on a 1.2 km link [18]. In Fig. 6.12 the average spacing between fades is about  $\Delta f = 0.3$  MHz. As the phase difference  $2\pi f(L_n - L_m)/c$  between two terms in Eq. (6.8) changes by  $2\pi$  the terms go in and out of phase. They return to the same relative phase in frequency interval  $\Delta f = c/(L_n - L_m)$ .

**FIG. 6.11**

Cumulative distribution functions of the received voltage in Fig. 6.10 normalized to the average.

**FIG. 6.12**

Frequency dependence of the radio channel centered at 910 MHz measured in an urban environment.

Source: © 1994 IEEE. Reprinted, with permission, from E.S. Sousa, V.M. Jovanovic, C. Daigneault, Delay spread measurements for the digital cellular channel in Toronto, *IEEE Trans. Veh. Technol.* 43 (1994) 837–847.

The fade spacing  $\Delta f = 0.3$  MHz therefore corresponds to differences in path length  $L_n - L_m$  on the order of 1 km. These frequency fading characteristics are related to the pulse response discussed in Section 6.5 below via the Fourier transform, and are considered further there.

If a signal transmission is spread over wide spectrum of narrowband channels with different center frequencies  $\omega_0$  and averaged, the spatial variation can be eliminated. This result can be seen from averaging the received power  $P_R(t; \omega_0)$  for each center frequency over a band  $\omega_1 \leq \omega_0 \leq \omega_2$ . Thus, the frequency averaged received power  $\langle P_R(t) \rangle$  is

$$\begin{aligned} \langle P_R(t) \rangle &= \frac{1}{\omega_2 - \omega_1} \int_{\omega_1}^{\omega_2} |V_R(t; \omega_0)|^2 d\omega_0 \\ &= \frac{1}{\omega_2 - \omega_1} \int_{\omega_1}^{\omega_2} \sum_n \sum_m a_n a_m e^{j(\phi_n - \phi_m)} e^{-j\omega_0(L_n - L_m)/c} d\omega_0. \end{aligned} \quad (6.13)$$

Because the amplitudes  $a_n$  and phases  $\phi_n$  are weak functions of frequency, the integration in Eq. (6.13) reduces to the last exponential. For wide enough frequency band the integral can be approximated by

$$\frac{1}{\omega_2 - \omega_1} \int_{\omega_1}^{\omega_2} e^{-j\omega_0(L_n - L_m)/c} d\omega_0 \approx \delta_{nm}, \quad (6.14)$$

where  $\delta_{nm}$  is the Kroneker delta. Hence

$$\langle P_R(t) \rangle = \sum_n a_n^2, \quad (6.15)$$

which is the sum of the individual ray powers and no longer exhibits spatial fading.

### 6.4.3 CORRELATION OF NARROWBAND SPATIAL FADING

Understanding the relation between the signals received by antennas at neighboring locations can be used to mitigate the effect of the fading through spatial diversity, or make use of the multipath, as in MIMO systems. This relation is embodied by the complex correlation function  $C(s)$  for points separated by a distance  $s$  along the  $x$ -axis. The correlation is defined as

$$C(s) = \left\{ \frac{1}{2W} \int_{-W}^W V_R(x) V_R^*(x-s) dx \right\} / \left\{ \frac{1}{2W} \int_{-W}^W |V_R(x)|^2 dx \right\}, \quad (6.16)$$

where the interval  $2W$  is large compared to  $s$ .

Using the approximation (Eq. 6.10) for the received voltage the numerator of Eq. (6.16) is seen to be

$$\begin{aligned} &\frac{1}{2W} \int_{-W}^W V_R(x) V_R^*(x-s) dx \\ &= \sum_n \sum_m a_n a_m e^{j(\phi_n - \phi_m)} e^{jk(L_n - L_m)} e^{-jks \cos \theta_m} \left\{ \frac{1}{2W} \int_{-W}^W e^{-jkx(\cos \theta_n - \cos \theta_m)} dx \right\}. \end{aligned} \quad (6.17)$$

The integral on the right in Eq. (6.17) will be unity for  $n = m$ . Under some circumstances, such as for reception at a street level mobile from an elevated base station, the angles  $\theta_n$  and  $\theta_m$  are not nearly equal for  $n \neq m$ . Assuming that  $W$  is large, the integral will be small so that the integral can be approximated by the Kroneker delta  $\delta_{nm}$ . With this approximation

$$\frac{1}{2W} \int_{-W}^W V_R(x) V_R^*(x-s) dx = \sum_n a_n^2 \exp(-jks \cos \theta_n). \quad (6.18)$$

The integral in the denominator of Eq. (6.16) is also approximated by setting  $s = 0$  in Eq. (6.18). The resulting expression is

$$\frac{1}{2W} \int_{-W}^W |V_R(x)|^2 dx = \sum_n a_n^2. \quad (6.19)$$

Eq. (6.19) can be interpreted as showing that when the received power is averaged over a sector, the resulting value is the same as would be found by summing the powers that would be obtained if ray contribution was received separately. With the help of Eqs. (6.18) and (6.19) it is seen from Eq. (6.16) that

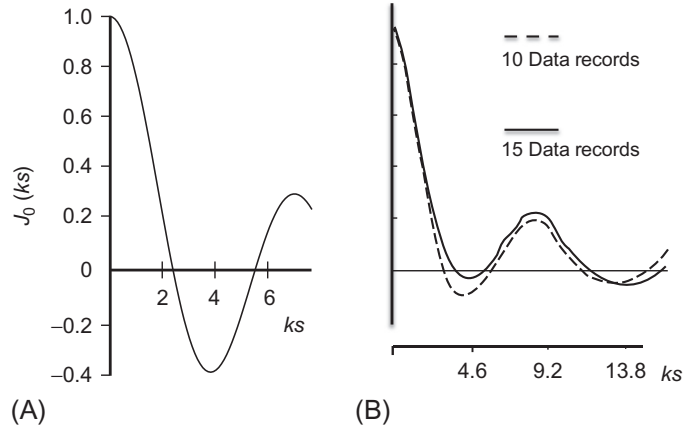
$$C(s) = \sum_n a_n^2 \exp(-jks \cos \theta_n) / \sum_n a_n^2. \quad (6.20)$$

For symmetric links where both antennas are among the scatterers, there will be some pairs of rays, such as Eqs. (6.1) and (6.2) in Fig. 6.3A, for which  $\theta_n$  and  $\theta_m$  at one end of the link can be nearly equal, even though the paths are very different at the other end of the link. In this case, averaging over both ends of the link is required to obtain the Kroneker delta approximation [19,20].

The *correlation function at street level*  $C_{SL}(s)$  can be further modeled by assuming that the rays arrive uniformly and densely distributed over all directions in the horizontal plane, so that the summation in Eq. (6.20) can be replaced by an integral over  $\theta$ . If all amplitude are further taken to have the same value  $a_n = A$ , then the correlation at street level becomes

$$C_{SL}(s) = \int_0^{2\pi} A^2 e^{-jks \cos \theta} d\theta / \int_0^{2\pi} A^2 d\theta = \frac{1}{2\pi} \int_0^{2\pi} e^{-jks \cos \theta} d\theta = J_0(ks). \quad (6.21)$$

Here  $J_0(ks)$  is the zero order Bessel function of the first kind and is plotted in Fig. 6.13A. If we consider the value  $C_{SL}(s) = 0.5$  to define the boundary between correlation and decorrelation, then the received signals decorrelate for distance such that  $ks = 2\pi s/\lambda > 1.6$ , or  $s > \lambda/4$ . For comparison with this simple expression, we have plotted in Fig. 6.13B the autocorrelation function  $C_{SL}(s)$  taken from measurement at 821 MHz [21]. While there are discrepancies between the model and measurements, the simple model works surprisingly well.

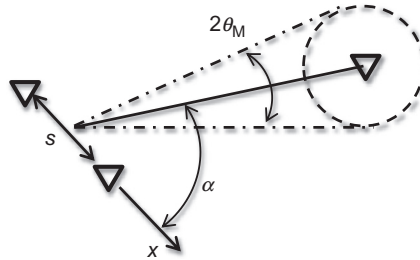
**FIG. 6.13**

Correlation function  $C(s)$  at street level: (A) as computed from a simple model of multipath; and (B) obtained from measurements.

Source: Based on measurements reported in S.-B. Rhee, G.I. Zysman, *Results of suburban base station spatial diversity measurements in the UHF band*, *IEEE Trans. Commun.* 22 (1974) 1630–1636.

The *correlation function at an elevated base station*  $C_E(s)$  can similarly be modeled. In this case the rays are limited to a narrow sector of angular width  $2\theta_M$  about the direction to the mobile, as indicated in Fig. 6.14. Two base station antennas are separated by a distance  $s$  that is taken to be along the  $x$ -axis. Assuming the rays to be densely and uniformly distributed in the sector and to have the same amplitudes, then replacing the summation by integration gives

$$C_E(s) \approx A^2 \int_{\alpha-\theta_M}^{\alpha+\theta_M} e^{-jks \cos \theta} d\theta / A^2 \int_{\alpha-\theta_M}^{\alpha+\theta_M} d\theta = \frac{1}{2\theta_M} \int_{\alpha-\theta_M}^{\alpha+\theta_M} e^{-jks \cos \theta} d\theta. \quad (6.22)$$

**FIG. 6.14**

Orientation geometry for determining the correlation between two base station antennas.

To evaluate the integral in Eq. (6.19) we make the substitution  $u = ks \cos \theta$  so that

$$C_E(s) = \frac{1}{2\theta_M} \int_{ks \cos(\alpha-\theta_M)}^{ks \cos(\alpha+\theta_M)} \frac{e^{-ju}}{(-ks \sin \theta)} du. \quad (6.23)$$

If the angular sector is small, the term  $\sin \theta$  in the denominator will have only small variation over the interval of integration and can be replaced by  $\sin \alpha$ . With this approximation

$$\begin{aligned} C_E(s) &\approx \frac{1}{2\theta_M(-ks \sin \alpha)} \int_{ks \cos(\alpha-\theta_M)}^{ks \cos(\alpha+\theta_M)} e^{-ju} du \\ &= \frac{\sin(ks \sin \alpha \sin \theta_M)}{\theta_M ks \sin \alpha} e^{-jks \cos \alpha \cos \theta_M} \end{aligned} \quad (6.24)$$

or

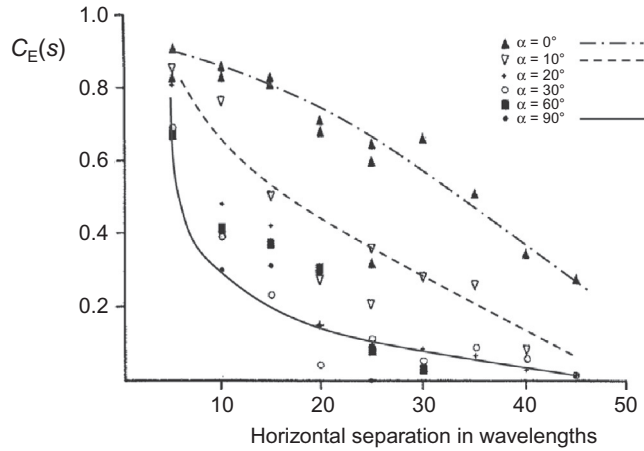
$$|C_E(s)| \approx \left| \frac{\sin(ks \theta_M \sin \alpha)}{ks \theta_M \sin \alpha} \right|. \quad (6.25)$$

Taking decorrelation to occur when  $|C_E(s)| = 0.5$ , then the two base station antennas in Fig. 6.14 are decorrelated when  $ks \theta_M \sin \alpha > 1.9$  or  $s > 0.302\lambda / (\theta_M \sin \alpha)$ . The decorrelation distance is smallest when the axis of antenna separation is perpendicular to the direction towards the mobile (when  $\alpha = 90$ ) degrees and becomes infinite when the axis of separation is in the direction of the mobile (when  $\alpha = 0$  degrees). Taking  $\theta_M = 5$  degrees or 0.087 radians, then for  $\alpha = 90$  degrees the distance for decorrelation is  $s = 3.5\lambda$ .

For comparison with the foregoing model, results from measurements made at 900 MHz in Liverpool [22] are shown in Fig. 6.15. For these measurements the correlation function was determined from the magnitude of the received voltage, rather than the complex voltage employed in Eq. (6.16). Correlation of the voltage magnitude is not simply related to phasor voltage correlation defined in Eq. (6.16), but does show the same dependence on  $\alpha$ . Curves that approximately fit the measurement points have been drawn in for  $\alpha = 0, 10$ , and 90 degrees. For  $\alpha = 90$  degrees, decorrelation occurs at about  $s = 5\lambda$  and increases significantly as  $\alpha$  decreases to zero.

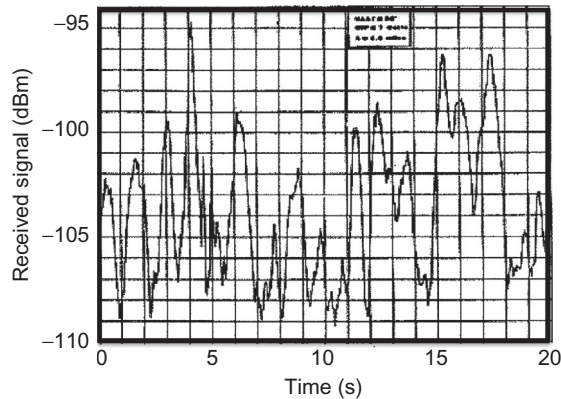
#### 6.4.4 TIME DEPENDENCE AND DOPPLER SPREAD OF NARROW BAND SIGNALS

Fig. 6.2 suggests two sources of time dependence of the received signal for narrow band signals. One source is due to the motion of scattering objects in the vicinity of the mobile, such as moving vehicle, pedestrian traffic, or wind-blown trees. The time variation of the voltage measured by a stationary receiver in an urban setting for a constant amplitude 900 MHz sine wave transmission [23] is shown in Fig. 6.16.

**FIG. 6.15**

Correlation of received voltage envelopes measured at 900 MHz for elevated base station antennas in Liverpool, England.

Source: Based on F. Adachi, M.T. Feeney, J.D. Parsons, A.G. Williamson, *Cross correlation between the envelopes of 900 MHz signals received at a mobile radio base station site*, *IEEE Proc.* 133 (Pt. F) (1980) 506–512.

**FIG. 6.16**

Time variation of signal received by a stationary mobile for constant amplitude transmission at 900 MHz in an urban environment.

Source: © 1988 IEEE. Reprinted, with permission, from N.H. Shepherd, *Special issue on radio propagation*, *IEEE Trans. Veh. Technol.* 37 (1988) 45.

Fade depth is typically about 10 dB and the time between successive fades is about 1 s. Fading due to pedestrian traffic is very important for indoor links and has been widely measured—see, for example, [24,25].

A second source of time variation is motion of the mobile through the standing wave pattern in space. This variation will have the same dependence as shown in Fig. 6.10 with  $x$  replaced by  $vt$  where  $v$  is the speed of the mobile. Both the time dependent effects can of course be viewed as imparting a spread in the received frequencies. The Doppler spread for high speed mobiles is especially important.

Doppler shift  $\Delta f$  for a mobile moving with velocity  $v$  at an angle  $\theta$  to the direction of a single arriving ray, is given by  $\Delta f = (vf/c) \cos \theta$ . When many rays arrive at the mobile from different directions, the distribution of power over the range of Doppler frequencies is given by the power spectral density, which can be found from the autocorrelation function (Eq. 6.16) [26]. The correlation function (Eq. 6.16) can be viewed as resulting from the displacement  $s = v\tau$  of the mobile in time  $\tau$ . If  $\Delta\omega = 2\pi\Delta f$  is the deviation of the angular frequency from  $\omega_0$ , then the power spectral density  $P(\Delta\omega)$  is given by the Fourier transform of  $C(v\tau)$ , or

$$P(\Delta\omega) = \int_{-\infty}^{\infty} C(v\tau) e^{-j\Delta\omega\tau} d\tau. \quad (6.26)$$

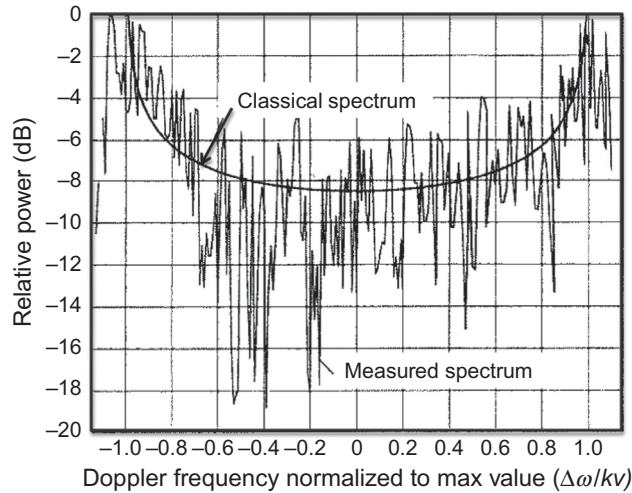
Using the simple model of the correlation function (Eq. 6.21) for street level mobiles, the power spectral density can be evaluated in closed form [27] and is found to be

$$P(\Delta\omega) = \int_{-\infty}^{\infty} J_0(kv\tau) e^{-j\Delta\omega\tau} d\tau = \frac{2/kv}{\sqrt{1 - (\Delta\omega/kv)^2}} U(kv - |\Delta\omega|). \quad (6.27)$$

A plot of Eq. (6.27) labeled Classical Spectrum is shown in Fig. 6.17 as a function of the Doppler shift  $\Delta\omega$  normalized to the maximum value  $v\omega_0/c = kv$ . The singular behavior in Eq. (6.27) at  $\Delta\omega = \pm kv$  is a result of assuming all of the rays to arrive in the horizontal plane. For comparison, a spectrum measured at 1800 MHz is shown in Fig. 6.17 [14]. The fact that the rays do not arrive at the mobile uniformly distributed over a continuum of directions in the horizontal plane is evident in the deviations from the classical spectrum. Since the Doppler shift is related to the angle of arrival  $\theta$ , the presence and absence of contributions in the measured spectrum indicates that the rays arrive at discrete angles.

## 6.5 MEASURES OF MULTIPATH FOR WIDEBAND SIGNALS AND DIRECTIVE ANTENNAS

In order to improve the reliability and capacity of radio communication systems, various modulation and multiple access schemes have been developed that spread the transmission over a wide bandwidth. Other schemes have been proposed that make use of directive antennas. It is therefore of interest to understand the channel

**FIG. 6.17**

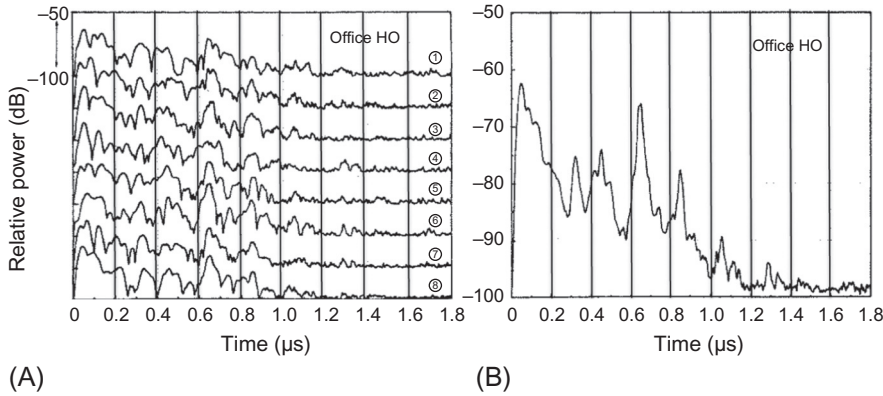
Power spectral density of Doppler spread observed by a mobile at 1800 MHz as compared to the classical spectrum of the simplified ray model.

Source: Reprinted with editor's permission from K.I. Pedersen, P.E. Mogensen, B.H. Fleury, F. Frederiksen, K. Olesen, S.L. Larsen, *Analysis of time, azimuth and Doppler dispersion in outdoor radio channels*, in: *Proceedings of ACTS*, 1997.

response to wideband signals in the presence of directive antennas, as exemplified in Fig. 6.8 and [4–7,9]. For simplicity we first consider channel measures for wideband transmission using antennas that are not very directive. Subsequently we consider measures of the channel for directive antennas.

### 6.5.1 SPATIAL VARIATION OF PULSE RESPONSE

In any finite bandwidth system some of the received multipath signals will overlap in time, as suggested in Fig. 6.5. Because the phases of the individual terms in Eq. (6.7) depend on the lengths of the individual paths, the power delay profile  $P_R(t)$  will vary with position over distances on the order of a wavelength. An example of this variation is shown in Fig. 6.18 for measurements made on an indoor link with one antenna moved over eight different positions located around a  $1.2 \text{ m}^2$  [28]. The eight power delay profiles are offset vertically in steps of 50 dB for clarity. It is seen that at a given time after the onset of the signal, there can be a local peak at one location but a local minimum at a different location due to the multipath interference. For indoor links, both ends are located in the clutter, and moving either end of the link will produce local fading [19,20]. In order to characterize the response in a small area, the spatial average  $\langle P_R(t) \rangle$  (in watts) of the power delay profiles has been introduced. The average of the eight individual profiles is shown in

**FIG. 6.18**

Power delay profiles measured as one end of an indoor link: (A) as antenna is moved around a 1.2 m square (individual profiles are offset vertically by 50 dB for clarity); and (B) the average in watts of the eight profiles.

Source: © 1987 IEEE. Reprinted, with permission, from D.M.J. Devasirvatham, *Multipath time delay spread in the digital portable radio environment*, *IEEE Commun. Mag.* 25 (1987) 13–21.

**Fig. 6.18.** As in the case of narrowband transmission, spatial averaging removes multipath interference effects and the attendant frequency sensitivity. Removing frequency sensitivity allows comparison of the delay profiles in different frequency bands. Measurements on indoor links indicate that the spatial average power delay profiles are nearly the same at 850 MHz, 1.7 GHz, and 4.0 GHz [29], suggesting that the scattering mechanisms responsible for multipath have only weak frequency dependence.

### 6.5.2 DELAY SPREAD FOR WIDEBAND CHANNEL RESPONSE

The RMS delay spread is primary measure of channel response to short pulse excitation. Using the power delay profile  $P_R(t)$ , as shown in Fig. 6.6, we first define the mean delay  $T_0$  using the equation

$$T_0 = \int_0^\infty t P_R(t) dt / \int_0^\infty P_R(t) dt. \quad (6.28)$$

The RMS delay spread  $\tau_{\text{RMS}}$  is then defined by

$$\tau_{\text{RMS}}^2 = \int_0^\infty (t - T_0)^2 P_R(t) dt / \int_0^\infty P_R(t) dt. \quad (6.29)$$

In Eqs. (6.28) and (6.29) it is assumed that the time origin is chosen in any way such that  $P_R(t) = 0$  for  $t < 0$ . Note that  $T_0$  depends on the choice of starting time, but

$\tau_{\text{RMS}}$ , which is a measure of the width of the power delay profile, is independent of the starting time. When evaluating the integral in Eq. (6.29) it is important that a threshold be defined just above the noise floor and that  $P_R(t)$  be taken as zero when it falls below the threshold [30]. The denominator in Eqs. (6.28) and (6.29) is the total energy  $E_0$  of the received power delay profile.

Since  $\tau_{\text{RMS}}$  is an important parameter for determining capacity of communication systems, it has been measured extensively—see, for example, [29–33]. One way to represent the totality of measurements in an area is to create a CDF, such as shown in Fig. 6.19 [31]. The delay spread is smaller in suburban areas than in urban areas. In these measurements the mobile station had a vertically polarized antenna, while reception at the base station was via both vertically and horizontally polarized antennas. Polarization is seen to have only limited effect on delay spread.

Measurements and simulations indicate that as the separation  $R$  between antennas increases, the delay spread  $\tau_{\text{RMS}}$  increases [34,35]. Based on a survey of measurements, Greenstein et al. propose that the mean value of the delay spread increase as  $R^n$  with  $n$  between 0.5 and 1.0 [36]. For indoor links a linear dependence has been proposed [34].

While power delay profiles reported in the literature take many forms, typically the time variation is like that seen in Figs. 6.6 and 6.18, which suggest that the power in decibel decrease approximately linearly with time. This decrease of power

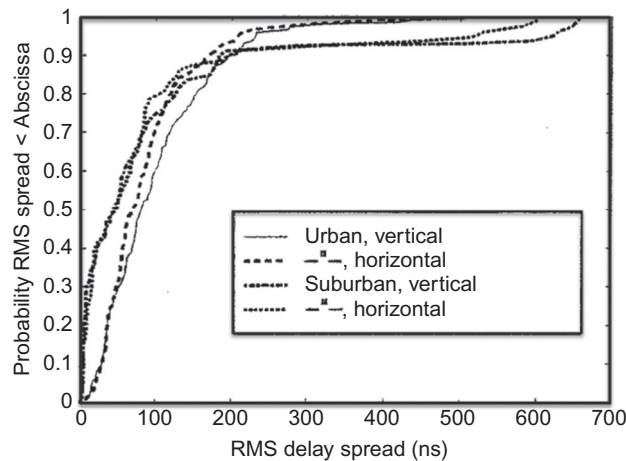


FIG. 6.19

Cumulative distribution function of RMS delay spread measured at 1800 MHz in suburban and urban areas in Sweden.

Source: © 1999 IEEE. Reprinted, with permission, from M. Nilsson, B. Lindmark, M. Ahlberg, M. Larsson, C. Beckmann, *Measurements of the spatio-temporal polarization characteristics of a radio channel at 1800 MHz*, in: *Proceedings of the IEEE Vehicular Technology Conference*, 1999, pp. 386–391.

in decibel corresponds to an exponential decrease of  $P_R(t)$  in watts. For a given total pulse energy  $E_0$  and RMS delay spread  $\tau_{\text{RMS}}$ , exponential time dependence of the received power takes the form

$$P_R(t) = \frac{E_0}{\tau_{\text{RMS}}} \exp(-t/\tau_{\text{RMS}}) U(t), \quad (6.30)$$

where  $U(t)$  is the unit step function. If the delay spread  $\tau_{\text{RMS}}$  increases with antenna separation  $R$ , then the peak amplitude  $E_0/\tau_{\text{RMS}}$  of the received power will decrease more rapidly with  $R$  than the total energy  $E_0$  [34]. This observation indicates that as the dominant ray propagates through a region, scattering causes it to lose energy to the multipath fields, which continue to reverberate in the environment.

### 6.5.3 COHERENCE BANDWIDTH

The dependence on the center frequency of a narrow band transmission, as shown in Fig. 6.12, represents the channel transfer function  $H(\omega)$  and is the Fourier transform of the response  $V_R(t)$  for a short transmitted pulse. The coherence function of the channel  $C(\Delta\omega)$  is the expectation value  $E\{H(\omega)H^*(\omega + \Delta\omega)\}$ . Using the Fourier transform of  $V_R(t)$  for  $H(\omega)$  and making the spatial ergodic assumption, the coherence function can be found from the Fourier transform of the spatial average received power  $\langle |V_R(t)|^2 \rangle = \langle P_R(t) \rangle$ . This equation takes the form [30,37]

$$C(\Delta\omega) = \int_{-\infty}^{\infty} \langle P_R(t) \rangle e^{j\Delta\omega t} dt / \int_{-\infty}^{\infty} \langle P_R(t) \rangle dt. \quad (6.31)$$

If we use expression Eq. (6.30) for the spatial average received power, then

$$C(\Delta\omega) = \int_0^{\infty} \frac{1}{\tau_{\text{RMS}}} \exp(-t/\tau_{\text{RMS}}) e^{j\omega t} dt = \left[ \frac{1}{1 + j\Delta\omega\tau_{\text{RMS}}} \right]. \quad (6.32)$$

The magnitude of the coherence function is given by

$$|C(\Delta\omega)| = 1 / \sqrt{1 + (\Delta\omega\tau_{\text{RMS}})^2}. \quad (6.33)$$

The coherence function has amplitude 0.5 when  $\Delta\omega = \sqrt{3}/\tau_{\text{RM}}$ . Thus, the coherence bandwidth of the narrow band response is inverse to the delay spread of the response to a pulsed source.

### 6.5.4 ANGLE SPREAD FOR HIGHLY DIRECTIVE ANTENNAS

In designing systems that use antenna directivity to assist in reducing user interference or as a basis for multiple access, it is important to understand the range of angle over which multipath signals arrive at the base station from individual mobiles. Fig. 6.8 shows an example of the multipath arrivals from a mobile as measured at

an elevated base station using an antenna that is highly directive in azimuth [14]. Ignoring the differences in time delay of the individual arrivals, it is possible to compute the angle spread  $AS$  for all arrivals taken together.

Let  $\psi_n$  be the direction of the arrival as measured from any choice of the  $x$ -axis. Then the mean angle of arrival  $\Psi_0$  is

$$\Psi_0 = \sum_n \psi_n a_n^2 / \sum_n a_n^2. \quad (6.34)$$

The expression for  $AS$  is then given by

$$(AS)^2 = \sum_n |\psi_n - \Psi_0|^2 a_n^2 / \sum_n a_n^2. \quad (6.35)$$

In reporting on measurements of angle spread, it is common to provide a CDF of the measurements for many mobile locations, as shown in Fig. 6.20. This figure is based on measurement in Sweden at 1800 MHz for a vertically polarized mobile and both horizontally and vertically polarized receivers at the base station [31]. The angles of arrival are spread over about  $\pm 5$  degrees in the suburbs and over  $\pm 10$  degrees in urban areas. Several studies have sought to find a correlation between the

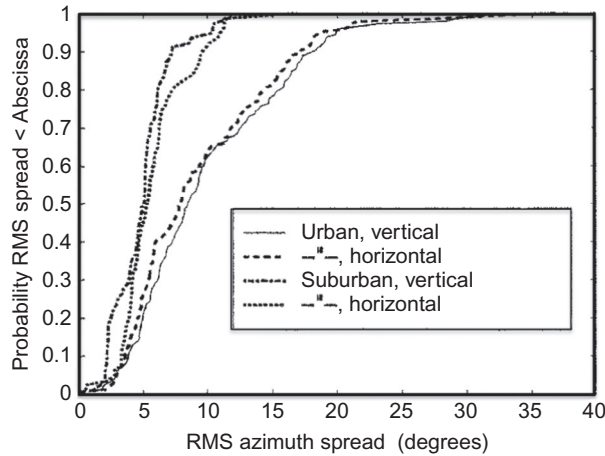


**FIG. 6.20**

Cumulative distribution of angle spread measured in urban and suburban areas of Sweden at 1800 MHz.

Source: © 1999 IEEE. Reprinted, with permission, from M. Nilsson, B. Lindmark, M. Ahlberg, M. Larsson, C. Beckmann, *Measurements of the spatio-temporal polarization characteristics of a radio channel at 1800 MHz*, in: *Proceedings of the IEEE Vehicular Technology Conference*, 1999, pp. 386–391.

delay spread and angle spread and to model them via scattering in some choice of geometric region about the radio link [38].

## 6.6 SHADOW FADING, RANGE DEPENDENCE, AND CROSS-POLARIZATION

In addition to the effects associated with multipath scattering, buildings, and other objects along the radio link cause shadow fading and alter the range dependence of the received signal. Scattering also generates coupling from the radiated polarization into orthogonal polarizations. In this section we show how shadow fading and range dependence are extracted from measurements in the classical narrow band mobile radio setting, and briefly discuss the statistical properties of cross-polarization. Because these properties depend only weakly on frequency, the characteristics observed for narrow band transmission apply to a wide range of communication systems.

In the development of narrow band mobile radio, signal strength measurements have been recorded as a vehicle-mounted receiver is driven over urban streets. Along a block, the recorded received signal exhibits variations similar to that seen in the simulation of Fig. 6.21. As previously discussed the received power undergoes multipath fading (also called fast fading) over distances less than a wavelength. The multipath fading can be removed by averaging the received power in watts over a small distance or area called a sector whose dimension is on the order of  $20\lambda$ . (Note that for a Rayleigh distribution  $\langle |V_R|^2 \rangle = (4/\pi)(\langle |V_R| \rangle)^2$ , so that averaging power is 1 dB different than squaring the average voltage.) Let  $U_k = 10 \log \langle P_R \rangle$  be the average

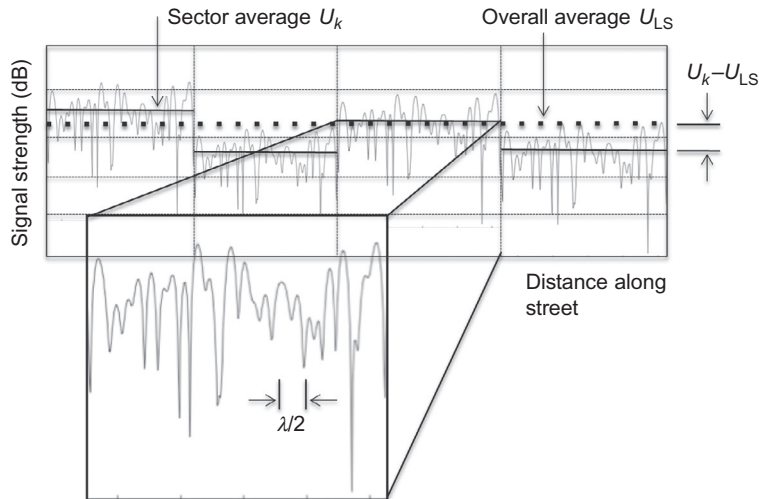


FIG. 6.21

Characteristic variations of a narrow band received signal observed along a street.

power in the  $k$ th sector expressed in decibel, as suggested in Fig. 6.21. As the mobile passes different buildings and open spaces, such as parking lots and intersections, the differences in shadowing and scattering will cause  $U_k$  to vary along the street.

### 6.6.1 SEPARATING SHADOW FADING FROM RANGE DEPENDENCE

In order to characterize the variation of  $U_k$ , it is common to plot its value in decibel versus the distance  $R$  between the antennas plotted using a log scale. Such a plot is shown in Fig. 6.22 for transmission from an elevated base station antenna in Philadelphia [39]. The individual dots represent individual values of  $U_k$ . A line  $U_{LS}(R)$  is then drawn through the dots using the least squares fit criterion. This line represents the range dependence of the received power, and the deviation of the dots from the line is referred to as shadow fading (also called slow fading). The straight line in Fig. 6.22 corresponds to the simple range dependence

$$P_{LS}(R) = P_T A / R^n. \quad (6.36)$$

When expressed in decibel, using  $U_{LS}(R) = 10 \log P_{LS}(R)$ , Eq. (6.36) plots as a straight line versus  $\log R$  with slope  $10n$ . In the case of Fig. 6.22, the slope corresponds to  $n = 3.7$ , which is in the range typical for macrocell. In other physical environments, the range dependence can take other forms. For example, a two-slope

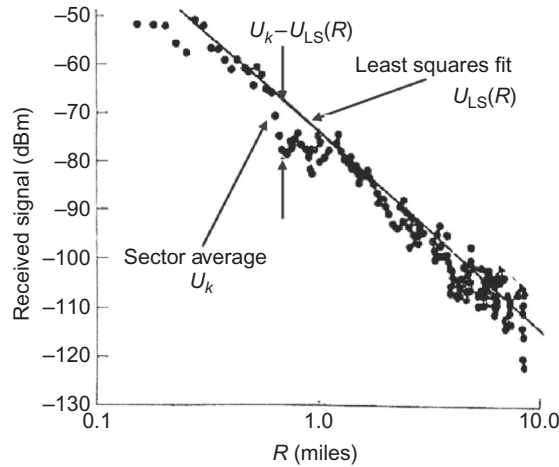
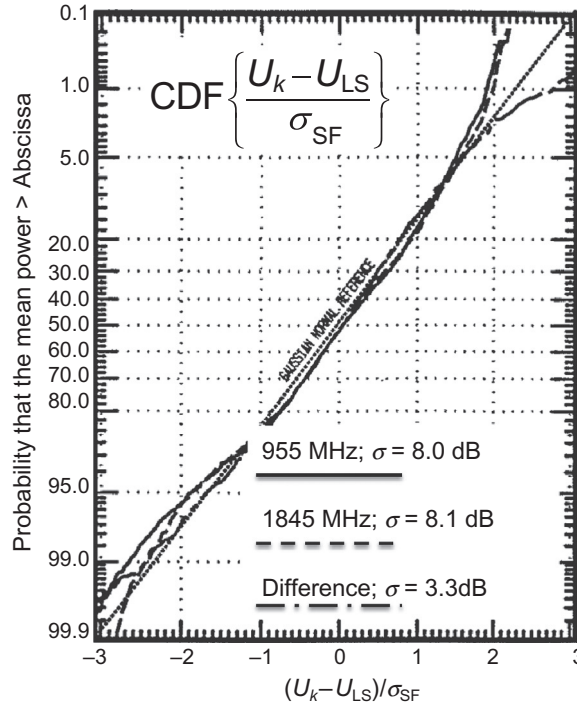


FIG. 6.22

Sector averaged power received from an elevated base station in Philadelphia versus distance  $R$  on a log scale.

Source: Based on measurements reported in G.D. Ott, A. Plitkins, *Urban path-loss characteristics at 820 MHz*, *IEEE Trans. Veh. Technol.* 27 (1978) 199–197.

**FIG. 6.23**

Comparison of cumulative distribution functions of shadow fading at 955 and 1845 MHz in Copenhagen with a Gaussian distribution.

Source: © 1991 IEEE. Reprinted, with permission, from P. Morgensen, P. Eggers, C. Jensen, J.B. Andersen, Urban area radio propagation measurements at 955 and 1845 MHz for small and micro cells, in: *Proceedings of Globecom'91*, vol. 2, 1991, pp. 1297–1302.

regression fit is found to be useful for LOS conditions [40], while an additional exponential factor has been used for propagation over one floor of a large building [41].

The deviation  $U_k - U_{LS}(R)$  of the small area (sector) averages from the least squares fit line is typically found to have Gaussian distribution whose probability distribution function (PDF) is given by

$$\text{PDF}(U_k - U_{LS}) = \frac{1}{\sqrt{2\pi}\sigma_{SF}} \exp \left[ -(U_k - U_{LS})^2 / 2\sigma_{SF}^2 \right], \quad (6.37)$$

where  $\sigma_{SF}$  is the standard deviation. For macrocells in cities,  $\sigma_{SF}$  is typically in the range of 8–10 dB. Fig. 6.23 compares the CDF of the shadow fading measured at

955 and 1855 MHz in Copenhagen with the mathematical CDF corresponding to a Gaussian distribution [42]. The plot has a distorted vertical scale such that a Gaussian distribution plots as a straight line. All random variables have been normalized to their standard deviations, which were 8.0 dB at 955 MHz and 8.1 dB at 1845 MHz. The two measurement derived distributions are seen to be a good fit to the Gaussian over the 5–95% range.

The Gaussian nature of the shadow fading depicted in Fig. 6.23 has been observed in many different cities. In order to explain the Gaussian nature of shadow fading, it has been proposed that the signal undergoes a sequence of shadowing events that multiply the power by random amplitudes [43]. When expressed in decibel, such random events add together, and the sum tends to a Gaussian. Shadowing events have weak frequency dependence, so that shadow fading should be nearly independent of frequency. This is supported by the observation that  $\sigma_{SF}$  is nearly the same for 955 and 1845 MHz. Moreover, in making the measurements in Copenhagen, at each sector the difference  $U_k(955) - U_k(1845)$  was recorded. While the mean difference was 10.5 dB, due to variations in system and antenna performance, the standard deviation of the difference was only 3.3 dB. Thus, although the plot of sector average for each frequency varies over  $\pm 8$  dB, the two plots track each other to within  $\pm 3.3$  dB. Fig. 6.23 also contains a plot of the CDF for the difference, which is seen to have a Gaussian distribution.

The performance of early narrow band cellular mobile radio systems was constrained by presence of the frequency dependent multipath fading. Moving to digital systems eliminated the problems caused by multipath, and through the advent of MIMO was in fact able to make use of multipath to increase capacity. Shadow fading on the other hand is nearly independent of frequency and therefore has the same effect on digital systems as it does on narrow band systems.

### 6.6.2 CROSS-POLARIZATION COUPLING

The electromagnetic waves scattered by objects of almost any shape will exhibit coupling from the incident polarization into orthogonal polarizations. For example, if the radiated electric field is polarized in the vertical direction, the field incident on the receiving antenna will have both vertical and horizontal components. Measurements at 900 MHz and 2.0 GHz have shown that for transmission from a vertically polarized mobile antenna, the multipath fading of the vertical and horizontal polarizations received at a base station are uncorrelated [44]. This property can be used to achieve polarization diversity reception, and permits MIMO operation by co-located antennas.

The relative strength of the sector averaged vertical and horizontal polarization components have also been measured for various mobile antenna configurations, and in urban and suburban environments [45]. Coupling ranges from  $-13$  dB for a roof-mounted antenna in a spread-out suburb to  $-1$  dB for an indoor portable in a city. Roof-mounted mobiles show the least coupling and indoor portables the most, and more coupling is found in urban environments than suburban.

## REFERENCES

- [1] H.L. Bertoni, *Radio Propagation for Modern Wireless Systems*, Prentice Hall, Upper Saddle River, NJ, 2000.
- [2] T.S. Rappaport, R.W. Heath, R.C. Daniels, J.N. Murdock, *Millimeter Wave Wireless Communications*, Prentice Hall, Upper Saddle River, NJ, 2015.
- [3] C.A. Balanis, *Theory Antenna*, third ed., Wiley-Interscience, Hoboken, NJ, 2005.
- [4] K. Kalliola, H. Laitinen, P. Vaninikainen, M. Toeltsch, J. Laurila, E. Bonek, 3-D double-directional radio channel characterization for urban macrocellular applications, *IEEE Trans. Antennas Propag.* 51 (2003) 3122–3133.
- [5] M. Ghoraiishi, J. Takada, T. Imai, Identification of scattering objects in microcell urban mobile propagation channel, *IEEE Trans. Antennas Propag.* 54 (2006) 3473–3480.
- [6] M.R.J.A.E. Kwakkernaat, Y.L.C. de Jong, R.J.C. Bultitude, M.H.A.J. Herben, High-resolution angle-of-arrival measurements on physically-nonstationary mobile radio channels, *IEEE Trans. Antennas Propag.* 56 (2008) 2720–2729.
- [7] M.R.J.A.E. Kwakkernaat, M.H.A.J. Herben, Diagnostic analysis of radio propagation in UMTS networks using high-resolution angle-of-arrival measurements, *IEEE Antennas Propag. Mag.* 53 (2011) 66–75.
- [8] T. Taga, Analysis for mean effective gain of mobile antennas in land mobile radio environments, *IEEE Trans. Veh. Technol.* 39 (1990) 117–131.
- [9] J. Fuhl, J.-P. Rossi, E. Bonek, High-resolution 3-D direction-of-arrival determination for urban mobile radio, *IEEE Trans. Antennas Propag.* 45 (1997) 672–682.
- [10] C. Zhou, R.C. Qiu, Pulse distortion caused by cylinder diffraction and its impact on UWB communications, *IEEE Trans. Veh. Technol.* 56 (2007) 2385–2391.
- [11] R. Aiello, A. Batra (Eds.), *Ultra Wideband Systems*, Elsevier, Amsterdam, 2006.
- [12] Experimental License Progress Report to FCC from Telesis Technology Laboratory, Walnut Creek, CA, Aug. 1991.
- [13] S. Salous, Indoor and outdoor UHF measurements with a 90 MHz bandwidth, in: *Proceedings of the IEE Colloquium on Propagation Characteristics and Related System Techniques for Beyond Line-of-Sight Radio*, London, Nov. 24, 1997, pp. 8/1–8/6 (INSPEC No. 589129).
- [14] K.I. Pedersen, P.E. Mogensen, B.H. Fleury, F. Frederiksen, K. Olesen, S.L. Larsen, Analysis of time, azimuth and Doppler dispersion in outdoor radio channels, in: *Proceedings of ACTS*, 1997.
- [15] A.A.M. Saleh, R.A. Valenzuela, A statistical model for indoor multipath propagation, *IEEE J. Sel. Areas Commun.* 5 (2) (1987) 128–137.
- [16] N. Czink, E. Bonek, X. Yin, B. Fleury, Cluster angular spreads in a MIMO indoor propagation environment, in: *Proceedings of the IEEE 16th International Symposium on Personal, Indoor and Mobile Radio Communications*, 2005, pp. 664–668.
- [17] T. Rappaport, *Wireless Communications: Principles and Practice*, second ed., Prentice Hall, Upper Saddle River, NJ, 2000, pp. 210–214.
- [18] E.S. Sousa, V.M. Jovanovic, C. Daigneault, Delay spread measurements for the digital cellular channel in Toronto, *IEEE Trans. Veh. Technol.* 43 (1994) 837–847.
- [19] W. Honcharenko, H.L. Bertoni, J. Dailing, Bi-lateral averaging over receiving and transmitting areas for accurate measurements of sector average signal strength inside buildings, *IEEE Trans. Antennas Propag.* 43 (5) (1995) 508–512.
- [20] R.A. Valenzuela, O. Landron, D.L. Jacobs, Estimating local mean signal strength of indoor multipath propagation, *IEEE Trans. Veh. Technol.* 46 (1997) 203–212.

- [21] S.-B. Rhee, G.I. Zysman, Results of suburban base station spatial diversity measurements in the UHF band, *IEEE Trans. Commun.* 22 (1974) 1630–1636.
- [22] F. Adachi, M.T. Feeney, J.D. Parsons, A.G. Williamson, Cross correlation between the envelopes of 900 MHz signals received at a mobile radio base station site, *IEEE Proc.* 133 (Pt. F) (1980) 506–512.
- [23] N.H. Shepherd, Special issue on radio propagation, *IEEE Trans. Veh. Technol.* 37 (1988) 45.
- [24] A. Kara, H.L. Bertoni, Effect of people moving near short-range indoor propagation links at 2.45 GHz, *J. Commun. Netw.* 8 (2006) 286–289.
- [25] R. Rosini, R. Verdone, R. D’Errico, Body-to-body indoor channel modeling at 2.45 GHz, *IEEE Trans. Antennas Propag.* 62 (2014) 5807–5819.
- [26] A. Papoulis, *Probability, Random Variables and Stochastic Process*, McGraw Hill, New York, 1991, pp. 319–332.
- [27] M. Abramowitz, I.A. Stegun (Eds.), *Handbook of Mathematical Functions*, Dover Publications, New York, 1965.
- [28] D.M.J. Devasirvatham, Multipath time delay spread in the digital portable radio environment, *IEEE Commun. Mag.* 25 (1987) 13–21.
- [29] D.M.J. Devasirvatham, M.J. Krain, D.A. Rappaport, C. Banerjee, Radio propagation measurements at 850 MHz, 1.7 GHz and 4 GHz inside two dissimilar office buildings, *Electron. Lett.* 26 (1990) 445–447.
- [30] S. Kim, H.L. Bertoni, M. Stern, Pulse propagation characteristics at 2.4 GHz inside buildings, *IEEE Trans. Veh. Technol.* 45 (1996) 579–592.
- [31] M. Nilsson, B. Lindmark, M. Ahlberg, M. Larsson, C. Beckmann, Measurements of the spatio-temporal polarization characteristics of a radio channel at 1800 MHz, in: *Proceedings of the IEEE Vehicular Technology Conference*, 1999, pp. 386–391.
- [32] H. Asplund, K. Larsson, P. Okvist, How typical is the “Typical Urban” channel model? in: *Proceedings of the IEEE Spring 2008 Vehicular Technology Conference*, 2008, pp. 340–343.
- [33] M. Kim, J. Takada, Y. Chang, J. Shen, Y. Oda, Large scale characteristics of urban cellular wideband channels at 11 GHz, in: *Proceedings of the 9th European Conference on Antennas and Propagation (EuCAP)*, 2015, pp. 1–4.
- [34] K. Siwiak, H.L. Bertoni, S. Yano, On the relation between multipath and wave propagation attenuation, *Electron. Lett.* 35 (1) (2003) 142–143.
- [35] C. Cheon, G. Liang, H.L. Bertoni, Simulating radio channel statistics for different building environments, *IEEE J. Sel. Topics Commun.* 19 (11) (2001) 2191–2200.
- [36] L.J. Greenstein, V. Erceg, Y.S. Yeh, M.V. Clark, A new path gain/delay spread propagation model for digital cellular channels, *IEEE Trans. Veh. Technol.* 46 (1997) 477–485.
- [37] J.G. Proakis, *Digital Communications*, McGraw-Hill, New York, 1989, pp. 1702–1719.
- [38] T. Imai, T. Taga, Statistical scattering model in urban propagation environment, *IEEE Trans. Veh. Technol.* 55 (4) (1906) 1081–1093.
- [39] G.D. Ott, A. Plitkins, Urban path-loss characteristics at 820 MHz, *IEEE Trans. Veh. Technol.* 27 (1978) 199–197.
- [40] H.H. Xia, H.L. Bertoni, L.R. Maciel, A. Lindsay-Stewart, R. Rowe, Radio propagation characteristics for line-of-sight microcellular and personal communications, *IEEE Trans. Antennas Propag.* 41 (1994) 1439–1447.

- [41] D.M.J. Devasirvatham, C. Banerjee, M.J. Krain, D.A. Rappaport, Multi-frequency radiowave propagation measurements in the portable radio environment, in: Proceedings of IEEE ICC'90, vol. 4, 1990, pp. 1334–1340.
- [42] P. Morgensen, P. Eggers, C. Jensen, J.B. Andersen, Urban area radio propagation measurements at 955 and 1845 MHz for small and micro cells, in: Proceedings of Globecom'91, vol. 2, 1991, pp. 1297–1302.
- [43] C. Chrysanthou, H.L. Bertoni, Variability of sector averaged signals for UHF propagation in cities, IEEE Trans. Veh. Technol. 39 (4) (1990) 352–358.
- [44] J.J.A. Lempiainen, J.K. Laiho-Steffens, The performance of polarization diversity schemes at a base station in small/micro cells at 1800 MHz, IEEE Trans. Veh. Technol. 47 (1998) 1087–1092.
- [45] F. Lotse, J.E. Berg, U. Forssen, P. Idahl, Base station polarization diversity reception in macrocellular systems at 1800 MHz, in: Proceedings of the Vehicular Technology Conference, 1996, pp. 1643–1646.

# Synchronization of digital signals

# 7

**N. Noels, M. Moeneclaey**  
Ghent University, Ghent, Belgium

## CHAPTER OUTLINE

<b>7.1</b>	<b>Introduction</b> .....	227
<b>7.2</b>	<b>System Model</b> .....	230
<b>7.3</b>	<b>Effect of Channel Estimation Errors</b> .....	233
7.3.1	Perfect Estimation of $\tau$ .....	234
7.3.2	Perfect Estimation of $(A, \theta, F)$ .....	239
<b>7.4</b>	<b>Results from Estimation and Decision Theory</b> .....	240
7.4.1	MAP Detection .....	242
7.4.2	MAP Estimation .....	243
7.4.3	The Expectation-Maximization Algorithm .....	244
7.4.4	Bounds on Estimation Performance .....	246
<b>7.5</b>	<b>Estimation Strategy</b> .....	247
<b>7.6</b>	<b>NDA Coarse Frequency Estimation</b> .....	250
<b>7.7</b>	<b>NDA Symbol Timing Estimation</b> .....	252
<b>7.8</b>	<b>PA ML Estimation of <math>(A, \theta, F_{\text{res}}, k_{\tau})</math></b> .....	254
<b>7.9</b>	<b>CA ML Estimation of <math>(A, \theta, F_{\text{res}}, k_{\tau})</math></b> .....	259
<b>7.10</b>	<b>Evaluation of Modified Cramer-Rao Bounds</b> .....	263
<b>7.11</b>	<b>Performance Evaluation</b> .....	264
7.11.1	Simulation Setup .....	264
7.11.2	NDA Frequency and Symbol Timing Estimation .....	266
7.11.3	PA Estimation .....	266
7.11.4	CA Estimation .....	268
<b>7.12</b>	<b>Conclusions and Remarks</b> .....	275
<b>Appendix A</b>	<b>Averaged Likelihood Functions</b> .....	276
<b>Appendix B</b>	<b>MFIM Computation</b> .....	278
<b>References</b>	.....	279

## 7.1 INTRODUCTION

When transmitting data symbols over a channel that introduces a scaling factor  $A$ , a phase shift  $\theta$ , a frequency offset  $F$ , and a time delay  $\tau$ , the receiver has

to compensate for these channel parameters before detecting the data. Typically, these parameters are not known in advance, so they need to be estimated by the receiver. The estimation of and compensation for the parameters  $(\theta, F, \tau)$  is referred to as *synchronization*. When the data symbol constellation is not of the constant-modulus type, and/or advanced channel codes (such as turbo codes or LDPC codes) with maximum a posteriori bit detection are used, the scaling factor  $A$  must also be estimated. Therefore, this chapter deals with the estimation of all four channel parameters  $(A, \theta, F, \tau)$ .

Maximum-likelihood (ML) estimates asymptotically achieve a performance close to the Cramer-Rao bound, which is a theoretical lower bound on the mean-square estimation error [1]. However, obtaining the ML estimates of  $(A, \theta, F, \tau)$  is computationally very intensive: first, the likelihood function of  $(A, \theta, F, \tau)$  involves a summation over all allowed codewords (the number of terms in this summation grows exponentially with the frame length), and second, the computation of the ML estimates requires a search over the four-dimensional parameter space of  $(A, \theta, F, \tau)$ . Hence, simplifications must be introduced to obtain algorithms that are practically feasible. A traditional approach consists of evaluating the likelihood function of  $(A, \theta, F, \tau)$  under the assumption of uncoded transmission; the resulting computational complexity is linear (rather than exponential) in the frame length. This approach works well for channel codes with moderate coding gain, such as convolutional codes [2] and trellis codes [3,4]. The introduction of powerful channel codes (turbo codes [5,6] and LDPC codes [7,8]) allows the operating SNR to be lowered substantially when the receiver knows the channel parameters; however, at such a low SNR, the traditional channel estimation algorithms no longer provide accurate estimates, thereby considerably deteriorating the error performance of the communication system. Therefore, in this chapter we also pay attention to estimation algorithms that exploit the redundancy among the transmitted symbols, so that the coding gain becomes beneficial to the estimation accuracy as well; the resulting algorithms iterate between estimation and detection/decoding and achieve an excellent performance in the presence of powerful channel codes.

The system model to be investigated is presented in [Section 7.2](#). [Section 7.3](#) illustrates the effect of constant channel estimation errors on the error performance of the receiver and justifies the need for accurate channel estimates. In [Section 7.4](#) we give a brief overview of estimation and decision theory, dealing with generic parameter estimation and theoretical performance bounds (ie, the Cramer-Rao bound and the modified Cramer-Rao bound). In [Section 7.5](#) an estimation strategy is outlined, explaining the various approximations needed to achieve practically feasible algorithms. The specific estimation algorithms are derived in a systematic way in [Sections 7.6–7.9](#); it turns out that a one-dimensional search has to be executed to obtain an estimate of the integer part of the time delay, and closed-form expressions are found for the estimates of the remaining parameters. In [Section 7.10](#) we present closed-form expressions for the modified Cramer-Rao bounds and in [Section 7.11](#) the actual performance of the estimation algorithms and their effect on the error performance are investigated. Finally, conclusions are drawn in [Section 7.12](#).

The main variables used in this chapter are listed below.

$x(t)$	Transmitted signal
$y(t)$	Received signal
$v(t)$	AWGN in received signal
$N_0$	Spectral density of AWGN term $v(t)$
$\mathbf{s} = \{s_m\}$	Transmitted symbol sequence
$E_s$	Symbol energy
$h(t), H(f)$	Transmit filter impulse response and transfer function
$h^*(-t), H^*(f)$	Matched filter impulse response and transfer function
$T, 1/T$	Symbol interval and symbol rate
$A, \hat{A}$	Amplitude and its estimate
$\theta, \hat{\theta}$	Phase shift at $t=0$ and its estimate
$F, \hat{F}$	Frequency offset and its estimate
$\tau, \hat{\tau}$	Time delay, and its estimate
$\boldsymbol{\psi} = (A, \theta, F, \tau),$ $\hat{\boldsymbol{\psi}} = (\hat{A}, \hat{\theta}, \hat{F}, \hat{\tau})$	Vector of channel parameters and its estimate
$\lambda(\mathbf{s}, \boldsymbol{\psi})$	Likelihood function of $(\mathbf{s}, \boldsymbol{\psi})$
$z(t, \hat{F})$	Response of matched filter to $y(t)e^{-j2\pi\hat{F}t}$
$z_k(\hat{F}, \hat{\tau}) = z(t, \hat{F}) \Big _{t=kT+\hat{\tau}}$	Matched filter output sample
$u_k(\hat{\boldsymbol{\psi}}) = z_k(\hat{F}, \hat{\tau})e^{-j\hat{\theta}}/\hat{A}$	Sample used for detection
$\theta_{\text{tot}}(t) = 2\pi Ft + \theta,$ $\hat{\theta}_{\text{tot}}(t) = 2\pi\hat{F}t + \hat{\theta}$	Total phase, and its estimate
$e_A = (\hat{A} - A)/A$	Normalized amplitude error
$e_\theta = \hat{\theta} - \theta$	Phase error
$e_F = (\hat{F} - F)T$	Normalized frequency error
$e_\tau = (\hat{\tau} - \tau)/T$	Normalized timing error
$e_{\theta, \text{tot}}(t) = \hat{\theta}_{\text{tot}}(t) - \theta_{\text{tot}}(t)$	Total phase error
$g(t, e_F)$	Inverse Fourier transform of $H(f)H^*(f - \frac{e_F}{T})$
$t_c$	Instant of center of received frame
$e_{\theta, c} = e_{\theta, \text{tot}}(t_c)$	Total phase error at frame center
$K$	Number of symbols in frame
$K_p$	Number of pilot symbols in frame
$k_\tau T, \epsilon T$ ( $\tau = (k_\tau + \epsilon)T$ ); $\hat{k}_\tau T,$ $\hat{\epsilon} T$ ( $\hat{\tau} = (\hat{k}_\tau + \hat{\epsilon})T$ )	Integer and fractional part of delay and their estimates
$z_k$	Concise notation for $z(kT + \hat{\epsilon}T, \hat{F})$
$F_{\text{max}}$	Maximum of $F$
$\tau_{\text{min}}, \tau_{\text{max}}$	Minimum and maximum value of $\tau$
$F_{\text{res}}, \hat{F}_{\text{res}}$	Residual frequency offset after coarse frequency correction and its estimate
$\theta_{\text{res}}(t) = 2\pi F_{\text{res}}t + \theta,$ $\hat{\theta}_{\text{res}}(t) = 2\pi\hat{F}_{\text{res}}t + \hat{\theta}$	Residual total phase after coarse frequency correction and its estimate
$J_{\text{FIM}}, J_{\text{MFIM}}$	Fisher information matrix, modified Fisher information matrix

## 7.2 SYSTEM MODEL

We consider the transmission of a linearly modulated signal over an additive white Gaussian noise (AWGN) channel that is characterized by a number of parameters which are unknown to the receiver. At the transmitter, a binary information sequence is encoded, and the resulting coded bit sequence is mapped to a sequence  $\{s_m\}$  of data symbols, with  $E[s_m] = 0$  and  $E[s_{k+m}s_m^*] = \sigma_s^2 \delta_k$ , where  $\delta_k$  denotes the Kronecker delta function. The symbol sequence  $\{s_m\}$  is applied to a transmit filter with impulse response  $h(t)$  and transfer function  $H(f)$ . Using a complex baseband representation, the resulting transmitted signal  $x(t)$  is given by

$$x(t) = \sum_m s_m h(t - mT), \quad (7.1)$$

where  $T$  denotes the symbol interval (and correspondingly  $1/T$  is the symbol rate). According to Eq. (7.1), the symbol  $s_m$  is fed to the transmit filter at instant  $mT$ . We restrict our attention to the case where  $h(t)$  is a unit-energy square-root Nyquist pulse, ie,

$$\int h(kT + u)h^*(u)du = \delta_k, \quad (7.2)$$

so that the detection process does not suffer from intersymbol interference (ISI) when transmitting over an AWGN channel and using a receive filter which is matched to the transmit filter. In addition, we will assume that  $h(t)$  is real and even ( $h(t) = h^*(t) = h(-t)$ ), which is the case for many transmit pulses of practical interest, such as the square-root cosine-rolloff pulse; consequently,  $H(f)$  is real and even.

The received signal  $y(t)$  is given by

$$y(t) = Ae^{j\theta_{\text{tot}}(t)}x(t - \tau) + v(t), \quad (7.3)$$

where

$$\theta_{\text{tot}}(t) = 2\pi Ft + \theta \quad (7.4)$$

and  $(A, \theta, F, \tau)$  denote the channel parameters:  $A$  is a positive scaling factor,  $F$  is a frequency offset (representing the difference in frequency between the oscillators used for upconversion at the transmitter and downconversion at the receiver),  $\theta$  is a phase shift,  $\tau$  is a time delay, and  $v(t)$  denotes complex-valued AWGN with power spectral density  $N_0$  (ie,  $E[v(t+u)v^*(t)] = N_0\delta(u)$ , with  $\delta(u)$  denoting the Dirac delta function). We will refer to  $\theta_{\text{tot}}(t)$  as the total phase, which varies linearly with  $t$ ; note that  $\theta_{\text{tot}}(0) = \theta$ , so that the phase shift  $\theta$  in Eq. (7.4) is the value of the total phase at  $t = 0$ . The operations performed by the transmitter and the channel are illustrated in Fig. 7.1.

The resulting energy  $E_s$  per symbol interval at the receiver input is defined as

$$E_s = E \left[ \int_{-T}^T \left| A e^{j(2\pi Ft + \theta)} x(t - \tau) \right|^2 dt \right], \quad (7.5)$$

where the integration is over an interval of length  $T$  and the expectation is over the symbols. Using Eq. (7.1), Eq. (7.5) reduces to

$$\begin{aligned} E_s &= A^2 \sigma_s^2 \int_{-T}^T \sum_m |h(t - mT)|^2 dt \\ &= A^2 \sigma_s^2 \int_{-\infty}^{+\infty} |h(t)|^2 dt \\ &= A^2 \sigma_s^2, \end{aligned} \quad (7.6)$$

where the last line takes into account that  $h(t)$  has unit energy.

Stacking the transmitted symbols into the vector  $\mathbf{s}$  and introducing  $\boldsymbol{\psi} = (A, \theta, F, \tau)$ , the likelihood function  $\lambda(\mathbf{s}, \boldsymbol{\psi})$  [1] according to the observation Eq. (7.3) is given by

$$\lambda(\mathbf{s}, \boldsymbol{\psi}) = \exp \left( -\frac{1}{N_0} \int \left| y(t) - A e^{j(2\pi Ft + \theta)} x(t - \tau) \right|^2 dt \right). \quad (7.7)$$

Substituting Eq. (7.1) into Eq. (7.7), making use of Eq. (7.2), and removing terms not depending on  $(\mathbf{s}, \boldsymbol{\psi})$ , the log-likelihood function  $\ln(\lambda(\mathbf{s}, \boldsymbol{\psi}))$  is obtained as

$$\ln(\lambda(\mathbf{s}, \boldsymbol{\psi})) = \frac{A^2}{N_0} \left( 2\Re \left( \mathbf{s}^H \mathbf{u}(\boldsymbol{\psi}) \right) - |\mathbf{s}|^2 \right), \quad (7.8)$$

where  $\mathbf{u}(\boldsymbol{\psi})$  is defined as

$$\mathbf{u}(\boldsymbol{\psi}) = \frac{e^{-j\theta}}{A} \mathbf{z}(F, \tau). \quad (7.9)$$

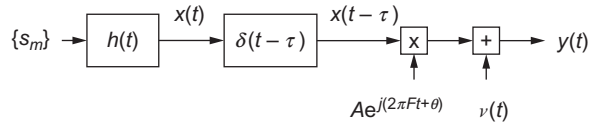


FIG. 7.1

Transmitter and channel.

The  $k$ th component of  $\mathbf{z}(F, \tau)$  in Eq. (7.9) is given by  $z_k(F, \tau) = z(t, F)|_{t=kT+\tau}$ , with

$$z(t, F) = \int h^*(u - t)y(u)e^{-j2\pi Fu} du, \quad (7.10)$$

denoting the output of a receive filter with transfer function  $H^*(f)$  (ie, matched to the transmit filter  $H(f)$ ), driven by  $y(t)e^{-j2\pi Ft}$ . As  $z_k(F, \tau)$  can be interpreted as the sample of  $z(t, F)$  at instant  $kT + \tau$ ,  $\mathbf{u}(\boldsymbol{\psi})$  represents a vector of scaled (by a factor  $1/A$ ) and rotated (over an angle  $-\theta$ ) matched filter output samples.

When the channel parameters  $\boldsymbol{\psi}$  are known to the receiver, the vector  $\mathbf{u}(\boldsymbol{\psi})$  from Eq. (7.9) is a sufficient statistic for detecting  $\mathbf{s}$ . Because of the property (7.2),  $z_k(F, \tau)$  can be decomposed as

$$z_k(F, \tau) = Ae^{j\theta} s_k + n_k, \quad (7.11)$$

where  $n_k$  is discrete-time complex AWGN with  $E[|n_k|^2] = N_0$ . Hence, the symbol  $s_k$ , that has been applied to the transmit filter at instant  $kT$ , appears without ISI at the matched filter output when sampling at  $kT + \tau$ . From Eq. (7.11) it follows that

$$u_k(\boldsymbol{\psi}) = s_k + w_k, \quad (7.12)$$

where  $u_k(\boldsymbol{\psi})$  is the  $k$ th component of  $\mathbf{u}(\boldsymbol{\psi})$  and  $w_k$  is discrete-time complex AWGN with  $E[|w_k|^2] = N_0/A^2$ . In order to extract the digital information contained in the symbol vector  $\mathbf{s}$ ,  $\mathbf{u}(\boldsymbol{\psi})$  is applied to an appropriate detector/decoder, the structure of which depends on the type of encoding and mapping that has been applied at the transmitter.

In the realistic case where  $\boldsymbol{\psi}$  is not known to the receiver, the following strategy (to be justified in Section 7.4) will be adopted: the receiver derives from  $y(t)$  an estimate  $\hat{\boldsymbol{\psi}} = (\hat{A}, \hat{\theta}, \hat{F}, \hat{\tau})$  of the channel parameters; this estimate is used to compute the vector of scaled and rotated matched filter output samples  $\mathbf{u}(\hat{\boldsymbol{\psi}}) = (e^{-j\hat{\theta}}/\hat{A})\mathbf{z}(\hat{F}, \hat{\tau})$ , which is then fed to the same detector/decoder as when  $\boldsymbol{\psi}$  is known. Fig. 7.2 illustrates the computation of  $u_k(\hat{\boldsymbol{\psi}})$ , when using estimated channel parameters. The multiplication of  $y(t)$  with  $e^{-j2\pi\hat{F}t}$ , the sampling at  $kT + \hat{\tau}$ , and the multiplication of the matched filter output sample  $z_k(\hat{F}, \hat{\tau})$  with  $e^{-j\hat{\theta}}/\hat{A}$  attempt to compensate for the frequency offset  $F$ , for the time delay  $\tau$ , and for both the phase

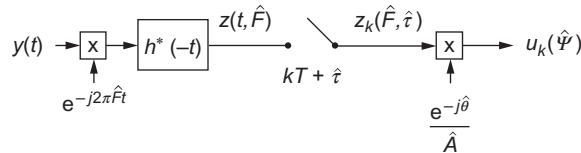


FIG. 7.2

Computation of  $u_k$  based on estimated channel parameters.

shift  $\theta$  and the scaling factor  $A$ , respectively. When  $\boldsymbol{\psi}$  is known to the receiver,  $u_k(\boldsymbol{\psi})$  is obtained by replacing in Fig. 7.2 the estimates  $(\hat{A}, \hat{\theta}, \hat{F}, \hat{\tau})$  by the actual parameter values  $(A, \theta, F, \tau)$ ; in this case the channel parameters are perfectly compensated for, yielding Eq. (7.12).

### 7.3 EFFECT OF CHANNEL ESTIMATION ERRORS

Here we point out how the channel estimation errors impact the vector of scaled and rotated matched filter output samples  $\mathbf{u}(\hat{\boldsymbol{\psi}}) = (e^{-j\hat{\theta}}/\hat{A})\mathbf{z}(\hat{F}, \hat{\tau})$ , and we illustrate how the resulting detection performance is degraded, compared to the (optimistic) case where the channel parameters are assumed to be known.

Let us introduce the dimensionless channel estimation errors  $(e_A, e_\theta, e_F, e_\tau)$ , defined as

$$(e_A, e_\theta, e_F, e_\tau) = \left( \frac{\hat{A} - A}{A}, \hat{\theta} - \theta, (\hat{F} - F)T, \frac{\hat{\tau} - \tau}{T} \right). \quad (7.13)$$

Note that  $e_A$  is the relative amplitude estimation error,  $e_\theta$  is the phase estimation error,  $e_F$  is the normalized (to the symbol rate  $1/T$ ) frequency estimation error, and  $e_\tau$  is the normalized (to the symbol interval  $T$ ) timing error.

Using Eq. (7.3) and Fig. 7.2, the scaled and rotated matched filter output sample  $u_k(\hat{\boldsymbol{\psi}})$  can be decomposed as

$$u_k(\hat{\boldsymbol{\psi}}) = \frac{e^{-je_{\theta,\text{tot}}(kT+\hat{\tau})}}{1+e_A} \sum_m s_{k-m} g(mT + e_\tau T, e_F) + w_k, \quad (7.14)$$

where  $w_k$  is discrete-time complex AWGN with  $E[|w_k|^2] = N_0/\hat{A}^2$ ,

$$e_{\theta,\text{tot}}(t) = \hat{\theta}_{\text{tot}}(t) - \theta_{\text{tot}}(t) = 2\pi e_F \frac{t}{T} + e_\theta \quad (7.15)$$

is referred to as the total phase error, and the pulse  $g(t, e_F)$  is defined as

$$g(t, e_F) = \int h^*(u) h(t+u) e^{-j\frac{2\pi}{T} e_F u} du. \quad (7.16)$$

Denoting by  $G(f, e_F)$  the Fourier transform of  $g(t, e_F)$ , we have

$$G(f, e_F) = H(f) H^* \left( f - \frac{e_F}{T} \right). \quad (7.17)$$

It follows from Eq. (7.2) that  $g(mT, 0) = \delta_m$ . Feeding  $u_k(\hat{\boldsymbol{\psi}})$  to a detector/decoder that assumes perfect channel estimates will give rise to an increased error probability due to the presence of channel estimation errors.

### 7.3.1 PERFECT ESTIMATION OF $\tau$

In order to facilitate the interpretation of Eq. (7.14), we assume that the time delay has been correctly estimated, ie,  $e_\tau = 0$ . In this case, Eq. (7.14) reduces to

$$u_k(\hat{A}, \hat{\theta}, \hat{F}, \tau) = \frac{e^{-je_{\theta, \text{tot}}(kT + \tau)}}{1 + e_A} \sum_m s_{k-m} g(mT, e_F) + w_k. \quad (7.18)$$

First, we consider the case where  $e_F = 0$ . Using  $g(mT, 0) = \delta_m$ , Eq. (7.18) simplifies to

$$u_k(\hat{A}, \hat{\theta}, F, \tau) = \frac{e^{-je_\theta}}{1 + e_A} s_k + w_k. \quad (7.19)$$

As compared to Eq. (7.12), we observe from Eq. (7.19) that amplitude and phase estimation errors affect the useful symbol  $s_k$  by introducing a scaling  $(1 + e_A)^{-1}$  and a phase shift  $-e_\theta$ , respectively.

**Example 7.1** (Effect of phase error and amplitude error on detection). Here we restrict our attention to constellations of the quadrature amplitude modulation (QAM) type. When it is assumed that 4-QAM transmission is affected by only a phase error  $e_\theta = -\pi/6$ , Fig. 7.3 shows the 4-QAM constellation along with the scatter

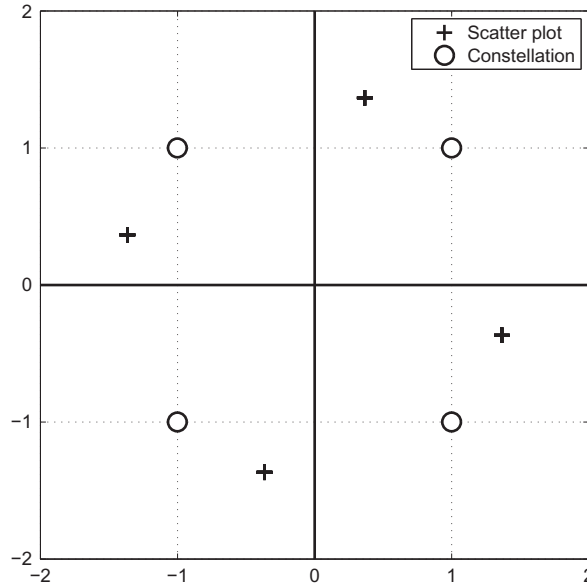


**FIG. 7.3**

4-QAM constellation and scatter diagram of  $u_k$  in the absence of noise, for  $e_\tau = e_F = e_A = 0$  and  $e_\theta = -\pi/6$ .

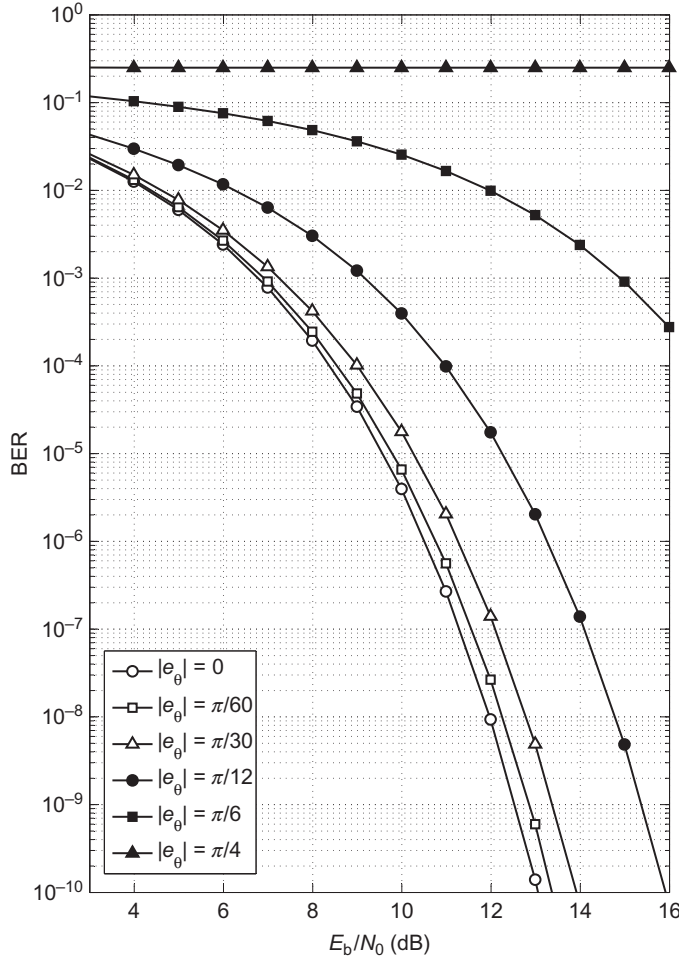


FIG. 7.4

BER of uncoded Gray-mapped 4-QAM, for  $e_r = e_f = e_A = 0$ .

diagram of  $u_k$  from Eq. (7.19) in the absence of noise, illustrating the phase shift of the original constellation points. Fig. 7.4 shows that the corresponding bit error rate (BER) for uncoded transmission with Gray-mapping degrades with increasing  $|e_\theta|$ . For 16-QAM transmission affected by only an amplitude error  $e_A = 0.2$ , the scaling of the original constellation points is illustrated in Fig. 7.5, which shows the 16-QAM constellation and the corresponding decision regions for uncoded transmission, along with the scatter diagram of  $u_k$  from Eq. (7.19) in the absence of noise. With increasing  $|e_A|$ , the BER performance for uncoded transmission with Gray-mapping degrades as shown in Fig. 7.6. For both cases, the deterioration of the BER performance is



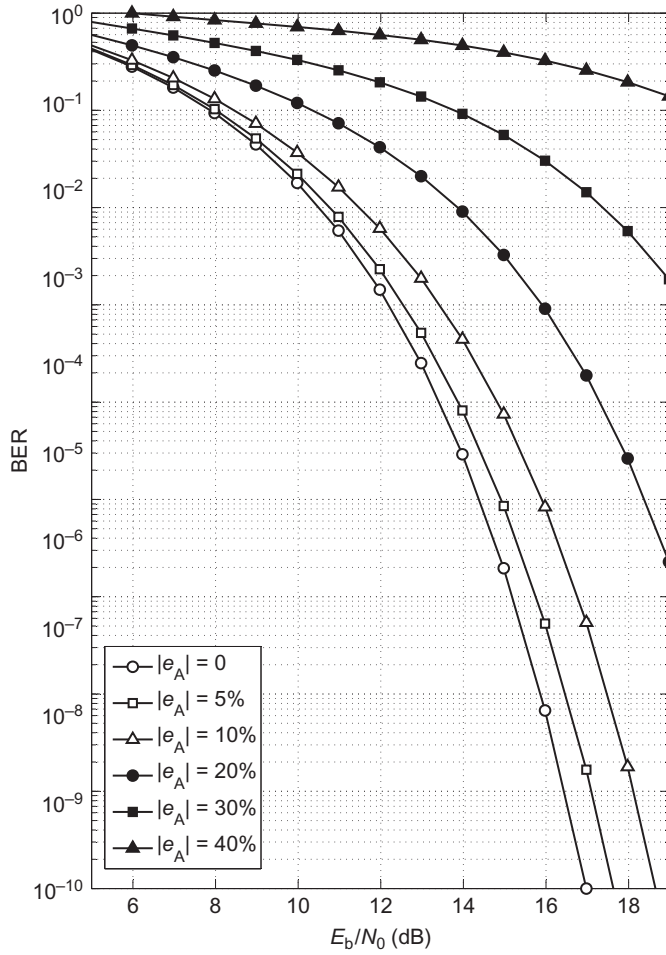


FIG. 7.6

BER of uncoded Gray-mapped 16-QAM, for  $e_\tau = e_F = e_\theta = 0$ .

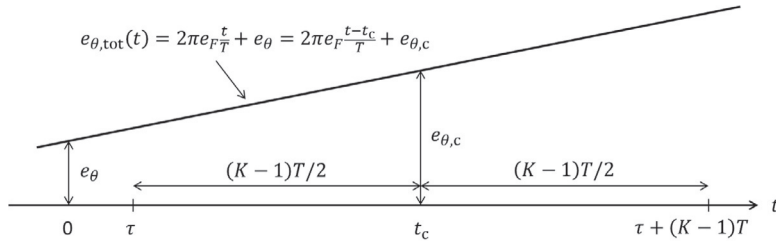


FIG. 7.7

Relation between  $e_\theta$ ,  $e_{\theta, c}$ , and  $t_c$ .

The symbol  $s_k$  is scaled by a factor  $(1 + e_A)^{-1}$  caused by the amplitude estimation error, and it is affected by a constant-speed rotation of  $-2\pi e_F$  rad per symbol interval caused by the frequency estimation error.

**Example 7.2** (Effect of frequency error on detection). Assuming 4-QAM transmission, perfect amplitude estimation (ie,  $e_A = 0$ ), and  $e_{\theta,c} = 0$ , Fig. 7.8 displays the scatter diagram of  $u_k$  from Eq. (7.20) in the absence of noise, for  $(e_F, K) = (10^{-3}, 101)$  (left) and  $(e_F, K) = (10^{-3}, 401)$  (right), respectively. The scatter diagram for  $K = 101$  shows four arcs, each centered at a constellation point and corresponding to an angle of  $2\pi(K-1)e_F = 0.2\pi$  rad (ie, 36 degrees); these arcs are located in the correct decision regions, so that no decision errors would occur in the absence of noise. For  $K = 401$ , the four arcs each correspond to  $0.8\pi$  rad (ie, 144 degrees); these arcs partly enter a wrong decision region, meaning that decision errors would occur in the absence of noise. This illustrates that for the given  $e_F$ , the effect of the constant-speed rotation increases with the frame length  $K$  and becomes detrimental for long frames.

When  $e_F$  is so large that the approximation  $g(mT, e_F) \approx \delta_m$  is no longer valid, we see from Eq. (7.18) that  $u_k$  depends not only on the symbol  $s_k$  but also on neighboring symbols: the frequency estimation error now gives rise to a constant-speed rotation and to ISI.

**Example 7.3** (Effect of frequency error on detection (cont'd.)). Fig. 7.9 shows the scatter diagram of  $u_k$  from Eq. (7.18) in the absence of noise, for 4-QAM transmission,  $e_{\theta,c} = 0$ ,  $e_A = 0$ , and  $(e_F, K) = (0.15, 101)$ . Because of the constant-speed rotation at  $-2\pi e_F = -0.3\pi$  rad (ie,  $-54$  degrees) per symbol interval, each

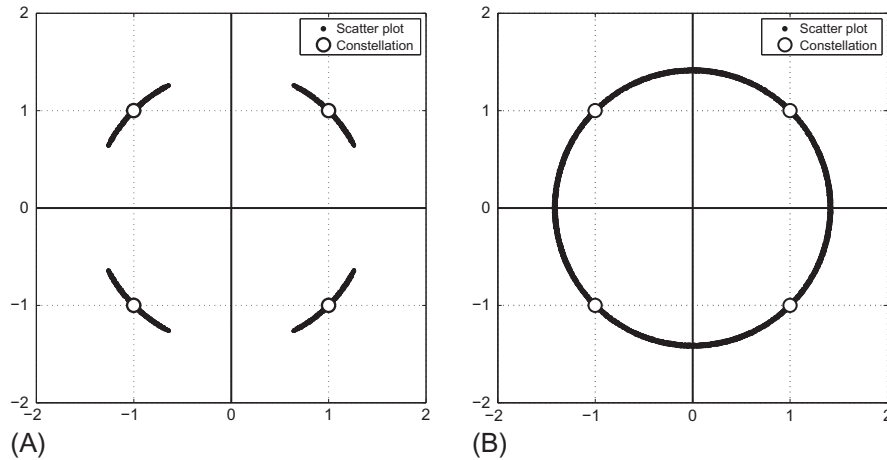


FIG. 7.8

4-QAM constellation and scatter diagram of  $u_k$  in the absence of noise, for  $e_{\tau} = e_A = e_{\theta,c} = 0$ ,  $e_F = 10^{-3}$  and  $K = 101$  (left),  $K = 401$  (right).

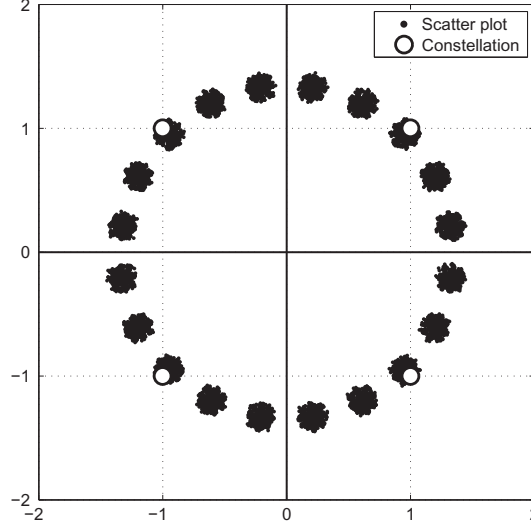


FIG. 7.9

4-QAM constellation and scatter diagram of  $u_k$  in the absence of noise, for  $e_\tau = e_A = e_{\theta,c} = 0$ ,  $e_F = 0.15$  and  $K = 101$ .

constellation point gives rise to the same set of 20 clusters spaced by  $0.1\pi$  rad (or 18 degrees), with the radius of the clusters giving an indication on the amount of ISI. Here too, decision errors will occur in the absence of noise.

### 7.3.2 PERFECT ESTIMATION OF $(A, \theta, F)$

Let us assume that  $(A, \theta, F)$  has been correctly estimated, but a time delay estimation error  $e_\tau$  is present. Defining the continuous-time signal  $u(t, A, \theta, F)$  as

$$u(t, A, \theta, F) = \frac{1}{A} \int h^*(u) y(t+u) e^{-je_{\theta, \text{tot}}(t+u)} du, \quad (7.21)$$

the condition  $e_A = e_\theta = e_F = 0$  reduces Eq. (7.14) to

$$\begin{aligned} u_k(A, \theta, F, \hat{\tau}) &= u(t, A, \theta, F)|_{t=kT+\hat{\tau}} \\ &= \sum_m s_m g(t - mT - \tau, 0)|_{t=kT+\hat{\tau}} + w_k \\ &= \sum_m s_{k-m} g(mT + e_\tau T, 0) + w_k. \end{aligned} \quad (7.22)$$

We see from Eq. (7.22) that  $u_k(A, \theta, F, \hat{\tau})$  contains not only the useful symbol  $s_k$ , but also symbols  $s_{k-m}$  with  $m \neq 0$ , which constitute ISI.

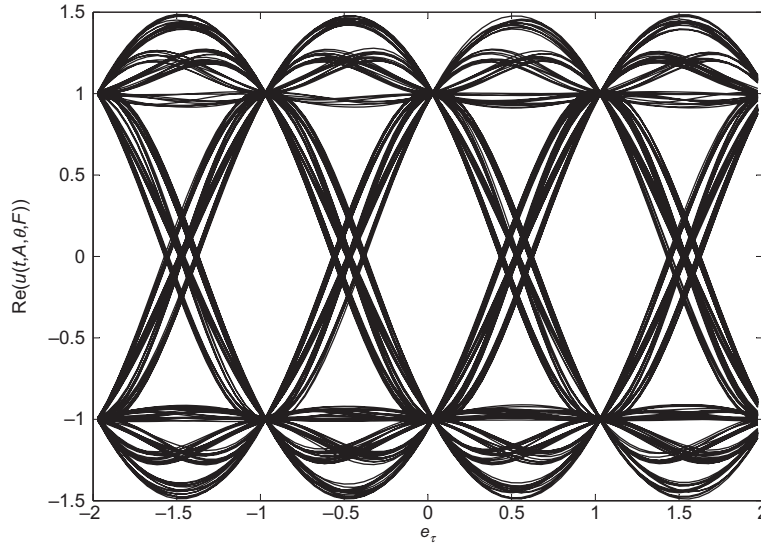


FIG. 7.10

Eye diagram of the in-phase component of  $u(t, A, \theta, F)$  in the absence of noise, assuming 4-QAM and square-root cosine-rolloff transmit filter with 50% rolloff.

**Example 7.4** (Effect of timing error on detection). Fig. 7.10 shows the eye diagram of the in-phase component of the signal  $u(t, A, \theta, F)$  in the absence of noise, assuming 4-QAM transmission, a square-root cosine-rolloff transmit filter with 50% rolloff, and  $\tau = 0$ . When sampling  $u(t, A, \theta, F)$  at instant  $kT + \tau$  (ie,  $e_\tau = 0$ ), ISI is absent:  $u_k(A, \theta, F, \tau) = s_k + w_k$ . We see from Fig. 7.10 that the vertical eye opening becomes zero at  $|e_\tau| \approx 0.4$ . For  $0 < |e_\tau| < 0.4$ , the time delay estimation error gives rise to ISI which reduces the noise margin as compared to  $e_\tau = 0$ . For  $0.4 < |e_\tau| < 0.5$ , the eye is closed, so that decision errors occur even in the absence of noise. For  $|e_\tau| > 0.5$ ,  $s_k$  is no longer the symbol having the largest contribution to  $u_k(A, \theta, F, \hat{\tau})$ , so also in this case decision errors occur in the absence of noise. Fig. 7.11 shows that the BER for uncoded 4-QAM transmission with Gray-mapping degrades with increasing  $|e_\tau|$ .

## 7.4 RESULTS FROM ESTIMATION AND DECISION THEORY

Estimation and decision theory is a branch of statistics involving the estimation of continuous parameters (“estimation”) and the detection of discrete parameters (“decision”).

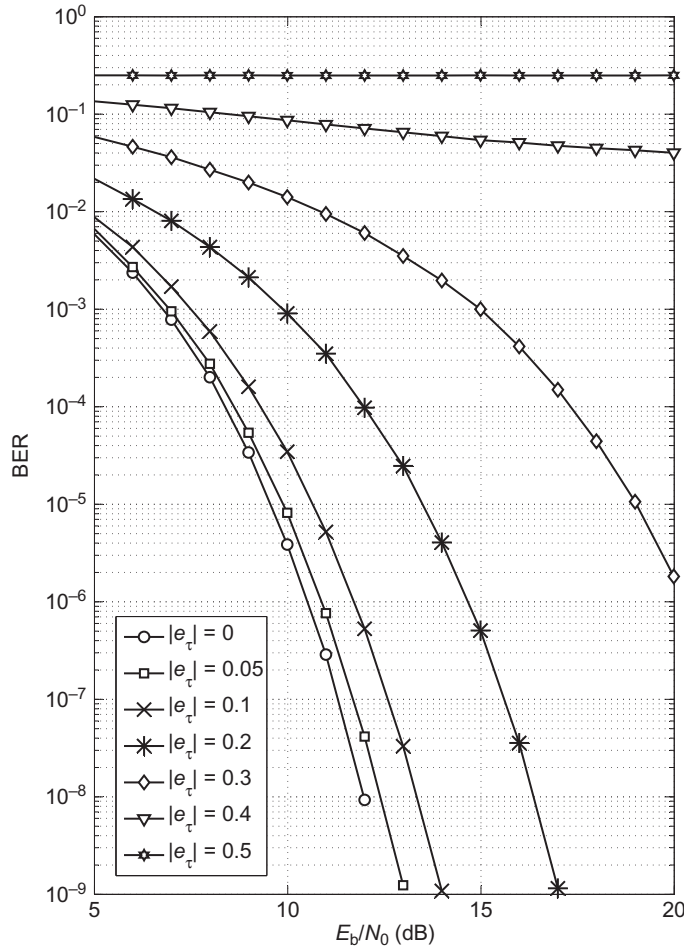


FIG. 7.11

BER of uncoded Gray-mapped 4-QAM, for  $e_A = e_F = e_\theta = 0$ .

In [Section 7.4.1](#) we consider maximum a posteriori (MAP) detection, which is optimum in terms of the decision error probability. We point out that MAP detection is hard to perform in the presence of unknown channel parameters because it involves averaging over the joint distribution of these parameters. Therefore, a simpler suboptimum detection is proposed, which makes use of estimates of the channel parameters. These estimates can be obtained using an MAP estimation algorithm, which is described in [Section 7.4.2](#). The MAP estimation algorithm makes use of the observed signal and of the a priori distribution of the channel parameters; we will assume that the channel parameters are uniformly distributed, in which case MAP

estimation simplifies to ML estimation. The presence of the unknown data symbols increases the complexity of the estimation of the channel parameters; in [Section 7.4.3](#) we describe the expectation-maximization (EM) algorithm, which is an iterative procedure allowing to obtain at reasonable complexity the MAP (or ML) channel estimates in the presence of the unknown data symbols. Finally, in [Section 7.4.4](#) we present fundamental lower bounds (ie, the Cramer-Rao bound (CRB) and the modified CRB (MCRB)) on the mean-square error (MSE) of (unbiased) estimates, which are useful as benchmarks for practical estimation algorithms.

### 7.4.1 MAP DETECTION

Basically, the main task of a receiver for digital communications is to detect the transmitted information bits. Let us consider an observation  $\mathbf{y}$ <sup>1</sup> characterized by a probability density function (p.d.f.)  $p(\mathbf{y}|\mathbf{b})$  that depends on the information bit sequence  $\mathbf{b}$ ; for the given  $\mathbf{y}$ , the conditional p.d.f.  $p(\mathbf{y}|\mathbf{b})$  seen as a function of  $\mathbf{b}$  is referred to as the likelihood function of  $\mathbf{b}$ . Let us denote by  $\hat{\mathbf{b}}$  the receiver's decision about the transmitted bit sequence  $\mathbf{b}$ . From decision theory [1] we know that the sequence error probability  $\Pr[\hat{\mathbf{b}} \neq \mathbf{b}]$  and the bit error probability  $\Pr[\hat{b}_j \neq b_j]$  regarding the  $j$ th bit  $b_j$  are minimized by the MAP sequence decision, given by

$$\hat{\mathbf{b}} = \arg \max_{\mathbf{b}} p(\mathbf{b}|\mathbf{y}) \quad (7.23)$$

and by the MAP bit decision, given by

$$\hat{b}_j = \arg \max_{b_j} p(b_j|\mathbf{y}) \quad (7.24)$$

respectively. In Eqs. (7.23) and (7.24),  $p(\mathbf{b}|\mathbf{y})$  and  $p(b_j|\mathbf{y})$  denote the a posteriori probability (APP) of the information bit sequence and of the  $j$ th information bit, respectively. The APP  $p(b_j|\mathbf{y})$  results from the marginalization of  $p(\mathbf{b}|\mathbf{y})$ , ie,

$$p(b_j|\mathbf{y}) = \sum_{\mathbf{b} \setminus b_j} p(\mathbf{b}|\mathbf{y}), \quad (7.25)$$

where the summation runs over all bits except the  $j$ th bit. According to Bayes' rule, we have

$$p(\mathbf{b}|\mathbf{y}) = \frac{p(\mathbf{y}|\mathbf{b})p(\mathbf{b})}{p(\mathbf{y})}, \quad (7.26)$$

which relates the APP  $p(\mathbf{b}|\mathbf{y})$  to the likelihood function  $p(\mathbf{y}|\mathbf{b})$  and the a priori probability  $p(\mathbf{b})$  of  $\mathbf{b}$ .

The application of the MAP decision rule becomes complicated when the p.d.f. of the observation depends not only on the bit sequence  $\mathbf{b}$ , but also on a “nuisance”

---

<sup>1</sup>In the case of a continuous-time observation  $y(t)$ ,  $\mathbf{y}$  denotes a vector representation of  $y(t)$ .

vector parameter  $\boldsymbol{\psi}$  (which in the context of digital communications consists of the channel parameters); in this case, the p.d.f. of  $\mathbf{y}$  is denoted  $p(\mathbf{y}|\mathbf{b}, \boldsymbol{\psi})$ , and for a given  $\mathbf{y}$ , represents the likelihood function of  $(\mathbf{b}, \boldsymbol{\psi})$ . For the linear modulation system considered in Section 7.2,  $p(\mathbf{y}|\mathbf{b}, \boldsymbol{\psi})$  equals the likelihood function  $\lambda(\mathbf{s}, \boldsymbol{\psi})|_{\mathbf{s}=\chi(\mathbf{b})}$  from Eq. (7.7), where  $\boldsymbol{\psi} = (A, \theta, F, \tau)$  and  $\mathbf{s} = \chi(\mathbf{b})$  denotes the relation between the symbol sequence  $\mathbf{s}$  and the information bits  $\mathbf{b}$ , imposed by the binary encoder and the mapper. The APP  $p(\mathbf{b}|\mathbf{y})$  can still be obtained as in Eq. (7.26), but the likelihood function of  $\mathbf{b}$  must now be computed as

$$p(\mathbf{y}|\mathbf{b}) = \int p(\mathbf{y}|\mathbf{b}, \boldsymbol{\psi}) p(\boldsymbol{\psi}) d\boldsymbol{\psi} \quad (7.27)$$

$$= E_{\boldsymbol{\psi}}[p(\mathbf{y}|\mathbf{b}, \boldsymbol{\psi})]. \quad (7.28)$$

In Eq. (7.27) we have assumed that the nuisance parameters are independent of the bit sequence. The high complexity of the MAP decision comes from the averaging of the likelihood function  $p(\mathbf{y}|\mathbf{b}, \boldsymbol{\psi})$  over the nuisance parameters, which involves multidimensional integration.

#### 7.4.2 MAP ESTIMATION

An alternative expression of the a posteriori probability  $p(\mathbf{b}|\mathbf{y})$  in the presence of nuisance parameters is obtained as

$$p(\mathbf{b}|\mathbf{y}) = \int p(\mathbf{b}|\mathbf{y}, \boldsymbol{\psi}) p(\boldsymbol{\psi}|\mathbf{y}) d\boldsymbol{\psi}. \quad (7.29)$$

If the receiver knows that the nuisance parameter  $\boldsymbol{\psi}$  takes a value  $\boldsymbol{\psi}_0$ , we have  $p(\boldsymbol{\psi}|\mathbf{y}) = \delta(\boldsymbol{\psi} - \boldsymbol{\psi}_0)$  irrespective of  $\mathbf{y}$ , in which case Eq. (7.29) simplifies to  $p(\mathbf{b}|\mathbf{y}) = p(\mathbf{b}|\mathbf{y}, \boldsymbol{\psi}_0)$ . For the linear modulation system considered in Section 7.2, the detection (7.23) or (7.24), based on  $p(\mathbf{b}|\mathbf{y}, \boldsymbol{\psi}_0)$  or on its marginals  $p(b_i|\mathbf{y}, \boldsymbol{\psi}_0)$ , consists of applying the samples  $\mathbf{u}(A, \theta, F, \tau)$  from Eq. (7.9) to the appropriate decoder/detector, which according to Eq. (7.12) is designed for operating on the noisy symbol sequence  $\mathbf{s} + \mathbf{w}$ .

When the value of the nuisance parameter  $\boldsymbol{\psi}$  is not known to the receiver, the observation  $\mathbf{y}$  provides information on  $\boldsymbol{\psi}$  through the a posteriori p.d.f.  $p(\boldsymbol{\psi}|\mathbf{y})$ . Let us introduce the MAP estimate  $\hat{\boldsymbol{\psi}}$  of the nuisance parameter  $\boldsymbol{\psi}$ , which is defined as [1]

$$\hat{\boldsymbol{\psi}} = \arg \max_{\boldsymbol{\psi}} p(\boldsymbol{\psi}|\mathbf{y}). \quad (7.30)$$

Assuming that  $p(\boldsymbol{\psi}|\mathbf{y})$  exhibits a sharp peak at the MAP estimate (this happens when  $\mathbf{y}$  provides reliable information on  $\boldsymbol{\psi}$ ), we can use in Eq. (7.29) the approximation  $p(\boldsymbol{\psi}|\mathbf{y}) \approx \delta(\boldsymbol{\psi} - \hat{\boldsymbol{\psi}})$ , which yields  $p(\mathbf{b}|\mathbf{y}) \approx p(\mathbf{b}|\mathbf{y}, \hat{\boldsymbol{\psi}})$ ; note that  $\hat{\boldsymbol{\psi}}$  is a function of  $\mathbf{y}$ . Performing detection/decoding based on this approximation has the advantage that we can use the same receiver (including the detector/decoder) as when the nuisance parameters are known, except that now the actual values of the nuisance

parameters are replaced by the nuisance parameter estimates; this involves the computation of  $\mathbf{u}(\hat{\boldsymbol{\psi}})$  and applying these samples to the detector/decoder that has been designed to operate on the noisy symbols  $\mathbf{s} + \mathbf{w}$ . This receiver strategy avoids the multidimensional integration from Eq. (7.27), but instead requires an estimator module that provides an estimate  $\hat{\boldsymbol{\psi}}$  of the nuisance parameters, based on the observation  $\mathbf{y}$ .

Using Bayes' rule, the a posteriori p.d.f.  $p(\boldsymbol{\psi}|\mathbf{y})$  can be written as

$$p(\boldsymbol{\psi}|\mathbf{y}) = \frac{p(\mathbf{y}, \boldsymbol{\psi})}{p(\mathbf{y})} = \frac{p(\mathbf{y}|\boldsymbol{\psi})p(\boldsymbol{\psi})}{p(\mathbf{y})}, \quad (7.31)$$

where  $p(\mathbf{y}|\boldsymbol{\psi})$  and  $p(\boldsymbol{\psi})$  are the likelihood function and the a priori p.d.f. of  $\boldsymbol{\psi}$ , respectively, and  $p(\mathbf{y}, \boldsymbol{\psi})$  denotes the joint p.d.f. of  $\mathbf{y}$  and  $\boldsymbol{\psi}$ . We will assume that the elements of  $\boldsymbol{\psi}$  are statistically independent and uniformly distributed, so that the a priori p.d.f.  $p(\boldsymbol{\psi})$  is uniform; in this case MAP estimation of  $\boldsymbol{\psi}$  reduces to ML estimation, ie, the maximization of the likelihood function  $p(\mathbf{y}|\boldsymbol{\psi})$ .

The MAP or ML estimation of  $\boldsymbol{\psi}$  requires a multidimensional maximization over all elements of  $\boldsymbol{\psi}$ . The computational complexity can be reduced by adopting an alternative approach, which consists of partitioning the parameter set  $\boldsymbol{\psi}$  into two subsets  $\boldsymbol{\psi}_1$  and  $\boldsymbol{\psi}_2$ , and estimating  $\boldsymbol{\psi}_1$  and  $\boldsymbol{\psi}_2$  separately instead of jointly. For instance, for  $\hat{\boldsymbol{\psi}}_1$  we take the ML estimate of  $\boldsymbol{\psi}_1$ , which maximizes the likelihood function  $p(\mathbf{y}|\boldsymbol{\psi}_1) = \int p(\mathbf{y}|\boldsymbol{\psi})p(\boldsymbol{\psi}_2)d\boldsymbol{\psi}_2$  of  $\boldsymbol{\psi}_1$ ; then we consider  $\hat{\boldsymbol{\psi}}_1$  as the actual value of  $\boldsymbol{\psi}_1$ , and obtain  $\hat{\boldsymbol{\psi}}_2$  by maximizing the likelihood function  $p(\mathbf{y}|\hat{\boldsymbol{\psi}}_1, \boldsymbol{\psi}_2) = p(\mathbf{y}|\boldsymbol{\psi})|_{\boldsymbol{\psi}_1=\hat{\boldsymbol{\psi}}_1}$  with respect to  $\boldsymbol{\psi}_2$ . As compared to MAP or ML estimation of  $\boldsymbol{\psi}$ , the alternative approach involves two lower-dimensional maximizations, which is less complex than a single maximization over all elements of  $\boldsymbol{\psi}$ .

### 7.4.3 THE EXPECTATION-MAXIMIZATION ALGORITHM

It follows from Eq. (7.31) that the MAP estimate  $\hat{\boldsymbol{\psi}}$  of a parameter  $\boldsymbol{\psi}$  from an observation  $\mathbf{y}$  can be obtained as  $\hat{\boldsymbol{\psi}} = \arg \max_{\boldsymbol{\psi}} \ln(p(\mathbf{y}, \boldsymbol{\psi}))$ , because  $p(\mathbf{y})$  does not depend on  $\boldsymbol{\psi}$ , and  $\ln(\cdot)$  is a monotonically increasing function of its argument. Let us consider the case where the observation  $\mathbf{y}$  is a many-to-one function of some vector  $\mathbf{y}_c$ , ie,  $\mathbf{y} = \mathbf{g}(\mathbf{y}_c)$ ;  $\mathbf{y}_c$  and  $\mathbf{y}$  are referred to as the complete data and the incomplete data, respectively. Denoting by  $p_c(\mathbf{y}_c, \boldsymbol{\psi})$  the joint p.d.f. of the complete data  $\mathbf{y}_c$  and the parameter  $\boldsymbol{\psi}$ , we have

$$p(\mathbf{y}, \boldsymbol{\psi}) = \int_{\{\mathbf{y}_c|\mathbf{y}=\mathbf{g}(\mathbf{y}_c)\}} p_c(\mathbf{y}_c, \boldsymbol{\psi})d\mathbf{y}_c. \quad (7.32)$$

Depending on the function  $\mathbf{g}(\cdot)$ ,  $p(\mathbf{y}, \boldsymbol{\psi})$  might be hard to compute even for simple  $p_c(\mathbf{y}_c, \boldsymbol{\psi})$ , in which case the MAP estimate based on  $\mathbf{y}$  is difficult to obtain.

The EM algorithm [9] provides a way to compute in an iterative way the MAP estimate based on  $\mathbf{y}$ . Denoting by  $\hat{\boldsymbol{\psi}}^{(i)}$  the estimate resulting from the  $i$ th iteration,

the estimate  $\hat{\psi}^{(i+1)}$  is obtained from  $\hat{\psi}^{(i)}$  and  $\mathbf{y}$  in two steps, ie, an expectation step and a maximization step. The expectation step consists of computing the function  $Q(\psi|\hat{\psi}^{(i)})$ , given by

$$\begin{aligned} Q(\psi|\hat{\psi}^{(i)}) &= \int \ln(p_c(\mathbf{y}_c, \psi)) p_c(\mathbf{y}_c|\mathbf{y}, \hat{\psi}^{(i)}) d\mathbf{y}_c \\ &= E \left[ \ln(p_c(\mathbf{y}_c, \psi)) | \mathbf{y}, \hat{\psi}^{(i)} \right]. \end{aligned} \quad (7.33)$$

The function  $Q(\psi|\hat{\psi}^{(i)})$  denotes the a posteriori expectation of  $\ln(p_c(\mathbf{y}_c, \psi))$ , which is obtained by averaging over the a posteriori p.d.f.  $p_c(\mathbf{y}_c|\mathbf{y}, \hat{\psi}^{(i)})$  of the complete data  $\mathbf{y}_c$ , conditioned on the incomplete data  $\mathbf{y}$  and the value  $\hat{\psi}^{(i)}$  of the parameter  $\psi$ , obtained in the  $i$ th iteration. The maximization step involves maximizing  $Q(\psi|\hat{\psi}^{(i)})$  with respect to  $\psi$ , ie,

$$\hat{\psi}^{(i+1)} = \arg \max_{\psi} Q(\psi|\hat{\psi}^{(i)}). \quad (7.34)$$

It can be shown that with an increasing iteration index  $i$ ,  $\hat{\psi}^{(i)}$  converges to a value  $\hat{\psi}^{(\infty)}$  that corresponds to a maximum of  $p(\mathbf{y}, \psi)$ , which depending on the starting value  $\hat{\psi}^{(0)}$ , might be a local rather than the global maximum. The EM algorithm can also be used for ML estimation; in this case, we simply have to replace in the above derivations the joint p.d.f.  $p_c(\mathbf{y}_c, \psi)$  by the likelihood function  $p_c(\mathbf{y}_c|\psi)$  based on the complete data  $\mathbf{y}_c$ .

Let us consider the MAP estimation of the channel parameters  $\psi$  from an observation  $\mathbf{y}$  that depends not only on  $\psi$  but also on the information bit sequence  $\mathbf{b}$ ; the associated likelihood function is  $p(\mathbf{y}|\mathbf{b}, \psi)$ . The MAP estimate  $\hat{\psi}$  maximizes the joint p.d.f.  $p(\mathbf{y}, \psi)$ , which can be expressed as  $p(\mathbf{y}, \psi) = \sum_{\mathbf{b}} p(\mathbf{y}, \mathbf{b}, \psi)$ ; this summation over all bit sequences  $\mathbf{b}$  precludes a simple computation of the MAP estimate  $\hat{\psi}$ . Instead, we will make use of the EM algorithm for obtaining the MAP estimate in an iterative way. As complete data, we choose  $\mathbf{y}_c = (\mathbf{y}, \mathbf{b})$ . In this case, the expectation step Eq. (7.33) becomes

$$\begin{aligned} Q(\psi|\hat{\psi}^{(i)}) &= \sum_{\mathbf{b}} \ln(p(\mathbf{y}, \mathbf{b}, \psi)) p(\mathbf{b}|\mathbf{y}, \hat{\psi}^{(i)}) \\ &= E \left[ \ln(p(\mathbf{y}, \mathbf{b}, \psi)) | \mathbf{y}, \hat{\psi}^{(i)} \right]. \end{aligned} \quad (7.35)$$

The expectation in Eq. (7.35) is with respect to  $p(\mathbf{b}|\mathbf{y}, \psi = \hat{\psi}^{(i)})$ , ie, the APP of  $\mathbf{b}$ , conditioned on  $\mathbf{y}$  and the value  $\hat{\psi}^{(i)}$  of the parameter  $\psi$ .

For the case of linear modulation, we will show in [Section 7.9](#) that  $Q(\psi|\hat{\psi}^{(i)})$  turns out to be a simple expression, involving the marginal a posteriori symbol probabilities which are obtained from the detector/decoder. Hence, the application of the EM algorithm yields a considerable complexity advantage compared to the maximization of  $p(\mathbf{y}, \psi) = \sum_{\mathbf{b}} p(\mathbf{y}, \mathbf{b}, \psi)$  over  $\psi$ , the latter requiring a summation over all information bit sequences.

#### 7.4.4 BOUNDS ON ESTIMATION PERFORMANCE

Here, we present two theoretical lower bounds on the MSE of unbiased estimates. These bounds can be computed from the likelihood function and serve as a useful benchmark for the MSE resulting from practical estimation algorithms.

Assume we have obtained from the observation  $\mathbf{y}$  an estimate (not necessarily MAP or ML)  $\hat{\psi}$  of  $\psi$ ; in order to emphasize the dependence of  $\hat{\psi}$  on  $\mathbf{y}$ , we will occasionally make use of the notation  $\hat{\psi}(\mathbf{y})$ . Consider the conditional expectation  $E[\hat{\psi}|\psi]$ , which is obtained as

$$E[\hat{\psi}|\psi] = \int \hat{\psi}(\mathbf{y})p(\mathbf{y}|\psi)d\mathbf{y}. \quad (7.36)$$

When  $E[\hat{\psi}|\psi] = \psi$ , the estimate  $\hat{\psi}$  is said to be unbiased. The CRB [\[1\]](#) is a theoretical lower bound on the MSE of unbiased estimates. Arranging  $\hat{\psi}$  and  $\psi$  as column vectors and defining the estimation error  $\mathbf{e} = \hat{\psi} - \psi$ , the estimation error correlation matrix for given  $\psi$  is given by  $E[\mathbf{e}\mathbf{e}^T|\psi]$ . The CRB states that  $E[\mathbf{e}\mathbf{e}^T|\psi] - \mathbf{J}_{\text{FIM}}^{-1}$  is a positive semi-definite matrix. Denoting the  $n$ th component of  $\hat{\psi}$  and  $\psi$  by  $\hat{\psi}_n$  and  $\psi_n$  respectively, it follows that the MSE of unbiased estimates is lower bounded as

$$E[(\hat{\psi}_n - \psi_n)^2|\psi] \geq (\mathbf{J}_{\text{FIM}}^{-1})_{n,n}. \quad (7.37)$$

In the above,  $\mathbf{J}_{\text{FIM}}$  denotes the Fisher information matrix (FIM), which is defined as

$$(\mathbf{J}_{\text{FIM}})_{m,n} = E \left[ \frac{\partial \ln(p(\mathbf{y}|\psi))}{\partial \psi_m} \frac{\partial \ln(p(\mathbf{y}|\psi))}{\partial \psi_n} \middle| \psi \right]. \quad (7.38)$$

As in [Eq. \(7.36\)](#), the conditional expectations in [Eqs. \(7.37\) and \(7.38\)](#) are over the p.d.f.  $p(\mathbf{y}|\psi)$ , so that these expectations in general depend on  $\psi$ . The CRB represents a fundamental lower bound on the MSE, and therefore serves as a useful benchmark for the MSE of practical estimation algorithms.

The p.d.f. of  $\mathbf{y}$  depends on the information bit sequence  $\mathbf{b}$  and the channel parameters  $\psi$ , so that  $\mathbf{b}$  acts as a nuisance parameter with respect to the estimation of  $\psi$ . The p.d.f.  $p(\mathbf{y}|\psi)$  needed for the computation of the CRB is given by

$$p(\mathbf{y}|\psi) = \sum_{\mathbf{b}} p(\mathbf{y}|\mathbf{b}, \psi)p(\mathbf{b}), \quad (7.39)$$

which involves a summation over all possible information bit sequences inside the logarithmic functions from Eq. (7.38). Hence the presence of the nuisance parameters considerably complicates the evaluation of the CRB. This problem can be circumvented by using a simpler but looser bound on the MSE of unbiased estimates, which is referred to as the MCRB [10,11]. According to the MCRB,  $\mathbf{E}[\mathbf{e}\mathbf{e}^T|\boldsymbol{\psi}] - \mathbf{J}_{\text{MFIM}}^{-1}$  is a positive semi-definite matrix, which limits the MSE of unbiased estimates as

$$\mathbf{E}[(\hat{\psi}_n - \psi_n)^2|\boldsymbol{\psi}] \geq (\mathbf{J}_{\text{MFIM}}^{-1})_{n,n}. \quad (7.40)$$

The matrix  $\mathbf{J}_{\text{MFIM}}$  denotes the modified FIM (MFIM), which is defined as

$$(\mathbf{J}_{\text{MFIM}})_{m,n} = \mathbf{E} \left[ \frac{\partial \ln(p(\mathbf{y}|\mathbf{b}, \boldsymbol{\psi}))}{\partial \psi_m} \frac{\partial \ln(p(\mathbf{y}|\mathbf{b}, \boldsymbol{\psi}))}{\partial \psi_n} \middle| \boldsymbol{\psi} \right]. \quad (7.41)$$

The expectation in Eq. (7.41) is over the joint conditional p.d.f.  $p(\mathbf{y}, \mathbf{b}|\boldsymbol{\psi}) = p(\mathbf{y}|\mathbf{b}, \boldsymbol{\psi})p(\mathbf{b})$ . As the summation over the information bit sequences is no longer present inside the logarithmic functions from Eq. (7.41), the MCRB has lower computational complexity than the CRB. When the observation  $y(t)$  can be decomposed as  $y(t) = x(t, \mathbf{b}, \boldsymbol{\psi}) + v(t)$ , where  $v(t)$  denotes complex-valued AWGN with power spectral density  $N_0$ , it can be verified from Eq. (7.41) that

$$(\mathbf{J}_{\text{MFIM}})_{m,n} = \frac{2}{N_0} \Re \left( \mathbf{E} \left[ \int \frac{\partial x(t, \mathbf{b}, \boldsymbol{\psi})}{\partial \psi_m} \frac{\partial x^*(t, \mathbf{b}, \boldsymbol{\psi})}{\partial \psi_n} dt \right] \right), \quad (7.42)$$

where the expectation is over  $\mathbf{b}$ .

A simplification in the computation of the CRB or the MCRB consists of partitioning the set of channel parameters  $\boldsymbol{\psi}$  into two subsets  $\boldsymbol{\psi}_1$  and  $\boldsymbol{\psi}_2$ , and computing the (M)CRB for one subset of parameters, assuming that the parameters from the other subset are known to the receiver. This approach gives rise to a looser bound, which however, is simpler to evaluate. The same looser bound is obtained from Eq. (7.37) or Eq. (7.40) by setting to zero the elements of the (M)FIM for which the row index and the column index refer to different parameter subsets.

## 7.5 ESTIMATION STRATEGY

We consider the estimation of the channel parameters  $(A, \theta, F, \tau)$  from the received signal  $y(t)$  given by Eq. (7.3). The estimation of  $\theta$ ,  $F$ , and  $A$  is referred to as carrier phase synchronization, carrier frequency synchronization, and amplitude estimation, respectively. In the following, we will decompose the time delay  $\tau$  as  $\tau = (k_\tau + \epsilon)T$ , where  $k_\tau$  is integer and  $|\epsilon| < 1/2$ ;  $k_\tau T$  and  $\epsilon T$  denote the integer delay and the fractional delay. The estimation of  $k_\tau$  and  $\epsilon$  is referred to as frame synchronization and symbol timing synchronization. The receiver is assumed to know the uncertainty intervals of  $F$  and  $\tau$ , ie,  $|F| \leq F_{\max}$  and  $\tau_{\min} \leq \tau \leq \tau_{\max}$ .

The joint ML estimation of the parameters  $\boldsymbol{\psi} = (A, \theta, F, \tau)$  would involve a four-dimensional maximization of the corresponding likelihood function  $\lambda(\boldsymbol{\psi})$ ; moreover, this likelihood function must be obtained as the expectation of the likelihood function from Eq. (7.7) over all allowed symbol sequences, ie,  $\lambda(\boldsymbol{\psi}) = \text{E}_s[\lambda(\mathbf{s}, \boldsymbol{\psi})]$ , involving a summation over all codewords. Obviously, this is much too complex for practical implementation. Therefore, some simplifications that reduce the complexity must be introduced.

We propose an estimation strategy, where first a coarse estimate  $\hat{F}$  of the frequency offset  $F$  is obtained, based on maximizing (an approximation of) the likelihood function  $\lambda(F) = \text{E}_{\mathbf{s}, A, \theta, \tau} [\lambda(\mathbf{s}, \boldsymbol{\psi})]$  with respect to  $F$ . Next, we make use of  $\hat{F}$  to derive an estimate  $\hat{\epsilon}$  of the normalized fractional time delay  $\epsilon$ , by maximizing (an approximation of) the likelihood function  $\lambda(\hat{F}, \epsilon) = \lambda(F, \epsilon)|_{F=\hat{F}}$  with respect to  $\epsilon$ , where

$$\lambda(F, \epsilon) = \text{E}_{\mathbf{s}, A, \theta, k_\tau} [\lambda(\mathbf{s}, \boldsymbol{\psi})|_{\tau=(k_\tau+\epsilon)T}]. \quad (7.43)$$

The corresponding estimation algorithms are referred to as *nondata-aided* (NDA), because they result from likelihood functions that have been averaged over the symbol vector  $\mathbf{s}$ .

Having obtained the NDA estimates  $\hat{F}$  and  $\hat{\epsilon}$ , the receiver computes the matched filter output samples  $z_k = z(kT + \hat{\epsilon}T, \hat{F})$ , which we model as

$$z_k = A e^{j\theta_{\text{res}}(kT + \hat{\epsilon}T)} s_{k-k_\tau} + n_k, \quad (7.44)$$

where  $n_k$  is discrete-time complex AWGN with  $\text{E}[|n_k|^2] = N_0$ ; in Eq. (7.44),

$$\theta_{\text{res}}(t) = 2\pi F_{\text{res}}t + \theta \quad (7.45)$$

denotes the time-varying residual total phase after applying the frequency correction  $e^{-j2\pi\hat{F}t}$  to the received signal  $y(t)$ , and  $F_{\text{res}} = F - \hat{F}$  represents the corresponding residual frequency offset. The observation model (7.44) is based on the assumptions that (i) the symbol timing estimation error  $\hat{\epsilon} - \epsilon$  is sufficiently small, so that  $\tau - \hat{\epsilon}T \approx k_\tau T$ ; and (ii) the residual frequency error  $F_{\text{res}}$  is sufficiently small, so that  $g(mT, -F_{\text{res}}T) \approx \delta_m$ , but not small enough to ignore the residual constant-speed rotation (at  $2\pi F_{\text{res}}T$  rad per symbol interval) of the signal component of  $z_k$ . We will make use of the observation model (7.44) to derive estimates of  $(A, \theta, F_{\text{res}}, k_\tau)$ . In practice, the (small) nonzero values of  $\hat{\epsilon} - \epsilon$  and  $g(mT, -F_{\text{res}}T)$  for  $m \neq 0$  give rise to some (small) ISI in Eq. (7.44), which will adversely affect the estimation and detection performance.

In order to assist the estimation of  $(A, \theta, F_{\text{res}}, k_\tau)$ , the transmitter sends pilot symbols (ie, symbols that are known to the receiver) among the unknown data symbols. By setting to zero the data symbols in Eq. (7.44) and keeping only the pilot symbols, the resulting likelihood function contains no unknown data symbols. The estimates of  $(A, \theta, F_{\text{res}}, k_\tau)$  are obtained by maximizing this pilot-only likelihood

function, yielding a simple estimation algorithm because no averaging over the data symbols is required. The resulting estimation algorithms are referred to as *pilot-aided* (PA).

The estimates resulting from the pilot-aided algorithms make use of the pilot symbols, but not of the data symbols. Improved estimates of  $(A, \theta, F_{\text{res}}, k_\tau)$  based on the observation  $\{z_k\}$  from Eq. (7.44) that also includes the data symbols will be obtained by means of the EM algorithm (see Section 7.4.3). Application of the EM algorithm involves iterating between estimation and decoding; therefore, the corresponding estimation algorithms are referred to as *code-aided* (CA).

Having obtained the (PA or CA) estimates  $(\hat{A}, \hat{\theta}, \hat{F}_{\text{res}}, \hat{k}_\tau)$ , the receiver computes the scaled and rotated matched filter output samples  $\{u_k\}$  that will be applied to the detector/decoder, where

$$\begin{aligned} u_k &= \frac{1}{\hat{A}} z_{k+\hat{k}_\tau} e^{-j\hat{\theta}_{\text{res}}(kT+\hat{\tau})} \\ &= \frac{1}{\hat{A}} z_{k+\hat{k}_\tau} e^{-j(\hat{\theta}_{\text{res}}(\hat{\tau})+2\pi\hat{F}_{\text{res}}kT)}. \end{aligned} \quad (7.46)$$

In Eq. (7.46),  $\hat{\tau} = (\hat{k}_\tau + \hat{\epsilon})T$  and  $\hat{\theta}_{\text{res}}(t) = 2\pi\hat{F}_{\text{res}}t + \hat{\theta}$  are the estimates of  $\tau$  and  $\theta_{\text{res}}(t)$ .

In Sections 7.6–7.9 we derive specific algorithms for estimating the channel parameters. We use the notations  $\tilde{\psi}$  and  $\hat{\psi}$  to denote a trial value and the estimate, respectively, of a parameter vector  $\psi$ . The estimation algorithms will be derived under the assumption that the transmitter sends a single frame consisting of  $K$  symbols  $(s_0, \dots, s_{K-1})$ , and that the observation interval  $(t_{\min}, t_{\max})$  is sufficiently long to capture the entire useful signal. Taking into account the uncertainty interval  $\tau_{\min} \leq \tau \leq \tau_{\max}$ , Fig. 7.12 illustrates that we require  $t_{\min} < \tau_{\min}$  and  $t_{\max} > (K-1)T + \tau_{\max}$ , in order for the observation interval to contain the tails of all  $K$  transmitted pulses, for any allowed value of the time delay  $\tau$  within the uncertainty interval; typically,  $KT \gg \tau_{\max} - \tau_{\min}$ , which yields  $KT/T_0 \approx 1$ , with  $T_0 = t_{\max} - t_{\min}$  denoting the length of the observation interval. The performance of the resulting algorithms will be evaluated in Section 7.11, also when the transmitter sends a sequence of frames (rather than just a single frame); in this case, the observation

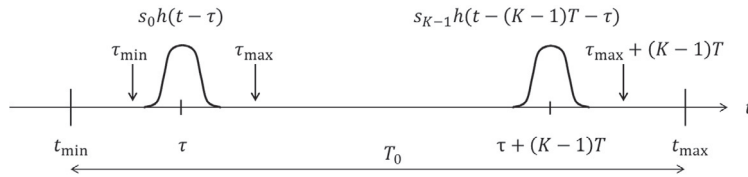


FIG. 7.12

Illustration of observation interval  $(t_{\min}, t_{\max})$ .

interval  $(t_{\min}, t_{\max})$  also contains pulse tails from adjacent frames, which might affect the performance of the algorithms that have been derived under the assumption of single-frame transmission.

## 7.6 NDA COARSE FREQUENCY ESTIMATION

The frequency estimate  $\hat{F}$  is obtained by maximizing (an approximation of) the likelihood function  $\lambda(\tilde{F})$ . We point out in [Appendix A](#) that  $\lambda(\tilde{F}) \approx \lambda_{\text{app}}(\tilde{F})$  with

$$\lambda_{\text{app}}(\tilde{F}) = \frac{1}{T_0} \int g^*(u, 0) e^{-j2\pi\tilde{F}u} \left( \int_{t_{\min}}^{t_{\max}} y(t) y^*(t - u) dt \right) du, \quad (7.47)$$

where  $g(u, 0)$  follows from Eq. (7.16) and  $y(t)$  is the signal (7.3) at the receiver input. In order to allow digital signal processing, we replace in Eq. (7.47) the integrations by summations of samples:

$$\lambda_{\text{app}}(\tilde{F}) = \sum_l e^{-j2\pi\tilde{F}lT_s} g^*(lT_s, 0) r_{y_{AA}}(lT_s), \quad (7.48)$$

where

$$r_{y_{AA}}(lT_s) = \frac{1}{M_0} \sum_{m=m_0}^{m_0+M_0-1} y_{AA}(mT_s) y_{AA}^*(mT_s - lT_s) \quad (7.49)$$

is the time-autocorrelation function of the sequence  $\{y_{AA}(mT_s)\}$  over  $M_0$  samples, corresponding to a time shift  $lT_s$ ; we assume  $T_0 = M_0T_s$  and  $t_{\min} = m_0T_s$ . The sequence  $\{y_{AA}(mT_s)\}$  is obtained by applying  $y(t)$  to an anti-aliasing filter  $H_{AA}(f)$  and sampling the resulting signal  $y_{AA}(t)$  at a properly selected (see further) rate  $1/T_s$ . The anti-aliasing filter  $H_{AA}(f)$  has a unit gain at  $f = 0$  and a bandwidth  $B_{AA}$  (ie,  $H_{AA}(0) = 1$  and  $H_{AA}(f) = 0$  for  $|f| > B_{AA}$ ), and it should not distort the useful signal in  $y(t)$ . Hence, for a frequency uncertainty interval  $F \leq |F_{\max}|$  and a transmit filter with bandwidth  $B$  (ie,  $H(f) = 0$  for  $|f| > B$ ), the passband of  $H_{AA}(f)$  should not be less than  $B + F_{\max}$ , yielding  $B_{AA} > B + F_{\max}$ , as indicated in [Fig. 7.13](#).

Maximizing Eq. (7.48) over  $\tilde{F}$  does not yield a closed-form solution. Therefore, we will further approximate  $\lambda(\tilde{F})$  by  $\lambda_{\text{app,tr}}(\tilde{F})$ , which is obtained by truncating in Eq. (7.48) the sum over  $l$  to only two terms, ie, the terms with  $l = l_0$  and  $l = -l_0$ . This leads to

$$\lambda_{\text{app,tr}}(\tilde{F}) = 2\Re \left( e^{-j2\pi\tilde{F}l_0T_s} g^*(l_0T_s, 0) r_{y_{AA}}(l_0T_s) \right). \quad (7.50)$$

Maximization of Eq. (7.50) over  $\tilde{F}$  yields the closed-form solution

$$\hat{F} = \frac{1}{2\pi l_0 T_s} \arg \left( g^*(l_0T_s, 0) r_{y_{AA}}(l_0T_s) \right). \quad (7.51)$$

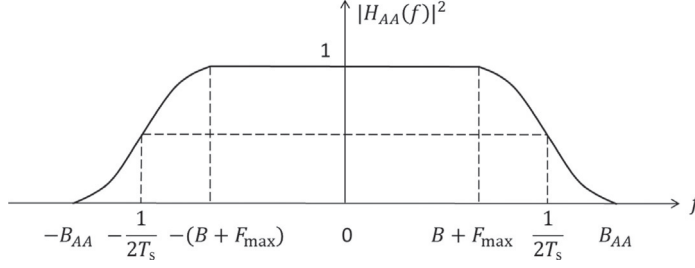


FIG. 7.13

Anti-aliasing filter.

When the transmit pulse  $h(t)$  is real, the corresponding  $g(t, 0)$  is also real; taking into account that  $g(mT, 0) = \delta_m$ , it is possible to select  $l_0T_s < T$  such that  $g^*(l_0T_s, 0)$  is positive, in which case  $g^*(l_0T_s, 0)$  can be removed from Eq. (7.51). The resulting NDA estimation algorithm is referred to as delay-and-multiply frequency estimation [12, Section 3.6]; the corresponding block diagram is shown in Fig. 7.14.

Understanding the operation of the delay-and-multiply frequency estimation can be gained from decomposing  $y_{AA}(t)y_{AA}^*(t - l_0T_s)$  as the sum of its expectation (over data symbols and noise)  $E[y_{AA}(t)y_{AA}^*(t - l_0T_s)]$  and a zero-mean disturbance  $\eta_1(t)$ . Taking into account that the anti-aliasing filter  $H_{AA}(f)$  does not distort the useful signal term of  $y(t)$ , this yields

$$y_{AA}(t)y_{AA}^*(t - l_0T_s) = A^2\sigma_s^2 e^{j2\pi Fl_0T_s} \rho(t) + R_{n_{AA}}(l_0T_s) + \eta_1(t), \quad (7.52)$$

where

$$\rho(t) = \sum_{k=0}^{K-1} h(t - kT - \tau)h^*(t - l_0T_s - kT - \tau) \quad (7.53)$$

and  $R_{n_{AA}}(u) = E[n_{AA}(t + u)n_{AA}^*(t)]$  is the statistical autocorrelation function of the noise at the output of the anti-aliasing filter;  $R_{n_{AA}}(u)$  equals the inverse Fourier transform of  $N_0|H_{AA}(f)|^2$ . The important observation is that by multiplying  $y_{AA}(t)$

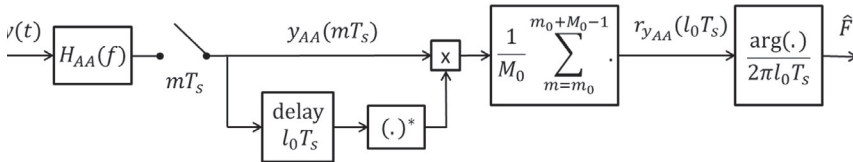


FIG. 7.14

Delay-and-multiply frequency estimation.

and  $y_{AA}^*(t - l_0 T_s)$ , the constant-speed rotation  $e^{j2\pi Ft}$ , which is present in  $y(t)$  and in  $y_{AA}(t)$ , is converted into a constant phase shift  $e^{j2\pi Fl_0 T_s}$  in Eq. (7.52). As  $r_{y_{AA}}(l_0 T_s)$  from Eq. (7.49) is a time average of  $y_{AA}(t)y_{AA}^*(t - l_0 T_s)$  over an interval of duration  $T_0$ , we obtain

$$r_{y_{AA}}(l_0 T_s) = \frac{KT}{T_0} \frac{E_s}{T} e^{j2\pi Fl_0 T_s} g(l_0 T_s, 0) + R_{n_{AA}}(l_0 T_s) + \frac{1}{M_0} \sum_{m=m_0}^{m_0+M_0-1} \eta_1(m T_s), \quad (7.54)$$

where we have used that each term in the summation (7.53) has a time average equal to  $g(l_0 T_s, 0)/T_0$ . Note that  $KT/T_0 \lesssim 1$ , and  $E_s/T$  denotes the received useful signal power. Selecting  $l_0 T_s$  such that  $R_{n_{AA}}(l_0 T_s) \approx 0$ , the second term in Eq. (7.54) can be safely ignored; when  $H_{AA}(f)$  is a square-root Nyquist filter with respect to the sampling interval  $T_s$  (see Fig. 7.13), we automatically have  $R_{n_{AA}}(l_0 T_s) = 0$  for all nonzero integers  $l_0$ . Disregarding for a moment the last term of Eq. (7.54), we obtain  $\arg(r_{y_{AA}}(l_0 T_s)) = 2\pi Fl_0 T_s$ , which would yield  $\hat{F} = F$ . The actual estimate (7.51) deviates from  $F$  because of the zero-mean third term in Eq. (7.54). As the arithmetical average over  $m$  acts as a lowpass filter with a bandwidth of about  $1/(KT)$  operating on  $\eta_1(m T_s)$ , the effect of this term is reduced by increasing the frame length  $K$ .

Noting that the function  $\arg(\cdot)$  returns an angle in the interval  $(-\pi, \pi)$ , it follows that in order to avoid phase wrapping, the angle of  $r_{y_{AA}}(l_0 T_s)$  should not exceed the  $\pm\pi$  boundaries; this yields the necessary condition  $F_{\max} l_0 T_s \leq 1/2$ . However, if  $F_{\max} l_0 T_s$  is less than but close to  $1/2$ , phase wrapping can still occur due to the third term in Eq. (7.54); hence, it is safer to adopt a more conservative condition, eg,  $F_{\max} l_0 T_s \leq 1/4$ .

## 7.7 NDA SYMBOL TIMING ESTIMATION

The symbol timing estimate  $\hat{\epsilon}$  is obtained by maximizing (an approximation of) the likelihood function  $\lambda(\hat{F}, \tilde{\epsilon})$ , where  $\hat{F}$  denotes an available frequency estimate. In Appendix A it is shown that  $\lambda(\hat{F}, \tilde{\epsilon}) \approx \lambda_{\text{app}}(\hat{F}, \tilde{\epsilon})$  with

$$\lambda_{\text{app}}(\hat{F}, \tilde{\epsilon}) = \Re \left( e^{-j2\pi \tilde{\epsilon}} C(\hat{F}) \right) \quad (7.55)$$

and

$$C(\hat{F}) = \frac{1}{T_0} \int_{t_{\min}}^{t_{\max}} |z(t, \hat{F})|^2 e^{j2\pi \frac{t}{T}} dt, \quad (7.56)$$

where  $z(t, \hat{F})$  results from applying  $y(t)e^{-j2\pi \hat{F}t}$  to the matched filter  $H^*(f)$ .

The maximization of  $\lambda_{\text{app}}(\hat{F}, \tilde{\epsilon})$  from Eq. (7.55) yields the closed-form solution  $\hat{\epsilon} = \arg(C(\hat{F})) / (2\pi)$ . In a practical implementation, a discrete-time matched filter will be fed with samples  $y_{AA}(m T_s)e^{-j2\pi \hat{F}m T_s}$ , yielding matched filter output samples  $z(m T_s, \hat{F})$ . In this case, the symbol timing estimate becomes

$$\hat{\epsilon} = \frac{1}{2\pi} \arg \left( \frac{1}{M_0} \sum_{m=m_0}^{m_0+M_0-1} |z(mT_s, \hat{F})|^2 e^{j2\pi \frac{m}{N_s}} \right), \quad (7.57)$$

where  $N_s = T/T_s$  denotes the oversampling factor. Taking into account that  $|z(t, \hat{F})|^2$  has a bandwidth of  $2B$ , the oversampling factor must satisfy the condition  $N_s > 2BT + 1$  in order to avoid aliasing. A convenient value of the oversampling factor is  $N_s = 4$ , in which case  $e^{j2\pi \frac{m}{N_s}} \in \{1, j, -1, -j\}$ , so that the computation of Eq. (7.57) is simplified considerably; the use of  $N_s = 4$  requires  $BT < \frac{3}{2}$ , which holds for a square-root cosine-rolloff transmit filter. The symbol timing estimator (7.57) has originally been proposed by Oerder and Meyr [13]. The block diagram of the Oerder-and-Meyr symbol timing estimator operating on the anti-aliasing filter output samples is shown in Fig. 7.15.

In order to gain understanding about the operation of the symbol timing estimation algorithm (7.57), we proceed in a similar way as for the delay-and-multiply frequency estimation from Section 7.6. We decompose in Eq. (7.56)  $|z(t, \hat{F})|^2$  as the sum of its expectation  $E[|z(t, \hat{F})|^2]$  over the data symbols and the noise and a zero-mean fluctuation  $\eta_2(t)$ , yielding

$$|z(t, \hat{F})|^2 = A^2 \sigma_s^2 \sum_{k=0}^{K-1} |g(t - kT - \tau, F_{\text{res}}T)|^2 + \eta_2(t). \quad (7.58)$$

Substituting Eq. (7.58) into Eq. (7.56), we obtain

$$C(\hat{F}) = \frac{KT}{T_0} \cdot \frac{E_s}{T} e^{j2\pi\epsilon} \int |g(t, -F_{\text{res}}T)|^2 \cos\left(\frac{2\pi t}{T}\right) dt + \frac{1}{T_0} \int_{t_{\min}}^{t_{\max}} e^{j2\pi \frac{t}{T}} \eta_2(t) dt. \quad (7.59)$$

Note that  $\epsilon$  appears in Eq. (7.59) as a constant phase shift  $e^{j2\pi\epsilon}$ . As it can be shown from Eq. (7.16) that the integral in the first term of Eq. (7.59) is positive, we have  $\arg(C(\hat{F})) = 2\pi\epsilon$  when disregarding  $\eta_2(t)$ , which would yield  $\hat{\epsilon} = \epsilon$ . The presence of  $\eta_2(t)$  gives rise to an actual estimate  $\hat{\epsilon}$  which deviates from  $\epsilon$ ; the effect of  $\eta_2(t)$  decreases with increasing frame length  $K$ , because the time-averaging in the second term of Eq. (7.59) can be interpreted as a lowpass filter with bandwidth  $1/T_0 \approx 1/(KT)$  operating on  $e^{j2\pi \frac{t}{T}} \eta_2(t)$ .

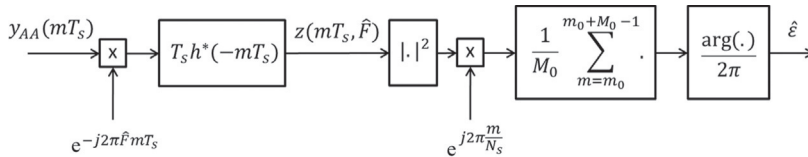


FIG. 7.15

Oerder-and-Meyr symbol timing estimation.

Having obtained the estimate  $\hat{\epsilon}$  from Eq. (7.57), the receiver must compute  $z_k = z(kT + \hat{\epsilon}T, \hat{F})$  from the available samples  $\{z(mT_s, \hat{F})\}$ . This is accomplished by means of interpolation. Introducing the decomposition  $kT + \hat{\epsilon}T = (i_k + \Delta_k)T_s$  with  $i_k = \lfloor (k + \epsilon)N_s \rfloor$ ,  $z(kT + \hat{\epsilon}T, \hat{F})$  is approximated by  $z_{\text{IP}}(kT + \hat{\epsilon}T, \hat{F})$ , given by

$$z_{\text{IP}}(kT + \hat{\epsilon}T, \hat{F}) = \sum_n \alpha_n(\Delta_k) z((i_k - n)T_s, \hat{F}). \quad (7.60)$$

For instance, in the case of (rather coarse) linear interpolation, Eq. (7.60) contains only two terms:  $\alpha_0(\Delta_k) = 1 - \Delta_k$ ,  $\alpha_{-1}(\Delta_k) = \Delta_k$ ,  $\alpha_n(\Delta_k) = 0$  otherwise. In practice, more sophisticated interpolators are used such as Lagrange interpolators and interpolators with optimized coefficients  $\{\alpha_n(\Delta_k)\}$  [14, 15].

## 7.8 PA ML ESTIMATION OF $(A, \theta, F_{\text{res}}, k_\tau)$

Having obtained a coarse frequency estimate  $\hat{F}$  and a symbol timing estimate  $\hat{\epsilon}$ , the receiver computes the matched filter output samples  $\{z_k\}$ , with  $z_k = z(kT + \hat{\epsilon}T, \hat{F})$ . The log-likelihood function based on Eq. (7.44) is given by

$$\ln(\lambda(\mathbf{s}, A, \theta, F_{\text{res}}, k_\tau)) = \frac{1}{N_0} \sum_{k=0}^{K-1} \left( 2A \Re \left( e^{-j\theta_{\text{res}}(t_k)} s_k^* z_{k+k_\tau} \right) - A^2 |s_k|^2 \right), \quad (7.61)$$

where  $t_k$  is a short-hand notation for  $(k + k_\tau + \hat{\epsilon})T$ .

We consider the case where the transmitter sends pilot symbols (ie, symbols that are known to the receiver) among the unknown symbols, in order to assist the estimation. More specifically, we consider the transmission of a frame consisting of  $K$  symbols, as illustrated in Fig. 7.16; the first and the last  $K_d$  symbols are data symbols that are separated by  $K_p$  pilot symbols ( $K = 2K_d + K_p$ ). Hence,  $s_k$  represents a data symbol for  $k \in \{0, \dots, K_d - 1\} \cup \{K - K_d, \dots, K - 1\}$  and a pilot symbol for  $k \in \{K_d, \dots, K_d + K_p - 1\}$ .

In order to avoid the averaging of the likelihood function  $\lambda(\mathbf{s}, A, \theta, F_{\text{res}}, k_\tau)$  over the data symbols, the estimation algorithm will assume that only the  $K_p$  pilot symbols have been transmitted, ie, the  $2K_d$  data symbols in Eq. (7.61) are set to

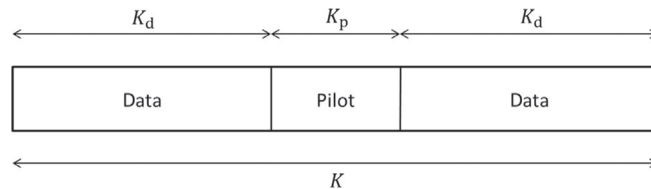


FIG. 7.16

Frame structure.

zero. The estimates  $(\hat{A}, \hat{\theta}, \hat{F}_{\text{res}}, \hat{k}_{\tau})$  are obtained by maximizing the corresponding log-likelihood function, which is obtained by restricting in Eq. (7.61) the summation index  $k$  to the range  $\{K_d, \dots, K_d + K_p - 1\}$ . The resulting estimation algorithms are referred to as PA.

In the case of constant-magnitude pilot symbols (ie,  $|s_k| = s_p$  for  $k \in \{K_d, \dots, K_d + K_p - 1\}$ ), the maximization of Eq. (7.61), with the summation interval restricted to the pilot symbol positions, yields

$$(\hat{F}_{\text{res}}, \hat{k}_{\tau}) = \arg \max_{(\tilde{F}_{\text{res}}, \tilde{k}_{\tau})} |M_p(\tilde{F}_{\text{res}}, \tilde{k}_{\tau})|, \quad (7.62)$$

$$\hat{\theta} = \arg(M_p(\hat{F}_{\text{res}}, \hat{k}_{\tau})), \quad (7.63)$$

$$\hat{A} = \frac{1}{s_p^2} |M_p(\hat{F}_{\text{res}}, \hat{k}_{\tau})|, \quad (7.64)$$

where

$$M_p(\tilde{F}_{\text{res}}, \tilde{k}_{\tau}) = \frac{1}{K_p} \sum_{k=K_d}^{K_d+K_p-1} z_{k+\tilde{k}_{\tau}} s_k^* e^{-j2\pi \tilde{F}_{\text{res}}(k+\tilde{k}_{\tau}+\hat{\epsilon})T}. \quad (7.65)$$

According to Eq. (7.62), the estimate  $(\hat{F}_{\text{res}}, \hat{k}_{\tau})$  is obtained by performing a two-dimensional search over the continuous variable  $\tilde{F}_{\text{res}}$  and the discrete variable  $\tilde{k}_{\tau}$ . For a given trial value  $\tilde{k}_{\tau}$ , we have to look for the value of  $\tilde{F}_{\text{res}}$  that maximizes the magnitude  $|M_p(\tilde{F}_{\text{res}}, \tilde{k}_{\tau})|$ ; this magnitude has to be computed and maximized over  $\tilde{F}_{\text{res}}$  for all trial values  $\tilde{k}_{\tau}$ , and the pair  $(\hat{F}_{\text{res}}, \hat{k}_{\tau})$  yielding the overall largest magnitude is selected. From  $M_p(\hat{F}_{\text{res}}, \hat{k}_{\tau})$ , the estimates  $\hat{\theta}$  and  $\hat{A}$  are obtained analytically according to Eqs. (7.63) and (7.64), respectively.

The two-dimensional search resulting from Eq. (7.62) can be avoided by making a simplifying approximation, similar to the approach in Section 7.6. First, we note that replacing in Eq. (7.62)  $|M_p(\tilde{F}_{\text{res}}, \tilde{k}_{\tau})|$  by  $|M_p(\tilde{F}_{\text{res}}, \tilde{k}_{\tau})|^2$  does not change the estimates  $(\hat{F}_{\text{res}}, \hat{k}_{\tau})$ . Expanding this squared magnitude yields

$$|M_p(\tilde{F}_{\text{res}}, \tilde{k}_{\tau})|^2 = \sum_{k_1, k_2=K_d}^{K_d+K_p-1} z_{k_1+\tilde{k}_{\tau}} z_{k_2+\tilde{k}_{\tau}}^* s_{k_1}^* s_{k_2} e^{-j2\pi \tilde{F}_{\text{res}}(k_1-k_2)T}. \quad (7.66)$$

The simplification consists of keeping in Eq. (7.66) only the terms with  $k_1 - k_2 = D$  and  $k_1 - k_2 = -D$ , where  $D$  is an integer design parameter, with  $0 < D < K_p$ ; denoting the resulting truncation of Eq. (7.66) by  $L_p(\tilde{F}_{\text{res}}, \tilde{k}_{\tau})$ , we obtain

$$L_p(\tilde{F}_{\text{res}}, \tilde{k}_{\tau}) = 2\Re(e^{-j2\pi \tilde{F}_{\text{res}}DT} N_p(\tilde{k}_{\tau})), \quad (7.67)$$

where

$$N_p(\tilde{k}_\tau) = \frac{1}{K_p - D} \sum_{k=K_d}^{K_d+K_p-1-D} z_{k+D+\tilde{k}_\tau} z_{k+\tilde{k}_\tau}^* s_{k+D}^* s_k \quad (7.68)$$

denotes the time-crosscorrelation over  $K_p - D$  samples of the sequences  $\{z_{k+D} z_k^*\}$  and  $\{s_{k+D} s_k^*\}$  for a time-shift  $\tilde{k}_\tau$ . Maximization of  $L_p(\tilde{F}_{\text{res}}, \tilde{k}_\tau)$  over  $(\tilde{F}_{\text{res}}, \tilde{k}_\tau)$  yields

$$\hat{k}_\tau = \arg \max_{k_{\tau,\text{max}} \leq \tilde{k}_\tau \leq k_{\tau,\text{min}}} |N_p(\tilde{k}_\tau)|, \quad (7.69)$$

$$\hat{F}_{\text{res}} = \frac{1}{2\pi DT} \arg(N_p(\hat{k}_\tau)). \quad (7.70)$$

Note that we end up with a one-dimensional search over the discrete variable  $\tilde{k}_\tau$ , whereas the estimate  $\hat{F}_{\text{res}}$  is obtained in closed form; the algorithms (7.69) and (7.70) are based on [16, Section 8.4.3]. After performing the frame synchronization followed by the fine frequency estimation according to Eqs. (7.69) and (7.70), the estimation of phase and amplitude are according to Eqs. (7.63) and (7.64). The corresponding block diagrams are shown in Figs. 7.17–7.19; note that the phase estimate in Fig. 7.19 equals

$$\begin{aligned} \hat{\theta}_{\text{res}}(\hat{\tau}) &= \hat{\theta} + 2\pi \hat{F}_{\text{res}}(\hat{k}_\tau + \hat{\epsilon})T \\ &= \arg \left( \frac{1}{K_p} \sum_{k=K_d}^{K_d+K_p-1} z_{k+\hat{k}_\tau} s_k^* e^{-j2\pi \hat{F}_{\text{res}} k T} \right) \end{aligned}$$

(rather than  $\hat{\theta}$  from Eq. (7.63)), which according to Eq. (7.46) can be used directly to compute the samples  $u_k$  to be supplied to the detector/decoder.

The operation of the frame synchronization algorithm (7.69) and the frequency estimation algorithm (7.70) can be understood by decomposing  $z_{k+D} z_k^*$  as the sum of its average (over the noise)  $E[z_{k+D} z_k^*]$  and a zero-mean disturbance  $\eta_{3,k}$ . This yields

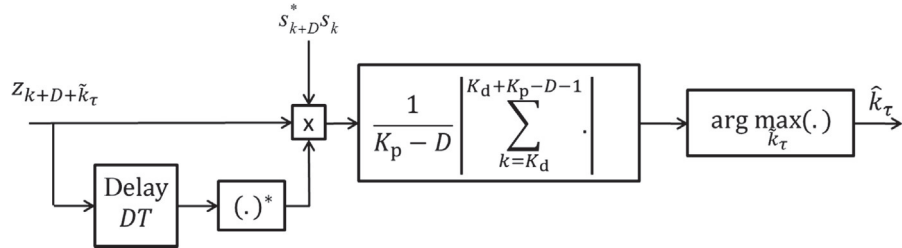
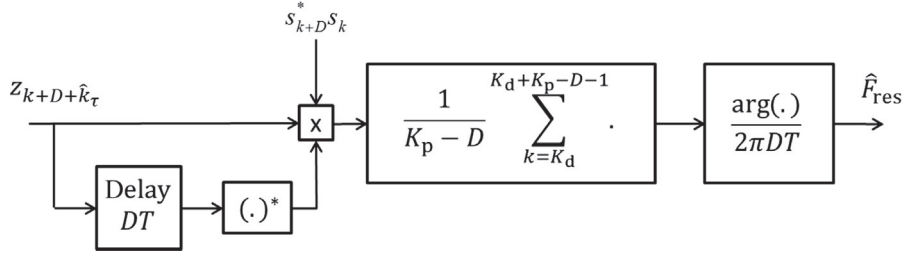
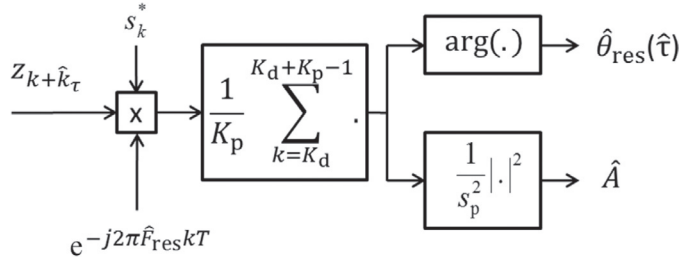


FIG. 7.17

Frame synchronization.


**FIG. 7.18**

Fine frequency estimation.


**FIG. 7.19**

Phase and amplitude estimation.

$$z_{k+D}z_k^* = A^2 e^{j2\pi F_{\text{res}}DT} s_{k+D-k_{\tau}} s_{k-k_{\tau}}^* + \eta_{3,k}. \quad (7.71)$$

Note that the multiplication of  $z_{k+D}$  and  $z_k^*$  turns the constant-speed rotation  $e^{j2\pi F_{\text{res}}kT}$ , which is present in  $z_k$ , into a constant phase shift  $e^{j2\pi F_{\text{res}}DT}$ . Substituting Eq. (7.71) into Eq. (7.68) with  $\hat{k}_{\tau} = k_{\tau}$ , we obtain

$$N_p(\hat{k}_{\tau}) = \frac{1}{K_p - D} \sum_{k=K_d}^{K_d+K_p-1-D} \left( A^2 e^{j2\pi F_{\text{res}}DT} c_{k+k_e} c_k^* + \eta_{3,k+\hat{k}_{\tau}} s_{k+D}^* s_k \right), \quad (7.72)$$

where  $k_e = \hat{k}_{\tau} - k_{\tau}$  denotes the frame synchronization error, and

$$c_k = \begin{cases} s_{k+D} s_k^*, & k \in \{K_d, \dots, K_d + K_p - 1 - D\}, \\ 0, & k \notin \{K_d, \dots, K_d + K_p - 1 - D\}. \end{cases} \quad (7.73)$$

When the contribution of  $\eta_{3,k}$  to Eq. (7.72) is ignored, the Cauchy-Schwarz inequality<sup>2</sup> indicates that  $N_p(\hat{k}_\tau)$  achieves a maximum magnitude of  $s_p^4 A^2$  at  $k_e = 0$  (ie,  $\hat{k}_\tau = k_\tau$ ). For nonzero  $\eta_{3,k}$ , the maximum magnitude of  $N_p(\tilde{k}_\tau)$  might occur for  $k_e \neq 0$ ; however, the probability that  $k_e \neq 0$  decreases with increasing  $K_p - D$ , because the arithmetical average of  $\eta_{3,k+\hat{k}_\tau} s_{k+D}^* s_k$  in Eq. (7.72) can be interpreted as lowpass filtering with a bandwidth of  $1/((K_p - D)T)$ . Hence, as far as the frame synchronization is concerned, the best performance is obtained for  $D = 1$ .

Assuming  $\hat{k}_\tau = k_\tau$ , we obtain from Eq. (7.72) that  $N_p(k_\tau) = s_p^4 A^2 e^{j2\pi F_{\text{res}}DT} + \delta_1$ , where  $\delta_1$  denotes the zero-mean contribution from  $\eta_{3,k}$ . Disregarding  $\delta_1$ , Eq. (7.70) yields  $\hat{F}_{\text{res}} = F_{\text{res}}$ . Actually, the disturbance term  $\delta_1$  will give rise to a nonzero normalized frequency estimation error  $e_F = (\hat{F}_{\text{res}} - F_{\text{res}})T$ . While the variance of  $\delta_1$  decreases with increasing  $K_p - D$ , the contribution of  $\delta_1$  to  $e_F$  is, according to Eq. (7.70), obtained by dividing by  $2\pi D$  the difference  $\arg(N_p(\hat{k}_\tau)) - 2\pi F_{\text{res}}DT$ , caused by  $\delta_1$ ; hence, the effect of  $D$  on the frequency estimation performance is rather complicated. In order to avoid phase wrapping in Eq. (7.70), the phase of  $N_p(\hat{k}_\tau)$  should not cross the  $\pm\pi$  boundaries; a necessary condition is  $|F_{\text{res}}|DT < 1/2$ ; because of the presence of  $\delta_1$ , it is safer to take a more conservative condition, eg,  $|F_{\text{res}}|DT < 1/4$ . Note that the value of  $D$  used for frequency estimation in Eq. (7.70) can be different from the one used for frame synchronization in Eq. (7.69); this allows the separate optimization of both estimation algorithms.

In order to gain more insight in the operation of the phase estimation algorithm (7.63) and the amplitude estimation algorithm (7.64), we assume perfect frame synchronization ( $\hat{k}_\tau = k_\tau$ ) and symbol timing estimation ( $\hat{\epsilon} = \epsilon$ ) but consider a nonzero frequency estimation error. Decomposing  $z_{k+k_\tau} s_k^*$  as the sum of its average (over the noise)  $E[z_{k+k_\tau} s_k^*]$  and a zero-mean disturbance  $\eta_{4,k}$ , we obtain

$$z_{k+k_\tau} s_k^* = A s_p^2 e^{j\theta} e^{j2\pi F_{\text{res}}(kT+\tau)} + \eta_{4,k}. \quad (7.74)$$

Substituting Eqs. (7.74) in (7.65) for  $(\tilde{F}_{\text{res}}, \tilde{k}_\tau) = (\hat{F}_{\text{res}}, k_\tau)$  yields

$$\begin{aligned} M_p(\hat{F}_{\text{res}}, k_\tau) &= \frac{1}{K_p} \sum_{k=K_d}^{K_d+K_p-1} \left( A s_p^2 e^{j\theta} e^{-j2\pi e_F(k+\frac{t_c}{T})} + \eta_{4,k} e^{-j2\pi \hat{F}_{\text{res}}(k+k_\tau+\epsilon)T} \right) \\ &= A s_p^2 e^{j(\theta-2\pi e_F \frac{t_c}{T})} \frac{\sin(\pi K_p e_F)}{K_p \sin(\pi e_F)} + \delta_2, \end{aligned} \quad (7.75)$$

where  $t_c = \frac{(K-1)T}{2} + \tau$  denotes the instant that corresponds to the center of the frame at the receiver side, and  $\delta_2$  represents the contribution from  $\eta_{4,k}$ . Assuming  $K_p |e_F| < 1$ , it follows from Eqs. (7.63) and (7.75) that the phase estimation error  $e_\theta = \hat{\theta} - \theta$  is given by

<sup>2</sup>The Cauchy-Schwarz inequality states that  $|\sum_m a_m b_m^*|^2 \leq (\sum_m |a_m|^2) (\sum_m |b_m|^2)$ ; equality holds for  $a_m = \gamma b_m$  with arbitrary  $\gamma$ .

$$e_\theta = -2\pi e_F \frac{t_c}{T} + \phi, \quad (7.76)$$

where  $\phi$  is the zero-mean contribution from the disturbance  $\delta_2$  to the phase estimation error. We observe that for a given normalized frequency estimation error  $e_F$ , the phase estimate  $\hat{\theta}$  exhibits a nonzero bias  $E[e_\theta]$ , which equals the first term of Eq. (7.76). Now we consider the estimate of the residual total phase  $\theta_{\text{res}}(t)$ , computed as  $\hat{\theta}_{\text{res}}(t) = 2\pi \hat{F}_{\text{res}} t + \hat{\theta}$ ; for the corresponding estimation error, we obtain

$$\begin{aligned} e_{\theta, \text{res}}(t) &= \hat{\theta}_{\text{res}}(t) - \theta_{\text{res}}(t) \\ &= 2\pi e_F \frac{t}{T} + e_\theta \\ &= 2\pi e_F \frac{t - t_c}{T} + \phi. \end{aligned} \quad (7.77)$$

We observe from Eq. (7.77) that the bias of  $\hat{\theta}_{\text{res}}(t)$  varies linearly over the frame; the bias is zero at the center of the frame ( $t = t_c$ ) and achieves its largest magnitude  $\pi |e_F| (K - 1)$  at the edges of the frame (ie, for  $|t - t_c| = \frac{(K-1)T}{2}$ ).

It follows from Eqs. (7.64) and (7.75) that

$$\hat{A} = A \left| \frac{\sin(\pi K_p e_F)}{K_p \sin(\pi e_F)} \right| + \delta_3, \quad (7.78)$$

where  $\delta_3$  represents the contribution from the zero-mean disturbance  $\eta_{4,k}$  to the amplitude estimation error. From Eq. (7.78) we observe that the normalized frequency estimation error  $e_F$  introduces a bias, which is limited to 10% (to 1%) for  $K_p |e_F|$  equal to 0.25 (to 0.08).

## 7.9 CA ML ESTIMATION OF $(A, \theta, F_{\text{res}}, k_\tau)$

While in Section 7.8 we exploited only the pilot symbols for estimation purposes, here we will apply the EM algorithm in order to also benefit from the presence of the unknown data symbols. According to Eq. (7.61), the expectation step (7.35) (with  $\mathbf{y}$  replaced by the observation  $\mathbf{z}$ ) yields

$$Q(\boldsymbol{\psi} | \hat{\boldsymbol{\psi}}^{(i)}) = \frac{1}{N_0} \sum_k \left( 2A \Re \left( e^{-j\theta_{\text{res}}(t_k)} m_{1,k}^{(i)*} z_{k+k_\tau} \right) - A^2 m_{2,k}^{(i)} \right), \quad (7.79)$$

where  $t_k = (k + k_\tau + \hat{\epsilon})T$  and

$$m_{1,k}^{(i)} = E \left[ s_k | \mathbf{z}, \hat{\boldsymbol{\psi}}^{(i)} \right], \quad (7.80)$$

$$m_{2,k}^{(i)} = E \left[ |s_k|^2 | \mathbf{z}, \hat{\boldsymbol{\psi}}^{(i)} \right] \quad (7.81)$$

depend on the estimates obtained during the  $i$ th iteration. Considering the similarity between the expressions (7.79) and (7.61), we follow the same approach as in

Section 7.8 for deriving the estimation algorithms. More specifically, the maximization step gives rise to

$$\hat{k}_\tau^{(i+1)} = \arg \max_{k_\tau} |N^{(i)}(k_\tau)|, \quad (7.82)$$

$$\hat{F}_{\text{res}}^{(i+1)} = \frac{1}{2\pi DT} \arg \left( N^{(i)}(\hat{k}_\tau^{(i+1)}) \right), \quad (7.83)$$

$$\hat{\theta}^{(i+1)} = \arg \left( M^{(i)}(\hat{F}_{\text{res}}^{(i+1)}, \hat{k}_\tau^{(i+1)}) \right), \quad (7.84)$$

$$\hat{A}^{(i+1)} = \left( \frac{1}{K} \sum_{k=0}^{K-1} m_{2,k}^{(i)} \right)^{-1} |M^{(i)}(\hat{F}_{\text{res}}^{(i+1)}, \hat{k}_\tau^{(i+1)})|, \quad (7.85)$$

where

$$N^{(i)}(k_\tau) = \frac{1}{K-D} \sum_{k=0}^{K-1-D} z_{k+D+k_\tau} z_{k+k_\tau}^* m_{1,k+D}^{(i)*} m_{1,k}^{(i)}, \quad (7.86)$$

$$M^{(i)}(F_{\text{res}}, k_\tau) = \frac{1}{K} \sum_{k=0}^{K-1} z_{k+k_\tau} m_{1,k}^{(i)*} e^{-j2\pi F_{\text{res}}(k+k_\tau+\hat{\epsilon})T}. \quad (7.87)$$

The EM iterations are initialized by taking for  $\hat{\boldsymbol{\psi}}^{(0)}$  the pilot-based estimates of  $(A, \theta, F_{\text{res}}, k_\tau)$  from Section 7.8. The corresponding block diagrams are similar to those from Figs. 7.17–7.19, but now the summations run over all  $K$  symbol positions (rather than only the  $K_p$  pilot symbol positions), and  $m_{1,k}^{(i)}$  and  $\frac{1}{K} \sum_{k=0}^{K-1} m_{2,k}^{(i)}$  are substituted for  $s_k$  and  $s_p^2$ .

The quantities  $m_{1,k}^{(i)}$  and  $m_{2,k}^{(i)}$  denote the a posteriori expectations of  $s_k$  and  $|s_k|^2$ . Expressing that the symbol  $s_k$  is a function of the information bit sequence  $\mathbf{b}$ , ie,  $s_k = \chi_k(\mathbf{b})$ , we obtain

$$m_{1,k}^{(i)} = \sum_{\mathbf{b}} \chi_k(\mathbf{b}) p(\mathbf{b} | \mathbf{z}, \hat{\boldsymbol{\psi}}^{(i)}),$$

$$m_{2,k}^{(i)} = \sum_{\mathbf{b}} |\chi_k(\mathbf{b})|^2 p(\mathbf{b} | \mathbf{z}, \hat{\boldsymbol{\psi}}^{(i)}),$$

which involves averaging over the joint a posteriori distribution of the information bits. These a posteriori expectations can be transformed into considerably simpler expressions involving only the marginal a posteriori symbol probabilities  $p(s_k | \mathbf{z}, \hat{\boldsymbol{\psi}}^{(i)})$ , ie,

$$m_{1,k}^{(i)} = \sum_{s_k} s_k p(s_k | \mathbf{z}, \hat{\boldsymbol{\psi}}^{(i)}), \quad (7.88)$$

$$m_{2,k}^{(i)} = \sum_{s_k} |s_k|^2 p(s_k | \mathbf{z}, \hat{\boldsymbol{\psi}}^{(i)}), \quad (7.89)$$

where the summation is over the constellation points. For  $K_d \leq k \leq K_d + K_p - 1$ , the symbol  $s_k$  is a pilot symbol known by the receiver; this yields  $m_{1,k}^{(i)} = s_k$  and  $m_{2,k}^{(i)} = s_k^2$ . For  $k \in \{0, \dots, K_d - 1\} \cup \{K - K_d, \dots, K - 1\}$ , the marginal a posteriori symbol probabilities can be computed by the detector/decoder that operates on the sequence  $\{u_k^{(i)}\}$ , where

$$u_k^{(i)} = \frac{1}{\hat{A}^{(i)}} e^{-j\hat{\theta}_{\text{res}}^{(i)}(kT + \hat{\tau}^{(i)})} z_{k+\hat{k}_d^{(i)}}. \quad (7.90)$$

Fig. 7.20 shows a generic factor graph [17,18] of a communication system that converts  $J$  information bits  $\mathbf{b} = (b_0, \dots, b_{J-1})$  into a frame of  $K$  symbols  $\mathbf{s} = (s_0, \dots, s_{K-1})$ , whose operation is represented as  $\mathbf{s} = \chi(\mathbf{b})$ . The upper and lower function nodes represent the likelihood function  $p(\mathbf{z} | \mathbf{s}, \hat{\boldsymbol{\psi}}^{(i)})$  and the indicator function  $\mathbb{I}[\mathbf{s} = \chi(\mathbf{b})]$ , respectively; note that the upper function node depends on the EM iteration number  $i$ . The variable nodes represent the symbols and the information bits. Factor graph messages are computed according to the sum-product algorithm.

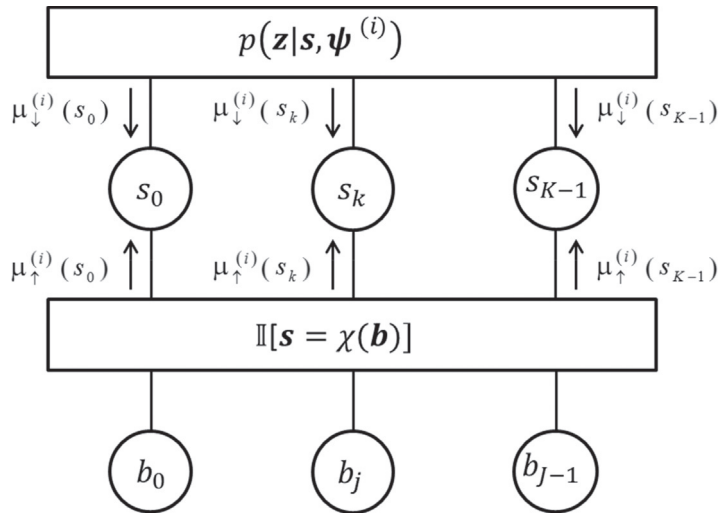


**FIG. 7.20**

Generic factor graph of communication system.

The a posteriori probability of  $s_k$  based on the estimates  $\hat{\psi}^{(i)}$  from the  $i$ th EM iteration equals the product of the messages  $\mu_{\downarrow}^{(i)}(s_k)$  and  $\mu_{\uparrow}^{(i)}(s_k)$ . From these a posteriori probabilities, the expectations  $m_{1,k}^{(i)}$  and  $m_{2,k}^{(i)}$  are computed according to Eqs. (7.88) and (7.89), and the channel estimates are updated to obtain  $\hat{\psi}^{(i+1)}$ . This process is repeated until convergence occurs.

In the case of uncoded transmission, the a posteriori probabilities of the data symbols are obtained as

$$p(s_k | \mathbf{z}, \hat{\psi}^{(i)}) = \left( \sum_{s'_k} T^{(i)}(s'_k) \right)^{-1} T^{(i)}(s_k), \quad (7.91)$$

where

$$T^{(i)}(s_k) = \exp \left( \frac{-1}{N_0} \left| z_{k+\hat{k}_\tau^{(i)}} - \hat{A}^{(i)} e^{j\hat{\theta}_{\text{res}}^{(i)}(kT + \hat{\tau}^{(i)})} s_k \right|^2 \right). \quad (7.92)$$

Through the marginal a posteriori symbol probabilities, the estimates benefit from the presence of a channel code; therefore, the estimation is referred to as CA. Assuming that, after conversion of the EM algorithm,  $m_{1,k}^{(\infty)} \approx s_k$  and  $m_{2,k}^{(\infty)} \approx |s_k|^2$ , the situation is as if all  $K$  symbols are pilot symbols; as typically  $K \gg K_p$ , a considerable estimation performance improvement compared to PA estimation is achieved.

It is convenient to modify Eq. (7.83) as

$$\hat{F}_{\text{res}}^{(i+1)} = \frac{1}{2\pi DT} \arg \left( N^{(i)}(\hat{k}_\tau^{(i+1)}) e^{-j2\pi \hat{F}_{\text{res}}^{(0)} DT} \right) + \hat{F}_{\text{res}}^{(0)}. \quad (7.93)$$

In this case, the condition on  $D$  to avoid phase wrapping is  $|F_{\text{res}} - \hat{F}_{\text{res}}^{(0)}|DT < 1/4$  rather than  $|F_{\text{res}}|DT < 1/4$ , which gives more freedom when selecting the value of  $D$ .

Some simplifying alternatives involve (i) computing the a posteriori symbol probabilities according to Eq. (7.91) even when a channel code is present (in this case the estimator does not benefit from the code); (ii) replacing  $m_{1,k}^{(i)}$  and  $m_{2,k}^{(i)}$  by  $\hat{s}_k^{(i)}$  and  $|\hat{s}_k^{(i)}|^2$ , respectively, with  $\hat{s}_k^{(i)}$  denoting the receiver's decision (either the decision made by the decoder or the symbol-by-symbol decision based on Eq. (7.90)) about  $s_k$  during the  $i$ th iteration; (iii) updating only a subset of the estimates during the EM iterations and keeping the other estimates equal to their values obtained during the pilot-based estimation.

## 7.10 EVALUATION OF MODIFIED CRAMER-RAO BOUNDS

We will evaluate the MCRBs related to the estimation of the unknown channel parameters  $\boldsymbol{\psi} = (A, \theta, F, \tau)$ , based on the received signal  $y(t)$  from Eq. (7.3) and involving the transmission of  $K$  symbols  $(s_0, \dots, s_{K-1})$ . The corresponding MFIM has been evaluated in Appendix B. Assuming that the transmit pulse  $h(t)$  is real and even (this is the case for many popular transmit pulses, such as the square-root cosine-rolloff pulse) the MFIM turns out to be block-diagonal: among the off-diagonal elements, only  $(\mathbf{J}_{\text{MFIM}})_{2,3}$  and  $(\mathbf{J}_{\text{MFIM}})_{3,2}$ , associated with  $\theta$  and  $F$ , are nonzero.

Considering the estimation errors  $(e_A, e_\theta, e_F, e_\tau)$  from Eq. (7.13), the corresponding MCRBs related to the estimation of  $(A, F, \tau)$  are obtained as

$$E[e_A^2]_{\text{MCRB}} = \frac{1}{K} \frac{N_0}{2E_s}, \quad (7.94)$$

$$E[e_F^2]_{\text{MCRB}} = \frac{3}{\pi^2} \frac{1}{K^3} \frac{N_0}{2E_s}, \quad (7.95)$$

$$\begin{aligned} E[e_\tau^2]_{\text{MCRB}} &= \frac{1}{\int |T\dot{h}(t)|^2 dt} \frac{1}{K} \frac{N_0}{2E_s} \\ &= \frac{1}{\int 4\pi^2 f^2 T^2 |H(f)|^2 df} \frac{1}{K} \frac{N_0}{2E_s}, \end{aligned} \quad (7.96)$$

where  $\dot{h}(t) = dh(t)/dt$  and the estimation errors have been defined in Eq. (7.13). The expression for  $E[e_F^2]_{\text{MCRB}}$  holds for large  $K$ . The above MCRBs are inversely proportional to  $E_s/N_0$ . The MCRBs related to  $(e_A, e_\tau)$  and  $e_F$  are inversely proportional to  $K$  and  $K^3$ , respectively. Only  $E[e_\tau^2]_{\text{MCRB}}$  depends on the shape of  $h(t)$ :  $E[e_\tau^2]_{\text{MCRB}}$  is inversely proportional to the energy of the derivative  $\dot{h}(t)$  of  $h(t)$ , and therefore,  $E[e_\tau^2]_{\text{MCRB}}$  decreases with the bandwidth of  $h(t)$ ; this makes sense, because we expect a better symbol timing estimation accuracy from narrower pulses.

As far as phase estimation is concerned, it is relevant to consider the MCRB corresponding to the estimation of the total phase  $\theta_{\text{tot}}(t) = 2\pi Ft + \theta$  (rather than  $\theta$ ). This is because Eq. (7.14) shows that the total phase estimation error  $e_{\theta, \text{tot}}(kT + \hat{\tau})$  (rather than  $e_\theta$ ) affects the symbol  $s_k$  at the input of the detector/decoder. Taking into account that  $e_{\theta, \text{tot}}(t) = 2\pi e_F \frac{t}{T} + e_\theta$ , the following is obtained for large  $K$ :

$$E[e_{\theta, \text{tot}}^2(t)]_{\text{MCRB}} = \left(1 + 12 \left(\frac{t - t_c}{KT}\right)^2\right) \frac{1}{K} \frac{N_0}{2E_s}, \quad (7.97)$$

where  $t_c = \tau + \frac{(K-1)T}{2}$  denotes the center of the frame, observed at the receiver input. Note that  $E[e_{\theta, \text{tot}}^2(t)]_{\text{MCRB}}$  achieves a minimum value of  $N_0/(2KE_s)$  at the center of the burst (ie,  $t = t_c$ ), which corresponds to the estimation of  $\theta_{\text{tot}, c} = \theta_{\text{tot}}(t_c)$ . At the edges of the frame (ie,  $t = t_c \pm \frac{K-1}{2}T$ ),  $E[e_{\theta, \text{tot}}^2(t)]_{\text{MCRB}}$  is essentially four times as large as at the center. The MCRB related to the estimation of  $\theta = \theta_{\text{tot}}(0)$  is obtained by setting  $t = 0$  in Eq. (7.97). If the frequency offset estimation error was zero, we would have  $e_{\theta, \text{tot}}(t) = e_\theta$  and  $E[e_{\theta, \text{tot}}^2(t)]_{\text{MCRB}} = E[e_\theta^2]_{\text{MCRB}} = N_0/(2KE_s)$ , which equals the minimum value of Eq. (7.97) and coincides with Eq. (7.94).

## 7.11 PERFORMANCE EVALUATION

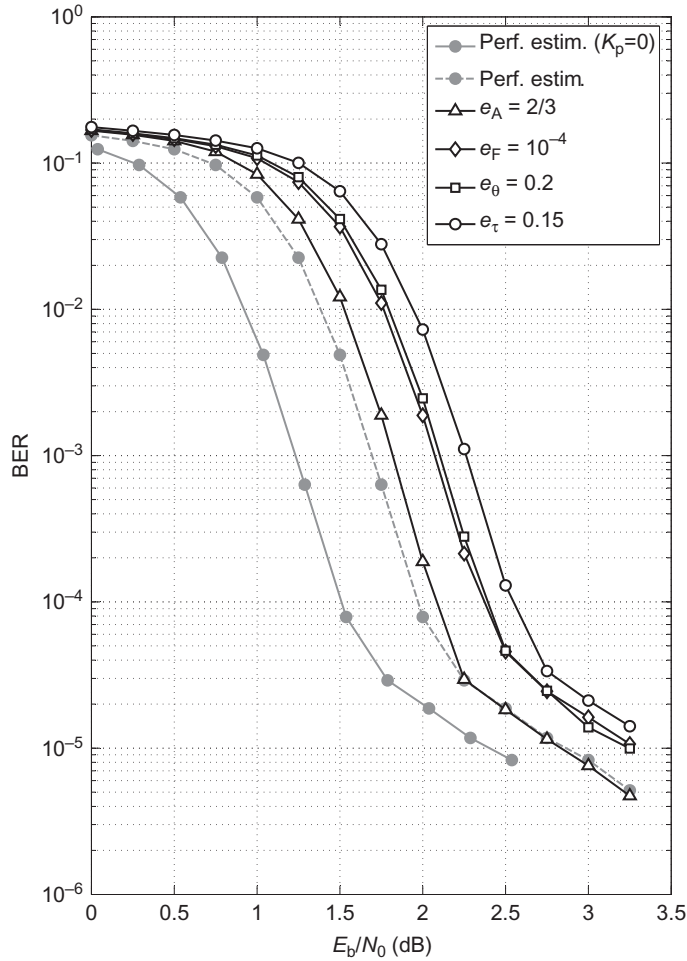
In the following we investigate by means of computer simulations the performance of the estimators derived in the previous sections. The considered performance measures are the MSE of the estimates and the resulting BER of the receiver, which will be compared to the MCRB and to the BER under perfect channel estimation, respectively.

### 7.11.1 SIMULATION SETUP

We consider a rate 1/2 turbo-coded system with Gray-mapped 4-QAM signaling and iterative decoding. The transmit filter is a square-root cosine-rolloff filter with 50% rolloff, yielding  $B = 3/(4T)$ . The turbo code consists of the parallel concatenation of two recursive systematic convolutional codes with octal generators (37,21), using a pseudo-random interleaver of 900 bits. The resulting 1800 turbo encoder output bits are Gray-mapped to 900 4-QAM data symbols. In accordance with Fig. 7.16, each frame consists of two parts of  $K_d = 450$  data symbols separated by  $K_p$  4-QAM pilot symbols; unless mentioned otherwise, we take  $K_p = 101$  yielding a frame size of  $K = 1001$  symbols. The pilot symbols are generated randomly for each frame. The received signal is applied to an anti-aliasing filter  $H_{AA}(f)$ , followed by sampling using an oversampling factor  $N_s = 4$ ;  $H_{AA}(f)$  is a square-root Nyquist filter with respect to the sampling interval  $T_s = T/4$ .

Fig. 7.21 shows the BER performance of the above turbo code after 20 decoder iterations as a function of  $E_b/N_0$ , with  $E_b$  denoting the energy per information bit;  $E_b/N_0$  and  $E_s/N_0$  are related by  $E_s/N_0 = \frac{900}{900+K_p}(E_b/N_0)$ , such that for a given  $E_b/N_0$  an increase of  $K_p$  reduces  $E_s/N_0$ . The BER curves for  $K_p = 0$  and  $K_p = 101$ , both under perfect channel estimation, show that the latter is degraded by  $10 \log \frac{1001}{900} \approx 0.46$  dB in  $E_b/N_0$  compared to the former, because of the addition of pilot symbols; irrespective of  $K_p$ , a BER of  $2 \times 10^{-5}$  is obtained at  $E_s/N_0 \approx 2$  dB. We have also displayed BER curves for  $K_p = 101$  in the presence of fixed channel estimation errors, causing degradations (in addition to the 0.46 dB degradation due to the 101 pilot symbols) in  $E_b/N_0$  of up to roughly 0.5 dB near  $\text{BER} = 10^{-5}$ ; these curves correspond to  $(e_A, e_{\theta,c}, e_F, e_\tau) = (2/3, 0, 0, 0)$ ,  $(0, 0.2, 0, 0)$ ,  $(0, 0, 10^{-4}, 0)$ ,  $(0, 0, 0, 0.15)$ , where  $e_{\theta,c} = e_{\theta,\text{tot}}(t_c)$  denotes the total phase error at the center of the frame. Compared to the case of  $K_p = 101$  and perfect estimation, a 0.5 dB degradation results from a very small normalized frequency estimation error of about  $10^{-4}$  (for  $K = 1001$  and  $e_{\theta,c} = 0$ , this corresponds to a maximum total phase estimation error of about 0.3 rad at the frame edges), a phase estimation error of about 0.2 rad, or a normalized timing error of about 0.15; the BER performance is less sensitive to amplitude estimation errors because for Gray-mapped QAM the amplitude estimation error only affects the scaling of the log-likelihood ratio of the coded bits.

For uncoded QAM transmission, the values of  $e_{\theta,c}$  and  $e_\tau$  that give rise to a 0.5 dB degradation at  $\text{BER} = 10^{-5}$  (see Figs. 7.4 and 7.11) are smaller than for turbo-coded QAM transmission, indicating a higher robustness of the latter. The turbo-coded

**FIG. 7.21**

Effect of estimation errors on the BER of turbo coded 4-QAM system.

system has a higher robustness because it operates at a lower  $E_s/N_0$ , compared to the uncoded system (the difference in operating  $E_s/N_0$  is roughly 10 dB at  $\text{BER} = 10^{-5}$ ); while for a given  $E_s$  and  $e_\tau$  the same amount of ISI is generated for uncoded and coded transmission, the relative importance of the ISI compared to the noise level is less for the coded system, which operates at the lower  $E_s/N_0$ ; a similar reasoning applies when comparing both systems for a given  $E_s$  and  $e_{\theta,c}$ .

In the following sections, the MSE performance of the individual estimation algorithms will be investigated, and these algorithms will be optimized such that

the estimation errors give rise to a negligibly small error performance degradation of the turbo decoder near  $\text{BER} = 10^{-5}$ , compared to the case of  $K_p = 101$  and perfect estimation.

### 7.11.2 NDA FREQUENCY AND SYMBOL TIMING ESTIMATION

We investigate the delay-and-multiply frequency estimation and the Oerder-and-Meyr symbol timing estimation from Sections 7.6 and 7.7, respectively, considering (i) the transmission of a single frame of  $K$  symbols and an observation interval of duration  $(K + 15)T$ , the center of which coincides with the center of the frame, and (ii) the continuous transmission of consecutive frames and an observation interval of duration  $KT$ .

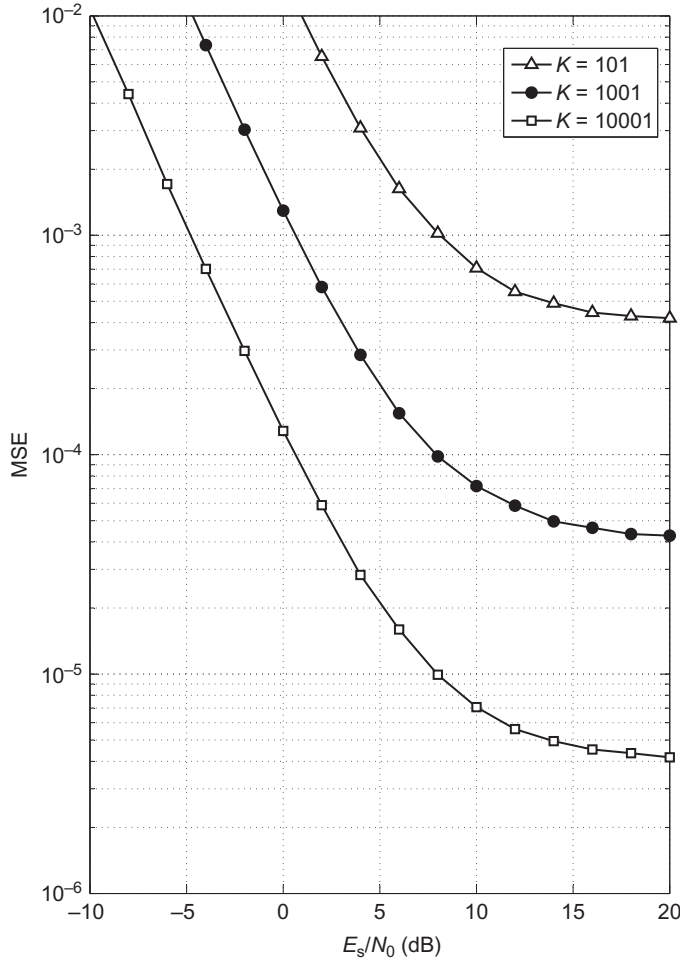
Fig. 7.22 shows the MSE  $E[e_F^2]$  resulting from the delay-and-multiply frequency estimator (7.51) as a function of  $E_s/N_0$  for  $l_0 = 1$ ; when imposing the (conservative) condition  $|F|l_0T_s < 1/4$  in order to avoid phase wrapping, the frequency estimator can handle frequency offsets satisfying  $|F| < 1/T$ . Continuous transmission and single-frame transmission yield virtually the same MSE. The MSE is observed to be inversely proportional to  $K$ . The MSE converges to an MSE floor at a high  $E_s/N_0$ ; this floor is caused by the self-noise, ie, the statistical fluctuation of  $y_{AA}(t)y_{AA}^*(t - l_0T_s)$  which is due to the random nature of the data symbols. It is easily verified from Eq. (7.95) that for all considered values of  $K$  and  $E_s/N_0$ , the estimator performs several orders of magnitude worse than the corresponding MCRB which, for large  $K$ , is inversely proportional to  $K^3E_s/N_0$ .

Fig. 7.23 shows the MSE  $E[(\hat{\epsilon} - \epsilon)^2]$  resulting from the Oerder-and-Meyr symbol timing estimator (7.57), for  $K = 101, 1001$ , and  $10001$ , as a function of  $E_s/N_0$ , assuming  $e_F = 0$ . The corresponding MCRBs are also shown. In the case of single-frame transmission, the Oerder-and-Meyr symbol timing estimator performs close to the MCRB, which is inversely proportional to  $KE_s/N_0$ . With continuous transmission the same performance is observed at low and moderate  $E_s/N_0$ , but at a high  $E_s/N_0$  the self-noise introduces an MSE floor, which is inversely proportional to  $1/K^2$ ; the self-noise originates from the statistical fluctuation of  $|z(t, F)|^2$  caused by the tails of the pulses associated with the data symbols outside the observation interval.

### 7.11.3 PA ESTIMATION

To illustrate the MSE performance of the PA estimation algorithms from Section 7.8, we consider the transmission of  $K_p$  known pilot symbols (no data symbols are transmitted, ie,  $K_d = 0$ ) and assume that the receiver uses perfect NDA estimates  $(\hat{F}, \hat{\epsilon}) = (F, \epsilon)$  to compute the matched filter output samples  $\{z(kT + \hat{\epsilon}T, \hat{F})\}$ .

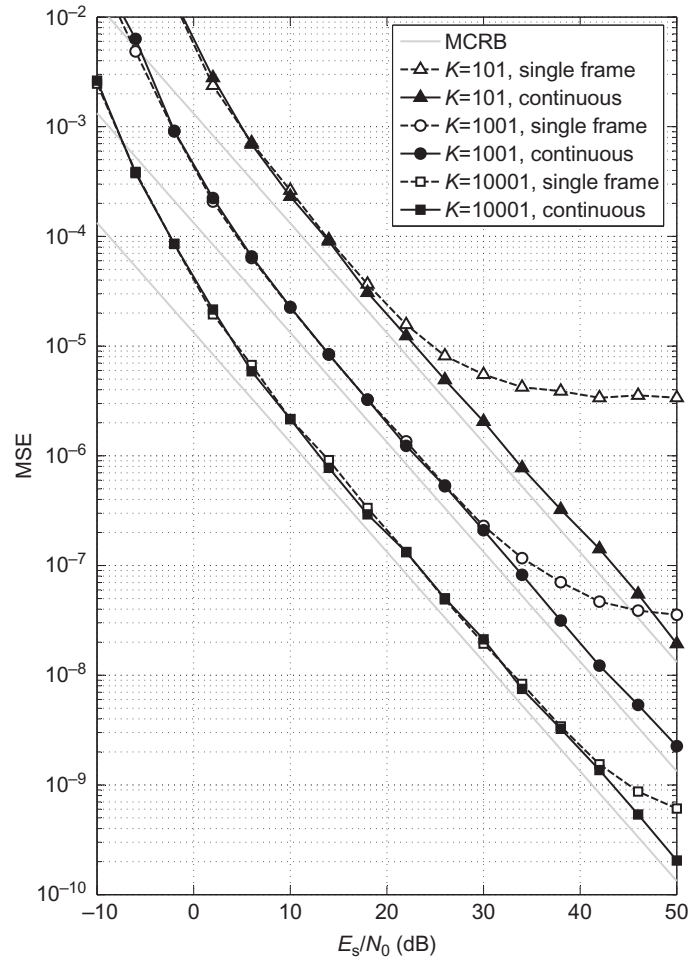
Fig. 7.24 shows the frame synchronization error probability (FSEP),  $\Pr[\hat{k}_\tau \neq k_\tau]$ , resulting from the maximization (7.69) with  $D = 1$  over the uncertainty range  $-5 \leq \tilde{k}_\tau \leq 5$ . We observe that for a given  $E_s/N_0$ , the FSEP spectacularly drops with an increasing  $K_p$ .

**FIG. 7.22**

MSE for NDA frequency estimation from 4-QAM signal.

Fig. 7.25 shows the MSE  $E[(\hat{F}_{\text{res}} - F_{\text{res}})^2 T^2]$  corresponding to the frequency estimate (7.70) for several values of  $D$ , assuming  $\hat{k}_\tau = k_\tau$  and  $K_p = 101$ , along with the MCRB. We observe that for properly selected  $D$ , the MSE is close to the MCRB at a moderate to high  $E_s/N_0$ .

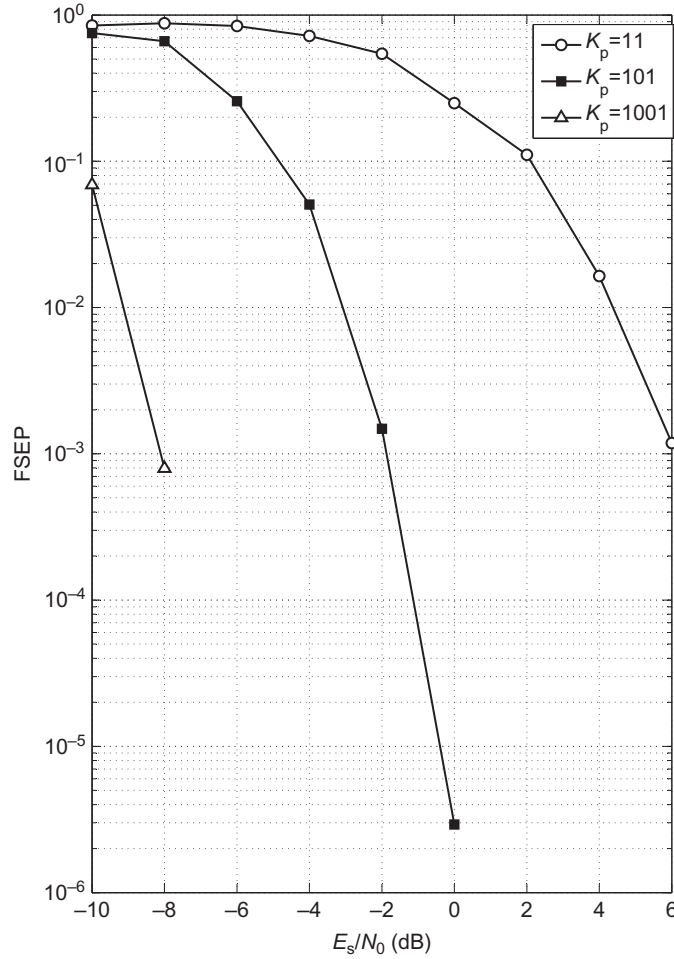
Finally, Fig. 7.26 shows the MSEs  $E[e_A^2]$  and  $E[e_\theta^2]$  resulting from Eqs. (7.64) and (7.63), assuming  $\hat{k}_\tau = k_\tau$  and  $\hat{F}_{\text{res}} = F_{\text{res}}$ , as a function of  $E_s/N_0$ . We observe that both estimators perform very closely to the MCRB, even for values of  $K_p$  as small as 11.

**FIG. 7.23**

MSE for NDA symbol timing estimation from 4-QAM signal, for  $e_F = 0$ .

#### 7.11.4 CA ESTIMATION

Taking into account that estimation errors should not degrade the turbo decoder performance at  $\text{BER} = 2 \times 10^{-5}$  by more than a small fraction of a dB, we first determine which estimates need to be refined by means of CA estimation. As the turbo decoder achieves  $\text{BER} = 2 \times 10^{-5}$  at  $E_s/N_0 \approx 2$  dB in the absence of estimation errors, we consider the performance of the NDA and PA algorithms at  $E_s/N_0 = 2$  dB.

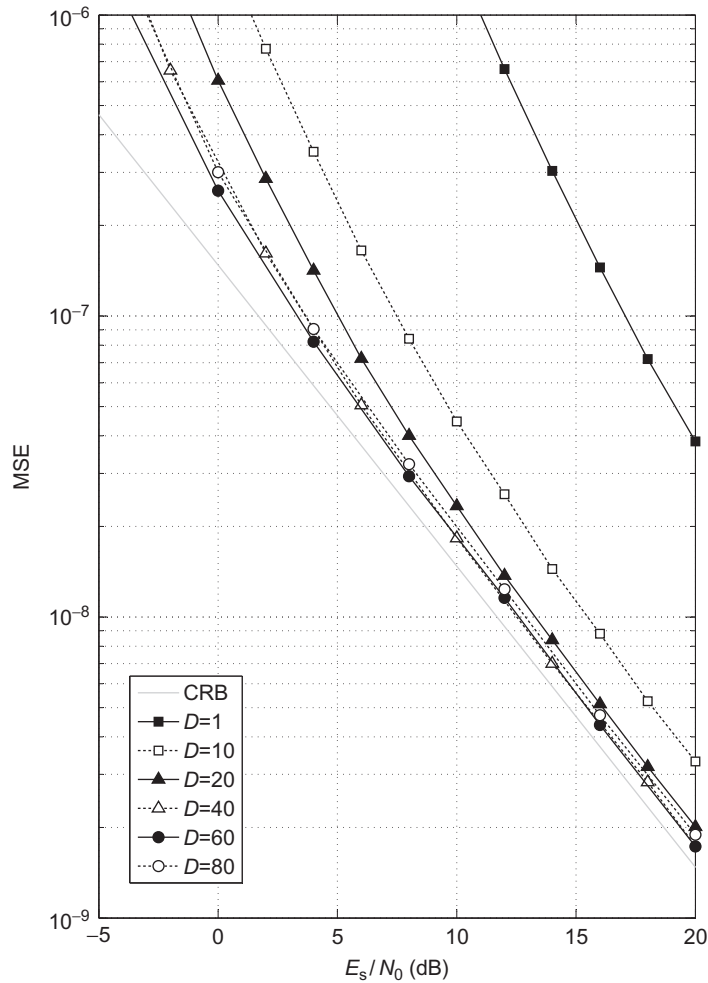
**FIG. 7.24**

FSEP for PA frame synchronization with  $D = 1$  for  $\hat{F} = F$ ,  $\hat{\epsilon} = \epsilon$ .

In the following, we make use of the fact that the magnitude of an estimation error is likely not to exceed three times the root mean-square (rms) estimation error.<sup>3</sup>

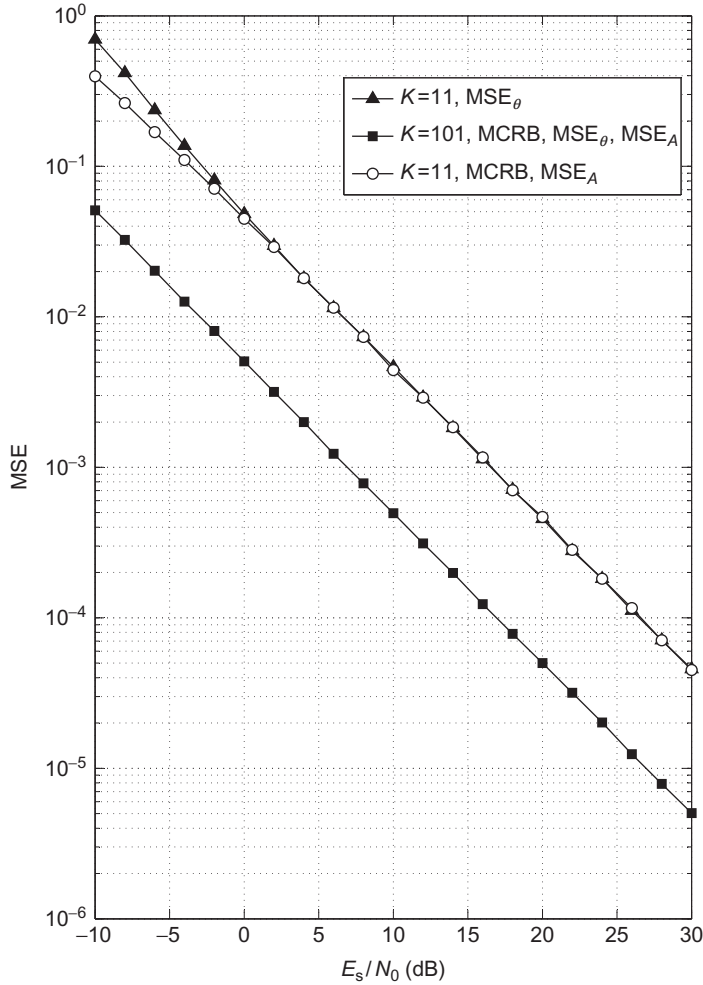
- From Fig. 7.24 it follows that at  $E_s/N_0 = 2$  dB, the PA frame synchronization algorithm for  $K_p = 101$  yields a FSEP which is several orders of magnitude lower than the BER of a perfectly synchronized system. Hence, the frame synchronization errors will barely affect the overall BER performance.

<sup>3</sup>The probability that the magnitude of a zero-mean Gaussian random variable exceeds 3 times its rms value equals 0.0027.

**FIG. 7.25**

MSE of PA frequency estimation for  $\hat{F} = F$  and  $e_\tau = 0$ .

- Fig. 7.23 indicates that at  $E_s/N_0 = 2$  dB, the MSE resulting from the NDA symbol timing estimation for  $K = 1001$  amounts to  $2 \times 10^{-4}$ . The corresponding rms error equals  $1.4 \times 10^{-2}$ , so that the corresponding estimation error  $e_\tau$  is likely to be much smaller than 0.15, the value that according to Fig. 7.21 gives rise to a degradation in error performance of roughly 0.5 dB.
- Similarly, it follows from Fig. 7.26 that the rms errors related to PA amplitude and phase estimation for  $K_p = 101$  both equal about  $5.5 \times 10^{-2}$  at  $E_s/N_0 = 2$  dB. The resulting estimation errors  $e_A$  and  $e_\theta$  are typically smaller

**FIG. 7.26**

MSE of PA amplitude and phase estimation for  $e_F = e_\tau = 0$ .

than 2/3 and 0.2, respectively, for which the corresponding BER curves are shown in Fig. 7.21.

- According to Fig. 7.22, the NDA frequency estimation at  $E_s/N_0 = 2$  dB yields an rms error of about  $2.4 \times 10^{-2}$  for  $K = 1001$ . Considering the MCRB (7.95), the rms error resulting from the PA frequency estimation for  $K_p = 101$  is lower bounded by about  $3 \times 10^{-4}$  at  $E_s/N_0 = 2$  dB. This indicates that neither the NDA nor the PA frequency estimation errors are likely to be smaller than  $10^{-4}$ , the value that according to Fig. 7.21 gives rise to 0.5 dB degradation in error performance.

The above analysis indicates that the NDA symbol timing estimation, the PA frame synchronization, the PA phase estimation, and the PA amplitude estimation are sufficiently accurate to yield an acceptable BER degradation of the turbo decoder; therefore, these estimates will not be refined by means of CA estimation. The NDA and PA frequency estimation errors, however, are too large, and we will therefore consider CA frequency estimation to reduce these errors. During the EM iterations, only the frequency estimate will be updated, while the estimates of the other parameters will be kept at their values resulting from NDA estimation (fractional time delay) and PA estimation (integer time delay, amplitude, and total phase at the frame center). To reduce the overall computational complexity of the receiver, these EM iterations will be intertwined with the iterations of the turbo-decoder: during the  $i$ th receiver iteration, first the messages  $\mu_{\downarrow}^{(i)}(s_k)$  from Fig. 7.20 are computed based on the current parameter estimates, subsequently one decoder iteration is performed (without resetting inside the decoder the messages from the previous iteration), after which the messages  $\mu_{\uparrow}^{(i)}(s_k)$  are generated, and finally, the frequency estimate is updated to obtain  $\hat{F}^{(i+1)}$  according to Eq. (7.93).

Assuming  $e_A = e_{\theta_c} = e_{\tau} = 0$ , Fig. 7.27 shows the BER resulting from CA frequency estimation after 20 receiver iterations at  $E_s/N_0 = 2$  dB, as a function of the frequency estimation error  $e_F^{(0)}$  at the start of the iterations, for several values of the delay  $D$  in Eq. (7.86); we observe that for  $D = 500$  the CA frequency estimation introduces virtually no BER degradation as compared to the case where  $F$  is known, provided that  $|e_F^{(0)}|$  does not exceed about  $2.5 \times 10^{-4}$ . Also shown is the BER after 20 decoder iterations, when the frequency estimate is not updated and the estimation error is maintained at  $e_F^{(0)}$ ; in this case,  $|e_F^{(0)}|$  should not exceed about  $0.5 \times 10^{-4}$  (which is 5 times less than when using CA frequency estimation) in order to achieve an acceptable BER degradation. In the following we investigate how the condition on  $|e_F^{(0)}|$  can be met by the PA frequency estimation algorithm that makes use of the matched filter output samples  $\{z(kT + \hat{\tau}; \hat{F})\}$ , with  $\hat{F}$  denoting the NDA frequency estimate.

As the NDA frequency estimate with  $K = 1001$  yields an rms error of about  $2.4 \times 10^{-2}$  at  $E_s/N_0 = 2$  dB, the magnitude of the resulting frequency estimation error is likely to be less than about  $7.2 \times 10^{-2}$ . For  $F_{\text{res}}T = 7.2 \times 10^{-2}$ , the PA frequency estimation algorithm requires  $D \leq 3$  in order to avoid phase wrapping. However, at  $E_s/N_0 = 2$  dB, the PA frequency estimation with  $D \leq 3$  and  $K_p = 101$  yields an rms error much larger than  $10^{-4}$ , so that the condition  $|e_F^{(0)}| < 0.5 \times 10^{-4}$  (PA estimation only) or  $|e_F^{(0)}| < 2.5 \times 10^{-4}$  (CA estimation) cannot be met. Taking into account that the frequency offset  $F$  remains constant over many frames, this problem can be solved by applying NDA and PA frequency estimation based on the observation of multiple frames, rather than a single frame; this is accomplished by extending the summations in Eqs. (7.49) and (7.68) over  $N_{\text{fr}}$  frames, as far as frequency estimation is concerned; the estimation of the other parameters remains on a per-frame basis. The condition  $|e_F^{(0)}| < 2.5 \times 10^{-4}$ , required for CA frequency

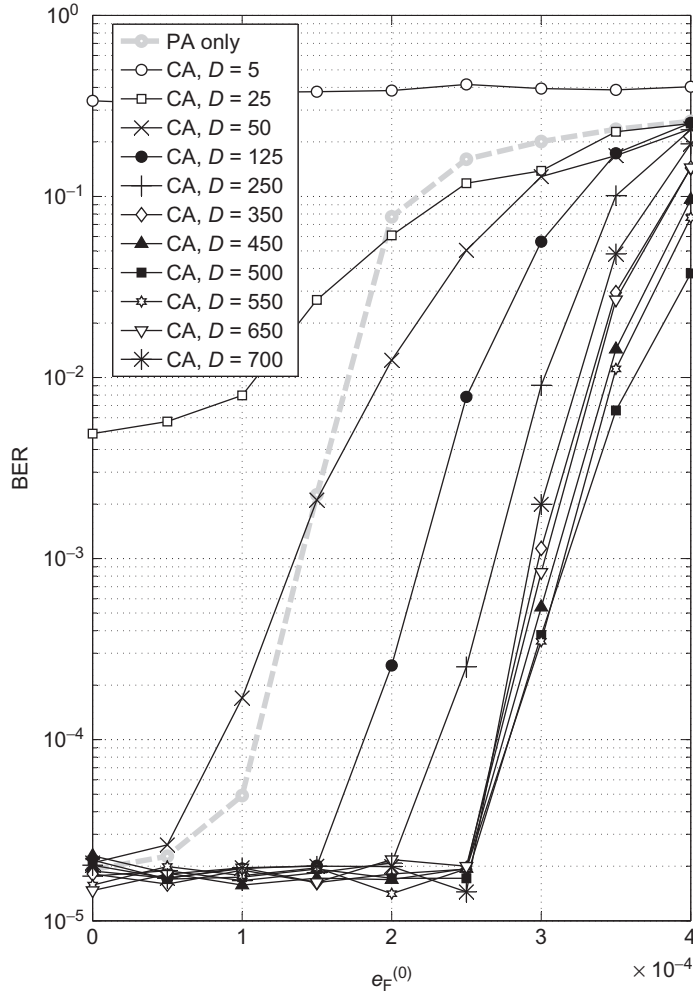
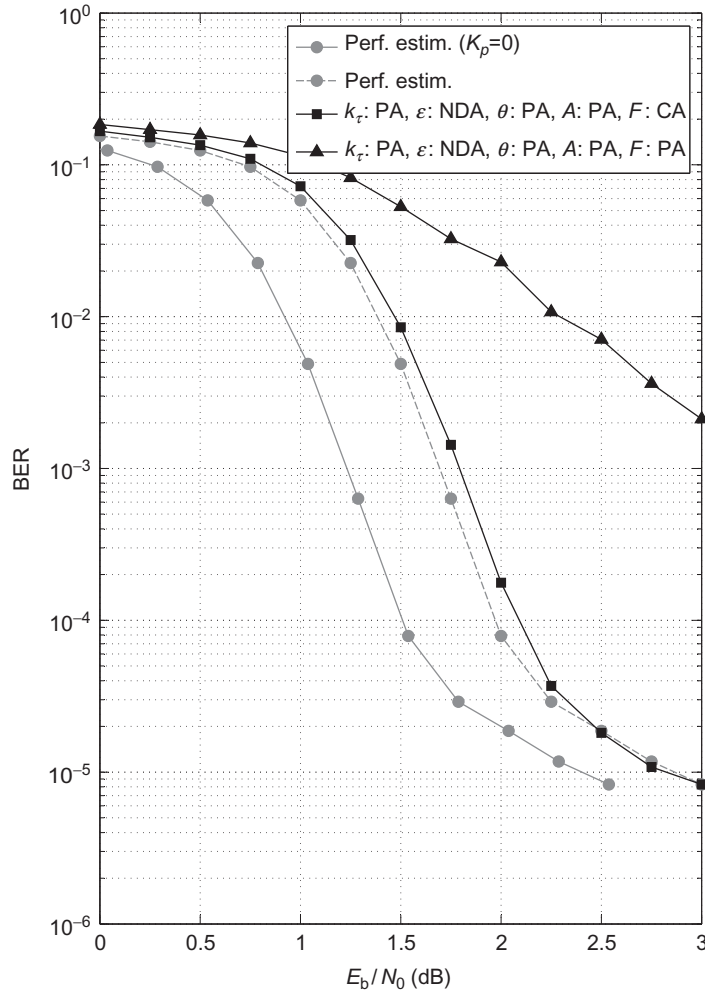


FIG. 7.27

BER for turbo-coded 4-QAM system at  $E_s/N_0 = 2$  dB as a function of the PA frequency estimation error  $e_F^{(0)}$ , assuming PA frequency estimation only or CA frequency estimation.

estimation, can be achieved for various pairs  $(N_{\text{fr}}, D)$ ; it turns out that this condition is met for the minimum  $N_{\text{fr}}$  when  $(N_{\text{fr}}, D) = (30, 20)$ . For the stronger condition  $|e_F^{(0)}| < 0.5 \times 10^{-4}$ , required when PA frequency estimation is not further refined by CA estimation, we would need  $N_{\text{fr}} > 100$ .

Fig. 7.28 shows the BER performance of a receiver when all parameters are estimated, ie, the receiver performs, on a per-frame basis, NDA symbol timing

**FIG. 7.28**

BER performance of receiver with iterative CA frequency estimation versus receiver without CA frequency estimation.

estimation (7.57) with  $N_s = 4$ , PA frame synchronization (7.69) using  $D = 1$ , PA phase estimation (7.63), PA amplitude estimation (7.64), and CA frequency estimation (7.93) with  $D = 500$ . The phase and amplitude estimates make use of the PA frequency estimate that is used to initialize the EM iterations. This frequency estimate results from first applying NDA coarse frequency estimation (7.51) with  $l_0 = 1$  and  $N_s = 4$ , followed by PA frequency estimation (7.70) with  $D = 20$ ; both

the NDA and PA frequency estimation algorithms operate on  $N_{\text{fr}} = 30$  consecutive frames. In Fig. 7.28 we observe that the proposed receiver has only a small BER degradation as compared to a system with perfect channel estimation and  $K_p = 101$ ; this degradation amounts to about 0.12 dB in the waterfall region of the BER curve, and it is negligibly small for  $\text{BER} < 2 \times 10^{-5}$ . Also, the BER of the receiver with iterative CA frequency estimation is seen to be much lower than the BER of the same receiver without iterative CA frequency estimation (with the NDA and PA frequency estimation still based on 30 frames). A value of  $N_{\text{fr}}$  larger than 100 would be required for the latter receiver to achieve a BER close to that of the system with perfect channel estimation.

---

## 7.12 CONCLUSIONS AND REMARKS

In this chapter we have considered the estimation of amplitude, phase shift, frequency offset, and time delay in the context of the transmission of digital signals. In a systematic way, we have derived several estimation algorithms that are based on the maximization of (an approximation of) the proper likelihood functions. Whereas the estimation of the integer part of the time delay requires a one-dimensional search, closed-form expressions have been obtained for the estimates of the other parameters. By means of computer simulations, we have assessed the resulting MSE of the estimates and the effect of estimation errors on the BER of a rate 1/2 turbo-coded system, which transmits frames containing 900 coded 4-QAM symbols and 101 pilot symbols. In order to achieve a negligible error performance degradation (compared to a system with 101 pilot symbols and perfect estimation) near  $\text{BER} = 10^{-5}$  (corresponding to an operating point  $E_s/N_0 \approx 2$  dB), it is sufficient to perform, on a per-frame basis, NDA estimation of the fractional time delay, along with PA estimation of the integer time delay, the amplitude, and the phase. However, to achieve the error performance target, a very accurate frequency estimate is required, which is obtained by applying three consecutive algorithms, ie, a NDA and a PA algorithm (both operating on 30 frames), followed by a (per-frame) iterative CA algorithm.

The estimation algorithms covered in this chapter are a representative subset of existing algorithms. The NDA and PA algorithms considered in this chapter are of the feedforward (“open loop”) type: parameters are estimated from the received signal, and the estimates are used to apply a correction that compensates for these parameters. Parameters can also be estimated using feedback (“closed loop”) algorithms: a correction is applied to the received signal using a trial value of the parameter, the corrected signal is fed to an error detector which outputs an indication about the difference between the trial value and the actual parameter value, and the trial value is updated according to the error detector output; this leads to a steady-state where the error detector output has zero mean. Usually, feedback algorithms are simpler to implement than their feedforward counterparts, but they might require long acquisition times, so that they are less suited for burst transmission systems.

Additional feedforward/feedback NDA and PA algorithms have been introduced in several papers contained in the special journal issues [19,20] and in the representative selection of papers [21–27]. The two textbooks [12,16] (and the bibliographical notes therein) deal with the systematic derivation of various synchronization algorithms, present their performance analysis, and cover the implementation of these algorithms in digital receivers.

The iterative CA estimation algorithms considered in this chapter are of the feedforward type and are limited to the estimation of amplitude, phase, frequency, and integer time delay. Other CA feedforward algorithms (including estimation of fractional time delay) and CA feedback algorithms can be found in the overview papers [28,29] (and the references therein) and in the representative selection of papers [30–32].

---

## Appendix A AVERAGED LIKELIHOOD FUNCTIONS

The likelihood function  $\lambda(F, \tau)$  of  $(F, \tau)$  is obtained by averaging  $\lambda(\mathbf{s}, \boldsymbol{\psi})$  over  $(\mathbf{s}, A, \theta)$ , ie,  $\lambda(F, \tau) = E_{\mathbf{s}, A, \theta}[\lambda(\mathbf{s}, \boldsymbol{\psi})]$ , with  $\boldsymbol{\psi} = (A, \theta, F, \tau)$ . Noting that  $\lambda(\mathbf{s}, \boldsymbol{\psi}) = \exp(\ln(\lambda(\mathbf{s}, \boldsymbol{\psi})))$ , we will perform the term-wise averaging of the following truncated Taylor series approximation:

$$\exp(\ln(\lambda(\mathbf{s}, \boldsymbol{\psi}))) \approx 1 + \ln(\lambda(\mathbf{s}, \boldsymbol{\psi})) + \frac{1}{2} (\ln(\lambda(\mathbf{s}, \boldsymbol{\psi})))^2. \quad (7.98)$$

We assume that (i) the symbol constellation has a symmetry angle of  $2\pi/N$  with  $N > 2$  (eg,  $N = 4$  for QAM constellations,  $N = M$  for  $M$ -PSK constellations with  $M > 2$ ), the symbols are pairwise uncorrelated and all constellation points have the same a priori probability; (ii) the phase  $\theta$  has a uniform a priori p.d.f. over the interval  $(-\pi, \pi)$ ; (iii) the amplitude  $A$  has an arbitrary a priori p.d.f.

Considering Eq. (7.98) and taking Eq. (7.8) into account, the likelihood function  $\lambda(F, \tau)$  can be approximated as

$$\lambda(F, \tau) \approx 1 + \mu_1(F, \tau) + \mu_2(F, \tau), \quad (7.99)$$

where

$$\mu_n(F, \tau) = \frac{1}{n!} N_0^{-n} E_{\mathbf{s}, A, \theta} \left[ \left( 2A \Re \left( e^{-j\theta} \mathbf{s}^H \mathbf{z}(F, \tau) \right) - A^2 |\mathbf{s}|^2 \right)^n \right]. \quad (7.100)$$

It is easily verified that  $\mu_1(F, \tau) = C_1$  and  $\mu_2(F, \tau) = C_2 |\mathbf{z}(F, \tau)|^2 + C_3$ , with  $\{C_i\}$  not depending on  $(F, \tau)$  and  $C_2 > 0$ . Hence, removing from Eq. (7.99) terms and factors which do not affect the maximization over  $(F, \tau)$ , we have  $\lambda(F, \tau) \approx |\mathbf{z}(F, \tau)|^2$ . It follows from Eq. (7.10) that

$$|\mathbf{z}(F, \tau)|^2 = \iint_{t_{\min}}^{t_{\max}} y_F(t_1) y_F^*(t_2) H_0^{K-1}(t_1, t_2, \tau) dt_1 dt_2, \quad (7.101)$$

where  $y_F(t) = y(t)e^{-j2\pi Ft}$ , and  $H_{k_1}^{k_2}(t_1, t_2, \tau)$  is defined as

$$H_{k_1}^{k_2}(t_1, t_2, \tau) = \sum_{k=k_1}^{k_2} h^*(t_1 - kT - \tau) h(t_2 - kT - \tau). \quad (7.102)$$

As a further approximation of  $\lambda(F, \tau)$ , we replace in Eq. (7.101)  $H_0^{K-1}(t_1, t_2, \tau)$  by  $H_{-\infty}^{+\infty}(t_1, t_2, \tau)$ , which is periodic in  $\tau$  with period  $T$ . The Fourier series expansion of  $H_{-\infty}^{+\infty}(t_1, t_2, \tau)$  w.r.t.  $\tau$  is given by

$$H_{-\infty}^{+\infty}(t_1, t_2, \tau) = \sum_n c_n(t_1, t_2) \exp(j2\pi n\tau/T), \quad (7.103)$$

with

$$\begin{aligned} c_n(t_1, t_2) &= \frac{1}{T} \int_{-\infty}^{+\infty} h^*(t_1 - u) h(t_2 - u) e^{-j2\pi \frac{nu}{T}} du \\ &= \frac{1}{T} \int_{-\infty}^{+\infty} H^*(f) H\left(f - \frac{n}{T}\right) e^{-j2\pi ft_1} e^{j2\pi (f - \frac{n}{T})t_2} df. \end{aligned} \quad (7.104)$$

This yields

$$\begin{aligned} \lambda(F, \tau) &\approx \sum_n e^{j2\pi \frac{n\tau}{T}} \iint_{t_{\min}}^{t_{\max}} y_F(t_1) y_F^*(t_2) c_n(t_1, t_2) dt_1 dt_2 \\ &= \frac{1}{T} \sum_n \int_{t_{\min}}^{t_{\max}} |z(t, F)|^2 e^{-j2\pi \frac{n(t-\tau)}{T}} dt. \end{aligned} \quad (7.105)$$

Decomposing the time delay as  $\tau = (k_\tau + \epsilon)T$ , where  $k_\tau T$  and  $\epsilon T$  denote the integer part and the fractional part of  $\tau$ , we observe that Eq. (7.105) does not depend on  $k_\tau$ ; hence,  $\lambda(F, \epsilon) = \mathbb{E}_{k_\tau}[\lambda(F, \tau)]$  is simply given by  $\lambda(F, \tau)|_{\tau=\epsilon T}$ .

The likelihood function  $\lambda(F)$  is obtained as  $\mathbb{E}_\epsilon[\lambda(F, \epsilon)]$ . After term-wise averaging Eq. (7.105) over  $\epsilon$ , only the term with  $n = 0$  remains. Taking into account that  $c_0(t_1, t_2) = g^*(t_1 - t_2, 0)/T$  with  $g(t, e_F)$  defined in Eq. (7.16), it follows that  $\lambda(F) \approx \lambda_{\text{app}}(F)$ , where (within irrelevant terms and factors)

$$\lambda_{\text{app}}(F) = \frac{1}{T_0} \int g^*(u, 0) e^{-j2\pi Fu} \left( \int_{t_{\min}}^{t_{\max}} y(t) y^*(t - u) dt \right) du \quad (7.106)$$

and  $T_0 = t_{\max} - t_{\min}$ .

Assuming an estimate  $\hat{F}$  is available, an estimate of  $\epsilon$  is obtained by maximizing  $\lambda(\hat{F}, \epsilon)$ . In the practically interesting case where the bandwidth  $B$  of the transmit filter is between  $1/(2T)$  and  $1/T$ , it follows from Eq. (7.104) that only the terms with  $n \in \{-1, 0, 1\}$  contribute to Eq. (7.105). Taking into account that the term with  $n = 0$  does not depend on  $\epsilon$ , we have  $\lambda(\hat{F}, \epsilon) \approx \lambda_{\text{app}}(\hat{F}, \epsilon)$ , where (within irrelevant factors and terms)

$$\lambda_{\text{app}}(\hat{F}, \epsilon) = \Re \left( e^{-j2\pi\epsilon} \frac{1}{T_0} \int_{t_{\min}}^{t_{\max}} |z(t, \hat{F})|^2 e^{j2\pi \frac{t}{T}} dt \right). \quad (7.107)$$

The approximate likelihood function  $\lambda_{\text{app}}(\hat{F}, \epsilon)$  can also be used when the bandwidth  $B$  exceeds  $1/T$ , but then the nonzero terms with  $|n| > 1$  in Eq. (7.105) are ignored.

---

## Appendix B MFIM COMPUTATION

Making use of Eqs. (7.42), (7.3), and (7.1), we obtain the following, with  $\boldsymbol{\psi} = (A, \theta, F, \tau)$ :

$$\begin{aligned} (\mathbf{J}_{\text{MFIM}})_{1,1} &= \frac{2}{N_0} \int E[|s(t)|^2] dt = \frac{2}{N_0} K \sigma_s^2, \\ (\mathbf{J}_{\text{MFIM}})_{2,2} &= \frac{2}{N_0} A^2 \int E[|s(t)|^2] dt = \frac{2}{N_0} K A^2 \sigma_s^2, \\ (\mathbf{J}_{\text{MFIM}})_{3,3} &= \frac{2}{N_0} A^2 \int 4\pi^2 t^2 E[|s(t)|^2] dt \\ &= \frac{2}{N_0} A^2 \sigma_s^2 4\pi^2 \left( D(K) + K t_c^2 \right), \\ (\mathbf{J}_{\text{MFIM}})_{4,4} &= \frac{2}{N_0} A^2 \int E[|\dot{s}(t)|^2] dt = \frac{2}{N_0} K A^2 \sigma_s^2 \int |\dot{h}(t)|^2 dt, \\ (\mathbf{J}_{\text{MFIM}})_{2,3} &= (\mathbf{J}_{\text{MFIM}})_{3,2} = \frac{2}{N_0} A^2 \left( \int 2\pi t E[|s(t)|^2] dt \right) = \frac{2}{N_0} A^2 \sigma_s^2 2\pi K t_c, \end{aligned}$$

where  $s(t) = \sum_m s_m h(t - mT - \tau)$ ,  $\dot{s}(t) = ds(t)/dt$ ,  $t_c = \tau + \frac{(K-1)T}{2}$ ,  $D(K) = KI + S(K)T^2$ ,  $I = \int t^2 |h(t)|^2 dt$ , and

$$\begin{aligned} S(K) &= \sum_{m=0}^{K-1} \left( m - \frac{K-1}{2} \right)^2 \\ &\approx \int_{-K/2}^{K/2} x^2 dx = \frac{K^3}{12}. \end{aligned}$$

Taking into account that the expectation  $E[|s(t)|^2]$  is real, and that for a real and even pulse  $h(t)$ , the expectation  $E[\dot{s}(t)s^*(t)]$  is real and the integral  $\int E[\dot{s}(t)s^*(t)] dt$  is zero,

it easily follows that the remaining elements of  $\mathbf{J}_{\text{MFIM}}$  are zero; hence,  $\mathbf{J}_{\text{MFIM}}$  has a block-diagonal structure.

Now we consider the computation of the elements of  $\mathbf{J}_{\text{MFIM}}^{-1}$ ; we restrict our attention to  $(\mathbf{J}_{\text{MFIM}}^{-1})_{2,2}$ ,  $(\mathbf{J}_{\text{MFIM}}^{-1})_{3,3}$ , and  $(\mathbf{J}_{\text{MFIM}}^{-1})_{2,3}$  ( $= (\mathbf{J}_{\text{MFIM}}^{-1})_{3,2}$ ) because obtaining the remaining elements is trivial. A straightforward evaluation of the inverse of a  $2 \times 2$  matrix yields

$$(\mathbf{J}_{\text{MFIM}}^{-1})_{2,2} = \frac{N_0}{2E_s} \left( \frac{1}{K} + \frac{t_c^2}{D(K)} \right),$$

$$(\mathbf{J}_{\text{MFIM}}^{-1})_{2,3} = (\mathbf{J}_{\text{MFIM}}^{-1})_{3,2} = -\frac{N_0}{2E_s} \frac{t_c}{2\pi D(K)},$$

$$(\mathbf{J}_{\text{MFIM}}^{-1})_{3,3} = \frac{N_0}{2E_s} \frac{1}{4\pi^2 D(K)}.$$

The MCRB related to the estimation of  $\theta_{\text{tot}}(t) = \begin{pmatrix} 1 & 2\pi t \end{pmatrix} \begin{pmatrix} \theta \\ F \end{pmatrix}$  is obtained as

$$\begin{aligned} E[\theta_{\text{tot}}^2(t)]_{\text{MCRB}} &= \begin{pmatrix} 1 & 2\pi t \end{pmatrix} \begin{pmatrix} (\mathbf{J}_{\text{MFIM}}^{-1})_{2,2} & (\mathbf{J}_{\text{MFIM}}^{-1})_{2,3} \\ (\mathbf{J}_{\text{MFIM}}^{-1})_{3,2} & (\mathbf{J}_{\text{MFIM}}^{-1})_{3,3} \end{pmatrix} \begin{pmatrix} 1 \\ 2\pi t \end{pmatrix} \\ &= \frac{N_0}{2E_s} \left( \frac{1}{K} + \frac{(t - t_c)^2}{D(K)} \right) \\ &\approx \frac{N_0}{2E_s} \frac{1}{K} \left( 1 + \frac{12(t - t_c)^2}{K^2 T^2} \right). \end{aligned} \quad (7.108)$$

In the last line of Eq. (7.108), we used the approximation  $D(K) \approx S(K)T^2 \approx K^3 T^2/12$ , which is accurate for a large  $K$ .

## REFERENCES

- [1] H.L. Van Trees, *Detection, Estimation, and Modulation Theory, Part 1*, Wiley, New York, 2004.
- [2] R. Johannesson, K.Sh. Zigangirov, *Fundamentals of Convolutional Coding*, Wiley, New York, 2015.
- [3] G. Ungerboeck, Channel coding with multilevel/phase signals, *IEEE Trans. Inform. Theory* 28 (1982) 55–67.
- [4] E. Biglieri, D. Divsalar, P.J. McLane, M.K. Simon, *Introduction to Trellis-Coded Modulation With Applications*, Macmillan, New York, 1991.
- [5] C. Berrou, A. Glavieux, P. Thitimajshima, Near Shannon limit error-correcting coding and decoding: turbo-codes, in: *IEEE International Conference on Communications, ICC'93*, Geneva, Switzerland, May 1993, pp. 1064–1070.
- [6] B. Vucetic, J. Yuan, *Turbo Codes: Principles and Applications*, Springer Science & Business Media, Dordrecht, 2012.

- [7] R.G. Gallager, Low Density Parity Check Codes, MIT Press, Cambridge, MA, 1963.
- [8] D.J.C. MacKay, R.M. Neal, Near Shannon limit performance of low density parity check codes, *Elect. Lett.* 1645–1646.
- [9] A.P. Dempster, N.M. Laird, D.B. Rubin, Maximum likelihood from incomplete data via the EM algorithm, *J. R. Stat. Soc. B* 39 (1) (1977) 1–38.
- [10] A.N. D’Andrea, U. Mengali, R. Reggiannini, The modified Cramer-Rao bound and its application to synchronization problems, *IEEE Trans. Comm.* 42 (2/3/4) (1994) 1391–1399.
- [11] F. Gini, R. Reggiannini, U. Mengali, The modified Cramer-Rao bound in vector parameter estimation, *IEEE Trans. Comm.* 46 (1) (1998) 52–60.
- [12] U. Mengali, A.N. D’Andrea, *Synchronization Techniques for Digital Receivers*, Plenum Press, New York, 1997.
- [13] M. Oerder, H. Meyr, Digital filter and square timing recovery, *IEEE Trans. Commun.* 36 (1988) 605–612.
- [14] F.M. Gardner, Interpolation in digital modems—I. Fundamentals, *IEEE Trans. Commun.* 41 (3) (1993) 501–507.
- [15] L. Erup, F.M. Gardner, R.A. Harris, Interpolation in digital modems—II. Implementation and performance, *IEEE Trans. Commun.* 41 (6) (1993) 998–1008.
- [16] H. Meyr, M. Moeneclaey, S. Fechtel, *Digital Communication Receivers — Synchronization*, Wiley, New York, 1997.
- [17] F.R. Kschischang, B.J. Frey, H.-A. Loeliger, Factor graphs and the sum-product algorithm, *IEEE Trans. Inform. Theory* IT-47 (2001) 498–519.
- [18] H.-A. Loeliger, An introduction to factor graphs, *IEEE Signal Process. Mag.* 21 (2004) 28–41.
- [19] Special issue on synchronization, *IEEE Trans. Commun.* 28 (1980) 1105–1334.
- [20] Special issue on signal synchronization in digital transmission systems *J. Select. Areas Commun.* 19 (2001) 2293–2419.
- [21] K.H. Mueller, M. Müller, Timing recovery in digital synchronous data receivers, *IEEE Trans. Commun.* 24 (1976) 516–531.
- [22] F.M. Gardner, A BPSK/QPSK timing-error detector for sampled receivers, *IEEE Trans. Commun.* 34 (1986) 423–429.
- [23] F.M. Gardner, Frequency detectors for digital demodulators via maximum likelihood derivation, ESA-ESTEC Final Report: Part 2, ESTEC Contract No 8022/88/NL/DG, March 1990.
- [24] S. Kay, A fast and accurate single frequency estimator, *IEEE Trans. Acoust. Speech, Signal Process.* 37 (1989) 1987–1990.
- [25] M.P. Fitz, Further results in the fast estimation of a single frequency, *IEEE Trans. Commun.* 42 (1994) 862–864.
- [26] M. Luise, R. Reggiannini, Carrier frequency recovery in all-digital modems for burst—mode transmissions, *IEEE Trans. Commun.* 43 (1995) 1169–1178.
- [27] A.J. Viterbi, A.M. Viterbi, Nonlinear estimation of PSK modulated carrier phase with applications to burst digital transmission, *IEEE Trans. Inform. Theory* 32 (1983) 543–551.
- [28] C. Herzet, N. Noels, V. Lottici, H. Wymeersch, M. Luise, M. Moeneclaey, L. Vandendorpe, Code-aided turbo synchronization, *Proc. IEEE* 95 (2007) 1255–1271.
- [29] A. Anastasopoulos, K.M. Chugg, G. Colavolpe, G. Ferrari, R. Raheli, Iterative detection for channels with memory, *Proc. IEEE* 95 (2007) 1272–1294.

- [30] H. Wymeersch, H. Steendam, H. Bruneel, M. Moeneclaey, Code-aided frame synchronization and phase ambiguity resolution, *IEEE Trans. Signal Proc.* 54 (2006) 2747–2757.
- [31] N. Noels, H. Steendam, M. Moeneclaey, Performance analysis of ML-based feedback carrier phase synchronizers for coded signals, *IEEE Trans. Signal Proc.* 55 (2007) 1129–1136.
- [32] C. Herzet, H. Wymeersch, M. Moeneclaey, L. Vandendorpe, On maximum-likelihood timing synchronization, *IEEE Trans. Comm.* 55 (2007) 1116–1118.

# Equalization

# 8

**J. Barry**

*Georgia Institute of Technology, Atlanta, GA, United States*

## CHAPTER OUTLINE

<b>8.1 Motivation .....</b>	<b>284</b>
<b>8.2 Models and Metrics.....</b>	<b>284</b>
8.2.1 Discrete-Time Intersymbol Interference Model .....	285
8.2.2 Arithmetic, Harmonic, and Geometric Means .....	287
8.2.3 Shannon Capacity .....	288
8.2.4 SNR Benchmarks: The MF Bound and Shannon SNR .....	289
<b>8.3 Optimum Trellis-Based Detectors .....</b>	<b>291</b>
8.3.1 The Trellis Diagram .....	291
8.3.2 MAP or ML Sequence Detection: The Viterbi Algorithm .....	295
8.3.3 APP Detection: The BCJR Algorithm .....	301
<b>8.4 Linear Equalization .....</b>	<b>305</b>
8.4.1 The Matched Filter.....	306
8.4.2 ZF Linear Equalization .....	307
8.4.3 MMSE Linear Equalization .....	308
<b>8.5 Decision-Feedback Equalization.....</b>	<b>311</b>
8.5.1 The ZF DFE .....	312
8.5.2 Error Propagation.....	314
8.5.3 The Minimum-MSE DFE .....	316
8.5.4 DFE via Noise Prediction .....	318
<b>8.6 Tomlinson-Harashima Precoding .....</b>	<b>319</b>
<b>8.7 Comparing Performance: A Case Study.....</b>	<b>322</b>
8.7.1 ZF Linear Equalizer .....	325
8.7.2 MMSE Linear Equalizer .....	325
8.7.3 ZF DFE.....	326
8.7.4 MMSE DFE.....	327
8.7.5 ZF Tomlinson-Harashima Precoding.....	327
8.7.6 MMSE THP .....	328

8.7.7 Viterbi Algorithm .....	329
8.7.8 BCJR Algorithm .....	329
<b>8.8 Summary</b> .....	<b>330</b>
<b>References</b> .....	<b>331</b>

---

## 8.1 MOTIVATION

In Chapter 4 there was only one impediment to reliable communication: additive noise. Here, we consider the more realistic case where, in addition to adding noise, the channel *filters* the transmitted signal. Such filtering arises in nearly every practical scenario: A wireless channel filters because the transmitted signal bounces off of different reflectors with different path lengths before arriving at the receiver; an electronic cable filters because different frequencies are attenuated by different amounts; a fiber-optic cable filters because different wavelengths propagate at different speeds. This seemingly modest change to the channel model has profound implications on how communications systems are designed and implemented. *Equalization* is broadly defined as any signal processing aimed at counteracting the dispersive effects of such a filtering channel. As we will see, the equalization process can range from a simple linear filter to a sophisticated signal processing algorithm, and it can be performed in advance (at the transmitter) or after the fact (at the receiver).

Equalization plays a central role in most communications applications, ranging from wireless to wired to storage devices. Equalization is thus a fundamental and important topic in its own right. Moreover, the problem of equalization has at its core the problem of mitigating interference, namely interference between one information symbol and another. As such, the concepts developed in this chapter readily extend to a much broader class of interference problems, many of which at a glance have no obvious connection to the linear filter model considered here, including co-channel interference, multiuser interference, intercell interference, and multiple-input multiple-output communications.

---

## 8.2 MODELS AND METRICS

The nature of the equalization problem is strongly impacted by the type of modulation scheme being used. In this chapter, we will limit our discussion to a communication system that uses a single-carrier passband version of pulse-amplitude modulation such as quadrature-amplitude modulation (QAM) and phase-shift keying (PSK), as opposed to nonlinear alternatives such as continuous-phase frequency-shift keying or pulse-position modulation. Our motivation for this restriction is threefold: (1) A wide variety of applications use QAM and its variations; (2) the mere presence of a dispersive channel suggests that a spectrally efficient modulation scheme like

QAM is an appropriate design choice; and (3) linear modulation schemes like QAM are more amenable to equalization through signal processing.

In a QAM or PSK system, the transmitter conveys a sequence of  $L$  *information* or *message* symbols  $\{a_0 \cdots a_{L-1}\}$  by transmitting a signal whose complex envelope (see Chapter 4) has the following form:

$$x(t) = \sum_{k=0}^{L-1} a_k g(t - kT), \quad (8.1)$$

where  $g(t)$  is the transmit pulse shape,  $a_k$  is the  $k$ th information symbol chosen from a complex alphabet  $\mathcal{A}$  (typically QAM or PSK), and  $T$  is the signaling period. This equation describes a pulse train, where a new pulse is sent every  $T$  seconds, and the amplitude of the  $k$ th pulse is modulated by the  $k$ th symbol  $a_k$ .

The impact of a dispersive channel is to filter the transmitted signal. Filtering a PAM signal yields another PAM signal, where the pulse shape after the filter is simply a filtered version of the pulse shape before the filter. Therefore, the complex envelope of the received waveform after a channel that first filters and then adds noise can be written as

$$y(t) = \sum_{k=0}^{L-1} a_k h(t - kT) + v(t), \quad (8.2)$$

where the received pulse shape  $h(t)$  is the filtered version of the transmit pulse shape  $g(t)$ , and where  $v(t)$  is the complex envelope of the additive noise, assumed to have independent real and imaginary parts, each of which is white and Gaussian with power-spectral density (PSD)  $N_0/2$ .

### 8.2.1 DISCRETE-TIME INTERSYMBOL INTERFERENCE MODEL

The change in pulse shape is more problematic than it may at first seem because it generally leads to interference between neighboring symbols, a phenomenon known as *intersymbol interference* (ISI). Even when the transmitter carefully chooses its transmit pulse shape  $g(t)$  so that the set of translated pulses  $\{g(t - kT)\}$  in Eq. (8.1) are mutually orthogonal, the dispersive channel destroys that orthogonality, so that the set of translated pulses  $\{h(t - kT)\}$  seen at the receiver are not orthogonal.

If  $\{h(t - kT)\}$  were orthogonal, the detection problem would simplify dramatically: The receiver could apply the received waveform to a filter matched to  $h(t)$  and sample the matched filter (MF) output at the symbol rate; the  $k$ th sample would be a sufficient statistic for optimal detection of the  $k$ th symbol, and it could be passed to a simple memoryless quantizer to arrive at the corresponding symbol decision. In other words, if  $\{h(t - kT)\}$  were orthogonal, the optimal receiver could make symbol-by-symbol decisions, considering each symbol in isolation.

It can be shown that a filter matched to  $h(t)$  followed by a symbol-rate sampler is an optimal front end (providing sufficient statistics) even when the received pulses  $\{h(t - kT)\}$  are not orthogonal [1]. The cascade of this sampled MF and a subsequent discrete-time noise-whitening filter is known as the whitened MF, and it is a common starting point for front-end processing for the general case [2]. However, in this chapter we opt for a simpler presentation based on an assumption that the transmitter pulse shape is the minimum-bandwidth Nyquist pulse shape, that is, that  $g(t) = \sin(\pi t/T)/(\pi t/T)$ . Our motivation for this choice is based on two observations:

- A practical transmitter will often either aim to implement this pulse shape exactly or will implement a close approximation (such as a square-root-raised-cosine pulse shape with a modest amount of excess bandwidth).
- Using the ideal minimum-bandwidth pulse simplifies our exposition without obscuring the main conceptual problem of equalization. Extensions to handle arbitrary pulse shapes are more cumbersome but straightforward.

Since the received pulse shape is a filtered version of the transmitted pulse shape, the bandwidth of the received pulse will match that of the transmit pulse. Therefore, our assumption that the transmitter uses a minimum-bandwidth pulse, whose bandwidth is  $1/(2T)$ , implies that the bandwidth of the received pulse  $h(t)$  will also be  $1/(2T)$ . Furthermore, this implies that the received signal (before noise) will similarly be bandlimited to  $1/(2T)$ . We can thus pass the noisy received signal  $r(t)$  through an ideal low-pass filter with cutoff frequency  $1/(2T)$  without losing any information about the transmitted symbols; the low-pass filter will only reject out-of-band noise that is irrelevant to the detection problem. Further, the fact that the filter output is bandlimited enables us to sample it at the symbol rate  $1/T$  without losing any information. Applying Eq. (8.2) to such a low-pass filter that is scaled to have unit energy and then sampling at the symbol rate  $1/T$  leads to the following equivalent discrete-time model for the channel:

$$r_k = \sum_{i=0}^{L-1} a_i h_{k-i} + n_k, \quad (8.3)$$

or more compactly  $r_k = a_k * h_k + n_k$ , where  $h_k = \sqrt{T}h(kT)$  is a scaled and sampled version of the received pulse shape and where  $\{n_k\}$  is a complex-valued circularly symmetric white-Gaussian noise process with PSD  $N_0$ , so that its real and imaginary parts are mutually independent, each being white and Gaussian with PSD  $N_0/2$ . A block diagram is shown in Fig. 8.1.

The discrete-time model of Eq. (8.3) and Fig. 8.1C will be our starting point for the remainder of the chapter. The discrete-time impulse response  $h_k$  captures the severity of the ISI, and it will be referred to as the ISI response. To be concrete we will assume that the impulse response is causal, starting at time 0, and has memory  $\mu$ , so that the only nonzero coefficients are  $h_0$  through  $h_\mu$ . We will at times require that the memory be finite,  $\mu < \infty$ .

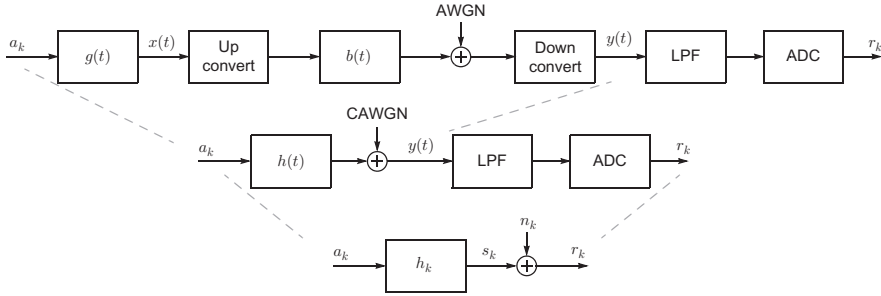


FIG. 8.1

Three equivalent views of the channel model, from top to bottom: passband model; baseband continuous-time model; baseband discrete-time model.

To recap, here are the key assumptions that we make in this chapter, limiting its scope:

- We assume a single-carrier passband linear modulation (such as QAM or PSK).
- We assume a minimum-bandwidth pulse shape.
- We assume a linear time-invariant ISI response with additive white Gaussian noise.
- We assume perfect channel knowledge available at the transmitter (for precoding schemes only) and at the receiver (for all schemes).
- We assume perfect synchronization.

See [Section 8.8](#) for further reading on the situation where one or more of these assumptions is violated.

### 8.2.2 ARITHMETIC, HARMONIC, AND GEOMETRIC MEANS

For any real and nonnegative function  $S(e^{j\theta})$  over  $\theta \in [-\pi, \pi)$ , including, for example, any valid PSD, let us define three mean operators as follows:

$$\text{Arithmetic mean: } \mathcal{A}\{S(e^{j\theta})\} = \frac{1}{2\pi} \int_{-\pi}^{\pi} S(e^{j\theta}) d\theta,$$

$$\text{Harmonic mean: } \mathcal{H}\{S(e^{j\theta})\} = \frac{1}{\frac{1}{2\pi} \int_{-\pi}^{\pi} \frac{1}{S(e^{j\theta})} d\theta},$$

$$\text{Geometric mean: } \mathcal{G}\{S(e^{j\theta})\} = \exp \left\{ \frac{1}{2\pi} \int_{-\pi}^{\pi} \log S(e^{j\theta}) d\theta \right\}.$$

These will prove to be useful throughout the chapter. A few comments:

- In all three cases, the mean of a constant is that same constant.
- All three means can be seen as a special case of the transformation  $f^{-1}(\frac{1}{2\pi} \int_{-\pi}^{\pi} f(S(e^{j\theta})) d\theta)$ , or equivalently  $f^{-1}(\mathcal{A}\{f(\cdot)\})$ , where either  $f(x) = x$ ,  $f(x) = 1/x$ , or  $f(x) = \log(x)$ .

- As written, the logarithm in the geometric mean is base  $e$ , although any other base will yield the same result, as long as the outer exponential operator is changed to be its inverse.
- All three can be seen as the limiting case (as  $N \rightarrow \infty$ ) of first taking  $N$  equally spaced samples  $S_k = S(e^{jk2\pi/N})$  for  $k \in 0, \dots, N-1$ , and second applying the corresponding means to the resulting finite set of real numbers. For example, when  $N = 2$  the arithmetic mean is  $(S_0 + S_1)/2$ , the harmonic mean is  $2/(1/S_0 + 1/S_1)$ , and the geometric mean is  $\sqrt{S_0 S_1}$ .
- The three means satisfy

$$\mathcal{H}\{S\} \leq \mathcal{G}\{S\} \leq \mathcal{A}\{S\}, \quad (8.4)$$

for any real and nonnegative function  $S = S(e^{j\theta})$ . Equalities are met if and only if  $S(e^{j\theta})$  is a constant, independent of  $\theta$ .

- When  $S(e^{j\theta})$  is the PSD of a random sequence  $x_k$ , the arithmetic mean reduces to  $\mathcal{A}\{S(e^{j\theta})\} = E(|x_k|^2)$ , the power in the random sequence.
- When  $S(e^{j\theta})$  is the PSD of a random sequence  $x_k$ , the geometric mean reduces to the mean-squared error of an optimal linear predictor  $\hat{x}_k = \sum_{i=1}^{\infty} p_i x_{k-i}$ , whose predictor coefficients  $\{p_i\}$  are chosen to minimize the mean-squared error [3], that is,  $\mathcal{G}\{S(e^{j\theta})\} = \min_{\{p_i\}} E(|\hat{x}_k - x_k|^2)$ .
- The arithmetic mean operator is linear, so that  $\mathcal{A}\{a_1 S_1 + a_2 S_2\} = a_1 \mathcal{A}\{S_1\} + a_2 \mathcal{A}\{S_2\}$ . In contrast, neither the harmonic nor geometric mean operators is linear.
- The geometric mean involving a product or ratio satisfies  $\mathcal{G}\{a \frac{S_1 S_2}{S_3}\} = a \frac{\mathcal{G}\{S_1\} \mathcal{G}\{S_2\}}{\mathcal{G}\{S_3\}}$ .
- It can be shown that  $\mathcal{G}\{|1 + be^{-j\theta}|^2\} = 1$  for any constant  $b$  satisfying  $|b| \leq 1$ . Combined with the previous fact, this implies that  $\mathcal{G}\{|M(e^{j\theta})|^2\} = 1$  for any rational, monic, and minimum phase filter of the form  $M(z) = 1 + m_1 z^{-1} + m_2 z^{-2} + \dots$ .

### 8.2.3 SHANNON CAPACITY

The Shannon capacity is an upper bound on how fast one can communicate reliably. The Shannon capacity of the ISI channel with AWGN of Eq. (8.3), subject to a power constraint on the input of  $E(|a_k|^2) \leq E_a$ , can be expressed in terms of the discrete-time Fourier transform  $H(e^{j\theta}) = \sum_k h_k e^{-jk\theta}$  of the ISI response, according to [4]:

$$C = \frac{1}{2\pi} \int_{-\pi}^{\pi} \log_2 \left( 1 + \frac{S_a(e^{j\theta}) |H(e^{j\theta})|^2}{N_0} \right) d\theta \quad (8.5)$$

$$= \frac{1}{2\pi} \int_{-\pi}^{\pi} \log_2 (1 + \text{SNR}(\theta)) d\theta \quad (8.6)$$

$$= \log_2 \mathcal{G}\{1 + \text{SNR}(\theta)\} \text{ bits/symbol}, \quad (8.7)$$

where for convenience we have introduced the *signal-to-noise ratio (SNR) spectral density*, defined by:

$$SNR(\theta) = \frac{S_a(e^{j\theta})|H(e^{j\theta})|^2}{N_0},$$

which can be interpreted as the SNR per unit frequency. The capacity formula (8.5) is not complete until the PSD  $S_a(e^{j\theta})$  of the transmitted symbols is specified: The capacity-achieving PSD can be found via a procedure with a geometrical interpretation known as *waterpouring*, according to the following:

$$S_a(e^{j\theta}) = \max[0, \lambda - N_0|H(e^{j\theta})|^{-2}], \quad (8.8)$$

where the water-level parameter  $\lambda$  is adjusted until the power constraint is met with equality,  $\frac{1}{2\pi} \int_{-\pi}^{\pi} S_a(e^{j\theta}) d\theta = E_a$ .

**Example 8.1.** The waterpouring procedure is shown in Fig. 8.2 for the case when the channel ISI response is  $H(z) = 1 + (0.6 + 0.6j)z^{-1} + 0.6jz^{-2}$ , the transmit power constraint is  $E_a = 1$ , and the noise PSD is  $N_0 = 0.25$ , which corresponds to a channel SNR of 9.2 dB. As the figure shows, the optimal PSD concentrates its power at those frequencies for which the channel gain is large, while avoiding those frequencies for which the channel gain is small.

Rather than adopting the optimal waterpouring spectrum, if the transmitted symbols are instead chosen independently and identically distributed (iid) with a uniform distribution from an alphabet with energy  $E_a$ , so that  $S_a(e^{j\theta}) = E_a$ , the formula (8.5) would no longer be the capacity of the channel; nevertheless, it would represent an upper bound on the achievable rate for any input meeting the iid constraint.

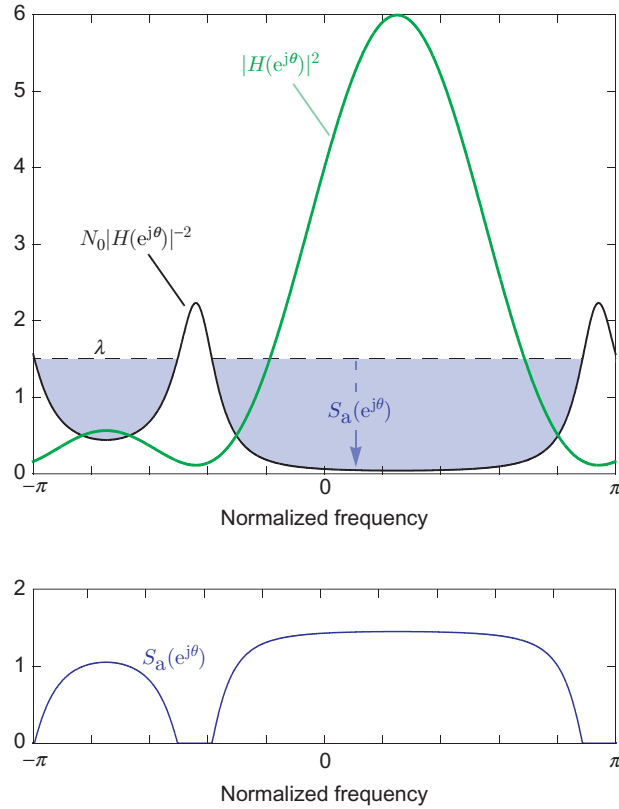
In the special case of a channel with no ISI, both the channel magnitude response and the optimal waterpouring spectrum are flat, namely  $|H(e^{j\theta})| = |h_0|$  and  $S_a(e^{j\theta}) = E_a$ , so that the SNR spectral density reduces to the constant  $SNR_0 = E_a|h_0|^2/N_0$ , independent of  $\theta$ ; in this case, the capacity formula of Eq. (8.5) reduces to the familiar form  $C = \log_2(1 + SNR_0)$ .

## 8.2.4 SNR BENCHMARKS: THE MF BOUND AND SHANNON SNR

We will encounter two types of SNRs in this chapter, and it will be important to not confuse the two:

- *Channel SNR:* This is the SNR of the underlying ISI channel, and it is, by definition, the ratio of the power in the received signal (the first term in Eq. 8.3) divided by the power in the received noise (the second term in Eq. 8.3), namely,

$$SNR = \frac{E(|\sum_i a_i h_{k-i}|^2)}{E(|n_k|^2)} = \frac{\frac{1}{2\pi} \int_{-\pi}^{\pi} S_a(e^{j\theta})|H(e^{j\theta})|^2 d\theta}{N_0} = \mathcal{A}\{SNR(\theta)\}, \quad (8.9)$$

**FIG. 8.2**

Geometric interpretation of the waterpouring procedure (Eq. 8.8) for determining the capacity-achieving transmit spectrum: water is poured into the “bowl”  $N_0|H(e^{j\theta})|^{-2}$  until the average water depth matches the power constraint; the depth of the water at each frequency is then the optimal PSD, illustrated separately in the *bottom figure*.

where  $SNR(\theta) = S_a(e^{j\theta})|H(e^{j\theta})|^2/N_0$ . This is the SNR of the ISI channel itself, before any attempts at equalization are made.

- *Postequalization SNR*: Also referred to as the *equalizer SNR*, this is the SNR after equalization. Importantly, this generally applies only to the class of equalizers that strive to *transform the ISI channel into an ISI-free channel*; these include the linear equalizers of Section 8.4, the decision-feedback equalizers of Section 8.5, and the precoding strategies of Section 8.6. The performance of any such equalizer is then easily and effectively quantified by the SNR of the resulting ISI-free channel.

The postequalization SNR is an effective metric for comparing equalizer alternatives. The higher the postequalization SNR, the better the equalizer. A particularly useful bound for the postequalization SNR of any practical equalization strategy is the so-called *matched-filter bound* on the postequalization SNR, which is based on the unrealistic assumption that the receiver has (genie-aided) knowledge of all of the interfering symbols. In other words, when making a decision about the  $i$ th symbol  $a_i$ , the receiver somehow knows all of the interfering symbols  $\{a_{k \neq i}\}$ . A receiver with this knowledge can do no better than to reconstruct the ISI from the known interfering symbols and subtract it from the channel output Eq. (8.3), yielding the ISI-free channel  $z_k = a_i h_{k-i} + n_k$ . Subtracting the ISI in this way clearly transforms the ISI channel into an ISI-free channel whose SNR is:

$$SNR_{\text{MFB}} = \frac{E_a \sum_k |h_k|^2}{N_0}. \quad (8.10)$$

When the transmit PSD is flat ( $S_a(e^{j\theta}) = E_a$ ), which is often the case, this SNR is identical to the SNR of the underlying channel in Eq. (8.9). Otherwise, in the general case, we use  $E_a = \mathcal{A}\{S_a(e^{j\theta})\}$  in Eq. (8.10). The reason that the MFB is a bound for the postequalization SNR is because it arises from optimal processing with genie-aided knowledge of the interfering symbols; optimal (or suboptimal) processing without such knowledge can only perform worse.

An alternative upper bound on the postequalization SNR of any practical equalization strategy is the “effective SNR”  $SNR_{\text{Shannon}}$  achieved by a capacity-achieving system, which can be found by setting Eq. (8.5) to equal  $\log_2(1 + SNR_{\text{Shannon}})$  and solving for  $SNR_{\text{Shannon}}$ , yielding:

$$SNR_{\text{Shannon}} = \mathcal{G}\{1 + SNR(\theta)\} - 1.$$

The inequality in Eq. (8.4) directly leads to the conclusion that the effective SNR of a capacity-achieving system cannot exceed the SNR of the underlying channel:

$$SNR_{\text{Shannon}} \leq SNR,$$

with equality being reached only when  $SNR(\theta)$  is a constant, independent of  $\theta$ , which can happen only when the channel has no ISI.

## 8.3 OPTIMUM TRELLIS-BASED DETECTORS

### 8.3.1 THE TRELLIS DIAGRAM

Before adding noise, the channel model in Eq. (8.3) applies the sequence of information symbols  $a_k$  to a linear filter with impulse response  $h_k$ , producing the filter output  $s_k = a_k * h_k$ . For the case when the channel memory is finite ( $\mu < \infty$ ), it will be convenient to view this filter as a *finite-state machine (FSM)*. In particular, let  $\theta_k = [a_{k-1}, a_{k-2}, \dots, a_{k-\mu}]$  denote the filter *state* at time  $k$ . Because each symbol  $a_k \in \mathcal{A}$  is chosen from a finite alphabet, the number of such states is clearly finite,

namely  $Q = |\mathcal{A}|^\mu$ . More than just having a finite number of states, the filter is an FSM because it further satisfies two additional properties. First, the current output  $s_k$  is uniquely determined by the pair  $(a_k, \theta_k)$ , a fact that becomes clear when we rewrite the convolution  $s_k = a_k * h_k$  as follows:

$$s_k = h_0 a_k + [h_1, h_2, \dots, h_\mu] \theta_k^T. \quad (8.11)$$

Second, the next state  $\theta_{k+1}$  is also uniquely determined by the pair  $(a_k, \theta_k)$ ; this is also clearly true, since the next state  $\theta_{k+1}$  can be formed by concatenating the current input  $a_k$  with the first  $\mu - 1$  entries of the current state  $\theta_k$ . The key to the FSM formulation is that the state sequence satisfies the Markov property  $P(\theta_{k+1} | \theta_0, \theta_1, \dots, \theta_k) = P(\theta_{k+1} | \theta_k)$ . Intuitively, this means that knowledge of the state at time  $k$  tells us everything we need to know about what the next state at time  $k + 1$  might be; the history of how we got there is irrelevant. Two tapped-delay line models for the FSM are shown in Fig. 8.3.

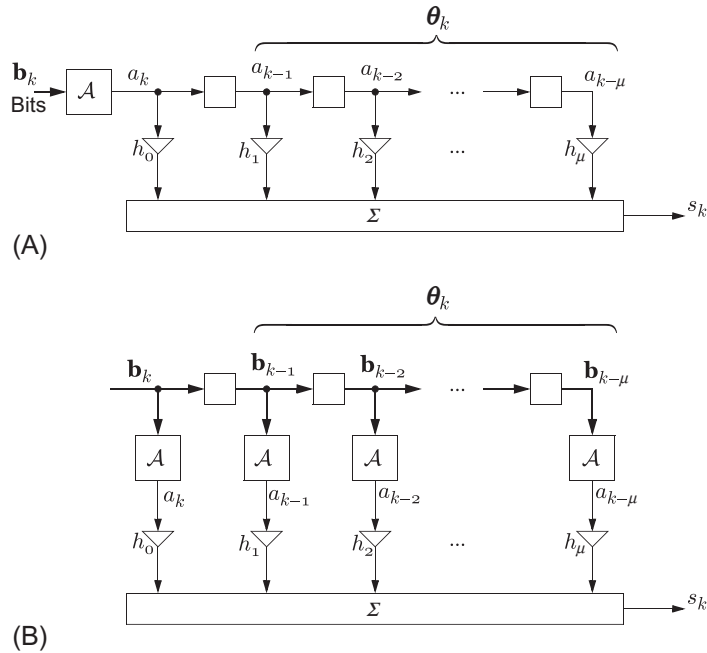


FIG. 8.3

Two equivalent views of the ISI filter as a finite-state machine. In both cases the state of the filter is the contents of its memory elements. In (A) the memory stores the information symbols, while in (B) the memory stores the corresponding message bit blocks, where  $\mathbf{b}_k$  denotes the unique block of  $\log_2 |\mathcal{A}|$  bits associated with the symbol  $a_k \in \mathcal{A}$ . The model of (B) is preferred when computing probabilities for the message bits using the Bahl-Cocke-Jelinek-Raviv algorithm.

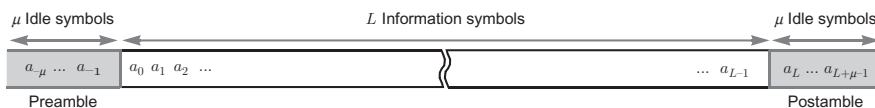


FIG. 8.4

We assume that the  $L$  information symbols are sandwiched between a preamble and postamble, both consisting of a block of  $\mu$  idle symbols.

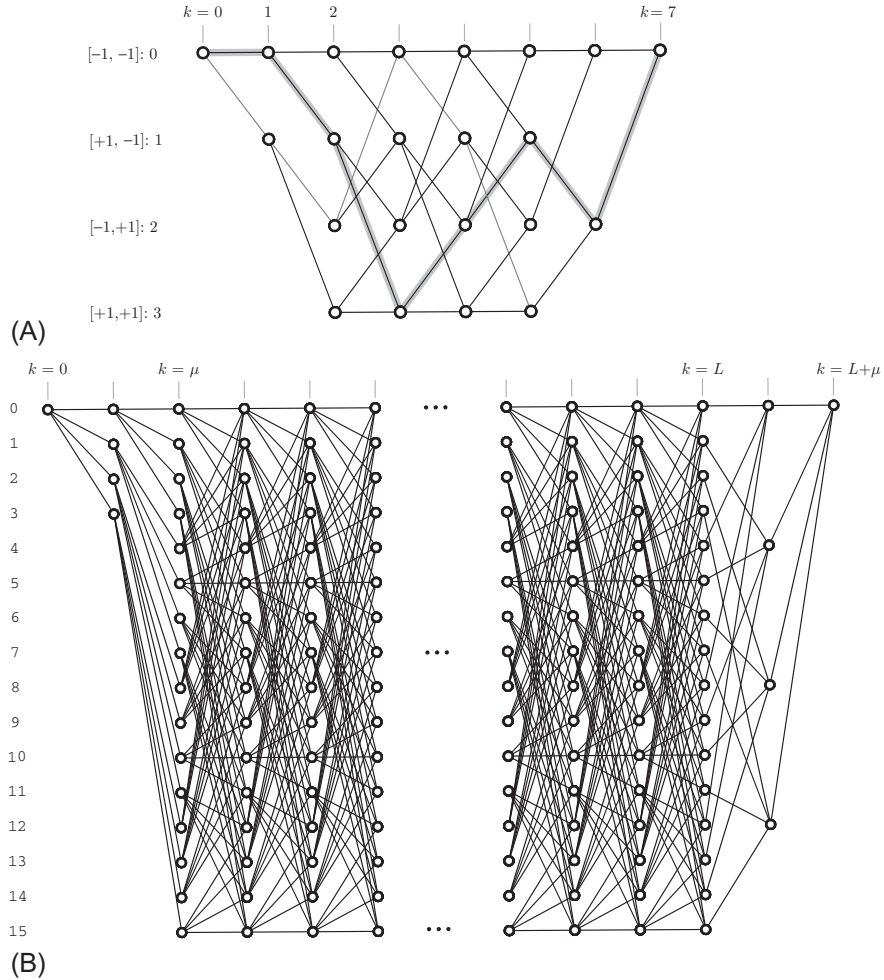
So far, we have assumed that the transmitter sends a symbol sequence of length  $L$ , starting with  $a_0$  and ending with  $a_{L-1}$ . To proceed further we need to clarify what happens before  $a_0$  and after  $a_{L-1}$ . While it might seem natural to assume that nothing is transmitted before and after, namely to assume that  $a_k = 0$  for all  $k \notin \{0, \dots, L-1\}$ , this can be problematic when  $0 \notin \mathcal{A}$ , because it would require that an augmented alphabet  $\mathcal{A} \cup \{0\}$  is used to define the states during the transients at the beginning and ending of the message. Besides, in practice it is more common to use preambles or postambles of noninformation-bearing symbols for tasks such as frame synchronization and channel estimation. To better capture this reality we will identify one symbol from the alphabet as the *idle* symbol, denoted  $a^0 \in \mathcal{A}$ , and we will assume that the transmitter uses both a preamble and a postamble, each consisting of a block of  $\mu$  idle symbols. In other words, we assume that  $a_k = a^0$  for  $k \in \{-\mu, \dots, -1\}$  and  $k \in \{L, \dots, L + \mu - 1\}$ . The preamble and postamble are shown in Fig. 8.4. The preamble ensures that the state is in the all-idle state at time 0, namely  $\theta_0 = [a^0, \dots, a^0]$ , while the postamble ensures that the state is in the all-idle state at time  $L + \mu$ , namely  $\theta_{L+\mu} = [a^0, \dots, a^0]$ .

In what follows we associate an integer label  $p \in \{0, \dots, Q-1\}$  with each state, and we will reserve the zero label for the all-idle state; with this notation, the preamble and postamble ensure that both  $\theta_0 = 0$  and  $\theta_{L+\mu} = 0$ . The symbols in the postamble are sometimes referred to as *termination* symbols, since their purpose is to terminate the trellis to a known state (namely, state 0).

The *trellis diagram* is defined simply as a plot of all possible states versus time.

**Example 8.2.** Suppose a block of  $L = 5$  binary symbols  $\mathcal{A} = \{\pm 1\}$  are transmitted across an ISI channel with memory  $\mu = 2$ , sandwiched between a preamble and postamble of two idle symbols  $a^0 = -1$ . There are four possibilities for the state  $\theta_k = [a_{k-1}, a_{k-2}]$ : it can be  $[-1, -1]$ ,  $[+1, -1]$ ,  $[-1, +1]$ , or  $[+1, +1]$ , which are assigned the integer labels 0, 1, 2, and 3, respectively. The corresponding trellis diagram is shown in Fig. 8.5A. The preamble ensures that the state begins at state 0 at time 0. The state at time 1 is either 0 or 1, depending on the value of  $a_0$ . The trellis terminates at state 0 at time 7. The path corresponding to the message  $[a_0, \dots, a_4] = [-1, +1, +1, -1, +1]$  is highlighted. In all, there are  $|\mathcal{A}|^L = 2^5 = 32$  distinct paths through this trellis, one for each possible message.

Longer messages, larger alphabets, and higher ISI memory can lead to a more complicated trellis.

**FIG. 8.5**

Examples of trellis diagrams: (A) A relatively simple trellis diagram for a message of length  $L = 5$ , alphabet size  $|\mathcal{A}| = 2$ , and channel memory  $\mu = 2$ . There are  $Q = |\mathcal{A}|^\mu = 4$  states; and (B) a more complicated trellis diagram for alphabet size  $|\mathcal{A}| = 4$  and channel memory  $\mu = 2$ , with  $Q = |\mathcal{A}|^\mu = 16$  states. Each message sequence  $\mathbf{a}$  corresponds to a unique “path” through the trellis that begins at state 0 at time 0 and ends at state 0 at time  $L + \mu$ .

**Example 8.3.** Suppose a block of  $L$  symbols chosen from an alphabet of size  $M = |\mathcal{A}| = 4$  (such as 4-QAM or 4-PSK) is transmitted across an ISI channel with memory  $\mu = 2$ . In this case the state  $\theta_k = [a_{k-1}, a_{k-2}]$  is the previous two symbols, so that the number of states is  $Q = |\mathcal{A}|^\mu = 16$ . The preamble and postamble ensure

that the starting state (at time  $k = 0$ ) and the ending state (at time  $k = L + \mu$ ) are both zero. The corresponding trellis diagram is shown in Fig. 8.5B. The trellis diagram has a total of  $L + \mu$  stages. The first  $L$  stages of the trellis correspond to the  $L$  message symbols. In these stages there are  $M = |\mathcal{A}| = 4$  branches emanating from each node, one for each possible message symbol. The last  $\mu$  stages of the trellis correspond to the postamble idle symbols. In these stages there is only one branch emanating from each node, namely the branch corresponding to the idle symbol.

### 8.3.2 MAP OR ML SEQUENCE DETECTION: THE VITERBI ALGORITHM

The maximum-a-posteriori (MAP) estimate of the message is the message  $\mathbf{a} = [a_0, \dots, a_{L-1}] \in \mathcal{A}^L$  that maximizes the a posteriori probability (APP),  $P(\mathbf{a}|\mathbf{r}) = f(\mathbf{r}|\mathbf{a})P(\mathbf{a})/f(\mathbf{r})$ , or equivalently maximizes just the numerator  $f(\mathbf{r}|\mathbf{a})P(\mathbf{a})$ . When all messages are equally likely, the MAP sequence decision reduces to the maximum-likelihood (ML) sequence decision, which is the symbol sequence  $\mathbf{a} \in \mathcal{A}^L$  that maximizes the likelihood  $f(\mathbf{r}|\mathbf{a})$ . A brute-force search for either type of decision would require that  $f(\mathbf{r}|\mathbf{a})$  be computed for each of the  $|\mathcal{A}|^L$  possible message sequences. The complexity of such an exhaustive search would thus grow exponentially with the message length  $L$ . In this section we describe an efficient solution to the MAP or ML sequence detection problem whose complexity grows only linearly with  $L$ .

Every message  $\mathbf{a} \in \mathcal{A}^L$  uniquely determines a “path” through the trellis, as specified by the state sequence  $\boldsymbol{\theta} = [\theta_0, \dots, \theta_{L+\mu}] \in \mathcal{A}^{\mu(L+\mu+1)}$ . The reverse is true as well, that is, every path through the trellis uniquely specifies the corresponding message sequence. Therefore, to find the MAP estimate of the message, we only need to find the MAP estimate for the *path* through the trellis, which is the state sequence  $\boldsymbol{\theta} \in \mathcal{A}^{\mu(L+\mu+1)}$  that maximizes the APP  $P(\boldsymbol{\theta}|\mathbf{r}) = f(\mathbf{r}|\boldsymbol{\theta})P(\boldsymbol{\theta})/f(\mathbf{r})$ , or equivalently maximizes just the numerator  $f(\mathbf{r}|\boldsymbol{\theta})P(\boldsymbol{\theta})$ . Because the noise components are independent, and because the noiseless channel output  $s_k$  depends only on the states at time  $k$  and time  $k + 1$ , this numerator reduces to the following:

$$\begin{aligned} f(\mathbf{r}|\boldsymbol{\theta})P(\boldsymbol{\theta}) &= \prod_{k=0}^{L+\mu-1} f(r_k | s_k = s^{(\theta_k, \theta_{k+1})}) P(a_k = a^{(\theta_k, \theta_{k+1})}) \\ &= \prod_{k=0}^{L+\mu-1} \gamma_k(\theta_k, \theta_{k+1}), \end{aligned} \quad (8.12)$$

where  $\gamma_k(p, q) = f(r_k | s^{(p, q)})P(a_k = a^{(p, q)})$  can be interpreted as a *branch metric* for the branch in the trellis diagram from state  $p$  at time  $k$  to state  $q$  at time  $k + 1$ . Here we use  $a^{(p, q)} \in \mathcal{A}$  to denote the unique input symbol associated with the transition from state  $p \in \{0, \dots, Q - 1\}$  to state  $q \in \{0, \dots, Q - 1\}$ . (When such a transition is impossible, we take the corresponding probability to be zero.) Similarly, we use  $s^{(p, q)}$  to denote the unique FSM output associated with a transition from state  $p$  to state  $q$ , as defined by Eq. (8.11). This means that an FSM that starts out in state  $p$  will output  $s^{(p, q)}$  and move to state  $q$  when the input symbol is  $a^{(p, q)}$ . Intuitively, the

branch metric for a branch from one state to another is a measure of how probable that particular transition is; the smaller the branch metric, the less likely the state transition along the corresponding branch occurred. The extreme case of a zero branch metric indicates an impossible state transition; this generally arises because the second factor  $P(a_k = a^{(p,q)})$  is zero, meaning that it is impossible to make a transition from state  $p$  to state  $q$ .

In effect, Eq. (8.12) rephrases the MAP sequence detection problem as the problem of finding a path through the trellis with the largest path metric, where the metric for a path is defined as the product of the branch metrics in its path, according to Eq. (8.12). The *Viterbi algorithm* is an efficient solution to this problem whose complexity grows only linearly with the message length  $L$  [2]. Let us define the *survivor* for the node  $(p, k)$  as the partial path to that node (ie, the partial path starting at node  $(0, 0)$  and ending at node  $(p, k)$ ) with maximal metric. Further, let  $\hat{\alpha}_k(p)$  denote this maximal survivor metric.<sup>1</sup> The decision path can thus be thought of as the survivor path for ending the node of the trellis, namely the node  $(0, L + \mu)$ . The key to the Viterbi algorithm is the observation that the survivors for the states at time  $k + 1$  will always build on the survivors at time  $k$ . In particular, the survivors for the states  $q \in \{0, 1, \dots, Q - 1\}$  at time  $k + 1$  can be computed recursively from the  $Q$  survivors at time  $k$  according to

$$\hat{\alpha}_{k+1}(q) = \max_p \{\hat{\alpha}_k(p) \gamma_k(p, q)\}, \quad (8.13)$$

with initialization  $\hat{\alpha}_0(p) = \delta_p$ , to account for the fact that the state is initially  $p = 0$  at time 0.

The Viterbi algorithm starts at the zeroth stage of the trellis, computes the survivors for the nodes at time  $k = 1$  based on the above recursion, then moves on to the next stage, computes the survivors for the nodes at time  $k = 2$ , and so on. It continues moving through the trellis from left to right and computes the survivors recursively, according to the above recursion, and further stores for each node the index of the previous state that was selected by the maximization of Eq. (8.13). At any time  $k$  the Viterbi algorithm need only track  $Q$  survivors, independent of  $k$ , one for each possible state at time  $k$ . This represents a significant amount of pruning, since the number of partial paths to any node at time  $k$  grows exponentially with  $k$ . Further, observe that the complexity at the  $k$ th stage of the trellis is fixed, independent of the value of  $k$ ; the number of computations required to implement Eq. (8.13) does not depend on  $k$ . This makes the overall complexity of the Viterbi algorithm a *linear* function of the sequence length  $L$ , in stark contrast to the exponential dependence on  $L$  that would be required by an exhaustive search for the best message.

The Viterbi algorithm described above is *multiplicative* because the path metric Eq. (8.12) is the product of all of the branch metrics in its path; because the logarithm

---

<sup>1</sup>The reason for the “hat” is that this metric can be interpreted as an estimate or approximation of a quantity that will be denoted  $\alpha_k(p)$  in the next section.

is monotonic, we can equivalently maximize the logarithm of Eq. (8.12), that is, maximize  $\sum_k g_k(\theta_k, \theta_{k+1})$ , which leads to an *additive* version of Eq. (8.13):

$$\lambda_{k+1}(q) = \max_p \{\lambda_k(p) + g_k(p, q)\}, \quad (8.14)$$

where  $\lambda_k(p) = \log \hat{\alpha}_k(p)$  and  $g_k(p, q) = \log \gamma_k(p, q)$ . Exploiting the fact that the noise is Gaussian, the branch metric  $\gamma_k(p, q) = f(r_k | s^{(p,q)}) P(a^{(p,q)})$  reduces to

$$\gamma_k(p, q) = \frac{1}{\pi N_0} e^{-|r_k - s^{(p,q)}|^2 / N_0} P(a_k = a^{(p,q)}), \quad (8.15)$$

so that a negatively scaled version  $\mu_k(p, q) = -N_0 g_k(p, q)$  of the additive branch metric is

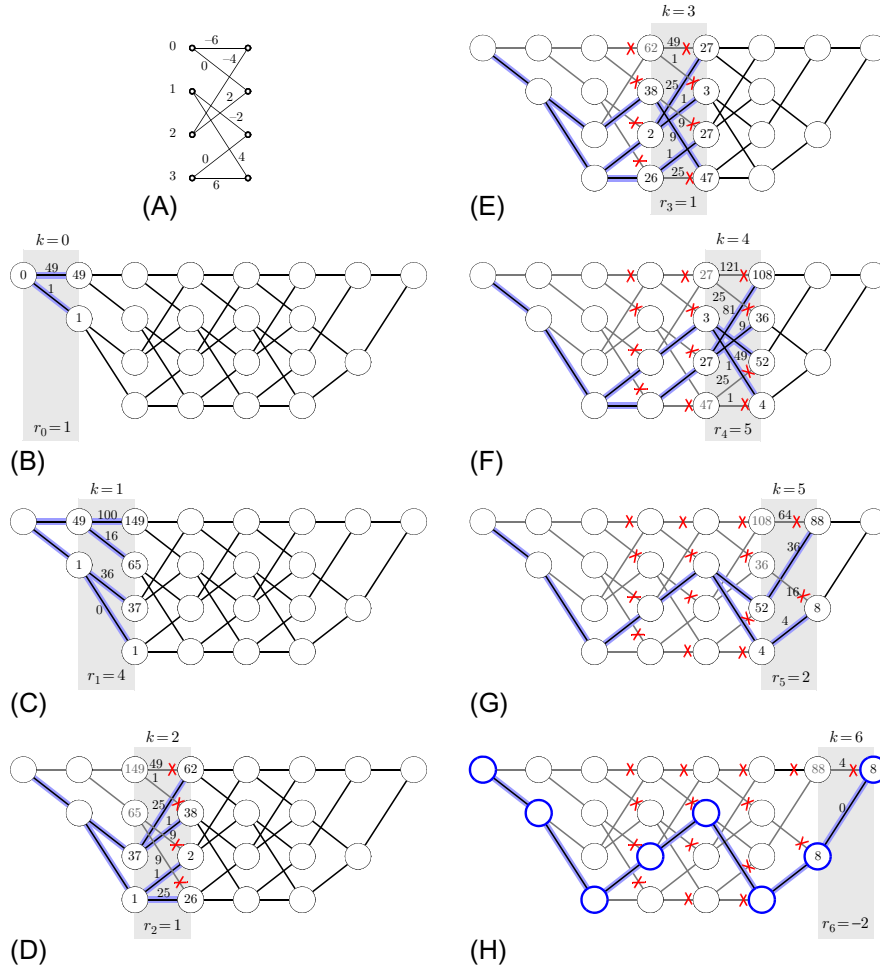
$$\mu_k(p, q) = |r_k - s^{(p,q)}|^2 - N_0 \log \frac{P(a_k = a^{(p,q)})}{\pi N_0}. \quad (8.16)$$

The negative scaling factor means that, instead of maximizing the sum  $\sum_k g_k(\theta_k, \theta_{k+1})$  of the original additive branch metrics, the MAP detector can now equivalently *minimize* the sum  $\sum_k \mu_k(\theta_k, \theta_{k+1})$  of the new branch metrics. Furthermore, when all symbols are equally likely, the subtracted term in Eq. (8.16) will be independent of  $p$  and  $q$  and thus the same for every branch in the trellis, meaning that the MAP detector (which reduces to the ML detector in the case when all symbols are equally likely) can be based on an additive version of the Viterbi algorithm with the simplified branch metric  $\hat{\mu}_k(p, q) = |r_k - s^{(p,q)}|^2$ . This last branch metric has a simple geometric interpretation as the squared Euclidean distance between the  $k$ th observation and what that observation should have been, had the particular transition from state  $p$  to state  $q$  actually occurred. The Viterbi algorithm with this branch metric is also commonly known as the minimum-distance sequence detector, or the maximum-likelihood sequence detector when the noise is white and Gaussian. The solution is the message sequence that maximizes the likelihood  $f(\mathbf{r}|\mathbf{a})$ , or equivalently minimizes the energy in the error between the observation sequence  $r_k$  and the filtered message  $a_k * h_k$ .

**Example 8.4.** Suppose a sequence  $\mathbf{a} = [a_0, \dots, a_4]$  of  $L = 5$  binary symbols chosen independently and uniformly from the BPSK alphabet  $\mathcal{A} = \{\pm 1\}$  is transmitted across an ISI channel with real-valued impulse response  $H(z) = 3 + 2z^{-1} + z^{-2}$ , which has memory  $\mu = 2$ , with a preamble and postamble each consisting of a pair of idle symbols  $a^0 = -1$ . In this example we illustrate how to use the Viterbi algorithm to find the ML decision sequence, given that the noisy channel output<sup>2</sup> (after additive white Gaussian noise) is  $\mathbf{r} = [r_0, \dots, r_6] = [1, 4, 1, 1, 5, 2, -4]$ .

The state  $\theta_k = [a_{k-1}, a_{k-2}]$  can be  $[-1, -1]$ ,  $[+1, -1]$ ,  $[-1, +1]$ , or  $[+1, +1]$ , which are labeled by the integers 0, 1, 2, and 3, respectively. A transition from state  $\theta_k = [a_{k-1}, a_{k-2}]$  at time  $k$  to state  $\theta_{k+1} = [a_k, a_{k-1}]$  at time  $k + 1$  uniquely

<sup>2</sup>In practice, neither the channel ISI coefficients nor the noisy channel outputs will be integer-valued; nevertheless, we assume they are integers in this example to simplify the branch metric computations.

**FIG. 8.6**

The Viterbi algorithm example: (A) shows the expected outputs  $\{s^{(p,q)}\}$ , while (B) through (H) show the branch metrics and add-compare-select results for stage 0 through stage 6, respectively.

determines the “expected” filter output  $s_k = 3a_k + 2a_{k-1} + a_{k-2}$  at time  $k$  (see Eq. 8.11). The expected filter outputs for all possible state transitions are summarized in Fig. 8.6A. On the left of the figure is a set of four nodes, one for each possible value for the state  $p \in \{0, 1, 2, 3\}$  at time  $k$ . On the right is another set of four nodes, one for each possible state  $q \in \{0, 1, 2, 3\}$  at time  $k+1$ . A branch from state  $p$  to state  $q$  indicates that a transition from state  $p$  to state  $q$  is possible. The label on each such

branch in Fig. 8.6A is the corresponding expected output  $s_k = 3a_k + 2a_{k-1} + a_{k-2}$  at time  $k$ .

The diagram in Fig. 8.6A can be used as an alternative to convolution for computing the ISI filter output in response to an input sequence. For example, consider the input sequence  $\mathbf{a} = [a_0, \dots, a_4] = [-1, +1, +1, -1, +1]$ . The path for this sequence is highlighted in Fig. 8.5A. Each branch in this path has an expected output, as indicated in Fig. 8.6A, so that the expected ISI filter output in response to this input sequence can be read off from the branches in Fig. 8.6A as  $\mathbf{s} = [s_0, \dots, s_6] = [-6, 0, 4, 0, 2, -2, 4]$ .

Each message has its own unique path, and hence, from Fig. 8.6A, its own expected output sequence  $\mathbf{s}$ . The ML sequence detection problem for this AWGN channel reduces to that of finding the message  $\mathbf{a}$  whose expected filter output  $\mathbf{s}$  is closest to the observation  $\mathbf{r} = [r_0, \dots, r_6]$ , in the sense that it minimizes  $\|\mathbf{r} - \mathbf{s}\|^2 = \sum_{k=0}^6 |r_k - s_k|^2$ . Let us label the branch from state  $p$  at time  $k$  to state  $q$  at time  $k+1$  with the additive branch metric  $|r_k - s^{(p,q)}|^2$  (which is equivalent to Eq. 8.16 given our assumption that the symbol distribution is uniform), where  $s^{(p,q)}$  is the expected output associated with a transition from state  $p$  to state  $q$ , as summarized in Fig. 8.6A. The ML cost  $\|\mathbf{r} - \mathbf{s}\|^2$  for a particular message can then be computed by summing the branch metrics in its corresponding path; this branch label thus reduces the ML sequence detection problem to the problem of finding a path through the trellis (from state 0 at time 0 to state 0 at time 7) whose path metric (equal to the sum of its branch metrics) is as small as possible.

The Viterbi algorithm efficiently finds the path through the trellis with minimum cost. For each node  $(p, k)$  in the trellis, the algorithm keeps track of both the survivor path to that node (which is the lowest-cost path to that node) and its corresponding cost, call it  $\alpha_k(p)$ . The algorithm is depicted in Fig. 8.6B through Fig. 8.6H. Fig. 8.6B highlights stage  $k = 0$  of the trellis, with the corresponding noisy observation  $r_0 = 1$  written below it. The two branch metrics for this stage are computed by computing the square of the difference between the *actual* observation ( $r_0 = 1$ ) and the *expected* observation ( $s^{(p,q)}$ ) for the transition, as indicated in Fig. 8.6A. In particular, since  $s^{(0,0)} = -6$  in Fig. 8.6A, the upper branch metric in Fig. 8.6B is  $|r_k - s^{(0,0)}|^2 = |1 - (-6)|^2 = 49$ . Similarly, since  $s^{(0,1)} = 0$  in Fig. 8.6A, the lower branch metric in Fig. 8.6B is  $|r_k - s^{(0,1)}|^2 = |1 - 0|^2 = 1$ .

In the figure, the number written inside each node  $(p, k)$  is the survivor metric  $\alpha_k(p)$  for that node's survivor; that is, it is the cost of the lowest-cost partial path to that node. The cost at the beginning of the trellis (state 0 at time 0) is initialized to zero. At time 1 only two of the four states are reachable, with costs 49 and 1, as shown in Fig. 8.6B.

In Fig. 8.6C we highlight stage  $k = 1$  of the trellis, with the corresponding noisy observation  $r_1 = 4$  written below. As before, the branches are labeled by the squared difference between the actual observation  $r_1 = 4$  and the expected observation for the corresponding transition, as indicated in Fig. 8.6A. For example, since  $s^{(0,0)} = -6$  in Fig. 8.6A, the upper branch metric in Fig. 8.6C is  $|r_k - s^{(0,0)}|^2 = |4 - (-6)|^2 = 100$ , and since  $s^{(1,2)} = -2$  in Fig. 8.6A, the corresponding branch metric in Fig. 8.6B is

$|r_k - s^{(1,2)}|^2 = |4 - (-2)|^2 = 36$ . The survivor metrics are then computed and stored by adding the previous survivor metrics to the corresponding branch metrics.

It is not until stage  $k = 2$  of the trellis, as highlighted in Fig. 8.6D, that the pruning of paths begins. The noisy observation for this stage is  $r_2 = 1$ , which is written below. The branch metrics are labeled as before (by computing the square of the difference between  $r_2$  and the expected outputs from Fig. 8.6A). Next, the survivors for the states at time  $k = 3$  are computed. For example, the figure shows that there are two ways to get to node  $(0, 3)$ :

- we could start at node  $(0, 2)$ , which has a cost of 149, and traverse the upper branch, which has a cost of 49, for a total cost of 198;
- we could start at node  $(2, 2)$ , which has a cost of 37, and traverse the lower branch, which has a cost of 25, for a total cost of 62.

The Viterbi algorithm selects the second option because of its lower cost. In the figure, we indicate this selection by crossing out the branch that was not selected (the upper branch in this case). We further store the new metric by writing the cost of 62 into node  $(0, 3)$ . A similar *add-compare-select* procedure is implemented for the remaining three nodes at time  $k = 3$ : the lower branch is selected for node  $(1, 3)$ , since  $37 + 1 = 38 < 149 + 1 = 150$ ; the lower branch is selected for node  $(2, 3)$ , since  $1 + 1 = 2 < 65 + 9 = 74$ ; and the lower branch is selected for node  $(3, 3)$ , since  $1 + 25 = 26 < 65 + 9 = 74$ .

The algorithm then moves on to stage  $k = 3$ , as shown in Fig. 8.6E, performing four *add-compare-select* operations, one for each possible state, and storing the new survivor metrics. The same operations are performed for stage 4, as shown in Fig. 8.6F, and then again for stage 5, as shown in Fig. 8.6G, and then again for the last stage, as shown in Fig. 8.6H.

The decision path is the survivor path for the last node of the trellis. It can be found by starting at the ending node of the trellis and tracing backwards, at each stage choosing the branch that was not discarded (ie, not crossed out); the resulting decision path is highlighted in Fig. 8.6H. The decision path in turn determines the decision message, since there is a one-to-one mapping between paths and messages. In particular, since the states were ordered so that the lower branch emanating from any node always corresponds to an input of  $+1$ , the fact that the decision path transitions are lower-lower-upper-lower-lower-upper-upper indicates that the ML decision sequence is  $\hat{\mathbf{a}} = [+1, +1, -1, +1, +1]$ . (The last two transitions correspond to the postamble and are not a part of the message decision.)

Observe that the survivor metric for the last node of the trellis is  $\alpha_7(0) = 8$ . This is the smallest cost  $\|\mathbf{r} - \mathbf{s}\|^2$  that is achieved by the decision sequence. Indeed, we can confirm this value by computing the expected output sequence from the decision sequence  $\hat{\mathbf{a}}$  (via Fig. 8.6A) as  $\mathbf{s} = [0, 4, 0, 2, 4, 0, -4]$ , and verifying that the squared distance to  $\mathbf{r} = [1, 4, 1, 1, 5, 2, -4]$  is indeed  $\|\mathbf{r} - \mathbf{s}\|^2 = 8$ .

We close this section with a summary of the key properties of the Viterbi algorithm, as described so far:

- It makes a decision about the entire sequence all at once, either the MAP or ML decision, depending on how the branch metrics are defined.
- It waits until the entire message has been transmitted before making its decision.
- It is built on a trellis diagram consisting of  $L + \mu$  stages (in the horizontal dimension) and  $Q = |\mathcal{A}|^\mu$  states (in the vertical dimension).
- The storage requirement for the survivor paths is roughly  $QL$ .
- The complexity of each stage is roughly proportional to the number of branches in each stage, namely  $|\mathcal{A}|^{\mu+1}$ , so that it requires a constant computation rate that is independent of the message length.

To reduce the storage requirements and delay, in practice the Viterbi algorithm is typically modified to operate over a window of, say,  $D$  stages of the trellis, from time  $k - D$  to time  $k$ . At each time  $k$ , the survivor node with the best survivor metric is traced back to determine the decision at time  $k - D$ . This approach reduces the decoding delay from approximately  $L$  to  $D$ , and it reduces the storage required from approximately  $QL$  to approximately  $QD$ . The window depth parameter  $D$  can then be tuned to trade-off performance versus complexity and delay. The optimal performance of the original Viterbi algorithm is achieved as  $D$  grows large, but small values are often sufficient; values of  $D$  on the order of  $5\mu$  are often sufficient to make the performance degradation negligible.

The Viterbi algorithm is an effective solution to the problem of estimating the inputs to an FSM based on a noisy observation of the FSM output, and it is used in a wide variety of applications beyond equalization of ISI channels, including error-control decoding for convolutional and trellis codes and demodulation of continuous-phase modulation [2].

### 8.3.3 APP DETECTION: THE BCJR ALGORITHM

The MAP decision found by the Viterbi algorithm of the previous section is optimal in the sense that it minimizes the probability that the message decision is incorrect. What could be better? Note that the MAP decision produced by the Viterbi algorithm is a *hard* decision about the *entire* message sequence. Here we describe the *Bahl-Cocke-Jelinek-Raviv (BCJR)* algorithm [5,6] that differs on both fronts:

- Instead of making one decision about the *entire* message, the BCJR algorithm makes *separate* decisions about each bit of the message.
- Instead of making *hard* decisions about the message bits, the BCJR algorithm makes *soft* decisions in the form of APPs.

The “soft” decisions of the BCJR algorithm are the APPs  $P(b_{k,i} = 1|\mathbf{r})$  for each message bit  $b_{k,i}$ , for  $k \in \{0, \dots, L - 1\}$ , and for  $i \in \{0, \dots, \log_2 |\mathcal{A}| - 1\}$ . The BCJR algorithm is thus an APP computer. If we were to quantize each bit’s APP we would arrive at hard decisions that would at times disagree with those of the Viterbi algorithm. In fact, these quantized APPs would be optimal in the sense that they minimize the probability that each message bit is incorrect.

The fact that the quantized APPs from BCJR minimize the *bit*-error probability, as opposed to the *word*-error probability minimized by the Viterbi decision, is not what makes BCJR valuable. Indeed, in practice the performance difference between the two is often negligible. In other words, the fact that BCJR makes separate decisions about each bit is not what makes it valuable. Instead, the value of BCJR is the soft outputs (APPs) themselves, not their quantized versions. An equalizer that passes hard decisions to another receiver computation block (such as synchronization, estimation, or error-control decoding) is throwing away useful information. Overall performance can be improved significantly when the equalizer instead passes soft decisions to these other receiver blocks. For example, an error-control decoder operating on soft decisions can significantly outperform a decoder operating on hard decisions. Extraordinary gains can be achieved when such blocks iteratively cooperate by sharing soft decisions according to the turbo principle [7]. Indeed, the BCJR algorithm is a key building block for turbo decoding of convolutional codes [8] and turbo equalization of ISI channels [7].

We now describe the BCJR algorithm, which is built on precisely the same trellis as the Viterbi algorithm. Let us associate with each node  $(p, k)$  in the trellis the *forward metric*  $\alpha_k(p) = f(\theta_k = p, r_0^{k-1})$ , which is within a scaling constant of being the APP  $P(\theta_k = p | r_0^{k-1})$  of being in that state  $p$  at that time  $k$ , given all of the “past” observations  $r_0^{k-1} = \{r_0, r_1, \dots, r_{k-1}\}$ . These metrics can be computed recursively, that is, knowledge of the  $Q$  metrics  $\alpha_k(0)$  through  $\alpha_k(Q-1)$  at time  $k$  can be used to compute the  $Q$  metrics  $\alpha_{k+1}(0)$  through  $\alpha_{k+1}(Q-1)$  at time  $k+1$ , according to the following:

$$\alpha_{k+1}(q) = \sum_{p=0}^{Q-1} \alpha_k(p) \gamma_k(p, q), \quad \text{for } q \in \{0, 1, \dots, Q-1\}, \quad (8.17)$$

where, again,  $\gamma_k(p, q)$  denotes the branch metric from state  $p$  at time  $k$  to state  $q$  at time  $k+1$  and is precisely the same as the branch metric for the Viterbi algorithm, namely  $\gamma_k(p, q) = f(r_k | s^{(p,q)}) P(a^{(p,q)})$ . The forward recursion of Eq. (8.17) is initialized in the same way as the Viterbi algorithm, namely  $\alpha_0(p) = \delta_p$ , to account for the fact that the state is initially  $p = 0$  at time 0.

Comparing the recursion Eq. (8.17) to the Viterbi recursion in Eq. (8.13) we see that they are nearly the same; the only difference is that the maximum operation  $\max_p$  of Eq. (8.13) has been replaced by a sum operation  $\sum_p$  in Eq. (8.17). This difference means that, while only the largest term contributes in the Viterbi recursion, *all* terms contribute in the BCJR recursion. The difference is not always significant, however, because at high SNR, it is common for one term to dominate anyway. We can thus view the Viterbi survivor metric  $\hat{\alpha}_k(p)$  in Eq. (8.13) as a high-SNR approximation of the BCJR metric  $\alpha_k(p)$  in Eq. (8.17).

Similarly, let us associate with each node  $(p, k)$  in the trellis the *backward metric*  $\beta_k(p) = f(r_k^{L+\mu-1} | \theta_k = p)$ , which is a function of the “future” observations,  $r_k^{L+\mu-1} = \{r_k, \dots, r_{L+\mu-1}\}$ . These metrics can also be computed recursively, using

the same type of recursion as in Eq. (8.17), except that it starts at the end of the trellis and moves backwards, so that the backward metrics at time  $k$  can be computed from those at time  $k + 1$  according to the following:

$$\beta_k(p) = \sum_{q=0}^{Q-1} \gamma_k(p, q) \beta_{k+1}(q), \quad \text{for } p \in \{0, 1, \dots, Q-1\}, \quad (8.18)$$

where, again,  $\gamma_k(p, q) = f(r_k | s^{(p,q)}) P(a^{(p,q)})$ . The backward recursion of Eq. (8.18) is initialized by  $\beta_{L+\mu}(q) = \delta_q$ , to account for the fact that the ending state at time  $k = L + \mu$  is fixed at  $q = 0$ .

Key to the BCJR algorithm is the fact that the APP of a state transition, say a transition from state  $p$  at time  $k$  to state  $q$  at time  $k + 1$ , can be expressed in terms of the forward, backward, and branch metrics as follows:

$$P(\theta_k = p, \theta_{k+1} = q | \mathbf{r}) = \alpha_k(p) \gamma_k(p, q) \beta_{k+1}(q) / f(\mathbf{r}). \quad (8.19)$$

Therefore, according to the law of total probability, we can compute the APP for a particular bit, say the  $i$ th bit, of the  $k$ th symbol by summing over all state transitions for which the  $i$ th bit is one:

$$P(b_{k,i} = 1 | \mathbf{r}) = \frac{1}{f(\mathbf{r})} \sum_{(p,q) \in \mathcal{B}_i} \alpha_k(p) \gamma_k(p, q) \beta_{k+1}(q), \quad (8.20)$$

where  $\mathcal{B}_i$  denotes the subset of branches  $\{(p, q) : p, q \in \{0, \dots, Q-1\}\}$  for which the  $i$ th bit of the symbol associated with that transition is one.

Rather than computing Eq. (8.20) directly, it is much more convenient (and hence much more common) to compute the so-called “ $L$ ” values, which are defined as the logarithm of the ratio of the APPs [9]:

$$L_{k,i} = \log \left( \frac{P(b_{k,i} = 1 | \mathbf{r})}{P(b_{k,i} = 0 | \mathbf{r})} \right). \quad (8.21)$$

These  $L$  values are the soft information provided by the BCJR algorithm. They have several useful properties:

- The sign of the  $L$  values determines the optimal MAP decision (ie, the decision that minimizes the probability of being incorrect), according to  $\hat{b}_{k,i}^{\text{MAP}} = 1_{L_{k,i} > 0}$ .
- A zero value ( $L_{k,i} = 0$ ) indicates complete uncertainty in the value of the corresponding bit; that is,  $b_{k,i}$  is equally likely to be a 0 and a 1.
- More generally, the magnitude  $|L_{k,i}|$  is a measure of certainty regarding the hard decision; small magnitudes indicate a small amount of confidence that the hard decision is correct, while large magnitudes indicate a high amount of confidence that the hard decision is correct.
- The a posteriori bit probability in Eq. (8.20) can be recovered from the  $L$  value via  $P(b_{k,i} = 1 | \mathbf{r}) = 1 / (1 + e^{-L_{k,i}})$ .

Substituting Eq. (8.20) and its complement into Eq. (8.21) yields the following expression for the  $L$  values, expressed in terms of the  $\alpha$ ,  $\beta$ , and  $\gamma$  parameters:

$$L_{k,i} = \log \left( \frac{\sum_{(p,q) \in \mathcal{B}_i} \alpha_k(p) \gamma_k(p,q) \beta_{k+1}(q)}{\sum_{(p,q) \in \bar{\mathcal{B}}_i} \alpha_k(p) \gamma_k(p,q) \beta_{k+1}(q)} \right). \quad (8.22)$$

The set  $\bar{\mathcal{B}}_i$  in the denominator denotes the complement of  $\mathcal{B}_i$ , that is, the set of branches corresponding to a zero bit. The scaling factor  $1/f(\mathbf{r})$  in Eqs. (8.19) and (8.20) can be ignored because it is common to both the numerator and the denominator in Eq. (8.22), so it will cancel.

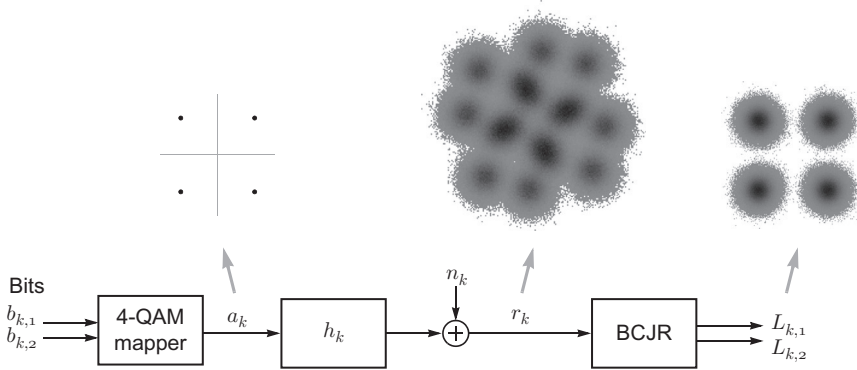
We can now summarize the BCJR algorithm for APP computation after an ISI channel:

1. Compute the forward metrics  $\{\alpha_k(p)\}$  recursively using the forward recursion Eq. (8.17), moving through the trellis from left to right.
2. Compute the reverse metrics  $\{\beta_k(p)\}$  recursively using the backward recursion Eq. (8.18), moving through the trellis from right to left.
3. Use Eq. (8.22) to compute the APP values for each bit of the message.

Each pass through the trellis has complexity roughly comparable to that of the Viterbi algorithm, making the BCJR algorithm roughly twice as complex.<sup>3</sup> The computation of the APP  $L$  values has a further cost in complexity.

**Example 8.5.** Suppose a sequence of symbols chosen from the 4-QAM alphabet  $\mathcal{A} = \{\pm 1 \pm j\}$  is transmitted over the ISI channel  $H(z) = h_0 + h_1 z^{-1} + h_2 z^{-2}$ , where  $h_0 = 1 + 0.3j$ ,  $h_1 = 0.2 + 0.7j$ , and  $h_2 = 0.05 - 0.1j$ , and the noise power is  $N_0 = 0.18$ , so that  $\text{SNR} = E_a E_h / N_0 = 12.6$  dB. The message bits are iid uniform over  $\{0, 1\}$ . A block diagram is shown in Fig. 8.7, along with two empirically measured constellations: one for the output  $r_k$  of the noisy channel and another for the outputs  $L_{k,i}$  of the BCJR algorithm. The ISI in this example is severe enough to cause significant overlap of neighboring clouds. Some sort of equalization is clearly needed to reliably recover the transmitted message. The trellis diagram for this example is exactly as shown in Fig. 8.5B. In particular, since the alphabet size is  $|\mathcal{A}| = 4$  and the channel memory is  $\mu = 2$ , the number of states is  $Q = |\mathcal{A}|^\mu = 16$ . Also shown in the figure is a constellation for the fictitious signal  $L_{k,1} + jL_{k,2}$  after the BCJR algorithm. We see that it resembles a 4-QAM constellation with no ISI and with circularly symmetric Gaussian noise. The conditional distribution after the BCJR is approximately consistent Gaussian, meaning that the variance in each dimension is twice the conditional mean. Measuring the SNR after the BCJR algorithm yields  $\text{SNR} = 12.6$  dB, which is approximately the same as the underlying SNR. Evidently, in this example, the BCJR algorithm is able to eliminate the effects of the ISI without an appreciable penalty in SNR. This conclusion can be confirmed in terms of capacity [10].

<sup>3</sup>Although the traceback operation of the Viterbi algorithm can be viewed as a backward pass through the trellis, analogous to the backward recursion of BCJR, it does not require any computations.

**FIG. 8.7**

An example of equalization via BCJR for 4-QAM over the ISI channel  $H(z) = (1 + 0.3j) + (0.2 + 0.7j)z^{-1} + (0.05 - 0.1j)z^{-2}$ , with  $SNR = 12.6$  dB.

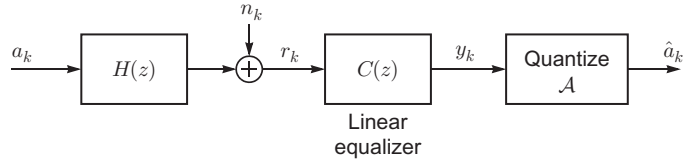
## 8.4 LINEAR EQUALIZATION

The trellis-based detectors of the previous section perform exceptionally well, but their complexity can be high. In particular, the complexity of both Viterbi and BCJR algorithms is exponential in both the spectral efficiency ( $\log_2 |\mathcal{A}|$ ) and channel memory ( $\mu$ ), and it can be prohibitive when the alphabet is large, the channel memory is large, or both. As an alternative, we consider in this section the class of *linear* detectors, which feature a complexity that is nearly independent of the alphabet size and channel memory, albeit with performance that can at times fall significantly short of the trellis-based detectors.

A linear equalizer is simply a linear time-invariant filter applied to the channel output. In this section we assume that the linear equalizer is designed with the expectation that the equalizer output will be applied to a *memoryless* quantizer that rounds the equalizer output to the nearest element of the symbol alphabet  $\mathcal{A}$ . In other words, the aim of the linear equalizer is to eliminate ISI, so that subsequent receiver processing can ignore ISI.<sup>4</sup>

A block diagram of a linear equalizer is shown in Fig. 8.8. In the following three sections we describe three special cases of the linear equalizer: (1) the MF, (2) the zero-forcing (ZF) linear equalizer, and (3) the minimum-mean-squared-error (MMSE) linear equalizer.

<sup>4</sup>This is in contrast to a partial-response equalizer, which aims not to eliminate ISI, but to mold it to match a desired target [11].

**FIG. 8.8**

A linear equalizer  $C(z)$  followed by memoryless quantizer results in decisions  $\hat{a}_k$  about the message symbols  $a_k$ .

### 8.4.1 THE MATCHED FILTER

If the transmitter were to send only a single symbol in isolation, so that  $L = 1$  in Eq. (8.1) and the channel model Eq. (8.3) reduces to  $r_k = a_0 h_k + n_k$ , the SNR after equalization (at time 0) is maximized when the linear equalizer  $C(z)$  in Fig. 8.8 is *matched* to the channel. In the time domain, the MF impulse response is a time-reversed and conjugated version of the ISI channel:

$$c_k = h_{-k}^*.$$

In the  $z$  domain,<sup>5</sup> this means that  $C(z) = H^*(1/z^*)$ , while in the frequency domain it means that  $C(e^{j\theta}) = H^*(e^{j\theta})$ . The MF equalizer gain at a particular frequency matches that of the channel at that frequency; frequencies that are amplified by the channel will be further and similarly amplified by the equalizer, while frequencies that are attenuated by the channel will be further and similarly attenuated by the equalizer.

In practice, the transmitter will send a sequence of symbols, not a single symbol in isolation. In this case the MF receiver may not at first glance appear to be an equalization strategy at all, since the net effect of the MF will be to *accentuate* the severity of the ISI rather than to eliminate it. However, as we will see below, the MF is an optimal linear equalizer in the limit of low SNR. Intuitively, this can be understood by observing that the ISI, no matter how severe, will eventually become negligible (falling below the noise floor) at a low enough SNR. Furthermore, in a direct-sequence code-division-multiple-access (DS-CDMA) application for which the transmit pulse shape  $g(t)$  of Eq. (8.1) has a bandwidth that is orders of magnitude greater than the signaling rate  $1/T$ , an oversampled version<sup>6</sup> of the MF is known as

<sup>5</sup>The  $z$  transform of a sequence  $x_k$  is a mapping from the complex  $z$  plane to  $X(z) = \sum_{k=-\infty}^{\infty} x_k z^{-k}$ , for those values of  $z$  for which the sum converges. Evaluating the  $z$  transform at  $z = e^{j\theta}$  results in the Fourier transform  $X(e^{j\theta})$ , when it exists.

<sup>6</sup>The broadband nature of a DS-CDMA signal violates the minimum-bandwidth assumption made in Section 8.2.1; hence the baud-rate sampled model considered in this chapter would need to be replaced by an oversampled model in order to accommodate the expanded bandwidth.

the RAKE receiver and is an effective method for compensating for the effects of a dispersive channel, at any SNR.

### 8.4.2 ZF LINEAR EQUALIZATION

The ZF strategy for the linear equalizer design is to choose the equalizer to be the inverse of the channel, when it exists, which will completely eliminate the ISI:

$$C_{ZF}(z) = \frac{1}{H(z)}. \quad (8.23)$$

This is called a ZF equalizer because the ISI is forced to zero. The ZF linear equalizer is in some sense the opposite of the MF: It attenuates at frequencies that are amplified by the channel, and it amplifies at frequencies that are attenuated by the channel.

Because the ZF linear equalizer completely eliminates ISI, its output can be written as follows:

$$y_k = a_k + e_k,$$

where  $e_k = n_k * c_k$  is the noise after being filtered by the equalizer. The PSD of the filtered noise is

$$S_e(e^{j\theta}) = N_0 |C(e^{j\theta})|^2 = \frac{N_0}{|H(e^{j\theta})|^2}.$$

The power of the filtered noise is  $E(|e_k|^2) = \mathcal{A}\{S_e(e^{j\theta})\}$ . Therefore, the SNR after the ZF equalizer, as seen by the memoryless quantizer, is simply

$$SNR_{ZF} = \frac{E(|a_k|^2)}{E(|e_k|^2)} = \frac{E_a}{\mathcal{A}\{S_e(e^{j\theta})\}} = \frac{1}{\mathcal{A}\{\frac{1}{SNR(\theta)}\}}, \quad (8.24)$$

or more compactly,

$$SNR_{ZF} = \mathcal{H}\{SNR(\theta)\}. \quad (8.25)$$

This is the postequalization SNR of the ZF linear equalizer. Note that this SNR does not account for the correlation in the noise after the linear equalizer because the memoryless quantizer has no way of exploiting this correlation. Thus, the SNR measure implicitly takes the memoryless constraint into account. (In contrast, an optimal way of exploiting the noise correlation would be to follow the equalizer by the inverse of the equalizer (!), which reverts back to the original channel output, and then to apply a trellis-based detector.)

The ZF linear equalizer performance is never better than the MF bound when the transmit spectrum is flat, since in this case the inequalities in Eq. (8.4) imply that  $SNR_{ZF} = \mathcal{H}\{SNR(\theta)\} \leq \mathcal{A}\{SNR(\theta)\} = SNR_{\text{MFB}}$ . The inequality becomes an equality if and only if there is no ISI, that is, if and only if  $SNR(\theta)$  is independent of  $\theta$ . Therefore, for any channel with ISI, the ZF linear equalizer always falls short of the

MFB. The nature of the harmonic mean implies that the gap in performance can be significant when the channel frequency response is small at one or more frequencies.

**Example 8.6.** Consider the performance of the ZF linear equalizer for a sequence of iid symbols chosen from the 4-QAM alphabet  $\mathcal{A} = \{\pm 1 \pm j\}$  over a channel with frequency response  $H(z) = 1 + bz^{-1}$  and noise PSD  $N_0 = 2$ ; in this case the SNR spectral density reduces to  $SNR(\theta) = |1 + be^{-j\theta}|^2$ , so that the SNR after a ZF linear equalizer is as follows:

$$\begin{aligned} SNR_{ZF} &= \mathcal{H}\{SNR(\theta)\} \\ &= \frac{1}{\frac{1}{2\pi} \int_{-\pi}^{\pi} \frac{1}{|1 + be^{-j\theta}|^2} d\theta} \\ &= 1 - |b|^2. \end{aligned}$$

If  $|b|$  is infinitesimal, this SNR is not much smaller than the MFB, namely  $SNR_{MFB} = 1 + |b|^2$ . However, as  $|b|$  grows large, the SNR decreases dramatically. In fact, as  $|b|$  approaches unity, the SNR approaches zero! The ZF linear equalizer thus incurs an infinite SNR penalty when  $|b| = 1$ . The reason can be easily understood in the frequency domain, for the channel magnitude response  $|H(e^{j\theta})| = |1 + be^{-j\theta}|$  has a *spectral null* at some frequency  $\theta$  (that depends on the angle of  $b$ ) when  $|b| = 1$ . In turn, this implies that the gain of the equalizer  $|C(e^{j\theta})| = \frac{1}{|H(e^{j\theta})|}$  grows to infinity at that same frequency. This amplifies the noise by an infinite amount, so that the noise totally swamps the desired signal.

It is generally true that a ZF linear equalizer suffers infinite noise enhancement whenever the channel magnitude response is zero at one or more frequencies, and it performs poorly whenever the channel has a near spectral null at one or more frequencies.

### 8.4.3 MMSE LINEAR EQUALIZATION

The fatal flaw of the ZF equalizer is its insistence on forcing ISI to zero, regardless of what impact it has on the noise. Forcing ISI to zero is overkill. In contrast, here we describe the MMSE equalizer, which chooses its coefficients so as to minimize the mean-squared error between the equalizer output and what we want it to be, namely to minimize  $MSE = E(|e_k|^2)$ , where  $e_k = y_k - a_k$ . The Fourier transform of the solution is

$$C_{MMSE}(e^{j\theta}) = \frac{H^*(e^{j\theta})}{|H(e^{j\theta})|^2 + \frac{N_0}{E_a}}. \quad (8.26)$$

The numerator represents an MF, which transforms the channel frequency response from its original form,  $H(e^{j\theta})$ , to  $|H(e^{j\theta})|^2$ . The presence of the constant  $N_0/E_a$  term in the denominator is the only thing that prevents the remainder of the MMSE equalizer from inverting this effective response. As such, this constant is the only thing that prevents the MMSE linear equalizer from being the ZF linear equalizer. Intuitively, we can think of the constant as a way of preventing the denominator

from being close to zero, even when the channel itself is zero or near zero at certain frequencies.

Two extremes are of special interest: high SNR and low SNR. At high SNR, one that is high enough that the  $N_0/E_a$  term in the denominator is negligible, the MMSE equalizer reduces to the ZF equalizer  $C_{ZF}(e^{j\theta}) = 1/H(e^{j\theta})$  of Eq. (8.23). This makes intuitive sense, because at a high enough SNR, any residual ISI after the equalizer will eventually dominate. At the other extreme, which is low SNR, so low that the  $N_0/E_a$  term in the denominator dominates, the MMSE equalizer reduces to within a constant scaling factor of the MF  $H^*(e^{j\theta})$ . This also makes sense intuitively, because at a low enough SNR the ISI will eventually fall below the noise floor and will become negligible.

The two extreme cases considered above help to clarify the tradeoff achieved by the MMSE solution. The error after the equalizer will have two components, one being residual ISI and the other being filtered noise. The aim of the MMSE equalizer is to minimize the sum of the power of both. In stark contrast, the ZF equalizer minimizes ISI while *ignoring* the noise. Similarly, the MF can be thought of as an equalizer that maximizes SNR while *ignoring* the ISI. Neither of these extremes achieves the optimal balance obtained by the MMSE equalizer. One final intuitive view of how the MMSE equalizer compares to the ZF equalizer: While the ZF equalizer forces ISI to zero at the expense of a potentially large enhancement of the noise power, the MMSE equalizer merely pushes the ISI to be roughly below the noise floor, without as much noise enhancement.

In order to accurately quantify the postequalization SNR of the MMSE equalizer, we need to account for the equalizer bias. Let  $\beta_k = h_k * c_k$  denote the impulse response of the cascade of the channel and any equalizer  $c_k$ . We say that an equalizer is *biased* whenever the zeroth coefficient  $\beta_0$  satisfies  $\beta_0 \neq 1$ , because the conditional mean of the equalizer output satisfies  $E(y_k|a_k) = \beta_0 a_k$ . For example, the ZF equalizer of the previous section is unbiased, because in that case  $\beta_0 = 1$ . On the other hand, the MMSE equalizer is biased because  $\beta_0 \neq 1$ , namely

$$\beta_0 = \frac{1}{1 + 1/\text{SNR}_{\text{MMSE-LE}}},$$

where  $\text{SNR}_{\text{MMSE-LE}}$  will be defined shortly (see Eq. 8.28). Scaling the equalizer by  $1/\beta_0$  removes the bias, leading to the so-called *unbiased* MMSE linear equalizer:

$$C_{\text{MMSE,U}}(e^{j\theta}) = \frac{\beta_0^{-1} H^*(e^{j\theta})}{|H(e^{j\theta})|^2 + \frac{N_0}{E_a}}. \quad (8.27)$$

At high SNR, there is not much difference in performance between the unbiased and biased equalizer. However, the unbiased version makes it easy to compute the postequalization SNR of the MMSE equalizer, because—unlike for the biased case—the equalizer error  $e_k = y_k - a_k$  after the unbiased equalizer will be *independent* of  $a_k$ , so that the SNR after this equalizer can be computed simply as follows:

$$SNR_{\text{MMSE-LE}} = \frac{E(|a_k|^2)}{E(|e_k|^2)} \quad (8.28)$$

$$= \mathcal{H}\{1 + SNR(\theta)\} - 1. \quad (8.29)$$

Comparing this SNR to that of the ZF linear equalizer, and exploiting the inequality Eq. (8.4), we conclude the following:

$$SNR_{\text{MMSE-LE}} \geq SNR_{\text{ZF-LE}},$$

with equality if and only if the channel has no ISI. Thus, when faced with ISI, the MMSE linear equalizer always outperforms the ZF linear equalizer. The difference in performance can be significant at a low SNR, or for channels with severe ISI, while the difference can be small at a high SNR, or for channels with mild ISI.

**Example 8.7.** Consider a channel with transfer function  $H(z) = 1 + h_1 z^{-1} + h_2 z^{-2} + h_3 z^{-3}$ , where  $h_1 = 0.4 - 0.1j$ ,  $h_2 = 0.1 + 0.5j$ , and  $h_3 = 0.3 + 0.8j$ . The magnitude response  $|H(e^{j\theta})|$  is shown in Fig. 8.9, where we see deep spectral nulls that are attenuated by as much as 32 dB relative to the peak response. Since the MF and the channel share the same magnitude response, this same curve also

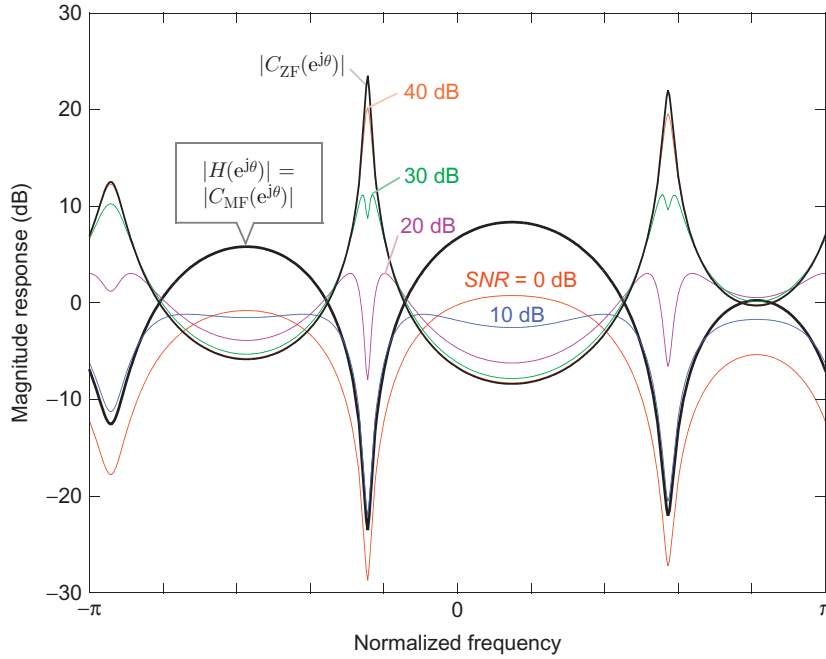


**FIG. 8.9**

An illustration of how the magnitude response of the MMSE linear equalizer ranges from that of an MF to that of a ZF linear equalizer, depending on the SNR.

depicts the magnitude response of the MF. Also shown in the figure is the magnitude response  $|C_{ZF}(e^{j\theta})| = 1/|H(e^{j\theta})|$  of the ZF linear equalizer. Observe that the ZF linear equalizer has a high gain of over 20 dB at the frequency most attenuated by the channel. The remaining five curves show the magnitude response of the unbiased MMSE linear equalizer for five different SNR values, ranging from 0 to 40 dB. At low SNR, the MMSE equalizer has roughly the same shape as the MF. At high SNR, the MMSE equalizer closely approximates the ZF linear equalizer. At moderate SNR, the MMSE linear equalizer resembles neither the MF nor the ZF linear equalizer over the entire frequency range. Instead, at 20 dB SNR, for example, we see that the MMSE linear equalizer behaves like the MF at frequencies near the channel null, while it behaves more like the ZF linear equalizer at all other frequencies.

## 8.5 DECISION-FEEDBACK EQUALIZATION

The decision-feedback equalizer (DFE) is a nonlinear equalization strategy that can significantly outperform a linear equalizer, with comparable complexity. The DFE is based on the concept of *interference cancellation*, where interference is estimated at the receiver and subtracted. As a motivating example, let us begin our discussion by supposing that the channel impulse response has most of its energy concentrated in the zeroth coefficient  $h_0$ , so that the channel output  $r_k = a_k * h_k + n_k$  can be broken down into three terms:

$$r_k = \underbrace{h_0 a_k}_{\text{desired}} + \underbrace{\sum_{i=1}^{\mu} h_i a_{k-i}}_{\text{ISI}} + \underbrace{n_k}_{\text{noise}}.$$

The first term represents the desired signal, the second term is the ISI, and the third term is the channel noise. Suppose further that, at time  $k$ , the receiver has access to the prior decisions  $\{\hat{a}_{k-1}, \hat{a}_{k-2}, \dots\}$ . In this case, the receiver can reconstruct an estimate  $\sum_{i=1}^{\mu} h_i \hat{a}_{k-i}$  of the ISI and subtract this estimate from the channel output, and further scale by  $1/h_0$ , resulting in the following:

$$\begin{aligned} z_k &= \frac{1}{h_0} \left( r_k - \sum_{i=1}^{\mu} h_i \hat{a}_{k-i} \right) \\ &= a_k + \frac{1}{h_0} \sum_{i=1}^{\mu} h_i (a_{k-i} - \hat{a}_{k-i}) + n_k/h_0. \end{aligned} \quad (8.30)$$

When the  $\mu$  relevant decisions are correct, this reduces to

$$z_k = a_k + n_k/h_0.$$

Like the ZF linear equalizer, this DFE has completely eliminated ISI. Unlike the linear equalizer, however, the noise here has not been enhanced. Instead, the noise

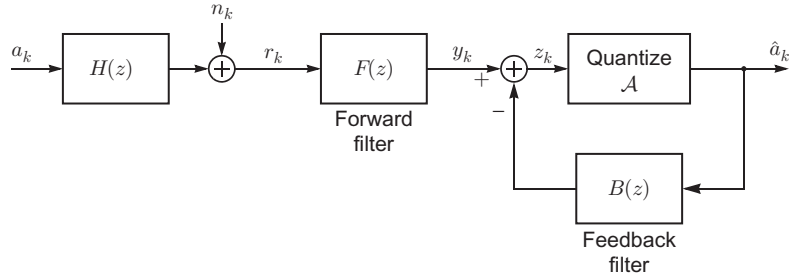


FIG. 8.10

The DFE has two filters: a forward filter for mitigating ISI from future symbols and a feedback filter for mitigating ISI from past symbols.

term  $n_k$  in the above equation is the noise  $n_k$  of the original channel. This DFE thus eliminates ISI without any noise enhancement.

In the general case when  $h_0$  is not large, the receiver can first apply the channel output to a linear “forward” filter whose purpose is to transform the cascade of the channel and the equalizer into an effective channel whose zeroth tap is large. This leads to the DFE structure shown in Fig. 8.10. The equalizer output (or equivalently, the input to the decision device) for the DFE is as follows:

$$z_k = r_k * f_k - \sum_{i=1}^{\infty} b_i \hat{a}_{k-i}, \quad (8.31)$$

where  $f_k$  is the impulse response of the forward filter and where  $b_k$  is the impulse response of the feedback filter. To be implementable, the feedback filter must be *strictly* causal, that is, it must satisfy  $b_k = 0$  for all  $k \in \{0, -1, -2, \dots\}$ , so that  $B(z) = \sum_{k=1}^{\infty} b_k z^{-k}$ . The motivating example of the previous paragraph is a special case when the forward filter is the scaling factor  $F(z) = 1/h_0$ , and the feedback filter is the strictly causal “tail” of the normalized channel,  $B(z) = (H(z) - h_0)/h_0 = h_0^{-1} \sum_{k=1}^{\mu} h_k z^{-k}$ .

### 8.5.1 THE ZF DFE

A ZF DFE is one for which the DFE output  $z_k$  depends only on the  $k$ th symbol  $a_k$ , with no residual ISI from the others. Of the many DFEs that satisfy this ZF property, we will prefer the one that results in the highest SNR, or, equivalently, the one that minimizes the  $MSE = E(|z_k - a_k|^2)$ . This version of the ZF DFE is unique and is given by [1]:

$$F(z) = \frac{H^*(1/z^*)}{\gamma^2 M^*(1/z^*)}, \quad (8.32)$$

$$B(z) = M(z) - 1, \quad (8.33)$$

which are defined in terms of the following spectral factorization of  $H(z)H^*(1/z^*)$ :

$$H(z)H^*(1/z^*) = \gamma^2 M(z)M^*(1/z^*), \quad (8.34)$$

where  $M(z) = 1 + m_1 z^{-1} + m_2 z^{-2} + \dots$  is monic (ie, satisfying  $m_0 = 1$ ), loosely minimum phase (ie, all of its poles are inside the unit circle, and all of its zeros are either inside or on the unit circle), and where

$$\gamma^2 = \mathcal{G}\{|H(e^{j\theta})|^2\}$$

is the geometric mean of the magnitude squared of the channel frequency response. With this choice for the forward filter, it is easy to see that the cascade of the channel and the forward filter reduces to  $H(z)F(z) = M(z)$ . Thus, the forward filter transforms the original channel with the transfer function  $H(z)$  into an effective channel with transfer function  $M(z)$ . Of all transfer functions having the same magnitude response as the original channel, the minimum-phase factor  $\gamma M(z)$  has the desirable property that its energy is maximally concentrated at time 0. Observe further that the optimal ZF forward filter is a scaled all-pass filter, which ensures that it does not enhance the noise; the noise after the forward filter is still white. One final observation: If the original channel happens to be a minimum phase from the beginning, the minimum-phase factor reduces to  $\gamma M(z) = H(z)$ . This means that the forward filter reduces to a scaling constant  $F(z) = 1/\gamma = 1/h_0$ , and the feedback filter reduces to  $B(z) = H(z)/h_0 - 1$ , so that the optimal ZF DFE reduces to the original motivating example provided at the beginning of this section.

To compute the SNR of the ZF DFE, observe that the net effect of the forward filter  $F(z)$  from Eq. (8.32) is to transform the channel from  $H(z)$  to the channel-filter cascade  $H(z)F(z) = M(z)$ . Because the forward filter is a scaled all-pass filter, the noise after the forward filter is still white and Gaussian. The scaling constant changes the noise PSD from  $N_0$  to  $N_0/\gamma^2$ . The feedback filter eliminates the ISI without any impact on this noise, so that the SNR after the ZF DFE, assuming correct decisions, is simply:

$$SNR_{\text{ZF-DFE}} = \frac{E_a}{N_0/\gamma^2} = \frac{E_a}{N_0} \mathcal{G}\{|H(e^{j\theta})|^2\} = \mathcal{G}\{SNR(\theta)\}. \quad (8.35)$$

(The last equality requires that the transmit spectrum be flat,  $S_a(e^{j\theta}) = E_a$ .) This is the postequalization SNR for the ZF DFE. Exploiting the inequality Eq. (8.4), we conclude the following:

$$SNR_{\text{ZF-DFE}} \geq SNR_{\text{ZF-LE}},$$

with equality if and only if the channel has no ISI. The DFE thus always outperforms the linear equalizer for channels with ISI. One caveat to keep in mind for the DFE is that the above SNR measure is based on an assumption that decisions are correct; the

actual SNR (that accounts for occasional errors) will be slightly lower. The impact of errors is considered next.

### 8.5.2 ERROR PROPAGATION

The DFE was designed and analyzed in the previous section with an assumption that the receiver decisions are correct. In practice, there will be occasional errors that tend to increase the probability of a subsequent error, a phenomenon known as *error propagation*. A single error will often lead to a burst of many errors. Looking closer at Eq. (8.30), we see that any error among  $\{\hat{a}_{k-1}, \dots, \hat{a}_{k-\mu}\}$  will lead to the corresponding ISI being *added* (in effect, doubled) instead of subtracted, which will in turn significantly increase the probability of a subsequent error. The error burst effect ends whenever  $\mu$  consecutive correct decisions are made. The impact of error propagation on the overall performance depends on the value of SNR: At a high SNR the impact can be negligible, while at a low SNR the impact can be more severe.

Fortunately, we can analyze the impact of error propagation in a straightforward way and quantify the overall performance that takes into account the possibility of error propagation. We illustrate this analysis with a simple example.

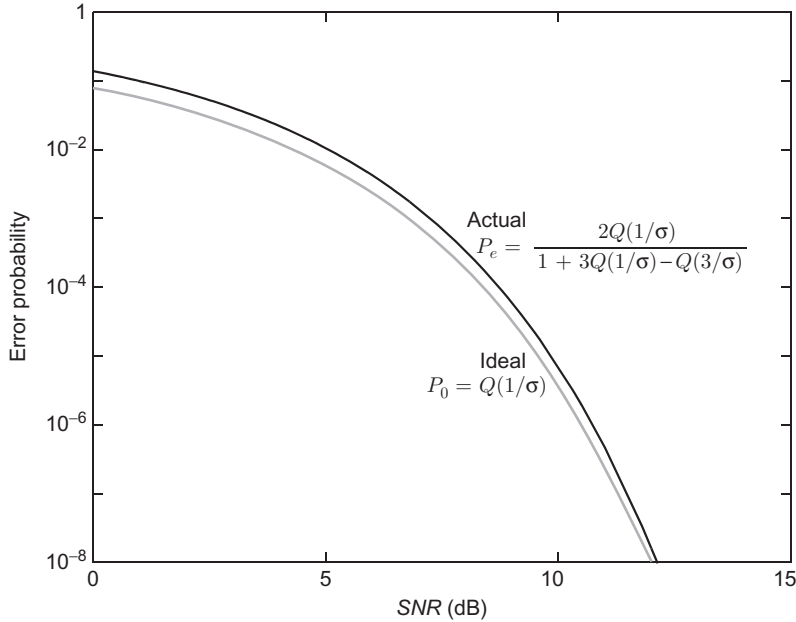
**Example 8.8.** Consider the channel  $r_k = a_k + a_{k-1} + n_k$ , where the symbols are chosen uniformly and independently from the BPSK alphabet  $\mathcal{A} = \{\pm 1\}$ , and where the independent noise is white with variance  $\sigma^2 = N_0/2$ . The forward filter of the ZF DFE in this case is the identity,  $F(z) = 1$ , while the feedback filter is the impulse response tail, namely  $B(z) = z^{-1}$ . The  $k$ th decision is then  $\hat{a}_k = \text{sign}(z_k)$ . Let  $p_0 = P(\hat{a}_k \neq a_k | \hat{a}_{k-1} = a_{k-1})$  denote the conditional probability of error for the  $k$ th decision, given that the previous decision was correct. Under this condition, Eq. (8.31) reduces to  $z_k = a_k + n_k$ , from which we conclude that  $p_0 = Q(1/\sigma)$ . Similarly, let  $p_1 = P(\hat{a}_k \neq a_k | \hat{a}_{k-1} \neq a_{k-1})$  denote the conditional probability of error for the  $k$ th decision, given that the previous decision was incorrect. Under this condition, Eq. (8.31) reduces to  $z_k = a_k + a_{k-1} - \hat{a}_{k-1} + n_k = a_k + 2a_{k-1} + n_k$ . The doubling of the ISI in this case is clearly evident. From this equation we conclude that the conditional error probability for  $\hat{a}_k = \text{sign}(z_k)$  is  $p_1 = \frac{1}{2}(1 - Q(1/\sigma) + Q(3/\sigma))$ . From the law of total probability, the overall probability of error  $P_e = P(\hat{a}_k \neq a_k)$  can then be written as follows:

$$\begin{aligned} P_e &= P(\hat{a}_k \neq a_k | \hat{a}_{k-1} = a_{k-1})P(\hat{a}_{k-1} = a_{k-1}) \\ &\quad + P(\hat{a}_k \neq a_k | \hat{a}_{k-1} \neq a_{k-1})P(\hat{a}_{k-1} \neq a_{k-1}) \\ &= p_0(1 - P_e) + p_1 P_e. \end{aligned}$$

Solving this equation for  $P_e$  yields the following:

$$P_e = \frac{p_0}{1 + p_0 - p_1} = \frac{2Q(1/\sigma)}{1 + 3Q(1/\sigma) - Q(3/\sigma)}.$$

The denominator quickly approaches unity as SNR increases, so the dominant impact of error propagation can be seen from the numerator: Error propagation

**FIG. 8.11**

The impact of error propagation on the performance of the ZF DFE, for the channel  $H(z) = 1 + z^{-1}$ . The lower curve is the performance of the genie-aided (ideal) DFE that somehow has access to correct decisions. The *upper curve* is the performance that takes into account the impact of decision errors in the feedback process. The SNR penalty due to error propagation is 0.17 dB at  $P_e = 10^{-7}$ .

approximately doubles the overall error probability in this example. This result is plotted in Fig. 8.11 versus SNR (upper curve), along with the performance of the ideal DFE (lower curve) that somehow has access to correct decisions when canceling the ISI. While it is true that the error propagation effectively doubles the error probability at moderate to high SNR, which may sound severe, the actual degradation when measuring the horizontal distance between the two curves is small. This is a result of the fact that the Q function decays rapidly. In fact, the horizontal distance between the two curves is only 0.17 dB at  $P_e = 10^{-7}$ , implying that the SNR penalty due to error propagation is only 0.17 dB at this probability.

The broad conclusions from the above example generalize to a wide range of alphabets and ISI responses: The impact of error propagation is rarely, if ever, catastrophic. Instead, it results in a modest SNR penalty when compared to the ideal DFE, a penalty generally small enough that even with error propagation the DFE will outperform the linear equalizer. (We will see another example in Section 8.7 where the error propagation penalty is about 0.5 dB.)

### 8.5.3 THE MINIMUM-MSE DFE

The DFE output  $z_k$  will generally contain both ISI and noise. The ZF DFE described in the previous section forces the ISI to zero, without regard to the impact on the noise. In this section we describe the MMSE DFE, which chooses the forward and feedback filters to minimize MSE instead, thus accounting for both ISI and noise. In particular, the MMSE DFE chooses  $F(z)$  and  $B(z)$  to minimize  $MSE = E(|z_k - a_k|^2)$ , where, again, the DFE output  $z_k$  is given by Eq. (8.31). The MMSE solution is as follows [1]:

$$F(z) = \frac{H^*(1/z^*)}{\tilde{\gamma}^2 \tilde{M}^*(1/z^*)}, \quad (8.36)$$

$$B(z) = \tilde{M}(z) - 1, \quad (8.37)$$

where  $\tilde{\gamma}$  and  $\tilde{M}(z)$  are defined by the following spectral factorization:

$$H(z)H^*(1/z^*) + \frac{N_0}{E_a} = \tilde{\gamma}^2 \tilde{M}(z)\tilde{M}^*(1/z^*), \quad (8.38)$$

where, again,  $\tilde{M}(z)$  is monic and minimum phase. Like the linear MMSE equalizer, this MMSE DFE is biased; removing the bias means scaling the forward filter by  $1 + 1/SNR_{\text{MMSE-DFE}}$ . The resulting SNR of the MMSE DFE is

$$SNR_{\text{MMSE-DFE}} = G\{1 + SNR(\theta)\} - 1. \quad (8.39)$$

In light of the inequalities in Eq. (8.4) we conclude that, for any channel with ISI, the MMSE DFE will always outperform the ZF DFE, the MMSE LE, and the ZF LE.

A summary of the linear and DFE equalizers is provided in Table 8.1. The rows are sorted roughly from best to worst, according to their SNR. The sorting is rough because it is possible for an MMSE linear equalizer to outperform a ZF DFE, if the channel ISI response and SNR are carefully chosen. But the other rankings are universal; we always have the following:

$$SNR_{\text{MFB}} \geq SNR_{\text{Shannon}} = SNR_{\text{MMSE-DFE}} \geq SNR_{\text{ZF-DFE}},$$

and

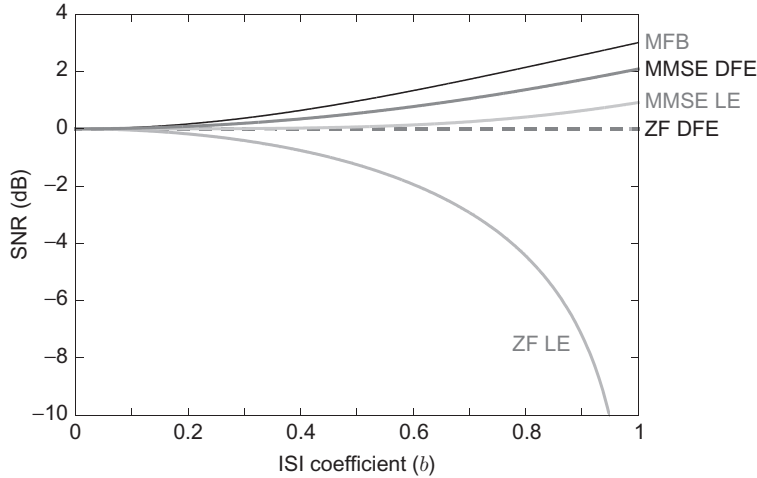
$$SNR_{\text{MMSE-LE}} \geq SNR_{\text{ZF-LE}}.$$

**Example 8.9.** Consider a 4-QAM alphabet  $\mathcal{A} = \{\pm 1 \pm j\}$  over the ISI channel  $H(z) = 1 + bz^{-1}$  with noise PSD  $N_0 = 2$ , so that the SNR spectral density is  $SNR(\theta) = |1 + be^{-j\theta}|^2$ . The severity of the ISI in this example is captured by the value of the ISI coefficient  $h_1 = b$ . At one extreme,  $b = 0$  corresponds to the case of an ideal ISI-free channel. At the other extreme,  $b = 1$  corresponds to severe ISI, where the energy of the interfering symbol is the same as the energy of the

**Table 8.1** Summary of Structure and Performance of the Linear and DFE Equalizers

	Forward $F(z)$	Feedback $B(z)$	SNR
MFB			$\mathcal{A}\{SNR(\theta)\}$
Shannon			$\mathcal{G}\{1 + SNR(\theta)\} - 1$
MMSE DFE	$\frac{\beta_0^{-1} H^*}{\tilde{\gamma}^2 \tilde{M}^*}$	$(\tilde{M}(z) - 1)/\beta_0$	$\mathcal{G}\{1 + SNR(\theta)\} - 1$
ZF DFE	$\frac{H^*}{\gamma^2 M^*}$	$M(z) - 1$	$\mathcal{G}\{SNR(\theta)\}$
MMSE linear	$\frac{\beta_0^{-1} H^*}{HH^* + \frac{N_0}{E_a}}$	0	$\mathcal{H}\{1 + SNR(\theta)\} - 1$
ZF linear	$\frac{1}{H(z)}$	0	$\mathcal{H}\{SNR(\theta)\}$

Notes: The first row shows the matched-filter bound on SNR for the case of a flat transmit spectrum ( $S_a(e^{j\theta}) = E_a$ ), for comparison. The bias coefficient  $\beta_0$  of both MMSE equalizers is related to the corresponding SNR (last column) by  $\beta_0^{-1} = 1 + 1/SNR$ .

**FIG. 8.12**

SNR after equalization versus the severity of the ISI, as captured by the value of the ISI coefficient  $h_1 = b$ .

desired symbol. In Fig. 8.12 we plot the SNR after equalization versus the channel coefficient  $b$ , as  $b$  ranges from 0 to 1. For small values of  $b$  we see that all equalizers perform about the same. For large values of  $b$ , however, we see that the MMSE versions significantly outperform the ZF counterparts. Further, we see that the DFE significantly outperforms the LE. Of particular note is the poor performance of the ZF LE as  $b$  grows large, which is the result of noise enhancement: As  $b$  approaches 1,

the channel frequency response develops a spectral null; an equalizer that attempts to invert this null will end up amplifying the noise by an infinite gain.

#### 8.5.4 DFE VIA NOISE PREDICTION

The DFE was introduced above as an instance of interference cancellation, where the feedback filter reconstructs the ISI from past decisions and subtracts it. Here we describe an alternative viewpoint, namely that the DFE can be viewed as a combination of linear equalization and *noise prediction*. To see how, let us start with the ZF linear equalizer  $C(z) = 1/H(z)$ , whose output is  $y_k = a_k + \eta_k$ , where  $\eta_k$  is the filtered (enhanced) noise:

$$\eta_k = n_k * c_k,$$

which has the PSD

$$\begin{aligned} S_\eta(z) &= N_0 C(z) C^*(1/z^*) \\ &= \frac{N_0}{H(z) H^*(1/z^*)}. \end{aligned}$$

The fact that this noise PSD is not white implies that the filtered noise values  $\{\eta_k\}$  are correlated and that knowledge of the past values can be used to predict the next value. Let  $\hat{\eta}_k = \sum_{i=1}^{\infty} p_i \eta_{k-i}$  be a linear predictor. In terms of the spectral factorization  $H(z) H^*(1/z^*) = \gamma^2 M(z) M^*(1/z^*)$  of Eq. (8.34), the prediction coefficients  $\{p_i\}$  that minimize the mean-squared error  $E(|\hat{\eta}_k - \eta_k|^2)$  are defined by  $P(z) = 1 - M(z)$ . While the receiver does not have access to the filtered noise  $\eta_k$  directly, it does have access to the receiver decisions  $\hat{a}_k$ , and therefore it can compute the difference  $y_k - \hat{a}_k$ , which reduces to  $\eta_k$  whenever the corresponding decision is correct. Therefore, under the assumption that the past decisions are correct, the linear predictor  $\hat{\eta}_k = \sum_{i=1}^{\infty} p_i \eta_{k-i}$  for the  $k$ th filtered noise sample can be rewritten as follows:

$$\hat{\eta}_k = \sum_{i=1}^{\infty} p_i (y_{k-i} - \hat{a}_{k-i}).$$

The receiver can then subtract this predicted value for  $\eta_k$  from the equalizer output, as shown in the block diagram of Fig. 8.13. The impact of this subtraction changes the noise that is seen at the decision device: Instead of being  $\eta_k$ , which has power  $E(|\eta_k|^2) = \mathcal{A}\{N_0 |H(e^{j\theta})|^{-2}\}$ , the noise after subtraction is  $\eta_k - \hat{\eta}_k$ , which has power  $E(|\eta_k - \hat{\eta}_k|^2) = \mathcal{G}\{N_0 |H(e^{j\theta})|^{-2}\}$ , when the prediction coefficients  $\{p_i\}$  are chosen optimally, and assuming the relevant past decisions are correct. The geometric mean is always less than the arithmetic mean whenever there is ISI, so the use of noise prediction will always lead to a performance improvement.

Perhaps unexpectedly, the noise prediction strategy described above and shown in Fig. 8.13 is actually precisely equivalent to the ZF DFE described earlier. In other words, linear prediction does not lead to a new receiver strategy; it merely provides

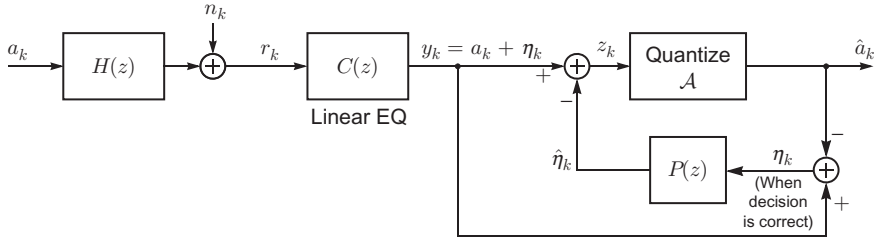


FIG. 8.13

An alternative interpretation of the DFE based on linear prediction of the noise. Both the ZF and MMSE DFE have this interpretation, depending on whether the front-end linear equalizer is the ZF or MMSE linear equalizer.

an alternative viewpoint for interpretation of the DFE strategy. Indeed, looking closer at the prediction architecture in Fig. 8.13, we see that it can be viewed as an instance of the DFE structure in Fig. 8.10, when the forward filter is  $F(z) = C(z)(1 - P(z))$  and the feedback filter is  $B(z) = -P(z)$ . Furthermore, when substituting the optimal linear prediction coefficients  $P(z) = 1 - M(z)$ , the forward and feedback filters reduce to the optimal forward and feedback filters of the ZF DFE, as described by Eqs. (8.32), (8.33).

While we have restricted our attention here to the ZF DFE, the noise predictive architecture of Fig. 8.13 applies equally well to the MMSE DFE; the only change is that the front-end linear equalizer is not the ZF but the MMSE linear equalizer, and the predictor is predicting the resulting error at the output, which includes residual ISI as well as noise. When the prediction coefficients are chosen optimally, the predictive architecture is equivalent to the MMSE DFE as defined by Eqs. (8.36), (8.37).

## 8.6 TOMLINSON-HARASHIMA PRECODING

The theory of the previous section shows that the ideal performance of the MMSE DFE is sufficient to achieve the Shannon capacity of the ISI channel. This is a remarkable result because it implies that the more complicated trellis-based detectors (such as Viterbi and BCJR) are not ideally necessary to approach capacity. However, this theoretical result is based on an assumption that the DFE has *instantaneous* access to *correct* decisions, which is nearly impossible to achieve in practice. Decisions that are instantaneous cannot tolerate the long decoding delay of powerful error-control codes and are hence unlikely to be correct; decisions that are likely to be correct require a significant decoding delay that prevents them from being instantaneous. In this sense, the DFE is fundamentally incompatible with powerful error-control codes.

Tomlinson-Harashima precoding (THP) is an alternative to the DFE with a similar performance that is compatible with error-control coding [12,13]. In a sense, THP can be thought of as a way of implementing the DFE *at the transmitter* instead of at the receiver. Since the transmitter knows the symbols it transmits, there is no chance for error propagation. However, as we will see, this benefit comes at the cost of (1) a slight increase in transmit power, which translates to a small SNR penalty, and (2) the requirement that the channel ISI response be known precisely at the transmitter. THP is thus not a good match for rapidly varying channels as well as other situations where it is difficult to get precise channel knowledge to the transmitter.

The relationship between THP and DFE is shown in Fig. 8.14. The top of the figure shows the channel model followed by the DFE of Fig. 8.10. As a reminder, for the ZF case, the forward filter transforms the channel into its monic and minimum-phase equivalent form, so that  $H(z)F(z) = M(z) = 1 + m_1z^{-1} + m_2z^{-2} + \dots$ , and the feedback filter is the tail  $B(z) = M(z) - 1$  of this channel.

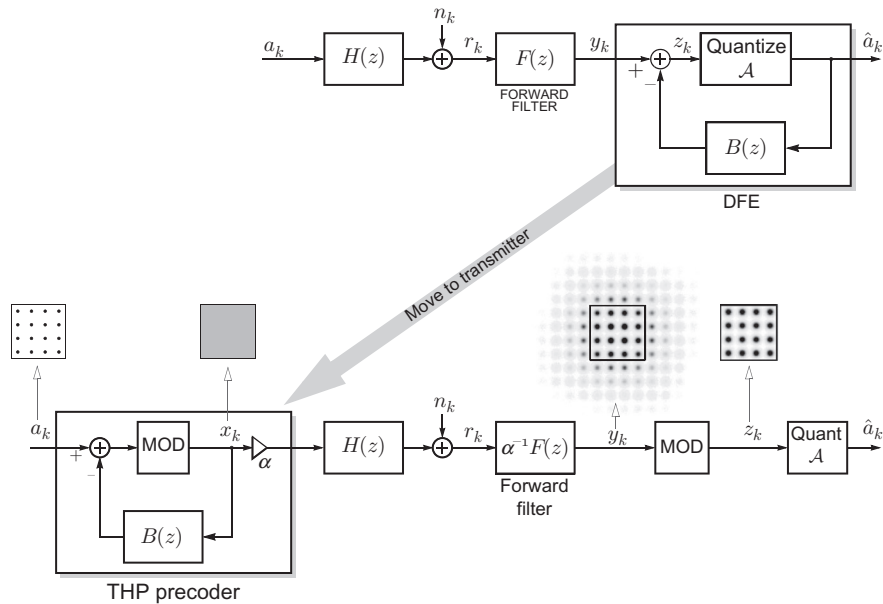


FIG. 8.14

The relationship between DFE and THP. The *top* of the figure shows the channel model followed by the DFE from Fig. 8.10. The *bottom* part of the figure shows Tomlinson-Harashima precoding (THP) implemented at the transmitter, before the channel, with additional processing performed by the receiver. The feedback filter of the DFE has been moved to the transmitter, but with two modifications: (1) the quantizer of the DFE is replaced by a modulo device for THP; (2) there is a scaling constant  $\alpha$  in THP to avoid any signal power amplification. Also shown in the figure are constellations at various points of the THP system, for a 16-QAM alphabet and a particular ISI response at  $\text{SNR} = 16$  dB.

The Tomlinson-Harashima precoder is shown at the bottom of Fig. 8.14. The THP principle requires that the message symbols  $\{a_k\}$  be chosen from an  $M$ -ary QAM alphabet, say  $\text{Re}\{\mathcal{A}\} = \text{Im}\{\mathcal{A}\} = \{\pm 1, \pm 3, \dots, \pm(K-1)\}$ , where  $K = \sqrt{M}$ . Instead of transmitting  $\{a_k\}$  directly, the  $k$ th symbol  $\alpha x_k$  transmitted by THP is computed recursively according to the following:

$$x_k = \left[ a_k - \sum_{i=1}^{\infty} m_i x_{k-i} \right]_{2K}, \quad (8.40)$$

where  $m_k$  is the impulse response of the monic and minimum-phase equivalent channel  $M(z)$ , and where we have introduced the complex modulo operator:

$$[z]_{2K} = z + 2K(p + jq),$$

where  $p$  and  $q$  are integers chosen so that the result  $[z]_{2K}$  falls within the complex square centered at the origin with sides of length  $2K$ . Looking at it another way: the modulo operator adds an integer multiple of  $2K$  to both the real and imaginary parts of its input, and it chooses these two integers so that the *modulo output is as close to the origin as possible*. The modulo operator thus maps any point in the complex plane to a point inside the  $2K$ -by- $2K$  square centered at the origin.

THP is known as “DFE at the transmitter” because the mapping from  $a_k$  to  $x_k$  of Eq. (8.40) is identical to the second-half of the DFE, with the feedback filter  $M(z) - 1$ , except that the decision device of the DFE is replaced by the complex modulo operation.

One way to motivate the modulo operation is to recognize that, without the modulo operator, the mapping in Eq. (8.40) would be a recursive implementation of a filter with transfer function  $1/M(z)$ . In other words, without the modulo operator, the mapping in Eq. (8.40) would be a *ZF linear equalizer at the transmitter*. And just like linear equalization at the receiver suffers from noise enhancement, linear equalization at the transmitter suffers from what might be called *signal enhancement*: the filter could potentially amplify the transmit signal power by a significant amount, especially when the channel ISI is severe. One way to compensate for this signal amplification is to follow the linear filter by a compensating attenuator. (Doing so would lead to the conclusion that linear equalization at the transmitter performs identically to linear equalization at the receiver; performance-wise it is neither better nor worse.) THP compensates for the signal amplification in a nonlinear way using the modulo operation, which removes nearly all of the signal amplification, while at the same time allowing the receiver to compensate (with high probability) for the modulo operation with another modulo operation.

For most channels the output of the THP modulo operator will be approximately uniformly distributed over the  $2K$ -by- $2K$  square in the complex plane, which makes its energy  $E_x = E(|x_k|^2) = 2K^2/3$ . In contrast, the energy before the precoder is  $E_a = 2(K^2 - 1)/3$ . The THP precoder thus includes an attenuation factor of  $\alpha = \sqrt{E_a/E_x}$  and transmits  $\alpha x_k$  as the  $k$ th transmitted symbol. This attenuation makes for a fair

comparison because it ensures that the energy of the symbols transmitted by a THP precoder is the same as the energy of the original alphabet  $\mathcal{A}$ . We see that  $\alpha$  will be a number only slightly less than unity, and it will approach unity as the size of the alphabet grows large. For example, the value of  $\alpha$  is 0.866, 0.968, 0.992, and 0.998 for QAM alphabets  $\mathcal{A}$  of size 4, 16, 64, and 256, respectively.

At the receiver, the THP uses a scaled version of the same front end as the DFE, namely the linear filter  $\alpha^{-1}F(z)$ , where  $H(z)F(z) = M(z)$ . The purpose of the gain factor  $\alpha^{-1}$  in the receiver is to cancel the attenuation factor of  $\alpha$  that was introduced at the transmitter. Since the forward filter satisfies  $H(z)F(z) = M(z)$ , and since the precoder inverts  $M(z)$  and effectively adds a complex integer  $2K(p_k + jq_k)$  to each information symbol  $a_k$ , it follows that the output of the scaled forward filter at the receiver will be the following:

$$y_k = a_k + 2K(p_k + jq_k) + n_k/\alpha. \quad (8.41)$$

The first term is the desired information symbol, which lies within the  $2K$ -by- $2K$  square. When the noise  $n_k/\alpha$  is small enough, the second term can be cleanly wiped away by a modulo operator, yielding  $[y_k]_{2K} = a_k + n_k/\alpha$ . Motivated by this observation, the receiver applies the forward filter output to the same modulo operator that was used at the transmitter. It then follows with a standard memoryless quantizer, which rounds each input to the nearest element of the alphabet  $\mathcal{A}$ .

**Example 8.10.** Consider a  $K^2 = 16$  QAM alphabet with  $\text{Re}\{\mathcal{A}\} = \text{Im}\{\mathcal{A}\} = \{\pm 1, \pm 3\}$ , so that  $K = 4$ . Assume the ISI channel is  $H(z) = 1 + (0.4 - 0.1j)z^{-1} + (0.1 + 0.5j)z^{-2} + (0.3 + 0.8j)z^{-3}$ , and the SNR is 16 dB. Shown in Fig. 8.14 are the constellations for several of the signals at various points in the THP system. First, the constellation for the information symbols  $a_k$  is shown, along with the 8-by-8 square. The output  $x_k$  of the modulo operator is empirically measured to be approximately uniform over the 8-by-8 square, so that its constellation is represented by a shaded square. After the forward filter, the constellation for  $y_k$  of Eq. (8.41) is shown. The constellation clearly extends well beyond the 8-by-8 square. Applying  $y_k$  to another modulo operator yields the final decision variable  $z_k$ , whose constellation is strictly confined to the 8-by-8 square. It closely resembles a simple 16-QAM alphabet that has been perturbed by Gaussian noise.

## 8.7 COMPARING PERFORMANCE: A CASE STUDY

There is no definitive ranking of the various equalization strategies described in this chapter; they all have their merits, and it will be the specific details of the application scenario that will dictate which choice is best. For example, fiber-optic links and other high-data-rate applications will often not have enough computational power to implement trellis-based detectors, and they hence will favor the reduced-complexity alternatives. Rapidly varying channels may not easily acquire knowledge of the channel at the transmitter, and they hence will avoid transmitter-based equalization

strategies like THP. High-performance links that operate at low SNR and use powerful error-control strategies will avoid DFE, since the decoding delay prevents the DFE from having timely and reliable decisions. The severity of the ISI also plays a major role when comparing various strategies. For example, linear equalization is generally not a viable option when the ISI is severe, while linear equalization is generally a preferred option when the ISI is mild (and there is not much to be gained by the more complex alternatives).

To close out this chapter, we will compare equalizer performance for one particular example. The reader is cautioned against drawing any universal conclusions from this one example; as the previous paragraph points out, a different example might reveal very different quantitative results. Nevertheless, the example we consider will be a valuable tool for pointing out the various qualitative differences between approaches.

Suppose a sequence of independent and uniformly distributed 16-QAM symbols is transmitted over an ISI channel with AWGN, whose impulse response is  $H(z) = 1 + h_1 z^{-1} + h_2 z^{-2} + h_3 z^{-3}$ , where  $h_1 = 0.4 - 0.1j$ ,  $h_2 = 0.1 + 0.5j$ , and  $h_3 = 0.3 + 0.8j$ . The same ISI response was considered in the example of Section 8.4.3. This channel is monic ( $h_0 = 1$ ) and minimum phase, which avoids the need for forward filters for the ZF DFE and THP strategies. The monic and minimum-phase condition is chosen for convenience, but it is not a limiting constraint on the channel, because any nonmonic and nonminimum-phase channel with AWGN can always be transformed into a monic and minimum-phase channel by a front-end all-pass filter. In effect, by starting with the minimum-phase channel, we are absorbing this all-pass filter into the definition of the channel. The magnitude response of the channel is shown in Fig. 8.15, where we see deep spectral nulls that are 32 dB below the peak magnitude response. The ISI in this example is severe.

Because the transmit PSD is flat, the underlying channel SNR and the MFB Eq. (8.10) on postequalization SNR are identical, namely  $SNR = E_a \sum_k |h_k|^2 / N_0$ . Some equalization strategies, like the linear and decision feedback equalizers, strive to transform the ISI channel into an effective memoryless (ISI-free) channel. When successful, the performance after such an equalizer can be quantified using the classical closed-form expression for the symbol-error probability of an ML detector in AWGN for 16-QAM (eg, Eq. 5.113 in [1]):

$$P_e = 3Q\left(\sqrt{SNR_{eq}/5}\right) - 2.25Q^2\left(\sqrt{SNR_{eq}/5}\right), \quad (8.42)$$

where  $SNR_{eq}$  is the SNR at the output of the equalizer. In the process of this transformation, the equalizer typically introduces a penalty in SNR, so that SNR after the equalizer is strictly less than the SNR of the underlying channel. In the previous sections we derived theoretical expressions for this postequalizer SNR for various strategies and compared them. Here, we instead look at the performance as measured by the symbol-error probability  $P_e$ .

The error-probability performance of eight different equalizers is shown in Fig. 8.16. In the following we will discuss the results for each strategy, one by one:

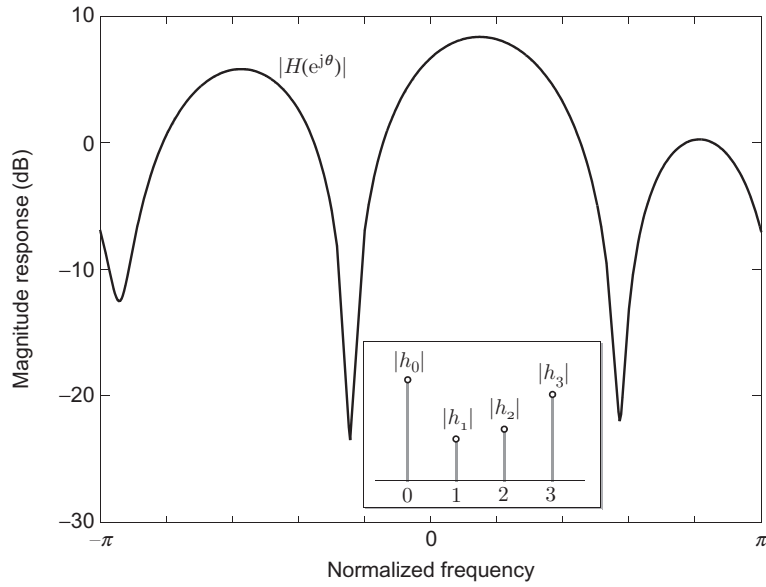


**FIG. 8.15**

The channel magnitude response for the case study example, which varies by 32 dB. The *inset* shows the magnitude of the impulse response coefficients in the time domain.

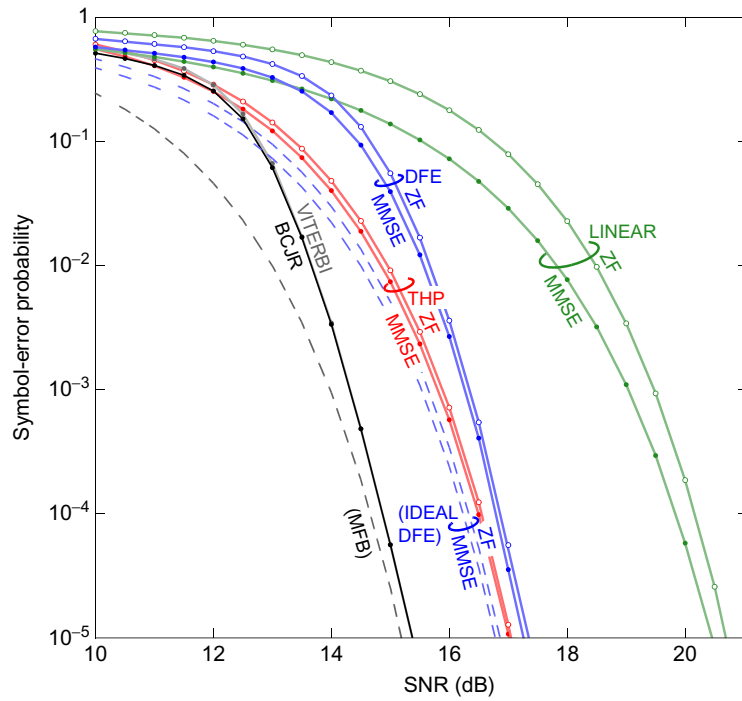


**FIG. 8.16**

Error probability comparison of various equalizers for the case study example.

### 8.7.1 ZF LINEAR EQUALIZER

- *Implementation:* Because the channel is FIR, its linear inverse (ie, the ZF linear equalizer of Eq. 8.23) cannot be implemented as an FIR transversal filter. (It would require an infinite number of coefficients.) However, because the channel has been reduced to its monic and minimum-phase form, its inverse can be implemented recursively via  $y_k = r_k - \sum_{i=1}^{\mu} h_i y_{k-i}$ , where  $r_k$  is the equalizer input and  $y_k$  is the equalizer output, so that the ZF linear equalizer can be implemented with only  $\mu = 3$  (feedback) coefficients.
- *Performance:* The right-most curve in Fig. 8.16 shows the error probability performance of the ZF linear equalizer. It performs worse than all other options, requiring nearly 21 dB to achieve a symbol-error probability of  $P_e = 10^{-5}$ . This curve (like most of the others) was generated via Monte Carlo simulations over millions of independent realizations of the symbols and noise. However, because the ZF linear equalizer exactly transforms the ISI channel into an ISI-free channel, we could instead use the closed-form equation of Eq. (8.42) for this error-probability curve, with  $SNR_{eq}$  set to the SNR after the ZF linear equalizer, namely the harmonic mean  $SNR_{ZF}$  of the SNR spectral density, as specified in Eq. (8.25).

### 8.7.2 MMSE LINEAR EQUALIZER

- *Implementation:* Unlike the ZF case, the MMSE linear equalizer of Eq. (8.27) cannot be implemented in exact form using a finite number of coefficients. Instead, a finite-coefficient version of the MMSE was implemented, with the number of coefficients chosen to be 200, which is large enough to mimic the performance of the theoretical infinite-coefficient case. The magnitude of the 200 MMSE linear equalizer coefficients for this example is shown in Fig. 8.17 for the case when  $SNR = 15$  dB.
- *Performance:* The MMSE linear equalizer outperforms the ZF linear equalizer in this example at all SNR values. The advantage of MMSE over ZF is seen to decrease as the SNR grows; the horizontal spacing between the MMSE and ZF linear curves is only about 0.2 dB at  $P_e = 10^{-5}$ . This trend confirms the fact that MMSE and ZF converge at high SNR, as expected because of the fact the MMSE equalizer of Eq. (8.26) reduces to the ZF equalizer as  $N_0 \rightarrow 0$ . We can use Eq. (8.42) to predict performance for the MMSE linear equalizer, with  $SNR_{eq}$  set to  $SNR_{MMSE}$  from Eq. (8.27). The resulting curve is no longer exact, however, because the MMSE equalizer only approximately transforms the ISI channel into an ISI-free channel, leaving some residual ISI that is subsequently treated as noise. The fact that the distribution of this residual ISI is not precisely Gaussian is what makes the expression in Eq. (8.42) an approximation. Nevertheless, the central-limit theorem ensures that it is close to Gaussian, and the curve predicted by Eq. (8.42) (not shown) is indistinguishable from the actual performance curve (generated via Monte Carlo simulation).

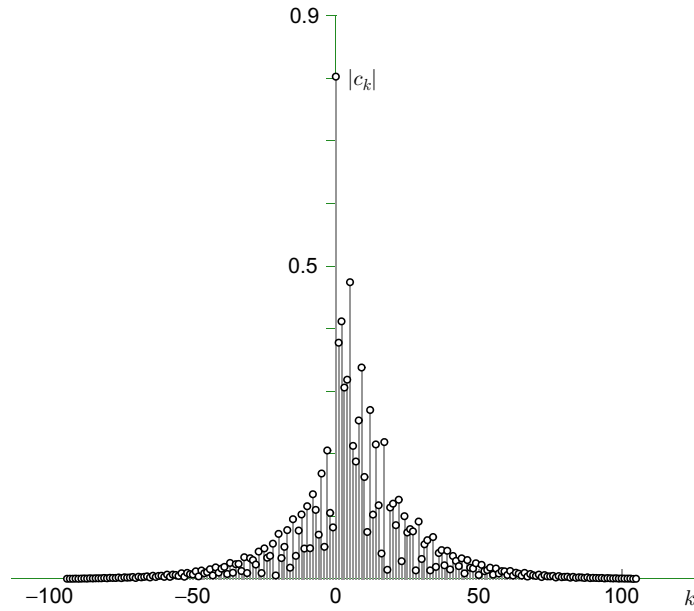


FIG. 8.17

The magnitude of the 200 coefficients of the MMSE linear equalizer for the case study, when  $\text{SNR} = 15$  dB. The leading and trailing coefficients are close to zero, suggesting that 200 coefficients is enough to mimic the infinite-coefficient theoretical MMSE linear equalizer.

### 8.7.3 ZF DFE

- Implementation:** The ZF DFE is described by Eq. (8.31). Because the channel is minimum-phase and monic, the forward filter of Eq. (8.32) reduces to the identity,  $F(z) = 1$  (requiring no coefficients), and the feedback filter of Eq. (8.33) reduces to the impulse response tail  $B(z) = H(z) - 1 = h_1 z^{-1} + h_2 z^{-2} + h_3 z^{-3}$ , requiring only  $\mu = 3$  coefficients. The complexity (as measured by the number of coefficients) of the ZF DFE is thus no greater than that required by the ZF linear equalizer. Furthermore, by the same complexity metric, the complexity of the ZF DFE is significantly *less* than that of the MMSE linear equalizer (which requires in theory an infinite number of coefficients or, as implemented, 200 coefficients).
- Performance:** The ZF DFE is seen to significantly outperform both linear equalizers. Remarkably, this performance advantage comes at essentially no cost in complexity. The dashed curve labeled “ideal ZF DFE” shows the performance predicted by Eq. (8.42) with  $\text{SNR}_{\text{eq}}$  set to  $\text{SNR}_{\text{ZF-DFE}}$  from Eq. (8.35); we see that this bound is not an accurate predictor of performance because Eq. (8.35) does not take into account the effects of error propagation. The impact of error

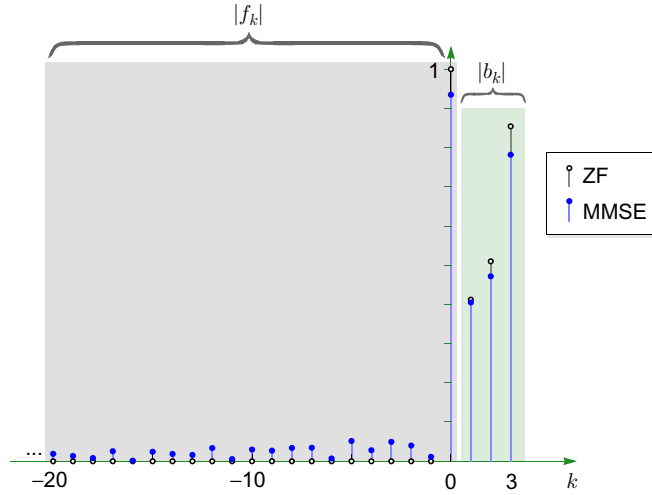
propagation can be quantified by comparing the dashed and solid curves for the ZF DFE. Error propagation is especially detrimental at low SNR, as might be expected, but its impact decreases rapidly at high SNR. At  $P_e = 10^{-5}$ , the SNR penalty due to error propagation for the ZF DFE is 0.5 dB. Comparing ZF DFE to the linear equalizers, we see that the ZF DFE always outperforms the ZF linear equalizer in this example, regardless of SNR, and regardless of error propagation. Comparing the ZF DFE to the MMSE linear equalizer, we see a crossover point: At a high enough SNR the ZF DFE is better, while at a low enough SNR the MMSE linear equalizer is better.

### 8.7.4 MMSE DFE

- *Implementation:* The MMSE DFE is described by Eqs. (8.31), (8.36), and (8.37). Because the channel  $H(z)$  in this example is minimum phase, the forward filter  $F(z)$  of Eq. (8.36) is anticausal, satisfying  $f_k = 0$  for all  $k > 0$ . In theory this  $F(z)$  requires an infinite number of equalizer coefficients. Like the linear case, however, we can approximate the infinite-coefficient case by using a finite number of coefficients and choosing this number to be large. For this example, the MMSE DFE was implemented using a forward filter having 200 coefficients, that approximates the infinite-coefficient filter of Eq. (8.36). The MMSE DFE feedback filter from Eq. (8.37) has only  $\mu = 3$  nonzero coefficients. The magnitudes of the forward and feedback coefficients for the MMSE are shown in Fig. 8.18, where they are compared to those for the ZF case.
- *Performance:* The MMSE DFE is seen to outperform the ZF DFE at all values of SNR. The performance gain is most significant at a low SNR, it decreases as SNR increases. At  $P_e = 10^{-5}$ , the advantage of MMSE DFE over ZF DFE is only 0.1 dB. This gain comes at the cost of an increase in complexity due to the increased number of filter coefficients. The dashed curve labeled “ideal MMSE DFE” shows the performance predicted by Eq. (8.42) with  $SNR_{eq}$  set to  $SNR_{MMSE-DFE}$  from Eq. (8.39); as for the ZF case, this bound is not an accurate predictor of performance because it neglects error propagation. Furthermore, again as in the ZF case, the penalty due to error propagation at  $P_e = 10^{-5}$  for the MMSE DFE is 0.5 dB.

### 8.7.5 ZF TOMLINSON-HARASHIMA PRECODING

- *Implementation:* The ZF THP precoded symbols  $x_k$  are generated according to Eq. (8.40), where—because  $H(z)$  is already monic and minimum phase in this example— $M(z)$  is set to  $H(z)$ . This will only be possible when the transmitter knows the channel, perhaps through a feedback mechanism from the receiver. To avoid the signal-enhancement effect of the modulo device, these symbols are attenuated in amplitude by a factor of  $\alpha = \sqrt{E_a/E_x} = \sqrt{10/(32/3)} \approx 0.9682$  before transmitting (see Fig. 8.14). The forward filter  $F(z)$  reduces to unity in

**FIG. 8.18**

Comparison of the ZF and MMSE forward and feedback coefficients (magnitudes) for the case study example, when  $SNR = 15$  dB. The coefficients in the *left box* are the anticausal forward filter coefficients  $f_k$ . For the ZF the only nonzero forward coefficient is  $f_0 = 1$ , while for the MMSE case there are 200 nonzero coefficients (not all are shown). The coefficients in the *right box* are the strictly causal feedback filter coefficients  $b_1$  through  $b_3$ .

this example. The receiver thus directly scales the channel output and applies a modulo device, yielding  $z_k = [r_k/\alpha]_8$ , which is then rounded to the nearest alphabet symbol to arrive at the decision.

- *Performance:* ZF THP is similar to ZF DFE but with one big advantage: by moving the feedback filter from the receiver to the transmitter (see Fig. 8.14), THP avoids the problem of error propagation. In Fig. 8.16 we see that ZF THP outperforms ZF DFE at all SNR values and that the gap in performance is especially large at a low SNR, where error propagation is most severe. However, the performance of ZF THP is seen to fall short of the performance of the ideal ZF DFE (dashed curve) that feeds back correct decisions; this gap is due to a combination of the attenuation factor  $\alpha$  and the loss inherent in the modulo device at the receiver.

### 8.7.6 MMSE THP

- *Implementation:* In theory, the MMSE THP forward filter  $F(z)$  is the MMSE DFE forward filter of Eq. (8.36), and the precoded symbols  $x_k$  are generated according to Eq. (8.40), where the feedback filter  $M(z) - 1$  is the MMSE DFE feedback filter of Eq. (8.37). As before, the attenuation factor is  $\alpha = \sqrt{E_a/E_x} \approx 0.9682$ . The forward filter was implemented using 200

coefficients, enough to emulate the infinite-coefficient filter specified by Eq. (8.36). The receiver scales by  $1/\alpha$  and filters by the MMSE forward filter  $F(z)$ , as shown in Fig. 8.14, applies a modulo device, and then rounds to the nearest alphabet symbol to arrive at the decision.

- *Performance:* In Fig. 8.16 we see that MMSE THP is slightly but consistently better than ZF THP at all SNR values. As in the ZF case, the MMSE THP closely approaches the performance of the ideal MMSE DFE; it falls short because of a combination of the attenuation factor  $\alpha$  and the modulo loss. It is worth emphasizing that THP is a transmitter-based equalization strategy that requires knowledge of the channel at the transmitter; as such it will be incompatible with many rapidly varying applications, as well as with many broadcast (one-to-many) applications.

### 8.7.7 VITERBI ALGORITHM

- *Implementation:* The Viterbi algorithm is implemented according to Eq. (8.14), where in place of  $g_k(p, q)$  we use the simplified additive branch metric  $\hat{\mu}_k(p, q) = |r_k - s^{(p,q)}|^2$ . There is no a priori term in the branch metrics, because all transmitted symbols are independent and uniformly distributed over the 16-QAM alphabet. Because the channel memory is  $\mu = 3$  and the alphabet size is  $M = 16$ , the number of states in the trellis is  $M^\mu = 4096$ . Furthermore, there will be  $M = 16$  branches emanating from each node in the trellis. The overall complexity is thus extremely high, significantly higher than the suboptimal equalizers considered above.
- *Performance:* The gray curve in Fig. 8.16 shows the performance of the Viterbi algorithm. At high SNR, the Viterbi algorithm significantly outperforms all of the linear, decision feedback, and THP strategies. At  $P_e = 10^{-5}$ , the SNR advantage of Viterbi over MMSE THP is 1.7 dB, and the advantage over ZF LE is more than 5.3 dB. Interestingly, the performance advantage of Viterbi is not as significant at extremely low SNR values. In fact, when the SNR is so low that the error probability exceeds 20%, the Viterbi algorithm is seen to perform slightly worse than the significantly less complex THP strategies. The dashed curve labeled “MFB” shows the error probability of the matched-filter bound, which is computed by substituting Eq. (8.10) into Eq. (8.42). The Viterbi algorithm closely approaches the MFB at high SNR, falling only 0.2 dB short at  $P_e = 10^{-5}$ .

### 8.7.8 BCJR ALGORITHM

- *Implementation:* The BCJR is implemented using the same 4096-state trellis as Viterbi, with a multiplicative branch metric  $\gamma_k(p, q) = e^{-|r_k - s^{(p,q)}|^2/N_0}$  that is a simplified version of Eq. (8.15). (Factors in the branch metric that are common to all branches—like the a priori probability factor—are ignored, to reduce complexity.) The forward and backward recursions are implemented according

to Eqs. (8.17), (8.18). The scaled APPs for each QAM symbol are computed according to  $P(a_k = a|\mathbf{r}) = \sum_{(p,q) \in \mathcal{B}_a} \alpha_k(p) \gamma_k(p, q) \beta_{k+1}(q)$ , where  $\mathcal{B}_a$  is the set of branches  $(p, q)$  corresponding to an input symbol of  $a \in \mathcal{A}$ . The maximum such APP determines the MAP decision,  $\hat{a}_k = \arg \max_{a \in \mathcal{A}} P(a_k = a|\mathbf{r})$ .

- *Performance:* The hard-output BCJR detector, which minimizes symbol-error probability, is seen to be almost indistinguishable from the Viterbi algorithm, which minimizes sequence-error probability. At a high SNR they perform identically, while at a low SNR we see a slight advantage for BCJR over Viterbi. This result reinforces a point that was made earlier: hard-output BCJR is not typically worth the trouble, the Viterbi algorithm is simpler to implement and performs nearly the same. The story would change if we were to expand the case study to include error-control coding, however; in that case, the soft outputs of BCJR would become extremely valuable, and the performance after error-control decoding would be significantly better with BCJR than with Viterbi.

---

## 8.8 SUMMARY

This chapter has reviewed an array of strategies for dealing with the ISI that arises because of dispersive channels. Linear and decision-feedback equalizers transform the ISI channel into an effective ISI-free channel, which enables us to quantify their performance by the postequalization SNR. This postequalization SNR was in turn shown to be related in a simple way to the harmonic and geometric means of the SNR spectral density. These results are tabulated in Table 8.1. In practice the DFE SNR falls short of the SNR predicted by this theory because of error propagation; in the case study example the penalty was seen to be about 0.5 dB. The Viterbi and BCJR detectors have no notion of a postequalization SNR, although their performance is bounded and typically close to the matched-filter bound at low error probabilities. Which strategy to choose for a particular design scenario will depend on many factors, including the severity of the ISI, the computational resources, and the availability of reliable channel knowledge at the transmitter.

This chapter's focus was limited to classical equalization strategies for single-carrier systems. Space limitations prevented us from exploring several alternative equalizers and related concepts. For example, we assumed throughout that the channel response was known. Channel estimation [14] and adaptive equalization [15] for finite-coefficient equalizers [1] are important topics for the realistic case. We assumed perfect synchronization at all levels (eg, frame, symbol, carrier phase). Synchronization strategies are explored in Chapter 7. Fractionally spaced equalizers [16] are robust to timing errors and to signals with excess bandwidth (beyond the minimum bandwidth assumed in this chapter), while passband equalizers [17] are robust to carrier phase errors. A combination of partial-response linear equalization and trellis-based detection has been effectively used for hard-disk drives for decades [11]. Single-carrier frequency-domain equalization (as used in LTE-A uplink) is

a reduced-complexity alternative for implementing either a linear equalizer or the forward filter of a DFE [18]. Multicarrier strategies such as orthogonal-frequency-division multiplexing (OFDM) are immensely important strategies for communication over ISI channels; conceptually, the idea is to transmit data independently across numerous subchannels, each of whose bandwidth is so narrow that a simple one-coefficient linear “equalizer” is enough to compensate for the dispersive channel. Chapter 10 is devoted to OFDM and related concepts.

---

## REFERENCES

- [1] J.R. Barry, E.A. Lee, D.G. Messerschmitt, *Digital Communication*, Springer-Verlag GmbH, 2004.
- [2] G.D.J. Forney, The Viterbi algorithm, *Proc. IEEE* 61 (3) (1973) 268–278.
- [3] J. Makhoul, Linear prediction: a tutorial review, *Proc. IEEE* 63 (4) (1975) 561–580.
- [4] W. Hirt, J.L. Massey, Capacity of the discrete-time Gaussian channel with intersymbol interference, *IEEE Trans. Inf. Theory* 34 (3) (1988) 38.
- [5] L. Bahl, J. Cocke, F. Jelinek, J. Raviv, Optimal decoding of linear codes for minimizing symbol error rate (corresp.), *IEEE Trans. Inf. Theory* 20 (2) (1974) 284–287.
- [6] A.J. Viterbi, An intuitive justification and a simplified implementation of the map decoder for convolutional codes, *IEEE J. Sel. Areas Commun.* 16 (2) (1998) 260–264.
- [7] M. Tuchler, A.C. Singer, Turbo equalization: an overview, *IEEE Trans. Inf. Theory* 57 (2) (2011) 920–952.
- [8] C. Berrou, A. Glavieux, P. Thitimajshima, Near Shannon limit error-correcting coding and decoding: turbo-codes. 1, in: *IEEE International Conference on Communications, 1993. ICC '93, Geneva. Technical Program, Conference Record*, vol. 2, 1993, pp. 1064–1070.
- [9] J. Hagenauer, E. Offer, L. Papke, Iterative decoding of binary block and convolutional codes, *IEEE Trans. Inf. Theory* 42 (2) (1996) 429–445.
- [10] R. Muller, W.H. Gerstacker, On the capacity loss due to separation of detection and decoding, *IEEE Trans. Inf. Theory* 50 (8) (2004) 1769–1778.
- [11] R.D. Cideciyan, F. Dolivo, R. Hermann, W. Hirt, W. Schott, A PRML system for digital magnetic recording, *IEEE J. Sel. Areas Commun.* 10 (1) (1992) 38–56.
- [12] M. Tomlinson, New automatic equaliser employing modulo arithmetic, *Electron. Lett.* 7 (5) (1971) 138–139.
- [13] H. Harashima, H. Miyakawa, Matched-transmission technique for channels with intersymbol interference, *IEEE Trans. Commun.* 20 (4) (1972) 774–780.
- [14] J.K. Tugnait, L. Tong, Z. Ding, Single-user channel estimation and equalization, *IEEE Signal Process. Mag.* 17 (3) (2000) 16–28.
- [15] S.U.H. Qureshi, Adaptive equalization, *Proc. IEEE* 73 (9) (1985) 1349–1387.
- [16] J.R. Treichler, I. Fijalkow, C.R. Johnson, Fractionally spaced equalizers, *IEEE Signal Process. Mag.* 13 (3) (1996) 65–81.
- [17] J.F. Hayes, R.D. Gitlin, S.B. Weinstein, *Data Communication Principles*, Springer-Verlag, 1992.
- [18] F. Pancaldi, G.M. Vitetta, R. Kalbasi, N. Al-Dhahir, M. Uysal, H. Mheidat, Single-carrier frequency domain equalization, *IEEE Signal Process. Mag.* 25 (5) (2008) 37–56.

# Multicarrier transmission in a frequency-selective channel

# 9

S.K. Wilson\*, O. A. Dobre†

*Santa Clara University, Santa Clara, CA, United States\** *Memorial University, St. John's, NL, Canada†*

## CHAPTER OUTLINE

<b>9.1 Introduction</b> .....	333
<b>9.2 Early OFDM</b> .....	334
9.2.1 Frequency Shift Keying .....	334
9.2.2 Analog OFDM .....	340
<b>9.3 Digital OFDM</b> .....	342
9.3.1 The FFT and the Cyclic Prefix .....	342
9.3.2 Zero-Padding: An Alternative to the Cyclic Prefix .....	347
<b>9.4 Diversity and Frequency Modulation</b> .....	352
9.4.1 Probability of Error for Uncoded OFDM .....	352
<b>9.5 OFDM: Power-Loading and Bit-Loading</b> .....	355
<b>9.6 OFDM: Diversity and Coding</b> .....	357
9.6.1 OFDM and Coding .....	357
9.6.2 Outage Capacity and OFDM .....	361
<b>9.7 Conclusions</b> .....	363
<b>Appendix Correlated Diversity Signals</b> .....	364
<b>References</b> .....	366

## 9.1 INTRODUCTION

Orthogonal frequency division multiplexing (OFDM) is a modulation technique that is used in several applications ranging from cellular systems (3G/LTE, WiMAX), wireless local area networks (LANs), digital audio radio, underwater communications, and even optical light modulation. OFDM combines several signals operating at different frequencies simultaneously. These frequencies are known as subcarriers or tones. If single-carrier systems are like single notes in music played quickly, OFDM comprises multiple tones and a chord, played simultaneously over a longer period.

In a single-carrier system, frequency selectivity demands some type of equalization. In OFDM, because constellations values are mapped onto narrow-band tones, equalization is relatively simple. Because each symbol is mapped onto a single tone with a single-valued gain and phase component, it is an attractive modulation technique for transmission schemes that are based on flat-fading channels, such as multiple-input-multiple-output (MIMO) systems.

OFDM has existed in one form or another since 1958 [1–4]. However, up until the late 1970s, OFDM was essentially an analog system, ie, transmitting multiple signals from widely-spaced carriers with guard bands. Though there existed high frequency (HF) OFDM modems used by the government, eg, [5], OFDM was primarily used in telephone lines, ie, relatively static channels.

A major breakthrough for digital OFDM was the introduction of the use of the fast Fourier transform (FFT) and cyclic prefix (CP) in Ref. [6]. In the late 1980s, digital OFDM was proposed (and eventually adopted) for digital subscriber twisted copper lines. However, one of the first times OFDM was proposed for a wireless channel was in Ref. [7]. Unlike most of today's OFDM wireless systems, this was OFDM operating in a flat but fast-fading environment. It was established as a viable modulation technique in frequency-selective channels when it became the standard for the European Digital Audio Broadcast (DAB) system [8].

OFDM had been seen as problematic for frequency-selective channels because each subcarrier had a different SNR and hence a different probability of error. In a wireline, static system, the transmitter can learn the location of the low SNR subcarriers and choose not to use them or only assign a few bits to those subcarriers [9]. But in a wireless system where the channel is changing, or in a broadcast system where each user experiences a different frequency response, adapting the bit assignment to the SNR of each subcarrier is problematic. In a frequency-selective channel, there is a good probability that many of the subcarriers' SNRs will be poor and hence dominate the probability of error for the entire OFDM symbol. To overcome this, the DAB standard proposed coded OFDM (COFDM). The idea was that coding and interleaving across the OFDM tones would compensate for deep fades.

This chapter discusses OFDM in fading channels. It begins with the predecessor to OFDM, frequency shift keying (FSK). It then moves on to digital OFDM and its implementation, including the use of the CP and methods to shape the spectrum. Finally, how coding and interleaving affect diversity and performance is introduced.

---

## 9.2 EARLY OFDM

### 9.2.1 FREQUENCY SHIFT KEYING

Frequency shift keying (FSK) was proposed in the early twentieth century by Fessenden [10], among others. In FSK, different frequencies are used to signal

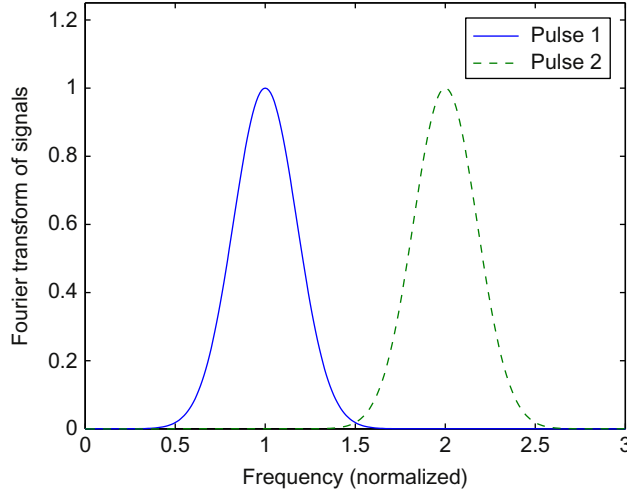
**FIG. 9.1**

Illustration of a 1-bit FSK signal set. The data rate for this signal set is  $1/2$  bits/s/Hz. At any one time, a user would transmit one of the two pulses with a normalized bandwidth of 2. This illustration assumes a Gaussian pulse shape.

different messages. Unlike modern OFDM, FSK sends one frequency at a time. The receiver listens to a set of frequencies and determines which frequency has the largest signal. This frequency represents a specific bit combination. A 1-bit FSK frequency response is illustrated in Fig. 9.1.

### 9.2.1.1 Modulation

Given a bandwidth allocation  $B$  and  $M$  frequency signals, we require a modulating pulse whose bandwidth is relatively narrow-band, ie, proportional to  $B/M$  (Hz). Thus, for example, given a pulse,  $p(t)$ , the user can send  $M$  messages by transmitting one of the following baseband signals:

$$p(t) \exp(j2\pi f_i t),$$

where  $f_i$  is one of  $M$  center frequencies.

Given a flat-fading channel, the receiver would see the following:

$$y(t) = p(t) \exp(j2\pi f_i t) + v(t), \quad (9.1)$$

where  $v(t)$  is complex-valued zero-mean additive Gaussian noise with variance  $\mathcal{N}_0$ . (We assume that we are working with a baseband signal, but without loss of generality, we can translate all calculations to the carrier frequency of interest.)

The maximum-likelihood receiver would apply  $M$  matched filters:

$$\begin{aligned} z_k &= \int y(t)p(t)^* \exp(-j2\pi f_k t) dt \\ &= \int |p(t)|^2 \exp(j2\pi(f_i - f_k)) dt + n_k, \end{aligned} \quad (9.2)$$

where  $n_k = \int n(t)p(t) \exp(-j2\pi f_k t) dt$  is zero-mean Gaussian noise with variance  $\mathcal{N}_0 \|p\|^2$  and  $\|p\|^2 = \int |p(t)|^2 dt$ .

We choose the most likely transmitted message to be the  $l$ th one if  $z_l$  is greater than all other  $z_k$ .

As the number of signals increases, the bandwidth also increases. As such, this type of system is bandwidth inefficient: the data rate is on the order of  $\frac{\log_2(M)}{MB}$  bits/s/Hz. This ratio goes to zero as  $M$  increases.

**Example 9.1.** Suppose you have a 1-bit FSK system with  $p(t) = \frac{1}{\sqrt{T_0}} \text{sinc}(t/T_0)$  and  $f_1 = 0$  and  $f_2 = \frac{\alpha}{T_0}$ , where  $\alpha$  represents an overlap factor. For example, if  $\alpha = 0$  the frequency pulses overlap (and there is no differentiation), but if  $\alpha = 1$ , there is no overlap. Each  $f_i$  corresponds to a message and the receiver's goal is to determine which message was most likely sent.

The transmitter sends  $x(t) = \frac{1}{\sqrt{T_0}} \text{sinc}(t/T_0) \exp(j2\pi f_i t)$  and the received signal is  $y(t) = x(t) + n(t)$ , where  $n(t)$  is additive white Gaussian noise (AWGN) with power spectral density  $S_n(f) = \mathcal{N}_0$  W/Hz.

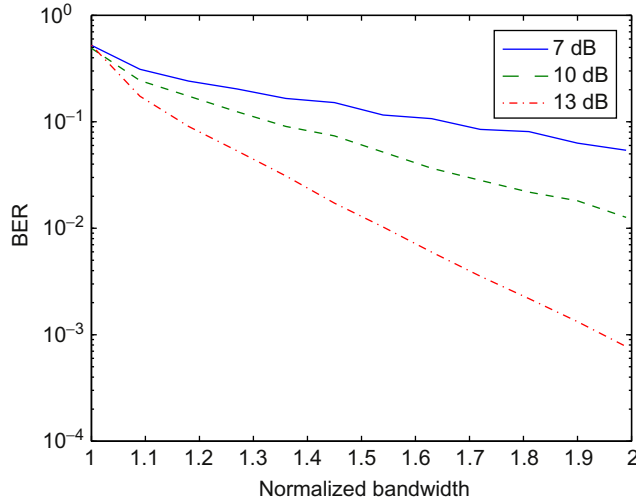
The receiver chooses the message to be  $\hat{i}$  if  $z_i + n_i > z_k + n_k$  for all other  $k$ . The resulting BER for different overlap values of  $\alpha$  are shown in Fig. 9.2. The SNR is measured as the energy of one frequency pulse divided by the energy of the resulting noise,  $\int n(t)x(t)^* dt$ .

Note that in Fig. 9.2 as the normalized bandwidth increases (and the effective bit rate decreases) the probability of error decreases. However, one can also see that some overlap between the signals is not that harmful.

### 9.2.1.2 Orthogonal signals

Two vectors are orthogonal if there is a 90 degree angle between them. One can test if two vectors are orthogonal by taking the inner product of the two:  $\langle \mathbf{x}_1, \mathbf{x}_2 \rangle = \sum_{i=1}^N x_{1,i} x_{2,i}$ ; if the inner product is zero, the vectors are orthogonal. Similarly, functions can be orthogonal. For example,  $x_1(t) = \cos(2\pi f_c t)$  and  $x_2(t) = \sin(2\pi f_c t)$  are orthogonal. If the inner product of two functions,  $\langle x_1(t), x_2(t) \rangle = \int x_1(t)x_2(t) dt$ , is zero, the two functions are orthogonal.

From a communications point of view, if  $x_1(t)$  and  $x_2(t)$  are orthogonal, they are easily separable. One can transmit both simultaneously, yet still discriminate one from the other. In a communications system, we map a finite set of, for example,  $M$  signals to a set of messages. These  $M$  signals can be mapped onto a finite set of  $N \leq M$  orthonormal basis functions [4,11].

**FIG. 9.2**

Plot of symbol error probability versus normalized bandwidth, ie, bandwidth divided by the bandwidth of a single pulse. The SNRs used in this plot are 7, 10, and 13 dB.

A set of functions  $\phi_i(t)$ ,  $i = 1, \dots, N$  are orthonormal if

$$\int \phi_i(t) \phi_k(t) dt = \begin{cases} 1, & i = k, \\ 0, & \text{otherwise.} \end{cases} \quad (9.3)$$

An  $M$ -point FSK constellation with zero correlation between signals can be modeled as follows:

$$x_i(t) = x \phi_i(t), \quad (9.4)$$

where  $M = N$ , ie, there is one symbol for each basis function. For FSK constellations,  $\phi_i(t)$  are not only orthonormal, but the center frequencies differ. So unlike in [Example 9.1](#), in this example, we require the functions to be orthogonal. Rather than use sinc functions as the basic pulse, as in [Example 9.1](#), the FSK signals can have the following form:

$$\phi_n(t) = \frac{1}{\sqrt{NT}} e^{j \frac{2\pi n t}{NT}} \Pi\left(\frac{t}{NT}\right),$$

where  $\Pi(t) = \begin{cases} 1, & t \in [-1/2, 1/2], \\ 0, & \text{otherwise.} \end{cases}$  Note that this is an orthonormal set of functions and the center frequencies of each of subcarriers are spaced  $\frac{1}{NT}$  Hz apart.

In any case, the FSK signals can be represented as vectors:

$$\begin{aligned}\mathbf{x}_1 &= x(1, 0, 0, \dots, 0), \\ \mathbf{x}_2 &= x(0, 1, 0, \dots, 0), \\ &\vdots \\ \mathbf{x}_M &= x(0, 0, \dots, 0, 1).\end{aligned}$$

Given  $\mathbf{y} = \mathbf{x}_i + \mathbf{n}$ , where  $\mathbf{n}$  is a vector of independent identically-distributed (iid) zero-mean Gaussian noise with variance  $\sigma^2$ , the probability of error is as follows:

$$P_e = (M-1)Q(\sqrt{\text{SNR}/2}), \quad (9.5)$$

where  $Q(x) = \int_x^\infty \frac{1}{\sqrt{2\pi}} \exp(-s^2/2) ds$ , and the SNR is  $\frac{x^2}{\sigma^2}$ .

As a comparison, for  $M$ -QAM constellations,  $P_e \approx 3Q\left(\sqrt{\frac{3\text{SNR}}{M-1}}\right)$  [1,12]. The probability of error for  $M$ -FSK and  $M$ -QAM is plotted in Fig. 9.3 for an SNR of 13 dB. Though FSK has better performance than QAM as the bit rate increases, this is at the expense of a large increase in bandwidth. In a frequency-selective channel, individual FSK signals can experience a loss in SNR. This is because in a frequency-selective channel, some part of the spectrum will have a much lower SNR than others. This in turn implies that some FSK signals will have a lower SNR than others.

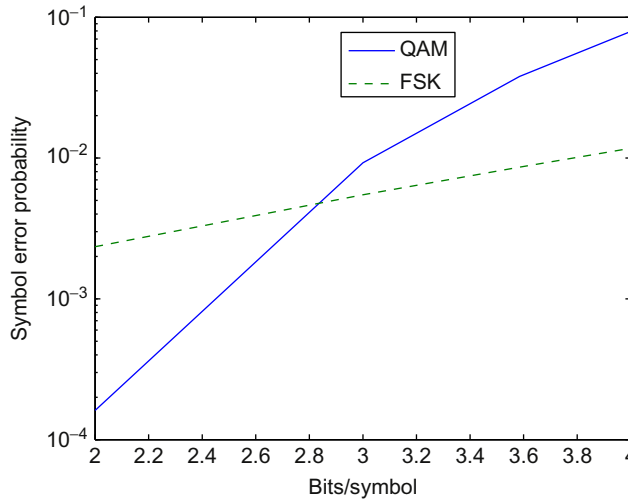


**FIG. 9.3**

Plot of symbol error probability versus bits/symbol for FSK versus QAM (SNR = 13 dB).

### 9.2.1.3 FSK and frequency-selective channels

Suppose you have a frequency-selective channel, modeled by an impulse response  $h(t) = \sum_{k=0}^{L-1} \alpha_k \delta(t - \Delta_t k)$ , where  $\alpha_k$  are uncorrelated zero-mean, complex-valued Gaussian random variables. This is a model [13] that represents the changing gain and phase due to a rich multipath environment. The probability of error for a given frequency pulse will be affected by the frequency response of the channel.

**Example 9.2.** Suppose you have a 2-FSK system and the frequency response for each frequency is  $H_i$ , where  $H_1$  and  $H_2$  are independent and  $E[|H_i|^2]/\sigma^2 = \Gamma$ , where  $\sigma^2$  is the variance of the noise in each dimension.

We can model each symbol as follows:

$$\begin{aligned}\mathbf{x}_1 &= H_1(1, 0, 0, 0), \\ \mathbf{x}_2 &= H_2(0, 1, 0, 0).\end{aligned}$$

Suppose  $\mathbf{x}_1$  is transmitted. Then, the square-law detector would see  $y_1 = H_1 + n_1$  and  $y_2 = n_2$  and choose between  $z_1 = |H_1 + n_1|^2$  and  $z_2 = |n_2|^2$ .

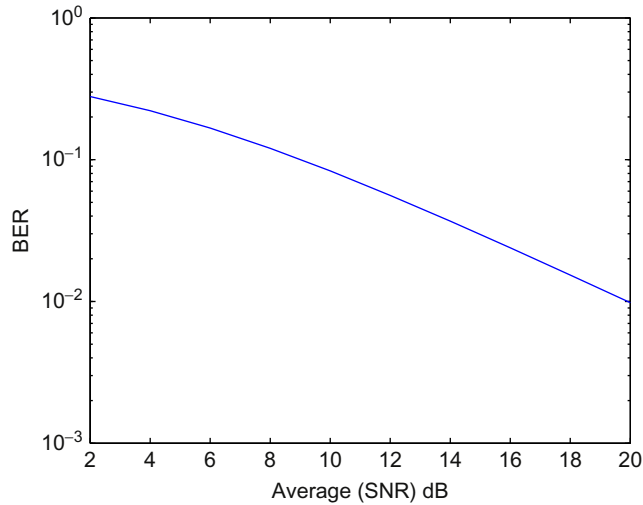
The probability of being correct in this case is as follows:

$$\begin{aligned}P(z_2 > z_1) &= \int_0^\infty \frac{1}{\sigma^2} \exp\left(-\frac{\gamma_1}{\sigma^2}\right) d\gamma_1 \int_{\gamma_1}^\infty \frac{1}{\Gamma + \sigma^2} \exp\left(-\frac{\gamma_2}{\Gamma + \sigma^2}\right) d\gamma_2 \\ &= \int_0^\infty \frac{1}{\sigma^2} \exp\left(-\frac{\gamma_1}{\sigma^2}\right) d\gamma_1 \exp\left(-\frac{\gamma_1}{\Gamma + \sigma^2}\right) d\gamma_1 \\ &= \int_0^\infty \frac{1}{\sigma^2} \exp\left(-\gamma_1 \left(\frac{1}{\sigma^2} + \frac{1}{\Gamma + \sigma^2}\right)\right) d\gamma_1 \\ &= \int_0^\infty \frac{1}{\sigma^2} \exp\left(-\gamma_1 \frac{\Gamma + 2\sigma^2}{\sigma^2(\Gamma + \sigma^2)}\right) d\gamma_1 \\ &= \frac{\Gamma + \sigma^2}{\Gamma + 2\sigma^2} \\ &= \frac{\text{SNR} + 1}{\text{SNR} + 2},\end{aligned}$$

which means that the probability of error is  $P_e = 1 - \frac{\text{SNR}+1}{\text{SNR}+2} = \frac{1}{\text{SNR}+2}$ . The BER for this scheme is shown in Fig. 9.4.

### 9.2.1.4 Data rate

With FSK, given  $M$  messages, the bandwidth will be proportional to  $MB_1$ , where  $B_1$  (Hz) is the bandwidth of the subcarrier and its guardband. As stated earlier, the normalized bandwidth  $\frac{\log_2(MB_1)}{MB} \rightarrow 0$  as  $M \rightarrow \infty$ . The key to increasing the efficiency of this system is to take advantage of the orthogonality of the frequency signals and send them simultaneously.

**FIG. 9.4**

Plot of BER for a 2-FSK signal in a frequency-selective fading channel.

### 9.2.2 ANALOG OFDM

Analog OFDM [1,3] took advantage of the fact that multiple signals separated in frequency could be transmitted simultaneously. This meant that the data rate could be significantly increased over what was offered by FSK. Before the advent of the FFT, this was done using analog filters, either by using non-overlapping or overlapping frequency division multiplexing.

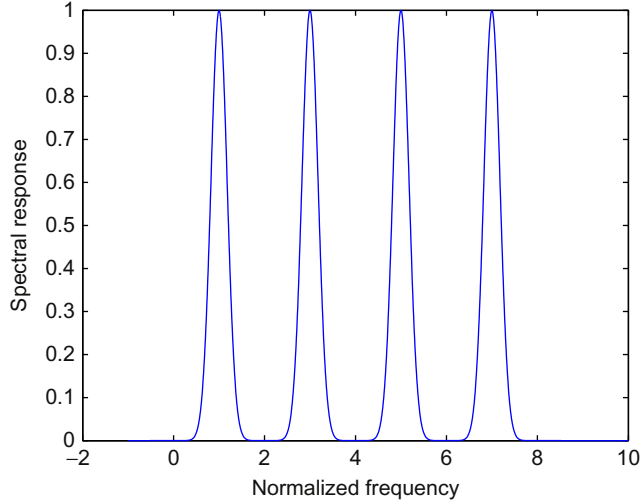
In all cases, the baseband transmitted signal was of the following form:

$$x(t) = \sum_{k=1}^K c_k p(t) e^{j2\pi k \Delta_f t}, \quad (9.6)$$

where  $\Delta_f$  is the frequency separation between the different pulses. Typically, in the modems described,  $c_k$  was a binary pulse.

For the non-overlapping case, if  $P(f)$  is the Fourier transform of the pulse,  $\Delta_f$  is large enough so that  $P(f)$  and  $P(f + \Delta_f)$  have minimal overlap. The problem with this method was that the data rate was limited by the separation between channels; the further apart the spectral pulses, the less efficient the data rate was. An example of a four-subcarrier analog OFDM signal is shown in Fig. 9.5. This problem was solved in Ref. [2] by alternating in-phase and quadrature modulation on adjacent subcarriers.

**Example 9.3.** Consider an  $N$ -subcarrier analog OFDM system with full-cosine roll-off as in Ref. [2]. The bandwidth of each 100% roll-off pulse is  $\frac{2}{T}$ .

**FIG. 9.5**

Example of the frequency response of a four-subcarrier, analog OFDM signal. Note that the effective symbol rate would be  $\frac{4b}{8}$  bits/s/Hz. This is due to the need for guardbands between the analog subcarriers.

In a non-overlapping pulse system, the bit rate would be less than  $R_n = \frac{Nb}{T} \frac{1}{\frac{N}{2T}} = b/2$  bits/s/Hz.

But in an overlapping system, where orthogonality is preserved by modulating adjacent subcarriers 90 degrees out-of-phase, the data rate is  $b$  bits/s/Hz.

The overlapping analog system described above had an inherently limited data rate for two reasons. In the 1960s, multi-level transmission was not feasible due to channel variation and the electronics of the time. In addition, full modern quadrature transmission was not feasible either. This meant that the bit rate described in [Example 9.3](#) had a maximum value of 1 bit/s/Hz. Increasing the bit rate in this fashion while preserving the orthogonality of the signals required an efficient way to transmit and receive multi-amplitude constellations. In addition, it required a static channel or knowledge of the channel at the transmitter to preserve orthogonality between subcarriers. Given knowledge of the channel at the transmitter, the pulse response of the transmitter could be shaped to ensure orthogonality at the receiver. The requirement for a static channel is illustrated in the following example.

**Example 9.4.** Suppose you transmit 1 bit on each subcarrier and receive the following:

$$x(t) = \sum_{k=0}^{N-1} b_k p(t) e^{j(2\pi k \Delta_f t + \phi_k)},$$

where  $\phi_{2k} = 0$  and  $\phi_{2k+1} = \pi/2$ , ie, the adjacent subcarriers are 90 degrees out-of-phase. In addition, suppose  $p(t)$  is a square-root Nyquist pulse with 100% roll-off as in Ref. [2] and

$$P(f) = \sqrt{T} \cos(\pi T f / 2) \cap \left( \frac{fT}{2} \right).$$

Using Rayleigh's theorem, note that

$$\int p(t) e^{j2\pi \Delta f t + j\phi_k} (p(t) e^{j2\pi l \Delta f t + j\phi_l})^* dt = e^{j(\phi_k - \phi_l)} \int P(f - k\Delta f) P(f - l\Delta f)^* df.$$

Letting  $\Delta f = \frac{1}{T}$ ,

$$\begin{aligned} & e^{j(\phi_k - \phi_{k-1})} \int P\left(f - k\frac{1}{T}\right) P\left(f - (k-1)\frac{1}{T}\right) df \\ &= T e^{j\pm\pi/2} \int_{-0}^{\frac{1}{2T}} \cos(\pi T f / 2) \cos\left(\pi T \left(f - \frac{1}{T}\right) / 2\right) df = \pm j/2. \end{aligned}$$

A similar result holds for  $\int p(t) e^{j2\pi \frac{k}{T} t + j\phi_k} (p(t) e^{j2\pi \frac{k-1}{T} t + j\phi_{k-1}})^* dt$  and the inner product of all other pulses with  $p(t) e^{j2\pi \frac{k}{T} t + j\phi_k}$  would be zero.

Using this,

$$\int x(t) p(t) e^{j(2\pi k \frac{f}{T} - \phi_k)} dt = b_k \pm j/2 b_{k+1} + \mp j/2 b_{k-1},$$

and because the in-phase and quadrature components are orthogonal, the receiver can recover the symbol-of-interest,  $b_k$ .

## 9.3 DIGITAL OFDM

Digital OFDM not only includes the use of digital techniques such as the FFT, but also coincides with the rise of digital communications research in the 1970s and digital communications implementation in the 1990s. Not only is it more bandwidth efficient than analog OFDM, but it also provides a means for interleaving and error-control coding of data.

### 9.3.1 THE FFT AND THE CYCLIC PREFIX

A breakthrough method for OFDM was presented in Ref. [6]<sup>1</sup> and introduced the use of the discrete Fourier transform (DFT) in the form of the FFT and the cyclic prefix. One of the issues of any communications system is to have the maximum data rate for the minimum bandwidth (and of course, power). Using the DFT and the cyclic

<sup>1</sup>Note that the concept of the cyclic prefix used in Ref. [6] was explicitly championed in Ref. [14].

prefix provided a way to set up orthogonal signals that retain their orthogonality in the presence of a channel unknown to the transmitter.

As shown above, it is not simple to find functions that are orthogonal in frequency at the receiver in the presence of an unknown channel. A key breakthrough in Ref. [6] was the use of an FFT and a non-linear receiver method to ensure orthogonality.

### 9.3.1.1 The discrete Fourier transform

With continuous signals, convolution in the time domain is equivalent to multiplication in the frequency domain. However, with discrete signals, multiplication in the frequency domain is equivalent to cyclic convolution in the time domain. That is, the cyclic convolution between two discrete and finite sequences of length  $N$ ,  $h_n$ , and  $x_n$ , is defined as follows:

$$h_n \otimes x_n = \sum_{k=0}^{N-1} h_{\text{mod}(n-k, N)} x_k.$$

For example, given  $N = 4$ ,  $(h_n \otimes x_n)_{n=2} = h_2x_0 + h_3x_1 + h_0x_2 + h_1x_3$ .

The DFT of a sequence of length  $N$  is

$$X_n = \sum_{k=0}^{N-1} x_k e^{-j2\pi kn/N},$$

and the inverse DFT (IDFT) of a sequence of length  $N$  is

$$x_k = \frac{1}{N} \sum_{n=0}^{N-1} X_n e^{j2\pi kn/N}.$$

The DFT of  $x_n \otimes h_n$  is  $X_n \times H_n$ . The cyclic aspect of the convolution is the key point here. It must be considered to ensure orthogonality between subcarriers in OFDM.

### 9.3.1.2 Modulation of OFDM with the IDFT and the cyclic prefix

In digital OFDM,

$$x(t) = \sum_{k=0}^{N-1} c_k e^{j2\pi kt/NT} \quad (9.7)$$

if  $t \in [0, NT + \Delta]$ , and 0 otherwise.

Note that the period of this signal is  $1/(NT)$ , but we extend the length of the signal by  $\Delta$  seconds. This extension, which we think of as coming in advance of the signal, is the *cyclic prefix*.

Rather than taking the DFT of the signal, we are applying the IDFT. This is done only to emphasize the fact that the constellations are mapped to symbols in the frequency domain. Mathematically, there is no reason to choose one over the other.

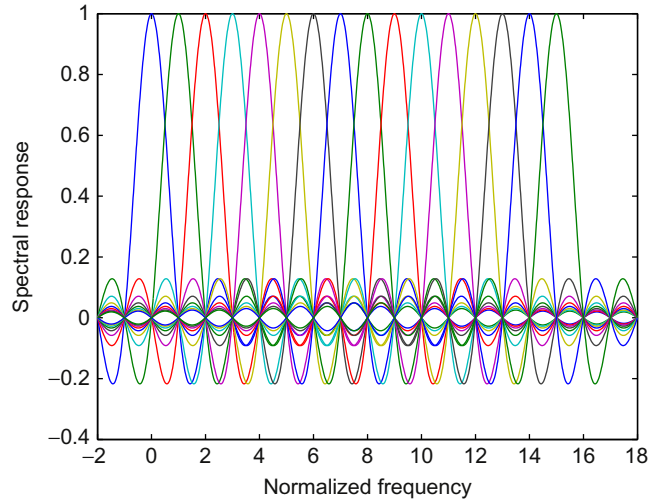


**FIG. 9.6**

An illustration of the overlapping sinc pulses found in the spectrum of a digital OFDM signal. In this example, there are 16 subcarriers. The effective data rate of this signal (excluding the cyclic prefix overhead) is  $\frac{b16}{16} = b$  bits/s/Hz, where  $b$  is the number of bits per subcarrier.

Suppose the impulse response of the channel,  $h(t)$ , is essentially zero outside the region  $[0, T_h]$ , then

$$\begin{aligned} x(t) * h(t) &= \int_0^{\min(t, T_h)} x(t - \tau) h(\tau) d\tau \\ &= \sum_{k=0}^{N-1} c_k e^{\frac{j2\pi kt}{NT}} \int_0^{\min(t, T_h)} h(\tau) e^{-\frac{j2\pi k\tau}{NT}} d\tau. \end{aligned} \quad (9.8)$$

Note that the upper-limit of the integral is the minimum of  $t$  and the length of the channel response,  $T_h$ , because of the start-up period of the convolution. The right-hand side of Eq. (9.8),  $\int_0^{\min(t, T_h)} h(\tau) e^{-\frac{j2\pi k\tau}{NT}} d\tau$ , almost looks like the Fourier transform of  $h(t)$  evaluated at frequency  $k/(NT)$ , except for the non-linear  $\min(t, T_h)$  term.

However, if the guard period,  $\Delta$ , is greater than  $T_h$ , then for  $t \geq \Delta$ ,

$$\int_0^{\min(t, T_h)} h(\tau) e^{-\frac{j2\pi k\tau}{NT}} d\tau = \int_0^{T_h} h(\tau) e^{-\frac{j2\pi k\tau}{NT}} d\tau = H_k.$$

So by using a modulating square pulse as the pulse which is equivalent to using a DFT as a modulation tool, we have improved the efficiency of the overlapping pulses. An illustration of the overlapping sinc pulses for each subcarrier of a digital OFDM signal is shown in Fig. 9.6. By extending the length of the modulating pulse, and then

using the non-linear step of throwing away the first  $\Delta$  seconds of the received pulse, we ensure the orthogonality of the signal. That is, for  $t \geq \Delta$ ,

$$x(t) * h(t) = \sum_{k=0}^{N-1} c_k H_k e^{\frac{j2\pi kt}{NT}}.$$

The impulse response of the channel does not impact the orthogonality of the system, but it shows up at the receiver as a gain and phase shift of the received signal. Hence the cyclic prefix makes linear convolution look cyclic and ensures orthogonality; it also acts as a guard period between adjacent OFDM symbols. The downside of the cyclic prefix is the loss of data rate due to the additional overhead.

### 9.3.1.3 Data rate and the cyclic prefix

This leads to the need for a system where the signal is long enough, ie,  $NT \gg \Delta$  so that the addition of the cyclic prefix is not wasteful. This also has an implication about the bandwidth of the system. The effective bandwidth of the OFDM signal is  $\frac{1}{T}$ .

**Example 9.5.** Suppose you have the two-tap channel,  $h(t) = \alpha_1 \delta(t) + \alpha_2 \delta(t - \tau)$ , where  $\tau < \Delta$ .

As in Ref. [15], we consider the effect of the CP on the performance of an OFDM signal with and without the CP.

For a system with the CP, let  $y(t) = x(t) * h(t) + v(t)$ , where  $v(t)$  is AWGN:

$$\begin{aligned} y(t) &= \sum_{k=0}^{N-1} c_k e^{\frac{j2\pi kt}{NT}} * (\alpha_1 \delta(t) + \alpha_2 \delta(t - \tau)) \\ &= \begin{cases} \sum_{k=0}^{N-1} c_k (\alpha_1 e^{\frac{j2\pi kt}{NT}}) t \in [0, \tau) \\ \sum_{k=0}^{N-1} c_k (\alpha_1 + \alpha_2 e^{-\frac{j2\pi k\tau}{NT}}) e^{\frac{j2\pi kt}{NT}}. \end{cases} \end{aligned}$$

If we throw away the portion of the signal in the CP, sample the remaining signal every  $T$  seconds and take the IDFT, we have  $z_l = H_l c_l + v_l$ . Given perfect knowledge of the frequency response, the probability of error for each subcarrier is

$$P_{e,l} \approx N_e Q\left(\frac{|H_l| d_{\min}}{2\sigma}\right),$$

where  $N_e$  is the number of nearest neighbors,  $d_{\min}$  is the minimum distance of the constellation from which  $c_l$  is chosen, and  $\sigma^2$  is the variance of the noise term,  $n_l$ . Two factors affect the probability of a symbol error here: the amplitude of the frequency response at the subcarrier and the AWGN process.

If there were no CP, then the sampled signal would be as follows:

$$y_n = \begin{cases} \alpha_1 \sum_{k=0}^{N-1} c_k e^{\frac{j2\pi nk}{N}} + v_n, & n \leq L-1, \\ \sum_{k=0}^{N-1} (\alpha_1 + \alpha_2 e^{-j2\pi \frac{k\tau}{NT}}) c_k + v_n, & n > L, \end{cases}$$

where  $L - 1 = \lfloor \tau/T \rfloor$ . In this case, the DFT of the signal would yield the following:

$$\begin{aligned}
 z_l &= \frac{1}{N} \sum_{n=0}^{L-1} y_n e^{-\frac{j2\pi nl}{N}} + \frac{1}{N} \sum_{n=L}^{N-1} y_n e^{-\frac{j2\pi nl}{N}} \\
 &= \alpha_1 \frac{1}{N} \sum_{n=0}^{L-1} \sum_{k=0}^{N-1} c_k e^{\frac{j2\pi(k-l)n}{N}} + \frac{1}{N} \sum_{n=L+1}^{N-1} \sum_{k=0}^{N-1} H_k c_k e^{\frac{j2\pi(k-l)n}{N}} \\
 &= \alpha_1 \frac{1}{N} \sum_{k=0}^{N-1} c_k e^{\frac{j\pi(k-l)(L-1)}{N}} \frac{\sin\left(\frac{\pi(k-l)L}{N}\right)}{\sin\left(\frac{\pi(k-l)}{N}\right)} + \frac{1}{N} \sum_{k=0}^{N-1} H_k c_k e^{\frac{j\pi(k-l)(2L-1)}{N}} \frac{\sin\left(\frac{\pi(k-l)(N-L)}{N}\right)}{\sin\left(\frac{\pi(k-l)}{N}\right)} \\
 &= \left( \frac{\alpha_1 L}{N} + \frac{N-L}{N} \left( \alpha_1 + \alpha_2 e^{-\frac{j2\pi k\tau}{NT}} \right) \right) c_l + \text{ICI},
 \end{aligned}$$

where the ICI is the intercarrier interference, ie, the extra terms in the sum.

There are two observations here. The first is that the data symbol,  $c_l$ , is not a multiple of the frequency response  $H_k$  but a combination of the first tap,  $\alpha_1$ , and the frequency response,  $H_k$ . The second is that the channels are no longer orthogonal and there is ICI. The energy of the ICI is as follows:

$$\begin{aligned}
 \mathcal{E}_{ICI} &= E \left[ \frac{1}{N} \sum_{k \neq l} \frac{c_k e^{j\pi(k-l)(L-1)N}}{\sin(\pi(k-l)/N)} (\alpha_1 \sin(\pi(k-l)L/N) \right. \\
 &\quad \left. + H_k e^{j\pi(k-l)L/N} \sin(\pi(k-l)(N-L)/N)) \right]^2 \\
 &= \frac{1}{N} \mathcal{E}_c \sum_{k \neq l} \frac{|\alpha_1 \sin(\pi(k-l)L/N) + H_k e^{j\pi(k-l)L/N} \sin(\pi(k-l)(N-L)/N)|^2}{\sin(\pi(k-l)/N)^2}.
 \end{aligned}$$

In the last step we are assuming that the constellation values  $c_k$  are iid with energy  $\mathcal{E}_c$ .

### 9.3.1.4 Demodulation of OFDM

For modern OFDM with a cyclic prefix, demodulation of  $y(t) = x(t) * h(t) + n(t)$  involves the following:

1. Throw away the cyclic prefix.
2. Sample the remaining signal every  $T$  seconds. (Note these two steps can be reversed.)
3. Take the DFT of the sampled signal, so that we have

$$\begin{aligned}
 z_l &= \text{DFT}(y(nT)) \\
 &= \frac{1}{N} \sum_{n=0}^{N-1} \left( \sum_{k=0}^{N-1} c_k H_k e^{\frac{j2\pi knT}{NT}} \right) + v(nT) e^{-\frac{j2\pi nl}{NT}} \\
 &= c_k H_k + n_k.
 \end{aligned}$$

4. Find the best estimate of the frequency response  $\hat{H}_l$ , for each of the  $N$  subcarriers and find  $\hat{c}_l$  from  $z_l/\hat{H}_l$ .

### 9.3.2 ZERO-PADDING: AN ALTERNATIVE TO THE CYCLIC PREFIX

The cyclic prefix has two roles: to preserve orthogonality and serve as a guard time between the current signal and the previous one.

An alternative to the cyclic-prefix is zero-padding, ie, instead of a cyclic prefix, have a guard period of zeros of length  $\Delta$ . Though it does prevent intersymbol interference between two adjacent OFDM symbols, provided  $\Delta$  is greater than the length of the channel, it does not ensure orthogonality as the cyclic prefix does. However, orthogonality can be ensured through the process of *overlap-and-add* [16].

$$\text{Consider a zero-padded signal } x(t) = \begin{cases} 0 & t \in [0, \Delta), \\ \sum_{n=0}^{N-1} c_n e^{j\frac{2\pi n t}{NT}} & t \in [\Delta, NT + \Delta] \end{cases}$$

Then, given a channel impulse response,  $h(t)$ ,

$$y(t) = \begin{cases} \int_0^{t-\Delta} x(t-\tau)h(\tau)d\tau, & t \in [\Delta, 2\Delta), \\ \int_0^{\Delta} x(t-\tau)h(\tau)d\tau, & t \in [2\Delta, NT], \\ \int_{t-NT}^{\Delta} x(t-\tau)h(\tau)d\tau, & t \in [NT, NT + \Delta]. \end{cases}$$

The key point here, which is illustrated in Fig. 9.7, is the following. In the start-up phase of the convolution, the first part of the channel impulse response is used, while in the ending phase of the convolution, the latter part of the channel is used. Note that in the zero-padding period belonging to OFDM symbol 2, the payload data from OFDM symbol 2 does not show up; only the tail end of OFDM symbol 1 shows up.

So orthogonality can be restored by overlapping and adding the tail end of the received OFDM signal with the initial end. Hence this process is called *overlap-and-add* [16].

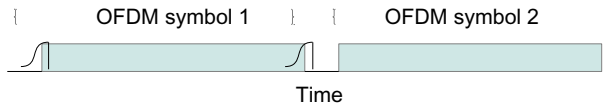


FIG. 9.7

Two adjacent OFDM symbols with zero-padding. Just before the start of the first OFDM symbol, we see the reversed channel indicating convolution at that point. At the end of the first OFDM symbol, we see the reversed channel again indicating convolution at this later point in time. Note that if we add the convolution at the beginning of the OFDM signal to the convolution at the end of the OFDM signal, we will have the effective “cyclic” convolution.

So,

$$\begin{aligned}
 y_{oa}(t) &= \begin{cases} y(t + \Delta) + y(t + NT + \Delta), & t \in [0, \Delta], \\ y(t + \Delta), & t \in [\Delta, NT], \\ 0, & \text{otherwise} \end{cases} \\
 &= \int_0^\Delta h(\tau)x(t + \Delta - \tau)d\tau \\
 &= \sum_{k=0}^{N-1} c_k H_k e^{j2\pi kt/NT}.
 \end{aligned}$$

However, if noise is present, we have an additional noise term for the overlapped part, that is,

$$y_{oa}(t) = \begin{cases} \sum_{k=0}^{N-1} c_k H_k e^{j2\pi kt/NT} + n(t + \Delta) + n(t + NT + \Delta), & t \in [0, \Delta], \\ \sum_{k=0}^{N-1} c_k H_k e^{j2\pi kt/NT} + n(t + \Delta), & \text{otherwise.} \end{cases}$$

Whether to use zero-padding or the cyclic prefix is not a simple decision. The zero-padding option uses less energy, but it lacks the redundancy found in the cyclic prefix. This redundancy can have other uses such as synchronization [17]. However, it can be argued that the quick drop in signal that is found in a zero-padded OFDM signal can also be used for synchronization [16].

### 9.3.2.1 Windowing and frequency characteristics

One of the key issues in any modulation technique is its frequency spectrum and bandwidth. OFDM is made of multiple subcarriers, each with an energy spectrum that decays at a rate that is inversely proportional to the frequency (Fig. 9.8).

Consider an OFDM signal with a cyclic prefix:

$$\begin{aligned}
 x(t) &= \sum_{k=0}^{N-1} c_k e^{j2\pi \frac{kt}{NT}} \Pi\left(\frac{t}{NT + \Delta}\right), \\
 X(f) &= (NT + \Delta) \sum_{k=0}^{N-1} c_k \text{sinc}\left(\left(f - \frac{k}{NT}\right)(NT + \Delta)\right), \\
 G(f) &= E[|X(f)|^2] \\
 &= (NT + \Delta)^2 \sum_{k=0}^{N-1} \mathcal{E}_c \text{sinc}\left(\left(f - \frac{k}{NT}\right)(NT + \Delta)\right)^2.
 \end{aligned}$$

To determine how quickly the sum rolls off outside the main frequency window, note that for  $f > 0$ ,  $\text{sinc}\left(\left(f - \frac{k}{NT}\right)(NT + \Delta)\right)^2 \leq \frac{1}{\pi^2 (NT + \Delta)^2 \left(f - \frac{k}{NT}\right)^2}$ ; and approximating the sum by an integral, for  $f$  outside the bandwidth,  $\left[0, \frac{1}{T}\right]$ ,

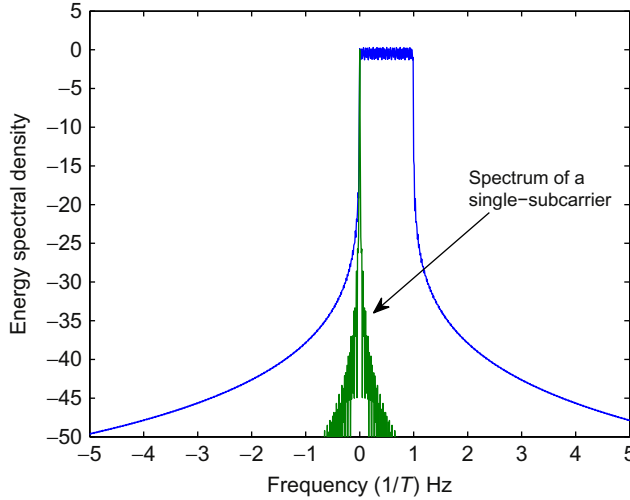


FIG. 9.8

Spectrum of an OFDM symbol with 128 subcarriers, along with that of a single subcarrier.

$$\begin{aligned}
 G(f) &\approx (NT + \Delta)^2 \mathcal{E}_c \int_0^{N-1} \frac{1}{\pi^2 (NT + \Delta)^2 \left(f - \frac{x}{NT}\right)^2} dx \\
 &= \mathcal{E}_c \frac{NT}{\pi^2 f} \frac{1}{\left(f - \frac{N-1}{NT}\right)}.
 \end{aligned}$$

The main point here is that the frequency will still roll off by a factor of  $1/f^2$  outside the bandwidth, but the drop from 1 to  $\frac{1}{(NT+\Delta)^2}$  is decreased by the factor of  $NT$  in the numerator. That is, by summing the  $N$  sinc-squared terms, we are increasing the out-of-band spectrum by a factor of  $N$ .

The square pulse is responsible for the relatively high out-of-band spectrum values. One way to reduce the out-of-band spectrum, and hence narrow the effective bandwidth, is the use of windowing.

### 9.3.2.2 Extra windowing and the preservation of orthogonality

By extending the OFDM symbol with a windowed version of the signal, eg, a Hanning window,  $w(t) = (1 - \cos(2\pi t f_0))/2$ , the out-of-band spectrum can be narrowed but with the penalty of additional overhead and the resulting loss in data rate.

So suppose your OFDM symbol,  $x(t)$ , has width  $NT + \Delta$  seconds; as a result, one can add extensions before and after the symbol. Let  $x_e(t)$  be the cyclically extended version of  $x(t)$ , and then multiply it by the window:

$$w(t) = \begin{cases} \frac{1}{2}(1 + \sin(\pi(t + \alpha/2)\alpha)), & t \in [-\alpha, 0], \\ 1, & t \in [0, NT + \Delta], \\ \frac{1}{2}\left(1 - \sin\left(\frac{\pi(t - (NT + \Delta + \alpha/2))}{\alpha}\right)\right), & t \in [NT + \Delta, NT + \Delta + \alpha]. \end{cases}$$

Note that with some manipulation the Fourier transform of  $w(t)$  is found to be the following:

$$W(f) = \frac{e^{-j\pi f B}}{2\pi} (\sin(\pi(NT + \Delta + 2\alpha)) + \sin(\pi(NT + \Delta))) \left( \frac{1}{f} - \frac{f}{f^2 - \frac{1}{(2\alpha)^2}} \right).$$

Even though we have added an additional  $2\alpha$  seconds to the symbol period, the loss in rate is the same as if we only add  $\alpha$  seconds. This is because we throw away the  $2\alpha + \Delta$  seconds of the symbol, and the next OFDM symbol can start at time  $NT + \Delta$ ; hence, the decrease in data rate is  $\frac{NT + \Delta}{NT + \Delta + \alpha}$ .

Fig. 9.9 shows a dramatic decrease in spectrum outside the payload region of  $[0, 1/T]$  Hz of the OFDM signal. So the bandwidth can be reduced, but at a cost. When designing these systems, one must consider if the need for bandwidth reduction is a function of the physics of the channel or a need for more spectrum. If it is the latter, the following question arises: Is the net result of a window in time, which in turn leads to a bandwidth reduction, a net gain or a net loss?

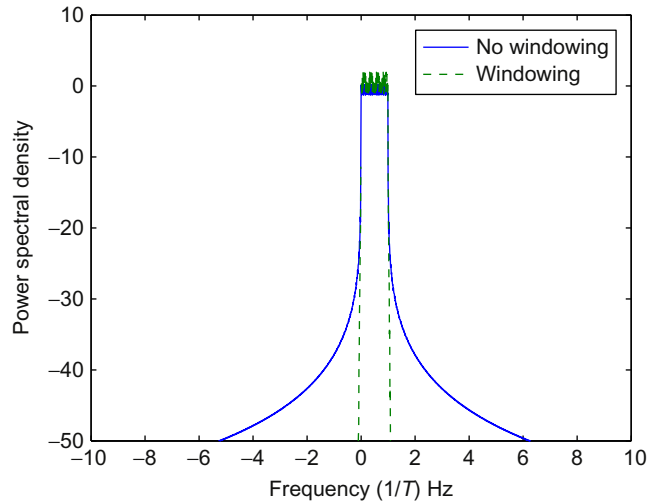


FIG. 9.9

Spectrum of an OFDM symbol with 128 subcarriers with no windowing and with a window where  $\alpha = \Delta$ .

An alternative to increasing the time period of the signal is to window the signal within the existing OFDM signal. So the window is now the following:

$$w(t) = \begin{cases} \frac{1}{2} \left(1 - \cos\left(\frac{\pi t}{\alpha}\right)\right), & t \in [0, \alpha], \\ 1, & t \in [\alpha, NT + \Delta - \alpha], \\ \frac{1}{2} \left(1 + \cos\left(\frac{\pi(t - (NT + \Delta))}{\alpha}\right)\right), & t \in [NT + \Delta - \alpha, NT + \Delta]. \end{cases}$$

The downside of this approach is that the subcarriers are no longer orthogonal. However, one could argue that the correlation is minimal and the errors that may result can be mitigated through extra error control. Again, this is mitigating data loss in one regime (time) but increasing data loss through the need for extra coding. Fig. 9.10 displays the BER curves for an OFDM symbol in multipath channels with and without windowing. Though the windowing will bring down the spectral wings, it will lead to an error floor and require additional coding. The designer must decide between large spectral wings or loss of data rate due to windowing. The loss of data rate due to windowing is the result of either adding extra length to the symbol, with no loss of orthogonality, or the result of adding no extra length to the symbol but requiring extra coding due to the increase in bit errors.

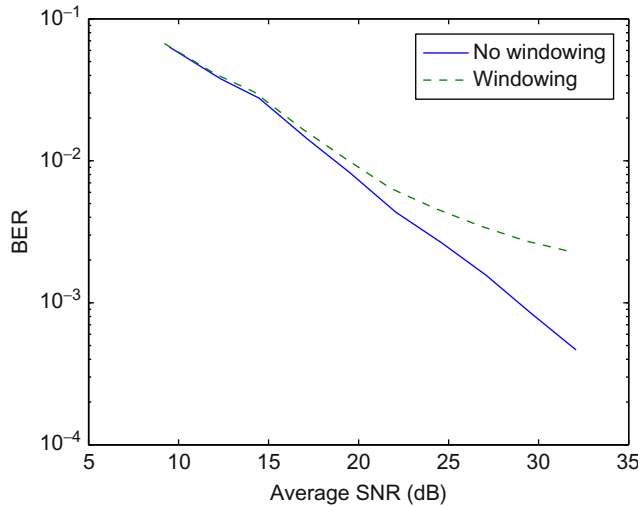


**FIG. 9.10**

Plot of BER for different channels for a 128 subcarrier OFDM system with and without windowing. The cyclic prefix size is  $\Delta = 12$  samples and the width of the window wings is  $\alpha = 6$  samples. In this case, the windowing is part of the OFDM symbol, so the length does not change.

## 9.4 DIVERSITY AND FREQUENCY MODULATION

For any modulation in a Rayleigh fading channel, some sort of diversity is necessary to avoid high error rates. In a single-carrier system, the equalizer acts as a diversity combiner. However, in a narrow band FSK or an OFDM system, frequency diversity is needed to overcome the high probability of error brought on by nulls in a frequency-selective channel.

Error control coding is used with frequency interleaving to achieve diversity and a resulting decrease in probability of error in OFDM. Error-control coding is a subject beyond the scope of this chapter but can be studied in books such as Ref. [18]. However, the main points to know about error control coding with respect to diversity are as follows:

1. A code consists of multiple codewords; a good code has a large distance between codewords while minimizing the required increase in rate.
2. The large distance between codewords decreases the probability of error. In general, the probability of error for a code is bounded above by the *minimum distance* between codewords.
3. Frequency diversity can be induced by a code through frequency interleaving. An interleaver takes the inputs to the codewords and separates adjacent elements of a codeword to ensure that not all elements of a codeword experience a low SNR.

This section describes how frequency selectivity affects the uncoded probability of error. It then discusses how coding and interleaving can decrease the probability of error in a frequency-selective channel.

### 9.4.1 PROBABILITY OF ERROR FOR UNCODED OFDM

In a frequency-selective channel, the average probability of error is dominated by the subcarrier with the lowest SNR. That is, given that the received signal on each subcarrier is  $y_k = H_k c_k + n_k$ , the probability of error for each subcarrier is approximately  $N_e Q\left(\sqrt{\frac{|H_k|^2 \mathcal{E}_c}{\sigma_n^2} K_c}\right)$ , where  $N_e$  is the number of nearest neighbors,  $\mathcal{E}_c$  is the energy of the constellation that  $c_k$  comes from,  $\sigma_n^2$  is the variance of the frequency domain noise, and  $K_c$  is a term that compensates for the size of the constellation. Therefore, the average probability of error for the uncoded OFDM signal is

$$P_e = \frac{1}{N} \sum_{k=0}^{N-1} N_{e,k} Q\left(\sqrt{K_{c,k} \frac{|H_k|^2 \mathcal{E}_c}{\sigma_n^2}}\right),$$

where  $N_{e,k}$  is the number of nearest neighbors for the constellation on the  $k$ th subcarrier, and  $K_{c,k}$  is the adjustment in the argument due to the constellation size. For example, for a quadrature phase shift keying (QPSK) constellation,  $N_{e,k} = 2$ , and  $K_c = 1$ , while for quadrature amplitude modulation (QAM) with 16 points in

the signal constellation,  $N_e = 3$  and  $K_c = 1/5$ . If  $K_{c,k}$  and  $N_{e,k}$  are the same for all subcarriers, the only part that changes as a function of frequency is the effective SNR  $\frac{|H_k|^2}{\sigma_n^2}$ .

Note that if the sampled noise in the time domain is AWGN, the sampled noise in the frequency domain is also AWGN. This can be shown by noting that the FFT of AWGN is as follows:

$$n_k = \frac{1}{N} \sum_{k=0}^{N-1} w_k e^{-j2\pi kn/N}$$

and

$$\begin{aligned} E[n_k] &= 0, \\ \sigma_n^2 &= E[|n_k|^2] \\ &= \frac{1}{N} \sigma_w^2. \end{aligned}$$

Note that the original noise came from a random process with a bandwidth of  $N/T$ . The subcarrier noise has a bandwidth that is on the order of  $1/T$ , hence the factor of  $N$  reduction in variance. However, the factor  $1/N$  is also a product of the normalization of the FFT.

**Example 9.6.** Suppose you have a 128-subcarrier OFDM signal with a baseband channel  $h(t) = \delta(t) + (0.8 + 0.4j)\delta(t - .9T)$ , and each subcarrier is modulated by 16-QAM, where  $\mathcal{E}_c = E[|c_k|^2] = 1$ , while the variance of the frequency domain noise  $E[|n_k|^2] = 0.05$ .

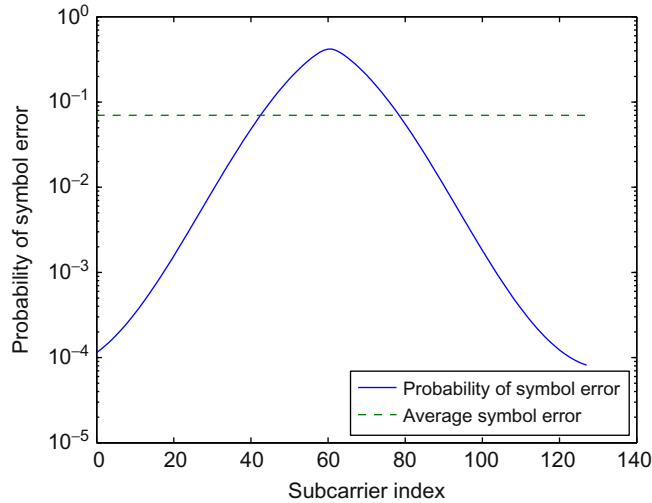
The SNR on each subcarrier is as follows:

$$\begin{aligned} \text{SNR}_k &= \frac{\mathcal{E}_c |H_k|^2}{E[|n_k|^2]} \\ &= 20 |1 + (0.8 + 0.4j)e^{-\frac{j2\pi 0.9Tk}{NT}}|^2 \\ &= 20(1.8 + 1.79 \cos(2\pi 0.9k/N + 0.15\pi)). \end{aligned}$$

Because of 16-QAM, the probability of error for each subcarrier is as follows:

$$\begin{aligned} P_{e,k} &= 3Q(\sqrt{20(1.8 + 1.79 \cos(2\pi 0.9k/N + 0.15\pi)/5)}) \\ &= 3Q(\sqrt{4(1.8 + 1.79 \cos(2\pi 0.9k/N + 0.15\pi))}). \end{aligned}$$

The average  $P_e = \frac{1}{128} \sum_{k=0}^N P_{e,k} = 0.07$ . A plot of the probability of symbol error versus the subcarrier index is shown in Fig. 9.11. Note that even though some subcarriers, eg, those close to the edges of the symbol, have a low probability of error, around  $10^{-4}$ , the subcarriers close to the middle (where the argument of the cosine would be  $\pi$ ) have a probability of error of around  $1/2$ . That means that the bits modulated on those subcarriers have very little chance of being correct.

**FIG. 9.11**

Plot of symbol error probability versus subcarrier index for the example given in Example 9.6.

In Example 9.6, we had a static, frequency-selective channel. If the taps of channels are Rayleigh-fading, ie, zero-mean, complex-valued Gaussian random variables, the frequency response of the channel,  $H_k$ , is also Rayleigh fading. In this case, the average probability of error for an OFDM signal in a frequency-selective Rayleigh-fading channel is

$$E[P_e] \approx \frac{1}{N} \sum_{k=0}^{N-1} N_{e,k} E[Q(\sqrt{\gamma_k K_k})],$$

where  $\gamma_k = \mathcal{E}_c |H_k|^2 / \sigma_n^2$ . Note that  $\gamma_k$  has an exponential distribution. Most OFDM systems in wireless channels use the same constellation type over all subcarriers. This means that the term  $E[Q(\sqrt{\gamma_k K_k})]$  is a constant and is equal to  $1/2 \left(1 - \sqrt{\frac{\Gamma}{\Gamma+2}}\right)$ , where  $\Gamma = K \frac{\mathcal{E}_c \sigma_h^2}{\sigma_n^2}$ . This can be found by noting that  $E[Q(\sqrt{\gamma_k K_k})]$  is a double-integral. By exchanging the order of integration and integrating over  $\gamma_k$  first, the result follows.

As such, the average probability of error in a fading channel for an OFDM system is

$$P_e(\Gamma) = 1/2 \left(1 - \sqrt{\frac{\Gamma}{\Gamma+2}}\right).$$

In the limit,  $\left(1 - \sqrt{\frac{\Gamma}{\Gamma+2}}\right)$  is inversely proportional to  $\Gamma$ . This can be shown by using L'Hôpital's rule.

Accordingly, an uncoded OFDM symbol in a Rayleigh fading channel has an average probability of error that is inversely proportional to the average SNR. In contrast to this, in an AWGN channel, the probability of error decreases exponentially for a large SNR.

**Example 9.7.** Suppose the SNR of the channel for the QPSK constellation in an AWGN channel is 10 dB and the probability of error is  $10^{-3}$ . An additional 3 dB of transmit power will result in a probability of error on the order of  $10^{-6}$ . For a fading channel with an average SNR of 10 dB, the probability of error will be

$$\begin{aligned}\bar{P}_e &= 1/2(1 - \sqrt{10/12}) \\ &= 0.04.\end{aligned}$$

A 3 dB increase in transmit power will result in

$$\begin{aligned}\bar{P}_e &= 1/2(1 - \sqrt{20/22}) \\ &= 0.02,\end{aligned}$$

which is only a decrease in BER of a factor of 2.

Even in a non-fading channel, as long as the channel is frequency-selective, uncoded OFDM will have a rather high probability of error due to low-SNR subcarriers. In static channels where the channel information can be forwarded to the transmitter, waterfilling and bit-loading can be used to compensate for low-SNR subcarriers [9]. When the transmitter knows that there is a subcarrier with an SNR of, say 0 dB, the transmitter may allocate no power to bits to that subcarrier.

However, given a broadcast channel where the transmitter cannot know the channel of every user or if the channel is changing so rapidly that channel information is outdated quite quickly, diversity methods are used to combat the presence of low SNR subcarriers. The diversity method of choice for OFDM is coding and interleaving across the subcarriers. The next two sections discuss bit-loading systems where timely feedback is feasible and coding and diversity for those where feedback is not practical.

---

## 9.5 OFDM: POWER-LOADING AND BIT-LOADING

When a channel is relatively static and the transmitter can adapt the power and modulation for an individual user, power-loading and bit-loading are methods that combat the frequency selectivity of the channel. Power loading assigns the most power to the subcarriers with strong SNR and the least to those with weak SNR. Bit-loading assigns different bits to each subcarrier so that the probability of error on each tone is relatively equal.

Given a frequency-selective channel with frequency response  $H_k$  on each of the subcarriers and a power budget  $P$ , one question is how to assign the power to each subcarrier to maximize the rate.

The capacity for an OFDM system is expressed as

$$C = \sum_{n=0}^{N-1} \log_2 \left( 1 + \frac{P_n |H_n|^2}{\sigma^2} \right), \quad (9.9)$$

where  $\sum_{n=0}^{N-1} P_n = P$  is the power budget.

How to assign the power is solved by taking the derivative of the capacity with respect to  $P_n$  and with the Lagrange multiplier constraint,  $\lambda(P - \sum_{n=0}^{N-1} P_n)$  as well as the additional constraint that  $P_n > 0$  for all  $n$ . This leads to allocating power according to the *waterfilling* method:

$$P_n = \begin{cases} \nu - \frac{\sigma^2}{|H_n|^2}, & \nu > \frac{\sigma^2}{|H_n|^2}, \\ 0, & \text{otherwise,} \end{cases} \quad (9.10)$$

where  $\nu$  is chosen so that  $\sum_{n=0}^{N-1} P_n = P$ . This is called waterfilling, as one can think of inverting channels, ie, examining the inverse of the channel SNR  $\frac{|H_n|^2}{\sigma^2}$ , and filling up the resulting signal with water until it reaches the level  $\nu$ .

**Example 9.8.** Suppose  $N = 16$  and  $\frac{|H_k|^2}{\sigma^2}$  equal to 100 for  $k = 0, 1, 2, \dots, 9$  and equal to 1 for  $k = 11, \dots, 15$ .

In the first case, let us assume that the power budget is only 1 W. (Note that in most real systems, the allocated power will be on the order of milliwatts, not watts. Here, we are using simple numbers for illustrative purposes.) Then we want to find  $\nu$  such that  $P_n > 0$  and  $P = 1$ . Then, by setting  $\nu = 1/9.1$ ,  $P_n = 0.1$  for  $n = 0, \dots, 9$ , and 0 otherwise. In this case, power is allocated exclusively to the first 10 subcarriers.

Note that the capacity for the system with waterfilling is  $C = 10 \times \log_2(1 + 10) = 34.6$  bits. In a system with equal power allocation across all bits, ie,  $P_n = 1/16$ , the capacity would be  $C = 10 \times \log_2(1 + 100/16) + 6 \times \log_2(1 + 1/16) = 29$  bits. In this case, waterfilling increases the capacity of the OFDM signal.

In the second case, let us assume that the power budget is 100 W. In this case, if  $\nu = 6.63$ , then  $P_n = 6.62$  for  $n = 0, \dots, 9$  and 5.63 for the last six subcarriers.

In this case, the power is much more equally divided. With the higher power budget, with waterfilling  $C = 10 \log_2(1 + 663) + 6 \log_2(1 + 5.63) = 110.1$  bits while with uniform distribution, the capacity is  $C = 10 \log_2(1 + 100 \times 100/16) + 6 \log_2(1 + 100/16) = 110$  bits.

Note that as the power budget increases, the water-filling as in the last example evens out. Waterfilling displays a large difference in power allocation when the SNRs between the subchannels are significantly different or when the power budget is low, leading to a low-water level. This is analogous to a tidal river. When the river is high, bumps in the waterbed are not visible. Only as the water level decreases does one see the differences in the signal.

Waterfilling can also be seen as finding the appropriate subband for transmission. On-off waterfilling [19,20] assigns equal power to those subcarriers that have reasonable SNR and no power is assigned to the remaining subcarriers. On-off waterfilling can have virtually the same rate as a water-filled signal and is much simpler to implement.

**Example 9.9.** Suppose  $H_k = 1 + 0.5e^{j2\pi k/N}$ ,  $N = 16$  and  $\sigma^2 = 1$ . Furthermore, suppose that  $P = 1$ .

Then  $|H_k|^2 = 2 + \cos(2\pi k/N)$ , and then if  $\nu = 0.66$ ,  $P_n = 0.2156, 0.2, 0.15, 0.05$  for  $n = 0, 1, 2, 3$   $P_n = 0.05, 0.15, 0.2$  for  $n = 13, 14, 15$ , and zero otherwise.

In this case, the capacity is  $C = 2.57$  bits. If, instead of assigning the power as above, one assigns equal power to subcarriers 0, 1, 2, 14, and 15,  $P_n = 0.2$ , the capacity is 2.53 bits.

In general, judicious power allocation is a reliable way to improve throughput when the channel is one-to-one and stable enough to ensure reliable feedback.

Whether waterfilling, on-off power allocation or equal power allocation is used, the SNR on each subcarrier will most likely vary. Given a reasonable estimate of the channel at the transmitter, the transmitter can adjust the constellation size for each subcarrier to ensure that the probability of error across all subcarriers does not vary significantly. Determining how to assign the bits to each subcarrier is an art. There are several algorithms for bit-loading that can be found in references such as [9].

## 9.6 OFDM: DIVERSITY AND CODING

Diversity is a way to decrease the probability of error when the channel is unknown at the transmitter. One cannot assign bits and power to the strong subcarriers, but one can use the diversity of the channel to decrease the probability of error.

The basic idea behind diversity is the following. One signal alone can fade unpredictably and can lead to poor error rates. But if one has two or more versions of the same information and each version of the signal is faded independently, the likelihood that all the signals have poor SNR is quite low. With diversity, the designer is banking on the probability that there will exist strong signal versions of the data that can boost the success of the weak signals.

### 9.6.1 OFDM AND CODING

As shown in Section 9.4.1, the probability of error for uncoded OFDM (with an equal number of bits on each subcarrier) is high due to the variation of the SNR across subcarriers. When power- and bit-loading are impractical, most OFDM systems use forward error-control (FEC) coding and interleaving to overcome the difficulties of low-SNR subcarriers. In a frequency-selective channel, error-control coding reduces the probability of error by increasing the effect.

When decoding, an error-control code one can make *hard* decisions or *soft* decisions. The term “hard decision” implies that the demodulator has mapped the received signal to bit values before the decoder. The term “soft decision” implies that the decoder has some information about the reliability of the signal. Sometimes this can be a quantized value, and sometimes this relates to the relative SNR of the symbol whence the bit came. A measure for the performance of the code is the minimum distance between code words. The larger the distance between code

words, the lower the probability that one code word is mistaken for another. When soft decisions are used, the distance between codewords is affected by the SNR of the individual components of the codewords.

For an OFDM signal with a frequency-selective channel, without prior knowledge at the transmitter, one cannot predict where the low SNR subcarriers will lie. FEC produces codewords that differ by at least  $d_{\text{free}}$  bits. The effective SNR of the coded system increases by this distance  $d_{\text{free}}$ . Ideally, one distributes the codeword across several subcarriers so that elements of a codeword have both high and low SNR. However, if adjacent bits in the codeword are found on successive subcarriers, the SNR on all the bits will have similar values. This is because the frequency response on adjacent channels will be highly correlated.

**Example 9.10.** Suppose you have a linear error control code with a codeword of length 8 bits and the codewords are 00000000, 01010101, 10101010, and 11111111.

Further suppose that you have 8 subcarriers with BPSK modulation on each one and the frequency response is  $H_k = 1 + e^{j2\pi k/8}$ . The distance-squared between the codewords would be as tabulated below:

Codeword 1	Codeword 2	Distance Squared Between Codewords
00000000	01010101	$\sum_{k=1,3,5,7} (2 + 2 \cos(2\pi k/8)) / \sigma^2 = 8$
00000000	10101010	$\sum_{k=0,2,4,6} (2 + 2 \cos(2\pi k/8)) / \sigma^2 = 8$
00000000	11111111	$\sum_{k=1,2,\dots,7} (2 + 2 \cos(2\pi k/8)) / \sigma^2 = 16$
01010101	10101010	$\sum_{k=1,2,\dots,7} (2 + 2 \cos(2\pi k/8)) / \sigma^2 = 16$
01010101	11111111	$\sum_{k=0,2,4,6} (2 + 2 \cos(2\pi k/8)) / \sigma^2 = 8$
10101010	11111111	$\sum_{k=1,3,5,7} (2 + 2 \cos(2\pi k/8)) / \sigma^2 = 8$

So in this case, the minimum distance-squared between codewords is 8. Note that if our codewords had been 00000000, 11110000, and 00001111 instead, where each bit is assigned to its respective subcarrier, the distance-squared between codewords would be as follows:

Codeword 1	Codeword 2	Distance Squared Between Codewords
00000000	11110000	$\sum_{k=0,1,2,3} (2 + 2 \cos(2\pi k/8)) / \sigma^2 = 10$
00000000	00001111	$\sum_{k=4,5,6,7} (2 + 2 \cos(2\pi k/8)) / \sigma^2 = 6$
00000000	11111111	$\sum_{k=1,2,\dots,7} (2 + 2 \cos(2\pi k/8)) / \sigma^2 = 16$
11110000	00001111	$\sum_{k=1,2,\dots,7} (2 + 2 \cos(2\pi k/8)) / \sigma^2 = 16$
11110000	11111111	$\sum_{k=4,5,6,7} (2 + 2 \cos(2\pi k/8)) / \sigma^2 = 6$
00001111	11111111	$\sum_{k=0,1,2,3} (2 + 2 \cos(2\pi k/8)) / \sigma^2 = 6$

This example shows how the ordering of the bits in a codeword with respect to the subcarriers of the OFDM signal can affect the performance. For a given code, one can change the order of the components of the codeword through interleaving.

In OFDM, error control coding is applied with interleaving across the subcarriers to mitigate the poor performance of the low SNR subcarriers. Suppose you have a frequency-selective channel with the following frequency responses:  $H_k$ ,  $k = 1, \dots, N$ . Coded bits correspond to modulated symbols. One can change the order and SNR of the modulated symbols through interleaving.

**Example 9.11.** Suppose you have QPSK modulation on every tone,  $N = 128$  subcarriers and a rate 1/2 convolutional encoder. After the encoder, each 2-bit output can be mapped directly to a QPSK constellation value  $\mathbf{c}_1, \dots, \mathbf{c}_N$ .

A *block* encoder with interleaver depth 8 would map out the 128 symbols as follows:

$$\begin{array}{ccccccc} \mathbf{c}_1 & \mathbf{c}_2 & \dots & \mathbf{c}_{16}, & & & \\ \mathbf{c}_{17} & \mathbf{c}_{18} & \dots & \mathbf{c}_{32}, & & & \\ & & \vdots & & & & \\ \mathbf{c}_{113} & \mathbf{c}_{114} & \dots & \mathbf{c}_{128}. & & & \end{array}$$

The vertical lines are read out first so that  $\mathbf{c}_1$  maps to  $H_1$ ,  $\mathbf{c}_{17}$  maps to  $H_2$ , etc. So the bits fed into the decoder would be from  $H_1\mathbf{c}_1, H_9\mathbf{c}_2, H_{17}\mathbf{c}_3, H_{25}\mathbf{c}_4, \dots, H_{128}\mathbf{c}_{128}$ . Note that rather than interleave constellation symbols, one can interleave the bits directly before modulation as in bit-interleaved coded modulation [21].

If the minimum path between two code words is  $d_{\min, \text{coded}}^2 = \sum_{k \in \mathcal{I}} |H_k|^2 d_k^2 \geq d_{\min}^2 \sum_{k \in \mathcal{I}} |H_k|^2$ , where  $\mathcal{I}$  is the indexing set across frequency subcarriers, the question is, how much diversity can be found in an OFDM coded system? The key lies in the correlation of the frequency response and the depth of the interleaving. As in Refs. [22–24], the probability of error for a linear code word is upper bounded by

$$P_e \leq N_e Q \left( \sqrt{\frac{d_{\min}^2 \sum_{i_k \in \mathcal{I}_{d_{\text{free}}}} |H_{i_k}|^2}{\sigma^2}} \right), \quad (9.11)$$

where  $\sigma^2$  is the variance of the noise,  $d_k$  is the minimum distance between the modulated bits,  $\mathcal{I}_{d_{\text{free}}}$  is an index of points that have a minimum distance from the all-zeros codeword, and  $N_e$  is the number of paths that are  $d_{\text{free}}$  bits away. Note that if we have a large constellation, the distance between bits from the codeword may differ. For example, if a path of a convolutional code is  $d_{\text{free}}$  bits from the all-zeros path, the soft-distance between bits may vary depending on whether the two bits come from adjacent points in the constellation or points that are at opposite ends of the constellation.

Based on Eq. (9.11) the average  $P_e$  can be bounded by noting that for Rayleigh-fading,  $H_k$  are correlated, Gaussian random variables. As in Refs. [22–24] the covariance matrix can be found by noting that for a time domain channel  $h(t) = \sum_{k=1}^L \alpha_k \delta(t - \tau_k)$ ,

$$|H(i_k)|^2 = \alpha^* \mathbf{F}_{i_k}^* \mathbf{F}_{i_k} \alpha,$$

where  $\mathbf{E}_{i_k} = \begin{pmatrix} 1 \\ e^{-\frac{j2\pi\tau_1 i_k}{NT}} \\ \vdots \\ e^{-\frac{j2\pi\tau_L i_k}{NT}} \end{pmatrix}$ , assuming without loss of generality that  $\tau_1 = 0$ ,

$\alpha = \begin{pmatrix} \alpha_1 \\ \vdots \\ \alpha_L \end{pmatrix}$  and  $\mathbf{E}_{i_k} \alpha = H_{i_k}$ .

If  $\alpha_1, \dots, \alpha_L$  are independent, identically-distributed zero-mean complex-valued Gaussian random variables, then as in Ref. [25],

$$\sum_{i_k \in \mathcal{I}_{d_{\text{free}}}} |H_{i_k}|^2 = \begin{pmatrix} u_1 & \dots & u_L^* \end{pmatrix} \mathbf{S} \begin{pmatrix} u_1 \\ \vdots \\ u_L \end{pmatrix},$$

where  $\mathbf{U}\mathbf{S}\mathbf{U}'$  is the singular value decomposition of  $R_\alpha^{1/2} \sum_{i_k \in \mathcal{I}_{d_{\text{free}}}} \mathbf{E}_{i_k}^* \mathbf{E}_{i_k} R_\alpha^{1/2}$ . Note that this is the same as the singular value decomposition of  $R_\alpha \sum_{i_k \in \mathcal{I}_{d_{\text{free}}}} \mathbf{E}_{i_k}^* \mathbf{E}_{i_k}$ . This in turn means that  $\sum_{i_k \in \mathcal{I}_{d_{\text{free}}}} |H_{i_k}|^2$  is a random variable whose distribution is the same as  $\sum_{i=1}^L \lambda_i |v_i|^2$ , where  $v_i$  is a zero-mean complex-valued Gaussian random variable variance and therefore,  $|u_i|^2$  is an exponentially distributed Gaussian random variable with parameter 1 and the  $\lambda_i$ s are the singular values of  $R_\alpha \sum_{i_k \in \mathcal{I}_{d_{\text{free}}}} \mathbf{E}_{i_k}^* \mathbf{E}_{i_k}$ .

So how much diversity is present in coded OFDM with interleaving across the tones? It depends on the number of non-zero eigenvalues. This in turn is bounded by the rank of  $\sum_{i_k \in \mathcal{I}_{d_{\text{free}}}} \mathbf{E}_{i_k}^* \mathbf{E}_{i_k}$ . This rank is bounded by two factors:  $L$ , the number of taps in the channel and  $d_{\text{free}}$ , the number of differences in the code path calculation.

Note that while each individual matrix  $\mathbf{E}_{i_k}^* \mathbf{E}_{i_k}$  has rank 1, the sum  $\sum_{i_k \in \mathcal{I}_{d_{\text{free}}}} \mathbf{E}_{i_k}^* \mathbf{E}_{i_k}$  has a rank that is less than or equal to the number of addends in the sum. But as  $\sum_{i_k \in \mathcal{I}_{d_{\text{free}}}} \mathbf{E}_{i_k}^* \mathbf{E}_{i_k}$  is an  $L \times L$  matrix, it cannot exceed  $L$  nor can it exceed  $d_{\text{free}}$ . When designing a code for diversity, the amount of diversity is dependent both on the minimum distance of the code and the number of independent taps in the time domain channel.

**Example 9.12.** Suppose  $N = 128$  and  $h(t) = \alpha_1 \delta(t) + \alpha_2 \delta(t - 1.5T)$ , where  $\alpha_1$  and  $\alpha_2$  are zero-mean complex-valued Gaussian random variables. Further, suppose that the interleaving depth is 8 and the minimum distance between the paths in convolutional code is  $d_{\text{free}} = 5$ .

Therefore,

$$\begin{aligned} \sum_{i_k \in \mathcal{I}_{d_{\text{free}}}} \mathbf{E}_{i_k} \mathbf{E}_{i_k}^* &= \sum_{k=0}^4 \begin{pmatrix} 1 & e^{-\frac{j2\pi(k+i) \times 8 \times 1.5}{128}} \\ e^{\frac{j2\pi(k+i) \times 8 \times 1.5}{128}} & 1 \end{pmatrix} \\ &= \begin{pmatrix} 5 & e^{-j2\pi i 12/128} \frac{1 - e^{-j2\pi 60/128}}{1 - e^{-j2\pi 12/128}} \\ e^{j2\pi i 12/128} \frac{1 - e^{j2\pi 60/128}}{1 - e^{j2\pi 12/128}} & 5 \end{pmatrix}. \end{aligned}$$

and the eigenvalues of  $R_\alpha \sum_{i_k \in \mathcal{I}_{d_{\text{free}}}}$  are  $\lambda_1 = 6.48 \frac{\Gamma \sigma^2}{1.5}$  and  $\lambda_2 = \frac{1.02 \Gamma \sigma^2}{1.5}$ . The average probability of error for such a code would be bounded by

$$P_e \leq N_e/2 \left( 1.19 \left( 1 - \sqrt{\frac{\frac{6.48\Gamma}{1.5}}{\frac{6.48\Gamma}{1.5} + 2}} \right) - 0.19 \left( 1 - \sqrt{\frac{\frac{1.02\Gamma}{1.5}}{\frac{1.02\Gamma}{1.5} + 2}} \right) \right).$$

Though  $d_{\text{free}} = 5$ , we have only 2-path diversity. However, the difference between  $d_{\text{free}} = 5$  and the diversity level of two shows up as an increase in the effective average SNR. The two eigenvalues,  $\lambda_1$  and  $\lambda_2$ , sum to  $5\Gamma\sigma^2$ , ie, a 5-fold increase in the average SNR. The bounded probability of error is shown in Fig. 9.12.

So frequency diversity in OFDM can be achieved through coding and interleaving across subcarriers. However, this diversity is limited by three factors: the amount of diversity inherent in the channel itself, the interleaving scheme of the code, and the minimum distance of the code.

### 9.6.2 OUTAGE CAPACITY AND OFDM

The above analysis focuses on the average probability of error of a coded system. However, the average probability of error only gives part of the picture. Most wireless systems transmit a block of data and can tolerate a small percentage, say 5%, of those

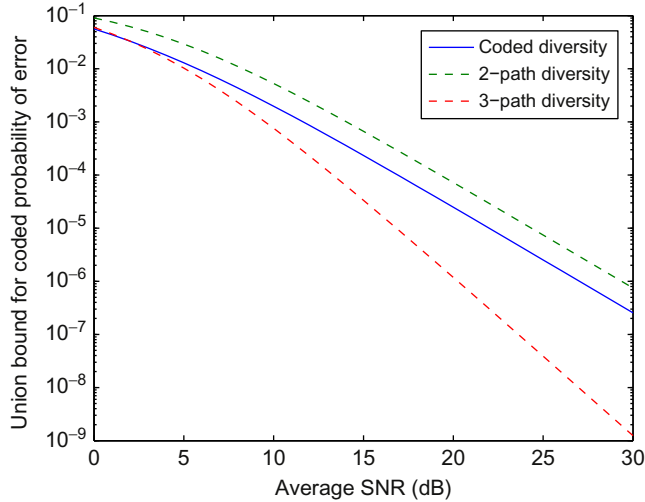


FIG. 9.12

Plot of union bound for average probability of error for the code given in Example 9.12. This is plotted along with the average probability of error for 2- and 3-path diversity. Note that though  $d_{\text{free}} = 5$ , the diversity of the system is at most 2.

blocks being in error. As such, the *outage capacity* of an OFDM symbol is of interest. Given an instantaneous OFDM symbol with equal power on every subcarrier, the normalized capacity of that symbol is

$$C_i = \sum_{n=1}^N \log_2(1 + |H_{i,n}|^2 \Gamma) / N.$$

Over a collection of frequency responses,  $\{H_{i,n}\}$ ,  $n = 1, \dots, N$ , there will be a set of capacities,  $\{C_i\}$ . Let  $C_X$  be the capacity value such that  $1 - X\%$  of the capacity values are greater than  $C_X$ . Then in theory, we can transmit outage free  $1 - X\%$  of the time as long as  $R \leq C_X$ .  $C_X$  is the  $X\%$  outage capacity.

**Example 9.13.** Suppose  $h(t) = \delta(t) + \alpha_1 \delta(t - T)$ , where  $\alpha_1$  is a zero-mean complex-valued Gaussian random variable with variance 1. Suppose  $N = 128$ , then

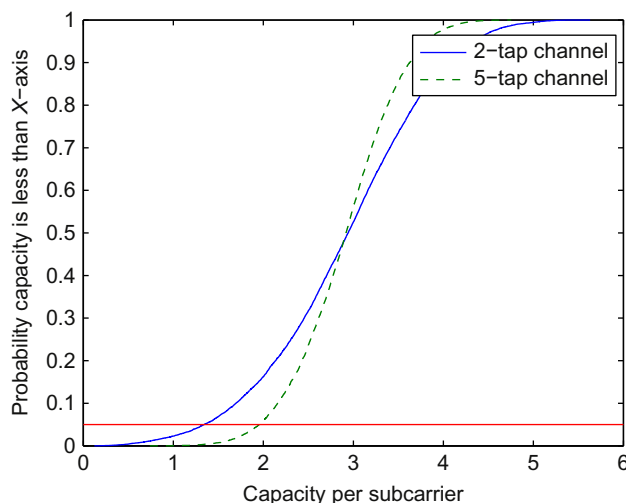
$$H_k = \alpha_0 + \alpha_1 \exp(-j2\pi k/N),$$

$$|H_k|^2 = |\alpha_0|^2 + |\alpha_1|^2 + 2|\alpha_1||\alpha_0| \cos(2\pi k/N + \theta_1 - \theta_0),$$

where  $\alpha_1 = |\alpha_1|e^{j2\pi\theta_1}$  and  $\alpha_0 = |\alpha_0|e^{j2\pi\theta_0}$ . The cumulative density function (cdf) of the capacity  $C_i$  for the 2-tap channel is found in Fig. 9.13. From the cdf one can see that the 5% outage capacity is around 1 bit/s/Hz and that there is wide variation in the capacities for a two-tap channel. If we repeat this for a 5-tap channel, assuming a uniform delay spread, then the outage capacity is increased by 1 bit. This is also shown in Fig. 9.13. If we found the average capacity of both channels, it would be the same, 2.9 bits.

The reason the 2-tap channel has a lower outage capacity than the 5-tap channel is the following. In a 2-tap channel, there is less variability in the channel's frequency response than there that of 5-tap channel. So the more taps in the channel, the more likely is for a subset of subcarriers with large enough SNR to dominate the capacity calculation. For the two-tap channel, the maximum SNR is proportional to the random variable  $|\alpha_0|^2 + |\alpha_1|^2 = \gamma$ . This random variable has the probability density function (pdf),  $\frac{\gamma}{\Gamma^2} \exp(-\gamma/\Gamma)u(\gamma)$ , when both  $\alpha_0$  and  $\alpha_1$  are identically-distributed complex-valued zero-mean Gaussian random variables. So the probability that the maximum value of  $|H_k|^2 < X$  is small, but not zero. However, when the maximum SNR is proportional to  $\gamma = \sum_{i=1}^L |\alpha_i|^2$  where  $L > 2$ , the probability that the maximum capacity across all subcarriers is less than 1 bit is much, much smaller.

The smaller the variability of the frequency response, the larger the variety of capacity values over a set of channels. But when there is large variability within the frequency response of the channel, it is more likely that some subcarriers' SNRs will be large enough to ensure a larger outage capacity. In summary, both the SNR and the delay spread of the channel determine the outage capacity and the rate at which one can transmit in the presence of uncertainty.

**FIG. 9.13**

Cumulative density function for capacity for a 2-tap channel and 5-tap channel and a 128-subcarrier OFDM signal. The average SNR is 10 dB.

The outage capacity argument provides for a non-zero period where transmission will fail, but most communications are designed to have a certain percent, eg, 10% failure or retransmission rate.

In Ref. [26] the outage capacity was found using fixed constellation size. Typically, OFDM system designers will adapt the number of bits on each subcarrier based on the average SNR. The implications from Ref. [26] are that rather than reducing the number of bits on each subcarrier, the designer could keep a constant modulation on every subcarrier and adapt the coding rate in a diversity-rich environment. This allows the code to take advantage of the high SNR subcarriers. The trick is designing high-rate codes that can take advantage of this SNR.

## 9.7 CONCLUSIONS

OFDM is an excellent choice for wireless communications. It is flexible and does not require complicated equalization. Because it divides the spectrum into multiple subcarriers, it can be designed to avoid interference within the spectrum. Diversity and improved performance can be attained through coding and interleaving. It is an elegant solution for any technique that requires non-frequency-selective signals, eg, MIMO. It also provides a useful starting point for researchers and system designers.

## Appendix CORRELATED DIVERSITY SIGNALS

Suppose you have  $L$  received values,  $y_i = \alpha_i x + n_i$ , but now the  $\alpha_i$  received zero-mean complex-valued Gaussian values are correlated, rather than independent. This could occur if the antennas receiving the values are closely spaced or in the case of OFDM, if the different values are closely spaced in frequency. How does this affect the diversity receiver?

Finding the symbol error rate for maximum ratio combining with correlated signals is relatively easy thanks to a trick from Turin [25]. Suppose you have  $L$  correlated zero-mean, complex-valued Gaussian random vectors,  $\alpha = (\alpha_1, \dots, \alpha_L)$ . We are interested, as before, in the sum  $\gamma = \sum_{i=1}^L |\alpha_i|^2$ , which is the inner product of  $\alpha$  with itself.

First suppose that the covariance matrix for  $\alpha$  is  $\mathbf{R}$ .

The random vector  $\tilde{\alpha} = \mathbf{u}\mathbf{R}^{1/2}$ , where  $\mathbf{u} = (u_1, \dots, u_L)$  is a vector of zero-mean, unit-variance, independent complex-valued Gaussian random variables that behaves like  $\alpha$ . Both  $\alpha$  and  $\tilde{\alpha}$  are zero-mean complex-valued Gaussian random variables, and the covariance matrix of  $\tilde{\alpha}$  is the same as  $\alpha$  by construction. So

$$\begin{aligned}\tilde{\gamma} &= \langle \tilde{\alpha}, \tilde{\alpha}^* \rangle \\ &= \mathbf{u}\mathbf{R}^{1/2}\mathbf{R}^{H/2}\mathbf{u}^* \\ &= \mathbf{u}\mathbf{R}\mathbf{u},\end{aligned}$$

so the inner product of the correlated Gaussian random variables acts like a modified inner product with the Hermitian symmetric matrix  $\mathbf{R}$  in the middle. The trick from Turin is to decompose  $\mathbf{R}$  into unitary and diagonal matrices. One can use the singular-value decomposition and find

$$\tilde{\gamma} = \mathbf{u}\mathbf{E}\mathbf{S}\mathbf{E}^*\mathbf{u}^*,$$

where  $\mathbf{E}\mathbf{E}^* = \mathbf{E}^*\mathbf{E} = \mathbf{I}$  the identity matrix and  $\mathbf{S}$  is a diagonal matrix of the eigenvalues of  $\mathbf{R}$ ,  $\lambda_i \geq 0$ .

The new vector  $\mathbf{v} = \mathbf{u}\mathbf{E}$  is zero-mean, complex-valued Gaussian, identically distributed with unit variance 1. The advantage of this way of writing the decision metric  $\gamma$  is that it is now the sum of independent random variables. So

$$\begin{aligned}\tilde{\gamma} &= \mathbf{v}\mathbf{S}\mathbf{v}^* \\ &= \sum_{i=1}^L \lambda_i |v_i|^2,\end{aligned}$$

and the inner product of correlated Gaussian random vectors behaves like the inner product of independent Gaussian random variables, each with a different variance.

To find the pdf of  $\gamma$ , one can use characteristic functions. The characteristic function of  $\gamma$  is

$$\begin{aligned}\Phi(f) &= \prod_{i=1}^L \frac{1}{j2\pi f\lambda_i + 1} \\ &= \sum_{i=1}^L \frac{A_i}{j2\pi f\lambda_i + 1},\end{aligned}$$

where

$$A_i = \frac{\lambda_i^{L-1}}{\prod_{k \neq i} (\lambda_i - \lambda_k)}.$$

This leads to the pdf of  $\gamma$  as

$$f(\gamma) = \sum_{i=1}^L \frac{A_i}{\lambda_i} \exp\left(-\frac{\gamma}{\lambda_i}\right).$$

From this, the average probability of error assuming distinct  $\lambda_i$ s is

$$E[P_e] = \sum_{i=1}^L \frac{A_i}{2} (1 - \sqrt{\lambda_i} 2 + \lambda_i).$$

For large  $\lambda_i$ ,

$$\begin{aligned} E[P_e] &\approx \sum_{i=1}^L \frac{A_i}{2\lambda_i} \\ &= \frac{\sum_{i=1}^L A_i \prod_{k \neq i} \lambda_k}{2 \prod_{i=1}^L \lambda_i}. \end{aligned}$$

Note that this means with  $L$  correlated paths, we can still achieve diversity. However, the diversity is limited by the correlation.

**Example I.14.** Suppose you apply maximum ratio combining with three different versions of the signal,  $y_i = \alpha_i x + n_i$ ,  $i = 1, \dots, 3$ , and the covariance matrix

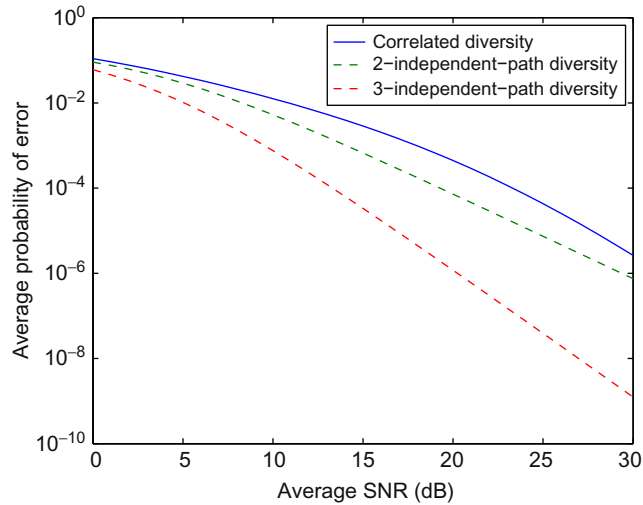
$$\mathbf{R} = \Gamma \begin{pmatrix} 1 & 0.99 & 0.97 \\ 0.99 & 1 & 0.99 \\ 0.97 & 0.99 & 1 \end{pmatrix}.$$

The singular values of this matrix are  $2.97\Gamma$ ,  $.03\Gamma$ , and  $.003\Gamma$ . Then, the random variable  $\gamma = \sum_{i=1}^3 |\alpha_i|^2$  has the same probability density function as  $\tilde{\gamma} = \Gamma(2.97|v_1|^2 + 0.03|v_2|^2 + 0.003|v_3|^2)$ . The partial fraction expansion coefficients are

$$\begin{aligned} A_1 &= 1.0113, \\ A_2 &= -0.0115, \\ A_3 &= 0.0001. \end{aligned}$$

For a BPSK channel,

$$\begin{aligned} E[P_e] &\approx 1/2(1.0113(1 - \sqrt{2.97\Gamma} 2 + 2.97\Gamma) \\ &\quad - 0.045(1 - \sqrt{0.03\Gamma} 2 + 0.03\Gamma) \\ &\quad + 0.0001(1 - \sqrt{0.0001\Gamma} 2 + 0.0001\Gamma)). \end{aligned}$$

**FIG. I.14**

Plot of the average probability of error for the correlated paths given in [Example I.14](#).

The probability of error for this case is plotted in [Fig. I.14](#). Because the 3 paths are so highly correlated, only one path dominates the distribution of the SNR and the resulting average probability of error.

Depending on the relative correlation of the components, the amount of diversity that results will vary and depends on the number and relative spread of the eigenvalues of the covariance matrix of the complex-valued Gaussian random variables that represent the gain and phase of each path.

## REFERENCES

- [1] R.R. Mosier, R.G. Clabaugh, Kineplex, a bandwidth-efficient binary transmission system, *Trans. Am. Inst. Elect. Eng.* 76 (6) (1958) 723–728.
- [2] B. Saltzberg, Performance of an efficient parallel data transmission system, *IEEE Trans. Commun. Tech.* 15 (6) (1967) 805–811.
- [3] M. Zimmerman, A.L. Kirsch, The AN/GSC-10 (KATHRYN) variable rate data modem for HF radio, *IEEE Trans. Commun. Tech.* 15 (2) (1967) 197–204.
- [4] R. Chang, R. Gibby, A theoretical study of performance of an orthogonal multiplexing data transmission scheme, *IEEE Trans. Commun. Tech.* 16 (4) (1968) 529–540.
- [5] B. Pierce, D. Sworder, Effective application of forward-acting error-control coding to multichannel HF data modems, *IEEE Trans. Commun. Tech.* 18 (4) (1970) 281–294.
- [6] S. Weinstein, P. Ebert, Data transmission by frequency-division multiplexing using the discrete Fourier transform, *IEEE Trans. Commun. Tech.* 19 (5) (1971) 628–634.
- [7] L.J. Cimini, Jr., Analysis and simulation of a digital mobile channel using orthogonal frequency division multiplexing, *IEEE Trans. Commun.* 33 (7) (1985) 665–675.

- [8] B. LeFloch, R. Halbert-Lassalle, D. Castelain, Digital sound broadcasting to mobile receivers, *IEEE Trans. Consumer Elect.* 35 (3) (1989) 493–503.
- [9] T. Starr, J.M. Cioffi, P.J. Silverman, *Understanding Digital Subscriber Line Technology*, Prentice-Hall, Upper Saddle River, NJ, 1999.
- [10] R.A. Fessenden U.S. Patent US 960,631, June 7, 1907.
- [11] J.M. Wozencraft, I.M. Jacobs, *Principles of Communication Engineering*, Wiley, New York, 1965.
- [12] J.M. Cioffi, Reader for a course in Digital Communications: Signal Processing, <http://www.stanford.edu/group/cioffi/ee379a/>, 2013.
- [13] W. Jakes, *Microwave Mobile Communications*, Wiley-IEEE Press, Piscataway, NJ, 1994.
- [14] A. Peled, A. Ruiz, Frequency domain data transmission using reduced computational complexity algorithms, in: *IEEE International Conference on Acoustics, Speech and Signal Processing (ICASSP'80)*, 1980, pp. 964–967.
- [15] J.L. Seoane, S.K. Wilson, S. Gelfand, Analysis of intertone and interblock interference in OFDM when the length of the cyclic prefix is shorter than the impulse response of the channel, in: *Global Telecommunications Conference, Globecom '97*, 1997, pp. 32–36.
- [16] B. Muquet, Z. Wang, G.B. Giannakis, M. DeCourville, P. Duhamel, Cyclic prefixing or zero padding for wireless multicarrier transmissions?, *IEEE Trans. Commun.* 50 (12) (2002) 2136–2148.
- [17] J.-J. van de Beek, M. Sandell, M. Börjesson, ML estimation of time and frequency offset in OFDM Systems, *IEEE Trans. Signal Process.* 45 (7) (1997) 1800–1805.
- [18] D. Declercq, M. Fossorier, E. Biglieri (Eds.), *Channel Coding: Theory, Algorithms, and Applications*, Academic Press Library in Mobile and Wireless Communications, Elsevier, San Diego, CA, 2014.
- [19] P. Chow, Bandwidth optimized digital transmission techniques for spectrally shaped channels with impulse noise, Ph.D. thesis, Stanford University, Stanford, CA, 1993.
- [20] W. Yu, J.M. Cioffi, Constant-power waterfilling: performance bound and low-complexity implementation, *IEEE Trans. Commun.* 54 (1) (2006) 23–28.
- [21] G. Caire, G. Taricco, E. Biglieri, Bit-interleaved coded modulation, *IEEE Trans. Inform. Theory* 44 (3) (1998) 927–946.
- [22] S.K. Wilson, *Digital Audio Broadcasting in a fading and dispersive channel*, Ph.D. thesis, Stanford University, Stanford, CA, 1994.
- [23] A. Chini, *Multi-Carrier Modulation in Frequency Selective Fading Channels*, Ph.D. thesis, Carleton University, Ottawa, Canada, 1994.
- [24] E. Akay, E. Ayanoglu, Achieving full frequency and space diversity in wireless systems via BICM, OFDM, STBC, and Viterbi decoding, *IEEE Trans. Commun.* 54 (12) (2006) 2164–2172.
- [25] G.L. Turin, On optimal diversity reception, II, *IRE Trans. Commun. Syst.* 10 (1) (1962) 22–31.
- [26] G. Lim, S.K. Wilson, L.J. Cimini, Jr., D.P. Taylor, On higher order modulations for OFDM in frequency-selective fading channels, *IEEE Commun. Lett.* 17 (4) (2013) 641–644.

# Spread spectrum signaling in wireless communications 10

S.L. Miller\*

*Texas A&M University, College Station, TX, United States*

## CHAPTER OUTLINE

<b>10.1 Fundamentals of Spread Spectrum Communications .....</b>	<b>369</b>
10.1.1 Motivation.....	369
10.1.2 Low Probability of Intercept/Anti-Jam Capabilities .....	370
10.1.3 Direct Sequence Spread Spectrum .....	372
10.1.4 FH Spread Spectrum.....	375
10.1.5 Code Division Multiple Access.....	376
10.1.6 Code Sequences .....	381
<b>10.2 Spread Spectrum and CDMA for Wireless Channels.....</b>	<b>386</b>
10.2.1 DS-SS in a Wireless Channel: RAKE Receivers .....	386
10.2.2 Multicarrier CDMA .....	391
10.2.3 Cellular CDMA.....	392
<b>10.3 CDMA Standards .....</b>	<b>393</b>
10.3.1 2G Cellular CDMA: IS-95.....	393
10.3.2 3G Cellular CDMA .....	395
<b>References.....</b>	<b>396</b>

## 10.1 FUNDAMENTALS OF SPREAD SPECTRUM COMMUNICATIONS

### 10.1.1 MOTIVATION

In many applications, a digital communication system must operate in the presence of other impairments in addition to just thermal noise. The technique of spread spectrum was initially developed to provide a digital communication system the capability of being somewhat robust to various forms of intentional interference found in military environments [1–5]. However, it has been seen that many of these military communication techniques have important commercial applications as well [6,7]. In addition to providing robustness to intentional jamming, spread spectrum techniques

also provide robustness to a variety of unintentional forms of interference that are found in today's wireless world.

We start by examining the effect a typical interferer might have on a very simple BPSK-based communication system. Suppose the system transmits one data symbol every  $T_s$  seconds and let  $B$  be the bandwidth the BPSK signal occupies. For example, if “sinc” pulse shapes were used, the bandwidth of the system would be  $B = 1/T_s$  Hz. Now suppose that in addition to the desired signal and the usual white noise, the received signal also has an interference component,  $j(t)$ . Furthermore, assume that the interfering signal has a total power of  $J$  spread over the bandwidth  $B$  so that the spectral density of the interferer's signal is equal to

$$S_{jj}(f) = \frac{J}{2B}, \quad |f - f_c| < B/2.$$

The white noise is taken to have a spectral density of  $N_o/2$ .

In order to make the problem easy to analyze, it is assumed that the interfering signal can be modeled as Gaussian noise. Assuming the white noise and the interference are independent, the interfering signal has the effect of adding to the spectral density of the noise, and the resulting probability of error of a typical detector is then

$$P_e = Q\left(\sqrt{\frac{2E_s}{N_o + J/B}}\right) = Q\left(\sqrt{\frac{2E_s/N_o}{1 + \frac{J E_s R_s}{S N_o B}}}\right),$$

where  $R_s = 1/T_s$  is the symbol rate and  $S = E_s/T_s$  is the desired signal's power. The loss in this system relative to a system with no interference is [8]

$$L = 1 + \frac{J E_s R_s}{S N_o B}.$$

As indicated by the previous expression, we can reduce the amount of loss in three ways. First and most obvious, we can try to increase our own signal's power relative to the interference power. Second, we can try to design a system that will operate at a lower signal-to-noise ratio (SNR). This could be done, for example, through the use of low rate coding [9]. Finally, we could increase our bandwidth beyond that which is typically needed for communication.

This final approach provides the motivation for spread spectrum communication. Loosely speaking, spread spectrum is any technique whereby the transmitted signal occupies a much larger bandwidth than is needed. In a stricter sense, spread spectrum communication systems require some sort of “code key” to recognize the waveform.

### 10.1.2 LOW PROBABILITY OF INTERCEPT/ANTI-JAM CAPABILITIES

It is instructive to quantify what damage the above interference has on our communication system. Define an effective SNR as

$$\left(\frac{E_s}{N_o}\right)_{\text{eff}} = \frac{E_s/N_o}{1 + \frac{J}{S} \frac{E_s}{N_o} \frac{R_s}{B}}.$$

Suppose, for example, the receiver needs to achieve an error rate of  $10^{-3}$ . This requires an effective SNR of about  $(E_s/N_o)_{\text{eff}} = 6.8$  dB (in an additive white Gaussian noise [AWGN] channel). Then  $J/S$  must satisfy

$$\frac{J}{S} < \frac{0.21 - \frac{1}{E_s/N_o}}{R_s/B}.$$

If  $R_s/B = 1$  (which is what would be achieved with sinc pulses), the received power of the desired signal must be at least 4.8 times stronger than the received power of the interferer. If both the desired and interfering transmitters are sending equal power, this implies that the interferer must be farther away from the receiver than the desired transmitter. How much farther depends on the propagation model. For example, for a fourth law propagation model, the interferer must be about 1.5 times farther from the receiver than the desired transmitter.

Now suppose we use a signaling scheme which expands our bandwidth by a factor of 100 so that  $R_s/B = 1/100$ . Now the interferer can be as much as 21 times stronger than the desired signal. Alternatively, the interferer can be as much as 2.1 times closer than the desired transmitter for fourth law propagation and still obtain acceptable error rates. In a military environment this is known as anti-jam (AJ) capability (see Peterson et al. [5], Chapter 6 and the references therein). The idea is to force a potential jammer to be closer to the receiver than he would be comfortable doing. This same idea is used in cellular systems to reduce the frequency reuse distance.

Alternatively, consider the power-spectral density (PSD) of the desired signal at the receiver. If a total power of  $S$  is received over a bandwidth of  $B$ , then the (two-sided) PSD is  $S/2B$ . For a traditional unspread system (where  $R_s/B = 1$ ), the PSD is  $S/2B = E_s/2$ . In order to achieve a bit error rate of  $10^{-3}$  at the receiver, the PSD of the desired signal must be somewhat larger than the PSD of the noise ( $E_s/N_o > 4.8 (= 6.8 \text{ dB})$ ). As a result, the PSD of the desired signal must be about five times stronger than the noise floor. This makes it easy for a potential eavesdropper to intercept the signal. On the other hand, for a spread system with  $R_s/B = 1/100$ , the PSD of the desired signal will be  $S/2B = E_s/200$  and the desired signal's PSD can be a factor of 20 (13 dB) below the noise floor and still maintain the desired error rate. This makes it difficult for a potential eavesdropper to intercept the signal or to even know (detect) that it is there. In a military context, these capabilities are referred to as low probability of interception (LPI) and low probability of detection (LPD) (see Peterson et al. [5], Chapter 10, and the references therein). Alternatively, in a commercial environment, there may be receivers from other systems near the transmitter. If the signal is well beneath the noise floor, the system will have minimal effect on the other systems. This is the idea behind the current industrial, scientific, and medical radio bands whereby various users

can access these bands in an unlicensed fashion, provided they adhere to minimal spreading requirements that will allow different applications to coexist without harming one another.

### 10.1.3 DIRECT SEQUENCE SPREAD SPECTRUM

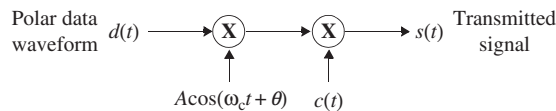
The two most common forms of spread spectrum are direct sequence (DS) and frequency hopping (FH). In this section and the next, we provide an overview of these basic spread spectrum techniques.

In DS-SS, the transmitted data signal,  $d(t)$ , is multiplied by a high rate pseudo-random sequence,  $c(t)$ , causing a significant expansion of the transmission bandwidth. This operation is known as spreading. A BPSK DS-SS transmitter is shown in Fig. 10.1. The transmitted signal will be described in terms of its base band complex envelope,  $x_{bb}(t)$ :

$$x_{bb}(t) = \begin{cases} d(t), & \text{without SS,} \\ d(t)c(t), & \text{with SS.} \end{cases}$$

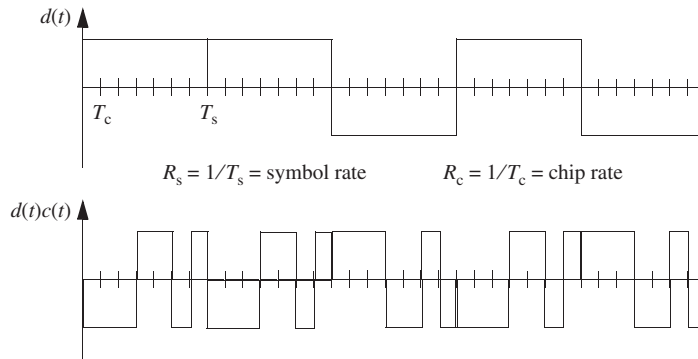
Typical waveforms are shown in Fig. 10.2. As usual,  $R_s = 1/T_s$  is the symbol rate, and now  $R_c = 1/T_c$ , the rate of the pseudo-random sequence, is called the chip rate. Without the spread spectrum, the occupied bandwidth is proportional to  $R_s$ , while with the spread spectrum it is proportional to  $R_c$ . Thus the ratio of  $R_c/R_s$ , the spreading factor, is a measure of how much bandwidth expansion is caused by the presence of the pseudo-random spreading sequence. Some typical waveforms, as viewed in the frequency domain, are shown in Fig. 10.3. At the receiver, the received signal is premultiplied by  $c(t)$  before detection. This operation is known as despreading. This multiplication by  $c(t)$  at the receiver brings the bandwidth of the desired signal down to  $\sim R_s$  while expanding the bandwidth (BW) of any interference present to  $\sim R_c$ . The signals present are illustrated in the frequency domain after despreading in Fig. 10.4.

Note that the matched filter (or correlator) used by the demodulator can be thought of as a filter with a bandwidth equal to the bandwidth of the desired signal (unspread). As a result, most of the interference power will be suppressed by this filter. If the interference is spread over a bandwidth of  $\sim R_c$ , and the signal occupies a BW of  $\sim R_s$ , then after filtering, the total interference power has been reduced by  $R_c/R_s$ .

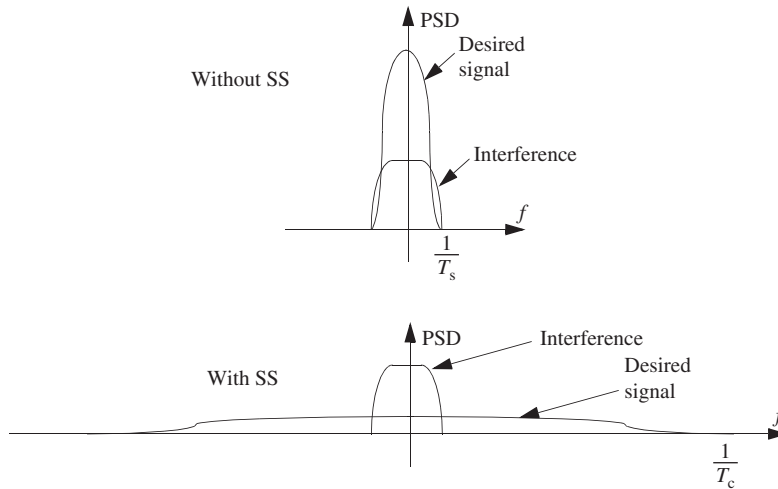


**FIG. 10.1**

A BPSK DS-SS transmitter.


**FIG. 10.2**

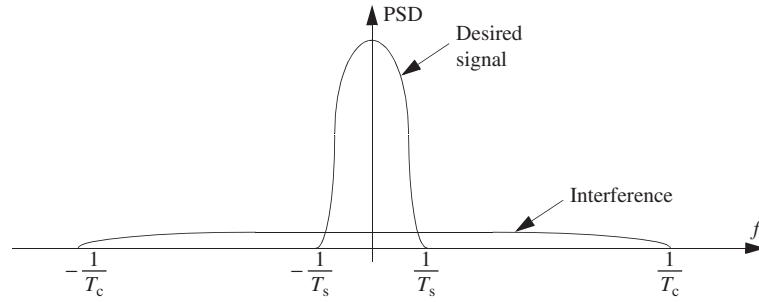
Complex envelopes of typical DS-SS waveforms.


**FIG. 10.3**

Typical waveforms in the frequency domain (base band).

This ratio of the spread bandwidth to the unspread bandwidth is called the processing gain. Other definitions of processing gain are also common.

Fig. 10.5 shows the spreading and despreading process in the time domain. In part A of the figure, a low rate data sequence is spread by a high rate spreading waveform where in this case the spreading sequence has seven chips per data symbol. This number is just for convenient illustration. In practice, much larger spreading factors are used. Part B shows successful despreading of the signal. After the signal at the


**FIG. 10.4**

Typical despread waveforms in the frequency domain (base band).

		Data symbol interval	Chip interval	
Data:	$d(t)$	+1	-1	-1
Spreading:	$c_1(t)$	+1+1+1-1+1-1-1	+1+1+1-1+1-1-1	+1+1+1-1+1-1-1
Spread data:	$d(t) c_1(t)$	+1+1+1-1+1-1-1	-1-1-1+1-1+1+1	-1-1-1+1-1+1+1
<b>(A)</b>				
Received:	$r(t)$	+1+1+1-1+1-1-1	-1-1-1+1-1+1+1	-1-1-1+1-1+1+1
(De)spreading:	$c_1(t)$	+1+1+1-1+1-1-1	+1+1+1-1+1-1-1	+1+1+1-1+1-1-1
Despread data:	$r(t) c_1(t)$	+1+1+1+1+1+1+1	-1-1-1-1-1-1-1	-1-1-1-1-1-1-1
<b>(B)</b>				
Received:	$r(t)$	+1+1+1-1+1-1-1	-1-1-1+1-1+1+1	-1-1-1+1-1+1+1
(De)spreading:	$c_2(t)$	-1-1+1-1+1+1+1	-1-1+1-1+1+1+1	-1-1+1-1+1+1+1
Despread data:	$r(t) c_2(t)$	-1-1+1+1+1-1-1	+1+1-1-1-1+1+1	+1+1-1-1-1+1+1
<b>(C)</b>				
Received:	$r(t)$	+1+1+1-1+1-1-1	-1-1-1+1-1+1+1	-1-1-1+1-1+1+1
(De)spreading:	$c_1(t-T_c)$	-1+1+1+1-1+1-1	-1+1+1+1-1+1-1	-1+1+1+1-1+1-1
Despread data:	$r(t) c_1(t-T_c)$	-1+1+1-1-1-1+1	+1-1-1+1+1+1-1	+1-1-1+1+1+1-1
<b>(D)</b>				

**FIG. 10.5**

An example of DS spreading and despreading in the time domain. (A) DS spreading at the transmitter; (B) correct despreading at the receiver; (C) incorrect despreading at the receiver, wrong code sequence; and (D) incorrect despreading at the receiver, delayed code sequence.

receiver is multiplied by the correct spreading waveform, the resulting signal can be downsampled back to the original data rate. In part C of the figure, it is seen that if the wrong spreading sequence is used at the receiver, the signal will not be despread correctly. This property will be important in the context of code division multiple access (CDMA). Finally, Fig. 10.5D shows what happens at the receiver if the correct spreading code is used but is not synchronized correctly. In this case, the spreading waveform has been delayed at the receiver by one chip interval, and once again, the signal is not successfully despread. This property will be important in our later discussion of RAKE receivers.

#### 10.1.4 FH SPREAD SPECTRUM

In FH-SS, the carrier frequency is pseudo-randomly hopped over many possible frequencies. A typical modulator and demodulator for FH-SS are shown in Figs. 10.6 and 10.7. The FH signal can be viewed as randomly changing “channels” which are commonly referred to as frequency bins. If any one (or a few) of the bins is being

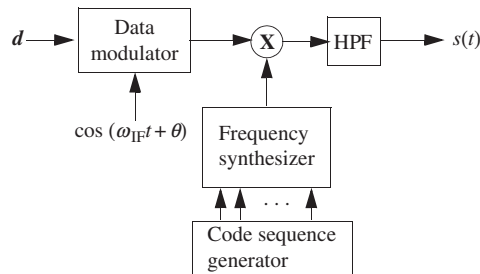


**FIG. 10.6**

FH-SS modulator.

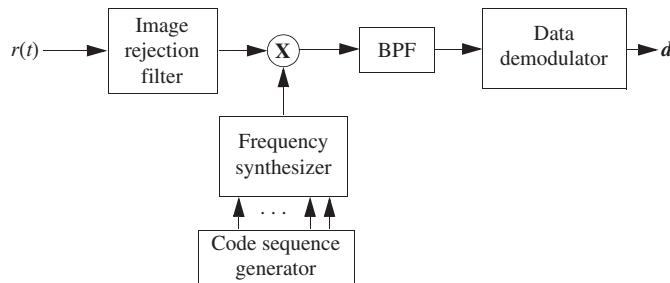


**FIG. 10.7**

FH-SS demodulator.

interfered with, the system will experience degradation only a small percentage of the time. This can be overcome with intelligently designed error correction coding. Any interferer which effects all (or most) of the bins will have its power spread over a large bandwidth, and hence the PSD in any one bin will be reduced to a manageable level. This provides AJ capability as well as robustness to many forms of unintentional interference. The LPI/LPD capability is provided by the fact that if the carrier is hopped fast enough, it never stays in one place long enough to be detected. The hopping is typically provided by the use of a programmable frequency synthesizer which is driven by some pseudo-random sequence. The demodulator works in a manner very similar to a superheterodyne radio (eg, Couch [10, pp. 283–288]). The received signal is down converted to an intermediate frequency (IF) which is the same regardless of the current carrier frequency. Naturally, this requires the receiver to generate the same sequence present at the transmitter and it must be synchronous in time. After the signal has been converted to the IF (dehopped), a standard demodulator is used.

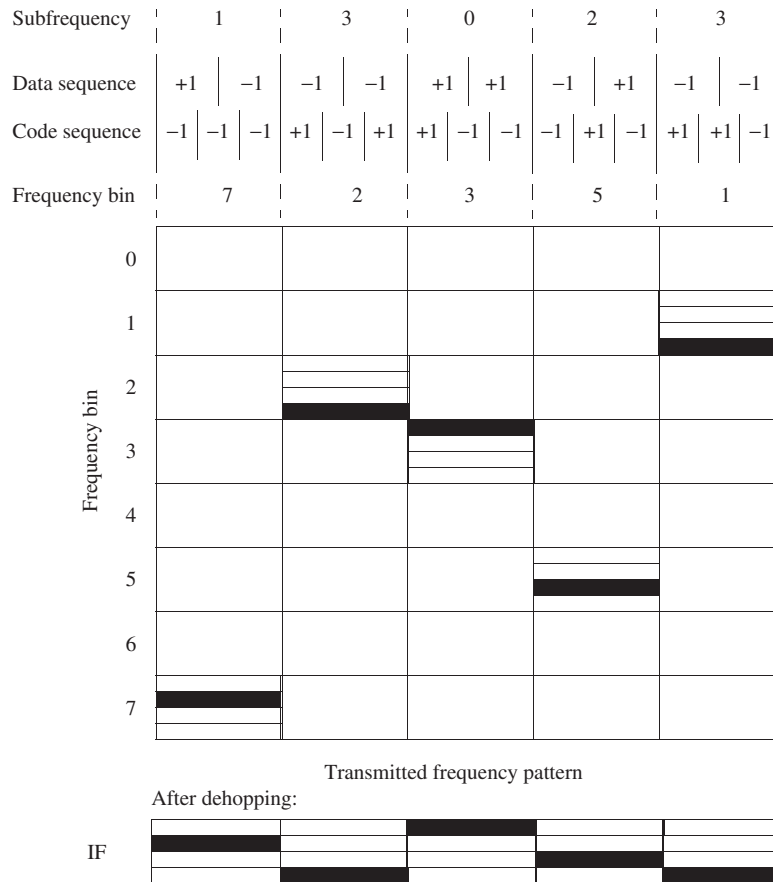
If the hopping rate is slower (or the same) than the symbol rate, then the FH is referred to as slow FH (multiple symbols per hop). If the hopping rate is faster than the symbol rate then the FH is fast (multiple hops per symbol). Since the carrier frequency is continually changing, it can be practically difficult for the receiver to perform phase synchronization on the received signal. As a result, data modulation formats which can be noncoherently demodulated are generally used in FH systems. *M*-ary FSK is the most common. For illustration purposes, an example of a 4-FSK-based FH system with eight hop bins with a rate of one hop per symbol is shown in Fig. 10.8.

### 10.1.5 CODE DIVISION MULTIPLE ACCESS

The use of spread spectrum, either DS or FH, can also provide multiple access capability. In multiple-access systems, several users must share the communication medium. The traditional approaches are to use frequency division multiple access (FDMA) or time division multiple access (TDMA), where the users are coordinated in frequency or time, respectively. In CDMA, the other system users can be viewed as interference. Since the spread spectrum system is robust to interference, a number of users can coexist without causing too much mutual harm to one another.

In DS-CDMA, each user is assigned a different spreading sequence and all users occupy the entire frequency band at all times. At each receiver, only the desired signal is despread properly. All unwanted signals (ie, signals from the other users) remain spread and are largely suppressed by filtering in the demodulator. This was shown in Fig. 10.5C.

In FH-CDMA, each user follows a different hopping pattern. Occasionally two or more users will hop to the same frequency at the same time and data will often be lost on that hop. This is accounted for with an appropriate amount of error control coding.

**FIG. 10.8**

An example of a 4-FSK-based slow FH system.

Unlike FDMA or TDMA, CDMA not only supports multiple users but is also robust to interference from nonsystem sources. Such interference might include intentional jamming in a military network, multipath interference, co-channel or adjacent channel interference (in a cellular system), or miscellaneous radio frequency (RF) interference [11].

CDMA systems can be either synchronous or asynchronous. In synchronous DS-CDMA, the various users' transmissions are synchronized in time so that the beginning of chips and data symbols are aligned. This makes it easier to design code sequences which reduce the mutual interference. In asynchronous DS-CDMA, no such attempt is made to align the various users' signals. Likewise, in synchronous FH-CDMA, the hopping of the various users is synchronized so that all signals hop simultaneously. In asynchronous FH-CDMA, different users hop at different times.

This can cause partial hits to occur more frequently, but each partial hit may not cause quite as much damage to the users involved.

Before concluding this brief introduction to CDMA, we present a very crude capacity analysis of both DS and FH CDMA to gain insight into how many simultaneous users can be supported by such multiple access schemes. Consider first an asynchronous DS-SS receiver. Suppose there are a total of  $K$  simultaneous users sharing the channel on a DS-SS basis. Let user #1 be the desired signal and all others are treated as interference. To make the analysis simple we treat the  $k$ th interfering DS-SS signal as Gaussian noise with a spectral density of  $P_k/2B$  for  $|f - f_c| < B/2$ , where  $P_k$  is the received power from the  $k$ th interferer and  $B$  is the total system bandwidth. If we lump this interference in with the thermal noise, the total noise plus interference spectral density is

$$S(f) = \frac{N_o}{2} + \sum_{k=2}^K \frac{P_k}{2B}.$$

The probability of error for our DS-SS receiver (assuming BPSK modulation) for the desired user would be

$$P_e = Q\left(\sqrt{\frac{2E_b}{N_o + \frac{1}{B} \sum_{k=2}^K P_k}}\right) = Q\left(\sqrt{\frac{2E_1/N_o}{1 + \frac{R_s}{B} \sum_{k=2}^K E_k/N_o}}\right),$$

where  $E_k$  is the received energy per bit of the  $k$ th received signal. Note that the bandwidth of our system will be proportional to the chip rate,  $R_c = NR_s$ . So the term  $R_s/B$  that appears in the previous expression will be proportional to  $N$ , the number of chips per symbol. A more careful analysis reveals that it is appropriate to take the constant of proportionality so that  $R_s/B = 2/3N$  and hence [12]

$$P_e = Q\left(\sqrt{\frac{2E_1/N_o}{1 + \frac{1}{3N} \sum_{k=2}^K 2E_k/N_o}}\right) = Q\left(\sqrt{\frac{2E_1/N_o}{1 + \frac{2}{3N} \frac{E_1}{N_o} \sum_{k=2}^K \frac{P_k}{P_1}}}\right).$$

While this result is based on some assumptions that may or may not be accurate (eg, Gaussian distribution of interference, truly random codes), it does bring out some of the gross characteristics of DS-SS. Consider first the case where all users carefully adjust their transmitted power so that all signals are received at the same energy level (perfect power control),  $P_k = P_1$ , so that

$$P_e = Q\left(\sqrt{\frac{2E_1/N_o}{1 + \frac{2(K-1)}{3N} \frac{E_1}{N_o}}}\right).$$

A typical plot of this error probability formula is shown in Fig. 10.9 for a DS-SS system that uses  $N = 100$  chips per bit. First note the appearance of error floors. From the previous expression, it can be seen that as  $E_1/N_o \rightarrow \infty$ , the error probability will approach the floor value of  $P_e = Q(\sqrt{3N/(K-1)})$ . From this we conclude that for

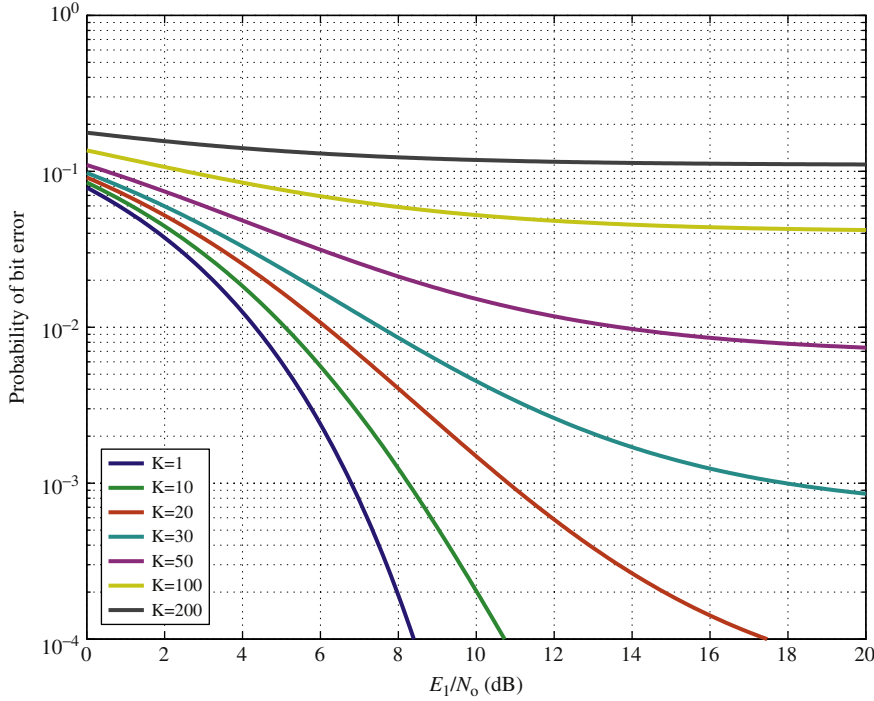


**FIG. 10.9**

Probability of bit error for a BPSK-based DS-CDMA system with  $N = 100$  chips/bit. Curves from bottom to top represent user loadings of  $K=1, 10, 20, 30, 50, 100, 200$  users, respectively.

an application that needs to maintain an uncoded bit error rate of  $p$ , the number of users that can be supported is limited by

$$K \leq \frac{3N}{(Q^{-1}(p))^2} + 1 \Rightarrow \frac{K}{N} \leq \frac{3}{(Q^{-1}(p))^2} + \frac{1}{N}.$$

Typically, the second term is negligible so that the system loading (as a percentage of the bandwidth expansion factor) can be determined directly from the required bit error probability. The capacity of a BPSK-based DS-CDMA system with perfect power control is shown in [Table 10.1](#) for different required system error rates. To put these numbers in context, consider an FDMA system that was allowed a bandwidth expansion factor of  $N$ . Such a system could have  $N$  different frequency channels and could therefore support  $K = N$  users (100% loading). Similarly, a TDMA system would have  $N$  time slots and could also support  $K = N$  users. A DS-CDMA system with powerful error correction coding could possibly tolerate uncoded bit error rates near 10% and hence may be able to handle loading beyond that of FDMA/TDMA

**Table 10.1** Maximum User Loading for a BPSK-Based DS-CDMA System

BER, $p$	AWGN, %	Three Channel FS, %	Flat RF, %
0.1	183	145	38
0.01	55	30	2.7
0.001	31	11	0.27
0.0001	22	4.7	0.027

Note: Loading is expressed as  $K/N \times 100\%$ .

(>100%). Even in situations where a CDMA system must operate at system loadings lower than 100%, the CDMA system still offers the advantage that it provides robustness to other forms of interference. In some applications, this can be a very important consideration.

It is a fairly straightforward exercise to adjust the user loading calculations above to other channel models. For example, if a flat Rayleigh fading channel is used, the error probability behaves in the following manner [13]:

$$P_{e,\text{avg}} = \frac{1}{2} - \frac{1}{2} \sqrt{\frac{1}{1 + \frac{1}{E_b/N_0}}}.$$

Proceeding as was done for the AWGN channel, replacing in the previous equation with  $3N/2(K-1)$  and solving for  $K/N$  one obtains the relationship for the user load of a BPSK DS-CDMA system on a flat Rayleigh fading channel to be

$$\frac{K}{N} \leq \frac{2}{3} \left( \frac{1}{(1-2p)^2} - 1 \right) + \frac{1}{N}.$$

This leads to the user loading numbers shown in the last column of Table 10.1. Note that the system user capacity is substantially lower in a flat Rayleigh fading channel.

As will be seen in a later section, the use of broadband signaling (ie, DS-SS) will often cause a fading channel to behave in a frequency selective manner and the resulting error probability may be more like a Rayleigh fading channel with a few diversity branches. As an example, if there are three equal power diversity channels over a Rayleigh fading channel, the error probability for BPSK will be as follows (eg, Eq. 14.4-15 of Proakis [13]):

$$P_{e,\text{avg}} = \left( \frac{1-\mu}{2} \right)^3 \left[ 1 + 3 \left( \frac{1+\mu}{2} \right) + 6 \left( \frac{1+\mu}{2} \right)^2 \right],$$

where  $\mu = (1 + 3/(E_b/N_0))^{-1/2}$ . For a desired average error probability, one can solve for the required value of  $E_b/N_0$  (numerically) and then find the DS-CDMA system loading according to  $K/N \leq ((2/3)E_b/N_0)^{-1}$ . Results are shown in the middle column of Table 10.1 for the three-branch frequency selective Rayleigh fading channel.

It should be noted that if any one of the interfering signals is significantly stronger than the desired signal then the bit error rate (BER) will be substantially degraded. From the BER expression, it is clear that one interfering signal that is 10 times stronger than the desired signal will have the same effect as 10 interfering signals with the same strength as the desired signal. This is referred to as the near-far problem and occurs when the interfering signal's transmitter is much closer to the receiver than the desired signal's transmitter. Typically, this problem is dealt with by the use of transmitter power control whereby the receiver will continually send side information to each transmitter instructing them how to adjust their transmit power so that all signals arrive at the receiver at approximately the same power level [14].

Finally, we examine an FH-CDMA system. To make the analysis simple, it is assumed that any time two or more users hop to the same frequency bin at the same time, a hit occurs and all users involved in the hit lose their data during that hit. Also, for convenience, it is assumed that all users hop synchronously (all shift frequencies at the same time) so that we do not have to worry about partial hits. Finally, assume that the SNR is large enough so that the probability of error is negligible when there is no hit. Under these assumptions, the bit error rate is just the probability that one or more of the interfering users use the same frequency bin of the desired user. If the hopping patterns are truly random for each user, then

$$P_c = Pr(\text{correct}) = Pr(\text{no hit}) = \left(1 - \frac{1}{N}\right)^{K-1}$$

$$P_e = Pr(\text{error}) = 1 - \left(1 - \frac{1}{N}\right)^{K-1} \approx \frac{K-1}{N}.$$

In the above expressions  $N$  is the number of hop bins and is also the bandwidth expansion factor. Note that the number of users the FH-CDMA system can support is basically given by  $K = pN$ , where  $p$  is the required BER. Note if a BER of  $10^{-2}$  is required then the number of simultaneous users that can be supported is roughly 1% of the bandwidth expansion. This number can be improved somewhat through the use of error control coding, but the capacity of an FH system will still typically be less than what can be achieved with a DS system. For this reason, DS is much more commonly used in CDMA systems. On the other hand, the FH system has no near-far problem and hence in an environment where power control is not possible, FH-CDMA may be a better option than DS-CDMA.

### 10.1.6 CODE SEQUENCES

In SS systems, the code sequences that are used should follow a deterministic format so that they can be identically reproduced at the transmitter and receiver, yet they should exhibit properties of randomness so that it is difficult for a potential eavesdropper to identify the sequence being used. Additionally, in order to ease the process of code synchronization at the receiver, it is desirable that the sequence used

is as different as possible from any time shifted version of itself. In other words, the auto-correlation function of the code sequence should be uniformly low for all possible nonzero offsets.

It is common in SS systems to use code sequences which are the output of a binary shift register (SR) with feedback. A generic  $n$ -stage SR is shown in Fig. 10.10. The SR is described in terms of a set of feedback connections,  $h_0, h_1, \dots, h_n$ , where  $h_i = 1$  indicates the presence of a feedback connection at the  $i$ th position, and  $h_i = 0$  indicates no connection. It is common to describe the feedback connections in terms of a polynomial:

$$h(x) = h_0 + h_1x + h_2x^2 + \dots + h_nx^n.$$

The SR, when clocked, produces a periodic sequence of 0 and 1 s. Since there are  $n$  binary storage elements, there are a total of  $2^n$  possible states in which the SR can be. Once it returns to its starting state it will repeat the output sequence it has produced up to that point. The all-zero state needs to be avoided since once the SR enters the all-zero state it will be stuck there and will produce an (undesirable) output sequence of all zeros. Therefore, there are a maximum of  $2^n - 1$  states the SR can cycle through and hence the SR produces a periodic output sequence whose period is no longer than  $2^n - 1$  bits. An SR which produces an output sequence which achieves this maximum period is called a maximal length linear feedback shift register (MLLFSR) and the sequences they produce are called MLLFSR sequences. Since this acronym is longer than most people prefer, the shortened term  $m$ -sequence<sup>1</sup> is more commonly used.

Not every polynomial,  $h(x)$ , will produce an  $m$ -sequence. Polynomials which do produce an  $m$ -sequence are known as primitive polynomials. Tables of primitive polynomials can be found in many books on spread spectrum (eg, Peterson et al. [5]) or error correction coding (eg, Peterson and Weldon [15]) and are often given in

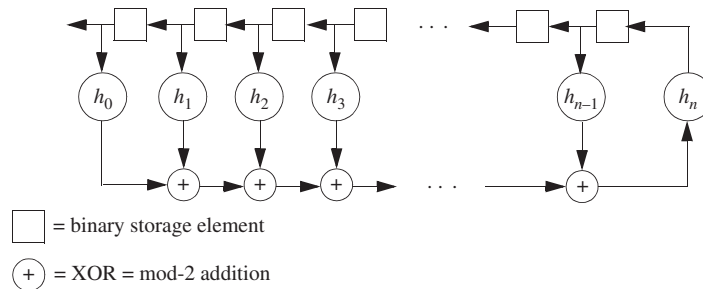


FIG. 10.10

A binary linear feedback shift register.

<sup>1</sup>Engineers are known to use excessive acronyms. In the ultimate of engineering jargon, the term  $m$ -sequence is an acronym of an acronym.

octal form. A short table is provided in Table 10.2. As an example of how to use that table, the  $n = 5$  entry will provide a primitive polynomial which will produce an  $m$ -sequence of length  $2^5 - 1 = 31$ . The octal entry 45 converts to the binary number 100101 which defines the polynomial  $h(x) = 1 + x^2 + x^5$ . The corresponding five-stage MLLFSR is shown in Fig. 10.11. Also, if  $h(x)$  is a polynomial of degree  $n$  which produces an  $m$ -sequence of length  $N = 2^n - 1$ , then its reciprocal (defined as  $x^n h(x^{-1})$ ) also generates an  $m$ -sequence. Typically, tables of primitive polynomials do not include both a polynomial and its reciprocal. So there are actually six  $m$ -sequences of degree 5 (length 31) although the table only lists 3.

In the context of DS-SS, a binary code sequence is converted to a spreading waveform by first converting the bits from a  $\{0, 1\}$  format to a  $\{+1, -1\}$  format and then modulating the sequence of bits with a chip waveform. So if  $\mathbf{b}$  is a sequence of bits with  $b_i \in \{0, 1\}$ , then form the sequence  $\mathbf{c}$  where  $c_i = (-1)^{b_i}$ . Finally, create the spreading waveform according to

$$c(t) = \sum_k c_k p(t - kT_c), \quad (10.1)$$

where  $p(t)$  is the chip pulse shape (often rectangular pulses are used but other options are possible). For a code sequence of period  $N$ , this will produce a spreading waveform which is periodic with a period of  $NT_c$ . In some applications, we may

**Table 10.2** Primitive Polynomials in Octal Form

Degree ( $n$ )	Polynomial (Octal)
2	7
3	13
4	23
5	45, 75, 67
6	103, 147, 155
7	211, 217, 235, 367, 277, 325, 203, 313, 345
8	435, 551, 747, 453, 545, 537, 703, 543

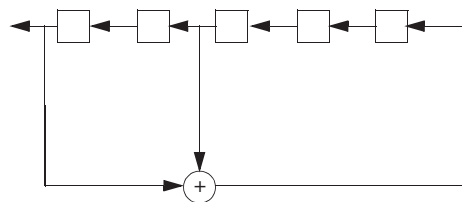


**FIG. 10.11**

The five-stage MLLFSR specified by the octal number 45.

choose the period of the code sequence such that the spreading waveform repeats once every symbol interval (ie,  $N = T_s/T_c$ ). Such a code is referred to as a short code. Alternatively, it is also common to use codes that have a very long period so that the resulting spreading waveform does not repeat for many symbol intervals. Such codes are called long codes. Fundamentally, it is nothing about the code that really makes it long or short. Rather it is the ratio of the number of chips per bit in the SS system and how that relates to the period of the code sequence that distinguishes a short code from a long one.

In FH-SS, an  $N = 2^k$ -ary hopping pattern could easily be formed from a binary code sequence by grouping the code sequence into  $k$ -bit segments. Suppose, for example, our FH system uses 64 hopping bins. Starting with a binary  $m$ -sequence of period 255 and grouping the bits into 6-bit words would produce a sequence of 64-ary numbers that appear random. Also, since 6 and 255 are relatively prime, the resulting 64-ary sequence would still have a period of 255. Naturally, many other possibilities abound for mapping a binary code sequence into a nonbinary hopping pattern.

In the context of DS-CDMA where multiple different DS-SS signals must be created, it is necessary to use a set of code sequences that have good cross-correlation properties. That is, each user should have a code sequence that is as dissimilar as possible to every other code sequence in the set. In the case of synchronous CDMA where we do not have to worry about the different users signals being offset in time with respect to one another, it is common to use a set of orthogonal sequences, the most common of which are the so-called Walsh codes, which are taken as rows from a Hadamard matrix. These sequences can be generated through a simple recursion as follows. Define the matrix,  $\mathbf{H}_0 = [1]$  then create a sequence of matrices,  $\mathbf{H}_n$ ,  $n = 1, 2, 3, \dots$  according to the recursion

$$\mathbf{H}_{k+1} = \begin{bmatrix} \mathbf{H}_k & \mathbf{H}_k \\ \mathbf{H}_k & -\mathbf{H}_k \end{bmatrix}.$$

The resulting Hadamard matrix  $\mathbf{H}_n$  will be a  $2^n \times 2^n$  matrix whose elements are  $\pm 1$  valued and whose rows constitute an orthogonal set. That is, if  $\mathbf{c}_k$  is the sequence corresponding to the  $k$ th column of the matrix  $\mathbf{H}_n$ , then  $\mathbf{c}_k^T \mathbf{c}_m = 0$  for all  $k \neq m$ . The construction of a few short Walsh codes is shown in Fig. 10.12.

In asynchronous DS-CDMA, we want each code sequence to be uncorrelated to not only every other code sequence in the set, but also to any time shift of any other code sequence in the set. Let  $c_k(t)$  be the spreading waveform assigned to user  $k$ . In order to keep the mutual interference to a minimum that each user's signal presents to another user's receiver, the spreading waveforms should be designed such that  $\int_{T_s} c_k(t - \tau_k) c_m(t - \tau_m) dt \approx 0$  for any values of the time delays  $\tau_k$  and  $\tau_m$  and for any  $k \neq m$ . The period of integration for the correlation integral is the symbol duration. For CDMA systems employing short codes, this corresponds to the period of the spreading waveforms, so we wish to keep the periodic cross-correlation function of the spreading waveforms uniformly low. For a CDMA system

$$\begin{aligned}
H_1 &= \begin{bmatrix} +1 & +1 \\ +1 & -1 \end{bmatrix} \quad \text{fi} \quad c_1 = \begin{bmatrix} +1 \\ +1 \end{bmatrix} \quad c_2 = \begin{bmatrix} +1 \\ -1 \end{bmatrix} \\
H_2 &= \begin{bmatrix} +1 & +1 & +1 & +1 \\ +1 & -1 & +1 & -1 \\ +1 & +1 & -1 & -1 \\ +1 & -1 & -1 & +1 \end{bmatrix} \quad \text{fi} \quad c_1 = \begin{bmatrix} +1 \\ +1 \\ +1 \\ +1 \end{bmatrix}, \quad c_2 = \begin{bmatrix} +1 \\ -1 \\ +1 \\ -1 \end{bmatrix}, \quad c_3 = \begin{bmatrix} +1 \\ +1 \\ -1 \\ -1 \end{bmatrix}, \quad c_4 = \begin{bmatrix} +1 \\ -1 \\ -1 \\ +1 \end{bmatrix} \\
H_3 &= \begin{bmatrix} +1 & +1 & +1 & +1 & +1 & +1 & +1 & +1 \\ +1 & -1 & +1 & -1 & +1 & -1 & +1 & -1 \\ +1 & +1 & -1 & -1 & +1 & +1 & -1 & -1 \\ +1 & -1 & -1 & +1 & +1 & -1 & -1 & +1 \\ +1 & +1 & +1 & +1 & -1 & -1 & -1 & -1 \\ +1 & -1 & +1 & -1 & -1 & +1 & -1 & +1 \\ +1 & +1 & -1 & -1 & -1 & -1 & +1 & +1 \\ +1 & -1 & -1 & +1 & -1 & +1 & +1 & -1 \end{bmatrix} \quad \text{fi} \quad c_1 = \begin{bmatrix} +1 \\ +1 \\ +1 \\ +1 \\ +1 \\ +1 \\ +1 \\ +1 \end{bmatrix}, \quad c_2 = \begin{bmatrix} +1 \\ -1 \\ +1 \\ -1 \\ +1 \\ -1 \\ +1 \\ -1 \end{bmatrix}, \quad c_3 = \begin{bmatrix} +1 \\ +1 \\ -1 \\ -1 \\ +1 \\ -1 \\ -1 \\ +1 \end{bmatrix}, \quad c_4 = \begin{bmatrix} +1 \\ -1 \\ -1 \\ +1 \\ +1 \\ -1 \\ -1 \\ +1 \end{bmatrix} \\
&\quad c_5 = \begin{bmatrix} +1 \\ +1 \\ +1 \\ +1 \\ -1 \\ -1 \\ -1 \\ -1 \end{bmatrix}, \quad c_6 = \begin{bmatrix} +1 \\ -1 \\ -1 \\ +1 \\ -1 \\ +1 \\ -1 \\ +1 \end{bmatrix}, \quad c_7 = \begin{bmatrix} +1 \\ +1 \\ -1 \\ -1 \\ -1 \\ +1 \\ +1 \\ +1 \end{bmatrix}, \quad c_8 = \begin{bmatrix} +1 \\ -1 \\ -1 \\ +1 \\ -1 \\ +1 \\ +1 \\ -1 \end{bmatrix}
\end{aligned}$$

FIG. 10.12

Generation of an orthogonal set of Walsh codes.

with long codes, the period of integration may be only a small fraction of the period of the spreading waveform, and therefore, the resulting correlation is only a partial correlation function.

For the case of short codes, there are a number of families of codes that have been designed to have good cross-correlation and auto-correlation properties. Many are constructed from pairs of  $m$ -sequences that are known to have good cross-correlation values. To describe such families of sequences, using the notation of Sarwate and Pursely [16], let  $\mathbf{b}$  be an  $m$ -sequence of length  $N$ , and let  $T$  be the right cyclic shift operator so that  $T\mathbf{b}$  is equal to the sequence  $\mathbf{b}$  cyclically shifted one place to the right.  $T^m\mathbf{b}$  would then cyclically shift  $\mathbf{b}$  by  $m$  places to the right.

A set of  $N + 2$  sequences of length  $N$  can be formed from two  $m$ -sequences of length  $N$ ,  $\mathbf{b}_1$  and  $\mathbf{b}_2$ , by constructing the following set

$$G = \left\{ \mathbf{b}_1, \mathbf{b}_2, \mathbf{b}_1 \oplus \mathbf{b}_2, \mathbf{b}_1 \oplus T\mathbf{b}_2, \mathbf{b}_1 \oplus T^2\mathbf{b}_2, \dots, \mathbf{b}_1 \oplus T^{N-1}\mathbf{b}_2 \right\}.$$

This set is known as the set of Gold codes [17,18] and has the property that if  $\mathbf{b}_1$  and  $\mathbf{b}_2$  have a peak cross-correlation of  $r$ , then all pairs of codes in the Gold set will also have a peak cross-correlation of  $r$ . Hence, if we can find one pair of  $m$ -sequences with good cross-correlation, then we can construct a family of  $N + 2$  sequences, all of which have equally good cross-correlation.

Another common family of sequences is the so-called Kasami set [19,20]. In this case, we choose  $\mathbf{b}_1$  to be an  $m$ -sequence of length  $N = 2^n - 1$ , where  $n$  is an even integer. Next, choose  $\mathbf{b}_2$  to be an  $m$ -sequence of length  $2^{n/2} - 1 = \sqrt{N + 1} - 1$ . The Kasami set then consists of the set of  $\sqrt{N + 1}$  sequences:

$$\mathbf{K} = \left\{ \mathbf{b}_1, \mathbf{b}_1 \oplus \mathbf{b}_2, \mathbf{b}_1 \oplus T\mathbf{b}_2, \mathbf{b}_1 \oplus T^2\mathbf{b}_2, \dots, \mathbf{b}_1 \oplus T^{2^{n/2}-2}\mathbf{b}_2 \right\}.$$

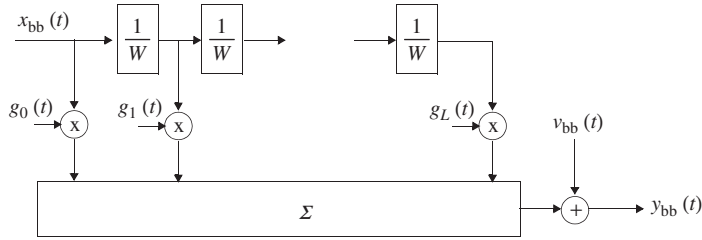
The peak cross-correlation of this set will be  $(\sqrt{N + 1} + 1)/N$ . For example, if we choose  $N = 63$ , the Kasami set will provide a set of 8 sequences of length 63 with a peak cross-correlation of 9/63. By comparison, the Gold set will provide 65 sequences of length 63 whose peak cross-correlation is 17/63.

In closing, it should be pointed out that there is a direct relationship between families of sequences that are commonly considered for spreading codes and codewords that are found in certain low-rate cyclic block codes [16]. It turns out that the set of Gold codes are nothing more than a subset of the codewords of a BCH code. For example, the length 63 Gold codes previously mentioned are found in the set of codewords of a (63, 10) binary cyclic BCH code. The point here is that if you want a set of sequences with good cross-correlation properties, you need not search any further than a book on error correction codes.

## 10.2 SPREAD SPECTRUM AND CDMA FOR WIRELESS CHANNELS

### 10.2.1 DS-SS IN A WIRELESS CHANNEL: RAKE RECEIVERS

One of the key advantages of the DS-SS signaling format is that it allows one to fairly easily take advantage of the natural diversity offered by a frequency selective communications channel. To start with, we will use the tapped delay line model for a frequency selective fading channel shown in Fig. 10.13. The parameter  $L$ , which determines the number of taps in the delay line, is specified by  $L = W\tau_m$ , where  $W$  is the bandwidth of our transmitted signal and  $\tau_m$  is the delay spread of the channel. In our case, the transmitted signal will be the complex envelope of a DS-SS signal, and the bandwidth will be on the order of  $W = 1/T_c$ . Since the taps in this model are spaced by delays of  $1/W$ , it is appropriate to take the delay intervals of the delay line to be a chip duration,  $T_c$ . The number of taps in the delay line will then be specified by  $L = \tau_m/T_c$ . By choosing our chip rate to be high enough so that  $T_c < \tau_m$ , we can ensure that there will be multiple taps in our delay line model and the channel will behave in a frequency-selective manner. On the other hand, if we do not employ any

**FIG. 10.13**

Tapped delay line model for a frequency selective fading channel.

spreading, the bandwidth of our signal will be on the order of  $W \sim 1/T_s$  and as a result,  $L \sim \tau_m/T_s$ . If the symbol duration is small compared to the delay spread, the same channel that was frequency selective to our spread system will behave as a flat fading channel to the unspread system.

Now consider the signal as seen by the SS receiver in our wireless channel (at complex base band).

$$y_{bb}(t) = \sum_{k=0}^L g_k(t)x_{bb}(t - kT_c) + v_{bb}(t).$$

The receiver sees the sum of several delayed versions of the transmitted signal, each one multiplied by an independent complex Gaussian fading process whose PSD might follow something like a traditional bathtub spectrum. While the fading can wreak havoc on the performance of a digital communication system, the presence of multiple independent fading processes allows us the potential for diversity which can greatly improve the performance of the system. In order to take advantage of this natural diversity provided to us by the frequency selective channel, we will need to separate each term in the sum so that we can then combine them in perhaps something like a maximal ratio combining scheme. Fortunately, the nice auto correlation properties possessed by typical spreading waveforms will provide just what we need to easily manage the diversity combining.

For simplicity, consider a BPSK-based DS-SS signal so that the transmitted signal is of the form

$$x_{bb}(t) = \sum_m s_m c(t - mT_s).$$

In an unspread system,  $c(t)$  might represent a traditional pulse shape such as a root raised cosine, but in the SS system,  $c(t)$  will be our spreading waveform. The received signal, as it depends on the data symbols,  $s_m$ , is

$$y_{bb}(t) = \sum_m s_m \sum_{k=0}^L g_k(t)c(t - mT_s - kT_c) + v_{bb}(t).$$

In order to make a decision on the  $m$ th data symbol, we should form the correlation statistic

$$z_m = \int y_{bb}(t) \sum_{k=0}^L g_k^*(t) c(t - mT_s - kT_c) dt.$$

Assuming the fading processes do not change substantially over the duration of a data symbol (ie, no fast fading), each of the  $g_k(t)$  can be treated as constants over the region of integration, and the above decision statistic can be rewritten as

$$z_m = \sum_{k=0}^L g_k^* \int y_{bb}(t) c(t - mT_s - kT_c) dt. \quad (10.2)$$

These statistics can be formed with a filter matched to the spreading waveform,  $c(t)$ , sampled at the appropriate points in time, and then by combining the samples with the appropriate weights, specified by the  $g_k$ . The form of this decision statistic suggests the receiver structure shown in Fig. 10.14, known as a RAKE receiver [13,21,22].<sup>2</sup>

To see how the RAKE receiver effectively combines the diversity offered by the multipath channel, consider the decision statistic (neglecting the noise) as given in Eq. (10.2):

$$\begin{aligned} z_m &= \sum_{k=0}^L g_k^* \int y_{bb}(t) c(t - mT_s - kT_c) dt \\ &= \sum_{k=0}^L g_k^* \int \sum_q s_q \sum_{l=0}^L g_l c(t - qT_s - lT_c) c(t - mT_s - kT_c) dt \\ &= \sum_q s_q \sum_{k=0}^L \sum_{l=0}^L g_k^* g_l \int c(t - qT_s - lT_c) c(t - mT_s - kT_c) dt \\ &= \sum_q s_q \sum_{k=0}^L \sum_{l=0}^L g_k^* g_l R_{cc}((m - q)T_s + (k - l)T_c), \end{aligned}$$

where  $R_{cc}(\tau) = \int c(t) c(t + \tau) dt$  is the auto-correlation function of the spreading waveform. In DS-SS, the code sequences are designed so that the auto-correlation function behaves such that  $R_{cc}(\tau) \approx 0$  for all  $|\tau| \geq T_c$ . As a result, the only terms in the above series that contribute significantly are the ones where  $q = m$  and  $l = k$ . Therefore, the decision statistic for the  $m$ th data symbol is well approximated by the following (assuming  $c(t)$  has been normalized such that  $R_{cc}(0) = 1$ ):

$$z_m \approx s_m \sum_{k=0}^L |g_k|^2.$$

<sup>2</sup>The term “RAKE” is not an acronym but rather refers to the structure having the form of a garden rake with many fingers to collect the energy from each resolvable multipath.

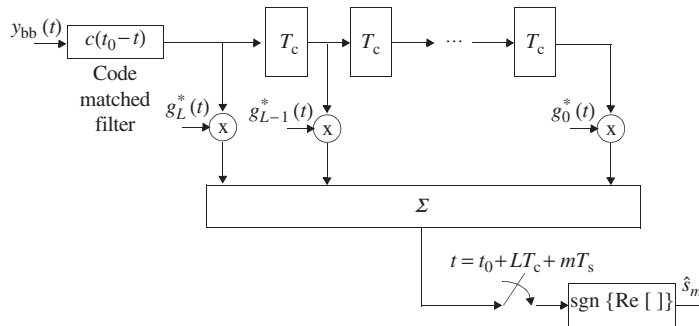


FIG. 10.14

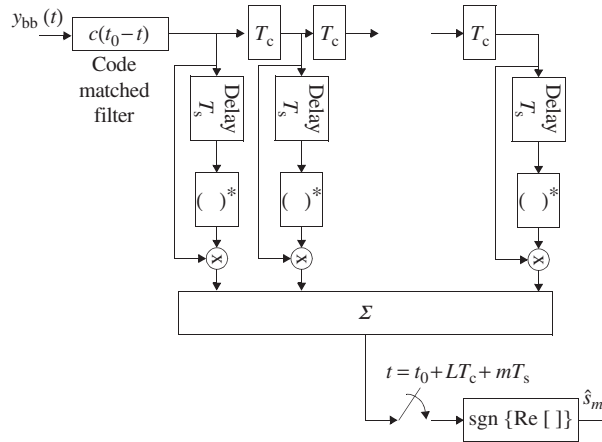
A RAKE receiver for DS-SS in a multipath fading channel.

This is exactly the result we would see in a diversity system with maximal ratio combining.

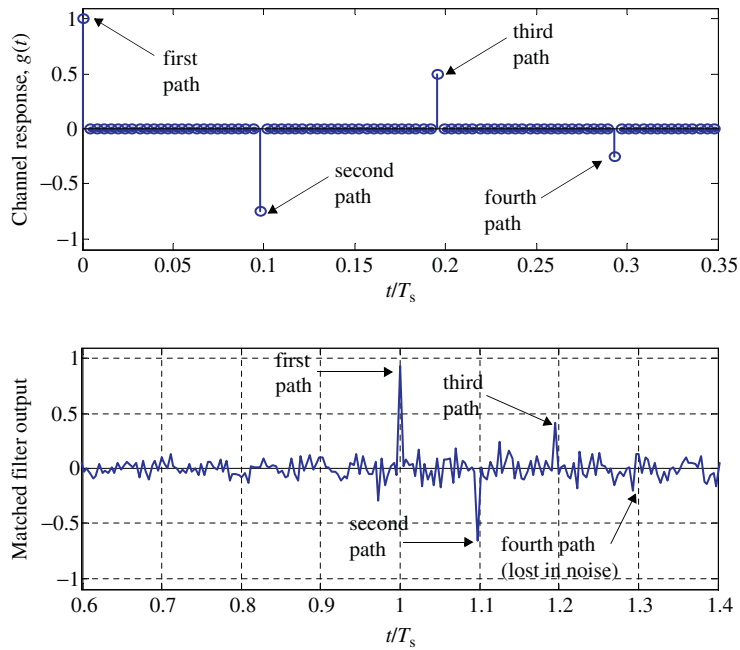
The following will include some statements about practical implementation of the RAKE receiver. In a channel where the delay spread is long compared to the chip duration, the number of taps in the RAKE receiver as presented in Fig. 10.14 may get too large. In that case, we may choose to implement a RAKE receiver that does not try to collect all of the energy from all multipaths, but rather just selects a few of the strongest paths and then ignores the rest. We would then track the gain and delays of, say, the three or four strongest paths. The delay line in this implementation would then have variable delays (rather than a fixed delay line structure) which would be updated as the channel changed.

In a time-varying multipath channel, the tap weights on the RAKE fingers (ie, the  $g_k$ ) have to be periodically updated. So the receiver has the responsibility of estimating these tap weights. This can be done based on the received signal in a manner similar to what is done with adaptive equalization, or it is often accomplished using a pilot signal on a side channel. Naturally, the frequency at which these tap weights have to be updated will depend on how fast the channel is changing. This typically depends on the amount of motion at the transmitter and/or the receiver and perhaps also motion in the surrounding environment. In pedestrian environments where the fading rates may be on the order of a few hertz, these updates may only need to happen a few times per second. However, in vehicular applications, fading rates on the order of 100 Hz can easily be encountered, in which case the RAKE finger weights may need to be updated every few milliseconds. In cases where we are either unwilling or unable to adequately track the channel variations, there is an alternative structure known as a differential RAKE receiver [13,22], which does not require knowledge of the channel tap gains. The structure assumes an underlying DPSK modulation format and is shown in Fig. 10.15.

Fig. 10.16 shows a simple illustration of the operation of a RAKE receiver. The top plot in this figure shows an example channel response where there are four paths


**FIG. 10.15**

A differential RAKE receiver for DPSK DS-SS.


**FIG. 10.16**

An example showing the response of a DS-SS signal to a multipath channel.

with varying strengths and whose delay spread is small compared to the symbol interval,  $T_s$ . Our DS-SS signal is transmitted over this channel and the lower plot shows the output of the receiver filter matched to the code waveform. Due to the fact that the code waveform has an autocorrelation function which is narrow relative to the delay spread of the channel (in this example we used a spreading factor of 256), we can clearly resolve the response due to each of the individual paths. These individual responses can then be isolated, weighted, and appropriately combined to extract a diversity advantage. It is also noted that in this example, the response due to the fourth (weakest) path is lost in the noise; so in this case we might choose to only track the three stronger paths with our RAKE combiner.

### 10.2.2 MULTICARRIER CDMA

Multicarrier CDMA (MCCDMA) [23,24] is a combination of the ideas of DS-CDMA and orthogonal frequency division multiplexing (OFDM). In MCCDMA, the chips associated with a given data symbol are transmitted down separate subcarriers similar to the way data bits are transmitted in OFDM. A generic block diagram of an MCCDMA transmitter is shown in Fig. 10.17. In the figure,  $M$  subcarriers are used, each employing a DS-SS format with  $N/M$  chips per symbol. At one extreme, if  $M = 1$ , this is just traditional DS-CDMA whereby the data symbols are spread with a spreading waveform using  $N$  chips/bit. At the other extreme where  $M = N$ , we have pure MCCDMA where the data symbol is repeated over  $N$  different carriers, each using a DS spreading code with only 1 chip per symbol. For in between values  $M$  such that  $M < N$ , this is referred to as hybrid DS/MC-CDMA. One practical advantage of MCCDMA is that the high chip rate modulators needed for DS-CDMA can be avoided since the use of  $M$  carriers reduces the chip rate of each individual modulator by a factor of  $M$ .

In a frequency selective channel, if the frequency subcarriers are contiguous, MCCDMA offers the same diversity advantage (no more, no less) as DS-CDMA with a RAKE receiver. In the case of MCCDMA, the diversity is achieved by using coding across the frequency subcarriers similarly to what is done in OFDM. By choosing the frequency subchannels to be disjoint, a diversity gain can be achieved even if the

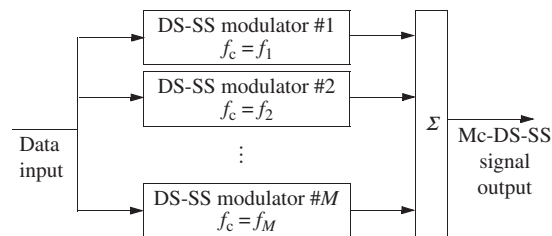


FIG. 10.17

A multicarrier CDMA transmitter.

spread bandwidth (in a DS system) is not enough to make the channel behave in a selective manner.

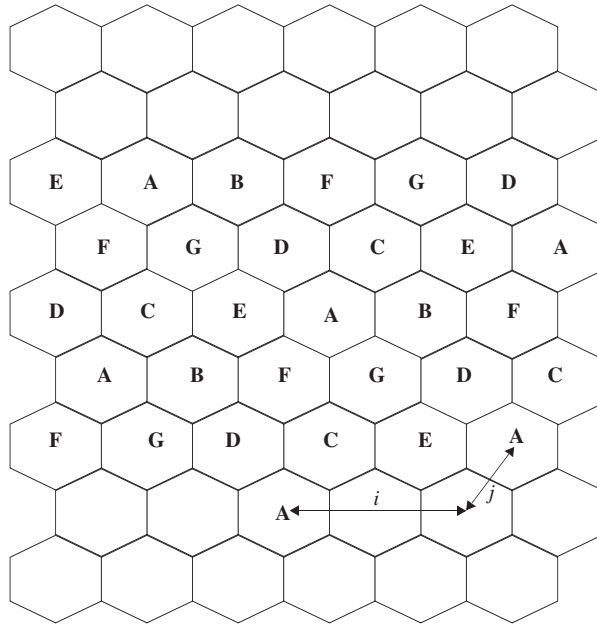
### 10.2.3 CELLULAR CDMA

One of the biggest applications for DS-CDMA over the last few decades has been in the area of cellular telephony. In this section, we discuss a few of the issues that arise in the context of cellular CDMA. To start with, consider the effect that the use of CDMA has on the frequency reuse in a cellular system. A generic cellular layout is shown in Fig. 10.18. Each cell in the figure that is labeled with the same letter reuses the same frequency. In this particular figure, a seven-cell frequency reuse pattern is employed. If an FDMA or hybrid FDMA/TDMA system were employed, each cell would only use one-seventh of the available system channels. This is done to limit the amount of interference caused by users in adjacent cells that are using the same frequency band. By using a high enough reuse factor, this adjacent cell interference can be kept to a manageable level. Alternatively, if DS-CDMA is used, the underlying modulation format is more robust to interference and frequencies can be reused more often. In practice, each frequency is typically reused in every cell (reuse factor of 1) in a cellular CDMA system. So, while the user loading in a CDMA system as shown in Table 10.1 may be below 100%, the advantage gained due to superior frequency reuse often more than makes up for that loss [11,25].

Furthermore, the user capacity in a CDMA system is not limited by the number of channels as in FDMA or TDMA, but rather by the amount of interference that we can tolerate from other users. Anything that can be done to lower the level of self-interference in the CDMA system will result in a direct increase in the number of users the system can support. One such technique is the concept of sectoring [26], whereby each cell is divided into several sectors through the use of directional antennas. Suppose, for example, that at the center of each cell in Fig. 10.18 is a base station that serves that cell. If that base station uses three directional antennas that each receives signals from a 120-degree sector, the amount of interference seen by each antenna will be reduced by roughly a factor of three. In a CDMA system, that will allow us to support thrice as many users. In practice the gain will not be quite a factor of three since there will be some overlap in the antenna gain patterns, but the improvement in user capacity will be substantial. The same concept can be applied to an FDMA-based system, but the gains may not be as great due to trunking inefficiencies.<sup>3</sup>

---

<sup>3</sup>Trunking efficiency measures how well we use the channels that are shared between multiple users that demand access in a random fashion. Trunking efficiency is higher when there are a larger number of channels serving a larger number of users. When FDMA systems use sectoring, the total number of channels available are divided amongst the cells in a frequency reuse pattern and then by the number of sectors per cell. Hence, in such a system, each sector has a smaller number of users served by a smaller number of channels and the trunking efficiency decreases.

**FIG. 10.18**

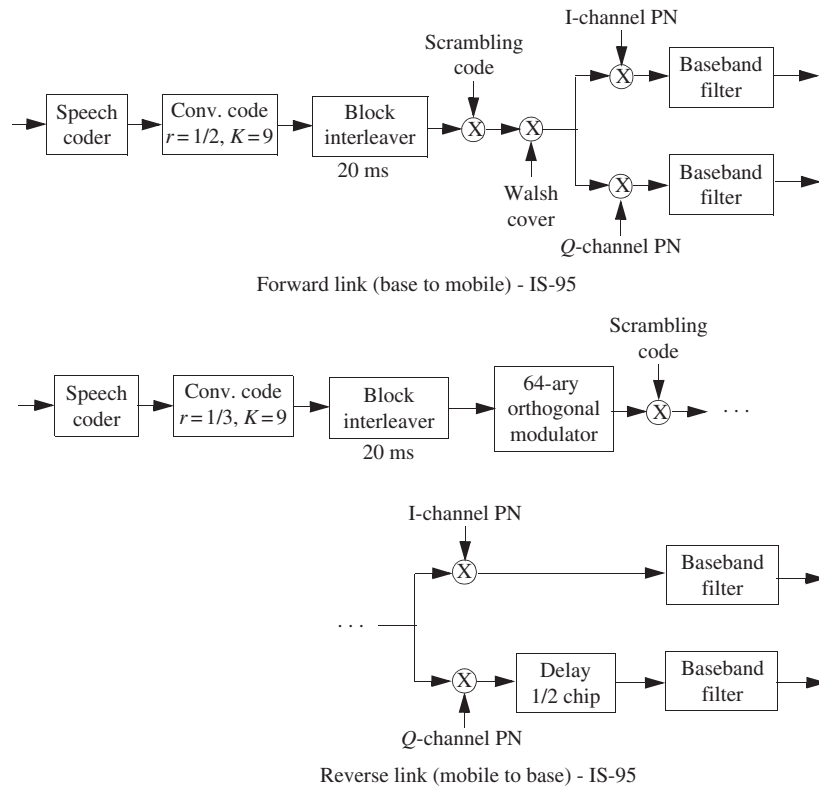
Frequency reuse in a cellular system.

Another technique commonly employed in voice-based cellular CDMA systems is that of voice activity detection [27]. In a typical voice call, each user's voice is active only about 40% of the time. It is relatively simple for a transmitter in a CDMA system to detect when a user's voice is inactive and transmit the corresponding frames at a greatly reduced power. This will result in a significant reduction in the amount of interference presented to the rest of the system and a corresponding increase in the system user capacity.

## 10.3 CDMA STANDARDS

### 10.3.1 2G CELLULAR CDMA: IS-95

The first standard for Cellular CDMA was the so-called Interim Standard 95 (IS-95) [28]. An overview of some of the features of this signaling format are shown in Fig. 10.19. First, the signaling formats are different for the forward link (ie, the downlink) from the base station to the mobile units and the reverse link (the uplink) from the mobiles to the base station. In both cases, the speech coder uses a 9600 bps code excited linear prediction vocoder [29]. The speech coding rate can be lowered to

**FIG. 10.19**

A block diagram of the IS-95 signaling format.

4800, 2400, or 1200 bps if the voice is detected to be inactive. By doing so, this lowers the transmitter power and decreases the interference that the transmitter presents to the rest of the system. In the forward link, the data bits from the speech coder are protected from channel errors using a rate  $1/2$ , constraint length 9, convolutional code. This produces a coded bit rate of 19.2 kbps. The coded bits are interleaved with a  $24 \times 16$  block interleaver. This serves to randomize the burst errors that tend to occur on wireless fading channels. The 384 bits in the interleaving block correspond to a 20-ms speech frame. The coded data bits are then spread further by a pair of spreading codes, one long code and one short code, both of which use a spreading factor of 64 chips/coded bit producing a chip rate of 1.2288 Mchips/s. The long code is an  $m$ -sequence of period  $N = 2^{42} - 1$  and is used to scramble the signal. At the chip rate of 1.228 Mchips/s, this code repeats once every 41.4 days! The short code is a Walsh code of length 64 chips. Each user is assigned one of the 64 codes. One of the Walsh codes is reserved as a pilot (carries no user data) to be used for channel

estimation. Finally, there are separate long codes used on the I and Q channels. These codes are  $m$ -sequences of length  $N = 2^{15} - 1$ . All users in the same sector use the same I and Q codes.

Signaling on the reverse link has several differences. The convolutional encoder uses a rate 1/3 code rather than the rate 1/2 code used on the forward link, and as a result, the coded bit rate is 28.8 kbps. The interleaver still uses 20 ms blocks, but since the input bit rate to the interleaver is higher, the block size is larger. Therefore, a  $32 \times 18$  block interleaver is used on the reverse link. The Walsh codes of length 64 chips are used in a completely different fashion on the reverse link. These codes form the constellation for a 64-ary orthogonal signal set. Each 6 bit word from the output of the interleaver specifies which of the 64 Walsh codes is sent. At this point the chip rate is  $28.8 \text{ kbits/s} \times (64 \text{ chips/6 bits}) = 307.2 \text{ kchips/s}$ . The scrambling codes and the I/Q codes are the same as the forward link, but in this case they further spread the signal by a factor of four producing the 1.2288 Mchips/s rate. In the reverse link, the Q channel is delayed by 1/2 a symbol relative to the I-channel producing an OQPSK type signal. This is done to reduce the peak-to-average power ratio of the transmitted signal in the mobile units in attempt to maximize the efficiency of the power amplifier and preserve battery life. Since the base stations do not need to run on batteries, this is not a concern in the forward link.

In the forward link, signal detection is accomplished using a coherent RAKE receiver. Channel estimates are obtained from the pilot channel. On the reverse link, a noncoherent RAKE is used since no pilot channel is available. Antenna sectorization is employed with three sectors per cell. As discussed previously, this increases the system user capacity but also increases the number of hand offs needed. Voice activity detection is also used to increase the number of users that can be supported. Inactive users lower their transmit power by as much as 9 dB. Each CDMA channel is reused in every cell/sector. To combat the near/far problem on the reverse link, closed loop power control is used. To keep up with a time-varying fading channel, the mobile transmit power is updated at a rate of 800 times/s.

### 10.3.2 3G CELLULAR CDMA

While 2G cellular systems were primarily designed for voice traffic with some small data capabilities, 3G systems were intended to provide much greater data capabilities and hence could handle a mixture of both voice and data. The 3G CDMA standards have many of the same features exhibited in the 2G CDMA standard, but the details are somewhat different, as described below.

#### 10.3.2.1 CDMA 2000

CDMA 2000 [30] is an evolution of the IS-95 system which attempts to meet some of the 3G goals for cellular systems. Transmission can be in multiples of 1, 3, 6, 9, or 12 of the IS-95 chip rate of 1.2288 Mchips/s. This is achieved through either MCCDMA or pure DS-CDMA. In the forward link, QPSK modulation is used with 128 Walsh chips per bit. More codes allow for more users on the forward

link. The 64-ary orthogonal modulation of the IS-95 reverse link was replaced with BPSK. One of the problems with IS-95 was that the voice quality was not great with the 9600 bps vocoder. CDMA 2000 allowed for a second rate set at 14.4 kbps, producing higher voice quality. Options for packet data transmission at rates from 9600 bps to 2.4576 Mbps are available. The spreading gain is variable to allow for different bit rates. Changes in the coding format were also made in CDMA 2000. The convolutional code rate was lowered to 1/4 on the reverse link and the convolutional code can be replaced with a turbo code for data applications. Another new feature introduced in CDMA2000 was the use of transmit diversity. This could be achieved through antenna diversity, through multicarrier diversity, or through a hybrid of both.

### 10.3.2.2 WCDMA

Wideband CDMA (WCDMA) [31,32] is the 3G evolution of the GSM standard. It is referred to as “wideband” since it uses a 5 MHz bandwidth, which is achieved through a 3.84 Mcips/s DS-SS format. The wider bandwidth leads to more multipath resolution and hence more diversity in a wireless channel. On the downlink, the spreading factor can range from 4 to 256, while on the uplink the spreading factor can be as large as 512 depending on the data rates required. Downlink users are kept orthogonal by the use of orthogonal variable spreading factor codes [33]. In WCDMA, pilots are used in both directions so that coherent RAKE detectors can be used. On the downlink, a pilot channel is included with each base station and pilot symbols are also multiplexed into each user’s data stream. On the uplink, no separate pilot channel is used, but pilot symbols are used. Error correction coding of variable rates are employed by puncturing a rate 1/3 or a rate 1/2, constraint length 9, convolutional code. There is also an option to use a rate 1/3 Turbo code. Interleaving is generally over a 10-ms frame. Options are also available to interleave over 20, 40, or 80 ms when the delay constraints allow. Transmission power control information is sent in both directions at a rate of 1400 Hz. Channel feedback information is also sent in both directions to allow the system to employ transmit antenna diversity. Data rates of up to 384 kbps are allowed on circuit switched connections and up to 2 Mbps on packet switched connections.

---

## REFERENCES

- [1] R.A. Scholtz, The spread spectrum concept, *IEEE Trans. Commun.* 25 (1977) 748–755.
- [2] J.K. Holmes, *Coherent Spread Spectrum Systems*, Wiley, 1982.
- [3] M.K. Simon, J.K. Omura, R.A. Scholtz, B.K. Levitt, *Spread Spectrum Communications*, Vol. I, II, III, Computer Science Press, 1985.
- [4] J.K. Nicholson, *Spread Spectrum Signal Design: LPE and AJ Systems*, Computer Science Press, 1988.
- [5] R.L. Peterson, R.E. Ziemer, D.E. Borth, *Introduction to Spread Spectrum Communications*, Prentice-Hall, 1995.

- [6] R.C. Dixon, *Spread Spectrum Systems With Commercial Applications*, third ed., Wiley, 1994.
- [7] A.J. Viterbi, *CDMA, Principles of Spread Spectrum Communications*, Addison Wesley, 1995.
- [8] A.J. Viterbi, Spread spectrum communications: myths and realities, *IEEE Commun. Mag.* 17 (1979) 11–18.
- [9] A.J. Viterbi, Very low rate convolutional codes for maximum theoretical performance of spread-spectrum multiple-access channels, *IEEE J. Sel. Areas Commun.* 8 (1990) 641–649.
- [10] L.W. Couch, *Digital and Analog Communication Systems*, 7th ed., Prentice-Hall, 2007.
- [11] A.J. Viterbi, Wireless digital communication: a view based on three lessons learned, *IEEE Commun. Mag.* 29 (1991) 33–36.
- [12] M.B. Pursley, Performance evaluation for phase-coded spread-spectrum multiple access communication—part I: system analysis, *IEEE Trans. Commun.* 25 (1977) 795–799.
- [13] J.G. Proakis, *Digital Communications*, fourth ed., McGraw-Hill, 2001.
- [14] A.J. Viterbi, A.M. Viterbi, E. Zehavi, Performance of power controlled wideband terrestrial digital communication, *IEEE Trans. Commun.* 41 (4) (1993) 559–569.
- [15] W.W. Peterson, E.J. Weldon, *Error Correcting Codes*, MIT Press, 1972.
- [16] D.W. Sarwate, M.B. Pursely, Crosscorrelation properties of pseudorandom and related sequences, *Proc. IEEE* 68 (1980) 593–619.
- [17] R. Gold, Optimal binary sequences for spread spectrum multiplexing, *IEEE Trans. Inf. Theory* 13 (1967) 619–621.
- [18] R. Gold, Maximal recursive sequences with 3-valued recursive cross-correlation functions, *IEEE Trans. Inf. Theory* 14 (1968) 154–156.
- [19] T. Kasami, Weight distribution formula for some class of cyclic codes, Technical Report R-285 (AD 632574), Coordinated Science Lab., Univ. Illinois, Urbana, 1966.
- [20] T. Kasami, *Weight Distribution of Bose-Chaudhuri-Hocquenghem Codes*, Combinatorial Mathematics and Its Applications, University of North Carolina Press, 1969.
- [21] R. Price, P.E. Green, A communication technique for multipath channels, *Proc. IRE* 46 (1958) 555–570.
- [22] G.L. Turin, Introduction to spread-spectrum antimultipath techniques and their application to urban digital radio, *Proc. IEEE* 68 (1980) 3285–3353.
- [23] S. Kondo, L.B. Milstein, Performance of multicarrier DS CDMA systems, *IEEE Trans. Commun.* 44 (1996) 238–246.
- [24] E.A. Sourour, M. Nakagawa, Performance of orthogonal multicarrier CDMA in a multipath fading channel, *IEEE Trans. Commun.* 44 (1996) 356–367.
- [25] K.S. Gilhousen, I.M. Jacobs, R. Padovani, A.J. Viterbi, L.A. Weaver, C.E. Wheatley, On the capacity of a cellular CDMA system, *IEEE Trans. Veh. Technol.* 40 (1991) 303–312.
- [26] A.F. Naguib, A. Paulraj, T. Kailath, Capacity improvement with base-station antenna arrays in cellular CDMA, *IEEE Trans. Veh. Technol.* 43 (1994) 691–698.
- [27] A.M. Viterbi, A.J. Viterbi, Erlang capacity of a power controlled CDMA system, *IEEE J. Sel. Areas Commun.* 11 (1993) 57–65.
- [28] T.I. Standard-95, *Mobile Station—Base Station Compatibility Standard for Dual Mode Wideband Spread Spectrum Systems*, Telecommunications Industry Association, Washington, D.C.

- [29] A. DeJaco, W. Gardner, P. Jacobs, C. Lee, QCELP: the North American CDMA digital cellular variable rate speech coding standard, in: IEEE Workshop on Speech Coding for Telecommunications, 1993, pp. 5–6.
- [30] E.G. Tiedemann, CDMA2000-1X: new capabilities for CDMA networks, IEEE Veh. Technol. Soc. Newslett. 48 (2001).
- [31] A. Toskala, H. Holma, P. Muszynski, ETSI WCDMA for UMTS, in: IEEE 5th International Symposium on Spread Spectrum Techniques and Applications, 1998, pp. 616–620.
- [32] R. Prasad, T. Ojanpera, A survey on CDMA: evolution towards wideband CDMA, in: IEEE 5th International Symposium on Spread Spectrum Techniques and Applications, 1998, pp. 323–331.
- [33] F. Adachi, M. Sawahashi, K. Okawa, Tree-structured generation of orthogonal spreading codes with different lengths for forward link of DS-CDMA mobile radio, Electron. Lett. 33 (1997) 27–28.

# MIMO communication for wireless networks

# 11

**C.B. Papadias**

*Athens Information Technology, Athens, Greece*

## CHAPTER OUTLINE

<b>11.1 Introduction</b> .....	399
<b>11.2 The Single-User MIMO Link</b> .....	401
11.2.1 Spatial Modes and Spatial Multiplexing .....	402
11.2.2 Full Channel Knowledge at Both the Transmitter and the Receiver .....	404
11.2.3 Full Channel Knowledge Only at the Receiver .....	405
11.2.4 Transceiver Techniques .....	406
11.2.5 Precoding Techniques .....	416
<b>11.3 Limited Feedback Techniques</b> .....	418
11.3.1 MIMO Multiple Access Channel (MAC) .....	420
11.3.2 MIMO Broadcast Channel (BC) .....	422
11.3.3 Multiple MIMO Base Stations .....	424
<b>11.4 Standards</b> .....	425
11.4.1 LTE/LTE-Advanced .....	425
11.4.2 802.11n/802.11ac .....	429
<b>11.5 Future Trends</b> .....	430
<b>Acknowledgments</b> .....	431
<b>References</b> .....	431

## 11.1 INTRODUCTION

Multiple-input/multiple-output (MIMO) systems emerged about two decades ago, as the latest episode/crown achievement of a long period of research in the area of antenna arrays and multidimensional signal processing. Array processing, a field that originated in the 1970s, originally in the analog and soon after in the digital domain, had already offered at the time a plethora of signal processing techniques in order to handle a number of signals that are either transmitted or (most often) received via an antenna array, that is, a group of neighboring antenna elements

with joint combining capability. The key attributes of these systems were their ability to shape arbitrary—within the constraints of the array topology—radiation patterns (“beams”), and to identify the direction(s) of the arrival of impinging waves, making them popular, originally, in military and TV broadcasting applications. Wireless personal communication applications followed suit, since these features translate in the ability to boost the signal-to-noise (SNR) or signal-to-interference-plus-noise (SINR) ratio of wanted signals and to attenuate unwanted interference. Furthermore, antenna arrays provide robustness against signal variability (fading) by offering multiple copies of the same signal that may have traveled through different channels, and hence have undergone different levels of attenuation—what is called antenna diversity. Mobile cellular networks benefited from antenna arrays already in 1st generation analog networks, which included sectorization (ie, the splitting of a wireless cell service area in a number (typically 3) of adjacent angular sections (“sectors”) that are separated from each other via fixed beams that each cover the corresponding sector in a pie-like fashion) [1]. This reduced greatly the interference from adjacent sectors and other co-channel interference in the network (depending on the employed frequency reuse pattern). Antenna-diversity reception at the uplink of the base station was the main extra feature in 2nd generation cellular networks (IS-54/IS-136 in the US, GSM in Europe), including even some beam forming capabilities [2], always at the level of the base station.

While it had become clear that the various array processing techniques, depending on the application, eventually resulted in better SNRs, lower interference and hence better attainable link data rates (throughputs) and system capacity (number of served users within a given spectrum and with target performance requirements in a specific service area) [3] the spectral efficiency potential of wireless links that are equipped with antenna arrays had not been studied in a comprehensive fashion until the mid-1990s. Targeting precisely this topic, that is, the quantification of the maximum attainable throughput per Hertz (“capacity”) of multi-antenna wireless links, the two seminal papers of Telatar [4] and Foschini [5] gave an answer to the question, showing that, under mild propagation conditions, the capacity of such links scales linearly with the minimum of the number of antennas on each side of the link (early indications about this behavior can be also found in Ref. [6]). This remarkable finding (perhaps slightly less so in hindsight, yet still surprising at its time) opened up the new field of MIMO communications, since no other technique up to then (and even today) could offer this type of gain. Its commercial success, which was largely due to an early patent on MIMO communication for TV broadcasting that had been filed, ahead of its time, by Paulraj and Kailath at Stanford University [7], as well as to early validation of spatial-multiplexing (the main MIMO transmission mechanism) in over-the-air experiments at Bell Labs and AT&T, started soon after, along with contributions adopted by air interface standards (3G/HSPA/LTE on the cellular side and IEEE802.11n on the WiFi side). Combined with the exponentially growing demand for wireless services, the proliferation of mobile telephony/data and the expensive licensing fees paid by mobile cellular operators for spectrum

usage, MIMO communication has been since witnessing an explosive growth that has yet to be tamed.

In this chapter, we will attempt to offer an overview of the way MIMO techniques could be employed in a number of key wireless node configurations that correspond to relevant wireless networking scenarios. These will be related to the corresponding performance bounds, in terms of spectral efficiency. The adoption of such techniques in wireless standards will also be discussed, whereas some key emerging trends, pointing to the near-to-mid-term evolution of this breakthrough technology will be presented.

## 11.2 THE SINGLE-USER MIMO LINK

Fig. 11.1 shows the basic configuration of a point-to-point MIMO system in baseband representation. The transmitter and receiver are equipped with  $M$  and  $N$  antenna elements, respectively. We denote by  $s_m$  the baseband signal transmitted from the  $m$ th transmit antenna and by  $x_n$  the signal received by the  $n$ th receiver antenna. We also assume that the channel between each transmit-receive antenna pair is described by a complex scalar, representing a narrow-band (or otherwise frequency-flat) channel characteristic. The channel coefficient between the  $m$ th transmit antenna and the  $n$ th receiver antenna will be denoted by  $h_{nm}$ . We also denote by  $n_n$  the additive noise which is assumed to corrupt the received signal at the  $n$ th receiver antenna.

Since every receive antenna is “exposed” to all the transmit antennas, it will actually receive a linear combination of the signals transmitted by all the transmit antennas:

$$x_n = \sum_{m=1}^M h_{nm} s_m + n_n. \quad (11.1)$$

By stacking together the received signals from all  $N$  receiver antennas in a tall vector, we obtain the following input-output relationship for the MIMO point-to-point link:

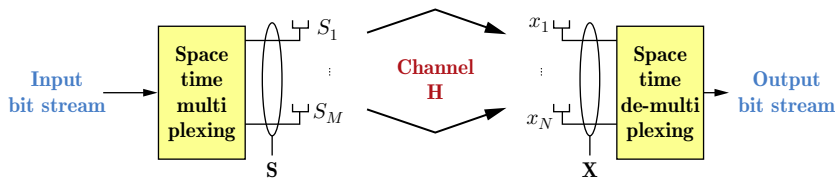


FIG. 11.1

The MIMO link setup.

$$\begin{bmatrix} x_1 \\ \vdots \\ x_N \end{bmatrix} = \begin{bmatrix} h_{11} & \cdots & h_{M1} \\ \vdots & \cdots & \vdots \\ h_{1N} & & h_{MN} \end{bmatrix} \begin{bmatrix} s_1 \\ \vdots \\ s_M \end{bmatrix} + \begin{bmatrix} n_1 \\ \vdots \\ n_N \end{bmatrix}, \quad (11.2)$$

which can be written in a more compact form as follows:

$$\mathbf{x} = \mathbf{H}\mathbf{s} + \mathbf{n}. \quad (11.3)$$

Eq. (11.3) is the well-known narrowband MIMO signal model, which was actually widely used a long time before MIMO systems were invented in several other fields (eg, array processing/direction finding, code division multiple access (CDMA) systems, and so on).

Unless mentioned otherwise, we will assume that  $\mathbf{H}$  is a  $N \times M$  matrix that is kept constant for the duration of transmission. Of course the statistical behavior of  $\mathbf{H}$  is of crucial importance when mutual information/capacity is evaluated—this aspect will be captured in certain performance curves.

It is now important to set forth the rules for transmission, since these will impact heavily the options for transmission methodologies. The most important rule is that the total power transmitted from all the antennas, denoted by  $P_T$ , must be kept constant, irrespective of the number of transmitter antennas  $M$ . As a result, the following equation holds:

$$P_T = \sum_{i=1}^M P_i = \sum_{i=1}^M E |s_i|^2 = \text{tr}(\mathbf{R}_{\mathbf{ss}}), \quad (11.4)$$

where  $P_m$  is the power of the zero-mean signal transmitted by the  $m$ th transmit antenna.  $\mathbf{R}_{\mathbf{ss}}$  is the covariance matrix of the vector of signals transmitted by all the  $M$  antennas:

$$\mathbf{R}_{\mathbf{ss}} = E(\mathbf{s}\mathbf{s}^\dagger), \quad (11.5)$$

where  $^\dagger$  denotes complex conjugate (Hermitian) transpose of a vector or matrix. It is also important to define the statistical properties of the involved signals, that is, the transmitted inputs and the noise. It is customary to model the transmitted signals  $\{s_m\}_{m=1}^M$  as independent and identically distributed (i.i.d.) stationary random processes that are zero-mean, have the same distribution, and are mutually independent. Even though in practice the transmitted signals will have a finite horizon (especially in packet data systems), this model is more convenient for reasons related mostly to capacity computation. For the same reason, we typically assume that each  $s_m$  is Gaussian distributed, hence it can be fully characterized by its mean (assumed zero as mentioned before) and variance  $E |s_m|^2$ .

### 11.2.1 SPATIAL MODES AND SPATIAL MULTIPLEXING

At this point we will provide a derivation of the mutual information (often called “capacity”) of the MIMO channel without channel knowledge at the transmitter. While the derivation would be a priori of secondary importance for this book, we will provide this sketchy proof because it reveals the important concept of

*spatial modes*. The proof is based in the orthogonalization of the channel, that is, its decomposition in non-interfering components, by use of the MIMO channel's singular value decomposition (SVD), which is given below:

$$\mathbf{H} = \mathbf{U}\mathbf{\Sigma}\mathbf{V}^\dagger, \quad (11.6)$$

where  $\mathbf{U}$  and  $\mathbf{V}$  are  $N \times N$  and  $M \times M$  unitary matrices, respectively ( $\mathbf{U}\mathbf{U}^\dagger = \mathbf{U}^\dagger\mathbf{U} = \mathbf{I}_N$ ,  $\mathbf{V}\mathbf{V}^\dagger = \mathbf{V}^\dagger\mathbf{V} = \mathbf{I}_M$ ) and  $\mathbf{\Sigma}$  is a  $N \times M$  diagonal matrix. Each element of  $\text{diag}(\mathbf{\Sigma})$  is a singular value of  $\mathbf{H}$ , or equivalently, the positive square root of an eigenvalue of:

$$\begin{cases} \mathbf{H}\mathbf{H}^\dagger, & \text{if } N \leq M, \\ \mathbf{H}^\dagger\mathbf{H}, & \text{if } N \geq M. \end{cases}$$

Moreover, the columns of  $\mathbf{U}$  are eigenvectors of  $\mathbf{H}\mathbf{H}^\dagger$ , whereas the columns of  $\mathbf{V}$  are eigenvectors of  $\mathbf{H}^\dagger\mathbf{H}$ . We can then write:

$$(\mathbf{H}\mathbf{H}^\dagger)\mathbf{u}_i = \lambda_i\mathbf{u}_i, \quad i = 1, \dots, N. \quad (11.7)$$

Combined with Eq. (11.1), this gives:

$$\begin{aligned} \mathbf{x} &= (\mathbf{U}\mathbf{\Sigma}\mathbf{V}^\dagger)\mathbf{s} + \mathbf{n}, \\ \Rightarrow \mathbf{U}^\dagger\mathbf{x} &= (\mathbf{U}^\dagger\mathbf{U})\mathbf{\Sigma}(\mathbf{V}^\dagger\mathbf{s}) + \mathbf{U}^\dagger\mathbf{n}, \\ \Rightarrow \mathbf{x}' &= \mathbf{\Sigma}\mathbf{s}' + \mathbf{n}'. \end{aligned} \quad (11.8)$$

Notice that Eq. (11.8) is equivalent to Eq. (11.1), since  $\mathbf{s}'$  is a rotated version of  $\mathbf{s}$  (rotation of coordinates). Notice also that the component equations of Eq. (11.8) are uncoupled, due to the diagonal structure of  $\mathbf{\Sigma}$ . Let us assume now that  $\text{rank}(\mathbf{H}) = r$  (where  $r \leq \min(M, N)$ ). Matrix  $\mathbf{\Sigma}$  will then have  $r$  non-zero diagonal elements. Then Eq. (11.8) can be equivalently written as:

$$x'_i = \sigma_i s'_i + n'_i \quad i = 1, \dots, r \quad (11.9)$$

(if  $r < \min(M, N)$  there are also  $\min(M, N) - r$  equations of the type  $x'_i = n'_i$ ,  $i = r + 1, \dots, \min(N, M)$ , which contain no input signal information, so they can be neglected). Notice that Eq. (11.9) describes an ensemble of  $r$  parallel, non-interfering single-input/single-output (SISO) channels, each of gain  $\sigma_i$ . As a result, we can depict the equivalent signal model as shown in Fig. 11.2:

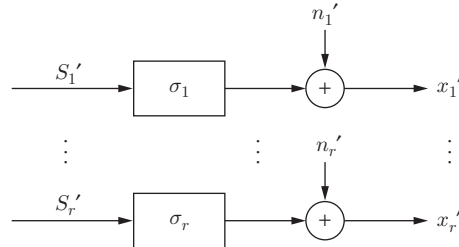


FIG. 11.2

Decomposition of the MIMO channel in constituent SISO channels.

### 11.2.2 FULL CHANNEL KNOWLEDGE AT BOTH THE TRANSMITTER AND THE RECEIVER

Assuming now that we can vary the Tx power of the different transmit antennas, the mutual information of the equivalent system depicted in Fig. 11.2 is given by:

$$C = \sum_{i=1}^r \log_2 \left( 1 + \frac{E |s_i|^2}{\sigma_n^2} \lambda_i \right) = \sum_{i=1}^r \log_2 \left( 1 + \frac{\gamma_i \lambda_i}{\sigma_n^2} \right), \quad (11.10)$$

where  $\gamma_i = E |s_i|^2$  and  $\sum_{i=1}^r \gamma_i = P_T$ .

The capacity of the system can then be found by maximizing the mutual information as follows:

$$\begin{aligned} \max_{\gamma_i} & \left( \sum_{i=1}^r \log_2 \left( 1 + \frac{\gamma_i \lambda_i}{\sigma_n^2} \right) \right) \\ \text{s.t.} & \sum_{i=1}^r \gamma_i = P_T. \end{aligned} \quad (11.11)$$

The expression in Eq. (11.11) is concave to the variables  $\gamma_i$  and can be maximized using Lagrangian methods, yielding the following solution:

$$\gamma_i^{\text{OPT}} = \left( \mu - \frac{\sigma_n^2}{\lambda_i} \right)^+ \quad \text{with} \quad \sum_{i=1}^r \gamma_i = P_T, \quad (11.12)$$

where  $(a)^+ = \max(a, 0)$ . The computation of these power allocations is done iteratively as per the waterfilling algorithm of Cover and Thomas [8]. The so-called closed-loop capacity of the channel is then given by:

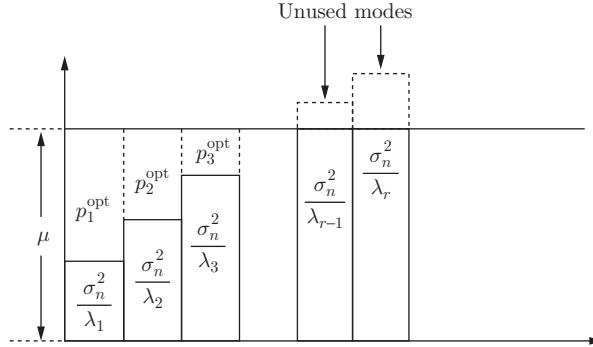
$$C_{\text{CL}} = \sum_{i=1}^r \log_2 \left[ 1 + \frac{1}{\sigma_n^2} \left( \lambda_i \mu - \sigma_n^2 \right)^+ \right]. \quad (11.13)$$

The covariance matrix of the Tx signal in that case is given by:

$$\mathbf{R}_{\text{ss}} = \mathbf{V} \text{diag}(\gamma_1, \dots, \gamma_M) \mathbf{V}^\dagger. \quad (11.14)$$

#### 11.2.2.1 Waterfilling algorithm

Fig. 11.3 depicts graphically the waterfilling technique, which remains the prime algorithm for the computation of the MIMO channel capacity, assuming full channel knowledge at both the transmitter and receiver.


**FIG. 11.3**

The waterfilling algorithm.

The algorithm is composed of the following steps:

1. Iteration count:  $c = 1 : \mu = \frac{P_T}{r - c + 1} \left[ 1 + \sigma_n^2 \sum_{i=1}^{r-c+1} (1/\lambda_i) \right]$ .  
Power computation:  $\gamma_i = (\mu - \sigma_n^2/\lambda_i) ; i = 1, \dots, r - c + 1$ .
2. If the energy allocated to the channel with the lowest gain is negative, that is,  $\gamma_{r-c+1} < 0$ , then we discard this channel by setting  $\gamma_{r-c+1} = 0$ . Then we rerun the algorithm with iteration count  $c$  incremented by 1.
3. The optimal waterfilling power allocation is found when power allocated to each spatial sub-channel (“spatial mode”) is non-negative.

### 11.2.3 FULL CHANNEL KNOWLEDGE ONLY AT THE RECEIVER

The spectral efficiency of the open-loop MIMO system can be computed by assuming that the transmission power is equally split across the spatial channels:

$$E |s_i|^2 = \frac{P_T}{\sigma_n^2}, \quad i = 1, \dots, r, \quad (11.15)$$

which gives, when substituted in Eq. (11.10):

$$C = \log_2 \left( 1 + \frac{\lambda_i P_T}{M \sigma_n^2} \right). \quad (11.16)$$

The MIMO link spectral efficiency with no channel knowledge at the transmitter (sometimes called “open-loop capacity”) would be maximized if each of its constituent capacities are maximized, leading to the expression

$$C = \sum_{i=1}^r \log_2 \left( 1 + \frac{P_T}{M\sigma_n^2} \lambda_i \right) \quad (11.17)$$

or equivalently

$$C = \log_2 \left[ \prod_{i=1}^r \left( 1 + \frac{P_T}{M\sigma_n^2} \lambda_i \right) \right]. \quad (11.18)$$

Note that in Eq. (11.18), the channel is only involved through its eigenvalues. The next question is how to further proceed with Eq. (11.18) to get to a simpler expression that does not involve eigenvalues but a direct channel expression. After some algebraic manipulation, Eq. (11.18) results in

$$C = \log \det \left( I_m + \frac{P_T}{M\sigma_n^2} \mathbf{Q} \right), \quad (11.19)$$

where

$$\begin{cases} \text{if } M \geq N : m = N & \& \quad \mathbf{Q} = \mathbf{H}\mathbf{H}^\dagger, \\ \text{if } M \leq N : m = M & \& \quad \mathbf{Q} = \mathbf{H}^\dagger\mathbf{H}. \end{cases}$$

This means that the mutual information for the open-loop MIMO channel with  $M$  transmit and  $N$  receiver antennas can be expressed as:

$$C = \log \det \left( I_N + \frac{P_T}{M\sigma_n^2} \mathbf{H}\mathbf{H}^\dagger \right). \quad (11.20)$$

Eq. (11.20) is the celebrated “log-det” formula that shows the potential of MIMO links with full channel knowledge at the receiver but no such knowledge on the side of the transmitter. It also leads to the subsequent realization that the capacity scales roughly linearly with the rank of the channel matrix (which is often the minimum of number of antennas between the transmitter and the receiver), even if no channel knowledge is available at the transmitter. Many extensions of this finding, which were first derived for the ergodic (average) capacity over narrowband Rayleigh i.i.d. MIMO channels have appeared since in the literature (see Refs. [4,5,10] for some early studies)—however, their detailed presentation is beyond the scope of this chapter.

### 11.2.4 TRANSCEIVER TECHNIQUES

Two original space-time multiplexing techniques were proposed in Foschini’s brilliant 1996 paper [5], where they were termed V-BLAST and D-BLAST, respectively<sup>1</sup> (see Fig. 11.4). Given the remarkable properties of these two spatial multiplexing schemes in terms of their spectral efficiency potential (realized fully after the paper

---

<sup>1</sup>The term “BLAST” stands for “Bell Labs lAyered Space-Time.”

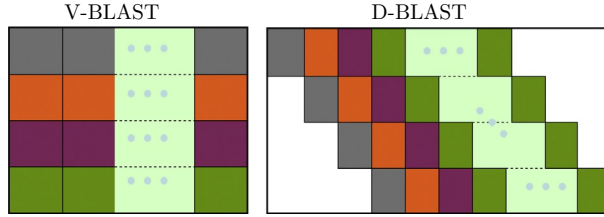


FIG. 11.4

V-BLAST vs. D-BLAST spatial multiplexing (horizontal vs. diagonal transmission).

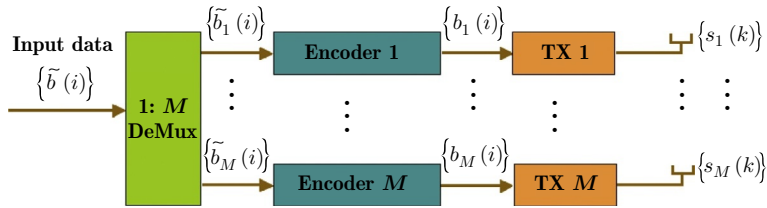


FIG. 11.5

The V-BLAST transmission architecture.

was written), as well as the fact that they cover a large range of trade-offs between performance and complexity, still making them very relevant to today's systems; we will outline their main attributes in this section.

#### 11.2.4.1 V-BLAST

The V-BLAST transmission architecture is shown in Fig. 11.5.

As can be seen in the figure, V-BLAST transmission consists of the following stages:

- *Stage 1:* The original input stream  $\{\tilde{b}(i)\}$  is first demultiplexed into  $M$  data sub-streams:

$$\{\tilde{b}_m(i)\} = \tilde{b}(M(i-1) + m), m = 1, \dots, M.$$

- *Stage 2:* Each of the  $M$  data sub-streams is then individually encoded:

$$\{b_m(k)\} = \text{enc} \{\tilde{b}_m(i)\}.$$

- *Stage 3:* Each of the encoded data sub-streams is then transmitted out of the antenna with the corresponding index:

$$\{s_m(k)\} = \mathbf{T} \{b_m(k)\}, \quad m = 1, \dots, M,$$

where  $\mathbf{T}$  represents all the transmission operations, such as modulation, up-conversion, filtering, etc., prior to transmission. In other words, there is no joint processing or encoding of the data sub-streams prior to transmission.

It should be noted that with V-BLAST:

- The demultiplexing operates on the original (uncoded) bit stream.
- Each data sub-stream is encoded individually.
- Different data sub-streams are transmitted from different antennas.

The term “vertical” BLAST stems from the fact that the original scalar process  $\{\tilde{b}(i)\}$  is converted into the vector process

$$\{\tilde{\mathbf{b}}(i)\} = \begin{bmatrix} \tilde{b}_1(i) \\ \vdots \\ \tilde{b}_M(i) \end{bmatrix}.$$

In hindsight, some people have suggested that a better term would have been “horizontal” BLAST, since each bit stream is encoded horizontally and independently of the other streams. In summary, “vertical” refers to the multiplexing operation, whereas “horizontal” refers to the encoding operation.

Recalling the narrowband MIMO signal of Eq. (11.3)  $[\mathbf{x}(k) = \mathbf{H}\mathbf{s}(k) + \mathbf{n}(k)]$ , the simplest processing option is to use a *linear* receiver. In this case, the received signal  $\mathbf{x}(k)$  is processed linearly, that is, it is multiplied by a  $M \times N$  matrix  $\mathbf{W}$  as follows:

$$\mathbf{z}(k) = \mathbf{W}^\dagger(k)\mathbf{x}(k),$$

where (by convention)  $^\dagger$  denotes Hermitian (ie, complex conjugate) transpose.

The two basic types of linear receivers are the well-known decorrelating (zero-forcing) and minimum mean squared error (MMSE) solutions are given below:

- Decorrelating (ZF) receiver:  $\mathbf{W}(k) = \mathbf{H}^\# = \mathbf{H}(\mathbf{H}^\dagger\mathbf{H})^{-1}$ .
- MMSE receiver:  $\mathbf{W}(k) = \left(\mathbf{H}\mathbf{H}^\dagger + \frac{M}{\text{SNR}}\mathbf{I}_N\right)^{-1}\mathbf{H}$ .

A number of nonlinear alternatives can be also used to offer better detection performance than their linear counterparts. These range from “decision-feedback-type” receivers to joint maximum likelihood receivers, providing a range of performance vs. complexity trade-offs. The most appealing architecture is based on ordered successive interference cancellation (SIC), based on successive nulling and cancellation (see Ref. [5] for more details).

### 11.2.4.2 Receiver options

We saw in detail the V-BLAST architecture and transmission/reception processing. A key performance feature of V-BLAST (as will be shown later) is that it falls short of capacity if only a single rate feedback is available at the transmitter. D-BLAST is a more complex technique that allows the attainment of the full log-det capacity of Eq. (11.20) with single rate feedback, which is why we describe it below.

In contrast to V-BLAST, in D-BLAST all sub-streams are exposed to all transmit antennas. Intuitively, this leads to a higher transmission rate, if for example we think of the pathological case of an antenna having a very bad (or completely broken) channel. As it turns out, this intuitive superiority indeed leads to a higher capacity potential. To better explain this transmission architecture, it is important that we define first the concept of “layer”: A layer is an encoded data sub-stream that is obtained after the original bit stream is de-multiplexed onto a number of sub-streams that are then each individually encoded, as shown in Fig. 11.6.

Having defined layers, the D-BLAST transmission architecture is shown in Fig. 11.7. In the figure, the Modulo- $M$  circular shift changes by a single step the layer-antenna association every  $t$  seconds. In other words, each layer is transmitted from an antenna for  $t$  seconds; then it is transmitted by the next (modulo  $M$ ) antenna

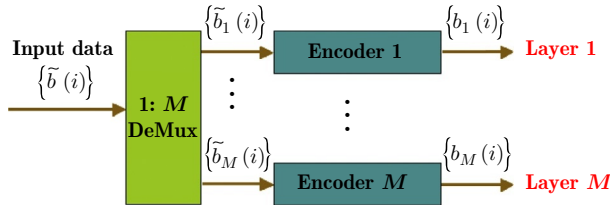


FIG. 11.6

The concept of a layer.

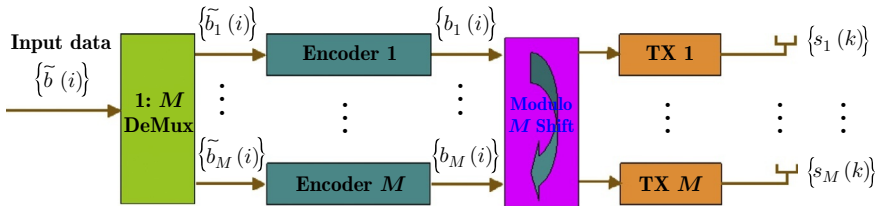


FIG. 11.7

The D-BLAST transmission architecture.

$\{\mathbf{b}_1(1)\}$	$\{\mathbf{b}_2(1)\}$	$\{\mathbf{b}_3(1)\}$	$\{\mathbf{b}_4(1)\}$	$\{\mathbf{b}_1(5)\}$	$\{\mathbf{b}_2(5)\}$	$\{\mathbf{b}_3(5)\}$	...
$\mathbf{0} \cdots \mathbf{0}$	$\{\mathbf{b}_1(2)\}$	$\{\mathbf{b}_2(2)\}$	$\{\mathbf{b}_3(2)\}$	$\{\mathbf{b}_4(2)\}$	$\{\mathbf{b}_1(6)\}$	$\{\mathbf{b}_2(6)\}$	...
$\mathbf{0} \cdots \mathbf{0}$	$\mathbf{0} \cdots \mathbf{0}$	$\{\mathbf{b}_1(3)\}$	$\{\mathbf{b}_2(3)\}$	$\{\mathbf{b}_3(3)\}$	$\{\mathbf{b}_4(3)\}$	$\{\mathbf{b}_1(7)\}$	...
$\mathbf{0} \cdots \mathbf{0}$	$\mathbf{0} \cdots \mathbf{0}$	$\mathbf{0} \cdots \mathbf{0}$	$\{\mathbf{b}_1(4)\}$	$\{\mathbf{b}_2(4)\}$	$\{\mathbf{b}_3(4)\}$	$\{\mathbf{b}_4(4)\}$	...

**FIG. 11.8**

The D-BLAST initialization procedure.

for another  $t$  seconds, and so on. The way streams are transmitted is shown in the right-hand side of Fig. 11.5.

Some comments are worth making regarding D-BLAST:

- The demultiplexing operates on the original (uncoded) bit stream.
- Each data sub-stream is encoded individually.
- The association between blocks of encoded data from each sub-stream (called layers) and transmit antennas is periodically shifted to the next antenna.
- As a result, the data stream that is transmitted out of each antenna contains segments of the encoded data of all the data sub-streams

Also, D-BLAST requires a specific initialization, whereby the first layer is first transmitted alone, then the second layer follows, and so forth. This transmission methodology can be depicted as in Fig. 11.8 (ways to avoid the waste of bandwidth that are related to this initialization were later devised).

In the figure,  $\{\mathbf{b}_m(l)\}$  represents a block of  $L$  encoded symbols—so the first layer can be depicted as

$\{\mathbf{b}_1(1)\}$	$\{\mathbf{b}_1(2)\}$	$\{\mathbf{b}_1(3)\}$	$\{\mathbf{b}_1(4)\}$
-----------------------	-----------------------	-----------------------	-----------------------

A similar termination mechanism is required at the end of the transmission as a consequence of the initialization procedure, as shown in Fig. 11.9.

Let us now examine a simple  $2 \times N$  case to show how the D-BLAST receiver operates:

We will denote the channel as  $\mathbf{H} = [\mathbf{h}_1 \quad \mathbf{h}_2]$ . Then the transmission can be depicted as follows for each transmission antenna:

**Antenna 1:**

$b_1(1) \cdots b_1(L)$	$b_2(1) \cdots b_2(L)$	$\mathbf{0} \cdots \mathbf{0}$
------------------------	------------------------	--------------------------------

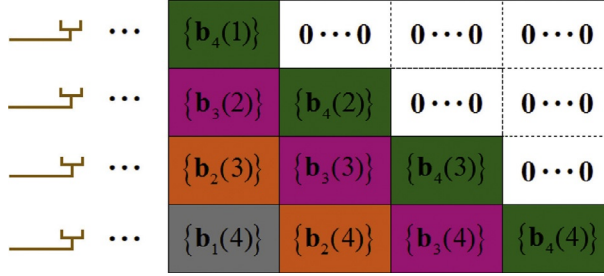


FIG. 11.9

The D-BLAST termination procedure.

### Antenna 2:

$$\begin{bmatrix} 0 & \dots & 0 & b_1(L+1) \dots b_1(2L) & b_2(L+1) \dots b_2(2L) \end{bmatrix}$$

Received signal during  $t = 1 : L$ :  $\mathbf{r}(i) = \mathbf{h}_1 b_1(i) + \mathbf{h}_2 \cdot 0 + \mathbf{n}(i)$ , which can be written equivalently as:  $\mathbf{r}(i) = \mathbf{h}_1 b_1(i) + \mathbf{n}(i)$ . In this case, simple matched filtering yields:

$$\hat{b}_1(i) = \frac{\mathbf{h}_1^\dagger \mathbf{r}(i)}{\|\mathbf{h}_1\|^2} = b_1(i) + \frac{\mathbf{h}_1^\dagger \mathbf{n}(i)}{\|\mathbf{h}_1\|^2},$$

thus recovering the part of the first layer  $\{b_1(1 : L)\}$ .

Now the received signal during  $t = L + 1 : 2L$  is given by:

$$\mathbf{r}(L+i) = \underbrace{\mathbf{h}_1 b_2(i)}_{\text{Interference}} + \underbrace{\mathbf{h}_2 b_1(L+i)}_{\text{Signal}} + \underbrace{\mathbf{n}(L+i)}_{\text{Noise}}.$$

The contribution from  $b_2(i)$  can be nulled out or projected away linearly or nonlinearly. A linear (zero-forcing) example is shown below:

- Signal model:  $\mathbf{r}' = \mathbf{r} - \mathbf{n} = \begin{bmatrix} \mathbf{h}_2 & \mathbf{h}_1 \end{bmatrix} \begin{bmatrix} b_1 \\ b_2 \end{bmatrix} = \mathbf{H}\mathbf{b}.$

- We want:  $W^\dagger \mathbf{r}' = 1 \cdot b_1 + 0 \cdot b_2 = \begin{bmatrix} 1 & 0 \end{bmatrix} \begin{bmatrix} b_1 \\ b_2 \end{bmatrix},$

which requires  $W^\dagger \mathbf{H}\mathbf{b} = \begin{bmatrix} 1 & 0 \end{bmatrix} \mathbf{b}, \forall \mathbf{b}$ , or equivalently

$$\begin{cases} W^\dagger \mathbf{h}_1 = 0 \Rightarrow W \perp \mathbf{h}_1, \\ W \mathbf{h}_2 = 1, \end{cases}$$

resulting in  $\mathbf{H}^\dagger \mathbf{W} = \begin{bmatrix} 1 \\ 0 \end{bmatrix} \Rightarrow$  a minimum-norm solution is

$\mathbf{W} = \mathbf{H} (\mathbf{H}^\dagger \mathbf{H})^{-1} \begin{bmatrix} 1 \\ 0 \end{bmatrix}$ , thus recovering the second part of the first layer,  $\{b_1(L+1 : 2L)\}$ . The recovery of the entire first layer is now complete.

For the detection of the 2nd layer now:

- Signal model for  $t = L+1 : 2L$ :  $\mathbf{r}(i) = \mathbf{h}_1 b_2(i) + \mathbf{h}_2 b_1(L+i) + \mathbf{n}(L+i)$ . But now,  $b_1(L+i)$  is known, thus allowing us to subtract it from the received signal, giving:

$$\tilde{\mathbf{r}}(i) = \mathbf{h}_1 b_2(i) + \mathbf{n}(L+i)$$

so that  $\{b_2(1 : L)\}$  can be easily detected.

- For  $t = 2L+1 : 3L$ :

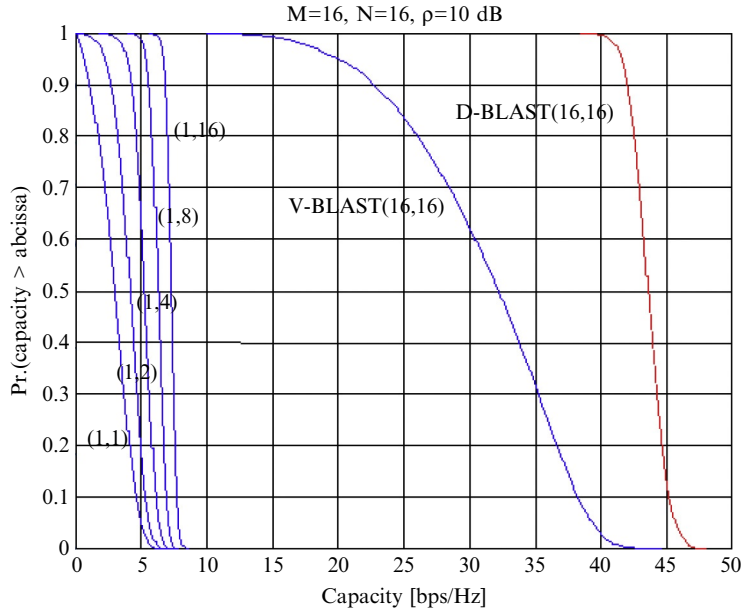
$$\mathbf{r}(2L+i) = \mathbf{h}_1 b_1(2L+i) + \mathbf{h}_2 b_2(L+i) + \mathbf{n}(2L+i)$$

Hence, simple matched filtering again yields  $b_2(L+1 : 2L)$ , thus concluding the recovery of the second layer as well!

The above mechanism was illustrative but can be easily generalized to an arbitrary number of  $M \leq N$  transmit antennas. It should be noted that the optimal linear projections are, again, MMSE filters. It should be also noted that the order in which the different sub-streams are processed is now fixed, based on the way the layers are arranged at the transmitter. Consistent with its philosophy (and assuming perfect detection at each stage), all sub-streams are exposed to the MIMO channel in the same way in D-BLAST.

Finally and most importantly, it should be noted that, in terms of performance, it was shown in Ref. [9] that the D-BLAST transmitter architecture, combined with optimal receiver processing, allows the attainment of the full open-loop capacity of the MIMO channel. It should be noted that D-BLAST is practically unique in its (at least theoretical) ability to attain the open loop channel capacity for i.i.d. channels in a universal fashion (ie, for arbitrary numbers of transmit and receive antennas—see Section 12.4.1 in Ref. [10]).

Based on all of the above, spectral efficiency curves as the one shown below can be drawn in order to see how the V-BLAST and D-BLAST schemes compare in terms of outage capacity—see Fig. 11.10 and also Ref. [11]. It should be also mentioned that, as was later shown in Ref. [12], if the strict “Open-loop” operation is relaxed at the V-BLAST transmitter in order to allow it to know the optimal rates of each stream, then, when combined with optimally ordered successive interference cancellation at the receiver, the V-BLAST technique can also attain the open-loop capacity. This technique is termed “per antenna rate control” (PARC) and achieves an excellent tradeoff between feedback burden and capacity attainment.

**FIG. 11.10**

Comparison of V-BLAST and D-BLAST in terms of outage capacity potential.

#### 11.2.4.3 Space-time block codes

As was mentioned earlier, the capacity scaling of MIMO channels is proportional (at best) to the minimum of the number of antennas between the transmitter and the receiver. As a result, in the case of a single antenna on the side of the receiver (as were most mobile terminals at the time of the introduction of the MIMO concept), the gains are expected to be very limited in terms of capacity scaling. However, there are important diversity gains that can be attained in this case. The introduction of MIMO has had, as a collateral benefit, the invention and study of so-called space-time coding techniques that are well suited for such asymmetrical channel configurations and extract diversity gains from these links.

In the following, we focus on the class of *space-time block codes*, which was historically the first one to be introduced and which contains some important techniques that are still used today as a building block of MIMO techniques in several wireless standards (as will be discussed later).

The basic space-time block coding transmission architecture is shown in Fig. 11.11.

In this architecture, the original bit stream is first encoded; the encoded data are then mapped onto blocks of vector data that are then transmitted out of the antennas. In this fashion, encoding and spatial multiplexing are decoupled: encoding

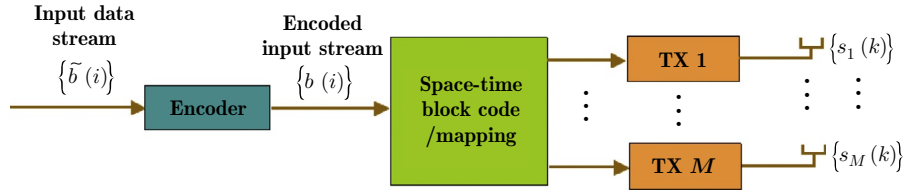


FIG. 11.11

A space-time block coding transmission architecture.

is a time-only operation, whereas the block code determines how the encoded data samples are mapped onto different antenna elements.

More specifically:

- The space-time block encoder is described by an  $M \times L$  matrix  $\mathbf{S}$  where  $M$  represents the number of transmit antennas and  $L$  represents the length of the code in symbol periods.
- The  $l$ th column of matrix  $\mathbf{S}$  represents the vector of encoded symbols that are transmitted from the  $M$  antennas during the  $l$ th symbol period within the block.
- Likewise, the  $m$ th row of matrix  $\mathbf{S}$  represents the sequence of encoded symbols that are transmitted by the  $m$ th transmit antenna over the  $L$  symbol periods (which constitute a coding block).
- Another important parameter besides  $M$  and  $L$  is the number of encoded input symbols that are contained in each space-time block  $\mathbf{S}$ : we denote this by  $Q$ . In other words,  $Q$  is the number of encoded sub-streams that are transmitted out of the  $M$  transmit antennas over the  $L$  symbol periods.

A generic space-time block code looks as follows:

$$\begin{array}{c}
 \text{Time} \longrightarrow \\
 \longleftarrow L \text{ columns} \longrightarrow \\
 \text{Space} \downarrow \\
 \mathbf{S} = \begin{bmatrix} (\pm) b_1^{(*)} & \dots & (\pm) b_J^{(*)} \\ \vdots & \dots & \vdots \\ (\pm) b_I^{(*)} & \dots & (\pm) b_F^{(*)} \end{bmatrix} \begin{array}{c} \uparrow \\ M \text{ rows} \\ \downarrow \end{array}
 \end{array}$$

In general, each  $s_{ij}$  is a linear combination of  $b_1, \dots, b_Q$  and  $b_1^*, \dots, b_Q^*$ . The code parameters are:

- $M$ : the number of transmit antennas;
- $L$ : the length of the code (in encoded symbol periods);
- $Q$ : the number of original encoded input symbols contained in  $\mathbf{S}$  (in other words,  $Q$  is the number of sub-streams mapped through  $\mathbf{S}$  onto the  $M$  transmit antennas).

Typically,  $M \leq L$ ;  $Q \leq L$ .

In terms of its properties, a space-time block code can be characterized by:

- Code rate:  $R = Q/L$  (eg, a code with  $R = 1$  is called “full rate”).
- Code delay:  $L \geq M$  (eg, a code with  $L = M$  is called “delay optimal”).
- Diversity order: defined as the magnitude of the slope of the average symbol error probability at the receiver vs. SNR (in a log-log scale).

The maximum diversity order equals  $M$  and can be achieved if  $\mathbf{S}$  satisfies the following equation:

$$\mathbf{S}\mathbf{S}^\dagger \propto \left( \sum_{q=1}^Q |b_q|^2 \right) \mathbf{I}_M \quad (11.21)$$

(This equation is derived from the theory of orthogonal designs [13].) A code that satisfies this equation achieves “maximum transmit diversity.” From the above, we conclude that the ideal space-time block code has the following properties:

1. It achieves full transmit diversity (order  $M$ )  $\Rightarrow$  it satisfies the condition Eq. (11.21).
2. It is full rate:  $R = 1 \Rightarrow Q = L$ .
3. It is delay optimal:  $L = M$ .

In summary, such a code has  $L = M = Q$  and satisfies

$$\mathbf{S}\mathbf{S}^\dagger \propto \left( \sum_{q=1}^Q |b_q|^2 \right) \mathbf{I}_M.$$

#### 11.2.4.4 An example for $M = 2$ : the Alamouti space-time code

A very popular (and remarkably efficient) space-time block code (the one that really defined the class of space-time block codes) is the so-called Alamouti space-time block code [14], which applies to the case of two transmit antennas and is simply defined as

$$\mathbf{S} = \begin{bmatrix} b_1 & -b_2^* \\ b_2 & b_1^* \end{bmatrix}.$$

The parameters of this code are  $Q = M = L = 2$ . Moreover, this code has

- Code rate:  $R = 1$ .
- Code delay:  $L = 2$ .
- Diversity order: 2.

In other words, the Alamouti space-time block code is:

- Full rate,
- Full diversity,
- Delay optimal.

Moreover, it has been shown that, quite remarkably, the Alamouti code allows the attainment of the open-loop capacity in the (2,1) case [15,16]. It should be noted that, to date, no other space-time block code is known that jointly satisfies these properties for any other  $M > 2$ . Not surprisingly, due to its remarkable properties, as will be seen later, the Alamouti code has been used in several wireless standards for improved link performance.

### 11.2.5 PRECODING TECHNIQUES

In cases where the channel is known perfectly on the side of the transmitter (such as in the case of the waterfilling algorithm presented earlier), the general class of techniques that can be used for MIMO transmission are termed as “precoding.” Linear precoding consists of a linear mapping between the original MIMO vector signal and its pre-coded version that is sent to the antennas for transmission over the channel. This linear mapping is usually denoted as

$$\mathbf{F} = \mathbf{\Phi} \mathbf{V}, \quad (11.22)$$

where  $\mathbf{V}$  is typically a rotation matrix and  $\mathbf{\Phi}$  a diagonal matrix. The role of  $\mathbf{V}$  is to rotate the transmitted way in a direction that is “friendly” to the channel, whereas the role of  $\mathbf{\Phi}$  is to load the independent spatial modes (columns) of  $\mathbf{V}$  with different powers according to a power constraint criterion. In most cases, the columns of  $\mathbf{V}$  are chosen to be the singular vectors of the channel matrix  $\mathbf{H}$ .  $\mathbf{F}$  is the last processing of the transmitted signal before it goes into the MIMO channel. Accordingly, a multiplying matrix  $\mathbf{G}$  is used at the receiver to process first the received vector signal.

The role of precoding is to make the entire spatial multiplexing/coding on the transmitter side and corresponding de-multiplexing/decoding on the receiver side simpler: it introduces some structure based on the knowledge of the channel that allows these operations to be less complex and more modular [17]. In all precoding/decoding designs, the matrices  $\mathbf{F}$  and  $\mathbf{G}$  exploit the eigen decomposition of the MIMO channel  $\mathbf{H}$ . It turns out that in all optimal designs, the optimal pairs of  $\mathbf{F}$  and  $\mathbf{G}$  are of the following form:

$$\begin{cases} \mathbf{F}_{\text{opt}} = \mathbf{V} \mathbf{\Phi}, \\ \mathbf{G}_{\text{opt}} = \mathbf{\Gamma} \mathbf{\Lambda}^{-1} \mathbf{V}^H \mathbf{H}^\dagger \mathbf{R}_{\text{nn}}^{-1}, \end{cases} \quad (11.23)$$

where  $\mathbf{\Phi}$  and  $\mathbf{\Gamma}$  are diagonal matrices. These designs apply even to the wideband (frequency selective, including intersymbol interference, ISI) MIMO channels, hence they are more general than the capacity-achieving waterfilling solution presented earlier. The simplicity achieved via linear precoding/decoding is manifested by the fact that, according to Eq. (11.23), the MIMO system is reduced into  $K$  parallel independent flat (ISI-free) scalar sub-channels, each of complex channel gain equal to  $\varphi_{kk} \gamma_{kk}$  and scalar additive Gaussian noise if variance  $1/\lambda_{kk}$  (the noise samples are uncorrelated between different sub-channels):

$$\hat{\mathbf{s}}_{ik} = \varphi_{kk}\gamma_{kk}\mathbf{s}_{ik} + \gamma_{kk}\beta_{ik}, \quad k = 1, \dots, K. \quad (11.24)$$

In the following section, we will describe the solutions to some well-known optimization criteria for linear precoding designs.

### 11.2.5.1 MSE-based criteria

The mean-squared error metric is defined as

$$\text{MSE}(\mathbf{F}, \mathbf{G}) = E \left\{ (\hat{\mathbf{s}}_i - \mathbf{s}_i) (\hat{\mathbf{s}}_i - \mathbf{s}_i)^\dagger \right\}. \quad (11.25)$$

For a given precoder  $\mathbf{F}$ , the matrix  $\mathbf{G}$  that minimizes (a function of) the MSE in (11.25) is given by [17]:

$$\mathbf{G}_{\text{opt}} = \sigma_{ss}^2 \mathbf{F}^\dagger \mathbf{H}^\dagger \left( \sigma_{ss}^2 \mathbf{H} \mathbf{F} \mathbf{F}^\dagger \mathbf{H}^\dagger + \mathbf{R}_{nn} \right)^{-1}. \quad (11.26)$$

To find the optimal  $\mathbf{F}$ , we need to also constrain the transmitted power. The following two criteria are commonly used:

- Fixing the average transmit power (per data block):

$$P_0 = E \|\mathbf{x}_i\|^2 = \text{tr}(\mathbf{F} \mathbf{R}_{ss} \mathbf{F}^\dagger).$$

- Fixing the peak power of the transmitted power, which amounts to fixing the maximum eigenvalue of  $\mathbf{F} \mathbf{F}^\dagger$ :

$$\mathcal{L}_0 = \lambda_{\max}(\mathbf{F} \mathbf{F}^\dagger).$$

Of the various combinations of constrained optimization criteria, perhaps the most interesting one is the following:

$$\begin{cases} \min_{\mathbf{F}} |\text{MSE}(\mathbf{F}, \mathbf{G}_{\text{opt}})|, \\ \text{s.t. } \text{tr}(\mathbf{F} \mathbf{F}^\dagger) \sigma_s^2 = P_0, \end{cases} \quad (11.27)$$

where  $\mathbf{G}_{\text{opt}}$  is given in Eq. (11.26). The solution to Eq. (11.27) is

$$\begin{aligned} \mathbf{F}_{\text{opt}} &= \mathbf{V} \Phi_{\text{opt}}, \\ [\Phi_{\text{opt}}]_{ij} &= \begin{cases} \left( \frac{P_0 + \sum_{k=1}^{\bar{N}} \lambda_{kk}^{-1}}{\bar{N} \sigma_s^2} - \frac{1}{\lambda_{ii} \sigma_s^2} \right)^+, & i = j, \\ 0, & i \neq j, \end{cases} \end{aligned} \quad (11.28)$$

where  $\bar{N}$  is the number of strictly positive  $|\varphi_{ii}|^2$ . Interestingly, the pair of solutions in Eqs. (11.26) and (11.28) also maximize the mutual information between the transmitter and receiver data! An alternative solution may be found if, instead of

the determinant of the MSE, its trace is used:

$$\begin{cases} \min_{\mathbf{F}} \text{tr}(\text{MSE}(\mathbf{F}, \mathbf{G}_{opt})), \\ \text{s.t. } \text{tr}(\mathbf{F}\mathbf{F}^\dagger) \sigma_s^2 = P_0. \end{cases} \quad (11.29)$$

The corresponding solution is as follows:

$$\begin{aligned} \mathbf{F}_{opt} &= \mathbf{V}\Phi_{opt} \\ [\Phi_{opt}]_{ij} &= \begin{cases} \left( \frac{P_0 + \sum_{n=1}^N \lambda_{nn}^{-1}}{\sigma_s^2 \sum_{n=1}^N \lambda_{nn}^{-1/2}} \lambda_{ii}^{-1/2} - \frac{1}{\lambda_{ii} \sigma_s^2} \right)^+, & i = j, \\ 0, & i \neq j. \end{cases} \end{aligned} \quad (11.30)$$

Other solutions can be found by using instead of average power a peak power constraint, as well as by replacing the MSE criteria by SNR-based criteria. More details can be found in Ref. [17].

The important two points to retain from the above discussion are:

1. Optimal precoding leads to the diagonalization of the overall MIMO channel and of the receive noise covariance.
2. The precoder/decoder pair that is optimal in terms of the determinant of the MSE metric subject to an average power constraint is also the solution that maximizes the mutual information between transmitter and receiver.

Solutions of similar structure stemming from similar criteria will emerge later on in multi-user MIMO settings.

---

### 11.3 LIMITED FEEDBACK TECHNIQUES

In cases where the channel is not known perfectly on the side of the transmitter, it is still possible to do precoding based on limited feedback from the receiver to the transmitter. These techniques mostly target Frequency Division Duplex (FDD) systems, wherein the channel from the transmitter to the receiver is weakly correlated to the channel from the receiver to the transmitter. In the general case, the transmitted signal is again weighted by a matrix  $\mathbf{F}$ , as well as typically power-scaled, resulting in a received signal of the following form:

$$\mathbf{x}(k) = \sqrt{\rho} \mathbf{H}(k) \mathbf{F}(k) \mathbf{s}(k) + \mathbf{n}(k), \quad (11.31)$$

where the dimension of  $\mathbf{F}(k)$  is  $M \times L$  where  $L \leq M$ . The idea is that  $\mathbf{s}(k)$  is chosen independently of the channel conditions, whereas the precoding matrix  $\mathbf{F}$  is chosen in order to temper the channel characteristics, based on some type of limited feedback from the receiver. Some typical limited feedback approaches are:

### Antenna subset selection

In this case  $\mathbf{F}(k)$  consists of  $L$  columns chosen from the  $M \times M$  identity matrix. These columns must be chosen by the receiver based on some criterion that takes advantage of its matrix channel estimate. Since there are  $\binom{M}{L}$  possible antenna subset selection matrices, the required feedback is  $\log_2 \binom{M}{L}$  bits [18].

### Antenna power adjustment

Another simple approach is to choose a diagonal  $\mathbf{F}(k)$  and only adjust the power of each antenna (sometimes called per antenna rate and power control). This is a straightforward limited feedback extension of conventional open-loop spatial multiplexing. As mentioned earlier, per antenna rate control alone, when combined with V-BLAST SIC-MMSE reception, allows the attainment of the open-loop mutual information of the MIMO channel. The extra degree of freedom provided by the power has the potential of offering further performance benefits [19].

### Subspace-based precoding

Ideally, one would of course want to design  $\mathbf{F}(k)$  so as to direct data towards “good” channel subspace directions [20]. Such precoding involves in a more substantial way the channel knowledge at the receiver. There are two schools of thought regarding the exploitation of channel state information (CSI) present at the receiver by the transmitter: in the first case, the channel matrix estimate is quantized and then sent to the transmitter, who then designs  $\mathbf{F}(k)$  based on the quantized channel estimate sent by the feedback channel. In the second case, the receiver chooses the preferred  $\mathbf{F}(k)$  and then quantizes it and sends it to the transmitter who then uses it without a need for further processing. In both cases, the employed vector quantization (VQ) techniques pick the matrix of choice from a set of  $2^B$  possible matrices based on some performance criterion and then use  $B$  bits of feedback in order to convey the chosen matrix to the transmitter.

In the case of subspace-based precoding, the employed performance criteria need to somehow involve metrics that include the distance between subspaces, which is an involved topic (in the special case of MISO channels, this reduces to Grassmanian line packing, for which several solutions exist, such as in Ref. [21]). Since most performance metrics depend on the product  $\mathbf{F}(k)\mathbf{F}^\dagger(k)$ , it is customary that  $\mathbf{F}(k)$  is chosen to be a unitary matrix ( $\mathbf{F}^\dagger(k)\mathbf{F}(k) = I_{L \times L}$ ). The approach can be then seen as a multidimensional eigenbeam-forming one.

### Covariance quantization

In this case, the transmitted signal is given by  $\sqrt{\rho}\mathbf{Q}^{1/2}(k)\mathbf{x}(k)$ , where  $\mathbf{Q}(k)$  is the covariance of the transmitted signal at the given channel instantiation and can include both spatial power allocation and unitary precoding. When a codebook of  $2^B$  possible covariance matrices  $\mathcal{Q} = \{\mathbf{Q}_1, \dots, \mathbf{Q}_{2^B}\}$  is employed, using a mutual information metric, the optimal precoder is found according to the following criterion:

$$n_{\text{opt}}(k) = \arg \max_{1 \leq n \leq 2^B} \log_2 \det \left[ I_N + \frac{\text{SNR}}{M} \mathbf{H}(k) \mathbf{Q}_n \mathbf{H}^\dagger(k) \right]. \quad (11.32)$$

Further improvements can be reached if temporal correlation between the channel fading blocks are taken into account (see [22] and other references in [18]).

### Rank-1 precoding

In the case of MISO channels, the precoding takes the form of  $\mathbf{x}(k) = \rho \mathbf{f}(k)s(k)$ . As in the MIMO case, the available options for choosing  $\mathbf{f}(k)$  include antenna selection, vector quantization either of the channel  $\mathbf{h}(k)$  or of the precoder  $\mathbf{f}(k)$  and Grassmanian line packing [21]. Another approach is random vector quantization (RVQ), where the codebooks are randomly generated (simultaneously at the transmitter and receiver) at each coding block, according to a given distribution of the optimal unquantized beam-forming vector. It should be noted that, even though these approaches are tailored to MISO channels, they can be also used in MIMO channels (reaching optimality when the MIMO channel is indeed rank 1, but providing variable gains in other cases as well).

The case of isolated MIMO links, as studied in the previous section, does not apply to most multi-user wireless network setups, wherein a number of wireless users are allocated within the same frequency band and are located close enough to each other so they interfere. The information theoretic analysis of multi-dimensional (MIMO) links has paved the way for the corresponding analysis of multi-user/multi-antenna network setups. The most important multi-user configurations are described below.

### 11.3.1 MIMO MULTIPLE ACCESS CHANNEL (MAC)

Fig. 11.12 shows a typical multi-access channel setup. We assume that  $K$  users, each equipped with an  $N$ -antenna terminal, occupy the same frequency band and are communicating in the uplink direction with a base station that is equipped with

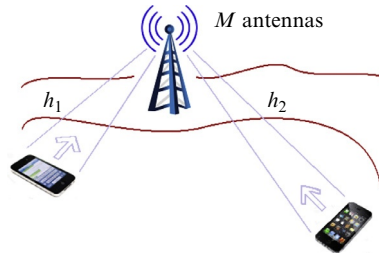


FIG. 11.12

A multi-access channel configuration.

$M$  antennas. The signal received at the base station array can be then expressed (in baseband) as follows:

$$\mathbf{x} = \sum_{k=1}^K \mathbf{H}_k^\dagger \mathbf{s}_k + \mathbf{n}, \quad (11.33)$$

where  $\mathbf{s}_k$  is the  $N \times 1$  signal transmitted from the  $k$ th user,  $\mathbf{H}_k^\dagger \in \mathbb{C}^{M \times N}$  is the complex channel matrix (assumed flat in frequency) between the  $k$ th user and the base station receiver, and  $\mathbf{n}$  is the  $M \times 1$  complex additive noise vector at the base station receiver ( $\mathbf{n} \in \mathbb{C}^{M \times 1}$ ). It is assumed that each  $\mathbf{s}_k$  contains the information of the corresponding vector symbol originating from user  $k$ , denoted as  $\mathbf{u}_k$ .

For a given set of MIMO channels  $\mathbf{H}_k^\dagger$  and power constraints  $P_k, k = 1, \dots, K$ , the capacity of the MIMO MAC channel (assuming that  $\mathbf{n}$  is a zero-mean Gaussian vector of i.i.d. variables with equal unit variance) is given by the following expression:

$$C_{\text{MAC}}(\mathbf{H}^\dagger, \mathbf{P}) \triangleq \bigcup_{\substack{\mathbf{Q}_1, \dots, \mathbf{Q}_K \\ \text{tr}(\mathbf{Q}_k) \leq P_k}} \left\{ (R_1, \dots, R_K) : \sum_{k \in S} R_k \leq \log \left| \mathbf{I} + \sum_{k \in S} \mathbf{H}_k^\dagger \mathbf{Q}_k \mathbf{H}_k \right|, \forall S \subseteq \{1, \dots, K\} \right\}, \quad (11.34)$$

where  $\mathbf{Q}_k \triangleq E[\mathbf{s}_k \mathbf{s}_k^H]$  is the covariance matrix of the  $k$ th user transmitted signal and  $P_k \in \mathbb{R}^+$  is the corresponding transmission power ( $\text{tr} \mathbf{Q}_k = P_k$ ). The expression in Eq. (11.34) is in general a polymatroid. In the special case of  $M = N = 1$  with  $K = 2$  users, it corresponds to the well-known pentagonal region described in Ref. [8]. The vertices of the capacity region can be achieved with a simple multi-user detector that uses Minimum Mean Squared Error (MMSE) detection in conjunction with successive interference cancellation [23]. Different vertices can be achieved by changing the order of the cancellation (see Ref. [24] for more details).

A capacity-achieving architecture for the MAC is shown in Fig. 11.13, taken from Ref. [24]:

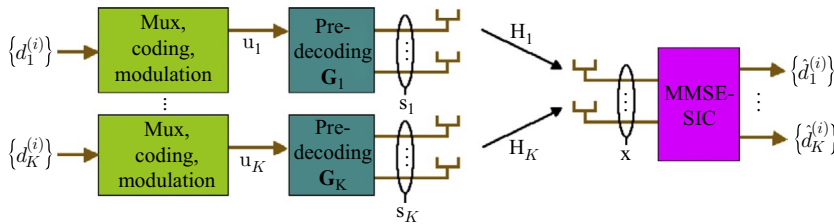


**FIG. 11.13**

A capacity-achieving architecture for the MAC channel.

User  $k$  de-multiplexes its information bits  $\{d_k^{(i)}\}$  into  $r_k \geq 1$  parallel streams, and then encodes and modulates each of these streams. The symbol vector  $\mathbf{u}_k \in \mathbb{C}^{r_k}$  is weighted by a precoding matrix  $\mathbf{G}_k \in \mathbb{C}^{M \times r_k}$  such that the transmitted signal is  $\mathbf{s}_k = \mathbf{G}_k \mathbf{u}_k$ . How are the transmit covariances  $\mathbf{Q}_1, \dots, \mathbf{Q}_K$  determined to achieve a particular rate vector on the capacity region boundary? Recall that for the single-user MIMO channel, the capacity-achieving covariance  $\mathbf{Q}$  is based on the SVD of the MIMO channel  $\mathbf{H}$ . For the MAC, if all the users' MIMO channels are mutually orthogonal (ie,  $\mathbf{H}_i^\dagger \mathbf{H}_j = 0_M$ , for all  $i \neq j$ ), then the capacity-achieving covariances for each user individually also achieve the MAC capacity region boundary. In general, however, because of the interaction of the users' MIMO channels, the MAC capacity region is not achieved using the optimal single-user covariances. Determining the capacity-achieving covariances for the MAC is not easy because of the channel interactions. While there is no known general closed-form expression for computing the optimal covariances for achieving the capacity region boundary, one can compute them numerically using iterative techniques described in Ref. [24, Section 3.5.1].

Fig. 11.14, also taken from Ref. [24], shows a block diagram for achieving the BC capacity region using DPC and precoding at the transmitter and MMSE-SIC at each receiver.

### 11.3.2 MIMO BROADCAST CHANNEL (BC)

Fig. 11.15 shows a typical broadcast channel configuration, where a base station equipped with  $M$  transmit antennas broadcasts (on the downlink) an  $M$ -dimensional vector signal  $\mathbf{s}$  that contains the user data of  $K$  users, each equipped with an  $N$ -element antenna array, that again, co-exist in the same frequency slot and interfere with each other. The signal received by each of the  $K$  receivers can be written as

$$\mathbf{x}_k = \mathbf{H}_k \mathbf{s} + \mathbf{n}_k, \quad (11.35)$$

where  $\mathbf{H}_k \in \mathbb{C}^{N \times M}$  is the complex channel (again assumed flat in frequency) between the  $M$ -antenna base station array and the  $k$ th user  $N$ -antenna receiver array and  $\mathbf{n}_k$  is the corresponding receiver  $N \times 1$  noise vector. In (11.35),  $\mathbf{s}$  contains the  $K$  users data vector data symbols, denoted as  $\mathbf{u}_k, k = 1, \dots, K$ .

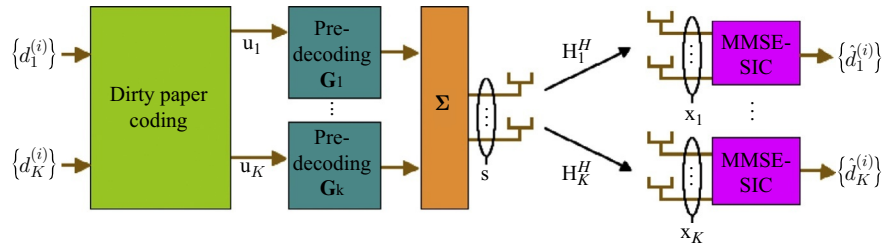
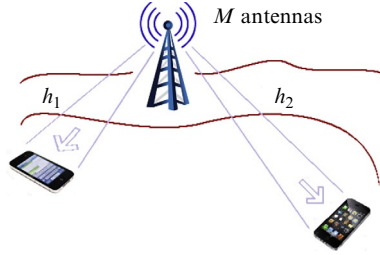


FIG. 11.14

A capacity-achieving architecture for the BC channel.



**FIG. 11.15**

A broadcast channel configuration.

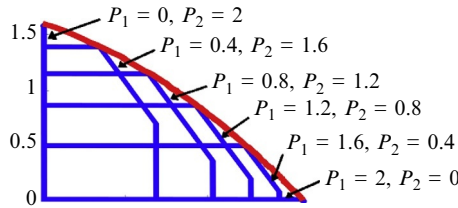


**FIG. 11.16**

BC capacity region as a union of MAC capacity regions.

For a given set of MIMO channels  $\mathbf{H}_k, k = 1, \dots, K$ , and power constraint at the base station array  $P$  and assuming, that each  $\mathbf{n}_k$  is a zero-mean Gaussian vector of  $N$  i.i.d. variables with equal unit variance, the sum capacity of the BC is given by

$$C_{\text{BC}}(\mathbf{H}, P) = \bigcup_{\substack{P_1, \dots, P_K \\ \sum_{k=1}^K P_k \leq P}} C_{\text{MAC}}(\mathbf{H}^\dagger, \mathbf{P}). \quad (11.36)$$

As can be seen from Eq. (11.36), the MIMO broadcast channel capacity is obtained as the union of the reverse MAC channel capacities, which is due to the remarkable duality between the BC and the MAC channel that was established in Refs. [25,26].

Fig. 11.16 shows an example of this for the simple case of  $K = 2$  users,  $M = N = 1$  antenna, a total power constraint of  $P = 2$  and SISO channels.

The MIMO BC capacity region can be achieved by the dirty paper coding technique of Costa [27], which constitutes a mirror-version of the successive interference cancellation technique mentioned earlier for the MAC channel (see Refs. [24,26] for more details). Zero-forcing block-diagonalization [28,29] is a simpler technique that performs almost as well (it has been shown to achieve the optimal capacity scaling as the number of users increases asymptotically).

In terms of scaling, it can be shown [30] that the maximum sum rate (assuming that  $M \geq N$ ) in the regime of asymptotically increasing number of users towards infinity is given by:

$$\lim_{K \rightarrow \infty} R_{\text{BC}}(\mathbf{H}(K), P) = \min(M, KN) \log(\log KN). \quad (11.37)$$

This means that the sum-rate capacity of the MIMO broadcast channel (assuming that usually  $M < KN$ ) grows linearly with  $M$  due to the spatial multiplexing of users (ie, within the spatial resolution of the base station antenna array) and very slowly (doubly logarithmically) with the total number of  $KN$ .

In the case of  $M \geq KN$ , the asymptotical BC capacity scaling becomes:

$$\lim_{K \rightarrow \infty} R_{\text{SU}}(\mathbf{H}(K), P) = N \log(\log K), \quad (11.38)$$

which shows a linear scaling with  $N$  in this case. It should be also noted that the gain of the sum-rate capacity of the MIMO BC over the MIMO single user link for large number of users scales as follows:

$$\lim_{K \rightarrow \infty} \frac{R_{\text{BC}}(\mathbf{H}(K), P)}{R_{\text{SU}}(\mathbf{H}(K), P)} = \frac{M}{N}, \quad (11.39)$$

which shows that the gains over single-user transmission diminish  $N$  grows, favoring strongly asymmetrical cases ( $M \gg N$ ). In the symmetric case  $M = N$ , the broadcast channel capacity is asymptotically equivalent to time division multiple access, where each user takes turns and operates in single-user MIMO fashion.

### 11.3.3 MULTIPLE MIMO BASE STATIONS

#### 11.3.3.1 MIMO interference channel

The MAC and BC multi-antenna setups discussed above correspond to situations where a single base station communicates with a number of user terminals (in the uplink or downlink direction, respectively). In the case of multiple base stations that communicate jointly with a number of user terminals, the corresponding setup is called cooperative MIMO. The most general case of base stations coordinating fully amongst them is called “Network MIMO,” wherein the antennas of all the base stations can be viewed as forming a super (virtual) array of distributed antennas. If full cooperation is assumed on the downlink (which implies that all base stations exchange both full channel state information of the channels between all the base stations and all the user terminals, as well as the corresponding data streams), the same results of the broadcast channel presented earlier hold, by replacing the number of base station antennas  $M$  by  $BM$ , where  $B$  is the number of cooperating base stations (see [25] and references therein). Similarly, on the uplink, Network MIMO can be implemented via multi-user detection of all the uplink signals by the virtual base station.

Since the exchange of full channel state and data information poses a huge burden on the backhaul, a more simple scenario is one where the corresponding bases need

to exchange only channel state information, but not the data streams of their users. A special case of this is the so-called “interference channel” described below.

As mentioned above, if the transmitting base stations are allowed to share channel state information but not their information-carrying data streams (a situation which is commonly referred to as the “interference channel,” see Fig. 11.17), then as was recently shown, the sum rate capacity scales as  $K/2$  times the capacity of the corresponding single links (assumed identical and in isolation). In the case of single antenna transmitters and receivers, this is expressed mathematically as

$$\lim_{\text{SNR} \rightarrow \infty} R_{\text{IA}}(\mathbf{H}(K, M)) = \frac{KM}{2} \log_2(\text{SNR}). \quad (11.40)$$

The technique through which this scaling can be attained is known as “interference alignment” (see Refs. [31–34], etc).

## 11.4 STANDARDS

MIMO technology has penetrated to date practically all the mobile and wireless broadband communication standards. In the following we provide a short summary of the current status of MIMO technology in two major wireless networking standards: LTE/LTE-Advanced in the area of mobile cellular networks and IEEE 802.11n in the area of broadband wireless local area networks. It is clear that these MIMO communication modes will keep evolving as the technology matures further and new service/networking paradigms emerge. What seems clear is that the technology will be an integral component of all future broadband wireless networks.

### 11.4.1 LTE/LTE-ADVANCED

The LTE (long-term evolution) and its latest version, LTE-Advanced, constitute the latest efforts of the 3GPP standardization body in the mobile cellular networking arena [35]. As will be briefly outlined below, LTE has embraced several single-user and even multi-user MIMO communication modes, while LTE-Advanced has moved one step further by including even multi-base cooperative MIMO techniques.

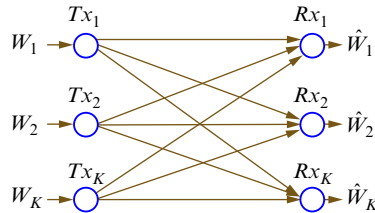


FIG. 11.17

The K-user interference channel.

### 11.4.1.1 LTE

LTE prescribes the following single-user multi-antenna communication modes, which correspond to different variants of the techniques presented earlier in the chapter. It should be mentioned at this point that LTE uses Orthogonal Frequency Division Multiplexing, which introduces the concept of sub-carriers. It should also be noted that, unlike its predecessors, UMTS and CDMA200, LTE has migrated to a packet-switching all-IP architecture (no circuit-switched transmission). Hence all communication techniques will take place over time/frequency packets, whereas multiple antennas offer yet a third signaling dimension. All employed MIMO techniques hence take into account the OFDM modulation structure, often resulting in replacing the time domain (in which MIMO techniques were originally developed) by the frequency (sub-carrier) domain. It should also be noted that all the techniques defined below are for downlink (DL) transmission. Since the mobile terminal (called “user equipment”—UE in LTE terminology) is assumed as comprising only a single signal chain, no single-user MIMO transmission is contemplated in the LTE uplink (only switch-antenna techniques could be envisioned).

- *Transmit diversity (TD)*: variants of the  $2 \times 1$  Alamouti technique are being used for transmit diversity-based transmission in LTE, for the cases of 2 and 4 transmitter antennas. In particular:
  - A frequency-domain variant of the  $2 \times 1$  Alamouti space-time code called SFBC (Space-Frequency Block Coding) is used for the case of two transmitter antennas [36]. It is identical to the Alamouti code with the different that time slots are replaced by frequency slots. As indicated earlier,  $2 \times 1$  Alamouti-based transmission could be also used when the receiver is equipped with multiple receiver antennas, by use, for example, of maximal ratio combining. In the particular case of two receiver antennas, the performance is close to the  $2 \times 2$  open-loop capacity of the system.
  - In the case of four transmitter antennas, a switched Alamouti scheme is being used: in particular the above SFBC scheme is switched between two different antenna pairs (see Ref. [36] for more details).
- *Open-loop spatial multiplexing*: Two different modes of open-loop spatial multiplexing are used in LTE, employing a maximum of four spatial streams (“layers”). However, only up to two independent codewords are being mapped to the four layers. In particular:
  - If the channel rank is 1, transmit diversity is used.
  - If the channel rank is higher than 1, then cyclic delay diversity (CDD) is used. This technique maps, as mentioned earlier, two independent codewords to a number of layers equal to the rank of the matrix (ie, up to 4)—the particular way this mapping takes place can be found in Ref. [36]. Furthermore, each layer is spatially precoded by a vector that cyclically progresses from each sub-carrier to the next. As a result CDD achieves a combination of spatial multiplexing and frequency diversity, which has been shown to have a good performance in LTE networks.

- *Closed-loop spatial multiplexing:* When reliable channel state information (CSI) is available at the transmitter, a number of different spatial multiplexing modes are possible in the LTE downlink. In LTE, to avoid an excessive burden on the uplink for CSI feedback from the receiver to the transmitter, a precoding matrix index (PMI) is fed back instead: this is an index that directs the transmitter to use one of a fixed set of pre-computed precoding matrices for downlink transmission. In this way, uplink feedback channel capacity burden is reduced at the cost of some lack of flexibility and resolution for downlink precoding. The following closed-loop modes are used for closed-loop single-user multi-antenna transmission:
  - In the case of two transmitter antennas, one out of three possible PMI precoding matrices is chosen based on the CSI.
  - In the case of four transmitter antennas, there are 16 possible PMI precoding matrices, depending on the channel rank (see Ref. [36] for more details). All precoding matrices have the constant modulus property, ensuring that the transmit power from each antenna will be equal (hence no power waterfilling is possible).
  - In the special case of rank-1 precoding, single-mode beamforming is used (again out of a predetermined set of possible beams when based on the PMI determined by the receiver). It is also possible for the transmitter to determine by itself the beamforming vector (eg, based on uplink channel measurements or based on uplink/downlink reciprocity in case of time division duplex (TDD) systems).

LTE also provides some support for MU-MIMO downlink transmission. This is rather basic, since it is limited to a single layer transmission per UE. Each participating UE feeds back a PMI indicating its preferred precoding vector, using the same codebook as for rank-1 transmission. The base station (eNodeB—eNB in LTE terminology) can then spatially multiplex the signals of multiple UEs (up to 4) by using collectively the corresponding preferred precoding vectors of each one. In practice, this mode is not used often, as the channel estimation at each UE in the presence of the others may be unreliable since no special provision has been taken in order to optimize it.

#### 11.4.1.2 LTE-advanced (LTE-A)

LTE-A provides important enhancements over LTE with regards to MIMO transmission. In particular, it allows up to  $8 \times 8$  MIMO on the downlink and up to  $4 \times 4$  MIMO on the uplink. The provision of proper uplink MIMO is an important breakthrough, probably the first to be included in a major standard. LTE-A also allows cooperative MIMO transmission via the renowned CoMP (cooperative multi-point) technique. This is another important milestone for the introduction of cooperative MIMO systems in real systems. The main MIMO modes of LTE-A are briefly outlined below:

- *Transmit diversity:* on the downlink, when up to four transmitter antennas the same TD modes as in standard LTE are used. When more than 4 (and up to 8)

antennas are available, these schemes are combined with a precoding scheme known as virtualization that chooses either 2 or 4 virtual antennas to which the standard TD scheme is applied [36]. Virtualization maps each diversity stream to a unique subgroup of physical antennas to form a virtual antenna while allowing all physical antennas to participate to the transmission. More advanced schemes are not used since it was found that there is very little benefit in open-loop transmit diversity techniques that use more than four transmitter antennas. In the case of uplink transmission and in the case of two transmitter antennas, a transmit diversity scheme called spatial orthogonal resource transmit diversity (SORTD) is used [37]. In the case of four transmitter antennas on the uplink, virtualization precoding is used first to form two virtual antennas, to which conventional transmit diversity is applied.

- *Spatial multiplexing*: on the downlink, LTE-A supports up to eight layers for the transmission of up to two codewords. When the transmission rank is up to 4, the same spatial multiplexing modes as in LTE are used. In the case of a higher transmission rank (ie, transmission of 5–8 layers), again only two codewords are used but each is mapped to between two and eight layers [36]. For the use of closed-loop spatial multiplexing, the same PMI-based mechanism of conventional LTE is used, where the PMI codebook is appropriately extended to include up to eight transmitter antennas. On the uplink, unlike conventional LTE, multiple signal chains are considered possible at the UE, thus allowing proper spatial multiplexing for uplink transmission. Up to two codewords can be mapped to up to four layers, used the same mappings as of the LTE downlink. Feedback provided by the eNB allows the UE to choose the appropriate precoding matrix. In particular, a fixed codebook-based beamforming is used for rank-1 uplink transmission and the identity matrix is used for rank-2 transmission in the case of two transmitter antennas; whereas precoder-based combinations are used for rank-1 to rank-3 transmissions and the identity matrix is used for rank-4 transmission in the case of four transmitter antennas [37].
- *Multi-user MIMO*: on the downlink, LTE-A contains important improvements over LTE in its multi-user transmission mode, notably, by allowing linear precoding of the block-diagonalization type, made possible by the introduction of extra feedback information (precoder settings). This builds upon the basic feedback structure of LTE, which remains the same [37]. On the uplink, MU-MIMO is supported by allowing to co-schedule multiple UEs on the uplink and letting the eNB perform multi-user detection (which is left for implementation to the equipment manufacturer and operator). The eNB has the ability to estimate the uplink channels reliably and instruct on the downlink the co-scheduled UEs as to which precoding matrices to use, using the same codebooks as for uplink SU-MIMO [36].
- *Cooperative multipoint*: As mentioned above, cooperative MIMO transmission, also known as Network MIMO, is an important feature of LTE-A. At the moment, LTE-A supports intra-eNB cooperative multipoint, that is, the cooperation takes place between antenna arrays (such as “remote radio

heads—RRHs”) that are controlled by the same base station (eNB) (see also [38]). Two categories of downlink CoMP transmission are supported: Joint Processing (JP) and Coordinated Scheduling/Beamforming (CS/CB). In JP, either coherent or incoherent joint transmission (JT) may take place. Coherent JT combines coherently all the transmitter antennas as belonging to a single distributed array—it has the best performance but has stringent synchronization and phase coherency requirements. The more relaxed incoherent JT mode performs macro-diversity combining, whereas a third JP mode, called dynamic cell selection, employs switching instead.

### 11.4.2 802.11N/802.11AC

IEEE 802.11n is well known in the MIMO community for being the first WLAN standard in the 802.11 family to introduce the use of MIMO [39]. In particular, it supports single-user MIMO transmission of, nominally, up to four spatial streams in the following ways:

- *Transmit diversity*: Standard Alamouti-based space-time block coding (in the time domain) is used for the case of two transmit antennas. Conventional maximal ratio combining can be used at the receiver, including the case of more than two receiver antennas. Furthermore, a cyclic shift delay may be added that delays the employed space-time streams in time. This feature is meant to prevent from unintentional beamforming and is transparent to the receiver.
- *Spatial multiplexing*: Three types of so-called Spatial Mapping are included in IEEE 802.11n. The *direct mapping* applies either an identity or a cyclic shift matrix to the TD technique described above. The *spatial expansion* expands the dimension of the produced signals by multiplying them (including the cyclic shift) with a spatial expansion matrix of orthogonal columns; this amounts to adding extra diversity to the order-2 TD scheme described above. Finally, *beamforming steering* is also supported, which adds extra beamforming gain.

Overall, 802.11 is more modest than LTE in terms of its MIMO features (eg, it has no multi-user MIMO modes); however it is similar in certain ways (allowing no more than two independent codewords (ie, spatial multiplexing order up to 2); using Alamouti-based space-time coding, etc.). Similar to the way LTE-A brings in much more advanced MIMO techniques to LTE, the emerging IEEE802.11ac standard, which operates at 5 GHz (as opposed to the 2.4 GHz of IEEE802.11n) also brings more advanced MIMO modes to IEEE802.11n and aims at up to  $8 \times 8$  MIMO communication. These attributes of IEEE802.11ac are briefly described below:

- *SU-MIMO*: A phased introduction of IEEE802.11ac targets up to three spatial streams in Wave 1, and up to eight spatial streams in Wave 2 of the standard. A maximum transmission rate of 1.3 Gbps is reached with  $3 \times 3$  MIMO transmission in Wave 1, compared to the corresponding 450 Mbps of

- IEEE802.11n, due to the higher employed bandwidth (up to 160 MHz via channel bonding, as opposed to the maximum 40 MHz of IEEE802.11n).
- *MU-MIMO*: The IEEE802.11ac standard supports Space Division Multiple Access (SDMA)-like MU-MIMO transmission, allowing the co-scheduling of up to four users. Combined with the channel bonding and up to eight spatial streams, this can provide rates of up to 9.6 Gbps. IEEE802.11ac chipsets have already been on the market for over 4 years, and continued improvements are expected.

---

## 11.5 FUTURE TRENDS

The material presented in this chapter is an attempted (non-all-inclusive) overview of the evolution of MIMO systems from their inception until today. In view of the upcoming next (5G) generation of wireless networks, it is clear that MIMO will remain an integral component of the corresponding standards. While 5G is not expected to reach commercial deployment before 2020, a number of trends (some whose commercial impact may happen even beyond 5G) that are already apparent/emerging are:

- Denser cell deployment,
- mmWave transmission,
- cloud radio networking,
- massive MIMO communication,
- spectrum sharing,
- full-duplex radio,
- terrestrial-satellite and backhaul/access/fronthaul convergence,
- miniaturized antenna arrays for various internet-of-things (IoT) nodes,
- visible light communication and photonic control circuits for fast-beam switching.

MIMO systems are expected to play an important role in all of the above areas. In the dense deployment of cells, cooperative MIMO will likely take advantage of the antennas positioned on small cells in order to better handle the interference and maximize the spectrum utilization [30–34]. In mmWave transmission [40], antenna arrays of a large number of elements will be most likely used in order to overcome the very low antenna gains that result in poor link budgets in such frequencies. Cloud radio access networks (C-RAN) will allow remote radio heads to be controlled by central nodes for more efficient cooperative MIMO transmission [38]. Massive MIMO [41] will allow certain line-of-sight links to carry very high throughputs over-the-air. Spectrum sharing will become much more aggressive and better controlled [42] and efficient by taking into account sensing in the spatial domain as well, enabled by MIMO transceivers [43]. Full-duplex radios [44] will equally benefit from the spatial dimension offered by multi-antenna arrays in order to offer further isolation between the two/multiple directions of communication. The

same will hold for co-existing segments (satellite/backhaul/access/fronthaul), which will tend to operate in the same bands as the frequencies keep increasing beyond 6 GHz [45]. Miniaturized antenna arrays (such as enabled by load-controlled and parasitic antenna arrays [46]) will enable MIMO capability on small nodes, such as low-power sensors, resulting not only in better sensing and link reliability, but also in power dissipation and battery life savings. Finally, visible light communication is poised to bring MIMO processing for signal and interference handling in the visible light spectrum [47], whereas fast photonic circuits will allow a faster and more efficient control of antenna arrays for highly spatial processing [48]. In a nutshell, while it is always risky trying to predict the future, the remarkable evolution of MIMO systems has opened a host of possibilities for better, greener, and more efficient communications that are foreseen to keep impacting future communication networks.

---

## Acknowledgments

The author would like to thank Ms. Foteini Verdou for her kind help with the editing of some of the chapter's figures.

---

## REFERENCES

- [1] W.C.Y. Lee, *Wireless and Cellular Communications*, third ed., McGraw Hill, Upper Saddle River, NJ, 2006.
- [2] S.C. Swales, M. Beach, D.J. Edwards, J.P. McGeehan, The performance enhancement of multibeam adaptive base-station antennas for cellular land mobile radio systems, *IEEE Trans. Veh. Tech.* 39 (1) (1990) 56–67.
- [3] A. Paulraj, C. Papadias, Space-time processing for wireless communications, *IEEE Signal Process. Mag.* 14 (6) (1997) 49–83.
- [4] E. Telatar, Capacity of multi-antenna Gaussian channels, AT&T-Bell Labs Technical Memorandum, June 1995.
- [5] G.J. Foschini, Layered space-time architecture for wireless communication in a fading environment when using multi-element antennas, *Bell Lab. Tech. J.* (1996) 41–59.
- [6] J. Winters, On the capacity of radio communication systems with diversity in a Rayleigh fading environment, *IEEE J. Sel. Areas Commun.* 5 (5) (1987) 871–878.
- [7] A. Paulraj, T. Kailath, Increasing capacity in wireless broadcast systems using distributed transmission/directional reception, US Patent #5,345,599, 1994.
- [8] T.M. Cover, J.A. Thomas, *Elements of Information Theory*, Wiley, New York, 1991.
- [9] S.L. Ariyavisitakul, Turbo space-time processing to improve wireless channel capacity, *IEEE Trans. Commun.* 48 (8) (2000) 1347–1359.
- [10] A. Paulraj, R. Nabar, D. Gore, *Introduction to Space-Time Wireless Communications*, Cambridge University Press, Cambridge, UK, 2003.
- [11] C. Papadias, G. Foschini, Capacity-approaching space-time codes for systems employing four transmitter antennas, *IEEE Trans. Inform. Theory* 49 (3) (2003) 726–732.
- [12] A. Lozano, Per-antenna rate and power control for MIMO layered architectures in the low- and high-power regimes, *IEEE Trans. Commun.* 58 (2) (2010) 652–659.

- [13] B. Vucetic, J. Yuan, *Space-Time Coding*, Wiley, Chichester, UK, 2003.
- [14] S.M. Alamouti, A simple transmitter diversity technique for wireless communications, *IEEE J. Special Areas Commun.* 16 (1998) 1451–1458.
- [15] C.B. Papadias, On the spectral efficiency of space-time spreading schemes for multiple antenna CDMA systems, in: 33rd Asilomar Conference on Signals, Systems and Computers, 1999, pp. 639–643.
- [16] S. Sandhu, A. Paulraj, Space-time codes: A capacity perspective, *IEEE Commun. Lett.* 4 (2000) 384–386.
- [17] A. Scaglione, P. Stoica, Linear Precoding for MIMO Channels, in: H. Bolcskei, D. Gesbert, C.B. Papadias, A.J. van der Veen (Eds.), *Space-Time Wireless Systems: From Array Processing to MIMO Communications*, Cambridge University Press, Cambridge, UK, 2006 (Chapter 9).
- [18] D.J. Love, R.W. Heath, V.K.N. Lau, D. Gesbert, B.D. Rao, M. Andrews, An overview of limited feedback in wireless communication systems, *IEEE J. Sel. Areas Commun.* 26 (8) (2008) 1341–1365.
- [19] S. Ekbatani, H. Jafarkhani, Combining beamforming and space-time coding using quantized feedback, *IEEE Trans. Wireless Commun.* 7 (2008) 898–908.
- [20] D.J. Love, R.W. Heath, Limited feedback unitary precoding for orthogonal space-time block codes, *IEEE Trans. Signal Process.* 53 (2005) 64–73.
- [21] D.J. Love, R.W. Heath, T. Strohmer, Grassmannian beamforming for multiple-input multiple-output wireless systems, *IEEE Trans. Inform. Theory* 49 (10) (2003) 2735–2747.
- [22] B.C. Banister, J.R. Zeidler, Feedback assisted transmission subspace tracking for MIMO systems, *IEEE J. Sel. Areas Commun.* 21 (3) (2003) 452–463.
- [23] S. Verdú, *Multiuser Detection*, Cambridge University Press, Cambridge, UK, 2008.
- [24] H. Huang, C.B. Papadias, S. Venkatesan, *MIMO Communication for Cellular Networks*, Springer, Berlin, 2011.
- [25] S. Vishwanath, N. Jindal, A. Goldsmith, Duality, achievable rates, and sum-rate capacity of MIMO Gaussian broadcast channels, *IEEE Trans. Inform. Theory* 49 (10) (2003) 2658–2668.
- [26] H. Weingarten, Y. Steinberg, S. Shamai (Shitz), The capacity region of the Gaussian multiple-input multiple-output broadcast channel, *IEEE Trans. Inform. Theory* 52 (9) (2006) 3936–3964.
- [27] M. Costa, Writing on dirty paper, *IEEE Trans. Inform. Theory* 29 (3) (1983) 439–441.
- [28] H. Viswanathan, S. Venkatesan, H. Huang, Downlink capacity evaluation of cellular networks with known-interference cancellation, *IEEE J. Sel. Areas Commun.* 21 (2003) 802–811.
- [29] Q.H. Spencer, A.L. Swindlehurst, M. Haardt, Zero-forcing methods for downlink spatial multiplexing in multiuser MIMO channels, *IEEE Trans. Signal Process.* 52 (2) (2004) 461–471.
- [30] M. Sharif, B. Hassibi, A comparison of time-sharing, DPC, and beamforming for MIMO broadcast channels with many users, *IEEE Trans. Commun.* 55 (1) (2007) 11–15.
- [31] V. Cadambe, S. Jafar, Interference alignment and degrees of freedom of the K-user interference channel, *IEEE Trans. Inform. Theory* 54 (8) (2008) 3425–3441.
- [32] I. Santamaria, O. Gonzalez, R.W. Heath, Jr., S.W. Peters, Maximum sum-rate interference alignment algorithms for MIMO channels, in: *Proc. IEEE Global Telecommunications Conference*, Miami, FL, USA, Dec. 6–10, 2010, pp. 1–6.

- [33] M. Rezaee, M. Guillaud, Limited feedback for interference alignment in the K-user MIMO interference channel, in: *Information Theory Workshop (ITW)*, Lausanne, Switzerland, Sep. 2012, pp. 3–7.
- [34] G.C. Alexandropoulos, C.B. Papadias, A reconfigurable iterative algorithm for the K-user MIMO interference channel, *Signal Process* 93 (12) (2013) 3353–3362 (Special Issue on Advances in Sensor Array Processing).
- [35] E. Dahlman, S. Parkvall, J. Skold, 4G: LTE/LTE-Advanced for Mobile Broadband, Academic Press, Oxford, 2011.
- [36] T. Derham, LTE and LTE-advanced, in: A. Sibille, C. Oestges, A. Zanella (Eds.) *MIMO: From Theory to Implementation*, Academic Press, New York, 2011 (Chapter 9).
- [37] UL single user MIMO schemes for LTE-Advanced, Technical Report R1-090727, 3GPP, 2009.
- [38] 7th Framework Program (FP7), High capacity network architecture with remote radio heads and parasitic antenna arrays (HARP), Collaborative research project funded by the European Commission's 7th Framework Program (FP7), <http://www.fp7-harp.eu/>.
- [39] Z. Zhao, IEEE 802.11n implementation, in: A. Sibille, C. Oestges, A. Zanella (Eds.) *MIMO: From Theory to Implementation*, Academic Press, New York, 2011 (Chapter 7).
- [40] R.W. Heath, J.N. Murdock, R.C. Daniels, T.S. Rappaport, *Millimeter Wave Wireless Communications*, Prentice Hall, Upper Saddle River, NJ, 2014.
- [41] E.G. Larsson, F. Tufvesson, O. Edfors, T.L. Marzetta, Massive MIMO for next generation wireless systems, *IEEE Commun. Mag.* 52 (2) (2014) 186–195.
- [42] A. Morgado, A. Gomes, V. Frascolla, K. Ntougias, C.B. Papadias, D. Slock, E. Avdic, N. Marchetti, N. Haziza, H. Anouar, Y. Yang, M. Pesavento, F.A. Khan, T. Ratnarajah, Dynamic LSA for 5G networks: the ADEL perspective, in: *European Conference on Networks and Communications*, Paris, France, June 29–July 2, 2015.
- [43] D. Wilcox, E.P. Tsakalaki, A. Kortun, T. Ratnarajah, C.B. Papadias, M. Sellathurai, On spatial domain cognitive radio using single-radio parasitic antenna arrays, *IEEE J. Sel. Areas Commun.* 31 (3) (2013) 571–580.
- [44] H.A. Suraweera, I. Krikidis, G. Zheng, C. Yuen, P.J. Smith, Low-complexity end-to-end performance optimization in MIMO full-duplex relay systems *IEEE Trans. Wireless Commun.* 13 (2014) 913–927.
- [45] E. Lagunas, S.K. Sharma, S. Maleki, S. Chatzinotas, B. Ottersten, Resource allocation for cognitive satellite communications with incumbent terrestrial networks, *IEEE Trans. Cogn. Commun. Network.* Nov. 2015.
- [46] A. Kalis, A. Kanatas, C.B. Papadias, *Parasitic Antenna Arrays for Wireless MIMO Systems*, Springer, New York, 2013.
- [47] B. Ghimire, H. Haas, Self organising interference coordination in optical wireless networks, *EURASIP J. Wireless Commun. Network.* <http://dx.doi.org/10.1186/1687-1499-2012-131>.
- [48] P. Ghelfi, F. Laghezza, F. Scotti, G. Serafino, S. Pinna, D. Onori, E. Lazzeri, A. Bogoni, Photonics in radar systems, *IEEE Microwave Mag.* 16 (8) (2015) 74–83.

# Multiple access control in wireless networks

# 12

H. Wymeersch\*, A. Eryilmaz†

*Chalmers University of Technology, Gothenburg, Sweden\** *Ohio State University, Columbus, OH, United States†*

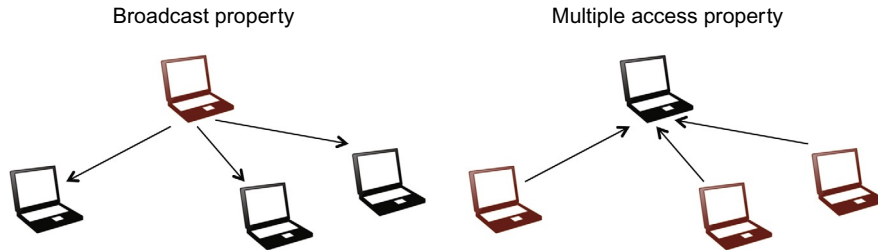
## CHAPTER OUTLINE

<b>12.1 Why Multiple Access Control?</b>	435
12.1.1 Motivation	435
12.1.2 Organization of This Chapter	437
<b>12.2 A Brief History</b>	437
12.2.1 Centralized Cellular Networks	437
12.2.2 Decentralized WLAN Networks	439
<b>12.3 Channels in Time, Frequency, and Space</b>	440
12.3.1 Orthogonal Channels	440
12.3.2 Nonorthogonal Channels	443
12.3.3 Example: Duplexing	443
<b>12.4 Centralized MAC in Cellular Networks</b>	444
12.4.1 Channelization	445
12.4.2 Channel and Traffic Models	447
12.4.3 Scheduling and Resource Allocation	449
<b>12.5 Decentralized MAC in Wireless Networks</b>	456
12.5.1 Channelization	456
12.5.2 Channel and Traffic Models	457
12.5.3 Scheduling and Resource Allocation	458
<b>12.6 Summary</b>	461
<b>References</b>	462

## 12.1 WHY MULTIPLE ACCESS CONTROL?

### 12.1.1 MOTIVATION

In both wired and wireless communication, there is a need for multiple users or multiple data streams to *access and share a common resource to satisfy demands*

**FIG. 12.1**

The broadcast and multiple access properties in wireless communications. The broadcast property enables multiple nodes to receive a signal from a common transmitter. The multiple access property forces transmitters to coordinate in order to reduce interference at a common receiver.

*of users/applications*. This resource could be a cable, a memory location, or a time slot over a wireless channel. In order for each user or stream to have the possibility to access this common resource, we can create different “channels” and assign each user/stream to its own channel, or have multiple users compete for the same channel.

In wireless communication systems, which will be the focus of this chapter, common resources appear naturally through the wireless channel [1,2]. The wireless channel is generally shared among different users, leading to the *broadcast property* and the *multiple access property*, illustrated in Fig. 12.1. The broadcast property means that a transmitter can be heard simultaneously by multiple receivers, while the multiple access property means that multiple active transmitters can cause interference at a common receiver. While the broadcast property can be considered a beneficial feature of the wireless channel, the multiple access property can lead to interference and is generally considered to be detrimental.

It is not sufficient for a communication system to simply provide channels to users: the system should operate so as to maximize a measure of system-wide utility (*efficiency*), while also giving each user fair access to the common resource (*fairness*). The aspects of fairness and efficiency appear once one considers the requirements of the users, which are ultimately the customers of the wireless network operators. First of all, not all users are equal, as some may be downloading a movie while others are idle. Users may also experience different channel conditions, with users closer to a transmitter having a better link quality and thus possibly having an unfair advantage. Hence, a simple way to avoid interference would be to assign users nonoverlapping time slots when transmitting to a common receiver, and cycle through the time slots in a round-robin fashion. While such a scheme is in some sense fair, it is not efficient if users have nothing to send. In addition, each user needs to know when its time slot starts and ends, requiring some form of synchronization. These aspects highlight several of the challenges in the design and implementation of multiple access communication.

In summary, the problem of multiple access control encompasses providing users with fair, efficient, and easy to implement access to the wireless channel [3]. The

problem is divided into (i) the creation of logical channels for each user and (ii) the optimization of how to use those channels. Strategies on how to address both aspects turn out to depend highly on the network topology (star or multihop), the channel dynamics (slow or fast, with or without channel state information), as well as the application requirements (throughput, delay, reliability).

### 12.1.2 ORGANIZATION OF THIS CHAPTER

This chapter will consider centralized and decentralized multiple access control and is organized as follows. In [Section 12.2](#), we provide a brief history of multiple access in both centralized (cellular) and decentralized (wireless local area networks (WLANs)) settings. In [Section 12.3](#), we describe the fundamental degrees of freedom offered by the wireless channel to give us logical channels. These degrees of freedom are time, frequency, and to a smaller extent, space. In [Sections 12.4](#) and [12.5](#), we go deeper into centralized and decentralized multiple access control, respectively. The centralized case relates mainly to cellular networks. We describe common ways of creating logical channels for cellular systems, how to efficiently use these channels through water-filling, and how to account for fairness among users. In [Section 12.5](#), we will see that decentralized systems are fundamentally different, both in how the channels are created, how interference is treated, and how efficient and fair use is enabled. Finally, we will provide concluding remarks in [Section 12.6](#).

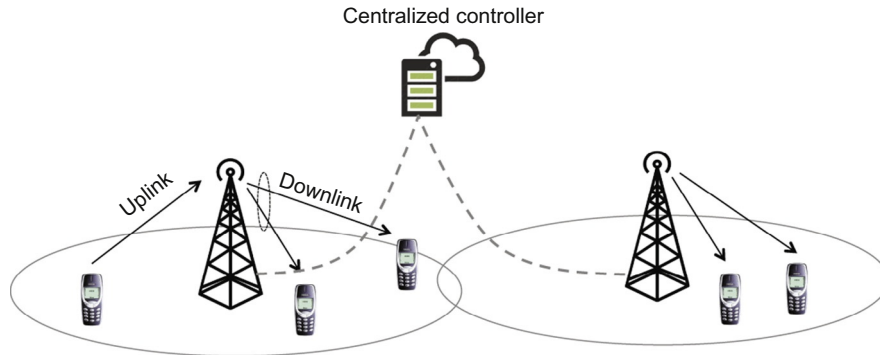
---

## 12.2 A BRIEF HISTORY

This chapter will separately consider centralized cellular networks and decentralized WLAN. In cellular networks, there are two classes of nodes, base stations (BSs) and mobiles, in which BSs are connected through a high-capacity backhaul network. The communication from BSs to mobiles is called the *downlink*, while the communication from mobiles to the BS is called the *uplink*. These concepts are depicted in [Fig. 12.2](#). In contrast, in WLAN all nodes are, in principle, equal and there is no central entity controlling the communication. This limits how logical channels are created and also renders fair and efficient use of these channels challenging.

### 12.2.1 CENTRALIZED CELLULAR NETWORKS

The first generation (1G) of cellular communication was active mainly during the 1980s. The main usage involved a low-rate, high delay sensitivity application: analog audio communication [\[4\]](#). Different countries relied on different standards (eg, Nordic Mobile Telephony in northern Europe [\[4\]](#)), though there were common features. In 1G systems, each BS was assigned a portion of the spectrum, ie, a set of channels. Each channel was divided into a downlink and an uplink, separated by a wide frequency margin, leading to frequency division duplexing (FDD). Uplink and downlink would be divided further to users within the cell, a principle known as

**FIG. 12.2**





A cellular system with two base stations and five mobiles. The centralized controller coordinates how logical channels are assigned and utilized across base stations. Downlink and uplink communication are highlighted.

frequency division multiple access (FDMA). The channels assigned to a BS could also be assigned to other BSs far away, provided the resulting interference was small. This concept is called *reuse*, and it was an important factor in the transition to digital cellular communications.

The first digital cellular standards, including the American IS-95 standard and the GSM standard [5], appeared in the 1990s and mark the second generation (2G) of cellular communication technologies. In digital cellular communication, voice signals are encoded into sequences of bits, which enables more sophisticated multiple access solutions. In fact, the different standards relied on different multiple access solutions, making them mutually incompatible. GSM was based on a combination of FDMA and time division multiple access (TDMA), where each BS is again assigned channels, but now these channels are divided up into short time slots. In contrast, the IS-95 standard allowed users to occupy the same bandwidth at the same time by creating logical channels through the use of near-orthogonal codes, known as code division multiple access (CDMA). By virtue of being digital, 2G was much more spectrally efficient and robust than 1G, and it was able to operate with shorter reuse distances. Nevertheless, data rates were only around 10 kbps for GSM, and up to 384 kbps for intermediate standards before the third generation (3G).

As users' appetites for higher and higher data rates increased, standards had to evolve to meet this need. Since 2001, 3G has provided high-rate access (up to around 2 Mbps) [6]. To accommodate more users in a given frequency spectrum, TDMA was largely abandoned in favor of CDMA. Separation of uplink and downlink is achieved either in frequency (FDD) or time domain, using time division duplexing (TDD).

Finally, the 4th generation of cellular technology (4G) is mainly associated with the worldwide Long-Term Evolution (LTE) standard [6], and it provides data rates similar to WLAN. These high rates are enabled through sophisticated design and

				
	1G	2G	3G	4G
Uplink	FDMA	FDMA+TDMA	CDMA	SC-FDMA
Downlink	FDMA	FDMA+TDMA	CDMA	OFDMA
Duplexing	FDD	FDD	FDD or TDD	FDD or TDD

**FIG. 12.3**

The evolution of multiple access in four generations of cellular communications.

signal processing. With increased sophistication in both BSs and handsets, more aggressive and flexible use of the spectrum became possible. Medium access relies on multicarrier orthogonal FMDA (OFDMA) in the downlink and single-carrier FDMA (SC-FDMA) in the uplink. Both FDD and TDD are currently available for duplexing.

[Fig. 12.3](#) provides an overview of the salient multiple access properties of each cellular generation. We will revisit these properties in [Section 12.4](#).

### 12.2.2 DECENTRALIZED WLAN NETWORKS

While cellular communications evolved into a complex system with a highly optimized medium access mechanism to achieve fair and efficient sharing of the channel, WLAN took a very different path [7,8]. In a WLAN, there are no BSs connected through a backhaul network, precluding the use of a central controller (see [Fig. 12.4](#)). The history of WLAN can be traced back to the ALOHAnet in Hawaii, which aimed to connect devices on different islands via decentralized operation. Medium access control was based on the simple, but highly inefficient Aloha protocol, whereby a node will try to transmit as soon as it has data to send. If the transmission was unsuccessful, the node tries again later at a random time. This idea of random access to the channel led to the carrier sense multiple access (CSMA) method, including CSMA with collision avoidance (CSMA/CA), which is used in the 802.11 standard. In CSMA/CA, nodes compete for access to the same channel (hence, such methods are called contention-based), but they do so in a way to cause as little interference as possible to ongoing transmissions. Such an approach works well, as long as nodes don't constantly send packets; this will be covered in more detail in [Section 12.5](#).

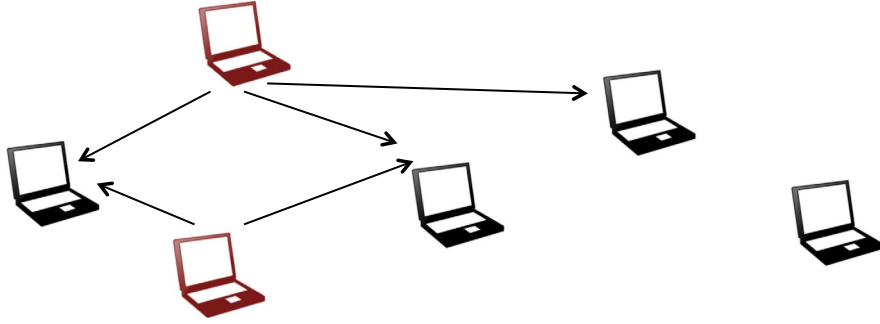


FIG. 12.4

A WLAN network with six nodes, of which two are actively transmitting.

## 12.3 CHANNELS IN TIME, FREQUENCY, AND SPACE

In this section, we will consider how to create channels from a physical communication channel, by dividing up the basic degrees of freedom given by nature: time, frequency, and space. Irrespective of which degree of freedom is used, we will see how to formulate a model for  $N$  channels in the form

$$\mathbf{y} = \mathbf{G}\mathbf{x} + \mathbf{v}, \quad (12.1)$$

in which  $\mathbf{x} \in \mathbb{C}^N$  represents the transmitted signals over the individual channels,  $\mathbf{y} \in \mathbb{C}^N$  represents the received signals over the individual channels,  $\mathbf{v} \in \mathbb{C}^N$  is observation noise, and  $\mathbf{G} \in \mathbb{C}^{N \times N}$  describes the interaction between the different channels. In later sections, we will then see how to provide fair access to these channels in a way that maximizes a system-wide objective.

### 12.3.1 ORTHOGONAL CHANNELS

A scalar signal with bandwidth  $W$  and duration  $T$  has approximately  $2WT$  real degrees of freedom [1]. From electromagnetic wave theory, it is known that space<sup>1</sup> can provide additional degrees of freedom, eg, through spatial modes. These degrees of freedom can enable information to be sent using orthogonal signals (interference-free) or nonorthogonal signals (interfering) [9].

We consider a scenario with  $N = 2$  channels, with two transmitters and one receiver, though the reasoning can also be applied to a scenario with one transmitter and two receivers, as well as scenarios with more than two transmitters or receivers. The transmitters wish to send data  $x_1$  and  $x_2$ , respectively. Transmitter  $i \in \{1, 2\}$  uses

<sup>1</sup>Including angle and polarization.

a dedicated signal  $\mathbf{w}_i$  to send  $x_i$  over a wireless channel characterized by  $\mathbf{H}_i$ . The receiver observes

$$[\mathbf{H}_1 \circ \mathbf{w}_1]x_1 + [\mathbf{H}_2 \circ \mathbf{w}_2]x_2 + \mathbf{v}, \quad (12.2)$$

in which  $[\cdot \circ \cdot]$  is an operator that represents the effect of the channel (to be specified later) and  $\mathbf{v}$  is observation noise. The receiver now applies a filter  $\tilde{\mathbf{w}}_i$  to recover the signal from user  $i$ . This leads to two observations:

$$y_1 = [\tilde{\mathbf{w}}_1 \bullet [\mathbf{H}_1 \circ \mathbf{w}_1]]x_1 + [\tilde{\mathbf{w}}_1 \bullet [\mathbf{H}_2 \circ \mathbf{w}_2]]x_2 + [\tilde{\mathbf{w}}_1 \bullet \mathbf{v}], \quad (12.3)$$

$$y_2 = [\tilde{\mathbf{w}}_2 \bullet [\mathbf{H}_1 \circ \mathbf{w}_1]]x_1 + [\tilde{\mathbf{w}}_2 \bullet [\mathbf{H}_2 \circ \mathbf{w}_2]]x_2 + [\tilde{\mathbf{w}}_2 \bullet \mathbf{v}], \quad (12.4)$$

in which  $[\cdot \bullet \cdot]$  is an operator that represents the receiver-side processing (again to be specified later). We will denote  $[\tilde{\mathbf{w}}_i \bullet \mathbf{v}]$  by  $v_i$ , and  $[\tilde{\mathbf{w}}_i \bullet [\mathbf{H}_j \circ \mathbf{w}_j]]$  by  $g_{ij}$ . We will assume that, without loss of generality,  $x_i \in \mathbb{C}$ ,  $g_{ij} \in \mathbb{C}$ ,  $y_i \in \mathbb{C}$ , and  $v_i$  is independent of  $v_{j \neq i}$  and independent of  $x_j$ .

Based on the above description, we obtain a general model for the communication of two transmitters to a receiver using dedicated signals and filters:

$$\begin{bmatrix} y_1 \\ y_2 \end{bmatrix} = \begin{bmatrix} g_{11} & g_{12} \\ g_{21} & g_{22} \end{bmatrix} \begin{bmatrix} x_1 \\ x_2 \end{bmatrix} + \begin{bmatrix} v_1 \\ v_2 \end{bmatrix}, \quad (12.5)$$

which is a special case of Eq. (12.1). The communication is said to be *orthogonal* if the following conditions hold: (i)  $g_{12} = g_{21} = 0$  (ie, no interuser interference), (ii)  $g_{11} \neq 0$  and  $g_{22} \neq 0$  (ie, there is useful remaining signal), and (iii) the noise terms  $v_1$  and  $v_2$  are mutually independent and independent of the transmitted signals. If orthogonal channels can be created, the receiver can recover  $x_i$  from  $y_i$ , without considering  $y_{j \neq i}$ . We will now consider three fundamental ways of creating orthogonal channels: frequency, time, and space.

### 12.3.1.1 Orthogonality in frequency

The oldest and most robust way to create orthogonal channels, both conceptually and implementation-wise, is by using nonoverlapping frequency bands (see Fig. 12.5).

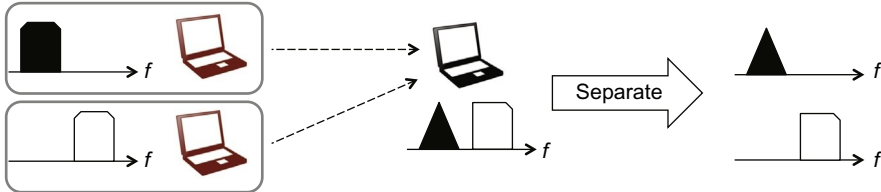


FIG. 12.5

The creation of orthogonal channels in frequency, where users are assigned nonoverlapping frequency bands. The receiver separates the signals from both users by filtering out the frequency band(s) of interest.

In this case,  $\mathbf{w}_i$  is a transmit waveform,  $\mathbf{H}_i$  represents a channel impulse response,  $\tilde{\mathbf{w}}_i$  is a receive filter,  $\circ$  represents convolution, and  $\bullet$  represents filtering with appropriate downsampling. In particular,  $\mathbf{w}_i$  corresponds to a waveform in a certain frequency band  $[f_i^s, f_i^e]$  such that  $[f_1^s, f_1^e] \cap [f_2^s, f_2^e] = \emptyset$  (ie, the frequency bands are nonoverlapping). The receiver-side  $\tilde{\mathbf{w}}_i$  corresponds to a bandpass filter over the frequency band  $[f_i^s, f_i^e]$ , matched<sup>2</sup> to  $[\mathbf{H}_i \circ \mathbf{w}_i]$ . This approach ensures orthogonality, *irrespective* of the channels  $\mathbf{H}_1$  and  $\mathbf{H}_2$ .

### 12.3.1.2 Orthogonality in time

Rather than divide channels into frequency bands, we can also divide channels into time-slots. Since different transmitters have different propagation delays to the receiver, accounting for the delays between users can be challenging, as shown in Fig. 12.6. As before,  $\mathbf{w}_i$  is a transmit waveform,  $\mathbf{H}_i$  represents a channel impulse response,  $\tilde{\mathbf{w}}_i$  is a receive filter,  $\circ$  represents convolution, and  $\bullet$  represents filtering with appropriate downsampling. However, now  $\mathbf{H}_i$  has a support over the delay interval  $[\delta_i^s, \delta_i^e]$ , ie, with delay spread  $\delta_i^e - \delta_i^s$ . The transmit waveforms  $\mathbf{w}_1$  and  $\mathbf{w}_2$  have the same bandwidth (ie,  $[f_1^s, f_1^e] = [f_2^s, f_2^e]$ ), but they are now distinguished through their time support:  $\mathbf{w}_i$  is nonzero only for times  $[t_i^s, t_i^e]$ . Finally,  $\tilde{\mathbf{w}}_i$  is a filter matched to  $[\mathbf{H}_i \circ \mathbf{w}_i]$ . Under the condition that  $[t_1^s + \delta_1^s, t_1^e + \delta_1^e] \cap [t_2^s + \delta_2^s, t_2^e + \delta_2^e] = \emptyset$  (ie, the time intervals do not overlap), orthogonality can be ensured. We see that  $\tilde{\mathbf{w}}_i$  should be designed to account for the delay spread of both channels and the relative propagation delays.

### 12.3.1.3 Orthogonality in space

Orthogonality in space can be achieved by using multiple antennas at transmitters and/or receivers. In this case,  $\mathbf{H}_i$  represents that channel matrix transmitter  $i$ , the receiver,  $\mathbf{w}_i$ , is a weighting vector at the transmitter, and  $\tilde{\mathbf{w}}_i$  is a weighting vector at the receiver. Moreover,  $\mathbf{H}_i \circ \mathbf{w}_i$  should be interpreted as the matrix-vector product

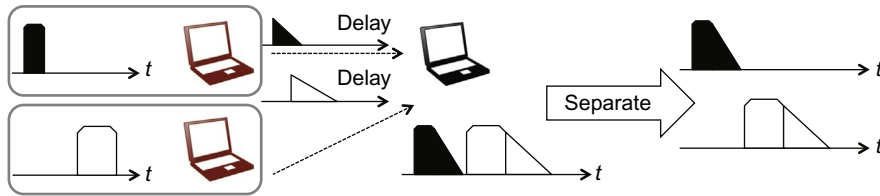


FIG. 12.6

The creation of orthogonal channels in time, where users are assigned nonoverlapping time slots. The receiver can separate the signals from both users as it receives the signals sequentially in time.

<sup>2</sup>In principle, a filter matched to  $\mathbf{w}_i$  is sufficient, provided additional processing is performed.

$\mathbf{H}_i \mathbf{w}_i$ , while  $\tilde{\mathbf{w}}_i \bullet \mathbf{x}$  represents  $\tilde{\mathbf{w}}_i^H \mathbf{x}$ . Proper design<sup>3</sup> of  $\mathbf{w}_i$  and  $\tilde{\mathbf{w}}_i$  as a function of both  $\mathbf{H}_1$  and  $\mathbf{H}_2$  can satisfy the orthogonality conditions.

### 12.3.2 NONORTHOGONAL CHANNELS

In practice, full orthogonality may not be possible to achieve, or it may even not be desirable in order to support more users than available through the physical degrees of freedom. We have already encountered this when we discussed reuse: a frequency band assigned to a BS in an cellular network may be assigned to another BS, provided the distance between the two BSs is sufficiently large. In such a case, the interference levels will be nonzero (ie,  $g_{12} \neq 0$  and  $g_{21} \neq 0$  in Eq. 12.5), but still manageable (ie,  $|g_{11}| \gg |g_{12}|$  and  $|g_{22}| \gg |g_{21}|$ ).

Interference can be treated in different ways when modeling, analyzing, and designing communication systems. The three common ways to treat interference are the collision model, the signal-to-noise-and-interference ratio (SINR) model, and the joint detection model.

- **Collision model:** In this model, it is assumed that it is only possible to recover  $x_1$  from  $y_1$  when  $g_{12} = 0$ , when  $g_{12} \neq 0$ ,  $x_1$  is lost.
- **SINR model:** In this model, it is possible to recover  $x_1$  when

$$\frac{|g_{11}|^2}{|g_{12}|^2 + \sigma^2} \geq \tau, \quad (12.6)$$

in which  $\sigma^2$  is the variance of  $v_1$ , and  $\tau$  is a suitable threshold. The left hand side of Eq. (12.6) is the SINR associated with user 1.

- **Joint detection model:** Here, we consider the full model (Eq. (12.5)) and solve for *both*  $x_1$  and  $x_2$ .

### 12.3.3 EXAMPLE: DUPLEXING

An example of orthogonal channels is *duplexing*, ie, the ability to provide separate channels for uplink and downlink in cellular networks (see Section 12.2.1), in frequency (FDD), time (TDD), and space (space division duplexing (SDD)).

#### 12.3.3.1 Frequency division duplexing (FDD)

FDD allows uplink and downlink transmission at the same time, but over different frequency bands. The bands are typically separated by a large margin to avoid

<sup>3</sup>Consider an example where nodes each have two antennas so that  $\mathbf{H}_1$  and  $\mathbf{H}_2$  are  $2 \times 2$  matrices, say  $\mathbf{H}_1 = [+1 \ +2; +3 \ +4]$  and  $\mathbf{H}_2 = [+3 \ +4; +2 \ +1]$ . Using the singular value decompositions  $\mathbf{H}_i = \mathbf{U}_i \mathbf{\Sigma}_i \mathbf{V}_i^H$ , setting  $\mathbf{w}_1$  to be the first column of  $\mathbf{V}_1$  and  $\tilde{\mathbf{w}}_1$  to be the first column of  $\mathbf{U}_1$ , we find that  $g_{11} = \tilde{\mathbf{w}}_1^H \mathbf{H}_1 \mathbf{w}_1 = 5.4650$  is the first singular value of  $\mathbf{H}_1$ . Choosing a  $\tilde{\mathbf{w}}_2$  that is orthogonal to  $\mathbf{H}_1 \mathbf{w}_1$  (eg,  $\tilde{\mathbf{w}}_2 = [+0.9145 \ -0.4046]^T$ ) and a  $\mathbf{w}_2$  orthogonal to  $\tilde{\mathbf{w}}_1^H \mathbf{H}_2$  (eg,  $\mathbf{w}_2 = [+0.7528 \ +0.6583]^T$ ), we find that  $g_{12} = g_{21} = 0$  and  $g_{22} = -5.3487$ .

leakage. FDD creates a channel that is always available and thus does not incur any delay. On the downside, the frequency bands are usually fixed by regulators, thus making FDD inflexible when uplink or downlink traffic requirements change. In addition, the nodes must be equipped with dedicated filters, which may be costly.

### 12.3.3.2 Time division duplexing (TDD)

TDD allows uplink and downlink to use the entire frequency spectrum, but in different time slots. Time is divided up into short slots and some are designated for uplink while others are designated for downlink. This approach enables asymmetric traffic and time-varying uplink and downlink demands. In addition, channel state information estimated in the uplink can be used in the downlink, under the assumption of channel reciprocity. The main drawbacks of TDD are latency (as information can only be sent when a channel becomes available) and the need for uplink synchronization (to account for differences in propagation time).

### 12.3.3.3 Space division duplexing (SDD)

Finally, SDD relies on the BS and mobile being equipped with multiple antennas and the creation of orthogonal spatial modes for uplink and downlink. In principle, this allows simultaneous uplink and downlink transmission over the entire frequency band. In practice, however, SDD is rarely used as leakage from transmit to receive antennas can lead to dominant interference [10].

---

## 12.4 CENTRALIZED MAC IN CELLULAR NETWORKS

In this section, we focus on the development of MAC strategies that have been driven by *cellular networks*, whereby channels are to be optimally split by a centralized coordinator (typically a BS or a set of BSs) amongst cellular mobile users. Accordingly, the aim is to maximize efficiency of the reserved resources to accommodate a large number of mobile users through optimized MAC strategies. The nature of the service is a mix of real-time voice/video services, along with an increasing percentage of data (eg, Internet surfing, texting, emails) services. A distinguishing feature of these systems, compared to their decentralized counterparts (to be discussed in [Section 12.5](#)), is the *continuous connectivity* of each member of the user population even when no active service is provided. This necessitates incessant implementation of synchronization, base-station assignment, and handoff operations between the cellular infrastructure and each of the mobile devices. When an active service request is generated by a mobile user, these background operations provide essential information about the channel conditions of the users to the BSs, and thereby enable the development of intelligent, and fairly sophisticated, MAC strategies—the *centralized* MAC strategies in our terminology. We will first describe different approaches to creating channels ([Section 12.4.1](#)) and then how to optimally allocate resources and users to those channels ([Section 12.4.3](#)).

### 12.4.1 CHANNELIZATION

In cellular networks, operators will reserve certain channels (eg, certain frequency bands) for *control channels*. These control channels provide means for new users to access the system, for the BS to assign channels to individual users, as well as for hand-off and synchronization. Due to the control channels, it is possible to provide sophisticated means of channelization, in time, frequency, and space. In this section, we will describe six important methods of channelization, starting with the three fundamental degrees of freedom [11,12] from Section 12.3, followed by three combinations of time and frequency.

#### 12.4.1.1 Frequency division multiple access (FDMA)

FDMA is the most basic way of creating channels, by assigning users to nonoverlapping frequency bands, it was used in first and 2G cellular systems. In a system with  $N$  users and a total bandwidth  $W$ , each user can be assigned a bandwidth of  $W/N$ .

*Implementation considerations:* To avoid leakage and interference due to imperfect filtering, frequency-domain guard-bands are required. In addition, hardware restrictions make it hard to assign more than one channel to a user. Care needs to be taken to avoid interference from nearby cells, so that channels can only be reused by BSs sufficiently far away.

#### 12.4.1.2 Time division multiple access (TDMA)

TDMA creates channels by assigning users nonoverlapping time slots, and it was used in 2G cellular networks. In a system with  $N$  users, each user can thus use the total bandwidth  $W$ , but only a fraction  $1/N$  of the time. This implies that TDMA, in contrast to FDMA, is not suitable for analog communication.

*Implementation considerations:* To implement TDMA, the uplink is more challenging than the downlink, since the transmissions from the mobiles must be synchronized such that they arrive at the appropriate time at the BS (also see Fig. 12.7). In addition, guard times need to be included to avoid interference between TDMA slots. As with FDMA, care needs to be taken to avoid interference from nearby cells, so that channels can only be reused by BSs sufficiently far away.



FIG. 12.7

The creation of orthogonal channels in space, where users utilize dedicated beamformers, in agreement with the receiver.

Nevertheless, TDMA is more flexible than FDMA, as it allows assigning a varying number of slots to users on a per-need basis.

#### **12.4.1.3 Space division multiple access (SDMA)**

SDMA users are assigned shaping and precoding matrices based on their multi-antenna channels, allowing them to use the same frequency band at all times. One realization of SDMA is the use of multiple antenna sectors at the BS, so that users in different sectors can be assigned the same time-frequency resource. *Implementation considerations:* SDMA relies on multiple antennas at either the BS and/or the mobile. The design of shaping and precoding relies on precise channel state information or highly directional antennas, thus making SDMA harder to implement for cellular systems. Nevertheless, SDMA will likely become more prominent in 5G networks, where the use of higher frequencies and a large number of antennas can lead to very focused spatial signals [13,14].

#### **12.4.1.4 Code division multiple access (CDMA)**

In CDMA, each user is assigned a unique spreading code in either time or frequency. Considering spreading in time, each user can use the entire frequency band  $W$  for all time but must use a spreading code of length  $K$ , which may be greater or smaller than  $N$ , the number of users in the cell. Hence, the effective data rate of each user drops from  $W$  to  $W/K$ . At the receiver, through suitable processing, the signal is despread with the spreading sequence to recover the data of each user.

#### **Implementation considerations**

In contrast to TDMA and FDMA, CDMA does not aim to achieve perfect orthogonality between users. In fact, it would be impossible to guarantee orthogonality in a dispersive channel and imperfect synchronization. Instead, CDMA relies on controlled, limited interference through design of the spreading codes in combination with power control (so that signals from nearby and faraway users arrive with the same power at the receiver). This approach avoids the need for reuse and can support more users per cell. These properties made CDMA a prime candidate for 3G cellular systems.

#### **12.4.1.5 Orthogonal frequency division multiple access (OFDMA)**

OFDMA is based on orthogonal frequency division multiplexing (OFDM), a powerful transmission technology that digitally (as opposed to in analog in FDMA) breaks up the spectrum in frequency-flat, overlapping channels (subcarriers). In OFDMA, users are assigned subcarriers or groups of nonoverlapping subcarriers. The guarantee of orthogonality with the increased flexibility of channelization made OFDMA the technology of choice for downlink for fourth generation cellular systems.

### Implementation considerations

OFDMA, being very similar to OFDM, suffers from many of the same drawbacks. Among these, the high peak-to-average power ratio (PAPR) stands out, forcing transmitters to operate their amplifiers in ways that consume large amounts of power. This, in conjunction with the tight synchronization requirements of the different subcarriers, makes OFDMA a suitable technology for downlink, but not for uplink.

#### 12.4.1.6 Single-carrier frequency division multiple access (SC-FDMA)

To complement OFDMA with a suitable uplink technology, SC-FDMA was introduced [15]. In SC-FDMA, the PAPR problem is avoided by letting data reside in the time domain (in contrast to OFDMA, where data resides in the frequency domain), and it relies on an additional fast Fourier transform<sup>4</sup> at the transmitter and receiver. In the frequency domain, each user is assigned a set of subcarriers, which is nonoverlapping with the subcarriers of any other user.

*Implementation considerations:* SC-FDMA combines many of the attractive properties of OFDMA but avoids high PAPR. The main drawback of SC-FDMA is the increased signal processing required at both the transmitter and receiver.

### 12.4.2 CHANNEL AND TRAFFIC MODELS

#### 12.4.2.1 Uplink/downlink channel models

The predominant types of wireless channels in cellular networks are *downlink* (Fig. 12.8) and *uplink* (Fig. 12.9) channels between mobile users and their assigned base stations (BSs). The BSs themselves form an interconnected network, either

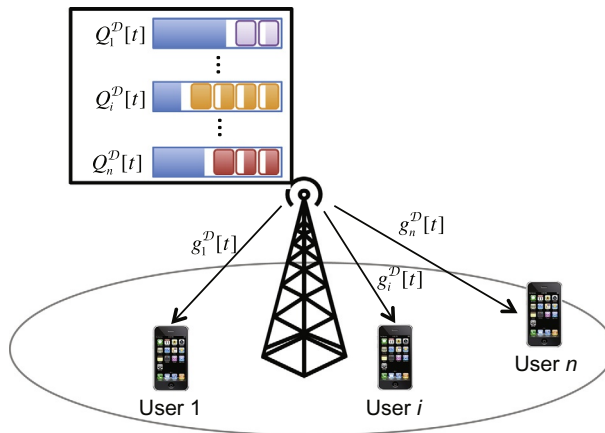
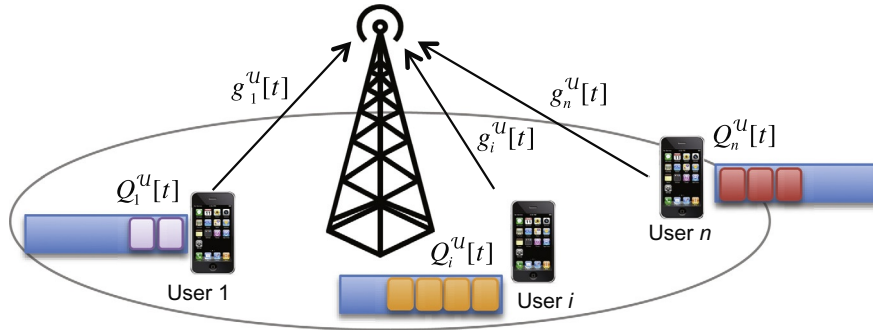


FIG. 12.8

Downlink scenario.

<sup>4</sup>The additional fast Fourier transform is of a smaller size than the main fast Fourier transform and can be seen as a type of precoding.

**FIG. 12.9**

Uplink scenario.

through wired or, less commonly, through wireless connections<sup>5</sup> that are outside the scope of our discussion in this section. Here, we focus on the multiuser MAC concerning the downlink/uplink communication at the edges of cellular networks, where the greatest congestion is observed.

Uplink and downlink wireless channels are subject to several degradations: *path loss* due to distance; *shadowing* due to environmental blockage and absorption; and *small-scale fading* due to constructive and destructive multipath signal overlap. The effects contribute to the channel characteristics at differing magnitudes and time scales. Also, they can differ based on frequency levels. The aim of this section is not to provide an exhaustive treatment of wireless channel modeling and analysis. We refer the interested reader to excellent sources on the modeling and capacity analysis of multiuser wireless channels [1,16,17]. Instead, we will present several essential MAC paradigms under commonly used physical-layer models that capture the collective impact of channel fading gains at a given time. In particular, we let the downlink and uplink channel gains at time slot<sup>6</sup>  $t$  between the BS and user  $i$  be denoted as  $\mathbf{g}^{\mathcal{D}}[t] \triangleq (g_i^{\mathcal{D}}[t])_i$  and  $\mathbf{g}^{\mathcal{U}}[t] \triangleq (g_i^{\mathcal{U}}[t])_i$ , respectively. Similarly, the downlink and uplink transmission powers at time  $t$  between the BS and user  $i$  are denoted as  $\mathbf{P}^{\mathcal{D}}[t] \triangleq (P_i^{\mathcal{D}}[t])_i$  and  $\mathbf{P}^{\mathcal{U}}[t] \triangleq (P_i^{\mathcal{U}}[t])_i$ , respectively. Finally, we use  $N_0$  for the noise power spectral density at the BS and at the  $n$  users.

In our discussion, we will assume FDD or TDD so that uplink and downlink transmissions do not interfere. We also assume that channel gains are available both at the transmitter and receiver, which can be achieved in current cellular systems

<sup>5</sup>The connections can take the form of satellite communication or millimeter-wave communications.

<sup>6</sup>We use the generic concept of a *time slot* as the smallest duration of time to perform resource allocation decisions in the wireless system. This duration is on the order of milliseconds in existing cellular systems.

through various estimation methods [18,19]. In downlink communication, we will consider the scenario where each user  $i$  is assigned an orthogonal frequency band of  $W_i$  Hz so that transmissions to users are noninterfering. In uplink communication, however, all users share the total bandwidth of  $W$  Hz. Accordingly, the downlink and uplink SINR for given channel gains  $\mathbf{g}^{\mathcal{D}}, \mathbf{g}^{\mathcal{U}}$ , given transmission powers  $\mathbf{P}^{\mathcal{D}}, \mathbf{P}^{\mathcal{U}}$ , and downlink orthogonal bandwidth allocation  $\mathbf{W} \triangleq (W_i)_i$  can be calculated as follows:

$$\gamma_i^{\mathcal{D}}(\mathbf{g}^{\mathcal{D}}, \mathbf{P}^{\mathcal{D}}, \mathbf{W}) = \frac{g_i^{\mathcal{D}}[t]P_i^{\mathcal{D}}}{W_i N_0}, \quad \gamma_i^{\mathcal{U}}(\mathbf{g}^{\mathcal{U}}, \mathbf{P}^{\mathcal{U}}) = \frac{g_i^{\mathcal{U}} P_i^{\mathcal{U}}}{W N_0 + \alpha \sum_{j \neq i} g_j^{\mathcal{U}} P_j^{\mathcal{U}}}, \quad (12.7)$$

for each user  $i$ , where the factor  $\alpha \in [0, 1]$  allows the incorporation of interference suppression techniques into the uplink SINR calculation, such as pseudo-orthogonalization that CDMA strategies enable. Assuming additive white Gaussian noise, these SINR levels can be mapped via Shannon's formula to maximum achievable rates for the given transmit powers and channel gains as follows:

$$R_i^{\mathcal{D}}(\mathbf{g}^{\mathcal{D}}, \mathbf{P}^{\mathcal{D}}, \mathbf{W}) = W_i \log(1 + \gamma_i^{\mathcal{D}}(\mathbf{g}^{\mathcal{D}}, \mathbf{P}^{\mathcal{D}}, \mathbf{W})), \quad (12.8)$$

$$R_i^{\mathcal{U}}(\mathbf{g}^{\mathcal{U}}, \mathbf{P}^{\mathcal{U}}) = W \log(1 + \gamma_i^{\mathcal{U}}(\mathbf{g}^{\mathcal{U}}, \mathbf{P}^{\mathcal{U}})). \quad (12.9)$$

### 12.4.2.2 Mobile user and traffic models

The mobile users are assumed to be continuously connected to their respective assigned BSs even when inactive. When a new demand is generated, a data queue  $\mathbf{Q} \triangleq (Q_i)_i$  (illustrated in Figs. 12.8 and 12.9) on the transmitting node (at the BS in downlink and at the mobile in uplink) buffers the generated content for transmission. The requirements of demands may be different based on the inherent quality-of-service (QoS) requirements of the applications that generate them. On the one hand, some applications, such as real-time voice/video communication, may require relatively fixed throughputs but delay-sensitive demand. On the other hand, some applications, such as data downloads or messaging services, may be more throughput greedy but less delay sensitive. We will discuss recent advances in the integration of these QoS requirements into the MAC design in the sequel.

## 12.4.3 SCHEDULING AND RESOURCE ALLOCATION

The main purpose of early cellular services was to provide voice services to cellular mobile users. Such services demand low-rate but regular service guarantees so that reliable communication can be assured between the end-parties. This has driven the development of early resource allocation strategies that separate available resources (time/frequency/energy) into orthogonal channels (see Section 12.3.1) and dedicate each to an ongoing call in order to guarantee reliable audio traffic between the parties. This may be viewed as a direct translation of the *circuit-switching* technology of early landline telephone networks to the wireless domain. It has the benefit of high-quality

service of admitted calls and simple resource allocation solutions. However, it suffers from inefficiency of circuit switching strategy in utilizing the available resources, and it became unsatisfactory as the intensity and nature of demand expanded over time.

Over many generations of wireless technologies, increasingly more sophisticated resource allocation and scheduling solutions have been developed to accommodate a growing population of users with increasingly diverse service demands, ranging from voice, to multimedia, to data. In the rest of this section, we outline some of the predominant resource allocation strategies employed by cellular MAC that are organized with respect to their objectives. An important point on channel models that concern multiuser access is the inherent asymmetry in the achievable set of rates that can be provided to users with widely different channel conditions (see discussion in [Section 12.4.2](#)). Especially, the users' proximity to their BS has a strong impact on their observable SINR level. As such, those users that happen to be close to the edge of a BS's coverage region can be at a great disadvantage in their rates. To accommodate these users, the MAC strategy may need to sacrifice some efficiency for fairness. The tradeoff between efficiency and fairness will be a driving factor in the following designs.

### 12.4.3.1 Waterfilling and channel inversion paradigms in power allocation

Two extreme power allocation strategies emerge in the power allocation of cellular systems, one (called *waterfilling allocation*) aiming for maximum efficiency and the other (called *channel inversion*) aiming for maximum fairness.

To explain and contrast these paradigms, we consider the downlink communication scenario where  $n$  users are active with given channel gains  $\mathbf{g}^{\mathcal{D}}$ . We assume that each user  $i$  is allocated an orthogonal band of unit length,<sup>7</sup> ie,  $W_i = 1$  for all  $i$  in Eq. (12.8), so that the decision of focus is on the power allocation. In particular, the objective of downlink power allocation  $\mathbf{P}^{\mathcal{D}}$  is to divide a bounded total power  $P_{\text{tot}}^{\mathcal{D}}$  amongst the  $n$  active users to maximize the total achieved rate, thereby achieving maximum efficiency. This can be posed as the sum rate maximization problem:

$$\begin{aligned} \bar{\mathbf{P}}^{\mathcal{D}} \triangleq (\bar{P}_i^{\mathcal{D}})_i &= \arg \max_{\{P_i^{\mathcal{D}} \geq 0\}_i} \sum_{i=1}^n R_i^{\mathcal{D}}(\mathbf{g}^{\mathcal{D}}, \mathbf{P}^{\mathcal{D}}, \mathbf{1}) \\ \text{s.t. } \sum_{i=1}^n P_i^{\mathcal{D}} &\leq P_{\text{tot}}^{\mathcal{D}}, \end{aligned} \quad (12.10)$$

<sup>7</sup>This assumption is made to allow presentation of closed-form expressions for the optimal allocations, which are insightful. It is possible to leave the bandwidth allocation  $\mathbf{W}$  as a decision variable to solve the joint bandwidth-power allocation problem. The problem still maintains the convex form, therefore it is amenable to efficient methods, but it does not yield a closed-form analytical solution.

where  $R_i^{\mathcal{D}}$  was defined in Eq. (12.8). This is a convex optimization problem that can be easily solved via optimization conditions to yield the following allocation rule:

$$\bar{P}_i^{\mathcal{D}} = \left( \lambda - \frac{N_0}{g_i} \right)^+, \quad \forall i \quad \text{and} \quad \sum_{i=1}^n \left( \lambda - \frac{N_0}{g_i} \right)^+ = P_{\text{tot}}^{\mathcal{D}}, \quad (12.11)$$

where  $(z)^+ := \max(0, z)$ . Then, the corresponding rates achieved by this power allocation rule are denoted by  $\bar{R}_i^{\mathcal{D}}$ . This is the *waterfilling* power allocation first observed in [20] based on the interpretation of the optimal allocation as filling a bucket with a nonuniform base (inversely related to the channel conditions) with a total amount of water to fill up to (but not above) the level  $\lambda$  as determined by Eq. (12.11).

Under the above waterfilling allocation, channels with favorable channel conditions receive a greater portion of the total power budget than those with worse conditions. This goes against the intuition of fairness, since users with poor channel conditions (eg, those that are close to the cell boundary) will suffer from very low rates, while users with good channel conditions (eg, those close to the BS with an unobstructed line-of-sight) will receive disproportionately high rates. In the interest of perfect fairness, the alternative to the waterfilling solution is the following power allocation problem that aims to equalize all achieved rates under the power budget:

$$\begin{aligned} \check{\mathbf{P}}^{\mathcal{D}} \triangleq (\check{P}_i^{\mathcal{D}})_i &= \arg \max_{\{P_i^{\mathcal{D}} \geq 0\}_i} \min_{\{i=1, \dots, n\}} R_i^{\mathcal{D}}(\mathbf{g}^{\mathcal{D}}, \mathbf{P}^{\mathcal{D}}, \mathbf{1}) \\ \text{s.t.} \quad &\sum_{i=1}^n P_i^{\mathcal{D}} \leq P_{\text{tot}}^{\mathcal{D}}. \end{aligned} \quad (12.12)$$

This also is an easily solvable problem with the following allocation rule:

$$\check{P}_i^{\mathcal{D}} = \frac{N_0}{g_i} \tau, \quad \forall i \quad \text{and} \quad \tau = \frac{P_{\text{tot}}^{\mathcal{D}}}{\sum_{i=1}^n N_0/g_i}. \quad (12.13)$$

This is the *channel inversion allocation*, whereby each user  $i$  is assured to receive the same rate level of  $\check{R}_i^{\mathcal{D}} = \log(1 + \tau)$  regardless of its channel gain and noise power values.

To understand the differences between waterfilling and channel inversion, let us consider an example with  $n = 20$  users with  $g_i/N_0$  values ranging from 0 to 20 dB and  $P_{\text{tot}}^{\mathcal{D}} = 10$ . Fig. 12.10 shows the allocated powers and corresponding rates of these two extreme paradigms for each user. It is readily verified that the sum-rate for channel inversion  $\sum_i \check{R}_i^{\mathcal{D}}$  is about 60% of the sum-rate of waterfilling,  $\sum_i \bar{R}_i^{\mathcal{D}}$ . It is apparent that, despite its throughput maximizing nature, the waterfilling power allocation can be highly unfair to users that have poor downlink channels from the BS, in particular those that are far from their assigned BSs. On the other hand, channel inversion completely eliminates the unfairness issues while exhausting much of its power budget on users with poor channels. It is therefore useful to consider a

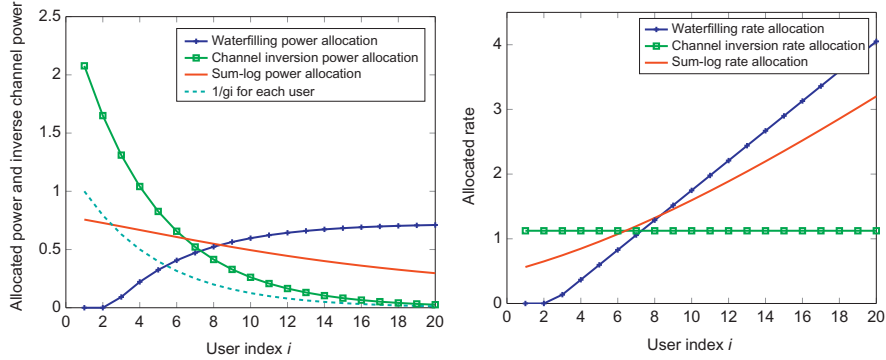


FIG. 12.10

Comparison of waterfilling, channel inversion, and sum-log optimal power allocations (left) and rate allocations (right) for  $n = 20$  users with  $g_i/N_0$  values ranging from 0 to 20 dB, and  $P_{\text{tot}}^D = 10$ . In terms of sum-rate, channel inversion and sum-log achieve 60% and 93% of the waterfilling performance, respectively.

balanced policy between these two extremes that trades off the efficiency and fairness characteristics. One such policy is the *sum-log* optimal allocation that solves the following:

$$\begin{aligned} \arg \max_{\{P_i^D \geq 0\}_i} & \sum_{i=1}^n \log(R_i^D(\mathbf{g}^D, \mathbf{P}^D, \mathbf{1})) \\ \text{s.t.} & \sum_{i=1}^n P_i^D \leq P_{\text{tot}}^D. \end{aligned} \quad (12.14)$$

The logarithmic function enforces the power allocation to be spread more fairly across users, while at the same time favoring channels with greater quality so that efficiency is also high. The resulting sum-log optimal allocation is depicted in Fig. 12.10 in contrast to the waterfilling and channel inversion scenarios. Under this allocation, the rates are allocated more fairly than waterfilling and more efficiently than channel inversion.

### 12.4.3.2 Opportunistic multiuser rate allocation over fading channels

The previous discussion concerned the tradeoff between efficiency and fairness for multiuser power allocation over static channels. In this discussion, we consider the multiuser rate allocation problem over fading channels where only a single transmission is allowed with a fixed power (ie, only a single user can be served at any time slot). Accordingly, we assume that the channel gain of user  $i$  in slot  $t$  is given by  $\{\mathbf{g}^D[t]\}_t$ , and we need to decide which user to serve in each slot at the rate  $R_i^D[t] := \log(1 + g_i^D[t]P_{\text{tot}}/N_0)$ .

If we target *maximum efficiency*, the choice would clearly be to choose the user that achieves the largest sum rate: Serve user  $\bar{i}[t] = \arg \max_i R_i^{\mathcal{D}}[t]$  in slot  $t$ . While this allocation will result in maximum total throughput achieved by the system, it will be unfair to users that fluctuate around low gains. As in the power allocation discussion, we can maximize the sum-log of throughputs to balance the fairness and efficiency objectives. The following iterative scheme provides such a long-term performance guarantee.

The nature of this allocation differs from the sum rate maximizing allocation in that its objective accounts not only for the instantaneously achievable rate  $R_i^{\mathcal{D}}[t]$  but also for the weighted average of the throughput  $T_i[t]$  for each user. In Fig. 12.11, we provide a numerical comparison of the sum-rate maximizing allocation (which serves the user with the best channel gain at any time) and the average rates achieved by the above proportionally fair allocation policy with  $\beta = 0.1$ . The figure clearly shows how the sum-rate maximizing policy can be significantly unfair to users with poor average channel conditions (those with smaller index values), while the proportionally fair allocation spreads its service across all users while still preferring users with better channels (those with larger index values) whenever possible. In fact, it can be shown [1,21] that Algorithm 1 maximizes  $\sum_i \log(T_i[\infty])$ , which is called the *proportionally fair allocation*. Consequently, if a user receives little throughput up to a given time  $t$ , its weight grows so that it receives a greater portion of the power budget. This balancing affect of this rule results in a proportionally fair allocation of rates amongst the users. This allocation rule found use in practical systems (eg, CDMA2000) to balance the fairness and efficiency of resource allocation in downlink MAC.

### 12.4.3.3 Energy minimizing uplink power allocation for targeted rates

The underlying aim of the previous resource allocation strategies has been to maximize a function of the throughput (either the linear, minimum, or logarithmic functions of it) with differing fairness and efficiency characteristics, under a power budget constraint. A reverse problem can also be posed that aims to guarantee a given throughput level per active connection with the smallest power consumption. This problem is especially important in the uplink scenario, whereby each device has a separate power budget to consume and would like to achieve a given SINR threshold  $\tau$  for reliable communication with the smallest power consumption. We can pose this problem assuming static channel conditions  $\{g_i^{\mathcal{U}}\}_i$  as follows:

$$\begin{aligned} \hat{\mathbf{P}}^{\mathcal{D}} \triangleq (\hat{P}_i^{\mathcal{D}})_i &= \arg \min_{\{P_i^{\mathcal{U}} \geq 0\}_i} \sum_{i=1}^n P_i^{\mathcal{U}} \\ \text{s.t. } \gamma_i^{\mathcal{U}}(\mathbf{g}^{\mathcal{U}}, \mathbf{P}^{\mathcal{U}}) &\geq \tau, \quad \text{for all } i, \end{aligned} \quad (12.15)$$

where  $\gamma_i^{\mathcal{U}}(\mathbf{g}^{\mathcal{U}}, \mathbf{P}^{\mathcal{U}})$  is the uplink SINR level as determined by Eq. (12.7). Such a problem is confronted in [22,23] to develop an iterative power allocation strategy that converges to the optimum solution  $\hat{\mathbf{P}}^{\mathcal{D}}$ , shown in Algorithm 2.

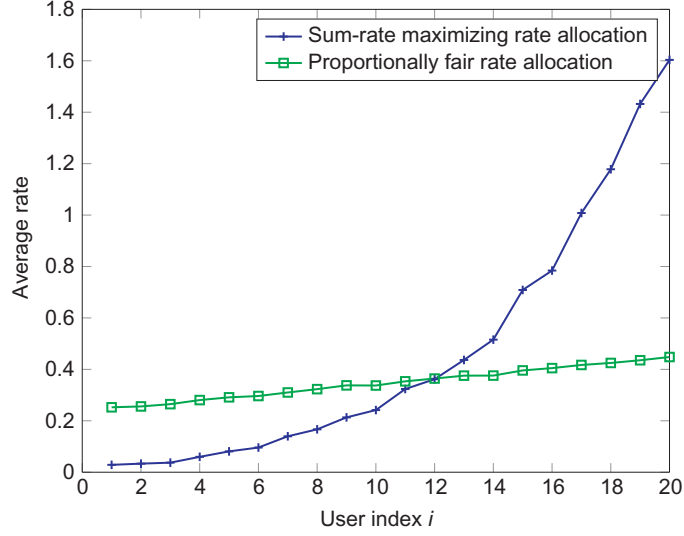


FIG. 12.11

Comparison of sum-rate maximizing (sum-rate  $\approx 7.1$ ) and proportionally fair (sum-rate  $\approx 5.0$ ) rate allocations for users with mean  $g_i/N_0$  values ranging from 0 to 20 dB and log-normal distribution 3 dB standard deviation for each user.

### ALGORITHM 1 PROPORTIONALLY FAIR RATE ALLOCATION

- 1: Input: a common constant  $\beta \in (0, 1)$
- 2: Set the value of  $T_i[0] = 1$  for all  $i$ , which aims to measure the weighted average of the throughput that user  $i$  receives
- 3: **for** at each time slot  $t$  **do**
- 4:     Determine a single user  $i^*[t]$  (break ties randomly in the case of multiple users) satisfying

$$i^*[t] \in \arg \max_{i=1, \dots, n} \tilde{R}_i^{\mathcal{D}}[t]/T_i[t]. \quad (12.16)$$

- 5:     Set the rate as

$$\tilde{R}_i^{\mathcal{D}}[t] = \begin{cases} \log(1 + g_i^{\mathcal{D}}[t]P_{\text{tot}}/N_0) & i = i^* \\ 0 & \text{else} \end{cases}. \quad (12.17)$$

- 6:     Update  $T_i[t+1] \leftarrow (1 - 1/\beta) T_i[t] + \tilde{R}_i^{\mathcal{D}}[t]/\beta, \forall i$
- 7: **end for**

**ALGORITHM 2 DISTRIBUTED UPLINK POWER ALLOCATION**

- 1: Input: a constant SINR threshold level  $\tau$
- 2: Set the value of  $P_i^{\mathcal{U}}[0]$  to a large enough power level  $P_{\max}$  for all  $i$ , and calculate the SINR  $\gamma_i^{\mathcal{U}}[0]$  at this power level for each user  $i$
- 3: **for** at each time slot  $t$  **do**
- 4:     Update the power allocation for each user  $i$  as

$$\tilde{P}_i^{\mathcal{U}}[t+1] = \arg \min_{P_i^{\mathcal{U}} \geq 0} P_i^{\mathcal{U}} \quad (12.18)$$

$$\text{s.t. } \frac{g_i^{\mathcal{U}} P_i^{\mathcal{U}}}{N_0 + \alpha \sum_{j \neq i} g_j^{\mathcal{U}} P_j^{\mathcal{U}}[t]} \geq \tau. \quad (12.19)$$

5: **end for**

This is a fully distributed allocation policy in which all users start from their maximum possible power allocations and iteratively *reduce* their power while maintaining the SINR threshold as described in Eq. (12.18), assuming all others to remain at their most recent power level. It is not difficult to observe that since the power levels can only decrease under this strategy, they must converge. It is shown in [22,23] that this limit point is in fact the solution  $\mathbf{P}^{\mathcal{D}}$  of Eq. (12.17). Therefore, this simple iterative rule provides the minimum energy solution for the uplink power control problem under the SINR threshold constraint.

**12.4.3.4 Birth of the cross-layer resource allocation framework**

The resource allocation rules outlined above have focused on various objectives ranging from sum rate maximization (Eq. 12.10), fairness (Eq. 12.15), and power minimization with rate guarantees (Eq. 12.17). In each case, the focus has been on the service side decisions with varying long-term performance objectives. Recently, there have been significant advances in generalizing and extending these efforts to cover more general wireless multiuser communication scenarios, incorporate traffic dynamics, account for variety of QoS requirements, and allow more general class of objective functions (also called *utility functions*). In particular, there has emerged a *cross-layer design framework* that provides a systematic design methodology for a network algorithm design that encompasses functionalities across multiple layers of the traditional network layering hierarchy, including power control, rate allocation, congestion control, scheduling, multihop routing, etc.

In contrast to the above MAC-layer allocation strategies, these cross-layer solutions account for the congestion levels of the buffers, the varying QoS requirements of the flows, the differences between the sensitivities of the applications, etc. To take an example in the context of downlink scheduling depicted in Fig. 12.8, a cross-layer strategy accounts for the state of the queues  $\mathbf{Q}^{\mathcal{D}}[t]$  at time  $t$  in deciding the service allocation. It is shown (eg, in [24–26]) that if in each slot  $t$  we serve the user

$i$  that maximizes  $(Q_i^D[t] \times R_i^D[t])$  amongst all users, then we can achieve maximum utilization of the available service rates for the system load. Note that this policy prioritizes the service of flows with high achievable rates and a high congestion level. As such, it exploits channel conditions as well as congestion conditions.

Such *queue-length-based* policies and their variants, have generated great interest due to their simplicity and performance guarantees. For example, the evolution-data optimized (EVDO) standard [18] utilizes such congestion information for efficient resource allocation in cellular systems. Many early works have built on the throughput-maximizing and stabilizing nature of queue-length-based designs in great generality (eg, [24,25,27–30]; see [31,32] for further references). Subsequently, this framework is extended within a *network utility maximization (NUM) framework* to cover congestion control and fairness objectives (eg, [30,33–37]; see [32,38,39] for further references). More recently, increasingly short-term requirements are incorporated into the design, such as deadline-constraints, regular service requirements, etc. [40–43]. The resulting cross-layer framework combines models and methods from optimization theory, stochastic control, and algorithm design and analysis to yield adaptive and dynamic resource allocation strategies with diverse QoS guarantees.

---

## 12.5 DECENTRALIZED MAC IN WIRELESS NETWORKS

The previous section has focused on the MAC strategies that are optimized for cellular networks and exhibit centralized characteristics due to the continuous connectivity of mobile users and information availability at the BSs. In this section, we move away from such cellular systems toward the MAC design for ad-hoc and Wi-Fi networks that can take a multihop structure and serve a dynamically changing population of users. These systems are far less structured in their deployment, usage, and traffic demands than their cellular counterparts. Moreover, they operate over an unlicensed spectrum that limits their control over the coordinated interference management. Therefore, their MAC must be designed to accommodate a dynamically changing and decentralized nature of operation.

In this section, we overview the key developments in the evolution of *decentralized* MAC strategies that are well-suited for these wireless networks.

### 12.5.1 CHANNELIZATION

The lack of central coordination and the dynamic nature of the network precludes the use of sophisticated channelization strategies, as in Section 12.4.1. The main resource that is considered in a decentralized setting is *time*. In other words, all users use a common bandwidth and compete for access (in the form of transmission times) to their receivers. In contrast to centralized MAC protocols, where the quality of a link was based on the SINR, decentralized MAC protocols have traditionally relied on collision-based models.

## 12.5.2 CHANNEL AND TRAFFIC MODELS

### 12.5.2.1 SINR and collision-based interference models

Interference management in multihop wireless networks is significantly more complex than in cellular networks due to the large-scale, dynamic, and decentralized nature of the operation. While it is possible to generalize the SINR-based interference models of [Section 12.4.2](#) to the multihop setting, this usually is counterproductive to developing decentralized solutions. Moreover, a complete SINR description may be an overkill as the dominant component of the interference at a receiver is governed by the nearby transmitters.

These considerations have prompted engineers and theoreticians to develop *collision-based* interference models whereby two transmissions within interference range of each other collide if they transmit simultaneously, in which case both transmissions fail. The interference range of a transmission is determined as a function of its transmission power as well as the distance and fading state between the transmitting and the receiving node. Such a model of interference facilitates tractable design of MAC strategies, and is employed in most practical standards. However, the collision-based model in multihop wireless networks also brings about new interference scenarios that did not exist in cellular context, namely *hidden* and *exposed* nodes. Next, we discuss these briefly.

### 12.5.2.2 Hidden nodes

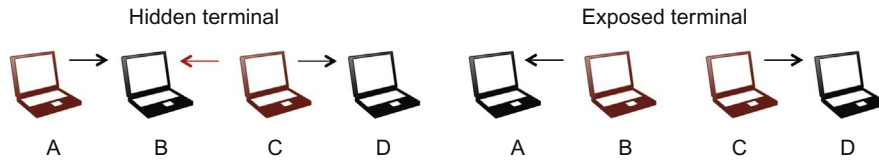
A receiver may be able to pick up transmissions from two nodes that are mutually out of reach. These transmitting nodes are said to be *hidden* from each other and may cause collision at the common receiver, regardless of whether the receiver was the intended recipient of the transmissions of either transmitting node.

### 12.5.2.3 Exposed nodes

Consider a scenario with two transmitter-receiver pairs, where each receiver is within communication range of its corresponding transmitter, but not of the other transmitter. When the transmitters are programmed to only start transmitting when the channel is unoccupied, only one transmitter will transmit at any given time, while in principle both transmitters could send signals to their respective receivers simultaneously without collision. This is known as the exposed node problem, and leads to underutilization of the channel ([Fig. 12.12](#)).

### 12.5.2.4 Mobile user and traffic models

In contrast to the cellular scenario, the mobile users in this scenario are assumed to appear and disappear intermittently in the network. Therefore, the dynamics of new users and their traffic becomes an integral part of the model for the operation and design of wireless networks. Assuming each user emerges with a small probability and independently of all others, the nature of these user appearances can be closely approximated by *Poisson* processes. A Poisson process is described by a single parameter  $\lambda$  that defines the mean rate arrivals per unit time. The key characteristic of this process is that at any time, the time to the next arrival is an exponentially

**FIG. 12.12**

Hidden and exposed nodes. On the left side, A transmits to B and C transmits to D. Since C is hidden from A, these simultaneous transmissions cause interference at node B. On the right side, B would like to transmit to A, and C to D. While simultaneous transmissions will not cause collisions at either A or D, if nodes are not allowed to transmit when the channel is busy, nodes B and C are not allowed to transmit at the same time, leading to a under utilization of the channel.

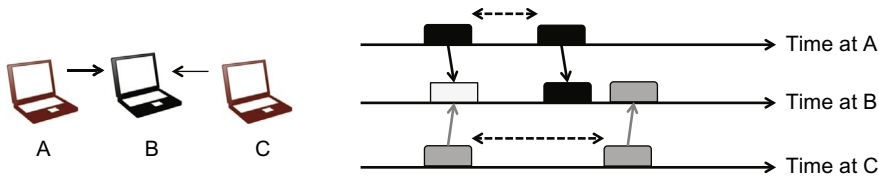
distributed random variable that is independent of the time of last arrival. This *memoryless* nature of the Poisson process facilitates a tractable analysis of the user dynamics, and it is the prominent model used in this literature. In addition to the user dynamics, each incoming user may have varying amounts and types of service demands from the system. These can be captured by random variables with distributions that depend on the particular scenario.

### 12.5.3 SCHEDULING AND RESOURCE ALLOCATION

The objective of this section is to provide a brief overview of the past and recent advances in the development of decentralized MAC strategies for ad hoc wireless networks. Throughout this section, we will assume a collision-based interference model (Section 12.5.2), which is the commonly used in the literature.

#### 12.5.3.1 Aloha-variant strategies

Aloha is arguably the most simple decentralized MAC protocol. It is built on the assumption that nodes will only sporadically send data, so that they will only need to utilize the channel a small fraction of the time. In *pure Aloha*, a node will transmit data as soon as it has a packet to send (Fig. 12.13). If it does not receive an acknowledgment from the receiver (or some other type of feedback), it will attempt again. Since the lack of an acknowledgment generally indicates that another transmitter was active and a collision has occurred, the transmitter should not retransmit immediately or retransmit at a fixed time later, since at least one other transmitter will attempt to retransmit as well, leading to a sequence of collisions. In order to resolve such ties in a decentralized manner, each transmitter will only retransmit after a random back-off time. The statistics of this random back-off must be adapted to the number of active users at the time, either assuming its knowledge or through adaptive updates. See [44,45] for an extended discussion. A variation of pure Aloha is *slotted Aloha*, where nodes can only transmit at the beginning of

**FIG. 12.13**

In Aloha, nodes A and C transmit when they have data to send. Since a collision occurs at node C, they each wait a random time before they try again. In this case, the second transmission is successful.

time slots. Such an organization prevents partial overlap between transmissions and thereby reduces the loss from collisions.

Aloha does not avoid hidden or exposed nodes and is generally inefficient in terms of usage of the channel: pure Aloha leads to a maximum efficiency of less than  $1/(2e) \approx 18.5\%$ , compared to a single user system. Slotted Aloha can utilize the channel up to nearly  $1/e \approx 37\%$ . More sophisticated versions of Aloha, called coded slotted Aloha, which rely on the joint detection principle from [Section 12.3](#), are able to reclaim much of this loss [\[46\]](#).

### 12.5.3.2 Carrier-sense multiple access (CSMA) strategies

The above Aloha strategies are based on backing off after collisions are experienced, for a random duration according to given distributions. Such strategies allow for nonnegligible occurrences of idle durations even when packets are awaiting service. These deficiencies have motivated the development of strategies that are based on sensing ongoing activity *before* attempting to capture the channels—so-called CSMA strategies.<sup>8</sup>

The core aim of CSMA strategies is to preserve the decentralized nature of Aloha strategies while reducing the amount of idle time spent in coordinating collisions. To that end, CSMA strategies are based on sensing idle channel conditions to attempt transmissions without too much extra delay. Still, users that sense idle channels must individually act to reduce the chances of delay. One advantage here is that if a user successfully captures the channel, its transmission will not be interrupted by any other transmitter within the transmission range of the transmitter. Also, the idle durations can be significantly reduced due to the sensing-based activity rather than random backoffs.

As in the pure Aloha case, there are numerous variants of CSMA strategies, including slotted, unslotted, collision avoidance (CSMA-CA), and collision detection

<sup>8</sup>Technically, CSMA strategies can still be considered as a variant of Aloha, and they are referred to as CSMA Aloha in some contexts. In our treatment, we prefer to refer to them as a separate class to avoid unnecessary confusion.

(CSMA-CD). All these share the essential characteristics of the above core CSMA construction principle. This basic CSMA strategy continues to suffer from the hidden and exposed nodes phenomenon. However, this can be prevented by a handshake between the transmitter-receiver pairs prior to transmission. Accordingly, short ready-to-send (RTS) and clear-to-send (CTS) packets are transmitted between the pair so that all potential transmitters around the receiver are silenced (thus avoiding the hidden node problem), while the other transmitters far away from the receiver can still be active (thus avoiding the exposed node problem).

In a single-hop setting where all transmissions are within the interference range of all others, which is the setting of connecting a common Wi-Fi router, such a CSMA-based strategy can be shown [44, Section 4.4] to achieve the full capacity of the shared wireless channel as the sensing delay becomes negligible compared to the packet transmission duration. Whether CSMA in multihop networks achieved capacity had been an open problem until it was shown in [47] that CSMA can achieve capacity asymptotically as the network size scales to infinity. This is a surprising and encouraging finding given the highly decentralized and low-complexity nature of CSMA. In the recent years, there have been further advances in the optimality characteristics of CSMA strategies in the sense that it is possible to determine CSMA design parameters to support any traffic load that is supportable by any other MAC strategy, including centralized ones (see [48] for an extended treatment with comprehensive references). Early investigations presume knowledge of traffic loads, which may be impractical. Later investigations released this assumption by developing adaptive strategies that determine CSMA parameters dynamically as a function of the local queue-lengths at the time [48,49]. This is achieved by carefully setting the CSMA parameters at different nodes as a function of their varying traffic loads and location in the network topology. By letting the data transmission duration increase relative to the sensing and collision durations, it is then shown that all nodes can support their traffic demands under the selected CSMA parameters as long as they are supportable by some other MAC solution.

These advances establish the potential power of CSMA strategy in achieving long-term throughputs when its parameters can be well-selected. While this sounds too good to be true, it comes with a serious handicap: *delay*. In a multihop scenario under CSMA-type decentralized operation, a user can only access the channel when one of its interfering neighbors are inactive. This becomes an unlikely event in a large network with high traffic load. In such a regime, users typically wait long intervals before they capture the channel, and they then get to use it for a long time to flush their buffers. Such intermittent and bursty service discipline is a classical example of a high-delay incurring service discipline. To understand and partially address this deficiency, there has been significant activity (eg, [50–54]). Some of these efforts focus on the design of new CSMA-type strategies that can be employed to improve delay performance with limited loss on throughput. Some of them focus on characterizing the throughput levels that CSMA can provide a good delay for. Some of them focus on understanding fundamental limits on the throughput-delay tradeoff of CSMA. All of these are still active fields of research.

### 12.5.3.3 Cross-layer decentralized MAC strategies

At the closing of [Section 12.4.3](#), we discussed the emergence of a unifying *cross-layer resource allocation* framework that enabled the systematic development of MAC solutions that incorporate new dynamics, generalizations, and more diverse QoS measures. In a nutshell, these strategies employ a combination of optimization models and methods, stochastic control techniques, and algorithm development to develop adaptive policies that utilize appropriate state information, eg, congestion states, and delay limitations to allocate resources. These policies, if implemented via centralized controllers, can be shown to achieve an increasing diversity of QoS-guarantees beyond throughput, including deadline-constrained streaming services, average delay guarantees, large-delay constraints, and regular service guarantees. However, the rules of allocation that emerge from these QoS-aware solutions typically assume repeated execution of centralized decisions. While these centralized operations can be integrated into cellular networks due to their centralized topology, they do not scale in multihop topologies that are the focus of this section. This reality has inspired an active effort in developing *decentralized* and *low-complexity* algorithms based the cross-layer design with performance guarantees. The vast and growing literature toward this end can be organized into the following categories:

- *Suboptimal low-complexity algorithms*: A group of works focus on the design and analysis of approximate algorithms that yield low-complexity decentralized implementations at the expense of performance loss from the centralized counterpart. These, in themselves, can be grouped under *greedy* algorithms (eg, [36,55–57]) and *randomized* algorithms (eg, [58–62]).
- *Optimal low-complexity algorithms*: Another set of works may be grouped as those that maintain optimality of centralized solutions, at least in an asymptotic sense and for the fundamental measures such as throughput and utility, but are also amenable to low-complexity implementation with guarantees on more complex QoS measures such as delay and outages. These include algorithms that employ *gradual search strategies* (eg, [63–65]), *random access strategies* (eg, [47,49,52,60,66–68]), and *queue-length-based variations* (eg, [69–71]).

We note that the above list can only cover a subset of works in this active area of research, and this is indicative of the productive nature of this algorithmic development space.

---

## 12.6 SUMMARY

In this chapter, we have provided a bird’s eye view of medium access control for wireless networks. Our treatment separated centralized cellular networks from decentralized WLAN-type networks. In centralized networks, the presence of channel state information and centralized control enables sophisticated ways of channelization and resource allocation. In decentralized networks, users compete for time slots, while access is controlled though decentralized strategies. Even though both types

of networks operate under different assumptions regarding the channel and traffic models, we have highlighted the common trend toward cross-layer design based on optimization theory and stochastic control.

---

## REFERENCES

- [1] D. Tse, P. Viswanath, *Fundamentals of Wireless Communication*, Cambridge University Press, 2005.
- [2] A.F. Molisch, *Wireless Communications*, Wiley Publishing, 2011.
- [3] A.C.V. Gummalla, J.O. Limb, Wireless medium access control protocols, *IEEE Commun. Surv. Tut.* 3 (2) (2000) 2–15.
- [4] J. Agar, *Constant Touch: A Global History of the Mobile Phone*, Icon Books, 2013.
- [5] M. Rahnema, Overview of the GSM system and protocol architecture, *IEEE Commun. Mag.* 31 (4) (1993) 92–100.
- [6] E. Dahlman, S. Parkvall, J. Skold, P. Beming, *3G Evolution: HSPA and LTE for Mobile Broadband*, Academic Press, 2010.
- [7] S. Kumar, V.S. Raghavan, J. Deng, Medium access control protocols for ad hoc wireless networks: a survey, *Ad Hoc Netw.* 4 (3) (2006) 326–358.
- [8] R. Jurdak, C.V. Lopes, P. Baldi, A survey, classification and comparative analysis of medium access control protocols for ad hoc networks, *IEEE Commun. Surv. Tut.* 6 (1) (2004) 2–16.
- [9] A.S. Poon, R.W. Brodersen, D.N. Tse, Degrees of freedom in multiple-antenna channels: a signal space approach, *IEEE Trans. Inform. Theory* 51 (2) (2005) 523–536.
- [10] D. Senaratne, C. Tellambura, Beamforming for space division duplexing, in: *IEEE International Conference on Communications*, 2011, pp. 1–5.
- [11] A. Jamalipour, T. Wada, T. Yamazato, A tutorial on multiple access technologies for beyond 3G mobile networks, *IEEE Commun. Mag.* 43 (2) (2005) 110–117.
- [12] H. Yin, H. Liu, Performance of space-division multiple-access (SDMA) with scheduling, *IEEE Trans. Wireless Commun.* 1 (4) (2002) 611–618.
- [13] J.G. Andrews, S. Buzzi, W. Choi, S.V. Hanly, A. Lozano, A.C.K. Soong, J.C. Zhang, What will 5G be? *IEEE J. Sel. Areas Commun.* 32 (6) (2014) 1065–1082.
- [14] T.S. Rappaport, S. Sun, R. Mayzus, H. Zhao, Y. Azar, K. Wang, G.N. Wong, J.K. Schulz, M. Samimi, F. Gutierrez, Millimeter wave mobile communications for 5G cellular: it will work! *IEEE Access* 1 (2013) 335–349.
- [15] G. Berardinelli, L.A. Ruiz de Temino, S. Frattasi, M.I. Rahman, P. Mogensen, OFDMA vs. SC-FDMA: performance comparison in local area IMT-A scenarios, *IEEE Wireless Commun.* 15 (5) (2008) 64–72.
- [16] T.S. Rappaport, *Wireless Communications: Principles and Practice*, Prentice Hall, 2001.
- [17] A. Goldsmith, *Wireless Communications*, Cambridge University Press, New York, NY, USA, 2005.
- [18] R.L.J. Li, X. Wu, *OFDMA Mobile Broadband Communications: A Systems Approach*, Cambridge University Press, New York, NY, USA, 2013.
- [19] H. Meyer, M. Moeneclaey, S.A. Fechtel, *Digital Communications Receivers*, Wiley-Interscience, 1997.
- [20] R. Knopp, P.A. Humblet, Information capacity and power control in single-cell multiuser communications, in: *Proceedings of the ICC*, Seattle, WA, 1995.

- [21] P. Viswanath, D. Tse, R. Laroia, Opportunistic beamforming using dumb antennas, *IEEE Trans. Inform. Theory* 48 (6) (2002) 1277–1294.
- [22] G.J. Foschini, Z. Miljanic, A simple distributed autonomous power control algorithm and its convergence, *IEEE Trans. Veh. Technol.* 42 (4) (1993) 641–646.
- [23] R.D. Yates, A framework for uplink power control in cellular radio systems, *IEEE J. Sel. Areas Commun.* 13 (7) (1995) 1341–1347.
- [24] L. Tassiulas, A. Ephremides, Dynamic server allocation to parallel queues with randomly varying connectivity, *IEEE Trans. Inform. Theory* 39 (1993) 466–478.
- [25] L. Tassiulas, Scheduling and performance limits of networks with constantly varying topology, *IEEE Trans. Inform. Theory* 43 (1997) 1067–1073.
- [26] A. Eryilmaz, R. Srikant, J.R. Perkins, Stable scheduling policies for fading wireless channels, *IEEE/ACM Trans. Netw.* 13 (2005) 411–425.
- [27] L. Tassiulas, A. Ephremides, Stability properties of constrained queueing systems and scheduling policies for maximum throughput in multihop radio networks, *IEEE Trans. Autom. Control* 36 (1992) 1936–1948.
- [28] M. Andrews, K. Kumaran, A. Ramanan, A. Stolyar, R. Vijayakumar, P. Whiting, Scheduling in a queueing system with asynchronously varying service rates, 2000, Bell Laboratories Technical Report.
- [29] M.J. Neely, E. Modiano, C.E. Rohrs, Dynamic power allocation and routing for time varying wireless networks, in: *Proceedings of the IEEE International Conference on Computer Communications (INFOCOM)*, San Francisco, CA, 2003.
- [30] A. Eryilmaz, R. Srikant, Fair resource allocation in wireless networks using queue-length based scheduling and congestion control, in: *Proceedings of the IEEE International Conference on Computer Communications (INFOCOM)*, Miami, FL, Mar. 2005.
- [31] L. Georgiadis, M.J. Neely, L. Tassiulas, Resource allocation and cross-layer control in wireless networks, in: *Foundations and Trends in Networking*, 2006. <http://www.nowpublishers.com/article/Details/NET-001>.
- [32] R. Srikant, L. Ying, *Communication Networks: An Optimization, Control and Stochastic Networks Perspective*, Cambridge University Press, New York, NY, USA, 2014.
- [33] D.P. Palomar, M. Chiang, A tutorial on decomposition methods for network utility maximization, *IEEE J. Sel. Areas Commun.* 24 (2006) 1439–1451.
- [34] A. Eryilmaz, R. Srikant, Joint congestion control, routing and mac for stability and fairness in wireless networks, *IEEE J. Sel. Areas Commun.*, special issue on Nonlinear Optimization of Communication Systems 14 (2006) 1514–1524.
- [35] A. Stolyar, Maximizing queueing network utility subject to stability: greedy primal-dual algorithm, *Queueing Syst.* 50 (4) (2005) 401–457.
- [36] X. Lin, N. Shroff, The impact of imperfect scheduling on cross-layer rate control in multihop wireless networks, in: *Proceedings of the IEEE International Conference on Computer Communications (INFOCOM)*, Miami, FL, 2005.
- [37] M.J. Neely, E. Modiano, C. Li, Fairness and optimal stochastic control for heterogeneous networks, in: *Proceedings of the IEEE International Conference on Computer Communications (INFOCOM)*, Miami, FL, 2005.
- [38] S. Shakkottai, R. Srikant, “Network Optimization and Control”, in *Foundations and Trends in Networking* vol. 2, Issue (3), Now Publishers Inc, ISBN-13: 978-1601981028, January 2008.
- [39] S. Shakkottai, A. Eryilmaz, Optimization and control of communication networks, in: W. Levine (Ed.), *The Control Handbook*, CRC Press, New York, 2010.

- [40] I.-H. Hou, V. Borkar, P.R. Kumar, A theory of QoS for wireless, in: Proceedings of the IEEE International Conference on Computer Communications (INFOCOM), Rio de Janeiro, Brazil, 2009.
- [41] J.J. Jaramillo, R. Srikant, L. Ying, Scheduling for optimal rate allocation in ad hoc networks with heterogeneous delay constraints, *IEEE J. Sel. Areas Commun.* 29 (5) (2011) 979–987.
- [42] R. Li, H. Gangammanavar, A. Eryilmaz, Optimal dynamic coding-window selection for serving deadline-constrained traffic over time-varying channels, *IEEE Trans. Inform. Theory* 58 (10) (2012) 6556–6571.
- [43] R. Li, A. Eryilmaz, B. Li, Throughput-optimal scheduling with regulated inter-service times, in: Proceedings of the IEEE International Conference on Computer Communications (INFOCOM), Turin, Italy, Apr. 2013.
- [44] D.P. Bertsekas, R.G. Gallager, P. Humblet, *Data Networks*, vol. 2, Prentice-Hall International, New Jersey, 1992.
- [45] B. Hajek, Communication network analysis, Course Notes, Dec. 2006.
- [46] G. Liva, Graph-based analysis and optimization of contention resolution diversity slotted ALOHA, *IEEE Trans. Commun.* 59 (2) (2011) 477–487.
- [47] P. Marbach, A. Eryilmaz, A. Ozdaglar, Asynchronous CSMA policies in multi-hop wireless networks with primary interference constraints, *IEEE Trans. Inform. Theory* 57 (2011) 3644–3676.
- [48] L. Jiang, J. Walrand, Scheduling and congestion control for wireless and processing networks, *Synthesis Lectures on Communication Networks*, Morgan & Claypool Publishers, 2010.
- [49] J. Ni, B. Tan, R. Srikant, Q-CSMA: queue-length-based CSMA/CA algorithms for achieving maximum throughput and low delay in wireless networks, *IEEE/ACM Trans. Netw.* 20 (3) (2012) 825–836.
- [50] M. Lotfinezhad, P. Marbach, Throughput-optimal CSMA protocols with order-optimal delay, in: Proceedings of the IEEE INFOCOM, 2011, pp. 2867–2875.
- [51] L. Jiang, M. Leconte, J. Ni, R. Srikant, J. Walrand, Fast mixing of parallel glauber dynamics and low-delay CSMA scheduling, *IEEE Trans. Inform. Theory* 58 (10) (2012).
- [52] B. Li, A. Eryilmaz, Optimal distributed scheduling under time-varying conditions: a fast-CSMA algorithm with applications, *IEEE Trans. Wireless Commun.* 12 (7) (2013) 3278–3288.
- [53] D. Shah, D.N.C. Tse, J.N. Tsitsiklis, Hardness of low delay network scheduling, *IEEE Trans. Inform. Theory* 57 (12) (2011).
- [54] P.-K. Huang, X. Lin, Improving the delay performance of CSMA algorithms: a virtual multi-channel approach, in: Proceedings of the IEEE INFOCOM, 2013, pp. 2598–2606.
- [55] X. Wu, R. Srikant, Regulated maximal matching: a distributed scheduling algorithm for multi-hop wireless networks with node-exclusive spectrum sharing, in: Proceedings of the IEEE Conference on Decision and Control, 2005.
- [56] A. Brzezinski, G. Zussman, E. Modiano, Enabling distributed throughput maximization in wireless mesh networks: a partitioning approach, in: Proceedings of the 12th Annual International Conference on Mobile Computing and Networking, MobiCom '06, 2006, pp. 26–37.
- [57] C. Joo, X. Lin, N.B. Shroff, Understanding the capacity region of the greedy maximal scheduling algorithm in multi-hop wireless networks, in: Proceedings of the IEEE International Conference on Computer Communications (INFOCOM), Phoenix, AZ, 2008.

- [58] B. Li, A. Eryilmaz, Exploring the throughput boundaries of randomized schedulers in wireless networks, *IEEE/ACM Trans. Netw.* 20 (4) (2012) 1112–1124.
- [59] P. Chaporkar, K. Kar, S. Sarkar, Throughput guarantees through maximal scheduling in wireless networks, in: *Proceedings of the Allerton Conference on Control, Communications and Computing*, 2005.
- [60] P. Gupta, A.L. Stolyar, Optimal throughput allocation in general random-access networks, in: *Proceedings of the 40th Annual Conference on Information Sciences and Systems*, 2006, pp. 1254–1259.
- [61] A. Gupta, X. Lin, R. Srikant, Low complexity distributed scheduling algorithms for wireless networks, *IEEE/ACM Trans. Netw.* 18 (2009) 1846 – 1859.
- [62] X. Lin, S. Rasool, Distributed and provably-efficient algorithms for joint channel-assignment, scheduling and routing in multi-channel ad hoc wireless networks, *IEEE/ACM Trans. Netw.* 17 (6) (2009) 1874–1887.
- [63] L. Tassiulas, Linear complexity algorithms for maximum throughput in radio networks and input queued switches, in: *Proceedings of the IEEE International Conference on Computer Communications (INFOCOM)*, San Francisco, CA, 1998.
- [64] E. Modiano, D. Shah, G. Zussman, Maximizing throughput in wireless networks via gossiping, in: *ACM SIGMETRICS/IFIP Performance*, 2006.
- [65] A. Eryilmaz, A. Ozdaglar, D. Shah, E. Modiano, Distributed cross-layer algorithms for the optimal control of multi-hop wireless networks, *IEEE/ACM Trans. Netw.* 18 (2010) 638–652.
- [66] L. Jiang, J. Walrand, A distributed CSMA algorithm for throughput and utility maximization in wireless networks, *IEEE/ACM Trans. Netw.* 18 (3) (2010).
- [67] J. Liu, Y. Yi, A. Proutiere, M. Chiang, H.V. Poor, Towards utility-optimal random access without message passing, *Wireless Commun. Mobile Comput.* 10 (1) (2010) 115–128.
- [68] L. Jiang, D. Shah, J. Shin, J. Walrand, Distributed random access algorithm: scheduling and congestion control, *IEEE Trans. Inform. Theory* 56 (12) (2010) 6182–6207.
- [69] H. Xiong, R. Li, A. Eryilmaz, E. Ekici, Delay-aware cross-layer design for network utility maximization in multi-hop networks, *IEEE J. Sel. Areas Commun.* 29 (5) (2011) 951–959.
- [70] L. Huang, M.J. Neely, Delay reduction via lagrange multipliers in stochastic network optimization, in: *Proceedings of the Seventh International Conference on Modeling and Optimization in Mobile, Ad Hoc, and Wireless Networks, WiOPT’09*, 2009.
- [71] L. Ying, S. Shakkottai, A. Reddy, On combining shortest-path and back-pressure routing over multihop wireless networks, in: *Proceedings of the IEEE International Conference on Computer Communications (INFOCOM)*, Rio de Janeiro, Brazil, 2009.

# Cognitive radio networks and spectrum sharing

# 13

**E. Hossain\*, K.G. Madushan Thilina\***

*University of Manitoba, Winnipeg, MB, Canada*

## CHAPTER OUTLINE

<b>13.1 Introduction</b>	468
13.1.1 Basics of Cognitive Radio	468
13.1.2 Cognitive Radio Network Architectures	469
13.1.3 Challenges in Cognitive Radio Networks	471
13.1.4 Regulatory Aspects and Standardization	474
<b>13.2 Spectrum Management Framework</b>	475
13.2.1 Spectrum Sensing	476
13.2.2 Spectrum Decision	478
13.2.3 Spectrum Sharing	480
13.2.4 Spectrum Mobility	481
<b>13.3 Spectrum Sensing Techniques</b>	482
13.3.1 Individual Spectrum Sensing-Based Spectrum Opportunity Detection	482
13.3.2 Cooperative Spectrum Sensing (CSS)-Based Spectrum Opportunity Detection	484
13.3.3 Fusion Techniques for CSS	485
13.3.4 Database-Centric Approach for Spectrum Sensing	491
<b>13.4 Resource Allocation in CRNs</b>	492
13.4.1 Elements of Resource Allocation Problems in CRNs	492
13.4.2 Resource Allocation Approaches in CRNs	493
<b>13.5 Medium Access Control for CRNs</b>	503
13.5.1 Cognitive Medium Access Control (C-MAC) Cycle	504
13.5.2 Dynamic Common Control Channel (DCCC)-Based MAC Protocol for Centralized CRNs	507
<b>13.6 In-Band Full-Duplexing-Enabled CRNs</b>	512
<b>13.7 Summary</b>	513
<b>References</b>	514

---

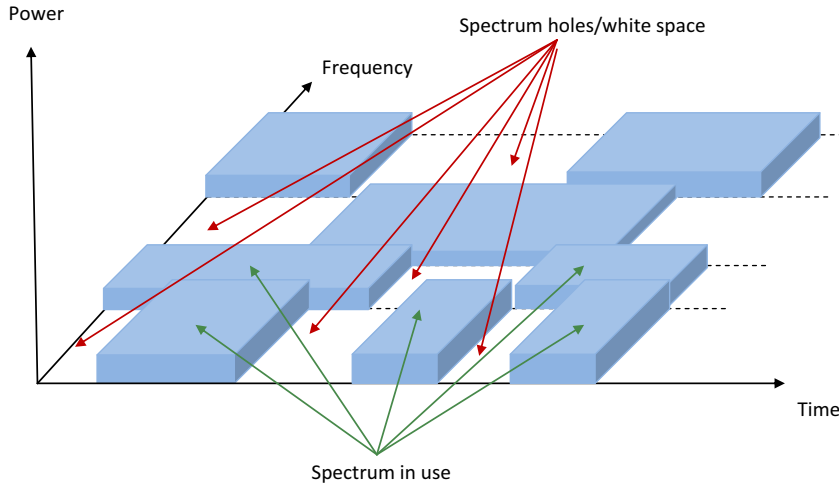
## 13.1 INTRODUCTION

The advancements in information and communication technology have resulted in an explosion in the demand for cellular and data traffic. It is projected that the demand for wireless Internet access through smartphones, tablets, and laptops will continually increase in the foreseeable future. The use of wireless communications applications goes beyond personal communications services; they are used for sensing, monitoring, and control systems (eg, in surveillance systems, embedded health monitoring systems, and traffic controlling systems). However, the proliferation of wireless communications services is somewhat limited by the scarcity of the radio spectrum, which, in most situations, has already been allocated by regulatory agencies for different types of applications and services. In particular, a large chunk of the available spectrum has already been assigned to network operators, thus granting them exclusive right to their usage for a long-term over vast geographical areas [1,2]. This static spectrum allocation to operators is governed by an auction process conducted by the regulatory authorities in a country (eg, Federal Communications Commission (FCC) in the United States). The traditional wireless communications systems have to utilize only their dedicated spectrum bands irrespective of the traffic condition. The long-term assignment of radio spectrum limits the feasibility of short-term licensing of spectrum bands to meet the temporary traffic demand. In addition, an allocated spectrum may not be efficiently utilized in a situation where there is a small number of users, whereas there are other users (eg, from other networks/operators) who are unable to access the spectrum. A study by the Spectrum Task Force (SPTF) of the FCC [2] has shown that a large portion of the licensed spectrum bands are partly or highly unoccupied in a given area at a given time. FCC's reference [3] states that the licensed spectrum utilization over the time and geographical location varies from 15% to 85%. It is worth mentioning that the unlicensed Industrial Scientific and Medical (ISM) bands have become crowded, and therefore also have a limited bandwidth availability for new wireless services.

The scarcity of the radio spectrum and exponential growth in the demand for wireless services have therefore motivated researchers to explore new design paradigms for wireless communications systems to provide ubiquitous, efficient, and seamless connectivity to wireless users.

### 13.1.1 BASICS OF COGNITIVE RADIO

Mitola [4] proposed a novel idea for the opportunistic use of the underutilized portion of the spectrum, while providing a solution to mitigate the spectrum scarcity problem. This proposed spectrum management paradigm creates a landscape for new wireless services using the novel idea of *cognitive radio* (CR). A CR is an intelligent wireless communications device which senses its operational electromagnetic environment and can dynamically and autonomously adjust its radio operating parameters [4–6]. In this context, opportunistic spectrum access (OSA) is a key concept which allows a CR device to opportunistically access the frequency band allocated to a licensed user when the transmission of the licensed user is detected to be inactive. The licensed

**FIG. 13.1**

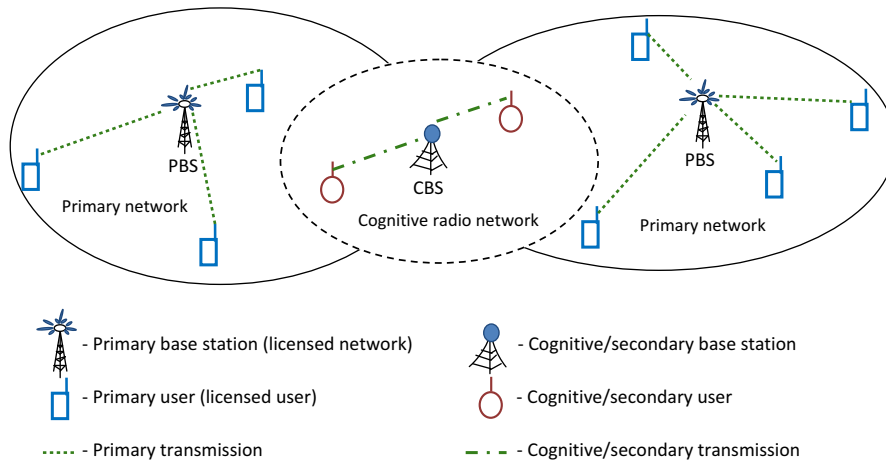
Spectrum holes or white spaces.

users' inactive spectrum bands are referred to as “spectrum holes” or “white spaces” (Fig. 13.1). These spectrum holes or white spaces are formally defined as [7] “a band of frequencies assigned to a primary user (PU) (licensed user), but at a particular time and specific geographic location, the band is not being utilized by that user.”

To achieve OSA by dynamically and autonomously adjusting its operating parameters, CRs should have two main characteristics [8]: cognitive capability and reconfigurability. The cognitive capability of a CR device is defined as the ability to sense the surrounding radio environment, analyze the sensed information, and make the spectrum access decision based on the analyzed information. Reconfigurability is defined as the ability of a CR to change its operating parameters based on the spectrum-analyzed information on-the-fly. Such CRs interconnect with other wireless devices opportunistically by forming cognitive radio networks (CRNs). In a CRN, the available radio spectrum has to be allocated intelligently and efficiently among the CRs using a smart spectrum management system.

### 13.1.2 COGNITIVE RADIO NETWORK ARCHITECTURES

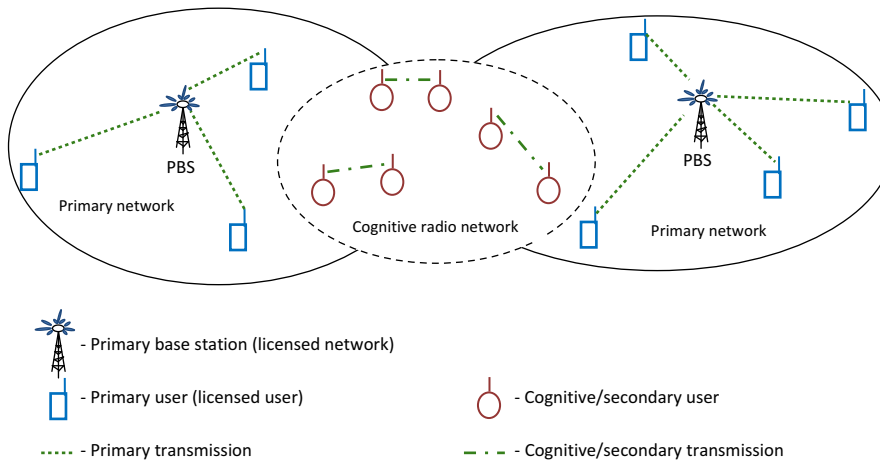
A CNR (referred to as a secondary network, unlicensed network, or dynamic spectrum access (DSA) network) coexists with primary networks (also referred to as licensed networks) within the same geographical area at the same time, and it utilizes the same frequency bands. The CRs (also referred to as secondary users [SUs]) in a CRN are not licensed to operate in the spectrum band. Only the PUs have the right to access the spectrum band. The primary network can be either a centralized (infrastructure-based) or a distributed (ad hoc) network based on the spectrum access model. Similarly, the CNR can be either a centralized (infrastructure) or

**FIG. 13.2**

Centralized/infrastructure-based cognitive radio network architecture.

a distributed (ad hoc) network based on its architecture, as shown in Figs. 13.2 and 13.3, respectively. Generally, the PUs and the primary base stations (PBSs) do not have the cognitive capabilities. It is the responsibility of the CRs (or SUs) to sense the channel before cognitive transmission and vacate immediately after the appearance of PUs. That is, the OSA mechanism implemented in the CRNs should guarantee the performance of primary network.

- **Centralized CNRs:** Centralized CRNs [5,8,9] have a central controller or coordinator (see Fig. 13.2), eg, a cognitive base station (CBS) or a central access point. This central controller can collect spectrum information from SUs over a licensed or unlicensed spectrum band (ie, control channel (CC)), analyze the information, and make the spectrum availability information (eg, information about channels in which PUs are absent) known to SUs via CCs. A cognitive CBS provides resource (eg, channel and power) for SUs. The IEEE 802.22 is the first standard for centralized CRNs [10].
- **Distributed CNRs:** Distributed CRNs [5,8,9] are ad hoc or point-to-point communications systems where SUs communicate over licensed or unlicensed bands opportunistically, as shown in Fig. 13.3. These distributed CRNs do not have a central controller to coordinate OSA, and the spectrum access, decisions are jointly coordinated via a common control channel (CCC) [11]. In distributed CRNs, the spectrum access decisions based on local information (instead of global network information) may not be optimal.
- **Spectrum access models and operating modes of CRs:** The DSA models in CRNs can be typically categorized into three access models [12–14]: spectrum exclusive-use model, spectrum shared-use model, and spectrum common-use

**FIG. 13.3**

Distributed/infrastructureless cognitive radio network architecture.

model. In the spectrum exclusive-use model, when the licensed users do not use the bands, the spectrum licensee grants the spectrum access right to the CRs under some constraints. In such a case the CRN operates in the *overlay* mode [5]. In the spectrum shared-use model, the CRs are allowed to access the spectrum simultaneously with PUs as long as CRs do not create harmful interference at the primary receivers (PRs). In this case, the CRN operates in the *underlay* mode. Such CRNs protect the PUs by enforcing a spectral mask that guarantees that the interference experienced at the PUs is below the acceptable noise floor. In the common-use model, the CRs have the same right to access the spectrum as other users and this spectrum is not licensed to any party (ie, spectrum access in the ISM bands).

### 13.1.3 CHALLENGES IN COGNITIVE RADIO NETWORKS

The CRNs should have additional capabilities compared to legacy wireless networks to access the unlicensed spectrum without causing harmful interference to the PUs. Specially, to accomplish the basic requirements of CRNs, the CRs should be equipped with additional functionalities such as spectrum sensing, learning, spectrum management, and opportunistic spectrum access.

#### 13.1.3.1 Spectrum management in CRNs

Spectrum management challenges for CRNs include those related to spectrum sensing and analysis, spectrum sharing, and spectrum mobility functionalities. The spectrum sensing and analysis method needs to answer questions like: where to

sense, what to sense, how to sense, how long to sense, and what are the allowable interference limits. The spectrum sharing method needs to answer questions such as how to access and how to allocate the PUs' idle channels. The questions related to the spectrum mobility functionality include the following: how to shift the cognitive communication to another channel in case PUs reappear in that channel and how to change configuration parameters for smooth operation. We will discuss these issues in more detail in [Section 13.2](#).

### ***13.1.3.2 Resource allocation in CRNs***

Resource allocation schemes for CRNs should be carefully designed due to the dynamic nature of spectrum access. The resource allocation method is responsible for avoiding harmful interference at the PUs while optimally utilizing the available resources (ie, power and spectrum). Spectrum allocation and interference mitigation in CRNs is challenging due to the imperfect radio environmental information at the CRs, ie, information about the channel gains between cognitive transmitters (cognitive receiver) and PRs (primary transmitter), and PUs' transmit power. Also, the resource allocation schemes need to consider the effect of PU activities in different spectrum bands or channels.

### ***13.1.3.3 Interference characterization and management in CRNs***

There are two types of interference: interference caused at the PRs by cognitive transmission and interference caused at the cognitive receivers by the primary transmission. Due to the lack of information about the current channel state and the modulation of the primary signals, the CRs may not be able to accurately calculate the interference to or from the PRs. Furthermore, the primary network may not provide the primary signal information to the CRs. The CRs may obtain the channel state information (CSI) through the radio environment map (REM) and calculate interference at the PRs based on this information [15,16]. Also, the aggregate interference, caused by the adjacent primary transmitters, can be estimated based on the power spectral density of the PU signals when the waveform of the PU signals is unknown [17].

One strategy that protects the PUs from interference due to cognitive transmissions is interference management. Interference management handles the trade-offs between spectral efficiency and interference mitigation. Certainly, the interference at the PUs can be eliminated by allowing cognitive transmissions only into the PUs' idle channels. However, this is not the most efficient way to optimize spectrum utilization in CRNs. Allocating transmit power to CRs to access the PU-occupied spectrum bands in the presence of imperfect CSI in order to maximize cognitive capacity, while minimizing interference at PUs, is a challenging task [18–20].

### ***13.1.3.4 Cross-layer design of communication methods in CRNs***

Conventional wireless devices often use a layered architecture and interaction between the layers is limited. This may not be flexible enough for OSA nor an optimal use of available resources. CRs may need to operate with sufficient flexibility

to directly access the information in different layers and need to adapt the control parameters in different layers [21–25]. However, developing a protocol stack which allows accessing information at the different layers through well-defined interfaces could be very challenging.

#### 13.1.3.5 Security threats in CRNs

CRNs are susceptible to traditional wireless network-specific attacks [26,27] such as radio frequency (RF) jamming (data and CC) [28,29], medium access control (MAC) address snooping [29], spurious MAC (eg, RTS, CTS, ACK) frame transmission [29], eavesdropping [30], and cheating on contention (violating back-off rules) [31]. In addition to these traditional attacks, due to the nature of spectrum access by the CRs, CRNs are also vulnerable to unique security attacks. The main CRN-specific attacks are listed as follows:

- Primary user emulation attacks (PUEA) [32–34]: At the appearance of PUs, the CRs vacate the spectrum bands they are occupying. Malicious users can mimic/imitate primary transmissions by forcing the CRs to vacate particular spectrum bands. This malicious behavior is known as PUEA.
- Spectrum sensing data falsification (SSDF) [35–37]: Unlike CRNs which rely on precomputed data, sensing-based CRNs continually update their information. These sensing-based networks are vulnerable to false information sent by malicious CRs. This type of attack is known as a SSDF.
- Beacon falsification (BF) [38,39]: In a centralized/infrastructure-based CRN, a central controller transmits beaconing signals for data integrity, synchronization, and authentication. A malicious user can transmit false or similar beaconing signals to interrupt the operation of the CRN.
- Cross-layer attacks [40–42]: When there is a cross-layer optimized communication protocol stack in a CRN, the network is more vulnerable to cross-layer attacks. An example of a cross-layer attack is the lion attack [42].

Different types of security threats that can make the CRNs vulnerable are shown in Fig. 13.4.

#### 13.1.3.6 Routing in multihop CRNs

The routing protocols used in traditional multihop wireless communications systems cannot be utilized in multihop CRNs due to the volatility and heterogeneity of the available spectrum for CRs. The spectrum bands that can be utilized for cognitive communication may vary from CR to CR. Finding a common channel in multihop CRNs therefore could be very challenging. Developing new routing protocols for multihop CRNs, which achieve high network throughput, low latency, and low packet loss, is a significant research problem. Packet routing depends on spectrum allocation in CRNs. Therefore, an efficient routing algorithm should adopt a spectrum-aware on-demand routing approach [9,43].

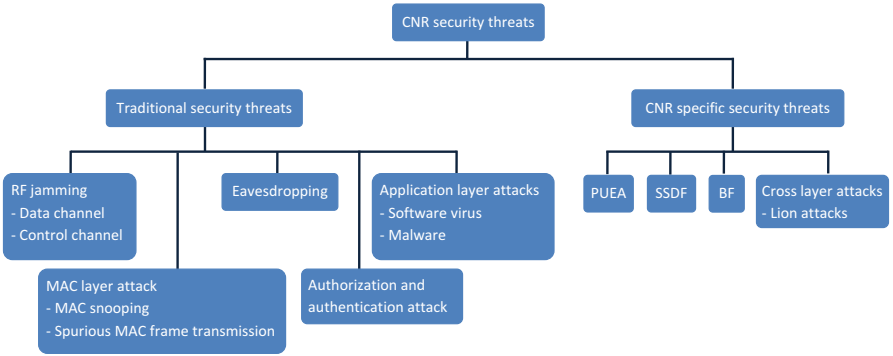


**FIG. 13.4**  
Different types of security threats in CRNs.

**13.1.4 REGULATORY ASPECTS AND STANDARDIZATION**

Significant efforts have been made toward the standardization of CNRs for different applications and regulation of CR-specific activities. IEEE 802.18 is a standards body which is responsible for monitoring standardization activities in different projects such as IEEE 802.11, IEEE 802.15, and IEEE 802.16. Other technical groups within the IEEE 802 Standards Committee working on CR include 802.19 and 802.22. Some of the application specific standards are listed in [Table 13.1](#) [44].

**Table 13.1** Application-Specific Standards

Application Scenario	Standards	Use Case
Wireless regional area networks (WRANs) using TV white space	IEEE 802.22	The fallow TV spectrum is used by centralized CRNs [38,39,45], eg, WRANs
Local area applications within buildings	European Computer Manufacture Association (ECMA)-392	Personal and portable devices exploiting TV white space [46]
Wi-Fi using spectrum holes in TV bands	IEEE 802.11af	IEEE 802.11 protocol stack is modified (ie, PHY and MAC layers) to meet the channel access and coexistence with other CRNs using the spectrum holes in TV bands [47]
Medical body area networks (MBANs)	IEEE 802.15.4j	Access 2.36–2.4 GHz band opportunistically for MBANs [48,49]
Public safety (FirstNet)	3GPP (LTE)	Provide spectrum with priority to public safety network in addition to the licensed bands [50,51]
Smart grid	Weightless	Automatic metering in TV white space [52]

- IEEE 802.22 WRANs: The IEEE 802.22 [45] is the first world-wide effort to define a standard air interface for centralized/infrastructure-based CRNs. It incorporates advanced CR capabilities including spectrum sensing, DSA, accurate geolocation techniques through GPS, incumbent database access, regulatory policies, and spectrum etiquette to utilize the fallow TV bands. The IEEE 802.22 standard specifies a silent period in which all the SUs in the network perform spectrum sensing and send the sensed information to the CBS. Then, the CBS fuses the sensed data with the occupancy data retrieved from the database to make a final decision about the channel availability for the CRs. Due to its simplicity and low computational overhead, IEEE 802.22 uses “energy detection” for spectrum sensing. The main objective of this standard is to support provisioning of broadband services to hard-to-reach and low-populated areas such as rural areas.
- IEEE 802.11af Wi-Fi: The IEEE 802.11af is a technical standard which was approved in February 2014 [53] and is currently being developed with the goal of providing high speed Wi-Fi connectivity in the fallow TV bands between 54 and 790 MHz. This standard is also referred to as “White-Fi” and “Super Wi-Fi.” The IEEE 802.11af standard will incorporate cognitive capabilities with legal requirements in spectrum management, PHY and MAC layer modifications, regulatory policies, and etiquette, which need to be considered when coexisting with the incumbent users. The 802.11af-based Wi-Fi potentially has higher coverage compared to all other 802.11 versions. The 802.11af standard may include the carrier aggregation techniques to improve system throughput [44].
- IEEE 802.15.4j MBANs: MBANs are mostly deployed in the ISM bands which are more likely to be busy when the network becomes crowded. This may lead to significant problems in deploying large-scale MBANs. Therefore, the FCC in the United States has allocated aeronautical mobile telemetry bands (2360–2400 MHz) for a cognitive-based MBANs. The IEEE 802.15 Task Group 4j is developing standards for 802.15.4j by modifying the IEEE 802.15.4 standard PHY and MAC layer requirements to support these cognitive MBANs [49].

---

## 13.2 SPECTRUM MANAGEMENT FRAMEWORK

The number of accessible channels available in traditional wireless networks is fixed whereas the number of channels available for cognitive transmission varies with time and space. The number of channels available for cognitive transmission changes with the appearance of a PU. This volatility of available spectrum imposes unique challenges for CR spectrum management system. These challenges include interference avoidance to PUs, quality-of-service (QoS) awareness, and seamless cognitive communication for CRs regardless of the primary appearance. In order to address these challenges, the CRNs should determine which portions of the spectrum bands are available for cognitive transmission, select the best channel to achieve the

required QoS, coordinate access to mitigate interference and collision, and vacate the channel at the reappearance of PUs. These capabilities are achieved by CRNs through four different spectrum management functionalities: spectrum sensing, spectrum decision, spectrum sharing, and spectrum mobility [8]. The relationships among the spectrum management functionalities are illustrated in Fig. 13.6. The spectrum-management functionalities involve all the layers in the protocol stack as illustrated in Fig. 13.5.

### 13.2.1 SPECTRUM SENSING

Spectrum sensing is a process (which is implemented in CRs) to obtain radio or spectrum information at a given time and a given location. The radio information obtained through spectrum sensing focuses on the following: obtaining PUs' idle channels, calculating interference experienced by PUs, learning the PU traffic condition to enhance CRN operation, and estimating channel gains between CRs. The CRN makes spectrum access and sharing decisions based on the sensed information. The spectrum sensing mechanism should provide answers to the following questions [8,44,54]:

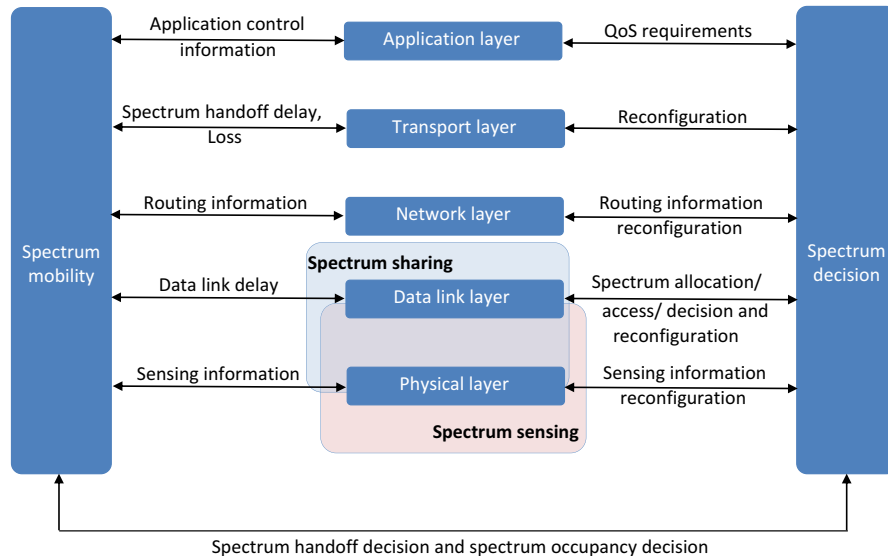


**FIG. 13.5**

The protocol stack and the spectrum management framework in CRNs.

*Courtesy: I.F. Akyildiz, W.-Y. Lee, M.C. Vuran, S. Mohanty, A survey on spectrum management in cognitive radio networks, IEEE Commun. Mag. 46 (4) (2008) 40–48.*

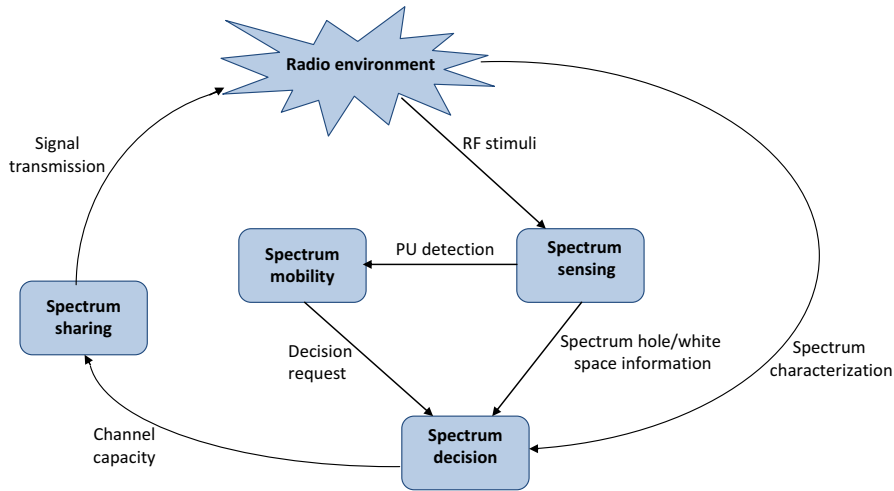


FIG. 13.6

Spectrum management framework in CRNs.

Courtesy: I.F. Akyildiz, W.-Y. Lee, M.C. Vuran, S. Mohanty, A survey on spectrum management in cognitive radio networks, *IEEE Commun. Mag.* 46 (4) (2008) 40–48.

- **When to sense:** To discover and keep track of the available spectrum opportunities, the CRs should execute spectrum sensing within the allocated sensing time. Based on the spectrum sensing time in the cognitive transmission frame, spectrum sensing can be either proactive or reactive [55]. Proactive sensing is performed periodically while reactive sensing is performed on demand. CRNs can implement both proactive and reactive spectrum sensing to improve the reliability of spectrum sensing. For example, the CRN can use proactive sensing to identify spectrum opportunities, and reactive spectrum sensing to improve the reliability of its sensing. With the intention of improving sensing reliability, the IEEE 802.22 standard has defined two types of spectrum sensing periods in the IEEE 802.22 frame as fast and fine sensing periods.
- **What and how to detect:** CRNs should decide what will be sensed by CRs for exploring and exploiting the PUs' idle channels. CRs are equipped with two types of detection techniques: blind detection and feature detection. In blind detection, the CRs blindly detect PU idle channel using energy detection or autocorrelation detection without any prior knowledge of the PUs signal [56]. On the other hand, the feature detection technique utilizes a priori knowledge of primary waveforms for PU idle channel detection [56,57]. To improve detection probabilities, CRNs utilize cooperative spectrum sensing techniques [58–61]. These detection techniques will be discussed in more detail in Section 13.3.
- **Where to sense:** The answer to this question depends on the capabilities of CR hardware and their operational mode. The number of spectrum bands which can

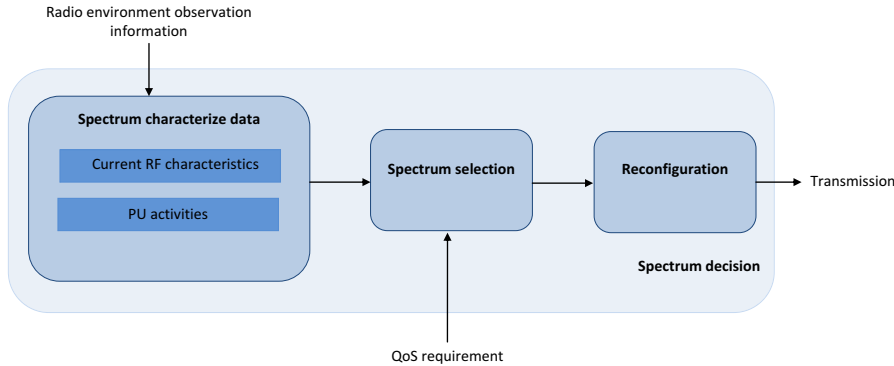
be sensed simultaneously within a single sensing period varies based on the operational mode. The CRs that operate in the wideband mode can perform simultaneous spectrum sensing in different bands at the expense of increased hardware cost whereas those which operate in the narrowband mode perform sequential sensing at a significantly low cost compared to wideband CRs [62].

- **How to sense:** This depends on spectrum sensing policies such as the number of spectrum bands sensed at a given time, the spectrum band sensing order, or whether CRs adopt learning-based or nonlearning-based spectrum sensing techniques. In narrow band multichannel CRNs, CRs have to decide the order and set of channels sensed in a given time slot. To improve the quality of the set of channel and sensing order selection, CRs can utilize learning techniques based on passed sensing information [63–65].
- **How long to sense:** The overall duration of spectrum sensing depends on the spectrum sensing technique used. Blind detection techniques such as energy detection require a shorter sensing period whereas a longer sensing duration is generally required for feature detection [56,57]. Feature detection-based spectrum sensing is particularly suitable for extremely low SNR environments, and it can be used when some information about the transmitted signals is known a priori. One example is cyclostationary detection, which exploits the periodicity in the modulated signals.

If CRNs use cooperative spectrum sensing, the sensing duration does not need to be as long as individual sensing. In narrowband sequential spectrum sensing, a CR can stop sensing as soon as it finds a PU idle channel [66] or it has sensed a predefined number of idle channels within a predefined duration [67]. Another approach is to stop sensing as soon as the sensing level exceeds the threshold before a given time [68]. The time expended for sensing directly affects the CRN performance as it constitutes part of the time that would otherwise have been used for data transmission.

### 13.2.2 SPECTRUM DECISION

The spectrum decision is required to select the best PU idle channel(s) to satisfy the QoS requirements of CRs without causing harmful interference to PUs. For this, the decision process first characterizes each PU idle spectrum band based on the spectrum sensing information and statistical information of PU activity [69]. Then, the most suitable bands are selected based on spectrum characterization. Once the most appropriate bands for cognitive transmission are identified, the transceiver parameters at the CR are configured to support cognitive transmission on the selected bands. The spectrum decision flow is illustrated in Fig. 13.7 and the main questions to be answered in performing these functionalities are as follows [70]: How are available spectrum bands characterized? How are the best PU idle bands selected to satisfy CRs' QoS? What is the best technique to configure cognitive transceivers for the bands selected?

**FIG. 13.7**

Spectrum decision flow.

- How to characterize the available spectrum bands: RF characterization of spectrum bands is achieved by estimating the following key elements:
  - Channel identification: Channel identification identifies traffic pattern (ie, deterministic or stochastic traffic) in the primary networks. The deterministic traffic exhibits a fixed or periodic ON and OFF period whereas the stochastic traffic exhibits a large variation in time and spectrum, which is modeled by applying probabilistic approaches [71].
  - Channel switching delay: CRs have to switch their operating spectrum bands once PUs become active in those bands or when there is a performance degradation in the presence of interference. At this point, all the switching CRs suspend their transmissions temporarily until a new spectrum opportunity is found. The delay due to this temporary suspension and transceiver reconfiguration is known as a channel switching delay [45,72,73].
  - Interference estimation: If not controlled properly, the coexistence of CRs with primary networks may create harmful interference to the PUs. Therefore, accurate interference estimation, analysis, and modeling is very important [74–76].
  - Channel capacity: Channel capacity is important in the RF characterization process because it helps to make spectrum decisions based on the CR's QoS requirement.
  - Channel holding time: This is the expected time duration that a particular CR can function until a PU interrupts its transmission. This is a regulatory aspect and can vary depending on the cognitive application [77,78].
  - Channel error rate: The bit-error rate can be estimated during RF characterization. Based on this, the frequency band and modulation scheme for cognitive transmission can be adapted [79,80].
  - User locations: User location information can be used to predict RF environment and spectrum holes. This information can be obtained by using in-built GPS systems or REMs.

Even though the PUs' idle channels are identified for transmissions by CRs, there is no guarantee that these channels will be available for the entire period of cognitive transmission. Therefore, it is important to predict the PU activities on the considered channels. The PU activities on different bands can be predicted by analyzing the historical spectrum usage data. PU activities can be modeled based on Poisson process models [69,81], spectrum availability statistics [71], and spectrum measured data [82]. In the Poisson process model, the PU traffic is modeled as a two state-date birth-death process assuming that traffic arrivals at the PUs follow independent Poisson processes. However, the Poisson process-based PU activity approximation techniques fail to capture the effect of bursty traffic, correlation within data, and short-term temporal fluctuation in data. The statistical PU activity modeling approach stores the spectrum band occupancy states in a binary database (ie, if a channel is free, then the state is set to 0, otherwise it is set to 1). Once the spectrum states are stored in the binary database, a classification algorithm runs for identifying PU activity for the given time.

Based on the PU activity information, not only can the CRs decide which spectrum bands are most suitable for their data transmissions, they can also give high priority to the bands, which have less PU activity, for spectrum sensing [70].

- How to select best PU idle band to satisfy the QoS of CRs: With the characterization of spectrum bands, the CRs know the list of available spectrum holes or the PUs' idle channels. The major task is to select the best PU idle channels in such a way that satisfies the CRs' QoS requirements while mitigating harmful interference at the PUs. This spectrum band selection approach mainly depends on the CRN architecture. Centralized CRNs use policy-based [83] and noncooperative game-based [84] approaches for spectrum selection. In distributed and multihop CRNs, spectrum selection is largely affected by the heterogeneity in spectrum availability in different hops [85].
- What is the best technique to configure cognitive transceivers for the selected bands: A CR should have high flexibility in configuring its transceiver parameters such as bandwidth, carrier frequency, modulation and coding scheme, and transmit power by considering its utility function and QoS constraints [86,87]. A CR may also change its radio access technology in order to improve its QoS performance [83].

### 13.2.3 SPECTRUM SHARING

The spectrum sharing functionality in CRNs is implemented in cognitive MAC protocols. In the context of spectrum sharing, the following aspects are important: CRNs architecture, spectrum allocation, and the spectrum access mechanism.

- Centralized and distributed spectrum sharing: In centralized spectrum sharing, spectrum allocation and access are controlled by a central controller [87–89], whereas in distributed CNRs the spectrum allocation and spectrum access are performed by each CR [88,90]. In the former case, the control information is

exchanged with the help of a dedicated CCC or a dynamic common control channel (DCCC) [91]. The centralized spectrum sharing generally provides a higher performance over distributed sharing; however, it is at the cost of a higher information exchange and complexity.

- How to allocate the spectrum: Spectrum allocation in CRNs can be classified into two categories: cooperative [92] and noncooperative [93] spectrum allocation. Cooperative spectrum sharing can achieve a higher performance compared to noncooperation spectrum sharing by exploiting cooperation among all the active CRs and/or cooperating with primary networks. Game theory-based approaches such as bargaining [94] and coalitional games [95] have been used for allocating the spectrum among CRs. In noncooperative spectrum sharing, CRs do not collaborate with each other and try to maximize their performances as much as possible in a selfish manner. Cooperative spectrum sharing can offer a higher spectral efficiency, certain level of fairness, and improved throughput compared to noncooperative spectrum sharing. Cooperative sharing achieves these gains at the cost of higher information exchange and complexity. On the contrary, with noncooperative spectrum sharing, CRs consume a relatively lower amount of energy compared to cooperative spectrum sharing due to lower signaling overhead and complexity.
- How to perform multiple access: In the case of centralized spectrum sharing, once the frequency bands (channels) are allocated to CRs, they should be informed of the allocation. Then spectrum access can be performed using technologies such as code-division multiple access (CDMA), orthogonal frequency division multiple access (OFDMA), time-division multiple access (TDMA), frequency-division multiple access (FDMA), or space-division multiple access (SDMA). The OFDMA access technology is particularly attractive for CRNs due to the capability of altering waveform and channel bandwidth. SDMA is a promising access technology for network MIMO-enabled CRs since the same frequency band can be utilized for multiple users simultaneously [96].

#### 13.2.4 SPECTRUM MOBILITY

The objective of spectrum mobility functionality in a CRN is to maintain an ongoing cognitive transmission by seamlessly switching between PUs' idle channels at the appearance of PUs or low channel quality [97]. For spectrum mobility, the following two processes need to be performed (Fig. 13.8): spectrum handoff and connection management. The spectrum handoff process is responsible for switching an ongoing transmission from one channel to another PU idle channel whereas the connection management process is responsible for adapting or reconfiguring the connection parameters. To reduce the latency in spectrum mobility, the CR protocol stack should provide flexible access to different layers. With regard to spectrum handoff due to channel quality degradation, CRs can adopt standard approaches in traditional wireless networks.

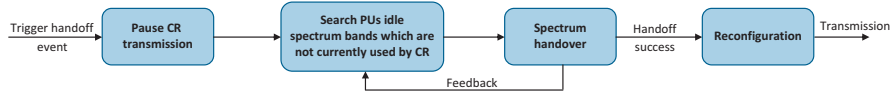


FIG. 13.8

Spectrum mobility in CRNs.

### 13.3 SPECTRUM SENSING TECHNIQUES

There are two basic approaches for identifying spectrum opportunities in licensed bands: database-centric approach and spectrum sensing approach. In the former approach, information about spectrum opportunities are exchanged through a central database. On the other hand, the spectrum-sensing based approach requires the CRs to explore the spectrum holes (ie, PUs' idle channels) so that they are able to exploit those spectrum opportunities. Spectrum sensing-based CRNs are more compatible and can coexist with the legacy wireless communications systems. In this type of CRN, either an individual or cooperative spectrum sensing-based scheme can be used.

#### 13.3.1 INDIVIDUAL SPECTRUM SENSING-BASED SPECTRUM OPPORTUNITY DETECTION

Either the blind detection [98] or feature detection [98,99] technique can be used for spectrum hole detection. Blind detection techniques characterize the available spectrum holes without having any prior knowledge of primary transmission. They are unable to differentiate a PU-transmitted signal from the coexisting CR-transmitted signal. Energy detection, autocorrelation detection, and higher-order-static detection are some of the well-known blind detection techniques studied for CRNs. Feature detection techniques utilize a priori knowledge of the primary transmission to detect spectrum holes and are able to differentiate PU signals from CR signals. Matched filter and cyclostationary detection are examples of feature detection techniques.

##### 13.3.1.1 Energy detection

The energy detection technique does not require any a priori knowledge about the primary transmission and it detects spectrum holes based on the sensed energy at the receiver [61,100]. To perform energy detection, a CR needs to estimate the energy level in a spectrum band (or channel) for a certain time duration  $\tau_s$ . If we denote the bandwidth by  $w$ , the energy detector takes  $w\tau_s$  baseband complex signal samples during  $\tau_s$ . Let  $Z_n(i)$  denote the  $i$ th signal sample taken by SU  $n$ ,  $1 \leq n \leq N$ , where  $N$  is the number of CRs in the CRN. The signal samples consist of the summation of the signals from all PUs in the active state and the thermal noise, that is,

$$Z_n(i) = \sum_{m=1}^M h_{m,n} X_m(i) + N_n(i), \quad (13.1)$$

where  $h_{m,n}$  denotes the channel gain from  $m$ th PU to  $n$ th CR,  $X_m(i)$  is the signal transmitted by  $m$ th PU,  $N_n(i)$  is the thermal noise at  $n$ th CR, and  $M$  is the number of PUs in the network. The energy detector of CR  $n$  estimates the energy level normalized by the noise spectral density, which is denoted by  $Y_n$ , from the signal samples as

$$Y_n = \frac{2}{\eta} \sum_{i=1}^{w\tau_s} |Z_n(i)|^2, \quad (13.2)$$

where  $\eta = E[|N_n(i)|^2]$  is the noise spectral density. The output of the  $n$ th CR's energy detector,  $Y_n$ , is compared with the energy threshold  $\Gamma_{th}$  and the spectrum availability decision is made as follows:

$$A_n = \begin{cases} 1, & \text{if } Y_n \geq \Gamma_{th} \\ -1, & \text{otherwise.} \end{cases} \quad (13.3)$$

If  $A_n = 1$  (ie, at least one PU is active), the channel is considered unavailable for the CR network to access. The channel is available only when there is no PU in the active state (ie,  $A_n = -1$ ).

### 13.3.1.2 Cyclostationary feature detector

A cyclostationary feature detector exploits the inherent periodicity of a PU's modulated signals for detecting spectrum holes. Specifically, a process is said to be wide-sense stationary if its mean and autocorrelation function are time-independent and it becomes cyclic stationary if it shows wide-sense stationary behavior periodically. This is the feature that a cyclostationary feature detector exploits in the process of PU idle channel detection. The periodicity property of a PU's modulated signal and the wide-sense stationary property of uncorrelated noise makes it possible for the decoder to easily differentiate noise from the PU's signal. Therefore, the detector calculates the cyclic spectral density or cyclic periodogram of a received signal as follows [99]:

$$S(f, \alpha) = \sum_{\tau=-\infty}^{\infty} R_Z^\alpha(\tau) e^{-j2\pi f\tau}, \quad (13.4)$$

where  $\alpha$  is the cyclic frequency or frequency separation and  $R_Z^\alpha(\tau)$  is the cyclic autocorrelation function of the received signal. The  $R_Z^\alpha(\tau)$  can be expressed as

$$R_Z^\alpha(\tau) = E[Z(t + \tau)Z^*(t - \tau)e^{j2\pi f\tau}]. \quad (13.5)$$

The cyclic spectral density function of the received signal given (13.4) yields peaks when the cyclic frequency is equal to the fundamental frequency when PUs transmit on that channel. Hence, the PUs availability (ie, CRs cannot transmit) on a given channel can be detected by identifying peaks at fundamental frequency.

### 13.3.2 COOPERATIVE SPECTRUM SENSING (CSS)-BASED SPECTRUM OPPORTUNITY DETECTION

The individual or noncooperative spectrum sensing-based detection is highly vulnerable to uncertainties, fading, shadowing, and the hidden terminal problem. It is possible for CRs to cooperate in order to achieve a higher sensing reliability than an individual CR does by yielding a better solution to the hidden PU problem that arises because of shadowing and multipath fading [98]. The hidden PU problem in CRNs due to shadowing is illustrated in Fig. 13.9. Based on the behavior of cooperation, the cooperative spectrum sensing (CSS) scheme is classified as centralized and distributed CSS. Irrespective of cooperation behavior, the CSS techniques show better PUs/spectrum hole detection accuracy by exploiting the diversity gain provided by different CRs. However, the benefits obtained by CSS appear at the cost of increasing signaling/traffic overhead, increased complexity, and increased power consumption due to heavy communication [100]. The required information in CSS is exchanged through the CCC which lies either in a licensed band or unlicensed band such as the ISM bands. The level of signaling/traffic overhead in CCC varies based on the type of the information exchange, eg, some CSS algorithms require a one-bit decision from cooperating CRs whereas other CSS algorithms require multiple bits of sensing information from the cooperating CRs. On the other hand, inappropriate clustering of CRs for cooperation may not give the expected performance gain in CSS. For example, the sensing information obtained from the CRs deployed in a small area may be highly correlated since the CRs may be located within the same shadowing and primary transmission area.

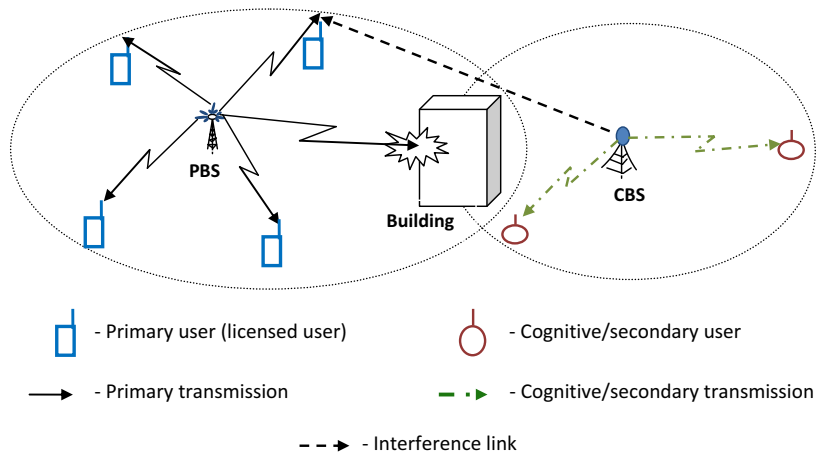


FIG. 13.9

Hidden PU problem due to shadowing.

In centralized CSS, the cooperating CRs sense the target unlicensed spectrum bands and report the sensed information (ie, sensed raw data or individual decision about their own detection) to the central data fusion center. The data fusion center fuses the received spectrum sensing results and estimates the status (ie, idle or active) of PU-available and idle spectrum bands. In distributed CSS, the CRs exchange their sensing information among each other through CCC and makes its own sensing decision by fusing the received sensing information.

### 13.3.3 FUSION TECHNIQUES FOR CSS

The commonly used fusion techniques for CSS can be classified as hard fusion, soft fusion, softened fusion, and learning-based fusion techniques. In the case of hard fusion, the CRs report only one-bit information to the fusion center, which indicate whether the sensed spectrum band is idle or not. The AND-rule, the OR-rule, the  $M$ -out-of- $N$  rule, and linear quadratic combining rules are commonly used for hard fusion-based cooperative spectrum sensing [101,102]. In the soft fusion algorithms, the exact sensing results are reported to the fusion center which then combines the individual sensing results using equal gain combining or maximal ratio combining technique that yields the PU detection decision [103,104]. In learning-based fusion, the fusion center adopts machine learning techniques for fusing the sensing information. Generally, the learning-based fusion outperforms the aforementioned fusion techniques due to its higher predictive power and adaptability to the environmental changes on-the-fly [60,105].

Learning-based CSS can be classified into two categories: supervised and unsupervised learning. Some of the learning-based fusion techniques used in literature are  $K$ -nearest neighbor (KNN) and support vector machine (SVM) fusion whereas  $K$ -means clustering and Gaussian mixture model (GMM) are examples of unsupervised learning-based fusion. In learning-based fusion, prior to the online PU idle channel detection, the classifier has to go through a training phase where it learns from the CSS-based training results. For the supervised learning techniques, the training results should be fed to the classifier with its label (ie,  $a^{(l)} = 1$ , if  $l$ th training sample for the PU active case, otherwise  $a^{(l)} = -1$ ), whereas unsupervised learning does not need labels for its training samples. The main advantages of learning-based fusion over the traditional soft, hard, and softened fusion are as follows:

1. Learning-based fusion techniques implicitly learn the radio environmental parameters (eg, PU and CR network topology and channel gain) in an online fashion. Therefore, learning-based techniques are more adaptive to environmental changes than the traditional fusing techniques.
2. Learning techniques can obtain more optimized decision regions for spectrum sensing decision and thus offer better detection performance. The scatter plots of energy vectors in Fig. 13.10 [60] show that learning techniques-based fusion can obtain the decision boundaries even when the transmit powers of primary transmitters are low.

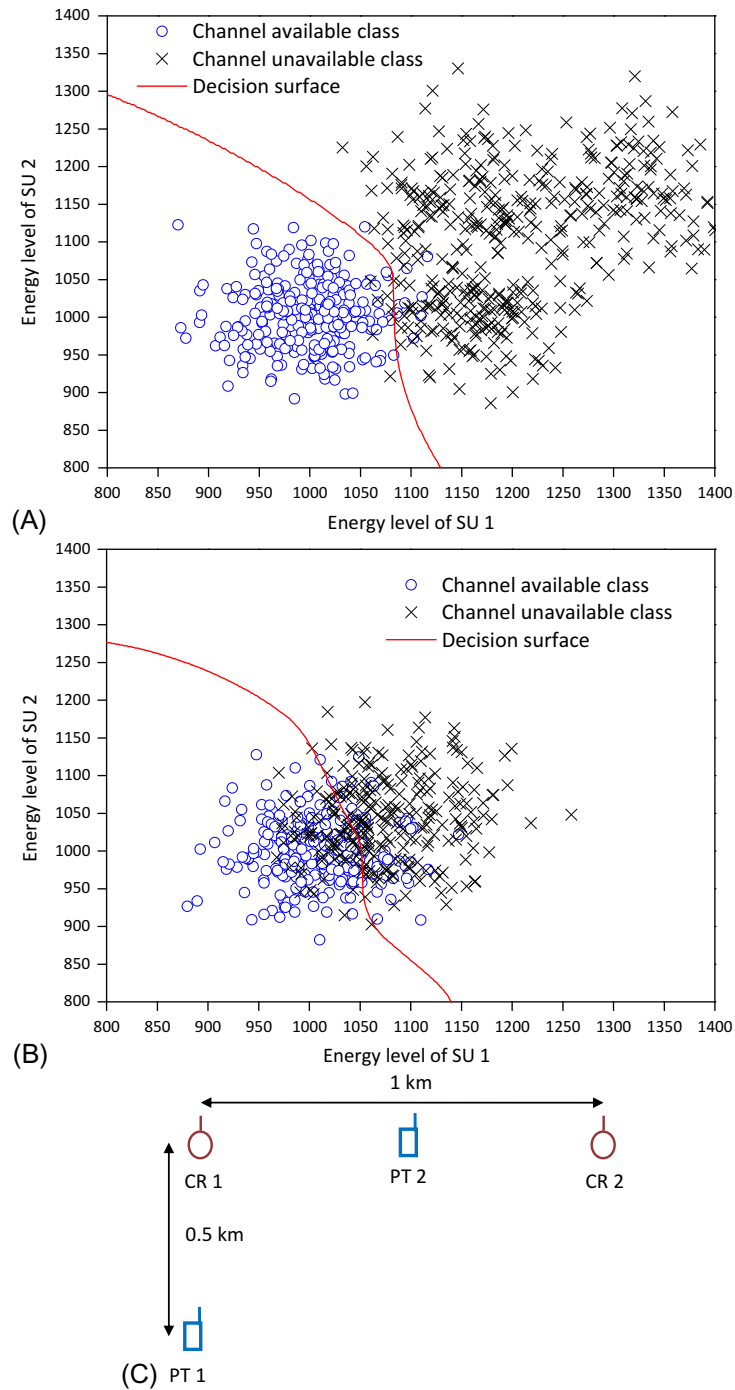


**FIG. 13.10**

Example scatter plots of energy vectors for the network scenario in (C) [60]. The decision surfaces in (A) and (B) are plotted using GMM-based fusion technique. (A) Scatter plot of energy vectors for network scenario in (C) when the transmit power of each primary transmitter is 200 mW. (B) Scatter plot of energy vectors for network scenario in (C) when the transmit power of each primary transmitter is 80 mW. (C) Simulation set up.

### 13.3.3.1 K-means clustering for CSS

*K*-means clustering is an unsupervised learning technique which is used in CSS-based CRNs for fusion of sensing data. The cooperating CRs report normalized received energy level, which is given by Eq. (13.2), to the fusion center. In the case of *K*-means clustering, only the training energy vectors (ie,  $\bar{\mathbf{y}} = \{\mathbf{y}^{(1)}, \dots, \mathbf{y}^{(L)}\}$ ) are fed into the classifier for training, where  $L$  is the number of training samples used for training and the dimensionality of a given sample is  $N$ . The dimensionality of a training sample becomes  $N$  since one training sample is a collection of  $N$  number of cooperating CRs sensing reports [60].

The unsupervised *K*-means clustering algorithm partitions a set of the training energy vectors (ie,  $\bar{\mathbf{y}} = \{\mathbf{y}^{(1)}, \dots, \mathbf{y}^{(L)}\}$ ) into  $K$  disjoint clusters. Let  $\mathcal{C}_k$  denote the set of the training energy vectors that belong to cluster  $k$  and  $\alpha_k$  is the centroid of the cluster  $k$ . Compared to the ordinary *K*-means clustering algorithm, the centroid of cluster 1 is fixed to the mean of  $\mathbf{Y}$ ,  $\mathbf{Y} = (Y_1, \dots, Y_N)^T$ , conditioned on  $\mathbf{S} = \mathbf{0}$ ,<sup>1</sup> that is,  $\alpha_1 = \mu_{\mathbf{Y}|\mathbf{S}=\mathbf{0}}$ , where  $\mu_{\mathbf{Y}}$  denotes the mean of  $\mathbf{Y}$ . Among all the clusters, only one cluster corresponding to the case that no PU is in the active state (ie,  $\mathbf{S} = \mathbf{0}$  for the zero vector  $\mathbf{0}$ ) can be mapped to the channel-available class for CRs, while all the other clusters are mapped to the channel-unavailable class for CRs. Hence, the cluster corresponding to the case that  $\mathbf{S} = \mathbf{0}$  is denoted as cluster 1. The CR network is aware of the parameters for the multivariate Gaussian distribution if and only if  $\mathbf{S} = \mathbf{0}$ . Therefore, cluster 1 can easily be identified by the mean vector  $\mu_{\mathbf{Y}|\mathbf{S}=\mathbf{0}}$  and the covariance matrix  $\Sigma_{\mathbf{Y}|\mathbf{S}=\mathbf{0}}$  while the other clusters should be blindly identified by unsupervised learning. For all other clusters, the centroid is defined as the mean of all training energy vectors in  $\mathcal{C}_k$  and can be calculated as follows:

$$\alpha_k = |\mathcal{C}_k|^{-1} \sum_{\mathbf{y}^{(l)} \in \mathcal{C}_k} \mathbf{y}^{(l)}, \quad \forall k = 2, \dots, K, \quad (13.6)$$

where  $|\mathcal{X}|$  denotes the number of elements in the set  $\mathcal{X}$ . The *K*-means clustering algorithm aims to find out  $K$  clusters,  $\mathcal{C}_1, \dots, \mathcal{C}_K$ , which minimize the within-cluster sum of squares as follows:

$$\operatorname{argmin}_{\mathcal{C}_1, \dots, \mathcal{C}_K} \sum_{k=1}^K \sum_{\mathbf{y}^{(l)} \in \mathcal{C}_k} \|\mathbf{y}^{(l)} - \alpha_k\|^2. \quad (13.7)$$

In *K*-means classification, the process of calculating cluster centroids is known as *K*-means classifier training and the cluster centroids for training samples are calculated by using Eq. (13.6).

<sup>1</sup>Let  $S_m$  denote the state of PU  $m$ . Then,  $S_m = 1$  if PU  $m$  is in the active state (ie, PU  $m$  transmits a signal); and  $S_m = 0$  otherwise. Let  $\mathbf{S} = (S_1, \dots, S_M)^T$  be the vector of the states of all PUs, where the superscript  $T$  denotes the transpose operation.

After the training is over, the classifier receives the test energy vector  $\mathbf{y}^*$  for classification. The classifier determines if the test energy vector belongs to cluster 1 or the other classes, based on the distance from the test energy vector to the centroids. The classifier classifies  $\mathbf{y}^*$  as the channel-unavailable class (ie,  $\hat{a} = -1$ ) if the following condition is met [60]:

$$\frac{\|\mathbf{y}^* - \boldsymbol{\alpha}_1^*\|}{\min_{k=1,\dots,K} \|\mathbf{y}^* - \boldsymbol{\alpha}_k^*\|} \geq \beta. \quad (13.8)$$

Otherwise,  $\mathbf{y}^*$  is classified as the channel-available class (ie,  $\hat{a} = 1$ ). The parameter  $\beta$  is the threshold to control the tradeoff between the misdetection and the false alarm probabilities. If  $\beta$  becomes high,  $\mathbf{y}^*$  is more likely to be classified as the channel-available class, which in turn increases the misdetection probability while decreasing the false alarm probability.

### 13.3.3.2 Support vector machine for CSS

The SVM-based CSS is a supervised learning technique which is used in CRNs to classify PUs' idle spectrum bands from PUs' active spectrum bands. The main difference between supervised learning and unsupervised learning is that each training energy vector  $\mathbf{y}^{(l)}$  is labeled with the corresponding PU's spectrum availability  $a^{(l)}$ . Therefore, to implement SVM-based CSS, the primary network should occasionally inform the PUs' active and idle spectrum bands to the CRN with some training energy vectors for the purpose of training. However, supervised learning-based SVM techniques perform better than unsupervised learning-based CSS techniques due to the additional information utilized in the SVM classifier training process [60].

The SVM tries to find a linearly separable hyperplane, with the help of support vectors (ie, energy vectors that lie closest to the decision surface), by maximizing the margin of the classifier while minimizing the sum of errors. Let's assume the training energy vectors (ie,  $\bar{\mathbf{y}} = \{\mathbf{y}^{(1)}, \dots, \mathbf{y}^{(L)}\}$ ) and the spectrum availability corresponding to each training energy vector (ie,  $\bar{a} = \{a^{(1)}, \dots, a^{(L)}\}$ ) are fed into the SVM classifier for training. However, the training energy vectors may not be linearly separable. Therefore, the SVM classifier maps the training energy vectors into a higher dimensional feature space by a nonlinear mapping function, denoted by  $\phi$ , to make the training samples linearly separable [106,107]. Hence, the classifier should satisfy the following condition for all  $l = 1, \dots, L$ :

$$\begin{aligned} \mathbf{w} \cdot \phi(\mathbf{y}^{(l)}) + w_0 &\geq 1, \text{ if } a^{(l)} = 1, \\ \mathbf{w} \cdot \phi(\mathbf{y}^{(l)}) + w_0 &\leq -1, \text{ if } a^{(l)} = -1, \end{aligned} \quad (13.9)$$

where  $\mathbf{w}$  is the weighting vector and  $w_0$  is the bias. The bias is used for shifting the hyperplane away from the origin.

Although the training energy vectors are mapped into a higher dimensional feature space, practically they cannot achieve a perfect linearly separable hyperplane that satisfies the condition in Eq. (13.9) for each  $\mathbf{y}^{(l)}$ . Therefore, the condition in Eq. (13.9) should be modified in such a way that addresses the possible errors in

classification. Hence, the condition in Eq. (13.9) is modified by introducing a slack variable  $\delta^{(l)}$  for possible classification errors as follows:

$$a^{(l)}[\mathbf{w} \cdot \phi(\mathbf{y}^{(l)}) + w_0] \geq 1 - \delta^{(l)}, \quad (13.10)$$

where  $\delta^{(l)} \geq 0$  for  $l = 1, \dots, L$ . For marginal classification errors, the slack variable lies in  $0 \leq \delta^{(l)} \leq 1$ , whereas  $\delta^{(l)} > 1$  for misclassification. Hence, the optimization problem for maximizing the margin classifier while minimizing the sum of errors can be written as follows [60]:

$$\text{minimize} \quad \frac{1}{2} \|\mathbf{w}\|^2 + \xi \sum_{l=1}^L I_{\{\delta^{(l)} > 1\}} \quad (13.11)$$

$$\text{s.t.} \quad a^{(l)}[\mathbf{w} \cdot \phi(\mathbf{y}^{(l)}) + w_0] \geq 1 - \delta^{(l)}, \quad \text{for } l = 1, \dots, L, \quad (13.12)$$

$$\delta^{(l)} \geq 0, \quad \text{for } l = 1, \dots, L, \quad (13.13)$$

where  $\|\mathbf{w}\|^2 = \mathbf{w} \cdot \mathbf{w}$ ,  $\xi$  is a soft margin constant [106], and  $I_{\{X\}}$  is the indicator function which is one if  $X$  is true and is zero, otherwise.

The optimization problem defined in Eqs. (13.11)–(13.13) is nonconvex due to  $I_{\{\delta^{(l)} > 1\}}$  in the objective function. Since  $\delta^{(l)} > 1$  for misclassification,  $\sum_{l=1}^L \delta^{(l)}$  gives a bound on the number of the misclassified training energy vectors. Therefore,  $\sum_{l=1}^L \delta^{(l)}$  can be used to measure the number of the training energy vectors which are misclassified by the decision surface  $\mathbf{w} \cdot \phi(\mathbf{y}^{(l)}) + w_0 = 0$ , as well as the number of the training energy vectors that are correctly classified but lie in the slab  $-1 < \mathbf{w} \cdot \phi(\mathbf{y}^{(l)}) + w_0 < 1$ . Hence, the optimization problem can be rewritten as a convex optimization problem as follows [60]:

$$\text{minimize} \quad \frac{1}{2} \|\mathbf{w}\|^2 + \xi \sum_{l=1}^L \delta^{(l)} \quad (13.14)$$

$$\text{s.t.} \quad a^{(l)}[\mathbf{w} \cdot \phi(\mathbf{y}^{(l)}) + w_0] \geq 1 - \delta^{(l)}, \quad \text{for } l = 1, \dots, L, \quad (13.15)$$

$$\delta^{(l)} \geq 0, \quad \text{for } l = 1, \dots, L. \quad (13.16)$$

This optimization problem can be solved by using the Lagrangian technique. Hence, the Lagrangian of Eqs. (13.14)–(13.16) can be written as

$$\begin{aligned} A(\mathbf{w}, w_0, \delta; \lambda, \gamma) = & \frac{1}{2} \|\mathbf{w}\|^2 + \xi \sum_{l=1}^L \delta^{(l)} - \sum_{l=1}^L \lambda^{(l)} \left\{ a^{(l)}[\mathbf{w} \cdot \phi(\mathbf{y}^{(l)}) + w_0] - 1 + \delta^{(l)} \right\} \\ & - \sum_{l=1}^L \gamma^{(l)} \delta^{(l)}, \end{aligned} \quad (13.17)$$

where  $\lambda^{(l)}$  and  $\gamma^{(l)}$  are Lagrangian multipliers. By applying the Karush-Kuhn-Tucker (KKT) conditions, we can obtain

$$\mathbf{w} = \sum_{l=1}^L \lambda^{(l)} a^{(l)} \phi(\mathbf{y}^{(l)}) \quad (13.18)$$

$$\sum_{l=1}^L \lambda^{(l)} a^{(l)} = 0 \quad (13.19)$$

$$\lambda^{(l)} = \xi - \gamma^{(l)}. \quad (13.20)$$

It is noticeable that  $\gamma^{(l)} \geq 0$  and  $0 \leq \lambda^{(l)} \leq \xi$ . The vector of  $\lambda^{(l)}$ 's is known as a support vector. Hence, we can obtain the dual problem in terms of the support vector as follows:

$$\text{maximize} \quad \sum_{l=1}^L \lambda^{(l)} - \frac{1}{2} \sum_{i=1}^L \sum_{j=1}^L \lambda^{(i)} \lambda^{(j)} a^{(i)} a^{(j)} \{\phi(\mathbf{y}^{(i)}) \cdot \phi(\mathbf{y}^{(j)})\} \quad (13.21)$$

$$\text{s.t.} \quad \sum_{l=1}^L \lambda^{(l)} a^{(l)} = 0 \quad (13.22)$$

$$0 \leq \lambda^{(l)} \leq \xi, \quad \text{for } l = 1, \dots, L. \quad (13.23)$$

The KKT conditions uniquely characterize the solution of the primal problem as Eqs. (13.18)–(13.20), and the dual problem has two active constraints  $\lambda^{(l)} \{a^{(l)} [\mathbf{w} \cdot \phi(\mathbf{y}^{(l)}) + w_0] - 1 + \delta^{(l)}\} = 0$  and  $\gamma^{(l)} \delta^{(l)} = (\xi - \lambda^{(l)}) \delta^{(l)} = 0$ . We can solve the optimization problem in Eqs. (13.21)–(13.23) by using standard techniques to solve a quadratic program. Let  $\tilde{\lambda}^{(l)}$  denote the solution of Eqs. (13.21)–(13.23).

Finally, the nonlinear decision function can be obtained as

$$d(\mathbf{x}) = \text{sgn} \left( \sum_{l=1}^L \tilde{\lambda}^{(l)} a^{(l)} \kappa(\mathbf{x}, \mathbf{y}^{(l)}) + w_0 \right), \quad (13.24)$$

where  $\text{sgn}$  is the sign function and  $\kappa(\mathbf{x}, \mathbf{y}) = \phi(\mathbf{x}) \cdot \phi(\mathbf{y})$  is the kernel function. Some of the commonly used kernel functions are linear, polynomial, and Gaussian radial basis functions [106]. After the classifier obtains the decision function, it can categorize the test energy vector  $\mathbf{y}^*$  as

$$\hat{a} = d(\mathbf{y}^*). \quad (13.25)$$

### 13.3.3.3 Comparison among different fusion techniques for CSS

The performance of different fusion techniques (ie, SVM with linear and polynomial kernel [107], KNN with Euclidean and Cityblock distances [60],  $K$ -means clustering [60], GMM [60], Fisher linear discriminant (Fisher) [105], OR and AND rule) used for CSS is shown in Fig. 13.11. The performance of the fusion techniques

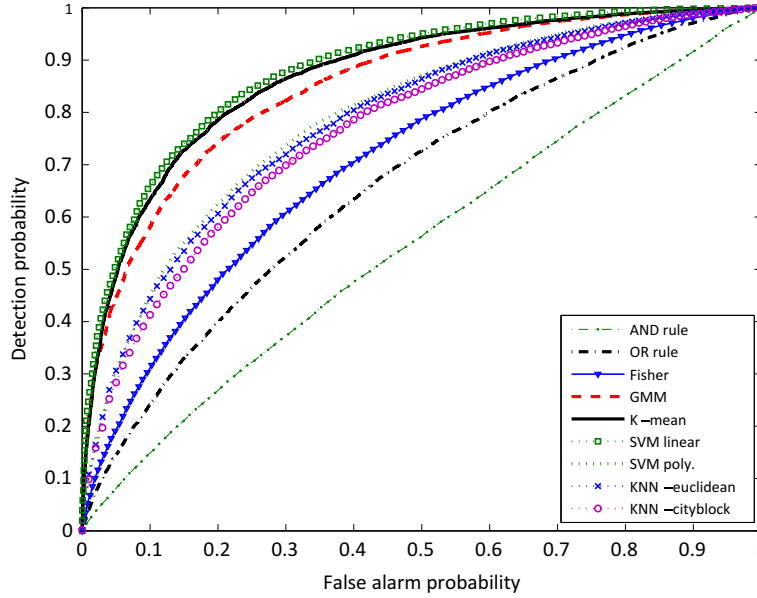


**FIG. 13.11**

The ROC curves when the bandwidth  $w$  is 5 MHz, the sensing duration  $\tau$  is 100  $\mu$ s, and the transmit power of each PU is 200 mW. The cooperating CRs are located in a 5-by-5 grid in a 4000 m  $\times$  4000 m area.

*Courtesy: K.M. Thilina, K.W. Choi, N. Saquib, E. Hossain, Machine learning techniques for cooperative spectrum sensing in cognitive radio networks, IEEE J. Sel. Areas Commun. 31 (11) (2013) 2209–2221.*

is characterized in terms of receiver operating characteristic (ROC) when there is a single PU and there are  $5 \times 5$  (ie, 25) CRs in the network. This figure clearly reveals that the SVM with linear kernel outperforms (ie, achieves a higher detection probability) all other classification techniques, and this performance gain is achieved by mapping the feature space to a higher dimension with the help of the linear kernel. Interestingly, the  $K$ -means unsupervised learning technique achieves a similar performance as the SVM-linear technique. Due to the simplicity of implementation (ie, it does not need training data with its label; therefore, it can learn the environment on the fly), lower training and classification delay, and higher detection probability,  $K$ -means clustering is a promising candidate for CSS.

### 13.3.4 DATABASE-CENTRIC APPROACH FOR SPECTRUM SENSING

With the database-centric mechanism, the CRNs acquire radio-environmental or spectrum information from a central database. The CRs do not require the spectrum-sensing capability since all the required environmental awareness

information for cognitive operation are acquired through the central database. Therefore, instead of spectrum-sensing capabilities, the CRs should have the capability to access the database through CCCs. However, implementing an up-to-date and highly reliable central database for all geographical locations can be very challenging. Therefore, researchers have proposed an information grid-based approach to update the central database and calculate spectrum specific information for other locations based on the information obtained through the grid points. Also, researchers have proposed a combined approach for improving the sensing performance by means of radio environmental maps (REM) [16,80,108]. The REM makes it possible to combine the spectrum-sensing system with the database-centric approach by providing different mechanisms and algorithms to collect, process, store, and retrieve different field measurements.

---

### 13.4 RESOURCE ALLOCATION IN CRNs

In the literature, extensive research has been carried out on resource allocation for conventional wireless networks. However, those approaches cannot be directly applied to resource allocation in CRNs due to the added limitation such as mutual interference among PUs and CRs and imperfect spectrum sensing. In this context, inefficient utilization of the available spectrum and other wireless resources in CRNs degrade not only the performance of CRNs but also the performance of primary networks. Therefore, in order to optimize the performance of both networks, it is very important to manage the mutual interference between CRs and avoid harmful interference at PUs. Hence, an efficient resource allocation algorithm should jointly consider the aforementioned aspects with spectrum management aspects [109–114].

#### 13.4.1 ELEMENTS OF RESOURCE ALLOCATION PROBLEMS IN CRNs

The main elements which need to be optimized in CR resource allocation problems are as follows:

- **Power allocation:** The power allocation schemes which have been developed for traditional wireless networks cannot be utilized directly in CRNs since the interference caused to the primary networks needs to be taken into account. The power allocation algorithms should always maintain the level of interference at the PRs under the acceptable interference limit.
- **Channel allocation:** The channel allocation algorithm in CRNs plays a significant role in mitigating harmful interference at PUs. As an example, in the spectrum underlay mode, the channel allocation scheme should allocate channels to the CRs which receive minimum interference from the PUs. Unlike traditional wireless channel allocation, the channel allocation algorithms in CRNs depend on the PU activities in the considered channels.

- User scheduling: The CR scheduling decision should be made by considering the CRs' channel conditions and their QoS requirements in such a way that it does not affect the QoS requirements of the PUs. The QoS requirement for the CRs could be a minimum rate requirement and a maximum packet error rate. The other QoS metrics could be response time, delay, outage, and blocking probability.
- Fairness: A CRN can achieve a higher system throughput or spectral efficiency while not being fair to all the CRs. This is a tradeoff between efficiency in resource allocation and fairness. The fairness can be achieved in terms of bandwidth fairness (equal amount of spectrum to all CRs), power fairness (equal portion of power from the total budget in downlink transmission), or rate fairness (allocate resources in such a way that all the CRs can achieve same rate).
- Relay selection: In a CRN, implementation of OSA for cell-edge CRs could be challenging since direct transmission from the CBS to the cell-edge CRs would require a high transmit power and generate interference to the PUs. This would lead to limited spectrum access for cell-edge users. Relay-assisted communication can provide an effective solution to this problem since it helps to reduce the transmit power required to service the cell-edge CRs. With an optimal relay selection mechanism, the spectral efficiency and network throughput can be enhanced while avoiding harmful interference at PUs.

### 13.4.2 RESOURCE ALLOCATION APPROACHES IN CRNs

The generic resource allocation problem for CRNs is shown in Table 13.2. The applicability of the input parameters, the constraints, and objective functions in the resource allocation optimization problem are based on the CRN architecture, communication protocols, and transmission scenario (downlink/uplink transmission).

The input parameters and the constraints for resource allocation problem are generally set by the network operators or regulatory authorities. As an example, the number of CRs admitted to the CRN is set by the network operators, whereas the interference thresholds at PUs are set by the regulatory authorities. The interference threshold levels allowed for underlay and overlay operational modes are not the same. The interference threshold for the underlay operation is less than that of overlay operation due to the simultaneous spectrum access by the PUs and CRs in the underlay operation. For resource allocation, CSI at the CRs is an important parameter. Most of the resource allocation algorithms assume that perfect CSI information is available at the CRs. However, in practical scenarios, this is not the case.

#### 13.4.2.1 Optimization model with typical objectives and constraints

Let us consider a downlink transmission model in an OFDMA-based multiuser CRN (Fig. 13.12). The number of SUs in the CRN is denoted by  $\mathcal{M}$ . The considered CRN coexists with a primary network which is denoted by  $\mathcal{P}$ . We assume that the downlink transmissions by the CBS in the CRN are synchronized with the uplink transmissions

**Table 13.2** General Resource Optimization Problem

Inputs/given (any combination)	Number of CRs in CRN/cluster/cooperate Number of channel or spectrum bands sensed Number of PUs Number of relays Interference thresholds at PUs CSI, geographic location of PUs and SUs Protocol and the protocol-specific parameters CRN-specific custom inputs
Find/decision variable (any combination)	Transmit power (CRs/CBS/relays) Allocation/assignment of spectrum bands (channels) and bandwidth User selection and scheduling Assignment/selection of relays
Constraints (any combination)	CRN-specific custom decision variables CBS/CR/cognitive relay specific power constraint Interference constraint at PUs Channel/bandwidth assignment constraint Relay selection/assignment constraint Fairness constraint Rate/delay constraint - QoS constraints Receiver sensitivity constraint CRN-specific topology constraint Outage constraint Revenue-specific constraint CRN-specific custom constraint
Objectives (any combination)	Minimize: Transmit power at CBS in downlink Per-CR transmit power in uplink transmission Generalized spectral footprints in CRNs Outage probability of CRs, interference outage at PUs Bit-error rate in cognitive transmission End-to-end transmission delay Maximize: Sum rate in CRNs, weighted Sum rate in CRNs Energy efficiency in CRNs Utility in CRNs Max-min: Worst CRs capacity/SNR/utility Max/Min: CRN specific custom objectives

*M. Naeem, A. Anpalagan, M. Jaseemuddin, D.C. Lee, Resource allocation techniques in cooperative cognitive radio networks, IEEE Commun. Surv. Tut. 16 (2) (2014) 729–744.*

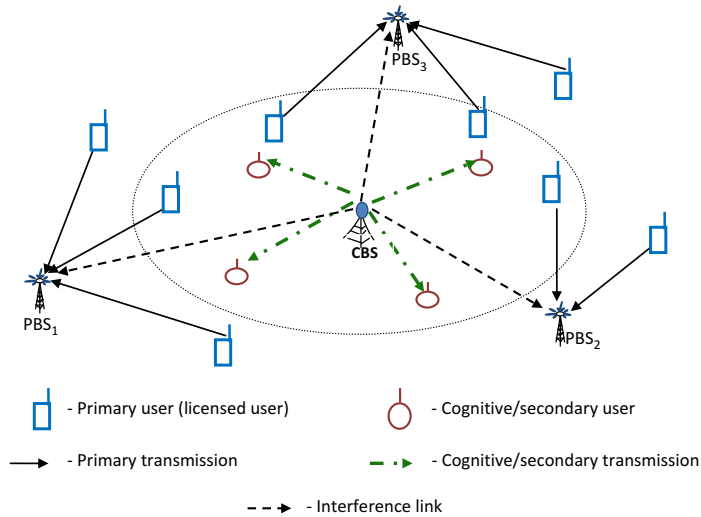


FIG. 13.12

A CRN model.

in the primary network [15,115,116]. The PUs transmit in the uplink and the PBSs are the PRs.

The total available spectrum band in the CRN is divided into  $\mathcal{K}$  equal independent subchannels each with bandwidth  $B$ . The channel realization from any transmitter (PU transmitter/CBS) to any receiver (PBS/SUs) is quasi-static for one frame duration and independent and identically distributed (i.i.d.) over different frames. The location information of the PBSs in the primary network can be obtained from the REM [15,115,116]. Furthermore, the waveform of the PU signal is unknown at the cognitive user on a given subchannel; hence the interference at the cognitive user is calculated by assuming power spectral density of that subchannel as given in [115, Section II.B]. We assume that at the beginning of every frame, the CBS obtains information such as the CSI between CBS and CRs and aggregate interference at the CRs caused by the PUs.

### 13.4.2.2 Optimization constraints

The commonly used optimization constraints in the resource allocation problems for a CRN are applied based on the system model discussed in Section 13.4.2.1. We set  $X_{m,k} = 1$  if the  $k$ th subchannel is allocated to the  $m$ th user; otherwise  $X_{m,k} = 0$ . With the OFDMA-based downlink transmission,  $P_{m,k}$  denotes the transmit power of the CBS on the  $k$ th subchannel assigned to the  $m$ th user.

### Interference constraint

The constraint which guarantees the interference caused at the  $p$ th PR on the  $k$ th subchannel can be expressed as

$$g_{p,k}P_{m,k} \leq I_{\text{th},k}^p, \quad \forall p \in \mathcal{P}, \forall k. \quad (13.26)$$

The interference threshold,  $I_{\text{th},k}^p$ , in Eq. (13.26) is defined by the regulatory authorities and the value of interference threshold depends on the operational mode (underlay/overlay) of CRs; additionally,  $g_{p,k}$  is the channel power gain from the CBS to the PRs (ie, PBS according to the considered system model).

### Rate constraint

In OFDMA CRNs, the number of subchannels allocated to a particular user to satisfy a given rate requirement varies with the channel conditions of the allocated subchannels. Furthermore, the CRs have different rate requirements and the rate constraint, which ensures that the  $m$ th CR achieves its minimum rate requirement of  $\phi_m$  can be expressed as follows:

$$\sum_{k=1}^{\mathcal{K}} X_{m,k} B \log \left( 1 + \frac{P_{m,k} h_{m,k}}{\eta + \sum_{p \in \mathcal{P}} I_{p,m,k}} \right) \geq \phi_m, \quad \forall m, \quad (13.27)$$

where  $\eta$  denotes the noise power,  $I_{p,m,k}$  denotes the interference caused by the PU  $p \in \mathcal{P}$  at the  $m$ th CR on the  $k$ th subchannel, and  $h_{m,k}$  is the channel power gain from CBS to the  $m$ th user on subchannel  $k$ .

### Total power constraint

The total power constraint is introduced in the downlink resource allocation problem to ensure that the power allocation to subchannels is not greater than the saturation power of the CBS transmitters. This constraint can be expressed as follows:

$$\sum_{m=1}^{\mathcal{M}} \sum_{k=1}^{\mathcal{K}} P_{m,k} \leq P^{\max}, \quad (13.28)$$

where  $P^{\max}$  is the maximum total transmit power in CBS.

### Subchannel allocation constraint

This constraint ensures that the  $k$ th subchannel is not allocated to more than one user in the cognitive network and can be expressed as follows:

$$\sum_{m=1}^{\mathcal{M}} X_{m,k} \leq 1. \quad (13.29)$$

Since  $X_{m,k}$ ,  $X_{m,k} \in \{0,1\}$  is a binary integer variable, most of the optimization problems in this case are convex/nonconvex/linear/nonlinear integer programs and hence have high complexity.

### Receiver sensitivity constraint

In the underlay CRNs, due to the simultaneous transmissions of CRs with PUs, the power allocated to some subchannels may not be enough to generate a strong signal at the CR receivers. A CR receiver may not be able to decode the received signal if the received signal strength is less than the receiver sensitivity. This effect may be more significant in the power minimization optimization problem in CRNs since the main objective of such a problem is to minimize total transmit power allocated to subchannels by utilizing as much bandwidth as possible. If the received signal at the CRs is lower than the receiver sensitivity, it is a waste of scarce radio resources (ie, spectrum bandwidth and power). The sensitivity constraint can be expressed as follows:

$$P_{m,k}h_{m,k} \geq \Gamma_m, \quad \forall m, \forall k, \quad (13.30)$$

where  $\Gamma_m$  is the sensitivity threshold of CRs.

#### 13.4.2.3 Optimization objectives

The essence of resource allocation in CRNs is to minimize the utilization of radio resources while avoiding harmful interference at the PUs and to satisfy the QoS requirements of CRs [117]. The most common types of objective functions used for optimizing resource allocation in CRNs are illustrated in Table 13.2.

An optimization problem with a maximization objective tries to maximize the system throughput (sum-rate or weighted sum-rate), or SNR at the cognitive receivers, or the total network utility. Game theory-based approaches are used for solving network utility maximization problems. The fairness in resource allocation indicates how equally the available scarce resources are distributed among the CRs in the network. Different fairness criteria such as the max-min fairness and the proportional fairness criteria can be used.

### Power minimization

The objective of power minimization in CRN downlink transmission is to mitigate harmful interference at the PUs while providing the required QoS to the CRs. In uplink cognitive transmission, the objectives of power minimization are as follows: mitigate interference at the PUs and protect scarce battery power in CR devices. An optimization problem with a power minimization objective function utilizes as much bandwidth as possible to minimize power allocation to subchannels (in an OFDMA CRN) while satisfying the cognitive transmission-specific constraints. The corresponding resource allocation scheme is generally known as the margin adaptive allocation scheme since it allocates power to subchannels until it satisfies the QoS requirements of the CR users [117], ie, no more power allocation is possible to subchannels to increase the QoS. The objective function for power minimization in the downlink transmission can be expressed as follows:

$$\min_{x_{m,k}, p_{m,k}} \sum_{m=1}^{\mathcal{M}} \sum_{k=1}^{\mathcal{K}} x_{m,k} p_{m,k}. \quad (13.31)$$

The objective function in Eq. (13.31) shows the summation of total power allocated to all of the PUs' idle subchannels. The iterative waterfilling algorithm [112] and Lagrangian-based dual decomposition algorithms are commonly used for solving power minimization optimization problems [118].

### Generalized spectral footprint

The traditional resource allocation techniques in CRNs try to utilize as much bandwidth as possible to minimize the transmit power and interference caused to the PU receivers [117]. However, it is reasonable to allow the CRs to keep transmitting until the interference caused by them reaches a predefined interference threshold. Thus, instead of utilizing all the available bands for transmission, the CRs can save some spectrum bands for other cognitive applications. This is a tradeoff between the allocation of power and spectrum band. The spectral footprint<sup>2</sup> minimization approach facilitates CRNs to reduce the number of channels used to satisfy the required QoS at the expense of slightly higher transmission power while maintaining the given interference threshold at the PU receivers. The generalized spectral footprint minimization objective can be written as follows: [109]:

$$\min \left[ \sum_{m=1}^{\mathcal{M}} \sum_{k=1}^{\mathcal{K}} \frac{BX_{m,k}}{(1-\omega_k)} \right]^{\alpha} \left[ \sum_{m=1}^{\mathcal{M}} \sum_{k=1}^{\mathcal{K}} P_{m,k} \right]^{\beta}. \quad (13.32)$$

The weighting parameters for the bandwidth-footprint and the power-footprint are  $\alpha (\geq 0)$  and  $\beta (\geq 0)$ , respectively. Moreover, for CRNs, a generalized spectral footprint-based allocation paves the way to optimally and opportunistically utilize the available radio resources (ie, by varying the values  $\alpha$  and  $\beta$ ) depending on the network operators' objectives. Note that the case with  $\alpha = 0$  and  $\beta = 1$  is the known power minimization objective. Here,  $\omega_k$  is the activity factor of PUs on the  $k$ th subchannel. Interestingly, the incorporation of PU activity in the optimization objective adds another dimension to the optimization problem by allocating the subchannels with lower PU activity to CRs while avoiding the subchannels with higher PU activity in the allocation process so that the spectral footprint is minimized.

### Rate maximization

The optimization problems in CRNs with a sum rate maximization objective aims to maximize total system throughput in CRNs with the interference constraints (ie, at the PUs) and total power constraints [119]. In the literature, this type of problem with the sum-rate maximization objective function is known as the rate-adaptive optimization problem. Specifically, the sum-rate maximization problem indirectly

---

<sup>2</sup>The spectral footprint is defined as a product of the bandwidth-footprint ( $F_B = \sum_{m=1}^{\mathcal{M}} \sum_{k=1}^{\mathcal{K}} \frac{BX_{m,k}}{(1-\omega_k)}$ ) and the power-footprint ( $F_P = \sum_{m=1}^{\mathcal{M}} \sum_{k=1}^{\mathcal{K}} P_{m,k}$ ) [118], where  $\omega_k$  is the activity factor of the PUs on the  $k$ th subchannel.

maximizes the spectral efficiency in CRNs. Hence, the sum-rate maximization objective that maximizes the spectral efficiency in CRNs can be written as follows:

$$\max_{X_{m,k}, P_{m,k}} \sum_{m=1}^{\mathcal{M}} \sum_{k=1}^{\mathcal{K}} X_{m,k} B \log \left( 1 + \frac{P_{m,k} h_{m,k}}{\eta + \sum_{p \in \mathcal{P}} I_{p,m,k}} \right). \quad (13.33)$$

It is important to note that the sum-rate maximization problems in CRNs maximize the individual CR rate in such a way that the total system throughput is increased. However, there is no guarantee for the satisfaction of an individual CR's minimum rate requirement unless constraints for individual rate requirements are also considered.

#### Utility maximization

Utility maximization-based resource allocation can achieve efficiency and fairness in resource optimization. CRNs can exploit the flexibility of defining utility functions in such a way that the unique requirements in CRNs can be satisfied. The logarithmic utility functions guarantee the fairness, concavity, optimality, and uniqueness of the optimal solution [120]. However, selecting an appropriate logarithmic utility function to satisfy efficiency and fairness in CRNs is challenging, and the utility function can vary from application to application. Game theory is a very good tool for solving utility maximization-based resource allocation problems for CRs [121–123].

#### 13.4.2.4 Approach to solve a resource allocation problem in CRNs

In this section, the joint subchannel and power allocation problem is formulated as a generalized spectral-footprint minimization problem for OFDMA-based CRNs with the rate, interference, total power, subchannel allocation, and receiver constraints. Hence, the optimization problem for minimizing the generalized spectral footprint for a CRN can be stated as follows [109]:

$$\min \left[ \sum_{m=1}^{\mathcal{M}} \sum_{k=1}^{\mathcal{K}} \frac{B X_{m,k}}{(1 - \omega_k)} \right]^{\alpha} \left[ \sum_{m=1}^{\mathcal{M}} \sum_{k=1}^{\mathcal{K}} P_{m,k} \right]^{\beta}, \quad (13.34)$$

$$\text{s.t. } \sum_{k=1}^{\mathcal{K}} X_{m,k} B \log \left( 1 + \frac{P_{m,k} h_{m,k}}{\eta + \sum_{p \in \mathcal{P}} I_{p,m,k}} \right) \geq \phi_m, \quad \forall m, \quad (13.34.1)$$

$$\sum_{m=1}^{\mathcal{M}} X_{m,k} \leq 1, \quad (13.34.2)$$

$$g_{p,k} P_{m,k} \leq I_{\text{th},k}^p, \quad \forall \omega_k \leq \omega_{\text{th}}, p \in \mathcal{P}, \forall k \quad (13.34.3)$$

$$\sum_{m=1}^{\mathcal{M}} \sum_{k=1}^{\mathcal{K}} P_{m,k} \leq P^{\max}, \quad (13.34.4)$$

$$P_{m,k} h_{m,k} \geq \Gamma_m, \quad \forall m, \forall k, \quad (13.34.5)$$

$$X_{m,k} \in \{0, 1\}, P_{m,k} \geq 0, \quad \forall m, k, \quad (13.34.6)$$

where  $X_{m,k}$  and  $P_{m,k}$  are the decision variables to be optimized. The PU activity threshold in a given subchannel is denoted by  $\omega_{th}$  and a particular subchannel is allocated for cognitive transmission if and only if the PU activity on that subchannel is less than or equal to  $\omega_{th}$ .

The optimization problem in Eq. (13.34) is a mixed-integer, nonlinear, and nonconvex programming problem. Furthermore, it is observable that the generalized spectral footprint minimization problem in Eq. (13.34) is a collection of two separable subproblems where one depends on the subchannel allocation and the other depends on the power allocation only. Hence, to make the optimization problem easier to solve without loss of generality, the decomposition technique [124] can be applied to convert Eq. (13.34) into subchannel allocation and power allocation subproblems. The subproblems can be coupled through an appropriate coupling constraint. In fact, the coupling constraint for the decomposed subproblems is the rate constraint defined in Eq. (13.34.1). The block diagram of the resource allocation algorithm which solves the subchannel allocation and power allocation subproblems iteratively for optimality is illustrated in Fig. 13.13.

### Initial solution

To start any iterative algorithm, the initial feasible solution needs to be found with some approximation. Specifically, the goodness of the initial feasible solution is important since it affects the number of iterations required for the algorithm to converge. Note that at first we do not know the exact number of subchannels required to achieve the given rate requirement of CRs. However, the minimum transmit power required to decode a signal on each subchannel for a given CR can be calculated by considering the equality of the sensitivity constraint in Eq. (13.34.5). This calculated power may violate the interference constraint in Eq. (13.34.3). Therefore, the violation of the interference constraint in Eq. (13.34.3) for the calculated power should be checked. If the interference constraint is not violated for the calculated power, the calculated power based on the sensitivity threshold can be treated as the feasible power, though we do not consider the rate constraint. This is acceptable

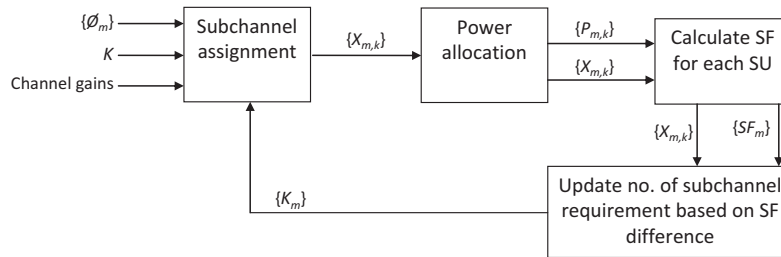


**FIG. 13.13**

Block diagram of the resource allocation process [109], where  $\{SF_m\}$  is the spectral footprint of  $m$ th user.

as a good starting point since we do not know the exact number of subchannels that should be allocated to achieve a given rate requirement of CRs. Furthermore, if the calculated minimum transmit power violates the interference constraint in Eq. (13.34.3), we do not allocate power on that subchannel.

#### Subchannel allocation subproblem

The subchannel allocation problem for the given initial feasible power  $P_{m,k}^*$  can be written as

$$\begin{aligned} & \min \left[ \sum_{m=1}^{\mathcal{M}} \sum_{k=1}^{\mathcal{K}} \frac{BX_{m,k}}{(1 - \omega_k)} \right]^{\alpha}, \\ & \text{s.t. } \sum_{k=1}^{\mathcal{K}} X_{m,k} B \log \left( 1 + \frac{P_{m,k}^* h_{m,k}}{\eta + \sum_{p \in \mathcal{P}} I_{p,m,k}} \right) \geq \phi_m, \quad \forall m, \\ & \quad \sum_{m=1}^{\mathcal{M}} X_{m,k} \leq 1, \\ & \quad X_{m,k} \in \{0, 1\}, \quad \forall m, k. \end{aligned} \tag{13.34}$$

The optimization problem in Eq. (13.34) becomes an integer programming problem for a given power allocation  $P_{m,k}^*$ . Therefore, this problem can be solved for optimality by using the basic Hungarian algorithm [125,126]. The authors in [115] proposed a modified Hungarian algorithm for resource allocation by directly allocating subchannels which are not candidate subchannels for other CRs. However, in each iteration, the modified Hungarian algorithm in [115] has to run from the very beginning to obtain the optimal solution. Therefore, the authors in [109] proposed a novel low-complexity modified Hungarian-based subchannel assignment algorithm which exploits the available local cost information to reduce the complexity from the first iteration onwards.

The integer program for the subchannel allocation problem in Eq. (13.34) can also be solved by relaxing the integer constraint, ie,  $X_{m,k}$ , and assigning the values within the interval [0,1]. With the help of this new continuous parameter, standard Lagrangian techniques can be used to obtain a solution for subchannel allocation. Due to the integer relaxation of  $X_{m,k}$ , a particular subchannel may be allocated to more than one user with time sharing within a considered time slot. This cannot be achieved in practical implementation. Therefore, the CR which gets the largest factor on a particular subchannel gets the assignment for its transmission [127]. However, there is no guarantee for the optimality of the solution.

#### Power allocation subproblem

With the optimal subchannel assignment,  $\mathbf{X}_{m,k}^*$ , which is obtained by solving Eq. (13.34), we can write the optimal power allocation that minimizes the spectral footprint as follows:

$$\begin{aligned}
& \min [F_B^*]^\alpha \left[ \sum_{m=1}^{\mathcal{M}} \sum_{k=1}^{\mathcal{K}} P_{m,k} \right]^\beta, \\
& \text{s.t. } \sum_{k=1}^{\mathcal{K}} X_{m,k}^* B \log \left( 1 + \frac{P_{m,k} h_{m,k}}{\eta + \sum_{p \in \mathcal{P}} I_{p,m,k}} \right) \geq \phi_m, \quad \forall m, \\
& \quad g_{p,k} P_{m,k} \leq I_{\text{th},k}^p, \quad \forall \omega_k \leq \omega_{\text{th}}, p \in \mathcal{P}, \forall k, \\
& \quad \sum_{m=1}^{\mathcal{M}} \sum_{k=1}^{\mathcal{K}} P_{m,k} \leq P^{\max} \\
& \quad P_{m,k} h_{m,k} \geq \Gamma_m, \quad \forall m, \forall k \\
& \quad P_{m,k} \geq 0, \quad \forall m, k,
\end{aligned} \tag{13.35}$$

where  $F_B^* = \sum_{m=1}^{\mathcal{M}} \sum_{k=1}^{\mathcal{K}} \frac{BX_{m,k}^*}{(1-\omega_k)}$ . The power allocation subproblem in Eq. (13.35) can be solved by formulating the Lagrangian as follows:

$$\begin{aligned}
\mathcal{L}(\mathbf{P}, \lambda, \mu, \gamma, \nu) = & [F_B^*]^\alpha \left[ \sum_{m=1}^{\mathcal{M}} \sum_{k=1}^{\mathcal{K}} P_{m,k} \right]^\beta + \sum_{p \in \mathcal{P}} \sum_{k=1}^{\mathcal{K}} \mu_{p,k} (g_{p,k} P_{m,k} - I_{\text{th},k}^p) \\
& + \sum_{m=1}^{\mathcal{M}} \lambda_m \left( \phi_m - \sum_{k=1}^{\mathcal{K}} X_{m,k}^* B \log \left( 1 + \frac{P_{m,k} h_{m,k}}{\eta + \sum_{p \in \mathcal{P}} I_{p,m,k}} \right) \right) \\
& + \sum_{m=1}^{\mathcal{M}} \sum_{k=1}^{\mathcal{K}} \nu_{m,k} (\Gamma_m - P_{m,k} h_{m,k}) + \gamma \left( \sum_{m=1}^{\mathcal{M}} \sum_{k=1}^{\mathcal{K}} P_{m,k} - P^{\max} \right),
\end{aligned} \tag{13.36}$$

where  $\mu_{p,k}$ ,  $\lambda_m$ ,  $\nu_{m,k}$ , and  $\gamma$  are Lagrangian multipliers [124]. Hence, the optimal power allocation at the  $(t+1)$ th iteration ( $P_{m,k}(t+1)$ ) for a given subchannel assignment can be obtained by yielding  $\frac{\partial \mathcal{L}(\mathbf{P}, \lambda, \mu, \gamma, \nu)}{\partial P_{mk}} = 0$  as in Eq. (13.37).

$$\begin{aligned}
P_{m,k}(t+1) = & \left[ \frac{B \lambda_m X_{m,k}^*}{\beta [F_B^*]^\alpha \left[ \sum_{m=1}^{\mathcal{M}} \sum_{k=1}^{\mathcal{K}} P_{m,k}(t) \right]^{\beta-1} + \sum_{p \in \mathcal{P}} \mu_{p,k} g_{p,k} + \gamma - \nu_{m,k} h_{m,k}} \right. \\
& \left. - \frac{\eta + \sum_{p \in \mathcal{P}} I_{p,m,k}}{h_{m,k}} \right]^+.
\end{aligned} \tag{13.37}$$

The Lagrange multipliers can be updated in each iteration as follows [124]:

$$\lambda_m(t+1) = \left[ \lambda_m(t) + \delta(t) \left( \phi_m - \sum_{k=1}^{\mathcal{K}} X_{m,k}^* B \log \left( 1 + \frac{P_{m,k}(t) h_{m,k}}{\eta + \sum_{p \in \mathcal{P}} I_{p,m,k}} \right) \right) \right]^+, \tag{13.38}$$

$$\mu_{p,k}(t+1) = \left[ \mu_{p,k}(t) + \delta(t) \left( g_{p,k} P_{m,k} - l_{th,k}^p \right) \right]^+, \quad (13.39)$$

$$v_{m,k}(t+1) = \left[ v_{m,k}(t) + \delta(t) \left( \Gamma_m - P_{m,k} h_{m,k} \right) \right]^+, \quad (13.40)$$

$$\gamma(t+1) = \left[ \gamma(t) + \delta(t) \left( \sum_{m=1}^{\mathcal{M}} \sum_{k=1}^{\mathcal{K}} P_{m,k} - P^{\max} \right) \right]^+, \quad (13.41)$$

where  $\delta(t)$  is the step size in the  $t$ th iteration. Hence, the optimal power allocation can be obtained by iteratively updating the power according to Eq. (13.37) and the Lagrange multipliers. The iteration stops once the power update difference between consecutive iterations falls below a predefined threshold.

The power and subchannel allocations for generalized spectral footprint minimization in Eq. (13.34) can be obtained by iteratively updating the solutions given by the subproblems (Eqs. 13.34 and 13.35). Due to the iterative resource allocation approach, the spectral footprint minimization problem converges to a local optimum. However, when the number of PU idle subchannels is high compared to the number of CRs in the network, the solution converges to the globally optimal solution most of the time.

---

### 13.5 MEDIUM ACCESS CONTROL FOR CRNs

Cognitive MAC protocols should adopt mechanisms which will allow peaceful coexistence of CRs with the licensed users. Such a cognitive MAC protocol should achieve a higher overall spectrum efficiency by detecting all possible spectrum opportunities, spectrum sharing, and accessing through adaptable controlling. The main functional requirements which need to be addressed by a cognitive MAC protocol are as follows:

- **Interference avoidance and mitigation:** The transmission of the coexisting CRs in the spectrum bands, which are licensed to the PUs, should avoid or mitigate harmful interference caused at the PUs (eg, in the underlay mode of operation).
- **Spectrum access:** The MAC protocol is responsible for DSA based on the spectrum sensing information or up-to-date spectrum information in databases so that the collision with PUs and CRs is minimized (eg, in the overlay mode of operation).
- **Spectrum sharing:** The spectrum sharing strategies implemented in cognitive MAC protocols are responsible for choosing an optimal set of spectrum bands and transmission parameters to maximize the overall performance of the CRN while avoiding harmful interference at the PUs.
- **Control signaling mechanism:** The efficiency of the control signaling mechanism (eg, establishment and management of reliable and secure control signaling) significantly impacts the performance of a cognitive MAC protocol.

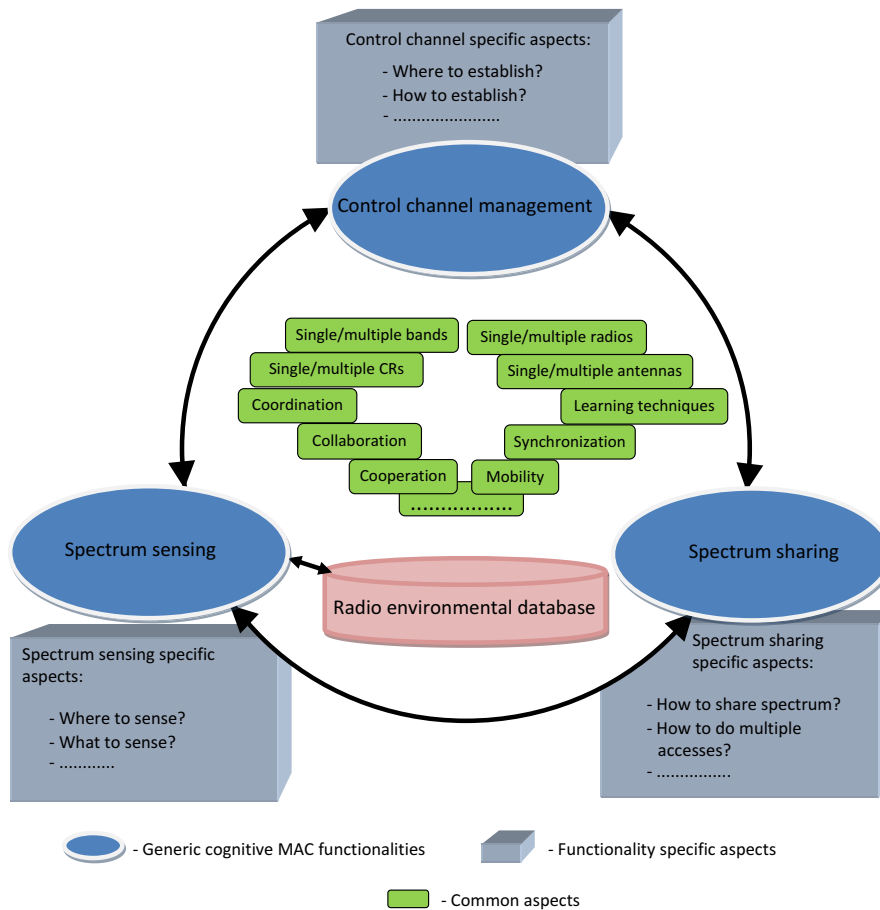
Cognitive MAC protocols can be categorized as either centralized [91,128] or distributed [129] MAC protocols based on the location of the spectrum management entity, which is responsible for spectrum access and allocation. Based on the presence, scope, and the characteristics of the CCC, the cognitive MAC protocols can be categorized as either local/global dedicated CCC [54] or dynamic CCC [91]-based MAC protocols. The behavior of the MAC protocols also varies with the degree of the CRs' interaction for spectrum sensing. Accordingly, the cognitive MAC protocols can be classified as either cooperative or noncooperative MAC protocols [129]. In CRNs, the spectrum access technique depends on the operational mode of CRs (ie, underlay or overlay). Accordingly, the cognitive MAC protocols can also be identified as either underlay or overlay MAC protocols [129]. The CRs equipped with a single radio transceiver access the spectrum by splitting the time frame for spectrum sensing and accessing, whereas the CRs equipped with multiple radios access the spectrum while simultaneously sensing the channels. The optimization and learning-based MAC protocols learn the radio environment and optimally utilize the available spectrum, whereas the other MAC protocols directly access the spectrum without adopting any learning capabilities [130].

### 13.5.1 COGNITIVE MEDIUM ACCESS CONTROL (C-MAC) CYCLE

The C-MAC cycle refers to a general design framework (as illustrated in Fig. 13.14) for cognitive MAC protocols which supports the following: the generic cognitive MAC functionalities, functionality-specific aspects, and common aspects [54]. The general functionalities in the C-MAC cycle are radio environmental data acquisition, spectrum sharing, and CC management. The radio environmental data acquisition techniques and relevant issues were discussed in detail in Sections 13.2.1 and 13.3. The spectrum-sharing functionality in the C-MAC cycle exploits the radio environmental data for efficient utilization and management of the PUs' idle spectrum. The issues related to spectrum sharing were discussed in Section 13.2.3. The CC management function is an integral function of the C-MAC cycle which is used to establish and manage secure and reliable control signaling among the CRs in the network. The common aspects include the number of radios per CR, number of antennas per CR, single/multiband operation, synchronization vs. asynchronous operation, and CR mobility, as well as those related to the techniques, principles, and solutions implemented for addressing the functionality specific challenges such as cooperation, collaboration, coordination, and learning mechanism.

The CC supports different CRN-specific operational aspects such as network coordination, cooperation, collaboration, network self-organization, data exchange, and spectrum mobility [54]. For this, the CC carries different types of control information such as sensing results, spectrum sharing information, spectrum access decisions, and system parameters.

- *Where to establish:* The CC can be established as an in-band or an out-of-band channel. If the CC is established within the spectrum band used for data

**FIG. 13.14**

General cognitive MAC cycle.

transmission, such a CC is known as an in-band CC. This in-band CC can be a dedicated control channel (DCC) or a nondedicated control channel (NCC). On the other hand, if the CC is established in a band separate from that used for data transmission, such a CC is known as an out-of-band CC. This out-of-band CC can be located in the licensed band or unlicensed bands such as the ISM bands.

- *How to establish:* The approaches for CC establishment can be divided into two main categories: DCC or NDCC establishment approaches. In the DCC approach, only the control information is exchanged in the channel, whereas for the NDCC approach, both the control and data information are exchanged in the

CC. A special type of DCC is one which is not fixed for a long period of time and used only during a specified time slot duration. The MAC protocols which do not use a static CC are known as dynamic CC-based MAC protocols [91].

- *DCC approach* can be categorized into the following: global, local, and dynamic DCC approaches. In the global DCC-based approach, all the CRs tune their radios to the global DCC to exchange control information. Since all the CRs tune to this channel, the global DCC-based approach is more susceptible to saturation. However, this approach provides a network-wide coordination among CRs and is suitable for centralized CRNs [131]. The local DCC-based approach mitigates the CC saturation problem at the cost of localized coordination among the CRs. In this approach, the CRs in a cluster exchange control information with the help of locally available DCC. The DCC localization within the cognitive network can be optimized by adopting a clustering mechanism for CRs [132]. In general, for both the global and local DCC approaches, the CC is allocated statistically for a long period of time. Therefore, both the approaches are more vulnerable to CC jamming and attacks. To address the problem of CC attacks and jamming, the dynamic common CC-based approach has been proposed. In this approach, the CC is not fixed for a long period of time and the allocated channel only serves for that time slot duration as the CC. In the next time slot, the CC may change. This type of CC is known as a dynamic CCC [91].
- *NDCC approach* eliminates the requirement of a DCC at the cost of transmission delay. Frequency hopping NDCC (FHNDCC) and rendezvous NDCC (RNDCC) are two different types of CC establishment methods. Frequency hopping and rendezvous NDCC-based MAC protocols mainly differ in the hopping sequences adopted by the CRs. In the FHNDCC-based MAC protocols, the CRs hop across the spectrum bands or frequency channels according to a predefined hopping list [133,134]. The CRs exchange their control information and data once the communicating pair hop to a particular channel in the hopping list. With the RNDCC-based approach for control information exchange, the CRs adopt different hopping sequences that overlap at certain places [135]. Once the overlapping occurs, the CRs exchange their control information through the overlapped channel. The RNDCC-based MAC protocols are much simpler compared to the FHNDCC-based MAC protocols since they do not require network-wide synchronization. The transmission delay in the RNDCC-based MAC protocols can be reduced by properly designing the hopping sequences. Another solution for NDCC establishment is the hybrid scheme which exploits the advantages of frequency hopping and rendezvous approaches. The CRs can adopt the rendezvous approach to find a common channel for initial control information exchange, and after that, they can follow a common hopping sequence as in FHNDCC hopping.

### 13.5.2 DYNAMIC COMMON CONTROL CHANNEL (DCCC)-BASED MAC PROTOCOL FOR CENTRALIZED CRNs

A DCCC-based MAC protocol eliminates the requirement of a dedicated channel for control information exchange which is referred to as the CCC. Due to the dynamic nature of the CCC, this DCCC-MAC protocol is able to withstand CC jamming and attack problems. This DCCC-MAC protocol should have the ability to learn from the surrounding radio environment in an online fashion and select a CCC from the set of in-band PUs' idle channels [91].

To describe a DCCC-MAC protocol, we use the system model described in Fig. 13.12 and assume that each of the CRs is equipped with a single half-duplex transceiver. We assume that due to hardware constraints, the CRs can sense only  $\tilde{K}$  channels out of  $K$  channels.

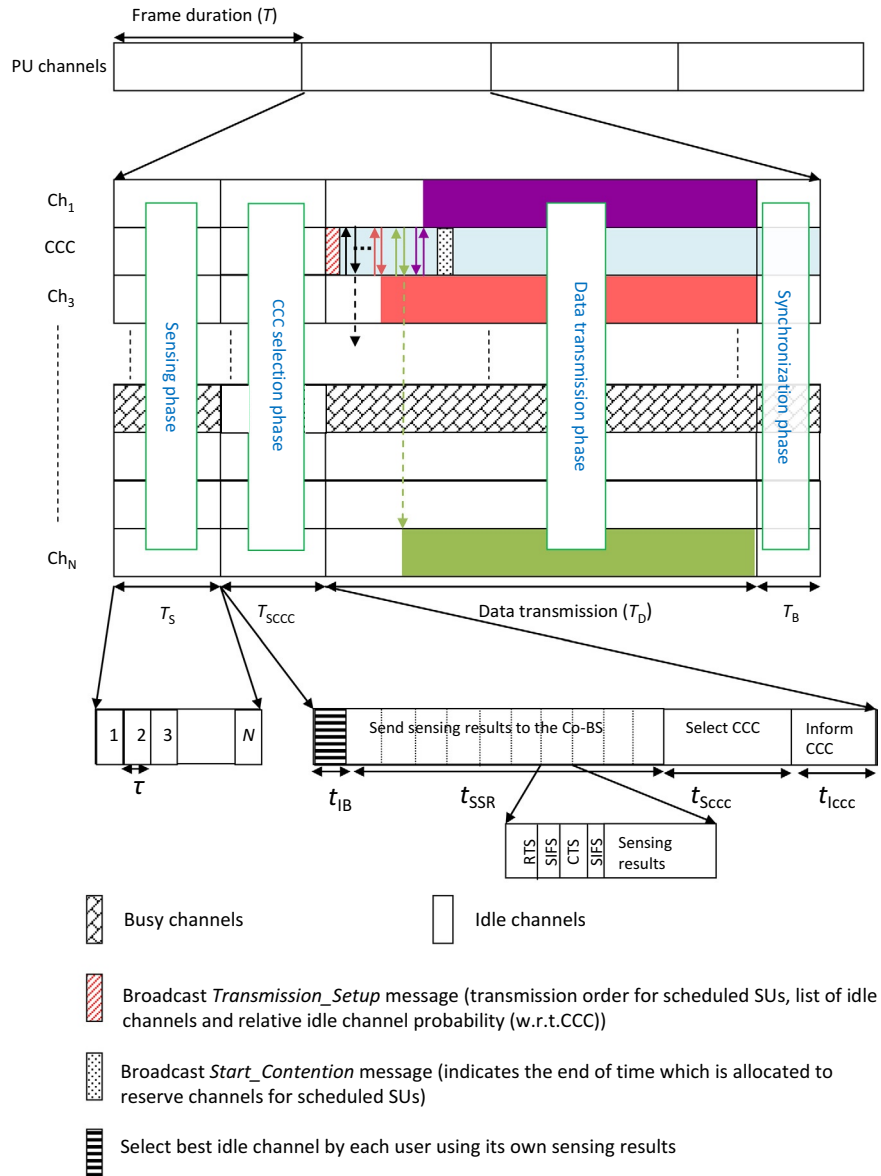
In the DCCC-MAC protocol, the CBS transmits a periodic beacon in all of the idle channels to synchronize the CRs. The beacon period (frame duration) is divided into four phases as shown in Fig. 13.15, and these phases are referred to as the sensing phase, CCC selection phase, data transmission phase, and synchronization phase. The operational flow of each phase is illustrated in the block diagram in Fig. 13.16. In the spectrum sensing phase, the CRs perform fast sensing in a given set of channels. The set of channels required to be sensed in the next frame is provided by the beacon at the end of the beacon period. At the beginning of the CCC selection phase, every CR informs its sensing result to the CBS through the best idle channel. Then, the CCC for the current frame duration is selected by using an SVM-based [60,91] algorithm. The CBS informs the CCC and the list of PUs' idle channels to all CRs by broadcasting in all the PUs' idle channels. The data transmission phase is utilized by the CRs for their communications while the synchronization is achieved by broadcasting a beacon in the synchronization phase. Each phase of the DCCC MAC protocol is presented in detail below.

#### 13.5.2.1 Spectrum sensing phase of the DCCC-MAC protocol

In the DCCC-MAC protocol, the CRs sense only a limited number of channels (eg, due to hardware limitations). In particular, the CRs sense only  $\tilde{K}$  channels out of  $K$  channels at a given frame duration. The list of channels to be sensed is broadcast by the CBS in the beacon at the end of the previous frame duration in the synchronization phase. In the case that a particular CR does not receive this information, that CR selects a random set of  $\tilde{K}$  channels and performs spectrum sensing. Every channel in the list is sensed in sequence by the CRs for a time duration of  $\tau$ . Hence, the received normalized energy at the  $n$ th CR on the  $k$ th channel within duration  $\tau$  is given by Eq. (13.2).

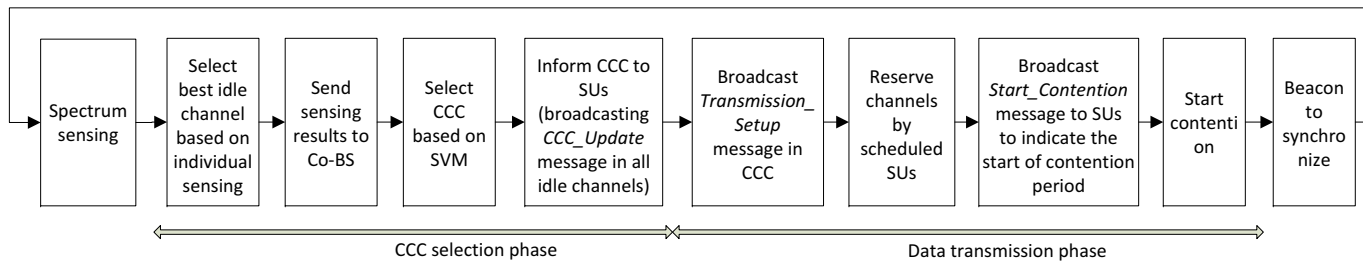
#### 13.5.2.2 CCC selection phase in the DCCC-MAC protocol

In the CCC selection phase, four main functionalities corresponding to CCC selection are executed. At the beginning of the CCC selection phase, every CR selects the best idle channel based on individual sensing and then makes available the sensing result to the CBS via the selected best channel. Then, the CBS selects the CCC for that


**FIG. 13.15**

Frame structure of the DCCC-MAC protocol.

Courtesy: K. Thilina, E. Hossain, DCCC-MAC: a dynamic common control channel-based MAC protocol for cellular cognitive radio networks, *IEEE Trans. Veh. Technol.* (99) (2015) pp. 3597–3613.

**FIG. 13.16**

The operation of the DCCC-MAC protocol.

Courtesy: K. Thilina, E. Hossain, *DCCC-MAC: a dynamic common control channel-based MAC protocol for cellular cognitive radio networks*, *IEEE Trans. Veh. Technol.* (99) (2015) pp. 3597–3613.

frame duration by utilizing an SVM-based cooperative spectrum sensing approach. Finally, the CBS broadcasts the information about the selected CCC and the list of idle channels to the CRs via all the idle channels (ie, outcome of the SVM based cooperative spectrum sensing).

- *Select the best idle channel based on individual sensing:* In the DCCC-MAC protocol, the CRs do not have any dedicated channel for sending the sensing results to the CBS without interfering with the PUs. Therefore, each CR needs to find a channel for sending the sensing result to the CBS. The best option is to select the channel which has the minimum received normalized energy as the candidate channel for the sending purpose. The candidate channel for the  $n$ th CR can be selected as follows:

$$\text{Ch}_{n,\text{best}} = \arg \min\{Y_{n,k}\}, \quad \forall k, \quad (13.42)$$

where  $Y_{n,k}$  is the normalized energy at the  $n$ th CR on the  $k$ th channel. Although  $\text{Ch}_{n,\text{best}}$  is the candidate channel for transmitting the sensing results, there is no guarantee that the PUs will be absent in the selected best channel (ie,  $\text{Ch}_{n,\text{best}}$ ). Therefore, the PUs can be protected from the harmful interference only by transmitting the sensing results if the received energy of the  $\text{Ch}_{n,\text{best}}$  is less than a predefined value  $\delta$  (ie,  $\min\{Y_{n,k}\} < \delta$ ). If  $\min\{Y_{n,k}\} \geq \delta$ , that particular CR does not transmit its sensing result to the CBS.

- *Transmit the sensing results to the CBS:* In the CCC selection phase, the time duration allocated to transmit the sensing results to the CBS is divided into mini-slots (see Fig. 13.15). Each CR transmits its sensing result within a mini-slot duration to the CBS if that CR has not successfully transmitted its sensing result in one of the previous mini-slots. At the beginning of each mini-slot in the CCC selection phase, the CRs transmit request-to-send (RTS) packets to the CBS with some probability. If the CBS receives that RTS without collision, the CBS then sends a clear-to-send (CTS) packet on that channel. Upon receipt of the CTS packet, that particular CR sends its sensing result to the CBS and receives acknowledgement (ACK) within the mini-slot. The transmission of the sensing result within a mini-slot is illustrated in Fig. 13.15. In case of RTS collision, the CRs wait for the next mini-slot to transmit the sensing results until the end of the time duration allocated to send the sensing results of the CRs to the CBS. The time duration allocated for sending sensing results varies from frame to frame based on the number of mini-slots required to send the sensing results from a particular number of CRs to the CBS. The number of mini-slots required to send the sensing results from a particular number of CRs to the CBS varies based on the number of CRs and the number of idle channels in the network [91]. The accuracy of the decision making process (in terms of selection of CCC and the PUs' idle channels) increases with the number of CRs sending sensing results to the CBS.
- *Select CCC:* In the CCC selection process, out of all the available idle channels, the channel which is more likely to be the most reliable idle channel is selected

as the CCC. For this, an SVM-based cooperative spectrum sensing mechanism which is described in Section 13.3.3 can be used. Hence, the CCC for the current time slot can be obtained by using Eq. (13.24) as follows:

$$\text{Ch}_{\text{CCC}} = \arg \min_{k \in \bar{\mathbf{K}}} \left\{ \sum_{l=1}^L \tilde{\lambda}^{(l)} a^{(l)} \kappa(\mathbf{x}_k, \mathbf{y}^{(l)}) + w_0 \right\}. \quad (13.43)$$

At the same time, the CBS can detect the availability of the  $k$ th channel for cognitive transmission as follows:

$$\hat{a}_k = \text{sgn} \left\{ \sum_{l=1}^L \tilde{\lambda}^{(l)} a^{(l)} \kappa(\mathbf{x}_k, \mathbf{y}^{(l)}) + w_0 \right\}, \quad (13.44)$$

where  $\text{sgn}$  is the sign function. If  $\hat{a}_k = 1$ , then the PUs are active on the  $k$ th channel. Otherwise, the PUs are idle on that channel and hence can be allocated to the CRs. Since the estimates  $\hat{a}_k$  are based on cooperative spectrum sensing, they are more reliable than the individual sensing-based estimates.

- *Inform the CCC to the CRs:* After deciding on the CCC, the CBS broadcasts a *CCC\_Update* message in all the idle channels. The CRs receive this update message since they listen to their best idle channels (ie, those determined based on individual sensing) after sending their sensing results. This *CCC\_Update* message only contains the index of the channel which is selected as the CCC for the current frame. Then, the CRs which receive the *CCC\_Update* message tune their radios to the CCC for exchanging control information to obtain a channel reservation.

### 13.5.2.3 Data transmission phase in the DCCC-MAC protocol

In the DCCC-MAC protocol, once the CCC is selected, it is used only for exchanging control information. The remaining time in the data transmission phase is divided into mini-slots in such a way that the mini-slot duration is good enough to send and receive the RTS and CTS messages, respectively. Although the CRs receive the CCC selection information and tune their radio to the CCC, they do not know the PUs' idle channels and CRs' scheduled information to start their communication. Therefore, the CBS broadcasts a *Transmission\_Setup* message containing the list of the scheduled CRs, channel reservation order for scheduled CRs, indices of the idle channels, and the relative channel idle probability with respect to the CCC. The CRs, which send their sensing results to the CBS for cooperative decision making, are treated as scheduled CRs.

The CRs which receive the *Transmission\_Setup* message know their channel reservation order and send the reservation requests in sequence. Therefore, every scheduled CR sends an RTS message with the index of its best available channel to the CBS, which in turn sends a CTS message confirming the reservation. The best available channel for a CR may be decided based on a combination of the

channel quality metric and the relative channel idle probability or any other metric corresponding to channel quality. With an allocation of a channel, every CR updates its possible channel allocation list by removing the index of the allocated channel from the list. This is possible since all the CRs can decode the RTS and CTS messages exchanged through the CCC. Therefore, the CRs know the list of channels currently available for possible allocation. This process continues until the end of scheduled channel reservation period or when all the idle channels have been allocated.

At the end of the scheduled channel reservation period, the CBS broadcasts a *Start\_Contention* message indicating the start of contention for the remaining CRs in the network. Then, the CRs which receive information about the CCC but are not scheduled (ie, the CRs which do not participate in the CCC selection process) start to contend for a channel. However, if all the idle channels are allocated among the scheduled CRs, then all the CRs who receive information about the CCC but are not allocated channels for data transmission have to wait until the next beacon since no more channel allocation is possible. First, the remaining synchronized CRs choose a random backoff value from a closed window  $[0, W - 1]$ , where  $W$  is the maximum size of the contention window. Until its backoff counter expires, the CRs have to listen to the CCC with the intention of updating the list of channels it may possibly access at the time of its channel reservation from the CBS. Once its backoff timer reaches zero, the CR starts the channel reservation process by transmitting an RTS packet with its best channel index. Right after receiving the CTS from the CBS, the CR starts its transmission on the reserved channel until the next beacon is received.

#### **13.5.2.4 Beacon phase in the DCCC-MAC protocol**

Synchronization is essential for the DCCC MAC protocol since it requires choosing the CCC dynamically for every frame or next frame. Therefore, at the end of every frame, the CBS broadcasts a beacon for synchronization in all the PU idle channels. With the beacon, the CBS transmits the list of channels to be sensed in the next frame and the minimum number of mini-slots required for a particular number of CRs to participate in the cooperative decision-making process (ie, to select the CCC channel and detect the idle channels). The number of mini-slots required for a particular number of CRs to cooperate in the CCC selection process and the algorithm for updating list of channels to be sensed in next frame are presented in [91].

---

### **13.6 IN-BAND FULL-DUPLEXING-ENABLED CRNs**

The concept of transmission and reception in the same spectrum band (referred to as in-band full-duplexing (FD) technology) did not seem very promising until very recently. The primary reason of this indifference is the overwhelming nature of the so-called self-interference which is generated by the transmitter to its own collocated receiver. This self-interference is generally assumed to be a fundamental bottleneck in the progress of FD technology [136,137]. Fortunately, with the recent

advancement in antenna, digital baseband, and RF interference-cancellation techniques, self-interference can be reduced close to the level of noise floor in low-power networks. Considering a point-to-point link and perfect self-interference cancellation, theoretically, the spectral efficiency of FD communication is equal to twice the spectral efficiency of half-duplex communication. This makes the FD technology very promising in different wireless communications scenarios, especially in those scenarios with low transmission power and distance requirements.

In half-duplex-based CRNs, the CRs sense the licensed spectrum for a short sensing period and transmit their data using PUs' idle channels during the transmission period. However, since the PU's behavior is random, a PU may become active on the channel which is currently being used by a CR. This change in PU activity on currently utilized transmission channels cannot be immediately detected by the CRs due to the inherent limitation of half-duplex communication. This may cause unexpected interference and delay to PU communication. This problem can be eliminated only by simultaneously sensing and transmitting on the same channel (ie, by using the FD technology).

FD-enabled CRs can operate in either simultaneous transmission-reception mode or simultaneous sensing-transmission mode. These modes offer a tradeoff between spectrum efficiency and spectrum awareness. The sensing-transmission mode increases spectrum awareness (ie, decreases the spectrum efficiency), whereas the transmission-reception mode increases spectrum efficiency (ie, decreases the spectrum awareness). The CRs can operate in the transmission-receiving mode in a spectrum band where the PU activity on that spectrum band is very low. In case of high PU activity, the CRs may need to operate in the sensing-transmission mode. The adaptive mode-switching between the simultaneous sensing-transmission and transmission-reception modes is a research area open for investigation.

---

## 13.7 SUMMARY

The motivations and basic concepts of CR have been discussed. The spectrum management framework is a key element for CNRs, which aims at satisfying the CR users, QoS requirements while protecting the PUs from unexpected interference. Spectrum sensing, spectrum decision, spectrum sharing, and spectrum mobility are the major spectrum management functionalities in CNRs and these have been discussed in detail. Resource allocation and MAC schemes are required for spectrum sharing. The basics of different resource allocation schemes with objectives such as power minimization, spectrum footprint minimization, sum rate maximization, and utility maximization have been illustrated. The main requirements for a cognitive medium access protocol have been discussed and the general framework for designing such a protocol has been illustrated. Finally, the concept of FD-enabled CRs has been introduced.

## REFERENCES

- [1] Federal Communications Commission (FCC), ET Docket No. 02-135, Spectrum policy task force report, Tech. Rep., 2002.
- [2] Federal Communications Commission (FCC), ET Docket No. 02-155, Spectrum policy task force report, Tech. Rep., 2002.
- [3] Federal Communications Commission (FCC), ET Docket No. 03-222, Notice of proposed rule making and order, Tech. Rep., 2003.
- [4] J. Mitola, Cognitive radio: an integrated agent architecture for software define radio, Ph.D. thesis, KTH, 2000.
- [5] E. Hossain, V.K. Bhargava, Cognitive Wireless Communication Networks, Springer, New York, NY, 2007.
- [6] S. Haykin, Cognitive radio: brain-empowered wireless communications, *IEEE J. Sel. Areas Commun.* 23 (2005) 201–220.
- [7] P. Kolotzy, Next generation communications: Kickoff meeting, in: Proceedings of DARPA, 2001.
- [8] I.F. Akyildiz, W.-Y. Lee, M.C. Vuran, S. Mohanty, A survey on spectrum management in cognitive radio networks, *IEEE Commun. Mag.* 46 (4) (2008) 40–48.
- [9] B. Wang, K.J.R. Liu, Advances in cognitive radio networks: a survey, *IEEE J. Sel. Topics Signal Process.* 5 (1) (2011) 5–23.
- [10] IEEE Working Group on Wireless Regional Area Networks, Enabling rural broadband wireless access using cognitive radio technology and spectrum sharing in TV white spaces, Tech. Rep., 2011.
- [11] B.F. Lo, A survey of common control channel design in cognitive radio networks, *Phys. Commun.* 4 (1) (2011) 26–39.
- [12] E. Hossain, D. Niyato, Z. Han, Dynamic Spectrum Access and Management in Cognitive Communication Networks, Cambridge University Press, Cambridge, UK, 2009.
- [13] J.M. Peha, S. Panichpapiboon, Real-time secondary market for spectrum, *Telecommun. Policy* 28 (7–8) (2004) 603–618.
- [14] G. Li, S. Srikanteswara, C. Maciocco, Interference mitigation for WLAN devices using spectrum sensing, in: Proceedings of the Fifth IEEE Consumer Communications and Networking Conference (CCNC), 2008, pp. 958–962.
- [15] Y. Zhao, L. Morales, J. Gaeddert, K.K. Bae, J.-S. Um, J.H. Reed, Applying REMs to cognitive wireless regional area networks, in: Proceedings of the Second IEEE International Symposium on New Frontiers in Dynamic Spectrum Access Networks (DySPAN), 2007, pp. 115–118.
- [16] Y. Zhao, D. Raymond, C. da Silva, J.H. Reed, S.F. Midkiff, Performance evaluation of radio environment map-enabled cognitive spectrum-sharing networks, in: Proceedings of the IEEE Military Communications Conference, 2007, pp. 1–7.
- [17] T. Weiss, J. Hillenbrand, A. Krohn, F.K. Jondral, Mutual interference in OFDM-based spectrum pooling systems, in: Proceedings of the 59th IEEE Vehicular Technology Conference (VTC), vol. 4, 2004, pp. 1873–1877.
- [18] A. Shojaeifard, H. Saki, M.M. Mahyari, M. Shikh-Bahaei, Resource allocation and interference management for adaptive modulation and coding-based OFDMA cognitive radio networks, in: Proceedings of the IEEE International Conference on Communications (ICC), 2014, pp. 5908–5913.
- [19] K. Yamamoto, H. Murata, S. Yoshida, Management of dominant interference in cognitive radio networks, in: Proceedings of the 21st IEEE International Symposium

- on Personal, Indoor and Mobile Radio Communications Workshops (PIMRC), 2010, pp. 451–455.
- [20] S.R. Aryal, H. Dhungana, K. Paudyal, Novel approach for interference management in cognitive radio, in: Proceedings of the Third Asian Himalayas International Conference on Internet (AH-ICI), 2012, pp. 1–5.
  - [21] A. Maharshi, L. Tong, A. Swami, Cross-layer designs of multichannel reservation MAC under Rayleigh fading, *IEEE Trans. Signal Process.* 51 (8) (2003) 2054–2067.
  - [22] G.A. Shah, V.C. Gungor, O.B. Akan, A cross-layer design for QoS support in cognitive radio sensor networks for smart grid applications, in: Proceedings of the IEEE International Conference on Communications (ICC), 2012, pp. 1378–1382.
  - [23] J. Wang, L. Li, S.H. Low, J.C. Doyle, Cross-layer optimization in TCP/IP networks, *IEEE/ACM Trans. Netw.* 13 (3) (2005) 582–595.
  - [24] C. Luo, F.R. Yu, H. Ji, V.C.M. Leung, Cross-layer design for TCP performance improvement in cognitive radio networks, *IEEE Trans. Veh. Technol.* 59 (5) (2010) 2485–2495.
  - [25] B. Van den Bergh, T. Vermeulen, M. Verhelst, S. Pollin, CLAWS: cross-layer adaptable wireless system enabling full cross-layer experimentation on real-time software-defined 802.15.4, *EURASIP J. Wireless Commun. Netw.* 1 (2014) 1–13, <http://dx.doi.org/10.1186/1687-1499-2014-187>.
  - [26] A.G. Fragkiadakis, E.Z. Tragos, I.G. Askoxylakis, A survey on security threats and detection techniques in cognitive radio networks, *IEEE Commun. Surv. Tut.* 15 (1) (2013) 428–445.
  - [27] A. Attar, H. Tang, A.V. Vasilakos, F.R. Yu, V.C.M. Leung, A survey of security challenges in cognitive radio networks: solutions and future research directions, *Proc. IEEE* 100 (12) (2012) 3172–3186.
  - [28] A. Fragkiadakis, V. Siris, N. Petroulakis, Anomaly-based intrusion detection algorithms for wireless networks, in: Proceedings of the Eighth WWIC, 2010.
  - [29] S. Mishra, M. Thamilarasu, R. Sridhar, A cross-layer approach to detect jamming attacks in wireless ad hoc networks, in: Proceedings of the Milcom'06, vol. 12, 2006, pp. 1–7.
  - [30] A. Houjeij, W. Saad, T. Basar, Evading eavesdroppers in adversarial cognitive radio networks, in: Proceedings of the IEEE Global Communications Conference (GLOBECOM), 2013, pp. 611–616.
  - [31] J. Hubaux, M. Raya, I. Aad, Domino: a system to detect greedy behavior in IEEE 802.11 hotspots, in: Proceedings of the MobiSys '04, 2010, pp. 1–8.
  - [32] Z. Jin, S. Anand, K.P. Subbalakshmi, Detecting primary user emulation attacks in dynamic spectrum access networks, in: Proceedings of the IEEE International Conference on Communications (ICC), 2009, pp. 1–5.
  - [33] Y. Liu, P. Ning, H. Dai, Authenticating primary users' signals in cognitive radio networks via integrated cryptographic and wireless link signatures, in: Proceedings of the IEEE Symposium on Security and Privacy (SP), 2010, pp. 286–301.
  - [34] A. Alahmadi, M. Abdelhakim, J. Ren, T. Li, Defense against primary user emulation attacks in cognitive radio networks using advanced encryption standard, *IEEE Trans. Inf. Forensics Security* 9 (5) (2014) 772–781.
  - [35] F.R. Yu, H. Tang, M. Huang, Z. Li, P.C. Mason, Defense against spectrum sensing data falsification attacks in mobile ad hoc networks with cognitive radios, in: Proceedings of the IEEE Military Communications Conference (MILCOM), 2009, pp. 1–7.

- [36] A.W. Min, K.G. Shin, X. Hu, Attack-tolerant distributed sensing for dynamic spectrum access networks, in: *Proceedings of the 17th IEEE International Conference on Network Protocols (ICNP)*, 2009, pp. 294–303.
- [37] Y.E. Sagduyu, Securing cognitive radio networks with dynamic trust against spectrum sensing data falsification, in: *Proceedings of the IEEE Military Communications Conference (MILCOM)*, 2014, pp. 235–241.
- [38] C. Cordeiro, K. Challapali, D. Birru, N. Sai Shankar, IEEE 802.22: the first worldwide wireless standard based on cognitive radios, in: *Proceedings of the First IEEE International Symposium on New Frontiers in Dynamic Spectrum Access Networks (DySPAN)*, 2005, pp. 328–337.
- [39] C. Stevenson, G. Chouinard, Z. Lei, W. Hu, S.J. Shellhammer, W. Caldwell, IEEE 802.22: The first cognitive radio wireless regional area network standard, *IEEE Commun. Mag.* 47 (1) (2009) 130–138.
- [40] O. Leon, J. Hernandez-Serrano, M. Soriano, A new cross-layer attack to TCP in cognitive radio networks, in: *Proceedings of the Second International Workshop on Cross Layer Design (IWCLD '09)*, 2009, pp. 1–5.
- [41] W. Wang, Y. Sun, H. Li, Z. Han, Cross-layer attack and defense in cognitive radio networks, in: *Proceedings of the IEEE Global Telecommunications Conference (GLOBECOM)*, 2010, pp. 1–6.
- [42] O. Aliu, A. Imran, M. Imran, B. Evans, A survey of self organisation in future cellular networks, *IEEE Commun. Surv. Tut.* 15 (2012) 336–361.
- [43] Q. Wang, H. Zheng, Route and spectrum selection in dynamic spectrum networks, in: *Proceedings of the Third IEEE Consumer Communications and Networking Conference (CCNC)*, vol. 1, 2006, pp. 625–629.
- [44] S.M. Dudley, W.C. Headley, M. Lichtman, E.Y. Imana, X. Ma, M. Abdelbar, A. Padaki, A. Ullah, M.M. Sohil, T. Yang, J.H. Reed, Practical Issues for Spectrum Management With Cognitive Radios, *Proc. IEEE* 102 (3) (2014) 242–264.
- [45] IEEE Standard for Information Technology Local Metropolitan Area Networks Specific Requirements, Part 22: cognitive wireless RAN medium access control (MAC) and physical layer (PHY) specifications: policies and procedures for operation in the TV Bands, in: *IEEE Std 802.22-2011*, 2011, pp. 1–680.
- [46] J. Wang, M.S. Song, S. Santhiveeran, K. Lim, G. Ko, K. Kim, S.H. Hwang, M. Ghosh, V. Gaddam, K. Challapali, First cognitive radio networking standard for personal/portable devices in TV white spaces, in: *Proceedings of the IEEE Symposium on New Frontiers in Dynamic Spectrum*, 2010, pp. 1–12.
- [47] K.G. Shin, H. Kim, A.W. Min, A. Kumar, Cognitive radios for dynamic spectrum access: from concept to reality, *IEEE Wireless Commun.* 17 (6) (2010) 64–74.
- [48] D. Wang, D. Evans, R. Krasinski, IEEE 802.15.4J: extend IEEE 802.15.4 radio into the MBAN spectrum [industry perspectives], *IEEE Wireless Commun.* 19 (5) (2012) 4–5.
- [49] IEEE Standard for Local Metropolitan Area Networks, Part 15.4: low-rate wireless personal area networks (LR-WPANs) amendment 4: alternative physical layer extension to support medical body area network (MBAN) services operating in the 2360 MHz 2400 MHz band, in: *IEEE Std 802.15.4j-2013 (Amendment to IEEE Std 802.15.4-2011 as amended by IEEE Std 802.15.4e-2012, IEEE Std 802.15.4f-2012, and IEEE Std 802.15.4g-2012)*, 2013, pp. 1–24.
- [50] T.L. Doumi, Spectrum considerations for public safety in the United States, *IEEE Commun. Mag.* 44 (1) (2006) 30–37.

- [51] N. Jesuale, B.C. Eydt, A policy proposal to enable cognitive radio for public safety and industry in the land mobile radio bands, in: *Proceedings of the Second IEEE International Symposium on New Frontiers in Dynamic Spectrum Access Networks (DySPAN)*, 2007, pp. 66–77.
- [52] U.S. Department of Energy, Communications requirements of smart grid technologies, Tech. Rep., 2010.
- [53] IEEE 802.11 Working Group, Official IEEE 802.11 working group project timelines, Tech. Rep., 2014, [http://grouper.ieee.org/groups/802/11/Reports/802.11\\_Timelines.htm](http://grouper.ieee.org/groups/802/11/Reports/802.11_Timelines.htm), Retrieved Nov. 26, 2014.
- [54] L. Gavrilovska, D. Denkovski, V. Rakovic, M. Angjelichinoski, Medium access control protocols in cognitive radio networks: overview and general classification, *IEEE Commun. Mag.* 16 (4) (2014) 2092–2124.
- [55] K. Challapali, C. Cordeiro, M. Ghosh, Cognitive PHY and MAC layers for dynamic spectrum access and sharing of TV bands, in: *Proceedings of the First International Workshop TAPAS*, Boston, MA, USA, 2006, pp. 1–10.
- [56] H. Kim, K.G. Shin, In-band spectrum sensing in cognitive radio networks: energy detection or feature detection? in: *Proceedings of the 14th ACM International Conference on Mobile Computing and Networking (MobiCom '08)*, 2008, pp. 14–25.
- [57] M. Oner, F. Jondral, On the extraction of the channel allocation information in spectrum pooling systems, *IEEE J. Sel. Areas Commun.* 25 (3) (2007) 558–565.
- [58] W. Han, J. Li, Z. Li, J. Si, Y. Zhang, Efficient soft decision fusion rule in cooperative spectrum sensing, *IEEE Trans. Signal Process.* 61 (8) (2013) 1931–1943.
- [59] J. Ma, Y. Li, Soft combination and detection for cooperative spectrum sensing in cognitive radio networks, in: *Proceedings of the IEEE Global Telecommunications Conference (GLOBECOM '07)*, 2007, pp. 3139–3143.
- [60] K.M. Thilina, K.W. Choi, N. Saquib, E. Hossain, Machine learning techniques for cooperative spectrum sensing in cognitive radio networks, *IEEE J. Sel. Areas Commun.* 31 (11) (2013) 2209–2221.
- [61] K.M. Thilina, K.W. Choi, N. Saquib, E. Hossain, Pattern classification techniques for cooperative spectrum sensing in cognitive radio networks: SVM and W-KNN approaches, in: *Proceedings of the IEEE Global Communications Conference (GLOBECOM)*, 2012, pp. 1260–1265.
- [62] W. Gabran, P. Pawelczak, D. Cabric, Throughput and collision analysis of multichannel multistage spectrum sensing algorithms, *IEEE Trans. Veh. Technol.* 60 (7) (2011) 3309–3323.
- [63] Z. Zhang, H. Jiang, P. Tan, J. Slevinsky, Channel exploration and exploitation with imperfect spectrum sensing in cognitive radio networks, *IEEE J. Sel. Areas Commun.* 31 (3) (2013) 429–441.
- [64] L. Wang, X. Chen, Z. Zhao, H. Zhang, Exploration vs exploitation for distributed channel access in cognitive radio networks: a multi-user case study, in: *Proceedings of the 11th International Symposium on Communications and Information Technologies (ISCIT)*, 2011, pp. 360–365.
- [65] M. Bkassiny, S.K. Jayaweera, Y. Li, K.A. Avery, Optimal and low-complexity algorithms for dynamic spectrum access in centralized cognitive radio networks with fading channels, in: *Proceedings of the 73rd IEEE Vehicular Technology Conference (VTC)*, 2011, pp. 1–5.

- [66] Z. Khan, J.J. Lehtomaki, L.A. DaSilva, M. Latva-aho, Autonomous sensing order selection strategies exploiting channel access information, *IEEE Trans. Mobile Comput.* 12 (2) (2013) 274–288.
- [67] S. Lim, T.-J. Lee, A self-scheduling multi-channel cognitive radio MAC protocol based on cooperative communications, *IEICE Trans. Commun.* 94-B (6) (2011) 1657–1668.
- [68] D. Hu, S. Mao, A sensing error aware MAC protocol for cognitive radio networks, *ICST Trans. Mobile Commun. Appl.* 12 (7-9) (2012) 1–22.
- [69] B. Canberk, I.F. Akyildiz, S. Oktug, Primary user activity modeling using first-difference filter clustering and correlation in cognitive radio networks, *IEEE/ACM Trans. Netw.* 19 (1) (2011) 170–183.
- [70] M.T. Masonta, M. Mzyece, N. Ntlatlapa, Spectrum decision in cognitive radio networks: a survey, *IEEE Commun. Surv. Tut.* 15 (3) (2013) 1088–1107.
- [71] S. Pollin, M. Hoyhtya, A. Mammela, Improving the performance of cognitive radios through classification, learning, and predictive channel selection, *Adv. Electron. Telecommun.* 2 (4) (2011) 28–38.
- [72] A. Azarfar, J.-F. Frigon, B. Sanso, Improving the reliability of wireless networks using cognitive radios, *IEEE Commun. Surv. Tut.* 14 (2) (2012) 338–354.
- [73] D. Xu, E. Jung, X. Liu, Optimal bandwidth selection in multi-channel cognitive radio networks: how much is too much? in: *Proceedings of the 3rd IEEE Symposium on New Frontiers in Dynamic Spectrum Access Networks (DySPAN)*, 2008, pp. 1–11.
- [74] H. Bogucka, A.M. Wyglinski, S. Pagadarai, A. Kliks, Spectrally agile multicarrier waveforms for opportunistic wireless access, *IEEE Commun. Mag.* 49 (6) (2011) 108–115.
- [75] S.M. Almalfouh, G.L. Stuber, Interference-aware radio resource allocation in OFDMA-based cognitive radio networks, *IEEE Trans. Veh. Technol.* 60 (4) (2011) 1699–1713.
- [76] M. Amir, A. El-Keyi, M. Nafie, Constrained interference alignment and the spatial degrees of freedom of MIMO cognitive networks, *IEEE Trans. Inform. Theory* 57 (5) (2011) 2994–3004.
- [77] R. Chandra, T. Moscibroda, Y. Yuan, P. Bahl, Y. Wu, Allocating dynamic time-spectrum blocks in cognitive radio networks, in: *Proceedings of the ACM International Symposium on Mobile Ad Hoc Networking and Computing Wireless Communications and Networking Conference*, 2007.
- [78] V. Pla, J.-R. Vidal, J. Martinez-Bauset, L. Guijarro, Modeling and characterization of spectrum white spaces for underlay cognitive radio networks, in: *Proceedings of the IEEE International Conference on Communications (ICC)*, 2010, pp. 1–5.
- [79] K.G.M. Thilina, E. Hossain, Optimal-switching adaptive modulation for multiuser relay networks with feedback delays, *IEEE Trans. Wireless Commun.* 12 (8) (2013) 3682–3695.
- [80] M. Mustonen, H. Sarvanko, A. Hekkala, M. Katz, A. Mammela, M. Kiviranta, M. Matinmikko, M. Hoyhtya, A. Kautio, Cognitive radio: an intelligent wireless communication system, *Tech. Rep.*, 2008.
- [81] W.-Y. Lee, I.F. Akyildiz, A spectrum decision framework for cognitive radio networks, *IEEE Trans. Mobile Comput.* 10 (2) (2011) 161–174.
- [82] J. Riihijarvi, P. Mahonen, M. Wellens, M. Gordziel, Characterization and modelling of spectrum for dynamic spectrum access with spatial statistics and random fields, in: *Proceedings of the IEEE 19th International Symposium on Personal, Indoor and Mobile Radio Communications (PIMRC)*, 2008, pp. 1–6.

- [83] K. Tsagkaris, K. Demestichas, P. Demestichas, G. Dimitrakopoulos, J. Adamopoulou, Reconfigurations selection in cognitive, beyond 3G, radio infrastructures, in: *Proceedings of the International Conference on Cognitive Radio Oriented Wireless Networks and Communications (CROWNCOM)*, Mykonos Island, Greece, 2006.
- [84] I. Malanchini, M. Cesana, N. Gatti, On spectrum selection games in cognitive radio networks, in: *Proceedings of the IEEE Global Telecommunications Conference (GLOBECOM)*, 2009, pp. 1–7.
- [85] I.F. Akyildiz, W.-Y. Lee, K.R. Chowdhury, CRAHNS: cognitive radio ad hoc networks, *J. Ad Hoc Netw.* 7 (2009) 810–826.
- [86] A.T. Hoang, Y.-C. Liang, A two-phase channel and power allocation scheme for cognitive radio networks, in: *Proceedings of the IEEE 17th International Symposium on Personal, Indoor and Mobile Radio Communications*, 2006, pp. 1–5.
- [87] M. Uddin, P. Kaur, A. Khosla, Adaptive bandwidth allocation scheme for cognitive radios *Int. J. Adv. Comput. Technol.* 2 (4) (2010) 35–41.
- [88] Q. Liang, S. Han, F. Yang, G. Sun, X. Wang, A distributed-centralized scheme for short- and long-term spectrum sharing with a random leader in cognitive radio networks, *IEEE J. Sel. Areas Commun.* 30 (11) (2012) 2274–2284.
- [89] K.B. Shashika Manosha, N. Rajatheva, M. Latva-aho, Overlay/underlay spectrum sharing for multi-operator environment in cognitive radio networks, in: *Proceedings of the 73rd IEEE Vehicular Technology Conference (VTC)*, 2011, pp. 1–5.
- [90] Q. Zhao, L. Tong, A. Swami, Y. Chen, Decentralized cognitive MAC for opportunistic spectrum access in ad hoc networks: a POMDP framework, *IEEE J. Sel. Areas Commun.* 25 (3) (2007) 589–600.
- [91] K. Thilina, E. Hossain, DCCC-MAC: a dynamic common control channel-based MAC protocol for cellular cognitive radio networks, *IEEE Trans. Veh. Technol.* (99) (2015) 3597–3613.
- [92] H.A. Bany Salameh, M. Krunz, O. Younis, Cooperative adaptive spectrum sharing in cognitive radio networks, *IEEE/ACM Trans. Netw.* 18 (4) (2010) 1181–1194.
- [93] H. Zheng, L. Cao, Device-centric spectrum management, in: *Proceedings of the First IEEE International Symposium on New Frontiers in Dynamic Spectrum Access Networks (DySPAN)*, 2005, pp. 56–65.
- [94] A. Attar, M.R. Nakhai, A.H. Aghvami, Cognitive radio game for secondary spectrum access problem, *IEEE Trans. Wireless Commun.* 8 (4) (2009) 2121–2131.
- [95] Z. Khan, S. Glisic, L.A. DaSilva, J. Lehtomaki, Modeling the dynamics of coalition formation games for cooperative spectrum sharing in an interference channel, *IEEE Trans. Comput. Intell. AI Games* 3 (1) (2011) 17–30.
- [96] D. Wilcox, E. Tsakalaki, A. Kortun, T. Ratnarajah, C.B. Papadias, M. Sellathurai, On spatial domain cognitive radio using single-radio parasitic antenna arrays, *IEEE J. Sel. Areas Commun.* 31 (3) (2013) 571–580.
- [97] I. Christian, S. Moh, I. Chung, J. Lee, Spectrum mobility in cognitive radio networks, *IEEE Commun. Mag.* 50 (6) (2012) 114–121.
- [98] T. Yucek, H. Arslan, A survey of spectrum sensing algorithms for cognitive radio applications, *IEEE Commun. Surv. Tut.* 11 (1) (2009) 116–130.
- [99] J. Dong, H. Liu, X. Wu, Spectrum sensing techniques in practical cognitive radio applications, in: *Proceedings of the 12th IEEE International Conference on Communication Technology (ICCT)*, 2010, pp. 293–296.
- [100] S. Atapattu, C. Tellambura, H. Jiang, Energy detection based cooperative spectrum sensing in cognitive radio networks, *IEEE Trans. Wireless Commun.* 10 (4) (2011) 1232–1241.

- [101] J. Unnikrishnan, V.V. Veeravalli, Cooperative sensing for primary detection in cognitive radio, *IEEE J. Sel. Topics Signal Process.* 2 (1) (2008) 18–27.
- [102] E.C.Y. Peh, Y.-C. Liang, Y.L. Guan, Y. Zeng, Optimization of cooperative sensing in cognitive radio networks: a sensing-throughput tradeoff view, *IEEE Trans. Veh. Technol.* 58 (9) (2009) 5294–5299.
- [103] J. Ma, G. Zhao, Y. Li, Soft combination and detection for cooperative spectrum sensing in cognitive radio networks, *IEEE Trans. Wireless Commun.* 7 (11) (2008) 4502–4507.
- [104] A.M. Aziz, A.M. ElBakly, M.H.A. Azeem, G.A. Hamid, A new soft-fusion approach for multiple-receiver wireless communication systems, *ETRI J.* 33 (3) (2011) 310–319.
- [105] K.W. Choi, E. Hossain, D.I. Kim, Cooperative spectrum sensing under a random geometric primary user network model, *IEEE Trans. Wireless Commun.* 10 (6) (2011) 1932–1944.
- [106] C. Cortes, V. Vapnik, Support-vector networks, *Mach. Learn.* 20 (3) (1995) 273–297.
- [107] J.S. Taylor, N. Cristianini, *Kernel Methods for Pattern Analysis*, Cambridge University Press, Cambridge, UK, 2004.
- [108] S. Grimoud, B. Sayrac, S. Ben Jemaa, E. Moulines, An algorithm for fast REM construction, in: *Proceedings of the 2011 Sixth International ICST Conference on Cognitive Radio Oriented Wireless Networks and Communications (CROWNCOM)*, 2011, pp. 251–255.
- [109] K. Thilina, E. Hossain, M. Moghadari, Cellular OFDMA cognitive radio networks: generalized spectral footprint minimization, *IEEE Trans. Veh. Technol.* PP (99) (2014) 1–1.
- [110] M. Naeem, A. Anpalagan, M. Jaseemuddin, D.C. Lee, Resource allocation techniques in cooperative cognitive radio networks, *IEEE Commun. Surv. Tut.* 16 (2) (2014) 729–744.
- [111] P. Li, S. Guo, W. Zhuang, B. Ye, On efficient resource allocation for cognitive and cooperative communications, *IEEE J. Sel. Areas Commun.* 32 (2) (2014) 264–273.
- [112] Q. Qi, A. Minturn, Y. Yang, An efficient water-filling algorithm for power allocation in OFDM-based cognitive radio systems, in: *Proceedings of the International Conference on Systems and Informatics (ICSAI)*, 2012, pp. 2069–2073.
- [113] L.B. Le, E. Hossain, Resource allocation for spectrum underlay in cognitive radio networks, *IEEE Trans. Wireless Commun.* 7 (12) (2008) 5306–5315.
- [114] L.B. Le, P. Mitran, C. Rosenberg, Queue-aware subchannel and power allocation for downlink OFDM-based cognitive radio networks, in: *Proceedings of the IEEE Wireless Communications and Networking Conference (WCNC)*, 2009, pp. 1–6.
- [115] Y. Tachwali, B.F. Lo, I.F. Akyildiz, R. Agusti, Multiuser resource allocation optimization using bandwidth-power product in cognitive radio networks, *IEEE J. Sel. Areas Commun.* 31 (3) (2013) 451–463.
- [116] Y. Zhao, D. Raymond, C. da Silva, J.H. Reed, S.F. Midkiff, Performance evaluation of radio environment map-enabled cognitive spectrum-sharing networks, in: *Proceedings of the IEEE Military Communications Conference (MILCOM)*, 2007, pp. 1–7.
- [117] S. Sadr, A. Anpalagan, K. Raahemifar, Radio resource allocation algorithms for the downlink of multiuser OFDM communication systems, *IEEE Commun. Surv. Tut.* 11 (3) (2009) 92–106.

- [118] D.T. Ngo, C. Tellambura, H.H. Nguyen, Resource allocation for OFDMA-based cognitive radio multicast networks with primary user activity consideration, *IEEE Trans. Veh. Technol.* 59 (4) (2010) 1668–1679.
- [119] L. Zheng, C.W. Tan, Maximizing sum rates in cognitive radio networks: convex relaxation and global optimization algorithms, *IEEE J. Sel. Areas Commun.* 32 (3) (2014) 667–680.
- [120] F.P. Kelly, Charging and rate control for elastic traffic, *Eur. Trans. Telecommun.* 8 (1997) 33–37.
- [121] O. El Ferkouss, W. Ajib, Game theory based resource allocation for cognitive radio networks, in: *Proceedings of the IEEE Global Communications Conference (GLOBE-COM)*, 2012, pp. 1174–1179.
- [122] K.B. Shashika Manosha, N. Rajatheva, Joint power and rate control for spectrum underlay in cognitive radio networks with a novel pricing scheme, in: *Proceedings of the 72nd IEEE Vehicular Technology Conference Fall (VTC)*, 2010, 2010, pp. 1–5.
- [123] K. Akkarajitsakul, E. Hossain, D. Niyato, Distributed resource allocation in wireless networks under uncertainty and application of Bayesian game, *IEEE Commun. Mag.* 49 (8) (2011) 120–127.
- [124] D.P. Palomar, M. Chiang, A tutorial on decomposition methods for network utility maximization, *IEEE J. Sel. Areas Commun.* 24 (8) (2006) 1439–1451.
- [125] Z. Jian, Z. Qi, A novel adaptive resource allocation algorithm for multiuser OFDM-based cognitive radio systems, in: *Proceedings of the International Conference on Network Computing and Information Security (NCIS)*, vol. 2, 2011, pp. 442–445.
- [126] H.W. Kuhn, The Hungarian method for the assignment problem, *Nav. Res. Log. Q.* 2 (1955) 83–97.
- [127] C.Y. Wong, R.S. Cheng, K.B. Lataief, R.D. Murch, Multiuser OFDM with adaptive subcarrier, bit, and power allocation, *IEEE J. Sel. Areas Commun.* 17 (10) (1999) 1747–1758.
- [128] T.V. Krishna, A. Das, A survey on MAC protocols in OSA networks, *J. Comput. Netw.* 53 (9) (2009) 214–218.
- [129] P. Ren, Y. Wang, Q. Du, J. Xu, A survey on dynamic spectrum access protocols for distributed cognitive wireless networks, *EURASIP J. Wireless Commun. Netw.* 2012 (2012) 60.
- [130] A. De Domenico, E.C. Strinati, M. Di Benedetto, A survey on MAC strategies for cognitive radio networks, *IEEE Commun. Surv. Tut.* 14 (1) (2012) 21–44.
- [131] K.R. Chowdhury, I.F. Akyldiz, OFDM-based common control channel design for cognitive radio ad hoc networks, *IEEE Trans. Mobile Comput.* 10 (2) (2011) 228–238.
- [132] T. Chen, M. Matinmikko, H. Zhang, A novel control channel management in CogMesh networks, in: *Proceedings of the IEEE Vehicular Technology Conference (VTC)*, 2011, pp. 1–6.
- [133] K. Bian, J.-M. Park, R. Chen, Control channel establishment in cognitive radio networks using channel hopping, *IEEE J. Sel. Areas Commun.* 29 (4) (2011) 689–703.
- [134] G.Y. Chang, W.-H. Teng, H.-Y. Chen, J.-P. Sheu, Novel channel-hopping schemes for cognitive radio networks, *IEEE Trans. Mobile Comput.* 13 (2) (2014) 407–421.

- [135] N.C. Theis, R.W. Thomas, L.A. DaSilva, Rendezvous for cognitive radios, *IEEE Trans. Mobile Comput.* 10 (2) (2011) 216–227.
- [136] E. Hossain, K.M. Thilina, H. Tabassum, D.I. Kim, Medium access control design for full-duplex wireless systems: challenges and approaches, *IEEE Commun. Mag.* 53 (5) (2015) 112–120.
- [137] M. Duarte, C. Dick, A. Sabharwal, Experiment-driven characterization of full-duplex wireless systems, *IEEE Trans. Wireless Commun.* 11 (12) (2012) 4296–4307.

# Digital wireline transmission standards 14

**S. Gorshe**

*PMC-Sierra, Portland, OR, United States*

## CHAPTER OUTLINE

<b>14.1 Introduction—Why Do We Need Standards for Wireline Networks?</b>	<b>524</b>
14.1.1 Historical Background	525
14.1.2 Summary of the Different Types of Standards Bodies	531
<b>14.2 Carrier Network Wireline Interface Standards</b>	<b>531</b>
14.2.1 ITU-T International Standards	532
14.2.2 Important Regional SDOs	537
14.2.3 The 19xx Standards Working Groups of IEEE Communications Society	541
<b>14.3 Data Network Wireline Interconnection Standards</b>	<b>541</b>
14.3.1 IEEE 802.1—Higher Layer LAN Protocols Working Group	541
14.3.2 IEEE 802.3—Ethernet Working Group	544
14.3.3 IEEE 1588 Precise Networked Clock Synchronization Working Group	546
14.3.4 INCITS T11 Fiber Channel	547
<b>14.4 Industry Forums</b>	<b>547</b>
14.4.1 Broadband Forum	548
14.4.2 Optical Internetworking Forum (OIF)	548
14.4.3 Metro Ethernet Forum (MEF)	550
<b>14.5 Important Industry Consortia</b>	<b>551</b>
14.5.1 Full-Service Access Network (FSAN) Consortium	553
14.5.2 Common Public Radio Interface (CPRI) Corporation	553
14.5.3 Open Base Station Architecture Initiative (OBSAI) Consortium	554
14.5.4 Ethernet Alliance (EA) Consortium	554
14.5.5 Wireline Networks for Wireless Fronthaul/Backhaul	554
<b>14.6 Other Significant Groups</b>	<b>555</b>
14.6.1 CableLabs and DOCSIS	556
14.6.2 Telecommunications Industry Association (TIA)	556
<b>14.7 Conclusions</b>	<b>556</b>
<b>References</b>	<b>558</b>
<b>Web Sites for Further Reading</b>	<b>558</b>

### 14.1 INTRODUCTION—WHY DO WE NEED STANDARDS FOR WIRELINE NETWORKS?

Wireline standards specify everything needed for two entities to be able to interconnect and interoperate across a copper or optical wireline link. These standards cover a range of applications including the interconnecting of different networks, equipment interconnections, and even interconnections between integrated circuits that are part of the ecosystem of the telecom or datacom networks or systems. Standards for wireline interconnectivity have largely been developed along four parallel tracks, which have become increasingly interdependent:

1. interconnection between and within public telecommunications carriers;
2. local area network (LAN) connections between computers and other equipments in business, home, and other localized environments;
3. interconnection of user networks and equipment to carrier networks for wide-area networks (WAN); and
4. device and infrastructure development that supports the prior three areas.

The intention of this chapter is to give the reader an introduction to several important wireline standards organizations and the nature and scope of their work. Fig. 14.1 illustrates the scope of wireline standards within the context of the 7-Layer OSI protocol stack, with the relative scope of some of the important wireline standards organizations discussed in this chapter. It is important to understand

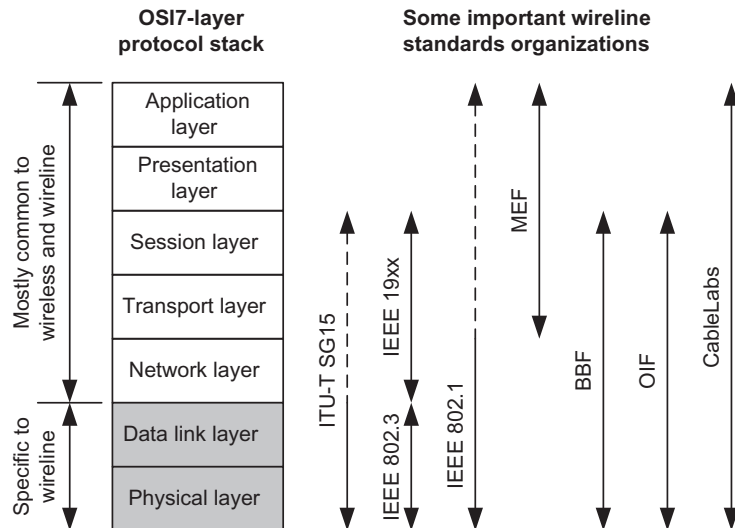


FIG. 14.1

Relationship of wireline standards and standards organizations to the OSI protocol model.

that wireline standards and wireless standards increasingly influence each other. For example, methods pioneered for digital subscriber line (DSL) (eg, bit-loading and dynamic spectrum management) are being adopted for wireless standards. As another example, the same medium access control (MAC) protocol was specified for both the Institute for Electrical and Electronics Engineers (IEEE) 802.16 WiMAX wireless networks and the data-over-cable service interface specification (DOCSIS) for cable TV networks. Orthogonal frequency division multiplexing (OFDM) is increasingly used in both wireless and wireline networks. As yet another example, the International Telecommunications Union—Telecommunication Standardization Sector (ITU-T) is working on a standard for carrying radio signals over fiber optic access networks. Beyond these cases of technology and protocol cross-pollination, there are important implications of the wireline standards to wireless networks that will be noted during the discussions of this chapter.

The chapter begins with some historical context regarding the appearance and evolution of the different standards bodies for the interested reader. The remainder of the chapter focuses on a brief description of different wireline standards organizations. Rather than attempting a comprehensive list, the emphasis is on ones of particular importance at the present time and the foreseeable future. Important interactions between some of the organizations are also described.

### 14.1.1 HISTORICAL BACKGROUND

Historically there were relatively few wireline standards organizations prior to the 1980s. The public telecommunications networks were dominated by government-owned or authorized carriers who defined their own standards, and LAN was limited to single vendor deployments of equipment from a small number of major computer companies. Standards development organizations (SDOs) grew as the need for them appeared, both for wide-area public interconnectivity and local area connections. The need was typically driven by the desire for ease of connectivity between entities and the desire for the advantages of increased competition and volumes of scale. The reader who is not interested in the history can jump ahead to [Section 14.1.2](#) for the description of the different types of standards bodies. However, the following two paragraphs on legal considerations are worth bearing in mind.

One of the key considerations for any SDO is that it does not violate antitrust laws by either intentionally or accidentally shutting out competitors from the standards process and hence hindering the competitors in the subsequent markets making use of these standards. Different bodies have taken somewhat different approaches to protect against this possibility, but most follow the following general set of principles. All interested corporations are allowed to become members, and in many cases the dues are based in part on the corporate revenue so that small companies can also participate. All decisions are made by consensus, if possible, but procedures are in place to ensure that dissenting companies have an opportunity to make the case for their positions, both during the discussions and in the ballot process for the standard. Discussions of cost and price are strictly forbidden so that there is no possibility for

collaborative price fixing. Note that industry consortiums do not always allow open membership; however, they typically do not produce standards of a nature that would shut nonmembers out of a market.

Another legal requirement addressed by each SDO is allowing all members access to the patented intellectual property that is required to implement the standard. The typical approach is to require every member to make all of their patents associated with a standard either available to all companies royalty-free, or to make them available on reasonable and nondiscriminatory (RAND) terms, such that the existence of a patent would not prevent another company from implementing the standard. Some SDOs require all member companies with a relevant patent or pending patent to announce it in advance of the standard going to ballot. Others allow the option for a member company to sign a blanket agreement that covers all current and future patents owned by the company that may be relevant to that SDO's standards rather than announcing them on a per-patent basis.

#### ***14.1.1.1 Public wide-area network (WAN) wireline standards***

Prior to the 1980s, the telephone network carriers within each country were typically owned by their national governments, and they had their own interconnection specifications. The United States and Canada took the approach of having private corporations own and operate telephone networks, but with government oversight at both the national and the state/provincial levels. Each of these North American carriers had a guaranteed and regulated monopoly for providing telephone service within their operating regions. This situation led to a number of different national and regional technologies and interface specifications. As the networks grew in size and importance, it became increasingly critical to have standards for interconnecting the different national networks. The primary focus of the telephone networks was voice, with data traffic beginning to become important in the late 1970s through modems that transmitted data signals over voice channels. The growing use of digital rather than analog signals for voice and data increased the need for standardized digitization, signal, and multiplexing formats.

The variety of local telephone network specifications meant that equipment vendors needed to make different equipment or versions of their equipment for each local or regional market. Standards that applied across wider regions reduced the development costs associated with the different equipment and allowed more economy of scale in manufacturing the equipment. Having common equipment types also allows for increased competition, which further brings down the equipment costs for the carriers. Common equipment and interface standards also greatly simplify the network management for the carriers. It is important to note that the ongoing cost of operating, administering, and maintaining their networks (ie, operational expense, or OPEX) is much more significant than the capital expense of the equipment (CAPEX) for carriers.

The first international body was the CCITT (International Telephone and Telegraph Consultative Committee, with the initials following the French version of the name). While the organization dates back to 1865 and telegraph standards, it began its

involvement in telephone network standards in 1925. It officially became the CCITT in 1956 when two subgroups merged. Since 1947, it has been a special agency of the United Nations, and it is now known as the ITU-T. Headquartered in Geneva, Switzerland, it has become the principal organization for global telecommunications network standards. The ITU-T produces standards, which they call “recommendations,” for both voice and data connectivity over public WANs, with a focus on public carriers.

In the United States, AT&T had operated roughly 90% of the telephone networks up to 1984. Consequently, the US “standards” for interconnection, and by default the Canadian ones as well, were a matter of what AT&T published as a technical requirement (TR) or a PUB (compatibility requirements publication) that specified what was needed to connect to the AT&T network. Beginning in 1984, the US Government required AT&T to go through divestiture, where its local service was divided into seven Regional Bell Operating Companies (RBOCs), with the long distance and equipment portions of the company remaining within AT&T. The Exchange Carrier Standards Association (ECSA) was then charged with creating US telecommunications standards under its new American National Standards Institute (ANSI)-accredited Committee T1. Subcommittee T1X1 was responsible for layer 1 network-network interface (NNI) carrier connection standards, and T1E1 (originally T1C1) was responsible for user-network interface (UNI). Other Committee T1 groups addressed other topics including exchanging call routing information and network management. As the scope of ECSA evolved, it changed its name to Alliance for Telecommunications Industry Solutions (ATIS) and decided to change the names of its then well-known subcommittees. T1X1 became OPTXS and T1E1 became NIPP, and both were finally merged to create Copper/Optical Access and Synchronization and Transport (COAST) Committee. Canadian carriers have always participated as members in the ECSA and ATIS organizations. As will be explained below, beginning in the 1990s, other SDOs sprouted in North America to address topics not being addressed by ATIS.

While AT&T’s Bell Labs was unquestionably a world leader in innovation, business considerations dictated that new innovations were introduced into their networks at a pace that allowed a return on the investment in the previous generation of technology. The AT&T divestiture allowed other equipment manufacturers to innovate and compete by driving and implementing new standards. The result was an explosion of new ideas and an accelerated pace of their introduction into the network. This was especially true for optical network standards. So, while the dismantling of Bell Labs’ protected environment for creating new innovations was a loss to the telecommunications community in some ways, the doors it opened for others to innovate more than offset this loss.

The opening of markets and the new innovations in the United States prompted many other governments around the world to deregulate or privatize their own telecommunications carriers, which led to a further opening of global markets for new innovations from many different vendors. All of this led to standards becoming increasingly important. In 1998, the European governments created the European

Telecommunications Standards Institute (ETSI) in order to create common standards for the interconnection between European nations and allow equipment vendors to build equipment that was not unique to each country. Japan also had its own national body, and China launched its China Communications Standards Association (CCSA) to create and promote standards most useful to China.

In time, however, each of the regional bodies, including ATIS, ETSI, and CCSA, became convinced that international standards were generally more valuable than regional ones. Each then shifted its focus to aiding their regional input to the ITU-T, and their own standards were only defined in areas that were either outside the focus of the ITU-T or were required for some national or region-specific context. As a special agency of the United Nations, the primary members of the ITU-T are the nation states. For many years, the US State Department required all national positions to be approved by, and US company contributions be reviewed by, recognized US standards bodies with the appropriate expertise. In most cases, this fell within the domain of ECSA/ATIS. Recently, this requirement has been relaxed for company contributions. Consequently, in December 2014 ATIS officially sunsetted all of the COAST committees, except the one working on network synchronization.

During the explosive growth of the Internet and carrier networks during the 1990s, carriers and equipment vendors became concerned that the traditional SDOs (eg, ITU-T, ATIS, ETSI) could not move quickly enough to create the standards required for new technology. The time frames of these SDOs were tailored to creating new standards when the technology and applications were reasonably stable, so that they would not become prematurely obsolete or irrelevant. Their processes were also tailored to rigorously account for the legal concerns discussed above. The drawback to this more deliberative approach was that equipment vendors often came out with different nonstandard or prestandard implementations of new technology and services that were not interoperable. Since carriers did not want to lock themselves into proprietary solutions from a single vendor, they pushed for the creation of more nimble industry forums. The forums were structured to adopt specifications and agreements for interworking on a more rapid time frame. The forums also allowed filling in other pieces of the ecosystem that were not being addressed by other SDOs. For example, the focus of some traditional SDOs was limited to interface specifications that allowed different vendor equipment to interconnect and interwork. Examples of the early forums were the SONET Interworking Forum, ATM Forum, and DSL Forum. As traditional SDOs revamped and streamlined their processes for more rapid standardization, the forums began focusing more on the ecosystem rather than early versions of the items being discussed in the other SDOs. For example, the Optical Internetworking Forum has led the way on defining the interfaces between chips and between printed circuits boards over a backplane within telecommunications systems. Their Common Electrical Interface (CEI) specifications are commonly adopted by other SDOs as the basis for their new intrasystem interface technologies. Several types of important and active forums are discussed below.

Another type of organization that functions somewhat like an SDO is an industry consortium. An industry consortium is a group of companies that work together to define common interface or equipment standards in order to provide new features or interoperation of new services. One example is the Full-Service Access Network (FSAN) consortium that has done much of the work defining new optical access networks (OANs). Another example is the Common Public Radio Interface (CPRI) consortium that has defined interfaces between wireless network base stations and the remote radio transmitters subtended from the base stations.

For completeness, it should also be mentioned that in the AT&T divestiture, part of Bell Labs was set aside as a new corporation called Bellcore. Bellcore was jointly owned by the seven RBOCs, and it performed many of the functions that Bell Labs had done for the local exchange carriers prior to divestiture. One of these functions was helping guide the RBOC input into ATIS and ITU-T, and in some cases directly defining network/equipment interfaces that would be internal to a carrier's network rather than between different carrier networks. Examples of such interface are ring networks optimized for metro/access applications, and the interfaces between central office (CO) switching equipment and remote multiplexing terminals closer to the subscriber. Over time, as this wireline standards work has evolved, Bellcore became Telcordia and was subsequently divided and sold to other entities. Consequently, Bellcore/Telcordia is not discussed below.

#### ***14.1.1.2 Local area network (LAN) wireline standards***

Computer data connections were initially proprietary links, largely between terminals and large mainframe computers, or between clusters of workstations or mini-computers. Remote connections used modem links over voice channels of the telephone network. Computer-to-computer connections were initially proprietary, but standardized protocols were driven by the US Government's Advanced Research Projects Agency (ARPA). The ARPA projects led a collaborative effort among the government, private industry, and universities to develop the Internet Protocol (IP) and Transmission Control Protocol (TCP) standards during the 1970s that launched the Internet. Internet standards work continues in the Internet Engineering Task Force (IETF). Since the IETF work focus is nearly always above Layer 1, it is not discussed further in this chapter.

Standardized LANs for computers came on the scene somewhat later. Ethernet was initially developed at the Xerox Palo Alto Research Center (PARC), and it was subsequently brought to the IEEE to become a public standard in 1981. IEEE 802.3 is responsible for Ethernet standards, while 802.1 is responsible for LAN bridge applications that are using Ethernet or interconnecting different IEEE 802 networks. Other LAN standards were developed for specific applications in other IEEE 802 groups and non-IEEE groups. For example, the International Committee for Information Technology Standards (INCITS) Committee T11 (INCITS group responsible for fiber channel [FC]) developed the FC standard as a method for ultra-reliable connections within enterprise data centers, both between computers

and between computers and disk storage systems, and subsequently for connecting computer centers across WANs.

Ethernet has become the dominant LAN technology due to its relatively low cost and the “plug-and-play” simplicity of setting up Ethernet networks. The plug-and-play property of Ethernet is made possible by various self-learning aspects of the Ethernet protocol, which allows entities on an Ethernet network to become aware of each other and how to forward packets to each other.

As with the telecom SDOs, industry forums and consortiums have appeared in the LAN space. Two prominent ones are the Metro Ethernet Forum (MEF) and Ethernet Alliance (EA) consortium. The MEF defines the services and service models that can be used when carriers provide Ethernet network connectivity over their networks. This puts MEF on the boundary between telecom networks and LANs. The EA primarily exists to promote the use of Ethernet in an expanding variety of applications and provide interoperability testing for these applications.

#### ***14.1.1.3 Interactions between SDOs***

The various SDOs typically have some degree of overlap, interdependencies, or cross-specification potential with one or more other SDOs. Examples include the following:

- The ITU-T optical transport network (OTN) provides WAN transport for the IEEE 802.3 Ethernet signals, and it can also use the optical interface modules that have been developed by IEEE 802.3 for Ethernet using similar rate signals.
- Multiple SDOs use the OIF CEI specifications as the basis for their intercomponent or intrasystem interfaces.
- FSAN defines required service rates and parameters and approaches for access networks, but it relies on the ITU-T to complete and publish the actual technical standards to implement them.

Communication between SDOs is typically done using formal liaisons. Liaisons commonly include official correspondence between the leaders of the respective groups, and there is also a designated person to present and clarify the correspondence to the other group. Examples of correspondence topics can include information about work being performed in the one SDO that may be of interest to the other SDO, questions for clarification from an SDO regarding how their standard could be used by the requesting SDO, and expressing compatibility concerns regarding the implications of the work of the other SDO on work in that SDO. The formality of the liaisons varies, depending on the groups involved.

As an illustration, an early incompatibility between the nominally 10 Gbit/s signal rates used by the ITU-T OTN and IEEE 802.3 standards created a number of difficulties for carrying 10 Gbit/s Ethernet over OTN. This situation prompted very close cooperation on subsequent higher rate interfaces to ensure that OTN could readily transport Ethernet signals and reuse their interface technologies.

Interactions between formal SDOs and industry consortiums can be problematic, since the consortiums typically lack either a designated leader with the authority

for liaison correspondence, or an ongoing formal organization that can respond to the liaison.

The most effective forms of liaison are when a designated liaison representative regularly attends both groups, and is thus fully aware of the work in each SDO. The liaison person can then clarify the intention behind the liaison correspondence and clarify the terminology and technology used by each.

### 14.1.2 SUMMARY OF THE DIFFERENT TYPES OF STANDARDS BODIES

The different types of wireline SDOs can be summarized as follows:

**International SDOs:** These bodies consist of members that are distributed around the world rather than within one nation or region of the world. The ITU-T is the most important telecommunications SDO. The IEEE committees, including 802, are the most prominent ones for LAN and WAN data communications.

**Regional and National SDOs:** These bodies focus on standards that meet requirements unique to their national or regional networks, or other needs. They can also coordinate national/regional input to the International SDOs. Examples include ATIS, ETSI, and CCSA.

**Industry Forums:** The forums provide a place to either develop prestandard agreements that allow for experimenting with new services or for developing standards that enable other aspects of the ecosystem. Examples include new services and intrasystem interfaces. Important wireline forums include the OIF, Broadband Forum (BBF), and MEF.

**Industry Consortium:** A consortium is a voluntary collaboration of multiple companies in order to enable aspects like common interfaces, common equipment reference designs, or service definitions. As with other standards, the intention is to allow both interoperability and economies of scale in design and component availability. They often arise when the member companies recognize a common goal or approach that is unlikely to be shared by a consensus of other companies who may have their own proprietary solutions. Important consortiums include the one responsible for CPRI.

**Industry Alliances:** An industry alliance will typically fall into a category somewhere between a forum and a consortium. An example is the EA that operates to promote the use of Ethernet technology.

---

## 14.2 CARRIER NETWORK WIRELINE INTERFACE STANDARDS

Public telecommunications network providers typically operate very large networks, and they are also typically subjected to some form of government supervision to ensure that they can provide universal interconnectivity in an open and reliable manner. The operating costs of these large networks are very significant and relative

to the cost of building the networks. Consequently, network operators rely on a small number of specialized SDOs to define the wireline interconnect standards and the associated network control, management, protection, and administration standards. As described in the introduction, the ITU-T has become the most important of these international standards bodies, with regional SDOs addressing matters of local or region concern.

### 14.2.1 ITU-T INTERNATIONAL STANDARDS

The ITU standards work is divided among two groups. ITU-R covers radio topics, which are outside the scope of this chapter. ITU-T (ITU Telecommunications Standardization Sector) covers wireline networks and other network topics outside of radio interfaces. The ITU-T is the primary wireline body upon which the global telecommunications network providers depend for their network standards.

The ITU-T work is divided among a number of study groups (SGs) that address specific topics. The work within an SG is divided into Working Parties that cover different subtopics, with the technical work being done in task groups called “Questions.” The name originated from the notion that the task group would address a particular question or narrower topic. The ITU-T uses a 4-year “study period” approach, in which the work is reorganized at the beginning of each study period. At that time, SGs and Questions that have effectively completed their work are dropped or merged into other SGs and Questions, new Questions or SGs are created to address new areas requiring standardization, work is transferred from one SG to one that is now a better fit for that work, and SGs and Questions that have ongoing work along the lines of their previous work are reaffirmed. A note on terminology: the abbreviation for a given question is

Q<question #> / <Study Group #> For example, Q11/15 is Question 11 of SG15.

As mentioned above in the introduction, the ITU is a special agency of the United Nations. Hence, the primary members of the ITU-T are nations. Public telecommunications network providers have their own class of membership. Scientific and industrial organizations also have a class of membership. In their case, being a Sector Member allows them to participate and access the documents of any of the SGs and also participate in the ballot process for new standards. It is also possible to be an “Associate” of a particular SG. Being an Associate allows full participation in the technical work of that SG for much lower annual dues, although an Associate is not allowed to vote or comment on standards in the ballot phase. Since the early 2000s, the ITU-T allows free access over the web to pdf versions of all its published standards.

Virtually all the ITU-T wireline network standards work is performed within SG15. The scope of this work includes “Layer 0” through Layer 5 topics for access and metro/core transport networks. Layer 0 includes the specifications of optical

fibers/cables, all physical infrastructure elements, and wavelength channels. Layer 1 covers the bit rates and frame formats of digital signals. Layers 2–4 include aspects of packet networks that are required to allow “carrier-grade” quality of service (QoS), and Layer 5 includes carrier network management protocols and interfaces. This wide range of topics is divided among three working parties:

- Working Party 1 (WP1), which covers access networks (Layers 1–5).
- Working Party 2 (WP2), which covers optical fiber networks (Layer 0).
- Working Party 3 (WP3), which covers transport networks (Layers 1–5 and equipment functional specifications).

Most of the standards developed in SG15 are published as part of the “G” and “L” series of standards (transmission systems and media, digital systems, and networks), which are designated as “Recommendation G.xxx” or “Recommendation L.xxx,” where the xxx is the number assigned to the standard. The work of each working party is summarized as follows. A list of some of the most active current wireline questions appears in [Tables 14.1–14.3](#).

In addition to the work in SG15, SG13 becomes involved in high-level work affecting the wireline network. For example, as this book was being written, SG13 launched a focus group to study the wireline network implications and requirements to support the “5G” mobile wireless network and the IMT-2020 work of ITU-R. Presumably, any wireline network standards recommended by the task force report would then be developed in SG15.

#### **14.2.1.1 WP1 “transport aspects of access, home, and smart grid networks”**

WP1 covers both optical and copper/electrical access networks. Key WP1 active work is summarized in [Table 14.1](#).

As noted above, the FSAN consortium has defined the types of OANs required by the carriers, and it does some of the initial protocol and technology studies. It then transitions this work to Q2/15 of WP1 for complete technical specification and standardization. Most of these are passive optical networks (PONs) in which an optical fiber tree topology is used, connecting multiple remote optical network units (ONUs) at or near the user premises with a single optical line terminal (OLT) at the carrier CO. Hence, a single optical interface at the OLT can serve multiple ONUs, thus saving optical component and fiber costs. The first of these FSAN PON standards was the gigabit per second-capable PON (G-PON) standards family, typically operating at approximately 2.5 Gbit/s downstream and 1.25 Gbit/s upstream shared among the ONUs on the PON. This work was followed by the XG-PON (10 Gbit/s-capable) protocol, which allowed roughly 10 Gbit/s downstream and 2.5 Gbit/s upstream. They are currently completing work on a family of “Next Generation” PON (NG-PON) protocols that allow for up to 40 Gbit/s downstream and 10 Gbit/s upstream, and they are considering technologies for even higher throughput. The PON bandwidth is shared among the end users, with dynamic

**Table 14.1** Key Current Questions in ITU-T SG15 Working Party 1

Question	Title	Description of Scope
2	Optical systems for fiber access networks	PON system architecture and technology and its evolution. This work includes long reach extensions, QoS, maximizing the service capability between PONs and wireless edge networks, energy saving for optical access equipment, video signal support, and carrying radio frequency (RF) radio signals directly over OANs
4	Broadband access over metallic conductors	Technology for broadband data communication over metallic telephone cable infrastructure. This work includes modulation and transport techniques, handshaking protocols, energy saving, physical layer management, and interconnection to higher network layers
15	Communications for smart grid	Technology and protocols for communications over power grid networks. These technologies include modulation and coding, digital signal processing, physical layer measurement methods, handshaking protocols, energy saving, and interconnection to higher network layers
18	Broadband in-premises networking	<p>Technology and protocols for in-premises networks over in-premises infrastructure. The technology includes modulation and transport techniques, protocols to coexist with powerline communications (PLC), physical layer measurement methods, handshaking protocols, energy saving, and interconnection to higher network layers.</p> <p>The in-premises network infrastructures include telephone wiring, powerline wiring, and coaxial cable (eg, installed for in-premises video distribution)</p>

*Note that the scope of all WP1 questions includes testing procedures and the requirement for optimized transport of Ethernet and IP-based services*

bandwidth allocation allowing individual users to burst data in either direction up to the full PON rate. Reach extension techniques are also defined with the end goal of replacing many telephone company COs with PON connections to a smaller number of regional COs that host the OLTs and switching/routing equipment. Q2/15 also defines the PON protection and the network management requirements and interfaces. Note that PON is expected to become increasingly important as a backhaul for wireless base stations or a “fronthaul” network for the connections between the base station and remote radios. See the discussion on CPRI below for more about the fronthaul application [1].

Q4/15 has developed the past several generations of DSL technologies, including very high-speed DSL (VDSL). DSL allows bidirectional high-speed data transmission over a twisted pair of telephone wires (ie, the subscriber line) that connect the user to the telephone network. VDSL2 vectoring allows access rates up to 250 Mbit/s. They are currently working on “G.fast,” which will allow access rates up to 1 Gbit/s by using an optimal combination of optical networks and DSL. An outgrowth of the Q4/15 DSL work has been two other copper cable standards areas. The first, covered by Q18/15, are network protocols that provide in-home broadband networking capability over existing wireline infrastructures, including telephone wiring, powerline wiring, and coaxial cable. Q15/15 works on narrowband powerline communication (NB-PLC) utilizing OFDM technology in order to use the existing utility power grid for the communications medium. NB-PLC allows the monitoring, analysis, and control of power usage, which is an important part of the emerging “smart grid” for more efficient power distribution [1].

#### **14.2.1.2 WP2 “optical technologies and physical infrastructures”**

WP2 covers various aspects associated with the lowest layer functions of optical fibers and networks. Key WP2 active work is summarized in [Table 14.2](#).

Q5/15 defines attributes, characteristics, and test methods for optical fibers and cables, including geometrical, physical, mechanical and environmental, and transmission characteristics. The Q5/15 work program also includes the description and testing of single-mode and multimode fibers for transport and access networks.

Q6/15 defines the optical characteristics and requirements for different types of optical systems and networks, and one of its most important outputs is standardized sets of wavelengths for use as channels in wavelength division multiplexed (WDM) networks. This set of wavelengths, referred to as a “grid,” allows higher volume manufacturing of standardized optical components.

Q7/15 covers aspects of the systems specifications. Specifically, it addresses specifications and requirements for components and subsystems. In that role, it serves as an interface to the component level standards generated outside of ITU-T in organizations such as International Electrotechnical Commission (IEC). The Q7/15 work program includes parameter definition and classification (eg, optical nonlinearities, polarization, dispersion, noise, optical surge); passive components (eg, splices and connectors, attenuators, terminators, splitters/combiners, optical multiplexers/demultiplexers, filters); and optical switches and dispersion compensators.

Q8/15 covers standards associated with undersea optical cables. The Q8/15 work had previously included standardizing or documenting forward error correction (FEC) codes. This work has now transitioned to Q11/15. The questions not listed in [Table 14.2](#) cover topics including optical components and subsystems, optical fiber and cable test methods, installation, and maintenance and operation of optical fiber cable networks.

Q16/15 addresses subscriber access network infrastructure. Their work program covers network infrastructure planning, cable construction, passive network elements

**Table 14.2** Key Current Questions in ITU-T SG15 Working Party 2

Question	Title	Description of Scope
6	Characteristics of optical systems for terrestrial transport networks	Various aspects of optical systems for transporting signals over fiber networks. These aspects include modulation formats, power budget calculation approaches, wavelength/frequency plans for WDM systems, dispersion management and compensation techniques, coherent detection, optical channel quality assessment (to enable routing in all-optical networks), application of FEC for terrestrial networks, the use of optical amplifiers and optical cross connects, and optical systems reliability. The work also includes optical link parameters such as optical interference and polarization mode dispersion (PMD). The goal in many cases is the specification of interoperable single channel and multichannel optical systems ("transverse compatibility"). The emphasis is on the transport of OTN, Ethernet, and legacy Synchronous Digital Hierarchy (SDH) signals
7	Characteristics of optical components and subsystems	The work includes active devices and subsystems (eg, optical fiber amplifiers and switches), parameter definitions and measurement (eg, optical nonlinearities, polarization, dispersion, noise, optical surge), passive components (eg, splices and connectors, attenuators and terminators, splitters/combiners), optical multiplexers/demultiplexers, and filters and isolators
8	Characteristics of optical fiber submarine cable systems	The work covers all aspects required for undersea (submarine) optical cable systems. The work includes interface specifications, cable transmission characteristics, mechanical considerations, WDM, introduction of different types of optical amplifiers, advanced FECs, repeaters with optical amplifiers, capability for partial network upgrades, integration of submarine and terrestrial networks, protection, repair procedures, and test methods. The work also includes the effects of chromatic and polarization mode dispersion and dispersion compensation techniques, as well as optical fiber nonlinearities, on the evolution to higher rate systems
16	Outside plant and related indoor installation	The work covers various aspects of OAN planning, construction, and components
17	Maintenance and operation of optical fiber cable networks	The work includes all aspects associated with optical fiber monitoring and testing, including functional requirements and interfaces and devices for these purposes

(for PON), and techniques and components for indoor and outside plant construction and operation.

Q17/15 focuses on optical fiber network maintenance and operation issues. Their program includes functional requirements, monitoring and testing methods, and maintenance functions and devices for monitoring and testing systems.

### **14.2.1.3 WP3 “transport network characteristics”**

WP3 covers various aspects of both circuit switched and packet switched metro/core transport networks. Key WP3 active work is summarized in [Table 14.3](#).

While this group also has responsibility for the legacy SDH networks, the primary focus of the WP3, since around 1999 and for the foreseeable future, is the OTN. The OTN standards have been developed to allow cost-effective use of WDM networks. The signal formats and overhead are optimized for simple transport signal processing and simplified network management. The OTN standards have evolved from a relatively basic transport protocol for legacy constant bit rate (CBR) SDH/SONET signals with rates up to 40 Gbit/s, to a very flexible multiplexing technology allowing efficient transport of a wide variety of both CBR and packet clients. These clients include Ethernet, multiprotocol label switching (MPLS), storage network connections (eg, FC), video (eg, SDI and DVB-ASI), and legacy telecom signals.

Current work in Q11/15 is extending OTN rates beyond 100 Gbit/s to allow up to multiple terabit per second transport signals. Q11/15 covers both the signal rates and formats, and also the equipment functional characteristic specifications so that the network can be managed effectively.

In addition to OTN protocols, WP3 works on extensions to the packet protocols of other standards bodies (eg, Ethernet and IP/MPLS) to allow carrier grade QoS guarantees and network protection. Another important aspect of the WP3 work, performed in Q13/15, is the synchronization of both time division multiplex (TDM) and packet networks, as well as specifications for jitter and wander for the TDM networks. (Jitter and wander are the high- and slow-rate variations induced by the network on the instantaneous phase of the transport signal.) Q9/15 develops protocols and techniques for the protection switching and restoration of TDM and packet networks in the presence of faults. One more important area for WP3 is the specification of network management and control plane protocols for operating transport networks [2].

## **14.2.2 IMPORTANT REGIONAL SDOs**

Regional SDOs primarily operate in regions of the world with significant growth in telecom network infrastructure and regions that have common needs that are specific to that region. For example, prior to around 2001, the North American networks were built using standards from ATIS/ECSA that grew from the unique aspects of the legacy North American networks. As China began the rapid modernization of its telecommunications infrastructure, they were relatively unencumbered by legacy

**Table 14.3** Key Current Questions in ITU-T SG15 Working Party 3

Question	Title	Description of Scope
9	Transport network protection/restoration	The focus of this group is protection architectures and protocols for both TDM and packet networks. These include SDH, OTN, MPLS, and Ethernet layer networks. It also includes multilayer survivability and protection interactions between the data/packet layers
10	Interfaces, interworking, OAM (operations, administration, and maintenance), and equipment specifications for packet-based transport networks	This group has the primary responsibility for carrier network standards associated with access and metro/core packet networks and the associated equipment functions. The emphasis is on supporting packet-based traffic for services including Ethernet, SAN, and Multiprotocol Label Switching-Transport Profile (MPLS-TP). This includes the necessary OAM requirements and mechanisms for both connection-oriented and connectionless packet transport networks of various topologies. While the work includes generic OAM principles for interworking of different network technologies, it also focuses on Ethernet and MPLS-TP. The OAM for MPLS-TP is done in cooperation with the IETF standards organization. The Ethernet work is done in cooperation with the IEEE and the MEF
11	Signal structures, interfaces, equipment functions, and interworking for transport networks	This group is responsible for the transport network digital signal rates and formats, as well as the associated equipment function specification. Its primary focus is on OTN, including optimizations for both CBR and packet client transport. Specific topics include packet encapsulation for transport over SDH/OTN, and FEC
12	Transport network architectures	The work of this group includes overall network architecture issues that are then reflected in the work of the other SG15 questions. The work includes circuit switching, including at the photonic layer, and packet switching capability for both metro/core and access networks. It also covers the converged multitechnology and multilayer transport networks

**Table 14.3** Key Current Questions in ITU-T SG15 Working Party 3—cont’d

Question	Title	Description of Scope
13	Network synchronization and time distribution performance	This group covers all aspects associated with distributing timing in networks and maintaining the required timing accuracy for signals carried through the networks. The timing distribution includes frequency and time-of-day and/or phase reference. These are covered for both TDM networks and packet networks. The work also covers jitter and wander specifications and requirements, including those required for supporting wireless networks, wireline access networks, and packet networks such as Ethernet and MPLS
14	Management and control of transport systems and equipment	This group is responsible for the various aspects associated with the management plane and control plane for both TDM and packet transport networks. The work also includes the management aspects of the associated network equipment

networks and were open to considering whether there were less expensive or more efficient telecom networks that could be built in that environment. CCSA plays the lead role in that effort. ETSI has led the way in coordinating telecom network positions and capabilities primarily among European carriers and their needs.

**14.2.2.1 ATIS**

ATIS covers a range of standards work and types of wireline and wireless standards. The wireline standards work of ATIS was merged into the COAST Committee. At this point in time, the only active COAST subcommittee is SYNC (Synchronization), which covers network synchronization topics for both circuit switched and packet switched networks. In December 2014, ATIS sunsetted three of its longstanding subcommittees: optical hierarchical interfaces (OHI), which covered technology and protocols related to intercarrier connections and intracarrier metro/core network interconnections; OANs, which covered OAN topic including PON; and network access interfaces (NAI), which covered the access interfaces between the carrier networks and the end users (eg, DSL and PON technologies). Historically, OHI and NAI (and the groups from which they directly descended) had been especially active since 1984. However, virtually all the work on these topics is currently being done

within the ITU-T SG15 discussed below. As noted in the introduction, the US State Department no longer requires a COAST review of ITU-T SG15 contributions by US companies.

One key SYNC topic is specifying the limits for jitter and wander of the client signal rate that can be introduced by equipment within the network and must be tolerated by the receiving equipment. Another SYNC topic is the distribution of reference frequency and phase information across the network in order to provide the desired network node synchronization. As packet-based network technologies are used for more applications, including carrying CBR services, there has been an increased need to define these parameters for packet networks. Since packet networks have not been defined around having highly accurate signal clock rates for CBR signals, the jitter/wander and timing distribution is much more challenging.

#### **14.2.2.2 ETSI**

ETSI had previously provided much of the European input to ITU-T standards. However, ETSI currently relies on European carriers and manufacturers to participate directly in the ITU-T. ETSI now focuses on related work, including equipment specifications and topics like network function virtualization (NFV). NFV defines the functions of different network equipment such that they can be implemented in software on commercial computing hardware (eg, blade servers in a data center) rather than on dedicated special-purpose equipment. This allows aspects like the functions associated with radio base stations, PON line terminals, and encryption, to be assigned as needed to different servers in the network via downloading and enabling the appropriate server software.

#### **14.2.2.3 CCSA**

Through the early 2000s, Chinese carriers had assumed that their networks were best served by inexpensive technologies with minimum functionality that were optimized for their network infrastructures and future plans. For example, the CCSA considered whether Ethernet would have cost advantages in applications where other carriers were using Internet-based protocols. The motivation was to reduce equipment cost and complexity in order to lower the CAPEX costs of building their burgeoning new networks. It subsequently became apparent to the Chinese carriers that in the long run, it was much more cost effective to actively participate in the ITU-T and use international standards. As their networks grew, the Chinese carriers also appreciated the ongoing OPEX advantages that had motivated the complexity behind the existing protocols. In some cases the CCSA still defines standards to meet specific needs of Chinese carriers. For example, CCSA specified an encryption protocol for PON that was available without needing to pay royalties, thus saving money in large-scale PON deployments.

### 14.2.3 THE 19XX STANDARDS WORKING GROUPS OF IEEE COMMUNICATIONS SOCIETY

IEEE Communications Society (ComSoc) identified the need for wireline standards in areas that were not currently being addressed by other SDOs. They were able to leverage a legacy of past ComSoc standards work, and they were also able to leverage the same organizational infrastructure provided by the IEEE Standards Association (SA) as the IEEE Computer Society uses for IEEE 802. They currently have two working groups (WGs) relevant to this chapter:

- 1904 Access Networks Working Group (ANWG);
- 1910 Loop-Free Switching and Routing Working group.

ANWG takes the system level access network view. It addresses functions and the protocols that are required for OAM in multiservice networks. [Table 14.4](#) provides a snapshot of recent or current ANWG work.

1910 is currently working on P1901.1, “Standard for Meshed Tree Bridging with Loop Free Forwarding.”

---

## 14.3 DATA NETWORK WIRELINE INTERCONNECTION STANDARDS

The most important standards organization for wireline data networks is IEEE 802 of the IEEE Computer Society. IEEE 802 covers a variety of wireless and wireline standards, with the key wireline standards covered in the 802.1 and 802.3 WGs. Other important groups include INCITS and IEEE 1588.

### 14.3.1 IEEE 802.1—HIGHER LAYER LAN PROTOCOLS WORKING GROUP

The group originated to develop methods for bridging between Ethernet and token ring networks. The charter of 802.1 is now necessarily broad, as it covers the 802 network architecture and interworking between different 802 technologies. For example, while the other 802 WGs typically cover a specific technology (eg, Ethernet or Wi-Fi), 802.1 covers 802 LAN/metropolitan area network (MAN) architecture, network interworking, higher layer protocols (above the MAC and logical link control [LLC] layers), security, and overall network management for 802 networks. The work of 802.1 is organized according to Task Groups, as illustrated in [Table 14.5](#).

Bridging is implemented by having each network node examine the source MAC addresses on the frames received on each port, and building a per-port table of these received source MAC addresses. The node then forwards (outputs) each frame on the port for which the frame’s destination MAC address matches a source address

**Table 14.4** Snapshot of IEEE 1904 Task Forces

Project	Title	Description of Scope
1904.1	Standard for Service Interoperability in Ethernet Passive Optical Networks (SIEPON)	While the IEEE 802.3 Ethernet specification covers all aspects related to Layers 1 and 2 of Ethernet Passive Optical Networks (EPON), there are many other aspects of EPON outside the scope of 802.3 that are needed for interoperable equipment and networks. The IEEE 1904.1 standard addresses such aspects as the definition of different services and how they are implemented over a PON, algorithms for MAC to share the PON bandwidth among the subscribers, mechanisms for power savings during periods of inactivity by PON terminals, QoS guarantees, discovering and authenticating remote PON terminals, and various management aspects. The work of 1904.1 is now complete, except for maintenance
1904.2	Standard for Management Channel for Customer-Premises Equipment Connected to Ethernet-based Subscriber Access Networks	When customer premises equipment (CPE) is served by an Ethernet-based access network, the potential exists to manage the CPE that lie beyond the PON ONU, Coaxial Network Unit (CNU), Residential Gateway, etc., in order to provide a variety of service capabilities. This group defines the required management channel, including message format, forwarding rules, and processing operations. The channel characteristics include the multihop capability to reach the CPE devices, secure communications (via encryption), the capability to simultaneously configure multiple devices, and the capability for extension to support new CPE device types and/or management protocols
1904.3	Standard for Radio Over Ethernet Encapsulations and Mappings	<p>The focus of this project is enabling wireless infrastructure signals (eg, CPRI) to use Ethernet encapsulation for transport over Ethernet-based radio access networks. The information carried is the digitized radio in-phase/quadrature phase (IQ) data, in addition to control channels. The signal structure is agnostic to the client in the sense that it can accommodate any such client by serving as an Ethernet container for the client frames.</p> <p>However, it is also structure-aware to appropriately accommodate the client's frame format structure. Note that this is only a partial specification of what is required for carrying radio over Ethernet, and it relies on IEEE 802.1 for additional specification</p>

**Table 14.5** IEEE 802.1 Active Task Groups

Task Group	Scope
Interworking	The work of this Task Group includes various aspects of bridging and link aggregation. The bridging work includes control functions such as resource reservation (eg, traffic engineering) and bridging between different 802 networks such as Ethernet and 802.11
Security	This WG covers the security protocols required for different types of 802 networks. For example, 802.11 and EPON communicate with subscribers over a shared medium, and hence they both require security for user privacy and authentication of users of the medium. Most operate at the MAC layer
Time sensitive networking	An increasing number of potential uses for Ethernet have required real-time critical information. This group defines the protocols to add these capabilities onto Ethernet or determine how to use other protocols (eg, IEEE 1588) for these applications. Considerations include communicating time/phase reference information for synchronization, as well as packet scheduling and priority mechanisms to guarantee the performance requirements of real-time critical information. One of the newer applications is carrying radio interface information over an Ethernet access infrastructure. (See also the discussions of IEEE 1904.3 and CPRI elsewhere in this chapter.)
Data center bridging	This Task Group addresses applications required by large data centers in their environments
OmniRAN	This Task Group is developing a reference model that allows all the various types of 802-based access networks to be managed in a consistent manner, both individually and in combination

received on that port. This information allows the construction of a filtering database, which in turn allows relaying Ethernet frames with different MAC addresses (MAC relay). The filtering also allows each node to recognize control frames destined for that node, which are hence not forwarded. This was originally defined in the 802.1D standard, but it is now defined in 802.1Q.

The 802.1 bridging work has resulted in the popular virtual LAN (VLAN) capabilities that create LAN-type privacy and functionality for individual users within a larger shared network. VLANs originated with 802.1Q, but they have been extended with several new varieties that add functionality or extensibility, including making them practical for use in carrier networks.

A fundamental aspect of the 802.1 bridging work was the spanning tree protocol (802.1D), which creates loop-free topologies for forwarding Ethernet frames. The spanning tree is built by network nodes (router/switches) handshaking with one another to discover the network topology. This work has also been extended with

variations including rapid spanning tree for faster topology discovery after a fault condition.

The Time Sensitive Network task group is developing several standards and tools that enable deterministic real-time performance in Ethernet bridged networks. This determinism in bridged networks expands the number of applications for which they can be used. Example applications include industrial control, and streaming of video and audio data, including in home networks. Extension to carrying mobile infrastructure information is under study in the 802.1CM project that was launched in 2015.

### 14.3.2 IEEE 802.3—ETHERNET WORKING GROUP

IEEE 802.3 is responsible for the definition of Ethernet. As such, it is one of the most successful and influential standards group in the world. The focus of the work is the physical layer through MAC and LLC sublayers (ie, Layers 1 and 2). Higher layer issues such as bridging are addressed by IEEE 802.1 and IEEE 1904. As Ethernet applications have expanded, so has the need for a variety of different physical interfaces and rates. A mid-2015 snapshot of some of the active 802.3 projects shown in [Table 14.6](#) gives the reader a sense of the scope of IEEE 802.3 work. At this point, the different types of media defined for carrying Ethernet signals of different rates includes coaxial copper cable, twisted-pair copper cable, printed circuit boards (eg, between chips on the same board), system backplanes, PON, serial transmission over a single fiber, parallel transmission over multiple channels (eg, different copper or optical cables, or optical wavelengths on the same fiber), and different types of fiber (single mode, multimode, and plastic optical fiber). Each type of interface has proven to be optimal in terms of cost and/or performance for an important Ethernet application. In some cases (eg, those addressed by 802.3bt and 802.3bu), power is also transmitted over the copper cables in order to run the equipment at the other end of the link rather than requiring it to have its own local power.

**Table 14.6** Snapshot of Some of the IEEE 802.3 Active Task Forces

Title	Scope
802.3bm	40 and 100 Gb/s Fiber Optic Task Force
802.3bn	EPON Protocol Over Coax (EPoC) Task Force
802.3bq	Interspersing Express Traffic Task Force
802.3bs	400 Gb/s Ethernet Task Force
802.3bt	DTE Power via MDI Over 4-Pair Task Force
802.3bu	1-Pair Power Over Data Lines (PoDL) Task Force
802.3bv	Gigabit Ethernet Over Plastic Optical Fiber Task Force
802.3by	25GBASE-T PHY Study Group

The Ethernet interfaces are typically identified according to the following nomenclature:

<MAC rate of the signal in Mbit/s>BASE-<type of medium>.

For example, 1000BASE-T is gigabit per second (ie, 1000 Mbit/s) over twisted-pair copper cable. 100GBASE-SR10 is a 100 Gbit/s interface using 10 electrical signals in parallel over a short reach electrical connection (eg, between chips). Note that the “MAC rate” means the signal rate between the MAC sublayer and the lower layers that adapt the signal to its physical transmission medium (eg, by applying a line code or FEC). Due to line coding, the signal rate over the medium will be somewhat higher. When referring to a family of Ethernet signals at the same line rate, it is most common to abbreviate as “<MAC rate of the signal in Mbit/s>bE.” For example, 10 Gbit/s Ethernet signals are typically collectively referred to as 10 GbE. Note that “BASE” refers to “baseband” signals, to distinguish them from broadband (BROAD) or passband (PASS) signals used in early generations of Ethernet. At this point, all Ethernet signals are designated as “BASE.”

Historically, the Ethernet rates increased by a factor of 10 with each generation: specifically 1 Mbit/s, 10 Mbit/s, 100 Mbit/s, 1 Gbit/s, and 10 Gbit/s. At each increment, the cost of the new interface was much less than using a combination of 10 of the previous interfaces. Clearly, such a logarithmic increase in rates could not continue forever. For rates above 10 Gbit/s, 802.3 began using other increments that were optimized for important applications. Consequently, the 40 and 100 Gbit/s interfaces were developed in parallel as part of the same project. These were the first interfaces that relied primarily on a parallel medium rather than a single serial stream. The highest signal rate currently under consideration is for 400 Gbit/s in 802.3bs. As the work on this project began, it became apparent that there were advantages to making incremental use of the rates being used on the parallel interface component signals. For example, the  $4 \times 25$  Gbit/s interfaces specified for 100 GbE can be used for sub-100 Gbit/s connectivity within the server racks of a data center (eg, to connect the server cards with the router at the top of the rack). This led to the launch of the 25 GbE 802.3by project. Some are working on expanding this concept with a modular approach referred to as “FlexEthernet,” which is primarily being defined in the OIF standards body, as discussed below.

In addition to different wireline media types, Ethernet also supports a variety of topologies at the physical layer. 10 Mbit/s Ethernet supported a fully shared broadcast medium (eg, through a shared coaxial cable or through expander equipment that emulated this function for Ethernet nodes connected to it over their own dedicated twisted pair cable). The legacy use of the CSMA-CD MAC (Carrier Sense Multiple Access—Collision Avoidance) protocol for shared media is the main reason that Ethernet signals continue to require a minimum number of interpacket characters between each Ethernet frame, and they have each frame begin with a preamble. This combination allows the destination receiver to align to the signal amplitude and clock rate of the received Ethernet frame before the packet information begins. As the rates increased, it became much more practical to have each Ethernet terminal

use a full-duplex signal over a point-to-point physical connection to a bridge or switch node. The extension of EPON created a one-to-multipoint topology. As Ethernet systems grew, it became important to define the system backplane as a cost-effective Ethernet medium within the system. The IEEE 802.3bj project added this capability.

While there was optional support for FEC coding with some Ethernet signal rates, the PON and backplane applications necessitated standardizing more powerful FEC coding. The more powerful FEC was optional for most applications but required for some. The 400 GbE standard will have a mandatory FEC.

It has become increasingly important for enterprise customers to be able to interconnect their local Ethernet networks across a WAN. Since the WAN is typically provided by the public telecom network providers, it was critical to define methods for encapsulating Ethernet for the WAN transport. This necessity has prompted an increasingly close cooperation between IEEE 802.3 and ITU-T SG15. At this point, Ethernet signals with rates from 1 to 100 Gbit/s have transparent mappings into the ITU-T-defined OTN, and 400 GbE will similarly support an OTN mapping. Note that in addition to transparent CBR Ethernet stream transport, OTN also supports mapping Ethernet on a frame-by-frame basis, in which it is possible to carry Ethernet flows at arbitrary rates desired by the user.

As noted, 802.3 supports access network applications between carriers and end users. These primarily use Ethernet-based PON. (See the above discussion on ITU-T Q2/15 for more on PON.) The PON rates currently supported are 1 Gbit/s symmetrical, 10 Gbit/s symmetrical, and 10 Gbit/s downstream with 1 Gbit/s upstream. The former is referred to as EPON, and the latter two as 10G-EPON. Work is beginning on higher rates. Of course the PON bandwidth is shared among the end users, which typically number in the 16–128 range. Dynamic bandwidth allocation allows individual users to burst data in either direction up to the full PON rate. In some applications, regions, or markets, the 802.3 PON protocols compete with the ITU-T G-PON protocol family. Each network provider makes its own choice for which technology to use. In addition to PON, Ethernet access transport has recently been defined for shared coaxial copper cable media such as that used by cable television network providers.

### **14.3.3 IEEE 1588 PRECISE NETWORKED CLOCK SYNCHRONIZATION WORKING GROUP**

This WG, sponsored by the IEEE Instrumentation and Measurement Society, specifies a precision time protocol (PTP) for carrying highly accurate timing information over Ethernet networks. While the initial applications were for aspects like industrial equipment control, version 2 was expanded to accommodate the growing use of Ethernet for telecom applications where high accuracy frequency and phase timing were required. The concept relies on the periodic transmission of special Ethernet frames from a master clock node that sends a timestamp in synchronization packets

and having intermediate nodes along the path update the timestamps based on the transit delay through that node. The node at the other end of the link sends a return timestamp updated based on its turnaround time. The master node can then determine the total time required to transmit a packet to the other node. With this information, it can communicate the information required to have the other nodes along the path maintain precise frequency and phase (eg, time of day [ToD]) alignment with the master node's clock.

ITU-T's Q13/15 defined a profile of IEEE 1588v2 for use in telecom applications. One of the most stringent applications is distributing precision timing to mobile network base stations over their Ethernet uplink to the metro/core network. The base stations can then use this information to establish the precision clocks for their radio interfaces, with a phase accuracy that allows the reliable handoff between cell sites. It can also be used as an alternative to legacy SONET/SDH signals for distributing precision clock information to telecom carrier COs in their networks. Yet another application is distributing precision timing and ToD information to CPE over different types of broadband access networks. IEEE 802.1AS specifies a profile of IEEE 1588 for carrying real-time information such as video signals over a bridged LAN.

#### 14.3.4 INCITS T11 FIBER CHANNEL

T11 is responsible for high performance computer interfaces. The most prominent of these is FC, which is a lossless datacom interface. It has been commonly used within enterprise computing and storage networks, and for interconnecting them over modest distances. The high performance and lossless reliability have enabled FC to remain popular in these applications, especially for storage area networks (SAN), even as the use of Ethernet has grown for data connectivity and the use of lower cost storage drive interfaces such as serial attached SCSI (SAS) and serial ATA (SATA) has grown in many cost-sensitive SAN applications. Note that SAS and SATA standards are developed in INCITS T10 and T13, respectively, and they are typically just used within a building rather than for MAN/WAN connectivity.

---

## 14.4 INDUSTRY FORUMS

As described in the introduction, industry forums came about as bodies for developing agreements in areas that were either outside the domain of existing SDOs or for which there was a desire for an early introduction of a capability in order to provide it on a limited basis until a full standard could be subsequently developed for network-wide use. For example, most telecom SDOs focus on standards for interface between different network providers. Other infrastructure related areas such as network architectures, service models, and useful interfaces within the systems

were hence outside their scope and taken up by the industry forums. The working methods of the forums can be looser than standards bodies since their specifications are often documented as industry agreements or technical recommendations rather than as full “standards” in the sense of those coming from a body like IEEE 802 or ITU-T.

### **14.4.1 BROADBAND FORUM**

The current BBF was formed in 2009 from the merger of the DSL Forum and the IP/MPLS Forum. The DSL Forum, founded in 1994, worked on standards related to broadband subscriber access using DSL technology. Their primary focus was on provisioning, creating reference models, network architectures, and best practices for carrying certain types of services. As its work expanded to include other broadband access technologies such as fiber, it changed its name to BBF in 2008. The predecessors of the IP/MPLS Forum are the ATM Forum, Frame Relay Forum, MFA Forum, and MPLS Forum. The focus of the IP/MPLS Forum was the promotion of MPLS and frame relay technologies.

The BBF is composed of 200 member organizations representing service providers, equipment manufacturers, and electronic chip suppliers, defines and facilitates next-generation broadband standards, best practices and solutions.

The BBF’s more recent work includes topics related to PON, Ethernet-based DSL (xDSL), and auto-configuration for CPE such as set-top box and Network Attached Storage units. In its 2014 work program, FTTdp (Fiber to the Distribution Point), xDSL interoperability, and NFV became central themes in the evolution of MultiService Broadband Network (MSBN) architecture and nodal requirements. Its technical recommendations (TRs) provide an integrated framework for managing different types of broadband access technologies and marketing reports (MRs) present technology overviews in support of specifications published in BBF TRs.

The work of the BBF is performed under two main working committees: the Technical Committee and the Marketing Committee, a joint technical and marketing WG: Service Innovation and Market Requirements (SIMR); and a special advisory group: the Service Provider Action Council (SPAC). The Technical Committee consists of six WGs, as described in [Table 14.7](#).

### **14.4.2 OPTICAL INTERNETWORKING FORUM (OIF)**

The OIF has been one of the most active and prolific telecom industry forums. Its focus is on developing implementation agreements (IAs) required for interoperability within the telecom network ecosystem. Their work also often provides valuable input to other SDOs. Their work is organized to address three areas:

- External network element interfaces for optical networking.
- Network element internal software interfaces.
- Interfaces between hardware components within a network element.

**Table 14.7** Key Current Working Groups in BBF Technical Committee

WG	Title	Description of Scope
BBHome	BroadbandHome	All aspects of in-premises device management; TR-069 (CPE WAN Protocol) updates with data model expansion to cover broader range of devices; functional requirements for residential and Internet gateway devices
E2EA	End-to-End Architecture	All aspects of MSBN architecture and requirements; current projects on NFV, FTTdp, hybrid access, and IPv6 transition
FAN	Fiber Access Network	All aspects of fiber-based MSBN requirements, including PON optical layer management; current projects on FTTdp functional requirements. Earlier projects included the global industry's first GPON interoperability program development
IP/MPLS and Core	IP/MPLS and Core	Current projects on IP network integration with optical transport aimed at packet network optimization by using DWDM interfaces
O&NM	Operations and Network Management	All aspects of protocol-independent management model development for MSBN; current projects on fiber infrastructure management (joint with FAN WG), FTTdp management architecture, and DSL quality management
MT	Metallic Transmission	All aspects of functional requirements and test methodology development for metallic wireline MSBN; current projects on FAST (G.Fast) certification test plan development, MSBN copper cable models, in-premises PLCs systems
SIMR	Service Innovation and Market Requirements	This group is responsible for expedited exploratory work on emerging MSBN technologies and description/development of use cases and market requirements. Current projects on high-level requirements and framework on NFV and software defined networking (SDN) in MSBN

Their work also includes interoperability testing and the marketing and promotion of the technologies and services they address. Organizationally, the OIF work is organized into two WGs:

- Physical and Link Layer Working Group/Physical Layer User Group Working Group.
- Networking and Operations Working Group/Carrier Working Group.

Examples of OIF projects in the Physical and Link Layer Working Group/Physical Layer User Group Working Group include the following:

- Common Electrical Interface (CEI) specifications.
  - These specifications are typically between chips, or between chips and modules, either on the same circuit board or across a backplane. They cover a range of different reaches and a discrete number of important interface rates.
- The multilink gearbox (MLG) for converting between a serial stream of data and a parallel interconnection. It defines the monitoring and control capabilities, as well as compatibility with the IEEE 802.3bj FEC specification.
- Thermal specifications for optical interface modules.
- Dense wavelength division multiplexing (DWDM) interfaces.

The CEI work has been especially important to other SDOs and, consequently, the telecom and datacom industries as a whole. For example, it has been used as the basis for electrical interfaces developed by IEEE 802.3, INCITS T10, and RapidIO. Consequently, IC vendors are very active in OIF.

Examples of OIF projects in the Networking and Operations Working Group/Carrier Working Group include the following:

- Framework document for transport network use of SDN.
- Application programming interfaces (APIs) for SDN in transport networks.
- Specifications for programmable virtual network services that could drive the deployment of SDN.

At the time this book was being written, the OIF was beginning a new project called “FlexEthernet” within the Physical and Link Layer Working Group/Physical Layer User Group Working Group. The concepts behind FlexEthernet were to decouple the Ethernet MAC and Physical Medium Dependent (PMD) sublayers, especially in terms of rates. It effectively extends the OIF MLG to provide a variety of subrates and also an efficient mechanism for bonding multiple parallel links. It allows multiple MAC flows that are each less than the PMD rate sharing a set of PMDs. It also allows MAC flows that are each more than the PMD rate to share a bonded set of PMDs.

The PMD signal is structured containing “calendar slots” that can be filled by 66-bit Ethernet characters (code words) on a periodic basis. Specifically, a 100 Gbit/s PMD signal contains 1023 sets of 20 calendar slots between each overhead calendar slot. A FlexE client signal can own any number of calendar slots that can either all be within the same PMD or spread over multiple PMDs. A FlexE client signal is a CBR-like signal that can be combined with other FlexE client signals through time division multiplexing via assignment to a set of the periodic calendar slots.

### **14.4.3 METRO ETHERNET FORUM (MEF)**

As the volume of data traffic began to overtake voice traffic in the carrier networks, Ethernet WAN connectivity became increasingly important. In order to provide

different types of WAN connections, especially when they cross carrier domains, it was important to have agreements on the types of services that would be supported. Specifically, carriers wanted to sell Ethernet connectivity services beyond just an emulation of a wire across their networks. For example, one important service is to provide Ethernet virtual connections with guaranteed performance, at rates lower than those of the customer networks. This allows customers to only pay for the WAN bandwidth that they require. Another example is providing tree or generalized LAN-type connection topologies between customer sites.

Providing such services within and across different service provider networks required defining the services in a standard manner, including characterizing the performance parameters and requirements. Since they needed to be well defined with appropriate service guarantees, such Ethernet services provided by the carriers are typically referred to as “carrier Ethernet” (CE) to distinguish them from the Ethernet LANs that often operate on a best-effort service basis. The MEF addresses the items necessary to meet these QoS expectations of CE. The MEF agreements also paved the way for carriers to directly use Ethernet technology in their own networks.

The first generation of MEF standards, called CE 1.0, specified the networks and services needed for delivering Ethernet services of a single carrier’s network. The second generation, called CE 2.0, adds multiple new services and manageability for interconnected carrier networks. Both port-based and VLAN-based services are supported. In other words, the underlying pillars of CE 2.0 are multiple service classes, interconnectedness, and manageability.

The MEF work is divided among four broad work areas:

- Services;
- Architecture;
- Management;
- Test and Measurement.

A partial list of the current MEF specifications is shown in [Table 14.8](#) in order to illustrate the scope of their work. With the exception of the addition of the information and data models, element management, and abstract test suites, the specifications in [Table 14.8](#) are the ones referenced in the ITU-T G.8011 (Ethernet over Transport—Ethernet service characteristics) recommendation.

---

## 14.5 IMPORTANT INDUSTRY CONSORTIUMS

As discussed in the introduction, an industry consortium is occasionally formed in order to effectively define standards for interworking on functions that are not being currently addressed in other standards organizations (eg, due to being out of scope). The smaller membership of a consortium allows definitions that are optimized for the needs of the consortium members. This section describes some of the more important consortiums for wireline networks.

**Table 14.8** Examples of MEF Specifications

Subject Area	Example MEF Specifications	
	#	Title
Carrier Ethernet Service Definitions	6.2	Metro Ethernet Services Definitions Phase 3
	22.1	Mobile Backhaul Phase 2 Implementation Agreement, and Amendment 1 (small cells)
	28	External Network-Network Interface (ENNI) Support for UNI Tunnel Access and Virtual UNI
	33	Ethernet Access Services Definition
Carrier Ethernet Service Attributes	10.3	Ethernet Services Attributes Phase 3
	23.1	Class of Service Phase 2 Implementation Agreement
	26.1	External Network-Network Interface (ENNI)—Phase 2
	45	Multi-CEN L2CP
Architecture	12.2	Carrier Ethernet Network Architecture Framework Part 2: Ethernet Services Layer
	13	User Network Interface (UNI) Type 1 Implementation Agreement
	20	UNI Type 2 Implementation Agreement
Information and Data Models	7.2	Carrier Ethernet Information Model
	31	Service OAM Fault Management Definition of Managed Objects (SNMP)
	40	UNI and Ethernet Virtual Circuit Definition of Managed Objects (SNMP)
Service Activation and Test	44	Virtual NID (vNID) Definition of Managed Objects (SNMP)
	46	Latching Loopback Protocol and Functionality
	48	Service Activation Testing
	49	Service Activation Testing Control Protocol and PDU Formats
Service OAM Fault & Performance Management	30.1	Service OAM Fault Management Implementation Agreement Phase 2, and amendment
	30.1.1	Service OAM Fault Management Implementation Agreement Phase 2 - Amendment 1
	35	Service OAM Performance Monitoring Implementation Agreement, and two implementation amendments
Element Management	15	Requirements for Management of Metro Ethernet Phase 1 Network Elements
	16	Ethernet Local Management Interface
Abstract Test Suites	9	Abstract Test Suite for Ethernet Services at the UNI
	14	Abstract Test Suite for Traffic Management Phase 1
	21	Abstract Test Suite for UNI Type 2 Part 1 Link OAM
	25	Abstract Test Suite for UNI Type 2 Part 3 Service OAM

### 14.5.1 FULL-SERVICE ACCESS NETWORK (FSAN) CONSORTIUM

The FSAN consortium originated with multiple telephone network carriers wanting to specify broadband technology beyond DSL that would allow them to compete with the coaxial cable broadband access networks from Cable Television providers. Having a common specification would be key to providing both the market competition and the volumes required to encourage the development of cost-effective technology. While IEEE 802.3 had developed EPON, it lacked some features needed for carrier networks. For example, it lacked a network management interface, specifications associated with bandwidth assignment, QoS guarantees, power saving, encryption, network protection, and multiservice delivery. Since the specifications involved many aspects beyond the Layers 1 and 2 protocols, no existing standards body was addressing the range of topics they needed. In other words, in order to be cost effective, the specifications had to include physical layer, MAC, service definitions, and network management.

Rather than developing and publishing its own standards, FSAN handed its requirements and technology investigations to the ITU-T for the detailed specification and standardization. As discussed above, this work takes place in Q2/15. FSAN initially defined the G-PON protocol with a wide variety of rates and features requested by its various members. In order to better facilitate the cost benefits of market volume, it subsequently defined a Common Technical Specification that specified a limited set of the most popular options. Subsequent work on higher rate PONs has also had the requirements and preliminary technology research performed in FSAN, with subsequent completion and publication by ITU-T.

### 14.5.2 COMMON PUBLIC RADIO INTERFACE (CPRI) CORPORATION

Mobile radio transmitter sites are simpler to construct when the radio functions do not need to be colocated with base station (BTS) functions. An industry consortium, initially consisting of five companies, defined a standard digital interface between the BTS and a remote radio head (RRH). The payload of this digital signal is the digitized radio in-phase/quadrature phase (IQ) data stream. Using a digital signal allows longer distance transmission than an analog radio signal, with immunity to noise and overall site power savings. This interface was initially used to reach between a BTS at the bottom of the radio antenna tower to the RRH at the top of the tower. It now supports several kilometers distance between the BTS and RRH, which allows centralizing the location of multiple BTSs. In the future, this topology allows performing much of the BTS processing function on data center servers rather than dedicated BTS hardware. This configuration using data center servers is referred to as Cloud-Radio Access Network (C-RAN).

Since the connections between the BTS and the metro/core networks are referred to as “backhaul” networks, the networks carrying the CPRI signals are commonly referred to as “fronthaul” networks.

In order to make the cost-effective use of the fronthaul physical layer network, it is desirable to multiplex multiple CPRI signals. However, there are many challenges associated with multiplexing CPRI-type signals. The challenges and the emerging standards work associated with this topic are discussed below in [Section 14.5.5](#).

### **14.5.3 OPEN BASE STATION ARCHITECTURE INITIATIVE (OBSAI) CONSORTIUM**

This industry consortium sought to define a standardized functional partition of the BTS, including interfaces between the functions. Their Reference Point 3 (RP3) serves essentially the same function as CPRI. While OBSAI is still used, CPRI has been more popular.

### **14.5.4 ETHERNET ALLIANCE (EA) CONSORTIUM**

The goal of this consortium is to promote the successful expansion of Ethernet technology. Its members include system and component vendors, as well as professionals from government and universities. It does not develop standards or specifications itself.

### **14.5.5 WIRELINE NETWORKS FOR WIRELESS FRONTHAUL/BACKHAUL**

A variety of standards groups and consortiums have been interested in the topic of using wireline networks for the fronthaul/backhaul of wireless network traffic. Rather than breaking this work down by group, this section provides a broader overview of the topic.

As discussed in other chapters of this book, increasing the per-user data rates in wireless networks is a matter of increasing the efficiency of using the available RF spectrum. One key method for increasing the efficiency is the spectrum reuse made possible by cellular topology where the same frequencies can be reused in nonadjacent cells, due to the power limitations on transmissions within each cell. The potential for frequency reuse is increased by going to smaller cells. Of course, using smaller cells requires more cells, and hence more radios. In order to make such an arrangement cost effective, CPRI is used to connect the radios to centralized base stations so that there are fewer base station locations. Shared base station locations are more cost effective due to being able to share common equipment and having reduced real estate costs and fewer sites to maintain.

In order to further reduce costs, the fronthaul wireline network carrying the CPRI signals must be shared. The main challenges with CPRI transport come from having the radio deriving its RF directly from the received CPRI signal. In order to allow handoffs between cell sites for mobile users (ie, where Doppler shift must be taken into account), the frequency accuracy and stability requirement allocated to the CPRI signal was specified to be 2 ppb. CPRI also includes stringent requirements for directional latency symmetry, latency variation, and overall latency.

These are important because the CPRI protocol measures the roundtrip latency of the connection between the BTS and RRH, and the BTS uses the propagation delay information to accommodate for its impact on the radio signal phase at the RRH. For protocol simplicity, the calculation assumes that latencies in the two directions are essentially equal. Hence, significant asymmetry impacts the accuracy of the phase impact calculation. WDM is the simplest multiplexing method to satisfy these requirements since each wavelength offers a transparent channel with minimum latency. However, WDM has been too expensive for carrying a single client signal per wavelength in fronthaul or access applications.

TDM is much less expensive than WDM for sharing the wireline fronthaul network; however, it can be difficult to adequately filter the jitter introduced in the CPRI signal by TDM and compensate for the latency and its directional delay variation. Carriers asked the ITU-T to define a TDM method for carrying CPRI over OTN. The ITU-T documented its OTN mappings for CPRI in informative text rather than normative text in order to make it clear that some degree of network engineering will be required to guarantee adequate performance. All aspects of carrying CPRI over OTN have been moved to a standalone informative supplement (ITU-T G.Sup56) to the OTN standard in order to highlight and clarify the requirements for the various proposed CPRI transport options. This ITU-T work was complicated by the consortium nature of the CPRI Corporation, making them not well structured to respond to liaison requests for clarifications on the nature and absolute limits of the CPRI specifications, as well as there being differences in how CPRI and ITU-T state their performance requirements. The CPRI Corp. has more recently expressed an interest in actively cooperating with the IEEE 802.1 group to work on CPRI transport using Ethernet technology in the 802.1CM project.

One new paradigm being explored is to decouple the IQ data transport from communicating the CPRI clock information. Conceptually, the different pieces of equipment in the fronthaul network can receive their RF clock and phase synchronization from something like a GPS satellite, or by using the IEEE 1588 protocol described above, rather than from the received CPRI signal rate. Having a separate means of communicating frequency and phase information, together with the mechanisms being defined in 802.1 and 1904.3, makes it feasible to use Ethernet for carrying the CPRI IQ data information.

Another network topology of interest is to move some of the BTS processing functions to the RRH location, such that the connection to the RRH is an Ethernet backhaul one rather than a CPRI fronthaul one. Carrying the information content of the baseband backhaul data requires much less bandwidth than carrying the raw IQ data samples via CPRI; therefore this allows for much more cost effective use of the wireline access network bandwidth.

---

## 14.6 OTHER SIGNIFICANT GROUPS

Other wireline SDOs exist to address specific areas. The two covered in this section are CableLabs and Telecommunications Industry Association (TIA).

### **14.6.1 CABLELABS AND DOCSIS**

CableLabs is a research laboratory jointly owned by US Cable Television Network Operators, and its work is funded by them and other cable operators from around the world. As such, it is not an SDO in the sense of the others covered above, but it functions as the primary standards setting body for the cable television industry. (Note that the Society of Cable Television Engineers (SCTE) also specifies some standards for the cable industry.) The early work of CableLabs focused on aspects like defining the spectrum usage within the coaxial cables in order to provide frequency division multiplexing channels for delivering analog video signals. As the coaxial cable infrastructure was upgraded to support bidirectional transmission, CableLabs defined the DOCSIS protocol to enable providing broadband data services over the cable television access network. DOCSIS specifies all aspects required for interoperability between the user cable modems (CMs) at the subscriber's premises and the network provider's cable modem terminating system (CMTS). For example, the areas defined by DOCSIS include frequency band allocations, modulation formats, the MAC layer, definition of services (including their QoS), IP address assignment, security, CM authentication, and network management. Over time, DOCSIS continues to evolve to provide even higher access bandwidth and additional features. See [1] for a tutorial on DOCSIS.

Note that DOCSIS has been extended by CableLabs and the IEEE 1904.1 work to allow carrying DOCSIS over Ethernet PON networks.

### **14.6.2 TELECOMMUNICATIONS INDUSTRY ASSOCIATION (TIA)**

TIA is an ANSI-accredited standards body covering a variety of specialized areas. It currently consists of 12 committees covering topics including wireless network infrastructure (private radio equipment, cell towers, satellites, and mobile device communications), terminal equipment (telephone and data), cabling, data centers, multimedia multicast, VoIP devices, accessibility, vehicular telematics, healthcare information communication, machine-to-machine communications, and smart utility networks. As evident by the scope of its work, TIA does not focus on interface agreements such as those covered in ITU-T SG15 and IEEE 802.3, but it is somewhat more like OIF in that it covers import infrastructure, device, and equipment standards that are required in the telecommunications and data communications ecosystems. However, some of its work provides input to the ITU.

---

## **14.7 CONCLUSIONS**

Wireline network standards continue to be a very active area, and they are especially important for building the core infrastructure of LAN and WAN. Understanding these network standards is very helpful for those involved in wireless networks, since the wireline networks are typically used as the backbone for connecting wireless networks, and many of the wireline network technologies find applications

in wireless networks. Table 14.9 provides a summary overview of which standards organizations play leading roles in different areas of technology. While this table is by no means comprehensive, it will provide the reader with important starting points for further study.

**Table 14.9** Some Important Wireline Technologies and Associated Key Standards Organizations

Technology	Lead Wireline Standards Organization(s)
Broadband access (wireline)	ITU-T SG15 Working Party 1 IEEE 802.3 FSAN CableLabs BBF (management)
DSL	ITU-T SG15 Q4
Ethernet interfaces	IEEE 802.3
Ethernet services	MEF IEEE 1904
Network management	ITU-T SG15 Q14 OIF IEEE 1904 MEF
Optical components	TIA ITU-T Working Party 2 OIF
Optical networking	ITU-T SG15 OIF
LAN	IEEE 802.3 IEEE 802.1 INCITS
OFDM	ITU-T SG15 Working Party 1 CableLabs
PON	ITU-T SG15 Working Party 1 IEEE 802.3 FSAN BBF (management)
Radio access networks	CPRI OBSAI IEEE 1904 IEEE 802.1
Synchronization	ITU-T SG15 Q13 IEEE 1588 IEEE 802.1

---

## REFERENCES

- [1] S. Gorshe, A. Raghavan, T. Starr, S. Galli, *Broadband Access: Wireline and Wireless—Alternatives for Internet Access*, Wiley, Chichester, UK, 2014.
- [2] Frame structures, mapping and multiplexing (sole author of section 2.2.2), “OTN mapping and multiplexing”, in: *Optical Transport Networks From TDM to Packet*, ITU-T, 2010.

---

## WEB SITES FOR FURTHER READING

<http://www.itu.int/en/ITU-T/studygroups/2013-2016/15/Pages/default.aspx>  
<http://www.ieee802.org/>  
[http://standards.ieee.org/develop/wg/1904\\_WG.html](http://standards.ieee.org/develop/wg/1904_WG.html)  
<http://grouper.ieee.org/groups/1904/>  
<http://www.mef.net/>  
<https://www.broadband-forum.org/>  
<http://www.oiforum.com/>  
<http://www.cpri.info/index.html>  
<https://www.fsan.org/>  
<http://www.tiaonline.org/>  
<http://www.cablelabs.com/>  
<http://www.ethernetalliance.org/>  
<http://www.incits.org/>  
<http://www.atis.org/>  
<http://www.etsi.org/>  
<http://www.ccsa.org.cn/english/>

# Wireless broadband standards and technologies 15

**S. Ahmadi**

*Xilinx Inc., San Jose, CA, United States*

## CHAPTER OUTLINE

<b>15.1 Introduction to Wireless Broadband Standards and Technologies .....</b>	<b>559</b>
<b>15.2 Wireless Broadband Standardization Organizations and Special Interest Groups .....</b>	<b>561</b>
15.2.1 IEEE 802 .....	561
15.2.2 3GPP .....	561
15.2.3 Wi-Fi Alliance .....	562
15.2.4 Bluetooth SIG .....	562
<b>15.3 Overview of Wireless Broadband Technologies .....</b>	<b>563</b>
15.3.1 IEEE 802.11 Family (Wi-Fi) .....	563
15.3.2 IEEE 802.16 Family (WiMAX) .....	571
15.3.3 IEEE 802.15 Family (Bluetooth) .....	583
15.3.4 3GPP Family (GSM, UMTS, LTE).....	590
<b>15.4 Conclusion and Remarks .....</b>	<b>618</b>
<b>References.....</b>	<b>619</b>

## 15.1 INTRODUCTION TO WIRELESS BROADBAND STANDARDS AND TECHNOLOGIES

Wireless communication comprises a wide range of technologies, services, and applications that have come into existence to meet the particular needs of users in different deployment scenarios. Wireless systems can be broadly characterized by content and services offered, reliability and performance, operational frequency bands, standards defining those systems, data rates supported, bidirectional and unidirectional delivery mechanisms, degree of mobility, regulatory requirements, complexity, and cost. The number of mobile subscribers has increased dramatically worldwide in the past two decades. The number of mobile devices is expected to continue to grow more rapidly

than nomadic and stationary devices, and mobile terminals are the most commonly used platforms for accessing and exchanging information. In particular, users expect dynamic applications, capabilities, and services that are ubiquitous and available across a range of devices using a single subscription and a single identity. Wireless multimedia traffic is increasing far more rapidly than voice and will increasingly dominate traffic flows. The paradigm shift from predominantly circuit-switched air-interface design to all IP-based systems has provided the users with the ability to more efficiently, more reliably, and more securely utilize multimedia services including email, file transfers, messaging, browsing, gaming, VoIP, and location-based and multicast and broadcast services. These services can be either symmetrical or asymmetrical (in terms of use of radio resources in the downlink or uplink) and real-time or nonreal-time with differing quality of service (QoS) requirements. The new applications consume relatively larger bandwidths, resulting in higher data rate requirements.

There are various types of broadband wireless access technologies that are classified based on the coverage and user mobility:

1. Body area network (BAN), also referred to as a body sensor network, is a network of wirelessly connected wearable devices/sensors. BAN devices may be embedded inside the body (implants), may be surface-mounted on the body in a fixed position (wearable technology), or may be accompanied devices which humans can carry in different positions, in clothes pockets, or in handbags.
2. Personal area network (PAN) is a wireless data network used for communication among data devices/peripherals around a user. The wireless PAN coverage area is typically limited to a few meters with no mobility. Bluetooth is an example of PAN technology.
3. Local area network (LAN) is a wireless or wireline data network used for communication among data/voice devices covering small areas such as home or office environments with limited or no mobility. Examples include Ethernet (fixed wired LAN) and Wi-Fi or IEEE 802.11 (wireless LAN for fixed and nomadic users).
4. Metropolitan area network (MAN) is a data network that connects a number of LANs or a group of stationary/mobile users distributed in a relatively large geographical area. Wireless infrastructure or optical fiber connections are typically used to link the dispersed LANs. Examples include IEEE 802.16-2004 (fixed WiMAX) and Ethernet-based MAN.
5. Wide area network (WAN) is a data network that connects geographically dispersed users via a set of interconnected switching nodes, hosts, LANs, etc. and covers a wide geographical area. Examples of WAN include the Internet and cellular networks such as 3GPP UMTS and LTE, and mobile WiMAX or IEEE 802.16-2012.

In this chapter, we will provide a high-level overview of the most common wireless standards and their developing standards organizations that fall into one of the above categories. References in this chapter will provide more in-depth resources for the interested readers.

---

## 15.2 WIRELESS BROADBAND STANDARDIZATION ORGANIZATIONS AND SPECIAL INTEREST GROUPS

Globally adopted wireless technology standards have been mainly developed by international standards development organizations such as IEEE, 3GPP, or ITU, as well as by special interest groups representing major industry proponents such as Bluetooth SIG or the Wi-Fi Alliance. The main objective of standardization is to ensure compatibility and interoperability of wireless system entities and interfaces across a large number of vendors. These technical standards are developed, maintained, and evolved by the corresponding standards organization through various releases of the baseline specifications. In this section, we will briefly introduce some of the standards developing organizations which have had significant impacts on the wireless industry in the past two decades.

### 15.2.1 IEEE 802

IEEE 802 refers to a family of IEEE standards developed for wired and/or wireless personal area, local area, and MANs [1]. The IEEE 802 LAN/MAN standards committee develops and maintains networking standards and recommended practices for personal, local, and metropolitan networks using an open and accredited process and advocates them on a global basis. The most widely used standards are for Ethernet, Bridging and Virtual Bridged LANs, Wireless LAN, Wireless PAN, Wireless MAN, Wireless Coexistence, Media Independent Handover Services, and Wireless RAN. Any individual working group provides the focus for each area. The services and protocols specified in IEEE 802 map to the lower two layers (data link and physical layers) of the seven-layer OSI networking reference model. In fact, IEEE 802 splits the OSI data link layer into two sublayers named logical link control (LLC) and medium access control (MAC), thus the layers and sublayers defined by IEEE 802 standards define the LLC sublayer, MAC sublayer, and physical layer.

### 15.2.2 3GPP

The Third Generation Partnership Project (3GPP) brings together a number of telecommunication standards development organizations (ARIB, ATIS, CCSA, ETSI, TTA, TTC), also known as Organizational Partners, and provides their members with stable technical baseline documents to transpose into their own specifications [2]. There are four technical specification groups in 3GPP which include radio access networks (RAN), service and systems aspects (SA), core network and terminals (CT), and GSM EDGE radio access networks (GERAN). Each technical group has a set of working groups and has a particular area of responsibility for the reports and specifications under its own terms of reference or group charter. 3GPP uses a system of parallel releases in order to provide device and network vendors as well as network operators with a stable platform for implementation and to allow the addition of new features required by the market. 3GPP has been credited for the development of some of the most important cellular standards—2G/GSM, 3G/UMTS, and 4G/LTE—over the past two decades.

### 15.2.3 Wi-Fi ALLIANCE

The Wi-Fi Alliance is a nonprofit organization that promotes Wi-Fi technology and certifies Wi-Fi products to ensure that they conform to certain standards of interoperability such that clients and access points manufactured by different vendors can work together [3]. Early IEEE 802.11 products suffered from interoperability issues because IEEE had no provision for testing equipment for compliance with its standards. The Wi-Fi Alliance owns and controls the “Wi-Fi Certified” registered trademark, which is permitted only on equipment that has passed the prescribed interoperability testing. A rigorous testing procedure is adopted because the standards involve not only radio and data format interoperability, but also security protocols, as well as optional testing for QoS and power management protocols. The user experience governs the overall approach of the Wi-Fi Alliance certification program. This pragmatic approach stems from three principles: (1) interoperability, which is the primary objective of certification and where stringent test cases are conducted to ensure that products from different equipment vendors can interoperate in a wide variety of configurations; (2) backward compatibility that has to be maintained in order to allow new equipment to work with the legacy counterparts, protecting investments in legacy Wi-Fi products and enables users to gradually upgrade and expand their networks; and (3) innovation that is supported through the introduction of new certification programs as the latest technology and specifications come into the marketplace. These certification programs may be mandatory or optional.

The Wi-Fi Alliance definition of interoperability surpasses the ability to work in a Wi-Fi network. To obtain certification under a specific program, products have to show satisfactory performance levels in typical network configurations and have to support both established and emerging applications. The Wi-Fi Alliance certification process includes three types of tests to ensure interoperability. The Wi-Fi Certified products are tested for compatibility, conformance, and performance.

### 15.2.4 BLUETOOTH SIG

The Bluetooth Special Interest Group (SIG) is a member-only industry association that oversees the development of Bluetooth standards and the licensing of the Bluetooth technologies and trademarks to device manufacturers [4]. Bluetooth is a short-range wireless technology originally developed as IEEE 802.15.1 for low-rate information exchange between compatible wireless devices such as mobile phones, laptops, computers, printers, and digital cameras over short distances via an ISM radio frequency band. The SIG owns the Bluetooth trademark and grants licenses to companies that incorporate Bluetooth wireless technology into their products. To become a licensee, a company must become a member of the Bluetooth SIG. The SIG also manages the Bluetooth SIG qualification program, a certification process required for any product using Bluetooth wireless technology and a precondition of the intellectual property license for Bluetooth technology. The main tasks for the

SIG are to publish the Bluetooth specifications, protect the Bluetooth trademarks, and promote Bluetooth technology.

To use Bluetooth technology, a device has to be able to interpret certain Bluetooth profiles, which are definitions of possible applications, and specify general behaviors that Bluetooth-enabled devices use to communicate with other Bluetooth devices. These profiles include settings to parameterize and to control the communication from the beginning of the session. Adherence to profiles saves time when transmitting the parameters again before the bidirectional link becomes effective. There are a wide range of Bluetooth profiles that describe many different types of applications or use cases for devices.

---

## 15.3 OVERVIEW OF WIRELESS BROADBAND TECHNOLOGIES

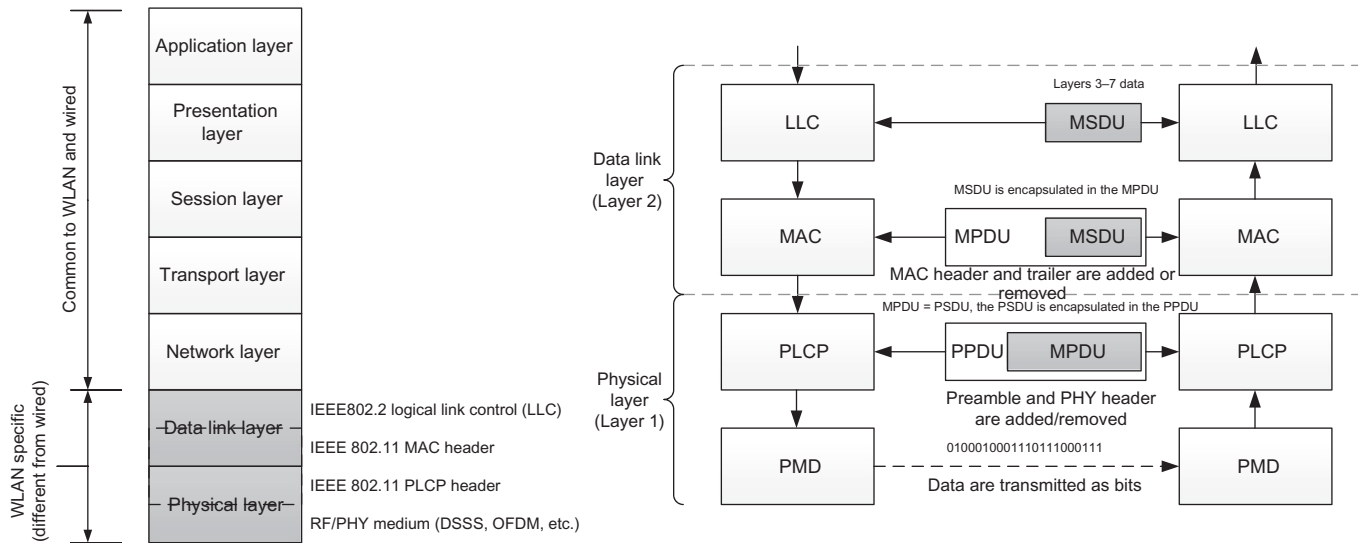
In this section, we provide an overview of some of the most commonly used radio access standards that have facilitated a large number of fixed, nomadic, and mobile services across various platforms in the past two decades.

### 15.3.1 IEEE 802.11 FAMILY (Wi-Fi)

The IEEE 802.11 family of standards is a group of wireless LAN radio access technologies developed by the IEEE 802 LAN/MAN Standards Committee. These standards define nonsynchronous contention-based multiple access schemes based on Carrier Sense Multiple Access with Collision Avoidance (CSMA/CA) [5].

IEEE 802.11 supports two network architecture types, namely, infrastructure and ad hoc modes. The basic service set (BSS) is the basic building block of an IEEE 802.11 network. Direct association of stations in an ad hoc network forms an Independent BSS or IBSS. The interconnection of a number of BSS through a distributed system creates an extended service set (ESS). IEEE 802.11 specifications define multiple physical layers and a common MAC layer for wireless LANs (as shown in [Fig. 15.1](#)). Another important aspect of this family is that they use an unlicensed spectrum in 2.4, 5, and 60 GHz for operation.

The IEEE 802.11 family comprises many technologies that have evolved from direct sequence spread spectrum (DSSS) and complementary code keying (CCK) in the first generation to orthogonal frequency division multiplexing (OFDM) waveforms combined with advanced coding and modulation techniques, as well as spatial division multiplexing (SDM) multiantenna schemes, in the latest generations. Depending on channel conditions, these features can provide data rates in the excess of a few gigabits per second within short distances. [Table 15.1](#) summarizes the key physical layer characteristics of IEEE 802.11 air-interface technologies. There are other IEEE 802.11 family members, and each provides an extension to the baseline standard by adding new features such as handover (HO) and roaming, mesh networking, QoS, security, regulatory aspects, and measurement for various regions of the world.

**FIG. 15.1**

OSI and IEEE 802.11 protocol relationships.

Based on, E. Perahia, R. Stacey, *Next Generation Wireless LANs: 802.11n and 802.11ac*, second ed., Cambridge University Press, Cambridge, UK, 2013.

**Table 15.1** Evolution of IEEE 802.11 Air-Interface Technologies

Standard	Frequency (GHz)	Bandwidth (MHz)	Transmission Scheme	Highest Order Modulation	Coding Rate	Spatial Streams	Data Rate (Mbps)
802.11	2.4	25	DSSS	–	Convolutional Coding with Coding Rates 1/2, 2/3, 3/4, and 5/6	1	1,2
802.11b	2.4	25	DSSS/CCK	–		1	1–11
802.11a	5	20	OFDM	64QAM		1	6–54
802.11g	2.4	25	OFDM, DSSS/CCK	64QAM		1	1–54
802.11n	2.4/5	20, 40	OFDM/SDM	64QAM		1–4	6.5–600
802.11ac	5	20, 40, 80, 160	OFDM/SDM/MU-MIMO	256QAM		1–8	6.5–6933.3
802.11ad	60	2160	OFDM	256QAM		1	up to 6912

Based on, E. Perahia, R. Stacey, *Next Generation Wireless LANs: 802.11n and 802.11ac*, second ed., Cambridge University Press, Cambridge, UK, 2013.

In IEEE 802.11, the stations and the access point are not synchronized except when they exchange data or control information in the downlink or uplink. A listen-before-talk method combined with CSMA/CA is used to gain access to the medium and to ensure collision avoidance with other contenders wishing to access the shared medium. The stations either passively scan the beacons transmitted by nearby access points or actively scan neighboring access points by transmitting a probe signal.

In IEEE 802.11, there are two options for medium access. The first is a centralized control scheme that is referred to as the point coordination function (PCF), and the second is a contention-based approach known as the Distributed coordination function (DCF). The PCF mode supports time-sensitive traffic flows where the access points periodically send beacon frames to communicate network management and identification which is specific to that WLAN. Between the sending of these frames, PCF splits the time frame into a contention-free period and a contention period. If PCF is enabled on the remote station, it can transmit data during the contention-free polling periods. However, the main reason why this approach has not been widely adopted is because the transmission times are not predictable. The other approach, DCF, relies on CSMA/CA scheme to send/receive data. Within this scheme, the MAC layer sends instructions for the receiver to look for other stations, transmissions. If it sees none, then it sends its packet after a given interval and awaits an acknowledgment. If one is not received, then it knows its packet was not successfully delivered. The station then waits for a given time interval and also checks the channel before retrying to send its data packet. This can be achieved because every packet that is transmitted includes a value indicating the length of time that the transmitting station expects to occupy the channel. This is noted by any station that receives the signal, and only when this time has expired may other stations consider transmitting. Once the channel appears to be idle, the prospective transmitting station must wait for a period equal to the DCF interframe spacing (DIFS). If the channel has been active, it must first wait for a time interval consisting of the DIFS plus a random number of backoff slot times. This is to ensure that if two stations are waiting to transmit, they do not transmit together and then do so repeatedly. A time known as a contention window (CW) is used for this purpose. This is a random number of backoff slots. If a transmitter intending to transmit senses that the channel becomes active, it must wait for a random period until the channel becomes free, this time allowing a longer CW. While the system works well in preventing stations from transmitting together, the result of using this access system is that if the network usage level is high, the time that it takes for data to be successfully transferred increases. This results in the system appearing to become slower for the users. In view of this, WLANs may not provide a suitable QoS in their current form for systems where real time data transfer is required (see [Fig. 15.2](#)).

To introduce QoS, a new MAC layer was developed as part of IEEE 802.11e. The user traffic is assigned a priority level prior to transmission. There are eight user priority levels. The transmitter prioritizes the data by assigning one of the four access categories. The QoS-enabled MAC layer has combined features from the DCF and PCF schemes into a hybrid coordination function (HCF). In this approach, the

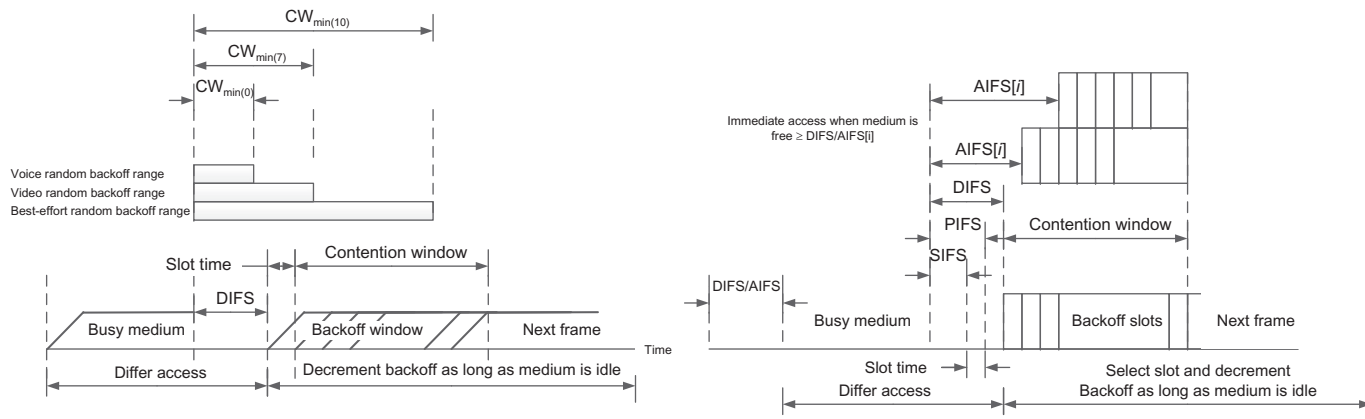


**FIG. 15.2**

Medium access methods in IEEE 802.11.

Based on, E. Perahia, R. Stacey, *Next Generation Wireless LANs: 802.11n and 802.11ac*, second ed., Cambridge University Press, Cambridge, UK, 2013.

modified elements of the DCF are termed the enhanced distributed channel access (EDCA), while the elements of the PCF are termed the HCF controlled channel access (HCCA). When using EDCA, a new class of interframe space called an arbitration inter frame space (AIFS) has been introduced. This is chosen such that the higher the priority the message, the shorter the AIFS, and associated with this, there is also a shorter CW. The transmitter then gains access to the channel in the normal way, but in view of the shorter AIFS and shorter CW, this means that the chance of it gaining access to the channel is higher. Although, statistically, a higher priority message will usually gain the channel, this will not always be the case.

The IEEE 802.11 frame contains a MAC header, a variable length frame body (0–2304 bytes), and a 32-bit frame check sequence (FCS). The MAC header contains information related to the type of frame, source and destination addresses, frame control, and, sequence control, as shown in [Fig. 15.3](#). The IEEE 802.11 standard defines three major frame types: (1) management frames which do not carry service data units; (2) control frames to assist delivery of data frames; and (3) data frames—some with service data units, some without service data units, and a null frame to inform the access point of a client’s power save status. The MAC frame format comprises a set of fields that occur in a fixed order in all frames. [Fig. 15.3](#) depicts the general MAC frame format. The first three fields (Frame Control, Duration/ID, and Address 1) and the last field (FCS) constitute the minimal frame format and are present in all frames, including reserved types and subtypes. The fields Address 2, Address 3, Sequence Control, Address 4, QoS Control, HT Control, and Frame Body are present only in certain frame types and subtypes. The format of each individual subtype of type of frame is defined in the standard. As shown in [Fig. 15.3](#), there are four different fields in the MAC header allocated for the address. The type of address is determined by “To DS” and “From DS” fields. Regardless of the contents in the frame, the structure of the MAC header is same.

The IEEE 802.11 physical layer is divided into two sublayers: Physical Layer Convergence Protocol (PLCP) sublayer and Physical Medium Dependent (PMD) sublayer. The PLCP sublayer receives a frame for transmission from the MAC sublayer and creates the PLCP Protocol Data Unit (PPDU). The PMD sublayer then modulates and transmits the data as bits. The MAC Protocol Data Unit (MPDU) that is delivered to the physical layer is referred to as the PLCP Service Data Unit (PSDU). As part of the processing, the PLCP sublayer adds a preamble and header to the PSDU. When the PLCP layer receives the PSDU from the MAC layer, the appropriate PLCP preamble and header are added to the PSDU to create the PPDU. When transmitting data, the transmitting station provides the receiving station with special synchronization sequences at the beginning of each transmission.

IEEE 802.11 defines three types of preambles: long PLCP preamble, short PLCP preamble, and OFDM PLCP preamble. The IEEE 802.11n amendment further defines three additional preambles in three different PPDU, namely nonhigh throughput (HT) legacy preamble, HT-mixed preamble, and HT-greenfield preamble, also known as OFDM training sequences. The OFDM training sequences consist of 10 short symbols and long symbols. A guard interval (GI) in the form of the cyclic

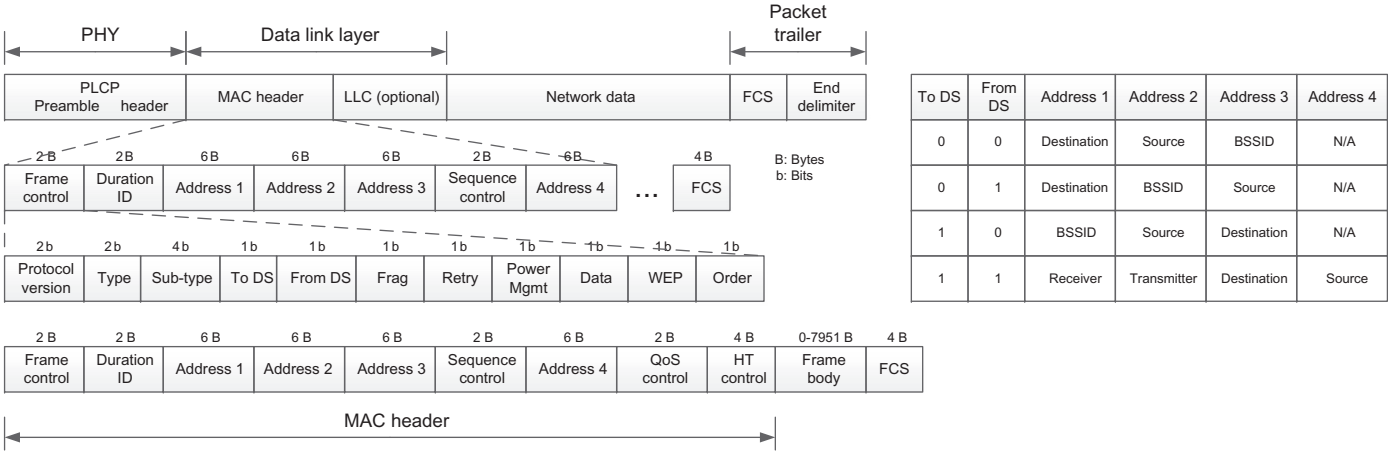


FIG. 15.3

IEEE 802.11 frame and MAC header formats.

Based on, E. Perahia, R. Stacey, *Next Generation Wireless LANs: 802.11n and 802.11ac, second ed.*, Cambridge University Press, Cambridge, UK, 2013.

prefix is added. The Signal and Data fields follow the PLCP preambles each with GI preceding them. The total training sequence length is 16  $\mu$ s. The short OFDM training symbol consists of 12 subcarriers, whereas the long OFDM training symbol consists of 53 subcarriers. The Signal field consists of 8 bits indicating which coding and modulation scheme is used for PSDU/MPDU. The Service field consists of 8 bits. The 16-bit Length field is used to indicate the number of microseconds that are required to transmit the PSDU. A 16-bit CRC provides protection for the preceding fields (signal, service, and length). In OFDM transmission, the SIGNAL field is 24 bits long.

The access point periodically broadcasts a special signal called a beacon (once every 102.4 ms). When the Wi-Fi communication module is turned on, the device first detects and decodes the beacon signal and establishes physical synchronization with the sender. After establishing synchronization, the access point and the device initiate the authentication procedure followed by the association procedure. There are two types of scanning: passive and active scanning. As shown in Fig. 15.4, during passive scanning, the device scans and detects the beacon signal from the access point

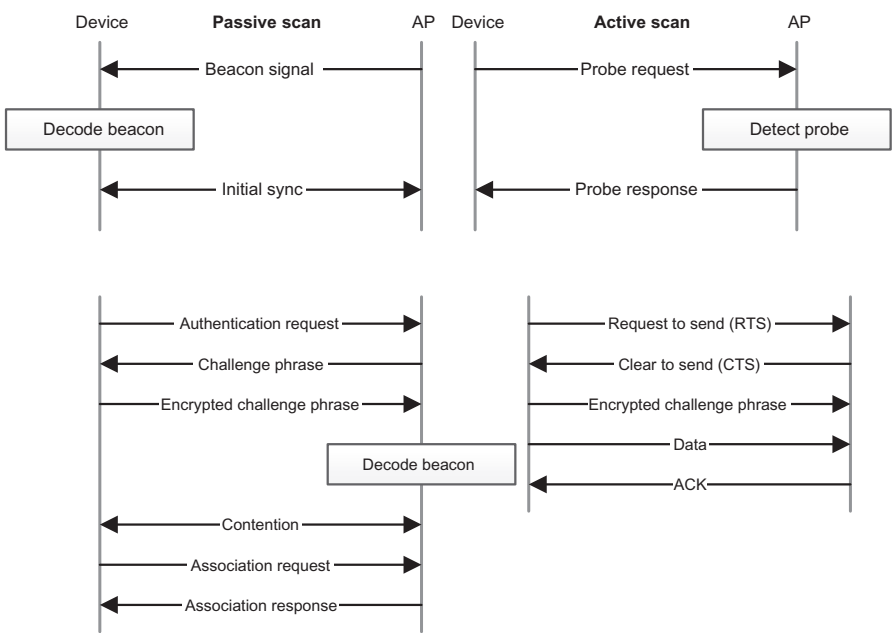


**FIG. 15.4**  
Scanning and association procedures.

Based on, E. Perahia, R. Stacey, *Next Generation Wireless LANs: 802.11n and 802.11ac*, second ed., Cambridge University Press, Cambridge, UK, 2013.

and establishes synchronization based on the beacon signal. In active scan mode, the device broadcasts a probe request to all access points or a specific access point. If there is any access point that detects the probe request, it sends a probe response to the device.

Once the client and the access point go through the Authentication and Association procedure, the client can send or receive data. Unlike cellular standards, IEEE 802.11 does not support dedicated control/traffic channels (TCHs) and it does not have the MAC scheduling functionality. The stations are allowed to transmit at any time, as long as the medium is not occupied by transmissions from other stations. In order to determine whether the medium is free and able to overcome the hidden-node problem, the station transmits a short Request to Send (RTS) frame containing the source address, destination address, and the duration of upcoming data transmission. Other stations located around the transmitting station may receive the RTS burst and check if the RTS is meant for them. If the RTS is meant for a station and the medium is free, the receiving device would transmit a Clear to Send (CTS) frame containing the duration of the transaction. At this time, other devices in the vicinity of the communicating stations know that the medium will be occupied for a certain duration and set their network allocation vector (NAV), which is a MAC level contention control timer, accordingly so that it would not try to sense the medium and transmit during that period.

When a packet arrives at the MAC layer from higher layers, a sequence number is assigned to it, and if the packet length is larger than a single MAC frame, it is segmented into multiple fragments. In this case, a fragment number is assigned to each segment. When a packet is segmented into multiple MAC frames, those fragmented frames are assigned the same sequence number and different values for the fragment number. IEEE 802.11 can transmit a maximum of 2304 bytes of higher layer data (Fig. 15.5).

### 15.3.2 IEEE 802.16 FAMILY (WIMAX)

This section provides an overview of the prominent functional features of IEEE 802.16m (mobile WiMAX) radio access technology [6]. Mobile WiMAX network architecture specifies a flat end-to-end network reference model. The network reference model is a logical representation of the network architecture that identifies functional entities and reference points over which interoperability is achieved (Fig. 15.6). The functions represented by the logical entities can be realized in a single physical entity or may be distributed over multiple physical entities. The reference model is used to ensure interoperability among different implementations of functional entities in the network. Thus, the functional entities on either side of a reference point represent a collection of control or data-plane terminations. The WiMAX architecture, developed by the WiMAX Forum, supports fixed, nomadic, and mobile operations. The WiMAX network architecture is based on an all-IP model and comprises three major elements:

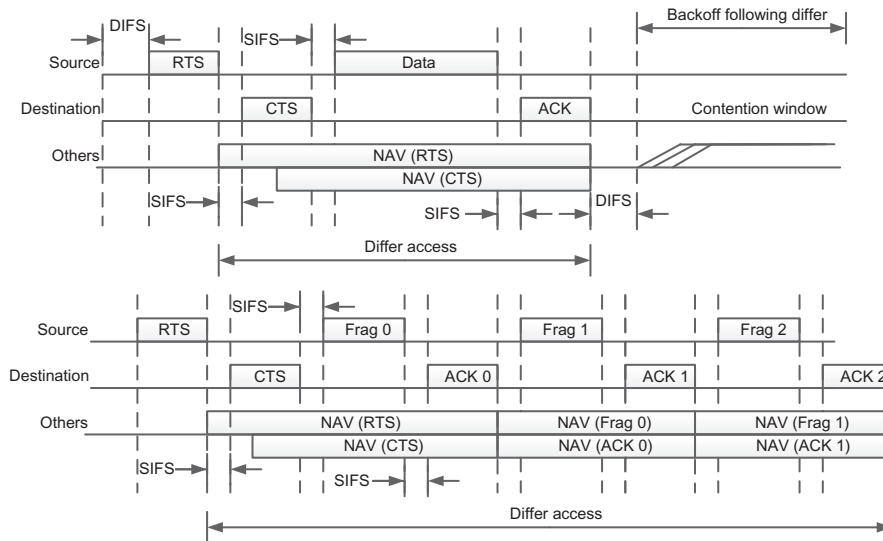


**FIG. 15.5**

Medium access and contention control in IEEE 802.11.

*Based on, E. Perahia, R. Stacey, Next Generation Wireless LANs: 802.11n and 802.11ac, second ed., Cambridge University Press, Cambridge, UK, 2013.*

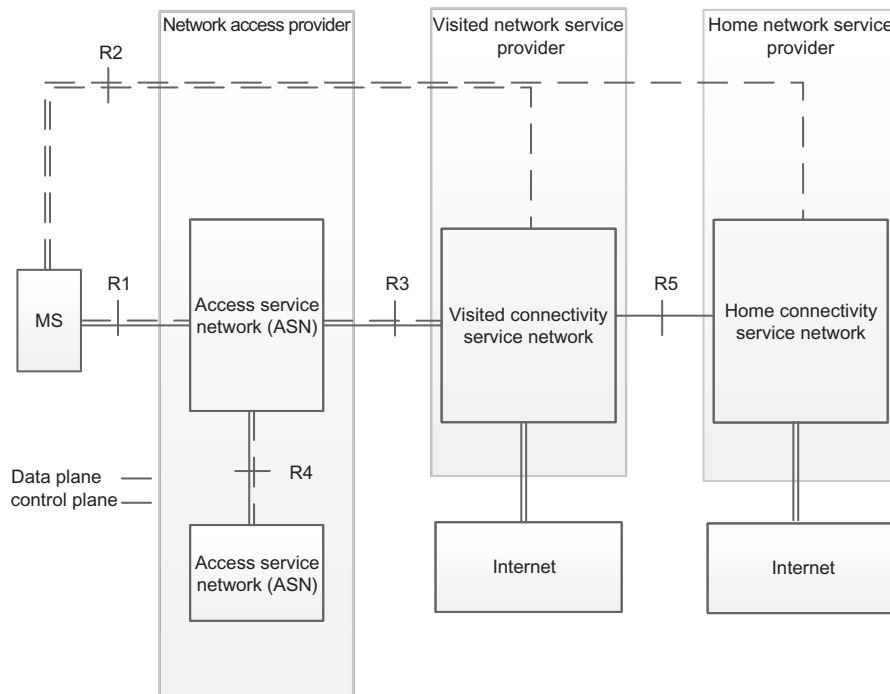


**FIG. 15.6**

Mobile WiMAX network reference model.

*Based on, S. Ahmadi, Mobile WiMAX: A Systems Approach to Understanding IEEE 802.16m Radio Access Technology, Academic Press, Oxford, UK, 2010.*

- Mobile stations (MS): These are the user equipments (UEs) that may be mobile or fixed and may be located in the premises of the user.
- Access service network (ASN): This is the area of the WiMAX network that forms the radio access network at the edge, and it comprises one or more base stations and one or more ASN gateways.
- Connectivity service network (CSN): This part of the WiMAX network provides the IP connectivity and all IP core network (CN) functions. It is the equivalent of the CN in cellular terminology.

The data link layer of IEEE 802.16 comprises three sublayers: (1) the service-specific Convergence Sublayer (CS) that provides any transformation or mapping of network-layer data packets into MAC SDUs. On the transmitter side, the CS receives the data packets through the CS Service Access Point (SAP) and delivers MAC SDUs to the MAC Common Part Sublayer (MAC CPS) through the MAC SAP. This includes classifying network-layer SDUs and associating them with the proper MAC Service Flow Identifiers (SFID) and Connection Identifiers (CID). The convergence sublayer also includes payload header suppression function to compress the higher-layer protocol headers. Multiple CS specifications are provided for interfacing with various network-layer protocols, such as Asynchronous Transfer Mode (ATM), and packet-switched protocols, such as IP or Ethernet. The internal format of the CS payload is unique to the CS, and the MAC CPS is not required to understand the format of or parse any information from the CS payload (Fig. 15.7).

The MAC CPS provides the core MAC functionality of system access, bandwidth allocation, connection establishment, and connection maintenance. It can receive data from the various convergence sublayers, through the MAC SAP classified into particular MAC connections. The QoS is further applied to the transmission and scheduling of data over the physical layer.

The MAC also contains a separate security sublayer providing authentication, secure key exchange, and encryption. The user data, physical layer control, and statistics are transferred between the MAC CPS and the physical layer (PHY) via the PHY SAP, which is implementation specific.

The IEEE 802.16m MAC common part sublayer is classified into a radio resource control (RRC) and management functional group and a MAC functional group. The control-plane functions and data-plane functions are also separately identified. The RRC and management functional group comprises several management functions including radio resource management, mobility management, network-entry management, location management, idle mode management, security management, system configuration management, and multicast and broadcast service. The MAC functional group, on the control-plane, includes functional blocks which are related to physical layer and link controls such as physical-layer control, control signaling, sleep mode management, QoS management, and scheduling. The MAC functional group on the data-plane includes functional blocks such as the fragmentation/packing block, automatic repeat request (ARQ) block, and MAC protocol data unit formation

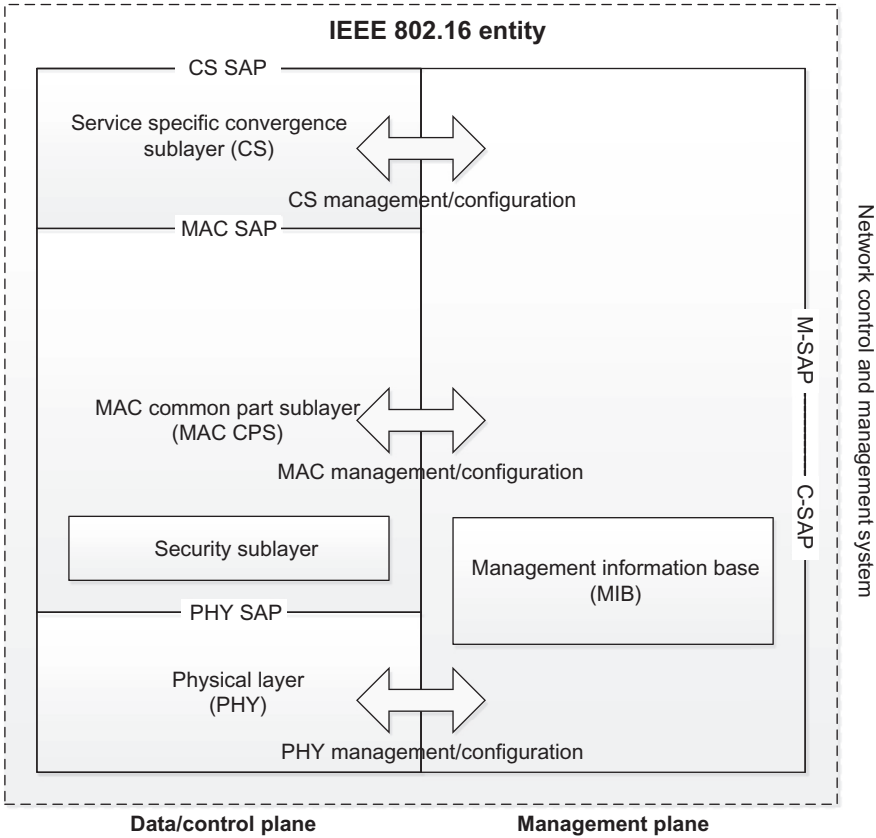


**FIG. 15.7**

IEEE 802.16 reference model.

*Based on, S. Ahmadi, Mobile WiMAX: A Systems Approach to Understanding IEEE 802.16m Radio Access Technology, Academic Press, Oxford, UK, 2010.*

block. The IEEE 802.16m protocol structure is similar to that of the legacy system with some additional functional blocks in the control plane for the new features such as relay, self-organization and self-optimization functions, and multicarrier functions. The multicarrier functions enable control and operation of a number of contiguous or noncontiguous RF carriers where the RF carriers can be assigned to unicast and/or multicast and broadcast services. A single MAC instantiation will be used to control several physical layers.

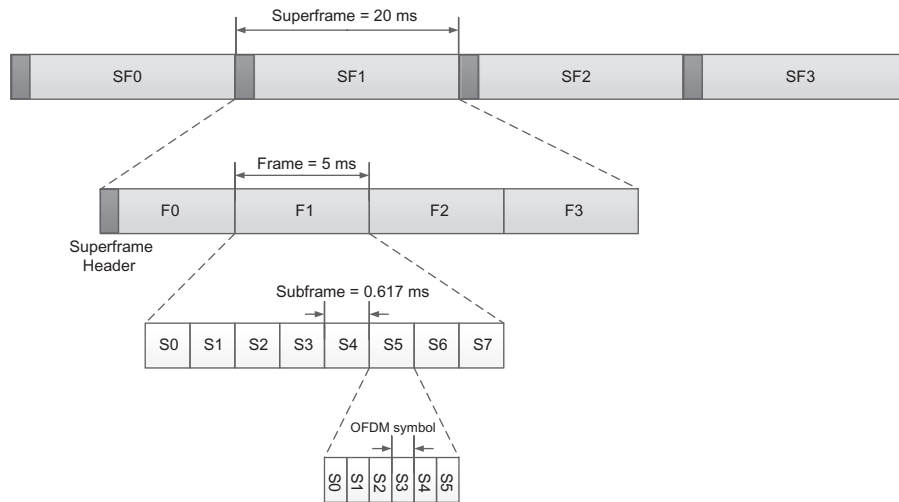
The IEEE 802.16m MS state diagram consists of the four states as follows:

- Initialization state: An MS without any connection performs cell selection by scanning and synchronizing to a BS and acquires the system information.
- Access state: The MS performs network entry to the selected base station through an initial ranging process.
- Connected state: In this state, the MS maintains at least one transport connection and two management connections with the serving BS. In order to reduce power consumption, the MS or BS can request a transition to sleep mode. The MS can also scan neighbor base stations to reselect a cell which provides more robust and reliable services.
- Idle state: In this state, the MS may save power by switching between paging available mode and paging unavailable mode. In the paging available mode, the MS may be paged by the BS. If the MS is paged, it transitions to the access state for its network reentry. The MS performs a location update procedure during the idle state.

IEEE 802.16m uses OFDMA as the multiple-access scheme in downlink and uplink. It further supports both TDD and FDD duplex schemes including H-FDD operation of the MSs in the FDD networks. The majority of the frame structure attributes and baseband processing are common for both duplex schemes. In the IEEE 802.16m frame structure, a superframe is defined as a collection of consecutive equally sized radio frames whose beginning is marked with a superframe header. The superframe header carries short-term and long-term system configuration information. In order to decrease the air-link access latency, the radio frames are further divided into a number of subframes where each subframe comprises an integer number of OFDM symbols. The transmission time interval (TTI) is defined as the transmission latency over the air-link and is equal to an integer multiple of subframe length (the default is one subframe). In the basic frame structure shown in Fig. 15.8, superframe length is 20 ms (comprising four radio frames), radio frame size is 5 ms (comprising eight subframes), and subframe length is 0.617 ms. The use of the subframe concept with the latter parameter set would reduce the one-way air-link access latency to less than 10 ms.

The downlink/uplink subframes are divided into a number of frequency partitions, where each partition consists of a set of physical resource units over the available number of OFDM symbols in the subframe. Each frequency partition can include localized and/or distributed physical resource units. Frequency partitions can be used for different purposes such as fractional frequency reuse (FFR).

Fig. 15.9 shows the channel coding and modulation procedures. A cyclic redundancy check (CRC) is appended to a burst (ie, a physical layer data unit) prior to partitioning. If the burst size including burst CRC exceeds the maximum block size, the burst is partitioned into a number of subblocks, each of which is encoded

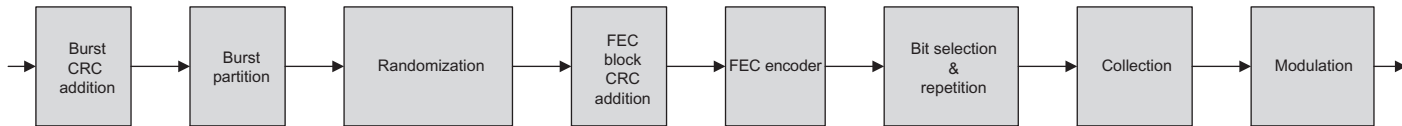
**FIG. 15.8**

IEEE 802.16m basic frame structure.

Based on, S. Ahmadi, *Mobile WiMAX: A Systems Approach to Understanding IEEE 802.16m Radio Access Technology*, Academic Press, Oxford, UK, 2010.

separately and appended with a CRC. The maximum block size is 4800 bits. IEEE 802.16m utilizes convolutional turbo code (CTC) with a code rate of 1/3. IEEE 802.16m supports QPSK, 16QAM, and 64QAM baseband modulation schemes in the downlink and uplink (uplink 64QAM is optional). The QAM symbols are then mapped to the input of the MIMO encoder.

The incremental redundancy HARQ (HARQ-IR) scheme is used in IEEE 802.16m by determining the starting position of the bit selection for HARQ retransmissions. Chase combining HARQ (HARQ-CC) is also supported and considered as a special case of HARQ-IR. The resource allocation and transmission formats in each retransmission in the downlink can be configured with control signaling. The resource allocation in each retransmission in the uplink can be fixed or adaptive, as configured by control signaling. IEEE 802.16m uses adaptive asynchronous and nonadaptive synchronous HARQ schemes in the downlink and uplink, respectively. The HARQ operation is relying on an  $N$ -process (multichannel) stop-and-wait protocol. In adaptive asynchronous HARQ, the resource allocation and transmission format for the HARQ retransmissions may be different from the initial transmission. In the case of retransmission, control signaling is required to indicate the resource allocation and transmission format along with other HARQ necessary parameters. A nonadaptive synchronous HARQ scheme is used in the uplink where the parameters and the resource allocation for the retransmission are known in advance.

**FIG. 15.9**

Coding and modulation procedure in IEEE 802.16m.

*Based on, S. Ahmadi, Mobile WiMAX: A Systems Approach to Understanding IEEE 802.16m Radio Access Technology, Academic Press, Oxford, UK, 2010.*

Transmission of pilot subcarriers in the downlink is necessary to allow channel estimation, channel quality measurement (eg, CQI), frequency offset estimation, etc. To optimize the system performance in different propagation environments, IEEE 802.16m supports both common and dedicated pilot structures. The common pilots can be used in distributed allocations by all MSs. The dedicated pilots can be used with both localized and distributed allocations and are associated with the user-specific pilot index. The dedicated pilots are associated with a specific resource allocation and are used by the MSs assigned to specific resource block (RB); therefore, they can be precoded in the same manner as the data subcarriers of the RB. The downlink pilot structure is defined for up to eight spatial streams, and the design of common and dedicated pilots is consistent. There is an equal pilot density per spatial stream; nevertheless, there is not necessarily equal pilot density per OFDM symbols. There is the same number of pilots for each physical resource unit allocated to a particular MS.

Downlink control channels carry essential information for system operation. Depending on the type of control signaling, information is transmitted over different time intervals (ie, from superframe to subframe intervals). The system configuration parameters are transmitted at the superframe intervals, whereas control signaling related to user data allocations is transmitted at the frame/subframe intervals.

The superframe header carries essential system parameters and configuration information. The content of superframe header is divided into two parts referred to as primary and secondary superframe headers. The information transmitted in the secondary superframe header is further divided into different subpackets. The primary superframe header is transmitted every superframe, whereas the secondary superframe header is transmitted over one or more superframes. The primary and secondary superframe headers are located in the first subframe within a superframe, and they are time-division-multiplexed with the preamble.

The Medium Access Protocol (MAP), which is a WiMAX term for scheduling and resource allocation control channels, consists of dedicated and common control information. The nonuser-specific control information includes information that is not dedicated to a specific user or a specific group of users. It contains information required to decode user-specific control signaling. User specific control information consists of information intended for one or more users. It includes scheduling assignment, power control, and HARQ ACK/NACK. Resources can be allocated persistently to the MSs. The periodicity of the allocation is configurable. A MAP allocation information element (IE) is defined as the basic element of unicast control signaling. A unicast control IE may be addressed to one user using a unicast identifier or to multiple users via the multicast/broadcast identifier. The CRC of the control channel is masked with a specific identifier for each specific allocation. It may contain information related to resource allocation, HARQ, MIMO transmission mode, etc. Each unicast control IE in IEEE 802.16m is coded separately. Note that this method is different from the legacy system control mechanism where the IEs of all users are jointly coded. Nonuser-specific control information is encoded separately from the user-specific control information. The transmission format of nonuser-specific

control information is predetermined. In the downlink subframes, each frequency partition may contain a control region.

MIMO feedback provides wideband and/or narrowband spatial characteristics of the channel that are required for MIMO operation. The MIMO mode, precoding matrix index, rank adaptation information, channel covariance matrix elements, and best subband index are examples of MIMO feedback information. HARQ feedback (ACK/NACK) is used to acknowledge downlink data transmissions. The uplink HARQ feedback channel starts at a predetermined offset with respect to the corresponding downlink transmission. The HARQ feedback channel is frequency-division-multiplexed with other control and data channels. Orthogonal codes are used to multiplex multiple HARQ feedback channels.

Bandwidth requests are used to indicate the amount of bandwidth required by a user, and they are transmitted through indicators or messages. A bandwidth request indicator notifies the base station of an uplink scheduling request by the MS. Bandwidth request messages can include information about the status of queued traffic at the MS such as buffer size and QoS parameters. Contention or noncontention-based random access is used to transmit bandwidth request information on this control channel.

Channel quality feedback provides information about channel conditions as seen by the user. This information is used by the base station for link adaptation, resource allocation, power control, etc. The channel quality measurement includes both narrowband and wideband measurements. The CQI feedback overhead can be reduced through differential feedback or other compression techniques. Examples of CQI include effective Carrier to Interference plus Noise Ratio (CINR), band selection, etc. The default subframe size for transmission of uplink control information is 6 OFDM symbols. The fast feedback channel carries channel quality and MIMO feedback.

The ranging channel is used for uplink synchronization. The ranging channel can be further classified into ranging for nonsynchronized and synchronized MSs. A random access procedure, which can be contention or noncontention based is used for ranging. The contention-based random access is used for initial ranging. The noncontention-based random access is used for periodic ranging and HO. The ranging channel for nonsynchronized MSs starts at a configurable location with the configuration signaled in a downlink broadcast control message. The ranging channel for nonsynchronized MSs is frequency-division multiplexed with other uplink control and data channels.

A power control mechanism is supported for downlink and uplink. The base station controls the transmit power per subframe and per user. Using downlink power control, user-specific information is received by the terminal with controlled power level. The downlink control channels are power-controlled based on the terminal uplink channel quality feedback. The uplink power control is supported to compensate the path loss, shadowing, fast fading, and implementation loss, as well as to mitigate inter- and intracell interference. The uplink power control includes open- and closed-loop power control mechanisms. The base station can transmit necessary information through control channels or MAC messages to terminals to support

uplink power control. The parameters of power control algorithm are optimized on a system-wide basis by the base station and broadcasted periodically or triggered by certain events. In high mobility scenarios, the power control scheme may not be able to compensate the fast fading channel effect because of the variations of the channel impulse response. As a result, the power control is used to compensate the distance-dependent path loss, shadowing, and implementation loss only. The channel variations and implementation loss are compensated via open-loop power control without frequently interacting with the base station. The terminal can determine the transmit power based on the transmission parameters sent by the serving base station, uplink channel transmission quality, downlink channel state information, and interference knowledge obtained in the downlink. Open-loop power control provides a coarse initial power setting for the terminal when an initial connection is established. The dynamic channel variations are compensated via closed-loop power control with power control commands from the serving base station. The base station measures uplink channel state and interference information using uplink data and/or control channel transmissions and sends power control commands to the terminal. The terminal adjusts its transmission power based on the power control commands from the base station.

IEEE 802.16m supports several advanced multiantenna techniques including single and multiuser MIMO (spatial multiplexing and beamforming), as well as a number of transmit diversity schemes. In a single user-MIMO (SU-MIMO) scheme, only one user can be scheduled over one (time, frequency, spatial) resource unit. In multiuser-MIMO (MU-MIMO), multiple users can be scheduled in one resource unit. Vertical encoding (or single codeword) utilizes one encoder block (or layer), whereas horizontal encoding (or multicodeword) uses multiple encoders (or multiple layers) in the transmit chain. A layer is defined as a coding and modulation input path to the MIMO encoder. A spatial stream is defined as the output of the MIMO encoder that is further processed through the beamforming or the precoder block. For spatial multiplexing, the rank is defined as the number of streams to be used for the user. Each SU-MIMO or MU-MIMO open-loop or closed-loop scheme is defined as a MIMO mode.

A number of antenna configurations and transmission rates are supported in uplink open-loop SU-MIMO including two and four transmit antennas with rate 1 (ie, transmit diversity mode) as well as two and four transmit antennas with rates 2, 3, and 4 (ie, spatial multiplexing). The supported uplink transmit diversity modes include two and four transmit antenna schemes with a rate of 1, such as Space Frequency Block Coding (SFBC) and dual-stream precoder. The spatial multiplexing modes supported in open-loop single-user MIMO include two and four transmit antenna rate-2 schemes with and without precoding, four transmit antenna rate-3 schemes with precoding, four transmit antenna rate-4 scheme. In FDD and TDD systems, unitary codebook-based precoding is supported. In this mode, an MS transmits a sounding reference signal in the uplink to assist the scheduling and precoder selection in the BS. The BS signals the resource allocation, MCS, rank, preferred precoder index, and packet size to the MS. The uplink MU-MIMO enables multiple MSs to be

spatially multiplexed on the same radio resources. Both open-loop and closed-loop MU-MIMO are supported. The MSs with a single transmit antenna can operate in open-loop SU-MIMO/MU-MIMO mode.

Network entry is the procedure through which an MS detects a cellular network and establishes a connection with that network. The network entry has the following steps:

- Synchronization with the BS by acquiring the preambles.
- Acquiring necessary system information such as BS and network service provider identifiers for initial network entry and cell selection.
- Initial ranging.
- Basic capability negotiation.
- Authentication/authorization and key exchange.
- Registration and service flow setup.

Neighbor search is based on the same downlink signals as initial network search except some information can be provided by the serving BS (ie, neighbor advertisement messages). The BS responds to the MS initial ranging code transmission by broadcasting a status indication message in a predefined downlink frame/subframe.

A connection is defined as a mapping between the MAC layers of a BS and one (or several) MS. If there is a one-to-one mapping between one BS and one MS, the connection is called a unicast connection; otherwise, it is called a multicast or broadcast connection. Two types of connections are specified: control connections and transport connections. Control connections are used to carry MAC control messages. Transport connections are used to carry user data including upper layer signaling messages. A MAC control message is never transferred over transport connection, and user data is never transferred over the control connections. One pair of bidirectional (DL/UL) unicast control connections is automatically established when an MS performs initial network entry. The user data communications are in the context of transport connections. A transport connection is unidirectional and established with a unique flow identifier. Each transport connection is associated with an active service flow to provide various levels of QoS required by the service flow. The transport connection is established when the associated active service flow is admitted or activated, and it is released when the associated service flow becomes inactive. Transport connections can be preprovisioned or dynamically created. Preprovisioned connections are those established by system for an MS during the MS network entry. On the other hand, the BS or the MS can create new connections dynamically if required.

IEEE 802.16m supports both network-controlled and MS-assisted HO. The HO procedure may be initiated by either MS or BS; however, the final HO decision and target BS selection are made by the serving BS. The MS executes the HO command as instructed by the BS or cancels the procedure through the HO cancellation message. The network reentry procedure with the target BS may be optimized, if the target BS obtains the MS context from the serving BS via CN. The MS may also maintain communication with serving BS while performing network reentry at target BS,

as directed by serving BS. The HO procedure is divided into three stages (1) HO initialization, (2) HO preparation, and (3) HO execution. Upon completion of HO execution, the MS is ready to perform network reentry with the target BS. In addition, the HO cancelation procedure is defined to allow an MS to cancel an HO procedure.

IEEE 802.16m provides power management functions including sleep mode and idle mode to reduce power consumption of the MSs. Sleep mode is a state in which an MS performs prenegotiated periods of absence from the serving BS. The sleep mode may be enacted when an MS is in the connected state. Using the sleep mode, the MS is provided with a series of alternative listening and sleep windows. The listening window is the time interval in which the MS is available for transmit/receive of control signaling and data. The IEEE 802.16m has the capability of dynamically adjusting the duration of sleep and listening windows within a sleep cycle based on changing traffic patterns and HARQ operations. When an MS is in the active mode, sleep parameters are negotiated between the MS and BS. The base station instructs the MS to enter sleep mode. MAC control messages can be used for sleep mode request/response. The period of the sleep cycle is measured in units of frames or superframes and is the sum of sleep and listening windows. During the MS listening window, the BS may transmit the traffic indication message intended for one or multiple MSs. The listening window can be extended through explicit/implicit signaling. The maximum length of the extension is to the end of the current sleep cycle.

Security functions provide subscribers with privacy, authentication, and confidentiality across IEEE 802.16m network. The MAC packet data units are encrypted over the connections between the MS and BS. The security architecture is divided into security management, encryption, and integrity protection logical entities. The security management functions include overall security management and control, Extensible Authentication Protocol (EAP) encapsulation/deencapsulation, privacy key management (PKM) control, security association management, and identity/location privacy. The encryption and integrity protection functions include user data encryption and authentication, management message authentication, and message confidentiality protection. Authorization is a process where base station and MS mutually authenticate the identity of each other. Authentication is performed during initial network entry after security capabilities and policies are negotiated. The basic MS capability negotiation is performed prior to authentication and authorization. Reauthentication is performed before the authentication credentials expire. Data transmission may continue during the reauthentication process. In the legacy system there is no explicit means by which the identity of a user is protected. During initial ranging and certificate exchange, the MS MAC address is transmitted over the air, revealing user identity or user location information that may result in compromising the security aspects of the system. IEEE 802.16m incorporates mechanisms such as pseudoidentity to mitigate this problem. IEEE 802.16m inherits the key hierarchies of the legacy system. The IEEE 802.16m uses the PKMv3 protocol to transparently exchange authentication and authorization messages. The PKM protocol provides mutual and unilateral authentication and establishes confidentiality between the MS

and the BS. Some IEEE 802.16m keys are derived and updated by both BS and MS. The key exchange procedure is controlled by the security key state machine, which defines the allowed operations in the specific states. The key exchange state machine is similar to that of the legacy system.

### 15.3.3 IEEE 802.15 FAMILY (BLUETOOTH)

The initial goal of Bluetooth technology was to enable the users to replace cables between devices such as printers, fax machines, desktop computers, and peripherals, as well as to wirelessly connect headsets to mobile phones [7]. Another application of Bluetooth technology was to provide a connection between an ad hoc wireless network and existing wired data networks. Bluetooth uses the license-free industrial, scientific, and medical (ISM) band at 2.4 GHz for its radio signals and enables communications to be established between devices to a maximum distance of 100 m.

The Bluetooth network often operates as a single connection or may include many devices. Bluetooth also allows for a scheme known as Bluetooth pairing, where devices can quickly associate with each other. There are various methods in which the Bluetooth networks can be set up. In the basic form known as pico-net topology, one device acts as the master and it is able to talk to a maximum of seven slave nodes. The limit of seven slave nodes is due to three-bit address that is used which reflects the number of active nodes in a Bluetooth network at any given time. Bluetooth network connections can support scatter-nets, although because of timing and memory constraints this form of Bluetooth network has rarely been implemented. For a Bluetooth scatter-net, a slave node or slave device is able to share its time between two different pico-nets. This enables large star networks to be created.

The way in which Bluetooth devices make connections is more complicated than what is associated with many other types of wireless devices. The reason for this is the frequency hopping nature of the devices. While the frequency hopping reduces the effects of interference, it makes connecting the devices more complicated. Bluetooth is a system in which connections are made between a master and a slave. These connections are maintained until they are broken, either by deliberately disconnecting the two or by the radio link quality becoming so poor that communications cannot be maintained. Typically, this occurs as the devices go out of range of each other. In the connection process, there are four types of Bluetooth connection channels:

- Basic pico-net channel: This channel is used only when all 79 channels are used within the hopping set.
- Adapted pico-net channel: This channel is used more widely and allows the system to use a reduced hopping set; that is, between 20 and 79 channels. Pico-net channels are the only channels that can be used to transfer user data.
- Inquiry channel: This channel is used when a master device finds a slave device or devices within its range.
- Paging channel: This channel is used where a master and a slave device make a physical connection.

Operating in the 2.4 GHz ISM band, the Bluetooth radio employs frequency hopping techniques with the carrier modulated using Gaussian frequency shift keying (GFSK). The frequency hopping mitigates cochannel interference by Bluetooth devices. A Bluetooth transmission only remains on a given frequency for a short time, and if any interference is present, the data will be resent later when the signal has changed to a different channel which is likely to be clear of other interfering signals. The standard uses a hopping rate of 1600 hops per second, and the system hops over the available frequencies using a predetermined pseudorandom hopping sequence based on the Bluetooth address of the master node in the network.

Bluetooth frequencies are located within the 2.4 GHz ISM band. The ISM band typically extends from 2400 to 2483.5 MHz (Fig. 15.10). The Bluetooth channels are spaced 1 MHz apart starting at 2402 MHz and ending at 2480 MHz. This can be calculated as  $2401 + n$ , where  $n$  varies from 1 to 79. The transmitter frequency

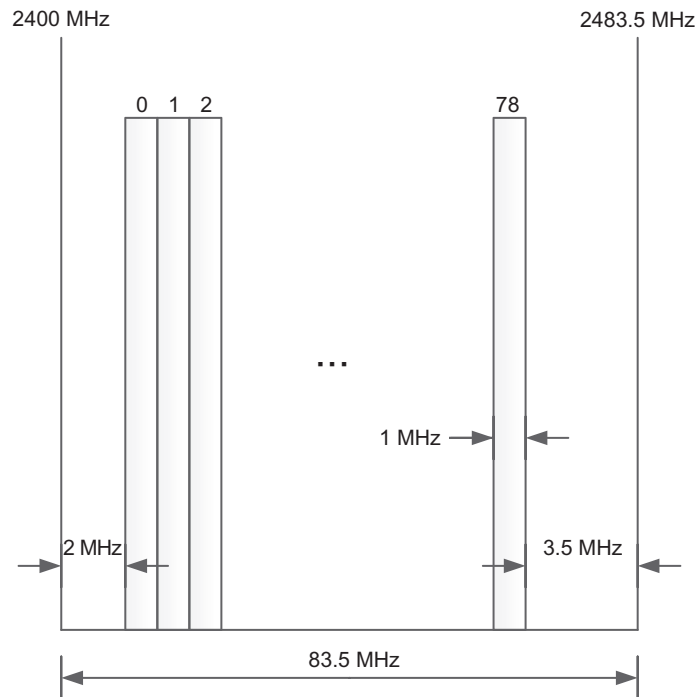


**FIG. 15.10**

Bluetooth channels in 2.4 GHz ISM band.

Based on, K. Townsend, et al., *Getting Started With Bluetooth Low Energy: Tools and Techniques for Low-Power Networking*, O'Reilly Media, Sebastopol, CA, 2014.

accuracy requirement for Bluetooth transmissions is  $\pm 75$  kHz from the receiver center frequency. The Bluetooth devices are identified by the 48-bit address.

The original modulation scheme for Bluetooth was GFSK; however, the requirement for higher data rates later necessitated the addition of two forms of phase shift keying for enhanced data rate (EDR) capability:  $\pi/4$  DQPSK (a form of phase shift keying known as  $\pi/4$  differential phase shift keying. It enables the raw data rate of 2 Mbps to be achieved) and 8DPSK (an eight point or eight-ary phase shift keying that is used when link conditions are good, and it allows raw data rates of up to 3 Mbps to be achieved). The enhanced data rate capability for Bluetooth modulation is implemented as an additional capability so that the system remains backward compatible. The Bluetooth modulation schemes and the general format do not lend themselves to carrying higher data rates. For Bluetooth v3, the higher data rates are not achieved by changing the format of the Bluetooth modulation, rather by integrating an IEEE 802.11g physical layer. In this way, data rates of up to 25 Mbps can be achieved.

A Bluetooth slot is made up of three major components (access code, header, and payload) as shown in Fig. 15.11. The fundamental length of the slot is 366  $\mu$ s, and depending on the length of payload, it can extend to 1.622 or 2.87 ms. The access code and header are always modulated with GFSK and the payload part is modulated using one of three different methods (GFSK,  $\pi/4$  DQPSK, 8DPSK) depending on packet type. Fig. 15.11 shows the frame structure for the most conventional Bluetooth slot structure. The maximum data rate that can be achieved with this structure is 1 Mbps, and this structure uses the GFSK modulation scheme across the slot.

Also shown in Fig. 15.11 is the frame structure for the high data rate Bluetooth slot structure. Using this frame structure, one can achieve a maximum data

Access code	Header	G T	Sync	Payload
GFSK 72 bits Used for inquiry and paging information	GFSK 54 bits Link control	5 $\mu$ s	11 $\mu$ s Synchronization Sequence	$\pi/4$ DQPSK (for 2 Mbps) and 8 DQPSK (for 3 Mbps) Data

Access code	Header	Payload
GFSK 72 bits Used for inquiry and paging information	GFSK 54 bits Link control	GFSK 224 bits (for DH1) 1480 bits (for DH2) 1278 bits (for DH3) Data

FIG. 15.11

Bluetooth common frame formats.

Based on, K. Townsend, et al., *Getting Started With Bluetooth Low Energy: Tools and Techniques for Low-Power Networking*, O'Reilly Media, Sebastopol, CA, 2014.

rate of 2–3 Mbps depending on the modulation scheme of the payload. The access code and header parts are modulated using GFSK and the payload part is modulated using  $\pi/4$  DQPSK for the 2 Mbps data rate and 8DPSK for 3 Mbps. This means that the modulation scheme changes within a slot. One additional component is that this frame format is the guard time (GT), giving the transmitter some time to switch the modulation scheme. Another additional component is the Sync field. In any  $I/Q$ -based modulation, sampling time is very important and the sync is part of reference signal so that the receiver can obtain proper timing reference.

The transmit power for Bluetooth devices is very low, although there are three different classes of output dependent upon the anticipated use and the range required. There are three power classes: Power Class 1 devices are designed for long range communications up to about 100 m, and this has a maximum output power of 20 dBm; Power Class 2 devices can cover a range up to about 10 m, with a maximum output power of 6 dBm; and Power Class 3 is for short range devices, and it supports communication only up to 10 cm and it has a maximum output power of 0 dBm. Power control is mandatory for Bluetooth Class 1, but it is optional for the other classes. The appropriate power level is chosen according to received strength signal indicator measurement. The Bluetooth specifications define a maximum bit error rate of 0.1% corresponding to a minimum requirement for the receive sensitivity level of  $-70$  dBm. This figure for sensitivity leads to the distances achievable for different power levels, although today's receivers are generally more sensitive than those that were used to baseline the specification.

Bluetooth data transfer can be achieved using a variety of different packet types and using different forms of links: asynchronous links and synchronous links. These different Bluetooth data file transfer formats provide flexibility, but they are transparent to the user who sees a connection being made and Bluetooth data being transferred. There are two main types of Bluetooth links that are available and can be set up: asynchronous connectionless communications link (ACL) and synchronous connection orientated communications link (SCO). The choice of the form of Bluetooth link depends on the type of Bluetooth data transfer that is required. ACL is the most widely used form of Bluetooth link. The ACL Bluetooth link is used for carrying framed data; that is, data submitted by an application to the logical link control and adaptation protocol channel. The channel may support either unidirectional or bidirectional Bluetooth data transfer. There are a variety of different ACL formats that can be used where most of them incorporate forward error correction to detect and correct errors that may occur over the radio link.

The asynchronous Bluetooth link provides connections for most Bluetooth applications. Data transfers are normally supported by profiles which allow the data to be incorporated into frames and transferred to the other end of the Bluetooth link, where it is extracted from the frames and passed to the relevant application. The Bluetooth v1 ACL enables data to be transferred at speeds up to the maximum rate of 732.2 kbps. This occurs when it is operating in an asymmetric mode. This is commonly used because for most applications, data is mostly asymmetrically transferred. When a symmetrical mode is needed with data transferred at the same rate in both directions, the data transfer rate falls to 433.9 kbps. The synchronous

links support two bidirectional connections at a rate of 64 kbps. The data rates are adequate for audio and most file transfers. With the Bluetooth v2 enhanced data rate, data rates of 2.1 Mbps may be achieved with QoS enabled on asynchronous links by setting the appropriate channel parameters.

The SCO link is used for streaming rather than framed-formatted data. The SCO can operate alongside the ACL channels, and in fact, one needs an ACL channel to configure the SCOs. A Bluetooth master node can support up to three simultaneous SCO channels and these can be split between up to three slave nodes. The idea of the SCO is to ensure that audio data can be streamed without suffering from delays as a result of waiting for frames or packet slots to become available. The SCO communication link is assigned guaranteed time slots so that they will be transported at the required time with a known maximum latency. Another link, known as eSCO or Extended SCO, was introduced with version 1.2 of the Bluetooth standard. Originally, no acknowledgment had been sent, whereas using the eSCO greater reliability is provided to the Bluetooth link by sending an acknowledgment and allowing a limited number of retransmissions if received data is corrupted. In view of the latency requirements, retransmissions are only allowable until the next guaranteed time slot; otherwise, new data would be delayed.

Within the core specification, there are a number of Bluetooth codec types that are relatively basic and are not used for audio, including stereo music applications which would use the ACL. Any Bluetooth codec is intended to provide telephone standard audio, limiting the audio bandwidth to around 4 kHz. The higher layer protocols within the Bluetooth stack are also known as the Bluetooth Host. This is responsible for the communications between the applications and the controller. Unlike the higher layer stack, the lower layers undertake the connections between devices with no need to reference the higher layers or Bluetooth host.

There are three main elements that are included in the higher layer stack or Bluetooth host: L2CAP, or Logical Link Control and Adaptation Protocol; SDP, or Service Discovery Protocol; and GAP, or Generic Access Protocol. These Bluetooth protocol stack components are fundamental to all profiles and transport types within the overall Bluetooth system (Fig. 15.12).

The Bluetooth L2CAP or logical link control and adaptation protocol is used to provide an interface for all data applications that use the ACL links. The Bluetooth L2CAP provides multiplexing between the higher layer protocols, enabling multiple applications to utilize the same lower layer links. The L2CAP transmits large data packets by segmenting and then, at the receiver, reassembling the packets so that the data can be fitted into the limits of the lower layer protocol data units. The L2CAP also supports flow control and retransmission, performing CRC checks. The latest specifications support two L2CAP modes over those originally included: that is, streaming mode and enhanced retransmission mode. Any error checking and reliability enhancements can be provided by the lower layers.

The SDP or service discovery protocol is a key element of the Bluetooth ad hoc networking capability. The Bluetooth SDP allows a Bluetooth device to discover and make many connections during the course of its life. It enables the devices to discover what services other Bluetooth devices support, and it also lists everything

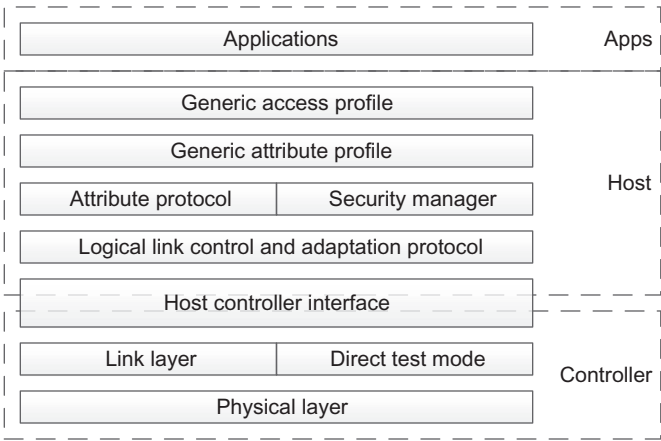


**FIG. 15.12**

Protocol layers in Bluetooth.

*Based on, K. Townsend, et al., Getting Started With Bluetooth Low Energy: Tools and Techniques for Low-Power Networking, O'Reilly Media, Sebastopol, CA, 2014.*

that the Bluetooth device is capable of supporting. All Bluetooth devices implement the features of an SDP client and SDP server database.

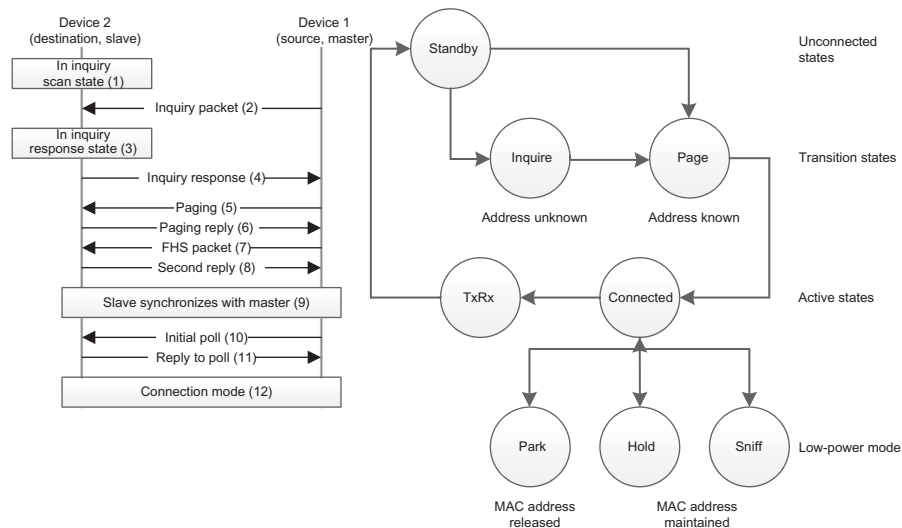
The Bluetooth GAP, or generic access protocol, defines the way that Bluetooth devices are able to discover each other and establish connections. It is one of the most basic Bluetooth profiles, but it is used by other profiles as the basis for establishing a link. The Bluetooth GAP can set the Bluetooth device into one of three different discovery modes: General discovery, Limited discovery, and Nondiscoverable. The Bluetooth GAP controls the formation of a connection by controlling the inquiry and paging routines. It also looks after pairing and controls the use of security and encryption. In order to enable Bluetooth devices to communicate properly with each other, Bluetooth profiles are used. A Bluetooth profile is effectively a wireless interface specification for communication between Bluetooth devices. In order to be able to operate, a Bluetooth device must be compatible with a subset of the available profiles sufficient to enable the desired Bluetooth services.

A Bluetooth profile resides on top of the Bluetooth core specification and possibly above any additional protocols that may be used. While a particular Bluetooth profile may use certain features of the core specification, specific versions of profiles are rarely linked to specific versions of the core specification, in order to facilitate the upgrades. The way a particular Bluetooth device uses Bluetooth technology depends on its profile capabilities. The Bluetooth profiles provide standards which manufacturers follow to allow devices to use Bluetooth in the intended manner. At a minimum, each Bluetooth profile specification contains details of the dependencies

on other formats, suggested user interface formats, and the specific parts of the Bluetooth protocol stack used by the profile. To perform its task, each profile uses particular options and parameters at each layer of the stack. This may include an outline of the required service record, if appropriate. As an example, the Advanced Audio Distribution Profile (A2DP) defines how stereo quality audio can be streamed from a media source to a sink. This Bluetooth profile defines two roles of an audio device: source and sink. A device is the source when it acts as a transmitter of a digital audio stream that is delivered to the sink on the pico-net. A device is the sink when it acts as a receiver of a digital audio stream delivered from the source on the same pico-net. There are over twenty different Bluetooth profiles, each having their own function. Some of these Bluetooth profiles are typically used more than others, but each one may be used in a variety of different scenarios and applications.

In order to connect the devices easily and quickly, a scheme known as Bluetooth pairing may be used. Once Bluetooth pairing has taken place, the two devices may communicate with each other. Bluetooth pairing is generally initiated manually by a device user. The Bluetooth link for the device is made visible to other devices. They may then be paired. The Bluetooth pairing process is typically triggered automatically the first time a device receives a connection request from a device with which it is not yet paired. In order to pair the Bluetooth devices, a password has to be exchanged between them, which is a code shared by both Bluetooth devices. It is used to ensure that both users have agreed to pair with each other.

The overall operational state diagram of a Bluetooth system is shown in [Fig. 15.13](#). When a Bluetooth device is turned on, it goes to standby mode and starts to inquire, broadcasting a message to all directions and asking if anyone is listening, and if there is a Bluetooth device, its address is requested. The initiating device may get a response from multiple devices. If it discovers any device that it wants to connect to, it sends a paging message to that device requesting a connection. If it receives an acceptance from the other party, both devices transition to the connected mode. Once in connected mode, both devices can transmit and receive data. If the devices are in the connected mode and there is no data to transmit, they may stay awake during that period, which would unnecessarily waste battery power. To reduce power consumption, Bluetooth supports three levels of energy saving known as sniff, hold, and park ([Fig. 15.13](#)). In sniff mode, the device maintains synchronization with the pico-net but transmit/receive cycles are reduced. This cycle is called sniff interval and is programmable based on the application. In hold mode, only the internal clock in the device is running and data transfer is not possible. However, if there is a need for data transfer, it can switch to active mode very quickly. The hold mode can be initiated either by the master or the slaves. In park mode, the device maintains synchronization with the pico-net but does not transmit or receive any data and releases the device's MAC address. In this mode, the device periodically wakes up and listens to the master. If it detects any signal from the master requesting data transaction, the device will initiate the connection establishment process. While it

**FIG. 15.13**

Bluetooth operating state diagram.

Based on, K. Townsend, et al., *Getting Started With Bluetooth Low Energy: Tools and Techniques for Low-Power Networking*, O'Reilly Media, Sebastopol, CA, 2014.

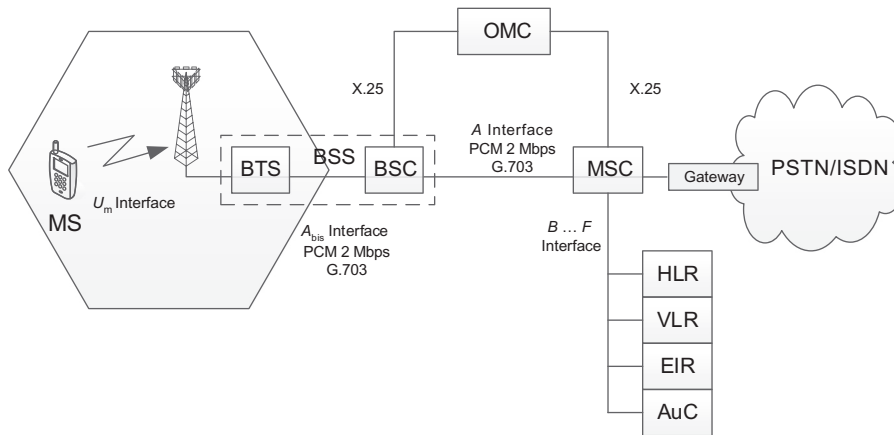
would take longer to reestablish the connection in this case, it would considerably save energy.

### 15.3.4 3GPP FAMILY (GSM, UMTS, LTE)

This section provides an overview of radio access technologies and their network architectures developed by 3GPP in the past two decades. These technologies evolved from GSM voice-centric and all circuit-switched systems to LTE all-IP systems that support wide range of IP-based rich multimedia services.

#### 15.3.4.1 GSM

GSM is a second-generation cellular system that has been widely deployed since its introduction in the late 1980s [8]. Voice services have been the primary service of GSM although subsequent improvements of the GSM system enabled low-rate data services as well. The GSM network architecture consists of three groups of entities, as shown in Fig. 15.14. It includes (1) MSs, (2) base station subsystems (BSS), and (3) CN entities. The MS includes a removable subscriber identity module, which provides the user with a unique identification number known as International Mobile Subscriber Identity (IMSI). Each MS is further assigned a unique hardware identification called the International Mobile Equipment Identity (IMEI). The BSS is made up of base station controllers (BSC) and base transceiver stations (BTS).

**FIG. 15.14**

GSM system architecture.

Based on, J. Eberspächer, et al., *GSM—Architecture, Protocols and Services*, third ed., Wiley, Chichester, UK, 2009.

The BSC uses the radio transceivers located at each BTS to connect the MSs to the cellular network and manages the radio resources for them. The BTS tasks include channel coding/decoding, modulation, and encryption/decryption. A BTS comprises radio transmitters and receivers, antennas, and the interface to the fixed and mobile network. The BTS may contain one or more transceivers to provide the required call handling capacity. A cell site may be omnidirectional or typically split into three directional cells. The MSs normally send a report of their received signal strength to the BSC every 480 ms. With this information, the BSC decides to initiate HO to other cells, change the BTS transmitter power, etc.

The network subsystem consists of mobile switching center (MSC), which acts as a standard exchange in a fixed network and additionally provides all necessary functionalities to manage the mobile subscribers. The main functions of MSC are registration, authentication, location update, HO, and call routing for a roaming subscriber. The signaling between functional entities in the network subsystem uses Signaling System 7 (SS7) standard. If the MSC also has a gateway function for communicating with other networks, it is called gateway MSC (GMSC). The Home Location Register (HLR) is a database used for management of mobile subscribers. It stores the international mobile subscriber identity, MS ISDN number, and current Visitor Location Register (VLR) address. The main information stored in this database concerns the location of each MS in order to be able to route calls to the mobile subscribers managed by each HLR. The HLR also maintains the services associated with each MS. One HLR can serve several MSCs. The visitor location register contains the current location of the MS and selected administrative

information from the HLR, necessary for call control and provision of the subscribed services, for each mobile currently located in the geographical area controlled by the VLR. A VLR is connected to one MSC and is normally integrated into the MSC's hardware. The authentication center (AuC) is a protected database that holds a copy of the secret key stored in each subscriber's SIM card, which is used for authentication and encryption over the radio channel. AuC provides additional security against fraud. It is normally located close to each HLR within a GSM network. The Equipment Identity Register (EIR) is a database that contains a list of all valid MS equipment within the network, where each MS is identified by its international mobile equipment identity. Operation and maintenance center (OMC) is a management system that oversees the GSM network functional blocks. The OMC assists the network operator in maintaining satisfactory operation of the GSM network. Hardware redundancy and intelligent error detection mechanisms help prevent network down-time. The OMC is responsible for controlling and maintaining the MSC, BSC, and BTS. The SMS gateway is the term that is used to collectively describe the two short message services gateways defined in the GSM standards. The two gateways handle messages sent in different directions. The Short Message Service Gateway Mobile Switching Center (SMS-GMSC) is used for short messages terminated at the MS, and the Short Message Service Interworking Mobile Switching Center (SMS-IWMSC) is used for short messages that originated from an MS. The SMS-GMSC's role is similar to that of the GMSC, whereas the SMS-IWMSC provides a fixed access point for the Short Message Service Center.

The nominal bandwidth for the GSM signal using GMSK is 200 kHz; that is, the channel bandwidth and spacing is 200 kHz. As GMSK modulation has been used, the unwanted or spurious emissions outside the nominal bandwidth are sufficiently low to enable adjacent channels to be used from the same base station. Typically, each base station will be allocated a number of carriers to enable it to achieve the required capacity. The data transported by the carrier serves up to eight different users under the basic system by splitting the carrier into eight time slots. The basic carrier is able to support a data throughput of approximately 270 kbps, but as some of this supports the management overhead, the data rate allotted to each time slot is only 24.8 kbps. In addition to this, error correction is required to overcome the problems of interference, fading, and general errors that may occur. This means that the available data rate for transporting the digitally encoded speech is 13 kbps for the basic vocoders.

GSM uses a combination of both TDMA and FDMA techniques. The FDMA element involves the division by frequency of the (maximum) 25 MHz bandwidth into 124 carrier frequencies spaced 200 kHz apart. The carriers are then divided in time, using a TDMA scheme. This enables different users of the single radio frequency channel to be allocated different time slots. They are then able to use the same RF channel without mutual interference. The slot is then the time that is allocated to the particular user, and the GSM burst is the transmission that is made in this time interval. As shown in [Fig. 15.15](#), each GSM slot, and hence each GSM burst period, is 0.577 ms. Eight of these burst periods are grouped into what is known

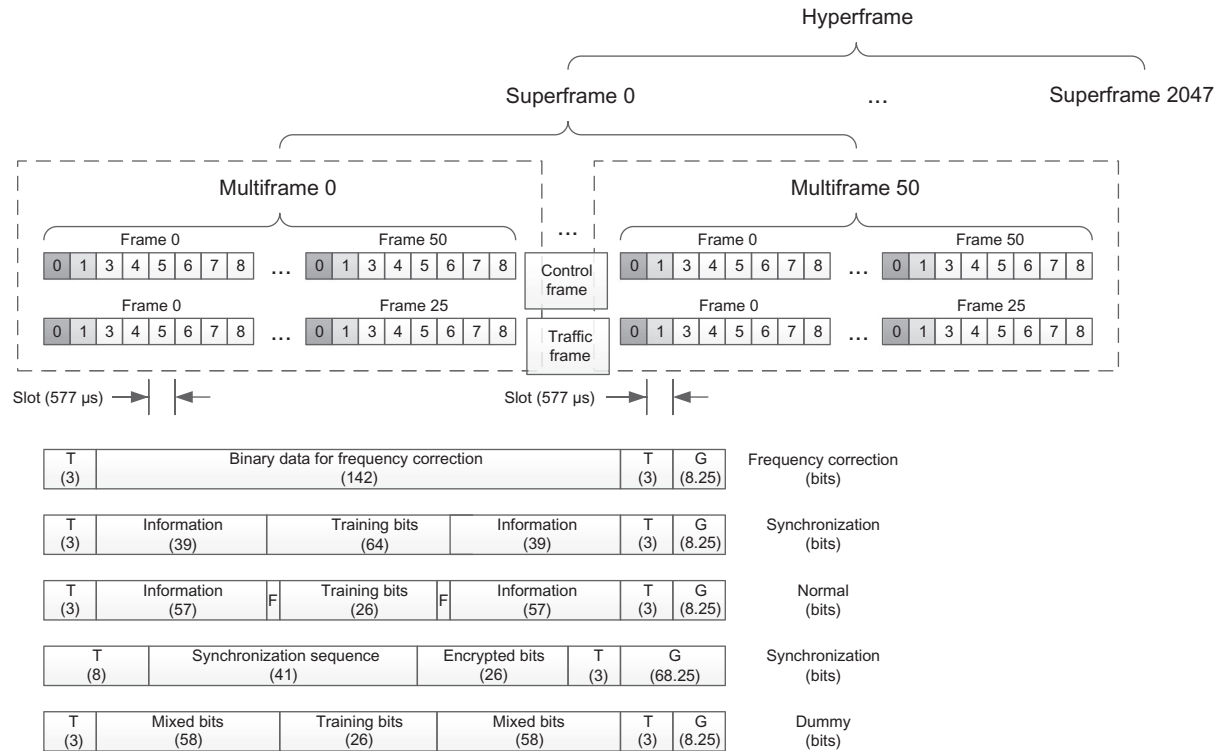


**FIG. 15.15**  
GSM frame structure.

Based on, J. Eberspächer, et al., *GSM—Architecture, Protocols and Services*, third ed., Wiley, Chichester, UK, 2009.

as a TDMA frame. This spans an interval of approximately 4.615 ms and it forms the basic unit for the definition of logical channels. One physical channel is one burst period allocated in each TDMA frame. There are different types of frames that are transmitted to carry different data, and the frames are organized into what are known as multiframe and superframes to provide overall synchronization.

A further power saving and interference reducing feature is the discontinuous transmission (DTX) capability that is incorporated within the specification. It is particularly useful because there are long pauses in conversational speech, for example, when the person using the mobile is listening. During these periods there is no need to transmit a signal. In fact it is found that a person speaks for less than 40% of the time during normal telephone conversations. The most important element of DTX is the voice activity detector, which distinguishes active voice from silence intervals. It is also necessary for the system to add background or comfort noise when the transmitter is turned off because complete silence can be very disconcerting for the listener. The noise is controlled by the silence indication descriptor.

GSM uses a variety of channels through which the data or control is carried (Fig. 15.16). In GSM, these channels are classified as physical channels and logical channels. The physical channels are determined by the timeslot, whereas the logical channels are determined by the information carried within the physical channel. In other words, several recurring timeslots on a carrier constitute a physical channel. These are then used by different logical channels to transfer information. These channels may either be used for user data or signaling to enable the system to properly operate. A TCH is used to carry speech and data traffic. TCHs are defined using

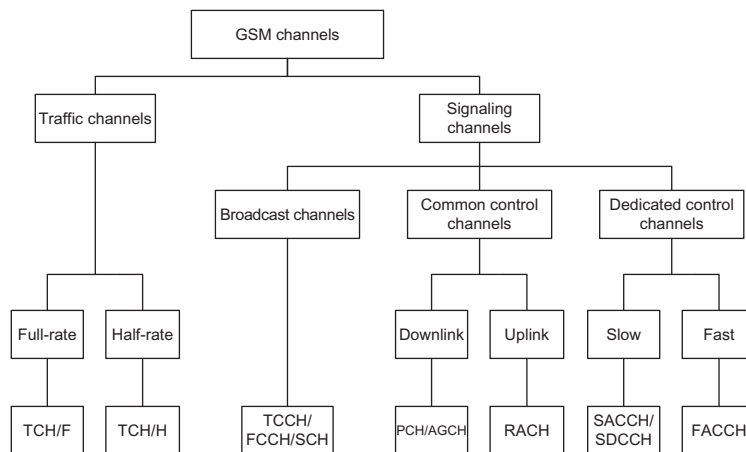


**FIG. 15.16**

Classification of GSM channels.

Based on, J. Eberspächer, et al., *GSM—Architecture, Protocols and Services*, third ed., Wiley, Chichester, UK, 2009.

a 26-frame multiframe, or group of 26 TDMA frames. The length of a 26-frame multiframe is 120 ms, which is how the length of a burst period is defined. Out of the 26 frames, 24 are used for traffic: one is used for the slow associated control channel (SACCH) and one is currently unused (Fig. 15.16). The TCHs for the uplink and downlink are separated in time by three burst periods so that the MS does not have to transmit and receive simultaneously, thereby simplifying the implementation. This method permits complex transmit/receive duplex filters to be avoided and thus helps reduce power consumption. In addition to these full-rate TCHs, half-rate TCHs are also defined. Half-rate TCHs double the capacity of a system effectively by making it possible to transmit two calls in a single channel. If a full-rate TCH is used for data communications, the usable data rate drops to 9.6 kbps due to the enhanced security algorithms. Eighth-rate TCHs are also specified and are used for signaling, referred to as stand-alone dedicated control channels (SDCCH) in the specifications.

The channels may also be divided into common and dedicated channels. The forward common channels are used for paging to inform a mobile of an incoming call, responding to channel requests, and broadcasting system information. The return common channel is a random access channel used by the mobile to request channel resources before timing information is conveyed by the BSS. The dedicated channels are of two main types: those used for signaling and those used for traffic. The signaling channels are used for maintenance of the call and for enabling call setup, providing features such as HO when the call is in progress and finally terminating the call. The TCHs convey the actual payload.

#### 15.3.4.2 UMTS

Universal Mobile Telecommunications System (UMTS) is the third-generation successor to the GSM-based cellular system, which also includes GPRS and EDGE [9]. Although UMTS uses a totally different air interface, the CN elements have been migrating toward the UMTS requirements with the introduction of GPRS and EDGE, making the transition from GSM to the 3G UMTS architecture smooth and less-costly. UMTS uses a wideband CDMA multiple access scheme. It employs a baseline 5 MHz channel bandwidth. The UMTS network architecture can be divided into three main elements (Fig. 15.17):

1. UE or the mobile terminal.
2. UMTS Terrestrial Radio Access Network (UTRAN): UTRAN provides and manages the air interface for the overall UMTS network which consists of two main components:
  - a. Radio Network Controller (RNC): This element of the radio network subsystem controls the NodeBs that are connected to it. The RNC undertakes the radio resource management and some of the mobility management functions. It is also the point at which the data encryption/decryption is performed to protect the user data privacy.
  - b. NodeB: NodeB is the term used in UMTS to denote the base station transceiver. It contains the transmitter and receiver to communicate with the

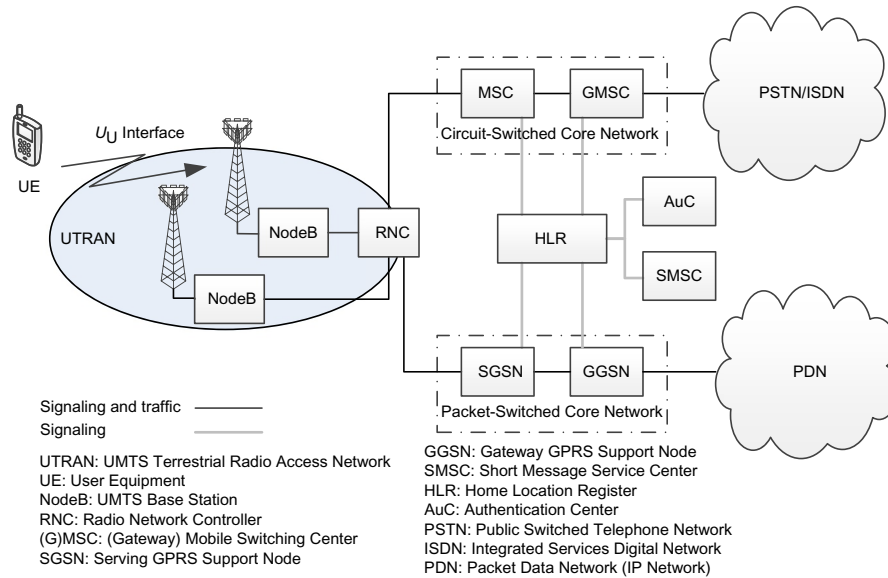


FIG. 15.17

UMTS network architecture.

*Based on, T. Chapman, et al., HSPA Evolution: The Fundamentals for Mobile Broadband, Academic Press, Oxford, UK, 2014.*

UEs within the cell. In order to facilitate effective HO between NodeBs under the control of different RNCs, the RNC communicates not only with the CN but also with neighboring RNCs.

3. Core network: The CN provides central processing and management for the system as well as interface to external networks, including [circuit-switched] public phone network and other cellular networks. The UMTS CN may be divided into two different areas:
  - a. Circuit-switched elements: These elements are primarily based on the GSM network entities and carry data in a circuit-switched manner; that is, a dedicated channel for the duration of the call.
  - b. Packet-switched elements: These network entities are designed to carry packet data. This enables much higher network usage as the capacity can be shared and data is carried as packets which are routed according to their destination.

The UMTS network architecture was required to provide a greater level of performance relative to GSM network. However, as many networks had migrated through the use of GPRS and EDGE, they already had the ability to carry data. Accordingly, many of the elements required for the UMTS network architecture were

seen as a migration. This considerably reduced the cost of implementing the UMTS network as many elements were in place or needed simple upgrades.

Some network elements in UMTS CN, particularly those that are associated with registration, are shared by both circuit-switched and packet-switched domains and operate in the same way as they did with GSM. Fig. 15.17 shows the UMTS CN architecture. The circuit-switched elements of the UMTS CN architecture include the following network entities:

- **MSC:** This entity is essentially the same as that in the GSM network and manages the circuit-switched call flows.
- **Gateway MSC (GMSC):** This is the interface to the external networks.

The packet-switched elements of the UMTS CN architecture include the following network entities:

- **Serving GPRS Support Node (SGSN):** This entity was first developed when GPRS was introduced, and its use has been carried over to the UMTS network architecture. The SGSN provides a number of functions within the UMTS network architecture including the following:
  - **Mobility management:** when a UE attaches to the packet-switched domain of the UMTS CN, SGSN generates mobility management information based on the mobile's current location.
  - **Session management:** SGSN manages the data sessions providing the required QoS and also managing what are referred to as the Packet Data Protocol (PDP) contexts; that is, data bearers.
  - **Interaction with other network elements:** SGSN is able to manage its elements within the network only by communicating with other areas of the network; for example, MSC and other circuit-switched areas.
  - **Billing:** SGSN is also responsible billing. It achieves this by monitoring the flow of user data across the GPRS network. Call detail records are generated by SGSN before being transferred to the charging entities.
- **Gateway GPRS Support Node (GGSN):** This entity was also first introduced in the GPRS network. GGSN is the central element within the UMTS packet-switched network. It handles interworking between the UMTS packet-switched network and external packet-switched networks and can be considered as a sophisticated router. In terms of operation, when GGSN receives data addressed to a specific user, it checks if the user is active and then forwards the data to the SGSN serving that particular UE.

Code Division Multiple Access (CDMA) is a multiple access technology where the users are separated by unique orthogonal codes, which means that all users can use the same frequency and transmit at the same time. In CDMA2000, a 1.25 MHz wide radio signal is multiplied by a spreading signal (which is a pseudo-noise code sequence) with a higher rate than the data rate of the message. The resulting signal appears as seemingly random, but if the intended recipient has the right code, this process is reversed and the original signal is extracted. The use of unique codes means

that the same frequency is repeated in all cells, which is commonly referred to as a frequency reuse of one. UMTS uses a 5 MHz wide radio signal and a chip rate of 3.84 Mcps, which is about three times higher than the chip rate of CDMA2000 (1.22 Mcps). As the form of modulation used is QPSK, this enables two bits of information to be transmitted for every symbol, thereby enabling a maximum data rate of twice the symbol rate or 7.68 Mbps. Therefore, if the actual rate of the data to be transmitted is 15 kbps, a spreading factor of 512 is required to bring the signal up to the required chip rate for transmission in the required bandwidth. If the data to be carried has a higher data rate, a lower spreading factor is required. It is worth remembering that changing the chip rate does change the processing gain of the overall system and this needs to be accommodated in the signal processing as well. Higher spreading factors are more easily correlated by the receiver and therefore a lower transmit power can be used for the same symbol error rate.

The codes required to spread the signal must be orthogonal to enable multiple users and channels to operate without mutual interference. The codes used in UMTS are orthogonal variable spreading factor (OVSF) codes, and they must remain synchronous for proper operation. As it is not possible to retain exact synchronization for this, a second set of scrambling codes is used to further mitigate the interference. This scrambling code is a pseudorandom number (PN) code. Thus there are two stages of spreading: the first using the OVSF code and the second using a scrambling PN code. These codes are used to provide different levels of separation. The OVSF spreading codes are used to identify the user services in the uplink and user channels in the downlink, whereas the PN code is used to identify the individual NodeB or UE. On the uplink, there is a choice of millions of different PN codes. These are processed to include a masked individual code to identify the UE. As a result, there are more than enough sufficient codes to accommodate the number of different UEs likely to access a network. For the downlink, a short code is used. There are a total of 512 different codes that can be used, one of which will be assigned to each NodeB.

In order for UMTS to work properly, several key features such as power control and soft HOs need to be enabled.

The power control adjusts the transmit power of the terminal and the base station, which results in less interference and allows more users on the same carrier. Transmit power adjustment thus provides more capacity in the network. With a frequency reuse of one, it is very important to have efficient power control in order to keep the interference at a minimum. For each subscriber service the aim is that the base station shall receive the same power level from all terminals in the cell regardless of distance from the base station. If the power level from one terminal is higher than needed, the QoS provided to the terminal will be better by taking a disproportionate share of the resources while generating unnecessary interference to the other subscribers in the network. On the other hand, if power levels are too low, this will result in poor link quality. In order to keep the received power at a suitable level, UMTS has a fast power control that updates power levels 1500 times/s. By doing that, the rapid change in the radio channel is mitigated. To ensure good performance, power control is implemented in both the uplink and downlink, meaning that the output powers of

the terminal and the base station are frequently updated. Power control also gives rise to a phenomenon called cell breathing, which is a trade-off between coverage and capacity, which means that the size of the cell varies depending on the traffic load. When the number of subscribers in the cell is low (low load), good quality can be achieved even at a long distance from the base station. On the other hand, when the number of users in the cell is high, the large number of subscribers generates higher interference levels and subscribers have to get closer to the base station to achieve better quality.

With soft HO functionality, the terminal can communicate simultaneously with two or more cells belonging to two or more base stations. The flexibility to make and maintain the connection to more than one base station results in fewer dropped calls, which is very important to the operators. To achieve good system performance with a frequency reuse of one and power control, soft and softer HO are required. Soft and softer HO enables the terminal to maintain the continuity and quality of the connection while moving from one cell to another. During soft or softer HO, the terminal will momentarily adjust its power to the base station that requires the smallest amount of transmit power and the preferred cell may change very rapidly. The difference between soft and softer HO is that during soft HO, the terminal is connected to multiple cells at different base stations, while during softer HO, the terminal is connected to multiple cells at the same base station. A drawback of soft HO is that it requires additional hardware resources on the network side, as the terminal has multiple connections. In a well-designed radio network, 30–40% of the users will be in soft or softer HO.

One of the basic requirements when UMTS was standardized was to avoid dependence on external systems for accurate synchronization of base stations. This has been achieved by a mechanism, where the terminal, when needed, measures the synchronization offset between the cells and reports this to the network. In addition, there is also an option to use an external source, such as GPS, for synchronizing the nodes. To provide the best solution, both asynchronous and synchronous nodes are supported.

The main service offered by UMTS RAN is the Radio Access Bearer (RAB). To establish a call connection between the terminal and the base station, an RAB is needed. Its characteristics are different depending on what kind of service/information is to be transported. The RAB carries the subscriber data between the terminal and the CN. It is composed of one or more radio access bearers between the terminal and the serving RNC, and one Iu bearer between the serving RNC and the CN. UMTS has defined four different quality classes of radio access bearers: Conversational (low delay, strict ordering), Streaming (moderate delay, strict ordering), Interactive (moderate delay), and Background (no delay requirement). Both Conversational and Streaming RABs require a certain reservation of resources in the network, and they are primarily meant for real-time services. They differ mainly in that the Streaming RAB tolerates a higher delay, appropriate for one-way real-time services. The Interactive and Background RABs are so-called best effort; that is, no resources are reserved and the throughput depends on the load in the cell. The only difference

is that the Interactive RAB provides a priority mechanism. The RAB is characterized by certain QoS parameters, such as bit rate and delay. The CN will select an RAB with appropriate QoS based on the service request from the subscriber, and it will ask the RNC to provide such an RAB.

The UTRAN protocol structure consists of a number of protocol layers, each providing a specific service to the next layer (Fig. 15.18).

The physical layer (Layer 1) provides transport channels to the MAC layer. There are different types of transport channels with different transmission characteristics. Common transport channels can be shared by multiple terminals (eg, FACH, RACH, DSCH, BCH, PCH). Dedicated transport channels (DCH) are assigned to only one terminal at a time. The transmission functions of the physical layer include channel coding and interleaving, multiplexing of transport channels, mapping to physical channels, spreading, modulation and power control, with corresponding functions for reception. A frequency and a code characterize a physical channel. The specifications include two duplex modes: frequency division duplex (FDD) and time division duplex (TDD).

The MAC protocol (Layer 2) provides logical channels to the layers above. The logical channels are distinguished by the different types of information they carry, and thus they include the dedicated control channel (DCCH), common control channel (CCCH), dedicated traffic channel (DTCH), common traffic channel (CTCH), broadcast control channel (BCCH), and paging control channel (PCCH).

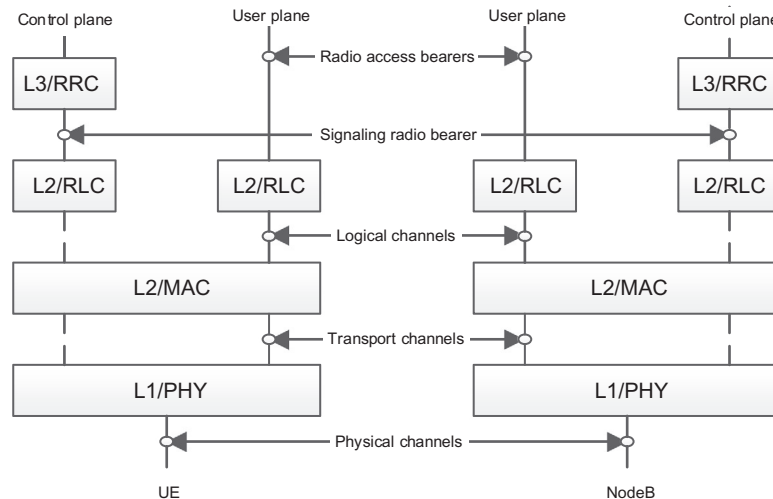


**FIG. 15.18**

UTRAN protocol structure.

Based on, T. Chapman, et al., *HSPA Evolution: The Fundamentals for Mobile Broadband*, Academic Press, Oxford, UK, 2014.

The MAC layer performs scheduling and mapping of logical channel data onto the transport channels provided by the physical layer. Also, for common transport channels, the MAC layer adds addressing information to distinguish data flows intended for different terminals. One major difference from GSM is the possibility to dynamically switch one logical channel (data flow) onto different transport channel types; for example, based on the activity of the subscriber. This is called channel type switching.

The radio link control (RLC) protocol (Layer 2) operates in one of three modes: transparent, unacknowledged, or acknowledged mode (AM). It performs segmentation/reassembly functions and, in AM, provides guaranteed delivery service by use of ARQ retransmission. The RLC layer provides services to the RRC signaling (the signaling radio bearer) and to the user data transfer (the radio access bearer).

The RRC protocol (Layer 3) provides control of the terminal from the RNC. It includes functions to control radio bearers, physical channels, mapping of the different channel types, HO, measurement, and other mobility procedures. An RRC state refers to different operational stages in which a UMTS UE or network can be after establishing a connection. As shown in Fig. 15.19, there are four states in RRC connected mode. In most cases, a UE can transition from its current state to any other states in a single step, but there are conditions where direct transition from one state to another state in a single step is not possible. For example, the UE cannot transition from CELL\_PCH to URA\_PCH or from CELL\_PCH to CELL\_DCH directly, but it can switch from CELL\_DCH to CELL\_PCH directly. The UMTS RRC states can be further characterized as follows:

- Idle mode: The UE in this state consumes the minimum amount of power and uses minimal network resources. The UE does not have a connection to NodeB. The UE's transceiver is turned off and the UE only wakes up periodically to check possible paging messages. The UE's mobility is controlled by the UE and it reselects a cell based on signal strength measurements.
- CELL\_PCH (paging channel): The UE in this state has an RRC connection, but cannot send or receive data. The network knows the location of the last cell where the UE was in CELL\_FACH (forward access channel) state. The UE must transition to CELL\_FACH to notify the network of cell reselection and the UE can be accessed through paging channel.
- URA\_PCH: This state is similar to CELL\_PCH, except the location of the UE is known in a paging area.
- CELL\_FACH: In this state, the UE does not have dedicated channels but can send or receive low-rate data on FACH and RACH. The mobility is controlled by the UE via cell reselection.
- CELL\_DCH (dedicated channel): In this state, the UE has dedicated control/TCHs, RRC connection, and the ability to transmit/receive data. The mobility is managed by the network by means of HO and soft HO. The UE power consumption and network resource usage are maximal.

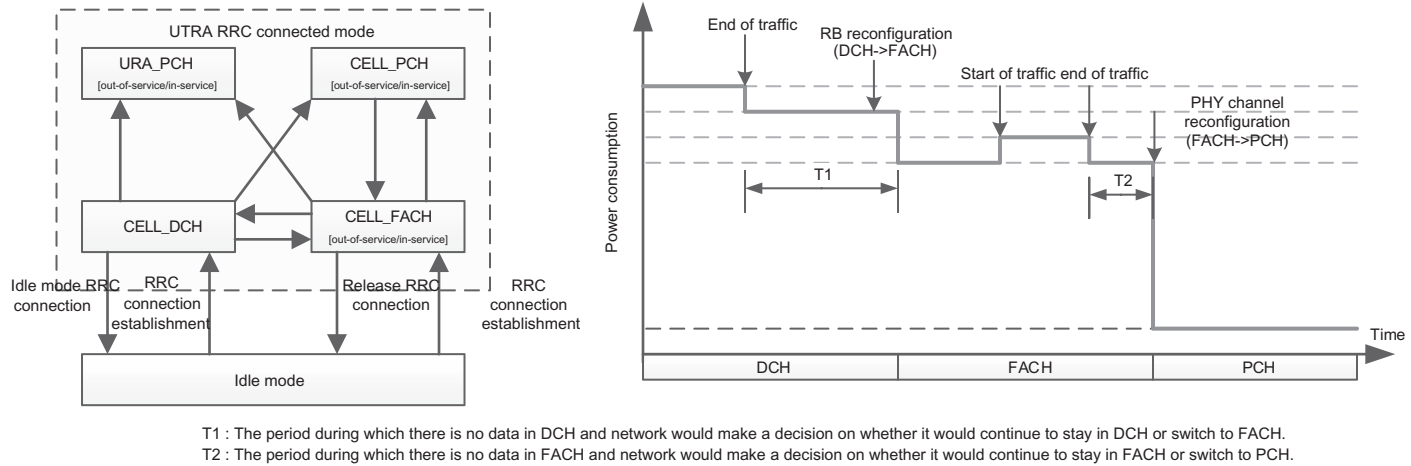


**FIG. 15.19**

RRC states in UMTS.

Based on, T. Chapman, et al., *HSPA Evolution: The Fundamentals for Mobile Broadband*, Academic Press, Oxford, UK, 2014.

### 15.3.4.3 LTE

The long-term evolution of UMTS systems (LTE) was a paradigm shift in the design of access network and CN architecture and technologies that was necessitated due to stringent requirements on system capacity, user throughput, reduced latency, QoS classes, variety of IP-based services, and reduced network and device complexity [10]. LTE has incorporated new all-IP flat network architecture and various techniques such as OFDM-based air interface, advanced multiantenna techniques, and sophisticated resource allocation and user scheduling techniques with minimal control/signaling overhead.

The Evolved UTRAN (E-UTRAN) is the LTE radio access network which consists of eNBs or equivalently E-UTRA base stations, providing the E-UTRA user-plane and control-plane protocol terminations toward the UE (MS). As part of the evolution from and enhancement of the legacy UMTS systems, the RNC functions have been included in the eNB to reduce the architectural complexity and further reduce the latency across the network. As illustrated in Fig. 15.20, the eNBs are interconnected with each other through the X2 interface. The X2 interface allows eNBs to communicate directly with each other and coordinate their activities.

The eNBs are also connected via the S1 interface to the Evolved Packet Core (EPC) or, more specifically, to the Mobility Management Entity (MME) through the S1-MME reference point and to the Serving Gateway (S-GW) via the S1-U interface. The S1 interface supports a multipoint connection among MMEs/serving gateways

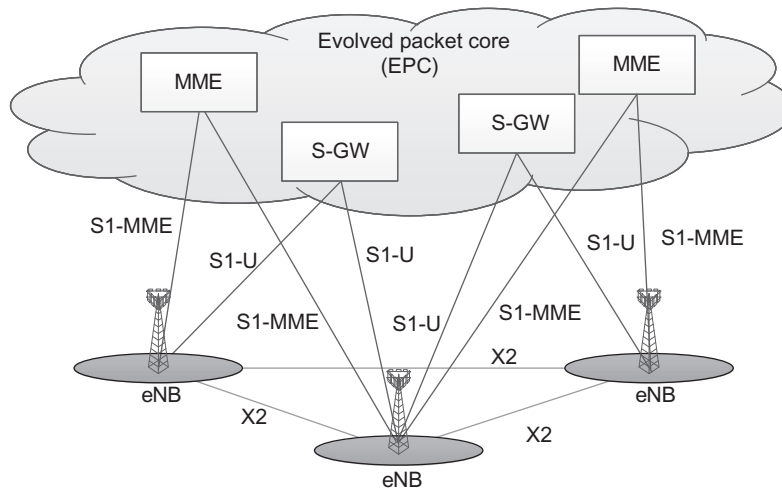


**FIG. 15.20**

E-UTRAN architecture.

Based on, S. Ahmadi, *LTE-Advanced: A Practical Systems Approach to Understanding 3GPP LTE Releases 10 and 11 Radio Access Technologies*, Academic Press, Oxford, UK, 2013.

and eNBs. The S1-MME is responsible for EPC bearer setup and release procedures, HO signaling, paging, and non-access stratum (NAS) signaling transport. Some general principles taken into consideration in the design of E-UTRAN architecture as well as the E-UTRAN interfaces are as follows:

- Signaling and data transport networks are logically separated.
- E-UTRAN and EPC functions are separated from transport functions. The addressing schemes used in E-UTRAN and EPC are not associated with the addressing schemes of transport functions. Some E-UTRAN or EPC functions reside in the same equipment.
- The mobility for RRC connection is controlled by the E-UTRAN.
- The interfaces are based on the logical model of the entity which is controlled through this interface.
- One physical network element can implement multiple logical nodes.

The MME is the key control node for the LTE access network. It is responsible for idle mode UE tracking and the paging procedure, including retransmissions. The MME functions include NAS signaling and NAS signaling security, inter-core-network signaling for mobility between 3GPP access networks, Idle mode UE accessibility (including control and execution of paging retransmission), tracking area list management (for UE in idle and active mode), packet data network (PDN) gateway and S-GW selection, MME selection for HOs with MME change, roaming, authentication of the users, and bearer management functions, including dedicated bearer establishment. The NAS signaling terminates at the MME and it is also responsible for generation and allocation of temporary identities to the UEs. It verifies the authorization of the UE to camp on the service provider's public land mobile network (PLMN) and enforces UE roaming restrictions.

The S-GW routes and forwards user data packets, while also acting as the mobility anchor for the user plane during inter-eNB HOs and as the anchor for mobility between LTE and other 3GPP technologies. The S-GW functions include being the local mobility anchor point for inter-eNB HO, mobility anchoring for inter-3GPP mobility, E-UTRAN idle mode downlink packet buffering and initiation of network triggered service request procedure, lawful interception, packet routing and forwarding, and transport-level packet marking in the uplink and the downlink.

The PDN gateway (P-GW) provides connectivity of the UE to external PDNs by being the point of exit and entry of traffic for the UE. A UE may have simultaneous connectivity with more than one P-GW for accessing multiple PDNs. The P-GW functions include per-user packet filtering, lawful interception, UE IP address allocation, and transport-level packet marking in the downlink.

In the control plane, the NAS functional block is used for network attachment, authentication, setting up bearers, and mobility management. All NAS messages are ciphered and integrity protected by the MME and UE. The RRC sublayer in the eNB makes HO decisions based on neighbor cell measurements reported by the UE, performs paging of the users over the air-interface, broadcasts system information, controls UE measurement and reporting functions such as the periodicity of channel

quality indicator (CQI) reports, and further allocates cell-level temporary identifiers to active users. It also executes transfer of UE context from the serving eNB to the target eNB during HO and performs integrity protection of RRC messages. The RRC sublayer is responsible for setting up and maintaining radio bearers.

In the user plane, the Packet Data Convergence Protocol (PDCP) sublayer is responsible for compressing or decompressing the headers of user-plane IP packets using Robust Header Compression (RoHC) to enable efficient use of air interface resources. This layer also performs ciphering of both user-plane and control-plane traffic. Because the NAS messages are carried in RRC, they are effectively double ciphered and integrity protected, once at the MME and again at the eNB.

The RLC sublayer is used to format and transport traffic between the UE and the eNB. The RLC sublayer provides three different reliability modes for data transport; that is, AM, unacknowledged mode (UM), and transparent mode (TM). The UM is suitable for transport of real-time services since such services are delay sensitive and cannot tolerate delay due to ARQ retransmissions. The AM is appropriate for nonreal-time services such as file transfers. The TM is used when the size of packet data units are known in advance such as for broadcasting system configuration information. The RLC sublayer also provides sequential delivery of service data units to the upper layers and eliminates duplicate packets from being delivered to the upper layers. It may also segment the service data units. Furthermore, there are two levels of retransmissions for providing reliability, the hybrid automatic repeat request (HARQ) at the MAC sublayer, and ARQ at the RLC sublayer. The ARQ is required to handle residual errors that are not corrected by HARQ. An  $N$ -process stop-and-wait HARQ protocol is employed that has asynchronous retransmissions in the downlink and synchronous retransmissions in the uplink. Synchronous HARQ means that the retransmissions of HARQ subpackets occur at predefined periodic intervals. Hence, no explicit signaling is required to indicate the retransmission schedule to the receiver. Asynchronous HARQ offers the flexibility of scheduling retransmissions based on air interface conditions (ie, scheduling gain).

LTE uses asymmetric multiple access schemes in the downlink and uplink; that is, the physical layer is based on Orthogonal Frequency Division Multiple Access (OFDMA) with a cyclic prefix in the downlink and Single Carrier Frequency Division Multiple Access (SC-FDMA) with cyclic prefix in the uplink. The OFDMA scheme is particularly suited for frequency-selective channels and high data rates. It transforms a wideband frequency-selective channel into a set of parallel flat fading narrowband channels. This, ideally, allows the receiver to perform a less complex equalization process in the frequency domain; that is, single-tap frequency-domain equalization.

The basic transmission scheme in the uplink is the single-carrier transmission (SC-FDMA) with cyclic prefix to achieve uplink interuser orthogonality and to enable efficient frequency-domain equalization at the receiver side. The frequency-domain generation of the SC-FDMA signal, also known as DFT-spread OFDM, is similar to OFDMA. This allows for a relatively high degree of commonality with the downlink OFDMA baseband processing using the same parameters; for

example, clock frequency, subcarrier spacing, FFT/IFFT size, etc. The use of SC-FDMA in the uplink is mainly due to relatively inferior peak to average power ratio (PAPR) properties of OFDMA that results in worse uplink coverage compared to SC-FDMA. The PAPR characteristics are important for cost-effective design of UE power amplifiers.

The E-UTRA is designed to operate in different frequency bands. The requirements were defined for 1.4, 3, 5, 10, 15, and 20 MHz bandwidth, with a specific configuration in terms of the number of RBs. Using carrier aggregation, a number of contiguous and/or noncontiguous frequency bands can be aggregated to create a virtually larger bandwidth.

Downlink and uplink transmissions are organized in the form of radio frames with 10 ms duration (Fig. 15.21). LTE supports two radio frame structures: Type 1, applicable to the FDD duplex scheme and Type 2, applicable to the TDD duplex scheme. In frame structure Type 1, each 10 ms radio frame is divided into 10 equally sized subframes. Each subframe consists of two equally sized slots. The cyclic prefix length is chosen to be longer than the maximum delay spread in the radio channel.

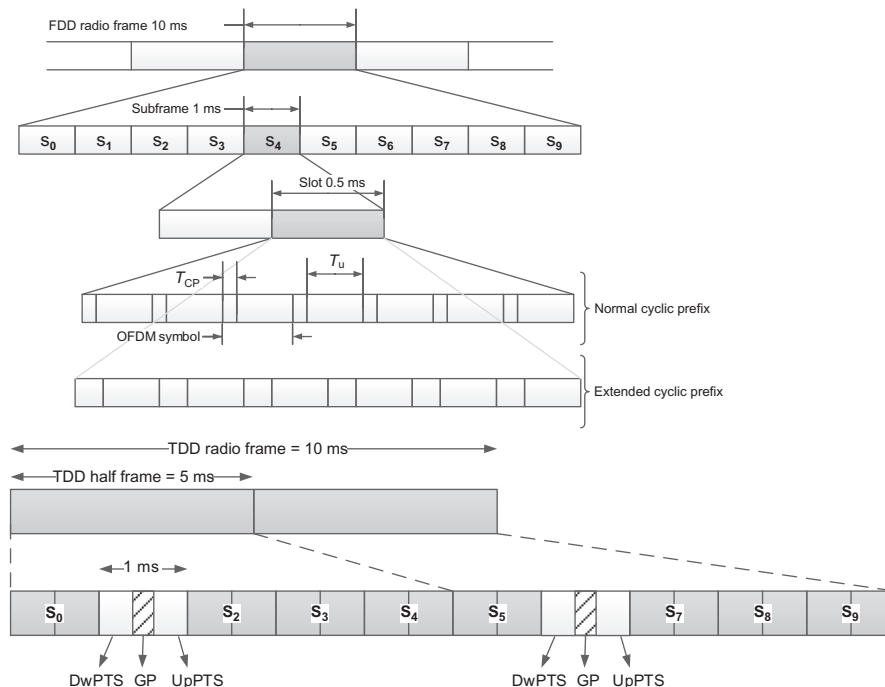


**FIG. 15.21**

LTE FDD and TDD frame structure.

Based on, S. Ahmadi, *LTE-Advanced: A Practical Systems Approach to Understanding 3GPP LTE Releases 10 and 11 Radio Access Technologies*, Academic Press, Oxford, UK, 2013.

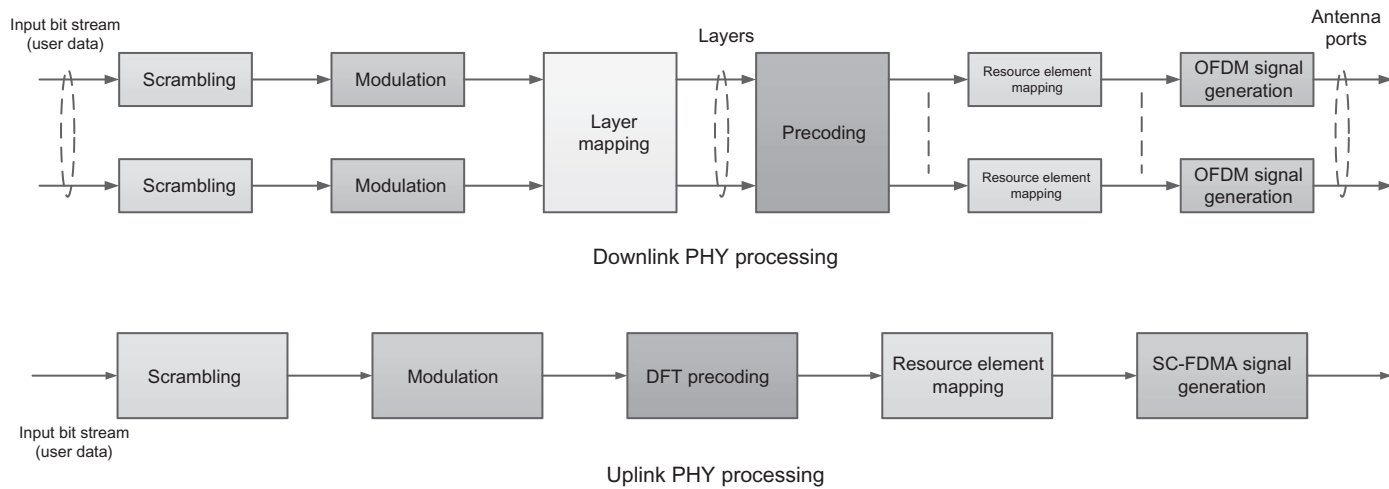
For FDD, 10 subframes are available for downlink transmission and 10 subframes are available for uplink transmissions in each radio frame. Uplink and downlink transmissions are separated in the frequency domain. The TTI of the downlink/uplink is 1 ms. To provide enhanced multicast and broadcast services, LTE has the capability to transmit multicast and broadcast over a single frequency network (MBSFN), where a time-synchronized common waveform is transmitted from multiple eNBs, allowing macro-diversity combining of multicell transmissions at the UE. The cyclic prefix is utilized to mitigate the difference in the propagation delays, which makes the MBSFN transmission appear to the UE as a transmission from a single large cell.

Frame structure Type 2 is illustrated in Fig. 15.21. Each 10 ms radio frame consists of two 5 ms half-frames. Each half-frame consists of eight slots of 0.5 ms length and three special fields: downlink pilot time slot (DwPTS), guard period (GP), and uplink pilot time slot (UpPTS). The length of DwPTS and UpPTS is configurable subject to the total length of DwPTS, GP, and UpPTS being equal to 1 ms. Both 5 and 10 ms switching-point periodicity are supported. The first subframe in all configurations and the sixth subframe in the configuration with a 5 ms switching-point periodicity consist of DwPTS, GP, and UpPTS. The sixth subframe in the configuration with a 10 ms switching-point periodicity consists of DwPTS only. All other subframes consist of two equally sized slots. For TDD systems, the GP is reserved for downlink to uplink transition. Other subframes/fields are assigned for either downlink or uplink transmission. Uplink and downlink transmissions are separated in the time domain.

The smallest time-frequency resource unit used for downlink/uplink transmission is called a resource element, defined as one subcarrier over one symbol. For both TDD and FDD duplex schemes, as well as in both the downlink and uplink, a group of 12 subcarriers contiguous in frequency over one slot in time form an RB. Transmissions are allocated in units of RB. One downlink/uplink slot using the normal cyclic prefix length contains seven symbols. There are 6, 15, 25, 50, 75, and 100 RBs corresponding to 1.4, 3, 5, 10, 15, and 20 MHz channel bandwidths, respectively. Note that the physical RB size is the same for all bandwidths.

The baseband modulation schemes supported in the downlink and uplink of LTE are QPSK, 16QAM, and 64QAM. The channel coding scheme for transport blocks in LTE is Turbo Coding, similar to UTRA, with the minimum coding rate of  $R = 1/3$ , two 8-state constituent encoders, and a contention-free quadratic permutation polynomial (QPP) turbo internal interleaver. Trellis termination is performed by taking the tail bits from the shift register feedback after all information bits are encoded. The tail bits are padded after the encoding of information bits. Before the turbo coding, transport blocks are segmented into octet-aligned segments with a maximum information block size of 6144 bits. Error detection is supported by the use of 24 bit CRC.

Fig. 15.22 illustrates different stages of LTE physical channel processing in the downlink and uplink. In the downlink, the coded bits in each of the codewords are scrambled for transmission on a physical channel. The scrambled bits are modulated to generate complex-valued modulation symbols that are later mapped to one or

**FIG. 15.22**

LTE downlink/uplink physical layer processing.

Based on, S. Ahmadi, *LTE-Advanced: A Practical Systems Approach to Understanding 3GPP LTE Releases 10 and 11 Radio Access Technologies*, Academic Press, Oxford, UK, 2013.

several transmission layers. The complex-valued modulation symbols on each layer are precoded for transmission and are further mapped to resource elements for each antenna port. The complex-valued time-domain OFDMA signal for each antenna port is then generated following these stages. In the uplink, the baseband signal is processed by scrambling the input coded bits and then by modulation of scrambled bits to generate complex-valued symbols. The complex-valued modulation symbols are transform-precoded (DFT-based precoding) and are later mapped to resource elements. The complex-valued time-domain SC-FDMA signal for each antenna port is then generated.

In LTE, five types of downlink reference signals are defined: wideband cell-specific reference signals associated with non-MBSFN transmission, MBSFN reference signals associated with MBSFN transmission, positioning reference signals, demodulation or UE-specific reference signals, and CSI reference signals. There is one cell-specific reference signal transmitted per downlink antenna port. Note that the antenna port is a logical entity and shall not be confused with the physical transmit antennas, although there is a mapping between the two entities during operation in various transmission modes. The cell-specific downlink reference signals consist of predetermined reference symbols that are inserted in the time-frequency grid over each subframe and are used for downlink channel estimation and physical layer identifier (cell identifier) detection. The exact sequence is derived from cell identifiers. The number of downlink antenna ports with cell-specific reference signals equals 1, 2, or 4. The reference signal sequence is derived from a pseudorandom sequence and results in a QPSK type constellation. Cell-specific frequency shifts are applied when mapping the reference signal sequence to the subcarriers. The two-dimensional reference signal sequence is generated as the symbol-by-symbol product of a two-dimensional orthogonal sequence and a two-dimensional pseudorandom sequence. There are 3 different two-dimensional orthogonal sequences and 168 different two-dimensional pseudorandom sequences. Each cell identity corresponds to a unique combination of one orthogonal sequence and one pseudorandom sequence, thus allowing for 504 unique cell identities.

The UE-specific reference signals are supported for transmission of a physical downlink shared channel and are transmitted on up to eight antenna ports; that is, up to eight spatial layers. The UE-specific reference signals can be precoded and support noncodebook-based precoding. The UE-specific reference signals are exclusively transmitted on the RBs in which the corresponding user data is mapped and they are precoded in the same way that user data is precoded.

Positioning reference signals are only transmitted in downlink subframes configured for positioning reference signal transmission. If both normal and MBSFN subframes are configured as positioning subframes within a cell, the OFDM symbols in an MBSFN subframe configured for positioning reference signal transmission use the same cyclic prefix as used for the first subframe. Otherwise, if only MBSFN subframes are configured as positioning subframes within a cell, the OFDM symbols configured for positioning reference signals in these subframes use the extended cyclic prefix. The positioning reference signals are transmitted on antenna port 6

and are not mapped to resource elements allocated to physical broadcast, primary, and secondary synchronization channels, regardless of their antenna port.

Channel state information reference signals (CSI-RS) are used to support measurement and reporting of channel-state information from the user terminals to the network. The CSI reference signals are sparse in the time and frequency and transmitted at a configurable periodicity. The physical resources at the locations of the reference signals of another antenna port are not used for data transmission on the other antenna ports.

The uplink reference signals, used for channel estimation for coherent demodulation, are transmitted in the middle SC-FDMA symbol in each slot assuming normal cyclic prefix. LTE uses UE-specific reference signals in the uplink. The uplink reference signal sequence length equals the size (number of subcarriers) of the assigned resource. The uplink reference signals are based on Zadoff-Chu sequences that are either truncated or cyclically extended to the desired length. There are two types of uplink reference signals: (1) the demodulation reference signal is used for channel estimation in the eNB receiver in order to demodulate control and data channels. It is located on the middle symbol in each slot (for normal cyclic prefix) and spans the same bandwidth as the allocated uplink data, and (2) the sounding reference signal provides uplink channel quality information as a basis for scheduling decisions in the base station. The UE sends a sounding reference signal in different parts of the bandwidths where no uplink data transmission is available. The sounding reference signal is transmitted in the last symbol of the subframe. The configuration of the sounding signal, for example, bandwidth, duration, and periodicity, are configured by higher layers.

The physical downlink control channel is primarily used to carry scheduling information to individual UEs; that is, resource assignments for uplink and downlink data and control information. It is located in the first few OFDM symbols of a subframe. An additional physical control format indicator channel, located on specific resource elements in the first OFDM symbol of the subframe, is used to indicate the number of OFDM symbols occupied by the physical downlink control channel (1, 2, 3, or 4 OFDM symbols may be consumed where four OFDM symbols are only used when operating in the minimum supported system bandwidth). The information carried in the physical downlink control channel is referred to as downlink control information, where depending on the purpose of the control message, different downlink control information formats are defined. This information enables the UE to identify the location and size of the resources in that subframe, as well as to provide the UE with information on the modulation and coding scheme and HARQ operation. As mentioned earlier, the information fields in the downlink scheduling grant are used to convey the information needed to demodulate the downlink shared channel. They include resource allocation information such as RB size and duration of assignment, transmission format such as multiantenna mode, modulation scheme, payload size, and HARQ operational parameters such as process number, redundancy version, and new data indicator. Similar information is also included in the uplink scheduling grants.

Control channels are formed by aggregation of control channel elements, and each control channel element consists of a set of resource elements. Different code rates for the control channels are realized by aggregating different numbers of control channel elements. QPSK modulation is used for all control channels. There is an implicit relationship between the uplink resources used for dynamically scheduled data transmission, or the downlink control channel used for assignment, and the downlink ACK/NACK resource used for feedback.

The physical uplink control channel is mapped to a control channel resource in the uplink. A control channel resource is defined by a code and two RBs, consecutive in time, with hopping at the slot boundary. Depending on presence or absence of uplink timing synchronization, the uplink physical control signaling can differ. In the case of time synchronization being present, the out-of-band control signaling consists of CQI, ACK/NACK, and a scheduling request. Note that a UE only uses a physical uplink control channel when it does not have any data to transmit in the uplink. If a UE has data to transmit, it would multiplex the control information with data on the physical uplink shared channel.

By use of uplink frequency hopping on PUSCH, frequency diversity effects can be exploited and interference can be averaged. The UE derives the uplink resource allocation as well as frequency hopping information from the uplink scheduling grant. The downlink control information format 0 is used on PDCCH to convey the uplink scheduling grant. LTE supports both intra-subframe and inter-subframe frequency hopping. The hopping pattern is configured per cell by higher layers. In intra-subframe hopping, the UE transmission hops to another frequency allocation from one slot to another within one subframe. In inter-subframe hopping, the frequency resource allocation changes from one subframe to another.

The CQI reports are provided to the scheduler by the UE, measuring the current channel conditions. If MIMO transmission is used, the CQI includes necessary MIMO-related feedback. The HARQ feedback in response to downlink data transmission consists of a single ACK/NACK bit per HARQ process. The PUCCH resources for scheduling requests and CQI reporting are assigned and can be revoked through RRC signaling. A scheduling request is not necessarily assigned to UEs acquiring synchronization through a random access channel (ie, synchronized UEs may or may not have a dedicated scheduling request channel).

In LTE, uplink control signaling consists of ACK/NACK, CQI, a scheduling request indicator, and MIMO feedback. When users have simultaneous uplink data and control transmission, control signaling is multiplexed with data prior to the DFT processing to preserve the single-carrier property in uplink transmission. In the absence of uplink data transmission, this control signaling is transmitted in a reserved frequency region on the band edges. Note that additional control regions may be defined as needed. Allocation of control channels with their small occupied bandwidth to band-edge RBs reduces out of band emissions caused by data resource allocations on inner band RBs and maximizes the frequency diversity for control channel allocations while preserving the single carrier property of the uplink waveform.

The random access procedure in LTE consists of four steps. In step 1, a random access preamble is sent by UE. The time/frequency resource where the random access preamble is sent is associated with a random access radio network temporary identifier. In step 2, a random access response is generated by eNB and is sent on the downlink shared channel. It is addressed to the UE using the random access identifier and contains a timing advance value, an uplink grant, and a temporary identifier. Note that eNB may generate multiple random access responses for different UEs which can be concatenated inside one MAC protocol data unit. The preamble identifier is contained in the MAC subheader of each random access response so that the UE can detect whether a random access response for the used preamble exists. In step 3, UE will send an RRC connection request message on the uplink common control channel, based on the uplink grant received in the previous step. In step 4, the eNB sends back a MAC message containing the uplink common control channel service data unit that was received in step 3. The message is sent on the downlink shared channel and addressed to the UE via the temporary identifier. When the received message matches the one sent in step 3, the contention resolution is considered successful; otherwise, the procedure is restarted at step 1.

Paging is used for setting up a network-initiated connection. A power-saving efficient paging procedure should allow the UE to sleep without having to process any information and only to briefly wake up at predefined intervals to monitor paging information (as part of control signaling in the beginning of each subframe) from the network.

Cell search is a procedure performed by a UE to acquire timing and frequency synchronization with a cell and to detect the cell identifier of that cell. LTE uses a hierarchical cell search scheme similar to UMTS. The E-UTRA cell search is based on successful acquisition of the following downlink signals: (1) the primary and secondary synchronization signals that are transmitted twice per radio frame, and (2) the downlink reference signals, as well the broadcast channel that carries system information such as system bandwidth, number of transmit antennas, and system frame number. The 504 available physical layer cell identities are grouped into 168 physical layer cell identity groups, each group containing 3 unique identities. The secondary synchronization signal carries the physical layer cell identity group, and the primary synchronization signal carries the physical layer identity 0, 1, or 2.

Uplink link adaptation is used in order to improve data throughput in a fading channel. This technique varies the downlink modulation and coding scheme based on the channel conditions of each user. Different types of link adaptation are performed according to the channel conditions, the UE capability (such as the maximum transmission power, maximum transmission bandwidth, etc.), and the required QoS (such as the data rate, latency, packet error rate, etc.). These link adaptation methods are as follows: (1) adaptive transmission bandwidth, (2) transmission power control, and (3) adaptive modulation and coding.

In LTE, a  $2 \times 2$  MIMO configuration is assumed to be the baseline in the downlink; that is, two transmit antennas at the base station and two receive antennas at the

terminal side. Configurations with four and eight transmit/receive antennas are also supported in the specification. Different downlink MIMO modes are supported in LTE, which can be adapted based on channel condition, traffic requirements, and the UE capability. In LTE spatial multiplexing, up to two codewords can be mapped to different layers. Each codeword represents an output from the channel coder. The number of layers available for transmission is equal to the rank of the channel matrix. Precoding in transmitter side is used to support spatial multiplexing. This is achieved by multiplying the signal with a precoding matrix prior to transmission. The optimum precoding matrix is selected from a predefined codebook which is known to both eNB and UE. The optimum precoding matrix is the one which maximizes the signal to noise ratio at the receiver.

The UE estimates the channel and selects the optimum precoding matrix. This feedback is provided to the eNB. Depending on the available bandwidth, this information is made available per RB or group of RBs, since the optimum precoding matrix may vary between RBs. The network may configure a subset of the codebook that the UE is able to select from. In case of UEs with high velocity, the quality of the feedback may deteriorate. Thus, an open-loop spatial multiplexing mode is also supported which is based on predefined settings for spatial multiplexing and precoding. In the case of four antenna ports, different precoders are assigned cyclically to the resource elements. The eNB will select the optimum MIMO mode and precoding configuration. The information is conveyed to the UE as part of the downlink control information on PDCCH. In order for MIMO schemes to work properly, each UE has to report information about the channel to the base station. Several measurement and reporting schemes are available which are selected according to MIMO mode and network preference. The reporting may include wideband or narrowband CQI, which is an indication of the downlink radio channel quality as experienced by this UE; Precoding Matrix Index (PMI), which is an indication of the optimum precoding matrix to be used in the base station for a given radio condition; and rank indication (RI), which is the number of useful transmission layers when spatial multiplexing is used.

In the case of transmit diversity mode, only one codeword can be transmitted. Each antenna transmits the same information stream, but with different coding. LTE employs SFBC as a transmit diversity scheme. A special precoding matrix is applied at the transmitter side in the precoding stage. Cyclic delay diversity (CDD) is an additional type of diversity which can be used in conjunction with spatial multiplexing in LTE. An antenna-specific delay is applied to the signals transmitted from each antenna port. This effectively introduces artificial multipath to the signal as seen by the receiver. As a special method of delay diversity, CDD applies a cyclic shift to the signals transmitted from each antenna port.

LTE supports uplink MU-MIMO where multiple user terminals may transmit simultaneously on the same RBs. The scheme requires only one transmit antenna at the UE side. The UEs sharing the same RB have to apply mutually orthogonal pilot patterns. To take advantage of two or more transmit antennas, transmit antenna selection can be used. In this case, the UE has two transmit antennas but only one

transmission chain. A switch will then choose the antenna that provides the best channel to the eNB.

The MIMO capabilities of LTE were extended by supporting up to eight downlink transmit antennas and up to four uplink transmit antennas. In addition to legacy MIMO transmission schemes, transmit diversity is now possible in both downlink and uplink directions. In the downlink, using the single-user spatial multiplexing scenario of LTE-Advanced, up to two transport blocks can be transmitted to a scheduled UE in one subframe per downlink component carrier. Each transport block is assigned its own modulation and coding scheme. For HARQ ACK/NACK feedback on uplink, one bit is used for each transport block. In addition to the spatial multiplexing scheme, the LTE-Advanced downlink reference signal structure has been modified to allow an increased number of antennas and PDSCH demodulation, as well as channel state information estimation for the purpose of CQI/PMI/RI reporting when needed.

The reference signals for physical downlink shared channel demodulation are UE-specific; that is, the data subcarriers and the demodulation reference signals intended for a specific UE are subject to the same precoding operation. Therefore, these reference signals are mutually orthogonal between the layers at the eNB. Reference signals targeting CSI estimation are cell specific, are sparse in the frequency and time domain, and are punctured into the data region of normal subframes.

With LTE-Advanced, a scheduled UE may transmit up to two transport blocks. Each transport block has its own modulation and coding scheme. Depending on the number of transmission layers, the modulation symbols associated with each of the transport blocks are mapped to one or two layers. The transmission rank can be dynamically adapted. Different codebooks are defined depending on the number of layers that are used. Furthermore, different precoding is used depending on whether two or four transmit antennas are available. Also, the number of bits used for the codebook index is different depending on the two and four transmit antenna case, respectively.

For uplink spatial multiplexing with two transmit antennas, a 3-bit precoding method is defined. In contrast to the LTE Rel-8 downlink scheme, where several matrices for full-rank transmission are available, only the identity precoding matrix is supported in the LTE-Advanced uplink direction. LTE-Advanced further supports transmit diversity in the uplink. However, for those UEs with multiple transmit antennas, an uplink single-antenna-port mode is defined. In this mode, the LTE Rel-10 UE behavior is the same as the one with a single antenna from eNB's point of view and it is always used before the eNB is aware of the UE antenna configuration. In the transmit diversity scheme, the same modulation symbol from the uplink channel is transmitted from two antenna ports, on two separate orthogonal resources.

The Layer 2 functions in LTE are classified into MAC, RLC, and PDCP sublayers. In the case of carrier aggregation, the multicarrier nature of the physical layer is only exposed to the MAC sublayer for which one HARQ entity is required per serving cell. In both uplink and downlink, there is one independent HARQ entity per serving

cell and one transport block is generated per TTI per serving cell in the absence of spatial multiplexing. Each transport block and the associated HARQ retransmissions are mapped to a single serving cell.

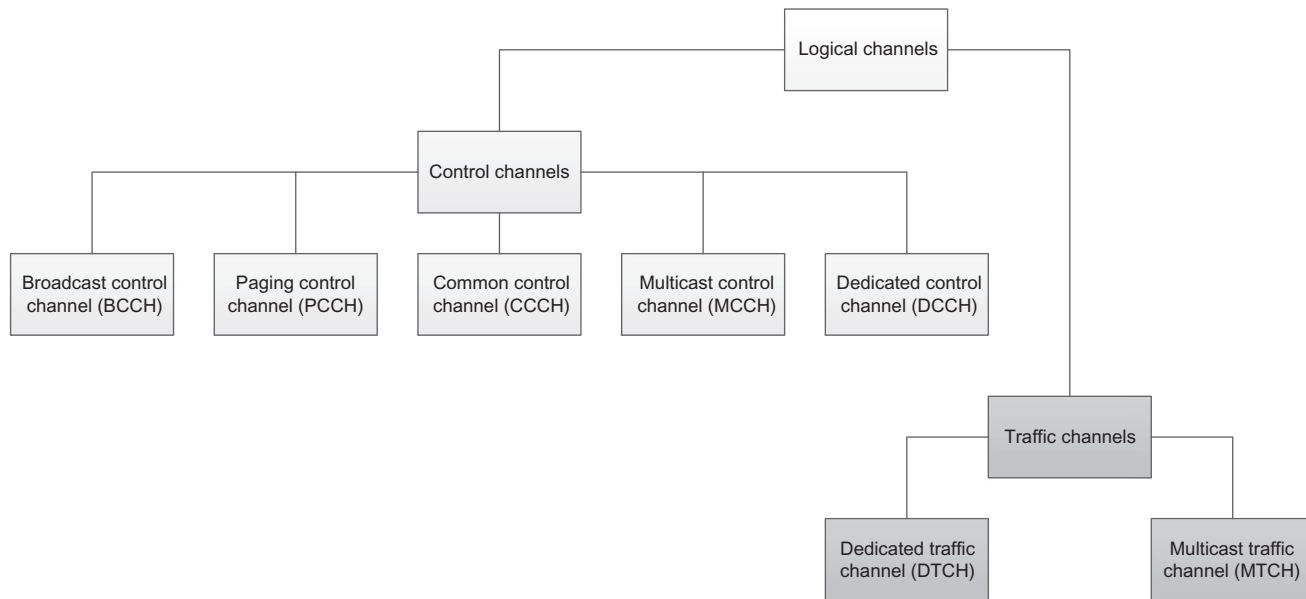
The services and functions provided by the MAC sublayer can be summarized as follows:

- Mapping between logical channels and transport channels.
- Multiplexing/demultiplexing of RLC protocol data units corresponding to one or different radio bearers into/from transport blocks delivered to/from the physical layer on transport channels.
- Traffic volume measurement reporting.
- Error correction through HARQ.
- Priority handling between logical channels of one UE.
- Priority handling between UEs through dynamic scheduling.
- Transport format selection.

The logical and transport channels in LTE are illustrated in [Fig. 15.23](#). Each logical channel type is defined by what type of information is transferred. The logical channels are generally classified into two groups: (1) control channels (for the transfer of control-plane information) and (2) TCHs (for the transfer of user-plane information).

The physical layer provides information transfer services to MAC and higher layers. The physical layer transport services are described by how and with what characteristics data are transferred over the radio interface. This should be clearly separated from the classification of what is transported, which relates to the concept of logical channels at MAC sublayer.

The main services and functions provided by the RLC sublayer include transfer of upper layer PDUs supporting AM or UM, TM data transfer, error correction through ARQ (since a CRC check is provided by the physical layer, no CRC is needed at RLC level), and segmentation according to the size of the transport. The E-UTRA provides ARQ and HARQ functionalities. The ARQ functionality provides error correction by retransmissions in the AM at Layer 2. The HARQ functionality ensures delivery between peer entities at Layer 1. The HARQ within the MAC sublayer is characterized by an N-process stop-and-wait protocol and retransmission of transport blocks upon failure of earlier transmissions. The ACK/NACK transmission in FDD mode refers to the downlink packet that was received four subframes earlier. In TDD mode, the uplink ACK/NACK timing depends on the uplink/downlink configuration. For TDD, the use of a single ACK/NACK response for multiple PDSCH transmissions is possible. A total of eight HARQ processes are supported. An asynchronous adaptive HARQ is utilized in the downlink. The uplink ACK/NACK signaling in response to downlink retransmissions is sent on uplink control or data channels. A synchronous HARQ scheme is supported in the uplink. The maximum number of retransmissions can be configured per UE basis as opposed to per radio bearer. The downlink ACK/NACK signaling in response to uplink retransmissions is sent on the downlink HARQ feedback channel.

**FIG. 15.23**

LTE logical channels.

Based on, S. Ahmadi, *LTE-Advanced: A Practical Systems Approach to Understanding 3GPP LTE Releases 10 and 11 Radio Access Technologies*, Academic Press, Oxford, UK, 2013.

The ARQ functionality within the RLC sublayer is responsible for retransmission of RLC PDUs or RLC PDU segments. The ARQ retransmissions are based on RLC status reports and optionally based on HARQ/ARQ interactions. The polling for the RLC status report is used when needed by RLC, and status reports can be triggered by upper layers.

Services and functions provided by the PDCP sublayer for the user plane include header compression and decompression, transfer of user data between the NAS and RLC sublayer, sequential delivery of upper layer PDUs at HO for RLC AM, duplicate detection of lower layer SDUs at HO for RLC AM, retransmission of PDCP SDUs at HO for RLC AM, and ciphering. Services and functions provided by the PDCP for the control plane include ciphering and integrity protection and transfer of control-plane data where PDCP receives PDCP SDUs from RRC and forwards it to the RLC sublayer and vice versa.

The main services and functions of the RRC sublayer include the following:

- broadcast of system information;
- paging;
- establishment, maintenance, and release of an RRC connection between the UE and E-UTRAN, including allocation of temporary identifiers between UE and E-UTRAN and configuration of signaling radio bearer(s) for RRC connection;
- security functions, including key management;
- establishment, configuration, maintenance, and release of point-to-point radio bearers;
- mobility functions, including UE measurement reporting and control of the reporting for intercell and inter-RAT mobility, HO, UE cell selection and reselection and control of cell selection and reselection, and context transfer at HO;
- establishment, configuration, maintenance, and release of radio bearers for MBMS services;
- QoS management functions; and
- UE measurement reporting and control of the reporting.

There are two RRC states in LTE:

- **RRC\_IDLE** is a state where a UE specific Discontinuous Reception (DRX) may be configured by upper layers. In the idle mode, the UE is saving power and does not inform the network of each cell change. The network knows the location of the UE to the granularity of a few cells, called the tracking area (TA). The UE monitors a paging channel to detect incoming traffic, performs neighboring cell measurements and cell selection/reselection, and acquires system information.
- **RRC\_CONNECTED** is a state where transfer of unicast data to/from UE is performed and the UE may be configured with a UE specific DRX or DTX. The UE monitors control channels associated with the shared data channel to determine if data is scheduled for it, sends channel quality and feedback

information, performs neighboring cell measurements and measurement reporting, and acquires system information.

In order to support mobility, a LTE-compliant UE must conduct intra/interfrequency or inter-RAT measurements (physical layer measurements include reference signal received power and E-UTRA carrier received signal strength indicator). Measurement commands are used by E-UTRAN to instruct the UE to start measurements, modify measurements, or stop measurements. The reporting criteria that are used include event triggered reporting, periodic reporting, and event triggered periodic reporting.

When carrier aggregation is configured, the UE only has one RRC connection with the network. At RRC connection establishment/reestablishment/HO, one serving cell provides the NAS mobility information, and at RRC connection reestablishment/HO, one serving cell provides the security input. This cell is referred to as the primary cell (PCell). In the downlink, the carrier corresponding to the PCell is the downlink primary component carrier, while in the uplink it is the uplink primary component carrier. Depending on UE capabilities, secondary cells (SCells) can be configured to form, together with the PCell, a set of serving cells. In the downlink, the carrier corresponding to a SCell is a downlink secondary component carrier, while in the uplink it is an uplink secondary component carrier. The configured set of serving cells for a UE always consist of one PCell and one or more SCells. For each SCell the usage of uplink resources by the UE in addition to the downlink ones is configurable. From the UE point of view, each uplink resource only belongs to one serving cell. The number of serving cells that can be configured depends on the aggregation capability of the UE. The PCell can only be changed with the HO procedure (ie, with a security key change and RACH procedure). The PCell is used for transmission of PUCCH, and unlike SCells, the PCell cannot be deactivated. The reestablishment is triggered only when the PCell experiences a radio link failure and not when the SCells experience radio link failure. The NAS information is obtained from PCell. The reconfiguration, addition, and removal of SCells can be performed by RRC signaling. In intra-LTE HO, RRC can also add, remove, or reconfigure SCells for usage with the target PCell. When adding a new SCell, dedicated RRC signaling is used for sending all required system information of the SCell; that is, while in connected mode, UEs do not need to acquire broadcasted system information directly from the SCells.

---

## 15.4 CONCLUSION AND REMARKS

This chapter provided an overview of the most prominent wireless technologies and their developing standards organizations. These technologies have been incorporated into numerous products, services, and networks in various industries across the globe and have changed our lifestyles in the past two decades. These technologies are continuously evolving and being improved in order to address the increasing user demand in a connected digital world.

---

## REFERENCES

- [1] IEEE 802 LAN/MAN Standards Committee, <http://www.ieee802.org/>.
- [2] 3rd Generation Partnership Project (3GPP), <http://www.3gpp.org/>.
- [3] Wi-Fi Alliance, <http://www.wi-fi.org/>.
- [4] Bluetooth Special Interest Group, <https://www.bluetooth.org>.
- [5] E. Perahia, R. Stacey, Next Generation Wireless LANs: 802.11n and 802.11ac, second ed., Cambridge University Press, Cambridge, UK, 2013.
- [6] S. Ahmadi, Mobile WiMAX: A Systems Approach to Understanding IEEE 802.16m Radio Access Technology, Academic Press, Oxford, UK, 2010.
- [7] K. Townsend, et al., Getting Started With Bluetooth Low Energy: Tools and Techniques for Low-Power Networking, O'Reilly Media, Sebastopol, CA, 2014.
- [8] J. Eberspächer, et al., GSM—Architecture, Protocols and Services, third ed., Wiley, Chichester, UK, 2009.
- [9] T. Chapman, et al., HSPA Evolution: The Fundamentals for Mobile Broadband, Academic Press, Oxford, UK, 2014.
- [10] S. Ahmadi, LTE-Advanced: A Practical Systems Approach to Understanding 3GPP LTE Releases 10 and 11 Radio Access Technologies, Academic Press, Oxford, UK, 2013.

# Power line communications 16

**L. Lampe<sup>\*</sup>, L.T. Berger<sup>\*,†</sup>**

*University of British Columbia, Vancouver, BC, Canada<sup>\*</sup> BreezeSolve, Paterna (Valencia), Spain<sup>†</sup>*

## CHAPTER OUTLINE

<b>16.1 Introduction</b>	621
16.1.1 Application Domains	622
16.1.2 Through the Grid	622
16.1.3 Terminology	623
16.1.4 Outline	623
<b>16.2 PLC Standards</b>	624
16.2.1 Ultra Narrowband PLC	624
16.2.2 Narrowband PLC	626
16.2.3 Broadband PLC	630
<b>16.3 Electromagnetic Compatibility Regulations</b>	634
16.3.1 Regulations for NB PLC	634
16.3.2 Regulations for Broadband PLC	636
<b>16.4 Power Line Channel</b>	637
16.4.1 Signal Propagation	638
16.4.2 Noise Characteristics	642
<b>16.5 Transmission Techniques</b>	643
16.5.1 Single-Carrier Transmission	644
16.5.2 Multicarrier Transmission	645
16.5.3 MIMO Transmission	645
16.5.4 Cognitive Transmission Techniques	647
<b>16.6 Final Remarks</b>	648
<b>References</b>	648

## 16.1 INTRODUCTION

Power line communications (PLC) reuse the existing power-grid infrastructure for the transmission of data signals. Since electrification generally preceded the roll-out of telecommunication infrastructures, it is not surprising that PLC has been used for a very long time.

### 16.1.1 APPLICATION DOMAINS

The original users of PLC have naturally been electric power utilities who own(ed) the power line networks. PLC has been suggested for remote meter reading [1] and remote load management [2] as early as around 1900 [3,4]. Following this, PLC was widely deployed to establish voice and data communication over medium-voltage (MV) and high-voltage (HV) transmission lines for telemetry, telecontrol, and teleprotection purposes and to perform load management tasks via so-called ripple control [5–7].

Today, both remote meter reading and load management, or more generally demand-side management, are part of the vision of smart grid [8]. Smart grid communication is thus a natural application domain for PLC technology [9–11]. Besides its more than 100-year track record of enabling power-grid control and automation, PLC has been identified as the “most adopted communication technology in smart meters” [12], with a concentration of deployments and trials in Europe, eg, [13–15]. Reliable two-way PLC systems have been installed for smart metering since the 1990s, and the recently developed suite of new PLC systems for smart grid applications employ signal transmission and processing techniques comparable to what we see in modern wireless or other wireline systems.

Power utilities have also explored the use of PLC for providing Internet access to customers through its overhead and/or underground power lines in the distribution grid. This started in the late 1990s [16,17] and led to renewed interest in this technology, coupled with a spur of innovation and the introduction of megabits per second communication over power lines. Similar PLC solutions have also penetrated the consumer market. While PLC has been applied for home and industry automation for decades [18], high-speed PLC for in-home multimedia communication has become a reality since the early 2000s [19,20]. PLC systems with data rates of originally a few megabits per second and later a few hundred megabits per second and even gigabits per second have been specified using modern multicarrier and multiple-input multiple-output (MIMO) techniques [21].

Most PLC systems have been deployed over AC power grids. Vehicles and more generally the transportation domain favor DC supply networks, which can be the medium for PLC signals. In particular, PLCs using the vehicle power harness can connect the electric components for vehicle control and passenger comfort and entertainment. This has been considered for cars, trucks, and trailers (eg, [22–24]), aircrafts (eg, [25–27]), spacecrafts (eg, [28,29]), and ships (eg, [30–32]); see [33] for an overview.

PLC has recently also been adopted for the communication between plug-in electric vehicles (PEVs) and charging infrastructures [34–37]. This is an important step toward integrating the growing electric vehicle fleets into the smart grid concept. Another interesting application of vehicle-to-infrastructure communication via PLC is for transit trains, which has been investigated in [38].

### 16.1.2 THROUGH THE GRID

A very specific feature of PLC systems is that their coverage and link performance depend on the topology of the electricity grid over which signals are transmitted. HV

transmission lines have little or no branches and carry PLC signals with relatively little attenuation over long distances. MV distribution lines can be overhead or underground and depending on the line or cable type and the level of branching, attenuation per line length can be notably increased [9, Table II]. However, the distances that need to be covered are generally shorter than for HV lines. The low-voltage (LV) distribution grid is typically the most challenging in terms of path loss for PLC. Also, distribution transformers strongly attenuate relatively high-frequency signals, thus often partially separating LV and MV grid domains. While this can be a desirable feature for reducing “intercell” interference in multicell PLC networks, it represents a challenge for economical deployment of PLC in grids where only a few consumer points are served by a single distribution transformer. In the latter case, either by-pass couplers and repeaters or low-frequency, and thus low data-rate (LDR), PLC transmission would be used.

The “through the grid” [9] nature of PLC and thus the intersection of communication engineering with power and energy engineering also show in another uniqueness of PLC, ie, the need for signal couplers that protect the communication equipment from the relatively higher voltages and currents carried by power lines. For example, the IEEE Power & Energy Society (PES) published [39] testing and verification standards for commonly used hardware and installation methods for broadband (BB) PLC systems, applicable to MV levels of up to 38 kV. Similarly, the IEEE PES standard [40] for “Power-Line Carrier Applications” includes a section dedicated to coupling components.

### 16.1.3 TERMINOLOGY

The brief discussion above alludes to the long history and the different application domains of PLC as well as the role of the grid and thus power engineering for PLC. These influences have led to a diverse terminology that is applied for PLC systems, often linked to a specific grid domain or application. For example, “power line carrier” has been a popular term that originated from the fact that not low-frequency (50/60 Hz) but carrier-modulated signals are transmitted over power lines. Similarly, “distribution line carrier (DLC)” refers to carrier-modulated signals, now also emphasizing their application in the distribution grid. Relatively newer terms are “broadband over power lines (BPL)” and “power line telecommunications (PLT),” which refer to systems with a signal bandwidth of tens of megahertz and data rates ranging from several megabits per second to hundreds of megabits per second.

The term “PLC” refers to all systems that use the power line medium for data communication and thus includes all of the above. It has widely been accepted in relevant research communities and in industry, so we will continue using it throughout this chapter.

### 16.1.4 OUTLINE

In the next section, we continue with a modern classification for PLC systems, which will lead to an overview discussion of popular PLC standards for smart grid communication, home and industry automation, and multimedia communication.

The regulatory environment for PLC will be outlined in [Section 16.3](#). In [Section 16.4](#), we introduce the fundamental characteristics and modeling approaches of signal propagation and noise when transmitting over power lines, which is followed by a presentation of transmission techniques applied in PLC in [Section 16.5](#). Final remarks in [Section 16.6](#) conclude this chapter.

Part of the material presented in this chapter has been adapted from [41] with friendly permission of the copyright holder CRC Press Taylor & Francis. Further details about the subjects discussed can be found in the books [41–43].

---

## 16.2 PLC STANDARDS

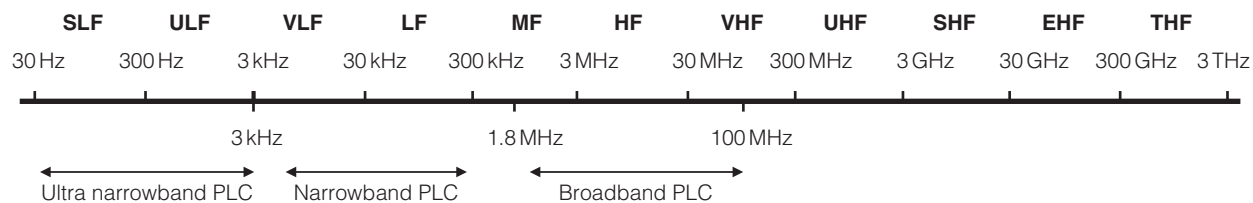
Before surveying the landscape of PLC standards, it is insightful to review the frequency bands that are used for PLC transmission. These are displayed in [Fig. 16.1](#) in relation to the radio bands defined in the International Telecommunication Union (ITU) Radio Regulations [44]. We observe three distinct bands for PLC technologies.

1. Ultra narrowband (UNB) technologies operate in the ultra low frequency band (ULF, 0.3–3 kHz) or in the upper part of the super low frequency band (SLF, 30–300 Hz).
2. Narrowband technologies operate at frequencies between 3 kHz up to around 500 kHz, ie, in the very low, the low, and in parts of the medium frequency (VLF/LF/MF) bands. For the following discussion of NB PLC standards, as well as regulations presented in [Section 16.3](#), we note that the European Comité Européen de Normalisation Électrotechnique (CENELEC) bands (3–148.5 kHz), the US Federal Communications Commission (FCC) band (10–490 kHz), the Japanese Association of Radio Industries and Businesses (ARIB) band (10–450 kHz), and the Chinese band (3–500 kHz) are located within this range.
3. Broadband (BB) technologies operate in the medium, high, or very high frequency bands (MF/HF/VHF) (1.8–250 MHz).

In the following, we will elaborate on specifications and standards developed for these bands. An overview of UNB-, NB-, and BB-PLC specifications and standards is presented in [Fig. 16.2](#).

### 16.2.1 ULTRA NARROWBAND PLC

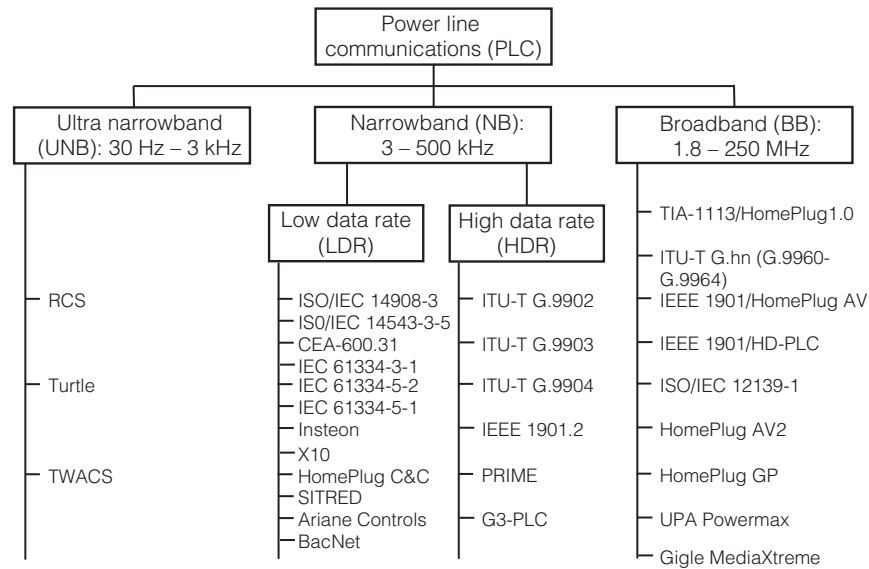
Ripple control systems (RCSs) [7] for remote load management are the earliest UNB PLC systems. RCSs enable unidirectional communication from a central control station located at the MV side to the consumers at the LV side of the grid. Other UNB PLC technologies include the Turtle system [45] and the more recent two-way automatic communications system (TWACS) [46,47], which have also been used for automated meter reading (AMR) and distribution automation [9]. The main advantage of UNB PLC technologies is that they can communicate over long



**FIG. 16.1**

Frequency bands used for PLC. The indicated frequency ranges and the acronyms on the top refer to the radio bands defined in the International Telecommunication Union (ITU) Radio Regulations [44].

*Source: Adopted from L.T. Berger, A. Schwager, P. Pagani, D.M. Schneider (Eds.), MIMO Power Line Communications: Narrow and Broadband Standards, EMC, and Advanced Processing, CRC Press—Taylor & Francis Group, New York, NY, 2014, Figure 1.1.*

**FIG. 16.2**

Overview of UNB-, NB-, and BB-PLC specifications and standards.

Source: Adopted from L.T. Berger, A. Schwager, P. Pagani, D.M. Schneider (Eds.), *MIMO Power Line Communications: Narrow and Broadband Standards, EMC, and Advanced Processing*, CRC Press—Taylor & Francis Group, New York, NY, 2014, Figure 10.1.

distances with their signals passing through distribution transformers. Hence, they have specifically been designed for efficient deployment in the distribution domain and scenarios with few consumers per distribution transformer using a minimal number of required modems and repeaters. A natural drawback of UNB PLC is the LDR that is achievable in the UNB, which is of the order of 0.001 bps for Turtle and two bits per mains frequency cycle for TWACS.

## 16.2.2 NARROWBAND PLC

NB PLC systems usually operate in the frequency range from 3 to 500 kHz. The class can be further divided into LDR and high data-rate (HDR) NB systems [9] (see Fig. 16.2).

### 16.2.2.1 Low data-rate narrowband PLC

“LDR” means that these systems only use a small fraction of the bandwidth in the 3–500 kHz band and enable data rates of typically a few kilobits per second. There are a number of LDR NB PLC systems specified for industry and home automation applications. An early example is the X10 standard developed in 1975, transmitting short bursts at the zero-crossing points of the AC power line cycle. Higher-rate successor developments include KNX and LonWorks, which are defined

for several physical media, including power lines and twisted pair wires. For PLC and home automation applications they use the CENELEC C-band (discussed further in [Section 16.3](#)) at 132 kHz, with a secondary frequency at 115 kHz for LonWorks systems. LonWorks PLC transceivers are also designed to operate at 85 and 75 kHz in the CENELEC A-band when used for power utility (ie, smart grid) applications. LonWorks became an ANSI and later an international standard as ISO/IEC 14908-3 [48,49]. Similarly, KNX is standardized as EN 50090 and ISO/IEC 14543-3-5 [50]. Another widely deployed set of LDR NB PLC technologies has been specified in the IEC 61334 series, in particular IEC 61334-5-1 and IEC 61334-5-2 [51,52], which operates in the CENELEC A band for power utility use.

### 16.2.2.2 High data-rate narrowband PLC

“HDR” refers to technologies capable of data rates ranging between tens of kilobits per second up to around 500 kbps. While all of the above-mentioned LDR NB PLC technologies use single-carrier transmission (as we will discuss further in [Section 16.5](#)), today’s HDR technologies are based on multicarrier and, in particular, orthogonal frequency division multiplexing (OFDM) modulation (see [Section 16.5](#)). A lot of emphasis for the development of such systems has been given to the distribution domain. Typical and important examples are the industry specifications DLC-2 [53], G3-PLC [54], and powerline related intelligent metering evolution (PRIME) [55] and the standards ITU-T 9902/03/04 [56–58] and IEEE 1901.2 [59]. To facilitate coexistence of these systems with the previous generation of LDR NB PLC technology, frequency separation, frequency notching, and preamble-based carrier-sense multiple-access (CSMA) mechanisms have been proposed [60] and adopted [59, Sec. 10, 61, Apps. A,B].

While the overview in this section and in [Fig. 16.2](#) focuses on the distribution domain, a similar evolution from LDR to HDR NB PLC has also occurred for transmission over HV lines [5]. For example, ABB’s ETL600 system “for the transmission of speech signals, data, and protection commands over HV transmission lines” supports data rates of 320 kbps in a 32 kHz bandwidth [62], and Selta’s STED system transmits 92.8 kbps in a 16 kHz bandwidth [63].

In the following, we provide a few more details for the PRIME and G3-PLC specifications. They are particularly relevant as they have also been adopted as international standards in ITU-T Recommendation G.9903 [57] and ITU-T Recommendation G.9904 [58], respectively. Furthermore, G3-PLC was used as the basis for the IEEE 1901.2 standard [59]. [Fig. 16.3](#) shows some milestones of the development of PRIME and G3-PLC specifications and the ITU-T and IEEE standards between 2008 and 2013.

#### PRIME

The PRIME specification was developed within the PRIME Alliance, with its steering committee chaired by the Spanish utility Iberdrola [55]. In 2012, PRIME version 1.3.6 became an international standard as ITU-T Recommendation G.9904 [58].

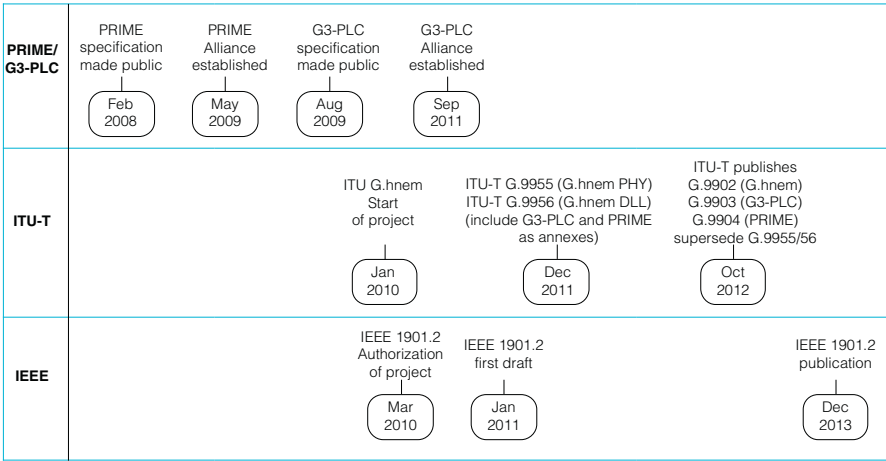


**FIG. 16.3**  
Development of HDR NB PLC specifications and standards (see also [64,65]).

The PRIME system uses OFDM with 97 active subcarriers and a subcarrier spacing of  $250/512 \approx 488$  Hz; the first and last subcarrier have a frequency of about 42 and 89 kHz, respectively, ie, within the CENELEC A-band reserved for utility applications. Accordingly, the OFDM symbol duration is 2240  $\mu$ s, which includes a 192  $\mu$ s cyclic prefix that is sufficient to deal with most commonly experienced linear distortions over power line channels. Modulation formats are differential binary, quaternary, and eight-ary phase-shift keying (DBPSK, DQPSK, and D8PSK), where differential encoding is across subcarriers. An optional 1/2-rate convolutional code is applied for improved transmission reliability. The physical-layer (PHY) data rates range from 21.4 to 128.6 kbps. In order to deal with unpredictable impulsive noise (discussed in Section 16.4) PRIME offers the option to implement automatic retransmission request (ARQ) based on the selective-repeat mechanism.

Turning to the system architecture, PRIME is forming subnetworks, where each subnetwork has one “base node” and several “service nodes.” The base node is the master that manages the subnetwork’s resources and connections using a periodically sent beacon signal. The base node is further responsible for PLC channel access arbitration. A contention free and a contention-based access mechanism exists, whose usage time and duration are decided by the base node. Within the contention-free channel access period, the base node assigns the channel to only one node at a time. The contention-based access uses CSMA with collision avoidance (CSMA/CA).

To interface the medium access control (MAC) and the application layer, PRIME defines a convergence layer (CL) between the two. The CL can be split into a common part convergence sublayer (CPCS) and a service specific convergence

sublayer (SSCS). The CPCS performs tasks of data segmentation and reassembling and is adjusted to the specific application. The SSCS defined in [58,66] include CLs for IPv4 and IPv6 traffic and for the data format according to the IEC 61334-4-32 standard [67]. The latter makes it easy to support advanced metering applications that make use of the standardized data models of IEC 62056-62 [68] and to replace existing deployments using single-carrier power line standard IEC 61334-5-1 [51].

For more details we refer to [58,66,69].

### G3-PLC

The G3-PLC specification was published in Aug. 2009. In 2012, members of the G3-PLC Alliance [54] brought the original G3-PLC specs into the ITU-T where they were enhanced and additional functionalities were added. The enhanced G3-PLC became an international standard in 2012 as ITU-T Recommendation G.9903 [57].

G3-PLC can be configured to operate in the frequency range from 10 to 490 kHz according to the so-called FCC, CENELEC, ARIB bands, which will be discussed in Section 16.3. Fig. 16.4 shows the frequency bands for G3-PLC and PRIME as well as the IEEE 1901.2 standard. Table 16.1 summarizes PHY parameters of G3-PLC for the different bandplans. Similar to PRIME, differential modulation is specified. However, differential encoding is applied in the time direction. Furthermore, an optional coherent mode with up to 16-ary quadrature amplitude modulation (QAM) is included in the standard. G3-PLC uses the concatenation of a rate-1/2 convolutional

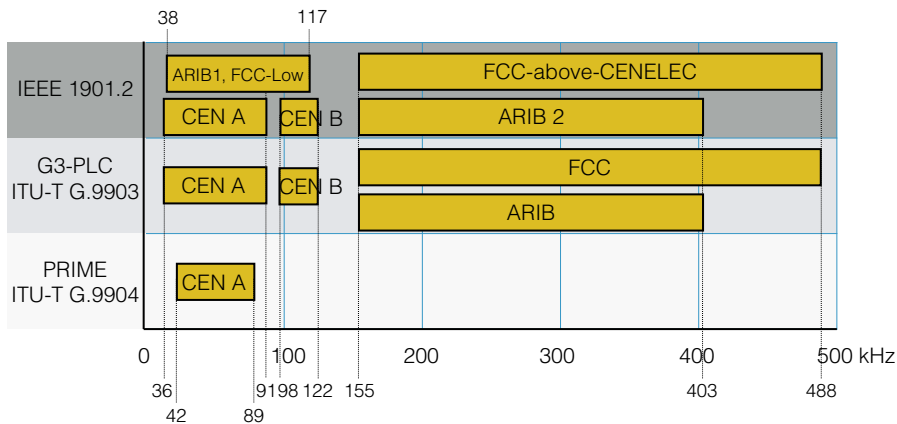


**FIG. 16.4**

Frequency bandplans for HDR NB PLC systems<sup>1</sup>. Figures are center frequencies of the start and end tone of each of the bands rounded to the next kilohertz-integer value.

Source: Modified from S. Galli, T. Lys, *Next generation narrowband (under 500 kHz) power line communications (PLC) standards*, China Commun. (2) (2015) 1–8.

<sup>1</sup>The PRIME v1.4 PHY specification extends the usable frequency band to 42–472 kHz.

**Table 16.1** Physical-Layer Parameters for G3-PLC and Its Different Bandplans

Band	CENELEC-A	CENELEC-B	FCC	ARIB
Subcarrier spacing (sampling frequency/FFT size)	400 kHz/256 $\approx$ 1.56 kHz		1200 kHz/256 $\approx$ 4.69 kHz	
Usable subcarriers	36	16	72	54
Cyclic prefix (CP) length (Nbr of CP samples/sampling frequency)	30/400 ms = 55 $\mu$ s		30/1200 ms $\approx$ 18.3 $\mu$ s	
Modulations	DBPSK, DQPSK, D8PSK, BPSK, QPSK, 8PSK, 16QAM			DBPSK, DQPSK, BPSK, QPSK, 8PSK

and the (255,239) Reed-Solomon (RS) code. The “robust” transmission (ROBO, for robust OFDM) modes use additional four- or six-times repetition, respectively. Coded bits are mapped to modulation symbols via time-frequency interleaving to mitigate the effects of impulse noise and deeply faded subcarriers. The latter is further countered through tone mapping that allows the transmitter to send dummy data on selected subcarriers. Typical PHY data rates, accounting for coding, frame control, and preamble overhead, are between 4 and 200 kbps [57, Sec. 7.3.1, 71].

The MAC layer is based on IEEE 802.15.4-2006 [72]. 6LoWPAN [73] is used to adapt the IEEE 802.15.4-2006 MAC to IPv6 [74].

A comparison between PRIME and G3-PLC focusing on physical layer aspects is presented in [75]. There it is found that G3-PLC performs more robust to impairments by the PLC channel than PRIME, while PRIME’s design paradigm is low complexity. As mentioned above, the G3-PLC specification was used as the basis for the IEEE 1901.2 PLC standard. Thus, there are technical similarities between ITU-T G.9903 and IEEE 1901.2, but there are also marked differences which make the two technologies noninteroperable. The differences between ITU-T G.9903 and IEEE 1901.2 are summarized in [70].

### 16.2.3 BROADBAND PLC

In the last decade, BB PLC chips by semiconductor vendors, such as Intellon,<sup>2</sup> DS2,<sup>3</sup> Gige,<sup>4</sup> and Panasonic, came to market that operate in the band from around 2 to 86 MHz and, in some cases, optionally up to 300 MHz. The chips are mainly based

<sup>2</sup>In 2009 acquired by Atheros; Atheros was acquired by Qualcomm in 2011.

<sup>3</sup>In 2010 acquired by Marvell.

<sup>4</sup>In 2010 acquired by Broadcom.

on three consortia-backed specifications developed within the frameworks of the HomePlug Powerline Alliance (HomePlug), the Universal Powerline Association (UPA; suspended activities in Nov. 2010), and the High Definition Power Line Communications (HD-PLC) Alliance. Related products allow data rates of around 200 Mbit/s and are not interoperable. However, to make BB PLC systems a broad success, internationally adopted standards became essential. Under the umbrella of ITU-T and IEEE, some of the industry specifications were consolidated in the ITU-T G.hn [76] and IEEE 1901 [77] standards.

ITU-T G.hn is not only applicable to power lines but also to phone lines and coaxial cables, therewith for the first time defining a single standard for all major wireline communications media. At the end of 2008, the PHY layer and the overall architecture were consented in ITU-T Recommendation G.9960 [78]. The Data Link Layer (DLL) Recommendation G.9961 [79] was approved in Jun. 2010, and a MIMO transceiver (see Section 16.5) extension G.9963 was consented in Sep. 2011 [80]. Additionally, the HomeGrid Forum was founded to promote the ITU-T G.hn standard and to address certification and interoperability issues [81].

Simultaneously, IEEE 1901 working group was working on the “Standard for Broadband over Power Line Networks: Medium Access Control and Physical Layer Specifications” [82]. It covers access and in-home BB PLC, as well as coexistence of access/in-home and in-home/in-home networks. The official IEEE Std 1901-2010 was published in Dec. 2010. To assure a broad industrial backing of IEEE 1901, two optional PHY technologies, namely FFT-PHY (based on HomePlug AV) and Wavelet-PHY (based on HD-PLC) were included in the standard. The HomePlug [83] serves as the certifying body for IEEE 1901 FFT-PHY compliant products, whereas the HD-PLC Alliance serves as the certifying body for IEEE 1901 Wavelet-PHY compliant products. While IEEE 1901 Wavelet-PHY/HD-PLC is presently mainly used in the Japanese market, IEEE 1901 FFT-PHY/HomePlug AV is used in many countries around the globe, with products of the HomePlug family currently possibly being the most deployed BB PLC technology worldwide.

In tandem with the introduction of MIMO to ITU-T G.hn, HomePlug introduced the HomePlug AV2 specification in Jan. 2012. The HomePlug AV2 specification includes features like MIMO with beamforming, an extended frequency range of up to 86 MHz, efficient notching, several transmit power optimization techniques, 4096-QAM, power save modes, and short delimiter and delayed acknowledgement, boosting the maximum PHY rate to around 2 Gbps. Further, to cover multiple home networking media under one umbrella, IEEE 1905.1 devised a “Standard for a Convergent Digital Home Network for Heterogeneous Technologies” [84]. It defines an abstraction layer for multiple home networking technologies like IEEE 1901, IEEE 802.11 (Wi-Fi), IEEE 802.3 (Ethernet), and MoCA 1.1, and it is extendable to work with other home networking technologies.

In the next two subsections, we first highlight some of the features of the IEEE 1901 and ITU-T G.hn. We then discuss the low-complexity profile of ITU-T G.hn together with the HomePlug Green PHY specification, which have been developed

as BB PLC solutions with lower complexity and power consumption suitable for smart grid applications.

### **16.2.3.1 IEEE 1901 and ITU-T G.hn**

IEEE 1901 uses the band from 2 MHz up to 50 MHz with services above 30 MHz being optional. ITU-T G.hn (G.9960/G.9961) operates from 2 MHz up to 100 MHz using bandwidth scalability, with three distinct and interoperable bands defined as 2–25, 2–50, and 2–100 MHz. The architectures defined by IEEE 1901 and ITU-T G.hn (G.9960/G.9961) are similar in several aspects. In ITU-T G.hn, one refers to a subnetwork as a “domain.” Operation and communication are organized by the domain master who communicates with various “nodes.” Similarly, the subnetwork in IEEE 1901 is referred to as the basic service set (BSS). The equivalent to the domain master is the BSS manager, which connects to so-called stations.

Even if many features appear to be individually developed by ITU-T and IEEE, several are actually identical. The fact that ITU-T G.hn and IEEE 1901 largely agree on channel coherence time, coherence bandwidth, guard interval, roll-off window timings, etc., shows that the BB PLC channel is analyzed similarly and that channels for comparable topologies are not very different around the globe. Similarities continue with PHY-frame header settings making use of QPSK, forward error-correction (FEC) coderate 1/2, and repetition codes. The segmentation process of embedding the application data into PLC convenient packets is similar and data are in both cases encrypted using AES-128 [85]. The MAC cycle or beacon period is selected to be two line cycles. The bit-loading of carriers can be line cycle dependent and immediate, and delayed acknowledgments are also possible.

The G.hn defines an OFDM PHY used for operation over any wireline medium. The OFDM parameters are adjusted to account for different medium dependent channel and noise characteristics and to allow for straightforward scaling when adjusting the parameters between one medium and another. IEEE 1901 defines two PHY referred to as FFT-PHY and Wavelet-PHY, respectively. The two physical layers are not interoperable but a mandatory coexistence protocol is standardized within IEEE 1901 as the intersystem protocol (ISP) (originally developed as inter-PHY protocol (IPP) [86]). The ISP also enables coexistence between IEEE 1901 and ITU-T G.hn devices. A nearly identical mechanism was standardized by ITU-T in Recommendation G.9972 [87], also known as G.cx. Technical contributions to ITU-T and IEEE from members of the Priority Action Plan 15 (PAP15) of the National Institute of Standards and Technology (NIST) assured the alignment of both standards. As a result, the NIST PAP 15 recommended to mandate that all BB PLC technologies implement Recommendation ITU-T G.9972 or ISP [88].

Two very different FECs, ie, low-density parity-check code (LDPC) in ITU-T G.hn and Turbo Code in IEEE 1901, were chosen (see [89] for a comparative analysis). Some have argued that this makes it more difficult (or costly) to implement both standards in a single chip, as the FEC part is, up to the present day, a nonnegligible cost/space factor when manufacturing wafers. However, dual mode devices have already started to appear on the market.

If ITU-T G.hn and IEEE 1901 modems are installed in the same home, the transmission from one modem is an unintended interferer for the other one. Confusion is avoided due to different preambles that are sent at the beginning of a frame. A correlator at the receiver is able to identify precise timing information of a frame by detecting the inverted transmitted preamble symbols. A PLC transmission is identified by verifying the timing results of the correlated received signals with an ITU-T G.hn or an IEEE 1901 mask. A multimode receiver could identify both correlation masks and forward the subsequent data signals to the corresponding decoding chain.

Another likely scenario is that same technology networks exist in close proximity, with the risk of so-called neighboring network interference. To deal with neighboring network interference ITU-T G.hn uses different preamble-symbol-seeds in each network. Therewith, ITU-T G.hn networks are able to coexist and communicate simultaneously, ie, not using time division. Instead, link adaptation procedures adjust the throughput to cope with degraded signal-to-interference-plus-noise ratios (SINRs). In many cases, the throughput will be throttled only slightly, allowing ITU-T G.hn networks to coexist nearly unimpeded. On the other hand, IEEE 1901 relies on a CSMA/CA medium access strategy, which may lead to an increased number of collisions. As a countermeasure, IEEE 1901 introduces a coordinated mode that allows neighboring networks to allocate times over the shared medium for specific communications. This coordinated time division multiple access (TDMA) mode enables traffic to get through unimpeded albeit at the price of time division (orthogonal throughput sharing).

### ***16.2.3.2 ITU-T G.hn low complexity profile and HomePlug green PHY***

In terms of data rate and silicon cost the full fledged ITU-T G.hn and IEEE 1901 systems are targeting primarily in-home data delivery, web-browsing, as well as audio and video distribution. To offer an alternative to automation and energy management tasks with respect to HDR NB-PLC, ITU-T G.hn includes a low complexity profile (LCP), while on the basis of IEEE 1901, HomePlug developed the HomePlug Green PHY (HPGP) specification.

The ITU-T G.hn LCP operates in the frequency range from 2 to 25 MHz and is still interoperable with the full G.hn profile. This allows for reduced component cost and power consumption in case G.hn nodes are embedded into smart grid home area network (SGH) devices in the future. Example SGH nodes could be heating and air conditioning appliances, as well as PEVs and electric vehicle supply equipment (EVSE). Together they form a multidomain home area network (HAN).

Similarly, the HPGP is a subset of HomePlug AV that is intended for use within smart grid applications. Optimized for low power applications and costs, HPGP uses the most robust communication mode of HomePlug AV technology. OFDM carrier spacing, preamble, frame control, and FEC are identical to HomePlug AV/IEEE 1901, resulting in identical coverage and reliability. CSMA/CA is used as a channel access scheme. Further, nodes may use long power save periods if a higher latency is acceptable. In the sleep state, modems have only a 3% power consumption compared

to the awake time, resulting in an average power reduction of more than 90% with respect to standard HomePlug AV products. In order to reliably perform PEV/EVSE association, a special feature called signal level attenuation characterization (SLAC) was designed into HPGP. Details of how to use HomePlug GP SLAC in automotive applications can be found in ISO/IEC 15118-3 [37].

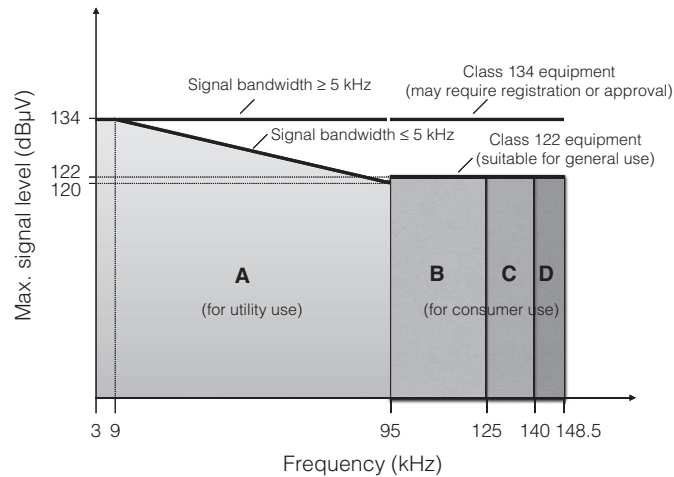
## 16.3 ELECTROMAGNETIC COMPATIBILITY REGULATIONS

The PLC systems according to the discussed standards and summarized in Fig. 16.2 do not work in isolation but over a shared medium. In particular, the power lines used to convey PLC signals are first and foremost deployed to supply energy to electrical loads such as machines, lighting devices, houses, and household appliances, etc. It is therefore not surprising that PLC devices are subject to regulations that limit the level of signals coupled into power lines, which are perceived by the power line network as conducted emissions. Furthermore, PLC systems are also subject to radiated emission limits, which can be critical considering that in the design of the power grid no effort has been made to mitigate electromagnetic radiation. A complicating factor for PLC regulation is that relevant emission standards differentiate between a mains and a telecommunication port of a device under test, which, however, are identical for PLC devices. Whereas a non-PLC device would not deliberately emit a signal over the mains port, this is intended for PLC devices. Hence, one may argue that existing measurement practices as well as emission limits should be adapted for PLC [90–92].

These issues of electromagnetic compatibility (EMC) of PLC are dependent on the frequency range used by PLC devices and are thus quite different for the NB and BB PLC systems. In general, NB PLC has enjoyed an unambiguous regulatory framework that has also facilitated the development of the NB PLC standards described in the previous section. The (more complicated) regulation for BB PLC has been quite contentious and subsequent to the specification and even deployment of BB PLC systems.

### 16.3.1 REGULATIONS FOR NB PLC

As stated in Section 16.2, NB PLC systems use frequencies between 3 and 500 kHz. An important European regulation that promoted the development of LDR and eventually HDR NB PLC systems is the European Norm (EN) 50065 issued by CENELEC in 1991 [93]. It defines transmission limits and their measurement procedures for the frequency range from 3 to 148.5 kHz. To this end, it distinguishes four frequency bands, which are referred to as CENELEC-A, CENELEC-B, CENELEC-C, and CENELEC-D band. Fig. 16.5 shows the frequency ranges and transmission limits for the four bands. These limits must be considered together with

**FIG. 16.5**

Frequency bands (so-called CENELEC bands) and in-band signal-level limits (for single phase installations) according to EN 50065.

*Source: Data from European Committee for Electrotechnical Standardization (CENELEC), Signalling on low-voltage electrical installations in the frequency range 3 kHz to 148.5 kHz—part 1: general requirements, frequency bands and electromagnetic disturbances, Standard EN 50065-1, 1991, 2001, 2011.*

the measurement procedures defined in [93]. As indicated in Fig. 16.5, EN 50065 also mandates that the CENELEC-A band may only be used by power utilities and their licensees, while the use of the other bands is limited to consumer installations. Furthermore, devices operating in the CENELEC-C band have to apply a CSMA/CA mechanism, which requires transmission and carrier sensing between 131.5 and 133.5 kHz and specifies maximum channel holding (1 s) and minimum pause (125 ms) periods.

In the United States, the FCC Code of Federal Regulations, Title 47, Part 15 (47 CFR §15), [94] applies for the regulation of PLC emissions. Section 15.3 clause (t) of [94] defines “power line carrier” systems, and Section 15.113 then specifies that power utilities can operate power line carrier systems within the 9–490 kHz band on an “unprotected, noninterference basis.” However, “electric lines which connect the distribution substation to the customer or house wiring” are explicitly excluded from this. Hence, we also need to consider “carrier current” systems, which are defined in clause (f) of Section 15.3. Fig. 16.6 shows the resulting sequence of clauses which set forth out-of-band conducted and in-band radiated emission limits for NB PLC operating in the 9–490 kHz band.

In Japan, the ARIB regulates and permits PLC transmission in the frequency band of 10–450 kHz. The standard [95] provides in-band and out-of-band transmission limits and the corresponding measurement procedures.

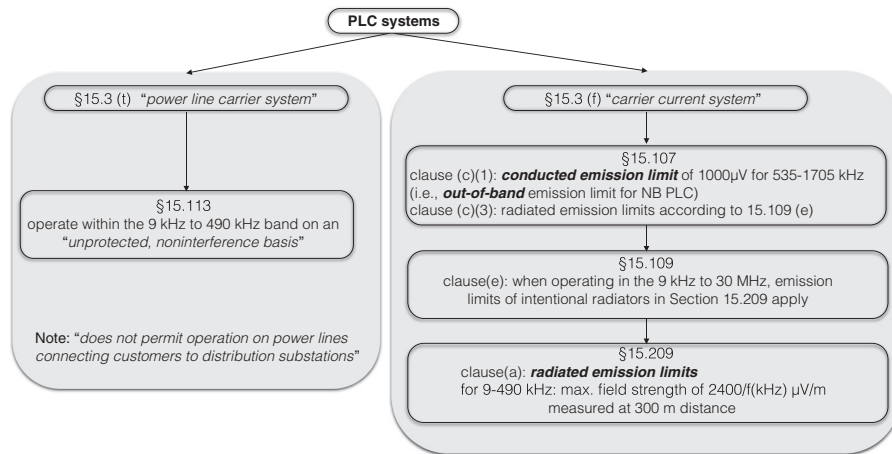


FIG. 16.6

Illustration of clauses from the U.S. FCC 47 CFR §15 [94] relevant for emissions from NB PLC systems.

### 16.3.2 REGULATIONS FOR BROADBAND PLC

The applicable EMC limits for BB PLC have been controversially discussed. Insightful accounts of the developments under the auspices of IEC's Comité International Spécial des Perturbations Radioélectriques (CISPR, International Special Committee on Radio Interference) and the European Telecommunications Standards Institute (ETSI) and CENELEC can be found in [91,92,96].

In Europe, EN 50561-1 [97] was approved in Nov. 2012. This standard “specifies limits and methods of measurement of radio disturbance characteristics for in-home communication apparatus that use the low voltage power installation as the transmission medium” and it applies to the frequency range 1.6065–30 MHz. It distinguishes between “AC mains power,” “telecommunications/network,” and “PLC” ports and specifies conducted emission limits and the corresponding measurement procedures. The standard requires a dynamic power control, ie, the reduction of the maximal transmitter power spectral density (PSD) level for low channel attenuation between two PLC devices, static frequency notching for specific frequency bands (amateur radio and aeronautical bands), and dynamic frequency notching for which the PLC equipment senses the presence of radio services and notches the affected frequencies for its own operation. At the time of writing, standard EN 50561-2 for “modems for access networks” has been sent out for comments to the National Committees. Furthermore, EN 50561-3 for “apparatus operating above 30 MHz,” which clarifies the transmission levels below the FM radio bands, is currently still under development.

In the United States, again the 47 CFR §15 [94] regulates electromagnetic emissions for BB PLC. In the jargon of [94], these are “BPL” systems, and it is distinguished between in-house and access BPL. The former send “radio frequency energy on frequencies between 1.705 and 80 MHz over medium voltage lines or over low voltage lines to provide BB communications and is located on the supply side of the utility service’s points of interconnection with customer premises,” while the latter use “electric power lines that are not owned, operated, or controlled by an electric service provider.” Both of them are subsets of carrier current systems. Hence, the paragraphs mentioned on the right-hand side of Fig. 16.6 generally apply. For access BPL, [94] includes a Subpart G, which further specifies that conducted emission limits are explicitly not applicable, BB PLC systems have to be able to notch certain frequencies that might be used by other services, excluding bands where no PLC signal shall be injected, as well as geographical exclusion zones close to which no access PLC systems may be deployed. Further, procedures in which service providers inform about prospective PLC access deployments, as well as complaint handling procedures, are a requirement.

The specific radiation limits are given in terms of field strength at a certain distance for BB PLC between 1.705 and 30 MHz and between 30 and 88 MHz, respectively. The latter distinguishes whether accessing PLC is over MV or LV lines, with an approximately 10 dB higher limit for the former. The translation of these radiation limits into PSD figures for PLC transmission is done via a coupling factor, which depends on a variety of factors related to topology, cabling, and symmetry of the power grid.

The application of BB PLC in Japan is limited to in-home power lines. The emission limits are specified for the 2–15 and 15–30 MHz bands in terms of the common mode current measured with a specified impedance stabilization that features a longitudinal conversion loss (LCL) of 16 dB [98]. The LCL quantifies the differential-mode (from the PLC device) to common-mode (mainly responsible for radiation) conversion and it is argued in [96] that 16 dB is a 99% worst-case value for typical power line networks found in Japanese homes.

Making some assumptions about network impedance, coupling factor, and common-mode impedance of a PLC modem, [96] presents limits for the average transmitter PSD for BB PLC for the three regions discussed in this section. These limits are illustrated in Fig. 16.7. We note the general drop of PSD levels at 30 MHz, which has been assumed 30 dB for deployments in Europe and the United States. This is consistent with the 30 dB drop in the PSD specifications in IEEE 1901 [82] and ITU-T G.9964 [99].

---

## 16.4 POWER LINE CHANNEL

The characterization of a communication channel usually comprises the description of signal propagation and disturbance effects. For the power line channel, the former is commonly assumed to be a linear transformation and thus linear system functions

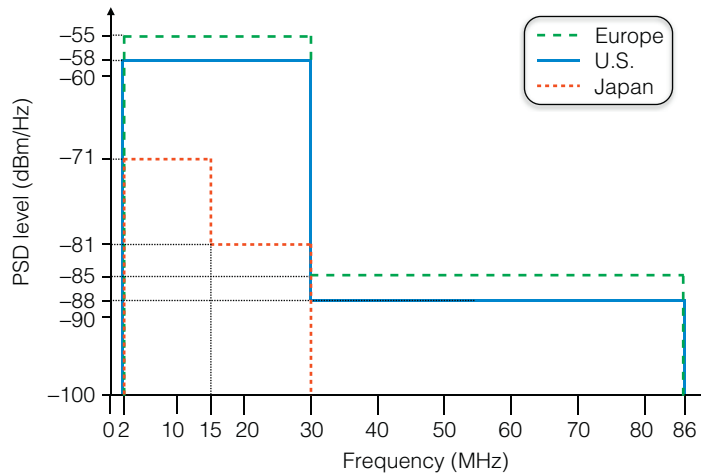
**FIG. 16.7**

Illustration of transmitter PSD limits. See discussion in [96] for assumptions and computation of PSD limits. Limits for Europe for above 30 MHz are pending regulation.

Source: Adopted from A. Schwager, L.T. Berger, *Power line communication electromagnetic compatibility regulations*, in: *MIMO Power Line Communications: Narrow and Broadband Standards, EMC, and Advanced Processing*, CRC Press—Taylor & Francis Group, New York, NY, 2014, Figure 6.3.

such as (time-varying) channel impulse response (CIR) and channel frequency response (CFR) are specified. Disturbance is represented through additive noise, which consists of several distinct components. The exact signal propagation and noise characteristics are very dependent on which grid and application domain are considered (see Sections 16.1.1 and 16.1.2), the topology details, wiring practices, and cable types; and it can also vary with the time of day as electric power consumption affects propagation and noise for PLC signals. In the following, we provide a fairly high-level overview about salient features of the power line channel and the corresponding modeling approaches.

## 16.4.1 SIGNAL PROPAGATION

### 16.4.1.1 Propagation effects

Similar to the wireless communication channel, the signal propagation effects for the power line channel could be classified into pathloss, shadowing, and multipath effects.

Pathloss describes the propagation losses along power lines due to resistive losses of the conductor and dielectric losses of the insulation material. These effects are quantified by the (effective) conductivity parameters [100]. Since the losses are frequency dependent, which for resistive losses is known as the skin effect, the

pathloss changes with frequency. In particular, the power line channel has a lowpass characteristic.

The term shadowing is not usually used to describe propagation effects for PLC. However, there is some similarity to “lognormal shadowing” often experienced in wireless communication. To see this, we consider the direct signal path between the PLC transmitter and receiver in a power line network illustrated in Fig. 16.8. At each point of impedance discontinuity, illustrated as line taps and labeled as A to G in Fig. 16.8, the transmitted signal undergoes reflection. Continuing along the transmission path to the receiver, this is accounted for through multiplication of the signal amplitude with the transmission coefficient  $t_x$ . For the example in Fig. 16.8, the direct path experiences a gain factor of  $t_{Tx-Rx,1} = t_A \times t_B \times \cdots \times t_F$ . We can consider the transmission coefficients  $t_x$  as random variables, with different power line networks or different states of the same network as the random events. Then, the fact that  $t_{Tx-Rx,1}$  is the product of those random variables gives rise to a lognormal distribution of  $t_{Tx-Rx,1}$  and thus the notion of lognormal shadowing.

Of course, part of the reflected signal eventually arrives at the receiver through the (infinitely) many indirect paths [101]. But before discussing this, we note that another factor that could be considered part of pathloss or shadowing is the presence of transformers, which can cause significant signal attenuation depending on the signal frequency and the state of the transformer. The combined effect of what we labeled pathloss and shadowing is often referred to as pathloss of the power line channel, and its per-distance value strongly depends on the grid domain (HV, MV, LV) and cable/wire type. Typical values have been reported in [9, Table II], which vary from 0.01–0.09 dB/km (HV) to 1.5–3 dB/km (LV) for PLC at 100 kHz and from 2–4 dB/km (HV) to 160–200 dB/km (LV) for PLC at 10 MHz, which also show the lowpass behavior of the power line channel.

Multipath propagation is caused by the same inhomogeneities mentioned above, where power line segments and connected loads with different impedances cause signal reflections. The effect is represented by reflection coefficients  $r_x$ , where  $|r_x| \leq 1$  and  $t_x = 1 + r_x$ . For example, Fig. 16.8 shows an indirect path with one reflection

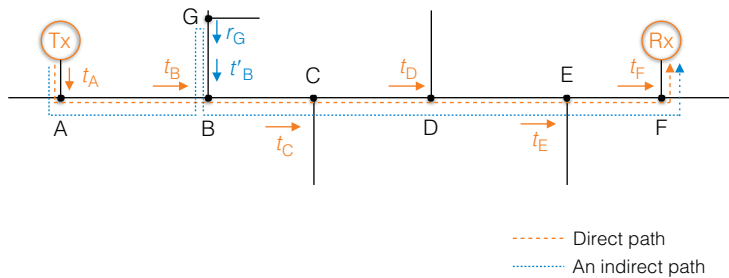


**FIG. 16.8**

Illustration of signal propagation in a power line network.

at discontinuity G. The signal components from the different paths superpose at the receiver. Since each of the path gains can be approximated as lognormally distributed, it has been argued that the sum of gains is also lognormally distributed [102]. If the path-length differences are sufficiently long compared to the wavelength of the PLC signal, or, in other words, the PLC signal is sufficiently BB, the power line channel becomes frequency selective due to multipath propagation. We note that because of the lowpass characteristic of the power line channel the overall CIR will appear as a superposition of relatively smooth and decaying pulses.

Finally, the power line channel is rather unique in that it is affected by the operation of power grid elements, or “loads.” Firstly, the channel may change abruptly when loads are switched on and off or are connected to and disconnected from the grid. Secondly, the high-frequency properties of the loads, namely their impedances, change as a function of the instantaneous value of the AC mains voltage. Hence, the load impedances are periodically time-varying, with the period being equal to the full or half the length of the mains cycle [103]. The overall power line channel is then represented by a linear periodically time-varying (LPTV) system.

#### 16.4.1.2 Modeling approaches

The effects described above are represented in PLC channel models, which can be grouped into two general classes. The first class is based on the actual propagation of electromagnetic signals in power line networks taking topology, power line (eg, cable) properties, and load impedances into account. This class can be referred to as “physical” models. The second class is based on observations of the propagation effects on the PLC signal, eg, through CIR and CFR measurements. The resulting models can be referred to as “empirical” models. These two classes can also be labeled as “bottom-up” and “top-down” [104], which also concisely identify the underlying approaches.

#### Empirical models

The originally and most widely used model that incorporates the above-described phenomenological propagation effects defines the CFR as [105–107]

$$H(f) = \sum_{i=1}^N g_i e^{-\alpha(f)\ell_i} e^{-j2\pi f\tau_i}, \quad (16.1)$$

where  $N$  represents the number of significant signal paths, and  $g_i$ ,  $\ell_i$ , and  $\tau_i$  are the gain factor, length, and signal delay for path  $i$ , respectively. The parameter  $\alpha(f) > 0$  is the frequency-dependent attenuation coefficient for the considered power line. We observe that the structure of  $H(f)$  in Eq. (16.1) explicitly accounts for multipath propagation and frequency-dependent pathloss. Using curve fitting based on measurements of CFRs, several reference channels with sets of parameters applicable to the BB PLC access domain have been specified in the Open PLC European Research Alliance (OPERA) project, see [42, Section 2.9]. Parameters for NB PLC channels are provided in [59, App. D].

References [108,109] present empirical values for distance-dependent attenuation as well as coupling losses for NB PLC in the CENELEC-A band over LV distribution lines, which can be considered as a single-tap version of Eq. (16.1). Furthermore, a simple two-tap channel model has been proposed in [102,110]. More specifically, the CIR is modeled as

$$h(t) = h\delta(t) + h\delta(t - \tau), \quad (16.2)$$

where  $\delta$  is the Dirac-delta function and  $\tau$  is the relative delay of the second path, and both taps have the same gain  $h$ . It has been recognized in [102,110] that the average channel gain and the root-mean-square delay spread (RMS-DS) are negatively correlated, lognormally distributed random variables. Thus, both  $h$  and  $\tau$  are obtained from a randomly chosen average channel gain to generate a sample CIR. It is argued that this simple model captures the essence of channel frequency-selectivity for NB PLC and can also be used for comparative analysis of BB PLC systems [111].

For in-house BB PLC and based on measurements of a total of 144 CFRs in the 30–100 MHz band in different types of homes, Tlich et al. [112] have proposed a random generator for CFRs. Nine classes of channels with their associated average attenuation models are defined, and the multipath nature is included through distributions for width, height, and number of peaks and notches in the CFR.

The measurement results reported in [112] were also used in [113,114] to present a different random CFR generator that closely matches the expression in Eq. (16.1). In particular, the parameters  $N$ ,  $g_i$ , and  $\ell_i$  are considered random variables, and their distribution parameters for the different classes identified in [112] have been obtained through a curve-fitting process [115].

Another empirical CFR generator has been presented in [116]. While verification that the generator creates representative CFRs in a statistical sense is based on results from a measurement campaign, the actual method of generation follows a physical model, as described in the next paragraph. Furthermore, it considers the presence of time-varying load impedances in LPTV channels. The CFR generators from [113, 116] are available as MATLAB code from the authors' websites.

### Physical models

This modeling approach describes the electric properties of a transmission line through the specification of line parameters, line length, the position of branches etc., and makes use of transmission line theory (TLT) to obtain CFRs or CIRs for specific PLC links. The underlying assumption is that the electro-magnetic (EM) field associated with the PLC signal has a transverse EM (TEM) or quasi-TEM structure [100]. Most physical models represent power line elements and connected loads through ABCD or S-parameter matrices or equivalently through their propagation constants and reflection coefficients, respectively [117]. These are then interconnected to produce the CFR, eg, [118–124]. Alternatively, one can consider a finite number  $N$  of paths and compute their gain factors  $g_i$  in Eq. (16.1)

following the transmission and reflection coefficients along those paths, as it is illustrated for two paths in Fig. 16.8; eg, [125,126].

Physical models also allow for incorporation and analysis of the effects of different wiring practices [120], time-varying load impedances [118], and multiconductor lines [121]. The latter makes use of multiconductor transmission line (MTL) theory [100], and its application can be extended to obtain channel realizations for the use of multiple conductors for MIMO transmission [127], which we will discuss further in Section 16.5. Through the application of statistical models for physical parameters of the considered grid topology, such as number of branches, branch lengths, load impedances, etc., CFR/CIR random generators can be developed [119,128]. Furthermore, the use of physical models is essential to capture interdependencies of channel responses for different links in the same network when considering cooperative or relay transmission [129–131].

While physical models are able to accurately represent the propagation of PLC signals over power lines, it may be considered a drawback that a significant amount of input data about the underlying grid structure and line elements, as well as some computational resources, are required to obtain CFR or CIR results. Hence, channel emulator software modules presented in [132,133] (based on [124]) and [134], which include the computation of transmission line parameters, can be useful. We note that physical models are also discussed in the relevant IEEE standardization documents [82, App. F, 59, App. D].

### 16.4.2 NOISE CHARACTERISTICS

The noise scenario experienced in power line networks is fairly diverse and richest in the distribution domain. This is because noise is not dominated by receiver noise but by unwanted signals injected into the power line channel. The classification of PLC noise into five different types according to [135] is illustrated in Fig. 16.9.

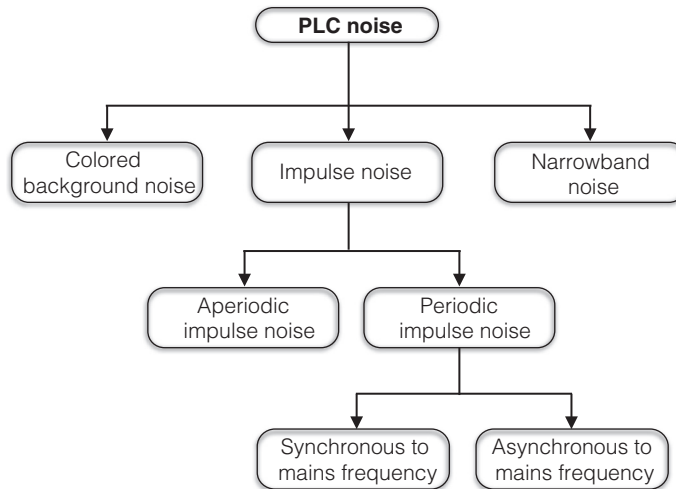
The first type of noise is colored background noise, whose PSD decreases with increasing frequency. Background noise comprises the effects of all noise sources which cannot be discerned otherwise. Typical PSD models are of the form

$$S(f) = -a + bf^{-c}, \quad \text{dBm/Hz} \quad (16.3)$$

where frequency  $f > 0$  and the parameters  $a, b, c > 0$  are chosen to define best and worst cases [119] or as random variables with a distribution [108].

The second noise type is narrowband noise, which is generated from the ingress of broadcasting radio stations. It is typically modeled as amplitude modulated sinusoids.

The third type of noise is impulse noise. This can be further classified into periodic and aperiodic impulse noise, where the latter is caused by switching transients in PLC networks and its occurrence is random. Periodic noise can further be classified into periodic noise synchronous to the AC mains frequency (50 or 60 Hz), commonly caused by silicon controlled rectifiers and diodes, and periodic noise asynchronous to the mains frequency, caused by switched mode power supplies. The asynchronous periodic impulse noise occurs in bursts which are periodic with

**FIG. 16.9**

Classification of PLC noise.

twice the mains cycle and consist of pulse trains with repetition rates in the kilohertz range [136].

A number of different modeling approaches to capture the effects of impulse noise in NB and BB PLC scenarios have been presented in the literature, eg, [119,135–141], and standards documents [82, App. F, 59, App. D]. The simplest models only consider the marginal amplitude distribution of impulse noise samples, for which Middleton’s class-A and two-term Gaussian mixture distributions have often been used. This has been extended to include temporal dependencies between impulse samples through Markov-chain models including the Gilbert-Elliott model. These models lead to bursty impulse noise representations. More refined models differentiate between the three subclasses of impulse noise and include temporal and spectral shaping of noise signals. For example, considering the periodic time-domain features synchronous to the mains cycle, [138] models impulse noise for NB PLC as a colored cyclostationary Gaussian process. This is extended in [140] in that the spectral shaping of the noise process is also periodically time-varying.

Finally, we note that physical propagation models discussed in the previous section also allow us to model the noise as generated at the source and to connect the noise sources to the PLC receiver through the power line network.

## 16.5 TRANSMISSION TECHNIQUES

In this section, we highlight the physical-layer transmission techniques that have been adopted for PLC. Following the historical development outlined in Section 16.1, we first consider single-carrier and then multicarrier transmission formats. The former

are mainly associated with UNB and LDR NB PLC systems (see Fig. 16.2). This is followed by a discussion of relatively recently introduced MIMO and cognitive transmission techniques, where the latter are a direct result of EMC regulations as presented in Section 16.3.

### 16.5.1 SINGLE-CARRIER TRANSMISSION

As mentioned in Section 16.2, RCSs are early implementations of UNB PLC that accomplish unidirectional communication from an MV injection point to consumers at the LV side. RCSs use frequencies in the range of about 125 Hz to 3 kHz, and the signal level is about 1–8% of the electric-power signal voltage level. This ensures that the PLC signal propagates with low pathloss and passes through the LV distribution transformers to reach the destination at the consumer end. Data are transmitted through a sequence of on-off pulses with a duration of several 100 ms, which corresponds to a data rate of about 1 bps. For two-way UNB PLC in the TWACS system [46,47] the AC mains signal is perturbed at around the AC zero crossing using a switched shunt. The resulting data signal is detected as a voltage (substation-to-end-user or outbound direction) or current (end-user-to-substation or inbound direction) pulse at the receiver. The maximal data rate would be two bits per mains cycle or 120 and 100 bps for a 60 and 50 Hz AC system, respectively. The basic outbound modulation is in differential form as a sequence of modulation and no-modulation over two mains cycles, corresponding to a data rate of 30 and 25 bps, respectively. The inbound modulation uses six binary channels created by four antipodal current pulses distributed over four mains cycles, which means a data rate of 90 bps at 60 Hz and 75 bps at 50 Hz [142].

Early LDR NB PLC systems used over MV and HV lines applied (single-sideband) amplitude modulation with channel bandwidths of a few kilohertz and signal power of a few tens of watts. Later, digital modulations in the form of on-off keying and frequency-shift keying (FSK) have been used. In the LV distribution grid domain, several digital communication formats have been used in PLC for building automation and control as well as remote meter reading. Typical modulation formats are binary phase-shift keying (BPSK) and binary FSK, where for the latter the frequency spacing is often much higher than the baud rate, which is referred to as spread-FSK (S-FSK). This spreading is done for better immunity to frequency-selective fading and narrowband interference. BPSK and (S-)FSK systems have been adopted in several standards, as mentioned in Section 16.2. Direct-sequence spread-spectrum and frequency-hopping spread-spectrum transmission have also been considered for narrowband PLC to improve robustness against channel impairments, eg, [143,144]. Another variant of spread-spectrum modulation is so-called differential code-shift keying (DCSK) [145], which is used in the HomePlug Command and Control specification. In DCSK, data are differentially encoded and mapped to cyclic shifts of the basic spreading waveforms such as chirp signals. Some particularly LDR transmission formats exploit the usually low-noise conditions [146] and the ability

to disconnect the distribution circuit from the power supply grid, to reduce cross-talk into the grid and increase network impedance [147], during the zero crossing of the AC power signal.

### 16.5.2 MULTICARRIER TRANSMISSION

Similar to narrowband transmission, spread spectrum modulation is also an option for BB PLC. Code-shift keying [148] and direct-sequence code-division multiple access (DS-CDMA) [149–151] have been investigated. Inspired by transmission methods used in digital subscriber line (DSL) systems, DS-CDMA with carrierless amplitude phase modulation (CAP) has been considered in [152]. This work compares CAP-CDMA with multicarrier modulation in the form of discrete multitone (DMT) for multiuser BB PLC transmission. While this comparison did not reveal a winner technology, multicarrier modulation has emerged as the most popular transmission format for BB and HDR NB PLC systems.

The modern use of multicarrier modulation and OFDM for PLC in particular, dates back to the 1990s, considering both HDR NB [153–157] and BB PLC systems [158–160]. Single-chip PLC OFDM solutions were presented by iAd GmbH at around 2000 [53,156], and the HomePlug 1.0 industry standard for BB PLC released in Jun. 2001 used OFDM [161]. OFDM specific features such as bit loading [162,163], multicarrier spread-spectrum [163], differential modulation [157,160], and cyclic prefix adaptation [164] have been investigated and in part have been adopted for BB and HDR NB PLC specifications.

Besides OFDM, discrete-wavelet multitone (DWTMT) modulation has been proposed and adopted for PLC in [165,166]. While DWTMT transmission over frequency-selective channels introduces interchannel interference, a simple one-tap equalizer (as in OFDM) has been suggested as sufficient to deal with interference experienced in typical indoor channels [167]. An advantage of DWTMT over OFDM is the absence of a cyclic prefix, leading to a potentially higher spectral efficiency. Perhaps more important for BB PLC applications is the better spectral containment of the DWTMT subchannels compared to OFDM. This facilitates narrowband interference suppression at the receiver and notching of frequency bands at the transmitter. For this purpose, the OFDM-based standards discussed in Section 16.2 apply pulse-shaping at the transmitter and windowing at the receiver to improve frequency confinement of OFDM subcarriers. Table 16.2 provides an overview of BB and HDR NB PLC industry and Standards Developing Organization (SDO) standards that use OFDM and DWTMT transmission.

### 16.5.3 MIMO TRANSMISSION

In many instances, PLC links make use of installations that feature more than two conductors. For example, in many in-home installations, outlets are connected via three wires: live or phase (L or P), neutral (N), and protective earth (PE). Similarly, MV underground cables and MV and HV overhead lines commonly have more than

**Table 16.2** Multicarrier Modulation Formats Used in BB and HDR NB PLC Systems

Broadband		High Data-Rate Narrowband	
HomePlug (AV/AV2/GP)	OFDM	DLC-2000	OFDM
DS2/UPA/OPERA	OFDM	PRIME/ITU-T G.9904	OFDM
HD-PLC	DWMT	G3-PLC/ITU-T G.9903	OFDM
IEEE 1901	OFDM/DWMT	IEEE 1901.2	OFDM
ITU-T G.9960	OFDM	ITU-T G.9902	OFDM

two conductors. This affects signal propagation properties, which, as we mentioned in [Section 16.4](#), can be captured through appropriate physical propagation models.

One can go one step further and make use of the presence of multiple conductors to transmit and/or receive multiple signals over the same PLC link. Following Kirchhoff's laws,  $N + 1$  conductors support the injection or extraction of  $N$  independent signals between the conductors. Hence, an  $(N + 1)$  conductor power line can be used as an  $N \times N$  MIMO channel. [Fig. 16.10](#) illustrates the PLC MIMO link for an  $(N + 1 = 3)$  conductor cable with L, N, PE. The number of signal ports at the transmitter ( $N_t$ ) and at the receiver ( $N_r$ ) need not be equal, and thus we can have an  $N_t \times N_r$  MIMO channel. While  $N_t, N_r \leq N$  should be the case,  $N_r > N$  has been found to provide performance benefits. This is can be accomplished through the extraction of a common-mode signal at the receiver, as indicated by the ground connection in [Fig. 16.10](#), which carries information about a differential-mode transmitted signal due to differential-to-common mode coupling along the power line network. Furthermore, it has been observed that processing of  $N + 1$  differential mode signals improves performance, which has been attributed to parasitic effects [21].

Combining MIMO with OFDM transmission, we can describe the MIMO PLC link per OFDM subcarrier through the vector channel

$$\mathbf{y} = \mathbf{H}\mathbf{x} + \mathbf{n}, \quad (16.4)$$

where  $\mathbf{y}$ ,  $\mathbf{H}$ ,  $\mathbf{x}$ , and  $\mathbf{n}$  are the  $N_r \times 1$  received vector,  $N_r \times N_t$  MIMO channel matrix,  $N_t \times 1$  transmit vector, and  $N_r \times 1$  noise vector, respectively. The well-known signal

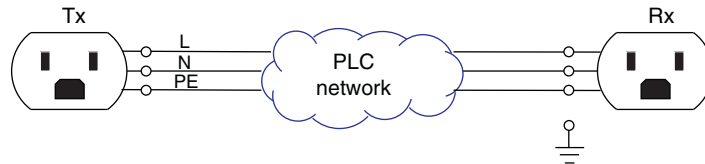
**FIG. 16.10**

Illustration of multiconductor power line enabling MIMO PLC.

**Table 16.3** Gain With MIMO BB PLC in Terms of 98th Percentile of Channel Capacity

MIMO Configuration	Europe	United States	Japan
$1 \times 1$	1	1	1
$1 \times 2$	1.55	1.65	3.63
$1 \times 4$	2.12	2.30	5.37
$2 \times 2$	1.87	1.94	3.52
$2 \times 4$	2.88	3.05	6.35

*Different transmit power masks are applied for different regions.*

*Source: Data from L.T. Berger, A. Schwager, P. Pagani, D.M.*

*Schneider, MIMO power line communications, IEEE Commun. Surv.*

*Tut. 17 (1) (2015) 106–124.*

processing methods for vector channels can now be applied. In particular, spatial multiplexing using linear precoding and space-time coding techniques have been investigated [21,168–171]. A specific feature of the PLC MIMO channel is that the components of the noise vector  $\mathbf{n}$  are often correlated. This applies to all the different noise types discussed in Section 16.4.2 [172]. Table 16.3 demonstrates the performance gains achievable by MIMO for BB PLC as reported in [21, Table III]. The figures represent the 98th percentile of the channel capacity computed based on channel and noise measurement results from different regions of the world. For these results, the total transmit power was kept constant for different  $N_t$ , and the PSD limits from Fig. 16.7 were applied.

### 16.5.4 COGNITIVE TRANSMISSION TECHNIQUES

Since the power grid behaves for the PLC signal as a broadcast medium, cognitive “radio” concepts can be applied to PLC for better resource utilization, eg, [173]. A more compelling argument for the use of cognitive principles arises from the EMC considerations presented in Section 16.3. In particular, radiated emissions from BB PLC systems can potentially interfere with wireless services in the HF band, including amateur radio (ham radio), short-wave radio broadcasting, and digital radio mondiale (DRM).

One approach to avoid interference between wireless and PLC systems is static notching, ie, the PLC signal is not transmitted in frequency bands used by wireless systems. However, since statically notching all possible bands in the HF frequency spectrum would have a significantly detrimental effect on achievable data rates, and since usually only a few wireless radio broadcast services are present at a specific location and time, dynamic notching appears to be a more suitable approach [174]. For the sensing step required for dynamic notching, the noise component of the PLC signal can be analyzed to detect narrowband radio signals using, eg, energy detection and thresholding methods [4, Ch. 5, 175]. Detection accuracy can be improved using cooperative sensing in a network of multiple PLC devices [176,177].

An alternative approach that makes maximal use of existing functionalities in a PLC modem is to consider signal-to-noise ratio measurements for sensing [177]. The use of databases with region-specific information on what bands are being used by wireless services has also been discussed [178]. Multicarrier transmission used in BB PLC facilitates the adaptive frequency notching step, which essentially consists of turning off subcarriers. Here, the tradeoff between data rate reduction and depth and width of notches favors DWT over OFDM methods. For OFDM, windowing at the transmitter helps achieve deeper notches. In addition, additional notch filters in the time-domain can be applied, eg, [4, Ch. 5].

As mentioned in Section 16.3, EMC norms and regulations already mandate the application of notching, including dynamic frequency notching [94,97].

---

## 16.6 FINAL REMARKS

In this chapter, we have attempted to provide a readable and concise overview of technical and regulatory aspects of PLC systems, intended especially for the reader who is not yet familiar with PLC. As we outlined in the Introduction section, PLC has a long history as a means to support the operation of the electric power grid. With the advent of sophisticated digital communication methods for wireline and wireless communication, PLC technology has also advanced significantly, and today, it applies the latest communication techniques including MIMO and cognitive radio transmission. From a communications engineering perspective, the PLC channel shares several similarities with a wireless communication channel, such as the broadcasting nature and frequency selectivity for BB signals. On the other hand, the determinism of the channel giving rise to physical models is what PLC has in common with other wireline media. A distinct feature of PLC is that it reuses the electric power grid. This means that high voltages and currents need to be dealt with when deploying PLC equipment. On the other hand, this also opens the door for grid diagnostics, optimization, and inference (eg, [179–182]), which are interesting directions for future research.

---

## REFERENCES

- [1] J. Routin, C.E.L. Brown, Improvements in and relating to electricity meters, Patent GB189 724 833, 1898.
- [2] C.R. Loubery, Einrichtung zur elektrischen Zeichengebung an die Teilnehmer eines Starkstromnetzes, Patent 118 717, 1901.
- [3] P.A. Brown, Power line communications—past present and future, in: Proceedings of the International Symposium on Power Line Communications and Its Applications (ISPLC), Lancaster, UK, 1999, pp. 1–8.
- [4] A. Schwager, Powerline communications: significant technologies to become ready for integration, Ph.D. thesis, University of Duisburg-Essen, Germany, 2010.
- [5] S. Ramseier, H. Spiess, Making power lines sing, ABB Rev. (2) (2006).

- [6] M. Schwartz, Carrier-wave telephony over power lines: early history [history of communications], *IEEE Commun. Mag.* 47 (1) (2009) 14–18.
- [7] D. Dzung, I. Berganza, A. Sendin, Evolution of powerline communications for smart distribution: from ripple control to OFDM, in: *Proceedings of the International Symposium on Power Line Communications and Its Applications (ISPLC)*, 2011, pp. 474–478.
- [8] L.T. Berger, K. Iniewski, *Smart Grid—Applications, Communications and Security*, John Wiley & Sons, Hoboken, NJ, 2012.
- [9] S. Galli, A. Scaglione, Z. Wang, For the grid and through the grid: the role of power line communications in the smart grid, *Proc. IEEE* 99 (6) (2011) 998–1027.
- [10] L. Lampe, A. Tonello, D. Shaver, Power line communications for automation networks and smart grid [guest editorial], *IEEE Commun. Mag.* 49 (12) (2011) 26–27.
- [11] L.T. Berger, A. Schwager, J.J. Escudero-Garz s, Powerline communications for smart grid applications, *Hindawi J. Electr. Comput. Eng.* 2013 (2013) Article ID 712376, 16 pages. <http://dx.doi.org/10.1155/2013/712376>.
- [12] A. Moscatelli, From smart metering to smart grids: PLC technology evolutions, in: *Proceedings of the International Symposium on Power Line Communications and Its Applications (ISPLC)*, Udine, Italy, 2011, Keynote Presentation, [http://www.ieee-isplc.org/2011/Moscatelli\\_talk.pdf](http://www.ieee-isplc.org/2011/Moscatelli_talk.pdf) (accessed Jun. 2015).
- [13] Landis+Gyr, White paper: introducing the power of PLC, 2012, [http://www.landisgyr.com/webfoo/wp-content/uploads/2012/11/LG\\_White\\_Paper\\_PLC.pdf](http://www.landisgyr.com/webfoo/wp-content/uploads/2012/11/LG_White_Paper_PLC.pdf) (accessed Jun. 2015).
- [14] The Meter on Consortium, Analysis of smart-metering projects, 2014, [http://www.meter-on.eu/file/2014/08/Meter-ON\\_Deliverable\\_D2.3\\_Analysis%20of%20smart%20metering%20projects%20Update%20n.2\\_Version%201.1\\_20140813.pdf](http://www.meter-on.eu/file/2014/08/Meter-ON_Deliverable_D2.3_Analysis%20of%20smart%20metering%20projects%20Update%20n.2_Version%201.1_20140813.pdf) (accessed Jun. 2015).
- [15] PRIME Alliance, Deployments, [http://www.prime-alliance.org/?page\\_id=249](http://www.prime-alliance.org/?page_id=249) (accessed Jun. 2015).
- [16] H.A. Latchman, L.W. Yonge, Power line local area networking (guest editorial), *IEEE Commun. Mag.* 31 (4) (2003) 32–33.
- [17] H. Hrasnica, A. Haidine, R. Lehnert, *Broadband Powerline Communications Networks: Network Design*, John Wiley & Sons, New York, NY, 2004.
- [18] G. Bumiller, G. Hallak, PLC for home and industry automation, in: L. Lampe, A. Tonello, T.G. Swart (Eds.), *Power Line Communications: Principles, Standards and Applications From Multimedia to Smart Grid*, second ed., John Wiley & Sons, New York, NY, 2016.
- [19] S. Galli, A. Scaglione, K. Dostert, Broadband is power: Internet access through the power line network (guest editorial), *IEEE Commun. Mag.* 31 (5) (2003) 82–83.
- [20] F.N. Pavlidou, H.A. Latchman, A.J. Han Vinck, R.E. Newman, Powerline communications and applications (guest editorial), *Int. J. Commun. Syst.* 16 (5) (2003) 357–495.
- [21] L.T. Berger, A. Schwager, P. Pagani, D.M. Schneider, MIMO power line communications, *IEEE Commun. Surv. Tut.* 17 (1) (2015) 106–124.
- [22] A. Schiffer, Design and evaluation of a powerline communication system in an automotive vehicle, Ph.D. thesis, Technical University of Munich, Germany, 2001, <http://tumb1.biblio.tu-muenchen.de/publ/diss/ei/2001/schiffer.html>.
- [23] F. Nouvel, P. Tanguy, S. Pillement, H.-M. Pham, Experiments of in-vehicle power line communications, in: K. Lovrecic (Ed.), *Vehicular Technologies*, Intech, 2011.

- [24] S. Barmada, M. Raugi, M. Tucci, Y. Maryanka, O. Amrani, PLC systems for electric vehicles and smart grid applications, in: *Proceedings of the International Symposium on Power Line Communications and Its Applications (ISPLC)*, Johannesburg, South Africa, 2013.
- [25] C.H. Jones, Communications over aircraft power lines, in: *Proceedings of the International Symposium on Power Line Communications and Its Applications (ISPLC)*, Orlando, FL, USA, 2006, pp. 149–154.
- [26] S. Dominiak, S. Serbu, S. Schnee, F. Nuscheler, T. Mayer, The application of commercial power line communications technology for avionics systems, in: *Proceedings of the IEEE/AIAA Digital Avionics Systems Conference*, 2012, pp. 7E1-1–7E1-14.
- [27] V. Degardin, I. Junqua, M. Lienard, P. Degauque, S. Bertuol, Theoretical approach to the feasibility of power-line communication in aircrafts, *IEEE Trans. Veh. Technol.* 62 (3) (2013) 1362–1366.
- [28] S. Galli, T. Banwell, D. Waring, Power line based LAN on board the NASA space shuttle, in: *Proceedings of the IEEE Vehicular Technology Conference (VTC)*, vol. 2, Milan, Italy, 2004, pp. 970–974.
- [29] J. Wolf, Power line communication (PLC) in space—current status and outlook, in: *Proceedings of the ESA Workshop on Aerospace EMC*, Venice, Italy, 2012, pp. 1–6.
- [30] J. Yazdani, M. Scott, B. Honary, Point to point multi-media transmission for marine application, in: *Proceedings of the International Symposium on Power Line Communications and Its Applications (ISPLC)*, Athens, Greece, 2002, pp. 171–175.
- [31] S. Tsuzuki, M. Yoshida, Y. Yamada, Characteristics of power-line channels in cargo ships, in: *Proceedings of the International Symposium on Power Line Communications and Its Applications (ISPLC)*, Pisa, Italy, 2007, pp. 324–329.
- [32] M. Antoniali, A.M. Tonello, M. Lenardon, A. Qualizza, Measurements and analysis of PLC channels in a cruise ship, in: *Proceedings of the International Symposium on Power Line Communications and Its Applications (ISPLC)*, Udine, Italy, 2011, pp. 102–107.
- [33] F. Nouvel, L. Lampe, PLC for vehicles, in: L. Lampe, A. Tonello, T.G. Swart (Eds.), *Power Line Communications: Principles, Standards and Applications From Multimedia to Smart Grid*, second ed., John Wiley & Sons, New York, NY, 2016.
- [34] SAE International, SAE J2931/2: inband signaling communication for plug-in electric vehicles, work in progress, <http://standards.sae.org/wip/j2931/2/>.
- [35] SAE International, SAE J2931/3: PLC communication for plug-in electric vehicles, work in progress, <http://standards.sae.org/wip/j2931/3/>.
- [36] SAE International, SAE J2931/4: broadband PLC communication for plug-in electric vehicles, 2014, [http://standards.sae.org/j2931/4\\_201410/](http://standards.sae.org/j2931/4_201410/).
- [37] Road vehicles—vehicle to grid communication interface—part 3: physical and data link layer requirements, ISO/IEC 15118-3 (2015).
- [38] P. Karols, K. Dostert, G. Griepentrog, S. Huettinger, Mass transit power traction networks as communication channels, *IEEE J. Sel. Areas Commun.* 24 (7) (2006) 1339–1350.
- [39] IEEE Standard for Broadband Over Power Line Hardware, IEEE STD 1675-2008 (2008) C1–C47, <https://standards.ieee.org/findstds/standard/1675-2008.html>.
- [40] IEEE Guide for Power-Line Carrier Applications, IEEE Std 643-2004 (Revision of IEEE Std 643-1980) (2005) 1–134, <http://standards.ieee.org/findstds/standard/643-2004.html>.

- [41] L.T. Berger, A. Schwager, P. Pagani, D.M. Schneider (Eds.), *MIMO Power Line Communications: Narrow and Broadband Standards*, EMC, and Advanced Processing, CRC Press—Taylor & Francis Group, New York, NY, 2014.
- [42] H.C. Ferreira, L. Lampe, J.E. Newbury, T.G. Swart (Eds.), *Power Line Communications: Theory and Applications for Narrowband and Broadband Communications Over Power Lines*, first ed., John Wiley & Sons, New York, NY, 2010.
- [43] L. Lampe, A. Tonello, T.G. Swart (Eds.), *Power Line Communications: Principles, Standards and Applications From Multimedia to Smart Grid*, second ed., John Wiley & Sons, New York, NY, 2016.
- [44] International Telecommunications Union (ITU), *ITU Radio Regulations*, 2012, <http://www.itu.int/pub/R-REG-RR-2012>.
- [45] D.E. Nordell, Communication systems for distribution automation, in: *Proceedings of the IEEE Transmission and Distribution Conference and Exposition*, Bogota, Colombia, 2008, pp. 1–14.
- [46] S. Mak, D. Reed, TWACS, a new viable two-way automatic communication system for distribution networks. Part I: outbound communication, *IEEE Trans. Power App. Syst.* 101 (8) (1982) 2941–2949.
- [47] S. Mak, T. Moore, TWACS, a new viable two-way automatic communication system for distribution networks. Part II: inbound communication, *IEEE Trans. Power App. Syst.* 103 (8) (1984) 2141–2147.
- [48] American National Standards Institute/Electronic Industries Association (ANSI/EIA), *Control Network Power Line (PL) Channel Specification*, 2006, ANSI/CEA-709.2-A.
- [49] International Organization for Standardization, *Interconnection of information technology equipment—control network protocol—part 3: power line channel specification 2011*, International Standard ISO/IEC 14908-3, Revision 11.
- [50] International Organization for Standardization, *Information technology—home electronic system (HES) architecture—part 3-5: media and media dependent layers—powerline for network based control of HES class 1*, 2007, International Standard ISO/IEC 14543-3-5, First edition.
- [51] International Electrotechnical Commission (IEC), *Distribution automation using distribution line carrier systems—part 5-1: lower layer profiles—the spread frequency shift keying (S-FSK) profile*, Standard IEC 61334-5-1, Ed. 2.0 2001.
- [52] International Electrotechnical Commission (IEC), *Distribution automation using distribution line carrier systems—part 5-2: lower layer profiles—frequency shift keying (FSK) profile*, Standard IEC 61334-5-2, Ed. 1.0, Geneva, Switzerland, 1998.
- [53] G. Bumiller, M. Deinzer, *Narrow band power-line chipset for telecommunication and Internet application*, in: *Proceedings of the International Symposium on Power Line Communications and Its Applications (ISPLC)*, Malmö, Sweden, 2001.
- [54] G3-PLC Alliance, <http://www.g3-plc.com>.
- [55] PRIME Alliance, *Powerline related intelligent metering evolution (PRIME)*, <http://www.prime-alliance.org>.
- [56] International Telecommunications Union (ITU)—Telecommunication Standardization Sector STUDY GROUP 15, *Narrowband orthogonal frequency division multiplexing power line communication transceivers for G.HNEM networks*, Recommendation ITU-T G.9902, 2012.
- [57] International Telecommunications Union (ITU)—Telecommunication Standardization Sector STUDY GROUP 15, *Narrowband orthogonal frequency division multiplexing*

- power line communication transceivers for G3-PLC networks, Recommendation ITU-T G.9903, 2014.
- [58] International Telecommunications Union (ITU)—Telecommunication Standardization Sector STUDY GROUP 15, Narrowband orthogonal frequency division multiplexing power line communication transceivers for PRIME networks, Recommendation ITU-T G.9904, 2012.
  - [59] IEEE standard for low-frequency (less than 500 kHz) narrowband power line communications for smart grid applications, IEEE Std 1901.2-2013 (2013) 1–269.
  - [60] National Institute of Standards and Technology, Smart Grid Interoperability Panel, Priority Action Plan 15, Guideline for the implementation of coexistence for low frequency narrowband power line communication standards in the smart grid, 2013, <http://dx.doi.org/10.6028/NIST.IR.7943>.
  - [61] International Telecommunications Union (ITU)—Telecommunication Standardization Sector STUDY GROUP 15, Narrowband orthogonal frequency division multiplexing power line communication transceivers—power spectral density specification, Recommendation ITU-T G.9901, 2014.
  - [62] ABB, ETL600 R4—Power Line Carrier System, <http://new.abb.com/network-management/communication-networks/power-line-carriers/etl600-r4> (accessed Jun. 2013).
  - [63] SELTA, Digital power line carrier transmission system for HV lines, <http://www.selta.it/ProductDetail?id=01t20000003nl0xAAA> (accessed Jun. 2013).
  - [64] I. Berganza, G. Bumiller, A. Dabak, R. Lehnert, A. Mengi, A. Sendin, PLC for Smart Grid, in: L. Lampe, A. Tonello, T.G. Swart (Eds.), *Power Line Communications: Principles, Standards and Applications From Multimedia to Smart Grid*, second ed., John Wiley & Sons, New York, NY, 2016.
  - [65] V. Oksman, J. Zhang, G.HNEM: the new ITU-T standard on narrowband PLC technology, *IEEE Commun. Mag.* 49 (12) (2011) 36–44.
  - [66] PRIME Alliance, Draft standard for powerline intelligent metering evolution, 2010, [http://www.prime-alliance.org/wp-content/uploads/2013/04/PRIME-Spec\\_v1.3.6.pdf](http://www.prime-alliance.org/wp-content/uploads/2013/04/PRIME-Spec_v1.3.6.pdf) (accessed Jun. 2015).
  - [67] International Electrotechnical Commission (IEC), Distribution automation using distribution line carrier systems—part 4: data communication protocols—section 32: data link layer—logical link control (LLC), 1997.
  - [68] International Electrotechnical Commission (IEC), Electricity metering—data exchange for meter reading, tariff and load control—part 62: interface classes, Standard IEC 62056-62, Ed. 2, 2006.
  - [69] I. Berganza, A. Sendin, J. Arriola, PRIME: powerline intelligent metering evolution, in: *CIREN Seminar 2008: SmartGrids for Distribution*, CIREN, Frankfurt, Germany, 2008, pp. 1–3.
  - [70] S. Galli, T. Lys, Next generation narrowband (under 500 kHz) power line communications (PLC) standards, *China Commun.* 12 (3) (2015) 1–8.
  - [71] K. Razazian, An overview to new PLC applications and new challenges, in: *Proceedings of the International Symposium on Power Line Communications and Its Applications (ISPLC)*, Udine, Italy, 2011, Keynote Presentation, [http://www.ieee-isplc.org/2011/Razazian\\_talk.pdf](http://www.ieee-isplc.org/2011/Razazian_talk.pdf) (accessed Jun. 2015).
  - [72] Institute of Electrical and Electronics Engineers, Local and metropolitan area networks—specific requirements—part 15.4: wireless medium access control (MAC) and physical layer (PHY) specifications for low-rate wireless personal area networks

- (WPANs), 2006, Standard for Information Technology—Telecommunications and Information Exchange Between Systems.
- [73] Z. Shelby, C. Bormann, 6LoWPAN: The Wireless Embedded Internet, John Wiley & Sons, New York, NY, 2009.
  - [74] S. Deering, R. Hinden, Internet Protocol, Version 6 (IPv6) Specification, RFC 2460, 1998, <http://tools.ietf.org/html/rfc2460> (accessed Feb. 2011).
  - [75] M. Hoch, Comparison of G3 PLC and PRIME, in: Proceedings of the International Symposium on Power Line Communications and Its Applications (ISPLC), Udine, Italy, 2011, pp. 165–169.
  - [76] V. Oksman, S. Galli, G.hn: the new ITU-T home networking standard, IEEE Commun. Mag. 47 (10) (2009) 138–145.
  - [77] S. Galli, O. Logvinov, Recent developments in the standardization of power line communications within the IEEE, IEEE Commun. Mag. 46 (7) (2008) 64–71.
  - [78] International Telecommunications Union (ITU), ITU-T Recommendation G.9960, Unified high-speed wire-line based home networking transceivers—foundation, 2009.
  - [79] International Telecommunications Union (ITU), ITU-T Recommendation G.9961, Data link layer (DLL) for unified high-speed wire-line based home networking transceivers, 2010, [http://www.itu.int/rec/dologin\\_pub.asp?lang=e&id=T-REC-G.9961-201006-I!!PDF-E&type=items](http://www.itu.int/rec/dologin_pub.asp?lang=e&id=T-REC-G.9961-201006-I!!PDF-E&type=items).
  - [80] International Telecommunications Union (ITU), ITU-T Recommendation G.9963, Unified high-speed wire-line based home networking transceivers—multiple input/multiple output (MIMO), 2011, ex G.hn-MIMO.
  - [81] HomeGrid Forum, <http://www.homegridforum.org/> (accessed Jun. 2015).
  - [82] Institute of Electrical and Electronics Engineers (IEEE) Standards Association, Working Group P1901, IEEE Standard for Broadband Over Power Line Networks: Medium Access Control and Physical Layer Specification, 2010, <http://standards.ieee.org/findstds/standard/1901-2010.html>.
  - [83] HomePlug Powerline Alliance, <http://www.homeplug.org> (accessed Jun. 2015).
  - [84] Institute of Electrical and Electronics Engineers, Standards Association, Working Group P1905.1, IEEE Standard for a Convergent Digital Home Network for Heterogeneous Technologies 2013, <http://standards.ieee.org/findstds/standard/1905.1-2013.html> (accessed Apr. 2013).
  - [85] National Institute of Standards and Technology (NIST), U.S. Department of Commerce, Specification for the Advanced Encryption Standard (AES), Federal Information Processing Standards Publication 197, 2001.
  - [86] S. Galli, A. Kurobe, M. Ohura, The inter-PHY protocol (IPP): a simple coexistence protocol for shared media, in: Proceedings of the International Symposium on Power Line Communications and Its Applications (ISPLC), Dresden, Germany, 2009, pp. 194–200.
  - [87] International Telecommunications Union (ITU), ITU-T Recommendation G.9972, Coexistence mechanism for wireline home networking transceivers, 2010.
  - [88] D. Su, S. Galli, PAP 15 recommendations to SGIP on broadband PLC coexistence, 2010, [http://collaborate.nist.gov/twiki-sggrid/pub/SmartGrid/PAP15PLCForLowBitRates/PAP15\\_-\\_Recommendation\\_to\\_SGIP\\_BB\\_CX\\_-\\_Final\\_-\\_APPROVED\\_2010-12-02.pdf](http://collaborate.nist.gov/twiki-sggrid/pub/SmartGrid/PAP15PLCForLowBitRates/PAP15_-_Recommendation_to_SGIP_BB_CX_-_Final_-_APPROVED_2010-12-02.pdf) (accessed Jun. 2015).
  - [89] S. Galli, On the fair comparison of FEC schemes, in: Proceedings of the IEEE International Conference on Communications (ICC), Cape Town, South Africa, 2010.

- [90] H. Hirsch, M. Koch, Electromagnetic compatibility, in: H.C. Ferreira, L. Lampe, J.E. Newbury, T.G. Swart (Eds.), *Power Line Communications: Theory and Applications for Narrowband and Broadband Communications Over Power Lines*, first ed., John Wiley & Sons, New York, NY, 2010.
- [91] S. Galli, M. Koch, H.A. Latchman, S. Lee, V. Oksman, Industrial and international standards on PLC-based networking technologies, in: H.C. Ferreira, L. Lampe, J.E. Newbury, T.G. Swart (Eds.), *Power Line Communications: Theory and Applications for Narrowband and Broadband Communications Over Power Lines*, first ed., John Wiley & Sons, New York, NY, 2010.
- [92] H. Hirsch, M. Koch, N. Weling, A. Zeddham, Electromagnetic compatibility, in: L. Lampe, A. Tonello, T.G. Swart (Eds.), *Power Line Communications: Principles, Standards and Applications From Multimedia to Smart Grid*, second ed., John Wiley & Sons, New York, NY, 2016.
- [93] European Committee for Electrotechnical Standardization (CENELEC), Signalling on low-voltage electrical installations in the frequency range 3 kHz to 148.5 kHz—part 1: general requirements, frequency bands and electromagnetic disturbances, Standard EN 50065-1 1991, 2001, 2011.
- [94] FCC, Title 47 of the Code of Federal Regulations (CFR), Tech. Rep. 47 CFR §15, U.S. Federal Communications Commission (FCC), <http://www.fcc.gov/encyclo-pedia/rules-regulations-title-47> (accessed Jun. 2015).
- [95] Association of Radio Industries and Businesses (ARIB), Power line communication equipment (10kHz–450kHz), 2002, sTD-T84, Ver. 1.0, (in Japanese), [http://www.arib.or.jp/english/html/overview/doc/1-STD-T84v1\\_0.pdf](http://www.arib.or.jp/english/html/overview/doc/1-STD-T84v1_0.pdf) (accessed Jun. 2015).
- [96] A. Schwager, L.T. Berger, Power line communication electromagnetic compatibility regulations, in: *MIMO Power Line Communications: Narrow and Broadband Standards, EMC, and Advanced Processing*, CRC Press—Taylor & Francis Group, New York, NY, 2014.
- [97] European Committee for Electrotechnical Standardization (CENELEC), Power line communication apparatus used in low-voltage installations—radio disturbance characteristics—limits and methods of measurement—part 1: apparatus for in-home use 2012.
- [98] Open PLC European Research Alliance (OPERA), Worldwide market research, Tech. Rep., 2007 OP\_WP6\_D37\_V1.0.doc.
- [99] International Telecommunications Union (ITU), ITU-T Recommendation G.9964, Unified high-speed wireline-based home networking transceivers power spectral density specification, 2011, <https://www.itu.int/rec/T-REC-G.9964> (accessed Jun. 2015).
- [100] C.R. Paul, *Analysis of Multiconductor Lines*, John Wiley & Sons, New York, NY, 1994.
- [101] L.T. Berger, G. Moreno-Rodríguez, Power line communication channel modelling through concatenated IIR-filter elements, *J. Commun.* 4 (1) (2009) 41–51.
- [102] S. Galli, A simplified model for the indoor power line channel, in: *Proceedings of the International Symposium on Power Line Communications and Its Applications (ISPLC)*, Dresden, Germany, 2009, pp. 13–19.
- [103] F.J. Cañete, J.A. Cortés, L. Díez, J.T. Entrambasaguas, J.L. Carmona, Fundamentals of the cyclic short-time variation of indoor power-line channels, in: *Proceedings of the International Symposium on Power Line Communications and Its Applications (ISPLC)*, 2005, pp. 157–161.

- [104] E. Biglieri, Coding and modulation for a horrible channel, *IEEE Commun. Mag.* 41 (5) (2003) 92–98.
- [105] H. Philipps, Modelling of powerline communication channels, in: *Proceedings of the International Symposium on Power Line Communications and Its Applications (ISPLC)*, Lancaster, UK, 1999, pp. 14–21.
- [106] M. Zimmermann, K. Dostert, A multi-path signal propagation model for the power line channel in the high frequency range, in: *Proceedings of the International Symposium on Power Line Communications and Its Applications (ISPLC)*, Lancaster, UK, 1999, pp. 45–51.
- [107] M. Zimmermann, K. Dostert, A multipath model for the powerline channel, *IEEE Trans. Commun.* 50 (4) (2002) 553–559.
- [108] O. Hooijen, A channel model for the low-voltage power-line channel: measurement and simulation results, in: *Proceedings of the International Symposium on Power Line Communications and Its Applications (ISPLC)*, Essen, Germany, 1997, pp. 51–56.
- [109] O. Hooijen, On the relation between network-topology and power line signal attenuation, in: *Proceedings of the International Symposium on Power Line Communications and Its Applications (ISPLC)*, Tokyo, Japan, 1998, pp. 45–56.
- [110] S. Galli, A simple two-tap statistical model for the power line channel, in: *Proceedings of the International Symposium on Power Line Communications and Its Applications (ISPLC)*, Rio de Janeiro, Brazil, 2010, pp. 242–248.
- [111] S. Galli, A novel approach to the statistical modeling of wireline channels, *IEEE Trans. Commun.* 59 (5) (2011) 1332–1345.
- [112] M. Tlich, A. Zeddani, F. Moulin, F. Gauthier, Indoor power line communications channel characterization up to 100 MHz—part I: one-parameter deterministic model, *IEEE Trans. Power Deliv.* 23 (3) (2008) 1392–1401.
- [113] A.M. Tonello, Wideband impulse modulation and receiver algorithms for multiuser power line communications, *EURASIP J. Adv. Signal Process.* (2007) 1–14, source code available at <http://www.diegm.uniud.it/tonello/plcresearch.html#tplc>.
- [114] A.M. Tonello, S. D'Alessandro, L. Lampe, Cyclic prefix design and allocation in bit-loaded OFDM over power line communication channels, *IEEE Trans. Commun.* 58 (11) (2010) 3265–3276.
- [115] A.M. Tonello, F. Versolatto, B. Bejar, S. Zazo, A fitting algorithm for random modeling the PLC channel, *IEEE Trans. Power Deliv.* 27 (3) (2012) 1477–1484.
- [116] F.J. Canete, J.A. Cortes, L. Díez, J.T. Entrambasaguas, A channel model proposal for indoor power line communications, *IEEE Commun. Mag.* 49 (12) (2011) 166–174.
- [117] D.M. Pozar, *Microwave Engineering*, third ed., John Wiley & Sons, New York, NY, 2005.
- [118] F.J. Canete, L. Díez, J.A. Cortés, J.T. Entrambasaguas, Broadband modelling of indoor power-line channels, *IEEE Trans. Consum. Electron.* 48 (1) (2002) 175–183.
- [119] T. Esmailian, F.R. Kschischang, P. Glenn Gulak, In-building power lines as high-speed communication channels: channel characterization and a test channel ensemble, *Int. J. Commun. Syst.* 16 (2003) 381–400.
- [120] S. Galli, T.C. Banwell, A deterministic frequency-domain model for the indoor power line transfer function, *IEEE J. Sel. Areas Commun.* 24 (7) (2006) 1304–1316.
- [121] T. Sartenauer, P. Delogne, Deterministic modeling of the (shielded) outdoor power line channel based on the multiconductor transmission line equations, *IEEE J. Sel. Areas Commun.* 24 (7) (2006) 1277–1291.

- [122] S. Barmada, A. Musolino, M. Raugi, Innovative model for time-varying power line communication channel response evaluation, *IEEE J. Sel. Areas Commun.* 7 (24) (2006) 1317–1326.
- [123] G. Moreno-Rodríguez, L.T. Berger, An IIR-filter approach to time variant PLC-channel modelling, in: *Proceedings of the International Symposium on Power Line Communications and Its Applications (ISPLC)*, Jeju, South Korea, 2008, pp. 87–92.
- [124] A.M. Tonello, F. Versolatto, Bottom-up statistical PLC channel modeling—part I: random topology model and efficient transfer function computation, *IEEE Trans. Power Deliv.* 26 (2) (2011) 891–898.
- [125] J.S. Barnes, A physical multi-path model for power distribution network propagation, in: *Proceedings of the International Symposium on Power Line Communications and Its Applications (ISPLC)*, Tokyo, Japan, 1998, pp. 76–89.
- [126] D. Anastasiadou, T. Antonakopoulos, Multipath characterization of indoor power-line networks, *IEEE Trans. Power Deliv.* 20 (1) (2005) 90–99.
- [127] F. Versolatto, A.M. Tonello, An MTL theory approach for the simulation of MIMO power-line communication channels, *IEEE Trans. Power Deliv.* 26 (3) (2011) 1710–1717.
- [128] A.M. Tonello, F. Versolatto, Bottom-up statistical PLC channel modeling—part II: inferring the statistics, *IEEE Trans. Power Deliv.* 25 (4) (2010) 2356–2363.
- [129] L. Lampe, R. Schober, S. Yiu, Distributed space-time block coding for multihop transmission in power line communication networks, *IEEE J. Sel. Areas Commun.* 24 (7) (2006) 1389–1400.
- [130] A.M. Tonello, F. Versolatto, S. D’Alessandro, Opportunistic relaying in in-home PLC networks, in: *Proceedings of the IEEE Globecom Conference (GLOBECOM)*, 2010, pp. 1–5.
- [131] L. Lampe, A.J.H. Vinck, On cooperative coding for narrowband PLC networks, *Int. J. Electron. Commun. (AEÜ)* 65 (8) (2011) 681–687.
- [132] G. Marrocco, D. Statovci, S. Trautmann, A PLC broadband channel simulator for indoor communications, Johannesburg, South Africa, 2013, source code available at <http://plc.ftw.at>.
- [133] F. Aalamifar, A. Schlögl, D. Harris, L. Lampe, Modelling power line communication using network simulator-3, in: *Proceedings of the IEEE Globecom Conference (GLOBECOM)*, 2013, pp. 2969–2974, source code available at <http://www.ece.ubc.ca/lampe/PLC>.
- [134] F. Gruber, L. Lampe, On PLC channel emulation via transmission line theory, in: *Proceedings of the IEEE International Symposium on Power Line Communications and Its Applications (ISPLC)*, Austin, TX, USA, 2015, source code available at <http://www.ece.ubc.ca/lampe/MIMOPLC>.
- [135] M. Zimmermann, K. Dostert, Analysis and modeling of impulsive noise in broadband powerline communications, *IEEE Trans. Electromagn. Compat.* 44 (1) (2002) 249–258.
- [136] J.A. Cortés, L. Díez, F.J. Ca nete, J.J. Sánchez-Martínez, Analysis of the indoor broadband power line noise scenario, *IEEE Trans. Electromagn. Compat.* 52 (4) (2010) 849–858.
- [137] M.H.L. Chan, R.W. Donaldson, Amplitude, width, and interarrival distributions for noise impulses on intrabuilding power line communication networks, *IEEE Trans. Electromagn. Compat.* 31 (3) (1989) 320–323.

- [138] M. Katayama, T. Yamazato, H. Okada, A mathematical model of noise in narrowband power line communication systems, *IEEE J. Sel. Areas Commun.* 24 (7) (2006) 1267–1276.
- [139] L. Di Bert, P. Caldera, D. Schwingshackl, A.M. Tonello, On noise modeling for power line communications, in: *IEEE Intl. Symp. on Power Line Commun. and Its Appl. (ISPLC)*, 2011, pp. 283–288.
- [140] M. Nassar, K. Gulati, Y. Mortazavi, B.L. Evans, Statistical modeling of asynchronous impulsive noise in powerline communication networks, in: *Proceedings of the IEEE Global Telecommunications Conference (GLOBECOM 2011)* 2011, pp. 1–6.
- [141] M. Nassar, A. Dabak, I. Kim, T. Pande, B.L. Evans, Cyclostationary noise modeling in narrowband powerline communication for smart grid applications, in: *Proceedings of the IEEE International Conference on Acoustics, Speech and Signal Processing*, 2012, pp. 3089–3092.
- [142] S.T. Mak, R.L. Maginnis, Power frequency communication on long feeders and high levels of harmonic distortion, *IEEE Trans. Power Deliv.* 10 (4) (1995) 1731–1736.
- [143] P.K. van der Gracht, R.W. Donaldson, Communication using pseudonoise modulation on electric power distribution circuits, *IEEE Trans. Commun.* 9 (33) (1985) 964–974.
- [144] K. Dostert, Frequency-hopping spread-spectrum modulation for digital communications over electrical power lines, *IEEE J. Sel. Areas Commun.* 8 (4) (1990) 700–710.
- [145] D. Raphaeli, Spread spectrum communication system utilizing differential code shift keying, US Patent 6,064,691, 2000.
- [146] X-10 Home Automation Specification, <http://ww1.microchip.com/downloads/en/AppNotes/00236a.pdf>.
- [147] G. Dickmann, digitalSTROM®: A centralized PLC topology for home automation and energy management, in: *Proceedings of the IEEE International Symposium on Power Line Communications and Its Applications (ISPLC)*, Udine, Italy, 2011.
- [148] D. Raphaeli, A. Grauer, A new power-line communications modem based on a novel modulation technique, in: *Proceedings of the International Symposium on Power Line Communications and Its Applications (ISPLC)*, Limerick, Ireland, 2000.
- [149] E. Del Re, R. Fantacci, S. Morosi, R. Seravalle, G. Pieraccioli, Orthogonal direct sequence code division multiple access for broadcast communications on power lines, in: *Proceedings of the International Symposium on Power Line Communications and Its Applications (ISPLC)*, Limerick, Ireland, 2000, pp. 60–67.
- [150] W. Hachem, P. Loubaton, S. Marcos, R. Samy, Multiple access communication over the power line channel: a CDMA approach, in: *Proceedings of the IEEE Globecom Conference (GLOBECOM)*, vol. 1, 2001, pp. 420–424.
- [151] L. Ouvry, D. Lattard, M. Laugeois, M. Combet, D. Chagnot, B. Piaget, A spread spectrum based implementation for powerline transmission system, in: *Proceedings of the International Symposium on Power Line Communications and Its Applications (ISPLC)*, Athens, Greece, 2002.
- [152] T. Sartenar, F. Horlin, L. Vandendorpe, Multiple access techniques for wideband upstream powerline communications: CAP-CDMA and DMT-FDMA, in: *Proceedings of the IEEE International Conference on Communication (ICC)*, vol. 2, 2000, pp. 1064–1068.
- [153] G. Dickmann, N.J. Fliege, Digital signal processing for multi-carrier data transmission on phase-controlled power lines with nonlinearities, in: *Proceedings of the*

- IEEE International Symposium on Circuits and Systems (ISCAS), vol. 2, 1995, pp. 889–892.
- [154] M. Ostertag, C. Imboden, A high data rate powerline communication system for combined DA/DSM, in: Proceedings of the International Symposium on Power Line Communications and Its Applications (ISPLC), Tokyo, Japan, 1998, pp. 141–152.
  - [155] S. Ramseier, M. Arzberger, A. Hauser, MV and LV powerline communications: new proposed IEC standards, in: Proceedings of the IEEE Transmission and Distribution Conference, vol. 1, 1999, pp. 235–239.
  - [156] M. Deinzer, M. Stöger, Integrated PLC-modem based on OFDM, in: Proceedings of the International Symposium on Power Line Communications and Its Applications (ISPLC), Lancaster, UK, 1999.
  - [157] D. Galda, T. Giebel, U. Zölzer, H. Rohling, An experimental OFDM-modem for the CENELEC B-band, in: Proceedings of the International Symposium on Power Line Communications and Its Applications (ISPLC), Lancaster, UK, 1999.
  - [158] C. Hensen, Data transmission applications via low voltage power lines using OFDM technique, in: IEEE 5th International Symposium on Spread Spectrum Techniques and Applications, vol. 1, 1998, pp. 210–214.
  - [159] T. Esmailian, P.G. Gulak, F.R. Kschischang, A discrete multitone power line communications system, in: Proceedings of the IEEE International Conference on Acoustics, Speech and Signal Processing, vol. 5, 2000, pp. 2953–2956.
  - [160] L. Lampe, J.B. Huber, Bandwidth efficient power line communications based on OFDM, *Int. J. Electron.* 54 (1) (2000) 2–12.
  - [161] M.K. Lee, R.E. Newman, H.A. Latchman, S. Katar, L. Yonge, HomePlug 1.0 powerline communication LANs—protocol description and performance results, *Int. J. Commun. Syst.* 46 (5) (2003) 447–473.
  - [162] S. Morosi, E. Del Re, R. Fantacci, D. Marabissi, N. Del Santo, A rate adaptive bit-loading algorithm for a discrete multi-tone modulation system in downstream power line communications, in: Proceedings of the International Symposium on Power Line Communications and Its Applications (ISPLC), Zaragossa, Spain, 2004.
  - [163] M. Crussière, J.-Y. Baudais, J.F. Héland, Robust and high-bit rate communications over PLC channels: a bit-loading multi-carrier spread-spectrum solution, in: Proceedings of the International Symposium on Power Line Communications and Its Applications (ISPLC), Vancouver, Canada, 2005.
  - [164] A.M. Tonello, S. D'Alessandro, L. Lampe, Cyclic prefix design and allocation in bit-loaded OFDM over power line communication channels, *IEEE Trans. Commun.* 58 (11) (2010) 3265–3276.
  - [165] M.C. Sun, D.P.K. Lun, Power-line communications using DWMT modulation, in: Proceedings of the IEEE International Symposium on Circuits and Systems (ISCAS), vol. 4, 2002, pp. IV-493–IV-496.
  - [166] H. Koga, N. Kodama, T. Konishi, High-speed power line communication system based on wavelet OFDM, in: Proceedings of the International Symposium on Power Line Communications and Its Applications (ISPLC), Kyoto, Japan, 2003, pp. 226–231.
  - [167] S. Galli, H. Koga, N. Kodama, Advanced signal processing for PLCs: wavelet-OFDM, in: Proceedings of the International Symposium on Power Line Communications and Its Applications (ISPLC), Jeju Island, Korea, 2008.
  - [168] C.L. Giovaneli, J. Yazdani, P. Farrell, B. Honary, Application of space-time diversity/coding for power line channels, in: Proceedings of the International Symposium on Power Line Communications and Its Applications (ISPLC), Athens, Greece, 2002.

- [169] H. Furukawa, H. Okada, T. Yamazato, M. Katayama, Signaling methods for broadcast transmission in power-line communication systems, in: *Proceedings of the International Symposium on Power Line Communications and Its Applications (ISPLC)*, Kyoto, Japan, 2003.
- [170] L. Stadelmeier, D. Schill, A. Schwager, D. Schneider, J. Speidel, MIMO for inhome power line communications, in: *Proceedings of the International ITG Conference on Source and Channel Coding (SCC)*, 2008, pp. 1–6.
- [171] D. Schneider, J. Speidel, L. Stadelmeier, D. Schill, Precoded spatial multiplexing MIMO for inhome power line communications, in: *Proceedings of the IEEE Globecom Conference (GLOBECOM)*, 2008, pp. 1–5.
- [172] P. Pagani, R. Hashmat, A. Schwager, D. Schneider, W. Baschlin, European MIMO PLC field measurements: noise analysis, in: *Proceedings of the IEEE International Symposium on Power Line Communications and Its Applications (ISPLC)*, 2012, pp. 310–315.
- [173] S.W. Oh, Y.L. Chiu, K.N. Ng, R. Mo, Y. Ma, Y. Zeng, A.A. Syed Naveen, Cognitive power line communication system for multiple channel access, in: *Proceedings of the International Symposium on Power Line Communications and Its Applications (ISPLC)*, Dresden, Germany, 2009, pp. 47–52.
- [174] A. Schwager, L. Stadelmeier, M. Zumkeller, Potential of broadband power line home networking, in: *IEEE Consumer Communications and Networking Conference (CCNC)*, Las Vegas, NV, 2005.
- [175] ETSI, Powerline telecommunications (PLT): coexistence between PLT modems and short wave radio broadcasting services (ETSI TS 102 578 V1.2.1), European Telecommunications Standards Institute, Sophia Antipolis, France, 2008.
- [176] B. Praho, M. Tlich, P. Pagani, A. Zeddami, F. Nouvel, Cognitive detection method of radio frequencies on power line networks, in: *Proceedings of the IEEE International Symposium on Power Line Communications and Its Applications (ISPLC)*, Rio de Janeiro, Brazil, 2010, pp. 225–230.
- [177] N. Weling, SNR-based detection of broadcast radio stations on powerlines as mitigation method toward a cognitive PLC solution, in: *Proceedings of the IEEE International Symposium on Power Line Communications and Its Applications (ISPLC)*, Beijing, China, 2012, pp. 52–59.
- [178] N. Weling, Feasibility study on detecting short wave radio stations on the powerlines for dynamic PSD reduction as method for cognitive PLC, in: *Proceedings of the IEEE International Symposium on Power Line Communications and Its Applications (ISPLC)*, Udine, Italy, 2011, pp. 311–316.
- [179] V. Taylor, M. Faulkner, Line monitoring and fault location using spread spectrum on power line carrier, *IEE Proc. C* 143 (5) (1996) 427–434.
- [180] A.N. Milioudis, G.T. Andreou, D.P. Labridis, Enhanced protection scheme for smart grids using power line communications techniques—part II: location of high impedance fault position, *IEEE Trans. Smart Grid* 3 (4) (2012) 1631–1640.
- [181] T. Erseghe, S. Tomasin, A. Vigato, Topology estimation for smart micro grids via powerline communications, *IEEE Trans. Signal Process.* 61 (13) (2013) 3368–3377.
- [182] M.O. Ahmed, L. Lampe, Power line communications for low-voltage power grid tomography, *IEEE Trans. Commun.* 61 (12) (2013) 5163–5175.

## Optical transmission

## 17

**M. Brandt-Pearce, M. Noshad***University of Virginia, Charlottesville, VA, United States***CHAPTER OUTLINE**

<b>17.1 Introduction</b>	662
<b>17.2 Device Properties</b>	662
17.2.1 Optical Transmitters	663
17.2.2 Optical Receivers	665
17.2.3 Other Components	666
<b>17.3 Channel Models</b>	666
17.3.1 Optical Wireless Channels	666
17.3.2 Optical Fiber Channels	671
<b>17.4 Modulation and Coding</b>	672
17.4.1 Intensity Modulation	672
17.4.2 Differential Modulation	674
17.4.3 Coherent Modulation	675
17.4.4 Error Control Coding	675
<b>17.5 Noise and Distortion</b>	675
17.5.1 Electrical Noise Model	676
17.5.2 Amplified Spontaneous Emission	676
17.5.3 Distortion and Interference Effects	677
<b>17.6 System Performance Analysis</b>	678
17.6.1 Direct Detection	679
17.6.2 Coherent Detection Performance	681
<b>17.7 Applications and Emerging Research Areas</b>	681
17.7.1 Free Space Optics	682
17.7.2 Deep Space Applications	682
17.7.3 Visible Light Communications	683
17.7.4 LANs and PONs	684
17.7.5 Long-Haul Transport Systems	685
17.7.6 Emerging Applications	685
<b>References</b>	685

---

## 17.1 INTRODUCTION

Within today's communications infrastructure, almost every transmission employs optical communications on at least a part of its path. Local area networks (LANs), access networks, cellular backhaul, and core transport systems practically all use fiber optics. Some of the most compelling new research areas in communications and information theory involve optical transmission, such as MIMO over fiber and optical wireless communications (OWCs). A description of transmission technologies would thus be incomplete without some discussion of optical communications.

In this chapter we address optical communications as a subject separate from other transmission systems because of their interdependence with optical technology and inherent differences due to the extremely high carrier frequencies. We present an overview of the devices necessary for this type of communication and then address design options and the applications they are best suited to. Our goal is not to present a complete description of optical communications; rather, we focus on the differences between RF and optical, hoping to provide classical communications engineers enough information to begin to explore this highly applicable huge-capacity communication medium.

Optical communications must be treated as a separate topic from RF or electrical communications for three fundamental reasons: (1) we currently do not have technology to directly sense the optical phase of the signal, ie, all optical sensors are optical power sensors, behaving nominally as square-law devices that discard the phase; we can obtain a measurement of the difference between two signal phases using a heterodyne receiver, adding significant complexity to the system; (2) the energy transmitted can be modeled as discrete valued due to the high energy per photon, and because of the basic uncertainty in these energy quanta, there is a fundamental SNR limit, called the *quantum limit*; (3) the bandwidth available, measured as even a small fraction of the carrier frequency, is still on the order of terahertz and therefore cannot be manipulated directly using modern electronics; multiplexing in the optical domain is necessary, typically done as wavelength division multiplexing (WDM). The implications of these differences on the design and performance of communications systems are addressed in this chapter.

Notation: all properties that refer to an optical signal are subscripted with an "O," while electrical notions are subscripted with an "E."

---

## 17.2 DEVICE PROPERTIES

Practically all optical systems today are device limited, meaning that the data rate and the performance are determined by a technological limit, not a fundamental one (such as the Shannon limit). Thus to understand optical transmission systems, one must consider the technologies being used and their properties. In this section, we discuss just enough about the devices needed to understand the design choices and their resulting performance.

### 17.2.1 OPTICAL TRANSMITTERS

Optical communication systems use either a light emitting diode (LED) or a laser diode (LD) to convert the electrical signal to the optical domain. Both devices impose two limits on the system, an *average* power limit and a *peak* power limit, the latter being a basic property of the device. The average power that can be transmitted is not subject to FCC regulations as in RF systems. However, eye-safety regulations, which differ based on the wavelength of transmission, do limit the average optical power that can be used.

#### 17.2.1.1 LEDs

LEDs are semiconductor devices that generate optical power approximately proportional to the positive electrical current flowing through them. The light generated is incoherent, exhibiting so much phase noise that the optical signal cannot be thought of as a sinusoidal carrier. Therefore, the optical frequency and phase of the device cannot be modulated, only the light intensity can. This is called *intensity modulation* and produces a nonnegative optical power signal  $P_O(t)$ ,

$$P_O(t) = F(s_E(t)), \quad (17.1)$$

where  $s_E(t)$  is the electrical signal to be transmitted and the operator  $F(\cdot)$  represents the LED's nonlinear response. A typical LED response to the input forward voltage is shown in Fig. 17.1, illustrating the nonnegative and saturating nature of the LED nonlinearity. Note that the modulating signal  $s_E(t)$  must itself be nonnegative or it will be severely clipped by the LED. The modulation speed of an LED is limited by the device rise time or modulation bandwidth. LEDs designed for communications can have bandwidths on the order of 100 MHz.

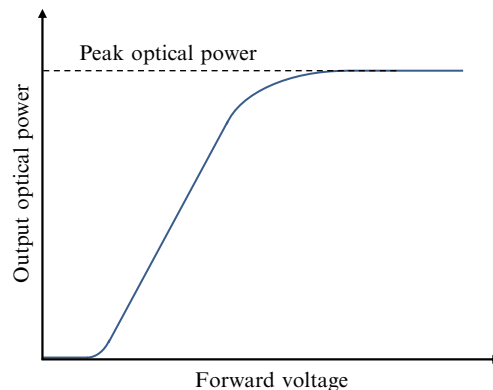


FIG. 17.1

Example of a nonlinear LED response to an input voltage.

As explained above, the optical signal produced,  $P_O(t)$ , is noncoherent so it does not contain a single frequency (or wavelength). The optical power is centered at a wavelength  $\lambda_O$  that depends entirely on the semiconductor material and has a wavelength range, called the *linewidth*, on the order of nanometers. LEDs are commercially available for wavelengths ranging from 210 to 4600 nm. Two noncoherent optical signals always add noncoherently, that is, the powers add (not the optical fields). This is fundamentally different from RF transmissions that normally add coherently when they are at the same frequency.

### 17.2.1.2 Lasers

Lasers are an alternative optical source when LEDs provide insufficient power or bandwidth. Lasers used for communications are typically semiconductor diodes like LEDs but produce a coherent light beam. Thus the signal can be described as a carrier with a single frequency experiencing some minor phase noise, the degree of which depends strongly on the design of the laser.

Lasers can be directly modulated by driving them with a nonnegative modulated current, resulting in intensity modulation similar to the LED. The signal produced is denoted as  $P_O(t)$ . The laser's response looks a bit different from the LED's, as shown in Fig. 17.2, where the slope of the linear portion can depend highly on the operating characteristics (temperature, etc.). Lasers require carefully designed drivers if they are to be operated as linear devices (current to optical power). For this reason, lasers are often on-off modulated, where the response nonlinearity can be largely ignored.

Alternatively, the laser can be operated as a continuous-wave (CW) source and the light can be modulated using an external modulator, such as a Mach-Zehnder modulator [1]. These devices can modulate both the amplitude and the phase of the optical field, so we need to refer to the signal produced as  $E_O(t) = A_O(t)e^{j(2\pi f_O t + \theta_O(t))}$ , the optical field where  $A_O(t)$  is the modulated optical

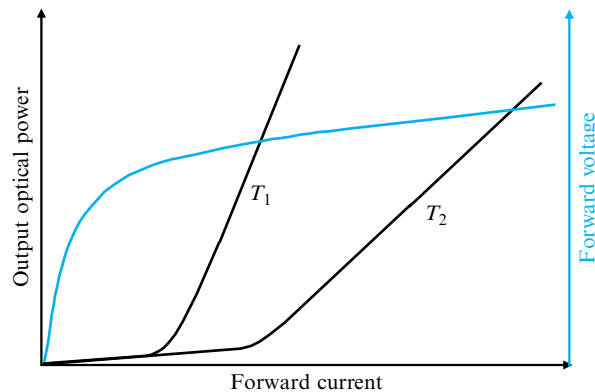


FIG. 17.2

Example of a nonlinear laser response to an input current.

amplitude,  $f_O$  is the optical frequency, and  $\theta_O(t)$  is the modulated optical phase (spatial parameters are omitted for clarity). Lasers put out polarized light (two orthogonal optical fields), and this affords one additional degree of freedom that can be used for modulation or multiplexing.

Lasers can introduce noise into the system in the form of phase noise and amplitude noise. These are not usually performance limiting, and they are not discussed here. The interested reader can refer to Ref. [2].

## 17.2.2 OPTICAL RECEIVERS

At the receiver the optical system needs a photodetector to convert the signal from the optical domain back to the electrical domain. One of two techniques can be used, as described here.

### 17.2.2.1 Direct detection

The first method is referred to as *direct detection* because the optical power is converted into an electrical current directly using a semiconductor photodetector. The photodetector is well modeled as a linear device with the output electrical current

$$s_E(t) = \rho P_O(t), \quad (17.2)$$

where the proportionality constant  $\rho$  is called the *responsivity* of the device and has units of A/W. The responsivity can be computed using

$$\rho = \frac{\eta q G}{h f_O}, \quad (17.3)$$

where  $\eta$  is the quantum efficiency of the photodetector (the fraction of photons that generate electrons),  $q$  is the charge of an electron,  $h$  is Planck's constant, and  $G$  is the gain of the device.

A low-cost and high bandwidth photodetector is the PIN diode, which is a positive-intrinsic-negative doped semiconductor that has unit gain,  $G = 1$ . These devices can have bandwidths of as high as 50 GHz. Instead, one can use an avalanche photodetector (APD) that has a high electric field avalanche region in the semiconductor, which results in a gain ranging from  $10 < G < 200$ , depending on the design. APDs are much slower devices, with bandwidths on the order of a few gigahertz, but the gain is useful in overcoming subsequent thermal/electronic noise.

### 17.2.2.2 Coherent receivers

For a coherent optical signal, instead of detecting the optical power, the optical field can be sensed by mixing the received signal with an optical signal generated locally (a local oscillator). This process requires the two equally polarized optical fields to be added prior to photodetection. Since the photodetector is effectively a square-law device, the resulting signal becomes

$$s_E(t) = \rho |E_{LO}(t) + E_O(t)|^2, \quad (17.4)$$

where  $E_{LO}(t)$  is the field of the local laser. If the lasers are perfect oscillators, ignoring the DC and second harmonics, the result creates an electrical current proportional to the modulating signal, carrying both the magnitude and phase:

$$s_E(t) \propto A_O(t)e^{j(2\pi f_{IF}t + \theta_{IF}(t))}, \quad (17.5)$$

where  $f_{IF}$  and  $\theta_{IF}$  are the intermediate frequency (IF) signal frequency and phase generated by the difference of the two optical signals. This type of detection is also called *heterodyne detection*. Heterodyning is expensive compared with direct detection, and it is currently only used in high-speed (100 Gbps or higher) fiber-optic links.

### 17.2.3 OTHER COMPONENTS

To construct an end-to-end optical system, many components are necessary, including optical filters, lenses, polarizers, couplers, etc. Most of these components are passive devices that affect the signal's amplitude at some particular optical frequency, but they can be considered frequency-flat over the signal bandwidth. These must be included in any link budget calculation, but they do not further affect the communication system, except in the case of multiple signals, where cross talk may leak through (in frequency, polarization, or space).

One important active optical device is the optical amplifier. These can be implemented either as semiconductors (SOA, semiconductor optical amplifier) or as doped fiber segments (eg, Erbium doped fiber amplifier, EDFA). Some optical amplifiers (notably the doped fiber) can be quite broadband, on the order of 10 THz, and low noise (noise figure on the order of 5 dB). The odd aspect of this optical noise is that it adds *before* the photodetector, which makes it fundamentally different from most noncoherent RF receivers. The consequences are discussed below in [Section 17.5.2](#).

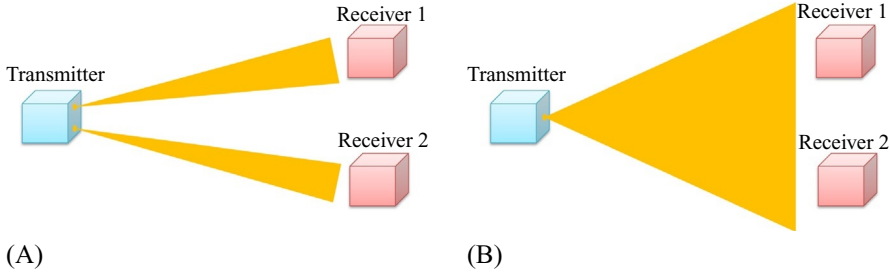
---

## 17.3 CHANNEL MODELS

Optical channels come in guided and unguided varieties, and each introduces its own distortions and limitations. We describe each channel by how it affects the transmitted signal.

### 17.3.1 OPTICAL WIRELESS CHANNELS

Wireless optical channels are the simplest to consider. The signal travels from the optical source to the optical sensor through what is called “free space,” meaning either the atmosphere, if the link is terrestrial, or a vacuum, if the link is in space. OWC has seen a resurgence in the last few years, fueled by the fear of an impending shortage of usable RF bandwidth.

**FIG. 17.3**

(A) Point-to-point optical link versus (B) diffuse optical channel.

### 17.3.1.1 Directed point-to-point channels

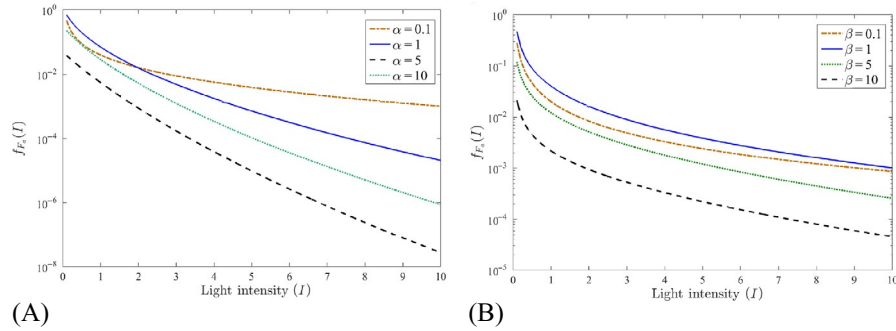
When an optical link uses a laser, the beam is so narrow that one can assume that a line-of-sight (LOS) is required between the source and the receiver, creating a point-to-point link (Fig. 17.3A). This type of transmission is often referred to as free-space optics (FSO), especially if the link is outdoors and terrestrial. Beamwidths ranging from fractions of a milliradian to just a few milliradians are standard. Terrestrial directed FSO links can range from one hundred meters to several hundred kilometers. For long links, the key design issue and the major system expense lie in the acquisition, pointing, and tracking (APT) mechanism.

Because no multipath can result from such narrow beams, the channel causes no temporal dispersion. For typical transmitted optical power levels, the channel can be assumed linear, causing no discernible nonlinear degradation. The only degradations suffered by the signal are attenuation and turbulence-induced fading. The relation between the transmitted optical power  $P_O^{(T)}$  and the received optical power  $P_O^{(R)}$  can be expressed as

$$P_O^{(R)} = P_O^{(T)} G_T G_R L_s L_a F_a, \quad (17.6)$$

where  $G_T$  is the transmitter antenna (optical lens or telescope) gain,  $G_R$  is the receiver antenna gain,  $L_s$  is the space loss,  $L_a$  is the atmospheric attenuation (slowly varying and modeled as deterministic), and  $F_a$  is the atmospheric fading (modeled as random). The attenuation results from three independent factors. The dominant factor is the loss due to beam spreading ( $G_T G_R L_s$ ), which occurs both in collimated and uncollimated beams. It is unusual for the entire beam to fall within the aperture of the receiver, so the portion of the power transmitted and not collected results in this loss factor. Since  $G_T$ ,  $G_R$ , and  $L_s$  in the link loss equation are the same as in RF systems, details about these are omitted here.

The second important factor is atmospheric loss,  $L_a$ , primarily due to weather. Fog, snow, and heavy rain can attenuate an optical wireless link by as much as 200 dB/km (for fog especially), making the link useless over a few hundred meters. The attenuation level depends on the wavelength used and the density of particulates in

**FIG. 17.4**

The pdf of  $f_{F_a}(I)$  for (A)  $\beta = 1$  and different  $\alpha$ 's, and (B)  $\alpha = 1$  and different  $\beta$ 's.

the air. In addition to this atmospheric effect that can be considered as a time invariant loss (changing over a matter of minutes or hours), the atmosphere can cause time-varying fading,  $F_a$ , that can have a time constant less than 1 ms. This is the third type of attenuation that must be considered as it can add over 15 dB of extra loss to the link. This fading is not caused by multipath and cannot be modeled as a Rayleigh random variable as in the RF case. It is caused by pockets of index of refraction inhomogeneities in the air, which can create a lens effect and scintillation. The statistics are dependent on the weather, so several models have been explored [3]. The most general is the Gamma-Gamma model, which gives a loss factor  $F_a$  with pdf illustrated in Fig. 17.4 and given as

$$f_{F_a}(I) = \frac{2(\alpha\beta)^{(\alpha+\beta)/2}}{\Gamma(\alpha)\Gamma(\beta)} I^{(\alpha+\beta)/2-1} K_{\alpha-\beta} \left( 2\sqrt{2\alpha\beta I} \right), \quad I > 0, \quad (17.7)$$

where  $\alpha$  is the small fading effect parameter,  $\beta$  is the large fading parameter,  $\Gamma(\cdot)$  is the gamma function, and  $K_\nu(\cdot)$  is the modified Bessel function of the second kind and order  $\nu$ .

### 17.3.1.2 Diffuse channels

Diffuse optical channels resemble classical wireless links: the optical source sends a broad beam meant to illuminate an entire area as shown in Fig. 17.3B. Any receiver in the broadcast area that can collect sufficient power can establish a link. Diffuse channels often use LEDs because they are naturally uncollimated, but in rare cases they can also use an artificially broadened laser beam. We will assume an LED is employed.

In a diffuse link the received power is a sum of the power received directly from the optical source, called the LOS component, and any power incident on the photodetector resulting from reflections of the light, called the nonline-of-sight (NLOS)

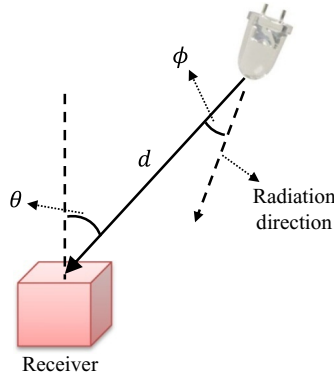


FIG. 17.5

Angles between the radiation direction and the path to user.

component. Assuming an LED total power of  $P_O^{(T)}$ , the general formula for the LOS channel loss between an LED and a photodetector can be written as follows [4]:

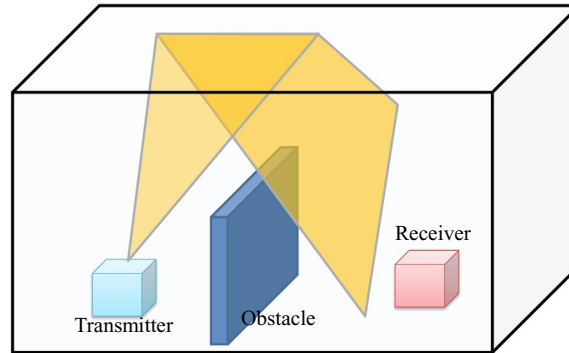
$$P_O^{(R)} = P_O^{(T)} \frac{A_r \cos \theta}{2\pi d^2} (m+1) \cos^m \phi, \quad (17.8)$$

where  $A_r$  is the receiver aperture,  $d$  is the distance between the LED transmitter and the receiver,  $\theta$  is the angle between the received light and the receiver's axis,  $\phi$  is the angle between the LED's axis and ray received by the user, and  $m$  is the Lambertian mode of the light source, which is related to the LED's semiangle  $\Phi_{1/2}$  by  $m = \frac{\ln 2}{\ln(\cos \Phi_{1/2})}$  and determines the beamwidth. This notation is illustrated in Fig. 17.5.

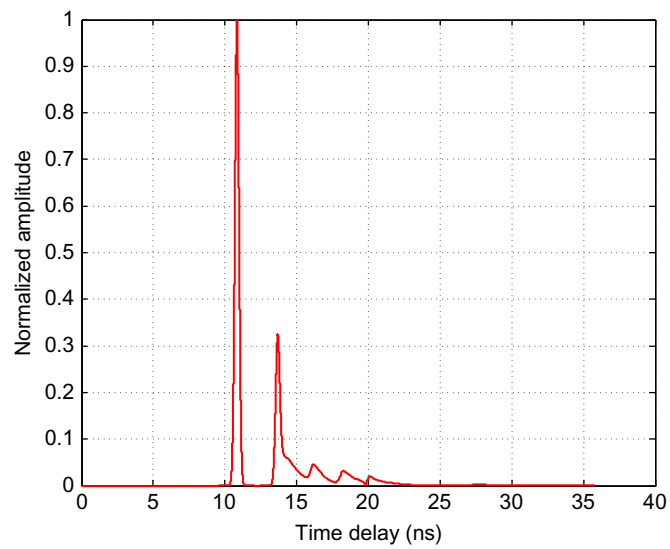
In indoor environments, the diffuse channel can have the LOS blocked, leaving reflected rays as the only contributors to the received power, as shown in Fig. 17.6. The reflected NLOS optical power typically contributes little to the received power compared with the LOS when both are present. Because the channel becomes a multipath channel, there can be degradation in the form of intersymbol interference (ISI) or fading. However, the form is somewhat different from the RF multipath channel in one fundamental aspect: the powers add noncoherently, so there is no phase offset, thus there is no signal cancellation. The impulse response is real and nonnegative, as illustrated in Fig. 17.7.

However, there is no fading of the optical carrier, in the sense that the optical powers cannot add destructively. If the information signal is intensity modulated onto a diffuse optical beam and experiences multipath, the intensity modulation can be faded by the multipath channel. Suppose the nonnegative electrical modulating signal is  $s_E(t)$  and that the received signal is due to two rays delayed by  $\tau$ . The received signal would be of the form

$$P_O^{(R)}(t) = \alpha_{\text{LOS}} s_E(t) + \alpha_{\text{NLOS}} s_E(t - \tau), \quad (17.9)$$

**FIG. 17.6**

NLOS optical link.

**FIG. 17.7**

Example of an impulse response for a diffuse indoor LED-based communication system obtained using ray-tracing.

Source: Adapted from J. Lian, *Multuser MISO indoor visible light communications*, Master's thesis, University of Virginia, Charlottesville, VA, 2014.

where the  $\alpha$ 's are attenuations, which would result in fading of sinusoidal components of  $s_E(t)$  with frequencies that are multiples of  $1/2\tau$  [5].

### 17.3.2 OPTICAL FIBER CHANNELS

By far, the most prevalent optical communications channel is the fiber optic channel, which is mainly used in medium and long-haul communication systems (10–10,000 km). An optical fiber is a cylindrical waveguide constructed as a thin strand of silica (highly transparent at infrared wavelengths) through which the optical signal travels. In this chapter, we briefly discuss the two most prevalent types of fiber links. Interested readers can learn more through optical fiber texts, such as Refs. [1,6,7].

#### 17.3.2.1 Single mode fiber

All long-haul and most metro systems use what is called a single-mode fiber (SMF). Without getting into any of the physics of propagation, one can think of it as a single spatial (cross-sectional distribution) electromagnetic mode that satisfies Maxwell's equations due to the properties of the fiber (index of refraction, diameter, etc.), thus if the optical signal input is coherent the signal inside the fiber can spatially and temporally be regarded as a single electromagnetic field in each of the two polarizations. At the receiver, this field can be directly or coherently detected.

The nonlinear Schrödinger (NLS) equation is used to model the propagation of optical pulses inside SMFs. For pulse widths  $T_0 > 5$  ps, the NLS equation is given by [6]

$$\frac{\partial A_O}{\partial z} = -\frac{\alpha}{2}A_O - \frac{i\beta_2}{2}\frac{\partial^2 A_O}{\partial t'^2} + i\gamma|A_O|^2A_O, \quad (17.10)$$

where  $A_O = A_O(t, z)$  is the slowly varying complex envelope of the propagating field;  $t$  is measured in a frame of reference moving with the pulses at the group velocity;  $z$  is the propagation distance measured along the fiber;  $\alpha$  is the attenuation constant;  $\beta_2$  is the group-velocity dispersion (GVD) parameter; and  $\gamma$  is the nonlinear parameter. The three terms on the right-hand side describe, respectively, the effects of fiber losses, dispersion, and nonlinearities on the pulses propagating through optical fibers.

The main effect of GVD is to broaden an optical pulse as it propagates through the fiber. Temporal spreads of neighboring bits overlap, leading to ISI. GVD in SMFs can be reduced by strategic use of dispersion compensation, a lumped device that introduces a negative dispersion, resulting in an equivalent zero (or small) pulse spreading. In addition to GVD-induced pulse broadening, polarization-mode dispersion (PMD) leads to distortion of optical pulses due to fiber birefringence. PMD is typically random, but slowly time varying and therefore relatively easy to compensate through signal processing.

Fiber nonlinearities can be classified into two types: Kerr effect and stimulated scattering [8]. Stimulated scattering leads to intensity-dependent gain or loss, the most detrimental of which is stimulated Raman scattering (SRS). The Kerr effect is due to the intensity dependence of the refractive index and causes an intensity-dependent phase shift experienced by an optical field during propagation in optical fibers [6]. Stimulated scattering is relatively small compared with the Kerr effect and is often ignored. In the case of successive transmissions of pulses in a multichannel system (WDM or OFDM), the Kerr effect combined with GVD leads to nonlinear interaction among optical pulses on the same channel (intrachannel effects), and among pulses on neighboring wavelengths in a WDM system (interchannel effects).

### 17.3.2.2 Multimode, multicore, and few-mode fibers

Multimode fibers are simultaneously an old and emerging technology within the context of optical systems. The first optical fiber systems back in the 1970s used multimode fibers. These fibers are identical to SMFs except that they have a wider diameter, thus allowing several transverse optical modes to propagate simultaneously. Depending on their cross-sectional index of refraction profiles, they suffer from varying degrees of what is called *modal dispersion*, where modes propagate at slightly different speeds resulting in pulse spreading. This limits the bandwidth-length product to about 100 MHz-km. Because of their larger size, they are easier to splice and couple, and they are generally less expensive to install. Older local-area and access networks still use multimode fibers.

There has recently been renewed interest in what are called few-mode fibers, which are multimode fibers that are just the right size where a few, say 3–10 modes, can propagate. Efforts to send multiple signals through these fibers, one per polarization per mode, a sort of MIMO transmission, has met some success [9,10]. Alternatively, MIMO can be accomplished using so-called *multicore* fibers, which are formed by placing several single-mode cores within one fiber [11,12].

---

## 17.4 MODULATION AND CODING

Each device and channel described above lends itself to a suite of modulation and coding schemes. We naturally separate the modulation schemes into those appropriate for noncoherent (direct detection) systems and those that can be used in coherent (heterodyne) systems.

### 17.4.1 INTENSITY MODULATION

When direct detection is employed, the easiest attribute of the optical signal to modulate is the light intensity. This yields a unipolar (nonnegative) one dimensional modulation. Since the phase of the optical signal is lost in the photodetection process, it cannot be used in modulation. Note that differential modulation cannot be directly used if the optical source is incoherent or if the phase is discarded at the receiver.

One important difference between optical and RF noncoherent systems is how the transmitted symbol is defined. In optical systems, the symbol  $X$  is the optical power, not the field. So the power consumed at the transmitter, a fundamental limitation in the system design, becomes proportional to  $E[X]$ , the expected value of the symbol, not  $E[X^2]$  as in RF systems. Of all the properties of optical systems, this is one that RF engineers transitioning to optical systems most often miss.

If baseband modulation is desired, pulse amplitude modulation (PAM) of the optical intensity is the simplest. In its binary form, this modulation is referred to as on-off keying (OOK), where  $X \in \{0, 1\}$ , and it is by far the most used intensity modulation; all 10 Gbps fiber systems use OOK. Because optical sources are difficult to operate linearly, higher-order PAM is not often used. OOK does not require linear operation of the optical source.

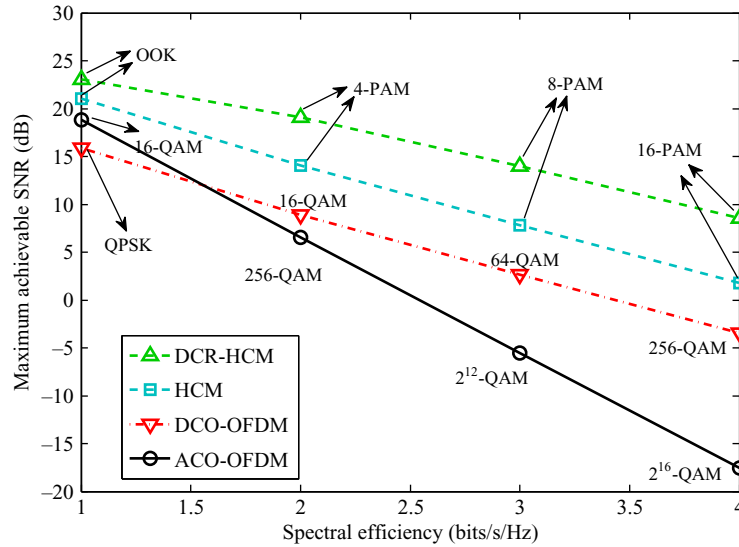
Another baseband modulation sometimes used is pulse position modulation (PPM). In standard PPM, the transmitted symbol is subdivided into  $M$  time slots and a pulse is sent in one of the slots, resulting in an  $M$ -ary modulation with spectral efficiency of  $\eta = \log_2(M)/M$ . Binary PPM, effectively identical to Manchester coding, is sometimes used in OWC systems because it does not require a detection threshold and the symbol clock is easily extracted, even in fading channels. High-order PPM modulation is used almost exclusively in deep space systems where the power efficiency is of paramount importance and the bandwidth is plentiful. One can send multiple pulses per symbol, a technique called multipulse PPM (MPPM). A generalized form of PPM called expurgated PPM (EPPM) is introduced in Ref. [13] to decrease the bit-error probability in optical systems with power-limited sources.

If the source can be operated such that the optical intensity is linearly related to the input signal (which requires a sophisticated driver circuit and a low modulation index), higher-order modulation can be accomplished by using subcarrier modulation. Any amplitude and/or phase modulation approach can be used to create a real-valued signal on an IF,  $s_{\text{IF}}(t)$ . This signal is then biased so that it is nonnegative, and the resulting current is used to intensity modulate the optical source, creating an optical power that can be written as

$$P_{\text{O}}(t) = \bar{P}_{\text{O}} + ms_{\text{IF}}(t), \quad (17.11)$$

where  $\bar{P}_{\text{O}}$  is the average power and  $m$  is the modulation index used. When the IF is in the RF range, this technique is called radio-over-fiber (RoF) or radio over FSO (RoFSO).

In RF wireless systems, OFDM has become the modulation of choice to combat temporal dispersion. Since the signals generated in OFDM systems are complex-valued, they cannot be directly used in direct detection optical systems. There are two basic ways to implement OFDM in optical systems [14]. One approach is to use subcarrier modulation as described above, replacing the IF signal with a real-valued OFDM signal, called DC offset OFDM (DCO-OFDM). Each OFDM subcarrier can be amplitude and/or phase modulated (QAM, for example). Alternatively, a technique called asymmetrically clipped OFDM (ACO-OFDM) has been adopted

**FIG. 17.8**

Spectral efficiency of different modulation schemes versus the maximum achievable SNR in peak-power-limited optical communication systems.

to work in energy efficient optical communications because of its better average-power efficiency compared to DCO-OFDM. The ACO-OFDM technique uses two symmetry properties to turn complex-valued signals into positive real data, which results in a loss in the spectral efficiency.

A pulsed-version of OFDM, where the FFT is replaced with a fast Hadamard transform, has recently been proposed [15,16]. This technique, called Hadamard coded modulation (HCM), performs better than OFDM in highly nonlinear environments. An alternative to HCM that removes unnecessary DC offset is termed DC-removed-HCM (DCR-HCM). Fig. 17.8 shows a comparison between the spectral efficiency of different modulation schemes versus the maximum achievable SNR in peak-power limited optical communication systems [15].

### 17.4.2 DIFFERENTIAL MODULATION

If a coherent optical source is used with an external amplitude and phase modulator, while still relying on the less-expensive direct detection receiver, differential detection can be a good intermediate-cost option. The signal modulates the difference between two successive pulses, as in conventional DPSK. At the receiver, successive pulses are added prior to photodetection so that a constructive versus destructive phase relation can be observed at the output of the photodetector [1]. Most 40 Gbps

WAN and core fiber systems are based on 20 Gbps differential QPSK. As coherent receivers have become less expensive, differential receivers have become less used.

### 17.4.3 COHERENT MODULATION

When the system uses a heterodyne receiver, both the amplitude and phase of the optical field can be modulated. The usual approach is to use standard quadrature modulation formats, such as M-ary QAM or OFDM. Independent modulation of the two polarizations doubles the throughput. Standard 100 Gbps systems use 50 Gbps on each polarization, with QPSK over a 25 Gbps (Gbaud) root-raised-cosine pulse (higher symbol rate if error control coding is used), typically centered within a 50 GHz WDM channel. To exploit the full bandwidth of the optical fiber, a technique called Nyquist-WDM has been proposed, where the Nyquist criterion for WDM channel independence is satisfied in the frequency domain [17,18]. WDM channels are then spaced with a frequency separation equal to the symbol rate. Alternatively, using standard OFDM modulation with coherent detection of one or more subcarriers has also been explored recently.

Since the polarization provides another dimension, some researchers have explored the idea of using a four-dimensional constellation instead of two parallel two-dimensional ones as described above [19,20]. As coherent detection is used primarily in long-haul fiber systems, and these suffer from significant linear and nonlinear effects, researchers have also proposed alternative two- or four-dimensional constellations that are less susceptible to these physical-layer impairments [21,22].

### 17.4.4 ERROR CONTROL CODING

There has been little effort to design forward error control (FEC) codes specifically for optical communication systems. Most optical systems employ standard codes developed for electrical or RF systems, such as LDPC codes. One effort to design LDPC codes specifically for optical channels notes that some general codes perform almost optimally over these channels [23]. Very high-speed systems often employ hard-decision versions, while the lower-speed systems can benefit from soft-decision decoding. Standard practice is to assume a required pre-FEC BER and assume the coding does as advertised. A recent paper questions this practice, as the coding gain depends substantially on the characteristics of the channel [24].

---

## 17.5 NOISE AND DISTORTION

Optical systems can be subject to shot noise and optical noise, in addition to the standard thermal noise. These require somewhat different models and performance expressions.

### 17.5.1 ELECTRICAL NOISE MODEL

Receiver noise in optical systems is a sum of electronic thermal noise from the front-end amplifier and shot noise. The thermal noise is well modeled as an additive white Gaussian noise (GN) with spectral density in units of  $A^2/Hz$  given as

$$S_{th} = \frac{4kT_p}{R_L}, \quad (17.12)$$

where  $k$  is Boltzmann's constant,  $T_p$  is the system temperature, and  $R_L$  is the load resistance as seen by the photodetector. For noise power, the spectral density can be simply multiplied by the receiver bandwidth  $\Delta f$ .

The shot noise results from the discrete nature of photons, and it can be modeled in one of two ways. Under the shot noise limit, the photodetection process can be analyzed using the semiclassical model, which takes the optical signal as behaving like a wave and the photoelectrons generated at the photodetector as particles. In this model, the received signal is represented as a Poisson process with photon arrival rate proportional to the incident optical power. If the optical power is high, the Poisson process can be approximated by a Gaussian process, simplifying the analysis. In this case, the power spectral density of the shot noise can be written as

$$S_{sh} = 2q\rho P_O \quad A^2/Hz, \quad (17.13)$$

where  $q$  is the electrical charge on an electron.

If the photodetector used is an APD, the shot noise is enhanced by the avalanche process. This occurs because the number of secondary electrons generated by each primary electron (one resulting directly from photon absorption) is random, creating more uncertainty. The statistics of this process are complex, thus the effect of the increased shot noise is often represented by a factor called the *excess noise factor*,  $F_E$ . The resulting shot noise spectral density for an APD with gain  $G$  becomes

$$S_{sh} = 2q\rho G^2 P_O F_E \quad A^2/Hz. \quad (17.14)$$

### 17.5.2 AMPLIFIED SPONTANEOUS EMISSION

Fiber-optic communication systems that use optical amplifiers are subject to optical noise, called amplified spontaneous emission (ASE) noise [25–27]. ASE noise is due to spontaneous emission of photons that adds optical noise to the signal during its amplification.<sup>1</sup> It can be modeled as a GN with a spectral density nearly constant (white noise) in the band of interest, which can be expressed by [1]

$$S_{ASE}(f_O) = n_{sp} h F_O (G - 1), \quad (17.15)$$

<sup>1</sup>In this description, we assume lumped amplification, but the model can be easily applied to distributed (Raman) amplification.

where  $n_{\text{sp}}$  is the spontaneous emission factor,  $h$  is Planck's constant,  $F_O$  is the optical carrier frequency of the signal being amplified, and  $G$  is the amplifier gain. The total ASE power for a chain of  $N$  equal-gain amplifiers through a linear fiber is approximated by [1]

$$P_{\text{ASE}} = 2NS_{\text{ASE}}\Delta_{f_O}, \quad (17.16)$$

where the factor of two takes into account the unpolarized nature of ASE noise and  $\Delta_{f_O}$  is the bandwidth of the optical filter at the receiver.

The photodetector acts as a band-limited square law device on the optical signal plus optical noise. The output of the matched filter can be roughly modeled as a sum of noncentral  $\chi$ -squared random variables, which is quite cumbersome. Instead, the noise is often modeled as Gaussian and comprised of three independent terms: a signal-noise beat term (signal dependent), a noise-noise beat term, and a shot noise term due to the ASE noise itself. Details can be found in Ref. [1].

### 17.5.3 DISTORTION AND INTERFERENCE EFFECTS

Narrow-beam optical wireless channels do not experience interference, temporal dispersion, or channel nonlinearities. Diffuse links can suffer from both multipath effects and additive interference from other user signals. These are dealt with as in wireless RF systems.

Short fiber channels can be modeled as linear and do not accumulate nonlinear impairments. The long-haul fiber channel is nonlinear and therefore so complex that it is difficult to give exact performance expressions. Various levels of modeling fidelity can be obtained, depending on the channel state known and the computational resources available. The classical method is to use the NLS equation, given in Eq. (17.10), which unfortunately does not give an input/output description amenable to analysis.

Alternatively, for a long-haul point-to-point optical fiber link with no optical dispersion compensation and known WDM channel utilization information, a more accurate model has recently become widely used, referred to as the GN model. The dispersion in the fiber serves to spread each symbol over hundreds or thousands of adjacent symbols, allowing us to use the central limit theorem to approximate the effect of both intra and interchannel nonlinear effects as an additive GN. The GN model provides an approximate expression for the physical layer impairments assuming a coherent polarization-multiplexed system, a rectangular channel spectrum, and perfect loss compensation. The nonlinear interference power spectral density per polarization for channel  $i$  can then be expressed as [28]

$$S_{\text{NLI}}^{(i)}(f_O^{(i)}) = \mu S_i \left( S_i^2 \operatorname{arcsinh} \left( \kappa \Delta_{f_O^{(i)}}^2 \right) + \sum_{\substack{j=1 \\ j \neq i}}^M S_j^2 \ln \left| \frac{|f_O^{(i)} - f_O^{(j)}| + \Delta_{f_O^{(j)}}/2}{|f_O^{(i)} - f_O^{(j)}| - \Delta_{f_O^{(j)}}/2} \right| \right), \quad (17.17)$$

where  $\mu = 3\gamma^2/(2\pi\alpha|\beta_2|)$ ,  $\kappa = \pi^2|\beta_2|/2\alpha$ ,  $M$  is the number of channels, and  $\Delta f_O^{(k)}, f_O^{(k)}$ , and  $S_k$  are the  $k$ th channel's bandwidth, center frequency, and signal power spectral density per polarization, respectively. The first term in Eq. (17.17) represents self-channel interference and the summation term is cross-channel interference.

Using this technique, one can predict performance for a point-to-point link. For networks, a coarse approach is to compute a worse case for a channel assuming that nonlinearities caused by WDM channels are at their maximum (all channels are used). This leads to an upper bound on the BER expected that must remain below a predetermined limit depending on the FEC chosen. This technique is commonly used in optical networks where dynamic channel usage makes it difficult for full channel state information to be known. Often the most meaningful measures for network design is the maximum length that a signal can propagate optically before it would require electronic regeneration, called the *transmission reach*.

The power penalty method is another commonly used approach for incorporating the effects of various distortions and impairments into fiber systems. For every impairment that acts on the signal independently, the impact on the optical signal power or the receiver sensitivity has been characterized, mostly experimentally or by simulation. A power penalty represents the equivalent power loss that would result in the same performance as the degradation under study. Many research efforts report on power penalties observed for various system configurations. From these, rules of thumb about the impact of each impairment have been generated [2].

## 17.6 SYSTEM PERFORMANCE ANALYSIS

To simplify the performance analysis in the presence of so many different impairments, only the dominant noise or distortions are usually considered, in both SNR and BER expressions, with the caveat that this is an approximation. If no optical amplifier is used, a PIN photodetector is used; if there is no strong background light, the system is usually thermal-noise-limited. The shot noise limit can be achieved with sufficient photodetection gain (APD gain), or if the received power level is quite high. When an optical amplifier is used, optical ASE noise normally dominates.

In optical communications using optical amplifiers, two signal-to-noise metrics can be defined: an optical SNR (OSNR) and an electrical SNR, simply called SNR. The OSNR is the optical signal to optical noise ratio, before photodetection, given by  $\text{OSNR} = P_O/P_{\text{ASE}}$ . In long-haul fiber systems, a lumped optical amplifier (an EDFA) is placed periodically along the fiber in such a way that the amplifier gain  $G$  compensates exactly for the attenuation. The noise from all the amplifiers in the chain accumulate and limit performance. In this case, using Eq. (17.15), for a fiber of length  $L$ , the OSNR be written as [1]

$$\text{OSNR} = \frac{P_O \ln G}{2n_{\text{sp}} h f_O \Delta f_O \alpha L (G - 1)}. \quad (17.18)$$

In short-haul, metro, or local area applications, and in FSO channels, optical amplifiers can be used to compensate for losses due to switching and fiber splits or for atmospheric losses in wireless channels. In this case, the performance may be limited by ASE noise or by electronic noise.

### 17.6.1 DIRECT DETECTION

In the thermal noise limit, the channel is an additive white GN channel, and the analysis used for RF communications through these types of channels applies directly. Similarly, if shot noise dominates and can be modeled as a Gaussian with constant signal-independent spectral density, as in the case of strong background noise, classical AWGN analysis applies as well. In this section, we discuss cases that deviate from these assumptions.

Shot noise is inconsequential in RF systems but fundamental and unavoidable in optical systems. It imposes a limit on the SNR that can be achieved; the largest possible SNR is referred to as the quantum limit, given by

$$\text{SNR}_q = \frac{\rho P_O}{q \Delta_f}. \quad (17.19)$$

This limiting SNR can be degraded by a detector noise figure, excess noise from an APD, or other power penalties.

Consider a binary OOK modulated signal, where  $X \in \{0, 1\}$  is the information signal, which is the simplest case for optical systems, and let the optical power received for  $X = i$  transmitted be denoted as  $P_O^{(i)}$ . In the thermal noise limit, the BER can be estimated as

$$\text{BER} = Q\left(\frac{\rho(P_O^{(1)} - P_O^{(0)})}{2\sigma}\right), \quad (17.20)$$

where  $\sigma^2 = S_{\text{th}} \Delta_f$ . Any power penalties would subtract from the received optical power levels, and any additional noise figures would add to the noise variance (in dB).

In the Poisson noise regime, it is common to measure the number of received photons for  $X = i$ , denoted  $n_i = P_O^{(i)} T_s / hf_O$ , where  $T_s$  is the symbol time. Under quantum-limited detection, we assume  $n_0 = 0$  and the  $\text{BER} = e^{-n_1}/2$ . Otherwise, the optimal threshold becomes  $\tau = (n_1 - n_0)T_s / \ln((n_1 + n_0)/n_0)$  and the resulting BER is given by

$$\text{BER} = \frac{1}{2} \sum_{k=0}^{\lfloor \tau \rfloor} \frac{n_1^k e^{-n_1}}{k!} + \frac{1}{2} \sum_{k=\lceil \tau \rceil}^{\infty} \frac{n_0^k e^{-n_0}}{k!}, \quad (17.21)$$

ignoring ties.

In the case where the shot noise can be modeled as a Gaussian process, the variance due to shot and thermal noise terms can add and result in an unequal noise level for  $X = 1$  and  $X = 0$ . This also occurs when the ASE noise dominates because the noise after photodetection contains signal-noise cross-terms (due to the

square-law operation). Letting the variance due to noise at the output of the receiver filter be  $\sigma_i^2$  for  $X = i$ , the BER becomes

$$\text{BER} = \frac{1}{2} \left[ Q \left( \frac{(\rho P_O^{(1)} - \tau)}{\sigma_1} \right) + Q \left( \frac{(\tau - \rho P_O^{(0)})}{\sigma_0} \right) \right], \quad (17.22)$$

where  $\tau$  is the decision threshold. The variances can be computed by adding the expressions in Eqs. (17.12) and (17.13), the latter depending on whether  $X = 0$  or  $X = 1$ .

If  $\sigma_0 \approx \sigma_1$ , a simpler approximate expression for the BER is

$$\text{BER} \approx Q \left( \frac{\rho(P_O^{(1)} - P_O^{(0)})}{\sigma_1 + \sigma_0} \right). \quad (17.23)$$

This expression comes from setting the threshold to  $\tau = \frac{\rho(P_O^{(1)}\sigma_0 + P_O^{(0)}\sigma_1)}{\sigma_1 + \sigma_0}$ , yielding equal error rates on  $X = 1$  and  $X = 0$ . Note that this threshold does not actually minimize the BER. The fraction inside the  $Q(\cdot)$  function is called the *Q-factor*, and it is often used as a figure of merit in optical systems and is related to the BER as shown in Fig. 17.9. Other modulations, such as PPM, lead to similar expressions based on simple detection theory.

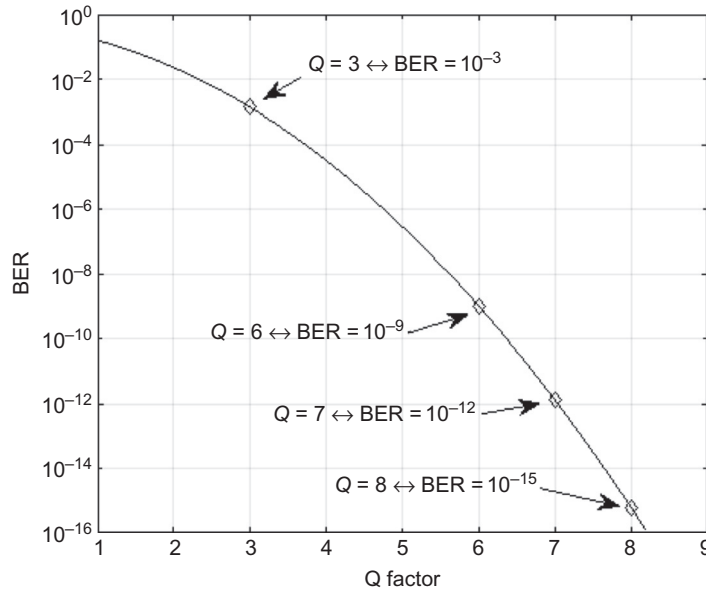


**FIG. 17.9**

BER as a function of the Q factor.

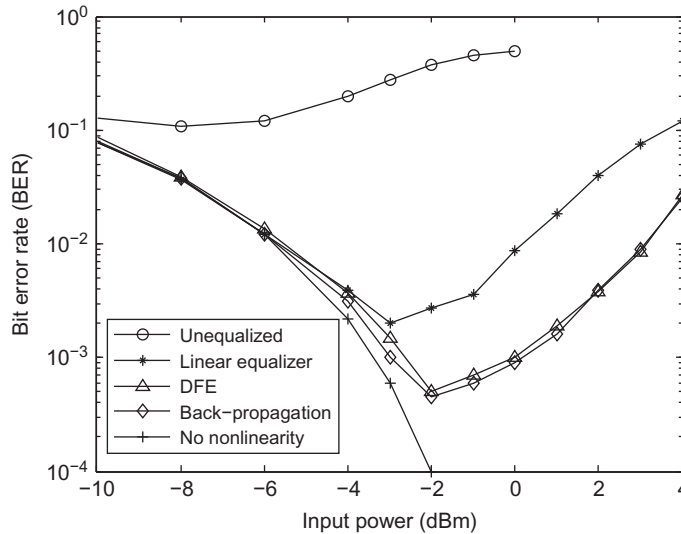


FIG. 17.10

BER of a long-haul fiber system with dispersion compensation and periodic amplification, 21.4 Gbit/s QPSK, 50 spans, 5 dB amplifier noise figure. The DFE used is described in Ref. [30].

## 17.6.2 COHERENT DETECTION PERFORMANCE

In coherent detection systems, the output of the receiver front-end (after high and low pass filtering) yields a signal proportional to the optical *field* down-converted to some appropriate IF, unlike direct detection, which produces a signal proportional to the optical *intensity*. The coherent scenario is thus completely analogous to RF communication systems. The most significant difference exists for long-haul fiber systems where the nonlinear degradations caused by the interplay between dispersion and Kerr effects can dominate performance. At lower signal-to-noise ratios, the system is ASE noise limited, and classical AWGN analysis holds, while at higher power levels the performance is determined by the nonlinear effects that couple with the noise introduced at the various stages of amplification, as shown in Fig. 17.10. Various signal processing techniques can be used to combat the physical impairments, such as digital back-propagation [29] and nonlinear equalization [30]. The performance becomes highly dependent on the specificity of the link design and the signal processing used. The interested reader can find more information in Ref. [2].

## 17.7 APPLICATIONS AND EMERGING RESEARCH AREAS

Because of their special properties, such as narrow beams and ultra-high bandwidths, optical communications can accomplish transmission unlike any RF or

electrical system. In this section, we describe some environments in which optical communications have been successfully used, as well as their properties.

### 17.7.1 FREE SPACE OPTICS

Terrestrial point-to-point links, referred to as FSO, provide an alternative to fiber and RF transmission when high-speed short-distance connectivity is needed. FSO links are much less expensive to deploy than fiber, as they do not require trenching. They can function at rates up to around 10 Gbps for short distances, for links of 100 m in very foggy weather and up to a few km in good weather. The primary application of FSO is as a last mile connection in urban areas, where retrofitting with fiber is difficult. Very short links, up to 200 m, are being considered as ideal approaches for backhauling signals from RF femtocells.

Recent research in FSO has focused on how to address limitations in performance caused by atmospheric fading and pointing errors. Great strides have been made in both statistical modeling of the physical channel limitations and signal processing to combat them [31,32]. MIMO processing has been shown to significantly help with both of these degradations.

There has been considerable interest also in using FSO systems to create networks by combining multiple point-to-point links. These are often envisioned as augmenting or complementing RF networks, forming so-called hybrid RF/FSO systems [33]. FSO links can serve as relays to each other or to RF links to connect locations that do not have a direct LOS [34].

### 17.7.2 DEEP SPACE APPLICATIONS

Laser communication systems have been a candidate for space communications to increase the speed of data transmission since the early days of laser development. Since 1995, there have been many laser communication system demonstrations from earth-orbiting spacecrafts to earth [35,36]. Table 17.1 lists some of the early historical milestones.

More recently, the Lunar Laser Communication Demonstration (LLCD), NASA's first high-rate, two-way space laser communications demonstration, was launched on September 6, 2013, and it set records for download and upload speeds to the Moon. This system employed 16-PPM with 1/2 rate code and interleaver to achieve data rates of 622 Mbps for the downlink (77 Mbps through thin clouds) and 20 Mbps for uplink. The first gigabit laser-based communication, called the European Data Relay System (EDRS), was achieved by the European Space Agency in November 2014. NASA's Optical Payload for Lasercomm Science (OPALS) on the International Space Station has been conducting cutting-edge research on data transmission since June 2014. In March 2015, researchers from NASA's Jet Propulsion Laboratory used OPALS to demonstrate that a laser signal from the space station can be focused into single-mode optical fibers on the ground.

**Table 17.1** Historical Milestones of Space Wireless Optical Communications

Year	Data Rate	Range
1995	1 Mbps	Ground-GTO
2001	1 Gbps	Ground-GEO
2001	50 Mbps	LEO-GEO
2005	50 Mbps	Ground-LEO
2006	50 Mbps	Aircraft-GEO
2008	5.6 Gbps	LEO-LEO

Source: Adapted from H. Hemmati, *Near-Earth Laser Communications*, CRC Press, 2009.

It is clear that optical communications will be an integral component of any future deep-space mission. It can provide 10× to 100× faster data transmission speed compared to present RF space communications. A high-speed deep space optical link will make the streaming of high-definition videos from spaceships possible, and it will enable the use of high data rate science instruments and tele-presence. Key areas of research include spacecraft disturbance isolation, photon-counting receivers, and high peak-to-average power laser transmitters.

17.7.3 VISIBLE LIGHT COMMUNICATIONS

To alleviate the RF spectral congestion problem, an idea has recently emerged to use optical energy to simultaneously provide lighting needs and downlink data transmission, so-called visible light communications (VLC), as illustrated in Fig. 17.11.

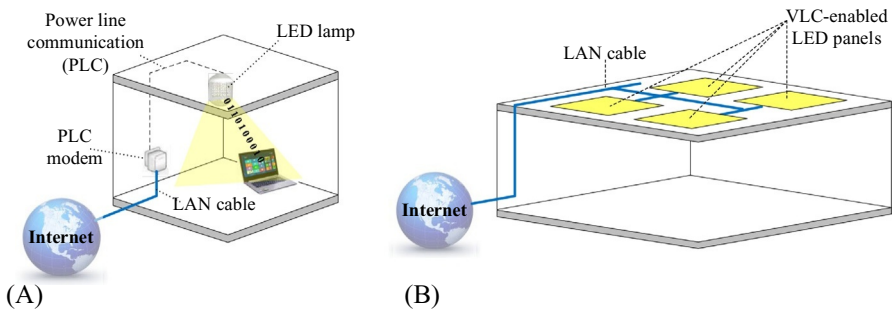


**FIG. 17.11**

Two likely visible light communication system scenarios.

Luminaires composed of dozens of white-light LEDs are mounted on the ceiling, connected to a wired network (either independent or via power-lines), and they serve as the transmission source for the downlink. Mobile users (laptop computers, cell phones, etc.) receive the signal via a photodetector that is either embedded or on a dongle. The uplink is accomplished independently using a complementary system such as RF or infrared.

VLC systems are challenging to design because they must provide high speed communications and also satisfy the lighting needs of the environment. Modern lighting systems based on LEDs are often designed to have desirable features such as dimming and color selection. Lighting systems must also be uniform (both spatially and temporally), or they can cause harm to humans; for example, *flicker* can trigger migraines or epileptic fits [37]. The design of high-rate multiuser VLC systems that conform to these features and address these health concerns is an open problem. Besides the lighting system needs, traditional technical solutions borrowed from the RF literature cannot be directly used because LEDs are incoherent sources, the transmit signal must be nonnegative, and the system tends to be limited by shot noise rather than additive white GN. An approach for resolving these issues can be found in Refs. [38,39].

One of the most compelling applications for VLC is for large unobstructed indoor spaces where many users desire simultaneous high-speed connectivity, such as conference centers and classrooms. This is an environment where Wi-Fi fails because it does not have the spectrum required and it cannot re-use its resources to provide adequate throughput. For VLC to work in these environments it must effectively provide its moderate bandwidth to many users simultaneously and, if possible, seamlessly and robustly. Many challenges remain in designing effective MAC layer support for these applications. CDMA coupled with MIMO processing could provide one viable solution [40,41].

#### 17.7.4 LANs AND PONs

Fiber systems are categorized as either long-haul or not, and their design approaches are quite different. Metro and LANs belong to the latter category. Short links often use older and less expensive technology, such as 10 Gbps OOK with direct detection. Systems are again divided into two types: passive and active. Passive optical networks (PONs) use passive optical splitters to connect a single fiber to multiple terminals, while active networks use switches and often employ optical amplifiers to reduce system losses. PONs are used for very short distances, such as distribution systems through buildings or neighborhoods, so-called last-mile solutions. Active LANs are needed for campus- and city-wide support. In recent years almost all fiber deployment, even for short links, has been SMF. Very short and inexpensive PONs sometimes use multimode or plastic fibers that are easier to splice.

### 17.7.5 LONG-HAUL TRANSPORT SYSTEMS

Our core long-haul information transport system is entirely based on WDM over SMFs using wavelength-selective switches, so-called ROADMs (reconfigurable optical add-drop multiplexers). A signal might travel optically over thousands of kilometers before being regenerated. There are millions of kilometers of fiber strung around the world, much of this under oceans, connecting all continents (except Antarctica).

Fiber optic transport networks have been evolving since the 1980s. A single fiber might carry a mixture of 10, 40, and 100 Gbps signals on various wavelengths. Older legacy systems operate at 10 Gbps using OOK and direct detection. The newer high-capacity links run at 100 Gbps using dual-polarization QPSK and coherent detection. Each fiber consists of as many as 80 wavelength channels with an equal spacing of 50 GHz.

Current estimates predict that the capacity of our fiber infrastructure will become insufficient within the next ten years or so. The majority of current research in this area attempts to address this problem, with a combination of statistical analysis, modulation/coding design, high-speed signal processing, and optical techniques [1, Ch 10].

### 17.7.6 EMERGING APPLICATIONS

Very recently there has been a surge of interest in using optics for applications that were previously ignored. Ultra-short optical links can be used on-chip as fast interconnects. Short ultra-high data rate FSO links have been proposed for use in data centers, to alleviate the clutter of fiber connections. Ultraviolet signals can be scattered by the atmosphere to create short non-LOS links that experience practically no background noise from the Sun. Underwater optical signals using blue-green lasers can transmit data over only several meters but can support Gbps rates; competing technology (acoustic communications) cannot achieve anywhere near such high data rates. As our technology continues to rely more and more on high-speed data transmission, we are bound to look towards optical communications to provide cost-effective and robust solutions.

---

## REFERENCES

- [1] G.P. Agrawal, *Fiber-Optic Communication Systems*, 4th edition, John Wiley & Sons, New York, USA, 2012.
- [2] M. Cvijetic, I. Djordjevic, *Advanced Optical Communication Systems and Networks*, Artech House, Norwood, MA, USA, 2012.
- [3] Z. Ghassemlooy, W. Popoola, S. Rajbhandari, *Optical Wireless Communications: System and Channel Modelling With Matlab®*, CRC Press, Boca Raton, FL, USA, 2012.
- [4] J.M. Kahn, J.R. Barry, Wireless infrared communications, *Proc. IEEE* 85 (2) (1997) 265–298.

- [5] V. Jungnickel, V. Pohl, S. Nönnig, C. Von Helmolt, A physical model of the wireless infrared communication channel, *IEEE J. Sel. Areas Commun.* 20 (3) (2002) 631–640.
- [6] G.P. Agrawal, *Nonlinear Fiber Optics*, fourth ed., Academic Press, San Diego, CA, 2006.
- [7] J.A. Buck, *Fundamentals of Optical Fibers*, John Wiley & Sons, Hoboken, NJ, USA, 2004.
- [8] P. Bayvel, R. Killey, Nonlinear optical effects in WDM transmission, in: I.P. Kaminow, T. Li (Eds.), *Optical Fiber Telecommunications IV-B: Systems and Impairments*, Academic Press, San Diego, CA, USA, 2002.
- [9] S. Randel, R. Ryf, A. Sierra, P.J. Winzer, A.H. Gnauck, C.A. Bolle, R.-J. Essiambre, D.W. Peckham, A. McCurdy, R. Lingle, et al.,  $6 \times 56$ -Gb/s mode-division multiplexed transmission over 33-km few-mode fiber enabled by  $6 \times 6$  MIMO equalization, *Opt. Express* 19 (17) (2011) 16697–16707.
- [10] R. Ryf, S. Randel, A.H. Gnauck, C. Bolle, A. Sierra, S. Mumtaz, M. Esmaeelpour, E.C. Burrows, R.-J. Essiambre, P.J. Winzer, et al., Mode-division multiplexing over 96 km of few-mode fiber using coherent  $6 \times 6$  MIMO processing, *J. Lightwave Technol.* 30 (4) (2012) 521–531.
- [11] D.J. Richardson, J.M. Fini, L.E. Nelson, Space-division multiplexing in optical fibres, *Nat. Photon.* 7 (5) (2013) 354–362.
- [12] R.G.H. Van Uden, R. Amezcua Correa, E. Antonio Lopez, F.M. Huijskens, C. Xia, G. Li, A. Schülzgen, H. de Waardt, A.M.J. Koonen, C.M. Okonkwo, Ultra-high-density spatial division multiplexing with a few-mode multicore fibre, *Nat. Photon.* 8 (11) (2014) 865–870.
- [13] M. Noshad, M. Brandt-Pearce, Expurgated PPM using symmetric balanced incomplete block designs, *IEEE Commun. Lett.* 16 (7) (2012) 968–971.
- [14] J. Armstrong, OFDM for optical communications, *J. Lightwave Technol.* 27 (3) (2009) 189–204.
- [15] M. Noshad, M. Brandt-Pearce, Hadamard coded modulation: an alternative to OFDM for wireless optical communications, in: *IEEE Global Communications Conference (GLOBECOM)*, IEEE, 2014, pp. 2102–2107.
- [16] M. Noshad, M. Brandt-Pearce, Hadamard coded modulation for visible light communications, *IEEE Trans. Commun.* 64 (3) (2016) 1167–1175.
- [17] G. Bosco, A. Carena, V. Curri, P. Poggiolini, F. Forghieri, Performance limits of Nyquist-WDM and CO-OFDM in high-speed PM-QPSK systems, *IEEE Photon. Technol. Lett.* 22 (15) (2010) 1129–1131.
- [18] O. Gerstel, M. Jinno, A. Lord, S.J. Ben Yoo, Elastic optical networking: a new dawn for the optical layer?, *IEEE Commun. Mag.* 50 (2) (2012) s12–s20.
- [19] M. Sjödin, P. Johannisson, H. Wymeersch, P.A. Andrekson, M. Karlsson, Comparison of polarization-switched QPSK and polarization-multiplexed QPSK at 30 Gbit/s, *Opt. Express* 19 (8) (2011) 7839–7846.
- [20] E. Agrell, M. Karlsson, Power-efficient modulation formats in coherent transmission systems, *J. Lightwave Technol.* 27 (22) (2009) 5115–5126.
- [21] M. Karlsson, E. Agrell, Four-dimensional optimized constellations for coherent optical transmission systems, in: *Proceedings of the 36th European Conference on Optical Communication*, Turin, Italy [Invited], 2010.
- [22] R.-J. Essiambre, G. Kramer, P.J. Winzer, G.J. Foschini, B. Goebel, Capacity limits of optical fiber networks, *J. Lightwave Technol.* 28 (4) (2010) 662–701.

- [23] T. Xie, S.G. Wilson, M. Brandt-Pearce, LDPC code design for OOK modulated Poisson optical channels, in: *Proceedings of the 47th Annual Conference on Information Sciences and Systems (CISS)*. IEEE, 2013, pp. 1–6.
- [24] A. Alvarado, E. Agrell, D. Lavery, R. Maher, P. Bayve, Replacing the soft FEC limit paradigm in the design of optical communication systems, *J. Lightwave Technol.* 33 (20) (2015) 4338–4352.
- [25] E. Basch, R. Egorov, S. Gringeri, S. Elby, Architectural tradeoffs for reconfigurable dense wavelength-division multiplexing systems, *IEEE J. Sel. Topics Quantum Electron.* 12 (4) (2006) 615–626.
- [26] A. Gnauck, R. Tkach, A. Chraplyvy, T. Li, High-capacity optical transmission systems, *J. Lightwave Technol.* 26 (9) (2008) 1032–1045.
- [27] M. Wu, W. Way, Fiber nonlinearity limitations in ultra-dense WDM systems, *J. Lightwave Technol.* 22 (6) (2004) 1483–1498.
- [28] L. Yan, E. Agrell, H. Wymeersch, P. Johannisson, R. Di Taranto, M. Brandt-Pearce, Link-level resource allocation for flexible-grid nonlinear fiber-optic communication systems, *IEEE Photon. Technol. Lett.* 27 (12) (2015) 1250–1253.
- [29] E. Ip, J.M. Kahn, Compensation of dispersion and nonlinear impairments using digital backpropagation, *J. Lightwave Technol.* 26 (20) (2008) 3416–3425.
- [30] D. Maiti, M. Brandt-Pearce, Modified nonlinear decision feedback equalizer for long-haul fiber-optic communication, *J. Lightwave Technol.* PP (99) (2015) 1–1.
- [31] H.G. Sandalidis, T. Tsiftsis, G.K. Karagiannidis, M. Uysal, et al., BER performance of FSO links over strong atmospheric turbulence channels with pointing errors, *IEEE Commun. Lett.* 12 (1) (2008) 44–46.
- [32] A. Farid, S. Hranilovic, et al., Diversity gain and outage probability for MIMO free-space optical links with misalignment, *IEEE Trans. Commun.* 60 (2) (2012) 479–487.
- [33] Y. Tang, M. Brandt-Pearce, Link allocation, routing, and scheduling for hybrid FSO/RF wireless mesh networks, *IEEE/OSA J. Opt. Commun. Netw.* 6 (1) (2014) 86–95.
- [34] M. Safari, M. Uysal, Relay-assisted free-space optical communication, *IEEE Trans. Wireless Commun.* 7 (12) (2008) 5441–5449.
- [35] V.W.S. Chan, Free-space optical communications, *J. Lightwave Technol.* 24 (12) (2006) 4750–4762.
- [36] H. Hemmati, *Near-Earth Laser Communications*, CRC Press, Boca Raton, FL, USA, 2009.
- [37] Epilepsy Foundation, Photosensitivity and seizures, <http://www.epilepsyfoundation.org/aboutepilepsy/seizures/photosensitivity/>.
- [38] M. Noshad, M. Brandt-Pearce, Application of expurgated PPM to indoor visible light communications—part I: single-user systems, *J. Lightwave Technol.* 32 (5) (2014) 875–882.
- [39] M. Noshad, M. Brandt-Pearce, Application of expurgated PPM to indoor visible light communications—part II: access networks, *J. Lightwave Technol.* 32 (5) (2014) 883–890.
- [40] M. Noshad, M. Brandt-Pearce, High-speed visible light indoor networks based on optical orthogonal codes and combinatorial designs, in: *IEEE Global Communications Conference (GLOBECOM)*. IEEE, 2013, pp. 2436–2441.
- [41] J. Lian, M. Noshad, M. Brandt-Pearce, Multiuser MISO indoor visible light communications, in: *Proceedings of the 48th Asilomar Conference on Signals, Systems and Computers*, November 2014, pp. 1729–1733.

# Baseband architectures to support wireless cellular infrastructure: History and future evolution

# 18

A. Gatherer\*, H. Zhu<sup>†</sup>, M. Erez<sup>†</sup>

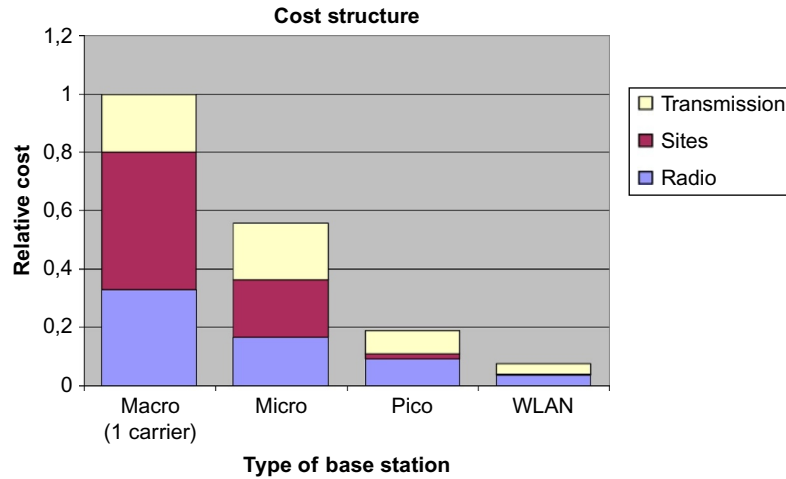
*Huawei United States, Plano, TX, United States\* University of Texas at Austin, Austin, TX, United States<sup>†</sup>*

## CHAPTER OUTLINE

<b>18.1 Overview of a Base Station and Its Components .....</b>	<b>689</b>
<b>18.2 From Voice to Broadband.....</b>	<b>691</b>
<b>18.3 From DSP + FPGA Through ASIC to SoC .....</b>	<b>693</b>
18.3.1 WCDMA and a Brief Period of Optimism in the FPGA Camp.....	693
18.3.2 DSP Plus ASIC and the Evolution of a High Bandwidth Interface....	695
18.3.3 DSP Plus ASIC to HAC-Enhanced DSP.....	696
<b>18.4 From Homogeneous Macros to Dense Small Cells and CRANs.....</b>	<b>696</b>
18.4.1 Traditional RAN Architecture.....	696
18.4.2 Dense Small Cells .....	697
18.4.3 CRAN and Resource Sharing.....	697
18.4.4 Emerging Trends .....	701
<b>18.5 Conclusions .....</b>	<b>703</b>
<b>References.....</b>	<b>704</b>

## 18.1 OVERVIEW OF A BASE STATION AND ITS COMPONENTS

The base station is the final hop provider in a large and complicated telecommunications network, bridging the last wireless gap between the operator equipment and the user's mobile device. However, the cost of the radio access part of the network is still significant, estimated at about 40% of the total cost [1], not including the cost of site build out, which is estimated at about 30–50% depending on the size of the network. So there is clear interest in reducing the cost of base station components, as well as reducing the cost of the site development for the base station. Within the

**FIG. 18.1**

Relative cost of different sized BTS.

Source: From J. Markendahl, O. Makitalo, J. Weiriding, *Analysis of cost structure and business model options for wireless access provisioning using femtocell solutions*, in: *Proceedings of the 19th European Regional ITS Conference, 2008*, pp. 18–20.

macro base station, the modem card itself can be the most expensive in the chassis and from Fig. 18.1 [2], the cost of a small (pico) cell base station is only about 20% of a macro.

Fig. 18.1 also shows that wireless LAN access points are less than half the cost of even a picocell. This is true even though a single cell of four antenna, 20 MHz LTE has a throughput of 300 Mbps compared to 600 Mbps for a four antenna, 40 Mbps 802.11n. Hence the throughput per hertz is very similar. The difference in cost can be related to the need for spectral efficiency in a multiuser environment in LTE where many users can be simultaneously supported, each using a fraction of the spectrum in which the user has good SNR for that symbol. Indeed, the silicon cost of supporting the management of all these users across the spectrum, called radio resource management, which is a layer 2 functionality, is comparable to the cost of the modem itself in layer 1. On top of that, the complexity of the layer 1 modem is significantly affected by the need to combine and separate many users, both in the cost of on chip memory and significant use of DDR on the board, needed for storage of a great amount of user data waiting for transmission to complete. These two requirements may greatly help explain the over 50% drop in complexity from LTE picocell to 802.11 LAN. The value of multiuser support in LTE needs to be justified at the network capacity layer. Studies have shown its clear value for macrocell networks, but the value is not so clear for a dense network of small cells where the number of users per cell is much smaller. At the same time, the value of

coordinated multipoint (CoMP), interference cancelation, and avoidance, as well as other interference management technologies becomes more apparent. This requires a significant change in the nature of the base station hardware, as well as the amount of control and interbase station signaling required.

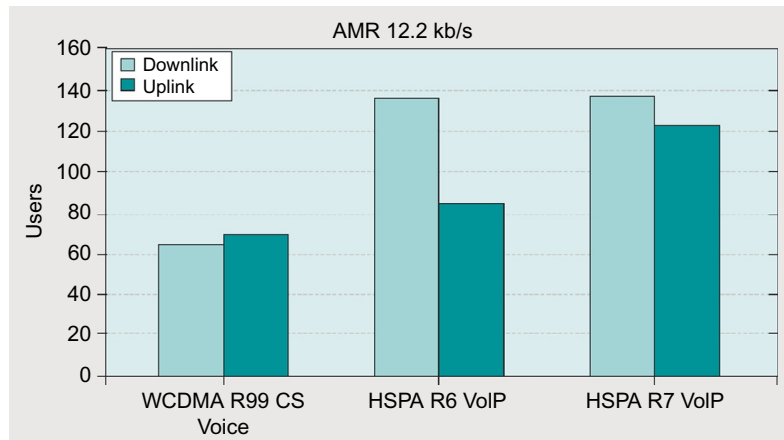
In Ref. [3], as well as other papers, we have seen a strong argument for the use of centralized RAN to increase the flexibility and coordination of base stations. This comes at the price of more backhaul from the Remote Radio Head (RRH), though the RRH is now much simpler, cheaper, and easier to install.

Though traditionally the majority of the power consumed by a base station was in the power amplifier (PA), the move to denser networks has changed this balance dramatically. Whereas a classical macro base station sector may have four antennas each radiating tens of watts at 20% efficiency, meaning the total PA dissipation is at 200 W or more, a small cell may have four antennas radiating at less than a watt each and an efficiency of 40%, giving a PA dissipation of 10 W. However, both systems will use a similar amount of baseband signal processing, probably in the range of 5 W/sector. Hence, the baseband power has become more critical to efficient processing.

---

## 18.2 FROM VOICE TO BROADBAND

Traditional 2G voice-only networks required a very specific amount of processing per cell. GSM capacity was measured in terms of users and the more complicated CDMA standard was measured in terms of “channel elements” (CEs). For CDMA, there was some efficiency to be gained by pooling the despreading resources, but many base station architectures assigned a fixed number of fingers per user and the operators measured the capacity for a worst-case scenario where the number of fingers per user was fixed. Hence, the original 2G baseband infrastructure architectures were conceptually simple, with each user being assigned a fixed portion of the hardware or being processed at a fixed time on a shared resource (as was common for viterbi decoding). If we fast forward to today, we see modems that must cope with a brand new set of users and their requirements every millisecond (probably going to 0.1 ms in 5G) with some users needing more resources than others for that millisecond. A requirement that could be analyzed by a systems engineer and “a worst case scenario” before the design was complete must now be calculated in one or, usually, multiple processors. The challenge is to know if a particular set of requirements is feasible, that is, can it be performed in real time by the hardware. This is a competing problem to the radio resource management problem, which attempts to make best use of the radio spectrum and therefore may request infeasible resource use to achieve its goal. This issue is not discussed in the literature as far as the authors are aware, but it appears in the literature to address the similar problem of managing network power. For instance, in Ref. [4] the energy efficiency of a network as the spectral efficiency changes is shown to have a maximum point with the energy efficiency then dropping off asymptotically, and often quite dramatically, to zero as we try to reach

**FIG. 18.2**

Voice capacity comparison for different versions of the WCDMA standard.

Source: From H. Holma, et al., *High speed packet access evolution in 3GPP release 7*, *IEEE Commun. Mag.* 45 (12) (2007) 29–35.

for higher spectral efficiency. We will examine this in more detail in [Section 18.4.4](#). The paradox for the system design engineer is that data can suffer more latency and even require opportunistic transmissions to increase spectral performance. This allows for much more creativity in how data is delivered and hence much more spectral capacity. It was shown as early as 2007 [5] that with the improvements in HSPA over WCDMA Rel.99, the HSPA packet network should achieve higher *voice* capacity than the Rel.99 system that was specifically designed for voice. This result is shown in [Fig. 18.2](#). But it must be noted that the industry still struggles to achieve this theoretical gain from voice over LTE (VoLTE).

Tipping to data-only allowed the PHY to employ new technologies and remove old ones. For instance, the soft handoff that was designed to improve voice quality as the mobile moved between sectors was replaced by cooperative multipoint (CoMP), intercell interference coordination (ICIC), and interference avoidance (IA), all of which were designed to maximize network capacity. These new technologies required much more processing power that is used in a speculative and sometimes recursive manner, making the total amount of processing required hard to predict.

The progression of the data transport standard in 3GPP from HSPA through LTE and now into 5G has shown some clear trends that pose clear challenges to hardware design:

1. Reduction in the size of the transport block (the TTI) from 10 to 1 ms now going down to 0.5 ms and even to 0.1 ms for 5G. This reduces the opportunity for parallelism in processing and places even more pressure on the critical path latency requirements for hardware.

2. Sophisticated radio resource management strategies require more processing to implement but also force much more storage on the system because packets of data are now waiting around for “just the right moment” to be transmitted. More spectrally, efficient strategies for redundant coding mean more access to these stored packets to update the state of the packet before it is completely transmitted. This puts an enormous strain on access to off-chip memory (universally implemented using DDR today), as there is not enough memory on the chip to store all this data.
3. CoMP requires different sectors to cooperate at the antenna level. Realistically, today, this can only occur for sectors supported on the same modem card or perhaps neighboring cards in the same chassis. But this means that a large chunk of the latency budget must be allocated to the time it takes to move antenna data between SoC on the board.

This trend toward more off chip storage along with lower latency to turn around a TTI put enormous pressure on the DDR memory interface. This is because the memory interface is not scaling with Moore’s law due firstly to its analog nature, interfacing to memory across the board, and secondly, due to its size being determined by the bump pitch of the package, which also is not scaling. The trend toward higher capacity DDR3 and now DDR4 has come with a lower total utilization of the DDR due to more complex access methods. Also, the shorter TTI means that DDR access can be bursty with a high peak to average ratio that is hard to schedule away.

Solving this issue may require new peripheral access technologies such as through silicon vias (TSVs). TSVs allow data to be removed from the chip over the whole volume, not just the edge, but they require significantly more expensive packaging technology, such as silicon interposers. This problem is also faced by high end computer server chips, but in that case the device cost is much larger than that of the base station, and therefore, the packaging cost is relatively inexpensive. Base station chips traditionally only budget less than a dollar per chip for packaging and use forced air cooling only. 3D, stacked die structures then become difficult to budget and even 2.5D structures, multichip modules (MCM) with silicon interposers, can be well out of the desired price range. We expect that as the industry struggles toward 5G cellular, it will have to change its cost structure and place a greater percentage cost on packaging and less on silicon.

---

## 18.3 FROM DSP + FPGA THROUGH ASIC TO SOC

### 18.3.1 WCDMA AND A BRIEF PERIOD OF OPTIMISM IN THE FPGA CAMP

The story of hardware development in cellular modems until now is of interest as many of the same industry dynamics exist today and will play out in the development of the 5G network. As the first WCDMA systems came online in the late 1990s, operators interested in maximizing their GSM investment encouraged the

development of new GSM-based TDMA technologies to create higher bandwidth in the existing system as well as more flexibility to support data services. This led to EDGE (enhanced data rate for GSM evolution), which significantly increased the complexity of GSM modems. EDGE took GSM from GMSK to 8PSK and added incremental redundancy. So both the computational complexity and the storage requirements increased. Evolved EDGE then added turbo codes. Several network OEMs, notably Ericsson and Nokia, competed for this rapidly evolving business and had solutions with a great amount of software to keep the solutions flexible for the new evolution. In the same time frame, Qualcomm provided many enhancements to CDMA, going to CDMA2000 and then onto EVDO, which was a data-only solution. As Qualcomm remained mostly in control of all these enhancements, it developed its own internal modem hardware to keep pace with their planned evolution. But their customers in the United States, Nortel, Motorola, and Lucent, also needed to support the emerging WCDMA standard, and as a result, we saw an opening up of the hardware and Qualcomm backed away from providing base station solutions in favor of handset silicon.

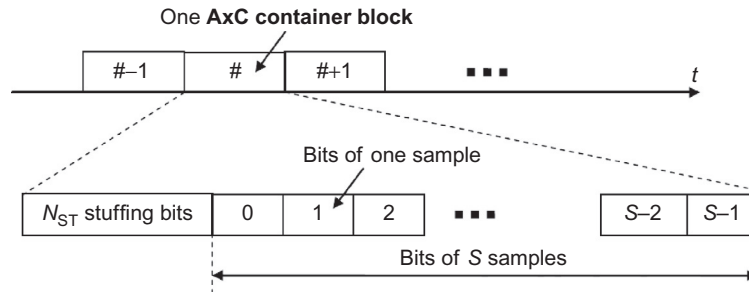
By the 2000s, most base station modems for the emerging WCDMA standard contained a DSP chip of some kind that supported symbol rate processing with on chip acceleration for turbo and Viterbi decoding. These chips came from silicon DSP vendors, TI, ADI, LSI, etc. They were a great example of “integration is king” because the OEMs initially thought they could differentiate with better architectures, and even algorithm improvements, for turbo and Viterbi decoding. But the cost of maintaining their own development teams, as well as the cost reduction they could get from the silicon vendors, integrated designs, forced them to hand error correction decoding to the silicon vendors. The rest of the modulation signal processing was supported on FPGA to allow for flexible upgrades in design. The FPGA companies, principally Xilinx and Altera, felt that this could become a long-term trend but they knew that they needed to move toward a complete solution. So the battle lines were drawn between the DSP and the FPGA suppliers to see who could provide a complete integrated solution. In the meantime, many OEMs looked toward developing their own ASICs to replace the FPGA and perhaps the DSP parts once the standard settled.

Unfortunately for the FPGA companies the trend as the silicon vendors’ integrated designs matured was toward hardening the high bandwidth, computing intensive operations such as FEC, spreading, bit processing, and leaving the lower computational complexity estimation algorithms programmable. Estimation algorithms such as channel estimation, frequency estimation, and complex decision processes to decide on parameter values tend to keep evolving as they are not part of the standard and small tweaks can produce decent capacity gains. But these algorithms were irregular and had many decision points and “change of flow” in them, and they were better suited to a DSP. Therefore the FPGA companies saw several years of hopeful progress but were eventually replaced by hardwired ASIC with DSP and CPU processors integrated into an SoC. We expect the same trend moving through 5G and therefore expect to see FPGA dominate the new modem cards, perhaps through 2020 or a little later, and it will then be gradually replaced by more hardwired solutions.

### 18.3.2 DSP PLUS ASIC AND THE EVOLUTION OF A HIGH BANDWIDTH INTERFACE

In the 1990s, the DSP chips were connected to the FPGAs or operator-developed ASICs using a memory interface, simply because that was available on the DSP. As DSPs became more common in wireless infrastructure, there was a recognized need for a more efficient interface between the DSPs and the ASIC/FPGA, as well as between DSPs. The industry gradually moved toward RapidIO as a solution. RapidIO is a peer-to-peer protocol, which initially came from the military space, with both an address-based format as well as a packet-based format. Connection between the DSPs quickly moved to RapidIO as the DSPs started to support it, but interconnection to the FPGAs often remained as a memory interface as the FPGAs did not support RapidIO as a hard macro, and therefore, RapidIO remained an expensive interface on the FPGA side. FPGAs supported PCI Express because of its connection to Intel processors, but this was not suitable for the kind of low latency, high reliability, and peer-to-peer connection required in wireless infrastructure. For a somewhat biased, but essentially correct, analysis of RapidIO versus PCIExpress, see Ref. [38]. In this article, there is also a comparison to Ethernet. In this case, the difference to RapidIO is not so severe and there exists a desire among chip developers that Ethernet could replace RapidIO, even if it is not quite as efficient, because we could then take advantage of lower cost Ethernet routers, as well as reduce the number of routers and lines on the modem card, as Ethernet has to be supported anyway. But this has yet to happen in the majority of chips for wireless infrastructure.

The other main interface on the wireless modem chip is the Common Public Radio Interface (CPRI), which is designed exclusively for the antenna data. This interface was standardized in order to allow different RF equipment to talk to the same baseband modem card. It was hoped that this would reduce the cost and increase flexibility in the network. It had a competitor standardization effort called Open Base Station Architecture Initiative (OBSAI) [6] that was generally less successful. The problem with both standards remains the use of a frame format for the data (see Fig. 18.3). This was adopted because it was how antenna data was usually input in proprietary formats, but also because it was seen as a low timing jitter solution. Low timing jitter is a critical requirement for antenna data as it is in the critical path of signal processing. However, this meant that the standard was inflexible to changes and different variants had to be added to support GSM, CDMA, WCDMA, WiMax, and LTE. Additionally, the addition of control and Ethernet over RapidIO led to more complexity. CPRI also suffered from many different formats to support individual OEM requirements, meaning that it was not tremendously interoperable. It is the authors' opinion that a packet-based protocol would have much more flexibility and a much lower gate count on the chip, and the jitter issue could be managed. But, at this time, CPRI will be the protocol for some time to come.

**FIG. 18.3**

Example frame structure with bit stuffing from CPRI standard.

Source: From Common Public Radio Interface (CPRI), [www.cpri.info](http://www.cpri.info).

### 18.3.3 DSP PLUS ASIC TO HAC-ENHANCED DSP

In the late 1990s and 2000s, the commercial DSP manufacturers pushed to get OEMs to buy an integrated chipset and stop doing their own SoCs. Analog Devices took the path of developing their own close to a traditional software-defined radio (SDR) [8] and other smaller companies also tried to develop soft modem solutions [9]. But these solutions proved to be expensive and difficult to program, and there simply was not enough variation in the implementations to warrant a flexible solution. Instead, more hardwired solutions became the norm, with Texas Instruments dominating the commercial chip vendors [10] using hardware accelerators to implement most of the high performance signal processing. The challenge to this strategy at the OEM was not only a loss of control of the ASIC implementation but also a loss of the ability to debug the ASIC/DSP interface on the board. This led to a great amount of focus on on-chip trace and debug technology, coupled with sophisticated system trace visualization software. Another challenge came when the process node allowed multi DSP SoC to be developed. This allowed greater channel density on-chip and therefore cheaper solutions, but this came with great challenges to the programming model, memory map, and trace and debug. Management of coherency of data, which was already a solved problem in standard multicore processors, became a big issue for modems because of the real time constraints of the chip.

## 18.4 FROM HOMOGENEOUS MACROS TO DENSE SMALL CELLS AND CRANS

### 18.4.1 TRADITIONAL RAN ARCHITECTURE

In the classical model of the cellular network, all cells are of the same size and have the same capacity. This would allow a single SoC to be efficient across all cells. However, in real networks, the cell size varies greatly, as does the capacity

of the cells. Different environments produce markedly different requirements on the modem. An example is the difference between a small, dense urban cell and a large, sparse rural cell. In WCDMA, the large rural cell will use most of its processing power to look for random access from new users. This is because the cell is large and the RACH channel has to search over the whole cell. In a dense urban environment, the RACH is a much smaller part of the processing and data and voice disspreading and decoding takes up most of the processing. Dense and rural cells are extremes but together may make up well over 20% of the total network deployment. The OEM is therefore faced with the problem of developing a chipset for the bulk of the network but also making it efficient for the extremes.

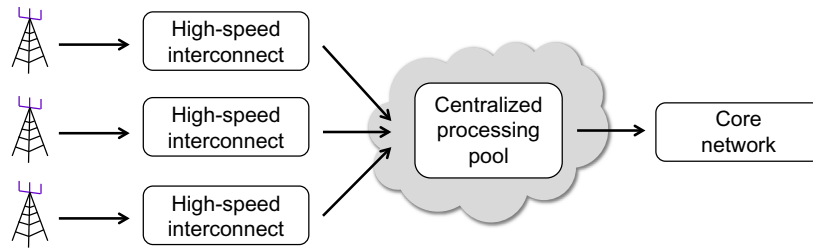
### 18.4.2 DENSE SMALL CELLS

Most capacity increase must be obtained by a reduction in cell radius. So the high density of antennas is a necessity in urban environments. For the modem SoC, this presents a problem as the cost of the chip does not scale down well with cell size. This is because much of the processing scales with user density rather than cell size. This is true of all control channel processing and estimation, generally. Symbol and bit processing scales with data rate rather than cell size and front-end signal processing scales somewhat with the number of antennas. A small cell also does not have a very stable user density over time as it is only supporting a relatively few users. Therefore it sees a “feast or famine” effect, where it may have zero users for a significant percentage of its time and then see a large data rate from a few users. This swing in processing requirements may occur over a relatively short time period. Small cells also need to cope with rapid handover as users pass quickly through their small cell size. Therefore the utilization of small cell hardware can be very low (less than 20% would not be surprising), and this leads to an expensive network solution compared to the traditional macrocell. “Hoteling” of resources into what is now called a Cloud RAN is therefore a seemingly attractive option, and we shall discuss this in some detail in the next section.

### 18.4.3 CRAN AND RESOURCE SHARING

A new architecture called Cloud RAN or CRAN has been proposed to reduce the ever-increasing cost of RAN [3]. The key idea is to deploy RRHs that are geographically separate from the baseband units (BBUs). A plurality of RRHs is connected to, and shares, a common baseband processing pool through a high-speed interconnection network. This architecture is illustrated in Fig. 18.4.

By separating the processing units from the radio units, baseband computation can be “virtualized” in the RAN, that is, the details of the computing resource organization are isolated from the rest of the network. This provides the radio network with the benefits cloud computing offers other industries, and additionally offers significant improvements unique to the RAN context. These benefits are detailed below.

**FIG. 18.4**

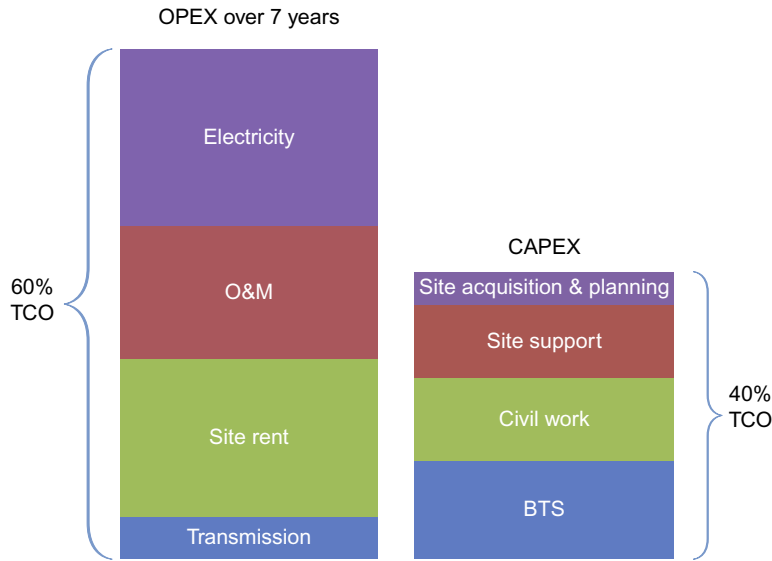
Structure of Cloud RAN.

### 18.4.3.1 Collaborative transmission technology

By centralizing the baseband processing of multiple cells, BBUs processing one cell can easily and rapidly exchange information with those BBUs working on adjacent cells. While there is nothing preventing base stations from exchanging information in a traditional RAN, the signal has to go through slower Ethernet and there are typically no direct links between base stations; the information would be stale by the time it arrives. CRAN solves the communication problem by collocating BBUs and connecting them to RRHs using a high-speed interconnection network. This enables more complex and aggressive radio transmission technology that optimizes on a global scale and improves performance for cell-edge users. An example of such a technology is intersite cooperative multipoint processing (CoMP) [11].

### 18.4.3.2 Statistical resource provision and lower CAPEX

Studies have shown that BBUs are not fully utilized at all times; rather, workloads for different cells fluctuate on many different time scales [3]. User migration between a business and residential area is one of the reasons that leads to this fluctuation, resulting in a tide-like workload variation throughout a day. On a finer scale, the number of active users in a cell and their activity are constantly changing too, leading to workload fluctuation occurring on the order of a minute or less. A traditional RAN architecture cannot efficiently handle such fluctuation. The typical solution is the overprovision resources to meet peak throughput demands. CRAN, on the other hand, can take advantage of the fluctuation and provision computing resources based on a statistical QoS guarantee to reduce the baseband hardware requirements [12,13]. The larger the coverage of a CRAN is, the more benefit it can provide by exploiting workload fluctuation. Pooling can also provide more reliable service: if a node in the baseband pool goes down, another node can easily pick up the work. As a result, CRAN can achieve the same level of service quality with much lower capital expenses. The famous diagram outlining the potential savings comes from a China Mobile study [3] and is shown in Fig. 18.5.

**FIG. 18.5**

CRAN CAPEX and OPEX.

Source: From Y. Chen, *Fundamental tradeoffs in green wireless networks*, *IEEE Commun. Mag.* 49 (6) (2011) 30-37; China Mobile Whitepaper, *CRAN the road towards green RAN*, 2011.

### 18.4.3.3 Transparent BBU pool scaling and virtualization

CRAN provides the wireless carriers with the flexibility of changing the amount of computing hardware after the RAN is built, thanks to the decoupling of BBUs from RRHs. Wireless carriers can easily expand the capacity of a baseband pool, which further helps to avoid resource overprovisioning by limiting initial investment to known needs. Decoupling the RRHs and BBUs also enables wireless carriers to virtualize BBUs. An example would be a complete SDR implementation of BBUs, where a wide range of baseband computation is done in software [14] and BBUs can be virtualized to support different wireless technology (2G, 3G, LTE, etc.) as they coexist. While this is an extreme case and may not be the most efficient one, CRAN certainly enables more freedom in resource organizing and sharing. Virtualization of the RRHs with respect to the BBU operation also allows for a virtualized association of antenna data and the baseband function, allowing dynamic management of cell size and shape to meet short-term user needs, even on a millisecond by millisecond basis, such as in the Airvana OneCell product [39].

### 18.4.3.4 Low OPEX

The most direct benefit of collocating the computing resource is the lower OPEX cost. Without the consolidation of CRAN, wireless operators must rent multiple geographically scattered sites, each of which houses and powers a small amount of

hardware. However, CRAN fundamentally changes the RAN architecture—all the BBUs can be housed, powered, and cooled together at a centralized location. Power can make up 50% of the OPEX, according to the China mobile report [3]. As a result, site rental costs drop significantly. Furthermore, powering and cooling BBUs is done at a higher density and at larger scale, and thus a higher efficiency.<sup>1</sup> Statistical provisioning of BBU resources and virtualization of BBUs can further reduce the power requirements of a CRAN. All these factors lead to much lower OPEX for CRAN compared to a traditional RAN architecture.

#### ***18.4.3.5 Progress in CRAN deployment***

Despite all the benefits CRAN can bring, many challenges still remain and many possible performance and efficiency optimizations remain unexplored. The interconnection network is a very expensive component, in particular when considering its large geographic span. Thus, available bandwidth is likely to be very limited and compression is necessary. However, baseband processing has stringent real-time constraints, which also constrain the latency of the network and the latency of compression/decompression, making the bandwidth problem even more challenging. There has been considerable commercial effort on antenna data compression and some academic work, but so far the amount of compression reported remains in the low single digits (around  $3\times$ ) [16,17]. There is also a large design space to explore in the BBU hardware organization. The options and tradeoffs are closely tied to the baseband processing algorithms because the algorithms specify the granularity of resource sharing, requirements of interconnection between BBU modules, efficiency of virtualization, etc. Problems like load scheduling and load balancing, which are typically found in traditional large-scale compute and cloud servers, are also likely to emerge. Finally, there are subtle trade-offs between the size of the CRAN and its efficiency. As the coverage of a CRAN becomes larger, the CAPEX and OPEX overhead becomes lower, while the radio transmission delay and management overhead take away time from baseband processing. Furthermore, different cells can have different activity levels, leading to a complex optimization process for deciding how to partition cells between multiple CRAN installations, where a single CRAN installation is limited in size by link length and total processing capability. At this time we expect, and indeed observe, that CRAN type architectures are gradually making progress, mainly in dense traffic areas, where there are many RRHs in a small region and the distance from the compute server and the RRHs is relatively small. We also note that CRAN has been most popular so far in Japan and parts of China due to the large amount of available fiber already installed in these areas.

The proposal of the CRAN structure is the result of continuous research in the RAN architectures and interconnection technologies. A similar concept named Base Station Hoteling was proposed in the early 2000s [18]. The idea of hoteling is

---

<sup>1</sup>Google estimates that its cloud computing service, Google Apps, can help reduce energy for powering and cooling servers by 70–90% [15].

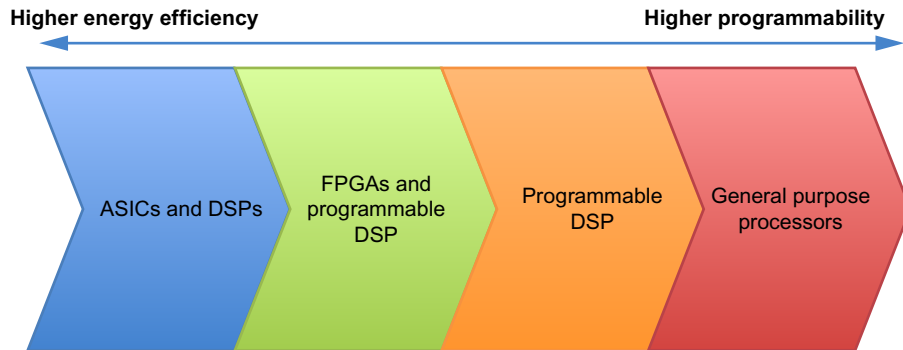
to geographically collocate BBUs for cells that were shrinking in size to reduce maintenance cost. CRAN differs mainly by enabling collaborative radio technologies such as CoMP and statistical BBU resource provision. There is another large body of research work on fiber interconnection carrying radio signals, or Radio over Fiber [19]. In terms of the logical partition of the RAN architecture, much work has been done in standardizing the interface between RRHs and the BBU pool such as CPRI [7] and OBSAI [6]. Finally, the radically new architecture of CRAN enables many other innovative technologies that have been common in the Internet world. For example, a wireless operator can create content caching local to the coverage of a CRAN to reduce the bandwidth requirement on the backhaul (connection between BBU pool and operator servers) [20].

#### 18.4.4 EMERGING TRENDS

Traditional baseband processing relies on multiple fixed-function accelerators that are each designed and tuned for a single specific wireless communication standard. This specialization helps in achieving required processing performance but comes with high development, manufacturing, and maintenance costs. With advances in VLSI technology, the necessary performance is now possible, even with programmable baseband processors—an approach known as SDR [21,22]. SDR is very appealing because it simultaneously increases hardware utilization and eases technology upgrades; instead of purchasing new hardware that must run simultaneously with older hardware to support transitioning to a new communication technology, hardware can be reprogrammed and resource allocations gradually adapted from older to newer standards. In addition, commodity programmable processors can be used to implement SDR, potentially further reducing cost.

While SDR offers significant benefits, important tradeoff decisions must still be made with respect to how generic and flexible the processors are [37]. Fig. 18.6 shows the spectrum of the processing options that have been explored over the years. Traditionally, most of the heavy lifting was carried out by various application-specific integrated circuits (ASICs) that had moderate programmability [10]. ASICs were necessary because processor performance was limited by transistor count. More recently, flexible solutions that use a reconfigurable processing element, such as field-programmable gate arrays (FPGAs) instead of ASICs, have been studied [23–25]. Unlike fixed-function ASICs, FPGAs can be reprogrammed dynamically, although the development effort is still high and significantly higher than writing new software. Therefore, there has also been significant interest in truly programmable baseband processors.

One style of programmable processors integrates the functionality of FPGAs or ASICs into enhanced digital signal processors (DSPs) [26–28]. These designs not only exploit the data level parallelism inherent to baseband processing workloads but also include domain-specific features that are tuned for baseband processing, such as specialized shuffle networks and arithmetic units. A more radical departure from specialized processors and the adoption of very general fully programmable hardware

**FIG. 18.6**

SDR processing option spectrum.

is an attempt to use off-the-shelf CPUs to process all the tasks of the physical layer processing [29,30]. Such solutions potentially enable wireless operators to further reduce the cost to build and upgrade RAN infrastructure with commodity off-the-shelf CPUs. Current CPUs have a large, and growing, number of cores and integrate single-instruction multiple-data (SIMD) units within each core. With this high level of parallelism, commodity CPUs can now meet the performance demands of even advanced physical-layer processing.

While there is a large spectrum for possible processing options, the fundamental tradeoffs remain the same. Programmable and reconfigurable processing elements are more flexible in that they can work with different signal frequencies, modulations, and coding schemes, and even completely different channel access methods and processing pipelines. This allows wireless operators to reuse hardware resources when migrating to new wireless technologies. Consolidating the functionality of ASICs into fewer processing elements also greatly reduces the cost of both hardware and software development. Finally, flexible RAN equipment can enable even better resource utilization through a more sophisticated resource scheduling strategy such as dynamic resource allocation between different wireless communication technologies. However, these benefits come at the price of energy efficiency and performance, because fewer opportunities for low-level specialization and hardware tuning are available with commodity parts than with specialized fixed-function accelerators. Previous work suggests that the performance and efficiency gap can be  $10\times$  to  $100\times$  between ASICs and general purpose processors [31]. With the expected slowdown of device scaling and the benefits it provides for performance and energy-efficiency, the tradeoff between energy efficiency and programmability in baseband processing hardware is becoming more important than ever.

In addition to the concept of programmable wireless communication, the proposal of SDR further led to other innovations in the RAN that are based on more flexible and intelligent systems, including CRAN, OpenRadio, and Cognitive Radio. CRAN,

for example, is an excellent match for baseband processing units that are enabled by SDR, even though such units are not required for CRAN.

Another example is OpenRadio, which is a technology that provides a clean interface between the RAN infrastructure and the service it provides [32,33]. This is in contrast to traditional RANs in which the hardware is tightly coupled with the wireless communication standard it supports. OpenRadio explicitly exploits the flexibility that SDR provides and allows easy deployment of software in the RAN equipment. All wireless transmission services in an OpenRadio system are represented using abstract and modularized control description, which in turn invokes predefined computing functions provided by the OpenRadio infrastructure. Details of the physical organization of the RAN, mappings of tasks onto the processing elements, and implementation of the computing functions are determined by the OpenRadio and hidden from programmers of the service. OpenRadio works like an operating system running on all the RAN equipment to allow wireless operators to manage the RAN resources more easily.

The last example of the possible impact of SDR is Cognitive Radio. The goal of Cognitive Radio is to improve the utilization of scarce radio resources by allowing devices to jump from busy frequency bands to vacant ones [34,35]. To achieve this goal, a Cognitive Radio system has to constantly change transmission parameters (including frequency, modulation, and even the wireless transmission technology) based on the interaction with the radio environment [36]. Therefore, such systems require great programmability and flexibility that can only be provided by SDR-enabled RAN equipment. By making full use of the radio frequency resource, Cognitive Radio can provide better connectivity for wireless devices as more clients are connected to the network.

---

## 18.5 CONCLUSIONS

This is a time of great change and challenge in infrastructure modem development. In the last 20 years, the baseband modem has gone from being a simple fixed-function bitpipe using several discrete chips, to a sophisticated heterogeneous multicore real-time system based on SoCs that support many channels and multimode operations. As we move on to 5G, higher user capacity and data throughput requirements demand even greater improvements in performance and efficiency from wireless infrastructure. On the network level, CRAN solutions are proposed to attack challenges in the dense cellular environment; CRAN allows wireless infrastructure to exploit the benefits of consolidated cloud computing infrastructure and enables more sophisticated physical layer processing. On the baseband architecture level, higher data capacity in the new standard requires new SoCs to address the bottlenecks in memory access latency and bandwidth. Evolution in the network level also brings new architecture challenges to the baseband modem SoC designs. Softening the baseband platforms allows more flexibility in scheduling and reusing hardware resources and reduces the cost for the wireless operators to upgrade their infrastructure. Overall, the wireless

infrastructure will continue to evolve with the drive from advancing VLSI and interconnection technology, as well as standardization efforts in the new wireless interface.

We have seen the wireless base station over the last 20 plus years, constantly changing in substantive ways, and we continue to expect it to do so. Most of the change is due to business, cultural (ecology, the rise of the emerging markets), and engineering capabilities, and it is not dominated just by changes to the cellular standards.

---

## REFERENCES

- [1] K. Johansson, Relation between basestation characteristics and cost structure in cellular systems, in: IEEE Symposium on PIMRC, 2004, pp. 5–8.
- [2] J. Markendahl, O. Makitalo, J. Weiriding, Analysis of cost structure and business model options for wireless access provisioning using femtocell solutions, in: Proceedings of the 19th European Regional ITS Conference, 2008, pp. 18–20.
- [3] China Mobile Whitepaper, CRAN the road towards green RAN, 2011.
- [4] Y. Chen, Fundamental tradeoffs in green wireless networks, *IEEE Commun. Mag.* 49 (6) (2011) 30–37.
- [5] H. Holma, et al., High speed packet access evolution in 3GPP release 7, *IEEE Commun. Mag.* 45 (12) (2007) 29–35.
- [6] Open Base Station Architecture Initiative (OBSAI), [www.obsai.com](http://www.obsai.com).
- [7] Common Public Radio Interface (CPRI), [www.cpri.info](http://www.cpri.info).
- [8] K. Lange, et al., A software solution for chip rate processing in CDMA wireless infrastructure, *IEEE Commun. Mag.* 40 (2) (2002) 163–167.
- [9] picoChip samples “software system on chip” (SSoC) to cut the cost of 3G infrastructure, <http://www.design-reuse.com/news/4864/picochip-samples-software-system-chip-ssoc-cut-cost-3g-infrastructure.html>.
- [10] Z. Lin, G. Wood, TI’s High-Performance LTE Physical Layer Solution, Texas Instruments, Dallas, TX, 2011.
- [11] R. Irmer, et al., Coordinated multipoint: concepts, performance, and field trial results, *IEEE Commun. Mag.* 49 (2) (2011) 102–111.
- [12] S. Bhaumik, et al., Cloudiq: a framework for processing base stations in a data center, in: Proceedings of the 18th Annual International Conference on Mobile Computing and Networking, ACM, 2012.
- [13] H. Zhu, A. Gatherer, M. Erez, Fog-RAN: hardware resource sharing in aggregated baseband processing systems, in: Design Automation Conference Poster, San Francisco, CA, 2014.
- [14] J. Mitola, Cognitive radio—an integrated agent architecture for software defined radio, PhD Thesis, Royal Institute of Technology (KTH), Sweden, 2000.
- [15] Google, Google Apps: energy efficiency in the cloud, 2012, [www.google.com/green/pdf/google-apps.pdf](http://www.google.com/green/pdf/google-apps.pdf).
- [16] B. Guo, W. Cao, A. Tao, D. Samardzija, CPRI Compression transport for LTE and LTE-A signal in C-RAN, in: Proceedings of the 7th International Conference on Communications and Networking in China (CHINACOM), 2012.

- [17] K.F. Nieman, B.L. Evans, Time-domain compression of complex-baseband LTE signals for cloud radio access networks, in: *Proceedings of the IEEE Global Conference on Signal and Information Processing (GlobalSIP)*, 2013.
- [18] D. Wake, Trends and prospects for radio over fibre picocells, in: *Proceedings of the IEEE International Topical Meeting on Microwave Photonics*, 2002.
- [19] H. Al-Raweshidy, S. Komaki, (Eds.), *Radio Over Fiber Technologies for Mobile Communications Networks*, Artech House, London, UK.
- [20] A. Vakali, G. Pallis, Content delivery networks: status and trends, *IEEE Internet Comput.* 7 (6) (2003) 68–74.
- [21] S.M. Blust, *Software Defined Radio-Industry Request for Information*, BellSouth Wireless, Inc., Atlanta, 1995.
- [22] J. Mitola, Software radio architecture: a mathematical perspective, *IEEE J. Sel. Areas Commun.* 17 (4) (1999) 514–538.
- [23] S. Haruyama, FPGA in the software radio, *IEEE Commun. Mag.* 37 (2) (1999) 109.
- [24] J.-P. Delahaye, et al., Software radio and dynamic reconfiguration on a DSP/FPGA platform, *Frequenz* 58 (5–6) (2004) 152–159.
- [25] D. Lund, B. Honary, M. Darnell, A new development system for reconfigurable digital signal processing, in: *Proceedings of the First International Conference on 3G Mobile Communication Technologies (Conf. Publ. No. 471)*, IET, 2000.
- [26] Y. Lin, H. Lee, SODA: a low-power architecture for software radio, in: *Proceedings of the 33rd International Symposium on Computer Architecture (ISCA'06)*, 2006.
- [27] M. Woh, et al., From SODA to scotch: the evolution of a wireless baseband processor, in: *Proceedings of the 41st IEEE/ACM International Symposium on Microarchitecture, MICRO-41*, IEEE, 2008.
- [28] M. Woh, et al., AnySP: anytime anywhere anyway signal processing, *IEEE Micro* 30 (1) (2010) 81–91.
- [29] K. Tan, et al., Sora: high-performance software radio using general-purpose multi-core processors, *Commun. ACM* 54 (1) (2011) 99–107.
- [30] Vanu, Inc., *The Vanu Anywave Base Station Subsystem*, Vanu, Inc., Cambridge, MA, 2006.
- [31] R. Hameed, et al., Understanding sources of inefficiency in general-purpose chips, *ACM SIGARCH Comput. Archit. News* 38 (3) (2010) 37–47.
- [32] M. Bansal, et al., OpenRadio: a programmable wireless dataplane, in: *Proceedings of the First Workshop on Hot Topics in Software Defined Networks*, ACM, 2012.
- [33] A. Gudipati, et al, SoftRAN: software defined radio access network, in: *Proceedings of the second ACM SIGCOMM Workshop on Hot Topics in Software Defined Networking*, ACM, 2013.
- [34] S. Haykin, Cognitive radio: brain-empowered wireless communications, *IEEE J. Sel. Areas Commun.* 23 (2) (2005) 201–220.
- [35] J. Mitola, G.Q. Maguire Jr., Cognitive radio: making software radios more personal, *IEEE Pers. Commun.* 6 (4) (1999) 13–18.
- [36] I.F. Akyildiz, NeXt generation/dynamic spectrum access/cognitive radio wireless networks: a survey, *Comput. Netw.* 50 (13) (2006) 2127–2159.
- [37] T. Ulversoy, Software defined radio: challenges and opportunities, *IEEE Commun. Surveys Tuts.* 12 (4) (2010) 531–550.
- [38] The Opportunity for Sub Microsecond Interconnects for Processor Activity, <http://www.rapido.org/technology-comparisons/>.
- [39] Airvana OneCell System, <http://www.airvana.com/products/enterprise/onecell>.

# Signal space concepts

In a signal space, waveforms are represented by vectors. By replacing signals with their vector representations, familiar vector concepts from linear algebra may be used to describe the waveforms, the relationships between waveforms, and some important waveform manipulations.

Let  $x(t)$  and  $y(t)$  be two complex-valued waveforms defined over the interval  $T_1 \leq t \leq T_2$ . The inner product of these waveforms is

$$\langle x(t), y(t) \rangle = \int_{T_1}^{T_2} x(t) y^*(t) dt. \quad (\text{A.1})$$

The norm of the waveform  $x(t)$  is the square root of its inner product with itself:

$$\|x(t)\| = \sqrt{\langle x(t), x(t) \rangle}. \quad (\text{A.2})$$

The energy in  $x(t)$  is the square of its norm:

$$E = \langle x(t), x(t) \rangle = \int_{T_1}^{T_2} |x(t)|^2 dt. \quad (\text{A.3})$$

The waveforms  $x(t)$  and  $y(t)$  are orthogonal, meaning that their inner product is zero:

$$x(t) \perp y(t) \Leftrightarrow \langle x(t), y(t) \rangle = 0. \quad (\text{A.4})$$

Equipped with these definitions, we are now in a position to describe span, linear dependence, and basis. Let  $\mathcal{X}$  be the set of  $K$  complex-valued waveforms,

$$\mathcal{X} = \{x_1(t), x_2(t), \dots, x_K(t)\}, \quad (\text{A.5})$$

defined on the interval  $T_1 \leq t \leq T_2$ . A waveform  $x(t)$  for  $T_1 \leq t \leq T_2$  is in the span of  $\mathcal{X}$ , which means that  $x(t)$  may be expressed as a linear combination of waveforms in  $\mathcal{X}$ :

$$x(t) \in \text{Span}\{\mathcal{X}\} \Leftrightarrow x(t) = c_1 x_1(t) + c_2 x_2(t) + \dots + c_K x_K(t) \quad (\text{A.6})$$

for a set of constants,  $c_k \in \mathbb{F}$ , where  $\mathbb{F}$  is any field, usually the set of real numbers or complex numbers. The set  $\mathcal{X}$  is linearly dependent, meaning that the solution to the following,

$$c_1 x_1(t) + c_2 x_2(t) + \dots + c_K x_K(t) = 0 \quad (\text{A.7})$$

involves at least one  $c_k \neq 0$  for  $k = 1, 2, \dots, K$ . Otherwise, the set  $\mathcal{X}$  is linearly independent.

The set  $\mathcal{X}$  may not be the minimum number of functions required to generate all the waveforms in  $\text{Span}\{\mathcal{X}\}$ . A minimal spanning set is called a basis. Let

$$\boldsymbol{\varphi} = \{\varphi_1(t), \varphi_2(t), \dots, \varphi_N(t)\} \quad (\text{A.8})$$

be a basis for  $\text{Span}\{\mathcal{X}\}$ . Clearly,  $N \leq K$ . The basis  $\boldsymbol{\varphi}$  is an orthonormal basis, which means the following:

$$\langle \varphi_m(t), \varphi_n(t) \rangle = \delta_K[m - n], \quad m, n = 1, 2, \dots, N, \quad (\text{A.9})$$

where  $\delta_K[n]$  is the Kronecker delta function. Let  $x(t)$  and  $y(t)$  be two waveforms in  $\text{Span}\{\boldsymbol{\varphi}\}$ . Then we may write the following:

$$x(t) = x_1\varphi_1(t) + x_2\varphi_2(t) + \dots + x_N\varphi_N(t), \quad (\text{A.10})$$

$$y(t) = y_1\varphi_1(t) + y_2\varphi_2(t) + \dots + y_N\varphi_N(t). \quad (\text{A.11})$$

Let the vectors

$$\mathbf{x} = \begin{bmatrix} x_1 \\ x_2 \\ \vdots \\ x_N \end{bmatrix} \quad \mathbf{y} = \begin{bmatrix} y_1 \\ y_2 \\ \vdots \\ y_N \end{bmatrix} \quad (\text{A.12})$$

be associated with the waveforms  $x(t)$  and  $y(t)$ , respectively. The relationship

$$\langle x(t), y(t) \rangle = \mathbf{y}^\dagger \mathbf{x} \quad (\text{A.13})$$

follows directly from the orthonormal property of  $\boldsymbol{\varphi}$ . Here,  $\mathbf{v}^\dagger$  is the conjugate transpose (or Hermitian) of  $\mathbf{v}$ . This shows that the energy in a waveform is the square of the length of its corresponding vector (or the square of the Euclidean distance between the  $N$ -dimensional point defined by its vector and the origin). If two waveforms are orthogonal, their corresponding vectors are orthogonal. The “distance” between the waveforms is

$$\sqrt{\langle x(t) - y(t), x(t) - y(t) \rangle} = \sqrt{(\mathbf{x} - \mathbf{y})^\dagger (\mathbf{x} - \mathbf{y})}. \quad (\text{A.14})$$

Because the right-hand side is the Euclidean distance between the points defined by the ends of the vectors  $\mathbf{x}$  and  $\mathbf{y}$ , the term  $\sqrt{\langle x(t) - y(t), x(t) - y(t) \rangle}$  is interpreted as the Euclidean distance between the waveforms  $x(t)$  and  $y(t)$ .

Let  $r(t)$  be a waveform defined on the interval  $T_1 \leq t \leq T_2$  that is not in  $\text{Span}\{\boldsymbol{\varphi}\}$ . We seek  $\hat{r}(t) \in \text{Span}\{\boldsymbol{\varphi}\}$  that is the best approximation to  $r(t)$ . We use as our definition of “best” the minimum error norm solution. For any  $x(t) \in \text{Span}\{\boldsymbol{\varphi}\}$ , the approximation error is  $e(t) = r(t) - x(t)$ . The approximation error norm is

$\langle e(t), e(t) \rangle$ . The minimum error norm approximation  $\hat{r}(t)$  is the member of  $\text{Span}\{\varphi\}$  that minimizes  $\langle e(t), e(t) \rangle$ . Using derivatives with respect to the coefficients, the solution is

$$\hat{r}(t) = \langle r(t), \varphi_1(t) \rangle \varphi_1(t) + \langle r(t), \varphi_2(t) \rangle \varphi_2(t) + \cdots + \langle r(t), \varphi_N(t) \rangle \varphi_N(t). \quad (\text{A.15})$$

An important property of  $\hat{r}(t)$  is that it is orthogonal to the approximation error  $e(t)$ :

$$\langle \hat{r}(t), e(t) \rangle = 0. \quad (\text{A.16})$$

# Index

Note: Page numbers followed by *f* indicate figures and *t* indicate tables.

## A

Adaptive channel equalizers, 20–21, 21*f*  
Additive white Gaussian noise (AWGN)  
  channel, 230, 371  
    MAP receiver, 137–138  
    ML detector, 141  
  maximum likelihood detector, 82, 101–102  
  spectral and power efficiency, 114, 115*f*  
ADSL. *See* Asymmetric digital subscriber line (ADSL)  
Advanced audio distribution profile (A2DP), 588–589  
Advanced mobile phone system (AMPS), 36–37  
Aliases, 66  
AlohaNet, 34  
Aloha-variant strategies, 458–459  
Amplified spontaneous emission, 676–677  
Amplitude-phase shift keying (APSK), 91–92  
Analog orthogonal frequency division multiplexing  
  baseband transmitted signal, 340  
  four-subcarrier, 340, 341*f*  
  Rayleigh’s theorem, 341  
Analog telephone (Alexander Graham Bell), 4  
Angle spread, for highly directive antennas, 217–219  
Antennas  
  directivity of, 194–195  
  effective receiving area, 196  
  gain, 194–196  
  multipath propagation models  
    directive antennas, channel response for, 202–204  
    elevated base station antenna, 197–198  
    isotropic antennas, channel response for, 199–201  
    radio links with symmetric ray distributions, 198, 199*f*  
Anti-aliasing filter, 250, 251*f*  
Anti-Gray mapping, 187, 188*t*  
Application-specific standards, 474*t*  
Asymmetric Digital Subscriber Line (ADSL), 22  
Asynchronous Bluetooth link, 586–587  
Asynchronous transfer mode (ATM), 31, 31*f*, 573.  
  *See also* Broadband ISDN (B-ISDN)  
Automatic request for retransmission (ARQ), 171–172  
Averaged likelihood functions, 276–278

## AWGN channel

coded binary modulation with  
  BPSK modulation, 177  
  channel decoding, 179–180  
  log-likelihood ratio, 178  
  MAP decoding rule, 179  
  soft demapping, 178–179

## B

Bahl–Cocke–Jelinek–Raviv (BCJR) algorithm  
  APP computation, 304  
  backward metric, 302–303  
  bit-error probability, 302  
  conditional distribution, 304  
  forward metric, 302  
  implementation, 329  
  “L” values, 303–304  
  performance, 330  
  “soft” decisions, 301  
Bandpass linear systems  
  bandpass filtering using  
    complex equivalent responses, 61, 61*f*  
    real functions, 61, 61*f*  
  description, 59  
  frequency response, 59*f*  
  impulse response, 60  
Bandpass random process  
  Gaussian process  
    description, 62–63  
    in-phase and quadrature components, 64, 64*f*  
  power spectral density, 62–63, 63*f*  
  wide-sense-stationary, 62  
Bandpass signals  
  in communication, 50  
  complex envelope representation, 50  
  description, 49  
  representation  
    analytic signal, 57–59  
    complex equivalent low-pass signal, 53  
    complex equivalent signal, frequency spectrum of, 52, 52*f*  
    energy/power calculations, 54–57  
    Fourier transform, 51–53  
    in frequency domain, 51, 51*f*  
    Hilbert transform, 58–59  
  sampling  
    alias-free sampling rate intervals, 67, 67*t*

- Bandpass signals (*Continued*)
    - heterodyning operation, 67–68
    - minimum acceptable sampling rate, 67, 68<sup>f</sup>
    - Nyquist rate, 66
  - Baseband architectures, wireless cellular infrastructure
    - base station and components, 689–691
    - DSP plus ASIC
      - to HAC-enhanced DSP, 696
      - high bandwidth interface, 695
    - from homogeneous macros to dense small cells and CRANS
      - CRAN and resource sharing, 697–701
      - dense small cells, 697
      - traditional RAN architecture, 696–697
    - from voice to broadband, 691–693
    - WCDMA systems, 693–694
  - Baseband modulation schemes, LTE, 607
  - Base station
    - primary, 469–470
    - secondary/cognitive, 470
  - Beacon falsification (BF), 473
  - Beacon, Wi-Fi, 570–571
  - BICM. *See* Bit-interleaved coded modulation (BICM)
  - BICM-ID. *See* Bit-interleaved coded modulation with iterative decoding (BICM-ID)
  - Binary modulation. *See* Coded binary modulation
  - Bit error probability and constellation labelings
    - a priori distribution, 157
    - average bit error probability, 158
    - binary labeling, 157
    - bit-to-signal-point mapping, 157
    - MAP and ML message decoder, 159
    - upper bound, 159
  - Bit-interleaved coded modulation (BICM), 173–174, 176, 182–187
  - Bit-interleaved coded modulation with iterative decoding (BICM-ID), 174, 176, 182–187
  - Bitwise MAP decoder, 160–163
  - Bluetooth. *See also* IEEE 802.15 (Bluetooth)
    - SIG, 562–563
    - transmission system, 44–45
  - Body area network (BAN), 560
  - BPSK DS-SS transmitter, 372, 372<sup>f</sup>
  - Broadband ISDN (B-ISDN), protocol reference model, 32, 33<sup>f</sup>
  - Broadband power line communications, 630–634
    - HD-PLC, 630–631
    - HomePlug, 630–631
    - IEEE 1901, 631–633
    - ITU-T G.hn, 631–634
  - Broadcast channel (BC), 422–424
- ## C
- Cable data networks, 24–25
  - CableLabs and DOCSIS, 556
  - Cable television (CATV), 24–25
  - Carrier network wire-line interface standards
    - ITU-T international standards, 532–537
    - regional SDOs, 537–540
      - ATIS, 539–540
      - CCSA, 540
      - ETSI, 540
      - IEEE Communications Society, 541
      - WP2, 535–537
      - WP3, 537
  - Carrier sense multiple access-collision avoidance (CSMA-CA), 44
  - Carrier sense multiple access-collision detection (CSMA-CD) scheme, 26–27
  - Carrier sense multiple access (CSMA) strategies, 459–460
  - CDMA2000 system, 39, 395–396
  - Cellular CDMA, 392–393
  - Cellular concepts
    - Advanced Mobile Phone System, 36–37
    - CDMA2000 system, 39
    - GSM time slot, 37–38, 38<sup>f</sup>
    - IMT-2000 concept, 39
    - IS-95 CDMA system, 38
    - MIMO spatial multiplexing, 39–40
    - sectorization, 36–37
    - TDMA standards, 37–38
    - Universal Mobile Telecommunications System, 39
  - Centralized cellular networks, MAC
    - American IS-95 standard, 438
    - channel and traffic models
      - mobile user and traffic models, 449
      - uplink/downlink channel models, 447–449
    - channelization
      - CDMA, 446
      - FDMA, 445
      - OFDMA, 446–447
      - SC-FDMA, 447
      - SDMA, 446
      - TDMA, 445–446
    - FDD, 437–439
    - GSM standard, 438
    - long-term evolution standard, 438–439
    - multiple access properties, 439, 439<sup>f</sup>

- scheduling and resource allocation
  - circuit-switching technology, 449–450
  - cross-layer resource allocation framework, 455–456
  - energy minimizing uplink power allocation, 453–455
  - opportunistic multiuser rate allocation over fading channels, 452–453
  - waterfilling and channel inversion paradigms, 450–452
- Channel allocation algorithm, 492
- Channel decoder, 174
- Channel estimation errors
  - dimensionless channel estimation errors, 233
  - and effects, 232*f*
  - perfect estimation
    - bit error rate, 234
    - frequency error effect, 238
    - Gray-mapping degradations, 234
    - quadrature amplitude modulation, 234
    - scatter diagram, 234
  - relative amplitude estimation error, 233
- Channel SNR, 289
- Channel state information (CSI), 472
- Channel state information reference signals (CSI-RS), 610
- Chase combining HARQ (HARQ-CC), 576
- Clear to send (CTS) frame, 571
- Cloud-RAN concept, 43, 43*f*
- Code-aided (CA) algorithm, 249
- Codebook, 172
- Coded binary modulation
  - with AWGN communication channel
    - BPSK modulation, 177
    - channel decoding, 179–180
    - log-likelihood ratio, 178
    - MAP decoding rule, 179
    - soft demapping, 178–179
  - Hamming code decoding, 180–182
- Code division multiple access (CDMA), 446
  - bit error rate, 381
  - BPSK-based DS-CDMA system, 378–379, 380*t*
  - broadband signaling, 380
  - CDMA 2000, 395–396
  - cellular, 392–393
  - DS spreading and despreading, 374*f*, 376
  - error probability formula, 378–379, 379*f*
  - flat Rayleigh fading channel, 380
  - hopping pattern, 376
  - MC-CDMA, 391–392
  - RAKE receivers, 386–391
  - synchronous/asynchronous, 377–378
  - total noise plus interference spectral density, 378
  - WCDMA, 396
- Coded-modulation systems, 172
  - binary codeword, 175–176
  - bit-interleaved coded modulation, 173–174
  - bit-to-symbol mapper function, 176
  - codebook, 172
  - coded binary modulation, 177–182
  - coded non-binary modulation, 182–190
  - codeword, 172
  - practical considerations, 173–174
  - simulated bit-error rate, 188*f*, 189*f*
  - spectral efficiency, 172–173
- Coded non-binary modulation
  - BICM-ID reception, 184–186
  - BICM reception, 182–184
- Coded OFDM (COFDM), 334
- Code sequences
  - binary shift register, 382
  - chip pulse shape, 383–384
  - Gold codes, 385
  - Hadamard matrix, 384
  - Kasami set, 386
  - long codes, 383–384
  - maximal length linear feedback shift register, 382
  - m*-sequences, 385
  - primitive polynomials, 382–383, 383*t*
  - short codes, 383–384
  - Walsh codes, 384
- Code-shift keying, 645
- Codeword, 172
- Coding
  - forward error-control, 357
  - hard decision, 357–358
  - linear error control code, 358
  - QPSK modulation, 359
  - soft decision, 357–358
  - zero-mean complex-valued Gaussian random variables, 360
- Cognitive capability, CR device, 469
- Cognitive medium access control (C-MAC) cycle, 504–506
- Cognitive radio (CN), 468–469
- Cognitive radio networks (CRN)
  - architectures, 469–471
  - centralized, 470
  - centralized/infrastructure-based architecture, 470*f*
  - challenges in, 471–473
    - cross-layer design of communication methods, 472–473
    - interference characterization and management, 472

- Cognitive radio networks (CRN) (*Continued*)
    - resource allocation, 472
    - routing in multihop, 473
    - security threats, 473, 474*f*
    - spectrum management, 471–472
  - distributed, 470
  - in-band full-duplexing-enabled, 512–513
  - medium access control for, 503–512
    - C-MAC cycle, 504–506
    - DCCC-based, 507–512
  - overlay mode, 470
  - regulatory aspects and standardization, 474–475
  - resource allocation in, 492–503
    - approaches, 493–503
    - elements of, 492–493
  - spectrum access models and operating modes, 470
  - underlay mode, 470
- Cognitive techniques, PLC, 647–648
- Coherence bandwidth, 217
- Coherent modulation, 675
- Coherent receivers, 665–666
- Common control channel (CCC), 470
  - cognitive MAC protocols, 504
  - dedicated/dynamic, 480, 507–512
- Common frame formats, 585*f*
- Common public radio interface (CPRI) corporation, 553–554
- Communication satellites, for backbone
  - transmission and broadcasting
    - C-band geosynchronous satellites, 16
    - Echo 1, 14–15
    - geosynchronous satellite with spot beams, 15, 15*f*
    - Intelsat satellites, 15
    - LEO satellite systems, 14–15
    - satellite propagation, 16
    - Syncom 3, 14–15
- Complementary code keying (CCK), 563
- Complex-valued baseband equivalent, of QAM, 80
- Connection identifiers (CID), 573
- Connectivity service network, 573
- Contention window (CW), 566
- Continuous phase modulation (CPM)
  - CPFSK, 108–109, 109*f*
  - and frequency modulation, 95–98
  - generation, 102, 103*f*
  - GMSK, 109–112, 111*f*
  - instantaneous frequency vs. phase, 96, 97*f*, 99*f*
  - instantaneous phase, 95
  - LREC and LRC pulse, 101, 101*f*
  - mathematical description, 98–102
  - minimum shift keying, 108–110
  - power efficiency, 113–114
  - power spectral density
    - characteristics, 104–107
    - minimum Euclidean distances and normalized power bandwidths, 104, 105*t*
  - IREC frequency pulse, 103, 105*f*
  - spectral efficiency, 113
  - “tilted phase” representation, 112
- Continuous phase version of frequency shift keying (CPFSK), 95, 108–109, 109*f*
- Control signaling mechanism, 503
- Convergence sublayer (CS), 573
- Cooperative multi-antenna communication, 424–425
- Cooperative spectrum sensing (CSS), 484–485
  - fusion techniques for, 485–491
    - K-means clustering, 487–488
  - performance, 490–491
  - support vector machine, 488–490
- Coordinated multipoint (CoMP), 690–693
- Correlated diversity signals, 364–366
- CPM. *See* Continuous phase modulation (CPM)
- CRAN and resource sharing, 697–701
  - collaborative transmission technology, 698
  - deployment, progress in, 700–701
  - low OPEX, 699–700
  - statistical resource provision and lower CAPEX, 698
  - transparent BBU pool scaling and virtualization, 699
- CRN. *See* Cognitive radio networks (CRN)
- Cross-layer attacks, 473
- Cross-layer decentralized MAC strategies, 461
- Cross QAM constellations, 90–91, 91*f*
- Crosstalk interference, xDSL systems, 24, 24*f*
- Cyclic redundancy check (CRC), 575–576
- Cyclostationary feature detector, 483
- ## D
- Database-centric approach, spectrum sensing, 491–492
- Data communication networks
  - Alohanet and Ethernet, 33–35
  - ATM and B-ISDN, 31–33
  - packet transmission, 28–31
- Data Over Cable Service Interface Specification (DOCSIS-1), 25
- Data transfer, Bluetooth, 586
- Decentralized wireless local area networks, MAC, 439
  - channel and traffic models
  - exposed nodes, 457

- hidden nodes, 457
- mobile user and traffic models, 457–458
- SINR and collision-based interference models, 457
- channelization, 456
- scheduling and resource allocation
  - Aloha-variant strategies, 458–459
  - carrier-sense multiple access strategies, 459–460
  - cross-layer decentralized MAC strategies, 461
- Decision-feedback equalizer (DFE)
  - error propagation, 314–315
  - feedback filter, 312, 312<sup>f</sup>
  - forward filter, 312, 312<sup>f</sup>
  - interference cancellation, 311–312
  - minimum-MSE, 316–318
  - via noise prediction, 318–319
  - ZF, 312–314
- Decisions regions, 168–169
  - for general detector, 144–145
  - for MAP detector, 148–149
  - for minimum-distance receiver, 146–148
- Dedicated control channel (DCC). *See* Non-dedicated control channel (NDCC) approach
- Deep space applications, optical transmission, 682–683
- Delay-and-multiply frequency estimation, 250–251, 251<sup>f</sup>
- Demodulation, 346–347
- Dense small cells, 697
- DFE. *See* Decision-feedback equalizer (DFE)
- Differential modulation, 674–675
- Diffuse channels, optical wireless channels, 668–671
- Digital access networking
  - cable data networks, 24–25
  - ISDN and DSL, 21–24
  - passive optical network, 26–27
  - voice channel modems, 17–21
- Digital signal detection
  - averaged likelihood functions, 276–278
  - CA ML estimation of  $(A, q, F_{\text{res}}, K_{\tau})$ , 259–262
  - channel estimation errors
    - dimensionless channel estimation errors, 233
    - perfect estimation of  $(A, q, F)$ , 239–240
    - perfect estimation of  $\tau$ , 234–239
    - relative amplitude estimation error, 233
  - estimation and decision theory
    - bounds on estimation performance, 246–247
    - expectation-maximization algorithm, 244–246
    - MAP detection, 242–243
    - MAP estimation, 243–244
    - estimation strategy, 247–250
    - maximum-likelihood, 228
    - MFIM computation, 278–279
    - modified Cramer-Rao bounds, 263
    - NDA coarse frequency estimation, 250–252
    - NDA symbol timing estimation, 252–254
    - performance evaluation
      - CA estimation, 268–275
      - NDA frequency and symbol timing estimation, 266
      - simulation setup, 264–266
    - synchronization, 227–228
    - system model, 230–233
- Digital transmission, 2
  - authentication, 3
  - communication satellites, 14–16
  - data communication networks
    - AlohaNet, 34
    - ATM and B-ISDN, 31–33
    - Ethernet, 34–35, 34<sup>f</sup>
    - packet transmission, 28–31
  - digital access networking
    - cable data networks, 24–25
    - ISDN and DSL, 21–24
    - passive optical network, 26–27
    - voice channel modems, 17–21
  - error detection and correction, 3
  - historical perspective
    - digital transmission hierarchy and SONET, 7–11
    - electrical telegraphy, 3–4
    - Huffman coding, 4
    - Morse code, 4, 4<sup>f</sup>
    - pulse code modulation, 6–7
    - sampling theorem, 4–6
  - microwave transmission, 11–12
  - optical transmission, 12–14
  - over noisy channels
    - bit-to-signal alternative mapping, 123, 124<sup>t</sup>
    - protocol stacks, 122
    - receivers, 124–125
    - signal alternatives, 123, 124<sup>f</sup>
    - transmitter, 123
  - secrecy, 3
  - wireless transmission systems
    - cellular mobiles, 36–42
    - in cloud, 42–43
    - history, 35–36
    - IEEE 802.11 (“WiFi”) networks, 43–45

- Digital wireline transmission standards
    - broadband forum, 548
    - CableLabs and DOCSIS, 556
    - historical background, 525–531
    - IEEE 802.1, 541–544
    - IEEE 802.3, 544–546
    - IEEE 1588, 546–547
    - INCITS T11 fiber channel, 547
    - industry forums, 547–551
    - local area network wireline standards, 529–530
    - metro ethernet forum, 550–551
      - common public radio interface corporation, 553–554
      - ethernet alliance consortium, 554
      - full-service access network consortium, 553
      - open base station architecture initiative consortium, 554
      - specifications, 552<sup>t</sup>
      - wireline networks, wireless
        - fronthaul/backhaul, 554–555
    - optical internetworking forum, 548–550
    - public wide-area network wireline standards, 526–529
    - vs. SDOs, 530–531
    - telecommunications industry association, 556
  - Digitized public telephone network, 8–9, 9<sup>f</sup>
  - Direct detection, 665
  - Directed point-to-point channels, 667–668
  - Directive antennas, channel response
    - angle spread, 217–219
    - clusters of related ray paths, 204
    - directive array antennas, 202
    - direct propagation over rooftops, 204
    - multipath components, 202–204, 203<sup>f</sup>
    - scattering from high-rise objects, 204
    - street-guided propagation, 204
  - Directivity, of antenna, 194–195
  - Direct-sequence code-division multiple access (DS-CDMA), 645
  - Direct sequence spread spectrum (DSSS), 372–375, 563
  - Discontinuous transmission (DTX) capability, 594
  - Discrete multitone (DMT), 22. *See also* Orthogonal frequency division multiplexing (OFDM)
  - Discrete-time intersymbol interference model, 285–287
  - Distortion and interference effects, 677–678
  - Distributed coordination function (DCF), 566
  - Diversity and frequency modulation, 352–355
  - DOCSIS 3.1 standard, 90–91
  - Doppler shift, 213
  - Doppler spread, for high speed mobiles, 213
  - Downlink and uplink transmissions, 606–607
  - DSL Access Multiplexer (DSLAM), 22
  - DSP plus ASIC
    - to HAC-enhanced DSP, 696
    - high bandwidth interface, 695
  - Duobinary partial response pulse, 19–20, 20<sup>f</sup>
  - Duplexing
    - frequency division, 443–444
    - space division, 444
    - time division, 444
  - Dynamic common control channel (DCCC)-based
    - MAC protocol
      - beacon phase, 512
      - CCC selection phase, 507–511
      - data transmission phase, 511–512
      - frame structure, 508<sup>f</sup>
      - operation of, 509<sup>f</sup>
      - spectrum sensing phase, 507
  - Dynamic spectrum access (DSA). *See* Cognitive radio networks (CRN)
- ## E
- Effective receiving area, antenna, 196
  - Electrical noise model, 675–678
  - Electrical telegraphy, 3–4
  - eNBs, 603–604
  - Energy detection, spectrum opportunity detection, 482–483
  - Equalization
    - decision-feedback equalizer
      - error propagation, 314–315
      - feedback filter, 312, 312<sup>f</sup>
      - forward filter, 312, 312<sup>f</sup>
      - interference cancellation, 311–312
      - minimum-MSE, 316–318
      - via noise prediction, 318–319
      - ZF, 312–314
    - linear equalizer
      - block diagram, 305, 306<sup>f</sup>
      - matched filter, 306–307
      - MMSE, 308–311
      - ZF, 307–308
  - models and metrics
    - discrete-time inter-symbol interference model, 285–287
    - information/message symbols, 285
    - pulse-amplitude modulation, 284–285
    - Shannon capacity, 288–289
    - SNR benchmarks, 289–291
  - optimum trellis-based detectors
    - BCJR algorithm, 301–304
    - trellis diagram, 291–295

- Viterbi algorithm, 295–301
  - orthogonal-frequency division multiplexing, 330–331
  - performance comparison
    - BCJR algorithm, 329–330
    - channel magnitude response, 323, 324f
    - error-probability performance, 323, 324f
    - MMSE DFE, 327
    - MMSE linear equalizer, 325–326
    - MMSE THP, 328–329
    - Viterbi algorithm, 329
    - ZF DFE, 326–327
    - ZF linear equalizer, 325
    - ZF THP, 327–328
  - single-carrier frequency-domain equalization, 330–331
  - Tomlinson–Harashima precoding
    - attenuation factor, 321–322
    - complex modulo operator, 321
    - desired information symbol, 322
    - error-control codes, 319
    - signal enhancement, 321
    - standard memoryless quantizer, 322
    - transmitter, 320
  - Equipment identity register (EIR), 591–592
  - Error control coding, 171–172, 675
  - Error probability, ML and MAP detectors, 149–156
  - Error propagation, 314–315
  - Estimation and decision theory
    - bounds on estimation performance, 246–247
    - expectation-maximization algorithm, 244–246
    - MAP detection, 242–243
    - MAP estimation, 243–244
  - Ethernet, 34–35, 34f
  - Ethernet alliance (EA) consortium, 554
  - Ethernet PON (EPON), 26–27
  - European Digital Audio Broadcast (DAB) system, 334
  - E-UTRA, 606
  - Evolved packet core (EPC), 603–604
  - Evolved UTRAN (E-UTRAN), 603
  - Expectation-maximization (EM) algorithm, 244–246
  - Exposed nodes, 457
  - Extra windowing and preservation of orthogonality, 349–351
  - Extrinsic information, 184–185
- F**
- FDD and TDD frame structure, 606f
  - FH spread spectrum, 375–376
  - Fiber channels, optical transmission, 671–672
  - Fifth generation (5G) cellular mobile
    - goal, 40–41
    - millimeter-wave frequencies, 41
    - ray tracing model, 41–42
    - transmission studies, 41
    - urban environments, 41
  - Finite-state machine (FSM), 291–292
  - First-generation (1G) cellular mobile, 36–37
  - Fisher information matrix (FIM), 246
  - Forward error-control (FEC) coding, 357
  - Forward error-correction, 632
  - Fourth-generation (4G) cellular mobile, 39
  - Frame and MAC header formats, 569f
  - Frame synchronization error probability (FSEP), 266, 269f
  - Free-space infrared optical communication, 45
  - Free space optics, optical transmission, 682
  - Free space path gain, 196
  - Frequency division duplexing (FDD), 17, 443–444
  - Frequency division multiple access (FDMA), 445
  - Frequency fading, of narrow band cellular mobile
    - radio channels, 206–208, 207f
  - Frequency-selective channels, 339
  - Frequency shift keying (FSK), 17
    - 1-bit frequency response, 334–335, 335f
    - data rate, 339
    - frequency-selective channels, 339
    - orthogonal signals, 336–338
  - Fresnel zones, 196–197
  - Fronthaul/backhaul, 554–555
  - Full response CPM, 98–101
  - Full-service access network (FSAN) consortium, 553
  - Fusion techniques, CSS, 485–491
    - K-means clustering, 487–488
    - performance, 490–491
    - support vector machine, 488–490
- G**
- Gaussian frequency shift keying (GFSK), 112, 584
  - Gaussian minimum shift keying (GMSK), 109–112, 111f
  - Gaussian nature, of the shadow fading, 221f, 222
  - Generalized Nyquist pulses, 88–89
  - Generic passive optical network (PON) architecture, 26f
  - GFSK. *See* Gaussian frequency shift keying (GFSK)
  - Gigabit-capable PON (GPON), 26–27
  - GMSK. *See* Gaussian minimum shift keying (GMSK)
  - G3-PLC, 629–630
  - Gray mapping, 187, 188f, 189

## GSM

- classification of channels, 594*f*
- discontinuous transmission capability, 594
- equipment identity register, 591–592
- frame structure, 593*f*
- groups of, 590–591
- international mobile equipment identity, 590–591
- mobile switching center, 591–592
- stand-alone dedicated control channels, 594–595
- system architecture, 591*f*

## H

- Half-sine pulse shape, 85, 86*f*
- Hamming code decoding, 180–182
- Hamming distance, 180–182
- Hard-decision decoder, 174
- HD-PLC, 630–631
- Hidden nodes, 457
- High frequency (HF) OFDM modems, 334
- HomePlug, 630–631
- HomePlug Green PHY (HPGP) specification, 633–634
- HomePlug Powerline Alliance (HomePlug), 630–631
  - HPGP specification, 633–634
- HSPA, 691–693
- Huffman coding, 4
- Hybrid-ARQ systems, 171–172
- Hybrid fiber-coaxial (HFC) CATV system, 24–25, 25*f*

## I

- IEEE 802, 561
- IEEE 802.1, 541–544
- IEEE 802.3, 544–546
- IEEE 802.11 (Wi-Fi), 425, 429–430
  - air-interface technologies, 565*t*
  - basic service set, 563
  - beacon, 570–571
  - Bluetooth, 44–45
  - carrier sense multiple access/collision avoidance, 44
  - clear to send frame, 571
  - complementary code keying, 563
  - contention window, 566
  - direct sequence spread spectrum, 563
  - distance and absorption indoor losses, 44, 45*t*
  - distributed coordination function, 566
  - frame and MAC header formats, 569*f*
  - medium access methods, 567*f*
  - network allocation vector, 571
  - PLCP protocol data unit, 568

- with relay and repeater extensions, 43–44, 44*f*
- request to send frame, 571
- scanning and association procedures, 570*f*
- spatial division multiplexing, 563

## IEEE 802.15 (Bluetooth)

- advanced audio distribution profile, 588–589
- asynchronous Bluetooth link, 586–587
- common frame formats, 585*f*
- Gaussian frequency shift keying, 584
- 2.4 GHz ISM band, 584*f*
- goal of, 583
- inquiry channel, 583
- logical link control and adaptation protocol, 587
- operating state diagram, 590*f*
- paging channel, 583
- pico-net channel, 583
- protocol layers, 588*f*
- SCO link, 587
- service discovery protocol, 587–588
- slot, 585
- transmit power, 586

## IEEE 802.16 (WiMAX)

- access service network, 573
- antenna configurations and transmission rates, 580–581
- channel quality feedback, 579
- Chase combining HARQ, 576
- coding and modulation procedure, 577*f*
- connectivity service network, 573
- convergence sublayer, 573
- cyclic redundancy check, 575–576
- medium access and contention control, 571–573, 572*f*
- medium access protocol, 578–579
- MIMO feedback, 579
- mobile stations, 573
- network entry, 581
- network reference model, 571–573, 572*f*
- power control mechanism, 579–580
- radio resource control, 573–574
- reference model, 574*f*
- transmission time interval, 575

## IEEE 802.18, 474

## IEEE 1588, 546–547

## IEEE 1901, 631–633

## IEEE 802.11af Wi-Fi, 475

## IEEE 802.15.4j MBANs, 475

## IEEE 802.22 WRANs, 475

## IMT-2000 concept, 39

## In-band full-duplexing-enabled, 512–513

## INCITS T11 fiber channel, 547

Individual spectrum sensing-based spectrum opportunity detection, 482–483

Instantaneous phase, of CPM carrier, 95

Integrated Services Digital Network (ISDN) and ADSL, 22

basic interface, 21, 22f

Intelsat satellites, 15

Intensity modulation, 672–674

Interference avoidance and mitigation, 503

Interference cancellation, 311–312

Interference channel, MIMO, 424–425

Interim Standard 95 (IS 95), 393–395

International mobile equipment identity (IMEI), 590–591

Intersymbol interference (ISI), 85–88, 230, 285

Irrelevance theorem, 141–144

ISDN. *See* Integrated Services Digital Network (ISDN)

Isotropic antennas, 195–196

channel response

- bandwidth influence, 199
- impulse response, 199–200
- power delay profiles, 201, 202f
- pulsed source, multipath response for, 199–200, 200f
- voltage envelopes of multipath components, 200–201, 201f

directivity, 195–196

ITU-T G.hn, 631–634

ITU-T international standards, 532–537

## K

K-nearest neighbor (KNN) fusion, 487–488

## L

Lagrange multipliers, 501–503

LANs and PONs, 684

Laser, 12–13

Laser diode, 663. *See also* Light emitting diode (LED)

Lasers, optical transmitters, 664–665

Length- $L$  rectangular (LREC) pulse, 101

Length- $L$  temporal raised-cosine (LRC) pulse, 101

Light emitting diode (LED), 663–664

Linear distortion, in telephone voice channel, 19–20, 20f

Linear equalization

- block diagram, 305, 306f
- matched filter, 306–307
- MMSE, 308–311
- ZF, 307–308

Linear, memoryless modulation. *See* Quadrature amplitude modulation (QAM)

Local area network (LAN), 524, 560

Logical link control and adaptation protocol (L2CAP), 587

Log-likelihood ratio (LLR), 178

Long-haul transport systems, 685

Long-haul WDM optical transmission, 13, 14f

Long-term evolution (LTE), 690–693

- MIMO communication, 425–429
- turbo codes, 189–190

of UMTS systems

- baseband modulation schemes, 607
- channel state information reference signals, 610
- downlink and uplink transmissions, 606–607
- eNBs, 603–604
- E-UTRA, 606
- evolved packet core, 603–604
- evolved UTRAN, 603
- FDD and TDD frame structure, 606f
- MAC sublayer, 615
- orthogonal frequency division multiple access, 605
- packet data convergence protocol sublayer, 605
- paging, 612
- PDN gateway, 604
- physical uplink control channel, 611
- positioning reference signals, 609–610
- RRC sublayer, 617
- SC-FDMA, 605–606
- S1-MME, 604
- uplink link adaptation, 612
- uplink reference signals, 610

Low earth orbiting (LEO) satellite systems, 14–15

Low-loss optical fiber, 12–13

LRC. *See* Length- $L$  temporal raised-cosine (LRC) pulse

LREC pulse. *See* Length- $L$  rectangular (LREC) pulse

## M

MAC. *See* Multiple access control (MAC)

Manchester pulse shape, 85, 86f

MAP receiver, 136–140

$M$ -ary phase shift keying (MPSK), 90

Matched filter, 306–307

- autocorrelation function, 164–165
- impulse response, 163–164
- property, 165–166
- signal-noise ratio, 165–166

- Maximal length linear feedback shift register (MLFSR), 382
- Maximum a posteriori
  - detection, 242–243
  - estimation, 243–244
- Maximum a posteriori probability decoding rule, 179
- Maximum a priori (MAP)
  - detector
    - decisions regions for, 148–149
    - irrelevance theorem, 142–144
    - upper bounds on error probability, 156
  - rule, 136–137
- Maximum-likelihood (ML) detector
  - AWGN channel, 141
  - bitwise ML detector, 161–163, 166–167
  - optimality properties, 140–141
  - upper bounds on error probability, 149–152, 154–155
- Medium access control (MAC), 473
  - cognitive radio networks, 503–512
    - C-MAC cycle, 504–506
    - DCCC-based, 507–512
- Medium access methods, Wi-Fi, 567f
- Medium access protocol (MAP), 578–579
- METIS simplified ray tracing model, 41–42, 42f
- Metro ethernet forum (MEF), 550–551
  - common public radio interface corporation, 553–554
  - ethernet alliance consortium, 554
  - full-service access network consortium, 553
  - open base station architecture initiative consortium, 554
  - specifications, 552t
  - wireline networks, wireless fronthaul/backhaul, 554–555
- Metropolitan area network (MAN), 560
- MFIM computation, 278–279
- Microwave relay, 11–12
- MIMO. *See* Multiple-input-multiple-output (MIMO)
- Minimum-distance receiver
  - distance between signals, 125
  - Gaussian random process, 127
  - signal alternatives, 126
- Minimum-mean-squared-error (MMSE)
  - DFE, 316–318, 327
  - linear equalizer, 308–311, 325–326
  - Tomlinson–Harashima precoding, 328–329
- Minimum probability of error constellations, 92–94, 93f, 94f, 116
- Minimum shift keying (MSK), 108–110
- Mobile stations, 573
- Mobile switching center (MSC), 591–592
- Mobile user and traffic models, 449, 457–458
- Modified Cramer-Rao bounds (MCRBs), 263
- Modulation, 335–336
  - and coding, optical transmission
    - coherent modulation, 675
    - differential modulation, 674–675
    - error control coding, 675
    - intensity modulation, 672–674
  - description, 74, 75f
- Morse code, 4, 4f
- MPSK. *See* M-ary phase shift keying (MPSK)
- MSK. *See* Minimum shift keying (MSK)
- Multicarrier CDMA (MC-CDMA), 391–392
- Multicarrier modulation, 74
- Multicarrier transmission, PLC, 645
- Multicore fibers, 672
- Multi-*h* CPM, 112
- Multimode fibers, 672
- Multipath narrowband signals
- Multiple access channel, 420–421
- Multiple access control (MAC)
  - broadcast property, 436
  - centralized cellular networks
    - American IS-95 standard, 438
    - channel and traffic models, 447–449
    - channelization, 445–447
    - FDD, 437–439
    - GSM standard, 438
    - long-term evolution standard, 438–439
    - multiple access properties, 439, 439f
    - scheduling and resource allocation, 449–456
  - decentralized WLAN networks, 439
    - channel and traffic models, 457–458
    - channelization, 456
    - scheduling and resource allocation, 458–461
- duplexing
  - frequency division, 443–444
  - space division, 444
  - time division, 444
- multiple access property, 436
- non-orthogonal channels, 443
- orthogonal channels
  - dedicated signals and filters, 441
  - electromagnetic wave theory, 440
  - frequency, 441–442
  - space, 442–443
  - time, 442
- sublayer, 615
- system-wide utility, 436

Multiple antennas in multiple antennas out spatial multiplexing, 39–40

Multiple-input-multiple-output (MIMO), 334, 645–647

- antenna power adjustment, 419
- antenna subset selection, 419
- broadcast channel, 422–424
- covariance quantization, 419–420
- feedback, 579
- full channel knowledge, 404–406
- interference channel, 424–425
- limited feedback techniques, 418–425
- multiple access channel, 420–421
- multiple base stations, 424–425
- precoding techniques, MSE-based criteria, 417–418
- rank-1 precoding, 420
- single-user link, 401–418
- spatial modes and spatial multiplexing, 402–404
- standards
  - LTE/LTE-advanced, 425–429
  - 802.11N/802.11AC, 429–430
- subspace-based precoding, 419
- transceiver techniques, 406–416
  - Alamouti space-time code, 415–416
  - receiver options, 409
  - space-time block codes, 413–415
  - V-BLAST, 407–408
- transmission, PLC, 645–647
- waterfilling algorithm, 404–405

Multiprotocol label switching (MPLS), 30–31

## N

Narrowband cellular mobile radio channels

- along streets
  - range dependence, 220–222
  - shadow fading, 220–222
  - signal strength measurements, 219–220, 219f
- coherence bandwidth, 217
- cross-polarization coupling, 222
- frequency fading, 206–208, 207f
- performance, 222
- spatial fading
  - correlation, 208–211
  - cumulative distribution functions, 205–206, 207f
  - Rayleigh distribution, 205–206
  - received voltage magnitude variation, 205, 206f
  - statistical models, 205–206
  - street level mobile, 204–205
- time dependence and Doppler spread, 211–213

Narrowband power line communication (PLC)

- high data-rate, 627–630
- low data-rate, 626–627

NDA coarse frequency estimation, 250–252

NDA symbol timing estimation, 252–254

Network allocation vector (NAV), 571

Network entry, 581

Network reference model, 571–573, 572f

Noise and distortion, optical transmission
 

- amplified spontaneous emission, 676–677
- distortion and interference effects, 677–678
- electrical noise model, 675–678

Non-binary modulation. *See* Coded non-binary modulation

Non-data-aided (NDA) algorithm, 248

Non-dedicated control channel (NDCC) approach, 506

Non-linear bandpass systems, 64–66

Non-orthogonal channels, 443

Non-return-to-zero pulse shape, 85, 86f

## O

Oerder-and-Meyr symbol timing estimation, 252–253, 253f

OFDM. *See* Orthogonal frequency division multiplexing (OFDM)

Offset QPSK (OQPSK), 94–95

Open base station architecture initiative (OBSAI) consortium, 554

Opportunistic spectrum access (OSA)
 

- cell-edge CRs, 493
- concepts of, 468–469
- mechanism, 469–470

Optical fiber channels
 

- multicore fibers, 672
- multimode fibers, 672
- single mode fiber, 671–672

Optical fiber transmission, 14

Optical internetworking forum (OIF), 548–550

Optical receivers, 665–666
 

- coherent receivers, 665–666
- direct detection, 665

Optical transmission
 

- applications and emerging research areas
  - deep space applications, 682–683
  - emerging applications, 685
  - free space optics, 682
  - LANs and PONs, 684
  - long-haul transport systems, 685
  - visible light communications, 683–684
- channel models
  - fiber channels, 671–672
  - wireless channels, 666–671

Optical transmission (*Continued*)

- device properties
  - receivers, 665–666
  - transmitters, 663–665
- modulation and coding
  - coherent modulation, 675
  - differential modulation, 674–675
  - error control coding, 675
  - intensity modulation, 672–674
- noise and distortion
  - amplified spontaneous emission, 676–677
  - distortion and interference effects, 677–678
  - electrical noise model, 675–678
- system performance analysis
  - coherent detection performance, 681
  - direct detection, 679–680
- Optical transmitters, 663–665
  - lasers, 664–665
  - LEDs, 663–664
- Optical wireless channels
  - diffuse channels, 668–671
  - directed point-to-point channels, 667–668
- Optimum message receivers
  - MAP receiver, 136–140
  - ML receiver, 140–141
- Optimum trellis-based detectors
  - BCJR algorithm, 301–304
  - trellis diagram, 291–295
  - Viterbi algorithm, 295–301
- Orthogonal channels
  - dedicated signals and filters, 441
  - electromagnetic wave theory, 440
  - frequency, 441–442
  - space, 442–443
  - time, 442
- Orthogonal frequency division multiple access (OFDMA), 446–447, 605
- Orthogonal frequency division multiplexing (OFDM), 13, 330–331
  - analog
    - baseband transmitted signal, 340
  - coding
    - forward error-control, 357
    - hard decision, 357–358
    - linear error control code, 358
    - QPSK modulation, 359
    - soft decision, 357–358
    - zero-mean complex-valued Gaussian random variables, 360
  - COFDM, 334
  - correlated diversity signals, 364–366
  - cyclic prefix, 334

## DAB system, 334

- digital
  - data rate and cyclic prefix, 345–346
  - demodulation, 346–347
  - discrete Fourier transform, 343
  - IDFT and cyclic prefix, 343–345
  - zero-padding, 347–351
- diversity and frequency modulation, 352–355
- fast Fourier transform, 334
- frequency shift keying
  - 1-bit frequency response, 334–335, 335<sub>f</sub>
  - data rate, 339
  - frequency-selective channels, 339
  - modulation, 335–336
  - orthogonal signals, 336–338
- MIMO systems, 334
- outage capacity, 361–363
- power-loading and bit-loading, 355–357
- subcarriers/tones, 333
- transmission system, 13, 22, 23<sub>f</sub>
- Orthogonal signals, 336–338
- Outage capacity, OFDM, 361–363

**P**

- Packet data convergence protocol (PDCP) sublayer, 605
- Packet transmission, 28
  - internet protocol
    - protocol data units, 29
    - reliability measures, 30
    - router/forwarder, 28–29
    - vs. X.25, 30
  - multiprotocol label switching, 30–31
- Paging channel, 583, 612
- PAM. *See* Pulse amplitude modulation (PAM)
- PA ML estimation of ( $A$ ,  $q$ ,  $F_{\text{res}}$ ,  $K_{\tau}$ )
  - amplitude estimation error, 259
  - Cauchy–Schwarz inequality, 256–258
  - constant-magnitude pilot symbols, 255
  - fine frequency estimation, 255–256, 257<sub>f</sub>
  - frame structure, 254, 254<sub>f</sub>
  - frame synchronization, 255–256, 256<sub>f</sub>
  - integer design parameter, 255–256
  - log-likelihood function, 254
  - nonzero normalized frequency estimation
    - error, 258
  - phase and amplitude estimation, 255–256, 257<sub>f</sub>
  - squared magnitude, 255–256
- Parabolic dish antennas, 195–196
- Partial response CPM, 98–101
- Passband signals. *See* Bandpass signals
- Passive optical network (PON)

- description, 26
- optical line termination, 26–27
- optical network termination, 26–27
- principal standards, 26–27
- PCM. *See* Pulse code modulation (PCM)
- PDN gateway (P-GW), 604
- Personal area network (PAN), 560
- Phase pulse, 98–101
- Phase-shift keying (PSK), 284–285
- Photodetector, 665–666, 676
- Physical uplink control channel, 611
- Pico-net channel, 583
- Pilot-aided (PA) algorithm, 248–249
- PLC. *See* Power line communications (PLC)
- PLCP Protocol Data Unit (PPDU), 568
- PON. *See* Passive optical network (PON)
- Positioning reference signals, 609–610
- Post-equalization SNR, 290
- Power allocation schemes, 492
- Power control mechanism, 579–580
- Power delay profiles, 201, 202*f*
  - spatial average, 214–215
  - width of, 215–216
- Power line channel
  - noise characteristics, 642–643
    - classification, 643*f*
    - colored background noise, 642
    - impulse noise, 642–643
    - narrowband noise, 642
  - signal propagation, 638–642
    - modeling approaches, 640–642
    - physical models, 641–642
    - propagation effects, 638–640
- Power line communications (PLC)
  - application domains, 622
  - electromagnetic compatibility regulations
    - broadband, regulations for, 636–637
    - NB, regulations for, 634–635
  - standards of
    - broadband, 630–634
    - narrowband, 626–630
    - ultra narrowband, 624–626
  - terminology, 623
  - through the grid, 622–623
  - transmission techniques
    - cognitive techniques, 647–648
    - MIMO transmission, 645–647
    - multicarrier transmission, 645
    - single-carrier transmission, 644–645
- Powerline related intelligent metering evolution (PRIME), 627–629
- Power-loading and bit-loading, 355–357

- Power spectral density (PSD), 62–63, 63*f*
  - CPM
    - characteristics, 104–107
    - LREC frequency pulse, 106, 106*f*
    - minimum Euclidean distances and normalized power bandwidths, 104, 105*t*
  - QAM
    - half-sine pulse shape, 85, 86*f*
    - intersymbol interference, 85–88
    - Manchester pulse shape, 85, 86*f*
    - modulated carrier, 84–85
    - non-return-to-zero pulse shape, 85, 86*f*
    - pulse shape, 84–85
    - raised cosine spectrum, 85–88, 88*f*
    - square-root Nyquist pulse shape, 88–89
    - square-root raised cosine pulse shape, 85–88, 88*f*
- Precoding techniques, MSE-based criteria, 417–418
- Primary base stations (PBSs), 469–470
- Primary ISDN interface, 21
- Primary user emulation attacks (PUEA), 473
- Pseudo-noise (PN) bit sequence, 38
- Public wide-area network (WAN) wireline
  - standards, 526–529
- Pulse amplitude modulation (PAM), 89
- Pulse code modulation (PCM), 6–7

## Q

- Quadrature amplitude modulation (QAM), 234, 284–285, 352–353
  - amplitude-phase shift keying, 91–92
  - complex-valued baseband equivalent, 80, 83
  - constellation, 75
    - cross QAM, 90–91, 91*f*
    - square QAM, 90–91, 91*f*
  - description, 75–76
  - generation, 83, 83*f*
  - $K$ -dimensional constellations, 95
  - $K$ -dimensional space, 79–80
  - linear digital modulation, 79–80
  - $M$ -ary phase shift keying, 90
  - mathematical description, 81–82
  - minimum probability of error constellations, 92–94, 93*f*, 94*f*, 116
  - offset QPSK, 94–95
  - orthonormal basis waveforms, 75, 76*f*
  - power efficiency, 113–114
  - power spectral density
    - half-sine pulse shape, 85, 86*f*
    - intersymbol interference, 85–88
    - Manchester pulse shape, 85, 86*f*
    - modulated carrier, 84–85

## Quadrature amplitude modulation (QAM)

*(Continued)*

non-return-to-zero pulse shape, 85, 86f

pulse shape, 84–85

raised cosine spectrum, 85–88, 88f

square-root Nyquist pulse shape, 88–89

square-root raised cosine pulse shape, 85–88, 88f

pulse amplitude modulation, 89

real-valued bandpass signal, 80, 82, 84

rectangular QAM, 90–91

spectral efficiency, 113

Quadrature phase shift keying (QPSK), 13, 352–353

Quantization noise, 3

**R**

Radio Access Network (RAN), 42–43

Radio channels

antenna gain, 194–196

cables and hardware, 194

path gain/loss, 196

Radio environment map (REM), 472

Radio over fiber (RoF) transmission, 43

Radio resource control (RRC), 573–574

Radio transmission properties, 193–194

Raised cosine spectrum, 85–88, 88f

RAKE receivers

decision statistics, 387–388

delay line, 389

independent complex Gaussian fading process, 387

*m*th data symbol, 388–389

multipath channel, 388

operation, 389–391, 390f

root raised cosine, 387

tapped delay line model, 386–387, 387f

time-varying multipath channel, 389

RAN. *See* Radio Access Network (RAN)

Rate-1/2 convolutional encoder, 187f, 188f

Real-valued bandpass QAM signal, 80, 82, 84

Reconfigurability, 469

Rectangular QAM, 90–91

Relay nodes, 43–44

Rendezvous NDCC (RNDCC), 506

Repeater extensions, 43–44

Request to send (RTS) frame, 571

Resource allocation, CRN, 472, 492–503

elements of, 492–493

generalized spectral footprint, 498

interference constraint, 496

optimization constraints, 495–497

optimization objectives, 497–499

power allocation subproblem, 501–503

power minimization, 497–498

rate constraint, 496

rate maximization, 498–499

receiver sensitivity constraint, 497

solution, 499–503

subchannel allocation constraint, 496

subchannel allocation subproblem, 501

total power constraint, 496

with typical objectives and constraints, 493–495

utility maximization, 499

RMS delay spread, 215–217

RRC sublayer, 617

**S**

Sampling, of bandpass signals

alias-free sampling rate intervals, 67, 67t

demodulation method, 69–71

heterodyning operation, 67–68

minimum acceptable sampling rate, 67, 68f

Nyquist rate, 66

Sampling theorem, 4–6

Satellite antenna, 194–195

SC-FDMA, 605–606

SCO link, 587

Second-generation (2G) cellular mobile, 37–38

Sectorization, 36–37

Service discovery protocol (SDP), 587–588

Service flow identifiers (SFID), 573

Shadow fading, 220–222

Shannon capacity, 288–289

Signal space concepts, 707–709

Signal-to-noise-and-interference ratio (SINR)  
model, 443, 633Signal-to-noise ratio (SNR) spectral density,  
288–289Single-carrier frequency division multiple access  
(SC-FDMA), 447

Single-carrier modulation

amplitude and frequency modulation, 73–74

nonlinear modulation. (*see* Continuous phase  
modulation (CPM))

quadrature amplitude modulation, 75–95

radio frequency systems, 73–74

Single-carrier transmission, PLC, 644–645

Single mode fiber, 671–672

SINR and collision-based interference models, 457

Slow fading. *See* Shadow fading

Smartphones, wireless internet access, 468

S1-MME, 604

Soft-decision decoder, 174

- Software-controlled electronic switching systems, 8–9
  - SONET. *See* Synchronous optical network (SONET)
  - Space division duplexing (SDD), 444
  - Space division multiple access (SDMA), 446
  - Spatial division multiplexing (SDM), 563
  - Spatial fading, of narrow band cellular mobile radio channels
    - correlation
      - definition, 208
      - at elevated base station, 210–211, 210f, 212f
      - at street level, 209, 210f
    - cumulative distribution functions, 205–206, 207f
    - Rayleigh distribution, 205–206
    - received voltage magnitude variation, 205, 206f
    - statistical models, 205–206
    - street level mobile, 204–205
  - Spatial multiplexing, 402–404
  - Spectrum access, 503
  - Spectrum decision, 478–480
  - Spectrum holes, 468–469, 469f
  - Spectrum management framework, 475–481
    - in CRNs, 477f
    - protocol stack and, 476f
  - Spectrum mobility, 481
  - Spectrum sensing, 476–478
    - database-centric approach for, 491–492
    - spectrum opportunity detection
      - cooperative spectrum sensing, 484–485
      - cyclostationary feature detector, 483
      - energy detection, 482–483
      - individual spectrum sensing-based, 482–483
  - Spectrum sensing data falsification (SSDF), 473
  - Spectrum sharing, 480–481, 503
  - Spectrum task force (SPTF), 468
  - Spread spectrum signaling
    - CDMA, wireless channels
      - CDMA 2000, 395–396
      - cellular, 392–393
      - IS-95, 393–395
      - MC-CDMA, 391–392
      - RAKE receivers, 386–391
      - WCDMA, 396
    - fundamentals
      - code division multiple access, 376–381
      - code sequences, 381–386
      - direct sequence spread spectrum, 372–375
      - FH spread spectrum, 375–376
      - low probability of intercept/anti-jam capabilities, 370–372
      - motivation, 369–370
  - Square QAM constellations, 90–91, 91f
  - Square-root Nyquist pulse shape, 88–89
  - Square-root raised cosine (SRRC) pulse shape, 85–88, 88f
  - Stand-alone dedicated control channels (SDCCH), 594–595
  - Support vector machine (SVM) fusion, 488–490
  - Symbol-to-waveform mapping, 74–75
  - Synchronous digital hierarchy (SDH), 10
  - Synchronous optical network (SONET), 7–8
    - description, 10
    - DS-1, 11
    - OC-1 frames, 10–11
  - Synchronous payload envelope (SPE), 10–11
  - System on chip (SoC), multi DSP development, 696
  - System performance analysis, optical transmission
    - coherent detection performance, 681
    - direct detection, 679–680
- ## T
- Telecommunications industry association (TIA), 556
  - Termination symbols, 293
  - Terrestrial radio links, in cities, 197
  - Third-generation (3G) cellular mobile, 39
  - Third generation partnership project (3GPP). *See* 3GPP
  - 3G cellular CDMA, 395–396
  - 3GPP, 561
    - GSM, 590–595
    - LTE, 603–618
    - long term evolution-advanced specifications, 39
    - UMTS, 595–603
  - THP. *See* Tomlinson–Harashima precoding (THP)
  - Time division duplexing (TDD), 444
  - Time division multiple access (TDMA), 445–446
  - Time-division multiplexed (TDM) transmission, 7–8
  - Tomlinson–Harashima precoding (THP)
    - attenuation factor, 321–322
    - complex modulo operator, 321
    - desired information symbol, 322
    - error-control codes, 319
    - signal enhancement, 321
    - standard memoryless quantizer, 322
    - transmitter, 320
  - Traditional RAN architecture, 696–697
  - Transmission techniques, PLC
    - cognitive techniques, 647–648
    - MIMO transmission, 645–647
    - multicarrier transmission, 645
    - single-carrier transmission, 644–645
  - Transmission time interval (TTI), 575

Trellis-coded modulation (TCM) system,  
173–174

Trellis diagram, 291–295

2.4 GHz ISM band, 584f

2G cellular CDMA, 393–395

## U

Ultra narrowband (UNB) technologies, 624–626

Universal mobile telecommunications system  
(UMTS), 39

basic requirements, 599

billing, 597

CELL\_DCH, 601

CELL\_FACH, 601

CELL\_PCH (paging channel), 601

circuit-switched elements, 596

code division multiple access, 597–598

core network, 596

gateway GPRS support node, 597

idle mode, 601

mobility management, 597

MSC, 597

network architecture, 595–596, 596f

orthogonal variable spreading factor codes, 598

packet-switched elements, 596

pseudorandom number code, 598

radio access bearer, 599–600

radio link control protocol, 601

RRC protocol, 601–603

serving GPRS support node, 597

session management, 597

URA\_PCH, 601

UTRAN protocol structure, 600, 600f

Uplink/downlink channel models, 447–449

Uplink link adaptation, 612

Uplink reference signals, 610

User scheduling decision, 493

## V

Vector channel

conversion between signals and signal vectors,  
127, 128f

generic signal projection onto signal space, 130

Gram–Schmidt procedure, 128

orthonormal bases, for signal alternatives,  
128, 128f

received signal and projections, 131, 132f

signal vectors, 129f

and waveforms, 133, 134f

Very high speed DSL (VDSL), 22, 24

Virtual circuits, 32

Visible light communications, optical transmission,  
683–684

Viterbi algorithm, 168

add-compare-select procedure, 300

a posteriori probability, 295

branch metric, 295–296

decision path, 296

decision sequence, 300

implementation, 329

lowest-cost partial path, 299

noise components, 295–296

performance, 329

properties, 300–301

real-valued impulse response, 297

Voice channel modems

adaptive channel equalizers, 20–21, 21f

data-driven echo cancellation, 17, 18f

dial-up access speed bottleneck, 17, 17f

pulse amplitude modulation, 17–19

self-tuning linear filters, 20–21

signal constellations, 19, 19f

Voice channels, in telephone network, 19, 20f

Voice over LTE (VoLTE), 691

Voronoi regions, 146, 147f, 148, 148f

## W

Waterfilling method, 356

and channel inversion paradigms, 450–452

Waterpouring, 288–289

Wavelength division multiplexing (WDM), 13

WDM PON, 27

White Gaussian noise vector, 134–136

White spaces. *See* Spectrum holes

Wide area network (WAN), 524, 560

Wideband CDMA (WCDMA), 396

Wideband channel response, delay spread for,  
215–217

Wi-Fi, 562. *See also* IEEE 802.11 (Wi-Fi)

WiMAX. *See* IEEE 802.16 (WiMAX)

Windowing and frequency characteristics, 348–349

Wireless broadband standards and technologies

Bluetooth SIG, 562–563

body area network, 560

IEEE 802, 561

IEEE 802.11 (Wi-Fi), 563–571

IEEE 802.15 (Bluetooth), 583–590

IEEE 802.16 (WiMAX), 571–583

local area network, 560

metropolitan area network, 560

personal area network, 560

3GPP, 561

GSM, 590–595

- LTE, 603–618
  - UMTS, 595–603
- wide area network, 560
- Wi-Fi alliance, 562
- Wireless channels, optical transmission, 666–671
- Wireless LAN, 690–691
- Wireless transmission systems
  - cellular mobiles, 36–42
  - in cloud, 42–43
  - history, 35–36
  - IEEE 802.11 (“WiFi”) networks, 43–45
- Wireline networks, wireless fronthaul/backhaul, 554–555
- Wireline transmission standards, digital
  - broadband forum, 548
  - CableLabs and DOCSIS, 556
  - historical background, 525–531
  - IEEE 802.1, 541–544
  - IEEE 802.3, 544–546
  - IEEE 1588, 546–547
  - INCITS T11 fiber channel, 547
  - industry forums, 547–551
  - local area network wireline standards, 529–530
  - metro ethernet forum, 550–551
    - common public radio interface corporation, 553–554
  - ethernet alliance consortium, 554

- full-service access network consortium, 553
  - open base station architecture initiative consortium, 554
  - specifications, 552<sub>t</sub>
  - wireline networks, wireless fronthaul/backhaul, 554–555
- optical internetworking forum, 548–550
- public wide-area network wireline standards, 526–529
- vs. SDOs, 530–531
- telecommunications industry association, 556
- types of, 531

## X

- xDSL access system, 22, 23<sub>f</sub>, 23<sub>t</sub>

## Z

- Zero-forcing (ZF)
  - DFE, 312–314, 326–327
  - linear equalizer, 307–308, 325
  - Tomlinson–Harashima precoding, 327–328
- Zero-padding
  - extra windowing and preservation of orthogonality, 349–351
  - windowing and frequency characteristics, 348–349